

SOURCE OR SINK? EROSIONAL AND DEPOSITIONAL SIGNATURES OF TECTONIC ACTIVITY IN DEEP-SEA SEDIMENTARY SYSTEMS

EDITED BY: Rob Butler, Fabiano Gamberi, Rosanna Maniscalco and Adam McArthur

PUBLISHED IN: Frontiers in Earth Science



frontiers

Frontiers eBook Copyright Statement

The copyright in the text of individual articles in this eBook is the property of their respective authors or their respective institutions or funders. The copyright in graphics and images within each article may be subject to copyright of other parties. In both cases this is subject to a license granted to Frontiers.

The compilation of articles constituting this eBook is the property of Frontiers.

Each article within this eBook, and the eBook itself, are published under the most recent version of the Creative Commons CC-BY licence.

The version current at the date of publication of this eBook is CC-BY 4.0. If the CC-BY licence is updated, the licence granted by Frontiers is automatically updated to the new version.

When exercising any right under the CC-BY licence, Frontiers must be attributed as the original publisher of the article or eBook, as applicable.

Authors have the responsibility of ensuring that any graphics or other materials which are the property of others may be included in the CC-BY licence, but this should be checked before relying on the CC-BY licence to reproduce those materials. Any copyright notices relating to those materials must be complied with.

Copyright and source acknowledgement notices may not be removed and must be displayed in any copy, derivative work or partial copy which includes the elements in question.

All copyright, and all rights therein, are protected by national and international copyright laws. The above represents a summary only. For further information please read Frontiers' Conditions for Website Use and Copyright Statement, and the applicable CC-BY licence.

ISSN 1664-8714

ISBN 978-2-83250-496-3

DOI 10.3389/978-2-83250-496-3

About Frontiers

Frontiers is more than just an open-access publisher of scholarly articles: it is a pioneering approach to the world of academia, radically improving the way scholarly research is managed. The grand vision of Frontiers is a world where all people have an equal opportunity to seek, share and generate knowledge. Frontiers provides immediate and permanent online open access to all its publications, but this alone is not enough to realize our grand goals.

Frontiers Journal Series

The Frontiers Journal Series is a multi-tier and interdisciplinary set of open-access, online journals, promising a paradigm shift from the current review, selection and dissemination processes in academic publishing. All Frontiers journals are driven by researchers for researchers; therefore, they constitute a service to the scholarly community. At the same time, the Frontiers Journal Series operates on a revolutionary invention, the tiered publishing system, initially addressing specific communities of scholars, and gradually climbing up to broader public understanding, thus serving the interests of the lay society, too.

Dedication to Quality

Each Frontiers article is a landmark of the highest quality, thanks to genuinely collaborative interactions between authors and review editors, who include some of the world's best academicians. Research must be certified by peers before entering a stream of knowledge that may eventually reach the public - and shape society; therefore, Frontiers only applies the most rigorous and unbiased reviews.

Frontiers revolutionizes research publishing by freely delivering the most outstanding research, evaluated with no bias from both the academic and social point of view. By applying the most advanced information technologies, Frontiers is catapulting scholarly publishing into a new generation.

What are Frontiers Research Topics?

Frontiers Research Topics are very popular trademarks of the Frontiers Journals Series: they are collections of at least ten articles, all centered on a particular subject. With their unique mix of varied contributions from Original Research to Review Articles, Frontiers Research Topics unify the most influential researchers, the latest key findings and historical advances in a hot research area! Find out more on how to host your own Frontiers Research Topic or contribute to one as an author by contacting the Frontiers Editorial Office: frontiersin.org/about/contact

SOURCE OR SINK? EROSIONAL AND DEPOSITIONAL SIGNATURES OF TECTONIC ACTIVITY IN DEEP-SEA SEDIMENTARY SYSTEMS

Topic Editors:

Rob Butler, University of Aberdeen, United Kingdom

Fabiano Gamberi, Institute of Marine Science, Department of Earth System Sciences and Technologies for the Environment, National Research Council (CNR), Italy

Rosanna Maniscalco, University of Catania, Italy

Adam McArthur, University of Leeds, United Kingdom

Citation: Butler, R., Gamberi, F., Maniscalco, R., McArthur, A., eds. (2022). Source or Sink? Erosional and Depositional Signatures of Tectonic Activity in Deep-Sea Sedimentary Systems. Lausanne: Frontiers Media SA.
doi: 10.3389/978-2-83250-496-3

Table of Contents

- 05 Editorial: Source or Sink? Erosional and Depositional Signatures of Tectonic Activity in Deep-Sea Sedimentary Systems**
A. D. McArthur, F. Gamberi, R. Maniscalco and R. Butler
- 09 Architectural Diversity of Submarine Lobate Deposits**
Tim R. McHargue, David M. Hodgson and Eitan Shelef
- 31 Seismic Characteristics of Paleo-Pockmarks in the Great South Basin, New Zealand**
Arunee Karaket, Piyaphong Chenrai and Mads Huuse
- 49 The Origin and 3D Architecture of a Km-Scale Deep-Water Scour-Fill: Example From the Skoorsteenberg Fm, Karoo Basin, South Africa**
L. A. S. Hansen, R. S. Healy, L. Gomis-Cartesio, D. R. Lee, D. M. Hodgson, A. Pontén and R. J. Wild
- 67 Evolution of a Fault-Controlled, Deep-Water Sub-Basin, Tabernas, SE Spain**
Lucie Baudouy, Peter D. W. Haughton and John J. Walsh
- 91 Substrate Entrainment, Depositional Relief, and Sediment Capture: Impact of a Submarine Landslide on Flow Process and Sediment Supply**
A. Martínez-Doñate, A. M-L. J. Privat, D. M. Hodgson, C. A-L. Jackson, I. A. Kane, Y. T. Sychala, R. A. Duller, C. Stevenson, E. Keavney, E. Schwarz and S. S. Flint
- 114 Thrust Faults Promoted Hydrocarbon Leakage at the Compressional Zone of Fine-Grained Mass-Transport Deposits**
Qiliang Sun, Xinong Xie, Shiguo Wu and Guorui Yin
- 126 Depositional Model for Turbidite Lobes in Complex Slope Settings Along Transform Margins: The Motta San Giovanni Formation (Miocene—Calabria, Italy)**
Sébastien Rohais, Julien Bailleul, Sandra Brocheray, Julien Schmitz, Paolo Paron, Francis Kezirian and Pascal Barrier
- 149 Forward Modelling for Structural Stratigraphic Analysis, Offshore Sureste Basin, Mexico**
Donald N. Christie, Frank J. Peel, Gillian M. Apps and David “Stan” Stanbrook
- 170 The Influence of Channel Planform and Slope Topography on Turbidity Current Overbank Processes: The Example of the Acquarone Fan (Southeastern Tyrrhenian Sea)**
Elena Scacchia, Roberto Tinterri and Fabiano Gamberi
- 192 Submarine Channel Mouth Settings: Processes, Geomorphology, and Deposits**
David M. Hodgson, Jeff Peakall and Katherine L. Maier
- 212 Contained-Reflected Megaturbidites of the Marnoso-arenacea Formation (Contessa Key Bed) and Helminthoid Flysches (Northern Apennines, Italy) and Hecho Group (South-Western Pyrenees)**
Roberto Tinterri, Tommaso Mazza and Pierre Muzzi Magalhaes

- 243** *Possible Tsunami-Induced Sediment Transport From Coral Reef to Deep Sea Through Submarine Canyons on the Southern Ryukyu Forearc, Japan*
Ken Ikehara, Toshiya Kanamatsu and Kazuko Usami
- 257** *Tectonic Influence on the Geomorphology of Submarine Canyons: Implications for Deep-Water Sedimentary Systems*
Laura H. Bührig, Luca Colombero, Marco Patacci, Nigel P. Mountney and William D. McCaffrey
- 287** *Coexistence of Adjacent Siliciclastic, Carbonate, and Mixed Sedimentary Systems: An Example From Seafloor Morphology in the Northern Lesser Antilles Forearc*
Pierre Morena, Gueorgui Ratzov, Antonio Cattaneo, Frauke Klingelhoefer, Christian Beck, Chloé Seibert, Boris Marcaillou and Nathalie Feuillet



OPEN ACCESS

EDITED AND REVIEWED BY
Valerio Acocella,
Roma Tre University, Italy

*CORRESPONDENCE
A. D. McArthur,
a.mcarthur@leeds.ac.uk

SPECIALTY SECTION
This article was submitted to
Sedimentology, Stratigraphy and
Diagenesis,
a section of the journal
Frontiers in Earth Science

RECEIVED 12 September 2022
ACCEPTED 13 September 2022
PUBLISHED 29 September 2022

CITATION
McArthur AD, Gamberi F, Maniscalco R
and Butler R (2022), Editorial: Source or
sink? Erosional and depositional
signatures of tectonic activity in deep-
sea sedimentary systems.
Front. Earth Sci. 10:1042473.
doi: 10.3389/feart.2022.1042473

COPYRIGHT
© 2022 McArthur, Gamberi, Maniscalco
and Butler. This is an open-access
article distributed under the terms of the
[Creative Commons Attribution License](#)
(CC BY). The use, distribution or
reproduction in other forums is
permitted, provided the original
author(s) and the copyright owner(s) are
credited and that the original
publication in this journal is cited, in
accordance with accepted academic
practice. No use, distribution or
reproduction is permitted which does
not comply with these terms.

Editorial: Source or sink? Erosional and depositional signatures of tectonic activity in deep-sea sedimentary systems

A. D. McArthur^{1*}, F. Gamberi², R. Maniscalco³ and R. Butler⁴

¹University of Leeds, Leeds, United Kingdom, ²University of Bologna, Bologna, Italy, ³University of Catania, Catania, Italy, ⁴University of Aberdeen, Aberdeen, United Kingdom

KEYWORDS

seafloor topography, sediment-gravity flow, deep-water fan, submarine channel, submarine canyon

Editorial on the Research Topic

Source or sink? Erosional and depositional signatures of tectonic activity
in deep-sea sedimentary systems

Introduction

A recent break-through in sedimentological research is the application of ‘source-to-sink’ type studies to aid our understanding of continental margin evolution (e.g., [Somme et al., 2009](#); [Carvajal and Steel 2011](#); [Helland-Hansen et al., 2016](#); [Snedden et al., 2018](#)). “Source-to-sink” being the study of sediments from their source area, their transport to, and deposition in a sink or basin. Whilst the continental slope was conventionally perceived to primarily experience sediment bypass in source-to-sink studies, the net bypass character of the slope is the result of alternation of deposition and erosion over various magnitudes and time-scales (e.g., [Prather et al., 2017](#)). Although the basin-plain is typically considered as a sink, the same concept applies, with varying degrees of erosion and deposition occurring in the deep-ocean (e.g., [Talling et al., 2022](#)). Hence, the deep-sea has a diverse capacity for sediment storage but also great potential for redistribution (e.g., [Shumaker et al., 2018](#)). Consequently, sediment routing may be divided into discrete cells with different sedimentary behaviour, due to a variety of processes, some affecting the land and the shelf, some the slope, and others the basin-plain (e.g., [Gamberi, 2020](#)). Amongst those occurring in the deep-sea, a major role is played by tectonics, which modify seafloor topography; this in turn dictates where and when sediments are generated, stored, and remobilised in the deep-sea (e.g., [Butler et al., 2020](#); [McArthur et al., 2022](#)).

This Research Topic aimed to assemble contributions that investigated the distribution of erosion and deposition in the deep-sea and to explore its linkage with

tectonic activity. A diverse range of fourteen papers cover the sedimentary processes (e.g., turbidity currents, mass-wasting), geomorphic elements (e.g., canyons, basins) and stratigraphic architectures (e.g., channels, lobes) that are indicative of tectonic shaping of the deep-sea environment across a range of tectonic settings, e.g., extensional, convergent, and strike-slip. Contributions covered a range of modern studies to those in deep geological-time and utilised a range of research approaches, from fieldwork to subsurface studies, to yield new insights on one or more of the research areas highlighted above. The resulting collection forms an anthology of Original Research and Reviews, which better constrain sediment routing systems in the slope and basin-plain and develops new concepts for the advancement of future source-to-sink studies. Hence, this Research Topic documents sedimentary processes, geomorphic elements and stratigraphic architectures of erosional and depositional signatures of tectonic activity in deep-sea sedimentary systems.

Sedimentary processes

The sedimentary processes that drive erosion and deposition in tectonically active deep-sea systems were given particular attention, from shelf incising submarine canyons, through deep-sea channels, their transition to terminal deposits, and into the abyssal plain.

[Ikehara et al.](#) considered the sedimentary processes in submarine canyons, giving particular attention to sediment transport and deposition by large tsunamis, which transferred carbonate material from the shelf to the deep-sea offshore of the Ryukyu subduction zone, Japan. This work highlights the source-to-sink transfer of carbonate material through the marine environment.

[Scacchia et al.](#) examined the deposits found overbank of submarine channels in a zone of active extensional tectonics, in the south-eastern Tyrrhenian Sea, Italy. This enabled documentation of how variation in flow type and flow interaction with tectonically modified seafloor topography act as a major control on the amount of overspill from a channel and the location of overbank depocenters.

[Hodgson et al.](#) reviewed modern seafloor studies of deep-sea channel mouths initially to explore the erosional and depositional processes and products of the channel-lobe transition zone (CLTZ). However, in doing so they recognised a new type of transition between channels and their terminal deposits, which they term ‘channel mouth expansion zones’ (CMEZs), which exhibit long and flared tracts between channels and lobes. These authors suggest previously documented CLTZs may need to be re-examined in light of the recognition of CMEZs.

[Martínez-Doñate et al.](#) Recorded erosion, transport and deposition by turbidity currents on top of kilometre-scale submarine landslides, with examples from Middle Jurassic

deep-water deposits from the Neuquén Basin, Argentina. This paper highlights the role of mass-transport deposits in generating seafloor topography, which may influence the erosional and depositional signatures of subsequent flows.

[Tinterri et al.](#) documented oversized deposits, here termed ‘megaturbidites’ from ancient outcropping deep-sea systems of the northern Apennines (Italy) and in the Pyrenees (Spain) to propose a new depositional model for such outsized events. The model proposes that deposition of these meters thick event beds occurs in confined basins by reflection of turbidity currents against obstacles, in these examples being basin margins.

Geomorphic elements

In this section geomorphic elements, such as carbonate shelves and volcanic arcs, canyons, and deep-water basins, were investigated for their erosional and depositional records across a range of tectonic settings. The role of tectonics is explored in: 1) shaping the seafloor and therefore creating an active topography interacting with flow dynamics, 2) changing the morphology from the shelf to the deep sea and the source to sink distribution; 3) modifying the source areas and therefore flow pathways.

[Hansen et al.](#) provided a unique outcrop example of scour field, preserved in the rock record, from the Permian Karoo Basin, South Africa, in a convergent setting (Cape Fold Belt). The scours and their subsequent sandstone fill at channel-lobe transition (with excellent sedimentary structures and architecture) inform of a change from erosion- and bypass-dominated flows to depositional flows.

[Baudouy et al.](#) delivered important evidence at outcrop for the interplay between tectonic deformation on the sea floor, slope instability and turbidity current behaviour. The strike-slip fault-controlled Deep Water Sub-Basin, Tabernas, SE Spain, is a case study revealing the role of tectonics on controlling basin morphology and stratigraphy.

[Christie et al.](#) explored the interplay between structural fold growth and sedimentation in mini-basins applying a fast computational method (Onlapse-2D) to basin forward modelling. Testing the match of model outputs to available subsurface control is performed through the case study of Sureste Basin, Gulf of Mexico.

[Morena et al.](#) discussed modern mixed carbonate/siliciclastic/volcaniclastic systems adjacent to carbonate platforms along active margins in the forearc zone of North Lesser Antilles. Sediment sources and pathways of gravity-driven currents from carbonate shelf, down to the slope and basin, reflect the major role played by tectonic activity and seismicity.

[Bühlig et al.](#) Questioned the role of tectonic setting (active vs passive margins and across different plate-boundary types) on canyon geomorphology, building a database-informed meta-study of globally distributed submarine canyons.

Stratigraphic architectures as records of tectonic activity in deep-sea sedimentary systems

The sedimentary facies and stratigraphic architectures produced by interaction of deep-water sedimentary processes with structurally modulated geomorphology was the subject of the final four papers, which aimed to describe deposition in the 'sink', subsequent burial, modifications (e.g., fluid flow and diagenesis), and the economic potential of such deposits.

McHargue et al. explored the diversity of architecture in lobes from intra-slope and basin plan settings with 3D seismic data, particularly focusing on the presence and style of distributary channels. The key influence on presence and style of distributary channels is inferred to be the lobe forming processes and type of sediment, with mud-rich systems producing lobes with multifaceted, branching distributary channels; whereas mud-poor lobes tend to lack resolvable channels. Hence, sediment source and type are shown to have a fundamental control on the resulting depositional style and stratigraphic architecture.

Rohais et al. continue the theme of lobe architectures, here with examples from outcrops of exhumed lobe complexes, which were deposited in a structurally confined intra-slope setting. Their key finding is that lobes on this transform margin are particularly small (ca. 300–3,000 m wide, 500–5,000 m long) and relatively thin (and 2–22 m thick), likely due to limited accommodation in such settings.

Sun et al. consider the effects of mass-transport deposits (MTDs) generated by tectonically induced slope failures on fluid migration through deep-water sedimentary systems. Although such slope derived MTDs are often considered mud-rich and potential barriers to flow, this example documents how minor compressional faults within the MTD act as conduits, permitting fluid flow through deposits often thought as good seals.

Karaket et al. continue the theme of fluid migration through deep-water stratigraphy, diving down to the basin plain, where the terminal deposits of a basin floor fan are overlain by a paleo-pockmark field. The authors suggest progradation of clastic sediments in the deep-sea provides permeable layers through which fluids migrate.

Perspectives and future research

To conclude, this Research Topic presents multidisciplinary investigations into erosional and depositional signatures of tectonic activity in deep-sea sedimentary systems, with

numerous implications for source-to-sink studies in the deep-sea. Seafloor, subsurface, and outcrop studies all contribute to demonstrating the diverse and dynamic nature of deep-sea sedimentation, with a variety of sedimentary processes, geomorphic elements and resulting stratigraphic architectures showcasing how tectonic forcing may alter the seafloor, driving both erosion and deposition.

Many of these studies will be of interest for academic and applied audiences, particularly for helping to understand subsurface sedimentary systems and seafloor hazards that may help or hinder the energy transition. However, avenues for future research remain to conduct source-to-sink studies in the deep-sea, including how coeval sedimentary systems evolve either side of active plate boundaries, how different sedimentary processes may interact (e.g., contour and turbidity currents), and how sedimentation and erosion may influence tectonics.

Author contributions

All authors listed have made a substantial, direct, and intellectual contribution to the work and approved it for publication.

Acknowledgments

We sincerely thank all the authors and reviewers who have participated in this Research Topic.

Conflict of interest

The authors declare that the research was conducted in the absence of any commercial or financial relationships that could be construed as a potential conflict of interest.

Publisher's note

All claims expressed in this article are solely those of the authors and do not necessarily represent those of their affiliated organizations, or those of the publisher, the editors and the reviewers. Any product that may be evaluated in this article, or claim that may be made by its manufacturer, is not guaranteed or endorsed by the publisher.

References

Butler, R. W., Pinter, P. R., Maniscalco, R., and Hartley, A. J. (2020). Deep-water sand-fairway mapping as a tool for tectonic restoration: Decoding miocene central

mediterranean palaeogeography using the numidian turbidites of southern Italy. *J. Geol. Soc. Lond.* 177, 766–783. doi:10.1144/jgs2020-008

- Carvajal, C., and Steel, R. (2011). "Source-to-sink sediment volumes within a tectono-stratigraphic model for a Laramide shelf-to-deep-water basin: Methods and results," in *Tectonics of sedimentary basins: Recent advances*, 131–151. New York, NY: Blackwell Publishing Ltd. doi:10.1002/9781444347166.ch7
- Gamberi, F. (2020). Systems supplying sediment to canyon heads (SSSCHs) in the Tyrrhenian Sea: The past and the present as a key to understanding deep-sea stratigraphy. *Mar. Pet. Geol.* 119, 104470. doi:10.1016/j.marpetgeo.2020.104470
- Helland-Hansen, W., Sømme, T. O., Martinsen, O. J., Lunt, I., and Thurmond, J. (2016). Deciphering earth's natural hourglasses: Perspectives on source-to-sink analysis. *J. Sediment. Res.* 86, 1008–1033. doi:10.2110/jsr.2016.56
- McArthur, A. D., Crisóstomo-Figueroa, A., Wunderlich, A., Karvelas, A., and McCaffrey, W. D. (2022). Sedimentation on structurally complex slopes: Neogene to recent deep-water sedimentation patterns across the central Hikurangi subduction margin, New Zealand. *Basin Res.* 34 (5), 1807–1837. doi:10.1111/bre.12686
- Prather, B. E., O'Byrne, C., Pirmez, C., and Sylvester, Z. (2017). Sediment partitioning, continental slopes and base-of-slope systems. *Basin Res.* 29, 394–416. doi:10.1111/bre.12190
- Shumaker, L. E., Sharman, G. R., King, P. R., and Graham, S. A. (2018). The source is in the sink: Deep-water deposition by a submarine volcanic arc, Taranaki Basin, New Zealand. *Sedimentology* 65, 2506–2530. doi:10.1111/sed.12475
- Snedden, J. W., Galloway, W. E., Milliken, K. T., Xu, J., Whiteaker, T., and Blum, M. D. (2018). Validation of empirical source-to-sink scaling relationships in a continental-scale system: The Gulf of Mexico basin Cenozoic record. *Geosph. (Boulder)*. 14, 768–784. doi:10.1130/GES01452.1
- Sømme, T. O., Helland-Hansen, W., Martinsen, O. J., and Thurmond, J. B. (2009). Relationships between morphological and sedimentological parameters in source-to-sink systems: A basis for predicting semi-quantitative characteristics in subsurface systems. *Basin Res.* 21, 361–387. doi:10.1111/j.1365-2117.2009.00397.x
- Talling, P. J., Baker, M. L., Pope, E. L., Ruffell, S. C., Jacinto, R. S., Heijnen, M. S., et al. (2022). Longest sediment flows yet measured show how major rivers connect efficiently to deep sea. *Nat. Commun.* 13, 4193. doi:10.1038/s41467-022-31689-3



Architectural Diversity of Submarine Lobate Deposits

Tim R. McHargue^{1*}, David M. Hodgson² and Eitan Shelef³

¹Department of Geological Sciences, School of Earth, Energy and Environmental Sciences, Stanford University, Stanford, CA, United States, ²Stratigraphy Group, School of Earth and Environment, University of Leeds, Leeds, United Kingdom, ³Department of Environmental Sciences, University of Pittsburgh, Pittsburgh, PA, United States

OPEN ACCESS

Edited by:

Rosanna Maniscalco,
University of Catania, Italy

Reviewed by:

Roberto Tinteri,
University of Parma, Italy
Yvonne Therese Spychala,
Leibniz University Hannover, Germany

*Correspondence:

Tim R. McHargue
timmchar@stanford.edu

Specialty section:

This article was submitted to
Sedimentology, Stratigraphy
and Diagenesis,
a section of the journal
Frontiers in Earth Science

Received: 19 April 2021

Accepted: 12 July 2021

Published: 27 July 2021

Citation:

McHargue TR, Hodgson DM and
Shelef E (2021) Architectural Diversity
of Submarine Lobate Deposits.
Front. Earth Sci. 9:697170.
doi: 10.3389/feart.2021.697170

Lobate deposits in deep-water settings are diverse in their depositional architecture but this diversity is under-represented in the literature. Diverse architectures result from multiple factors including source material, basin margin physiography, transport pathway, and depositional setting. In this contribution, we emphasize the impact of differing source materials related to differing delivery mechanisms and their influence on architecture, which is an important consideration in source-to-sink studies. Three well imaged subsurface lobate deposits are described that display three markedly different morphologies. All three lobate examples, two from intraslope settings offshore Nigeria and one from a basin-floor setting offshore Indonesia, are buried by less than 150 m of muddy sediment and are imaged with high resolution 3D reflection seismic data of similar quality and resolution. Distinctively different distributary channel patterns are present in two of the examples, and no comparable distributaries are imaged in a third example. Distributary channels are emphasized because they are objectively recognized and because they often represent elements of elevated fluid content within buried lobate deposits and thus influence permeability structure. We speculate that the different distributary channel patterns documented here resulted from different processes linked to source materials: 1) a lobate deposit that is pervasively channelized by many distributaries that have branched at numerous points is interpreted to result from comparatively mud-rich, stratified, turbulent flows; 2) an absence of distributaries in a lobate deposit is interpreted to result from collapse of mud-poor, turbulent flows remobilized from littoral drift; and 3) a lobate deposit with only a few, long, straight distributaries with few branching points is interpreted to be dominated by highly viscous flows (i.e., debris flows). We propose a conceptual model that illustrates the relationship between the proportion of mud in contributing flows and the relative size and runout distance of lobate deposits. We conclude that reconciling 3D seismic morphologies with outcrop observations of channels, scours, and amalgamation zones, and simple application of hierarchical schemes, is problematic. Furthermore, when characterizing unconfined deep-water deposits in the subsurface, multiple models with significant differences in predicted permeability structure should be considered.

Keywords: submarine fan, submarine lobe, submarine channel, turbidite, debris flow, distributary, seismic geomorphology

INTRODUCTION

Submarine fans and other submarine lobate deposits are repositories of continentally-derived coarse sediment in the deep sea (e.g., Normark, 1978), and are important archives of palaeoenvironmental change. The potentially large volumes of sand in lobate deposits make them important targets for hydrocarbon exploration and production (Weimer et al., 2000) as well as potentially important aquifers, or reservoirs for the sequestration of CO₂ or hazardous fluids (Ketzer et al., 2005). Simulations of fluid dynamics within lobate deposits designed to optimize performance, either during fluid injection or extraction, necessitate a detailed understanding of depositional architecture, heterogeneity distribution, and permeability structure.

Diverse conceptual models of submarine fan deposits have been proposed (e.g., Normark, 1970; Mutti and Ricci Lucchi, 1972; Walker, 1978; Stow, 1985; Stow, 1986; Reading and Richards, 1994). Tectonic setting, source terrain, sediment transport mechanisms, and bathymetric irregularities have long been acknowledged to be important when predicting the characteristics of submarine fans (Normark, 1970; Mutti and Ricci Lucchi, 1972; Stow, 1985; Stow, 1986; Reading and Richards, 1994). Early submarine fan models included a diverging set of channel-levee complexes each of which terminated at the distal end with a sand-rich “depositional lobe” (Normark, 1970; Mutti and Ghibaudo, 1972). More recent studies with more complete or detailed data demonstrate that lobate deposits at the terminus of each distributary channel complex typically consist of multiple smaller, nested or overlapping offset lobate to palmate bodies (e.g., Mutti, 1977; O’Connell et al., 1991; Lowry et al., 1993; Martinsen et al., 2000; Sullivan et al., 2000; Johnson et al., 2001; Gardner et al., 2003; Posamentier and Kolla, 2003; Hodgson et al., 2006; Deptuck et al., 2008; Prélat et al., 2009; Groenenberg et al., 2010; Mulder and Etienne, 2010; Prélat and Hodgson, 2013; Picot et al., 2016).

The presence of channels in at least some lobate deposits has long been recognized (Beaubouef et al., 1999; Carr and Gardner, 2000; Sullivan et al., 2000; Gardner et al., 2003). Normark (1970), in his classical and commonly cited model, included shallow distributary channels in the proximal portion of his definition of a lobe but few to none in the distal portion of the lobe. This model has been widely adopted and applied by many subsequent researchers (summarized in Mulder and Etienne, 2010). A distinct levee-confined distributary channel network is present in the proximal lobe, constructed as the upper mud-rich portion of mud-rich stratified flows over spills channel confinement. Resistance to shear of the mud-rich levees sustains confinement although levee height, shear resistance and channel depth decrease down flow. Farther down flow, as the turbulent flow becomes increasingly sand-rich, the basal part of the flow collapses at the distributary channel mouth and produces a tabular sand deposit.

More recent fan models (Prélat et al., 2009; Mulder and Etienne, 2010; Prélat et al., 2010) highlight the scaling of lobes, but do not emphasize distributary channels within depositional lobes. This is important because the potential

presence and distribution of channels within lobate deposits can strongly affect the permeability structure of the deposit. Relative to the non-channelized portion of a lobate deposit, sand caliber can be coarser, and thus permeability higher within channels so that channel deposits may be a preferred pathway for subsurface fluids (Pyles et al., 2014; Jones et al., 2015; Hofstra et al., 2017; Bell et al., 2018). In contrast, models of intraslope lobe complexes (Spychala et al., 2015; Jobe et al., 2017) or transient fans (Adeogba et al., 2005) above stepped submarine slope profiles, emphasise channels that cut through lobes after accommodation is healed.

In modern or near modern turbidite systems, distributary channels have been imaged within lobate deposits in some cases (O’Connell et al., 1991; Twichell et al., 1992; Kidd, 1999; Posamentier and Kolla, 2003; Hadler-Jacobson et al., 2005; Clark and McHargue, 2007; Hadler-Jacobson et al., 2007; Bourget et al., 2010; Bakke et al., 2013; Doughty-Jones et al., 2017; Howlett et al., 2020). However, even in modern submarine fan systems, detailed bathymetric records and sidescan sonar recordings often do not produce clear images of distributary channel networks within lobate deposits (Bonnell et al., 2005; Gervais et al., 2006; Jegou et al., 2008; Dennielou et al., 2009; Bourget et al., 2010; Hanquiez et al., 2010; Migeon et al., 2010) even though incisional transient fan channels, when present, may be well imaged (Johann et al., 2001; Adeogba et al., 2005; Gamberi and Rovere, 2011; Maier et al., 2011; Barton, 2012; Maier et al., 2012; Prather et al., 2012a; Maier et al., 2013; Yang and Kim, 2014).

Outcrop studies of lobate deposits with laterally extensive exposures have guided fundamental concepts of fan architecture and facies distribution (Mutti and Ricci Lucchi, 1972; Martinsen et al., 2000; Sullivan et al., 2000; Johnson et al., 2001; Gardner et al., 2003; Hodgson et al., 2006; Prélat et al., 2009; Groenenberg et al., 2010; Prélat and Hodgson, 2013). However, there are few opportunities to unambiguously document the three-dimensional relationships of architectural components within lobate deposits in outcrop exposures. Interestingly, these few examples display conspicuous differences. The somewhat lobate deposits of the Brushy Canyon Formation in Texas, United States, are extensively channelized with tabular sands in overbank positions (e.g., Gardner et al., 2003). The Ross Formation, Ireland, displays well developed tabular sandstone units associated with multiple channels (e.g., Martinsen et al., 2000; Sullivan et al., 2000; Pyles and Jennette, 2009; Pierce et al., 2018). In the Skoorsteenberg Formation in the Tanqua Karoo Basin, South Africa, the lobate deposits with the most continuous and extensive exposure (e.g., Johnson et al., 2001; Hodgson et al., 2006; Prélat et al., 2009; Groenenberg et al., 2010; Prélat and Hodgson, 2013), conventional channels, such as seen in the Ross Formation, are present only in the most proximal exposure of the lobate units (Johnson et al., 2001; Hodgetts et al., 2004; Hodgson et al., 2006; Hofstra et al., 2017). Distally, zones of amalgamation have been interpreted as possible channels within lobate depositional units (Johnson et al., 2001; Hodgetts et al., 2004). However, these outcrop examples lack constraints on source material, basin margin

TABLE 1 | Tabular summary of contextual data and observations associated with each of the three discussed lobate examples.

	Lobate examples		
	1	2	3
Water depth	2,250 m	1,275 m	2,000 m
Burial thickness	120 m	50 m	160 m
Seismic dominant frequency	60 Hz	60 Hz	50 Hz
Seismic resolution	8.3 m	8.3 m	10 m
Sediment source	Major delta	Major delta	Major delta
Sediment delivery	Large leveed channel complex	From littoral drift via multiple small non-leveed gullies	Large erosional channel complex
Depositional setting	Mid slope	Mid slope	Base of slope
Length (L)	12 km	14 km	7 km
Width (W)	14 km	6 km	7 km
Maximum thickness (T)	130 m	20 m	43 m
Aspect ratio (W/T)	108	300	163
Branching nodes	Pervasive	0	1
Distributary number	Pervasive	0	Few (~5)
Surface texture	Channelized	Smooth with scours	Nodular to smooth
Dominant process	Turbulent stratified flows with thick dilute layer	Collapse of turbulent stratified flows with thin dilute layer	Debris flows abundant to dominant

physiography, or transport pathways, and their control on depositional architecture, which limit their utility within source-to-sink contexts.

In deep subsurface examples, images of submarine lobate deposits, even in high quality 3D reflection seismic volumes, often reveal few, if any, details of architectural features within or on the surface of lobate deposits. In some cases, lens-shaped lobate deposits, typically stacked in a compensating pattern (*sensu* Mutti and Sonnino, 1981), can be recognized within a larger lobate system (e.g., Gervais et al., 2006; Deptuck et al., 2008; Saller et al., 2008; Bourget et al., 2010; Prélat et al., 2010; Yang and Kim, 2014), but even these gross features may not be resolved in the deep subsurface. Consequently, more often than not, the presence of distributary channels and other architectural features of lobate deposits are inferred based on models, about which there is considerable uncertainty.

We recognize that the range of architectures within lobate deposits is diverse and that this diversity is under-represented in the literature. Therefore, the objective of this paper is to emphasize this diversity by describing three examples of lobate deposits with fundamentally different architectures. We describe the context within which each lobate deposit is found and suggest possible controlling mechanisms. The sinuosity, distribution, and divergence of channels, if present, are key criteria for discriminating between these three examples. These examples were chosen because of their distinctly different architectures as imaged in 3D reflection seismic data with very similar resolution (Table 1). All three are likely late Pleistocene in age, buried by about 50–160 m of muddy sediment. All three are similar in size and located on passive margins offshore of large deltas, which are the source of their sediment. Two are located in intraslope basins offshore of the Niger Delta, Nigeria, while the third is located on the basin floor offshore of the Mahakam Delta, Kalimantan, Indonesia (Figure 1). No cores are available to confirm interpretations of sediment caliber and distribution. However, seismic Root Mean Squared (RMS)

amplitude displays provide an objective basis for a general interpretation of mud versus sand (Posamentier and Kolla, 2003).

DESCRIPTION OF THREE EXAMPLES

In the description of the three examples below we use the general term “lobate deposit” because hierarchical classification originally designed for two-dimensional reflection seismic and outcrop data (e.g., Deptuck et al., 2008; Prélat et al., 2009; Mulder and Etienne, 2010; Prélat and Hodgson, 2013) does not apply directly to deposits imaged by three-dimensional reflection seismic data. We revisit this topic in the discussion.

Lobate Example 1: A Pervasively Channelized Lobate Deposit

Example 1: Regional Setting

Lobate Example 1 (LE1) is located on the continental slope of the western Niger Delta approximately 95 km from the modern shelf edge beneath 2,250 m of water (Figure 1A). The general direction of sediment transport was from north to south or southwest. The continental slope in the study area is irregular (i.e., the stepped profile of Prather et al., 1998; Prather, 2003), including areas of both high and low gradient, as well as ridges that are elevated above the regional slope profile (Allen, 1965; Doust and Omatsola, 1990; Damuth, 1994; Pirmez et al., 2000; Steffens et al., 2003). The steep segments of the profile are formed on the seaward flanks of basinward verging thrusts cored by over-pressured buoyant mud. The areas of low gradient (i.e., steps of Prather et al., 1998) occur on the landward sides of the thrust ridges. LE1 accumulated within a sediment wedge on one of these steps in what has been called a slope apron (Gorseline and Emery, 1959; Barton, 2012; Prather et al., 2012a) within healed slope accommodation (Prather, 2000; Prather, 2003; Barton, 2012; Prather et al., 2012a; Sylvester et al., 2012).

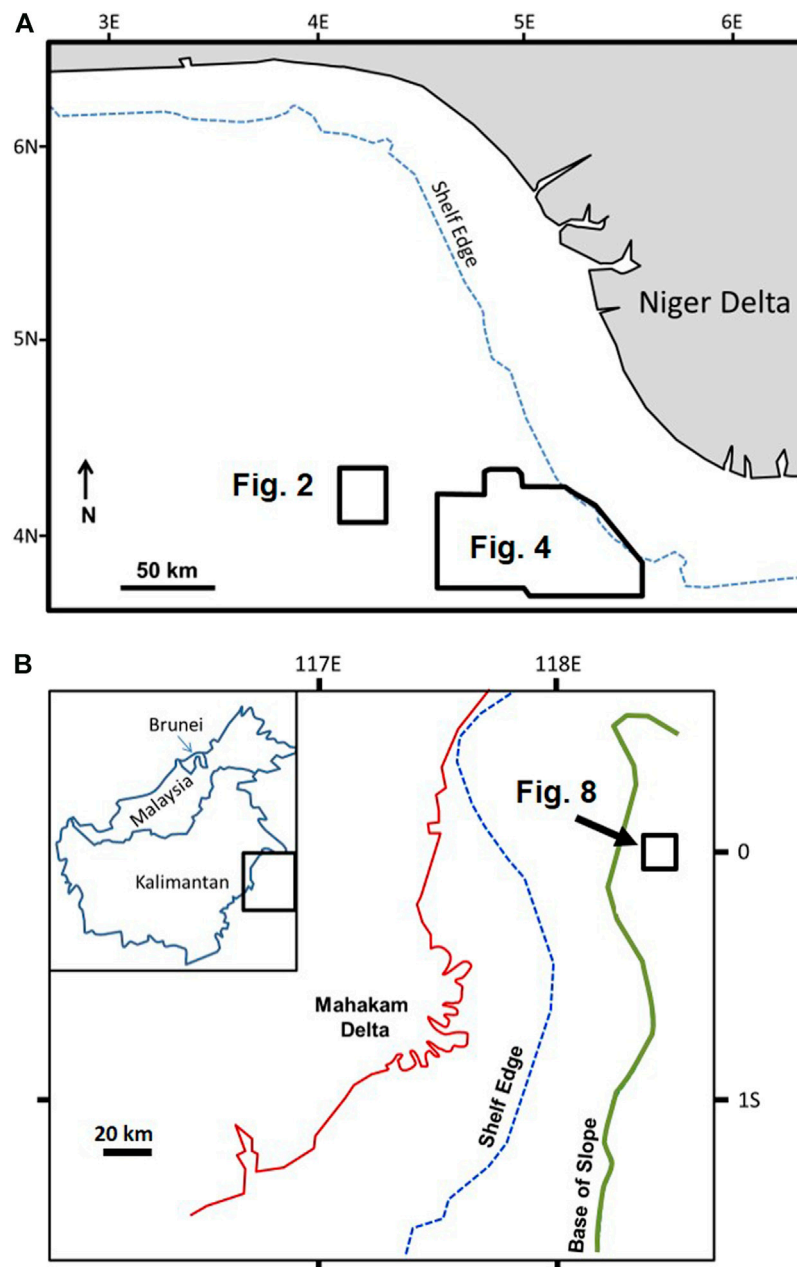


FIGURE 1 | (A) map of a portion of offshore Nigeria. The location of panels 2, 4 are indicated. **(B)** map of a portion of offshore Kalimantan, Indonesia. The location of panel 8 is indicated.

Example 1: Seismic Data

Images of LE1 (**Figures 2, 3**) are derived entirely from industry standard 3D reflection seismic data. The interpreted data have a dominant frequency of about 60 Hz at the shallow depth of the studied lobate deposit, which assuming an acoustic velocity of 2,000 m/sec (Flood et al., 1997), provides a nominal vertical resolution of approximately 8.3 m (**Table 1**). Sample spacing is 4 milliseconds (ms) and bin spacing is 12.5 m by 12.5 m. Planform images are horizon-referenced displays garnered from the uppermost 200 ms (200 m) of data below the seabed. The

contiguous seismic volumes that encompass LE1 cover an irregularly shaped area of approximately 5,500 km², of which, about 500 km² are displayed in **Figures 2, 3**. The seismic volumes extend from near the modern shelf edge to a position on the continental slope approximately 110 km seaward from the shelf edge.

Example 1: Description

LE1 (**Figures 2, 3**) has been described previously and called a lobe complex (Prélat et al., 2010, their Figure 5). These authors noted that LE1 is the youngest of several related lobate units. Each

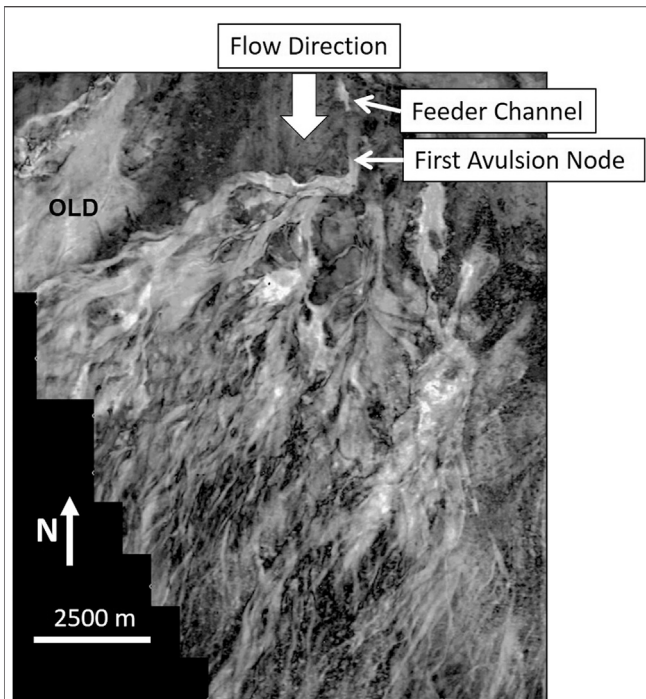


FIGURE 2 | An RMS (Root Mean Squared) amplitude extraction of LE1 from a 3D reflection seismic volume on the middle slope, offshore Nigeria (see **Figure 1** for location). Sediment transport is from north to south. The image is calculated from the interval between 10 and 20 ms from the top of the lobate deposit (see **Figure 3**). High RMS values are displayed as white to yellow colors. An older lobate deposit (marked OLD) is present to the west of LE1. Modified from Prélat et al. (2010).

lobate unit is displaced eastward of its predecessor, occupying low topography between the mounded sediment of the previous lobate deposit to the west and the regional southwest-dipping slope to the east (Prélat et al., 2010).

LE1 is approximately 14 km wide, in excess of 12 km long, with a maximum thickness of 130 m near the proximal (North) end of the lobe, yielding a width to thickness ratio of 108 (Prélat et al., 2010). LE1 is buried by approximately 120–170 m of mud-rich sediments. No core samples are available from LE1.

The single feeder channel complex (approximately 600–700 m wide) to LE1 was confined by a combination of erosion and outer, or external, levee aggradation (**Figures 3A,B**). Outer levees flanking the feeder channel complex are up to 50 m thick and 500 m wide, represented in reflection seismic data by low Root Mean Squared (RMS) amplitude values (**Figures 3A,B**). Sediment from the single levee-confined feeder channel complex was dispersed across LE1 via a system of distributary channels, each 300 m or less in width (**Figures 2, Figures 3A**). Numerous branching points resulting either from avulsion or bifurcation, are observed within the distributary channel system all across LE1 (**Figure 2**). For approximately 3 km down flow from the first, most proximal, branching point, distributary channels continue to be flanked by small outer levees, although levee height decreases down flow to the south until they are no longer resolvable on seismic profiles (**Figure 3C**). Fill

within these proximal distributary channels, as well as within the feeder channel complex, are recorded as high RMS values (**Figure 3**).

In a down-flow (southward) direction, each levee-confined distributary channel transitions into numerous sub-parallel to slightly diverging smaller channels (100 m or less in width) that form a 2–3 km wide cluster (**Figure 2**). The channel pattern in each cluster is achieved by increasing the number and frequency of branching points distally so that a few channels in a proximal position increase distally to a large number of closely spaced channels toward the fringe of LE1. Despite the fact that limited vertical resolution results in compositing multiple vertically juxtaposed channels within the same image, the entire lobate unit beyond the limit of levee confinement appears to consist of numerous channel clusters. The axis of each cluster follows a path that is sub-parallel to the axis of adjacent clusters and thus the overlap between adjacent clusters is minimal.

Within LE1, depositional lenses have been interpreted (Prélat et al., 2010) as lobes and can be resolved in at least some seismic profiles in the proximal to middle, high relief portion of LE1 (**Figures 3C,D**). Distally, the lenses gradually become flatter and thinner until they are no longer distinguishable (**Figure 3E**).

Lobate Example 2: A Lobate Deposit Without Distributary Channels

Example 2 Regional Setting

LE2 is located on the continental slope of the Niger Delta (**Figures 1, 4–7**), 70 km southeast of LE1 and approximately 45 km basinward of the modern shelf edge beneath 1,275 m of water (**Figure 1A**). The general direction of sediment transport was from northeast to southwest. As is the case with LE1, LE2 is in an area of relatively low gradient along an irregular stepped profile resulting from deep seated thrusts modified by diapiric deformation of buoyant shales (circular features near the head of LE2 in **Figure 6**) (Allen, 1965; Doust and Omatsola, 1990; Damuth, 1994; Pirmez et al., 2000; Steffens et al., 2003). LE2 accumulated as part of a slope apron (Gorseline and Emery, 1959; Barton, 2012; Prather et al., 2012a) within healed slope accommodation (Prather, 2000; Prather, 2003; Barton, 2012; Prather et al., 2012a; Sylvester et al., 2012).

Example 2 Seismic Data

Images of LE2 are derived entirely from industry standard 3D reflection seismic data of very similar vintage and quality to the data that are illustrated for LE1 (**Table 1**). About 6,000 km² of contiguous 3D reflection seismic data have been examined in the area around LE2 (**Figure 4**) including the shelf edge near LE2 as well as surrounding slope features. As with LE1, these interpreted data have a dominant frequency of about 60 Hz at the shallow depth of the studied lobate deposit, which assuming an acoustic velocity of 2,000 m/sec (Flood et al., 1997), provides a nominal vertical resolution of approximately 8.3 m (**Table 1**). Sample spacing is 4 milliseconds and bin spacing is 12.5 m by 12.5 m. The plan view images provided in this paper for LE2 are horizon-referenced displays of data between 50 and 150 milliseconds (50–150 m) below the seabed.

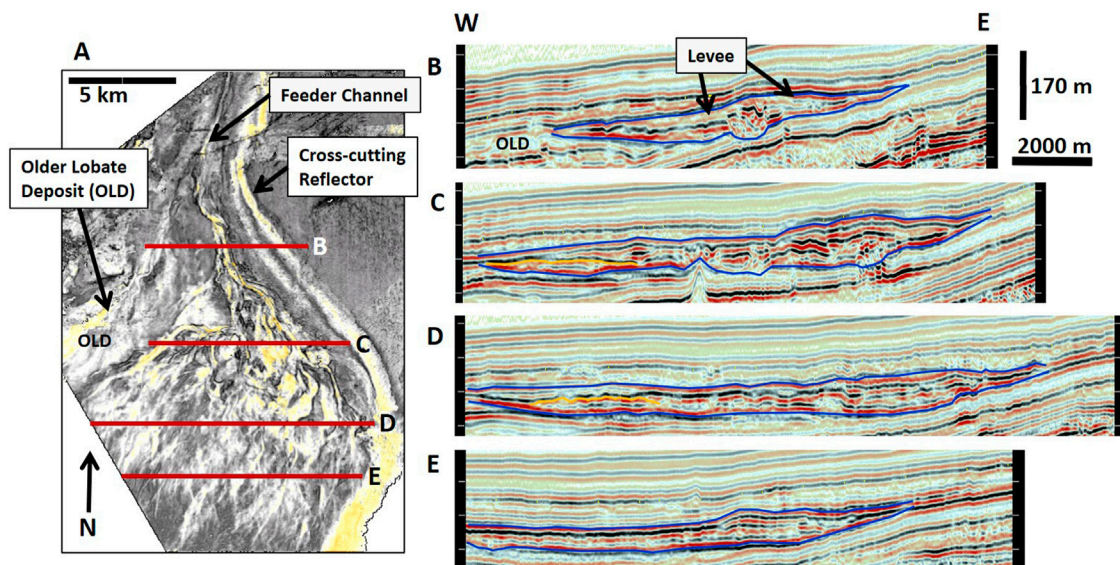


FIGURE 3 | Cross sections through LE1 from a 3D reflection seismic volume. **(A)** Plan view Root Mean Squared (RMS) amplitude extraction midway between the upper and lower bounding surfaces of LE1 [blue horizons in panels **(B–E)**] superimposed on a continuity display (lateral rate of change of RMS amplitude values from the same interval). High RMS values are displayed as white to yellow colors. Low continuity values are displayed as black. Modified from Prélat et al. (2010). The locations of cross-sections **(B–E)** are displayed as red lines. An older lobate deposit (OLD) is present to the west and beneath LE1. **(B)** Proximal section through the feeder channel complex for LE1. Prominent levees are present on both sides of the channel complex and thin away from the channel complex. **(C)** Seismic section through the proximal portion of LE1. This portion of the lobate deposit is characterized by highly discontinuous reflections resulting from the presence of numerous distributary channels. As an example, the top of a single lens-shaped unit within LE1 is highlighted as a yellow horizon. **(D)** Seismic section through the medial portion of LE1. This portion of the lobate deposit is characterized by moderately discontinuous reflections, resulting from the presence of numerous distributary channels. The top of one lens-shaped unit within LE1 is highlighted as a yellow horizon. **(E)** Seismic section through the distal portion of LE1. This portion of the lobate deposit is characterized by moderately continuous reflections. Very small distributary channels appear to be present in plan view but are too small (shallow) to break up reflection continuity in section view. Lens-shaped units within LE1 are not resolvable.

Example 2 Description

LE2 is approximately 6 km wide, 14 km long, and a maximum of 20 m thick yielding a width to thickness ratio of 300 (Table 1). LE2 is buried at approximately 50 m below the seabed. No core samples are available from LE2.

In cross-section, LE2 is tabular and thin (Figure 7) and distinct internal lens shapes, if present, are not resolved with available data. LE2 is a high amplitude feature (HAF) displayed in the RMS extractions of Figure 4 through Figure 7 as a light colored object (elevated RMS values). Several HAFs of diverse sizes and shapes are displayed on the continental slope surrounding LE2 including narrow linear HAFs, fan-shaped HAFs, and irregular broad HAFs that indicate the location and transport path of granular clastic material.

In the area north and east of LE2, the shelf edge has a generally smooth to slightly irregular northwest trend (Figure 4). No submarine canyon is imaged at or near the shelf edge. Instead, the shelf edge occasionally is offset landward by approximately 2 km by arcuate indentations that are 5–8 km wide (Figure 4). Numerous narrow and linear HAFs (interpreted as gullies) are imaged immediately basinward of the arcuate indentations (area X in Figure 4). Some of the linear HAFs appear to terminate down slope, after 5–10 km or less, in small divergent, fan shaped HAFs that are only one or 2 km wide and long (area X, Figure 4). Others continue farther down slope and are focused by bathymetry into larger HAFs with stronger amplitudes.

Directly up slope from LE2, the shelf edge is beyond the limit of the seismic volume (Figures 4, 5). In the most proximal portion of the seismic volume, numerous narrow linear HAFs each give way down slope to a wedge-shaped HAF consisting of a divergent collection of sharp to diffuse linear forms with elevated amplitude (area Y, Figures 4, 5). The wedge-shaped HAFs overlap to form an apron (sensu Reading and Richards, 1994). After crossing a zone of down-to-the-basin normal faults farther down slope, the apron of wedge-shaped HAFs merges into a single large HAF (area Z, Figure 5). Specific features within the HAF are indistinct although amplitude variations are elongate (channels?) and define a textural trend that is parallel to the local direction of maximum gradient. The HAF narrows down slope until it is funneled through bathymetric highs to emerge and form the single large HAF of LE2 (Figures 5, 6).

Sediment was supplied to LE2 through multiple entry points rather than through a single channel complex (Figures 5, 6). No outer levees are observed anywhere along the transport path to or within LE2. Sediment was dispersed across the bulk of LE2 without leaving evidence for either a distributary channel system or branching (Figure 6) comparable to LE1. Instead, elongate textures are imaged in RMS amplitude extractions, most prominently defined by dark elongate features (low RMS values), in LE2 that vary in morphology in planform from lenticular or irregularly shaped to continuous with slightly convergent or slightly divergent margins (Figure 6). The most continuous

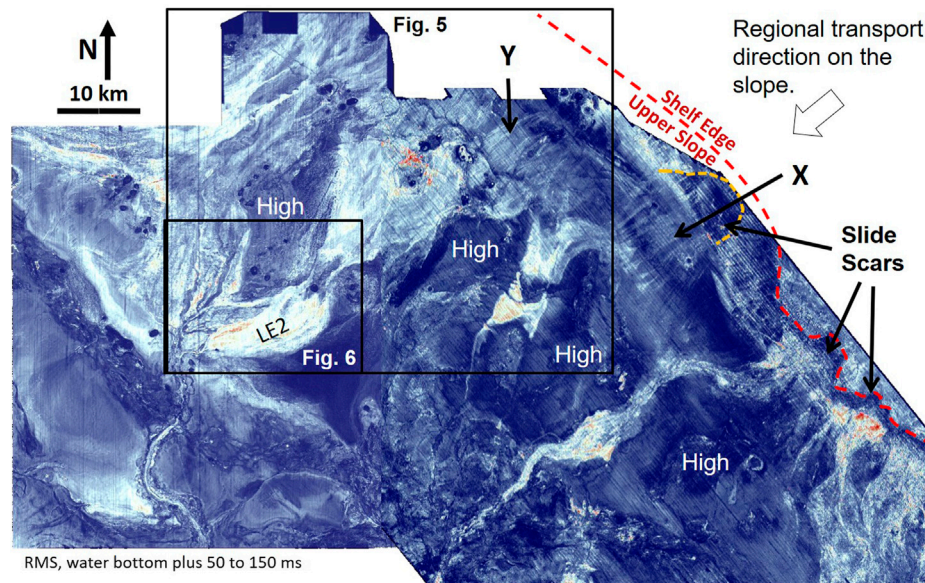


FIGURE 4 | A Root Mean Squared (RMS) amplitude extraction from 3D reflection seismic volumes on the middle to upper slope, off shore Nigeria (location in **Figure 1**). The image is calculated from the interval between 50 and 150 ms below seabed (approximately 100 m of sediment). Sediment transport is from northeast to southwest and water depth increases to the southwest. High RMS values are displayed as white to orange colors. The approximate position of the shelf edge is represented by a red dashed line. The edges of large slide complexes at the shelf edge are indicated by scallop-shaped indentations in the shelf edge. The edge of a large slide scar complex on the upper slope is indicated by an orange dashed line. Influential structural highs are annotated (High). The locations of panels 5, 6 are indicated. The location of LE2 is labeled as are the locations of areas X and Y (discussed in the text).

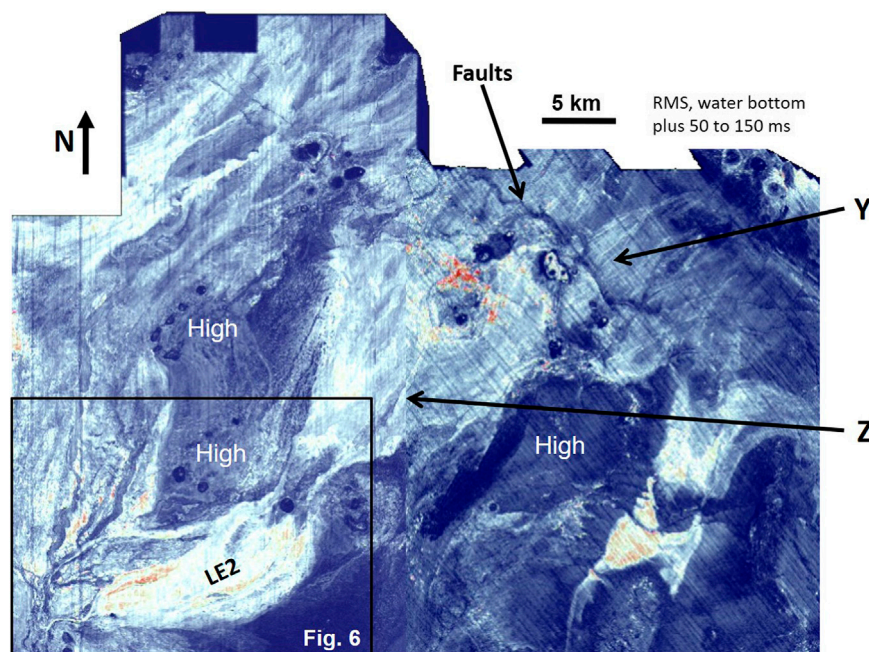


FIGURE 5 | A Root Mean Squared (RMS) amplitude extraction from two adjacent 3D reflection seismic volumes on the middle to upper slope, off shore Nigeria. See **Figure 4** for location. The image is calculated from the interval between 50 and 150 milliseconds (approximately 100 m of sediment) below seabed. High RMS values are displayed as white to orange colors. Sediment transport is from northeast to southwest. The location of panel 6 is indicated. Influential structural highs are annotated (High). The location of LE2 is labeled, as are the locations of areas Y and Z (discussed in the text).

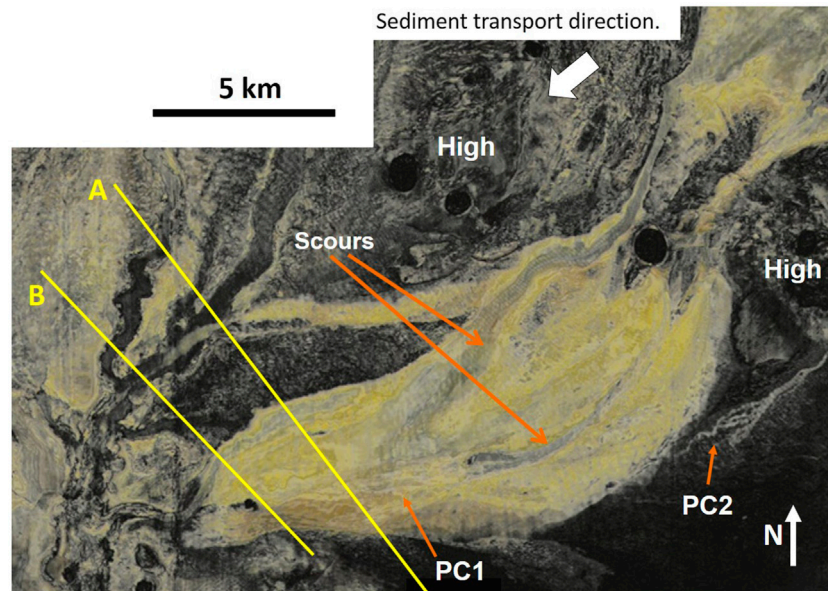


FIGURE 6 | A Root Mean Squared (RMS) amplitude extraction from a 3D reflection seismic volume on the middle slope, off shore Nigeria. See **Figures 4, 5** for location. The image, which includes LE2, is calculated from the interval between 50 and 100 ms (approximately 50 m of sediment) below seabed. The sampled interval corresponds to the interval between blue lines in **Figure 7**. High RMS values are displayed as white to yellow colors. Sediment transport is from northeast to southwest. Dark, elongate, low sinuosity features with non-parallel sides, interpreted as scours within LE2, are labeled (Scours). Small possible channel forms may be seen locally within LE2 (PC1) as well as outside of LE2 (PC2). Influential structural highs are annotated (High). The locations of seismic cross sections in **Figure 7** are indicated by yellow lines labeled (A) and (B).

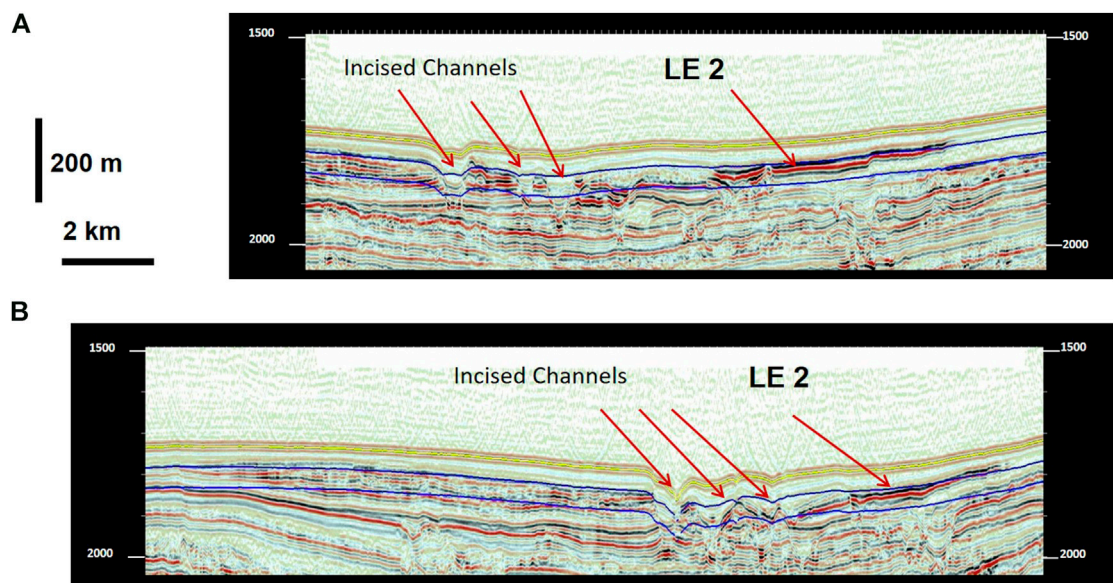
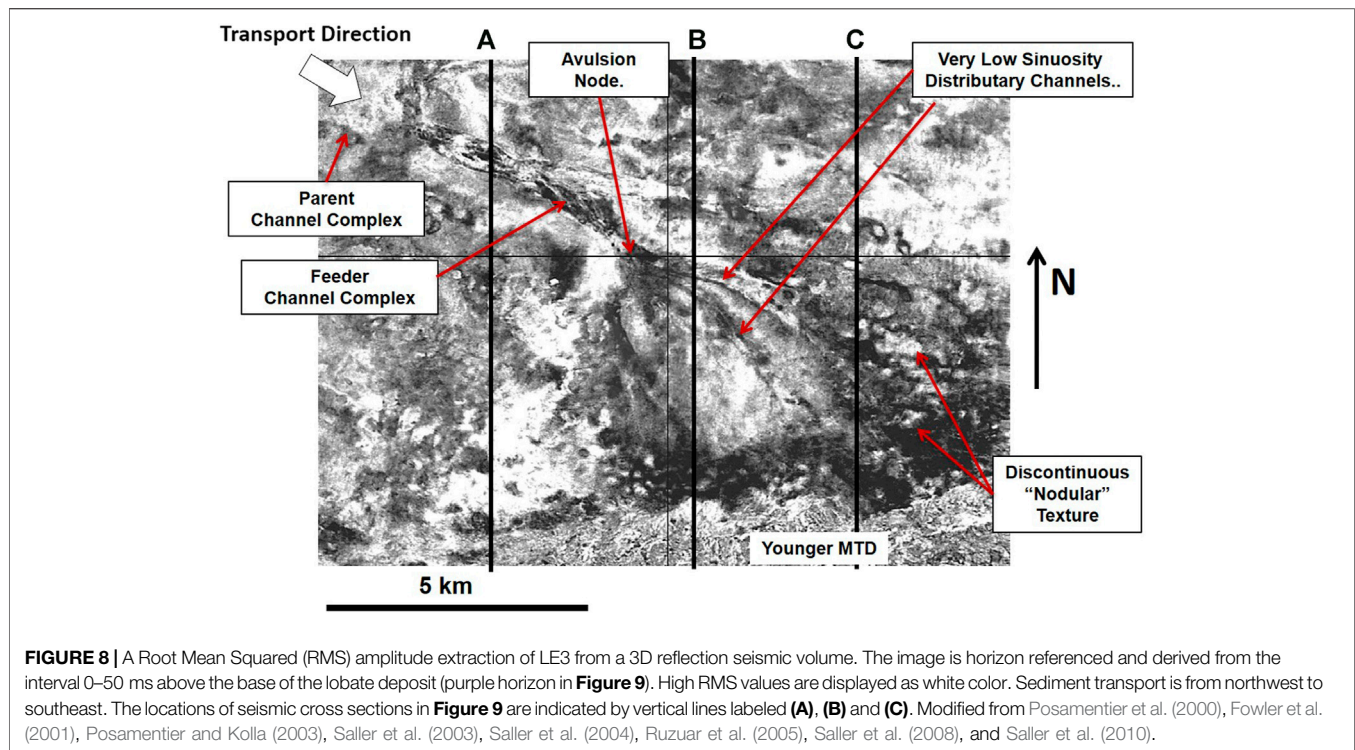


FIGURE 7 | Cross sections through LE2 from a 3D reflection seismic volume. See **Figure 6** for locations. The blue lines indicate the top and base of the interval from which the RMS (Root Mean Squared) values in **Figure 6** were calculated. (A) Seismic section through the distal portion of LE2. This portion of the lobate deposit is characterized by highly continuous reflections. Incisional bypass channels are evident to the west of LE2. (B) Seismic section through the terminus of LE2. LE2 continues to be characterized by a highly continuous reflection. The area to the west of LE2 is dominated by multiple incised channel.



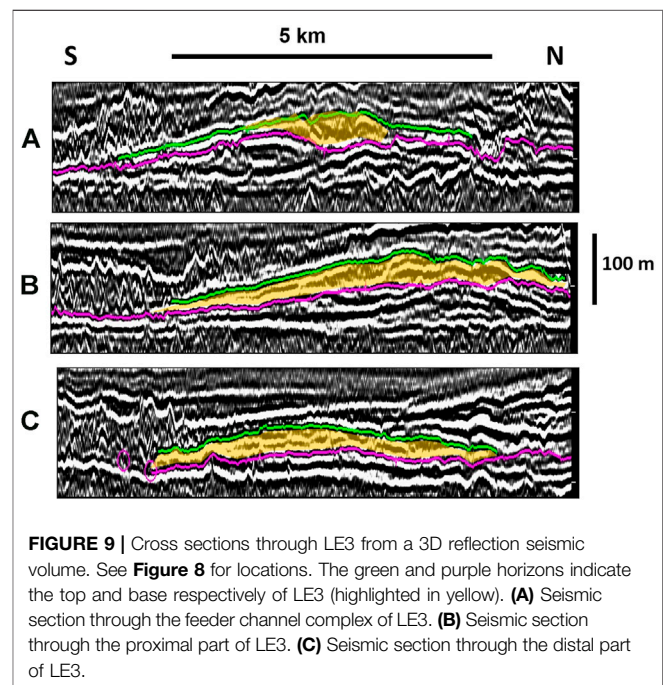
elongate features lack the sharply defined parallel margins of channels that are clearly imaged in LE1 (Figure 2). A possible exception to the absence of conventional channels is present in the southern part of LE2 where a slightly divergent set of narrow moderately high amplitude threads (PC, Figure 6) appear locally down flow from a prominent elongate low amplitude feature.

At the down-flow terminus of LE2, deeply incised channels are observed (Figures 6, 7). One is located at the terminus of the main part of LE2 (Figure 7B), while another is located at the terminus of a narrow arm of the HAF located to the west of LE2. These deeply incised channels are located at positions that would have, in combination, received any flows and transported sediments that bypassed LE2 (transient fan of Adeogba et al., 2005). These incised channels deepen along their path to the southwest and converge basinward with other erosional channels (Figure 4).

Lobate Example 3: A Channelized Lobate Deposit With Few Distributaries

Example 3 Regional Setting

LE3 (Figure 8) is located at the base of slope east of Kalimantan, Indonesia, in the Kutei Basin, Makassar Strait (Figure 1B). LE3 is part of a larger fan system on the basin floor, approximately 40 km from the shelf edge beneath about 2,000 m of water (Saller et al., 2008). Sediment transport generally was from west to east or southeast. The continental slope proximal to the fan that contains LE3 is irregular, including areas of both high and low gradient, as well as ridges that tend to stand above the regional slope profile. The stepped slope profile results from prominent toe thrusts that maintain a gradient of 2.1° at the base of slope compared to the basin floor gradient of 0.3° (Saller et al., 2004).



The fan, including LE3, has been imaged and interpreted multiple times (Posamentier et al., 2000; Fowler et al., 2001; Posamentier and Kolla, 2003; Saller et al., 2003; Saller et al., 2004; Ruzuar et al., 2005; Saller et al., 2008; Saller et al., 2010). The fan was deposited in association with a sea level lowstand about 240 ka (Saller et al., 2004). The submarine fan was both preceded

and followed immediately by substantial mass transport deposits (Posamentier et al., 2000; Fowler et al., 2001; Posamentier and Kolla, 2003; Saller et al., 2003; Saller et al., 2004; Ruzuar et al., 2005; Saller et al., 2008; Saller et al., 2010).

LE3 (Figures 8, 9) is located approximately midway within a strongly progradational and moderately aggradational succession of lobate bodies (Saller et al., 2008). Each lobate body was connected to the same feeder channel-levee complex. Deposition, avulsion and abandonment of each lobate body resulted in the progressive basinward offset of successive lobate deposits and progradation of the system. The youngest expression of the channel-levee complex culminated with a terminal lobate deposit (Posamentier et al., 2000; Fowler et al., 2001; Posamentier and Kolla, 2003; Saller et al., 2003; Saller et al., 2004; Ruzuar et al., 2005; Saller et al., 2008; Saller et al., 2010). At least one mass transport complex (MTC) was deposited within the fan during progradation (Posamentier and Kolla, 2003; Saller et al., 2008) and a younger MTC eroded the southern edge of LE3 (Figure 8).

Example 3 Seismic Data

Images of LE3 are derived entirely from industry standard 3D reflection seismic data acquired in 1998–1999 by WesternGeco as part of the much larger Makassar 3D survey. The interpreted data have a dominant frequency of about 50 Hz (Saller et al., 2008) at the shallow depth of the studied fan. Assuming an acoustic velocity of 2,000 m/sec (Flood et al., 1997), the nominal vertical resolution of these data is approximately 10 m (Table 1). The plan view image provided in this paper is a horizon-referenced RMS amplitude display garnered from the uppermost 200 milliseconds (200 m) of data below the seabed. Bin spacing is 12.5 m by 12.5 m. The studied portion of the seismic volume extends from near the modern base of slope to a position approximately 22 km to the east on the basin floor.

Example 3 Description

LE3 is approximately 7 km wide, more than 7 km long, and a maximum of approximately 43 m thick near the proximal (NW) end of the lobate deposit yielding a width to thickness ratio of 163 (Figures 8, 9; Table 1). LE3 is buried by approximately 160 m of mud-rich sediments. No core samples are available from LE3.

At the time of deposition, LE3 may have been a terminal lobe of the submarine fan (Posamentier and Kolla, 2003, their frontal splay). Alternatively, its single feeder channel complex (approximately 300–500 m wide) may have avulsed from a larger parent channel complex that extended into the basin as the fan prograded. Confinement of the parent channel complex was provided by a 110 m thick and 4,000 m wide outer levee (estimated from Posamentier and Kolla, 2003). The dimensions of the levee, if present, at the time of LE3 deposition are unknown.

The single feeder channel complex is about 5 km long between its connection to the larger parent channel complex and the apex of LE3 (Figure 8). The feeder complex appears to have been confined primarily by erosion although a contemporaneous levee cannot be discounted. Within the feeder channel, which is almost straight, smaller low sinuosity channel elements (*sensu* McHargue et al., 2011) are distinctly imaged. A branching point is present at the distal end of the feeder channel

marking the proximal end of a small number of long distributary channels (up to 5 km long and 100–300 m wide) with very low sinuosity (Figure 8). No other branching points are recognized within LE3. No finer scale channel forms are recognizable surrounding the distributary channels or at the distal end of the distributaries. Fill within the distributary channels is too thin to image distinctly in cross-section (Figure 9).

Except for the few distributary channels, plan-view imaging of the sediment within LE3 ranges from featureless to nodular (Figure 8). The nodular features are particularly prominent around the fringe of LE3, but subtle variation within the main part of the lobate unit suggests that the nodular texture may be present throughout LE3. Nodular texture also is present lateral to LE3 in adjacent lobate bodies (Figure 8). Individual nodular features can be up to 200 m wide although a full range of smaller sizes, down to the resolution limit of the data, are evident.

In cross-section, LE3 is markedly lenticular (highlighted in yellow, Figure 9). It overlies multiple older lenticular lobate units and, at its distal part, is overlain by at least one lobate unit before burial by the channel-levee complex. The sediment within LE3 is crudely layered and imaged with moderate amplitudes. Compensational stacking of the successive older and younger lobate lenses is evident surrounding the proximal part of LE3 (Figure 9, sections A and B) but becomes more subtle distally as lens relief decreases (Figure 9, section C).

INTERPRETATION

Lobate Example 1 Interpretation

The diversity of amplitudes suggests that LE1 received flows transporting a wide range of grain-sizes including both sands and muds. The feeder channel complex and proximal distributary channels of LE1 are confined primarily by outer levees (Figures 3B,C). Low seismic RMS amplitudes in the levees suggest that they are composed dominantly of mud. Low seismic RMS amplitudes within outer levees contrast with high seismic RMS amplitudes within the feeder channel complex and within distributary channels of LE1. High RMS amplitudes require strong contrasts in impedance and suggest the presence of mixed sand and mud within the channel-fills. Farther down flow, where levees are no longer discernable, it is suspected that overbank sediments continue to have higher mud content relative to channel sediments accounting for distinct, well imaged channels. The presence of well-developed levees confining the feeder and proximal distributary channels, as well as the acoustic variability required to yield well imaged channels, suggests that the contributing flows were density stratified (Kneller and Buckee, 2000; Peakall et al., 2000; Hansen et al., 2015). As each turbidity current crossed LE1, the top of the dilute layer was eventually lost overbank by flow stripping as levee height decreased down flow.

At the terminus of each levee-confined distributary channel, instead of unchanneled deposits, a pervasively channelized unit is present that is dominated by a cluster of sub-parallel to slightly divergent small channels. Adjacent clusters tend to be laterally offset from each other suggesting compensation. LE1

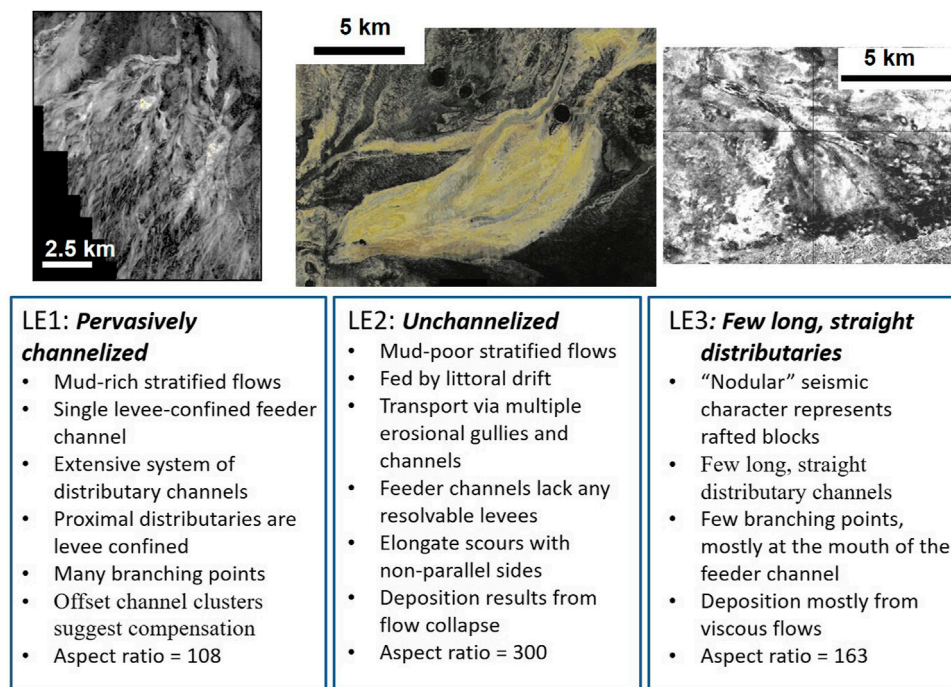


FIGURE 10 | Summary of distinctive characteristics of the three discussed lobate examples. See **Figures 2, 6, 8** for explanations of seismic RMS amplitude displays.

(**Figures 2, 10**) is covered by distributary channels with numerous branching points, an observation that, when combined with the presence of levee-confined distributaries, is compatible with the proposal of Mulder and Etienne (2010) that lobate deposits with a well-developed distributary channel system appear to be constructed from relatively mud-rich flows. However, even their model for channelized lobes does not illustrate the high density of distributary channels present across all of LE1 (**Figures 2, 10**).

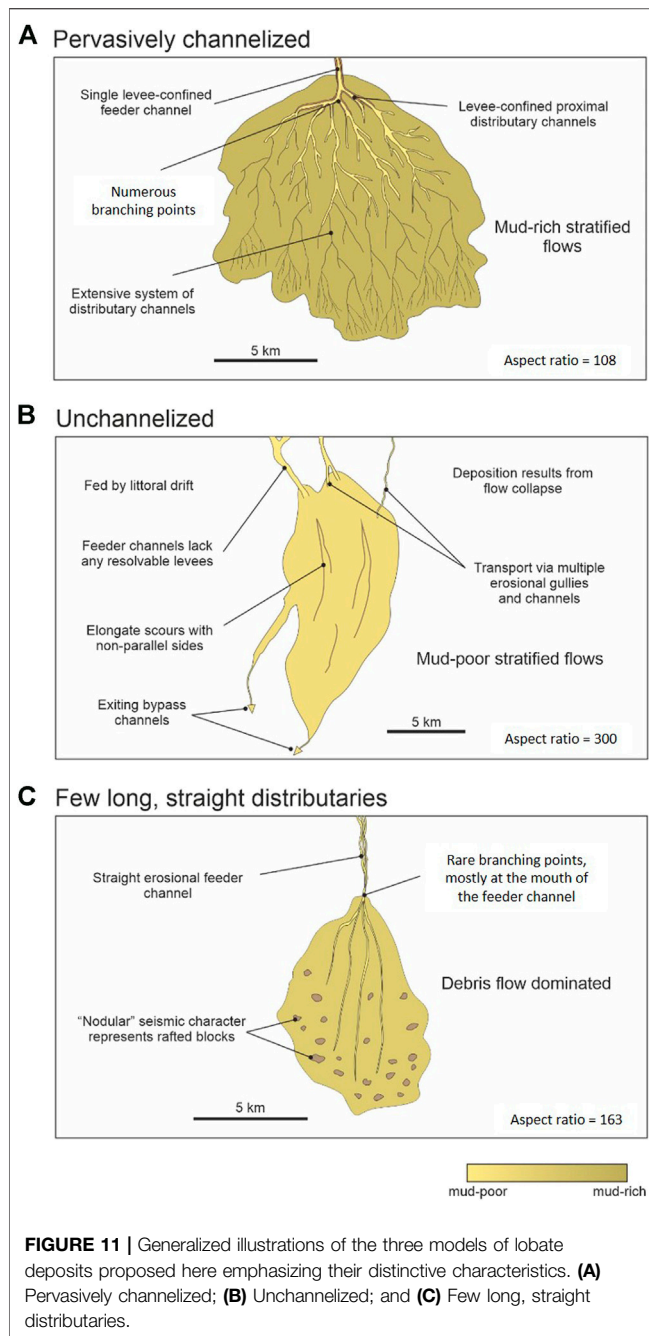
Summary

In summary, LE1 is interpreted to have a well-developed distributary channel system that is interpreted to display the following characteristics (**Figures 10, 11**):

- 1) Sediments were delivered to LE1 through a single levee-confined feeder channel complex.
- 2) Transported sediments were heterolithic, including enough mud in the upper dilute portion of flows to allow for outer levee construction.
- 3) Sediments were dispersed across LE1 via an extensive system of distributary channels.
- 4) The proximal distributary channels are interpreted to have been levee confined.
- 5) LE1 grew as a result of avulsions or bifurcations at numerous and diverse branching points along the distributary channel pathways.
- 6) The most distal visible channels form channel clusters that tend to be laterally offset relative to one another in a stacking pattern that suggests compensation.

Lobate Example 2 Interpretation

LE2 (**Figures 6, 10**) appears to have only sparse, fine-scale distributary channels and a much higher aspect ratio (300) than LE1 (108) (**Table 1**). Much can be inferred regarding the nature of the shelf edge and slope from the regional horizon-based RMS amplitude extraction (**Figure 4**). The sizes, shapes and linkages of the HAFs displayed on the continental slope indicate the locations of sediment transport paths and deposition. The presence of high amplitudes (light colors in **Figure 4** through **Figure 6**) within the HAFs suggests sand-rich sediments within the HAFs (Posamentier and Kolla, 2003). The source area on the shelf for the sediment within LE2 lies outside the available seismic coverage. However, the transport path from shelf to lobate deposits is well imaged for sediment immediately to the east (area X in **Figure 4**). Upper slope architectures are very similar in areas X and Y so, by analogy, we interpret that those similar conditions prevailed for both systems at the shelf edge. No submarine canyon is imaged at or near the shelf edge up slope from area X. Instead, arcuate indentations in the shelf edge and upper slope are well imaged and are interpreted as coalesced slide scars (**Figure 4**). Because these slide scars are well imaged, we infer that submarine canyons, if present, also would be imaged. The narrow and linear HAFs immediately down slope of the slide scars (area X in **Figure 4**) are interpreted to represent numerous slope gullies, some of which terminate in small fan-shaped deposits. Others coalesce and continue down slope to deliver sediment to large HAFs. Because of the spatial association of slide scars and the clustered transport paths (**Figure 4**), it is



inferred that the slide scars were integral to intercepting shelf sediments and directing them down slope within density currents. The gullies in area Y (**Figures 4, 5**) up slope of LE2 have very similar morphology and clustering as in area X and, assuming lateral continuity of the slide scar pattern, are inferred to have the same origin as those in area X. Therefore, although a degree of speculation is required, features in area Y are interpreted to represent the transport path of shelf sediments that were intercepted at slide scars and directed through multiple HAFs to LE2.

We speculate that the dominant source of sediment was from littoral drift. The Niger Delta is a wave-dominated system today

(Allen, 1965; Doust and Omatsola, 1990) with strong littoral cells (Burke, 1972; Biscara et al., 2013). Because littoral drift potentially is available all along the lowstand delta front, especially concentrated where slide scars intersect the shelf edge, it seems reasonable that gravity flows, consisting of sand-rich littoral deposits (Imhansoloeva et al., 2011), spilled over the indented lowstand shelf edge and traversed numerous gullies to coalesce in areas of decreased gradient as HAFs. No outer levees are observable anywhere within LE2, or along the train of HAFs leading to LE2, suggesting that the gravity flows that traversed the HAFs lacked sufficient mud caliber sediments to build outer levees (Posamentier and Kolla, 2003). Furthermore, these observations are consistent with the contention that the HAFs contain sand-rich sediment that originated from littoral drift on the shelf.

On LE2 (**Figure 6**), no large conventional distributary channels with parallel margins are observed. Instead, indistinct elongate textures are recorded by RMS amplitudes within LE2 (**Figure 6**). Some of the most continuous elongate features are slightly darker (lower RMS amplitude) than the surrounding deposits. Perhaps this amplitude distribution results from thinning of the sand-prone deposits within the linear features as a result of scouring reminiscent of the central feature of the Navy Fan (Carvajal et al., 2017). We further suggest that these elongate features served as conduits for sediment transport (De Leeuw et al., 2016; Ferguson et al., 2020). A possible exception occurs in a local area in the southern part of LE2 where fine-scale thread-like features (possible channels) appear to emanate from the distal end of one of the dark, elongate, linear features (PC1 in **Figure 6**). If these features are channels, analogous to the small channel threads to the east outside of LE2 (PC2 in **Figure 6**) they are markedly smaller than the channels in LE1. The origin of the possible fine-scale channels is unclear; they may be superficial, but they do demonstrate that channels, even fine-scale channels, when present, may be imaged successfully.

Deeply-incised channels at the terminus of LE2 deepen along their path to the southwest (**Figure 7**) and converge with other erosional channels (**Figure 4**). The strongly erosive character of these channels indicates that significant volumes of sediment periodically bypassed LE2 resulting in increased basal shear stress and scour (Adeogba et al., 2005; Gamberi and Rovere, 2011; Maier et al., 2011; Barton, 2012; Maier et al., 2012; Prather et al., 2012a; Maier et al., 2013; Yang and Kim, 2014). We reconcile these observations and the interpretation of sand-rich flows by speculating that deposition of LE2 occurred as flows slowed and collapsed at an area of relatively low gradient. Other flows had sufficient momentum to scour and bypass LE2 producing local erosion of linear troughs and incisional bypass-dominated channels. Compatible with this model, the dark, linear features are thought to have low RMS amplitude due to thinning or complete removal of sand by scour of more energetic flows.

Summary

LE2 is interpreted to have no conventional distributary channel system; rather it is interpreted to display, the following characteristics (**Figures 10, 11; Table 1**):

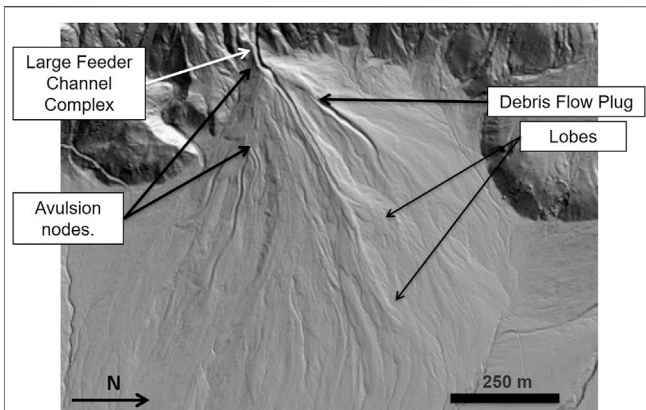


FIGURE 12 | Hill-shade map based on LiDAR produced topography of subaerial debris flow dominated fan in Saline Valley, California. Laminar flow of the subaerial debris flows has produced a surface distributary texture with long, nearly straight channels, sparse branching points, and narrow depositional bodies. This distributive architecture is reminiscent of LE3 (Figure 8). Source: Earthscope Eastern and Southern California. Resolution = 0.5 m. Lat. 36.824674°, Long. -117.919470°. The material for this example is based on services provided to the Plate Boundary Observatory by NCALM (<http://www.ncalm.org>). The Plate Boundary Observatory is operated by UNAVCO for EarthScope (<http://www.earthscope.org>) and supported by the National Science Foundation (No. EAR-0350028 and EAR-0732947).

- 1) LE2 likely is constructed of sediments derived from multiple points along the shelf edge (a line source) without evidence of a submarine canyon (a point source).
- 2) Transported sediments are interpreted to consist of mud-poor sandy littoral drift intercepted and remobilized at slide scars at or near the shelf edge.
- 3) The delivered sediments are transported from the shelf edge to LE2 via multiple erosional gullies or channels that are focused by slope topography toward the location of LE2.
- 4) Feeder channels and lobate deposits lack any resolvable levees suggesting that the delivered sediments are extremely sand-rich with minimal accompanying mud.
- 5) Large elongate scours with non-parallel sides are interpreted to be present.
- 6) No conventional distributary channel system is visible within the lobate deposit. Local thin threads (PC1 in Figure 6) near the southern margin may represent local distributaries.
- 7) Deposition is interpreted to result from collapse of sand-rich flows at decreased gradient although other, more robust flows scoured the deposits and bypassed LE2.

Lobate Example 3 Interpretation

LE3 (Figures 8, 10) displays only a few distributaries that diverge at the mouth of the feeder channel and extend without further branching points to the observed limits of the lobate deposit. The absence of secondary branching points and secondary distributaries coupled with the very low sinuosity of the primary distributaries is distinctive. The nodular texture of seismic RMS amplitudes, best displayed in planform (Figure 8), are interpreted to be rafted coherent to semi-coherent blocks of allochthonous sediment within a

surrounding mass of mud-rich sediment (e.g., Saller et al., 2008; Hodgson et al., 2016) and suggests the presence of abundant debrites. LE3 is crudely layered in cross-section (Figure 9) suggesting that multiple events are present. The fact that distributary channels and small nodular features are imaged suggests that secondary distributaries, if present, would be recognized in these data. The nodular texture, lack of observed secondary distributary channels, and the extremely low sinuosity of the primary distributary channels, are interpreted to result from deposition from viscous flows.

Interestingly, similar morphology of long, nearly straight distributary channels with few branching points, is well demonstrated for debris-flow dominated alluvial fans (Figure 12). In these alluvial fans, avulsion is triggered either by debris plugs and/or slow aggradation that fill the channel, or by unusually large events (De Haas et al., 2019); these mechanisms might apply to submarine systems as well.

Summary

LE3 is interpreted to have a small number of straight distributary channels and rare branching points (Figures 10, 11; Table 1), and is interpreted to display the following characteristics:

- 1) LE3 is located at the end of a straight, erosional conduit without discernible levees and with minor slightly sinuous channel elements within its fill.
- 2) It displays a prominent “nodular” seismic character in plan view, typical of debrites, with individual nodular seismic features interpreted to represent rafted blocks up to 200 m wide.
- 3) A small number of long, straight distributary channels diverge at the mouth of the feeder channel.
- 4) Distributaries extend without further branching to near the end of the lobate deposit.
- 5) The long, straight, non-branching channels are interpreted to result primarily from viscous flows (debris flows) although minor turbidite and hybrid event deposits also could be present.

DISCUSSION

Processes and Sediment Caliber

The three lobate examples illustrated here are visually distinct based on distributary architecture (Figures 10, 11). No core material is available from any of the three examples so interpretations of process and sediment caliber are conjectural, constrained by regional context, seismic response and depositional architecture (Figures 10, 11). Based on these observations, we propose that relatively mud-rich turbulent, density-stratified flows produce levee-confined feeder channels, leveed proximal distributaries, and multiple secondary and tertiary distributaries with many branching points (LE1, Figures 2, 3, 10). Mud-poor turbidity currents, likely sourced from littoral drift, or via effective filtering of mud through flow stripping in long slope conduits (e.g., McHargue et al., 2011; Hodgson et al., 2016), are prone to collapse and result in a lobate

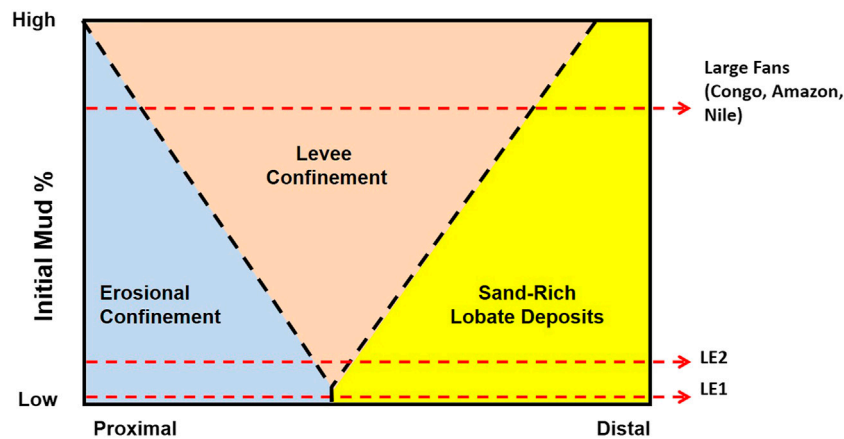


FIGURE 13 | Simplified schematic field diagram of the gross architectural succession from proximal to distal of a submarine turbidite system as a function of the abundance of initial mud in the average turbulent flow. Boundaries between fields are displayed as a linear function for simplicity but we acknowledge that these boundaries may be non-linear. The model is scale independent. Gradient is not considered here explicitly because mud-rich systems respond to gradient very differently than sand-rich systems. Mud is assumed to be located primarily in the upper dilute portion of highly stratified turbulent flows and to be consumed during transport primarily due to levee construction that shortens flow height. Levees decrease in height and decrease contribution to confinement down flow. Substrate entrainment is not considered. Also, this model does not consider the contribution of debris flows (LE3 does not apply). This model illustrates that systems with relatively high initial volumes of mud (higher on the Y axis) extend farther into the basin (more efficient) and tend to have larger sediment volume, larger levee volume, and more extensive levee-confined distributaries. Systems with relatively low initial volumes of mud (lower on the Y axis) extend a shorter distance into the basin (less efficient) and tend to have smaller sediment volume, smaller levee volume, increased reliance on erosional confinement, increased tendency to collapse, and increased sensitivity to gradient. Mud-rich systems, such as the Amazon, Nile or Congo Fans, are dominated by large levee-confined channels arranged in a distributary pattern. Extremely sand-rich systems, such as LE2 and Lobe X, are small, fed by erosional feeder channels with little to no distributary channels.

deposit with scour features but no distributaries (LE2, **Figure 4** through **Figures 7, 10**). Debris flow-dominated lobate features display straight, erosional feeder channels, a small number of straight distributary channels emanating from the mouth of the feeder channel, and few branching points (LE3, **Figures 8–10**).

Interpretations of LE1 and LE2 are consistent with the suggestions of Mulder and Etienne (2010). Although their proposal is intended to explain morphologically distinct portions within a single lobate deposit, we extrapolate their process-response model and the concept of flow efficiency proposed by Mutti and Normark (1987) to illustrate the relationship between the mud-richness of contributing flows and the relative size and runout distance of lobate deposits (**Figure 13**). Consistent with this model, the implications of varying mud-richness in fluvial versus littoral drift sediment supply on the size and runout distance of lobate deposits have been documented by Paumard et al. (2020). In addition, we propose that mud-poor flows produce poorly channelized lobate deposits whereas mud-rich stratified flows produce lobate deposits with a prominent distributary channel network (**Figures 10, 11**). Likewise, we suggest that the mode of feeder channel confinement serves as a useful proxy for sediment caliber: i.e., a levee-confined feeder channel implies mud-rich flows whereas erosionally-confined feeder channels without levees imply mud-poor flows.

Consistent with this proposal, LE1 displays a levee-confined feeder channel and an extensive system of distributary channels; in fact, except for its small size, LE1 has the morphology of a submarine fan (Normark, 1970). The volume of mud in a succession of mud-rich stratified flows feeds an increase in the

volume and length of levees around the feeder channel as well as distributary channels (**Figure 13**). This trend is one of the drivers for progradation of the lobate body (Ferguson et al., 2020). At some undefined size, the mud-rich lobate deposit is large enough to be called a submarine fan containing multiple subordinate lobate deposits, one at the terminus of each levee-confined distributary.

The LE2 feeder system lacks levees and LE2 does not display conventional distributary channels, only scours (**Figure 13**). In mud-poor sediments, cohesion is minimal and these sediments are easily scoured (e.g., Hir et al., 2008). Although initial erosion of the substrate may be a prerequisite for channel initiation (Fildani et al., 2013; De Leeuw et al., 2016), parallel sided channels did not form in LE2; consistent with features generated in non-cohesive sediments in flumes (e.g., Metivier et al., 2005, their Figure 2; and Cantelli et al., 2011, their Figures 1, 4) and with the conclusion of Rowland et al. (2010) that cohesive banks are necessary to produce parallel sided channels in flume experiments.

The morphology of LE3, the straight erosional feeder channel and sparse straight distributaries without secondary branches, is visually similar to elongate non-branching features produced in physical experiments from viscous flows, or at most weakly turbulent flows (Fernandez et al., 2014). Alfaro et al., 2014, their Figure 19) illustrated a lobate feature on the Caribbean margin of Colombia with characteristics similar to LE3 that they interpreted to consist of mixed slumps, debrites and turbidites, consistent with our interpretation of LE3.

For the three examples studied here (**Table 1**), relatively mud-rich turbulent flows, LE1, produce a thick deposit relative to

width ($W/T = 108$) whereas the collapse of sand-rich flows, LE2, produces a thin deposit ($W/T = 300$). The debris flow dominated deposit, LE3, displays intermediate dimensions and an intermediate aspect ratio ($W/T = 163$). The significance of differences in aspect ratios between the three lobate examples is unclear but likely is linked to the dominant depositional process. Furthermore, there are implications for source-to-sink investigations on the size, morphology, and runout distance of lobate deposits, which we interpret to be influenced by the varying character of sediment supplied by fluvial versus littoral drift systems. However, more lithological data from contemporary systems, where the source material and physiography are well constrained, are needed to test these controls on the architecture of lobate deposits in deep-water systems.

Seismically Imaged Subsurface and Modern Analogs

High resolution reflection seismic data of features at or near the seabed provide the most robust constraints on the 3D architecture of submarine lobate bodies. However, with few exceptions (e.g., Migeon et al., 2010; Jobe et al., 2017), core samples are sparse to non-existent. Additionally, because of resolution limitations, imaging of submarine lobes often reveals few details of architectural features within the lobe or even on the lobe surface. These fine-scale features are best revealed by high resolution bathymetric surveys (Maier et al., 2011; Carvajal et al., 2017; Maier et al., 2018; Droz et al., 2020; Maier et al., 2020). Such high resolution surveys illustrate the diversity of deep-water depositional systems but these surveys are rare. Given the relative sparsity of high resolution data on lobate deposits, it remains unclear whether the three examples shown here are representative of most such deposits. More data will help address this question.

In some cases, lens-shaped lobate deposits (Figure 9), typically stacked in a compensating pattern (*sensu* Mutti and Sonnino, 1981), can be recognized within a fan from reflection seismic data (e.g., Saller et al., 2008; Yang and Kim, 2014), but even these gross features may not be resolved unless near the seabed (e.g., Gervais et al., 2006; Deptuck et al., 2008; Bourget et al., 2010; Picot et al., 2016; Dennielou et al., 2017; Hamilton et al., 2017; Jobe et al., 2017).

Unambiguous images of distributary channel systems, as seen in LE1, have been recorded in some near surface seismic volumes of individual lobate deposits (Kidd, 1999; Posamentier and Kolla, 2003; Hadler-Jacobsen et al., 2005; Clark and McHargue, 2007; Hadler-Jacobsen et al., 2007; Prather et al., 2012b; Bakke et al., 2013; Oluboyo et al., 2014), or in high resolution bathymetric data (Maier et al., 2018). Curiously, in these examples, distributary channels tend to extend across the entire lobate body rather than just in the proximal portion. More common are lobate deposits with elongate to slightly divergent textures that might, ambiguously, be interpreted to represent distributaries (e.g., Jegou et al., 2008; Shanmugam et al., 2009; Bourget et al., 2010; Migeon et al., 2010; Sylvester et al., 2012; Egawa et al., 2013; Paumard et al., 2020).

If distributaries are not imaged, is that because they are present but difficult to image or because they are absent? Lobate deposits typically represent sand-rich environments both within and surrounding distributary channels. Therefore, it may be common that the acoustic properties of the channel fill are similar to those of surrounding overbank deposits. With little impedance contrast, imaging of distributaries is poor. Yet, in LE1 (Figure 2), distributaries are well imaged. Relatively mud-rich flows allowed for levee construction in proximal distributaries but also may have provided sufficient mud in overbank deposits of the middle to outer distributaries to provide impedance differentiation.

Distributaries may be present, even if not imaged, but it does not follow that one can assume their presence. For example, Lobe X of Prather et al. (2012a), Jobe et al. (2014), and Jobe et al. (2017) is located approximately 60 km to the northwest of LE1 and buried to a similar depth. Likewise, seismic data from Lobe X (60 Hz, 12.5 m \times 18.75 m bin spacing) is very similar in resolution to LE1 data (Figures 2, 3; Table 1). Multiple cores from Lobe X confirm that it is very sand-rich. However, in contrast to LE1, Lobe X displays neither levees nor distributaries. In that respect, it is similar to LE2.

Lobate deposits dominated by debrites, as in LE3 (Figure 8), have been imaged with sidescan data and confirmed with core from the Mississippi (Twichell et al., 1992; Twichell et al., 2009) and Nile (Ducassou et al., 2009; Migeon et al., 2010) submarine fans. However, given the very different tools with which these lobate bodies have been imaged versus LE3, the architecture is hard to compare. Nevertheless, these examples suggest that debrite dominated lobate deposits may be widespread.

Outcrop Analogs

We do not confidently recognize any outcrop analogs for any of the three examples of lobate deposits described here, although some partial analogs are suggested. It is challenging to reconcile architectural features illustrated in 3D reflection seismic data, even relatively high resolution data, with observations from outcrops because of poor resolution of seismic data relative to outcrop exposures and limited 3D exposure of even the best outcrops. Yet outcrop exposures are the principal way by which facies relationships within submarine lobate deposits are observed and documented.

An outcrop dominated by debrites, such as LE3 (Figures 8, 10), may not be recognized as a lobate deposit. Likewise, channels are so numerous in LE1 that, in outcrop, it might not be recognized as a lobate deposit. An extensively channelized distributary system has been recognized in outcrop in the Brushy Canyon Formation in the form of multiple erosional channels that diverge at an acute angle (Carr and Gardner, 2000; Gardner et al., 2003). Erosional distributary channels have been interpreted from 2D exposures of the Kaza Formation of the Windermere Group (Terlaky et al., 2016). However, channel density in the Kaza Formation apparently is inadequate to match that of LE1. In the Ross Formation of Ireland, feeder channels and incisional transient fan channels have been recognized and mapped, but not distributaries within lobes

(Elliott, 2000; MacDonald et al., 2011; Pyles et al., 2014; Pierce et al., 2018).

Likewise, in the Skoorsteenberg Formation of South Africa, probably the most extensively exposed lobate succession in the world, a distributary system is not recognized, at least not as conventional erosional channels (Hodgetts et al., 2004; Hodgson et al., 2006). The multiple feeder channels of the Ongeluk River outcrop of the Skoorsteenberg Formation might be considered proximal distributaries although they are absent in the rest of the outcrop belt (Johnson et al., 2001; Hodgetts et al., 2004; Hodgson et al., 2006). Instead, what are seen repeatedly within lobate deposits of the Skoorsteenberg Formation are scours and zones of bed amalgamation (Johnson et al., 2001; Hodgetts et al., 2004; Hodgson et al., 2006; Prélat et al., 2010; Hofstra et al., 2015). The lack of distinct channels can be compared to LE2 (Figures 6, 10), but there are few distinct features in LE2 to provide constraints.

Zones of bed amalgamation have been interpreted in the Skoorsteenberg Formation to represent the axes of distributive flows (depositional channels of Johnson et al., 2001). It is logical that zones of amalgamation represent locations of focused flow, and it is possible that these zones are present in a distributary pattern. Unfortunately, extensive work on these outcrops has not confirmed any particular pattern in map view (Hodgetts et al., 2004; Hodgson et al., 2006; Prélat et al., 2009). Also, it seems unlikely that the slight difference in the amount of mud within the preserved interbedded mud laminations of non-amalgamated areas versus zones of amalgamation would provide sufficient acoustic contrast to produce a channel image with distinct channel margins as displayed in reflection seismic images of LE1 (Figure 2).

Scours and zones of amalgamation also are common in other well exposed lobate deposits (e.g., Carr and Gardner, 2000; Elliott, 2000; Gardner et al., 2003; Remacha et al., 2005; MacDonald et al., 2011; Van der Merwe et al., 2014). In these systems, scours, or megaflutes, are interpreted to be local features rather than through going distributary channels (Elliott, 2000; Hodgson et al., 2006; MacDonald et al., 2011; Hofstra et al., 2016), although scours and scour trains (cyclic steps) have been proposed as possible channel precursors (Fildani et al., 2006; Maier et al., 2011; Armitage et al., 2012; Fildani et al., 2013; Maier et al., 2013; Covault et al., 2014; Covault et al., 2017).

Despite these challenges in determining the presence, absence, and distribution of distributaries in outcrop exposures, published illustrations of proposed models of unconfined units in outcrop routinely illustrate a few distributaries in the proximal lobe and none in the middle and distal lobe (e.g., Hirayama and Nakajima, 1977; Eschard et al., 2004; Hodgson, 2009; Prélat et al., 2010; Bernhardt et al., 2011; MacDonald et al., 2011; Brunt et al., 2013; Etienne et al., 2013; So et al., 2013; Grundvåg et al., 2014; Van der Merwe et al., 2014; Masalimova et al., 2016; Terlaky et al., 2016; Kane et al., 2017).

Classification

Normark (1970), Mutti and Ghibaudo (1972), and Normark (1978) loosely defined a lobe as part of a submarine fan consisting of a lobate sand-rich deposit at the distal end of a feeder channel and containing a distributary channel system in its

proximal part. However, lobate depositional bodies can be present at multiple scales with a variety of architectures and permeability structures. For flexibility, it seems advisable to use a broader definition of the term lobe and differentiate diverse architectures with a standardized set of descriptors such as “pervasively channelized lobe” or “unchannelized lobe.” This approach is flexible and can be adapted as new architectures are recognized. We are fully aware that the term “lobe” has been used to label a specific level within a hierarchy of lobate architectures (Prélat et al., 2009; Groeneweg et al., 2010; Mulder and Etienne, 2010; Prélat and Hodgson, 2013) defined by an empirical range of two-dimensional external dimensions (Prélat et al., 2009). We note that using a general and common morphological term such as lobe to describe one particular scale within a hierarchy of lobate bodies can cause confusion.

Hierarchy

The outcrop belt of lobate deposits that is most intensely studied and extensively exposed is the Skoorsteenberg Formation in the Tanqua Karoo Basin, South Africa (e.g., Johnson et al., 2001; Hodgson et al., 2006; Prélat et al., 2009; Groeneweg et al., 2010; Prélat and Hodgson, 2013). These deposits have been interpreted to display a hierarchy of tabular, lobate sandstone bodies that systematically increase in thickness and lateral extent with increasing rank. Furthermore, each higher rank within the sandstone hierarchy is separated by a siltstone unit that correspondingly also increases in thickness (Prélat et al., 2009), which is the fine-grained fringe of a body at the same hierarchical level (Prélat and Hodgson, 2013). This scheme has been adopted by other researchers for other lobate deposits (e.g., Mulder and Etienne, 2010; Grundvåg et al., 2014; Pierce et al., 2018).

Each unit within a hierarchical level is separated from the others by avulsion. A plan view map imaged by three-dimensional reflection seismic data is helpful for recognizing avulsions. However, it is difficult to assign a specific hierarchical term as defined by Prélat et al. (2009) based on reflection seismic data alone (i.e., without bed scale lithologic data) and thus it is not directly transferrable to the lobate units described here. Therefore, we choose to use the descriptive term “lobate” to refer to these seismically imaged examples.

LE1 Hierarchy

LE1 is a unit within a larger fan deposit (Prélat et al., 2010), suggesting that a hierarchical structure might be present. However, within LE 1 (Figure 1), many avulsions are imaged at many scales implying a large and unwieldy number of subordinate levels of hierarchy within the deposit. A distributary at one scale is a feeder channel at a finer scale and all lobate units, regardless of scale, are pervasively channelized. At multiple scales, each distributary channel avulses and feeds an additional cluster of distributary channels. Perhaps each channel cluster is analogous to a lobe in this case, or, an unchannelized and unresolved lobe is present at the distal end of each small distributary of each ultimate channel cluster. The latter option implies a very large number of strongly overlapping, unresolved, small lobes.

Perhaps, rather than a hierarchical architecture, LE1 has a fractal structure. Straub and Pyles (2012) provided a mechanism for testing hierarchical versus fractal structure with a modified compensational index. Unfortunately, this requires measurement of the thickness of all units at all scales and the vertical resolution of seismic profiles (**Figure 2**) of LE1 is inadequate for this purpose.

LE2 Hierarchy

LE2 is a solitary deposit, not a component of a larger submarine fan. Due to the absence of distributary channels and avulsions, the conventional basis for recognizing smaller hierarchical units within LE2 is lacking (**Figure 5**). Alternatively, because sediments enter LE2 from two entry points, the deposits derived from each entry point might form subunits within LE2. This setting is more likely to cause such subunits if the entry points were active at different times rather than simultaneously. Unfortunately, seismic resolution is inadequate to test this model. Interestingly, thin (meter scale) laterally offset lobate units within a potentially analogous deposit (Lobe X of Prather et al., 2012a; Jobe et al., 2017) have been confirmed with multiple cores. However, again, comparable lobate units, if present in LE2, are too thin to image with our available data.

LE3 Hierarchy

LE3 is a unit within a larger fan deposit (Saller et al., 2008), suggesting that a hierarchical structure might be present. The only recognized avulsion node of LE3 is located at the mouth of the feeder channel (**Figure 7**). The distributaries that diverge from that avulsion node might provide a basis for defining a hierarchy within LE3 if a separate lens of sediment is associated with each distributary. Unfortunately, no lense-shaped deposits are recognized unambiguously in cross-section within LE3 (**Figure 8**) perhaps due to limited vertical resolution. Consequently, the presence of an internal hierarchy within Lobate Example 3 remains speculative.

CONCLUSION

- 1) Three lobate examples (LE) presented here illustrate some diversity of lobate architectures and provide additional models to guide interpretation (**Figures 10, 11**).
- 2) Although speculative, we suggest a conceptual model for the morphology of lobate deposits and their associated channels as products of specific processes and mud concentration (**Figures 10–12**).
- 3) LE1: Relatively mud-rich turbidity currents produce levee-confined feeder channels, levee-confined proximal distributaries, and multiple secondary and tertiary distributaries with many branching points (**Figure 11A**).
- 4) LE2: Mud-poor turbulent flows, likely sourced from littoral drift, are prone to collapse and result in a lobate deposit with

scour features but no distributaries comparable to LE1 (**Figure 11B**).

- 5) LE3: Debris (viscous) flow dominated lobate features display straight, erosional feeder channels, a small number of straight distributary channels emanating from the mouth of the feeder channel, and minimal branching points (LE3, **Figure 11C**).
- 6) These lobate examples illustrate the important role of source material, basin margin physiography, and seabed topography in controlling the architecture of lobate features, and that these are important considerations in source-to-sink studies.
- 7) Outcrop analogs for the three lobate deposits described here are not obvious. For example, it is unclear if zones of amalgamation, which are common in outcrops of lobate deposits, will look like conventional channels or distributaries in horizon-referenced displays from 3D reflection seismic data or if they will be imaged at all.

DATA AVAILABILITY STATEMENT

The data analyzed in this study is subject to the following licenses/restrictions: The seismic data are petroleum company proprietary data to which we no longer have access. The illustrated images of seismic data are highly modified from previously published figures as referenced within the text. Requests to access these datasets should be directed to TM, timmmchar@stanford.edu.

AUTHOR CONTRIBUTIONS

TM is the principal author and primary seismic interpreter. DH interpreted the seismic data of example 3 and contributed significantly to writing and editing the paper. ES contributed significantly to discussions of processes involved in the deposition of the three examples, contributed significantly to writing and editing the paper, proposed the subaerial analog and secured the alluvial fan image used in **Figure 13**.

ACKNOWLEDGMENTS

The authors would like to thank Chevron Nigeria Ltd. and the Nigerian National Petroleum Co. for permission to publish data for this research. An earlier version of this paper was greatly improved by the thorough review by S. A. Grundvåg and an anonymous reviewer. The current version greatly benefited from reviews by R. Tinterri and Y. T. Sychala. The research was supported through the Stanford Project on Deepwater Depositional Systems by AERA, Anadarko, Aramco Services Company, California Resources Corporation, Chevron, Conoco-Phillips, Hess, Nexen, Pemex, PTTEP, RAG, Schlumberger, Shell, Woodside, and YPF, and the Lobe 3 Joint Industry Project by AkerBP, BHP, BP, Equinor, Hess, Neptune Energy, Petrobras, Petrochina, Total, Vår Energi, and Woodside.

REFERENCES

- Adeogba, A. A., McHargue, T. R., and Graham, S. A. (2005). Transient Fan Architecture and Depositional Controls from Near-Surface 3-D Seismic Data, Niger Delta continental Slope. *Bulletin* 89, 627–643. doi:10.1306/11200404025
- Alfaro, E., Holz, M., and Holz, M. (2014). Seismic Geomorphological Analysis of deepwater Gravity-Driven Deposits on a Slope System of the Southern Colombian Caribbean Margin. *Mar. Pet. Geology*. 57, 294–311. doi:10.1016/j.marpetgeo.2014.06.002
- Allen, J. R. L. (1965). Late Quaternary Niger Delta, and Adjacent Areas - Sedimentary Environments and Lithofacies. *Am. Assoc. Pet. Geologists Bull.* 49, 547–800.
- Armitage, D. A., McHargue, T., Fildani, A., and Graham, S. A. (2012). Postavulsion Channel Evolution: Niger Delta continental Slope. *Bulletin* 96, 823–843. doi:10.1306/09131110189
- Bakke, K., Kane, I. A., Martinsen, O. J., Petersen, S. A., Johansen, T. A., Hustoft, S., et al. (2013). Seismic Modeling in the Analysis of Deep-Water sandstone Termination Styles. *Bulletin* 97, 1395–1419. doi:10.1306/03041312069
- Barton, M. D. (2012). “Evolution of an Intra-slope Apron, Offshore Niger Delta Slope: Impact of Step Geometry on Apron Architecture,” in *Application of the Principles of Seismic Geomorphology to continental Slope and Base-Of-Slope Systems: Case Studies from Seafloor and Near-Seafloor Analogues*. Editors B. E. Prather, M. E. Deptuck, D. Mohrig, B. Van Hoorn, and R. B. Wynn (Tulsa, OK: SEPM Special Publication), 181–197. doi:10.2110/pec.12.99.0181
- Beaubouef, R. T., Rossen, C., Zelt, F. B., Sullivan, M. D., Mohrig, D. C., and Jennette, D. C. (1999). “Deep-Water Sandstones, Brushy Canyon Formation, West Texas,” in *AAPG Hedberg Field Research Conference* (Tulsa, Oklahoma, USA: American Association of Petroleum Geologists). doi:10.1306/ce40695
- Bell, D., Kane, I. A., Pontén, A. S. M., Flint, S. S., Hodgson, D. M., and Barrett, B. J. (2018). Spatial Variability in Depositional Reservoir Quality of Deep-Water Channel-Fill and Lobe Deposits. *Mar. Pet. Geology*. 98, 97–115. doi:10.1016/j.marpetgeo.2018.07.023
- Bernhardt, A., Jobe, Z. R., and Lowe, D. R. (2011). Stratigraphic Evolution of a Submarine Channel-Lobe Complex System in a Narrow Fairway within the Magallanes Foreland basin, Cerro Toro Formation, Southern Chile. *Mar. Pet. Geology*. 28, 785–806. doi:10.1016/j.marpetgeo.2010.05.013
- Biscara, L., Mulder, T., Hanquiez, V., Marieu, V., Crespin, J.-P., Braccini, E., et al. (2013). Morphological Evolution of Cap Lopez Canyon (Gabon): Illustration of Lateral Migration Processes of a Submarine canyon. *Mar. Geology*. 340, 49–56. doi:10.1016/j.marpetgeo.2013.04.014
- Bonnell, C., Dennielou, B., Droz, L., Mulder, T., and Berné, S. (2005). Architecture and Depositional Pattern of the Rhône Neofan and Recent Gravity Activity in the Gulf of Lions (Western Mediterranean). *Mar. Pet. Geology*. 22, 827–843. doi:10.1016/j.marpetgeo.2005.03.003
- Bourget, J., Zaragosi, S., Mulder, T., Schneider, J.-L., Garlan, T., Van Toer, A., et al. (2010). Hyperpynal-fed Turbidite Lobe Architecture and Recent Sedimentary Processes: A Case Study from the Al Batha Turbidite System, Oman Margin. *Sediment. Geology*. 229, 144–159. doi:10.1016/j.sedgeo.2009.03.009
- Brunt, R. L., Di Celma, C. N., Hodgson, D. M., Flint, S. S., Kavanagh, J. P., and van der Merwe, W. C. (2013). Driving a Channel through a Levee when the Levee Is High: An Outcrop Example of Submarine Down-Dip Entrenchment. *Mar. Pet. Geology*. 41, 134–145. doi:10.1016/j.marpetgeo.2012.02.016
- Burke, K. (1972). Longshore Drift, Submarine Canyons, and Submarine Fans in Development of Niger Delta. *Am. Assoc. Pet. Geologists Bull.* 56, 1975–1983.
- Cantelli, A., Pirmez, C., Johnson, S., and Parker, G. (2011). Morphodynamic and Stratigraphic Evolution of Self-Channelized Subaqueous Fans Emplaced by Turbidity Currents. *J. Sediment. Res.* 81, 233–247. doi:10.2110/jsr.2011.20
- Carr, M., and Gardner, M. H. (2000). “Portrait of a Basinfloor Fan for sandy deepwater Systems, Permian Lower Brushy Canyon Formation, West Texas,” in *Fine-grained Turbidite Systems*. Editors A. H. Bouma and C. G. Stone (American Association of Petroleum Geologists Memoir 72/SEPM Special Publication), 215–232.
- Carvajal, C., Paull, C. K., Caress, D. W., Fildani, A., Lundsten, E., Anderson, K., et al. (2017). Unraveling the Channel-Lobe Transition Zone with High-Resolution AUV Bathymetry: Navy Fan, Offshore Baja California, Mexico. *J. Sediment. Res.* 87, 1049–1059. doi:10.2110/jsr.2017.58
- Clark, J., and McHargue, T. (2007). *Stratigraphic and Spatial Changes in Channel Morphology Related to Deepwater Processes in Confined and Ponded Slope Mini-Basins, Angola*. Long Beach, California: American Association of Petroleum Geologists, AAPG Search and Discover Article #90063 AAPG Annual Convention.
- Covault, J. A., Kostic, S., Paull, C. K., Ryan, H. F., and Fildani, A. (2014). Submarine Channel Initiation, Filling and Maintenance from Sea-Floor Geomorphology and Morphodynamic Modelling of Cyclic Steps. *Sedimentology* 61, 1031–1054. doi:10.1111/sed.12084
- Covault, J. A., Kostic, S., Paull, C. K., Sylvester, Z., and Fildani, A. (2017). Cyclic Steps and Related Supercritical Bedforms: Building Blocks of Deep-Water Depositional Systems, Western North America. *Mar. Geology*. 393, 4–20. doi:10.1016/j.marpetgeo.2016.12.009
- Damuth, J. E. (1994). Neogene Gravity Tectonics and Depositional Processes on the Deep Niger Delta continental Margin. *Mar. Pet. Geology*. 11, 320–346. doi:10.1016/0264-8172(94)90053-1
- De Leeuw, J., Eggenhuisen, J. T., and Cartigny, M. J. (2016). Morphodynamics of Submarine Channel Inception Revealed by New Experimental Approach. *Nat. Commun.* 7 (1), 1–7. doi:10.1038/ncomms10886
- Dennielou, B., Droz, L., Babonneau, N., Jacq, C., Bonnel, C., Picot, M., et al. (2017). Morphology, Structure, Composition and Build-Up Processes of the Active Channel-Mouth Lobe Complex of the Congo Deep-Sea Fan with Inputs from Remotely Operated Underwater Vehicle (ROV) Multibeam and Video Surveys. *Deep Sea Res. Part Topical Stud. Oceanography* 142, 25–49. doi:10.1016/j.jdsr.2017.03.010
- Dennielou, B., Jallet, L., Sultan, N., Jouet, G., Giresse, P., Voisset, M., et al. (2009). Post-glacial Persistence of Turbiditic Activity within the Rhône Deep-Sea Turbidite System (Gulf of Lions, Western Mediterranean): Linking the Outer Shelf and the basin Sedimentary Records. *Mar. Geology*. 257, 65–86. doi:10.1016/j.marpetgeo.2008.10.013
- Deptuck, M. E., Piper, D. J. W., Savoye, B., and Gervais, A. (2008). Dimensions and Architecture of Late Pleistocene Submarine Lobes off the Northern Margin of East Corsica. *Sedimentology* 55, 869–898. doi:10.1111/j.1365-3091.2007.00926.x
- Doughty-Jones, G., Mayall, M., and Loneragan, L. (2017). Stratigraphy, Facies, and Evolution of Deep-Water Lobe Complexes within a Salt-Controlled Intraslope Minibasin. *Bulletin* 101, 1879–1904. doi:10.1306/01111716046
- Doust, H., and Omatsola, E. (1990). “Niger Delta,” in *Divergent/Passive Margin Basins*. Editors J. D. Edwards and P. A. Santagrossi (American Association of Petroleum Geologists Memoir), 201–238.
- Droz, L., Jégou, I., Gillet, H., Dennielou, B., Bez, M., Canals, M., et al. (2020). On the Termination of Deep-Sea Fan Channels: Examples from the Rhône Fan (Gulf of Lion, Western Mediterranean Sea). *Geomorphology* 369, 107368. doi:10.1016/j.geomorph.2020.107368
- Ducassou, E., Migeon, S. B., Mulder, T., Murat, A., Capotondi, L., Bernasconi, S. M., et al. (2009). Evolution of the Nile Deep-Sea Turbidite System during the Late Quaternary: Influence of Climate Change on Fan Sedimentation. *Sedimentology* 56, 2061–2090. doi:10.1111/j.1365-3091.2009.01070.x
- Egawa, K., Furukawa, T., Saeki, T., Suzuki, K., and Narita, H. (2013). Three-dimensional Paleomorphologic Reconstruction and Turbidite Distribution Prediction Revealing a Pleistocene Confined basin System in the Northeast Nankai Trough Area. *Bulletin* 97, 781–798. doi:10.1306/10161212014
- Elliott, T. (2000). “Depositional Architecture of a Sand-Rich, Channelized Turbidite System: The Upper Carboniferous Ross Sandstone Formation, Western Ireland,” in *Deep-Water Reservoirs of the World*. Editors P. Weimer, R. M. Slatt, J. Coleman, N. C. Rossen, H. Nelson, A. H. Bouma, et al. Gulf Coast Section SEPM Foundation 20th Annual Research Conference, Houston, TX, 342–373. doi:10.5724/gcs.00.15.0342
- Eschard, R., Albouy, E., Gaumet, F., and Ayub, A. (2004). Comparing the Depositional Architecture of basin Floor Fans and Slope Fans in the Pab Sandstone, Maastrichtian, Pakistan. *Geol. Soc. Lond. Spec. Publications* 222, 159–185. doi:10.1144/gsl.sp.2004.222.01.09
- Etienne, S., Mulder, T., Razin, P., Bez, M., Désaubliaux, G., Joussiaume, R., et al. (2013). Proximal to Distal Turbiditic Sheet-Sand Heterogeneities: Characteristics of Associated Internal Channels. Examples from the Trois Evêchés Area, Eocene-Oligocene Annot Sandstones (Grès d’Annot), SE France. *Mar. Pet. Geology*. 41, 117–133. doi:10.1016/j.marpetgeo.2012.03.007
- Ferguson, R. A., Kane, I. A., Eggenhuisen, J. T., Pohl, F., Tilston, M., Sychala, Y. T., et al. (2020). Entangled External and Internal Controls on Submarine Fan

- Evolution: an Experimental Perspective. *Depositional Rec.* 6 (3), 605–624. doi:10.1002/dep2.109
- Fernandez, R. L., Cantelli, A., Pirmez, C., Sequeiros, O., and Parker, G. (2014). Growth Patterns of Subaqueous Depositional Channel Lobe Systems Developed over a Basement with a Down-dip Break in Slope: Laboratory Experiments. *J. Sediment. Res.* 84, 168–182. doi:10.2110/jsr.2014.10
- Fildani, A., Hubbard, S. M., Covault, J. A., Maier, K. L., Romans, B. W., Traer, M., et al. (2013). Erosion at Inception of Deep-Sea Channels. *Mar. Pet. Geology* 41, 48–61. doi:10.1016/j.marpetgeo.2012.03.006
- Fildani, A., Normark, W. R., Kostic, S., and Parker, G. (2006). Channel Formation by Flow Stripping: Large-Scale Scour Features along the Monterey East Channel and Their Relation to Sediment Waves. *Sedimentology* 53, 1265–1287. doi:10.1111/j.1365-3091.2006.00812.x
- Flood, R. D., Pirmez, C., and Yin, H. (1997). “The Compressional-Wave Velocity of Amazon Fan Sediments: Calculation from Petrophysical Properties and Variation with clay Content,” in *Proceedings of the Ocean Drilling Project, Scientific Results 155*. R. D. Flood, D. J. W. Piper, A. Klaus, and L. C. Peterson (College Station, Texas: Ocean Drilling Program), 477–496.
- Fowler, J. N., Guritno, E., Sherwood, P., and Smith, M. J. (2001). IPA01-G-120. Depositional Architectures of Recent Deep Water Deposits in the Kutei Basin, East Kalimantan. In *Proceedings of the Annual Convention-Indonesian Petroleum Association* (Jakarta, Indonesia: Indonesian Petroleum Association), 409–422.
- Gamberi, F., and Rovere, M. (2011). Architecture of a Modern Transient Slope Fan (Villafranca Fan, Gioia basin-Southeastern Tyrrhenian Sea). *Sediment. Geology* 236, 211–225. doi:10.1016/j.sedgeo.2011.01.007
- Gardner, M. H., Borer, J. M., Melick, J. J., Mavilla, N., Dechesne, M., and Wagerle, R. N. (2003). Stratigraphic Process-Response Model for Submarine Channels and Related Features from Studies of Permian Brushy Canyon Outcrops, West Texas. *Mar. Pet. Geology* 20, 757–787. doi:10.1016/j.marpetgeo.2003.07.004
- Gervais, A., Savoye, B., Mulder, T., and Gonthier, E. (2006). Sandy Modern Turbidite Lobes: A New Insight from High Resolution Seismic Data. *Mar. Pet. Geology* 23, 485–502. doi:10.1016/j.marpetgeo.2005.10.006
- Gorsline, D. S., and Emery, K. O. (1959). Turbidity-current Deposits in San Pedro and Santa Monica Basins off Southern California. *Geol. Soc. America Bull.* 70, 279–290. doi:10.1130/0016-7606(1959)70[279:tdispa]2.0.co;2
- Groeneweg, R. M., Hodgson, D. M., Prêlat, A., Luthi, S. M., and Flint, S. S. (2010). Flow-Deposit Interaction in Submarine Lobes: Insights from Outcrop Observations and Realizations of a Process-Based Numerical Model. *J. Sediment. Res.* 80, 252–267. doi:10.2110/jsr.2010.028
- Grundvåg, S.-A., Johannessen, E. P., Helland-Hansen, W., and Plink-Björklund, P. (2014). Depositional Architecture and Evolution of Progradationally Stacked Lobe Complexes in the Eocene Central Basin of Spitsbergen. *Sedimentology* 61, 535–569. doi:10.1111/sed.12067
- Haas, T., Densmore, A. L., Hond, T., and Cox, N. J. (2019). Fan-Surface Evidence for Debris-Flow Avulsion Controls and Probabilities, Saline Valley, California. *J. Geophys. Res. Earth Surf.* 124, 1118–1138. doi:10.1029/2018jg004815
- Hadler-Jacobsen, F., Gardner, M. H., and Borer, J. M. (2007). “Seismic Stratigraphic and Geomorphic Analysis of Deep-marine Deposition along the West African continental Margin,” in *Seismic Geomorphology: Applications to Hydrocarbon Exploration and Production*. London. Editors R. J. Davies, H. W. Posamentier, L. J. Wood, and J. A. Cartwright (London: Geological Society Special Publication), 47–84. doi:10.1144/GSL.SP.2007.277.01.04
- Hadler-Jacobsen, F., Johannessen, E. P., Ashton, N., Henriksen, S., Johnson, S. D., and Kristensen, J. B. (2005). January. Submarine Fan Morphology and Lithology Distribution: a Predictable Function of Sediment Delivery, Gross Shelf-To-basin Relief, Slope Gradient and basin Topography. *Geol. Soc. Lond. Pet. Geology. Conf. Ser.* 6, 1121–1145. doi:10.1144/0061121
- Hamilton, P., Gaillet, G., Strom, K., Fedele, J., and Hoyal, D. (2017). Linking Hydraulic Properties in Supercritical Submarine Distributary Channels to Depositional-Lobe Geometry. *J. Sediment. Res.* 87, 935–950. doi:10.2110/jsr.2017.53
- Hanquiez, V., Mulder, T., Toucanne, S., Lecroart, P., Bonnel, C., Marchès, E., et al. (2010). The sandy Channel-Lobe Depositional Systems in the Gulf of Cadiz: Gravity Processes Forced by Contour Current Processes. *Sediment. Geology* 229, 110–123. doi:10.1016/j.sedgeo.2009.05.008
- Hansen, L. A., Callow, R. H., Kane, I. A., Gamberi, F., Rovere, M., Cronin, B. T., et al. (2015). Genesis and Character of Thin-Bedded Turbidites Associated With Submarine Channels. *Marine Petrol. Geol.* 67, 852–879.
- Hir, P. L., Cann, P., Waeles, B., Jestin, H., and Bassoullet, P. (2008). “Chapter 11 Erodibility of Natural Sediments: Experiments on Sand/mud Mixtures from Laboratory and Field Erosion Tests,” in *Proceedings in Marine Science 9*. Editors T. Kusuda, Y. Hiroyuki, J. Spearman, and J. Z. Gailani (Amsterdam: Elsevier), 137–153. doi:10.1016/s1568-2692(08)80013-7
- Hirayama, J., and Nakajima, T. (1977). Analytical Study of Turbidites, Otadai Formation, Boso Peninsula, Japan. *Sedimentology* 24, 747–779. doi:10.1111/j.1365-3091.1977.tb01914.x
- Hodgetts, D., Drinkwater, N. J., Hodgson, J., Kavanagh, J., Flint, S. S., Keogh, K. J., et al. (2004). “Three-dimensional Geological Models from Outcrop Data Using Digital Data Collection Techniques: an Example from the Tanqua Karoo Depocentre, South Africa,” in *Geological Prior Information: Informing Science and Engineering*. Editors A. C. Curtis and R. Wood (London: Geological Society Special Publication), 57–75. doi:10.1144/gsl.sp.2004.239.01.05
- Hodgson, D. M. (2009). Distribution and Origin of Hybrid Beds in Sand-Rich Submarine Fans of the Tanqua Depocentre, Karoo Basin, South Africa. *Mar. Pet. Geology* 26, 1940–1956. doi:10.1016/j.marpetgeo.2009.02.011
- Hodgson, D. M., Flint, S. S., Hodgetts, D., Drinkwater, N. J., Johannessen, E. P., and Luthi, S. M. (2006). Stratigraphic Evolution of fine-grained Submarine Fan Systems, Tanqua Depocenter, Karoo Basin, South Africa. *J. Sediment. Res.* 76, 20–40. doi:10.2110/jsr.2006.03
- Hodgson, D. M., Kane, I. A., Flint, S. S., Brunt, R. L., and Ortiz-Karpf, A. (2016). Time-transgressive Confinement on the Slope and the Progradation of basin-floor Fans: Implications for the Sequence Stratigraphy of Deep-Water Deposits. *J. Sediment. Res.* 86 (1), 73–86. doi:10.2110/jsr.2016.3
- Hofstra, M., Hodgson, D. M., Peakall, J., and Flint, S. S. (2015). Giant Scour-Fills in Ancient Channel-Lobe Transition Zones: Formative Processes and Depositional Architecture. *Sediment. Geology* 329, 98–114. doi:10.1016/j.sedgeo.2015.09.004
- Hofstra, M., Pontén, A. S. M., Peakall, J., Flint, S. S., Nair, K. N., and Hodgson, D. M. (2017). The Impact of fine-scale Reservoir Geometries on Streamline Flow Patterns in Submarine Lobe Deposits Using Outcrop Analogues from the Karoo Basin. *Pet. Geosci.* 23, 159–176. doi:10.1144/petgeo.2016.087
- Howlett, D. M., Gawthorpe, R. L., Ge, Z., Rotevatn, A., and Jackson, C. A. L. (2020). Turbidites, Topography and Tectonics: Evolution of Submarine Channel-lobe Systems in the Salt-influenced Kwanza Basin, Offshore Angola. *Basin Res.*
- Imhansiolewa, T. M., Akintoye, A. E., Mayowa, I. P., Abdulkarim, R., Oguwuike, I. D., Olubukola, S., et al. (2011). Numerical Assessment and Analysis of Textural Deposits of beach Sediment: A Case Study of Ajah (Okun Mopo) Beach Lagos South West Nigeria. *Nat. Sci.* 9, 165–174.
- Jegou, I., Savoye, B., Pirmez, C., and Droz, L. (2008). Channel-mouth Lobe Complex of the Recent Amazon Fan: the Missing Piece. *Mar. Geology* 252, 62–77. doi:10.1016/j.margeo.2008.03.004
- Jobe, Z. R., Sylvester, Z., Howes, N., Pirmez, C., Parker, A., Cantelli, A., et al. (2017). High-resolution, Millennial-Scale Patterns of Bed Compensation on a Sand-Rich Intraslope Submarine Fan, Western Niger Delta Slope. *Geol. Soc. America Bull.* 129, 23–37. doi:10.1130/b31440.1
- Jobe, Z. R., Sylvester, Z., Pirmez, C., Prather, B., El-Gawad, S. A., Minisini, D., et al. (2014). Ultra-high Resolution Modern Analog Dataset from the Western Niger Delta Slope: Facies Architecture and Application to Turbidite Reservoirs. *Gulf Coast Assoc. Geol. Societies Trans.* 64, 543–546.
- Johann, P., de Castro, D. D., and Barroso, A. S. (2001). Reservoir Geophysics: Seismic Pattern Recognition Applied to Ultra-deepwater Oilfield in Campos basin, Offshore Brazil. In *SPE Latin American and Caribbean Petroleum Engineering Conference*, Buenos Aires, Argentina (Richardson, TX: Society of Petroleum Engineers SPE), 69483. doi:10.2118/69483-MS
- Johnson, S. D., Flint, S., Hinds, D., and De Ville Wickens, H. (2001). Anatomy, Geometry and Sequence Stratigraphy of basin Floor to Slope Turbidite Systems,

- Tanqua Karoo, South Africa. *Sedimentology* 48, 987–1023. doi:10.1046/j.1365-3091.2001.00405.x
- Jones, D. W., Large, S., McQueen, A., and Helmi, A. (2015). Reservoir Geology of the Paleocene Forties Sandstone Member in the Fram Discovery, UK Central North Sea. *Geol. Soc. Lond. Spec. Publications* 403, 219–246. doi:10.1144/sp403.13
- Kane, I. A., Pontén, A. S. M., Vangdal, B., Eggenhuisen, J. T., Hodgson, D. M., and Sychala, Y. T. (2017). The Stratigraphic Record and Processes of Turbidity Current Transformation across Deep-marine Lobes. *Sedimentology* 64, 1236–1273. doi:10.1111/sed.12346
- Ketzer, J. M., Carpentier, B., Le Gallo, Y., and Le Thiez, P. (2005). Geological Sequestration of CO₂ in Mature Hydrocarbon Fields. Basin and Reservoir Numerical Modelling of the Forties Field, North Sea. *Oil Gas Sci. Tech. Rev. IFP* 60, 259–273. doi:10.2516/ogst.2005016
- Kidd, G. D. (1999). Fundamentals of 3-D Seismic Volume Visualization. *The Leading Edge* 18, 702–709. doi:10.1190/1.1438362
- Kneller, B., and Buckee, C. (2000). The Structure and Fluid Mechanics of Turbidity Currents: A Review of Some Recent Studies and Their Geological Implications. *Sedimentology* 47, 62–94.
- Lowry, P., Jenkins, C. D., and Phelps, D. J. (1993). January. Reservoir Scale Sandbody Architecture of Pliocene Turbidite Sequences, Long Beach Unit, Wilmington Oil Field, California. In SPE Annual Technical Conference and Exhibition, Houston, TX (Richardson, TX: Society of Petroleum Engineers), 26440. doi:10.2118/26440-ms
- MacDonald, H. A., Peakall, J., Wignall, P. B., and Best, J. (2011). Sedimentation in Deep-Sea Lobe-Elements: Implications for the Origin of Thickening-Upward Sequences. *J. Geol. Soc.* 168, 319–332. doi:10.1144/0016-76492010-0361
- Maier, K. L., Fildani, A., McHargue, T. R., Paull, C. K., Graham, S. A., and Caress, D. W. (2012). Punctuated Deep-Water Channel Migration: High-Resolution Subsurface Data from the Lucia Chica Channel System, Offshore California, U.S.A. *J. Sediment. Res.* 82, 1–8. doi:10.2110/jsr.2012.10
- Maier, K. L., Fildani, A., Paull, C. K., Graham, S. A., McHargue, T. R., Caress, D. W., et al. (2011). The Elusive Character of Discontinuous Deep-Water Channels: New Insights from Lucia Chica Channel System, Offshore California. *Geology* 39, 327–330. doi:10.1130/g31589.1
- Maier, K. L., Fildani, A., Paull, C. K., McHargue, T. R., Graham, S. A., and Caress, D. W. (2013). Deep-sea Channel Evolution and Stratigraphic Architecture from Inception to Abandonment from High-Resolution Autonomous Underwater Vehicle Surveys Offshore central California. *Sedimentology* 60, 935–960. doi:10.1111/j.1365-3091.2012.01371.x
- Maier, K. L., Paull, C. K., Caress, D. W., Anderson, K., Nieminski, N. M., Lundsten, E., et al. (2020). Submarine-fan Development Revealed by Integrated High-Resolution Datasets from La Jolla Fan, Offshore California, U.S.A. *J. Sediment. Res.* 90 (5), 468–479. doi:10.2110/jsr.2020.22
- Maier, K. L., Roland, E. C., Walton, M. A. L., Conrad, J. E., Brothers, D. S., Dartnell, P., et al. (2018). The Tectonically Controlled San Gabriel Channel-Lobe Transition Zone, Catalina Basin, Southern California Borderland. *J. Sediment. Res.* 88, 942–959. doi:10.2110/jsr.2018.50
- Martinsen, O. J., Lien, T., Walker, R. G., and Lien, T. (2000). “Upper Carboniferous Deep Water Sediments, Western Ireland: Analogues for Passive Margin Turbidite Plays,” in *Deep-Water Reservoirs of the World. Gulf Coast Section SEPM 20th Bob F. Perkins Research Conference*. Editors P. Weimer, R. M. Slatt, J. Coleman, N. C. Rosen, H. Nelson, A. H. Bouma, et al. 533–555. doi:10.5724/gcs.00.15.0533
- Masalimova, L. U., Lowe, D. R., Sharman, G. R., King, P. R., and Arnot, M. J. (2016). Outcrop Characterization of a Submarine Channel-Lobe Complex: the Lower Mount Messenger Formation, Taranaki Basin, New Zealand. *Mar. Pet. Geology* 71, 360–390. doi:10.1016/j.marpetgeo.2016.01.004
- McHargue, T., Pyrcz, M. J., Sullivan, M. D., Clark, J. D., Fildani, A., Romans, B. W., et al. (2011). Architecture of Turbidite Channel Systems on the continental Slope: Patterns and Predictions. *Mar. Pet. Geology* 28, 728–743. doi:10.1016/j.marpetgeo.2010.07.008
- Métivier, F., Lajeunesse, E., and Cacas, M.-C. (2005). Submarine Canyons in the Bathub. *J. Sediment. Res.* 75, 6–11. doi:10.2110/jsr.2005.002
- Migeon, S., Ducassou, E., Le Gonidec, Y., Rouillard, P., Mascle, J., and Revel-Rolland, M. (2010). Lobe Construction and Sand/mud Segregation by Turbidity Currents and Debris Flows on the Western Nile Deep-Sea Fan (Eastern Mediterranean). *Sediment. Geology* 229, 124–143. doi:10.1016/j.sedgeo.2010.02.011
- Mulder, T., and Etienne, S. (2010). Lobes in Deep-Sea Turbidite Systems: State of the Art. *Sediment. Geology* 229, 75–80. doi:10.1016/j.sedgeo.2010.06.011
- Mutti, E. (1977). Distinctive Thin-Bedded Turbidite Facies and Related Depositional Environments in the Eocene Hecho Group (South-central Pyrenees, Spain). *Sedimentology* 24, 107–131. doi:10.1111/j.1365-3091.1977.tb00122.x
- Mutti, E., and Ghibaudo, G. (1972). Un esempio di torbiditi di conoide sottomarina esterna: le Arenarie di San Salvatore (Formazione di Bobbio, Miocene) nell’Appennino di Piacenza. Torino, Italy: Accademia delle scienze, 40.
- Mutti, E., and Normark, W. R. (1987). “Comparing Examples of Modern and Ancient Turbidite Systems: Problems and Concepts,” in *Marine Clastic Sedimentology* (Dordrecht: Springer), 1–38. doi:10.1007/978-94-009-3241-8_1
- Mutti, E., and Ricci Lucchi, F. (1972). Le torbiditi del Appennino settentrionale: introduzione all’analisi di facies. *Memorie Società. Geologica Italiana* 11, 161–199.
- Mutti, E., and Sonnino, M. (1981). *Compensation Cycles: A Diagnostic Feature of Turbidite sandstone Lobes*. Bologna, Italy: International Association of Sedimentologists, 2nd European Regional Meeting, 120–123.
- Normark, W. R. (1978). Fan Valleys, Channels and Depositional Lobes on Modern Submarine Fans: Characteristics for Recognition of sandy Turbidite Environments. *Am. Assoc. Pet. Geologists Bull.* 62, 912–931.
- Normark, W. R. (1970). Growth Patterns of Deep Sea Fans. *Am. Assoc. Pet. Geologists Bull.* 54, 2170–2195.
- O’Connell, S., Ryan, W. B., and Normark, W. R. (1991). “Evolution of a Fan Channel on the Surface of the Outer Mississippi Fan: Evidence from Side-Looking Sonar,” in *Seismic Facies and Sedimentary Processes of Submarine Fans and Turbidite Systems*. Editors P. Weimer and M. H. Link (New York: Springer), 365–381.
- Oluboyo, A. P., Gawthorpe, R. L., Bakke, K., and Hadler-Jacobsen, F. (2014). Salt Tectonic Controls on Deep-Water Turbidite Depositional Systems: Miocene, Southwestern Lower Congo Basin, Offshore Angola. *Basin Res.* 26, 597–620. doi:10.1111/bre.12051
- Paumard, V., Bourget, J., Payenberg, T., George, A. D., Ainsworth, R. B., Lang, S., et al. (2020). Controls on Deep-Water Sand Delivery beyond the Shelf Edge: Accommodation, Sediment Supply, and Deltaic Process Regime. *J. Sediment. Res.* 90 (1), 104–130. doi:10.2110/jsr.2020.2
- Peakall, J., McCaffrey, B., and Kneller, B. (2000). A Process Model for the Evolution, Morphology, and Architecture of Sinuous Submarine Channels. *J. Sediment. Res.* 70 (3), 434–448.
- Picot, M., Droz, L., Marsset, T., Dennielou, B., and Bez, M. (2016). Controls on Turbidite Sedimentation: Insights from a Quantitative Approach of Submarine Channel and Lobe Architecture (Late Quaternary Congo Fan). *Mar. Pet. Geology* 72, 423–446. doi:10.1016/j.marpetgeo.2016.02.004
- Pierce, C. S., Haughton, P. D. W., Shannon, P. M., Pulham, A. J., Barker, S. P., and Martinsen, O. J. (2018). Variable Character and Diverse Origin of Hybrid Event Beds in a sandy Submarine Fan System, Pennsylvanian Ross Sandstone Formation, Western Ireland. *Sedimentology* 65, 952–992. doi:10.1111/sed.12412
- Pirmez, C., Beaubouef, R. T., Friedmann, S. J., and Mohrig, D. C. (2000). “Equilibrium Profile and Baselevel in Submarine Channels: Examples from Late Pleistocene Systems and Implications for the Architecture of Deepwater Reservoirs,” in *Deep-water Reservoir of the World*. Editors P. Weimer, R. M. Slatt, A. H. Bouma, and D. T. Lawrence Gulf Coast Section SEPM Foundation 20th Annual Research Conference, Houston, TX, 782–805. doi:10.5724/gcs.00.15.0782
- Posamentier, H. W., and Kolla, V. (2003). Seismic Geomorphology and Stratigraphy of Depositional Elements in Deep-Water Settings. *J. Sediment. Res.* 73, 367–388. doi:10.1306/111302730367
- Posamentier, H. W., Wisman, P. S., and Plawman, T. (2000). “Deep Water Depositional Systems-Ultra-Deep Makassar Strait, Indonesia,” in *Deep-Water Reservoirs of the World: Gulf Coast Society of the Society of Economic Paleontologists and Mineralogists Foundation, 20th Annual Research*

- Conference. Editors P. Weimer, R. M. Slatt, J. Coleman, N. C. Rosen, H. Nelson, A. H. Bouma, et al. 806–816. doi:10.5724/gcs.00.15.0806
- Prather, B. E., Booth, J. R., Steffens, G. S., and Craig, P. A. (1998). Classification, Lithologic Calibration and Stratigraphic Succession of Seismic Facies from Intraslope Basins, Deep Water Gulf of Mexico. *U.S.A. Am. Assoc. Pet. Geologists Bull.* 82, 701–728.
- Prather, B. E. (2000). Calibration and Visualization of Depositional Process Models for Above-Grade Slopes: a Case Study from the Gulf of Mexico. *Mar. Pet. Geology*. 17, 619–638. doi:10.1016/s0264-8172(00)00015-5
- Prather, B. E. (2003). Controls on Reservoir Distribution, Architecture and Stratigraphic Trapping in Slope Settings. *Mar. Pet. Geology*. 20, 529–545. doi:10.1016/j.marpetgeo.2003.03.009
- Prather, B. E., Pirmez, C., Sylvester, Z., and Prather, D. S. (2012a). “Stratigraphic Response to Evolving Geomorphology in a Submarine Apron Perched on the Upper Niger Delta Slope,” in *Application of the Principles of Seismic Geomorphology to continental Slope and Base-Of-Slope Systems: Case Studies from Seafloor and Near-Seafloor Analogues*. Editors B. E. Prather, M. E. Deptuck, D. Mohrig, B. Van Hoorn, and R. B. Wynn (Tulsa, OK: SEPM Special Publication), 145–161. doi:10.2110/pec.12.99.0145
- Prather, B. E., Pirmez, C., Winker, C. D., Deptuck, M. E., and Mohrig, D. (2012b). Stratigraphy of Linked Intraslope Basins: Brazos-Trinity System Western Gulf of Mexico. *SEPM, Spec. Publ.* 99, 83–109. doi:10.2110/pec.12.99.0083
- Prélat, A., Covault, J. A., Hodgson, D. M., Fildani, A., and Flint, S. S. (2010). Intrinsic Controls on the Range of Volumes, Morphologies, and Dimensions of Submarine Lobes. *Sediment. Geology*. 232, 66–76. doi:10.1016/j.sedgeo.2010.09.010
- Prélat, A., Hodgson, D. M., and Flint, S. S. (2009). Evolution, Architecture and Hierarchy of Distributary Deep-water Deposits: a High-resolution Outcrop Investigation from the Permian Karoo Basin, South Africa. *Sedimentology* 56, 2132–2154. doi:10.1111/j.1365-3091.2009.01073.x
- Prélat, A., and Hodgson, D. M. (2013). The Full Range of Turbidite Bed Thickness Patterns in Submarine Lobes: Controls and Implications. *J. Geol. Soc.* 170, 209–214. doi:10.1144/jgs2012-056
- P. Weimer, R. M. Slatt, J. Coleman, N. C. Rossen, H. Nelson, A. H. Bouma, et al. (2000). “Deep-water Reservoirs of the World,” in Gulf Coast Section SEPM Foundation 20th Annual Research Conference, Houston, TX.
- Pyles, D. R., and Jennette, D. C. (2009). Geometry and Architectural Associations of Co-genetic Debrite-Turbidite Beds in basin-margin Strata, Carboniferous Ross Sandstone (Ireland): Applications to Reservoirs Located on the Margins of Structurally Confined Submarine Fans. *Mar. Pet. Geology*. 26, 1974–1996. doi:10.1016/j.marpetgeo.2009.02.018
- Pyles, D. R., Strachan, L. J., and Jennette, D. C. (2014). Lateral Juxtapositions of Channel and Lobe Elements in Distributive Submarine Fans: Three-Dimensional Outcrop Study of the Ross Sandstone and Geometric Model. *Geosphere* 10, 1104–1122. doi:10.1130/ges01042.1
- Reading, H. G., and Richards, M. (1994). Turbidite Systems in Deep-Water basin Margins Classified by Grain Size and Feeder System. *Am. Assoc. Pet. Geologists Bull.* 78, 792–822.
- Remacha, E., Fernandez, L. P., and Maestro, E. (2005). The Transition between Sheet-like Lobe and basin-plain Turbidites in the Hecho Basin (South-Central Pyrenees, Spain). *J. Sediment. Res.* 75, 798–819. doi:10.2110/jsr.2005.064
- Rowland, J. C., Hilley, G. E., and Fildani, A. (2010). A Test of Initiation of Submarine Leveed Channels by Deposition Alone. *J. Sediment. Res.* 80, 710–727. doi:10.2110/jsr.2010.067
- Ruzuar, A. P., Schneider, R., Saller, A. H., and Noah, J. T., 2005. Linked Lowstand Delta to Basin-Floor Fan Deposition, Offshore East Kalimantan: An Analogue for Deep-Water Reservoir Systems. Proceedings, Indonesian Petroleum Association Thirtieth Annual Convention and Exhibition, 2005. 467–481.
- Saller, A., Dharmasamadhi, I. N. W., Lilburn, T., and Ryan, E. (2010). “Seismic Geomorphology of Submarine Slopes: Channel-Levee Complexes versus Slope Valleys and Canyons, Pleistocene, East Kalimantan, Indonesia,” in *Seismic Imaging of Depositional and Geomorphic Systems. Gulf Coast Section SEPM, 30th Annual Conference*. Editors L. J. Wood, T. T. Simo, and N. C. Rosen, 433–471. doi:10.5724/gcs.10.30.0433
- Saller, A. H., Noah, J. T., Ruzuar, A. P., and Schneider, R. (2004). Linked Lowstand delta to basin-floor Fan Deposition, Offshore Indonesia: An Analog for Deep-Water Reservoir Systems. *Bulletin* 88, 21–46. doi:10.1306/09030303003
- Saller, A. H., Noah, J. T., Schneider, R., and Ruzuar, A. P., 2003. Lowstand Deltas and a Basin-Floor Fan, Pleistocene, Offshore East Kalimantan, Indonesia. In: Margin deltas and linked down slope petroleum systems: Global significance and future exploration potential. Gulf Coast Section SEPM Foundation 23rd Annual Bob F. Perkins Research Conference. 421–439. doi:10.5724/gcs.03.23.0421
- Saller, A., Werner, K., Sugiaman, F., Cebastian, A., May, R., Glenn, D., et al. (2008). Characteristics of Pleistocene Deep-Water Fan Lobes and Their Application to an Upper Miocene Reservoir Model, Offshore East Kalimantan, Indonesia. *Bulletin* 92, 919–949. doi:10.1306/03310807110
- Shanmugam, G., Shrivastava, S. K., and Das, B. (2009). Sandy Debrites and Tidalites of Pliocene Reservoir Sands in Upper-Slope Canyon Environments, Offshore Krishna-Godavari Basin (India): Implications. *J. Sediment. Res.* 79, 736–756. doi:10.2110/jsr.2009.076
- So, Y. S., Rhee, C. W., Choi, P.-Y., Kee, W.-S., Seo, J. Y., and Lee, E.-J. (2013). Distal Turbidite Fan/lobe Succession of the Late Paleozoic Taean Formation, Western Korea. *Geosci. J.* 17, 9–25. doi:10.1007/s12303-013-0016-0
- Spychala, Y. T., Hodgson, D. M., Flint, S. S., and Mountney, N. P. (2015). Constraining the Sedimentology and Stratigraphy of Submarine Intraslope Lobe Deposits Using Exhumed Examples from the Karoo Basin, South Africa. *Sediment. Geology*. 322, 67–81. doi:10.1016/j.sedgeo.2015.03.013
- Steffens, G. S., Biegert, E. K., Scott Sumner, H., and Bird, D. (2003). Quantitative Bathymetric Analyses of Selected deepwater Siliciclastic Margins: Receiving basin Configurations for deepwater Fan Systems. *Mar. Pet. Geology*. 20, 547–561. doi:10.1016/j.marpetgeo.2003.03.007
- Stow, D. A. V. (1986). “Deep Clastic Seas,” in *Sedimentary Environments and Facies*. Editor H. G. Reading (Oxford: Blackwell Scientific Publications), 399–444.
- Stow, D. A. V. (1985). “Deep-sea Clastics: where Are We and where Are We Going?,” in *Sedimentology: Recent Developments and Applied Aspects*. Editors P. J. Brenchley and B. P. J. Williams (London: Geological Society [London] Special Publication), 67–93. doi:10.1144/gsl.sp.1985.018.01.05
- Straub, K. M., and Pyles, D. R. (2012). Quantifying the Hierarchical Organization of Compensation in Submarine Fans Using Surface Statistics. *J. Sediment. Res.* 82 (11), 889–898. doi:10.2110/jsr.2012.73
- Sullivan, M., Jensen, G., Goulding, F., Jennette, D., Foreman, L., and Stern, D. (2000). “Architectural Analysis of Deep-Water Outcrops: Implications for Exploration and Development of the Diana Sub-Basin, Western Gulf of Mexico,” in *Deep-Water Reservoirs of the World. Gulf Coast Section SEPM 20th Bob F. Perkins Research Conference*. Editors P. Weimer, R. M. Slatt, J. Coleman, N. C. Rosen, H. Nelson, A. H. Bouma, et al. 1010–1031. doi:10.5724/gcs.00.15.1010
- Sylvester, Z., Deptuck, M. E., Prather, B. E., Pirmez, C., and O’Byrne, C. (2012). “Seismic Stratigraphy of a Shelf-Edge delta and Linked Submarine Channels in the Northeastern Gulf of Mexico,” in *Application of the Principles of Seismic Geomorphology to continental Slope and Base-Of-Slope Systems: Case Studies from Seafloor and Near-Seafloor Analogues*. Editors B. E. Prather, M. E. Deptuck, D. Mohrig, B. Van Hoorn, and R. B. Wynn (Tulsa, OK: SEPM Special Publication), 31–59. doi:10.2110/pec.12.99.0031
- Terlaky, V., Rocheleau, J., and Arnott, R. W. C. (2016). Stratal Composition and Stratigraphic Organization of Stratal Elements in an Ancient Deep-marine basin-floor Succession, Neoproterozoic Windermere Supergroup, British Columbia, Canada. *Sedimentology* 63, 136–175. doi:10.1111/sed.12222
- Twichell, D. C., Schwab, W. C., Nelson, C. H., Kenyon, N. H., and Lee, H. J. (1992). Characteristics of a sandy Depositional Lobe on the Outer Mississippi Fan from SeaMARC IA Sidescan Sonar Images. *Geol.* 20, 689–692. doi:10.1130/0091-7613(1992)020<0689:coasdl>2.3.co;2
- Twichell, D., Nelson, C. H., Kenyon, N., and Schwab, W. (2009). “The Influence of External Processes on the Holocene Evolution of the Mississippi Fan,” in *External Controls on Deepwater Depositional Systems*. Editors B. Kneller, O. J. Martinsen, and W. D. McCaffrey (Tulsa, OK: SEPM Special Publication), 145–157. doi:10.2110/sepmssp.092.145

- Van der Merwe, W. C., Hodgson, D. M., Brunt, R. L., and Flint, S. S. (2014). Depositional Architecture of Sand-Attached and Sand-Detached Channel-Lobe Transition Zones on an Exhumed Stepped Slope Mapped over a 2500 Km² Area. *Geosphere* 10, 1076–1093. doi:10.1130/GES0103510.1130/ges01035.1
- Walker, R. G. (1978). Deep-water sandstone Facies and Ancient Submarine Fans: Models for Exploration for Stratigraphic Traps. *Am. Assoc. Pet. Geologists Bull.* 62, 932–966.
- Yang, S.-Y., and Kim, J. W. (2014). Pliocene basin-floor Fan Sedimentation in the Bay of Bengal (Offshore Northwest Myanmar). *Mar. Pet. Geology*. 49, 45–58. doi:10.1016/j.marpetgeo.2013.09.007

Conflict of Interest: The authors declare that the research was conducted in the absence of any commercial or financial relationships that could be construed as a potential conflict of interest.

Publisher's Note: All claims expressed in this article are solely those of the authors and do not necessarily represent those of their affiliated organizations, or those of the publisher, the editors and the reviewers. Any product that may be evaluated in this article, or claim that may be made by its manufacturer, is not guaranteed or endorsed by the publisher.

Copyright © 2021 McHargue, Hodgson and Shelef. This is an open-access article distributed under the terms of the Creative Commons Attribution License (CC BY). The use, distribution or reproduction in other forums is permitted, provided the original author(s) and the copyright owner(s) are credited and that the original publication in this journal is cited, in accordance with accepted academic practice. No use, distribution or reproduction is permitted which does not comply with these terms.



Seismic Characteristics of Paleo-Pockmarks in the Great South Basin, New Zealand

Arunee Karaket¹, Piyaphong Chenrai^{1,2*} and Mads Huuse³

¹Basin Analysis and Structural Evolution Research Unit (BASE RU), Department of Geology, Faculty of Science, Chulalongkorn University, Bangkok, Thailand, ²M.Sc. Program in Petroleum Geoscience, Faculty of Science, Chulalongkorn University, Bangkok, Thailand, ³Department of Earth and Environmental Sciences, University of Manchester, Manchester, United Kingdom

OPEN ACCESS

Edited by:

Adam McArthur,
University of Leeds, United Kingdom

Reviewed by:

Jess I T Hillman,
GNS Science, New Zealand
Ben Kilhams,
Shell, United Kingdom

*Correspondence:

Piyaphong Chenrai
piyaphong.c@chula.ac.th

Specialty section:

This article was submitted to
Sedimentology, Stratigraphy and
Diagenesis,
a section of the journal
Frontiers in Earth Science

Received: 21 March 2021

Accepted: 08 July 2021

Published: 30 August 2021

Citation:

Karaket A, Chenrai P and Huuse M
(2021) Seismic Characteristics of
Paleo-Pockmarks in the Great South
Basin, New Zealand.
Front. Earth Sci. 9:683617.
doi: 10.3389/feart.2021.683617

Globally, a wide range of pockmarks have been identified onshore and offshore. These features can be used as indicators of fluid expulsion through unconsolidated sediments within sedimentary basin-fills. The Great South Basin, New Zealand, is one such basin where paleo-pockmarks are observed at around 1,500 m below the seabed. This study aims to describe the characteristics of paleo-pockmarks in the Great South Basin. Numerous paleo-pockmarks are identified and imaged using three-dimensional seismic reflection data and hosted by fine-grained sediments of the Middle Eocene Laing Formation. The paleo-pockmarks are aligned in a southwest to northeast direction to form a fan-shaped distribution with a high density of around 67 paleo-pockmarks per square kilometre in the centre of the study area. The paleo-pockmarks in this area have a similar shape, varying from sub-rounded to a rounded planform shape, but vary in size, ranging from 138 to 481 m in diameter, and 15–45 ms (TWT) depth. The origin of the fluids that contributed to the paleo-pockmark formation is suggested, based on seismic observations, to be biogenic methane. The basin floor fan deposits beneath the interval hosting the paleo-pockmark might have enhanced fluid migration through permeable layers in this basin-fill. This model can help to explain pockmark formation in deep water sedimentary systems, and may inform future studies of fluid migration and expulsion in sediment sinks.

Keywords: paleo-pockmark, seismic interpretation, great south basin, biogenic methane, fluid expulsion

INTRODUCTION

Sediment remobilization and fluid flow features have been discovered on the present-day surface and subsurface in several geological settings worldwide (Pecher et al., 2001; Loncke et al., 2004; Cartwright, 2007; Plaza-Faverola et al., 2011; Anka et al., 2013; Luo et al., 2014). Fluid flow features, such as pipes, mud volcanoes, pockmarks, and polygonal fault systems on the seabed, and in the subsurface, have gained significant attention over the last few decades because of their relevance to hydrocarbon exploration and production, local biodiversity, and as a source of greenhouse gases in the atmosphere (Berndt, 2005; Judd and Hovland, 2007; Huuse et al., 2010; Andresen, 2012; Karstens and Berndt, 2015). Since fluid flow features have been identified in sedimentary basin-fills worldwide, including both passive and active continental margins, they have been applied in petroleum exploration as a hydrocarbon indicator (e.g., Hovland and Judd, 1988; Hurst et al., 2003; Andresen, 2012). However, the possible fluid types can be liquids, gases, or mixtures of any

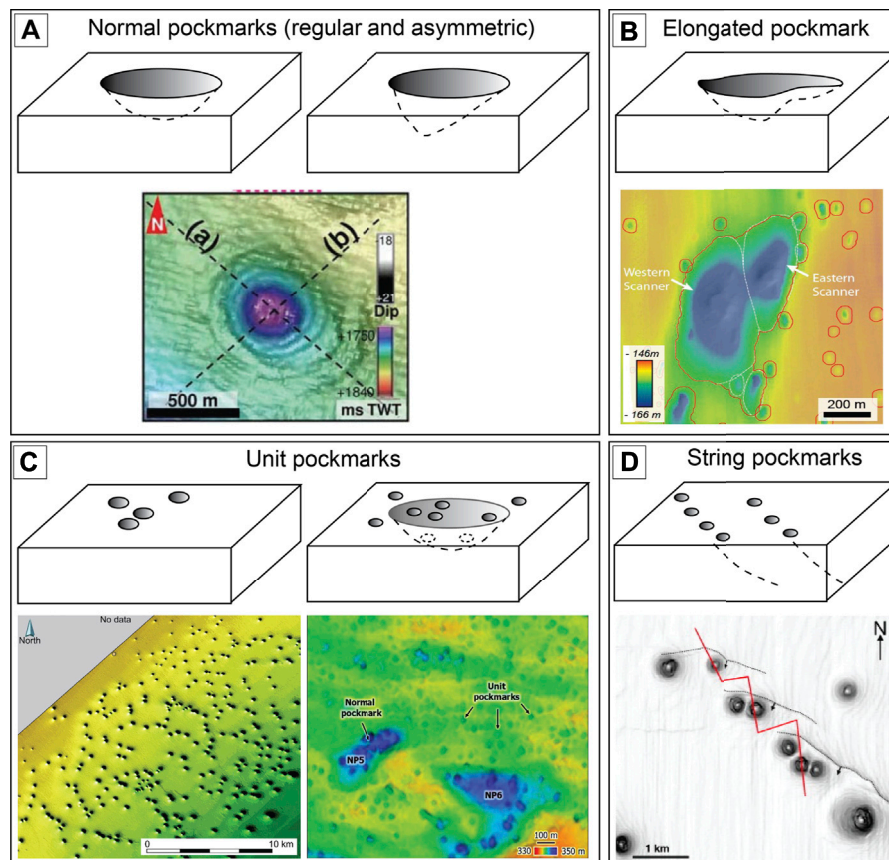


FIGURE 1 | The main classes of pockmarks are modified from Hovland et al. (2002). **(A)** Normal pockmarks, including regular and asymmetric shapes, and a top view of a normal pockmark (Ho et al., 2018); **(B)** top view of an elongated pockmark (Gafeira et al., 2018); **(C)** perspective view of unit pockmarks, with and without a “parental” normal pockmark (de Mahiques et al., 2017; Tasianan et al., 2018); and **(D)** top view of string pockmarks (Pilcher and Argent, 2007).

composition derived from within the Earth’s crust (Hovland and Judd, 1988; Judd and Hovland, 2007) such as hydrothermal fluid (Pickrill, 1993; Dimitrov and Woodside, 2003), fresh water (Hübscher and Borowski, 2006), and pore water (Cartwright et al., 2004). Despite many studies of detailed seismic characteristics that have these features, the fluids involved in the origin are still subject to debate, with many studies inferring that hydrocarbons are the main source of fluids contributing to these features (e.g., Gay et al., 2007; Judd and Hovland, 2007; Andresen, 2012; Kluesner et al., 2013; Donda et al., 2014). In addition, various types of fluids are expelled in different ways during basin burial and subsidence, and are inferred to involve different geological processes, such as the development of overpressure, abnormal gravitational loading, differential compaction, and eo- and meso-diagenesis.

Pockmarks are shallow seabed depressions that are usually interpreted as the result of fluids escaping through the sedimentary column to the seabed and are documented as an important fluid migration pathway at the seabed (King and MacLean, 1970; Paull et al., 1995; Gay et al., 2004; Judd and Hovland, 2007). Characteristics of pockmarks were first identified as circular and elliptical in shape (King and Maclean, 1970). Subsequently, other shapes of pockmarks, such as elongated,

eyed, and crescentic pockmarks have been found and classified (Andresen et al., 2008; Andresen and Huuse, 2011; Kilhams et al., 2011; Chen et al., 2015). The increased knowledge of pockmarks is due to the availability of three-dimensional (3D) seismic reflection data that have improved the resolution, providing subsurface information in great detail, including the seismic geomorphology and the geometry of pockmarks. Judd and Hovland (2007) suggested the classification of common pockmarks that occur in seas, oceans, and lakes worldwide by using their geometrical shapes (shape, size, and composite pattern). Accordingly, the types of pockmarks were classified into the six major classes of unit pockmarks, normal pockmarks, elongated pockmarks, eyed pockmarks, string of pockmarks, and complex pockmarks (Judd and Hovland, 2007). Furthermore, Chen et al. (2015) used the same criteria to identify various types of pockmarks in the northern Zhongjiannan Basin, South China Sea (Figure 1). Here, we used the geometrical shapes of pockmarks to classify the paleo-pockmarks in the Great South Basin (GSB). Hence, 3D seismic analysis can lead to an improved knowledge of large-scale fluid activity within sedimentary basins from the past to present day.

Paleo-pockmarks and present-day pockmarks have been found in New Zealand both in the North Island and South

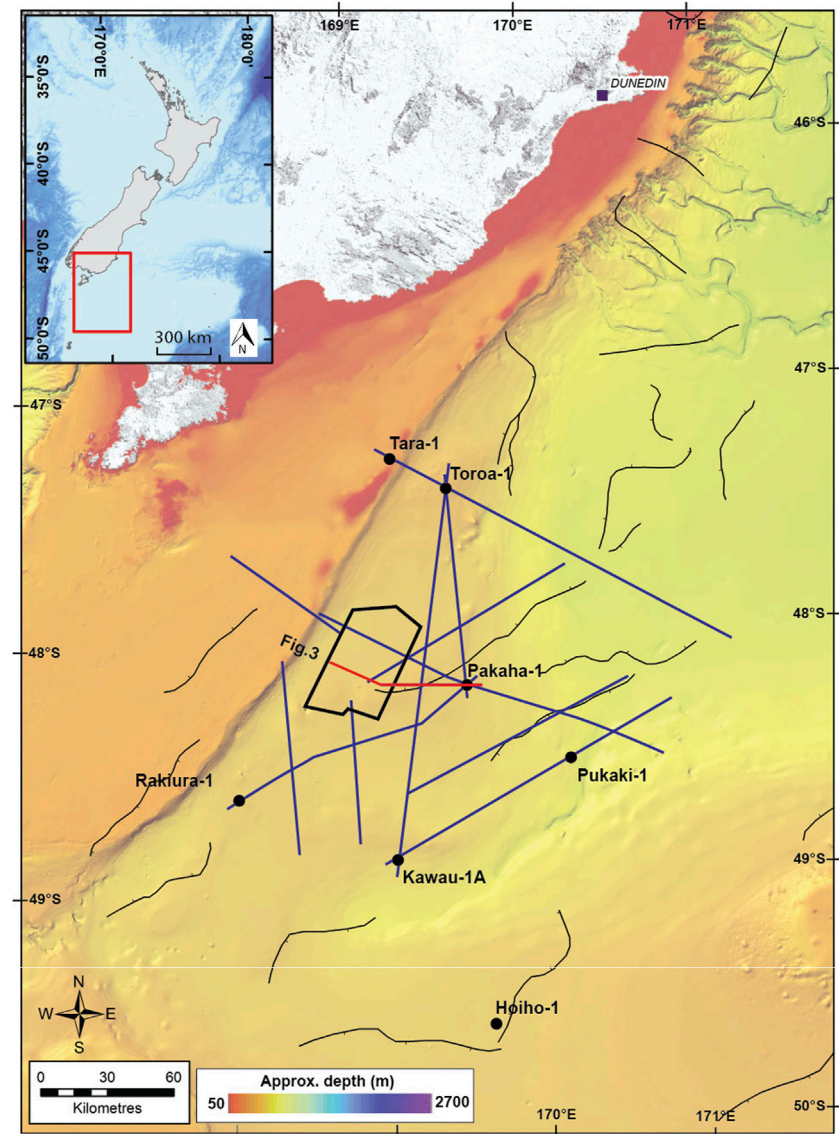


FIGURE 2 | Location map of the Great South Basin and study area. The GSB3D seismic survey is highlighted as a black polygon, and the two-dimensional seismic lines are highlighted as blue lines. The red line represents a regional seismic profile in **Figure 3**. The thin black lines represent tectonic faults in the basin. Well locations are highlighted as black dots.

Island regions (e.g., Pickrill, 1993; Chenrai and Huuse, 2017; Morley et al., 2017; Klaucke et al., 2018; Waghorn et al., 2018; Watson et al., 2020). Numerous paleo-pockmarks are shown in the GSB3D seismic reflection data, from the GSB of the South Island (**Figure 2**), which are associated with polygonal fault systems (Morley et al., 2017; Li et al., 2020; Jitmahantakul et al., 2020). Although petroleum fields in the GSB are not considered economically viable, they are still attractive and have potential for further exploration (Uruski et al., 2007; Uruski, 2010). This study may also be useful in other basins worldwide where current/future work might encounter similar fluid flow features. For example, a hydrocarbon-related pockmark can be used to indicate petroleum generation and maturation in a

sedimentary basin. Therefore, investigating fluid migration and the timing of petroleum formation is key to further our understanding of the petroleum plumbing system and large-scale fluid pathway of the basin. The paleo-pockmarks observed within the Paleocene to Eocene fine-grained sedimentary successions can be used to shed light on fluid expulsion at the seabed during Eocene time (**Figure 3**). Additionally, analysis of seabed-sediment remobilization and fluid flow in ancient sediment sinks, such as pockmarks in deep marine depositional systems, is more challenging than in modern deep marine systems. Morley et al. (2017) suggested that the Middle Eocene paleo-pockmarks and the “honeycomb structure” in this basin are related to opal-A/CT

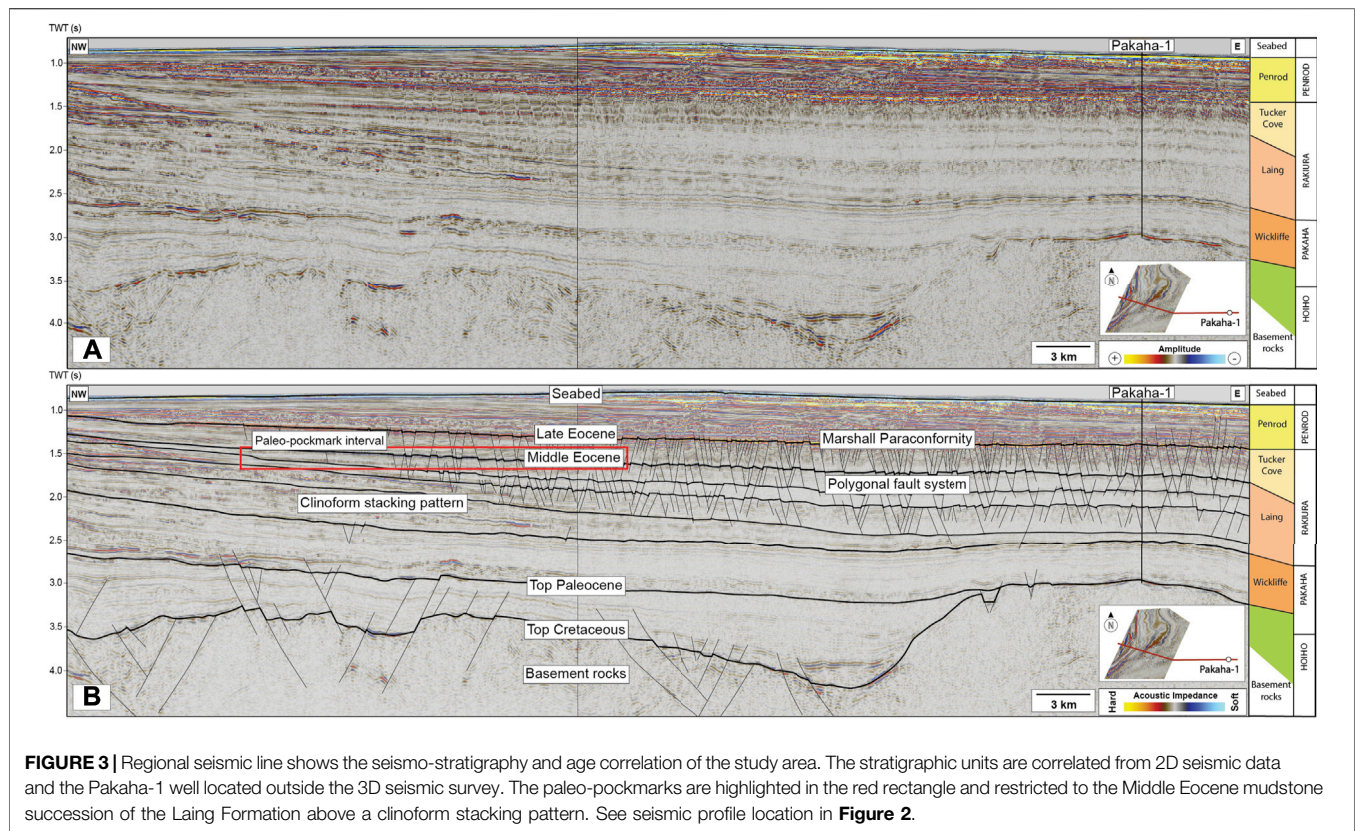


FIGURE 3 | Regional seismic line shows the seismo-stratigraphy and age correlation of the study area. The stratigraphic units are correlated from 2D seismic data and the Pakaha-1 well located outside the 3D seismic survey. The paleo-pockmarks are highlighted in the red rectangle and restricted to the Middle Eocene mudstone succession of the Laing Formation above a clinoform stacking pattern. See seismic profile location in **Figure 2**.

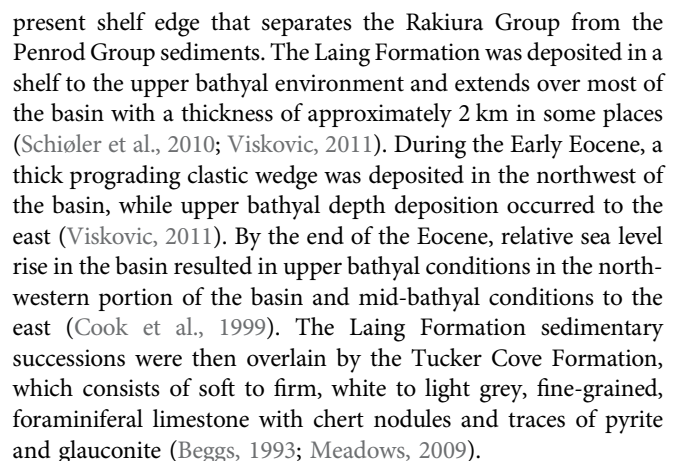
transformation, which is characterised by a high amplitude reflection. The uncertainty about the proposed opal-A/CT transformation-related pockmarks comes from lacking adequate data to constrain the lithology of the sedimentary succession, lacking depositional environment interpretation, and lacking temperature calculation at the opal-A/CT transformation interval in their study. Moreover, Omosanya and Harishidayat (2019) and Jitmahantakul et al. (2020) demonstrated that there are the Eocene clinoform reflections beneath the paleo-pockmark interval. Recent publications and seismic interpretation studies have also demonstrated a geomorphic analysis and characteristic description of pockmarks that can be used to compare and understand the mechanisms of pockmark formation in the GSB (e.g., Andresen, 2012; Gay et al., 2012; Rollet et al., 2012; Serié et al., 2012; Krabbenhoef et al., 2013; Chenrai and Huuse, 2017; Jatiault et al., 2019). Thus, this study aims to describe and identify the characteristics of the Middle Eocene paleo-pockmarks in the GSB, New Zealand, using the GSB3D seismic data in order to propose a hypothesis for the genesis of the paleo-pockmarks in the basin.

GEOLOGICAL SETTING AND STRATIGRAPHY

The GSB lies off the southern coast of the South Island of New Zealand in water depths of 300–600 m (**Figure 1**). The

basin consists of numerous sub-basins formed as a complex intra-continental rift of eastern Gondwana at approximately 105–100 Ma with grabens and half-grabens (Cook et al., 1998). The basement rocks include silicic-to-intermediate plutonics and metasedimentary rocks of about 92 Ma (Beggs, 1990). The stratigraphic framework of the GSB is based on (Constable et al., 2013; **Figure 4**).

The oldest known sedimentary sequence in the basin is the Hoiho Group, which consists of sandstones, shales, conglomerates, and coals during the Late Cretaceous (Cook et al., 1998). After the rifting phase, the Hoiho Group was deposited in a series of normal faulted depressions and sub-basins resulting in the deposition of fluvial and coal measure facies from braided floodplain and lacustrine environments (Meadows, 2009). The geochemistry of condensate in the Kawau-1, and oil shows in Kawau-1A and Toroa-1, suggest that mid-Cretaceous coaly facies are the main source rocks in the GSB (Killops et al., 1997; Sahoo et al., 2014). The Pakaha Group of Late Cretaceous to Paleocene sediments is characterised by widespread marine facies followed by shallowing to coastal environments during the Paleocene. The Pakaha Group is divided into the Kawau Sandstone, the Wickliffe Formation, and the Taratu Formation. The Kawau Formation is characterised by quartzose terrestrial sediments, which are the result of the increasing rate of subsidence from the intra-continental rifting to the seafloor spreading tectonic stage (Beggs, 1993). The Kawau Formation has high potential permeability and flow rates, and is a suitable reservoir for oil



The Penrod Group consists of mainly mid-Oligocene and younger carbonate sediments and is generally less than 500 m thick over most of the basin (Cook et al., 1999). The group has a complex internal structure caused by shelf effects, currents and changing tectonics (Viskovic, 2011). From the Oligocene to the present, tectonic activity has progressively increased in New Zealand (Nicol et al., 2007; McArthur et al., 2020). To the northeast of New Zealand, the Pacific plate is moving southwest and being subducted beneath the North Island. Within the South Island, the plate boundary transitions to dextral strike slip kinematics, moving to the western side of the island where the Australian plate then subducts beneath the Pacific plate (Carter and Norris, 1976; Lamb et al., 2016). The GSB is situated along the passive margin to the southeast of the South Island. The base of the Oligocene to recent sediments is marked by a significant change to more carbonate-rich sediments (chalks or foraminiferal oozes) in the southeast portions of the basin and an erosion surface along the north-western margin (Cook et al., 1999).

MATERIALS AND METHODS

The data presented here are from the GSB3D seismic survey acquired by a joint venture of ExxonMobil New Zealand (Exploration) Limited and Todd Exploration Limited during 2007–2009 (Figure 2). The seismic volume covers a surface area of 1,344 km² and is a full offset, post-stack, migrated volume, where acoustic impedance increases (“hard” reflections) are indicated by positive amplitudes (Hunt International Petroleum Company N.Z., 1977). The seismic data have a bin spacing of 12.5 × 25 m in crossline and inline directions, respectively. The seismic data are dominated by frequency of 40–60 Hz, resulting in a vertical resolution of about 8–12.5 m, using an average sediment velocity of 2.0 km/s for the Rakiura Formation (Hunt International Petroleum Company, N.Z., 1977). The horizontal resolution of about 16–25 m ensures confidence in the geomorphological interpretation of the paleo-pockmarks. The Pakaha-1 exploration well that was drilled adjacent to the 3D seismic survey was used to constrain the lithostratigraphy of the study area and correlate the information with 2D seismic sections (Hunt International Petroleum Company, N.Z., 1977). Seismic volume attributes such as variance, 3D curvature dip, and consistent dip, were used to identify the morphology of the paleo-pockmarks in this study. The surface attribute root mean square (RMS) amplitude was chosen to show the distribution of the paleo-pockmarks. A set of horizons was interpreted over the 3D seismic data by calibrating the Pakaha-1 well as presented in Figure 3. Based on our observations and data from the Pakaha-1 well, the paleo-pockmark interval is dominated by claystone and shale at the lower and upper parts of the Laing Formation, respectively. However, it should be noted that the well is located approximately 30 km east of the paleo-pockmark interval.

In this study, the geometrical characteristics (shape and size) of the paleo-pockmarks are described from a selected area of

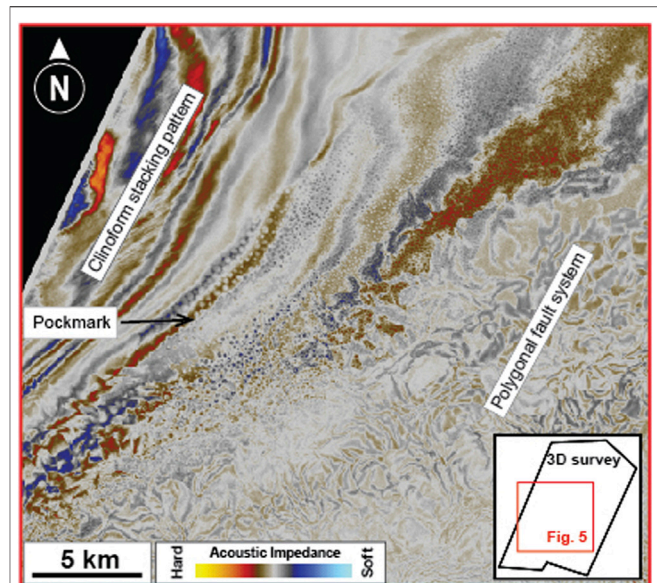


FIGURE 5 | Seismic time slice through 1,492 ms shows a wide area of paleo-pockmarks within the Middle Eocene mudstone succession.

approximately 5 km². The selected area is picked within the paleo-pockmark interval in order to represent the different paleo-pockmark characteristics in each zone. Then, obvious paleo-pockmarks above seismic resolution inside the selected areas are measured for their characteristics.

RESULTS

Paleo-Pockmark Distribution

Across the study area, numerous paleo-pockmarks are widespread laterally within basin floor deposits and are clearly displayed on the seismic time slice at 1,492 ms (TWT) (Figure 5). The paleo-pockmark interval is interpreted as the top of the Laing Formation by correlation with the 2D seismic line and the Pakaha-1 well (Figure 3). The RMS amplitude attribute is used to image the depositional element at the paleo-pockmark interval and shows a fan-shaped body with a high amplitude anomaly associated with the paleo-pockmarks from the proximal to distal fan as presented in Figure 6. Thus, the fan-shaped body, widening to the NE with an apex in the SW, is divided into three major zones, proximal, middle, and distal fans. Seismically, the fan-shaped body is bounded by onlapping or downlapping reflections with a flat reflection within the sedimentary package. Internal reflections are characterised by high to low, chaotic, and semi-continuous reflections. The fan-shaped body is lensoidal in the cross section with a maximum thickness of about 60 m and is an irregular ovoid in the map view (Figures 6, 7). The fan-shaped body preferentially dips to the NE direction and covers an area of more than 100 km². Thus, this fan-shaped body is interpreted as a lobe complex based on Pr  lat et al. (2009). To the west, an interpreted fine-grained interval with polygonal faults onlaps against older low-angle clinoform reflections

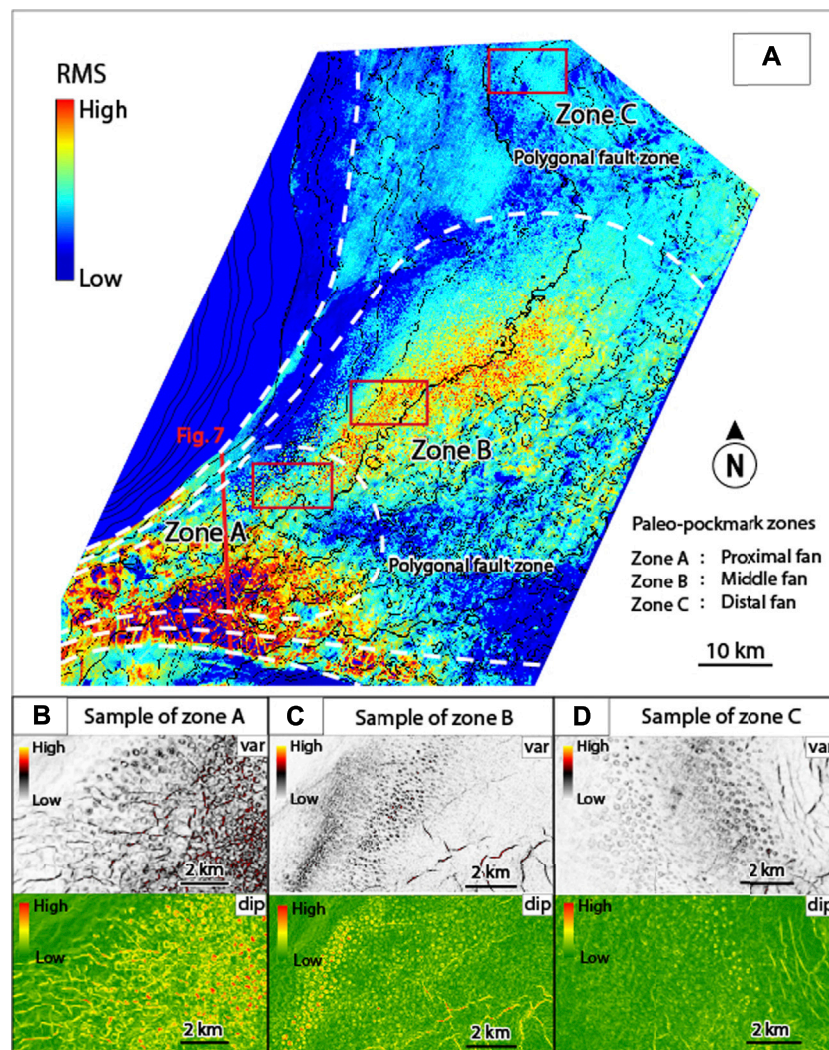


FIGURE 6 | (A) RMS amplitude attribute map extracted from the 0–50 ms (TWT) interval below the top surface of the Laing Formation. Paleo-pockmarks are distributed in a fan-shaped body. The variance (var) and consistent dip (dip) images show the samples of the paleo-pockmark from zones A, B, and C. **(B–D)** Zoom-in images from the selected locations show the geometric measurements which are indicated by red rectangles. White dashed lines are the boundary of the zones.

interpreted to be the progradation system at around 1.7–1.8 km beneath the paleo-pockmark interval (**Figure 7**). The RMS amplitude map presents an increasing number of paleo-pockmarks from the distal to proximal fan (**Figure 6**). Three areas, one within each the three major zones (A, B, and C) of the fan shape, are chosen to study the paleo-pockmark morphology and density (**Figure 6**). Variance and consistent dip attributes are used to image the characteristics of paleo-pockmarks in each zone. The variance attribute is used to measure the similarity of seismic reflections, while consistent dip attribute is used to calculate the dip angle of the paleo-pockmark craters (**Figure 6**).

Seismic Characteristics of Paleo-Pockmarks

Size measurements are described in terms of the width and depth of the paleo-pockmarks, where the width or diameter is a

measurement from the longest axis of the pockmark between pockmark edges, while the paleo-pockmark depth is the measurement in a vertical direction from the pockmark crater to the pockmark base (**Figure 8**). In total, 94 paleo-pockmark samples were measured from zones A, B, and C for the geometrical characteristics (see **Figure 6** for locations). Characteristics of the paleo-pockmarks of each zone are described in the next sections and summarised in **Table 1**. The paleo-pockmarks were classified as “normal pockmarks” based on Hovland et al. (2002) with a sub-round to round shape on the top view and a V- to U-shape in the vertical section (**Figures 9–11**). Their sizes mainly ranged from 131 to 481 m in diameter and 15–45 ms (TWT) in depth. The smallest paleo-pockmark was found in zone B with a diameter and depth of approximately 131 m and 16 ms (TWT), respectively (**Table 1**). The largest paleo-pockmark was found in zone A with a diameter and depth of approximately 481 m and 15 ms

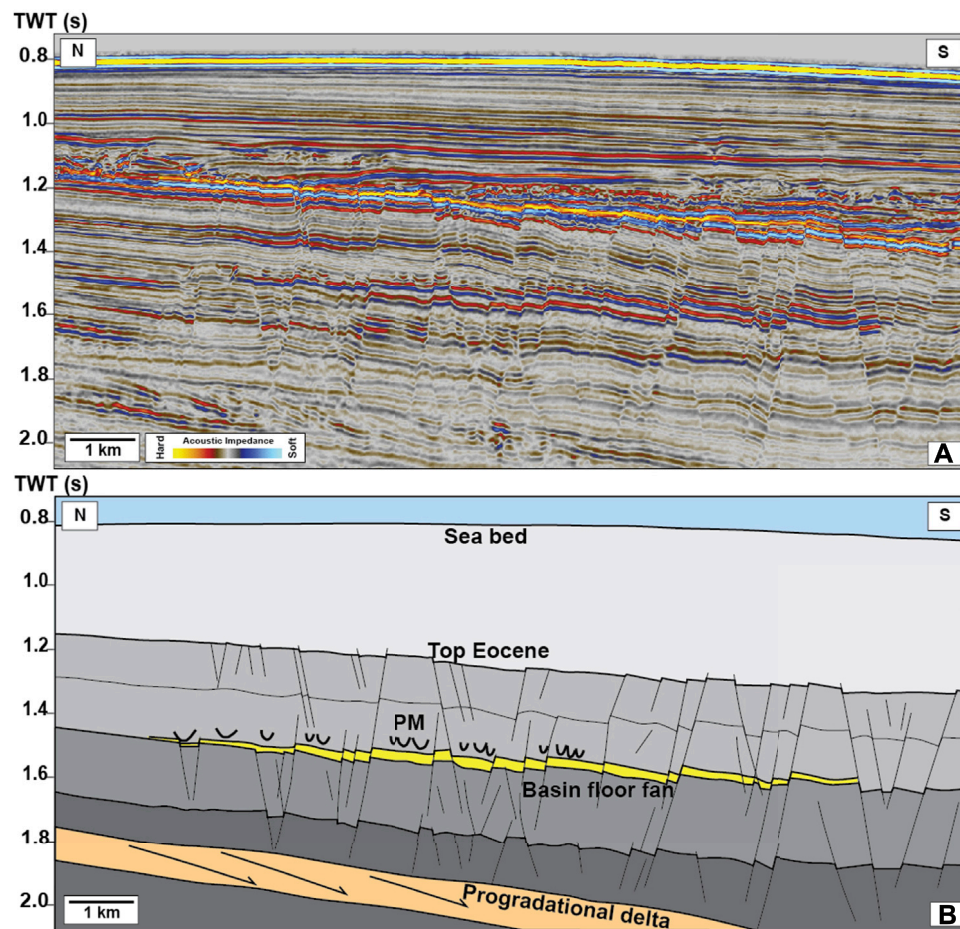


FIGURE 7 | (A) Un-interpreted and **(B)** interpreted 3D seismic profiles show paleo-pockmarks (PM) above a basin floor fan and polygonal faults in very fine-grained sedimentary successions above a progradational delta. See seismic profile location in **Figure 6**.

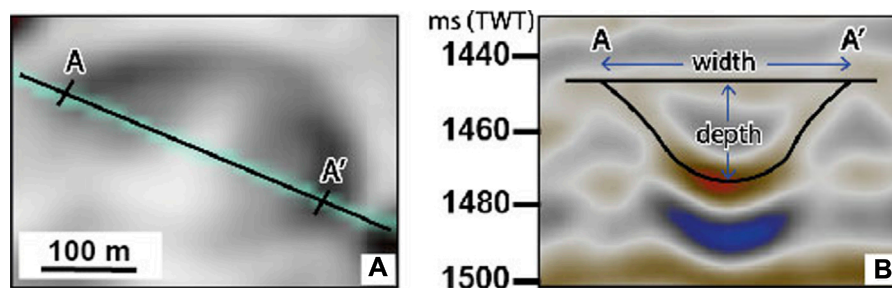


FIGURE 8 | Characteristics of a paleo-pockmark showing the **(A)** top view and **(B)** side view. The paleo-pockmark width and depth are measured in seismic section. Width is measured from the longest axis of pockmark between pockmark edges (A-A'), while depth is measured in a vertical direction from pockmark crater to pockmark base.

(TWT), respectively (**Table 1**). However, it should be noted that the geometry of the paleo-pockmarks is measured from compacted sedimentary strata. Thus, the paleo-pockmark depth and wall would have been deeper and steeper than the present day. There are no acoustic (amplitude) anomalies nor

signs of vertical seismic discontinuity beneath the paleo-pockmarks which could indicate a fluid origin from below the paleo-pockmark interval. The paleo-pockmarks are usually associated with a high amplitude anomaly (hard reflection) within the paleo-pockmark crater, especially in zone A.

TABLE 1 | Summary of the paleo-pockmark characteristics of each zone.

Zone	Paleo-pockmark density (per sq. km)	Paleo-pockmark wall dipping (degree)	Average diameter (m)	Diameter range (m)	Average depth (ms TWT)	Depth range (ms TWT)
A	32	7–15	340	204–481	24	15–45
B	67	4–15	226	131–350	26	15–45
C	21	4–7	195	163–281	22	16–37

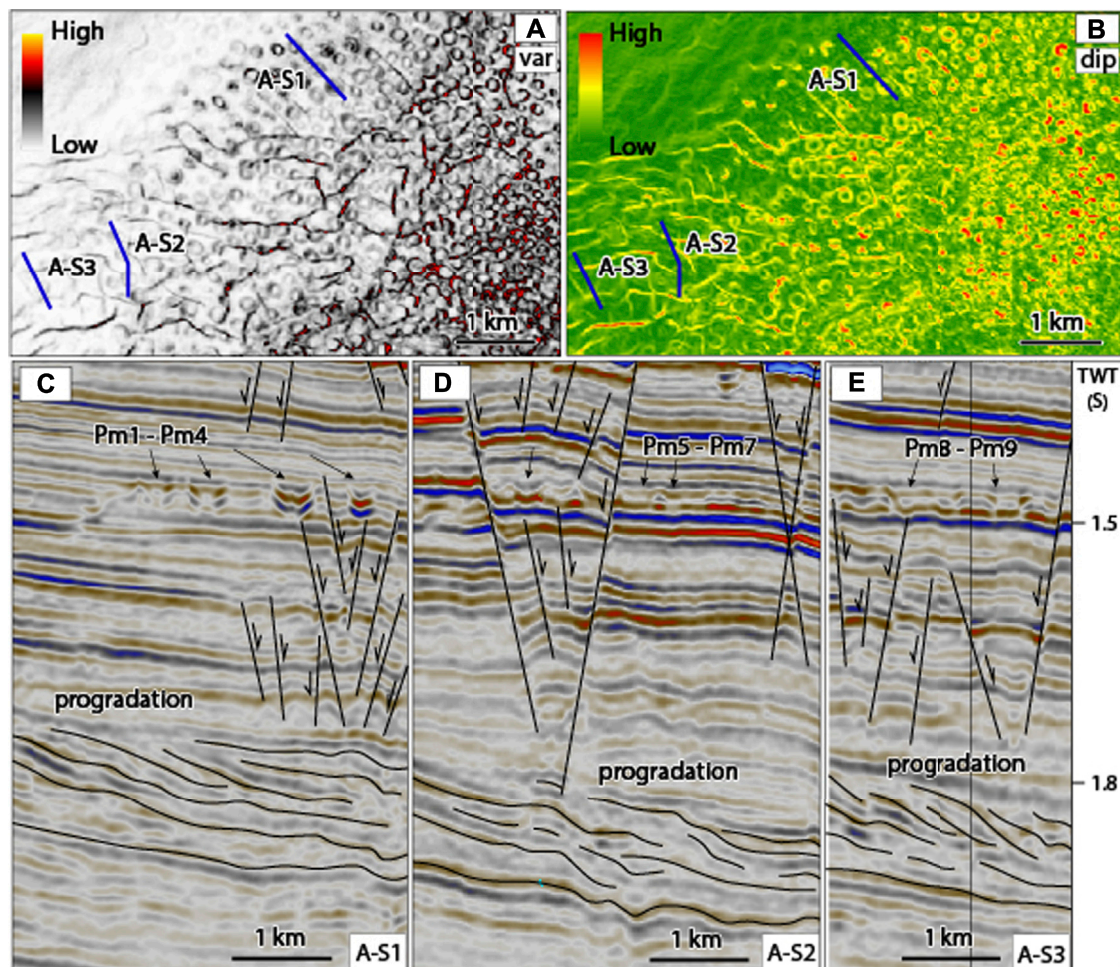


FIGURE 9 | (A) The variance map shows sub-round to round-shaped pockmarks on the top view with medium to high discontinuity values (0.5–0.8), while (B) the consistent dip map shows slope angles of paleo-pockmark walls between 7 and 15° (medium to high value). (C–E) Seismic sections A-S1 to A-S3 show the shape of nine paleo-pockmarks (Pm1–Pm9) in profile view. Pm1 and Pm2 are V-shaped pockmarks, while Pm3 to Pm9 are U-shaped pockmarks. Their size ranges from 204 to 382 m width and 19–45 ms (TWT) depth.

Zone A

The variance attribute map displays the sub-round to round paleo-pockmarks in shapes from the top view (Figure 9). In the profile view, U-shaped paleo-pockmarks were commonly observed (Figure 9). Slope angles of the paleo-pockmark walls are between 7 and 15°, as seen in the consistent dip attribute map. The paleo-pockmarks in zone A have a size range of 204–481 m diameter and 15–45 ms (TWT) depth. In

addition, the paleo-pockmarks in zone A are larger than those in the other zones (Table 1).

Zone B

The variance attribute map showed a common sub-round paleo-pockmark from the top view (Figure 10). In the profile view, U-shaped paleo-pockmarks were observed in the seismic sections. Slope angles of the paleo-pockmark walls are between

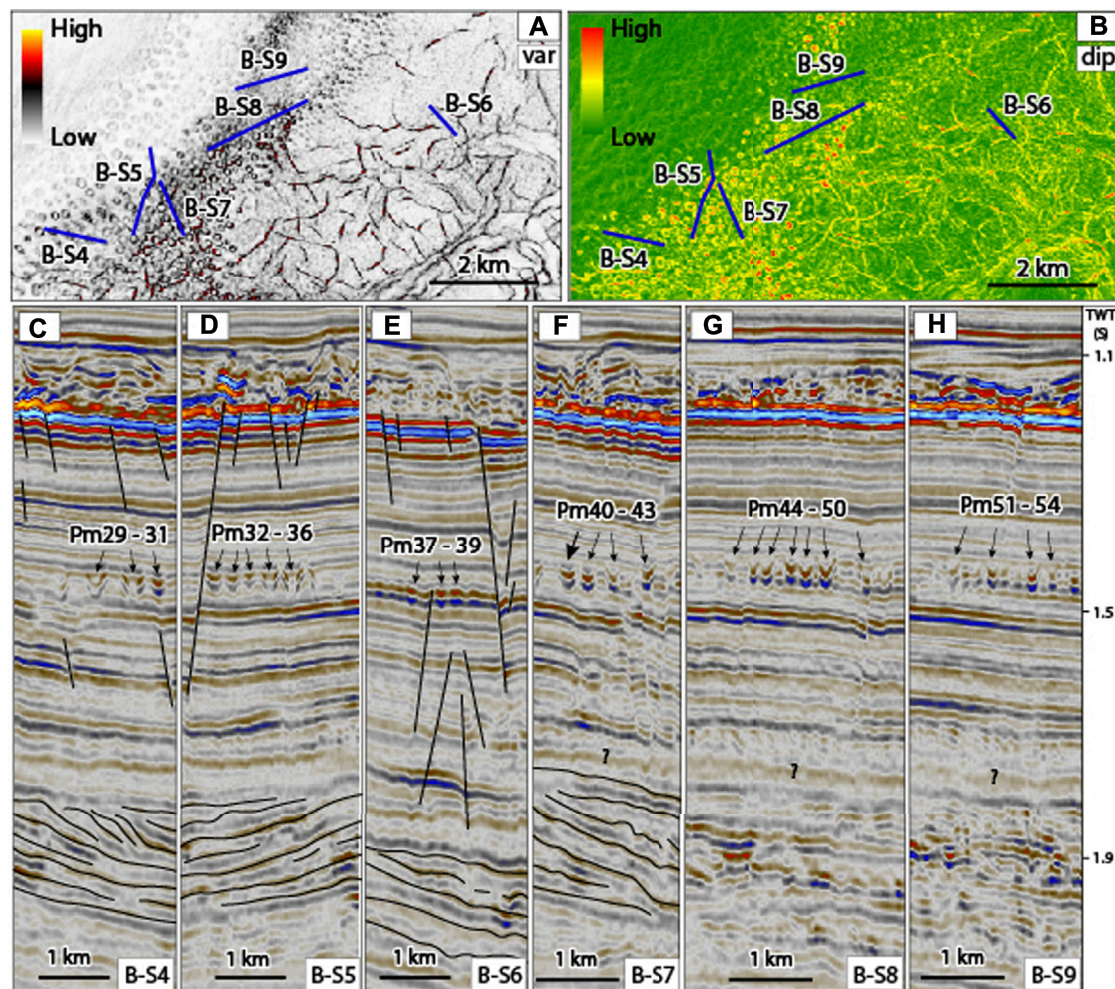


FIGURE 10 | (A) The variance map shows sub-round to round-shaped pockmarks on the top view with low to high discontinuity values (0.5–0.8), while **(B)** the consistent dip map shows slope angles of paleo-pockmark walls between 4 and 15° (low to high value). **(C–H)** Seismic sections B-S4 to B-S9 show the shape of 26 paleo-pockmarks (Pm29–Pm54) in profile view, as V- and U-shaped pockmarks with a size range from 131 to 350 m width and 16–45 ms (TWT) depth. The progradation seismic pattern of clastic sediments is observed beneath the paleo-pockmark interval.

4 and 15°, as observed in the consistent dip attribute map. The size of the paleo-pockmarks ranges from 131 to 350 m diameter and 15–45 ms (TWT) depth. The smallest paleo-pockmark is Pm37 with a 131 m diameter and 16 ms (TWT) depth and is located in the central part of this zone.

Zone C

The variance attribute map displayed sub-round to round paleo-pockmarks from the top view, while V- and U-shaped paleo-pockmarks (Pm82 to Pm94) were observed in the seismic sections (Figure 11). Slope angles of the paleo-pockmark walls are between 4 and 7°, as observed in the consistent dip attribute map. The size of the paleo-pockmarks ranges from 163 to 281 m diameter and 16–37 ms (TWT) depth. Generally, the paleo-pockmarks in this zone show a low relief pockmark. Due to their low relief and seismic resolution, internal structure is difficult to observe within the paleo-pockmarks. The paleo-pockmarks in zone C are usually observed below the polygonal fault interval.

Paleo-Pockmark Density

Curvature dip attribute describes how much the curve deviates at the edge and base of the paleo-pockmarks from a horizontal plane. This seismic attribute displays the paleo-pockmark shapes from the top view (Figure 12). The blue colour (positive curvature) and red colour (negative curvature) are identified as the edge and base of the paleo-pockmark, respectively (Figure 12F). The paleo-pockmark density, estimated by counting the number of paleo-pockmarks in a chosen 5 km² area (Figure 12D), was 32, 67, and 21 pockmarks/km² in zones A, B, and C, respectively.

DISCUSSIONS

Paleo-Pockmark Classification

In general, the paleo-pockmark characteristics in the GSB show similar shapes, but different sizes. In total, 94 paleo-pockmarks

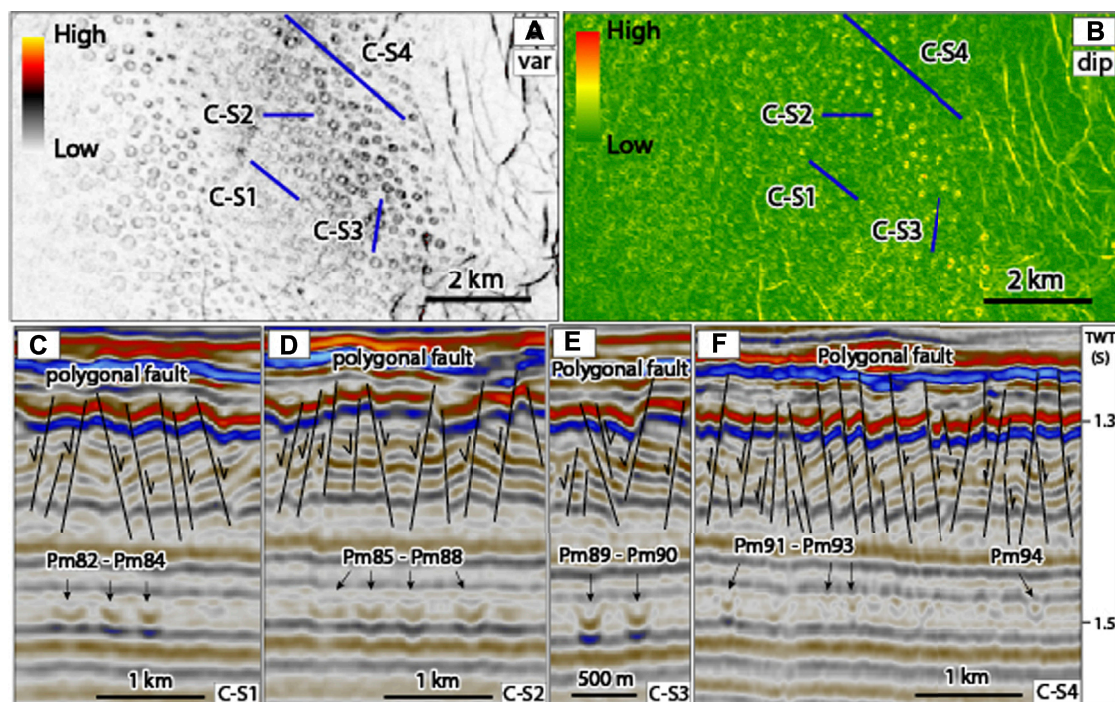


FIGURE 11 | (A) The variance map showing sub-round to round-shaped pockmarks on the top view with low to medium values (0.3–0.5) of discontinuity, while **(B)** the consistent dip map shows slope angles of paleo-pockmark walls between 4 and 7° (low to medium value). **(C–F)** Seismic sections C-S1 to C-S4 show the shape of 13 paleo-pockmarks (Pm82–Pm94) in profile view, as V- and U-shaped pockmarks with a size range from 163 to 281 m width and 16–37 ms (TWT) depth. The polygonal fault system is observed over the paleo-pockmark interval.

were selected to represent their shapes and sizes in both top and profile views. The selected paleo-pockmarks from zones A, B, and C showed the same characteristics of round to sub-round shapes in the top view and V- to U-shapes in the seismic profiles. However, the sizes of the paleo-pockmarks were diverse in each zone (Table 1). Thus, the size of the paleo-pockmarks in this area fits within the normal pockmark class of 131–481 m in diameter and up to 45 m depth (Hovland et al., 2002). A normal pockmark can be used as an indicator of both porewater and gas expulsions, and is usually found in basins that have low-energy currents (e.g., Nickel et al., 2012; Chenrai and Huuse, 2017; Mazzini et al., 2017). The size (diameter and depth) of the paleo-pockmarks in the GSB was plotted along with those previously reported around the world based on Pilcher and Argent (2007; Figure 13), and revealed that the sizes of the paleo-pockmarks in the GSB fall within an expected range. Moreover, the density of normal pockmarks can help to interpret the fluid source in the sedimentary basin-fill. For example, high-density normal pockmarks are mostly found in a large gas field, such as the Barents Sea (Mazzini et al., 2017) and the North Sea (Nickel et al., 2012).

Paleo-Pockmark Distribution

In this section, the comparative density of paleo-pockmarks in the study area was evaluated for zones A (proximal fan), B (middle fan), and C (distal fan). The paleo-pockmark density in zone B is the highest density zone, while zone C is the lowest density zone

(Table 1). It should be noted that the paleo-pockmark density in this study is calculated by counting the number of the paleo-pockmarks within the selected area (Figure 6). With respect to the paleo-pockmark distribution in each location, the clinoform facies beneath the paleo-pockmark interval possibly indicates a basin margin environment deposited from slope to basin (from southwest to northeast direction). Seismically, onlap reflections are observed on top of the clinoform facies indicating a transgressive marine system providing thick mudstone layers (up to 1,000 m) in the basin coinciding with previous studies (e.g., Schiøler et al., 2010). Omosanya and Harishidayat (2019) studied Eocene deltaic clinoforms in this area and observed distributary channels and mouth-bars within the clinoform reflections. These distributary channels are interpreted as sand-filled channels giving sand-prone deposits at proximal delta (Omosanya and Harishidayat, 2019; Jitmahantakul et al., 2020).

The basin floor fan deposits beneath the paleo-pockmarks area at zone A (proximal fan) and zone B (middle fan) may act as a pathway to bring fluids from the surrounding layers to the paleo-pockmark layers creating the paleo-pockmarks during the Middle Eocene. Furthermore, the paleo-pockmark sizes in zone A are larger than those in zone B and zone C (Table 1). It is possible that the size and density of the paleo-pockmarks in this area are controlled by lithology or fluid pathway. Based on the fact that fluids will migrate through coarse-grained sediments more readily than fine-grained sediments, the paleo-pockmarks at the proximal fan are usually larger than those in the distal fan.

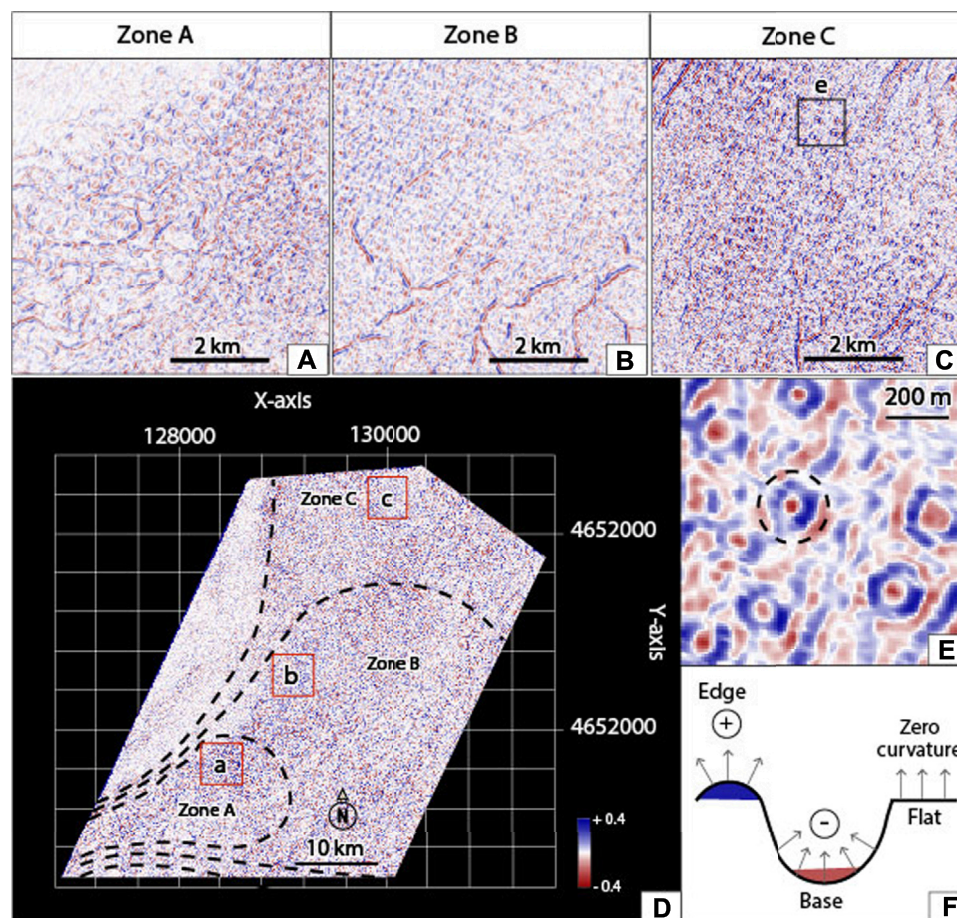


FIGURE 12 | Characteristics of paleo-pockmarks from the curvature dip map for zones (A) A, (B) B, and (C) C (locations in the red rectangles). Black-dashed lines are the boundaries of the three paleo-pockmark zones (D). Characteristics of paleo-pockmarks are shown in a dashed circle (blue colour is pockmark edge, and red colour is pockmark base) (E, F).

Potential Fluid Sources

The possible fluid sources (pore water, hydrothermal fluid and hydrocarbon fluid) that could contribute to the formation of the paleo-pockmarks in the study area are discussed in this section. These fluid types are commonly found and related to fluid flow process in offshore areas worldwide (Pickrill, 1993; Dimitrov and Woodside, 2003; Cartwright et al., 2004; Hübscher and Borowski, 2006; Chenrai and Huuse, 2017; Tasianas et al., 2018).

Pore Water Fluid

Pore water is water that is trapped between the sediment grains during or after sediment deposition. Generally, sediments are believed to be fully saturated in submarine environments at equilibrium stage, and pore water remains in pore spaces. Any reduction in pore spaces during burial, and compaction during diagenesis may cause the pore water to migrate laterally and upwards according to the hydraulic head. Thus, pore water is forced to migrate upwards until it is expelled at the seabed, displacing sediment and forming pockmarks. Pore water is one of the important fluid sources for pockmark generation (e.g., King and Maclean, 1970; Harrington, 1985; Chenrai and Huuse, 2017).

However, sediment compaction during diagenesis is not the only trigger for pore water escaping from sedimentary formation, as the escape of pore water can also be associated with other conditions such as earthquakes (Hovland, 2002), sea level change (Luo et al., 2014), and rapid sediment loading (Chenrai and Huuse, 2017).

In addition, pore water is relatively high within fine-grained sediments such as clay and silt compared to coarser sediments (Harrington, 1985). Based on the Pakaha-1 and Rakiura-1 wells, the paleo-pockmarks in the study area occurred on the surface of the Laing Formation which is dominated by mudstone and claystone. If the sedimentary layer in this formation is saturated with water, then pore water is potentially one of the fluid sources responsible for the paleo-pockmark formation in the study area. However, no seismic characteristics of fluid pathways, such as fluid pipes and chimneys, to the paleo-pockmarks are observed in the 3D seismic data. Thus, it is unclear if pore water from the compacting mudstone strata could have contributed to the paleo-pockmarks, and we were unable to either accept or refute pore water as a possible fluid source. In addition, if pore water driven by mudstone compaction occurred and migrated

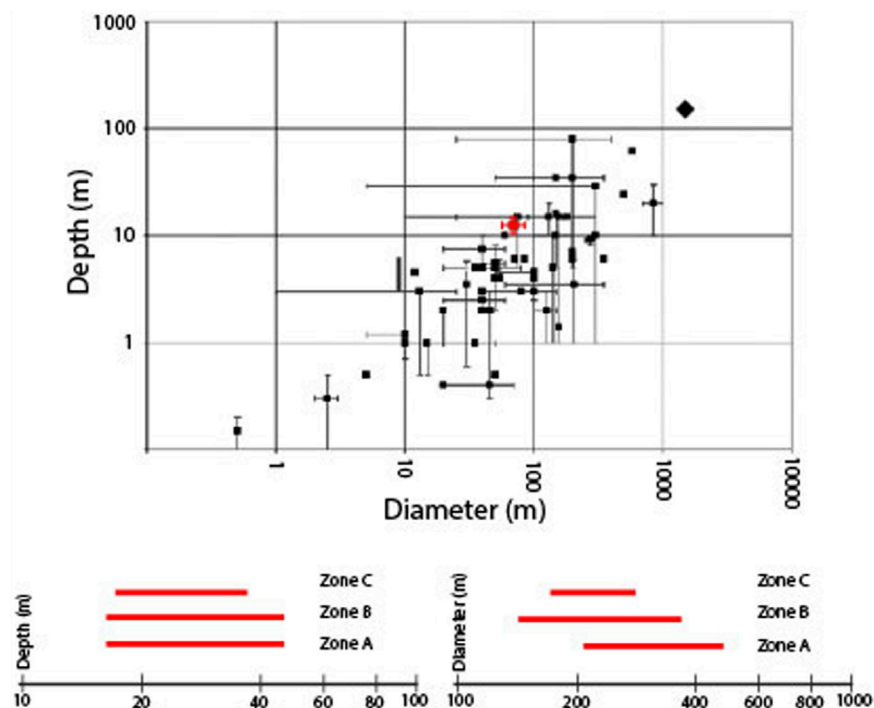


FIGURE 13 | Graph illustrates the pockmark geometry of previously studied pockmarks from 57 published sites, compiled by Pilcher and Argent (2007) in comparison with this study at the GSB. The X and Y scales are logarithmic. The paleo-pockmark geometry of this study is presented by a red cross-hair by applying a velocity of 2.0 km/s. Pilcher and Argent (2007) used single points to represent either measurements of single pockmarks or average measurements and used error bars to represent the range of sizes in a pockmark field.

into the paleo-pockmark layer, it would increase the pore fluid pressure within the layer leading to fluid expulsion resulting in the formation of paleo-pockmarks.

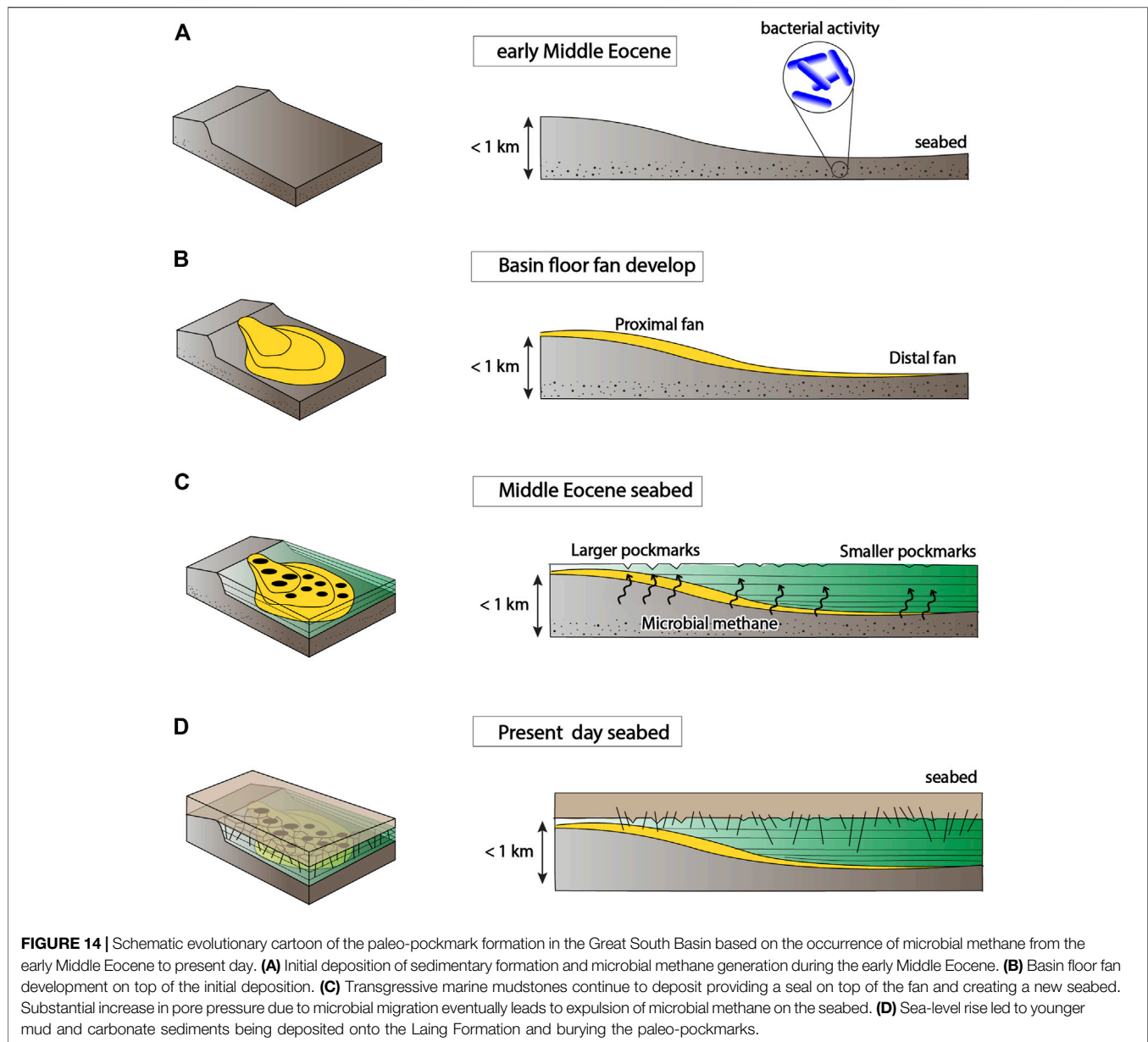
Hydrothermal Fluid

Hydrothermal activity is the process of heated subsurface water circulation (Colín-García et al., 2016). Subsurface water is heated near magma and volcanic rocks (batholiths, sills, and dykes) with temperatures up to 1,200°C (Judd and Hovland, 2009). Hydrothermal activity occurs in both the oceanic and continental crust, including mid-oceanic ridges, back-arc basins, and on submarine volcanic arcs (Norton, 1984; Hovland et al., 2005). Hydrothermal venting is one of the main processes that can form pockmarks on the seabed (Judd and Hovland, 2009). Volcanic activity was widespread in the Late Cretaceous and Cenozoic in New Zealand, forming volcanoes and igneous intrusions buried in sedimentary basins, including the Canterbury basin and GSB. Volcanoes and igneous intrusions have been widely recognised and mostly found within the Canterbury basin (e.g., Magee et al., 2019; Barrier et al., 2021). The GSB is located relatively close (~200 km) to the Alpine Fault, however the basin is considered to be relatively tectonically stable, and not influenced by back-arc extension or Alpine deformation (Phillips and Magee, 2020). However, volcanoes and igneous intrusions can be observed from 2D seismic lines outside the GSB3D seismic volume. Although hydrothermal fluids have been mentioned as a fluid source responsible for creating pockmarks in

Lake Rotoiti, New Zealand (Pickrill, 1993), hydrothermal fluids are not considered as a fluid source for the paleo-pockmarks in this study area because the paleo-pockmark field is closely linked with the occurrence of a slope-to-basin fan rather than any igneous phenomena. Also, no seismic characteristics of volcanic activities are found in the study area, and so there may have been no heat source from hydrothermal activity in this area. The standard temperature of the sedimentary formation is insufficient for formation of hydrothermal fluid. If hydrothermal fluids had been involved in fluid expulsion on the Middle Eocene seabed, the paleo-pockmarks should be linked with igneous structures, which should be clearly identified in the seismic data.

Hydrocarbon Fluid

The large distribution area of the paleo-pockmarks in this study suggests that fluids were also sourced from across a large area. The vitrinite reflectance of about 0.45% indicates a thermally immature source rock at a depth of about 3 km in Paleocene successions (Hunt International Petroleum Company, N.Z., 1977). Thus, only the Cretaceous source rock is thermally mature, while the younger Paleocene source rock is in an immature stage (Shalaby et al., 2020). Cretaceous source rocks at the depocenter of the GSB are predicted to have been expelled in the early Eocene (Kroeger and Funnell, 2012). Methane-dominated dry gas of possible biogenic origin is often documented in offshore wells at depths above 1,200 m (Hunt



International Petroleum Company, N.Z., 1977). However, if the thermogenic hydrocarbons from the Cretaceous source rocks have been generated, it is difficult for hydrocarbon fluid to migrate vertically into the Middle Eocene seabed during the paleo-pockmark formation. Seismically, there is no clear evidence of gas anomalies, such as gas chimneys, fluid pipes, or acoustic blanking underneath the paleo-pockmarks. Thus, local deep thermogenic hydrocarbon fluids are of lesser importance in forming the Middle Eocene paleo-pockmark. Biogenic methane can be generated at 0–80°C temperature with a low level of organic matter (total organic carbon, less than 0.5%) and low porosity/permeability (Rice and Claypool, 1981; Rice, 1992). Biogenic methane can be produced by several processes, but carbon dioxide reduction and acetate fermentation are very common within sedimentary successions (Judd and

Hovland, 2007; Katz, 2011). If biogenic methane was generated during the Middle Eocene, pore pressure within the sedimentary formation will be increased by adding methane fluid in the pore space, leading to the formation of paleo-pockmarks. Therefore, we propose that the fluid origin that created this paleo-pockmark field originated from biogenic gas. During the Middle Eocene, the Laing Formation was formed by deposition of muds and clays of the bathyal environment. This deposition may have involved organic-rich sediments that could provide or generate biogenic gas associated with microbial activity within the sedimentary successions. Biogenic gas from the microbial consumption of organic matter has previously been implicated in pockmark formation (e.g., Hovland et al., 2002; Judd and Hovland, 2007; Krämer et al., 2017).

The wide distribution of the low-relief pockmark in the study area, especially in zone C, is believed to be associated with a low fluid flux from the shallow subsurface. Most previous pockmark models suggested that pockmarks are formed by catastrophic fluid (mostly gas) expulsions (e.g., Hovland and Judd, 1988). However, the methane seep model of biogenic gas from a shallow subsurface does not require an overpressure condition to create a pockmark (Agirrezabala et al., 2013). This model can be used to support the Middle Eocene paleo-pockmark formation in the GSB. Thus, biogenic gas is a potential main fluid source for the paleo-pockmarks in the GSB.

Paleo-Pockmark Formation

Taking the main potential fluid origin of the Middle Eocene paleo-pockmarks in the GSB to be microbial methane produced during basin burial and subsidence, a model for the proposed formation of the paleo-pockmarks in the GSB is presented schematically in **Figure 14** and outlined below, based upon microbial methane production at a low temperature (<60°C) condition near the Middle Eocene seabed.

Early-Middle Eocene

Fine-grained sediment and organic matter were deposited on the seabed in the early stages. Bacteria accumulated and decomposed organic matter in the sediments, producing methane by carbon dioxide reduction and fermentation in anoxic conditions (Judd and Hovland, 2007; Katz, 2011).

Basin Floor Fan Development

Coarse- and fine-grained sediments began to be deposited in the slope area and formed the basin floor fan orientated from a southwest to northeast direction, possibly during the mid-Middle Eocene. Coarse-grained sediments were transported and deposited when the energy decreased at the proximal fan, while fine-grained sediments were transported to the distal fan (e.g., Hawie et al., 2019).

Middle Eocene Seabed

Transgressive marine mudstones of the Laing Formation overlie the basin floor fan. The thick bed of marine mudstone generated an overburden pressure in the basin floor fan package, which forced fluids to migrate upwards into the paleo-pockmark interval. Microbial methane from the mudstone strata below the paleo-pockmark interval could laterally and vertically migrate through the permeable layers within the basin floor fan until, eventually, the pore pressure exceeded the fracture gradient of the seal leading to the microbial methane escaping onto the paleo-seabed. Followed by fine-grained sediment compaction, the polygonal fault system then developed on the upper part of the Laing Formation in the study area.

Present Day Seabed

Sea-level rise led to mud and carbonate sediments of the Tucker Cover Formation and Penrod Group to deposit above the Laing Formation, and to bury the Middle Eocene paleo-pockmarks with these younger mud and carbonate sediments.

CONCLUSION

Fluid flow features recording fluid expulsion at the paleo-seabed are manifested in the Great South Basin as paleo-pockmarks that formed during the Middle Eocene. The paleo-pockmarks are observed along a trend that can be related to the distribution of underlying basin floor fan sediments in the ancient sediment-sink area. The evidence presented here shows that fluid flow activity in this basin has been active since at least the Middle Eocene. The analysis of the seismic data covering this paleo-pockmark field allowed the characterisation of the paleo-pockmark zone into three zones distributed in mudstones above basin floor fan deposits. The possible origin of fluids in this scenario is likely to be biogenic methane, suggesting that not all pockmarks should be used as indicators of thermogenic hydrocarbon expulsion. The progradational seismic pattern of clastic sediments beneath the paleo-pockmark interval possibly enhanced the fluid migration through the permeable layers. The proposed model may help to explain pockmark formation associated with basin floor fan deposits and inform future studies of fluid migration and expulsion within sedimentary basins.

DATA AVAILABILITY STATEMENT

The original contributions presented in the study are included in the article/supplementary material, further inquiries can be directed to the corresponding author.

AUTHOR CONTRIBUTIONS

All authors actively contributed to various parts of the manuscript and agreed with its contents. The data analysis and interpretation was conducted by AK and PC. The manuscript was also developed, written and revised by all authors.

FUNDING

This work was financially supported by the Research Grant for New Scholar Ratchadaphisek Somphot Endowment Fund, Chulalongkorn University.

ACKNOWLEDGMENTS

Schlumberger and IHS generously supplied Petrel and Kingdom licenses to Chulalongkorn University. The data were released by the New Zealand government. Reviewers are thanked for their useful and constructive comments. Specialty chief editor, David Mark Hodgson is thanked for valuable comments and suggestions. The authors thank the Office of Research Affairs, Chulalongkorn University, for assistance during manuscript preparation.

REFERENCES

- Agirrezabala, L. M., Kiel, S., Blumenberg, M., Schäfer, N., and Reitner, J. (2013). Outcrop Analogues of Pockmarks and Associated Methane-Seep Carbonates: a Case Study from the Lower Cretaceous (Albian) of the Basque-Cantabrian Basin, Western Pyrenees. *Palaeogeogr. Palaeoclimatol. Palaeoecol.* 390, 94–115. doi:10.1016/j.palaeo.2012.11.020
- Andresen, K. J. (2012). Fluid Flow Features in Hydrocarbon Plumbing Systems: What Do They Tell Us about the basin Evolution? *Mar. Geology*. 332–334, 89–108. doi:10.1016/j.margeo.2012.07.006
- Andresen, K. J., and Huuse, M. (2011). 'Bulls-eye' Pockmarks and Polygonal Faulting in the Lower Congo Basin: Relative Timing and Implications for Fluid Expulsion during Shallow Burial. *Mar. Geology*. 279, 111–127. doi:10.1016/j.margeo.2010.10.016
- Andresen, K. J., Huuse, M., and Clausen, O. R. (2008). Morphology and Distribution of Oligocene and Miocene Pockmarks in the Danish North Sea - Implications for Bottom Current Activity and Fluid Migration. *Basin Res.* 20 (3), 445–466. doi:10.1111/j.1365-2117.2008.00362.x
- Anka, Z., Ondrak, R., Kowitz, A., and Schödt, N. (2013). Identification and Numerical Modelling of Hydrocarbon Leakage in the Lower Congo Basin: Implications on the Genesis of Km-wide Seafloor Mounded Structures. *Tectonophysics* 604, 153–171. doi:10.1016/j.tecto.2012.11.020
- Barrier, A., Bischoff, A., Nicol, A., Browne, G. H., and Bassett, K. N. (2021). Relationships Between Volcanism and Plate Tectonics: A Case-Study from the Canterbury Basin, New Zealand. *Mar. Geol.* 433, 106397. doi:10.1016/j.margeo.2020.106397
- Beggs, J. M. (1993). Depositional and Tectonic History of the Great South Basin. *Sedim. Basins World* 2, 365–373.
- Beggs, J. M. (1990). "Seismic Stratigraphy of the Plio-Pleistocene Giant Foresets, Western Platform, Taranaki Basin," in New Zealand Oil Exploration Conference Proceedings (Queenstown: Ministry of Commerce), 201–207.
- Berndt, C. (2005). Focused Fluid Flow in Passive continental Margins. *Phil. Trans. R. Soc. A*. 363, 2855–2871. doi:10.1098/rsta.2005.1666
- Carter, R. M., and Norris, R. J. (1976). Cainozoic History of Southern New Zealand: an accord between Geological Observations and Plate-Tectonic Predictions. *Earth Planet. Sci. Lett.* 31, 85–94. doi:10.1016/0012-821x(76)90099-6
- Cartwright, J. (2007). The Impact of 3D Seismic Data on the Understanding of Compaction, Fluid Flow and Diagenesis in Sedimentary Basins. *J. Geol. Soc.* 164, 881–893. doi:10.1144/0016-76492006-143
- Cartwright, J., Wattrus, N., Rausch, D., and Bolton, A. (2004). Recognition of an Early Holocene Polygonal Fault System in Lake Superior: Implications for the Compaction of fine-grained Sediments. *Geol.* 32 (3), 253–256. doi:10.1130/g2012.1
- Chen, J., Song, H., Guan, Y., Yang, S., Pinheiro, L. M., Bai, Y., et al. (2015). Morphologies, Classification and Genesis of Pockmarks, Mud Volcanoes and Associated Fluid Escape Features in the Northern Zhongjiannan Basin, South China Sea. *Deep Sea Res. Part Topical Stud. Oceanography* 122, 106–117. doi:10.1016/j.dsr2.2015.11.007
- Chenrai, P., and Huuse, M. (2017). Pockmark Formation by Porewater Expulsion during Rapid Progradation in the Offshore Taranaki Basin, New Zealand. *Mar. Pet. Geology*. 82, 399–413. doi:10.1016/j.marpetgeo.2017.02.017
- Colín-García, M., Heredia, A., Cordero, G., Camprubí, A., Negrón-Mendoza, A., Ortega-Gutiérrez, F., et al. (2016). Hydrothermal Vents and Prebiotic Chemistry: a Review. *Bsgm* 68, 599–620. doi:10.18268/bsgm2016v68n3a13
- Constable, R. M., Langdale, S., and Allan, T. M. H. (2013). Development of a Sequence Stratigraphic Framework in the Great South Basin, In: *Proceedings of New Zealand Petroleum Conference*, Auckland, New Zealand, 1–21.
- Cook, R. A., Sutherland, R., and Zhu, H. (1999). *Cretaceous-Cenozoic Geology and Petroleum Systems of the Great South Basin*. New Zealand: Institute of Geological & Nuclear Sciences.
- Cook, R. A., Zhu, H., Sutherland, R., Killops, S., and Funnell, R. (1998). "Future Exploration of the Great South Basin," in New Zealand's basins of opportunity: New Zealand Petroleum Conference: proceedings.
- de Mahiques, M. M., Schattner, U., Lazar, M., Sumida, P. Y. G., and Souza, L. A. P. d. (2017). An Extensive Pockmark Field on the Upper Atlantic Margin of Southeast Brazil: Spatial Analysis and its Relationship with Salt Diapirism. *Heliyon* 3 (2), e00257. doi:10.1016/j.heliyon.2017.e00257
- Dimitrov, L., and Woodside, J. (2003). Deep Sea Pockmark Environments in the Eastern Mediterranean. *Mar. Geology*. 195, 263–276. doi:10.1016/s0025-3227(02)00692-8
- Donda, F., Forlin, E., Gordini, E., Panieri, G., Buenz, S., Volpi, V., et al. (2014). Deep-sourced Gas Seepage and Methane-Derived Carbonates in the Northern Adriatic Sea. *Basin Res.* 27, 531–545. doi:10.1111/bre.12087
- Gafeira, J., Dolan, M., and Monteys, X. (2018). Geomorphometric Characterization of Pockmarks by Using a GIS-Based Semi-automated Toolbox. *Geosciences* 8 (5), 154. doi:10.3390/geosciences8050154
- Gay, A., Lopez, M., Berndt, C., and Séranne, M. (2007). Geological Controls on Focused Fluid Flow Associated with Seafloor Seeps in the Lower Congo Basin. *Mar. Geology*. 244, 68–92. doi:10.1016/j.margeo.2007.06.003
- Gay, A., Lopez, M., Cochonat, P., and Sermondadaz, G. (2004). Polygonal Faults-Furrows System Related to Early Stages of Compaction - Upper Miocene to Recent Sediments of the Lower Congo Basin. *Basin Res.* 16, 101–116. doi:10.1111/j.1365-2117.2003.00224.x
- Gay, A., Mourgues, R., Berndt, C., Bureau, D., Planke, S., Laurent, D., et al. (2012). Anatomy of a Fluid Pipe in the Norway Basin: Initiation, Propagation and 3D Shape. *Mar. Geology*. 332–334, 75–88. doi:10.1016/j.margeo.2012.08.010
- Harrington, P. K. (1985). Formation of Pockmarks by Pore-Water Escape. *Geo-Marine Lett.* 5, 193–197. doi:10.1007/bf02281638
- Hawie, N., Covault, J. A., and Sylvester, Z. (2019). Grain-size and Discharge Controls on Submarine-Fan Depositional Patterns from Forward Stratigraphic Models. *Front. Earth Sci.* 7, 334. doi:10.3389/feart.2019.00334
- Ho, S., Imbert, P., Hovland, M., Wetzel, A., Blouet, J.-P., and Carruthers, D. (2018). Downslope-shifting Pockmarks: Interplay between Hydrocarbon Leakage, Sedimentations, Currents and Slope's Topography. *Int. J. Earth Sci. (Geol. Rundsch)* 107 (8), 2907–2929. doi:10.1007/s00531-018-1635-5
- Hovland, M., Gardner, J. V., and Judd, A. G. (2002). The Significance of Pockmarks to Understanding Fluid Flow Processes and Geohazards. *Geofluids* 2 (2), 127–136. doi:10.1046/j.1468-8123.2002.00028.x
- Hovland, M., and Judd, A. G. (1988). *Seabed Pockmarks and Seepages: Impact on Geology, Biology and the marine Environment*. London: Graham and Trotman, 293.
- Hovland, M. (2002). On the Self-Sealing Nature of marine Seeps. *Continental Shelf Res.* 22, 2387–2394. doi:10.1016/s0278-4343(02)00063-8
- Hovland, M., Svensen, H., Forsberg, C. F., Johansen, H., Fichler, C., Fosså, J. H., et al. (2005). Complex Pockmarks with Carbonate-Ridges off mid-Norway: Products of Sediment Degassing. *Mar. Geology*. 218, 191–206. doi:10.1016/j.margeo.2005.04.005
- Hübscher, C., and Borowski, C. (2006). Seismic Evidence for Fluid Escape from Mesozoic Cuesta Type Topography in the Skagerrak. *Mar. Pet. Geology*. 23, 17–28. doi:10.1016/j.marpetgeo.2005.07.004
- Hunt International Petroleum Company, N. Z. (1977); Pakaha-1 Well Completion Report. Ministry of Economic Development New Zealand unpublished petroleum report. PR703.
- Hurst, A., Cartwright, J., Huuse, M., Jonk, R., Schwab, A., Duranti, D., et al. (2003). Significance of Large-Scale Sand Injectites as Long-Term Fluid Conduits: Evidence from Seismic Data. *Geofluids* 3 (4), 263–274. doi:10.1046/j.1468-8123.2003.00066.x
- Huuse, M., Jackson, C. A.-L., Van Rensbergen, P., Davies, R. J., Flemings, P. B., and Dixon, R. J. (2010). Subsurface Sediment Remobilization and Fluid Flow in Sedimentary Basins: an Overview. *Basin Res.* 22 (4), 342–360. doi:10.1111/j.1365-2117.2010.00488.x
- Jatiaux, R., Loncke, L., Dhont, D., Imbert, P., and Dubucq, D. (2019). Geophysical Characterisation of Active Thermogenic Oil Seeps in the Salt Province of the Lower Congo basin Part I: Detailed Study of One Oil-Seeping Site. *Mar. Pet. Geology*. 103, 753–772. doi:10.1016/j.marpetgeo.2018.11.026
- Jay Katz, B. (2011). Microbial Processes and Natural Gas Accumulations. *Togeoj* 5, 75–83. doi:10.2174/1874262901105010075
- Jitmahantakul, S., Chenrai, P., Kanjanapayont, P., and Kanitpanyacharoen, W. (2020). Seismic Characteristics of Polygonal Fault Systems in the Great South Basin, New Zealand. *Open Geosci.* 12 (1), 851–865. doi:10.1515/geo-2020-0177
- Judd, A. G., and Hovland, M. (2007). *Seabed Fluid Flow: The Impact of Geology, Biology and the marine Environment*. Cambridge, UK: Cambridge University Press.
- Judd, A., and Hovland, M. (2009). *Seabed Fluid Flow: The Impact on Geology, Biology and the marine Environment*. Cambridge, UK: Cambridge University Press.

- Karstens, J., and Berndt, C. (2015). Seismic Chimneys in the Southern Viking Graben - Implications for Palaeo Fluid Migration and Overpressure Evolution. *Earth Planet. Sci. Lett.* 412, 88–100. doi:10.1016/j.epsl.2014.12.017
- Kilhams, B., McArthur, A., Huuse, M., Ita, E., and Hartley, A. (2011). Enigmatic Large-Scale Furrows of Miocene to Pliocene Age from the central North Sea: Current-Scoured Pockmarks? *Geo-mar. Lett.* 31, 437–449. doi:10.1007/s00367-011-0235-1
- Killops, S., Cook, R., Sykes, R., and Boudou, J. (1997). Petroleum Potential and Oil-Source Correlation in the Great South and Canterbury Basins. New Zealand *J. Geol. Geophys.* 40, 405–423. doi:10.1080/00288306.1997.9514773
- King, L. H., and MacLean, B. (1970). Pockmarks on the Scotian Shelf. *Geol. Soc. America Bull.* 81, 3141–3148. doi:10.1130/0016-7606(1970)81[3141:potss]2.0.co;2
- Klaucke, I., Sarkar, S., Bialas, J., Berndt, C., Dannowski, A., Dumke, I., et al. (2018). Giant Depressions on the Chatham Rise Offshore New Zealand - Morphology, Structure and Possible Relation to Fluid Expulsion and Bottom Currents. *Mar. Geology.* 399, 158–169. doi:10.1016/j.margeo.2018.02.011
- Kluesner, J. W., Silver, E. A., Bangs, N. L., McIntosh, K. D., Gibson, J., Orange, D., et al. (2013). High Density of Structurally Controlled, Shallow to Deep Water Fluid Seep Indicators Imaged Offshore Costa Rica. *Geochem. Geophys. Geosyst.* 14 (3), 519–539. doi:10.1002/ggge.20058
- Krabbenhoft, A., Bialas, J., Klaucke, I., Crutchley, G., Papenberg, C., and Netzeband, G. L. (2013). Patterns of Subsurface Fluid-Flow at Cold Seeps: The Hikurangi Margin, Offshore New Zealand. *Mar. Pet. Geology.* 39 (1), 59–73. doi:10.1016/j.marpetgeo.2012.09.008
- Krämer, K., Holler, P., Herbst, G., Bratek, A., Ahmerkamp, S., Neumann, A., et al. (2017). Abrupt Emergence of a Large Pockmark Field in the German Bight, southeastern North Sea. *Sci. Rep.* 7 (1), 5150–5158. doi:10.1038/s41598-017-05536-1
- Kroeger, K. F., and Funnell, R. H. (2012). Warm Eocene Climate Enhanced Petroleum Generation from Cretaceous Source Rocks: A Potential Climate Feedback Mechanism? *Geophys. Res. Lett.* 39 (4), L04701. doi:10.1029/2011GL050345
- Lamb, S., Mortimer, N., Smith, E., and Turner, G. (2016). Focusing of Relative Plate Motion at a continental Transform Fault: Cenozoic Dextral Displacement >700 Km on New Zealand's Alpine Fault, Reversing >225 Km of Late Cretaceous Sinistral Motion. *Geochem. Geophys. Geosyst.* 17, 1197–1213. doi:10.1002/2015gc006225
- Li, J., Mitra, S., and Qi, J. (2020). Seismic Analysis of Polygonal Fault Systems in the Great South Basin, New Zealand. *Mar. Pet. Geology.* 111, 638–649. doi:10.1016/j.marpetgeo.2019.08.052
- Loncke, L., Mascle, J., and Fanil Scientific Parties, F. S. (2004). Mud Volcanoes, Gas Chimneys, Pockmarks and mounds in the Nile Deep-Sea Fan (Eastern Mediterranean): Geophysical Evidences. *Mar. Pet. Geology.* 21 (6), 669–689. doi:10.1016/j.marpetgeo.2004.02.004
- Luo, M., Chen, L., Tong, H., Yan, W., and Chen, D. (2014). Gas Hydrate Occurrence Inferred from Dissolved Cl⁻ Concentrations and $\delta^{18}\text{O}$ Values of Pore Water and Dissolved Sulfate in the Shallow Sediments of the Pockmark Field in Southwestern Xisha Uplift, Northern South China Sea. *Energies* 7 (6), 3886–3899. doi:10.3390/en7063886
- Magee, C., Hoggett, M., Jackson, C. A. L., and Jones, S. M. (2019). Burial-Related Compaction Modifies Intrusion-Induced Forced Folds: Implications for Reconciling Roof Uplift Mechanisms Using Seismic Reflection Data. *Front. Earth Sci.* 7, 37. doi:10.3389/feart.2019.00037
- Mazzini, A., Svensen, H. H., Forsberg, C. F., Linge, H., Lauritzen, S.-E., Haflidason, H., et al. (2017). A Climatic Trigger for the Giant Troll Pockmark Field in the Northern North Sea. *Earth Planet. Sci. Lett.* 464, 24–34. doi:10.1016/j.epsl.2017.02.014
- McArthur, A. D., Claussmann, B., Bailleul, J., Clare, A., and McCaffrey, W. D. (2020). Variation in Syn-Subduction Sedimentation Patterns from Inner to Outer Portions of Deep-Water Fold and Thrust Belts: Examples from the Hikurangi Subduction Margin of New Zealand. *Geol. Soc. Lond. Spec. Publications* 490 (1), 285–310. doi:10.1144/sp490-2018-95
- Meadows, D. J. (2009). *Stable Isotope Geochemistry of Paleocene to Early Eocene Strata Around Southern New Zealand*. Msc thesis (Wellington, New Zealand: Victoria University of Wellington).
- Morley, C. K., Maczak, A., Rungprom, T., Ghosh, J., Cartwright, J. A., Bertoni, C., et al. (2017). New Style of Honeycomb Structures Revealed on 3D Seismic Data Indicate Widespread Diagenesis Offshore Great South Basin, New Zealand. *Mar. Pet. Geology.* 86, 140–154. doi:10.1016/j.marpetgeo.2017.05.035
- Nickel, J. C., di Primio, R., Mangelsdorf, K., Stoddart, D., and Kallmeyer, J. (2012). Characterization of Microbial Activity in Pockmark fields of the SW-Barents Sea. *Mar. Geology.* 332–334, 152–162. doi:10.1016/j.margeo.2012.02.002
- Nicol, A., Mazengarb, C., Chanier, F., Rait, G., Uruski, C., and Wallace, L. (2007). Tectonic Evolution of the Active Hikurangi Subduction Margin, New Zealand, since the Oligocene. *Tectonics* 26 (4). doi:10.1029/2006tc002090
- Norton, D. L. (1984). Theory of Hydrothermal Systems. *Annu. Rev. Earth Planet. Sci.* 12, 155–177. doi:10.1146/annurev.ea.12.050184.001103
- Omosanya, K. O., and Harishidayat, D. (2019). Seismic Geomorphology of Cenozoic Slope Deposits and Deltaic Cliniforms in the Great South Basin (GSB) Offshore New Zealand. *Geo-mar Lett.* 39 (1), 77–99. doi:10.1007/s00367-018-00558-8
- Paull, C. K., Ussler, W., III, Borowski, W. S., and Spiess, F. N. (1995). Methane-rich Plumes on the Carolina continental Rise: Associations with Gas Hydrates. *Geol.* 23 (1), 89–92. doi:10.1130/0091-7613(1995)023<0089:mrpotc>2.3.co;2
- Pecher, I. A., Kukowski, N., Huebscher, C., Greinert, J., and Bialas, J. (2001). The Link between Bottom-Simulating Reflections and Methane Flux into the Gas Hydrate Stability Zone—New Evidence from Lima Basin, Peru Margin. *Earth Planet. Sci. Lett.* 185 (3), 343–354. doi:10.1016/s0012-821x(00)00376-9
- Phillips, T. B., and Magee, C. (2020). Structural Controls on the Location, Geometry and Longevity of an Intraplate Volcanic System: The Tuatara Volcanic Field, Great South Basin, New Zealand. *J. Geol. Soc.* 177, 1039–1056. doi:10.1144/jgs2020-050
- Pickrill, R. A. (1993). Shallow Seismic Stratigraphy and Pockmarks of a Hydrothermally Influenced lake, Lake Rototiti, New Zealand. *Sedimentology* 40, 813–828. doi:10.1111/j.1365-3091.1993.tb01363.x
- Pilcher, R., and Argent, J. (2007). Mega-pockmarks and Linear Pockmark Trains on the West African continental Margin. *Mar. Geology.* 244, 15–32. doi:10.1016/j.margeo.2007.05.002
- Plaza-Faverola, A., Bünz, S., and Mienert, J. (2011). Repeated Fluid Expulsion through Subseabed Chimneys Offshore Norway in Response to Glacial Cycles. *Earth Planet. Sci. Lett.* 305 (3), 297–308. doi:10.1016/j.epsl.2011.03.001
- Prélat, A., Hodgson, D. M., and Flint, S. S. (2009). Evolution, Architecture and Hierarchy of Distributary Deep-water Deposits: a High-resolution Outcrop Investigation from the Permian Karoo Basin, South Africa. *Sedimentology* 56 (7), 2132–2154.
- Rice, D. D., and Claypool, G. E. (1981). Generation, Accumulation, and Resource Potential of Biogenic Gas. *Am. Assoc. Pet. Geol. Bull.* 65 (1), 5–25. doi:10.1306/2f919765-16ce-11d7-8645000102c1865d
- Rice, D. D. (1992). Controls, Habitat, and Resource Potential of Ancient Bacterial Gas. *Bacterial Gas*, 91–118.
- Rollet, N., McGivern, S., Hashimoto, T., Hackney, R., Petkovic, P., Higgins, K., et al. (2012). Seafloor Features and Fluid Migration in the Capel and Faust Basins, Offshore Eastern Australia. *Mar. Pet. Geology.* 35 (1), 269–291. doi:10.1016/j.marpetgeo.2012.03.011
- Sahoo, T., King, P., Bland, K., Strogon, D., Sykes, R., and Bache, F. (2014). Tectono-sedimentary Evolution and Source Rock Distribution of the Mid to Late Cretaceous Succession in the Great South Basin, New Zealand. *APPEA J.* 54 (1), 259–274. doi:10.1071/aj13026
- Schioler, P., Rogers, K., Sykes, R., Hollis, C. J., Ilg, B., Meadows, D., et al. (2010). Palynofacies, Organic Geochemistry and Depositional Environment of the Tarrant Formation (Late Paleocene), a Potential Source Rock in the Great South Basin, New Zealand. *Mar. Pet. Geol.* 27 (2), 351–369.
- Sérié, C., Huuse, M., and Schødt, N. H. (2012). Gas Hydrate Pingoes: Deep Seafloor Evidence of Focused Fluid Flow on continental Margins. *Geology* 40, 207–210. doi:10.1130/g32690.1
- Shalaby, M. R., Malik, O. A., Lai, D., Jumat, N., and Islam, M. A. (2020). Thermal Maturity and TOC Prediction Using Machine Learning Techniques: Case Study from the Cretaceous-Paleocene Source Rock, Taranaki Basin, New Zealand. *J. Petrol. Explor. Prod. Technol.* 10, 2175–2193. doi:10.1007/s13202-020-00906-4
- Tasianas, A., Bünz, S., Bellwald, B., Hammer, Ø., Planke, S., Lebedeva-Ivanova, N., et al. (2018). High-resolution 3D Seismic Study of Pockmarks and Shallow Fluid Flow Systems at the Snøhvit Hydrocarbon Field in the SW Barents Sea. *Mar. Geology.* 403, 247–261. doi:10.1016/j.margeo.2018.06.012
- Uruski, C. I. (2010). New Zealand's deepwater Frontier. *Mar. Pet. Geology.* 27 (9), 2005–2026. doi:10.1016/j.marpetgeo.2010.05.010
- Uruski, C., Kennedy, C., Harrison, T., Maslen, G., Cook, R. A., Sutherland, R., et al. (2007). Petroleum Potential of the Great South Basin, New Zealand—new Seismic Data Improves Imaging. *APPEA J.* 47 (1), 145–161. doi:10.1071/aj06008
- Viskovic, G. P. D. (2011). *Investigation of Fluid Migration Pathways in the Shallow Subsurface of the Great South Basin, through the Use of High-Resolution Seismic*

- Imaging of Fault and Fracture Systems*. MSc thesis (Dunedin, New Zealand: University of Otago).
- Waghorn, K. A., Pecher, I., Strachan, L. J., Crutchley, G., Bialas, J., Coffin, R., et al. (2018). Paleo-fluid Expulsion and Contouritic Drift Formation on the Chatham Rise, New Zealand. *Basin Res.* 30 (1), 5–19. doi:10.1111/bre.12237
- Watson, S. J., Mountjoy, J. J., Barnes, P. M., Crutchley, G. J., Lamarche, G., Higgs, B., et al. (2020). Focused Fluid Seepage Related to Variations in Accretionary Wedge Structure, Hikurangi Margin, New Zealand. *Geology* 48 (1), 56–61. doi:10.1130/g46666.1

Conflict of Interest: The authors declare that the research was conducted in the absence of any commercial or financial relationships that could be construed as a potential conflict of interest.

Publisher's Note: All claims expressed in this article are solely those of the authors and do not necessarily represent those of their affiliated organizations, or those of the publisher, the editors and the reviewers. Any product that may be evaluated in this article, or claim that may be made by its manufacturer, is not guaranteed or endorsed by the publisher.

Copyright © 2021 Karaket, Chenrai and Huuse. This is an open-access article distributed under the terms of the Creative Commons Attribution License (CC BY). The use, distribution or reproduction in other forums is permitted, provided the original author(s) and the copyright owner(s) are credited and that the original publication in this journal is cited, in accordance with accepted academic practice. No use, distribution or reproduction is permitted which does not comply with these terms.



The Origin and 3D Architecture of a Km-Scale Deep-Water Scour-Fill: Example From the Skoorsteenberg Fm, Karoo Basin, South Africa

L. A. S. Hansen^{1*}, R. S. Healy¹, L. Gomis-Cartesio², D. R. Lee¹, D. M. Hodgson¹, A. Pontén³ and R. J. Wild³

¹Stratigraphy Group, School of Earth and Environment, University of Leeds, Leeds, United Kingdom, ²Equinor ASA, Oslo, Norway, ³Equinor ASA, Trondheim, Norway

OPEN ACCESS

Edited by:

Fabiano Gamberi,
National Research Council (CNR), Italy

Reviewed by:

Roberto Tinteri,
University of Parma, Italy
Aggeliki Georgiopolou,
University of Brighton,
United Kingdom

*Correspondence:

L. A. S. Hansen
l.a.hansen@leeds.ac.uk

Specialty section:

This article was submitted to
Sedimentology, Stratigraphy and
Diagenesis,
a section of the journal
Frontiers in Earth Science

Received: 07 July 2021

Accepted: 19 August 2021

Published: 20 September 2021

Citation:

Hansen LAS, Healy RS,
Gomis-Cartesio L, Lee DR,
Hodgson DM, Pontén A and Wild RJ
(2021) The Origin and 3D Architecture
of a Km-Scale Deep-Water Scour-Fill:
Example From the Skoorsteenberg
Fm, Karoo Basin, South Africa.
Front. Earth Sci. 9:737932.
doi: 10.3389/feart.2021.737932

Scours, and scour fields, are common features on the modern seafloor of deep-marine systems, particularly downstream of submarine channels, and in channel-lobe-transition-zones. High-resolution images of the seafloor have improved the documentation of the large scale, coalescence, and distribution of these scours in deep-marine systems. However, their scale and high aspect ratio mean they can be challenging to identify in outcrop. Here, we document a large-scale, composite erosion surface from the exhumed deep-marine stratigraphy of Unit 5 from the Permian Karoo Basin succession in South Africa, which is interpreted to be present at the end of a submarine channel. This study utilizes 24 sedimentary logs, 2 cored boreholes, and extensive palaeocurrent and thickness data across a 126 km² study area. Sedimentary facies analysis, thickness variations and correlation panels allowed identification of a lower heterolithic-dominated part (up to 70 m thick) and an upper sandstone-dominated part (10–40 m thick) separated by an extensive erosion surface. The lower part comprises heterolithics with abundant current and sinusoidal ripples, which due to palaeocurrents, thickness trends and adjacent depositional environments is interpreted as the aggradational lobe complex fringes. The base of the upper part comprises 2–3 medium-bedded sandstone beds interpreted as precursor lobes cut by a 3–4 km wide, 1–2 km long, and up to 28 m deep, high aspect ratio (1:100) composite scour surface. The abrupt change from heterolithics to thick-bedded sandstones marks the establishment of a new sediment delivery system, which may have been triggered by an updip channel avulsion. The composite scour and subsequent sandstone fill support a change from erosion- and bypass-dominated flows to depositional flows, which might reflect increasingly sand-rich flows as a new sediment route matured. This study provides a unique outcrop example with 3D stratigraphic control of the record of a new sediment conduit, and development and fill of a large-scale composite scour surface at a channel mouth transition zone, providing a rare insight into how scours imaged on seafloor data can be filled and preserved in the rock record.

Keywords: scours, submarine lobes, channel-lobe-transition-zone, turbidites, karoo basin

INTRODUCTION

Scours are readily recognized erosional bedforms on modern seafloor datasets in deep-marine systems (Wynn et al., 2002; Bonnel et al., 2005; Fildani et al., 2006; Macdonald et al., 2011; Maier et al., 2011, 2020; Covault et al., 2014; Carvajal et al., 2017; Droz et al., 2020) and have been imaged in many high resolution seafloor data, providing more detail about their distribution and geometry (Carvajal et al., 2017; Droz et al., 2020; Maier et al., 2020, 2018). Scours are associated with slide scars (Pickering and Hilton, 1998; Lee et al., 2004; Moscardelli et al., 2006; Dakin et al., 2013), or located in channel-lobe-transition-zones (CLTZs) (Hofstra et al., 2015; Brooks et al., 2018a), or channel mouth settings prior to channel propagation (Carvajal et al., 2017; Droz et al., 2020; Maier et al., 2020; Pohl et al., 2020, 2019). Abundant examples of interpreted ancient small-scale scour-fills include the Ross Formation, Ireland (Elliott, 2000; Lien et al., 2003; Pyles et al., 2014), the Albian Black Flysch, Spain (Vicente Bravo and Robles, 1995), the Annot sandstone, France (Morris and Normark, 2000), the Windermere Group, Canada (Terlaky et al., 2016), the Karoo Basin, South Africa (Brooks et al., 2018a), the Macigno Costiero Formation, Italy (Eggenhuisen et al., 2011; Piazza and Tinterri, 2020), and the Boso Peninsula, Japan (Ito et al., 2014). Generally, the dimensions of these exhumed scour-fills are a few metres deep and 10–100s of metres long and wide, whilst scour dimensions described from modern systems are 10s of metres deep and 100–1000s of metres long and wide (e.g. Wynn et al., 2002; Macdonald et al., 2011; Carvajal et al., 2017). Large-scale scours infilled by turbidites are rarely documented from outcrop due to the high aspect ratio of the erosion surfaces and the difficulty in distinguishing them from channel-fills (Hofstra et al., 2015).

Stratigraphically, the presence of scour-fills can provide important insights into the evolution of deep-water system as whole, as they may mark a change in slope gradient, a temporal change in the nature of the flows, or changes in sediment supply. Changes in slope gradient and loss of confinement of a turbidity current can result in rapid flow transformation and enhanced basal shearing, which results in scouring via a process called “flow relaxation” (Komar, 1971; Mutti and Normark, 1987, 1991; García and Parker, 1993; Vicente Bravo and Robles, 1995; Wynn et al., 2002; Ito, 2008; Hofstra et al., 2015; Brooks et al., 2018a; Pohl et al., 2019). The depositional or erosional nature of flows either leads to infilling of the scour or further erosion where sediments are largely bypassed and deposited further downdip (Hofstra et al., 2015; Brooks et al., 2018a). Therefore, improved identification of scour-fills, and their stratigraphic evolution, can contribute to improved understanding of source-to-sink approaches.

The deep-marine stratigraphy of Unit 5 from the Permian Karoo Basin succession in South Africa, provides a unique outcrop where a large composite erosion surface can be mapped with three dimensional constraints. The presence of the erosion surface marks a significant and abrupt change from an up to 70 m thick lower package of heterolithics to a 40 m thick package of amalgamated sandstones. Unit 5 palaeogeography has been constrained by past studies (Hodgson et al., 2006; Hofstra et al., 2017; Johnson et al.,

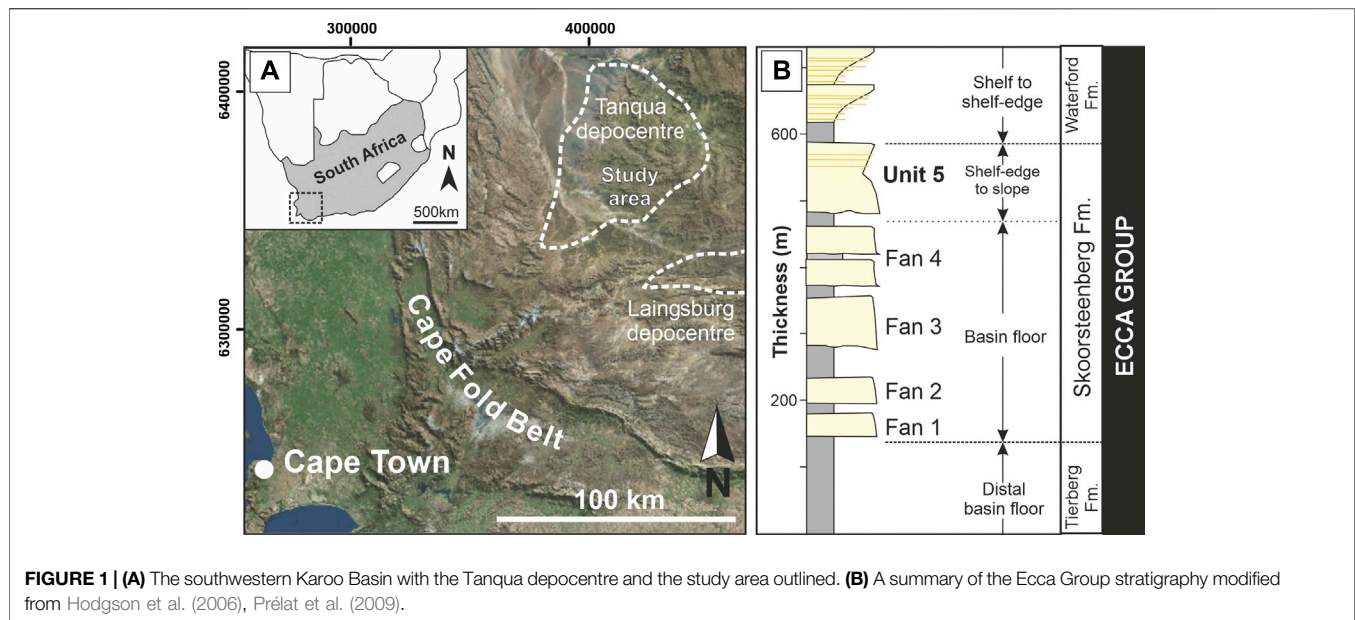
2001; Wild et al., 2009, 2005), and with the 3D outcrop control and research borehole data the following objectives are addressed: 1) to investigate the depositional environment of the thick basal package of heterolithics; 2) to document and establish the origin of the 3D erosion surface; and 3) to propose a palaeogeographic evolution of Unit 5 in the Skoorsteenberg area.

GEOLOGICAL SETTING

The Karoo Basin is bounded by the southern and western branches of the Cape Fold Belt (**Figure 1A**), and was traditionally interpreted as a retroarc foreland basin that developed from the early Permian (e.g., (De Wit and Ransome, 1992; Veevers et al., 1994; Visser and Praekelt, 1996; Visser, 1997; López-Gamundí and Rossello, 1998). However, recent models relate Permian subsidence to long-wavelength dynamic topography driven by the subducting palaeo-Pacific plate (Tankard et al., 2009), and no emergent Cape Fold Belt at the time of deep-water deposition (Blewett and Phillips, 2016). The Tanqua and Laingsburg depocentres make up the SW part of the Karoo Basin (**Figure 1A**), and are filled by the Late Carboniferous to Early Jurassic Karoo Supergroup (>5 km thick). Within the Tanqua depocentre, this succession comprises the glacial Dwyka Group, overlain by the post-glacial deep-marine to shallow-marine Ecca Group, and the non-marine Beaufort Group (**Figure 1B**). The Ecca Group is an approximately 1.4 km thick shallowing upward succession from deep-marine to fluvial settings (King et al., 2009; Flint et al., 2011). The 0.4 km thick Skoorsteenberg Formation is part of the Ecca Group and comprises four submarine fans (Fans 1–4) and an overlying succession termed Unit 5 (Bouma and Wickens, 1994; Morris et al., 2000; Johnson et al., 2001; Hodgson et al., 2006; Wild et al., 2009), which is the focus of this study. Several field studies (Bouma and Wickens, 1991; Johnson et al., 2001; Hodgson et al., 2006; Prélat et al., 2009; Kane et al., 2017; Hansen et al., 2019) and 11 research boreholes (Luthi et al., 2006; Sychala et al., 2017a; Hofstra et al., 2017) constrain the stratigraphic framework of the Skoorsteenberg Formation.

Originally, the distal (northern) area of Unit 5, at Skoorsteenberg, was recognised as Fan 5, and interpreted as a slope fan, and the southern, most proximal area, at Groot Hangklip, was referred to as Fan 6 (Wickens 1994; Basu and Bouma, 2000; Wach et al., 2000; Johnson et al., 2001; van der Werff and Johnson, 2003). Regional mapping of an overlying 12 m thick mudstone that correlated these sand-prone units led to the redefinition of Unit 5 (Wild et al., 2009).

In proximal (southern) areas of Unit 5 at Kleine Hangklip, stacked W-E and SW-NE orientated submarine slope channel complexes have been interpreted (Wild et al., 2005; Bell et al., 2020) that overlie the updip pinchout of Fans three and 4 (Hansen et al., 2019). In distal (northern) areas of Unit 5 submarine fan deposits have been mapped southeast of the study area at Blaukop, where sand-rich channel-fills incise into proximal lobes (Hofstra et al., 2017). This study focuses on the northern exposures of Unit 5 at Skoorsteenberg that are characterised by a thick lower part (~70 m) of thin-bedded



sandstones and siltstone, and an upper part (~40 m) of thick-bedded sandstones. Previous interpretations of these outcrops include “interfan deposits” overlain by a slump scar-fill towards the top (Johnson et al., 2001) and as an axial channel conduit (22 m thick, 8 km wide) that diverges downdip into three distributary channels (van der Werff and Johnson, 2003). Overall, published studies point towards Unit 5 being a deep-water slope apron fed by multiple W-E and SW-NE submarine channel-levees feeding lobes (Hodgson et al., 2006), with an overall younging direction of conduits along slope to the NW.

DATA AND METHODS

This study is based on 24 measured outcrop sections and 2 behind outcrop cores (NS1 and NS2) located to the east of the outcrop area (Figure 2A). These sections were logged at 1:50 scale (~1 km cumulative thickness), recording grain size, sedimentary structures and bounding surfaces. Two cores and three outcrop logs cover the whole thickness of Unit 5, which is defined by underlying and overlying regional mudstones (Wild et al., 2009). Fifteen outcrop logs focus on the sandstone-prone upper part of Unit 5 (Figure 2A).

For this study, Unit 5 is subdivided into a lower and upper part (Figure 2B) using a distinctive concretion marker bed, which was walked out in order to observe the spatial and temporal distribution of overlying sedimentary facies. Photo panels and photogrammetric models of the outcrop created from Uncrewed Aerial Vehicle (UAV) imagery (Stratigraphy Group, University of Leeds, 2021), using Agisoft Metashape and LIME, were used to document and interpret stratigraphic surfaces and architectural elements. Quantitative analysis of the thickness variations (using the inverse distance weighted (IDW) interpolation method in ESRI ArcGIS) of the whole of

Unit 5, and the lower and upper parts, was undertaken to determine regional changes.

SEDIMENTARY FACIES

Table 1 summarizes the sedimentary facies scheme (Figure 3), determined by their lithology, sedimentary structures, bed thickness, contacts and geometries.

MAP DATA

Unit 5 has been subdivided into two parts using a distinctive concretion marker bed (5–12 cm thick) that is resistant to weathering, at a consistent stratigraphic level and was walked out across the outcrop area. The lower part is dominated by thin-bedded heterolithics, and the upper part by medium-to thick-bedded sandstone (Figure 4). We present palaeocurrent and thickness data based on these two parts. The concretion marker bed is not identified in the NS1 and NS2 cores, which means the thickness of the lower and upper parts is poorly constrained.

Palaeocurrent Analysis

Four hundred and two palaeocurrent measurements were collected from current and climbing ripple lamination, groove marks, and orientation of margins of incision surfaces. The palaeocurrent data (Figures 5B,C) have a narrow spread from N to NE, which is consistent with the overall depositional dip direction for the Skoorsteenberg Fm. (e.g. Hodgson et al., 2006; Pr  lat et al., 2009; Hansen et al., 2019). The lower thin-bedded part is dominated by current and climbing ripple laminations trending towards the NE (average 084 , n = 207) (Figure 5B), with the upper part showing more dispersed trends to the N to NE (average 074 , n = 195) (Figure 5C).

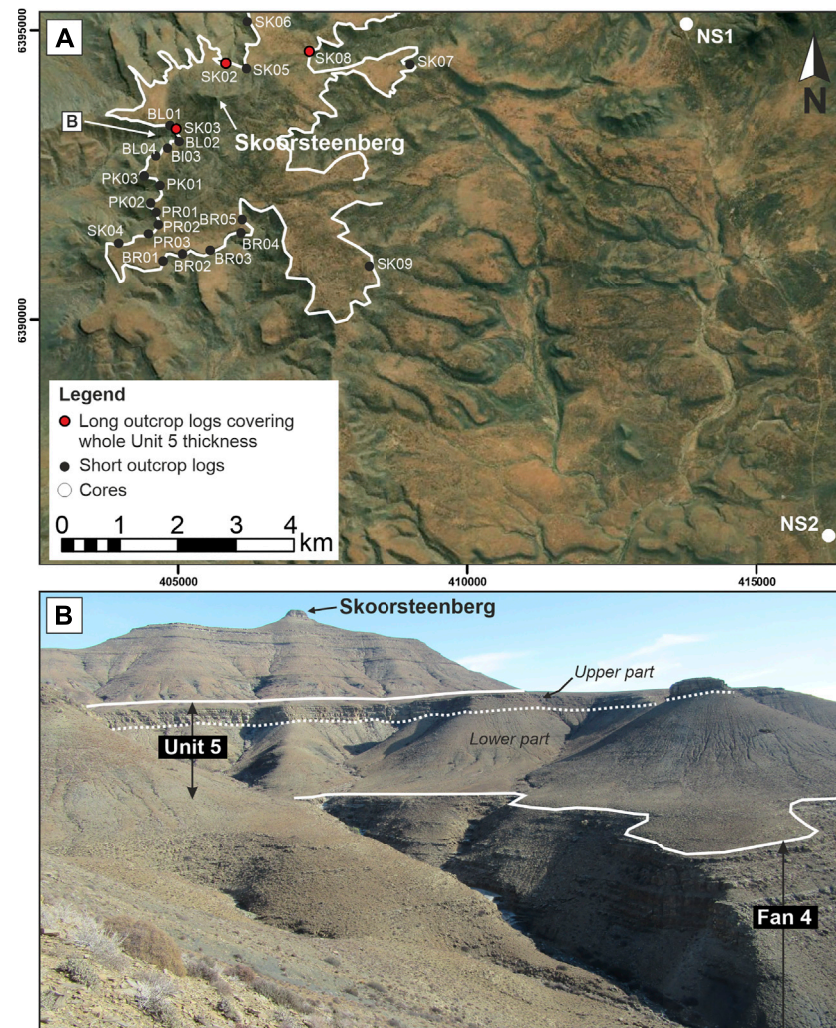


FIGURE 2 | (A) A detailed map of the study area with log locations indicated. **(B)** Overview photo of the study area showing Fan 4 and the partitioning seen in Unit 5.

Thickness Analysis

The Unit 5 isopach map shows eastward thinning from 120 m in the Skoorsteenberg area to 70 m at NS1 (Figure 5A). The lower thin-bedded part is bounded by the basal mudstone below Unit 5 and the concretion marked bed at the top (Figure 4), and thickens to the NW from 33 to 68 m thick (Figure 5B). The facies above the concretion marker bed change to medium-to thick-bedded, coarser grained sandstones, which are incised by a widespread erosion surface that can be correlated between field logs for kilometres (Figure 4). Overlying this erosion surface is filled by medium-to thick-bedded sandstones that thicken westward up to 40 m (Figure 5C).

ARCHITECTURE OF UNIT 5

Lower Part: Thin-Bedded Heterolithics

The thin-bedded lower succession overlies the basal mudstone that separates Fan 4 and Unit 5 and is characterised by siltstone- and

sandstone-prone heterolithics (FA2, FA3), dominated by sinusoidal, climbing, and current ripples (Figures 4A, 6). Sinusoidal lamination is a form of highly aggradational climbing-ripple cross-lamination (Jopling and Walker, 1968), which indicate persistent high rates of sediment deposition. This suggests that sediment gravity flows were expanding and depositing rapidly, either due to a change in gradient or an abrupt change in topographic confinement (Allen, 1973; Kneller, 1995; Jobe et al., 2012). Individual beds are normally graded, and coarsening- or fining-upwards packages (<5 m thick) are identified, but thicker grain-size or thickness trends are not present. A more sandstone-prone heterolithic unit, up to 12 m thick, is present towards the top of the succession (Figures 4, 6).

Upper Part: Medium-to Thick-Bedded Sandstone

The upper section of the Unit 5 stratigraphy is constrained using the concretion marker bed as a basal datum and the capping regional mudstone at the top of Unit 5 (Figures 4, 6). The

TABLE 1 | Unit 5 sedimentary facies classification, description and interpretation.

Sedimentary facies	Structures	Bed thickness	Bed boundaries	Outcrop thickness/ geometry	Bioturbation and other	Process interpretation
Mudstone (FA1)	Structureless, some thin-bedded (mm-scale) graded siltstone beds. Dark green, fissile to blocky	Up to 12 m	Gradational	Laterally extensive for tens of kilometres	Low bioturbation. Common concretion horizons, with thin ash layers (<0.01 m)	Hemipelagic suspension fallout. The coarser siltstones indicate deposition from low concentration turbidity currents (Boulestex et al., 2019)
Siltstone-prone heterolithics (FA2)	Structureless, planar and cross-ripple laminated siltstones, interbedded with very fine-grained sandstones, commonly ripple laminated, occasionally structureless or planar laminated	Thin-bedded (<0.15m, cm to mm-scale)	Gradational	Packages up to 10s of metres thick. Laterally extensive packages over kilometres	Low bioturbation	Deposited by dilute waning turbidity currents (Kneller and Buckee, 2000; Meiburg and Kneller, 2010)
Sandstone-prone heterolithics (FA3)	Planar or ripple-laminated, very fine-grained sandstone interbedded with ripple laminated siltstones. Common sinusoidal ripple laminations with stoss-side preserved, forming 3D aggrading asymmetric bedforms. Less frequently planar and current ripple laminated	Thin-bedded (<0.15m, cm to mm-scale)	Gradational	Packages up to 10s of meters thick. Laterally extensive for up to 100s of meters	Low bioturbation	Deposited by dilute turbidity currents with higher rate of deposition, by waning turbidity currents (Kneller and Buckee, 2000; Meiburg and Kneller, 2010). Sinusoidal lamination is a form of highly aggradational climbing-ripple cross-lamination (Jopling and Walker 1968). Persistent high rates of deposition suggests that sediment gravity flows were expanding and depositing rapidly (highly non-uniform; Kneller 1995)
Thin to medium-bedded sandstones (FA4)	Current and climbing ripple laminated, very fine to medium grained sandstones. Occasionally parallel laminated, and less commonly structureless beds	Up to 0.5 m thick	Locally beds have erosive bases lined with mudclasts	Laterally extensive for up to 10s of meters	Low bioturbation	Rapid deposition from high-density tractional turbidity currents with varying sedimentation rates
Medium to thick-bedded sandstones (FA5)	Predominantly structureless, very fine to fine grained sandstone, normally graded and pass upwards from structureless to parallel laminated or very low angle ripple laminated. Commonly amalgamated with loaded bases and flame structures	>0.5 m thick beds	Loaded and erosional bases mantled with mudclasts forming lag deposits	Laterally extensive for up to 10s of meters	Low bioturbation	Rapid deposition by high-density sediment gravity flows in high-energy depositional environments where sediment deposition suppresses the formation of sedimentary structures (Sumner et al., 2012). Mudclast lags indicative of bypassing flows (Stevenson et al., 2015)

concretion marker bed (5–12 cm thick) is identified by a distinctive brown-orange colour, is more resistant to weathering, and contrasts to the light grey to pale yellow of the surrounding stratigraphy (**Figure 4B**). The bed is laterally continuous for kms and was walked out between outcrop logs.

Concretion Marker Bed to Erosion Surface

The stratigraphy overlying the concretion marker bed consists of ~5 m of siltstone- and sandstone-prone heterolithics (FA2 and

FA3) above which two to three medium- to thick-bedded, sandstone beds are present (**Figures 4, 6, 7B–D**). These are truncated by an extensive erosion surface mantled by mudclasts (**Figure 7A**), which can be correlated between the outcrop logs. Multiple smaller erosion surfaces merge onto the larger surface indicating its composite nature (**Figure 7D**). To establish the shape and amount of erosion into the underlying stratigraphy, two measurement methods were employed (**Figure 8**): 1) measuring the stratigraphic thickness between

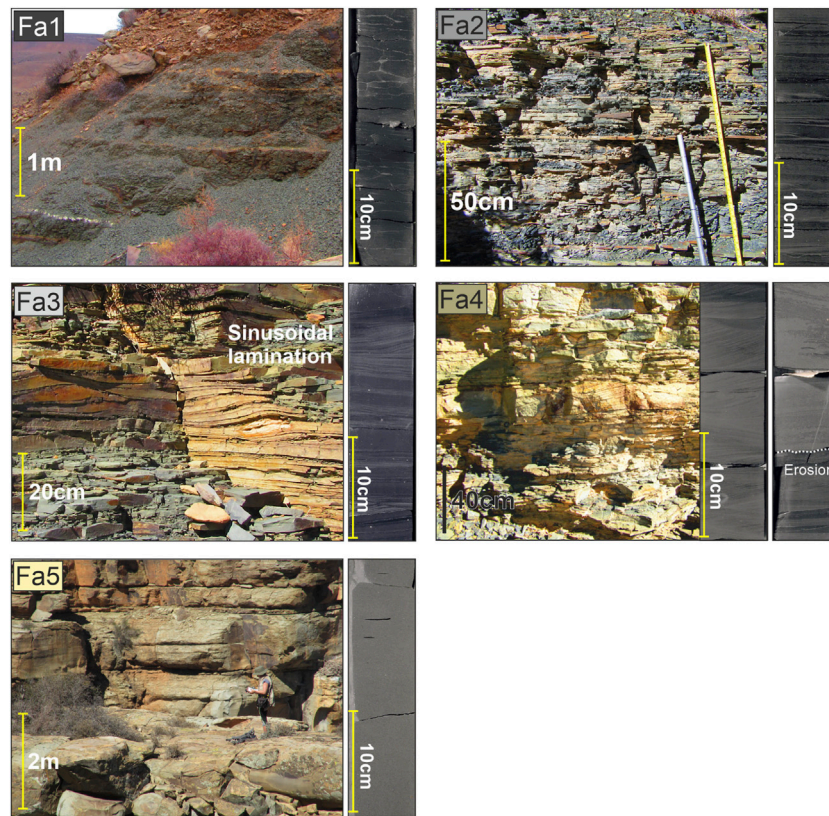


FIGURE 3 | Representative photographs of the five sedimentary facies in outcrop and core: FA1–Mudstone, FA2–Siltstone-prone heterolithics, FA3–Sandstone-prone heterolithics, FA4–Thin to medium-bedded sandstone, FA5–Medium to thick-bedded sandstone.

the concretion marker bed and the base of the erosion surface from the logs, which showed that net erosion is up to 28 m (**Figure 8A**), and 2) mapping the erosion surface using photogrammetric models of the outcrop built from UAV imagery to provide 3D constraints on the shape (**Figures 8B–D**), and the elevation change from inside to outside the cut to constrain erosion depth. The results of both methods showed that the area of maximum erosion is in the west of the study area, between logs SK03 and PK02 forming a deeper low aspect ratio heel of maximum erosion. The length of erosion is at least 1–2 km long in a downdip direction, and about 3–4 km wide in a strike section (**Figure 8**).

Erosion Surface to Top Unit 5

Above the laterally extensive erosion surface, and in the area of maximum erosion, the stratigraphy is characterised by a 40 m thick succession of amalgamated, structureless to parallel laminated, thick bedded sandstones (**Figures 4, 6, 9A,B**). In areas overlying less erosion, the succession is more stratified and characterised by ripple laminated medium-bedded sandstones (**Figures 6, 9C**).

Overlying this initial depositional phase, concave-up erosion surfaces 10–150 m wide, 1–8 m deep incise into underlying sandstones (**Figures 4C, 6, 9C**), and are overlain by medium-bedded structureless sandstones. Locally, the

larger erosion surfaces are mantled with mudstone and siltstone clasts.

The uppermost stratigraphy of Unit 5 comprises siltstone-prone, ripple laminated heterolithics, with rare sinusoidal laminations (**Figure 4**). The heterolithics fine upwards to a 12–15 m thick, capping mudstone, indicating the termination of Unit 5.

NS1 and NS2

In both cores, the base of Unit 5 is defined by a several metres thick mudstone (**Figure 10**), with the top of the boreholes sited close to the top of Unit 5. In NS1, Unit 5 is ~72 m thick, and consists of a basal ~25 m thick heterolithic unit, overlain by a ~20 m thick coarser grained, structureless to ripple laminated, medium to thick-bedded sandstone unit (**Figure 10**). Another siltstone-prone heterolithic unit is overlain by a ~15 m thick medium-to thick-bedded, structureless to ripple laminated sandstone package with mudclasts mantling erosion surfaces (**Figure 10**). Unit 5 in NS2 is ~91 m thick, with a lower ~30 m siltstone- and sandstone-prone heterolithic package (**Figure 10**). Above this a ~25 m thick, very fine to fine-grained, medium to thick-bedded sandstone package punctuates the succession, which is predominantly parallel and ripple laminated (**Figure 10**). Small (<1 cm diameter) mudclasts at bed bases and truncation of beds mark erosion surfaces. Some

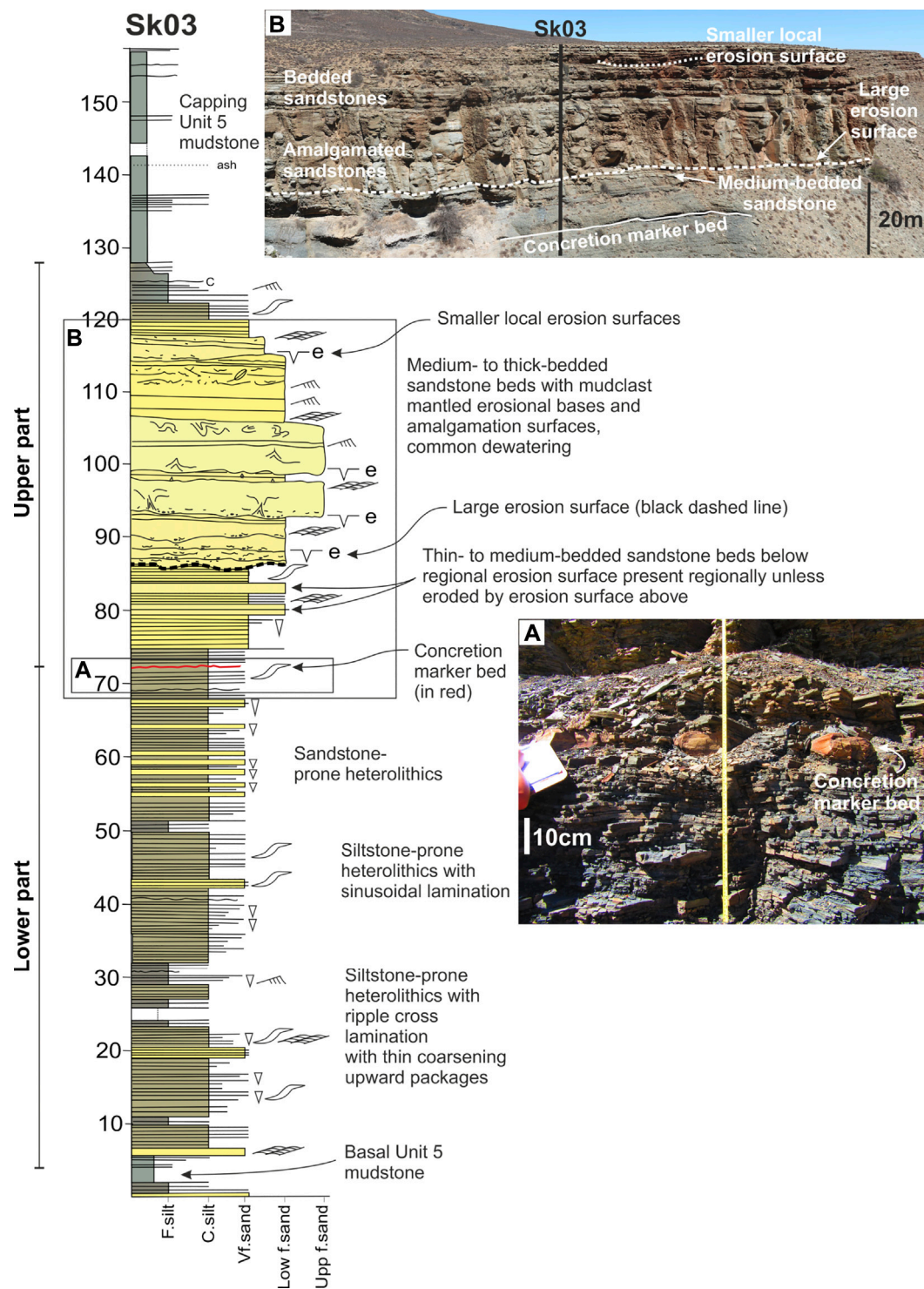


FIGURE 4 | Log SK03 showing an overview of the Unit 5 stratigraphy with the lower thin-bedded and upper sandstone-prone parts. The concretion marker bed and regional erosion surface are highlighted by a red solid and black dashed line respectively. **(A)** Photo of the thin-bedded succession with concretion marker bed. **(B)** Photo of log SK03 showing the concretion marker bed and the medium-bedded sandstone beds below the regional erosion surface. The sandstone fill of the large erosion surface can be seen as well as a small erosion surface towards the top of this fill.

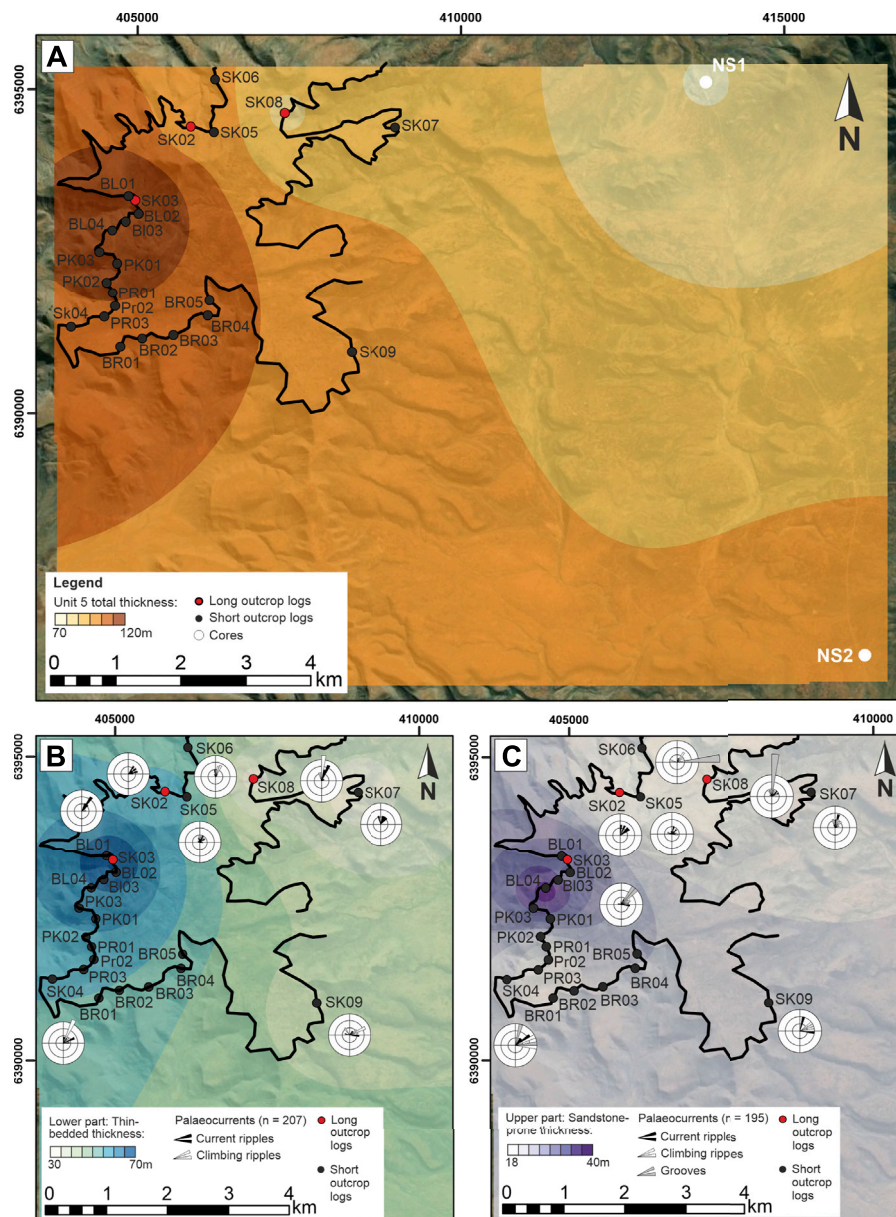


FIGURE 5 | (A) Unit 5 isopach map showing thickening to the NW; **(B)** Isopach map of the lower thin-bedded part showing thickening towards the W, with palaeoflow to the N and NE; **(C)** Isopach map of the upper sandstone-prone part showing thickening towards the W, with palaeocurrents indicating flow towards the N and NE. The black line indicates the outcrop belt of the upper division of Unit 5.

sandstones become argillaceous towards the bed tops, suggesting the presence of hybrid beds in this succession. Another heterolithic unit is overlain by a ~20 m thick unit of medium- to thick-bedded structureless and climbing rippled sandstones (Figure 10).

Fine-scale correlation of Unit 5 between the cores and outcrop logs is challenging in the absence of the concretion marker bed. Despite the 9 km distance between the cores, the two distinct sandstone packages may be correlated. However, their correlation with the Skoorsteenberg outcrops is uncertain. Nonetheless, the sedimentary facies observed in

both cores, particularly the argillaceous sandstone beds interpreted as hybrid beds in NS2, suggest that these sandstones represent lobe complexes. Lobes have also been interpreted 7 km to the south of NS2 in the lower part of Unit 5 at Blaukop and core BK1 (Hofstra et al., 2017). These associations support the lower part of Unit 5 in the cores being lobe complexes, with more evidence for erosion in the upper sandstone package, although the facies support an interpretation of more lobe axes in a lobe complex. The thin-bedded heterolithics between share affinities (bed thickness, ripple laminated sandstones) to a similar

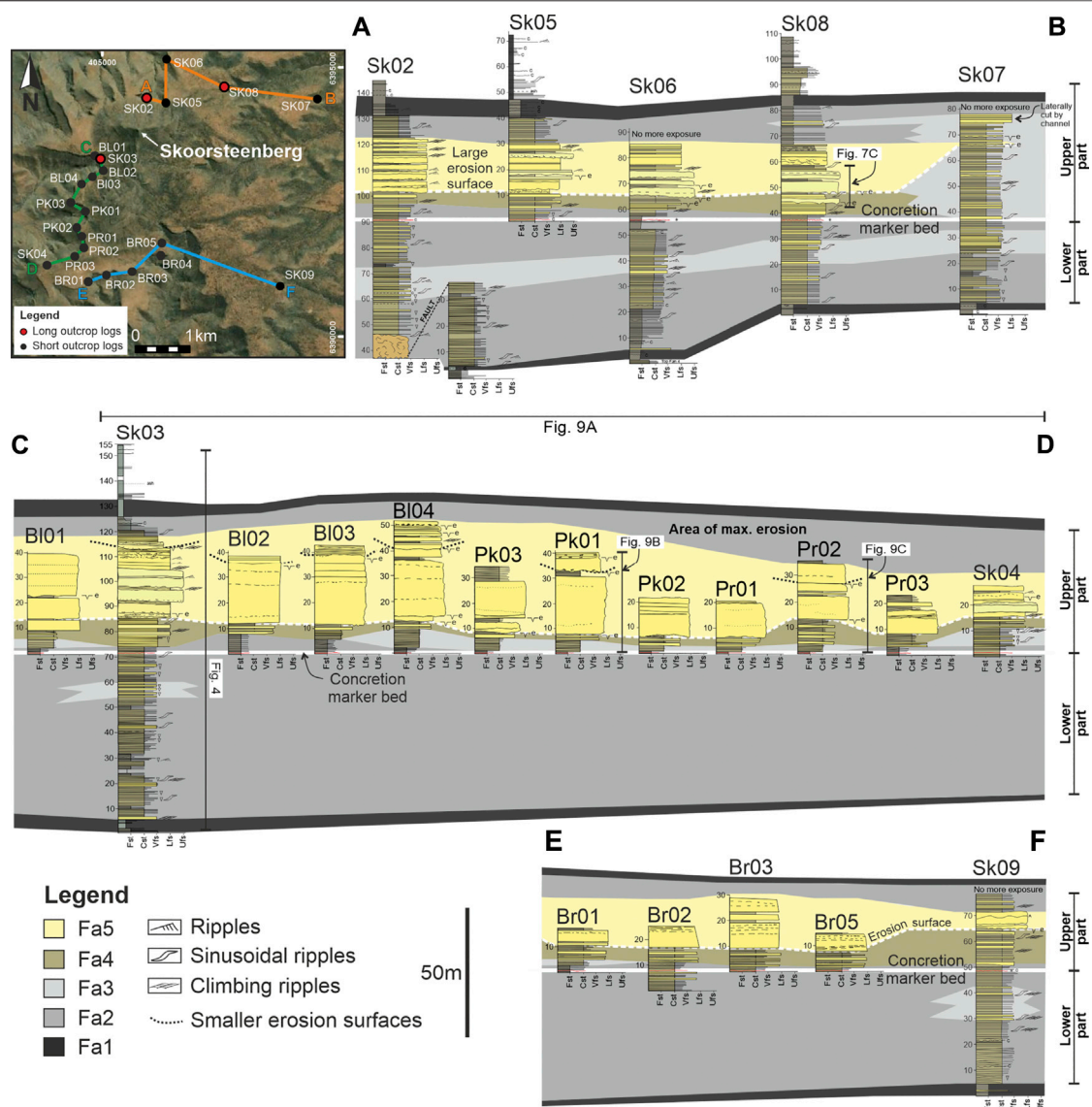


FIGURE 6 | Correlation panel of outcrop logs of Unit 5 flattened on the concretion marker bed on (the white solid line). The erosion surface is marked by the white dashed line with smaller erosion surfaces in the upper part shown by the black dashed lines. Locations of correlation panels **A-B**, **C-D** and **E-F** are shown in the map on the top left.

succession in Fan 4, and support a similar interpretation as the fringe of another lobe complex (Spychala et al., 2017a).

DISCUSSION

Depositional Environment of Lower Heterolithics-Prone Part

The heterolithic succession in the lower part of Unit 5 (70 m thick) has an abundance of sinusoidal, climbing and current ripples but no major coarsening- or fining-upwards trends. Thick accumulations of thin-bedded heterolithics in deep-water settings either occur in external levees adjacent to submarine channels, as internal levees and terrace deposits within large-scale erosion surfaces, or at lateral or distal lobe fringes and basin plain settings (Walker, 1975; Normark and Piper,

1991; Skene et al., 2002; Deptuck et al., 2003; Kane et al., 2007; Kane and Hodgson, 2011; Hansen et al., 2015; Sychala et al., 2017b). Sinusoidal ripples have previously been described in the Karoo Basin, in external and internal levees and aggradational lobe fringe deposits in the Fort Brown Formation in the Laingsburg depocentre (Kane and Hodgson, 2011; Morris et al., 2014a; Sychala et al., 2017b). Previous work has constrained the palaeogeographic context of the study area where there is a downdip architectural change from submarine channel complexes 25 km south of the study area (e.g. Wild et al., 2005; Bell et al., 2020) to lobe-dominated deposits mapped southwest of Skoorsteenberg (Hofstra et al., 2017).

Thick accumulations of heterolithics, or thin-bedded turbidites, in external levee successions have been observed from many outcrops, modern seafloor studies and in the subsurface (Clemenceau et al., 2000; Kane et al., 2007;

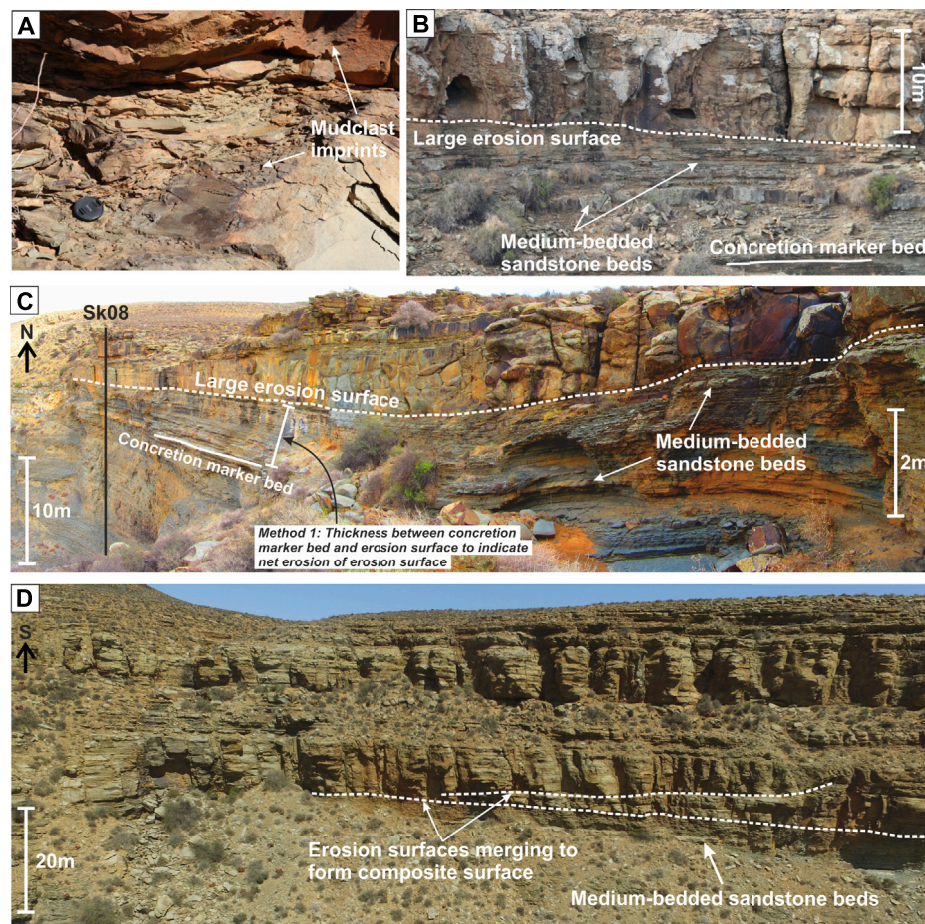


FIGURE 7 | (A) Photo of erosion surface mantled with mudclasts. (B,C) Photos of stratigraphy between concretion marker bed and the erosion surface with medium-bedded sandstone beds highlighted. The location of log SK08 is shown in (C) with the part of the log shown in the photo highlighted in Figure 6. Method 1 of measuring amount of erosion by the erosion surface is explained in Figure 8. (D) Photo of the upper sandstone-prone part of the stratigraphy showing multiple erosion surfaces merging indicating the composite nature of this surface.

Babonneau et al., 2010; Kane and Hodgson, 2011; Maier et al., 2012, 2013; Paull et al., 2013; Morris et al., 2014a; Hansen et al., 2015). Typical characteristics include underlying frontal lobes, thinning away from an adjacent submarine channel, and an overall fining- and thinning upwards trend attributed to levee growth and increased flow confinement allowing only the upper, fine-grained parts of turbidity currents to overspill and deposit sediments (Buffington, 1952; Manley et al., 1997; Skene et al., 2002; Deptuck et al., 2003; Kane et al., 2007; Kane and Hodgson, 2011; Nakajima and Kneller, 2013; Hansen et al., 2015). In the study area, the heterolithics do not show fining-upwards trends, and whilst thinning and palaeocurrent trends can be seen towards the NE (Figure 5), no contemporaneous submarine channel system is identified to account for flow stripping and overspilling of turbidity currents. Furthermore, the heterolithic package directly overlies the capping mudstone of the underlying Fan 4 system with no thicker sandstone beds that could be interpreted as frontal lobe present, thus making an external levee origin unlikely. An internal levee or terrace deposit interpretation is not supported due to the absence of

a confining erosion surface, and the consistent palaeocurrent directions.

Lobe fringes are also composed of packages of heterolithics but require certain conditions to accumulate packages of up to 70 m thick. Aggradational lobe fringes documented from the Laingsburg depocentre in the Karoo Basin, were pinned in one location by the presence of intrabasinal slopes (Spychala et al., 2017b). Aggradational onlaps form in weakly confined basins where the bounding slope angles are less than 1° (Smith, 2004; Smith and Joseph, 2004; Sychala et al., 2017b). The effects of subtle topography on sedimentary facies and depositional architectures in deep-water settings has been widely documented (Hansen et al., 2019; Pyles, 2008; Smith, 2004; Sychala et al., 2017b). The sedimentary structures in the lower part of Unit 5 indicate that the very fine-grained sandstones, sandy siltstones and siltstones with climbing and sinusoidal ripples were rapidly deposited from density stratified turbidity currents with high rates of suspended sediment load fallout. The lack of hybrid event beds within this succession supports these heterolithics being deposited in lateral rather than

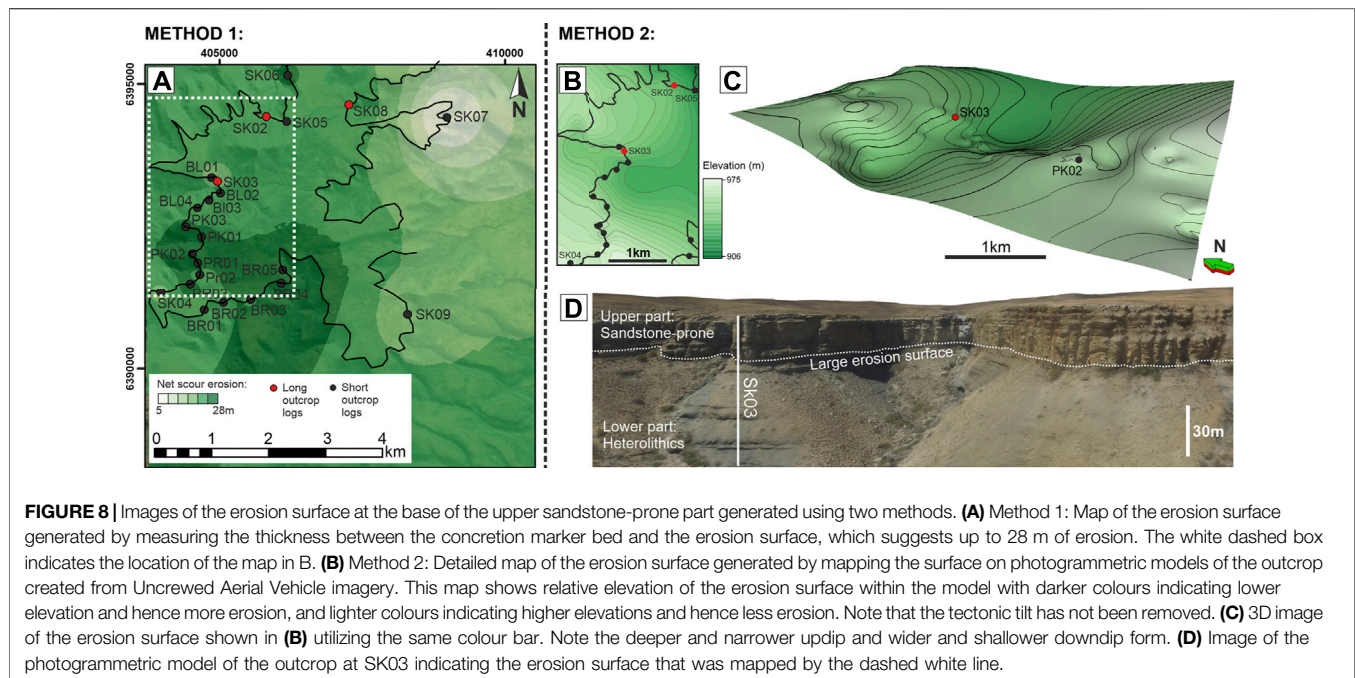


FIGURE 8 | Images of the erosion surface at the base of the upper sandstone-prone part generated using two methods. **(A)** Method 1: Map of the erosion surface generated by measuring the thickness between the concretion marker bed and the erosion surface, which suggests up to 28 m of erosion. The white dashed box indicates the location of the map in B. **(B)** Method 2: Detailed map of the erosion surface generated by mapping the surface on photogrammetric models of the outcrop created from Uncrewed Aerial Vehicle imagery. This map shows relative elevation of the erosion surface within the model with darker colours indicating lower elevation and hence more erosion, and lighter colours indicating higher elevations and hence less erosion. Note that the tectonic tilt has not been removed. **(C)** 3D image of the erosion surface shown in **(B)** utilizing the same colour bar. Note the deeper and narrower updip and wider and shallower downdip form. **(D)** Image of the photogrammetric model of the outcrop at SK03 indicating the erosion surface that was mapped by the dashed white line.

frontal lobe fringe settings (Hansen et al., 2019; Spychala et al., 2017a). However, the thickness of the heterolithic package is greatest in the west (Figures 5, 6), whereas if a SE-facing intrabasinal slope was present to pin the lobe fringe setting, a thinning trend would be predicted. The underlying upper Fan 4 deposits are also thickest in the Skoorsteenberg area (Spychala et al., 2017a), which initially might have formed a subtle high after deposition of the mudstone between Fan 4 and Unit 5. However, that Fan 4 and Unit 5 are thickest in the same location suggests increased subsidence rates may have affected this area during sedimentation allowing a greater thickness of thin beds to accumulate. Palaeocurrents towards the N and NE (Figure 5) indicate that turbidity currents were largely sourced from the south with the NE trend indicating that they were likely following the main downslope gradient at the time of deposition.

Origin of the Erosion Surface

The prominent large-scale erosion surface that widens and shallows downdip above the heterolithic succession is within the upper sandstone-prone part of Unit 5. In deep-water settings, large scale, high aspect ratio erosional surfaces of this geometry are likely scours that vary in dimensions from 10s of metres to multiple kilometres in width and length and cm to 10s of metres in depth (Ito et al., 2014; Hofstra et al., 2015). An alternative interpretation of a high aspect ratio channels would be sub-parallel sided and not shallow downdip so prominently. Large scour surfaces can form in the headwall areas of slide scars (e.g. Pickering and Hilton, 1998; Lee et al., 2004; Moscardelli et al., 2006; Dakin et al., 2013). Alternatively, scours are commonly concentrated in channel-lobe-transition-zones (CLTZs) (Hofstra et al., 2015; Brooks et al., 2018a), in channel mouth settings (Carvajal et al., 2017; Droz et al., 2020; Maier et al., 2020; Pohl et al., 2020, 2019), or have a multi-event origin.

Large-scale erosion surfaces formed by submarine landslides are associated with downdip Mass Transport Deposits (MTDs), and have been documented in slope settings in several subsurface examples (Moscardelli et al., 2006), modern seafloor datasets (Gamberi et al., 2011; Macdonald et al., 2011), and in some outcrop examples (Pickering and Hilton, 1998; Dakin et al., 2013; Brooks et al., 2018b). The erosion surface within Unit 5 has previously been interpreted as a slump scar (Johnson et al., 2001). In the translational domain, slump scar surfaces are the basal shear surface and are overlain by debrites or slumped sediments related to the initial sediment failure. In Unit 5, the erosion surface is infilled by turbidites, which if a slump origin is advocated points to the surface being in the proximal evacuation zone. The scale of the erosion surface described here would imply a large volume mass failure, and the absence of any slumped sediment or debrite above the erosion surface or downdip makes a slump scar origin unlikely.

High-resolution bathymetric data from modern deep-water systems have revealed extensive scouring in channel mouth settings, where the confining channel surface widens and shallows (Carvajal et al., 2017; Droz et al., 2020; Maier et al., 2020), rather than forming a discrete CLTZ between well-defined channels and well-defined lobes. Scouring of channel margins is shown to be extensive especially in areas with higher slope gradients ($>1^\circ$) (Carvajal et al., 2017). Coalescence of scour surfaces is likely a major driver for channel avulsion, inception and propagation resulting in further turbidity current confinement (Droz et al., 2020). In the La Jolla channel, these scours form laterally extensive erosion surfaces that can extend for kilometres downdip of the channel mouth (Maier et al., 2020). The scale and subtle relief of the scours reported from channel mouths is similar to the erosion surface seen in Unit 5. However, these scours have been shown to occur adjacent to, or within, channels. Although

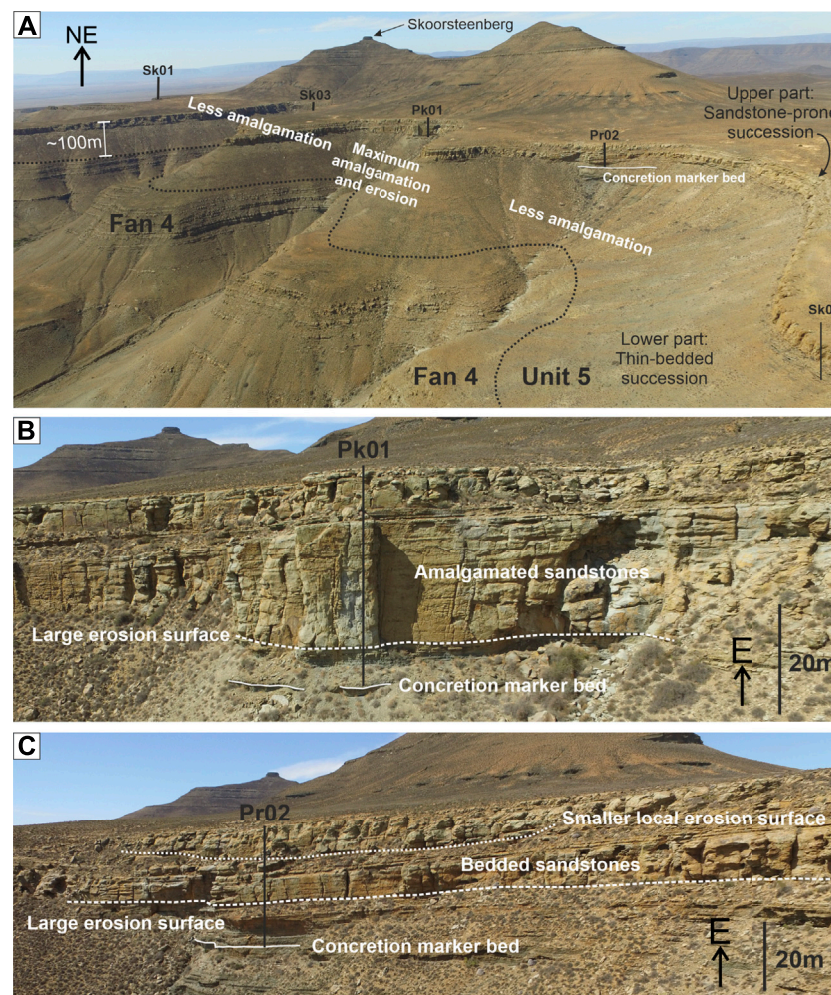


FIGURE 9 | (A) Uncrewed Aerial Vehicle imagery photograph of the western side of the outcrop indicating areas of maximum amalgamation and erosion in the upper sandstone-prone part of the stratigraphy. The part of the correlation panel shown in the photo is highlighted in **Figure 6**. **(B)** Photo of the amalgamated fill of the erosion surface at log PK01 (shown in **Figure 6**), with location indicated in **(A)**. **(C)** Photo of the bedded fill of the erosion surface at log PR02 (shown in **Figure 6**), with location indicated in **(A)**. An erosion surface present higher up the stratigraphy is also highlighted.

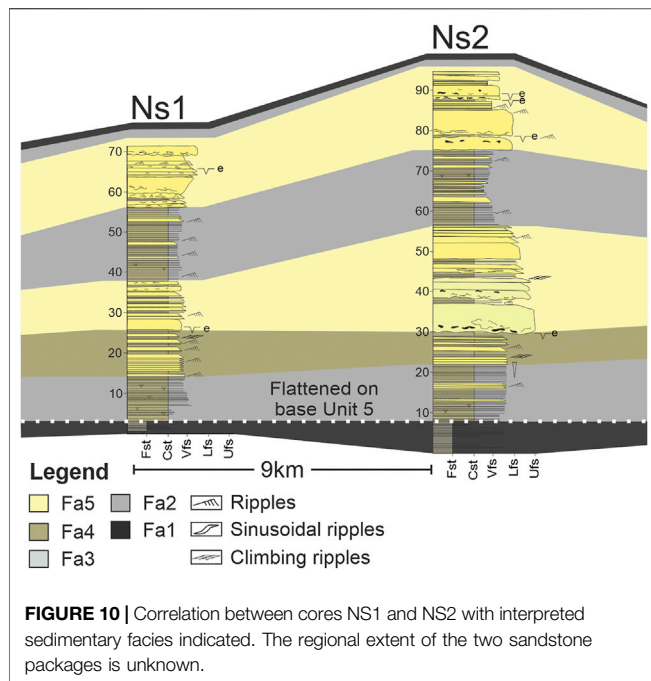
submarine channel complexes have been reported from updip areas, there is no evidence for a channel at this stratigraphic level in Unit 5 around Skoorsteenberg. If it is a channel mouth setting, then the channel did not propagate further into the basin.

Scouring is commonly reported from CLTZs where turbidity currents loose confinement resulting in rapid flow deformation and enhanced basal shearing of the turbidity current (Komar, 1971; Mutti and Normark, 1987, 1991; García and Parker, 1993; Vicente Bravo and Robles, 1995; Wynn et al., 2002; Ito, 2008; Hofstra et al., 2015; Brooks et al., 2018a) via a process referred to as “flow relaxation” (Pohl et al., 2019). Interpreted exhumed CLTZs are characterized by scour-fills, and thin and discontinuous structureless and structured sandstones dominated by ripple and climbing ripple lamination (García and Parker, 1993; Hofstra et al., 2015; Brooks et al., 2018a) that might be the remnants of sediment waves (Hofstra et al., 2018). Scours in CLTZs have been shown to vary in depth and

dimensions, and outcrop studies from the Karoo Basin suggest that they can form individual small-scale scours, or large-scale composite scours interpreted to represent prolonged periods of weakly confined sediment bypass (Hofstra et al., 2015; Brooks et al., 2018a). The 3D exposure of the erosion surface within Unit 5 indicates a 3–4 km wide, 1–2 km long, and up to 28 m deep surface. The scale of the surface is large compared to other outcrop studies, and suggests that this is a composite scour surface in a channel mouth transition zone that originated from bypassing flows that deposited sediment further downdip, with the main scour-fill infilled by subsequent flows.

Stratigraphic Evolution of Unit 5 at Skoorsteenberg

The stratigraphic evolution of Unit 5 at Skoorsteenberg (**Figure 11**) is based on our preferred interpretation of the



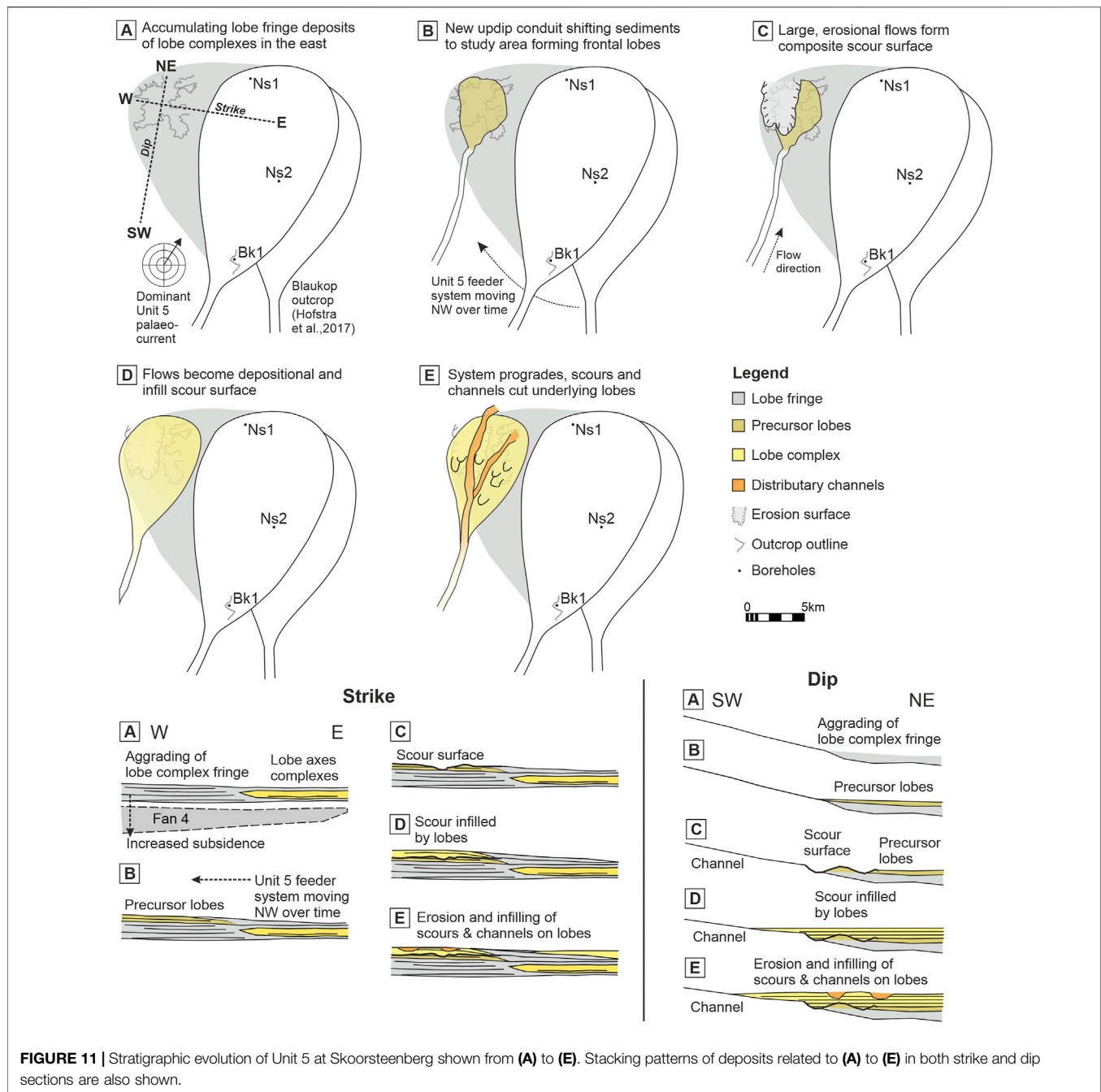
depositional environment of the lower heterolithic part and the origin of the erosion surface. The basal heterolithics are interpreted as the aggradational fringes of multiple stacked lobe complexes identified towards the E and SE (Hofstra et al., 2017), with lobe complexes also interpreted in cores NS1 and NS2. The aggradational lobe complex fringes are interpreted to have formed in an area that underwent preferential subsidence during sedimentation as the isopach thicks of Unit 5 and upper Fan 4 coincide, rather than representing the infill of pre-existing topography (**Figure 11A**).

Two to three ~0.5 m thick fine-grained sandstone beds are present above the package of heterolithics (**Figures 4, 6, 7**) across the entire outcrop areas unless cut out by the overlying erosion surface. Palaeocurrent trends are similar to the heterolithics package, i.e., towards the N and NE (**Figures 5B,C**). These sandstone beds appear abruptly without any coarsening- and thickening-upwards signature observed in the underlying heterolithics (**Figures 4, 6**). Hence, the abrupt appearance of these coarser and thicker sandstone beds below a thicker coarse-grained sandstone package mark the initiation of increased sediment supply to the area. A simple basinward progradation of the system would appear as a more gradual change, especially in distal settings of the basin described here. Similar deposits have been identified in the ancient deep-marine basin-floor successions of the Windermere Supergroup in Canada, where they have been interpreted as avulsion splays (Terlaky et al., 2016). However, these avulsion splays contain an abundance of fine-grained matrix and mudstone clasts, likely due to being the first flows that breach the levee updip and thus entraining mud-prone substrate (Terlaky et al., 2016). Mud-clast rich sandstone beds interpreted as crevasse splays (or “crevasse lobes”) were also observed in cores taken as part of IODP leg 155 in the Gulf of

Mexico (Pirmez et al., 1997). Similar fine-grained sandstones with abundant sinusoidal laminae and climbing ripples that have a mounded geometry were interpreted as frontal splays (or frontal lobes) in the Fort Brown Formation in the Karoo Basin (Morris et al., 2014b). The sandstone beds with some climbing-ripple and parallel lamination observed here are clean. This character and their abrupt appearance suggests that these sandstones either are 1) frontal lobes recording the establishment of a new slope conduit, or 2) avulsion splays where redirection of flows from an existing conduit eroded a sand-rich substrate. Establishment of a new slope conduit would follow the overall pattern in Unit 5 of submarine channels and lobes moving NW over time (**Figure 11B**). Slope submarine channel avulsions occur via a range of mechanisms (Jobe et al., 2020), including levee collapse and flow-stripping (Piper and Normark, 1983; Fildani et al., 2006), and/or channel aggradation (Kolla, 2007; Armitage et al., 2012), and drivers such as climate cyclicity (Picot et al., 2019). In more distal settings, an autogenic mechanism invoked is a downstream gradient decrease during lobe aggradation to a point where the channel will start to aggrade forcing it to migrate and/or avulse to find a new higher gradient downstream pathway (e.g., Groenenberg et al., 2010; Prélat et al., 2010) (**Figure 11B**).

Above these medium-bedded sandstones, the erosion surface incised up to 28 m into the substrate (**Figure 11C**) and was likely sculpted and widened by successive bypassing flows. The size of the erosion surface is similar in size to composite scour surfaces reported from modern seafloor datasets (Carvajal et al., 2017; Droz et al., 2020; Maier et al., 2020) and comparable to the largest reported from exhumed settings (Hofstra et al., 2015).

The subsequent filling of the erosion surface indicates that the flows transitioned from dominantly erosional and bypassing to dominantly depositional. It is not possible to resolve whether this is due to internal or external factors, or a combination of factors controlling the nature of the flows. Internal factors may include the flows becoming more sand prone and less efficient over time (Al Ja'Aidi et al., 2004; Heerema et al., 2020), as the feeder conduit matured, or that the new downstream pathway gradient decreased due to upstream erosion and downstream deposition resulting in aggradation (Prélat et al., 2010). External factors may include a transient period of decreased flow magnitude due to changes in sediment supply, for example caused by eustatic and climatic fluctuations. The sandstones that fill the erosion surface are thick-bedded, amalgamated, structureless to parallel laminated with no evidence for hybrid-bed prone facies. Furthermore, the lack of fine-grained heterolithics or bed tops suggest that the flows may have been stripped and finer grain-sizes deposited downdip, making these lobes more similar in character to intraslope lobes than basin-floor lobes (Spychala et al., 2015; Brooks et al., 2018c). Small-scale erosion surfaces towards the top of the sandstone-prone part of the succession are interpreted as either distributary channels where lags are present, or scour-fills, and are linked to a final phase of basinward progradation of the system (**Figure 11E**).



CONCLUSION

This study describes a unique outcrop in Unit 5 of the Karoo Basin, South Africa, where a large (2 long × 4 wide km) and high aspect ratio (28 m deep) erosion surface can be mapped with three dimensional constraints. The scale of the high aspect ratio erosion surface, and the geometry that widens and shallows downdip supports interpretation of a composite scour surface. The scour surface marks a significant and abrupt change from a lower package of heterolithics to an upper package of amalgamated sandstones, which indicates a change in sediment supply to the area, reflecting either establishment of a new

slope conduit, or an updip avulsion event. The underlying thick package of heterolithics is interpreted as aggradationally stacked lobe complex fringes that were deposited in an area of increased subsidence. Below the large scour surface multiple thin to medium-bedded sandstone beds are present, which are interpreted as frontal lobes before large, bypass dominated flows cut the substrate to form the scour surface. The upper sandstone-prone package is interpreted as lobe deposits that infill the scour surface and show a change from erosional and bypassing flows to depositional flows. Whilst large-scale scours are commonly observed on modern seafloor data, their preservation in outcrop is rare and provides a unique

opportunity into how the presence of scours and scour-fills can provide important insights into the source-to-sink configuration of deep-water systems.

DATA AVAILABILITY STATEMENT

The raw data supporting the conclusions of this article will be made available by the authors, without undue reservation.

AUTHOR CONTRIBUTIONS

DH, RH, LH, and AP coordinated the work. The main data collection was done by RH with the help of LG and DL. All authors discussed the results. LH wrote the manuscript, with support from DH, RH, LG, DL, AP, and RW.

REFERENCES

- Al Ja'Aidi, O. S., McCaffrey, W. D., and Kneller, B. C. (2004). "Factors Influencing the deposit Geometry of Experimental Turbidity Currents: Implications for Sand-Body Architecture in Confined Basins," in *Confined Turbidite Systems*. Editors S. A. Lomas and P. Joseph (London: Geol. Soc. London, Spec. Publ.), 222, 45–58.
- Allen, J. R. L. (1973). A Classification of Climbing-Ripple Cross-Lamination. *J. Geol. Soc. Lond.* 129, 537–541. doi:10.1144/gsjgs.129.5.0537
- Armitage, D. A., McHargue, T., Fildani, A., and Graham, S. A. (2012). Postavulsion Channel Evolution: Niger Delta continental Slope. *Am. Assoc. Pet. Geol. Bull.* 96, 823–843. doi:10.1306/09131110189
- Babonneau, N., Savoye, B., Cremer, M., and Bez, M. (2010). Sedimentary Architecture in Meanders of a Submarine Channel: Detailed Study of the Present Congo Turbidite Channel (Zaiango Project). *J. Sediment. Res.* 80, 852–866.
- Basu, D., and Bouma, A. H. (2000). Thin-Bedded Turbidites of the Tanqua Karoo: Physical and Depositional Characteristics. *Fine-Grained Turbid. Syst.* 72, 263–278.
- Bell, D., Hodgson, D. M., Pontén, A. S. M., Hansen, L. A. S., Flint, S. S., and Kane, I. A. (2020). Stratigraphic Hierarchy and Three-Dimensional Evolution of an Exhumed Submarine Slope Channel System. *Sedimentology* 67, 3259–3289. doi:10.1111/sed.12746
- Blewett, S. C., and Phillips, D. (2016). "An Overview of Cape Fold belt Geochronology: Implications for Sediment Provenance and the Timing of Orogenesis," in *Origin and Evolution of the Cape Mountains and Karoo Basin*. Editors B. Linol and M. de Wit (Cham: Springer), 45–55.
- Bonnel, C., Dennielou, B., Droz, L., Mulder, T., and Berné, S. (2005). Architecture and Depositional Pattern of the Rhône Neofan and Recent Gravity Activity in the Gulf of Lions (Western Mediterranean). *Mar. Pet. Geol.* 22, 827–843. doi:10.1016/j.marpetgeo.2005.03.003
- Boulesteix, K., Poyatos-Moré, M., Flint, S. S., Taylor, K. G., Hodgson, D. M., and Hasiotis, S. T. (2019). Transport and Deposition of Mud in Deep-Water Environments: Processes and Stratigraphic Implications. *Sedimentology* 66, 2894–2925. doi:10.1111/sed.12614
- Bouma, A. H., and Wickens, H. D. (1991). Permian Passive Margin Submarine Fan Complex, Karoo Basin, South-Africa: Possible Model to Gulf of Mexico. *Gulf Coast Assoc. Geol. Soc. Trans.* 41, 30–42.
- Bouma, A. H., and Wickens, H. D. (1994). "Tanqua Karoo, Ancient Analog for fine-grained Submarine Fans," in *Submarine Fans and Turbidite Systems*. Gulf Coast Section SEPM Foundation 15th Annual Research Conference. Editors P. Weimer, A. Bouma, and B. Perkins, 23–34.
- Brooks, H. L., Hodgson, D., Brunt, R. L., Peakall, J., and Flint, S. (2018a). Deepwater Channel-Lobe Transition Zone Dynamics — Processes and Depositional Architecture, an Example from the Karoo Basin, South Africa. *GSA Bull.* 130, 1723–1746. doi:10.1130/B31714.1
- Brooks, H. L., Hodgson, D. M., Brunt, R. L., Peakall, J., and Flint, S. S. (2018b). Exhumed Lateral Margins and Increasing Flow Confinement of a Submarine Landslide Complex. *Sedimentology* 65, 1067–1096. doi:10.1111/sed.12415
- Brooks, H. L., Hodgson, D. M., Brunt, R. L., Peakall, J., Poyatos-moré, M., and Flint, S. S. (2018c). Disconnected Submarine Lobes as a Record of Stepped Slope Evolution over Multiple Sea-Level Cycles. *Geosphere* 14, 1753–1779. doi:10.1130/GES01618.1
- Brunt, R., Di Celma, C., Hodgson, D., Flint, S., Kavanagh, J., and Van der Merwe, W. (2013). Driving a Channel through a Levee when the Levee Is High: An Outcrop Example of Submarine Down-Dip Entrenchment. *Mar. Pet. Geol.* 41, 134–145. doi:10.1016/j.marpetgeo.2012.02.016
- Buffington, E. C. (1952). Submarine "Natural Levees." *J. Geol.* 60, 473–479.
- Carvajal, C., Paull, C. K., Caress, D. W., Fildani, A., Lundsten, E., Anderson, K., et al. (2017). Unraveling the Channel-Lobe Transition Zone with High-Resolution AUV Bathymetry: Navy Fan, Offshore Baja California, Mexico. *J. Sediment. Res.* 87, 1049–1059. doi:10.2110/jsr.2017.58
- Clemenceau, G. R., Colbert, J., and Edens, D. (2000). "Production Results from Levee-Overbank Turbidite Sands at Ram/Powell Field, Deepwater Gulf of Mexico," in *Deep-Water Reservoirs of the World: GCSSEPM Foundation 20th Annual Research Conference*. Editors P. Weimer, M. Slatt, J. Coleman, N. Rosen, C. Nelson, A. Bouma, M. Styzen, and D. Lawrence, 241–251.
- Covault, J. A., Kostic, S., Paull, C., Ryan, H. F., and Fildani, A. (2014). Submarine Channel Initiation, Filling and Maintenance from Sea-Floor Geomorphology and Morphodynamic Modelling of Cyclic Steps. *Sedimentology* 61, 1031–1054. doi:10.1111/sed.12084
- Dakin, N., Pickering, K. T., Mohrig, D., and Bayliss, N. J. (2013). Channel-like Features Created by Erosive Submarine Debris Flows: Field Evidence from the Middle Eocene Ainsa Basin, Spanish Pyrenees. *Mar. Pet. Geol.* 41, 62–71. doi:10.1016/j.marpetgeo.2012.07.007
- De Wit, M. J., and Ransome, I. G. D. (1992). "Regional Inversion Tectonics along the Southern Margin of Gondwana," in *Inversion Tectonics of the Cape Fold Belt, Karoo and Cretaceous Basins of Southern Africa*. Editors M. J. D. Wit and I. G. D. Ransome (Rotterdam: Balkema), 15–21.
- Deptuck, M., Steffens, G. S., Barton, M., and Pirmez, C. (2003). Architecture and Evolution of Upper Fan Channel-Belts on the Niger Delta Slope and in the Arabian Sea. *Mar. Pet. Geol.* 20, 649–676. doi:10.1016/j.marpetgeo.2003.01.004
- Droz, L., Jégou, I., Gillet, H., Dennielou, B., Bez, M., Canals, M., et al. (2020). On the Termination of Deep-Sea Fan Channels: Examples from the Rhône Fan (Gulf of Lion, Western Mediterranean Sea). *Geomorphology* 369, 107368. doi:10.1016/j.geomorph.2020.107368
- EGgenhuisen, J. T., McCaffrey, W. D., Haughton, P. D. W., and Butler, R. W. H. (2011). Shallow Erosion beneath Turbidity Currents and its Impact on the Architectural Development of Turbidite Sheet Systems. *Sedimentology* 58, 936–959. doi:10.1111/j.1365-3091.2010.01190.x
- Elliott, T. (2000). "Depositional Architecture of Sand-Rich, Channelized Turbidite System: The Upper Carboniferous Ross Sandstone Formation, Western Ireland," in *Deep-Water Reservoirs of the World: GCSSEPM Foundation*

FUNDING

This research was funded by Equinor ASA.

ACKNOWLEDGMENTS

The manuscript has benefited from constructive reviews by Reviewer 1 and 2 and Associate Editor Fabiano Gamberi. This manuscript was a real team effort by all the authors. We thank the local farmers of the Tanqua region for permission to undertake field studies on their land, and especially De Ville Wickens. We are grateful for the financial support from Equinor that made this research work possible. The digital outcrop model of Unit 5 in the Skoorsteenberg area is publically available on the excellent V3Geo community resource: <https://v3geo.com/model/218>.

- 20th Annual Research Conference. Editors P. Weimer, R. Slatt, J. Coleman, N. Rosen, H. Nelson, A. Bouma, M. Styzen, and D. Lawrence.
- Fildani, A., Normark, W., Kostic, S., and Parker, G. (2006). Channel Formation by Flow Stripping: Large-Scale Scour Features along the Monterey East Channel and Their Relation to Sediment Waves. *Sedimentology* 53, 1265–1287. doi:10.1111/j.1365-3091.2006.00812.x
- Flint, S., Hodgson, D., Sprague, A. R., Brunt, R., Van der Merwe, W. C., Figueiredo, J., et al. (2011). Depositional Architecture and Sequence Stratigraphy of the Karoo basin Floor to Shelf Edge Succession, Laingsburg Depocentre, South Africa. *Mar. Pet. Geol.* 28, 658–674. doi:10.1016/j.marpetgeo.2010.06.008
- Gamberi, F., Rovere, M., and Marani, M. (2011). Mass-transport Complex Evolution in a Tectonically Active Margin (Gioia Basin, Southeastern Tyrrhenian Sea). *Mar. Geol.* 279, 98–110. doi:10.1016/j.margeo.2010.10.015
- García, M., and Parker, G. (1993). Experiments on the Entrainment of Sediment into Suspension by a Dense Bottom Current. *J. Geophys. Res.* 98, 4793–4807.
- Groeneweg, R. M., Hodgson, D., Prêlat, A., Luthi, S. M., and Flint, S. (2010). Flow-Deposit Interaction in Submarine Lobes: Insights from Outcrop Observations and Realizations of a Process-Based Numerical Model. *J. Sediment. Res.* 80, 252–267. doi:10.2110/jsr.2010.028
- Hansen, L. A. S., Callow, R. H. T., Kane, I., Gamberi, F., Rovere, M., Cronin, B. T., et al. (2015). Genesis and Character of Thin-Bedded Turbidites Associated with Submarine Channels. *Mar. Pet. Geol.* 67, 852–879. doi:10.1016/j.marpetgeo.2015.06.007
- Hansen, L. A. S., Hodgson, D. M., Pontén, A., Bell, D., and Flint, S. (2019). Quantification of basin-floor Fan Pinchouts: Examples from the Karoo Basin, South Africa. *Front. Earth Sci.* 7, 1–20. doi:10.3389/feart.2019.00012
- Heerema, C. J., Talling, P. J., Cartigny, M. J., Paull, C. K., Bailey, L., Simmons, S. M., et al. (2020). What Determines the Downstream Evolution of Turbidity Currents? *Earth Planet. Sci. Lett.* 532, 116023. doi:10.1016/j.epsl.2019.116023
- Hodgson, D. (2009). Distribution and Origin of Hybrid Beds in Sand-Rich Submarine Fans of the Tanqua Depocentre, Karoo Basin, South Africa. *Mar. Pet. Geol.* 26, 1940–1956. doi:10.1016/j.marpetgeo.2009.02.011
- Hodgson, D., Flint, S., Hodgetts, D., Drinkwater, N., Johannessen, E., and Luthi, S. (2006). Stratigraphic Evolution of Fine-Grained Submarine Fan Systems, Tanqua Depocenter, Karoo Basin, South Africa. *J. Sediment. Res.* 76, 20–40. doi:10.2110/jsr.2006.03
- Hofstra, M., Hodgson, D., Peakall, J., and Flint, S. (2015). Giant Scour-Fills in Ancient Channel-Lobe Transition Zones: Formative Processes and Depositional Architecture. *Sediment. Geol.* 329, 98–114. doi:10.1016/j.sedgeo.2015.09.004
- Hofstra, M., Peakall, J., Hodgson, D. M., and Stevenson, C. J. (2018). Architecture and Morphodynamics of Subcritical Sediment Waves in an Ancient Channel-Lobe Transition Zone. *Sedimentology* 65, 2339–2367. doi:10.1111/sed.12468
- Hofstra, M., Pontén, A. S. M., Peakall, J., Flint, S., Nair, K. N., and Hodgson, D. (2017). The Impact of fine-scale Reservoir Geometries on Streamline Flow Patterns in Submarine Lobe Deposits Using Outcrop Analogues from the Karoo Basin. *Pet. Geosci.* 23, 159–176. doi:10.1144/petgeo2016-087
- Ito, M. (2008). Downfan Transformation from Turbidity Currents to Debris Flows at a Channel-To-Lobe Transitional Zone: The Lower Pleistocene Otadai Formation, Boso Peninsula, Japan. *J. Sediment. Res.* 78, 668–682. doi:10.2110/jsr.2008.076
- Ito, M., Ishikawa, K., and Nishida, N. (2014). Distinctive Erosional and Depositional Structures Formed at a canyon Mouth: A Lower Pleistocene Deep-Water Succession in the Kazusa Forearc basin on the Boso Peninsula, Japan. *Sedimentology* 61, 2042–2062. doi:10.1111/sed.12128
- Jobe, Z. R., Howes, N. C., Straub, K. M., Cai, D., Deng, H., Laugier, F. J., et al. (2020). Comparing Aggradation, Superelevation, and Avulsion Frequency of Submarine and Fluvial Channels. *Front. Earth Sci.* 8, 53. doi:10.3389/feart.2020.00053
- Jobe, Z. R., Lowe, D., and Morris, W. (2012). Climbing-ripple Successions in Turbidite Systems: Depositional Environments, Sedimentation Rates and Accumulation Times. *Sedimentology* 59, 867–898. doi:10.1111/j.1365-3091.2011.01283.x
- Johnson, S., Flint, S., Hinds, D., and De Ville Wickens, H. (2001). Anatomy, Geometry and Sequence Stratigraphy of basin Floor to Slope Turbidite Systems, Tanqua Karoo, South Africa. *Sedimentology* 48, 987–1023. doi:10.1046/j.1365-3091.2001.00405.x
- Jopling, A. V., and Walker, R. B. (1968). Morphology and Origin of Ripple-Drift Cross-Lamination with Examples from the Pleistocene of Massachusetts. *J. Sediment. Petrol.* 38, 971–984.
- Kane, I., and Hodgson, D. (2011). Sedimentological Criteria to Differentiate Submarine Channel Levee Subenvironments: Exhumed Examples from the Rosario Fm. (Upper Cretaceous) of Baja California, Mexico, and the Fort Brown Fm. (Permian), Karoo Basin, S. Africa. *Mar. Pet. Geol.* 28, 807–823. doi:10.1016/j.marpetgeo.2010.05.009
- Kane, I., Kneller, B., Dykstra, M., Kassem, A., and McCaffrey, W. D. (2007). Anatomy of a Submarine Channel–Levee: An Example from Upper Cretaceous Slope Sediments, Rosario Formation, Baja California, Mexico. *Mar. Pet. Geol.* 24, 540–563. doi:10.1016/j.marpetgeo.2007.01.003
- Kane, I., Pontén, A. S. M., Vangdal, B., Eggenhuisen, J., Hodgson, D., and Spychala, Y. T. (2017). The Stratigraphic Record and Processes of Turbidity Current Transformation across Deep-marine Lobes. *Sedimentology* 64, 1236–1273. doi:10.1111/sed.12346
- King, R. C., Hodgson, D., Flint, S., Potts, G. J., and Van Lente, B. (2009). “Development of Subaqueous Fold Belts as a Control on the Timing and Distribution of Deepwater Sedimentation: An Example from the Southwest Karoo Basin, South Africa,” in *External Controls on Deep-Water Depositional Systems*. Editors B. C. Kneller, O. J. Martinsen, and W. D. McCaffrey (SEPM Special Publication), 92, 261–278.
- Kneller, B. (1995). “Beyond the Turbidite Paradigm: Physical Models for Deposition of Turbidites and Their Implications for Reservoir Prediction,” in *Characterisation of Deep Marine Clastic Systems*. Editors A. J. Hartley and D. J. Prosser (London: Geological Society Special Publications), 94, 31–49.
- Kneller, B., and Buckee, C. (2000). The Structure and Fluid Mechanics of Turbidity Currents: a Review of Some Recent Studies and Their Geological Implications. *Sedimentology* 47, 62–94. doi:10.1046/j.1365-3091.2000.047s1062.x
- Kolla, V. (2007). A Review of Sinuous Channel Avulsion Patterns in Some Major Deep-Sea Fans and Factors Controlling Them. *Mar. Pet. Geol.* 24, 450–469. doi:10.1016/j.marpetgeo.2007.01.004
- Komar, P. (1971). Hydraulic Jumps in Turbidity Currents. *Geol. Soc. Am. Bull.* 82, 1477–1488. doi:10.1130/0016-7606(1971)82
- Lee, S. E., Amy, L. A., and Talling, P. (2004). “The Character and Origin of Thick Base-Of-Slope sandstone Units of the Peira Cava Outlier, SE France,” in *Deep-Water Sedimentation in the Alpine Basin of SE France: New Perspectives on the Grès d’Annot and Related Systems*. Editors P. Joseph and S. A. Lomas (London: Geol. Soc. London, Spec. Publ.), 221, 331–347. doi:10.1144/GSL.SP.2004.221.01.18
- Lien, T., Walker, R., and Martinsen, O. J. (2003). Turbidites in the Upper Carboniferous Ross Formation, Western Ireland: Reconstruction of a Channel and Spillover System. *Sedimentology* 50, 113–148. doi:10.1046/j.1365-3091.2003.00541.x
- López-Gamundi, O. R., and Rossello, E. A. (1998). Basin Fill Evolution and Paleotectonic Patterns along the Samfrau Geosyncline: the Sauce Grande basin–Ventana Foldbelt (Argentina) and Karoo basin–Cape Foldbelt (South Africa) Revisited. *Geol. Rundschau* 86, 819–834. doi:10.1007/s005310050179
- Luthi, S. M., Hodgson, D., Geel, C. R., Flint, S., Goedbloed, J. W., Drinkwater, N. J., et al. (2006). Contribution of Research Borehole Data to Modelling fine-grained Turbidite Reservoir Analogues, Permian Tanqua-Karoo basin-floor Fans (South Africa). *Pet. Geosci.* 12, 175–190. doi:10.1144/1354-079305-693
- Macdonald, H. A., Peakall, J., and Wignall, P. B. (2011). Sedimentation in Deep-Sea Lobe-Elements: Implications for the Origin of Thickening-Upward Sequences. *J. Geol. Soc. Lond.* 168, 319–331. doi:10.1144/0016-76492010-036
- Maier, K., Fildani, A., McHargue, T., Paull, C., Graham, S. a., and Caress, D. W. (2012). Punctuated Deep-Water Channel Migration: High-Resolution Subsurface Data from the Lucia Chica Channel System, Offshore California. *U.S.A. J. Sediment. Res.* 82, 1–8. doi:10.2110/jsr.2012.10
- Maier, K., Fildani, A., Paull, C., Graham, S., McHargue, T., Caress, D., et al. (2011). The Elusive Character of Discontinuous Deep-Water Channels: New Insights from Lucia Chica Channel System, Offshore California. *Geology* 39, 327–330. doi:10.1130/G31589.1
- Maier, K., Fildani, A., Paull, C., McHargue, T., Graham, S., and Caress, D. (2013). Deep-sea Channel Evolution and Stratigraphic Architecture from Inception to Abandonment from High-Resolution Autonomous Underwater Vehicle Surveys Offshore central California. *Sedimentology* 60, 935–960. doi:10.1111/j.1365-3091.2012.01371.x
- Maier, K. L., Johnson, S. Y., and Hart, P. (2018). Controls on Submarine canyon Head Evolution: Monterey Canyon, Offshore central California. *Mar. Geol.* 404, 24–40. doi:10.1016/j.margeo.2018.06.014

- Maier, K. L., Paull, C. K., Caress, D. W., Anderson, K., Nieminski, N. M., Lundsten, E., et al. (2020). Submarine-fan Development Revealed by Integrated High-Resolution Datasets from La Jolla Fan, Offshore California, U.S.A. *J. Sediment. Res.* 90, 468–479. doi:10.2110/jsr.2020.22
- Manley, P., Pirmez, C., Busch, W., and Cramp, A. (1997). “3. Grain-Size Characterization of Amazon Fan Deposits and Comparison to Seismic Facies Units,” in *Proceedings of the Ocean Drilling Program, Scientific Results*, Vol. 155. Editors R. Flood, D. Piper, A. Klaus, and L. Peterson, 35–52. Meiburg, E., and Kneller, B. (2010). Turbidity Currents and Their Deposits. *Annu. Rev. Fluid Mech.* 42, 135–156. doi:10.1146/annurev-fluid-121108-145618
- Morris, E., Hodgson, D., Brunt, R., and Flint, S. (2014a). Origin, Evolution and Anatomy of silt-prone Submarine External Levées. *Sedimentology* 61, 1734–1763. doi:10.1111/sed.12114
- Morris, E., Hodgson, D., Flint, S., Brunt, R., Butterworth, P. J., and Verhaeghe, J. (2014b). Sedimentology, Stratigraphic Architecture, and Depositional Context of Submarine Frontal-Lobe Complexes. *J. Sediment. Res.* 84, 763–780. doi:10.2110/jsr.2014.61
- Morris, W., and Normark, W. (2000). “Sedimentologic and Geometric Criteria for Comparing Modern and Ancient sandy Turbidite Elements,” in *Deep-Water Reservoirs of the World: GCSSEPM Foundation 20th Annual Research Conference*. Editors P. Weimer, M. Slatt, J. Coleman, N. Rosen, C. Nelson, A. Bouma, M. Styzen, and D. Lawrence, 606–628.
- Morris, W., Scheihsing, M., Wickens, D., and Bouma, A. H. (2000). “Reservoir Architecture of Deepwater Sandstones: Examples from the Skoorsteenberg Formation, Tanqua Karoo Sub-Basin, South Africa,” in *Deep-Water Reservoirs of the World: GCSSEPM Foundation 20th Annual Research Conference*. Editors P. Weimer, M. Slatt, J. Coleman, N. Rosen, C. Nelson, A. Bouma, M. Styzen, and D. Lawrence, 629–666.
- Moscardelli, L., Wood, L., and Mann, P. (2006). Mass-transport Complexes and Associated Processes in the Offshore Area of Trinidad and Venezuela. *AAPG Bull.* 90, 1059–1088. doi:10.1306/02210605052
- Mutti, E., and Normark, W. (1991). “An Integrated Approach to the Study of Turbidite Systems,” in *Seismic Facies and Sedimentary Processes of Submarine Fans and Turbidite Systems*. Editors P. Weimer and M. Link (Berlin, Germany/New York: Springer-Verlag), 75–106.
- Mutti, E., and Normark, W. (1987). “Comparing Examples of Modern and Ancient Turbidite Systems: Problems and Concepts,” in *Marine Clastic Sedimentology*. Editors J. Leggett and G. Zuffa (London: Graham and Trotman), 1–38.
- Nakajima, T., and Kneller, B. (2013). Quantitative Analysis of the Geometry of Submarine External Levées. *Sedimentology* 60, 877–910. doi:10.1111/j.1365-3091.2012.01366.x
- Normark, W., and Piper, D. (1991). “Initiation Processes and Flow Evolution of Turbidity Currents: Implications for the Depositional Record,” in *SEPM Special Publication No. 46, from Shoreline to Abyss*. Editor R. H. Osborne, 207–230.
- Ortiz-Karpf, A., Hodgson, D. M., and McCaffrey, W. D. (2015). The Role of Mass-Transport Complexes in Controlling Channel Avulsion and the Subsequent Sediment Dispersal Patterns on an Active Margin: The Magdalena Fan, Offshore Colombia. *Mar. Pet. Geol.* 64, 58–75. doi:10.1016/j.marpetgeo.2015.01.005
- Paull, C., Caress, D., Lundsten, E., Gwiazda, R., Anderson, K., McGann, M., et al. (2013). Anatomy of the La Jolla Submarine Canyon System; Offshore Southern California. *Mar. Geol.* 335, 16–34. doi:10.1016/j.margeo.2012.10.003
- Piazza, A., and Tinterri, R. (2020). Cyclic Stacking Pattern, Architecture and Facies of the Turbidite Lobes in the Macigno Sandstones Formation (Chattian-Aquitian, Northern Apennines, Italy). *Mar. Pet. Geology* 122, 104704. doi:10.1016/j.marpetgeo.2020.104704
- Pickering, K. T., and Hilton, V. C. (1998). *Turbidite Systems of Southeast France: Application to Hydrocarbon Prospectivity*. London: Vallis Press.
- Picot, M., Marsset, T., Droz, L., Dennielou, B., Baudin, F., Hermoso, M., et al. (2019). Monsoon Control on Channel Avulsions in the Late Quaternary Congo Fan. *Quat. Sci. Rev.* 204, 149–171. doi:10.1016/j.quascirev.2018.11.033
- Piper, D., and Normark, W. (1983). Turbidite Depositional Patterns and Flow Characteristics, Navy Submarine Fan, California Borderland. *Sedimentology* 30, 681–694.
- Pirmez, C., Hiscott, R., and Kronen, J. D. (1997). “2. Sandy Turbidite Successions at the Base of Channel-Levee Systems of the Amazon Fan Revealed by FMS Logs and Cores: Unraveling the Facies Architecture of Large Submarine Fans,” in *Proceedings of the Ocean Drilling Program, Scientific Results*, Vol. 155. Editors R. D. Flood, D. J. W. Piper, A. Klaus, and L. C. Peterson, 7–33.
- Pohl, F., Eggenhuisen, J. T., Cartigny, M. J. B., Tilston, M. C., de Leeuw, J., and Hermidas, N. (2020). The Influence of a Slope Break on Turbidite Deposits: An Experimental Investigation. *Mar. Geol.* 424, 106160. doi:10.1016/j.margeo.2020.106160
- Pohl, F., Eggenhuisen, J. T., Tilston, M., and Cartigny, M. J. B. (2019). New Flow Relaxation Mechanism Explains Scour fields at the End of Submarine Channels. *Nat. Commun.* 10, 1–8. doi:10.1038/s41467-019-12389-x
- Prélat, A., Covault, J. A., Hodgson, D., Fildani, A., and Flint, S. (2010). Intrinsic Controls on the Range of Volumes, Morphologies, and Dimensions of Submarine Lobes. *Sediment. Geol.* 232, 66–76. doi:10.1016/j.sedgeo.2010.09.010
- Prélat, A., Hodgson, D., and Flint, S. (2009). Evolution, Architecture and Hierarchy of Distributary Deep-Water Deposits: a High-Resolution Outcrop Investigation from the Permian Karoo Basin, South Africa. *Sedimentology* 56, 2132–2154. doi:10.1111/j.1365-3091.2009.01073.x
- Pyles, D. (2008). Multiscale Stratigraphic Analysis of a Structurally Confined Submarine Fan: Carboniferous Ross Sandstone, Ireland. *Am. Assoc. Pet. Geol. Bull.* 92, 557–587. doi:10.1306/01110807042
- Pyles, D. R., Strachan, L. J., and Jennette, D. C. (2014). Lateral Juxtapositions of Channel and Lobe Elements in Distributive Submarine Fans: Three-Dimensional Outcrop Study of the Ross Sandstone and Geometric Model. *Geosphere* 10, 1104–1122. doi:10.1130/GES01042.1
- Skene, K. I., Piper, D., and Hill, P. S. (2002). Quantitative Analysis of Variations in Depositional Sequence Thickness from Submarine Channel Levees. *Sedimentology* 49, 1411–1430. doi:10.1046/j.1365-3091.2002.00506.x
- Smith, R., and Joseph, P. (2004). “Onlap Stratal Architectures in the Gres d’Annot: Geometric Models and Controlling Factors,” in *Deep-Water Sedimentation in the Alpine Basin of SE France: New Perspectives on the Grès d’Annot and Related Systems*. Editors P. Joseph and S. A. Lomas (London: Geol. Soc. London, Spec. Publ.), 221, 389–399. doi:10.1144/GSL.SP.2004.221.01.21
- Smith, R. (2004). “Turbidite Systems Influenced by Structurally Induced Topography in the Multi-Sourced Welsh Basin,” in *Confined Turbidite Systems*. Editors S. A. Lomas and P. Joseph (London: Geol. Soc. London, Spec. Publ.), 222, 209–228. doi:10.1144/GSL.SP.2004.222.01.11
- Spychala, Y. T., Hodgson, D., Flint, S., and Mountney, N. P. (2015). Constraining the Sedimentology and Stratigraphy of Submarine Intraslope Lobe Deposits Using Exhumed Examples from the Karoo Basin, South Africa. *Sediment. Geol.* 322, 67–81. doi:10.1016/j.sedgeo.2015.03.013
- Spychala, Y. T., Hodgson, D., Prélat, A., Kane, I., Flint, S., and Mountney, N. (2017a). Frontal and Lateral Submarine Lobe Fringes: Comparing Sedimentary Facies, Architecture and Flow Processes. *J. Sediment. Res.* 87, 75–96. doi:10.2110/jsr.2017.2
- Spychala, Y. T., Hodgson, D., Stevenson, C., and Flint, S. (2017b). Aggradational Lobe Fringes: The Influence of Subtle Intra-basinal Seabed Topography on Sediment Gravity Flow Processes and Lobe Stacking Patterns. *Sedimentology* 64, 582–608. doi:10.1111/sed.12315
- Stevenson, C., Jackson, C., Hodgson, D., Hubbard, S., and Eggenhuisen, J. (2015). Deep-water Sediment Bypass. *J. Sediment. Res.* 85, 1058–1081. doi:10.2110/jsr.2015.63
- Stratigraphy Group, University of Leeds (2021). Skoorsteenberg Digital Outcrop Model. Available at: <https://v3geo.com/model/218>.
- Sumner, E. J., Talling, P. J., Amy, L. A., Wynn, R. B., Stevenson, C. J., and Frenz, M. (2012). Facies Architecture of Individual basin-plain Turbidites: Comparison with Existing Models and Implications for Flow Processes. *Sedimentology* 59, 1850–1887. doi:10.1111/j.1365-3091.2012.01329.x
- Tankard, A., Welsink, H., Aukes, P., Newton, R., and Stettler, E. (2009). Tectonic Evolution of the Cape and Karoo Basins of South Africa. *Mar. Pet. Geol.* 26, 1379–1412. doi:10.1016/j.marpetgeo.2009.01.022
- Terlaky, V., Rocheleau, J., and Arnott, R. W. C. (2016). Stratal Composition and Stratigraphic Organization of Stratal Elements in an Ancient Deep-marine basin-floor Succession, Neoproterozoic Windermere Supergroup, British Columbia, Canada. *Sedimentology* 63, 136–175. doi:10.1111/sed.12222
- van der Werff, W., and Johnson, S. (2003). Deep-sea Fan Pinch-Out Geometries and Their Relationship to Fan Architecture, Tanqua Karoo basin (South Africa). *Int. J. Earth Sci.* 92, 728–742. doi:10.1007/s00531-003-0352-9
- Veivers, J. J., Cole, D. I., and Cowan, E. J. (1994). “Southern Africa: Karoo Basin and Cape Fold Belt,” in *Permian-Triassic Pangean Basins and Fold Belts along the Panthalassan Margin of Gondwanaland*. Editors J. J. Veivers and C. M. Powek (Boulder, Colorado, US: Geological Society of America), 184, 223–279.

- Vicente Bravo, J. C., and Robles, S. (1995). "Large-scale Mesotopographic Bedforms from the Albian Black Flysch, Northern Spain: Characterization, Setting and Comparison with Recent Analogues," in *Atlas of Deep Water Environments; Architectural Style in Turbidite Systems*. Editors K. T. Pickering, R. N. Hiscott, N. H. Kenyon, F. Ricci-Lucchi, and R. D. A. Smith (London: Chapman & Hall), 282–286. doi:10.1007/978-94-011-1234-5_32
- Visser, J. N. J. (1997). Deglaciation Sequences in the Permo- Carboniferous Karoo and Kalahari Basins of the Southern Africa: a Toll in the Analysis of Cyclic Glaciomarine basin Fills. *Sedimentology* 44, 507–521.
- Visser, J. N. J., and Praekelt, H. E. (1996). Subduction, Mega-Shear Systems and Late Palaeozoic basin Development in the African Segment of Gondwana. *Geol. Rundschau* 85, 632–646. doi:10.1007/BF02440101
- Wach, G., Lukas, T. C., Goldhammer, R. K., Wickens, H., and Bouma, A. H. (2000). Submarine Fan Through Slope to Deltaic Transition Basin-Fill Succession, Tanqua Karoo, South Africa. *Fine-Grained Turbid. Syst.* 72, 173–180.
- Walker, R. (1975). Upper Cretaceous Resedimented Conglomerates at Wheeler Gorge, California: Description and Field Guide. *J. Sediment. Petrol.* 45, 105–112.
- Wickens, H. deV. (1994). *Basin Floor Fan Building Turbidites of the Southwestern Karoo Basin, Permian Ecga Group, South Africa*. PhD dissert. (unpublished), University Port Elisabeth, South Africa. 233.
- Wild, R., Flint, S., and Hodgson, D. (2009). Stratigraphic Evolution of the Upper Slope and Shelf Edge in the Karoo Basin, South Africa. *Basin Res.* 21, 502–527. doi:10.1111/j.1365-2117.2009.00409.x
- Wild, R. J., Hodgson, D. M., and Flint, S. S. (2005). "Architecture and Stratigraphic Evolution of Multiple, Vertically-Stacked Slope Channel Complexes, Tanqua Depocentre, Karoo Basin, South Africa," in *Submarine Slope Systems: Processes and Products*. Editors D. M. Hodgson and S. S. Flint (London: Geol. Soc. Spec. Publ), 244, 89–111. doi:10.1144/GSL.SP.2005.244.01.06
- Wynn, R., Kenyon, N. H., Masson, D., Stow, D., and Weaver, P. (2002). Characterization and Recognition of Deep-Water Channel-Lobe Transition Zones. *Am. Assoc. Pet. Geol. Bull.* 86, 1441–1462. doi:10.1306/61EEDCC4-173E-11D7-8645000102C1865D

Conflict of Interest: Authors AP, RW and LG are employed by Equinor ASA.

The remaining authors declare that the research was conducted in the absence of any commercial or financial relationships that could be construed as a potential conflict of interest.

The authors declare that this study received funding from Equinor ASA. The funder had the following involvement in the study via collaboration with company staff who are co-authors: the collection, analysis, interpretation of data, and the writing of this article.

Publisher's Note: All claims expressed in this article are solely those of the authors and do not necessarily represent those of their affiliated organizations, or those of the publisher, the editors and the reviewers. Any product that may be evaluated in this article, or claim that may be made by its manufacturer, is not guaranteed or endorsed by the publisher.

Copyright © 2021 Hansen, Healy, Gomis-Cartasio, Lee, Hodgson, Pontén and Wild. This is an open-access article distributed under the terms of the Creative Commons Attribution License (CC BY). The use, distribution or reproduction in other forums is permitted, provided the original author(s) and the copyright owner(s) are credited and that the original publication in this journal is cited, in accordance with accepted academic practice. No use, distribution or reproduction is permitted which does not comply with these terms.



Evolution of a Fault-Controlled, Deep-Water Sub-Basin, Tabernas, SE Spain

Lucie Baudouy^{1,2*†}, Peter D. W. Haughton^{1‡} and John J. Walsh^{2‡}

¹UCD School of Earth Sciences, University College Dublin, Dublin, Ireland, ²Fault Analysis Group, UCD School of Earth Sciences, University College Dublin, Dublin, Ireland

OPEN ACCESS

Edited by:

Adam McArthur,
University of Leeds, United Kingdom

Reviewed by:

Roberto Tinteri,
University of Parma, Italy
Euan Lewis Soutter,
The University of Manchester,
United Kingdom

*Correspondence:

Lucie Baudouy
l.baudouy@fugro.com

†Present address:

Lucie Baudouy,
Fugro, Castries, France

[‡]All authors have contributed equally to this work and share first authorship

Specialty section:

This article was submitted to
Sedimentology, Stratigraphy and
Diagenesis,
a section of the journal
Frontiers in Earth Science

Received: 30 August 2021

Accepted: 20 October 2021

Published: 04 November 2021

Citation:

Baudouy L, Haughton PDW and
Walsh JJ (2021) Evolution of a Fault-
Controlled, Deep-Water Sub-Basin,
Tabernas, SE Spain.
Front. Earth Sci. 9:767286.
doi: 10.3389/feart.2021.767286

The Neogene Tabernas Basin, SE Spain, provides important evidence at outcrop for the interplay between tectonic deformation of the sea floor, slope instability and turbidity current behaviour. Dextral-oblique strike-slip faults and associated folds propagated along the basin axis to deform the palaeo-sea floor, creating structurally-controlled depressions in which turbidity currents were trapped and ponded. EW-trending syn-depositional faults define a narrow sub-basin that subsided asymmetrically as a negative flower structure. The sub-basin contains an expanded succession (>300 m of ponded turbidite sheets, debrites and slumps) along its northern margin flanked by the principal fault strand defined by a wide zone of sheared and calcite-veined marl. A narrower fault zone with a smaller displacement marks the southern margin of the sub-basin and the fill close to it is thin with internal discordances, evidence of local failure and southward thinning of sandstone sheets. Both northern and southern faults ‘died’ at the same stratigraphic level and were overstepped by basin floor turbidites showing evidence of weaker and longer-range topographic confinement. As turbidites healed and aggraded out of the sub-basin to progressively onlap the southern margin of the basin, major gravity failures occurred emplacing thick (>100 m) mass-transport complexes. The first initially reworked the southern part of the sub-basin fill together with the early onlap wedge, the second remobilised the onlap wedge, and the third records failure of the upper part of the slope well above the wedge. The first two were toe-confined failures, the third and furthest travelled was confined by basin axis topography. All three failures are lateral to or directly overlain by ‘megabed’ sheets on the basin floor, implying either a common trigger (earthquakes) or slope instability following reflection of large volume flows. Tabernas turbidites highlight the role of basin tectonics (as opposed to up-dip supply and sea level fluctuations) in directly impacting on deep-water processes and stratigraphy. Small deep-water transtensional sub-basins opened up along long transfer faults accommodating regional extension.

Keywords: ponded turbidites, mass-transport deposits, syn-depositional faulting, strike-slip faulting, negative flower structure

1 INTRODUCTION

Turbidity currents are extremely sensitive to slope (Britter and Linden, 1980; Kneller, 2003; Gray et al., 2005; Stevenson et al., 2013; Pohl et al., 2020) and respond to even subtle gradient changes induced by tectonic tilting or surface fault ruptures. Understanding the link between sea-floor deformation and sedimentation in deep-water successions has lagged behind that of more accessible fault-controlled terrestrial and shallow-water deposits. However, much recent progress has been made using seismic and bathymetric data from deforming continental slopes that demonstrate local flow ponding, transitions between channels and splays, and changes in channel sinuosity or position related to gradient breaks or lateral tilting (e.g. Pirmez et al., 2000; Heiniö and Davies, 2007; Caterall et al., 2010; Mayall et al., 2010; Doughty-Jones et al., 2017; Howlett et al., 2021; Pizzi et al., 2021). Nonetheless outcrop examples where tectonic control of sea floor gradients can be demonstrated are rare. Amongst those described are tectonically-forced lateral migration of channels and fans in the Ainsa Basin, northern Spain (Pickering and Corregidor, 2005; Tek et al., 2020), flow stripping across an emergent fault-scarp in the Annot Basin (Tomasso and Sinclair 2004), sandy lobes aggrading behind thrust-related folds in a trench slope setting on the Hikurangi Margin (McArthur et al., 2021), changes in bed type related to tectonic evolution of the Apennines foredeep (Tinterri and Muzzi Magalhaes, 2011; Tinterri and Piazza, 2019) and evidence for faulting on the floor of late Miocene basins in SE Spain (Haughton, 2000; Hodgson and Haughton, 2004). The study reported here builds on the first recognition of an important intrabasinal fault zone traversing the floor of the southern Tabernas Basin, SE Spain (Haughton, 2000). Here we demonstrate that the fault zone was part of a larger negative flower structure comprising several linked fault strands. These opened local fault-bounded accommodation (the Alfaro sub-basin) on the floor of a wider basin. The turbidite successions within and flanking the sub-basin record the history of sub-basin deepening, filling and healing that accompanied fault propagation to the sea floor. A significant feature of the sub-basin fill is the interplay between ponded turbidites and large-scale mass transport deposits (MTDs), particularly during healing of the basin floor. This interplay between tectonics, sea floor morphology and gravity current behaviour provides useful insight into processes operating in slope mini-basins with mobile shale or salt substrates.

The aims of this paper are to: 1) provide an improved tectonostratigraphic framework for the evolution of the Tabernas Basin and the associated Alfaro sub-basin based on new field mapping; 2) document the impact and displacement history of intrabasinal faults and show that these were part of a linked system sealed by the younger basin fill, 3) describe the pattern of sub-basin filling and healing as deformation transferred from intrabasinal faults to the basin margins, and 4) present evidence for onlap-wedge instability and the interplay between mass transport and turbidite systems as the structurally-generated topography was progressively buried. Evidence for the

behaviour of syn-depositional faults sealed by younger stratigraphy is important regionally as it helps resolve the rapidly evolving Neogene deformation conditions in SE Spain.

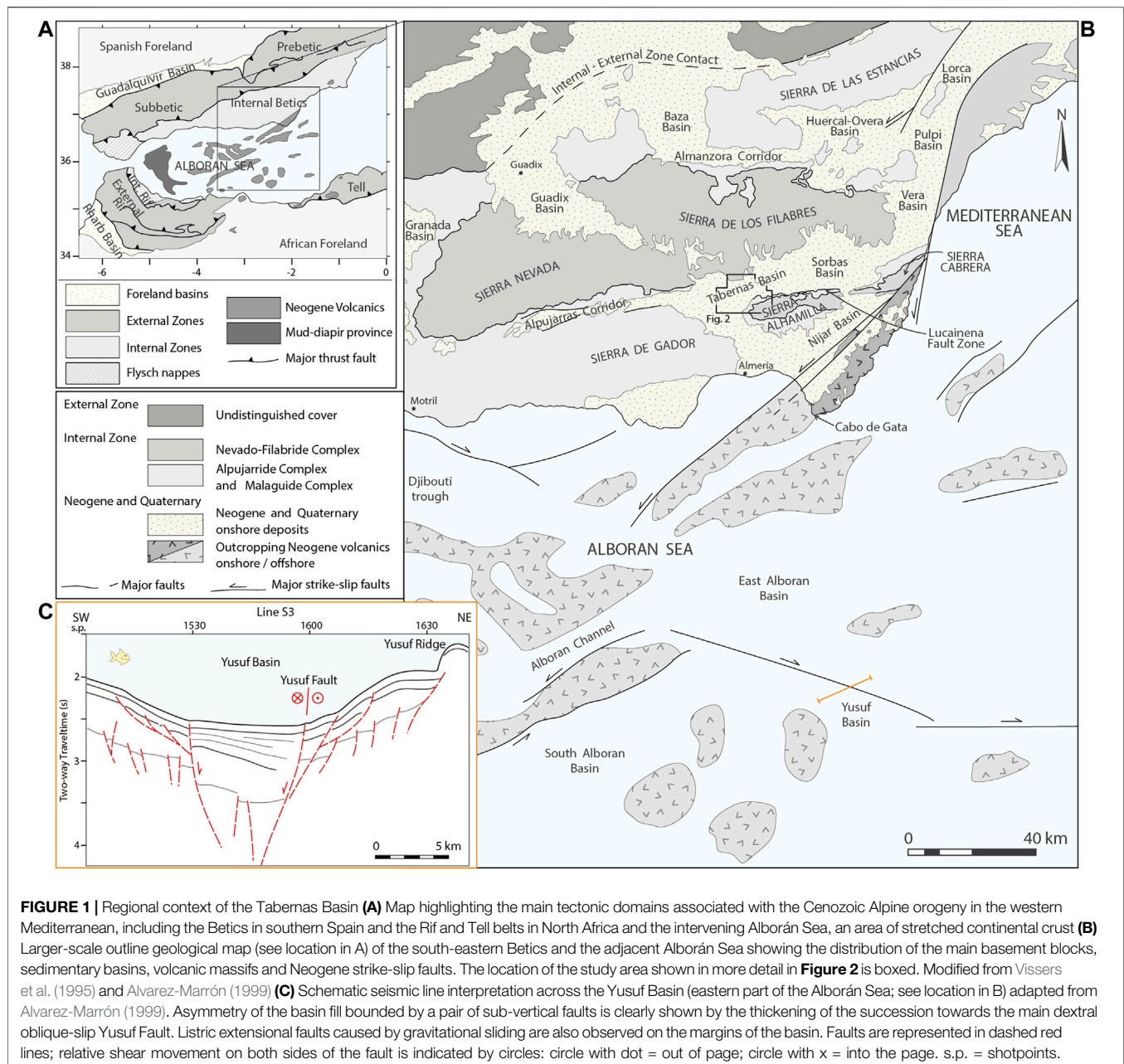
2 GEOLOGICAL SETTING

A network of small Neogene basins occurs throughout SE Spain and extends offshore into the Alboran Sea (**Figure 1**). The basins rest on exhumed basement rocks of the Internal Zone of the Betic Cordillera, the westernmost extension of the Alpine orogenic system (Lonergan and White 1997; Platt et al., 2013). The Tabernas Basin is typical of Neogene basins in the region in that it was a relatively narrow basin (~10 km wide, allowing for later compression) and elongated in an East-West direction. It is particularly well known for its deep-water fill first described by Kleverlaan (1989a,b). It was connected to the east with the Sorbas Basin and to the south with the Almería Basin (**Figure 1**), although each of the basins is characterised by a different subsidence pattern, fill, inversion and uplift history. The uplifted remnants of the Tabernas Basin are surrounded by basement cored mountains or sierras: the Sierra de los Filabres to the north composed mainly of high-grade metamorphic rocks (mainly dark mica-schist, gneiss and quartzite) assigned to the Nevado-Filabride Complex, and the Sierra Alhamilla and Sierra de Gádor to the south and south-west, respectively, which are dominated at surface by mainly lower-grade metamorphic rocks of the Alpujarride Complex (generally phyllites, psammites and dolomites). These basement highs and their extension to the west thus contributed compositionally distinct sediment to the adjacent basins (Koch and McCann 2020). Contemporary platform and pelagic carbonate production was also important, resulting in common mixed siliciclastic-carbonate sediment supply, as well as recycling of older Neogene basin fills.

3 TABERNAS BASIN

Kleverlaan (1989b) published the first detailed map and cross-sections of the Tabernas Basin fill. These illustrated the broad distribution of turbidite facies and highlighted the basin-wide distribution of a distinctive marker bed, a very thick (+ 60 m) debrite-turbidite couplet which was termed the Gordo Megabed (Kleverlaan 1987). Haughton (2000) subsequently provided a revised map for part of the southern section of the basin tracing distinctive stacked turbidite units assigned formation status in Hodgson and Haughton (2004). Since then, remapping has focussed on better integrating stratigraphic and structural aspects of the basin fill, and in particular in distinguishing syn and post-depositional faults. The result is the new map and cross-sections shown in **Figures 2, 3**.

The Tabernas Basin fill rests unconformably on the Sierra de los Filabres basement to the north and is up-ended and faulted against the Sierra Alhamilla basement in the south-east. The latter faulted contact is the westward extension of the Lucainena Fault Zone (Galdeano and Vera, 1992) that runs along the northern flank of the Sierra Alhamilla for over 35 km. East of

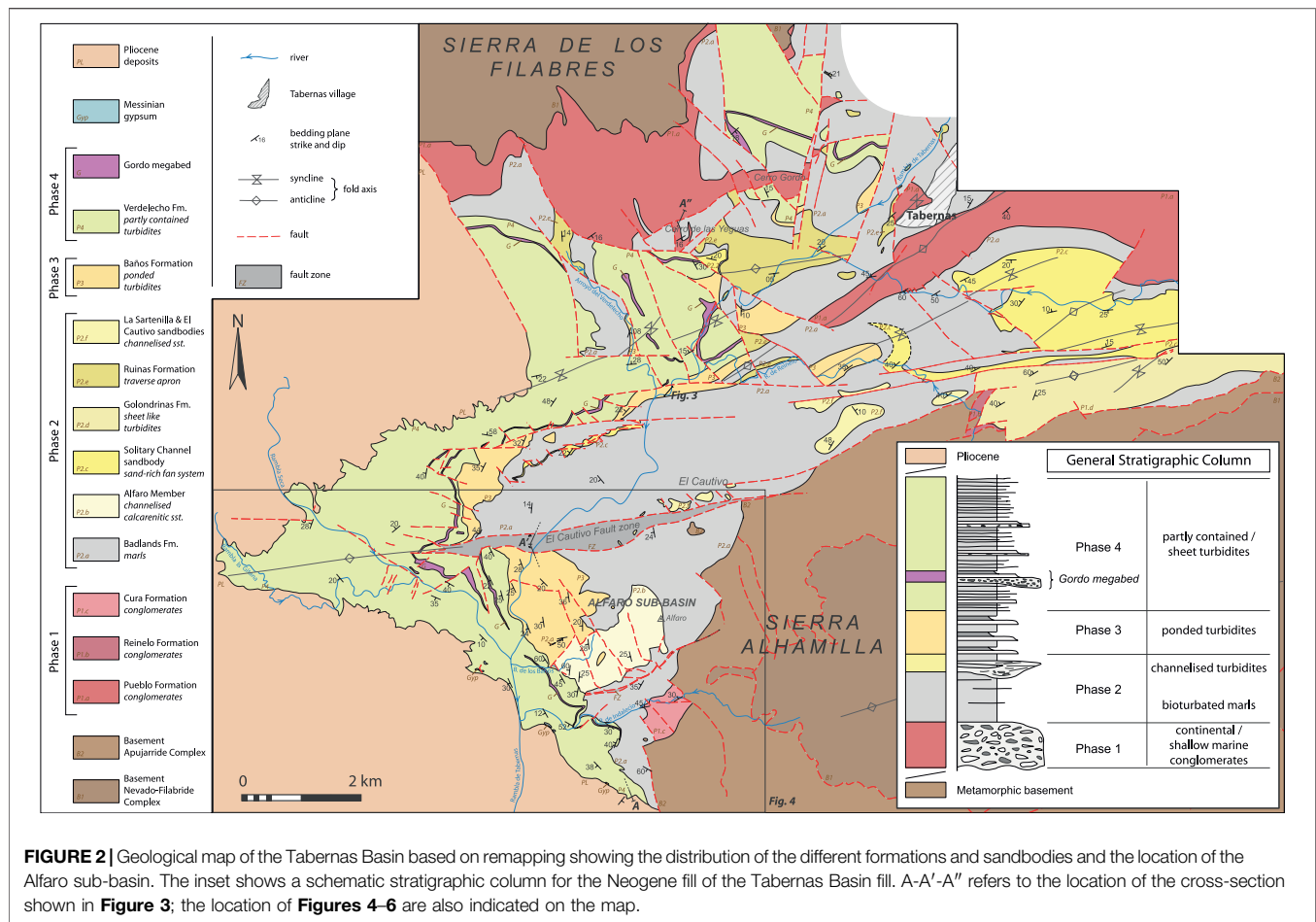


Lucainena, the Lucainena Fault Zone is unconformably overstepped by latest Tortonian-Messinian reefs and associated shallow marine deposits (Weijermars et al., 1985; Martín et al., 1998; Haughton, 2001). At the western plunge culmination of the Sierra Alhamilla, the fault propagates westwards up-dip into the Tabernas basin fill as the El Cautivo Fault Zone—but again it is overstepped by younger stratigraphy implying that it became inactive in the early Messinian. It is an area of stratigraphic expansion directly south of the El Cautivo Fault, here referred to as the Alfaro sub-basin, that is the subject of this paper. To the west, the deep-water fill to the Tabernas Basin is blanketed unconformably by younger Pliocene deposits locally affected by NNW-SSE

trending normal faults and E-W strike-slip faults (Sanz De Galdeano et al., 2010). To the east, it passes axially into the Sorbas Basin fill, although the Tabernas Basin remained a deep water basin at the end of the Tortonian whereas the Sorbas Basin was uplifted, eroded and became a shallower water platform.

Mapping of the Tabernas Basin fill reveals four distinct phases in basin development (**Figure 2**); these represent significant structurally-driven reconfigurations of the basin shape and sediment supply.

Phase 1 comprises an upward-fining succession of very coarse boulder conglomerates passing upwards into yellow-grey marine marls. The conglomerates rest unconformably on metamorphic basement along the foot of the Sierra de los Filabres, and are



brought to the surface in a pair of faulted anticlines at Cerro Gordo and south of Tabernas (**Figure 2**). The conglomerates record the early deposition of terrestrial alluvial fans that evolved to become fan deltas as a consequence of marine flooding (Dabrio, 1990; Doyle et al., 1996). This earlier phase of basin development is poorly dated but a Serravallian to early/mid Tortonian age has been inferred (Kleverlaan, 1987, 1989a; Poisson et al., 1999; Hodgson, 2002). Sediment dispersal was to the south and south-west from a source mainly comprising Nevado-Filabride basement lithologies (graphic schist and psammite). The conglomerates (several 100 m thick) may be related to Alpujarride-sourced conglomerates passing up into yellow-grey marls found in normal fault-contact with the Sierra Alhamilla east of Alfaro hill, and caught up as slivers in the fault zone juxtaposing the basin and basement along the north side of the Alhamilla (where they are locally unconformable on the Alpujarride basement and overstepped by younger late Tortonian turbidites). The early upward-fining successions may be remnants of the hanging-wall fill to extensional detachments formed during the later stages of an extensional event that regionally thinned the basement (Martínez-Martínez and Azañón, 1997; Martínez-Martínez and Azañón, 2002; Giaconia et al., 2014). This is consistent

with clast imbrication and grain size and facies trends suggesting flow to the SW (e.g. at Cerro Gordo west of Tabernas; **Figure 2**).

Phase 2 post-dates regional extension and was characterised by the development of an EW elongate depocentre in which a thick succession (>200 m) of late Tortonian grey marls initially accumulated in the basin axis, thinning onto the flanks of the basin. Towards the top of Phase 2, coarse grained sediment advanced into the basin, initially as northerly-derived, poorly sorted conglomerates and breccias interpreted as a deep-water apron related to reactivation of the northern basin margin (**Figure 3**). More mature W-derived conglomerates and sandstones filled a number of large axial slope channel fills in the basin axis and locally overlie the transverse apron south of the Cerro de las Yeguas (**Figure 2**). These were described by Haughton (2000) and interpreted as backfilled channels traversing an east-facing axial slope—they probably fed basin floor fans in the eastern Tabernas basin at this time and tapped a variable mix of Nevado-Filabride and Alpujarride sourced sediment supplied from the west.

Phase 3 represents a muddy phase of basin filling with the axial slope replaced by an uneven but relatively flat basin floor with depressions in which fully-contained (sensu Pickering and Hiscott, 1985) sheet turbidites accumulated. The term sheet is used here to

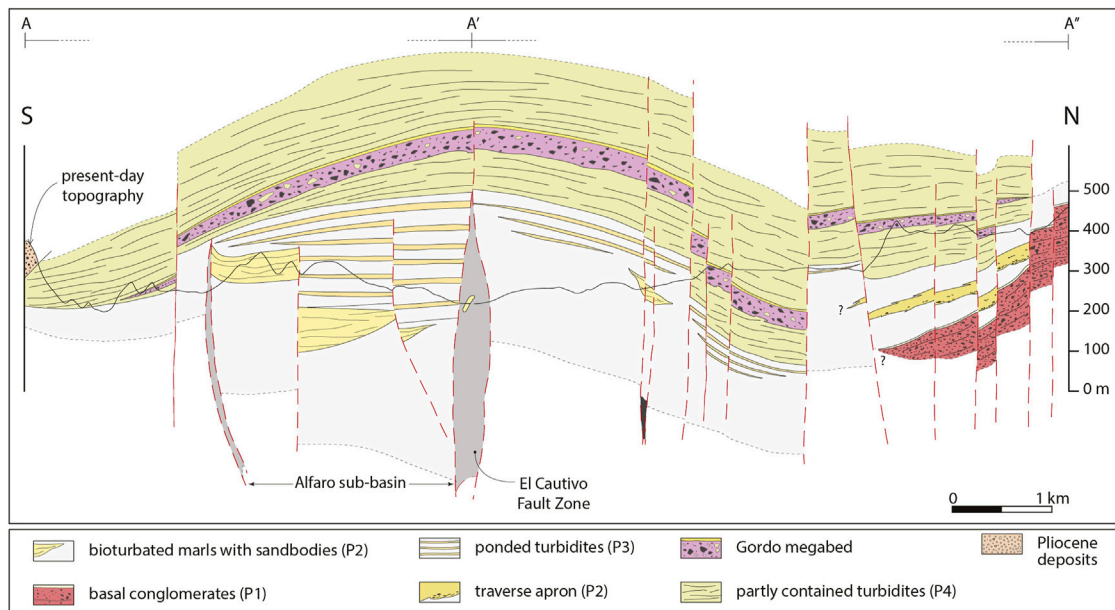


FIGURE 3 | N-S cross-section (vertical exaggeration of x4; see **Figure 2** for location) showing the stacked turbidite deposits of the central Tabernas Basin (identified by phase—see text for discussion) and the main faults. Note the Gordo megabed—an important marker horizon, and the presence of some faults that only affect the lower stratigraphic units. The position of the Alfaro-sub-basin is also indicated. Modified from Haughton (2000).

refer to laterally extensive single beds that extend across the area with minimal variation in thickness and which are limited by onlap onto topography or truncation against syn-depositional faults. Deposition was thus focussed across areas of deeper bathymetry; the sheets thin onto the basin margins and over intrabasinal highs (**Figure 2** and **Figure 3**). Turbidity currents were derived from the west with no evidence for sediment dispersed from the northern basin margin at this time; evidence for ponding of the flows implies there was now no exit for flows to the east and this probably corresponds to uplift of the southern part of the Sorbas Basin in the latest Tortonian/early Messinian.

Phase 4 (Messinian) saw a return to northerly-derived sediment following rejuvenation and uplift of the Filabres source; both transverse and larger volume axial turbidity currents spread sand across the basin floor, blanketing early intrabasinal structures, and onlapping unstable slopes on the south side of the basin. Phase 4 also saw the introduction of a series of megabeds, most spectacular of which was the Gordo Megabed of Kleverlaan (1987). The latter provides a useful datum for correlating stratigraphy across the basin. We distinguish here between megabeds, basin-wide large volume event beds comprising a basal breccia (debrite) overlain by a central sandstone grading upwards into a upper thick mudstone cap (a contained turbidite), and mass transport deposits, less well-organised and laterally more restricted products of slope failure involving slumping, sliding and local transformation to a debris flow.

The focus of this paper is on understanding phases 2, 3 and 4 of basin evolution in the area south of the El Cautivo Fault Zone in the southern part of the Tabernas Basin where an anomalously thick Phase 3 succession is preserved within the Alfaro sub-basin (**Figure 3**). The following sections first describe the margins of the sub-basin, concentrating on the southern margin which has not

been described before, and then analysing the fill and the relationship of the turbidite stratigraphy to early faults.

4 ALFARO SUB-BASIN

The Alfaro sub-basin fill is well exposed on the western flanks of Alfaro hill and in the Rambla de Tabernas (**Figure 4**). Its northern margin corresponds to the E-W trending El Cautivo Fault Zone described in detail by Hodgson and Haughton (2004). This dextral oblique soft-sediment shear zone is interpreted as a fault that propagated to the palaeo-sea floor through unconsolidated marl on account of its width (up to 350 m of muddy gouge including disrupted blocks of Phase 2 turbidite sand/sandstone), flared geometry and significant thickening of the Phase 3 ‘contained turbidite’ succession across it. The fault zone is characterised by a complex array of syn-kinematic fibrous calcite veins implying significant fluid movement during fault activity.

The succession immediately south of the El Cautivo Fault can be linked to that to the north, albeit with some important differences. Locally-derived basal conglomerates (up to 25 m thick) with an Alpujarride provenance and bioclastic components occur in normal-fault contact with Alpujarride basement. Hodgson (2002) has argued that these conglomerates contain evidence for syn-depositional NE-SW extension. They are overlain by yellow-grey marls with rare thin calcarenitic sandstone sheets that are well seen on the eastern counter-dip slopes of Alfaro hill. This fining upward conglomerate succession is tentatively assigned to Phase 1 (i.e. the early extensional phase of basin evolution), although it may not be age-equivalent to Phase 1 in the northern Tabernas Basin. However the

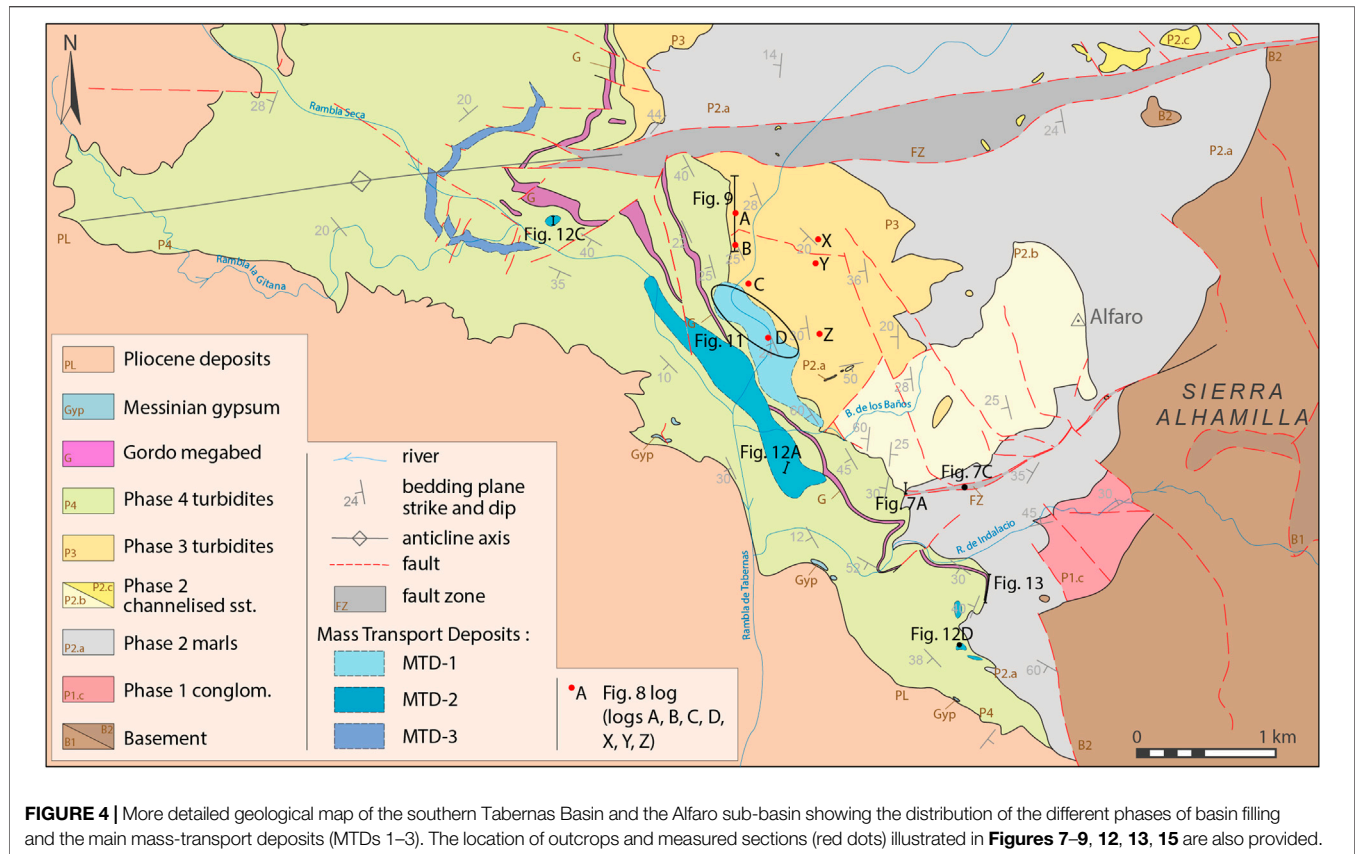


FIGURE 4 | More detailed geological map of the southern Tabernas Basin and the Alfaro sub-basin showing the distribution of the different phases of basin filling and the main mass-transport deposits (MTDs 1–3). The location of outcrops and measured sections (red dots) illustrated in **Figures 7–9, 12, 13, 15** are also provided.

thick muddy succession overlying the conglomerates is similar to the Phase 2 marls observed in the northern part of the basin.

A sharp erosional contact just beneath the crest of Alfaro hill separates the marls from an overlying stack of calcarenitic sandstones and microconglomerates (up to 70 m thick, Alfaro Member of Iaccarino et al., 1975). The calcarenites are rich in dolomite pebbles and contemporary bioclastic components and form two sandy packages separated by a 5 m thick discontinuous marl interval. Pebble imbrication indicates transport to the east. The calcarenites pass gradationally upwards into marl. The Alfaro Member is interpreted as two or more nested Phase 2 axial slope channels on the basis of the erosional bases, coarse grain size, amalgamation of sandstone beds and transport to the east similar to other Phase 2 channels (Haughton, 2000; Pickering et al., 2001). The channel bodies are overlain by up to 300 m of marls with thick ponded sandstone sheets [Unit C of Haughton (2000)] which occur on the western dip slope of Alfaro hill and in high cliffs along the western side of the Rambla de Tabernas. The sandstone sheets are dominantly of schistose metamorphic provenance, although there are some interleaved calcarenitic units (debrite-turbidite couplets). Most thicker sandstone beds have unbioturbated, more fissile capping mudstone divisions that are as thick or thicker than the underlying sandstones. This is the local expanded expression of Phase 3 deposition within the sub-basin (**Figure 5**). On the west side of Rambla de Tabernas, the change from Phase 3 to Phase 4 basin fill is marked by a step-change in the sandstone bed thickness distribution, bed frequency

and bed structure (Haughton, 2000). Thin and very thin beds are rare in the Phase 3 ponded fill, whereas these are common in Phase 4 and there is an attendant change in overall colour from grey to brown as well as an increase in bed frequency.

4.1 Stratigraphic Relationship Across the Northern Sub-basin Margin

Evidence for stratigraphic changes across the northern sub-basin margin has been addressed by Hodgson and Haughton (2004). Phase 3 sheets abut directly against the El Cautivo Fault Zone (ECFZ) which juxtaposes the ponded turbidite sheets to the south against thick marls to the north. There is no evidence for significant thinning of the turbidite sheets before they are cut by the fault zone. Only a thin interval of Phase 3 sheets (30 m thick) occurs directly north of the ECFZ just beneath the transition to Phase 4 fill. These cannot be tied at a bed level to sheets within the sub-basin. The sandier Phase 4 succession steps across the fault with only minor (m scale) later displacement.

Unlike the sheet turbidites, the underlying Alfaro Member calcarenites do not extend off the crest of Alfaro hill northwards as far as the ECFZ. Nested channel surfaces step up to the north and the calcarenites pinch out approximately 1 km south of the fault trace. Calcarenitic beds are however caught up in the thick gouge zone associated with the ECFZ. Calcarenitic beds also locally cap hills on the north side of the fault zone and are interpreted to represent the erosional remnants of another Phase

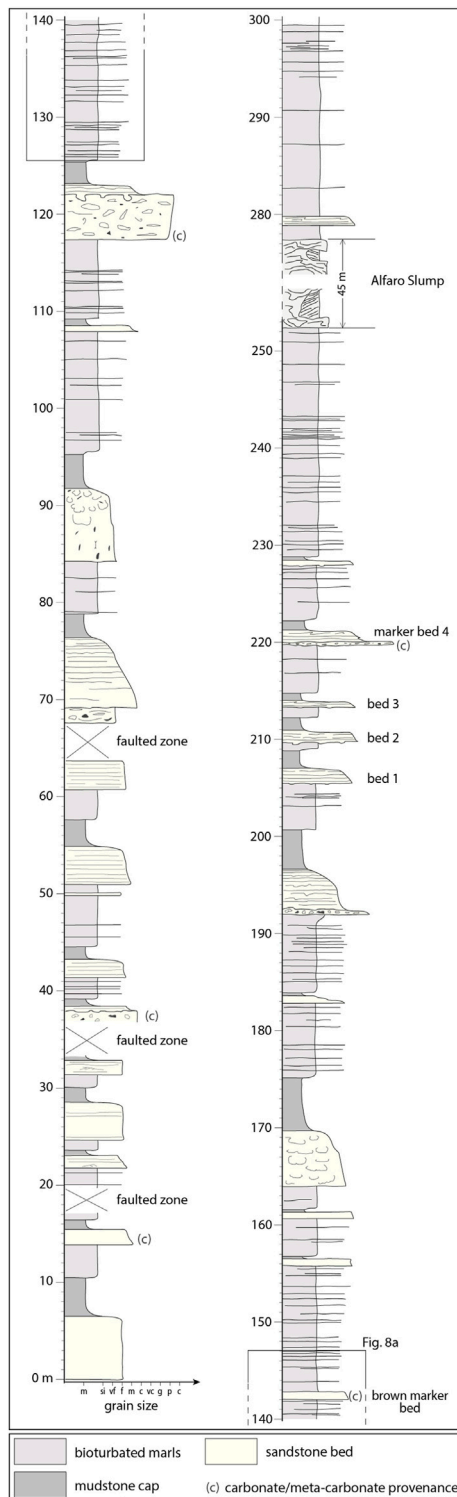


FIGURE 5 | Graphic log showing the character of the Phase 3 succession in the northern part of the Alfaro sub-basin where it is characterised by an expanded succession of thick megabeds and thinner contained turbidites. Log compiled from sections along the old N340 road and the Rambla de Tabernas. Extended from Houghton (2000). The stratigraphic position of the more detailed sections and beds illustrated in **Figure 8** is highlighted.

2 channel system, this one filled with sand with a mixed carbonate-siliciclastic provenance. At El Cautivo (**Figure 2**), this channel appears to have been truncated by the ECFZ to which it is oblique at a low angle in plan view.

Interpretation: Phase 4 sandstones overstep the ECFZ yet the Phase 3 sheet turbidites are truncated by the fault, implying the fault was active during or at least towards the end of Phase 3 deposition and then became inactive or buried by an increase in the rate of sediment accumulation. The expansion of the Phase 3 stratigraphy across the fault implies either an element of growth and/or lateral displacement of a thicker against a thinner sheet turbidite succession. The Alfaro calcarenite-filled channels step towards the fault zone but are separated from it suggesting the fault did not directly control the channel location. The northward stepping of channels may reflect early tilting towards the fault. The obliquity between channel orientations and the fault trend also suggests the fault was largely post channel formation, as do the large blocks of calcarenite resembling channel sediment (some cemented) that float within the fault gouge zone. The blocks were presumably entrained where the faults propagated to displace the channel fills cutting across the fault trace.

4.2 Phase 3 Sheets North of the Alfaro Sub-basin

The Phase 3 ponded sheet succession thickens northwards away from the sub-basin, reaching 100 m thick c.2 km north of the El Cautivo Fault before the sandstones pinch out laterally again into marl in the Arroyo del Verdelecho (**Figure 2**). The same sheets can also be traced eastwards 2.5 km in the Rambla de Reinelo where the thickest bed reaches >5 m thick. In general, however, the event beds are thinner than their equivalents in the expanded sub-basin succession and thick mudstone caps are less well developed. The character of the sheets outside the sub-basin is well illustrated by a large exposure in the Rambla de Tabernas (just upstream of its junction with the Arroyo del Verdelecho; **Figure 6**). Here a sandstone-mudstone couplet is characterised by a parallel-laminated sandstone with local convolute folding of the lamination upstream of a thinned part of the bed. The sandstone component of the event bed varies from 80 to 200 cm due to an irregular base as it rests on up to 10 m of remobilised marl. The bed is displaced by a series of normal listric faults orientated N115E and dipping to the south. The faults root out at the base of the muddy slumped interval but do not extend to the upper part of the outcrop to cut the next sandstone sheet. The fault planes have locally been intruded by marl.

Interpretation: Gradual expansion and then thinning of the Phase 3 sheet succession northwards away from the El Cautivo Fault Zone suggests that ponding of turbidity took place in gentle depressions up to 2 km across and > 3 km long, as well as in the deeper fault-controlled bathymetry of the sub-basin. The thickest sheets encountered outside of the sub-basin are in the Rambla de Reinelo and coincide with the hinge of a syncline. It is possible therefore that the basin floor outside of the sub-basin was warped by contemporary folding, with turbidites deposited along developing synclinal axes. Some of the sandstones directly overlie cohesive mudflow deposits suggesting that they were

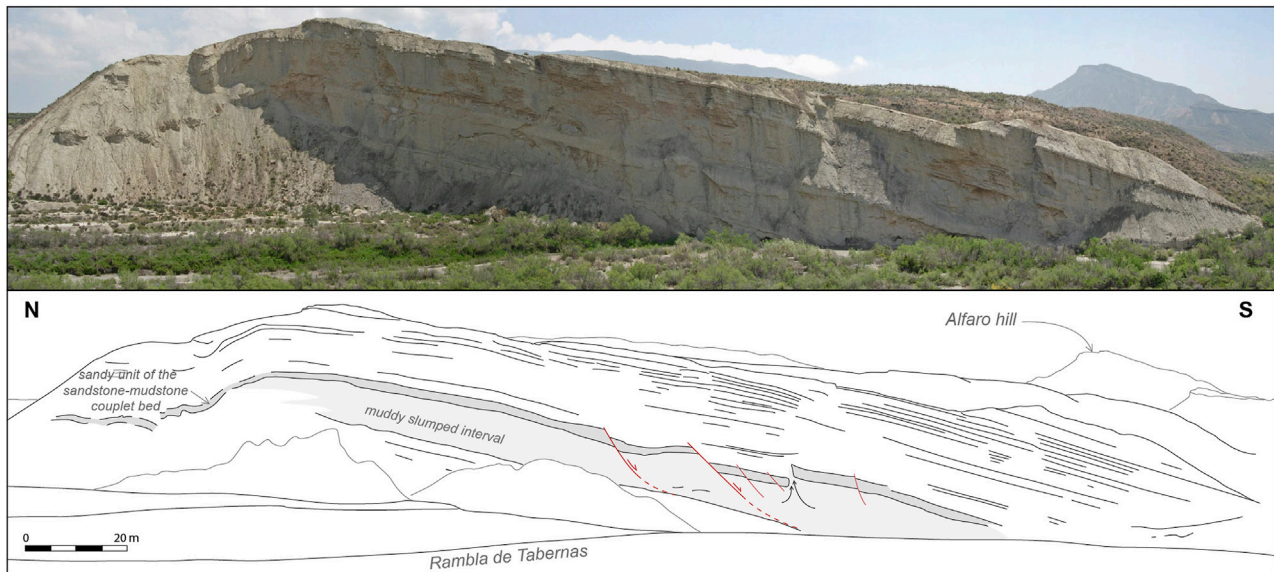


FIGURE 6 | Photograph and line drawing of part of Phase 3 succession due north of the Alfaro sub-basin in the Rambla de Tabernas (see **Figure 2** for location). Note the irregular thickness of the sandstone-mudstone couplet (highlighted in dark grey) deposited above a fine-grained slumped interval. Early listric faults (highlighted in red) locally intruded by mobile water saturated marls and rooting at the base of the slumped interval are also developed.

emplaced on mobile mud beds; turbidity currents may have either triggered local substrate flows or they may have interacted with mudflows released by the same external trigger (see below). The strongly layered nature of the sheet succession with sands encased in marls may have encouraged packet sliding off low gradient slopes, with gravity deformation continuing by brittle deformation and shallow faulting after emplacement of the sandstone and its associated mudstone cap.

4.3 Southern Margin of Sub-basin

The Alfaro Member calcarenites and overlying Phase 3 ponded turbidites can be followed southwards off the Alfaro ridge to the area north of Rambla de Indalecio where a series of exposures constrain the stratigraphic and structural geometry of the southern margin of the sub-basin. When traced down the dip slope to the southwest, the Alfaro Member calcarenites and basal part of the ponded sheets are overstepped by the Phase 4 basin fill. In the Barranco de los Baños, the Alfaro calcarenites are overlain by the basal part of the ponded sheet succession which is discordantly overlain by upper Phase 3 sheets. The result is that only a thin and incomplete interval (c. 50 m thick) of the Phase 3 fill is developed here (compared to >300 m to the north). Further south again, Alfaro calcarenites that floor the sub-basin to the north are progressively rotated to near vertical and juxtaposed against pale grey scaley marls by a decametre-wide vertical fault zone trending N090E (**Figure 7**). Ductile deformation of the adjacent, now cemented and brittle, calcarenites suggest that they were cohesive but not fully lithified at the time of deformation (**Figure 7B**). Mode I vuggy calcite veins occur in the fault zone and these have an average strike of N155E. Some sub-vertical dextral E-W shear planes are also developed in this fault zone and are occasionally

utilised by fibrous calcite veins. When the fault is traced 400 m to the east, calcarenites flanking the fault are incorporated into the fault zone and deformed to produced folds with axes orientated N070E which were then cut by minor N120E-trending dextral faults (**Figure 7C**). To the south of the fault, Alfaro calcarenites are not present, and Phase 2 marls are directly overlain by Phase 4 sheet turbidites. The contact is a sharp surface, generally planar but with local steps, against which the younger succession systematically onlaps in a south-easterly direction. The onlapping succession also contains evidence for significant gravity-induced deformation directed away from the slope (discussed in more detail below). The mapped distribution of the Phase 4 turbidites implies they extend without displacement across the shaley gouge zone that truncates the Alfaro calcarenites.

Interpretation: The scaley and calcite-veined gouge resembles a thinner version of the anomalously thick gouge zone bounding the northern side of the sub-basin. It is similarly interpreted as a syn-depositional fault, the key evidence being the overstep of the younger Phase 4 stratigraphy and the Gordo megabed embedded in it across the fault trace without displacement. The southern fault zone is orientated ENE-WSW and projects eastwards into a dextral step in the basement of c. 1 km. Overall the two bounding faults are slightly oblique to one another in map view and they converge to the east. As late uplift and subsequent erosion have produced an oblique slice, the geometry is interpreted as upward splaying of the principal displacement zone with the sub-basin sitting between two active strands of the same linked fault system. Small scale internal deformation features and vein orientations indicate the fault bounding the sub-basin to the south was a dextral fault zone (like the El Cautivo Fault

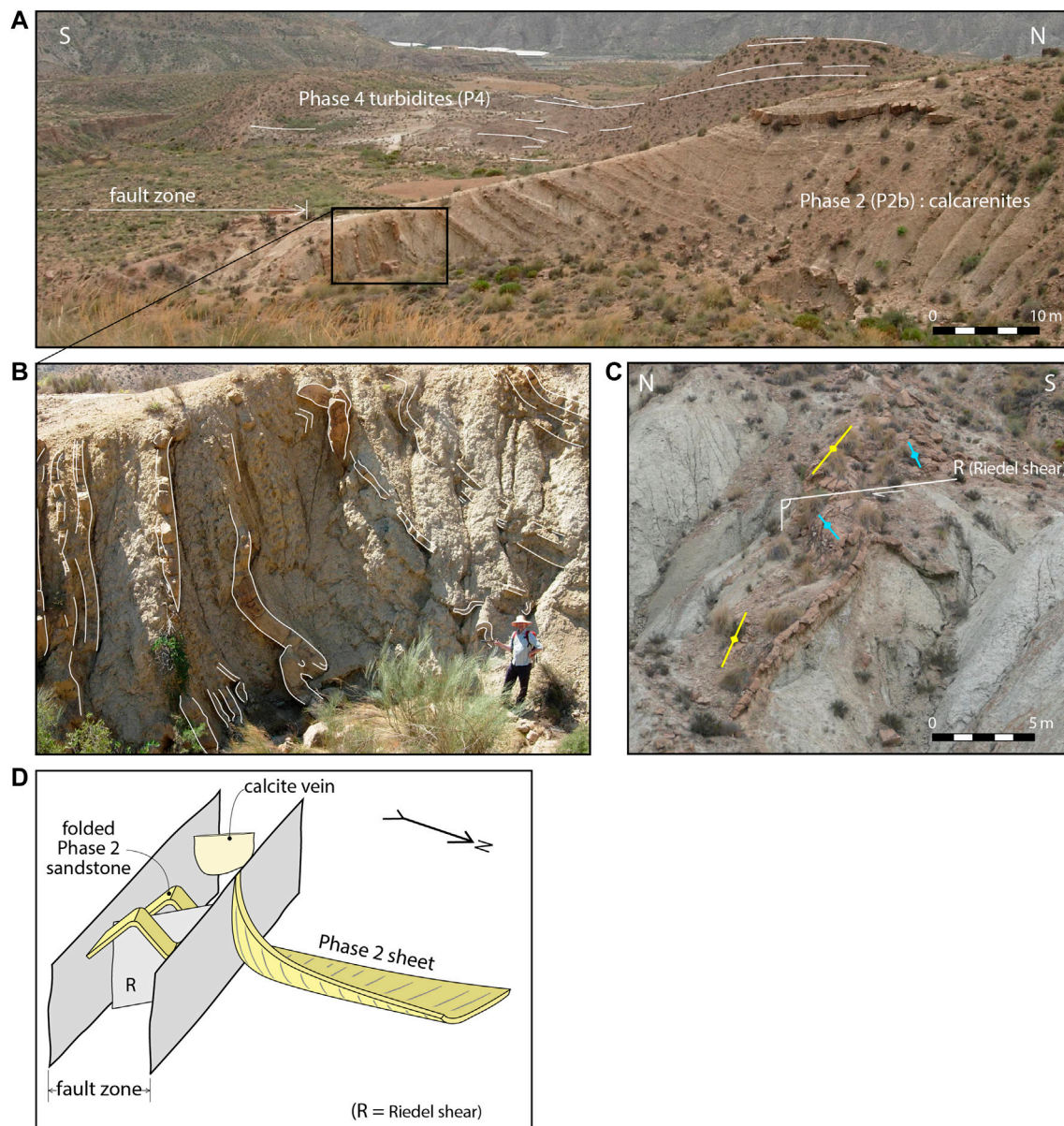


FIGURE 7 | Field photographs and fault reconstruction illustrating the character of the faulted southern margin of the Alfaro sub-basin (see **Figure 4** for location) **(A)** Progressive rotation of Phase 2 calcarenites against the northern side of the fault zone indicating dextral motion on the fault zone with a component of downthrow to the north. Relatively undisturbed Phase 4 turbidites occur on the far side of the fault (highlighted in white) and overstep it without displacement **(B)** Close-up of relatively ductile deformation of Phase 2 sandstone beds (highlighted in white) against the fault **(C)** Deformed calcarenitic sandstone bed within the southern margin fault zone exhibiting pair of very tight parallel anticlines (highlighted in yellow and blue) cut and offset by a dextral Riedel shear minor fault (highlighted in white) **(D)** Sketch summarising the deformation within and against the oblique slip fault on the southern margin of the Alfaro sub-basin (dextral strike-slip + downthrown to the north).

Zone) but in this case with a component of downthrow to the north (**Figure 7D**). Deformation flanking the fault zone to the south and/or longer wavelength uplift linked to the rise of the basement blocks may have tilted the muddy Phase 2 succession down to the north to provide the relatively smooth slope against which the younger Phase 4 stratigraphy laps out. The change from Phase 3 to Phase 4 turbidites coincides with overfilling of the sub-basin and a switch to deposition

over a wider area that draped the then-inactive faults and overlapped an unstable confining slope to the south.

4.4 Sub-Basin Fill and Stratigraphic Geometry

The sub-basin lying between the two fault strands is c.2 km wide and dominated by a succession of laterally extensive Phase 3

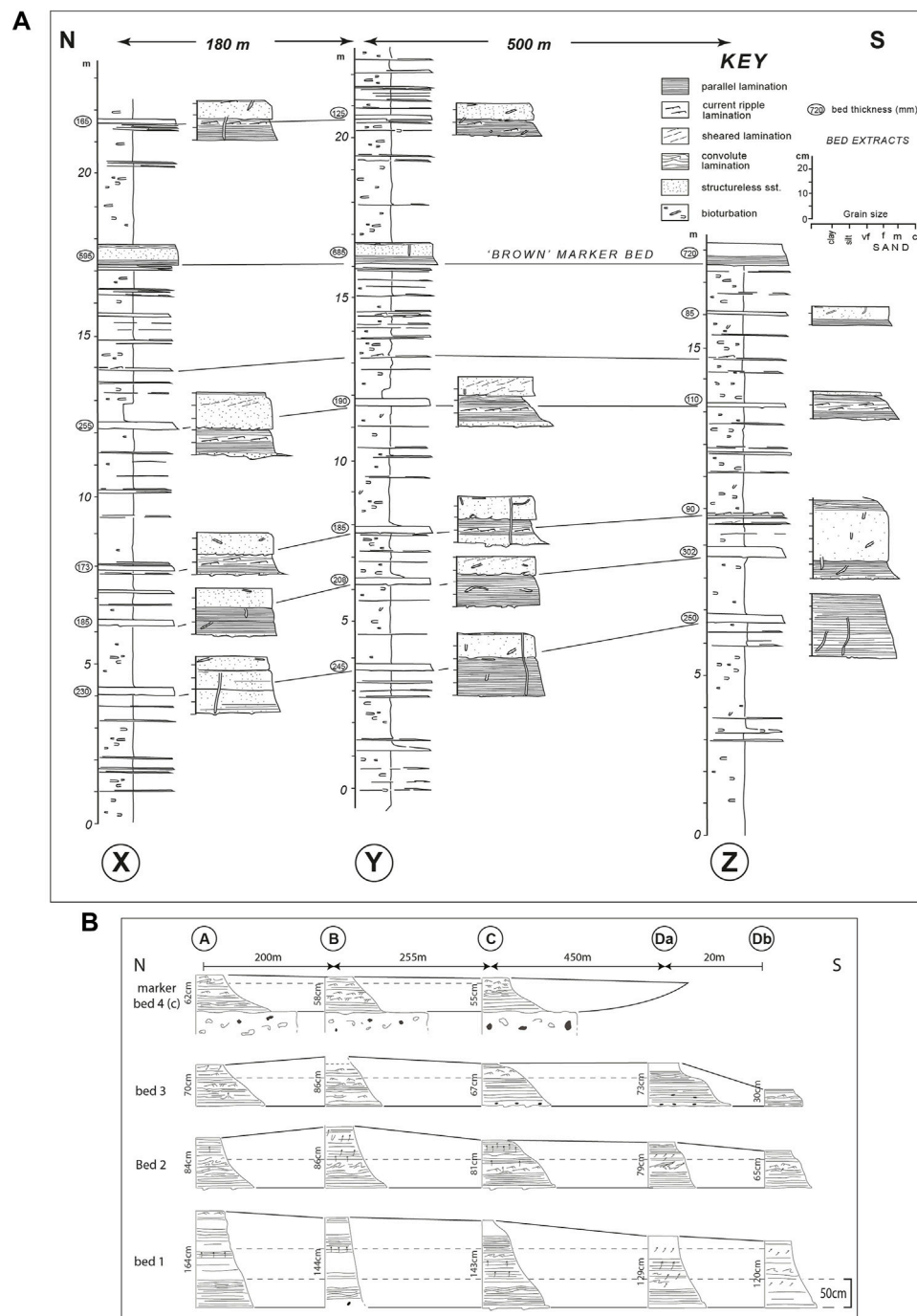
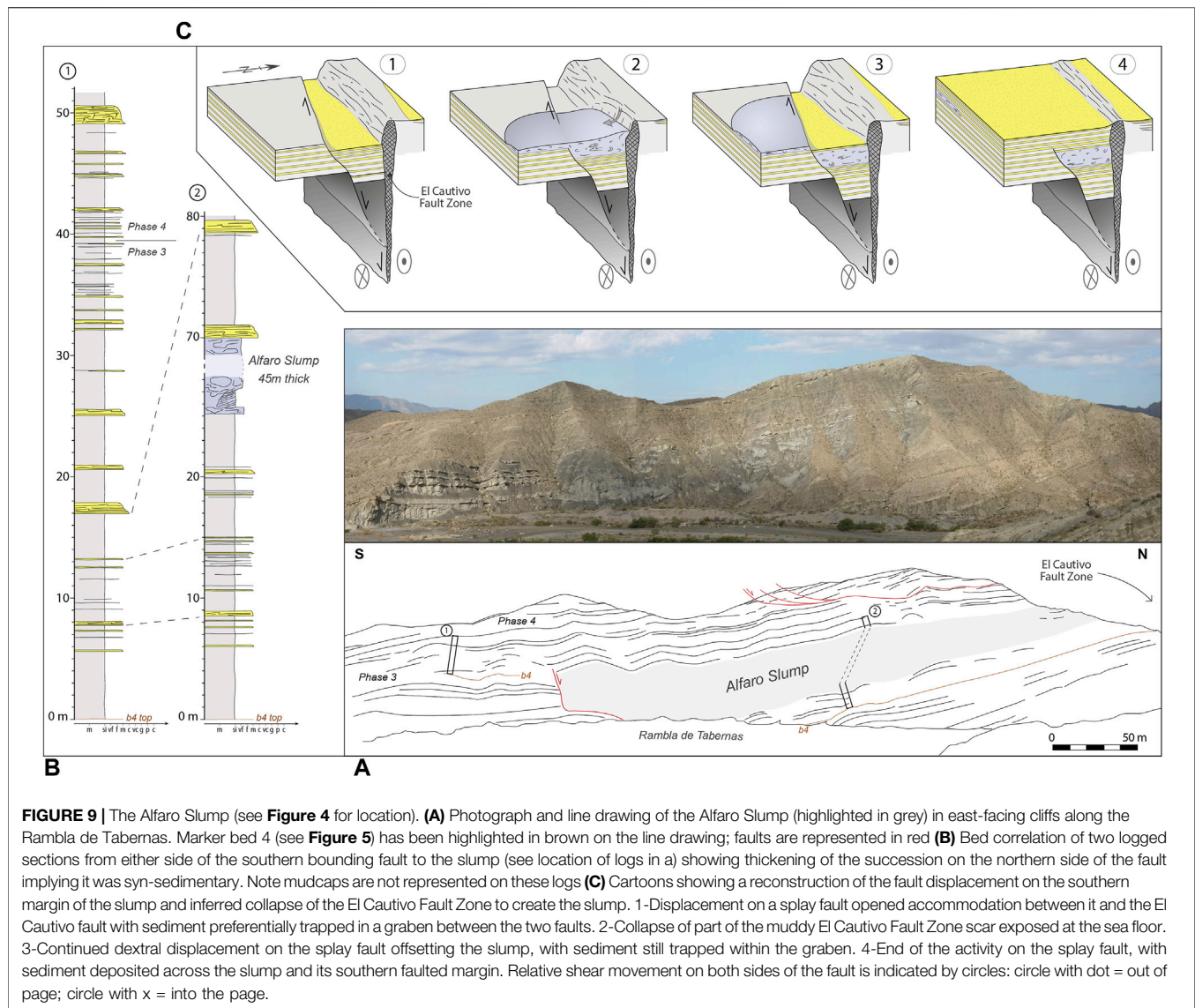


FIGURE 8 | Lateral correlation of Phase 3 sandy event beds filling the Alfaro sub-basin **(A)** N-S correlation of thin beds (stratigraphic location shown in **Figure 5**) over a distance of 680 m. More detailed log extracts illustrate the unusual character of the sandstones. See text for discussion **(B)** N-S correlation over a distance of 925 m of thicker event beds in the upper part the sub-basin fill showing thinning as the southern margin of the sub-basin is approached, and pinch-out of a bed with a carbonate provenance before those with a siliciclastic composition. Location of logged beds shown in **Figures 4, 5**.

ponded turbidite sheets (Haughton, 2000; Hodgson and Haughton, 2004) up to 300 m thick (**Figure 5**). The younger of these sheets extend across the full width of the sub-basin. They are dominantly siliciclastic sandstones, but include at least 5 sheets with a carbonate provenance (in all cases debrite-turbidite

couplets with the sand fraction dominated by bioclastic grains). A distinctive bundle of closely spaced beds c.140 m below the top of the sub-basin fill (highlighted on **Figure 5**) can be traced laterally between sections. Three stacked siliciclastic turbidite sheets (referred to as beds 1, 2 and 3) and an overlying calcarenite



sheet (marker bed 4) have a relatively constant thickness when traced north to south across the sub-basin floor for 800 m (**Figure 8B**), but thin as they approach the fault corridor at the south side of the sub-basin where the calcarenitic sheet pinches out completely, implying it thins laterally at a faster rate than siliciclastic sheets of similar thickness. Complete pinch out of the siliciclastic sheets cannot be demonstrated due to lack of outcrop in the main rambla bed. N-S section correlations of relatively thin sheets at a deeper stratigraphic level demonstrate subtle but systematic southward thinning of the succession, mainly involving thinning of the bioturbated sandy marls between the sheet sandstones (**Figure 8A**). Beneath the sheet succession, a marl interval occurs in the central sub-basin, resting on top of the Alfaro Member calcarenites. This marl is absent to the south where sheet sandstones higher in the section directly overlie the Alfaro Member. Just north of the Barranco de los Baños large calcarenite sandstone blocks (up to 70 m across) occur locally interleaved with the Phase 3 stratigraphy.

A major remobilised unit (referred to here as the Alfaro Slump; **Figure 9**) is intercalated with sheet turbidites within the sub-basin fill (c. 75 m below the top of Phase 3), but only in the northern part of the sub-basin. This is well exposed in high cliffs on the western margin of the Rambla de Tabernas (**Figure 9A**) immediately south of the El Cautivo Fault Zone. The slump is 45 m thick and is composed of chaotic sheared muddy matrix (more than 90%) with scattered deformed sandstone blocks (up to 1 m across) as well as poorly defined marl blocks which are recognised by their bedding-discordant fissility. It has a sheet-like geometry with no convergence of turbidite beds above and below. The slump has a planar base with the underlying marls and it sits stratigraphically above a distinctive calcarenite debrite-turbidite couplet (marker bed 4; see above). When followed to the north, the slump can be traced to within 10 s m of the El Cautivo Fault although recent erosion means the actual contact is no longer preserved. Sheet turbidites beneath the slump extend to and are truncated by the fault zone

and a similar relationship is inferred for the slump unit. No correlative of the slump can be found in the Phase 3 succession north of the El Cautivo Fault Zone. The slump can be followed 300 m south, along the Rambla de Tabernas to a sharp bend in the river where another fault with a strike of N120E truncates both the slump and underlying turbidite beds. The fault plane is sharp with a stepped geometry; a sub-vertical segment truncates the upper part of the slump, but the fault flattens close to ramble level. Significantly, the slump cannot be identified in the exposures south of the fault (contrast with Hodgson and Haughton, 2004). The geometry and timing of fault displacements have been documented by carefully logging the succession straddling the fault (**Figure 9B**) and by tracing beds using detailed photomontages. Marker bed 4 is displaced vertically c. 60 m by the fault. On the downthrown side (to the north), there are two bundles of thin beds in the 25 m thick section below the slump. Only the lower of these can be identified south of the fault in a similar position relative to bed 4. The slump cannot be correlated across the fault, but the turbidites above it forming the upper half of the cliff do not appear to be affected by the fault. Indeed the bed located at 17 m on the log south of the fault oversteps the fault and corresponds to the second thick bed above the slump (at 79 m on the northern log). The topmost beds on the cliff are composed of the lowermost beds of the Phase 4 (post sub-basin) fill. The boundary is placed at a step increase in the frequency of thin beds.

There is no bedding discordance at the top of sub-basin fill in the northern part of the sub-basin. However, the transition from Phase 3 isolated ponded sandstone sheets to Phase 4 fill is reworked by a major mass transport deposit in the southern part of the sub-basin (MTD-1 described in detail below). When the sub-basin fill dips are flattened by restoring the mean Phase 4 fill dips to horizontal, the residual dip is to the north implying tilting towards the El Cautivo Fault.

Interpretation: Filling of the sub-basin took place mainly by suspension settling of muds interspersed with sporadic turbidity currents, the larger volume of which became ponded and evolved to higher concentrations as sustained flows continued to drain into what must have been a relatively small bathymetric deep. Although the margins of the sub-basin are faulted, it was probably not greatly wider than the 2 km currently preserved. The strike extent of the sub-basin is speculative as it dips beneath younger stratigraphy to the west, and its eastern extent has been removed by erosion. Evidence for a thicker succession in the northern part of the sub-basin, thinning of individual sheets as the southern margin is approached, residual dip to the north and local angular discordances in the south suggest a wedge-shaped profile with greatest subsidence in the north. Tectonically-induced facies asymmetry has been noted in other deep-water basins, notably the Peira Cava Basin, SE France (Cunha et al., 2017) and the northern Apennines, Italy (Tinterri et al., 2017). If the Alfaro Member calcarenites fill channels at the base of the sub-basin as is suspected, their distribution (thicker to the south and lapping out to the north) implies initial subsidence may have been focussed further south and then migrated to adjacent to the main fault strand in the north when this propagated to the sea floor. Blocks of calcarenite within the sheet turbidites close to the

southern margin imply tilting may have led to uplift and reworking of the Alfaro Member next to the southern boundary fault.

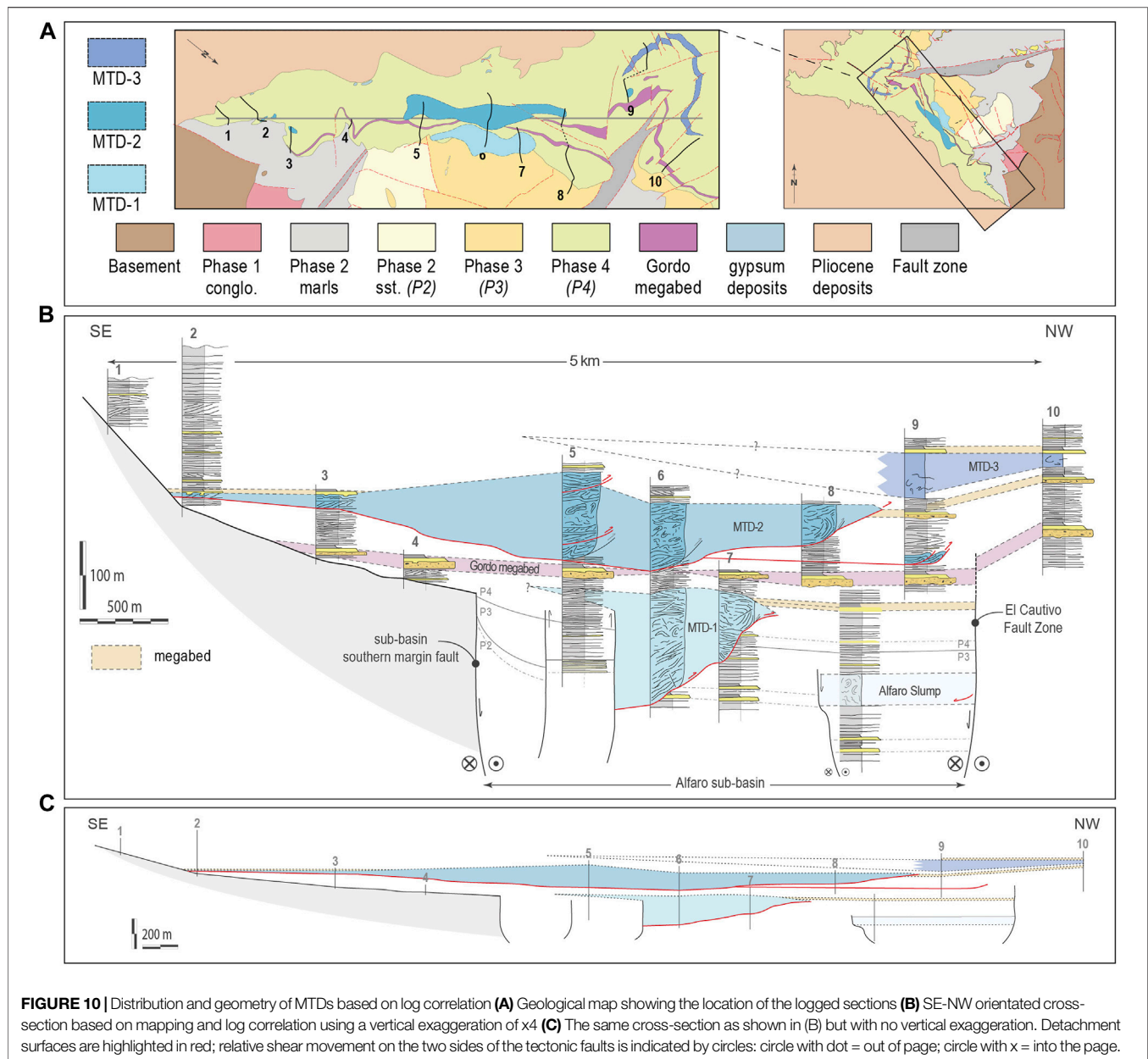
Younger Phase 3 sheets (and the marls between them) vary little in thickness across the floor of the sub-basin implying this was sub-horizontal by this stage. Thinning adjacent to the southern margin of the sub-basin reveals the presence of a fault-controlled, bounding slope. More rapid pinching out of the calcarenitic compared to the siliciclastic flows suggests a difference in the flow characteristics. The former may have been thinner with more concentrated lower portions as they tend to be coarser grained with less silty and micaceous components. The ponded suspensions may have inflated to differing extents, explaining the difference in pinchout geometry.

The thick interbedded slump has been attributed to local collapse of part of the El Cautivo Fault scar (Haughton, 2000; Hodgson, 2002). This is consistent with the muddy composition of the slump and its position adjacent to the El Cautivo Fault Zone. The analysis of the intra sub-basin fault limiting the slump to the south demonstrates that it was also active during deposition, initiating after the first bundle of thin beds above the bed 4 marker and ending shortly after slump deposition. The fault temporally partitioned the floor of the sub-basin providing deeper accommodation between it and the El Cautivo Fault. Occasional turbidity currents arriving from the west were preferentially trapped and confined on the downthrown block between the two faults (**Figure 9C**). Superficially the fault to the south appears extensional, but this would require an unrealistically high (>50 m) scarp to totally confine the slump. The major cross-sectional bend (step) on this fault requires a strike-slip component of displacement; furthermore bed geometries of sequences adjacent to this curved fault are incompatible with significant dip-slip displacement (**Figure 9A**). The preferred interpretation is therefore that the fault has laterally displaced the slump so that any overstep of the fault by the slump is out of the plane of section (**Figure 9C**); i.e. now below the ground for a dextral offset. The proximity and the angle between the faults bounding the slump suggest the small fault to the south formed a synthetic fault splaying from the dextral El Cautivo Fault.

The conformable contact between the Phase 3 sub-basin fill and the overstepping Phase 4 succession implies the fault-induced wedging and lateral displacement of the sub-basin had finished before Phase 4 deposition when the linked faults became inactive.

5 POST-FILL SLOPE ONLAP AND MASS WASTING

The overstepping Phase 4 succession progressively onlaps and wedges out against a rotated Phase 2 muddy succession directly south of the sub-basin. The Phase 4 turbidites show common evidence for sliding with rotated and internally-deformed bed packages several 10 s of m thick (e.g. in the Rambla de Indalecio). In addition, there are also three large mass transport deposits (MTDs 1–3) that rework the onlap wedge and slope. The MTDs



partly drape (and in the case of the oldest one, rework) the former fault-controlled sub-basin and they are enclosed largely within Phase 4 sheet turbidites. The larger scale architecture of the onlap-wedge has been captured in a series of logs (**Figure 10**) along a 5 km long SE-NW orientated transect that is approximately parallel to the slump transport direction. The three MTDs form lensoid bodies the thickest parts of which step basinwards with time. In addition, a very thick debrite-turbite couplet (the Gordo Megabed) occurs between MTD-1 and -2 and onlaps directly onto the north-facing slope.

5.1 MTD-1

MTD-1 differs from the younger failures in that it remobilised both Phase 4 and Phase 3 deposits. It is very well exposed in the

Rambla de Tabernas and in nearby road cuts giving a particularly good 3D insight into its internal structure and relationship to the undisplaced stratigraphy (**Figure 11A**). MTD-1 is up to 160 m thick centrally and about 50 m thick close to its toe. It can be followed laterally for up to 600 m, and extends about 350 m across the top of the sub-basin which it partly reworks. Phase 3 and 4 turbidite beds incorporated in MTD-1 are largely intact albeit complexly deformed, so much of the remobilisation can be classified as a slump (*sensu* Martinsen, 1994). In low cliffs on the east side of the Rambla de Tabernas, the basal detachment to the MTD is seen. This is a planar, bedding parallel bundle of clay-lined surfaces that lies stratigraphically about 10 m above marker bed 4 in the Phase 3 sub-basin fill (see earlier). The surfaces separate lensoid bodies of imbricated sandstone beds (duplexes)

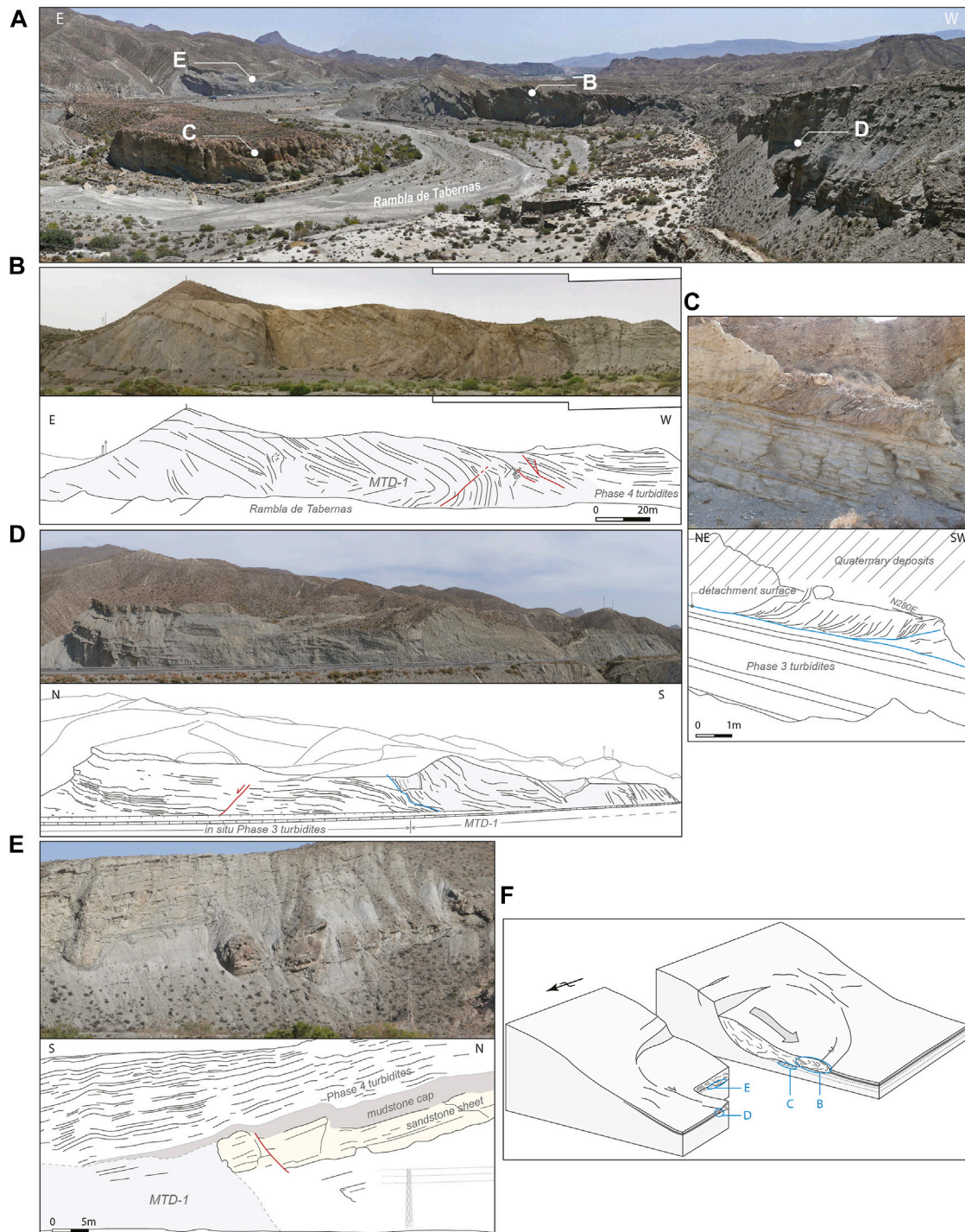


FIGURE 11 | Character of MTD-1 (see **Figure 4** for location) **(A)** General panorama of MTD-1 outcrops looking south down Rambla de Tabernas **(B)** Photograph and line drawing of a large recumbent fold at the toe of MTD-1 (highlighted in grey). In-situ Phase 4 turbidites draping the toe of MTD-1 occur on the western side of the outcrop. Faults developing within the fold are highlighted in red **(C)** Photograph and line drawing of the basal detachment zone characterised by the presence of duplexes formed by deformation of Phase 3 turbidites above the detachment surface (highlighted in blue). A westwards transport direction is deduced from the duplex orientation **(D)** Photograph and line drawing of the lateral detachment (blue) of MTD-1 (in grey) cutting through Phase 3 turbidites here observed along the N340 road **(E)** Photograph and line drawing of a Phase 4 megabed truncated by MTD-1 (highlighted in grey). Note the geometric relationship between the MTD and the megabed with the sandstone division of the megabed (highlighted in yellow) cut vertically by the lateral edge of the MTD but with the mudstone cap (highlighted in dark grey) overstepping the MTD **(F)** Schematic block diagram illustrating the 3D structure of MTD-1 (modified from Bradley and Hanson (1998)). The letters refer to the different components of the MTD illustrated in the preceding parts of the figure.

ranging from a few centimetres to a few tens of centimetres high. The slump transport direction deduced from the bed imbrication is from east (N100E) to west (**Figure 11C**).

The toe of MTD-1 is seen in a north-facing cliff (20 m high and 100 m long) at a prominent bend in the Rambla de Tabernas (**Figure 11B**). The basal detachment here is at rambla level and it has ramped up to within the overstepping Phase 4 turbidites. The ramp between here and where the basal detachment occurs on the east side of the rambla is estimated to be 40 m high. Both Phase 3 and 4 sheet turbidites are rafted intact above the detachment but roll into a large recumbent fold that is inclined to the west and corresponds to the toe of the failure. The toe is draped by in-situ Phase 4 turbidites in which there are many small dip discordances (**Figure 11B**).

Approximately 200 m to the north, MTD-1 truncates a 5 m thick sandstone sheet which can be mapped northwards away from the slump as part of an undisturbed succession of Phase 4 sheet turbidites. The thick sandstone is cut vertically by the lateral (northern) edge of the MTD, but a thick mudstone cap overlying the sandstone appears to overstep the junction between sandstone and the remobilised deposits, thinning and lensing out southwards over the MTD (**Figure 11E**).

MTD-1 is also seen beside the old N340 road in a high and unstable cut face north of Barranco de los Baños (a 300 m long and 30 m high exposure; **Figure 11D**). The northern end of the cliff preserves Phase 3 turbidite sheets (c. 50 m below marker bed 4), these are flexed down into MTD-1 which dominates the southern end of the exposure. Soft sediment deformation here has thus cut deeper still into the sub-basin fill. The eastern extension and headwall of the failure cannot be observed as this part of the MTD has been removed by recent erosion.

Interpretation: Exceptional exposure conditions encountered in the Tabernas Basin permits the reconstruction of the 3D geometry of MTD-1 (**Figure 11F**). An important feature of MTD-1 is that it is composed of local basin floor deposits, including translated ponded turbidites with thick mud caps that can only have formed on a relatively flat and deep part of the palaeo-sea floor. Phase 3 sandstone sheets preserved beneath the failure show evidence for thinning to the south suggesting proximity to a slope. Phase 4 turbidites that overstep the faulted southern margin of the sub-basin are also involved in the failure. A possible explanation is that gravity instability took place by sliding of the initial onlap wedge off the slope flanking the south-side of the sub-basin. This slide then interacted with and drove deformation of the earlier sub-basin fill. However, kinematic evidence from the stepped basal detachment, forced folds within the sliding mass and the position of the lateral limit of the failure suggests dominantly westward transport, parallel to the sub-basin margin. This suggests that failure may have been influenced by down to the west rotation of the sub-basin and its flanking slope (the Sierra Alhamilla to the east was uplifted to become emergent around this time). The large frontal fold may relate to a ramp on the underlying detachment, and to buttressing at the toe of the MTD. Minimal internal disaggregation is seen, at least in the section provided by the outcrop, consistent with limited transport and a low drop height due to the early stage in the onlap; MTD-1 involved slumping and sliding, but no transformation to a debris flow.

The trigger for the failure is uncertain, but the relationship with a large sandstone-mudstone couplet in the laterally equivalent undisturbed section to the north may be significant. The slump appears to cut the sandstone component of this bed, but to be onlapped by the mud produced by suspension fallout. This suggests MTD-1 may have been contemporary with a large-volume turbidity current, with failure occurring after the sand had fallen from suspension, but before the mud cloud rained out. Such a relationship could reflect a common trigger (seismic shaking) or a role for the large-volume (sloshing?) turbidity current in destabilising or loading the slope it impinged on. The former (common trigger) is perhaps less likely as the local slope failure might be expected to precede the arrival of the turbidity current.

5.2 MTD-2

A second more extensive slope failure associated with the southern onlap slope occurs approximately 20–80 m above the Gordo megabed although locally it cuts down to the level of the Gordo megabed. MTD-2 can be traced between a series of outcrops for a distance of c. 3.5 km parallel to the SE to NW transport direction (**Figure 10**) using the underlying Gordo event bed as a marker. Its width is unclear due to outcrop limitations. MTD-2 blanketed the southern part of the underlying sub-basin, and was sourced higher on the southern onlap surface. It is up to 130 m thick and characterised by a variable degree of internal disaggregation, locally forming blocks dispersed in a well-mixed matrix. The style of deformation also varies laterally along the failure. MTD-2 translated Phase 4 basin floor turbidites downslope, with no evidence for input of external slope-derived sediment. It does, however, locally contain pebbles and cobbles of Nevado-Filabride schist.

Close to the onlap surface (approximately 200 m from the projected onlap, and 100 m above the Gordo event bed), the inferred head region of the failure is seen. Here, a 6 m thick package of discordant inclined beds is overlain by a sandstone/mudstone couplet with an irregular base. When traced c.100 m to the NW, the basal deformed zone becomes more complex with several internal detachment levels (**Figure 12D**). There is also an increase in the deformation intensity with local folding beneath an irregular contact with the overlying sandstone-mudstone couplet.

A farther 1.8 km downslope, a large fresh road cut through the failure (200 m long and 15 m high) just south of Barranco de los Baños shows the deformation cuts down to within 20 m of the Gordo megabed (**Figure 12A**). The MTD here comprises upper and lower packages of soft-sediment deformed but coherent turbidites sandwiching a highly sheared and remoulded central part. The latter includes sheath folds (with SE-NW orientated stretching) and large (6 m across) folded and locally overturned rafts of Phase 4 turbidites floating in a poorly sorted, mud-rich matrix (**Figures 12A,B**). Significantly, extrabasinal clasts (mainly black schist and quartz vein pebbles up to 10 cm across) also float within the matrix. Overall, the deformed zone is estimated to be 130 m thick.

MTD-2 is also seen on the west side of the Rambla de Tabernas in an east-facing cliff up to 20 m high and 250 m long. The upper part of the MTD has been removed by recent

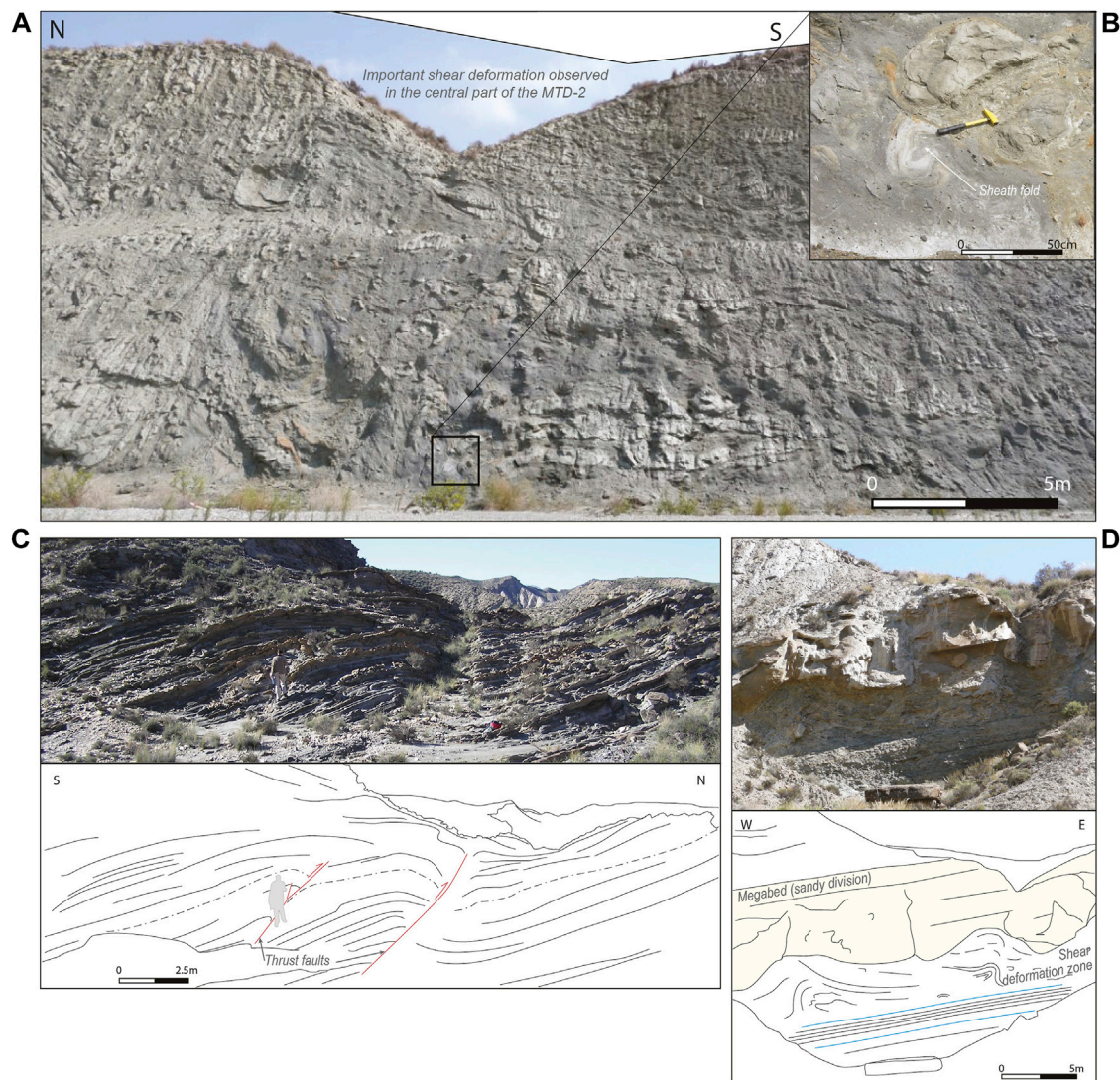


FIGURE 12 | Main features of MTD-2 (see **Figure 4** for location) **(A)** Zone of important shear deformation and mudstone/sandstone mixing characteristic of the debritic component of the central part of MTD-2 here observed along the N340 road (see **Figure 10**, log5). Large rafts of highly deformed and sheared Phase 4 turbidites are observed floating within a mud-rich matrix **(B)** Close-up photograph of a sheath fold attesting of the intense shearing inside the mass movement. Dark extrabasinal clasts (Nevado-Filabride schists) are also present **(C)** Photograph and line drawing of thrust faults cutting through Phase 4 turbidites here observed near the junction between the Rambla Seca and the Rambla la Gitana. Interpreted as soft-sediment deformation based on the presence of drag geometry on the hangingwall, these 075 oriented thrust faults are believed to be the result of compressional deformation occurring at the front of MTD-2 which occurs stratigraphically up-dip (see **Figure 10**, log9) **(D)** Photograph and line drawing showing remobilisation on the southern onlap slope interpreted as the source region of MTD-2 (see **Figure 10**, log3). Important shear deformation is observed immediately below the sandy division (highlighted in yellow) of a Phase 4 megabed. Bedding parallel detachment levels are also observed in the lower part of the outcrop (highlighted in blue).

erosion at this site. The Gordo event bed is also missing in this outcrop and deformation associated with MTD-2 merges downwards with MTD-1 deformation, making the base of MTD-2 hard to pick. MTD-2 deformation at this site is characterised mainly by multiple slide surfaces and discordances, particularly low in the body, with an increase in strain towards the central part of the MTD where tight folds and complex internal disruption are observed in rafts floating within a homogenised matrix.

The toe of the failure can be reconstructed from outcrops in the area close to the junction of the Rambla Seca with the Rambla

la Gitana. Here a large overturned fold (at least 30 m wavelength) of Phase 4 turbidites is developed. Further to the NW, the post-Gordo succession is largely intact but traversed by several soft-sediment thrust and reverse faults and associated forced folds (**Figure 12C**). Restoration of the fault geometry indicates compression from the south-east.

Interpretation: MTD-2 differs from MTD-1 in that it preserves evidence for internal disaggregation and matrix formation. This suggests that this failure initiated as a slide but locally broke up internally to become a debris flow. Transformation of just the

central section of the MTD may reflect a combination of partitioning of deformation in the lower part to the basal shear surface and reduced drainage of water from the central part, increasing pore fluid pressure. Alternatively, the failure may have occurred in two phases. MTD-2 transported Phase 4 turbidites blocks and is interpreted to have formed by collapse of part of the onlap-wedge. The toe of the failure was associated with a large fold and it is interpreted to have been frontally-confined like MTD-1. Compressional deformation spread out down slope from the confined front, deforming the basin floor that buttressed the failure. Transport was to the NW on the basis of internal and external shear indicators and the geometry of the inferred frontal fold.

A thick debrite-turbidite or megabed occurs stratigraphically 80 m above the Gordo megabed in the southern Tabernas Basin away from the onlap slope. Extrabasinal pebbles incorporated in MTD-2 resemble those in northerly-derived, large-volume event beds and are unlikely to have come off the southern slope. The thick sandstone–mudstone couplet also blankets headwall slides and slumps close to the onlap. The association between slumping and sliding and the emplacement of a large megabed is again significant and may suggest a link.

5.3 MTD-3

The youngest failure, MTD-3, occurs approximately 110 m above the Gordo megabed and is more difficult to link to the onlap surface and turbidite wedge, partly because it crops out remote from the onlap to the south and west of the junction of the Rambla la Gitana with Rambla Seca, beyond the confined toe of the underlying MTD-2. Although it is displaced on a series of NE-SW trending faults, it can be mapped over a strike length of at least 1.5 km. It is up to 65 m thick and dominated by white marl in which are dispersed sparse deformed clasts and rafts (up to 10 m long) of distinctive pebble-bearing calcarenites (locally micro-conglomerates). The marl unit thins northwards to c. 15 m over 1 km. The rafts tend to be folded. Rounded pebbles as clasts and within the rafts are dominantly basement dolomite, the surfaces of which are extensively bored. The calcarenites contain extensive shell fragments, including corals. MTD-3 is directly overlain by a thick sandstone–mudstone couplet, so the overall appearance of the unit is of a debrite-turbidite couplet; however, the capping sandstone is not a calcarenite. It is a siliciclastic sand of metamorphic provenance similar to the bulk of the basin floor turbidites making up the Phase 4 basin fill.

Interpretation: MTD-3 was not derived from the onlap wedge, but from higher on the southern slope. The pebble types and calcarenitic composition of the rafts in the lower muddy unit suggest emplacement as a mudflow dispersed from a southern or southwestern source (possibly the Sierra de Gádor). Abundant borings and coral fragments suggest a partly shallow water source, not the deep water reworking of basin-floor turbidites seen in the older MTDs. Whereas MTDs 1 and 2 were slope-attached and frontally-confined, MTD-3 appears to have more passively filled deep bathymetry without disturbing the onlap wedge. It was directly followed by a contained turbidite, not a trailing plume from the mudflow but a separate event dispersed from a different (siliciclastic) source. The sharp switch in

composition implies that this is unlikely to be a case of textural and compositional fractionation in a single flow. This again indicates a connection between different failure events, in this case possibly sharing the same trigger as there is little mixing between the two deposits. The stacking of event beds one on top of the other suggests little mounding on the top of the lower debrite, despite its thickness.

6 DISCUSSION

The re-analysis of the Tabernas Basin provides 1) new insight into the architecture of turbidite successions close to active faults and unstable slopes, and 2) improved understanding of the tectonic controls on sedimentation and Neogene basin development in this area of SE Spain.

6.1 Architecture of Turbidites Onlapping Active Slope Systems

Turbidity currents are commonly confined by lateral and/or distal slopes against which their deposits thin and pinch out. Outcrop examples of turbidites that can be traced laterally to onlap against slopes have been described from a number of basins (e.g. Sinclair 2000; McCaffrey and Kneller, 2001; Amy et al., 2004; Smith and Joseph 2004; Marini et al., 2015; Spychala et al., 2015). Most examples involve simple aggradation of confined turbidites against stable slopes that are either bare of sediment or draped by mud. Less is known about onlap settings where the onlap is inherently unstable and the slope/base of slope is modified by episodic slope failures, although this situation is likely to be common in basins on active substrates, such as slope minibasins in the Gulf of Mexico and elsewhere (Madof et al., 2009; Beaubouef and Abreu, 2010) or thrust-top basins (Tinterri and Tagliaferri, 2015). Onlaps associated with the Alfaro sub-basin are instructive on a number of counts:

Firstly, they show that the bed style can reflect the degree of confinement (see also Hodgson and Haughton 2004). Confined turbidites within the small sub-basin have a different vertical structure to those filling the enlarged but still confined basin once the sub-basin topography was healed. This is best seen in the thinner beds which in the Phase 3 fill comprise sandstone beds capped by structureless sandstone divisions interpreted as fallout from sandy suspensions ponded in local basin floor depressions. Once the depressions were filled, thinner turbidite beds show well laminated sandstone divisions throughout with evidence for flow reversals from ripple laminations. The flows reflected off the confining slopes but dissipated before sandy suspension clouds could form (a function of weaker containment).

Secondly, flows of different provenance (siliciclastic vs calcareous) can have different onlap geometries against the same slope. Calcarenitic sandstones pinch out laterally on the south side of the sub-basin before siliciclastic sandstones of similar thickness are lost. The former tend to be coarser grained and may have formed thinner flows and suspension clouds that did not inundate the slopes as much (McCaffrey and Kneller, 2001). The finer grained and polymodal siliciclastic flows produced thicker suspensions that extended further up slope.

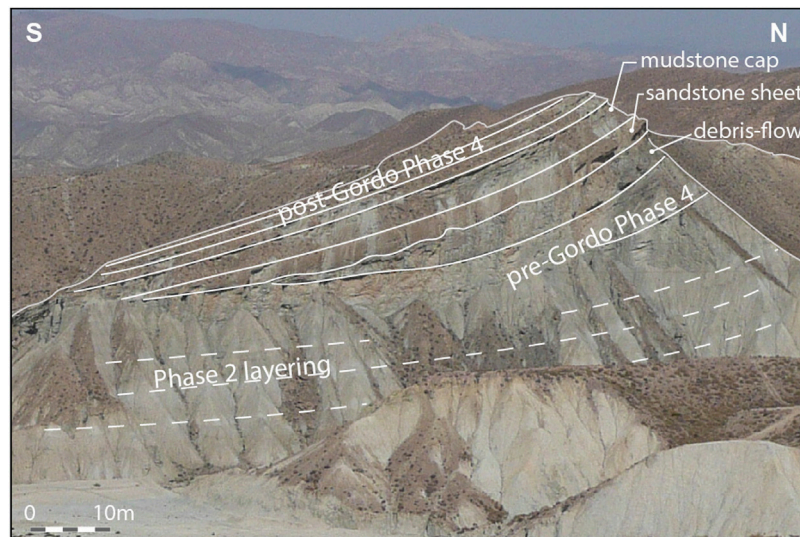


FIGURE 13 | Photograph and line drawing of the Gordo megabed onlapping directly onto tilted Phase 2 marls associated with the southern onlap slope (see **Figure 4** for location). Each division of the Gordo megabed (debris-flow, sandstone sheet and mudstone cap) pinches-out in turn against the slope.

Thirdly, when confinement is associated with an active fault, fault zone widening can trim the onlapping sandstones as has happened along the northern margin of the sub-basin. Pondered sheets show little thinning towards the fault due to the basin asymmetry, and are locally entrained as blocks in the fault zone.

Lastly, once the sub-basin was healed, the slope marking the southern limit of the basin was progressively onlapped but was subject to episodic collapse of the onlapping sediment wedge. Small scale slides involving thin bedded turbidites are common in the onlap area. Correlations using marker beds suggest a possible link between these slides and the thicker MTDs observed downslope on the floor of the basin. The slide complexes may record the instability leading to initiation of MTDs within the onlap wedge. MTDs 1 and 2 are composed mainly of wedge and basin floor turbidites and represent locally detached and frontally confined mass transport deposits with basal shear surface ramps, rafted blocks of remobilised turbidites, and well developed recumbent folds associated with frontal thrust propagation (Frey-Martínez et al., 2006; Moscardelli and Wood, 2008; Bull et al., 2009). The slump toes appear to have formed positive topography on the sea floor against which later turbidites onlap. MTD-3 was the furthest travelled and comprises exotic calcarenitic sandstone blocks, abundant borings, shells and coral fragments floating in a muddy background. The overall shape is also different with a more sheet-like geometry filling the deep bathymetry of the basin and draped by a thick pondered megabed (**Figure 10**).

Each of the local slope-sourced MTDs is associated with a thick, basin-wide megabed either lateral to it (MTD-1,-2) or directly on top of it (MTD-3). McCaffrey and Kneller (2001) drew attention to the possibility of debris flows triggered by turbidity currents impinging on distal slopes. Puigdefàbregas et al. (2004) describe outcrops of the Grés d'Annot onlap, SE France, showing evidence for deformation induced by flow

reflection against the basin confining slope. Overpressure in the slope muds associated with the sudden arrival of a large volume turbulent flow was thought to trigger injection, delamination and en-masse downslope movement. This sort of mechanism may explain the origin of MTD-1 and 2, particularly as large volume flows impinged on a slope that had been tectonically rotated and was being rapidly onlapped and loaded. One curious aspect of the slope stability is that the largest megabed event to impinge on the slope (Gordo megabed which occurred between MTD-1 and -2) did not trigger a failure. Instead, each of the three megabed elements (basal breccia or debrite, central graded sandstone and upper mudstone cap) lap out directly against the slope (**Figure 13**). It is possible the unusually thick basal debrite which contains abundant large intraclasts blanketed the slope protecting it from turbulent pressure fluctuations in the overlying expanded cloud. Alternatively, MTD-1 had already released the potential energy stored in the onlap wedge which was then relatively stable at this time.

This sort of distal failure triggering mechanism cannot apply for MTD-3 where the failure must have taken place high on the slope and did not involve remobilisation of the onlap wedge; the slope failure also preceded arrival of the megabed from a different source area. It is possible that in this case the separate slope failures had a similar trigger (a large earthquake?).

6.2 Tectonic Implications and Basin Development

Neogene basins in SE Spain have variously been interpreted as an extensional (Platt and Vissers, 1989; Vissers et al., 1995; Augier et al., 2005), thrust-top (Frizon De Lamotte et al., 1995) or strike-slip basins (Montenat et al., 1987a; Montenat et al., 1987b; Kleverlaan, 1989b; Haughton, 2000). The uncertainty

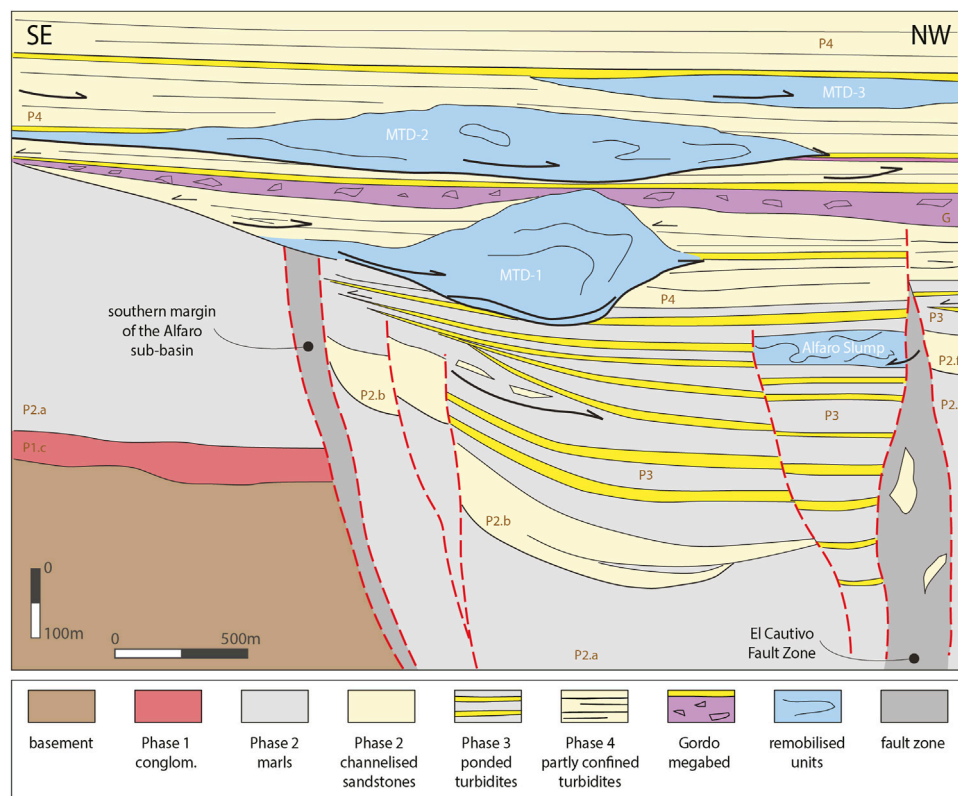


FIGURE 14 | Down-plunge schematic cross-section (vertical exaggeration of x2) of the southern part of the Tabernas Basin integrating evidence for syn-sedimentary faulting and major remobilisation described in this study and showing the inferred asymmetric character of the Alfaro sub-basin fill. Major detachment surfaces and displacement directions are indicated by thick dark arrows; onlap and bed pinch-outs are highlighted by thin dark arrows.

partly reflects the difficulty of linking faults to basin formation in areas where the stress field has evolved rapidly, where many of the faults are post-depositional, and where Neogene normal, thrust and strike-slip faults are all developed but are not necessarily directly related to basin formation. In addition, later rotation of earlier low-angle extensional structures to vertical can result in their misinterpretation as strike-slip faults (Valetti et al., 2019), and strike-faults can act as transfer structures in areas that are fundamentally undergoing heterogeneous extension (Martínez-Martínez, 2006; Giaconia et al., 2014).

Stratigraphic evidence discussed above (and in Hodgson and Haughton 2004) from the southern part of the Tabernas Basin strongly favours a strike-slip origin for the subsidence that opened up deep-water accommodation in that strike-slip faults are identified that were clearly active at the time of deposition. A wide range of different types of strike-slip basin have been described (e.g. Wood et al., 1994; Aksu et al., 2000; Lazar et al., 2006) ranging from fault-bend to stepover basins to basins formed between diverging or splaying faults. Other strike-slip basins form above relatively straight but divergent sectors of strike slip faults as negative flower structures (Bozkurt and Koçyiğit, 1996; Aksu et al., 2000; Barnes et al., 2001) or due to transform-normal extension (Ben-Avraham and Zoback, 1992).

The Alfaro sub-basin formed a narrow trough delimited to north and south by oblique-slip faults that displaced the sea-floor. Subsidence was demonstrably asymmetric, thickening towards the fault with the more extensive gouge zone (the El Cautivo Fault) and with local unconformities and evidence for uplift and gravity sliding of earlier deposits along the southern margin (Figure 14). Splays of the main bounding fault also propagated through the fill, creating subtle irregularities on the sea floor, uplifting areas which modified the flow pathways and capturing a slump failure thought to relate to collapse of the master fault scarp. The syn-sedimentary oblique slip faults are interpreted to converge downwards and to link to a master fault. Outside and to the northeast of the sub-basin, a series of folds with fold axis trending at an angle of 30 anticlockwise to the E-W Alfaro fault zone also deformed the sea floor, creating depressions into which sheet turbidites thicken and highs that created local slope instability.

The convergence of dextral-oblique strike-slip faults at depth, evidence for displacements with important dip-slip components, the narrow trough-like sub-basin and the oblique orientation of folds suggest the sub-basin formed above a negative flower structure associated with a divergent strand of the fault that projects eastwards along the northern flank of the Sierra Alhamilla (Sanz De Galdeano, 1989; Figure 15). As bed dips in the vicinity of the Alfaro sub-basin are low, this cannot be an

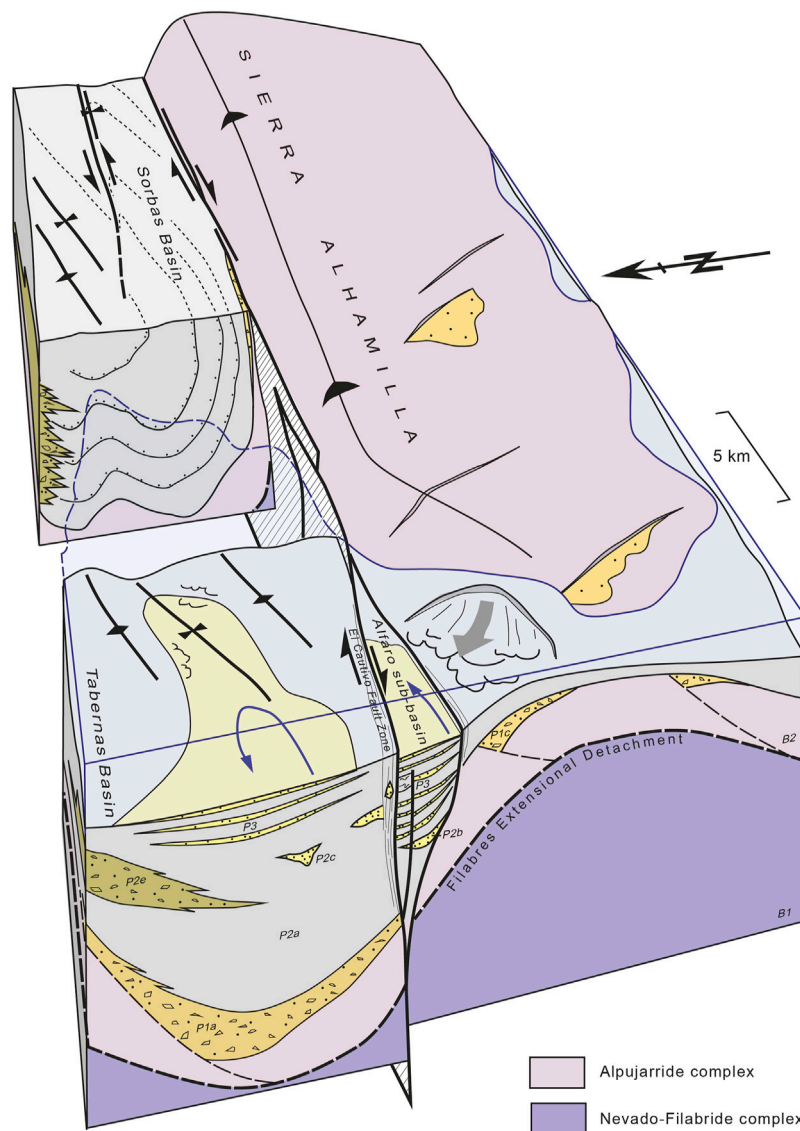


FIGURE 15 | Cartoon summarising the structural configuration of basins north of the Sierra Alhamilla basement block in the latest Tortonian. Sorbas Basin was being inverted in dextral transpression at the same time that dextral transtension drove opening of a narrow sub-basin in the Tabernas area. Subsidence in the area was initially driven by early (Serravalian) SW-directed extension (Martínez-Martínez and Azañón, 1997; Martínez-Martínez and Azañón, 2002) followed by strike-slip deformation and then regional buckling that differentially uplifted basement blocks flanking the basins. See caption to **Figure 2** for key to Tabernas basin fill components.

example of earlier extensional detachments that have been rotated to vertical to masquerade as strike-slip faults as has been argued elsewhere (Valetti et al., 2019). Evidence for folding and ponding of turbidites north-east of the sub-basin imply lateral changes between coeval transtension and transpression. In the Rambla de Reinelo area, the sea floor was gently warped, but moving further east, the earlier fill to the Sorbas Basin was already inverted in strong dextral transpression at this time (Haughton, 2001). The eastward change to transpressional deformation corresponds with the position of the western culmination of the Sierra Alhamilla. Northward translation of the Alhamilla as the regional folds amplified in

the late Tortonian may account for this. The western end of the Alhamilla also marks a change in the style of turbidite deformation from strong ponding in deep depressions to the west, to weak ponding in shallow fold axes in the eastern Tabernas Basin. Hodgson (2002) also suggested that the Phase 2 sandy fan system exposed in the eastern part of the Tabernas Basin was deformed by growing transpressional folds during an earlier phase of bypass and basin floor fan growth. Close to Tabernas, early Phase 1 conglomerates were uplifted in the core of transpressional anticlines (**Figure 2**) against which the sandy fan onlapped. In the Sorbas area close to Lucainena (c.25 km to the east; **Figure 1**) Tortonian ponded sheets exposed just north of the

Sierra Alhamilla closely resemble the Late Tortonian/early Messinian Alfaro sub-basin fill and may represent deposition within another but earlier transtensional depression later inverted in transpression.

Evidence for syn-depositional strike-slip deformation creating local accommodation on the sea floor in both the Tabernas and Sorbas basins is seemingly at variance with the recent focus on normal faults and regional extension in driving Late Miocene basin formation in the area (Andrić et al., 2018; Valetti et al., 2019). However, Giaconia et al. (2014) pointed to the importance of strike-slip transfer faults in areas undergoing regional heterogeneous extension and showed that these bound Tortonian depocentres in the eastern Sorbas Basin. Similarly the Alpujarras Corridor (Sanz De Galdeano et al., 1985; **Figure 1**) to the west of the Tabernas Basin has been interpreted as a dextral strike-slip fault zone transferring deformation between areas undergoing different styles and amounts of Miocene to Recent extension (Martínez-Martínez, 2006). The Alfaro sub-basin lies on the eastward projection of the Alpujarras structure to link with the fault zone on the northern flank of the Alhamilla. The implication is that transtension on long transfer faults opened up local depocentres (sub-basins) distinct from the titled fault-block depocentres in the hanging wall of the main detachment faults.

Basins resembling the Alfaro sub-basin are seen today on the floor of the Alboran Sea south of the Tabernas area where they have been imaged on seismic profiles. The Alboran Basin is divided into several small sub-basins which have mainly been controlled by active right-lateral transpression due to oblique Africa-Iberia convergence since the late Tortonian (Bourgeois et al., 1992; Comas et al., 1992; Woodside and Maldonado, 1992). Alvarez-Marrón (1999) interprets some of the sub-basins in the eastern Alboran Sea as negative flower structures. The Yusuf Basin is a 16 km long by 9 km wide depocentre bounded by a pair of sub-vertical faults. The dextral oblique-slip Yusuf Fault forms a master fault on the northern side of the basin. Subsidence in the basin was asymmetric wedging towards the Yusuf Fault (**Figure 1**). Subordinate faults on the south side of the basin step down into the basin. Moreover the downthrown/flexed basin margins are characterised by listric extensional faults caused by gravitational sliding.

7 CONCLUSION

Turbidite successions vary widely reflecting different combinations of up-dip supply, sea-level fluctuations and basin tectonics, as well as local factors (Reading, 1996). Tabernas turbidites are important in that they provide a rare outcrop example of a system strongly forced by changes in

receiving basin morphology—in this case driven by tectonic deformation of the sea bed. A phase of syndepositional faulting and folding controlled the location and wavelength of depocentres on the floor of the basin, the stability of slopes, failure triggering, flow pathways, and switching between bypass, confined fans and ponded flows. Dextral-oblique strike-slip faults linked to form a 2 km wide transtensional sub-basin filled by an expanded section of ponded turbidite sheets. Elsewhere, flows were also ponded in synclinal fold axes. The sub-basin was asymmetric, the fill thinning and onlapping to the south, with sheet turbidites juxtaposed against the main fault zone in the north. Sub-basin topography was rapidly buried as the faults became inactive with a series of large mass-transport deposits forming as an unstable (tectonically tilted) slope created in response to the compressional uplift of the western end of the Alhamilla block. This created a dynamic onlap slope very different in character to the generally more passive onlaps described from other basins. Small fault-controlled deep-water depocentres in SE Spain and the Alboran Sea analogous to the Alfaro sub-basin were developed more widely and may have been localised on long transfer faults accommodating heterogeneous extension. The well-exposed Tabernas example serves to highlight the complex interplay between tectonic deformation, flow processes and sea floor instability that can occur in deep-water sub-basins opened up on active strike-slip faults.

DATA AVAILABILITY STATEMENT

The raw data supporting the conclusion of this article will be made available by the authors, without undue reservation.

AUTHOR CONTRIBUTIONS

All authors listed have made a substantial, direct, and intellectual contribution to the work and approved it for publication.

FUNDING

Much of the work reported here was funded by a Science Foundation Ireland Research Frontiers grant 05/RFP/GEO028 to PDWH.

ACKNOWLEDGMENTS

We are very grateful to reviewers Roberto Tinterri, and Euan Soutter for their perceptive and helpful comments on an earlier version of this article.

REFERENCES

- Aksu, A. E., Calon, T. J., Hiscott, R. N., and Yasar, D. (2000). Anatomy of the North Anatolian Fault Zone in the Marmara Sea, Western Turkey: Extensional Basins above a Continental Transform. *GSA Today* 10, 3–7.
- Alvarez-Marrón, J. (1999). Pliocene to Holocene Structure of the Eastern Alboran Sea (Western Mediterranean). *Proc. Ocean Drill. Program Sci. Results* 161, 345–355. doi:10.2973/odp.proc.sr.161.224.1999
- Amy, L. A., McCaffrey, W. D., and Kneller, B. C. (2004). “The Influence of a Lateral basin-slope on the Depositional Patterns of Natural and Experimental Turbidity Currents,” in *Deep-Water Sedimentation in the Alpine Basin of SE*

- France: *New Perspectives on the Grès d'Annot and Related Systems*. Editors P. Joseph and S.A. Lomas. London: Geological Society, London, Special Publications, 221, 311–330. doi:10.1144/gsl.sp.2004.221.01.17
- Andric, N., Matenco, L., Hilgenand de Bresser, H. (2018). Structural Controls on Sedimentation During Asymmetric Extension: The Case of Sorbas Basin (SE Spain). *Glob. Planet. Change* 171, 185–206.
- Augier, R., Jolivet, L., and Robin, C. (2005). Late Orogenic Doming in the Eastern Betic Cordilleras: Final Exhumation of the Nevado-Filabride Complex and its Relation to basin Genesis. *Tectonics* 24. doi:10.1029/2004tc001687
- Barnes, P. M., Sutherland, R., Davy, B., and Delteil, J. (2001). Rapid Creation and Destruction of Sedimentary Basins on Mature Strike-Slip Faults: an Example from the Offshore Alpine Fault, New Zealand. *J. Struct. Geology* 23, 1727–1739. doi:10.1016/s0191-8141(01)00044-x
- Beaubouef, R. T., and Abreu, V. (2010). “MTCs of the Brazos-Trinity Slope System; Thoughts on the Sequence Stratigraphy of MTCs and Their Possible Roles in Shaping Hydrocarbon Traps,” in *Submarine Mass Movements and Their Consequences*. Editors D. C. Mosher, R.C. Shipp, L. Moscardelli, J.D. Chaytor, C.D.P. Baxter, H.J. Lee, et al. Advances in Natural and Technological Hazards Research. Dordrecht: Springer Science, 28, 475–490. doi:10.1007/978-90-481-3071-9_39
- Ben-Avraham, Z., and Zoback, M. D. (1992). Transform-normal Extension and Asymmetric Basins: An Alternative to Pull-Apart Models. *Geol* 20, 423–426. doi:10.1130/0091-7613(1992)020<0423:tneab>2.3.co;2
- Bradley, D., and Hanson, L. (1998). Paleoslope Analysis of Slump Folds in the Devonian Flysch of Maine. *Maine. J. Geol* 106, 305–318.
- Bourgeois, J., Mauffret, A., Ammar, A., and Demnati, A. (1992). Multichannel Seismic Data Imaging of Inversion Tectonics of the Alboran Ridge (Western Mediterranean Sea). *Geo-Marine Lett.* 12, 117–122. doi:10.1007/bf02084921
- Bozkurt, E., and Koçyiğit, A. (1996). The Kazova basin: an Active Negative Flower Structure on the Almus Fault Zone, a Splay Fault System of the North Anatolian Fault Zone, Turkey. *Tectonophysics* 265, 239–254. doi:10.1016/s0040-1951(96)00045-5
- Britter, R. E., and Linden, P. F. (1980). The Motion of the Front of a Gravity Current Travelling Down an Incline. *J. Fluid Mech.* 99, 531–543. doi:10.1017/s0022112080000754
- Bull, S., Cartwright, J., and Huuse, M. (2009). A Review of Kinematic Indicators from Mass-Transport Complexes Using 3D Seismic Data. *Mar. Pet. Geology* 26, 1132–1151. doi:10.1016/j.marpetgeo.2008.09.011
- Catterall, V., Redfern, J., Gawthorpe, R., Hansen, D., and Thomas, M. (2010). Architectural Style and Quantification of a Submarine Channel-Levee System Located in a Structurally Complex Area: Offshore Nile Delta. *J. Sediment. Res.* 80, 991–1017. doi:10.2110/jsr.2010.084
- Comas, M. C., García-Dueñas, V., and Jurado, M. J. (1992). Neogene Tectonic Evolution of the Alboran Sea from MCS Data. *Geo-Marine Lett.* 12, 157–164. doi:10.1007/bf02084927
- Cunha, R. S., Tinterri, R., and Muzzi Magalhaes, P. (2017). Annot Sandstone in the Peira Cava basin: An Example of an Asymmetric Facies Distribution in a Confined Turbidite System (SE France). *Mar. Pet. Geology* 87, 60–79. doi:10.1016/j.marpetgeo.2017.04.013
- Dabrio, J. (1990). “Fan-delta Facies Associations in the Late Neogene and Quaternary Basins of southeastern Spain,” in *Coarse-Grained Deltas*. Editors A. Colella and D.B. Prior. Oxford: Special Publication, International Association of Sedimentologists, 10, 91–111.
- De Galdeano, C. S., Rodriguez-Fernandez, J., and López-Garrido, A. C. (1985). A Strike-Slip Fault Corridor within the Alpujarra Mountains (Betic Cordilleras, Spain). *Geol. Rundsch.* 74, 641–655. doi:10.1007/bf01821218
- De Lamotte, D. F., Guezou, J.-C., and Averbuch, O. (1995). Distinguishing Lateral Folds in Thrust-Systems; Examples from Corbières (SW France) and Betic Cordilleras (SE Spain). *J. Struct. Geology* 17, 233–244. doi:10.1016/0191-8141(94)e0035-w
- Doughty-Jones, G., Mayall, M., and Lonergan, L. (2017). Stratigraphy, Facies, and Evolution of Deep-Water Lobe Complexes within a Salt-Controlled Intraslope Minibasin. *Bulletin* 101, 1879–1904. doi:10.1306/01111716046
- Doyle, P., Mather, A. E., Bennett, M. R., and Bussell, M. A. (1996). Miocene Barnacle Assemblages from Southern Spain and Their Palaeoenvironmental Significance. *Lethaia* 29, 267–274. doi:10.1111/j.1502-3931.1996.tb01659.x
- Frey-Martínez, J., Cartwright, J., and James, D. (2006). Frontally Confined versus Frontally Emergent Submarine Landslides: A 3D Seismic Characterisation. *Mar. Pet. Geology* 23, 585–604. doi:10.1016/j.marpetgeo.2006.04.002
- Galdeano, C. S., and Vera, J. A. (1992). Stratigraphic Record and Palaeogeographical Context of the Neogene Basins in the Betic Cordillera, Spain. *Basin Res.* 4, 21–36. doi:10.1111/j.1365-2117.1992.tb00040.x
- Giaconia, F., Booth-Rea, G., Martínez-Martínez, J. M., Azañón, J. M., Storti, F., and Artoni, A. (2014). Heterogeneous Extension and the Role of Transfer Faults in the Development of the southeastern Betic Basins (SE Spain). *Tectonics* 33, 2467–2489. doi:10.1002/2014tc003681
- Gray, T. E., Alexander, J., and Leeder, M. R. (2005). Quantifying Velocity and Turbulence Structure in Depositing Sustained Turbidity Currents across Breaks in Slope. *Sedimentology* 52, 467–488. doi:10.1111/j.1365-3091.2005.00705.x
- Haughton, P. (2001). Contained Turbidites Used to Track Sea Bed Deformation and basin Migration, Sorbas Basin, South-East Spain. *Basin Res.* 13, 117–139. doi:10.1046/j.1365-2117.2001.00143.x
- Haughton, P. D. W. (2000). Evolving Turbidite Systems on a Deforming basin Floor, Tabernas, SE Spain. *Sedimentology* 47, 497–518. doi:10.1046/j.1365-3091.2000.00293.x
- Heiniö, P., and Davies, R. J. (2007). Knickpoint Migration in Submarine Channels in Response to Fold Growth, Western Niger Delta. *Mar. Petrol. Geol.* 24, 424–449. doi:10.1016/j.marpetgeo.2006.09.002
- Hodgson, D. M., and Haughton, P. D. W. (2004). “Impact of Syndepositional Faulting on Gravity Current Behaviour and Deep-Water Stratigraphy: Tabernas-Sorbas Basin, SE Spain,” in *Confined Turbidite Systems*. Editors S. A. Lomas and P. Joseph. London: Geological Society, London, Special Publications, 222, 135–158. doi:10.1144/gsl.sp.2004.222.01.08
- Hodgson, D. M. (2002). Tectono-stratigraphic Evolution of a Neogene Oblique Extensional Orogenic basin, Southeast Spain. Ph.D. thesis. University of London.
- Howlett, D. M., Gawthorpe, R. L., Ge, Z., Rotevatn, A., and Jackson, C. A. L. (2021). Turbidites, Topography and Tectonics: Evolution of Submarine Channel-lobe Systems in the Salt-influenced Kwanza Basin, Offshore Angola. *Basin Res.* 33, 1076–1110. doi:10.1111/bre.12506
- Iaccarino, S., Morlotti, E., Papani, G., Pelosio, G., and Raffi, S. (1975). Lithostratigrafia e biostratigrafia di alcune serie Neogeniche della provincia di Almería (Andalusia orientale, Spagna). *Ateneo Parmense, Acta Naturalia* 11, 237–313.
- Kleverlaan, K. (1987). Gordo Megabed: a Possible Seismites in a Tortonian Submarine Fan, Tabernas basin, Province Almería, Southeast Spain. *Sediment. Geol.* 51, 181–213. doi:10.1016/0037-0738(87)90047-9
- Kleverlaan, K. (1989a). Neogene History of the Tabernas basin, (SE Spain) and its Tortonian Submarine Fan Development. *Geol. Mjnb.* 68, 421–432.
- Kleverlaan, K. (1989b). Three Distinctive Feeder-Lobe Systems within One Time Slice of the Tortonian Tabernas Fan, SE Spain. *Sedimentology* 36, 25–45. doi:10.1111/j.1365-3091.1989.tb00818.x
- Kneller, B. (2003). The Influence of Flow Parameters on Turbidite Slope Channel Architecture. *Mar. Pet. Geology* 20, 901–910. doi:10.1016/j.marpetgeo.2003.03.001
- Koch, H., and McCann, T. (2020). Petrological Characterisation and Provenance of the Shelf to Deep-marine Sandstones from the Neogene-Age Tabernas Basin, SE Spain. *zdg* 171, 521–549. doi:10.1127/zdg/2020/0245
- Lazar, M., Ben-Avraham, Z., and Schattner, U. (2006). Formation of Sequential Basins along a Strike-Slip Fault-Geophysical Observations from the Dead Sea basin. *Tectonophysics* 421, 53–69. doi:10.1016/j.tecto.2006.04.007
- Lonergan, L., and White, N. (1997). Origin of the Betic-Rif Mountain belt. *Tectonics* 16, 504–522. doi:10.1029/96tc03937
- Madof, A. S., Christie-Blick, N., and Anders, M. H. (2009). Stratigraphic Controls on a Salt-Withdrawal Intraslope Minibasin, north-central Green Canyon, Gulf of Mexico: Implications for Misinterpreting Sea Level Change. *Bulletin* 93, 535–561. doi:10.1306/12220808082

- Marini, M., Milli, S., Ravnås, R., and Moscatelli, M. (2015). A Comparative Study of Confined vs. Semi-confined Turbidite Lobes from the Lower Messinian Laga Basin (Central Apennines, Italy): Implications for Assessment of Reservoir Architecture. *Mar. Pet. Geology* 63, 142–165. doi:10.1016/j.marpetgeo.2015.02.015
- Martín, J. M., Braga, J. C., and Riding, R. (1998). “Messinian Reefs and Stromatolites of the Sorbas Basin, Almería, SE Spain,” in *15th IAS Field Trip Guide Book*. Editors A. Meléndez-Hevia and A.R. Soria. Alicante: Instituto Tecnológico Geominero de España, 111–125.
- Martínez-Martínez, J. M., and Azañón, J. M. (1997). Mode of Extensional Tectonics in the southeastern Betics (SE Spain): Implications for the Tectonic Evolution of the Peri-Alborán Orogenic System. *Tectonics* 16, 205–225. doi:10.1029/97tc00157
- Martínez-Martínez, J. M., and Azañón, J. M. (2002). Orthogonal Extension in the Hinterland of the Gibraltar Arc (Betics, SE Spain). *J. Virtual Explorer* 8, 3–22.
- Martínez-Martínez, J. M. (2006). Lateral Interaction between Metamorphic Core Complexes and Less-Extended, Tilt-Block Domains: The Alpujarras Strike-Slip Transfer Fault Zone (Betics, SE Spain). *J. Struct. Geology* 28, 602–620. doi:10.1016/j.jsg.2006.01.012
- Martinsen, O. (1994). “Mass Movements,” in *The Geological Deformation of Sediments*. Editors A. Maltman (London: Chapman and Hall), 127–165. doi:10.1007/978-94-011-0731-0_5
- Mayall, M., Lonergan, L., Bowman, A., James, S., Mills, K., Primmer, T., et al. (2010). The Response of Turbidite Slope Channels to Growth-Induced Seabed Topography. *Bulletin* 94, 1011–1030. doi:10.1306/101051009117
- McArthur, A. D., Bailleul, J., Mahieux, G., Claussmann, B., Wunderlich, A., and McCaffrey, W. D. (2021). Deformation-sedimentation Feedback and the Development of Anomously Thick Aggradational Turbidite Lobes: Outcrop and Subsurface Examples from the Hikurangi Margin, New Zealand. *J. Sedim. Res.* 91, 362–389. doi:10.2110/jsr.2020.013
- McCaffrey, W., and Kneller, B. (2001). Process Controls on the Development of Stratigraphic Trap Potential on the Margins of Confined Turbidite Systems and Aids to Reservoir Evaluation. *AAPG Bull.* 85, 971–988. doi:10.1306/8626ca41-173b-11d7-8645000102c1865d
- Montenat, C., Ott D’Estevou, P., De Larouziere, F. D., and Bedu, P. (1987a). Origine géodynamique des bassins Néogènes du domaine Bétique Oriental (Espagne). *Total Compagnie Française des Pétroles - Notes et Mémoires* 21, 11–49.
- Montenat, C., Ott D’Estevou, P., and Masse, P. (1987b). Tectonic-sedimentary Characters of the Betic Neogene Basins Evolving in a Crustal Transcurrent Shear Zone (SE Spain). *Bull. Cent. De Rech. Explor. Prod. Elf Aquitaine* 11, 1–22.
- Moscardelli, L., and Wood, L. (2008). New Classification System for Mass Transport Complexes in Offshore Trinidad. *Basin Res.* 20, 73–98. doi:10.1111/j.1365-2117.2007.00340.x
- Pickering, K. T., and Corregidor, J. (2005). Mass-transport Complexes (MTCs) and Tectonic Control on basin-floor Submarine Fans, Middle Eocene, South Spanish Pyrenees. *J. Sediment. Res.* 75, 761–783. doi:10.2110/jsr.2005.062
- Pickering, K. T., and Hiscott, R. N. (1985). Contained (Reflected) Turbidity Currents from the Middle Ordovician Cloridorme Formation, Quebec, Canada: an Alternative to the Antidune Hypothesis. *Sedimentology* 32, 373–394. doi:10.1111/j.1365-3091.1985.tb00518.x
- Pickering, K. T., Hodgson, D. M., Platzman, E., Clark, J. D., and Stephens, C. (2001). A New Type of Bedform Produced by Backfilling Processes in a Submarine Channel, Late Miocene, Tabernas-Sorbas Basin, SE Spain. *J. Sediment. Res.* 71, 692–704. doi:10.1306/2dc40960-0e47-11d7-8643000102c1865d
- Pirmez, C., Beaubouef, R. T., Friedmann, S. J., and Mohrig, D. C. (2000). “Equilibrium Profile and Baselevel in Submarine Channels: Examples from Late Pleistocene Systems and Implications for the Architecture of deepwater Reservoirs,” in GCSSEPM Foundation 20th Annual Research Conference, Deep-Water Reservoirs of the World, Houston, Texas, USA, 3–6 December 2000, 782–805. doi:10.5724/gcs.00.15.0782
- Pizzi, M., Whittaker, A. C., Lonergan, L., Mayall, M., and Mitchell, W. H. (2021). New Statistical Quantification of the Impact of Active Deformation on the Distribution of Submarine Channels. *Geology* 49, 926–930. doi:10.1130/g48698.1
- Platt, J. P., Behr, W. M., Johannesen, K., and Williams, J. R. (2013). The Betic-Rif Arc and its Orogenic Hinterland: a Review. *Annu. Rev. Earth Planet. Sci.* 41, 313–357. doi:10.1146/annurev-earth-050212-123951
- Platt, J. P., and Vissers, R. L. M. (1989). Extensional Collapse of Thickened continental Lithosphere: A Working Hypothesis for the Alboran Sea and Gibraltar Arc. *Geol.* 17, 540–543. doi:10.1130/0091-7613(1989)017<0540:ecotcl>2.3.co;2
- Pohl, F., Eggenhuisen, J. T., Cartigny-Tilston, M. J. B., Tilston, M. C., de Leeuw, J., and Hermidas, N. (2020). The Influence of a Slope Break on Turbidite Deposits: An Experimental Investigation. *Mar. Geology* 424, 106160. doi:10.1016/j.margeo.2020.106160
- Poisson, A. M., Morel, J. L., Andrieux, J., Coulon, M., Wernli, R., and Guernet, C. (1999). The Origin and Development of Neogene Basins in the SE Betic Cordillera (SE Spain): a Case Study of the Tabernas-Sorbas and Huercal Overa Basins. *J. Pet. Geol.* 22, 97–114. doi:10.1111/j.1747-5457.1999.tb00461.x
- Puigdefàbregas, C., Gjølberg, J., and Vaksdal, M. (2004). “The Grès d’Annot in the Annot Syncline: Outer basin-margin Onlap and Associated Soft-Sediment Deformation,” in *Deep-Water Sedimentation in the Alpine Basin of SE France: New Perspectives on the Grès d’Annot and Related Systems*. Editors P. Joseph and S. A. Lomas. London: Geological Society, London, Special Publications, 221, 367–388. doi:10.1144/gsl.sp.2004.221.01.20
- Reading, H. G. (1996). *Sedimentary Environments: Processes, Facies and Stratigraphy*. 3rd edn. Oxford: Blackwell Science, 688.
- Sanz De Galdeano, C. (1989). Las fallas de desgarre del borde Sur de la cuenca de Sorbas-Tabernas (norte de Sierra Alhamilla, Almería, Cordilleras Béticas). *Bol. Geol. y Min.* 101, 73–85.
- Sanz De Galdeano, C., Shanov, S., Galindo-Zaldívar, J., Radulov, A., and Nikolov, G. (2010). A New Tectonic Discontinuity in the Betic Cordillera Deduced from Active Tectonics and Seismicity in the Tabernas Basin. *J. Geodynamics* 50, 57–66. doi:10.1016/j.jog.2010.02.005
- Sinclair, H. D. (2000). Delta-fed Turbidites Infilling Topographically Complex Basins: A New Depositional Model for the Annot Sandstones, SE France. *J. Sediment. Res.* 70, 504–519. doi:10.1306/2dc40923-0e47-11d7-8643000102c1865d
- Smith, R., and Joseph, P. (2004). “Onlap Stratal Architectures in the Grès d’Annot: Geometric Models and Controlling Factors,” in *Deep-Water Sedimentation in the Alpine Basin of SE France: New Perspectives on the Grès d’Annot and Related Systems*. Editors P. Joseph and S. A. Lomas. London: Geological Society, London, Special Publications, 221, 389–399. doi:10.1144/gsl.sp.2004.221.01.21
- Spychala, Y. T., Hodgson, D. M., Flint, S. S., and Mountney, N. P. (2015). Constraining the Sedimentology and Stratigraphy of Submarine Intraslope Lobe Deposits Using Exhumed Examples from the Karoo Basin, South Africa. *Sediment. Geology* 322, 67–81. doi:10.1016/j.sedgeo.2015.03.013
- Stevenson, C. J., Talling, P. J., Wynn, R. B., Masson, D. G., Hunt, J. E., Frenz, M., et al. (2013). The Flows that Left No Trace: Very Large-Volume Turbidity Currents that Bypassed Sediment through Submarine Channels without Eroding the Sea Floor. *Mar. Pet. Geology* 41, 186–205. doi:10.1016/j.marpetgeo.2012.02.008
- Tek, D. E., Poyatos-Moré, M., Patacci, M., McArthur, A. D., Colomera, L., Cullen, T. M., et al. (2020). Syndepositional Tectonics and Mass-Transport Deposits Control Channelized, Bathymetrically Complex Deep-Water Systems (Ainsa Depocenter, Spain). *J. Sedim. Res.* 90, 729–762. doi:10.2110/jsr.2020.38
- Tinterri, R., Laporta, M., and Ogata, K. (2017). Asymmetrical Cross-Current Turbidite Facies Tract in a Structurally-Confined Mini-basin (Priabonian-Rupelian, Ranzano Sandstone, Northern Apennines, Italy). *Sed. Geol.* 352, 63–87. doi:10.1016/j.sedgeo.2016.12.005
- Tinterri, R., and Muzzi Magalhaes, P. (2011). Synsedimentary Structural Control on Foredeep Turbidites: An Example from Miocene Marnoso-Arenacea Formation, Northern Apennines, Italy. *Mar. Petrol. Geol.* 28, 629657. doi:10.1016/j.marpetgeo.2010.07.007

- Tinterri, R., and Piazza, A. (2019). Turbidites Facies Response to the Morphological Confinement of a Foredeep (Cervarola Sandstones Formation, Miocene, Northern Apennines, Italy). *Sedimentology* 66, 636–674. doi:10.1111/sed.12501
- Tinterri, R., and Tagliaferri, A. (2015). “The Syntectonic Evolution of Foredeep Turbidites Related to basin Segmentation: Facies Response to the Increase in Tectonic Confinement (Marnoso-Arenacea Formation, Miocene, Northern Apennines, Italy). *Mar. Pet. Geology* 67, 81–110. doi:10.1016/j.marpetgeo.2015.04.006
- Tomasso, M., and Sinclair, H. D. (2004). “Deep-water Sedimentation on an Evolving Fault-Block: the Braux and St Benoit Outcrops of the Grès d’Annot,” in *Deep-Water Sedimentation in the Alpine Basin of SE France: New Perspectives on the Grès d’Annot and Related Systems*. Editors P. Joseph and S. A. Lomas. London: Geological Society, London, Special Publications, 221, 267–283. doi:10.1144/gsl.sp.2004.221.01.14
- Valetti, L., Rutter, E., McCabe, A., and Mecklenburgh, J. (2019). On the Structure and Evolution of the Sorbas basin, S.E. Spain. *Tectonophysics* 773, 228230. doi:10.1016/j.tecto.2019.228230
- Visser, R. L. M., Platt, J. P., and Van Der Wal, D. (1995). Late Orogenic Extension of the Betic Cordillera and the Alboran Domain: a Lithospheric View. *Tectonics* 14, 786–803. doi:10.1029/95tc00086
- Weijermars, R., Roep, T. H. B., Van Den Eeckhout, B., Postma, G., and Kleverlaan, K. (1985). Uplift History of a Betic Fold Nappe Inferred from the Neogene-Quaternary Sedimentation and Tectonics (In the Sierra Alhamilla and Almería, Sorbas and Tabernas Basins of the Betic Cordillera, SE Spain). *Geol. Mijnb.* 64, 379–411.
- Wood, R. A., Pettinga, J. R., Bannister, S., Lamarche, G., and McMorran, T. J. (1994). Structure of the Hanmer Strike-Slip basin, Hope Fault, New Zealand. *Geol.Soc.Am.Bull.* 106, 1459–1473. doi:10.1130/0016-7606(1994)106<1459:sothss>2.3.co;2
- Woodside, J. M., and Maldonado, A. (1992). Styles of Compressional Neotectonics in the Eastern Alboran Sea. *Geo-Marine Lett.* 12, 111–116. doi:10.1007/bf02084920

Conflict of Interest: The authors declare that the research was conducted in the absence of any commercial or financial relationships that could be construed as a potential conflict of interest.

Publisher’s Note: All claims expressed in this article are solely those of the authors and do not necessarily represent those of their affiliated organizations, or those of the publisher, the editors and the reviewers. Any product that may be evaluated in this article, or claim that may be made by its manufacturer, is not guaranteed or endorsed by the publisher.

Copyright © 2021 Baudouy, Haughton and Walsh. This is an open-access article distributed under the terms of the Creative Commons Attribution License (CC BY). The use, distribution or reproduction in other forums is permitted, provided the original author(s) and the copyright owner(s) are credited and that the original publication in this journal is cited, in accordance with accepted academic practice. No use, distribution or reproduction is permitted which does not comply with these terms.



Substrate Entrainment, Depositional Relief, and Sediment Capture: Impact of a Submarine Landslide on Flow Process and Sediment Supply

A. Martínez-Doñate^{1*}, A. M-L. J. Privat², D. M. Hodgson², C. A-L. Jackson¹, I. A. Kane¹, Y. T. Sychala³, R. A. Duller⁴, C. Stevenson⁴, E. Keavney², E. Schwarz⁵ and S. S. Flint¹

¹School of Earth and Environmental Sciences, University of Manchester, Manchester, United Kingdom, ²School of Earth and Environment, University of Leeds, Leeds, United Kingdom, ³Institute for Geology, Leibniz University Hannover, Hannover, Germany, ⁴Department on Earth, Ocean, and Ecological Sciences, University of Liverpool, Liverpool, United Kingdom, ⁵Centro de Investigaciones Geológicas (CIG), La Plata, Argentina

OPEN ACCESS

Edited by:

Fabiano Gamberi,
Institute of Marine Science (CNR), Italy

Reviewed by:

Kei Ogata,
University of Naples Federico II, Italy
Victoria Valdez Buso,
Federal University of Paraná, Brazil
Mattia Marini,
University of Milan, Italy

*Correspondence:

A. Martínez-Doñate
ander.martinez-donate@
manchester.ac.uk

Specialty section:

This article was submitted to
Sedimentology, Stratigraphy and
Diagenesis,
a section of the journal
Frontiers in Earth Science

Received: 12 August 2021

Accepted: 27 October 2021

Published: 16 November 2021

Citation:

Martínez-Doñate A, Privat AM-LJ, Hodgson DM, Jackson CA-L, Kane IA, Sychala YT, Duller RA, Stevenson C, Keavney E, Schwarz E and Flint SS (2021) Substrate Entrainment, Depositional Relief, and Sediment Capture: Impact of a Submarine Landslide on Flow Process and Sediment Supply. *Front. Earth Sci.* 9:757617. doi: 10.3389/feart.2021.757617

Submarine landslides can generate complicated patterns of seafloor relief that influence subsequent flow behaviour and sediment dispersal patterns. In subsurface studies, the term mass transport deposits (MTDs) is commonly used and covers a range of processes and resultant deposits. While the large-scale morphology of submarine landslide deposits can be resolved in seismic reflection data, the nature of their upper surface and its impact on both facies distributions and stratal architecture of overlying deposits is rarely resolvable. However, field-based studies often allow a more detailed characterisation of the deposit. The early post-rift Middle Jurassic deep-water succession of the Los Molles Formation is exceptionally well-exposed along a dip-orientated WSW-ENE outcrop belt in the Chacay Melehue depocentre, Neuquén Basin, Argentina. We correlate 27 sedimentary logs constrained by marker beds to document the sedimentology and architecture of a >47 m thick and at least 9.6 km long debrite, which contains two different types of megaclasts. The debrite overlies ramps and steps, indicating erosion and substrate entrainment. Two distinct sandstone-dominated units overlie the debrite. The lower sandstone unit is characterised by: 1) abrupt thickness changes, wedging and progressive rotation of laminae in sandstone beds associated with growth strata; and 2) detached sandstone load balls within the underlying debrite. The combination of these features suggests syn-sedimentary foundering processes due to density instabilities at the top of the fluid-saturated mud-rich debrite. The debrite relief controlled the spatial distribution of foundered sandstones. The upper sandstone unit is characterised by thin-bedded deposits, locally overlain by medium-to thick-bedded lobe axis/off-axis deposits. The thin-beds show local thinning and onlapping onto the debrite, where it develops its highest relief. Facies distributions and stacking patterns record the progradation of submarine lobes and their complex interaction with long-lived debrite-related topography. The emplacement of a kilometre-scale debrite in an otherwise mud-rich basinal setting and accumulation of overlying sand-rich deposits suggests a genetic link between the mass-wasting event and transient coarse clastic sediment supply to an otherwise sand-starved part of the basin. Therefore, submarine landslides demonstrably

impact the routing and behaviour of subsequent sediment gravity flows, which must be considered when predicting facies distributions and palaeoenvironments above MTDs in subsurface datasets.

Keywords: foundering, dynamic topography, confinement, submarine landslide deposits, submarine lobe, Neuquén basin (Argentina)

INTRODUCTION

Submarine landslide deposits, olistostromes (Flores, 1955), or Mass Transport Deposits (MTDs) (Nardin et al., 1979), are sedimentary bodies that have been translated downslope from high to low gradient slopes as a result of mass failure and gravitational processes (Hampton et al., 1995; Moscardelli and Wood, 2008; Ogata et al., 2012; Festa et al., 2016; Kneller et al., 2016). The typically cohesive nature of the flows enables the transportation of large clasts (>4.1m diameter; herein named megaclasts, *sensu* Blair and McPherson, 1999) (Labaume et al., 1987; Payros et al., 1999; McGilvery and Cook, 2003; Lee et al., 2004; Jackson, 2011; Ogata et al., 2012; Hodgson et al., 2019; Nwoko et al., 2020a). Megaclasts within MTDs are sourced either from headwall areas or entrained from the substrate (Festa et al., 2016; Ogata et al., 2019). These features, accompanied by syn- and post-depositional faulting (Dykstra, 2005; Dykstra et al., 2011), generate the topographically irregular upper surfaces of MTDs (Moscardelli et al., 2006; Bull et al., 2009).

Deep-water sediment gravity flows interact with the rugose topography of MTDs, which influences flow behaviour, deceleration and steadiness (Lowe and Guy, 2000; Armitage et al., 2009; Jackson and Johnson, 2009; Fairweather, 2014; Ortiz-Karpf et al., 2015, 2017; Steventon et al., 2021), and therefore dispersal patterns and depositional architecture (Kneller et al., 2016). MTD surface relief has been shown to affect facies distribution and associated sedimentary architecture; this has been reported from both outcrop (Pickering and Corregidor, 2005; Armitage et al., 2009; Dykstra et al., 2011; Fallgatter et al., 2017; Brooks et al., 2018; Valdez et al., 2019) and subsurface studies (Ortiz-Karpf et al., 2017; Nwoko et al., 2020b). However, MTDs may continue to deform after initial emplacement through creeping processes (e.g. Butler and McCaffrey, 2010) or secondary mass movements (Sobiesiak et al., 2016). Furthermore, the high water content within newly deposited MTDs promotes active dewatering at their upper surface (Mulder and Alexander, 2001; Talling et al., 2012; Browne et al., 2020) associated with local instabilities and movement (Iverson, 1997; Major and Iverson, 1999; Van der Merwe et al., 2009). Fluids can also generate overpressure along with the interface between MTDs and its sediment cover, exploiting pathways created by internal MTD deformation (Ogata et al., 2012; Migeon et al., 2014). Therefore, the interaction between the initial topographic relief of MTDs, dewatering processes, post-depositional deformation and subsequent sediment gravity flows (and their deposits) is highly dynamic and inherently complex (e.g. Alves, 2015). A better understanding of sedimentary processes above MTDs can help subsurface predictions of facies distributions, which might

have been overlooked due to variable seismic resolution and core coverage. Therefore, detailed field-based studies can help to bridge the resolution gap.

Here, we aim to understand an exceptionally well-exposed debrite and overlying sand-rich strata in the Bathonian Los Molles Formation, which were physically correlated over 9.6 km along a depositional dip transect in the Chacay Melehue depocenter (Neuquén Basin, Argentina). The objectives of this study are to 1) document the anatomy and stratigraphic architecture of the debrite, 2) investigate the impact of the dynamic upper relief on the overlying heterolithic and sand-rich strata, and 3) discuss the role that mass-wasting processes may have played as a trigger for subsequent sand-rich sediment supply.

GEOLOGICAL SETTING

The Neuquén Basin is located in central-western Argentina and central-eastern Chile, covering an area of 160,000 km² (Figure 1A). The basin is bounded to the north-east by the Sierra Pintada, to the south by the North Patagonian Massif, and since the Early Jurassic, by the early Andean magmatic arc to the west (Legarreta and Gulisano, 1989; Suárez and de la Cruz, 1997; Franzese and Spalletti, 2001; Howell et al., 2005). The Neuquén Basin contains a >6 km-thick sedimentary succession that spans the Mesozoic to the Late Cenozoic and records several unconformities related to tectonic phases (Vergani et al., 1995; Legarreta and Uliana, 1996; Howell et al., 2005). Three key tectonic phases are recognised (Vergani et al., 1995; Franzese and Spalletti, 2001; Franzese et al., 2003): 1) Triassic-to-Early Jurassic rifting and the onset of subsidence; 2) Early Jurassic-to-Early Cretaceous post-rift thermal subsidence associated with the development of the Andean magmatic arc and back-arc basin; and 3) Late Cretaceous-to-Early Cenozoic Andean compression and foreland basin development. In the western sector of the Central Neuquén Basin, the deep- to shallow-marine deposits of the early post-rift Cuyo Group (Lower-to-Middle Jurassic) (Gulisano et al., 1984) unconformably overlie the continental syn-rift volcano-sedimentary deposits of the Precuyano Group (Gulisano et al., 1984; Gulisano and Gutiérrez Pleimling, 1995; Legarreta and Uliana, 1996; Pángaro et al., 2009; Leanza et al., 2013) or the Palaeozoic basement of the Choiyoi Group (Llambías et al., 2003, 2007) (Figure 2A).

Our investigation focuses on the Early Bathonian stratigraphy of the Upper Los Molles Formation, which forms a ~70 m thick interval characterised by ammonite-rich black shales and heterolithic successions comprising tuff layers with an intervening MTD and sandstone deposits (Figure 1B).

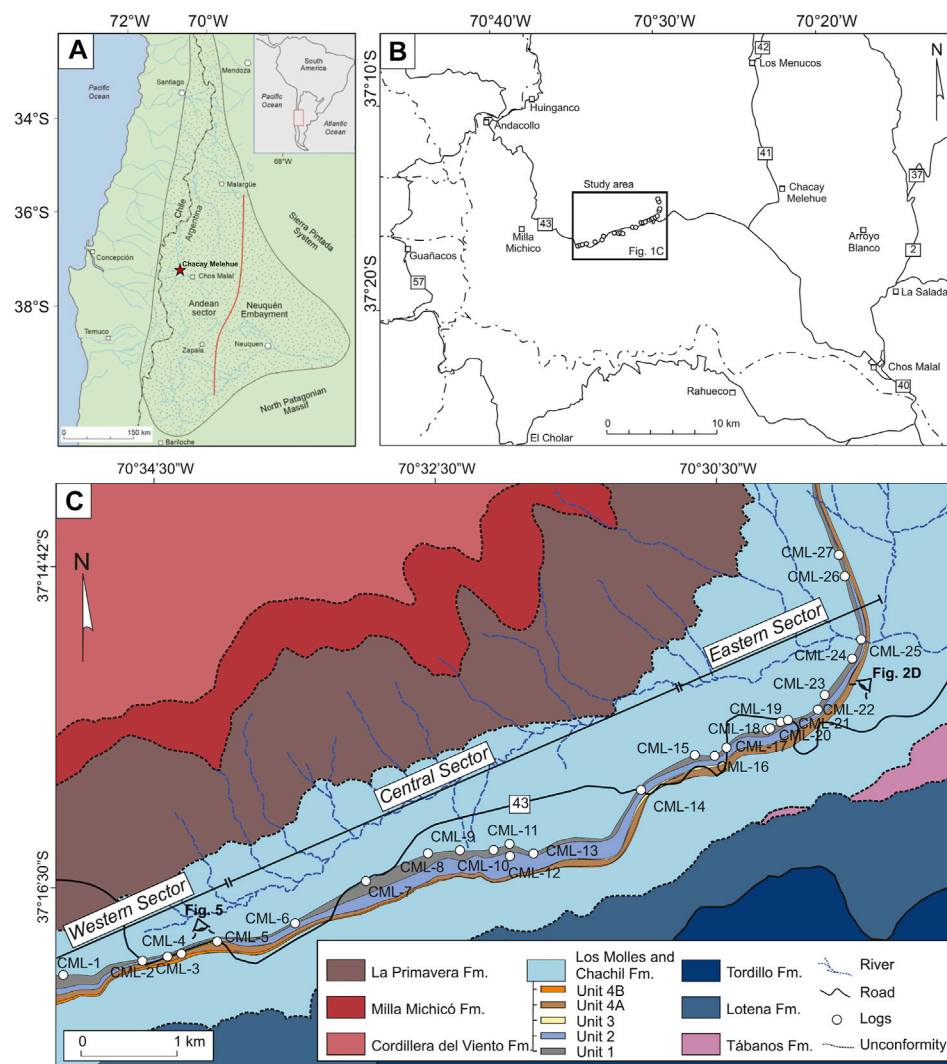
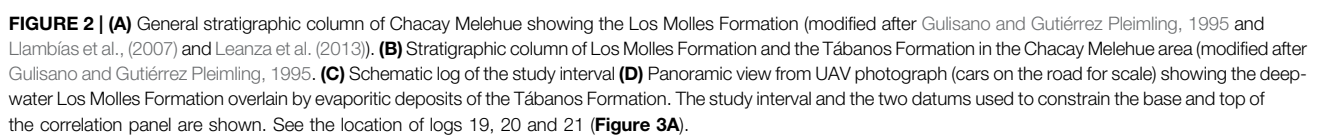


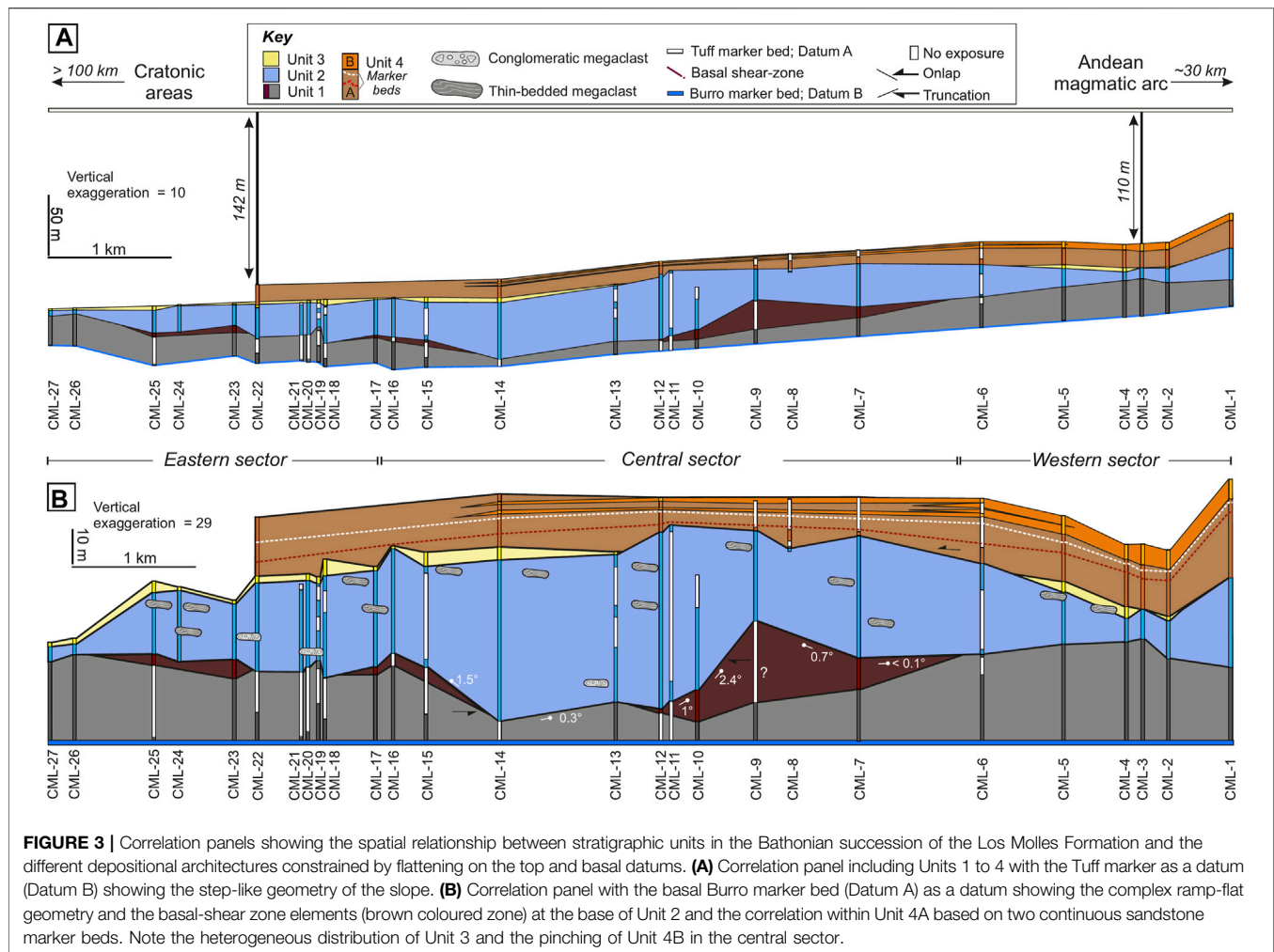
FIGURE 1 | (A) Location map of the Neuquén Basin and the study area Chacay Melehue (red star). **(B)** Local location map of the study area. **(C)** Map of the Chacay Melehue area with the formations [modified from Llambías et al. (2007)] and the locations of the logs. See the studied units and their distribution.

Study Area—Chacay Melehue Depocentre

The succession in the Chacay Melehue area was deposited in a half-graben (~20 km long) (Mancada and Figueroa, 1995; Llambías et al., 2007; Leanza et al., 2013) that occupied the western and deepest part of a broader early post-rift depocentre in the Central Neuquén Basin (~65 km long) (Mancada and Figueroa, 1995; Veiga et al., 2013). The half-graben shows a strong asymmetry due to a steep western margin characterised by the development of the early Andean magmatic arc and location of a major syn-rift fault (Mancada and Figueroa, 1995; Suárez and de la Cruz, 1997; Vicente, 2005), which contrasts with the stable and gently dipping eastern cratonic margin (Spalletti et al., 2012; Veiga et al., 2013). Deposition of the Los Molles Formation took place during a period of thermal subsidence and regional marine transgression across complex inherited rift topography, which promoted the reduction of sediment supply and sand starvation in this part of

the basin (Spalletti et al., 2012; Veiga et al., 2013). The proximity to the volcanic arc (~30 km to the west), the abundant volcanoclastic deposits (Zöllner and Amos, 1973; Rosenfeld and Volldaeimer, 1980; Gulisano and Gutiérrez Pleimling, 1995; Suárez and de la Cruz, 1997; Vicente, 2005; Llambías et al., 2007), and palaeocurrent measurements in sandstones indicating a general southeastwards trend reveals that sediment supply feeding the Chacay Melehue area during the post-rift was sourced from the western magmatic arc (Gulisano et al., 1984; Vicente, 2005). The deep-marine deposits of Los Molles Formation (Weaver, 1931) overlie shallow-marine tuffaceous clastic deposits (De La Cruz and Suarez, 1997; Llambías and Leanza, 2005) and carbonate deposits of the Chachil Formation (Pliensbachian to Early Weaver, 1942; Kamo and Riccardi, 2009; Leanza et al., 2013; Riccardi and Kamo, 2014), deposited with the first marine incursion in the basin (Gulisano and Gutiérrez Pleimling, 1995; Leanza et al.,





2013) (**Figure 2A**). Chronostratigraphic studies based on ammonite biostratigraphy (Gulisano and Gutiérrez Pleimling, 1995; Riccardi, 2008) and U-Pb radiometric dating (Kamo and Riccardi, 2009; Leanza et al., 2013; Riccardi and Kamo, 2014), place the Los Molles Formation in the Chacay Melehue region as Early Toarcian-to-Early Callovian in age (Gulisano and Gutiérrez Pleimling, 1995) (**Figure 2C**). The succession of the Los Molles Formation in the Chacay Melehue depocentre is 850 m thick (**Figure 2B**). A 55 m thick sandstone-prone interval in the lower succession represents an Aalenian turbidite system (interval II of Gulisano and Gutiérrez Pleimling, 1995). The overlying Bathonian section of the Los Molles Formation (up to 200 m thick) (**Figure 2B**) is mainly represented by mudstone and heterolithic successions, including a 70 m thick interval (study interval; **Figure 2C**) of deformed sand- and mud-rich deposits (interval IV of Gulisano and Gutiérrez Pleimling, 1995). The overlying Lower Callovian strata of the Los Molles Formation is characterised by a 300 m thick interval of thin-bedded mudstone. It is overlain by either the fluvial Lotena Formation (Gulisano and Gutiérrez Pleimling, 1995; Veiga et al., 2011) or evaporites (Tábanos Formation; **Figure 2D**), which record a period of

basin desiccation (Legarreta, 1991; Gulisano and Gutiérrez Pleimling, 1995; Legarreta and Uliana, 1996).

METHODOLOGY

The sedimentology and stratigraphic architecture of a 70 m thick interval (**Figures 2C, 3**) within the Upper Los Molles Formation were investigated along a 9.6 km long and WSW-ENE orientated outcrop belt (**Figures 1B,C**). The succession dips 10–20° to the SE, with minimal structural overprint from the later tectonic inversion. Twenty-seven (27) sedimentary logs were measured at 1:25 to 1:40 scale along this transect (CML-0 to CML-27 from SW to NE) to document the broad depositional architecture of 4 different units (Unit 1, 2, 3, 4A and B) (**Figure 1C**). Ten detailed logs were measured at a 1:2 scale at specific locations to document fine-scale thickness and facies changes. Four marker beds were used to build a robust physical correlation between sedimentary logs (**Figures 2, 3**). The marker beds are 1) Datum A, or the “Burro” marker bed, a light-grey indurated graded siltstone at the base of the study interval (**Figures 2A, 3, 4A**); 2) a gravelly thin-

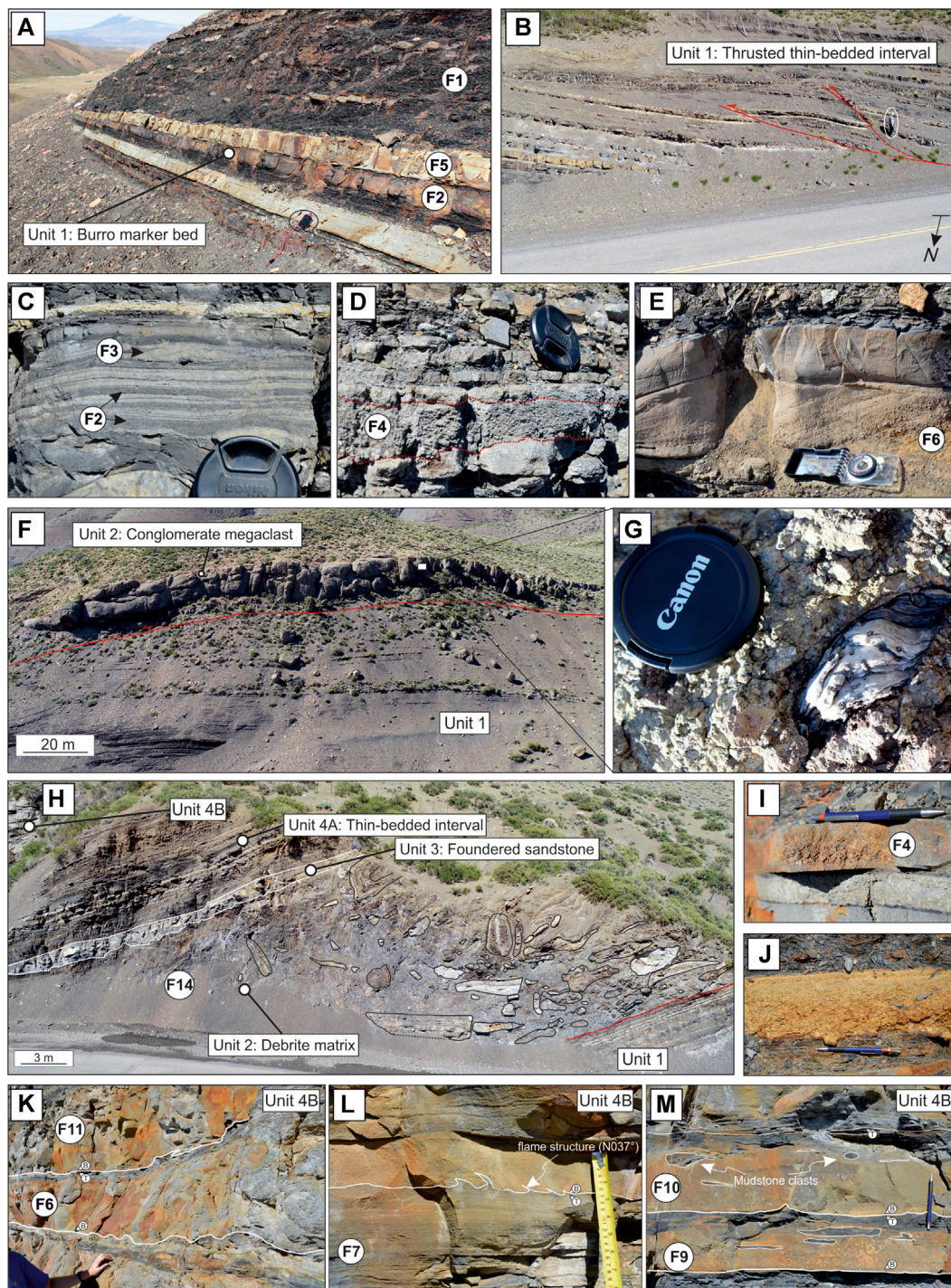


FIGURE 4 | Representative sedimentary facies photos. **(A)** Unit 1: Planar-laminated mudstone (F1) with a few thin- to medium-bedded intercalated siltstone beds (F2) (Burro marker bed; Datum A) and sandstone beds (F5). **(B)** Unit 1: Basal shear-zone characterised by imbricated thrusts with drag folding. **(C)** Unit 4A: Heterolithic deposits consisting in the alternation between siltstones (F2) to (very) fine-grained sandstones (F3). **(D)** Unit 4A: Gravelly thin bed (F4) locally eroded into fine-grained sandstones (F3). **(E)** Unit 4A: Medium-bedded sandstones with cross-bedding (F6). **(F)** Unit 2: 140 m long conglomerate megaclast, bearing oyster and belemnite fragments, and sitting above Unit 1. Oyster fragment highlighted in the inset box **(G)**. **(H)** Unit 2, 3 and 4A: Foundered sandstones onlapping the matrix-rich debris (F14) with deformed heterolithic megaclasts draped by the thin-bedded deposits of Unit 4A. **(I)** Unit 4A: Gravelly and **(J)** Tuff-marker bed within 4A. See the correlation **Panels 3B, 8** (red and white dashed lines). **(K)** Unit 4B: Amalgamated medium- (F6) to thick-bedded (F11) sandstones. **(L)** Unit 4B: Medium-bedded banded sandstone (F7) overlain by massive matrix-poor sandstones (F5). Note the vergent flame structures within the amalgamation surface **(M)** Unit 4B: Thin- (F9) and medium-bedded (F10) hybrid event beds type 2 (cf. Houghton et al., 2009) with a linked debris consisting of matrix-rich sandy division with elongated mudstone clasts.

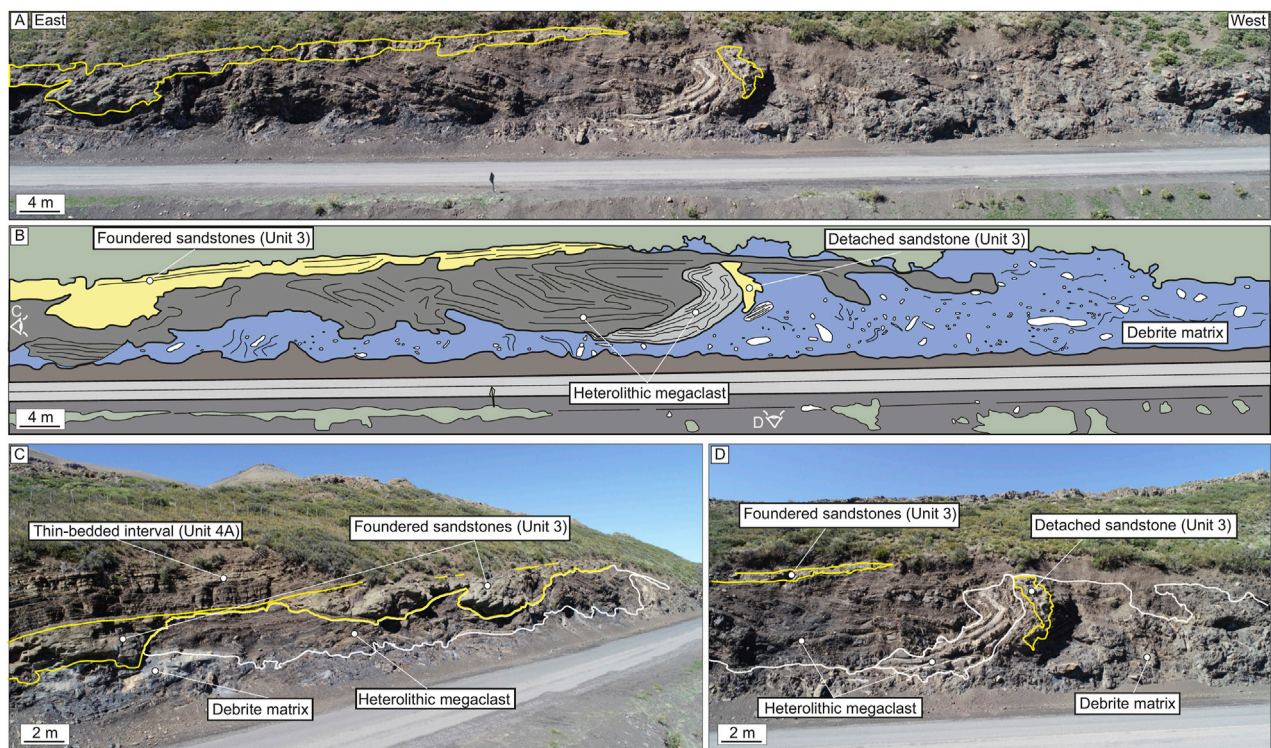


FIGURE 5 | (A) Panorama of the exposure showing the upper division of Unit 2 overlaid by Unit 3 foundered sandstone. **(B)** Sketched exposure of A. Note the matrix-supported texture and the chaotic distribution of clasts. **(C)** and **(D)** Same exposure of A from a different perspective. Note the unconformable base and conformable flat top interface of Unit 3 sandstones. See B for location.

bed (**Figure 4F**) and 3) a tuff layer (**Figure 4G**), both within one of the studied units (Unit 4A); and 4) Datum B, a tuff layer overlying the study interval (100–150 m above) across the study area (**Figures 2D, 3**). Uncrewed Aerial Vehicle (UAV) photogrammetry (**Figures 2D, 5**) was used in conjunction with standard field techniques, such as mapping and logging, to capture the micro- and macro-scale features of the investigated stratigraphic units. Fifty-eight (58) palaeocurrent measurements were collected from ripples, cross-bedding, flame structure and convolute lamination vergence from bed tops of sandstones, and plotted in rose diagrams.

RESULTS: SUBDIVISION AND CHARACTERISATION OF SEDIMENTARY UNITS 1–4

The study interval is subdivided informally into four different units (**Figure 2C**), based on their distinctive facies (**Table 1**) and stratal relationships.

Unit 1

Description: Unit 1 is 5.5–28 m thick and contains the Burro marker bed (Datum A) (**Figure 2C**), a light-grey indurated graded siltstone that is sharply overlain by light-grey fine-grained, planar-parallel laminated sandstone (**Figure 4A**). This

unit is truncated by the basal surface of Unit 2 and is thinnest in the central sector of the exposure (see sections CML-9 to CML-16 **Figure 3**). Unit 1 comprises a heterolithic succession of planar-parallel laminated mudstones (F1) and thin-bedded (<0.1 m thick) normally-graded, well-sorted siltstones (F2) to very fine-grained sandstones (F3), and occasional medium-bedded structureless sandstones (F5) (**Figures 4A,C**). When traced from west to east, the thin-bedded sandstones show subtle lateral fining and thinning, transitioning from heterolithic succession to mudstone-prone succession. Unit 1 is rich in ammonites, belemnite rostrums and bivalves, as well as calcareous concretions (Damborenea, 1990; Gulisano and Gutiérrez Pleimling, 1995; Riccardi et al., 2011).

The central and eastern sectors contain a discrete stratigraphic interval that exhibits deformed bedding (**Figure 4B**). This interval is thickest (at least 10 m; **Figure 3**) in the central sector, where, internally, it exhibits an array of imbricated decametre-scale east-verging thrusts (offset <2 m) and associated drag folds. The thrusts originate from a bed parallel surface, leaving the underlying bedding undeformed (**Figure 4B**). In the eastern sector, a thin (~5 m thick) interval of intense deformation is characterised by open folds and minor thrusts (offset <1 m) (**Figure 4B**). Unit 1 stratigraphy in the western sector lacks any deformation.

Interpretation: The laminated mudstones, graded siltstones and thin sandstone beds are interpreted as deposits of low-density

TABLE 1 | Descriptions of the facies recognised in the Los Molles stratigraphy of the Chacay Melehue area, including lithologies, thicknesses, and interpretations of their depositional processes.

Lithofacies	Lithology	Description	Thickness	Process interpretation
F1: Laminated mudstone	Mudstone	Dark-coloured planar parallel laminated mudstone with Ammonites. Concretionary horizons are common	0.1–3 cm	Deposits from very dilute sediment gravity under relative dysoxic-anoxic conditions (Trabucho-Alexandre et al., 2012; Könitzer et al., 2014)
F2: Graded siltstone	Graded siltstone	Normally-graded from silty bases to mud-rich tops. Usually structureless, although planar parallel-laminations are common	1–5 cm	Deposition under low-density turbidity current (Allen, 1971)
F3: Thin-bedded fine-grained sandstones	Very fine- to fine-grained sandstones	Normally-graded, well-sorted thin-beds. Fine-grained bases and very fine-grained tops. Structureless at the base with planar laminated tops. Rare starved ripple lamination at bed tops	1–10 cm	Deposition and tractional reworking by low-density turbidity current (Allen, 1971, 1982; Jobe et al., 2012)
F4: Thin-bedded granular sandstones	Granular- to medium-grained sandstones	Normally-graded, very well-sorted, coarse-grained to granular-sandstones. Sharp planar base and top	1–10 cm	Deposition from turbidity currents
F5: Medium-bedded sandstones	Very fine- to medium-grained sandstone	Structureless, normally-graded sandstones. Bed bases are medium-grained, grading up until fine-grained	10–50 cm	Deposition from medium-density turbidity currents. High-aggradation rates inhibited the formation of sedimentary structures (Talling et al., 2012)
F6: Thin-bedded cross-stratified sandstones	Granular- to medium-grained sandstones	Normally-graded, well-sorted thin-beds. Foreset heights range from 5 to 7 cm, and angles vary between 10° and 35°. Erosional bases are common—sharp contacts, with planar base and undulatory top	5–10 cm	Deposition and tractional reworking by turbidity currents (Tinterri, 2011)
F7: Medium-bedded banded sandstones	Banded sandstones with sharp alternation between darker and lighter bands. Lighter bands are grain-supported, while darker bands are matrix-supported and lack mudstone clasts	Sandstones comprising alternation between matrix-poor light bands and matrix-rich dark bands (0.2–2 cm thick). Similar grain size (fine to medium) along with different bands. Heterolithic bedforms and pinch-and-swell geometries can be developed. The bed bases can be structureless	10–50 cm	Deposits beneath mud-rich transitional plug flow formed by tractional reworking within the upper stage plane bed flow regime (Baas et al., 2009, 2011, 2016; Stevenson et al., 2020)
F8: Thick-bedded banded sandstones with mudstone clast	Banded sandstones with diffuse alternation between darker and lighter bands. Lighter bands are grain-supported, while darker bands are matrix-supported, with abundant mudstone clasts	Sandstones comprising banding between matrix-poor light bands and matrix-rich mudstone clast (millimetric scale) bearing dark bands (0.5–2 cm). Banding is diffuse and can be developed throughout the bed or from the middle to the top parts of a bed, commonly overlaid by convolute lamination. Laminae show local tilting and increasing spacing between laminae	50–150 cm	Rapid aggradation and episodic damping of near bed turbulence due to clay flocs disaggregation (Lowe and Guy, 2000). Increasing spacing between laminae is attributed to growth strata due to foundering processes
F9: Thin-bedded hybrid event beds	Silty sandstone	Matrix poor bases with linked argillaceous, ungraded and poorly-sorted top divisions	1–10 cm	Distal deposits are the product of en masse deposition and potentially behaving as transitional to laminar flows (Kane et al., 2017)
F10: Medium-bedded hybrid event beds	Bipartite sandstones with matrix-poor basal divisions and upper argillaceous mudstone-clast prone division	Bipartite sandstone beds are characterised by a matrix-poor structureless lower division passing gradually into linked mudstone clasts matrix-rich upper division	10–50 cm	Deposits formed under transitional flows. Erosion and incorporation of intrabasinal clasts. The entrained substrate was rapidly disaggregated within the flow resulting in clast-rich and clay-rich divisions at the bed top. The flows increased in concentration but had not developed stable density stratification (Haughton et al., 2003; Davis et al., 2009; Hodgson, 2009; Kane and Pontén, 2012; Kane et al., 2017)
F11: thick-bedded sandstones	Structureless sandstone	Structureless, thick-bedded argillaceous sandstones, lacking mudstone clasts. High amalgamation	0.5–1.2 m	Deposition under high-density turbidity currents (sensu Lowe, 1982), formed by incremental layer-by-layer deposition with (Continued on following page)

TABLE 1 | (Continued) Descriptions of the facies recognised in the Los Molles stratigraphy of the Chacay Melehue area, including lithologies, thicknesses, and interpretations of their depositional processes.

Lithofacies	Lithology	Description	Thickness	Process interpretation
F12: Thick-bedded structureless matrix-poor sandstones with normally-graded mudstone clast	Structureless sandstones with a mudstone clast at the base	rations and erosional beds when lying above fine-grained intervals. Banding is locally developed at bed tops, alternating between matrix-poor light bands and matrix-rich dark bands (0.2–2 cm thick). Similar grain size (fine to medium) along with different bands. Heterolithic bedforms and pinch-and-swell geometries can be developed. Structureless thick-bedded, medium- to coarse-grained, crudely normally-graded sandstones, with low-matrix content. They contain some mudstone clasts (0.1–1 m) with diffuse boundaries preferentially located at the base, which show coarse tail grading. Mudstone diapirs along the basal interface are common	0.5–2 m	high aggradation rates (Kneller and Branney, 1995; Sumner et al., 2008; Talling et al., 2012). The banding represents planar lamination (Bouma Tb division) (Stevenson et al., 2020)
F13: Thick-bedded structureless matrix-rich sandstones with ungraded mudstone clast	Argillaceous sandstone with abundant mudstone clasts	Structureless thick-bedded, fine- to medium-grained, ungraded sandstones with very high matrix content and abundant decimetric mudstone clasts (0.1–1 m) randomly distributed	0.5–2 m	Deposition under high-density turbidity currents (sensu Lowe, 1982), formed by incremental layer-by-layer deposition with very high aggradation rates (Kneller and Branney, 1995; Sumner et al., 2008; Talling et al., 2012). Mudstone clast is entrained due to erosion of an unconsolidated debrite (Unit 2) and syn-sedimentary buoyancy product of density instabilities (Owen, 1987, 2003)
F14: matrix-supported conglomerates	Mud-rich medium-grained sandstone to sandy mudstone	Poorly sorted, ungraded with a chaotic distribution of outsized clasts (up to 140 m long). Irregular and sharp contacts. Bases can be erosive and undulatory tops	7.4–47.9 m	Moderate-strength cohesive debris flows derived from mudstone clast entrainment and disaggregation. Mudstone clasts are supported by their positive buoyancy with respect to the surrounding matrix and the matrix strength (Talling et al., 2012). Cohesive debris-flow deposits (sensu Talling et al., 2012). with near-instantaneous deposition from a flow with high yield strength and buoyant support

turbidity currents (Allen, 1982; Trabucho-Alexandre et al., 2012; Könitzer et al., 2014), whereas the medium-bedded sandstones represent the deposits of medium- to high-density turbidity current (Talling et al., 2012). The laterally extensive character, mudstone dominance, and overall eastward (down-dip) fining and thinning trend of thin-bedded sandstones of Unit 1 suggest deposition from low-energy sediment gravity flows in distal areas (e.g., Mutti, 1977), with possible distal lobe fringe deposits (Boulestix et al., 2020). The discrete intervals of deformed bedding found in the upper parts of Unit 1 represent a post-depositional sheared zone linked to the overlying Unit 2.

Unit 2

Description: Unit 2 has an unconformable basal contact that truncates Unit 1 in the central sector (Figure 3). The relief of the basal contact is characterised by down- and up-stepping segments (ramps, >2°) linked by bedding-parallel segments (flats). The average thickness of Unit 2 is 20–30 m but can locally reach >47 m in the central sector and abruptly thins to <8 m towards the eastern and western sectors (Figure 3). This increase in thickness coincides with deeper erosion on the basal surface.

Unit 2 is characterised by a matrix-supported medium-grained muddy sandstone to sandy mudstone and is very poorly sorted throughout, ungraded, and with a chaotic distribution of outsized

clasts (F14; Figure 5). Clasts range in character and size from granular quartz grains and rounded volcanic epiclasts to much larger megaclasts (>4.1–140 m long) (Hodgson et al., 2019) of either conglomeratic or heterolithic lithology (Figures 2C,D, 4F, 5). The chaotic distribution of polymictic clast encased into a muddy sand matrix is responsible for the block-in-matrix fabric (e.g. Ogata et al., 2012). Typically, conglomeratic megaclasts are rounded, elongated and weakly deformed (Figures 2D, 4F,G) and are clast-supported, with well-rounded to sub-angular clasts (0.03–1 m diameter) and fragments of thick-shelled bivalves (oysters; Figure 4D). These oyster-bearing conglomeratic megaclasts are preferentially located near the base of Unit 2 (Figures 2C,D, 3B). In contrast, heterolithic megaclasts are angular and characterised by internally folded packages of planar laminated and normally graded thin-bedded material (Figures 2C, 5) and preferentially distributed toward the top of Unit 2 (Figures 3, 5). This heterogeneity promotes a homogeneous matrix-rich texture in the middle division.

Apart from the irregular basal contact of Unit 2, thickness changes within the unit are strongly controlled by the rugose upper surface. Kilometre-scale wavelength (1–3 km) and metre-scale amplitudes (0.5–8 m) are responsible for a complex supra debrite topography.

Interpretation: The sedimentary characteristics of this unit, such as the chaotic distribution of (mega)clast floating onto a

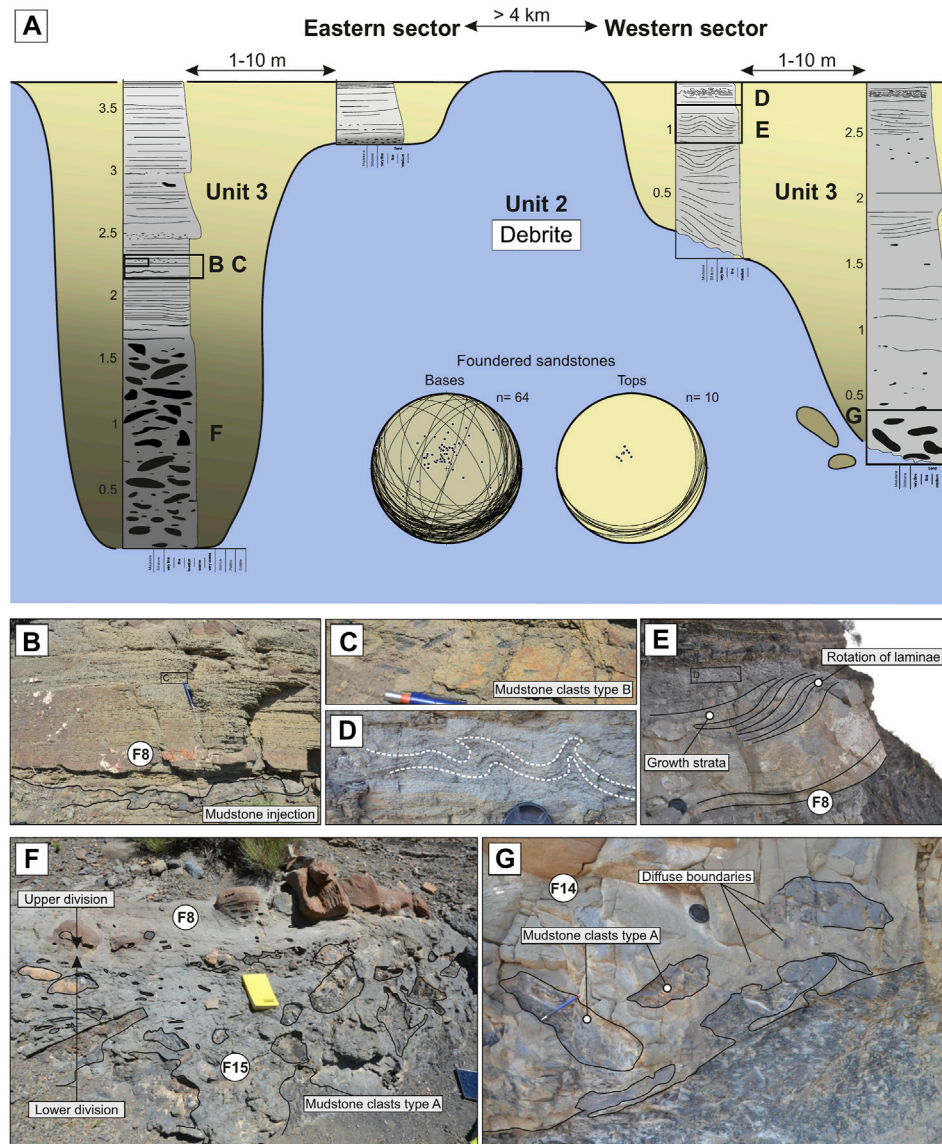
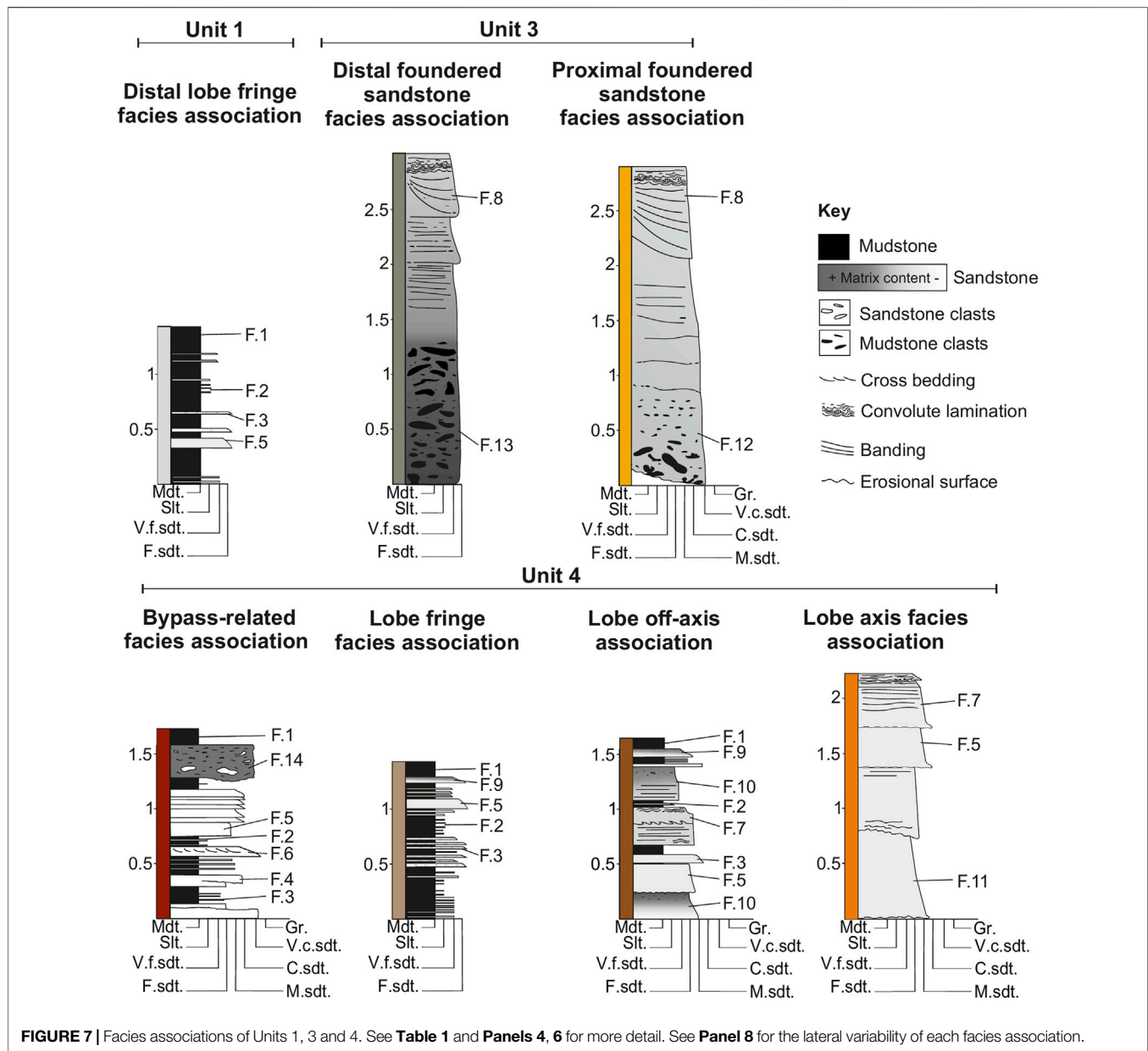


FIGURE 6 | Foundered sandstones (Unit 3) diagram. **(A)** Illustrative correlation of sandstone foundering (Unit 3) into debris (Unit 2). Note the difference between the conformable bed tops of matrix-poor and traction dominated sandstones (**right-hand stereonet**) and the mudstone clast- and matrix-rich sandstone texture near the unconformable bed bases (**left-hand stereonet**), which shows the architecture of these sandstone bodies. **(B)** Thick-bedded banded sandstones with bedding-parallel sill injection (F8). See mudstone clasts (type B) in the inset **(C)**. **(D)** Convolute-laminae with NE vergence. **(E)** Sandstones showing rotation and growth strata. **(F)** Lower division comprising thick-bedded structureless argillaceous (F13) sandstone division with a patchy and random distribution of mudstone clasts overlain by upper division comprising thick-bedded banded sandstones (F8). **(G)** Thick-bedded structureless sandstone with an undulating irregular base comprising decimetre-scale mudstone clasts (type A) (F12).

muddy sandstone to sandy mudstone matrix, suggest near-instantaneous deposition from a flow with high yield strength and buoyant support that could transport clasts up to 140 m long (Stow and Johansson, 2000; Mulder and Alexander, 2001). Using Datum A, the debris formed a long-wavelength mounded top (Figure 3), attributed to the parental flow's cohesive nature and en-masse freezing. We interpret Unit 2 as a cohesive debris flow deposit (Talling et al., 2012). The ramp and flat geometry at the base of Unit 2 indicate the debris flow's erosive nature (e.g., Lucente and Pini, 2003). The similarity in composition between

the heterolithic megacasts and underlying Unit 1 suggests entrainment of deep-marine substrate blocks due to the shear stress exerted by the overriding debris flow (Van der Merwe et al., 2009; Watt et al., 2012; Ogata et al., 2014a; Hodgson et al., 2019). In contrast, the sand content in the matrix and the oyster-bearing conglomerate megacasts suggest a shallow marine origin of the mass failure (e.g., Ogata et al., 2012). Alternatively, the megacast bearing shells could come from the remobilization of older slope strata, including shallow-marine deposits (La Primavera Fm; Suárez and de la Cruz, 1997; Llambías and Leanza, 2005). The



two distinct megaclast sources suggest long-distance transport of clasts and flow bulking through local substrate entrainment (e.g., Sobiesiak et al., 2016).

Unit 3

Description: Unit 3 (0–4 m thick) is composed of thick sandstone beds (0.5–2 m) with sharp, irregular concave-up bases and abrupt pinchout terminations, which result in a disconnected distribution of packages of wedge-shaped sandstone bodies (**Figure 6**) (see architecture section). Unit 3 is only present where Unit 2 is relatively thin (in the eastern-central and western sectors) and is absent in the central region where Unit 2 shows its maximum thickness (**Figure 3**). Where Unit 3 is absent, Unit 4 overlies Unit 2 (**Figure 3**). Unit 3 comprises bed

types characterised by two main amalgamated divisions (lower and upper divisions) with some grain size breaks lacking any mudstone- and siltstone-rich bounding intervals (**Figures 6A, 7**). The basal interface of these sandstone bodies shows centimetre-scale undulations characterised by abundant load casts, semi-detached ball structures, and mudstone intrusions (diapirs and injectites) originating from Unit 2 (**Figure 6G**).

Two different types of thick-bedded amalgamated sandstone facies dominate the lower division, which varies along the transect. Grain-size breaks define amalgamation surfaces within sandstones. In the western sector, and more rarely in the eastern sector, the lower divisions are characterised by thick-bedded (0.5–2 m thick), structureless, weakly normally-graded, moderately-to poorly-sorted sandstones (F12). At bed bases,

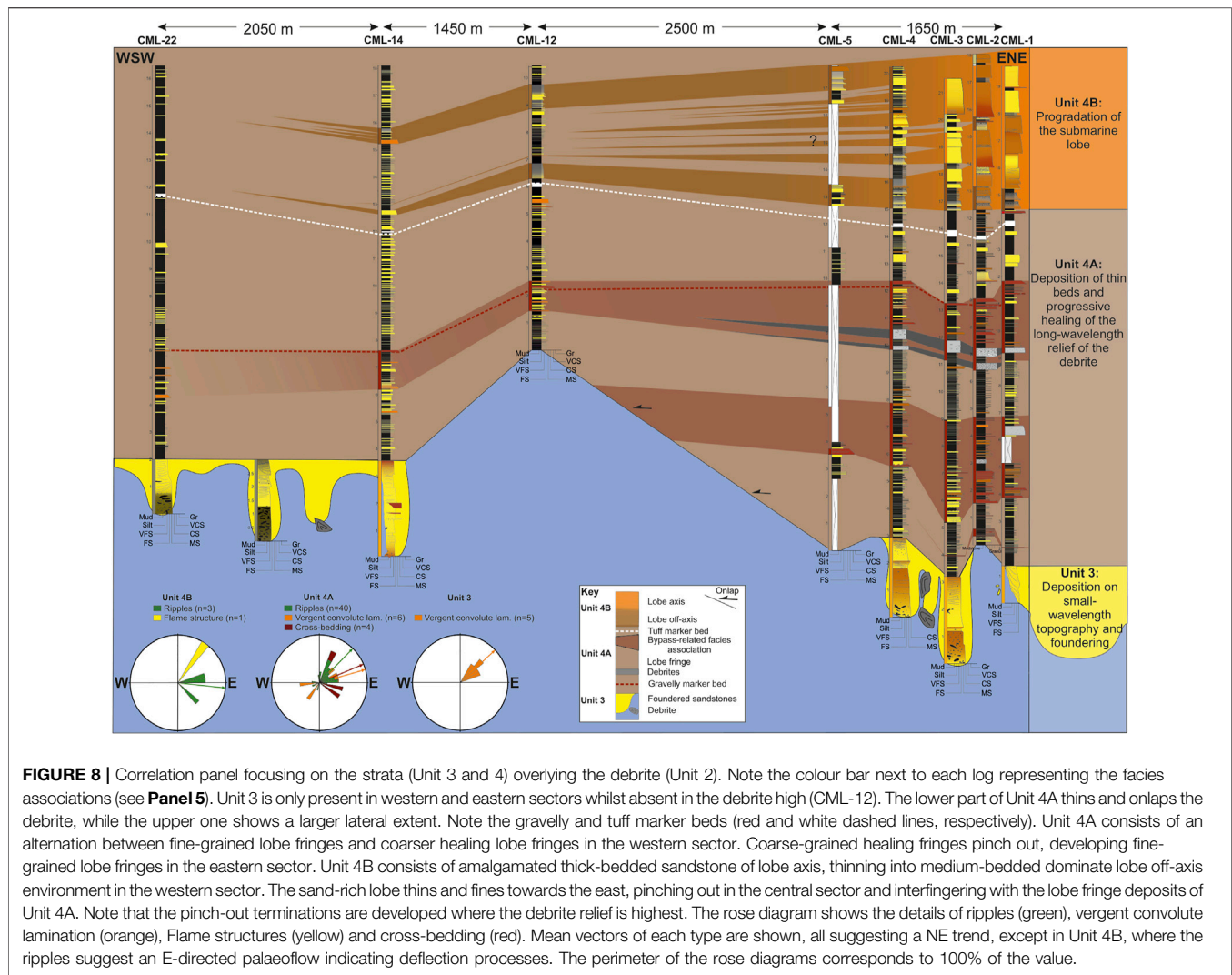


FIGURE 8 | Correlation panel focusing on the strata (Unit 3 and 4) overlying the debrite (Unit 2). Note the colour bar next to each log representing the facies associations (see **Panel 5**). Unit 3 is only present in western and eastern sectors whilst absent in the debrite high (CML-12). The lower part of Unit 4A thins and onlaps the debrite, while the upper one shows a larger lateral extent. Note the gravely and tuff marker beds (red and white dashed lines, respectively). Unit 4A consists of an alternation between fine-grained lobe fringes and coarser healing lobe fringes in the western sector. Coarse-grained healing fringes pinch out, developing fine-grained lobe fringes in the eastern sector. Unit 4B consists of amalgamated thick-bedded sandstone of lobe axis, thinning into medium-bedded dominate lobe off-axis environment in the western sector. The sand-rich lobe thins and fines towards the east, pinching out in the central sector and interfingering with the lobe fringe deposits of Unit 4A. Note that the pinch-out terminations are developed where the debrite relief is highest. The rose diagram shows the details of ripples (green), vergent convolute lamination (orange), Flame structures (yellow) and cross-bedding (red). Mean vectors of each type are shown, all suggesting a NE trend, except in Unit 4B, where the ripples suggest an E-directed palaeoflow indicating deflection processes. The perimeter of the rose diagrams corresponds to 100% of the value.

these sandstones comprise well-rounded (0.1–1 m diameter) mudstone clasts of low-sphericity and diffuse boundaries (mudstone clast type A), which show a coarse tail grading (**Figures 6A,G**). Locally, in the eastern sector, lower divisions of these sandstone bodies comprise thick-bedded, structureless, very poorly-sorted, more argillaceous sandstones with abundant mudstone clasts (0.1–1 m diameter) with very diffuse boundaries (mudstone clast type A), which are ungraded and randomly orientated (F13) throughout the encasing matrix (**Figure 5F**).

The lower division of Unit 3 sandstone bodies are overlain by an upper division (up to 2 m thick), which comprises coarse to very fine-grained, normally graded, moderately-to poorly-sorted sandstones (0.5–1.7 m) (**Figure 6A**). Banding can be developed throughout the bed or overlying a structureless division (**Figure 6A**). The banding is characterised by an alternation between lighter matrix-poor bands and darker matrix-rich bands that comprise bedding parallel millimetric mudstone clast with sharp boundaries (mudstone clast type B) (F8; **Figure 6C**). Contacts between bands are diffuse (**Figures 6B,F**). The spacing between the individual bands (0.5–2 cm)

increases from the margin to central parts of the sandstone body (**Figure 8**), commonly showing rotation (**Figure 6E**). These sandstones develop symmetrical and asymmetrical convolute lamination at bed tops (predominant vergence towards NE; **Figure 6D**). Decimetre-scale long and centimetre-scale thick mudstone injections can be observed within this division (**Figure 6B**).

Interpretation: The wedge-shaped and deformed concave-up basal contacts of the sandstone bodies beds in Unit 3 are interpreted to reflect the interaction with the rugose upper surface and syn-sedimentary foundering of sand into the underlying mud-rich debrite (**Figures 6, 9**). Foundering is driven by instability due to the density contrast between the sand deposited above a less dense debrite (density loading) and lateral changes in sediment load (uneven loading) (Owen, 1987, 2003) produced by the short-wavelength rugosity of the upper surface.

The lack of sedimentary structures in the lower divisions of bed types recognised in Unit 3 is interpreted as a product of hindered settling from highly-concentrated gravity-flows,

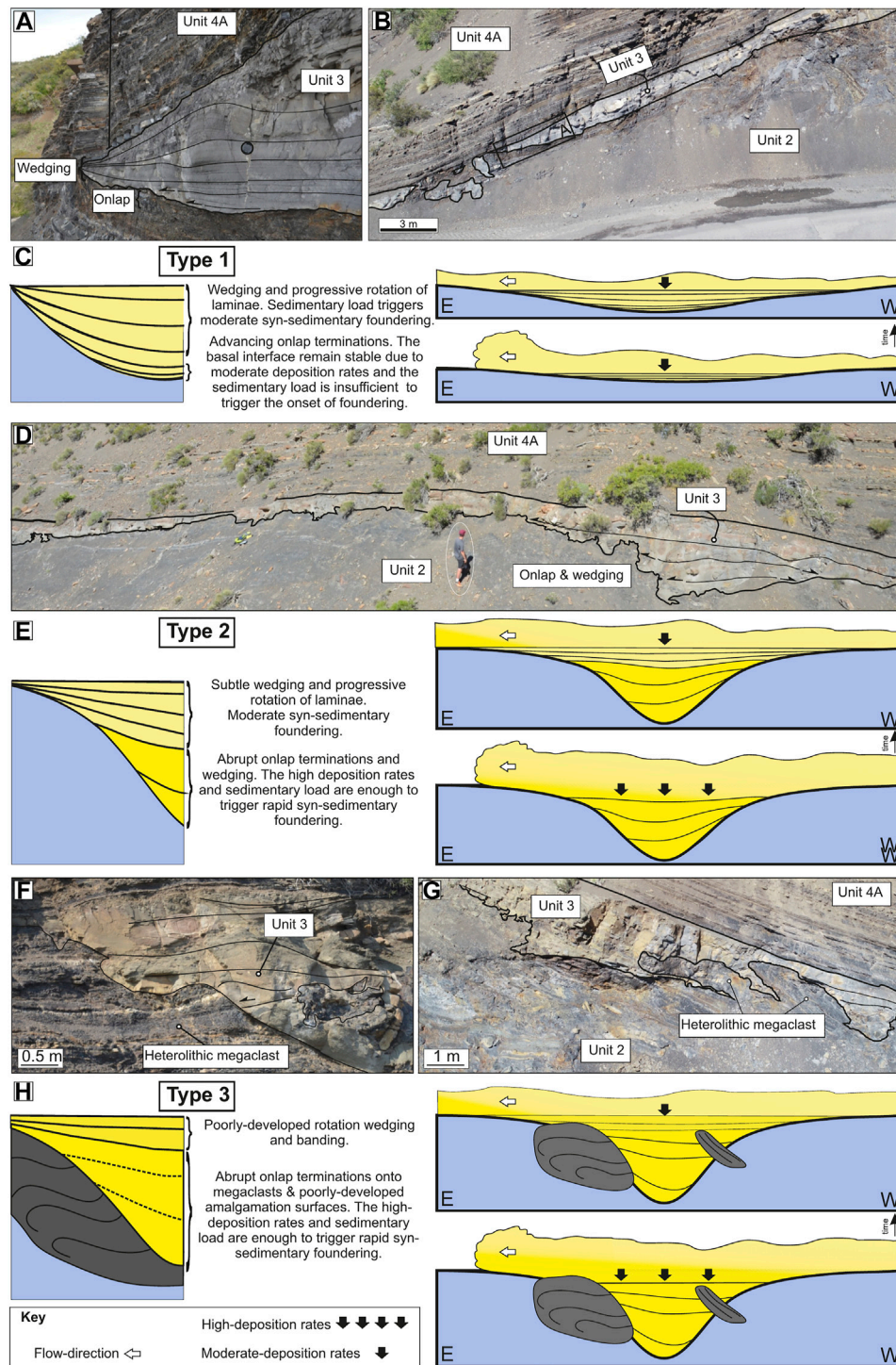


FIGURE 9 | Illustrative diagram of founded sandstone architecture and a model for their development. Type 1: **(A)** Thin-bedded sandstone with onlap termination at the base, indicating interaction with inherited relief and wedging associated with the syn-depositional foundering. **(B)** Bodies wedge smoothly, forming lenticular bodies with flat tops. Note the location of A) indicated by a black rectangle. **(C)** Sketch of the architecture and evolutionary model of Type 1 architecture: Initial deposition is insufficient to trigger the foundering. Type 2: **(D)** Thick-bedded founded sandstones with associated thinner margins. Central parts are composed of sandstones deposited by high-density turbidity currents, whereas the thinner margins are sandstones interpreted as being deposited under more fluidal sediment gravity flows (Transitional flows). **(E)** Sketch of the architecture and evolutionary model of Type 2 architecture: Initial deposition is enough to trigger the foundering. Type 3: **(F, G)** The shape of the thick-bedded sandstone bodies depends on the size and geometry of the thin-bedded megaclast. See **Panel 5** for more detail. **(H)** Sketch of the architecture and evolutionary model of Type 2 architecture: While foundering, the sandstone might be protruded by the megaclast due to its higher competence than the surrounding debrite matrix.

resulting in turbulence damping and rapid deposition (Talling et al., 2012), inhibiting any period of traction (Sumner et al., 2008). The normally-graded lower divisions were produced by incremental layer-by-layer deposition from high concentration gravity flows, such as high-density turbidity currents (*sensu* Lowe, 1982). In contrast, the thick-bedded argillaceous sandstones with ungraded mudstone clasts observed in the distal areas (eastern sector) are interpreted as moderate-strength cohesive debrites (*sensu* Talling et al., 2012). The decimetre-scale mudstone clasts (type A) were transported due to the matrix strength of the debris flows and their positive buoyancy with respect to the encasing matrix.

The lateral facies transition from high-density turbidites to moderate strength cohesive debrite suggest a flow transformation due to the entrainment of cohesive material from the underlying debrite (e.g., Kane and Pontén, 2012; Baker et al., 2017). The unconsolidated state of the debrite might have enhanced the substrate entrainment of decimetre-scale mudstone clasts (type A) and disaggregation (as indicated by the diffuse boundaries: **Figure 6G**), increasing the amount of mud and, therefore, the cohesiveness of the flow. Based on facies juxtaposition, the foundered sandstones can be subdivided into two different facies associations: 1) proximal and 2) distal, foundered sandstones facies associations (**Figure 7**). Both high-density turbidites and moderate strength cohesive debrites are characterised by rapid deposition (incremental deposition and *en masse* freezing, respectively), triggering the liquefaction of the fluid-saturated and unconsolidated upper surface of the debrite and foundering of sand (**Figure 9**). The undulations of the concave-up basal interface reflect complex interactions with the substrate: as the denser sand sank into the fluid-saturated muddy substrate, the buoyancy of mud promoted the syn- to post-depositional intrusion (mud diapirs and injectites) of the substrate into sandstones. The most advanced stage of foundering is observed when detached sand-balls develop (**Figure 5**; Owen, 2003; Tinterri et al., 2016).

In contrast, the banded sandstone characteristic of the upper divisions is interpreted to be formed under episodic near-bed turbulence damping at high rates of deposition (Lowe and Guy, 2000). The juxtaposition of the banded sandstones over the mudstone-clast bearing sandstones of the lower divisions suggests highly stratified flows, mixing and upwards transfer of centimetre-scale mudstone clast (type B) and the cohesive material from the disaggregation of the entrained decimeter-scale mudstone clast (type A). This enrichment in cohesive clayey material triggered the periodic suppression of turbulence and, therefore, banding development. The banding passes into convolute laminations towards the top, indicating moderate rates of deposition. The vergence of convoluted laminations suggests a syn-sedimentary shear-stress exerted by the overriding flow (McClelland et al., 2011; Butler et al., 2016) and flow-rebound produced by the underlying debrite relief (e.g., Tinterri et al., 2016).

Unit 4

Description: Unit 4 (10–27.3 m thick) has a sharp and concordant contact with the underlying Unit 2 and Unit 3

(**Figure 3**). It comprises two subunits: a lower heterolithic interval (Unit 4A) and an upper sandstone-prone interval (Unit 4B; **Figure 2C**).

Unit 4A is thin- to medium-bedded (0.01–0.5 m; **Figure 4H**) heterolithic succession (F1, F2, F3 and F5) with a maximum thickness of 22 m, thinning to 8 m in the central sector above where Unit 2 is thickest (**Figure 3**). Most of the thin-beds (0.01–0.1 m thick) are fine- to medium-grained normally-graded sandstones, matrix-poor, moderately well-sorted, and structureless with common planar-parallel lamination and/or starved-ripple lamination near bed tops (F3; **Figure 4C**). Palaeocurrent measurement shows a consistent flow trend towards the NE (**Figure 9**). Unit 4A also comprises coarse- to granular normal-graded sandstones, relatively low matrix content with common grain size-breaks (0.07–0.2 m thick), erosive bases and sharp-planar tops (F4; **Figure 4D**) and two medium-bedded matrix-supported conglomerates with sandstone clasts (F14; 0.25 and 0.35 m thick, respectively) that pinch out towards the central sector (**Figure 8**). One of these thin gravelly beds, which lacks any lateral thinning or fining trend (**Figure 4I**), was traced across the exposure (gravelly marker bed; dashed red line in **Figure 8**). In addition, a 0.15 m thick tuff layer (**Figure 4J**) was also used for correlation purposes (tuff marker bed; dashed white line in **Figure 3**). The medium-bedded sandstones (0.1–0.5 m thick) are structureless, ungraded, with planar-parallel and convolute lamination at bed tops, except one that shows cross-bedding (F6; **Figure 4D**). These sandstones have sharp bed bases and tops and lack mudstone clasts. In the eastern sector, Unit 4A is dominated by thin- to medium-bedded heterolithic succession that lacks any gravelly (F5) or matrix-supported conglomerate beds (F14).

Unit 4B (5.7 m thick in the western sector) thins eastwards along a 4.3 km transect until it pinches out, where Unit 2 is thickest (**Figure 3**). In the western sector, it dominantly comprises medium- (F5; **Figure 4K**) to thick-bedded sandstones (F11; **Figure 4K**), with less common “bipartite” sandstone beds (F9 and F10) composed of a matrix-poor lower division and a matrix-rich upper division with mudstone clasts. Conformable bases and sharp tops characterise the thick-bedded sandstones (0.5–1.2 m). Where the thick-bedded sandstones are not amalgamated and are intercalated centimetre-thick beds of fine-grained material (F1 and F2), bed bases are loaded locally. The thick-bedded sandstones are normally graded from medium to fine sand, well-sorted with rare centimetric mudstone clasts at the bed top. Soft-sediment deformation structures, such as centimetre-scale flames with NE vergence, are also common at bed bases and along amalgamation surfaces (**Figure 4L**). Banded sandstones are medium-bedded (0.1–0.5 m), fine- to medium-grained, and characterised by alternating between light- and dark-coloured bands, ranging from 0.2 to 2 cm thick (F7; **Figure 4L**). Both band types show a similar maximum grain size, although the darker bands are matrix-rich, and light bands are matrix-poor. Banding is generally sub-parallel to bedding. Although banded sandstones are more commonly associated with thick-bedded structureless sandstones, the banded sandstones can be individual event beds, with banding above the structureless basal division. The medium-bedded bipartite sandstone beds (0.1–0.5 m) consist of a

medium-grained, matrix-poor and structureless lower division, which is overlain by a fine-grained matrix-rich upper division characterised by poor sorting and abundant mudstone clasts (0.05–0.3 m) with low sphericity and variable roundness (F9 and F10; **Figure 4M**). The lower and upper divisions show a gradual upwards increase in matrix content rather than across a sharp boundary. When Unit 4B is traced eastwards towards the central sector, the sandstone package transitions into a few thin-beds (0.1 m thick) of weakly graded, very poorly-sorted matrix-rich sandstone, lacking the mudstone clasts observed in western areas. Unit 4B is absent in the eastern sector.

Interpretation: In Unit 4A, the thin sandstone beds showing planar and cross ripple laminations support an interpretation as low-to medium-density turbidites (Talling et al., 2012). The starved-ripple lamination observed in thin-bedded sandstones is interpreted as the reworking of sand deposited by dilute flows with low sedimentation rates (Talling et al., 2007; Jobe et al., 2012). The intercalation of thin-bedded sandstones with finer-grained deposits suggests a lobe fringe environment (Lobe fringe facies association, **Figure 5**) (Prélat et al., 2009; Spychala et al., 2017b). The abundant coarse-grained to gravelly thin-bedded sandstones in the western sector record intermittent energetic coarse-grained flows, suggesting sporadic sediment bypass processes (Stevenson et al., 2015). However, the low matrix content within the granular beds suggests a sediment source area where only coarse-to granular grain size was available. The intercalation of such different facies suggests the juxtaposition of depositional environments of contrasting energy and/or different sediment sources. Either scenario could be possible given the complex sediment routing patterns and multiple transverse or axial sources available in the Neuquén Basin during the early post-rift setting (Vicente, 2005; Privat et al., 2021) and by analogy to other post-rift settings (e.g., Lien, 2005; Fugelli and Olsen, 2007; Hansen et al., 2021). The mass failure would trigger a new coarse-grained source due to slide scar position and geometry, promoting intermittent sand supply to an otherwise sand-starved environment (see “Origin and role of the Mass-wasting process as a trigger for turbidite systems development” in discussion). The downdip variability in the thickness of Unit 4A (from 22 to 8.5 m thick), reduction in gravelly sandstone content and the stratigraphic thinning between the granular marker bed (red dashed line in correlation) and the top debrite (Unit 2) reveals the existence of subtle relief on the debrite surface (**Figure 3B**). Furthermore, the two poorly sorted ungraded muddy sandstones, which are interpreted to be debrites due to their chaotic distribution of clast within the argillaceous matrix, also pinch out towards the central sector. The ripples and convolute laminae with SW vergence (**Figure 3**) contrast with the consistent NE paleoflow, suggesting local flow deflection (cf. Tinterri et al., 2016) in the central sector, where the debrite relief is highest, indicating the interaction between sediment gravity-flows and the upper surface of the debrite.

Massive medium-to thick-bedded deposits of Unit 4B are interpreted as high-density turbidites formed by incremental layer-by-layer deposition with high aggradation rates (Kneller and Branney, 1995), interpreted to represent proximal lobe axis

environments (lobe axis facies association; **Figure 5**) (e.g., Prélat et al., 2009; Kane et al., 2017). The location of these facies in the westernmost sector, and the palaeoflow measurements, suggests that the western sector was relatively proximal. Banded sandstones represent the deposits of mud-rich transitional flows formed by tractional reworking (Stevenson et al., 2020). The bipartite beds consisting of a basal structureless to planar laminated sandstone division, overlain by a linked mudstone clast-rich upper division are interpreted as hybrid event beds (HEBs), formed from transitional flows deposited under high-deceleration rates (Haughton et al., 2009; Hodgson, 2009; Kane and Pontén, 2012) in more distal environments than the banded sandstones (Stevenson et al., 2020). The gradual and diffuse boundary between the basal turbidite and the upper debrite suggest vertical segregation of particles within the cohesive flow (Kane et al., 2017). The facies evolution of Unit 4B from proximal (western sector) to distal (eastern sector) of thick-bedded sandstones into hybrid event beds likely represents the downdip transition from lobe-axis/off-axis environments (lobe axis facies association: **Figure 5**) (sensu Prélat et al., 2009) into lobe-fringe environments (lobe fringe facies association; **Figure 5**) (e.g., Spychala et al., 2017a; Kane et al., 2017), persisting until the frontal/oblique pinchout (e.g. Hansen et al., 2019).

DEPOSITIONAL ARCHITECTURE OF THE DEBRITE AND OVERLYING UNITS

Large Scale Architecture: Debrite Relief

Using Datum A (“Burro” marker bed), the upper surface of the >9.6 km long debrite forms a broad convex-up relief that reaches a maximum in the central section coincident with the deepest incision (at least 22.5 m of erosional relief; **Figure 3B**). The spatial association of the thickest part of the debrite with the deepest incision support a genetic link between the geometry of the flat-ramp-flat shaped basal shear zone and the mounded top. The morphology of the basal surface can buttress material translated downslope and develop positive topographic features, such as pressure ridges (Moscardelli et al., 2006; Bull et al., 2009). Bed-by-bed correlation within Unit 4A shows that where the upper surface of the debrite develops the highest relief (~8 m of positive relief with respect to the western sector), Unit 3 is absent, and it is overlain by Unit 4A (**Figure 3**), showing a laterally continuous stratigraphic interval with metre-scale thickness variations (**Figure 8**). Unit 4A thins from 22 m (CML-1) and 13 m (CML-2) to 6 m (CML-12) across the highest part of the debrite (**Figure 3B**). The lower part of Unit 4A pinches out in the central sector, developing onlaps of individual beds, and supporting the existence of a gentle relief (Bakke et al., 2013; Soutter et al., 2019). In contrast, the upper part of Unit 4A shows tabular architecture with a lateral continuity of over 7 km.

Unit 4A is overlain by Unit 4B, which shows a progressive thinning of the submarine lobe from the western to the central sector over 5.6 km, from 5.7 m (CML-3) to 1.7 m (CML-12) and 1 m (CML-14) with a mean thinning rate of 0.9 m/km. The

submarine lobe pinches out between CML-14 and CML-22 (<2 km), interfingering with unit 4A (**Figure 3B**). The lack of onlap geometries against underlying deposits and subtle thinning rates consistent with unconfined settings (e.g., Prélat et al., 2009) suggests a lack of a pronounced pre-existing relief. However, the coincidence of lobe pinch-out in the area where the debrite relief is highest and where the underlying Unit 4A is thinnest might reflect subtle residual relief.

Small-Scale Architecture: Foundered Sandstones

The steeply-dipping unconformable base, internal deformation and abrupt thickness changes of Unit 3 sandstones contrast with their flat and conformable tops (see stereoplots in **Figure 6**). These sandstone bodies can be subdivided into three different types by their architecture.

Type 1

Description: The thinner foundered sandstone bodies range between 0.5 and 2 m thick and are only formed by the banded sandstones (**Figures 9A,B**). They are characterised by 5–25 m wide lenticular shapes, with thickness/width ratios varying from 1:5 to 1:18. These sandstone bodies show relatively constant thinning rates (~0.25 cm/m) towards their pinch outs. They are characterised by: 1) advancing onlap terminations onto Unit 2 at the base, and a vertical change into; 2) progressive rotation of laminae and the wedging of the sandstones (**Figure 9C**).

Interpretation: The onlap termination indicates the interaction between the parental sediment gravity flow and pre-existing debrite-related relief (e.g., Bakke et al., 2013), and the sediment load was insufficient to trigger the soft-sediment deformation along the upper surface. In contrast, the overlying rotation and wedging represent growth strata associated with the syn-sedimentary foundering. This juxtaposition of terminations indicates that foundering did not start since the onset of deposition of sand due to insufficient stress to trigger the soft-sediment deformation. This supports an incremental layer-by-layer deposition of these sandstones rather than the freezing of the parental flow.

Type 2

Description: Thick-bedded foundered sandstones (up to 4 m thick) are characterised by irregular stepped bases and abrupt thickness variations (up to 2 m thinning over 1 m laterally) (**Figure 9D**). They are composed by the juxtaposition of two different divisions: 1) lower and 2) upper divisions (**Figure 9E**). The lower divisions comprise structureless sandstones with poorly-developed amalgamation surfaces (F12 or F13). They rarely exceed 10 m laterally and 3 m in thickness (thickness/width 1:2 to 2:1) and are characterised by both abrupt onlaps terminations and wedging. In contrast, the upper divisions are characterised by banded sandstones (F8), which are more laterally extensive than the underlying division, with a maximum length of 50 m and rarely exceed 1 m in thickness, and thin laterally towards margins (thickness/width 1:10).

Interpretation: The coexistence of onlaps terminations and wedging indicate that the foundering began at the onset of deposition and the existence of pre-existing topography along the upper surface. The sediment load was enough to trigger the foundering because the debrite relief strongly influenced the initial high-concentration flows, which promoted a loss in flow capacity and deposition under high aggradation rates. The rapid deposition and foundering are responsible for the poorly-developed onlap terminations and amalgamation surfaces. The deposition of lower division deposits promoted a reduction in debrite rugosity due to the infilling of topographic lows, enabling the deposition of laterally more extensive deposits. The rotation and wedging in the banding of the upper division is less well developed than in Type 1 sandstone bodies. This suggests a progressive reduction in syn-sedimentary deformation and an increase in seafloor stability (e.g., Owen, 1987, 2003).

Type 3

Description: These sandstone bodies show similar facies juxtaposition as in Type 2. In this case, the sandstones terminate against heterolithic megaclasts due to their preferential location towards the top of the debrite (**Figures 5, 9F**). In these cases, the geometries of the foundered sandstones diverge from the concave-up geometry, dependent on the shape of the megaclast. Some megaclasts disconnect bodies laterally, whereas others only impact the base, with the top part of the sandstones undisturbed (**Figure 9G**).

Interpretation: The fluid-saturated matrix and rigid megaclast respond differently to the shear stress exerted by the deposition of sand creating. This differential compaction (Ogata et al., 2014b) controls the architecture of the foundered sandstones, creating complex bodies (**Figure 9H**).

DISCUSSION

Basal Shear Zone and Impact on the Substrate

As submarine landslides travel across the seafloor, they exert shear stress on the substrate, coupled with significant over-pressure (Bull et al., 2009; Hodgson et al., 2019; Payros and Pujalte, 2019). This leads to substrate entrainment (Eggenhuisen et al., 2011; Hodgson et al., 2019) and/or deformation (Butler and McCaffrey, 2010; Watt et al., 2012; Dakin et al., 2013; Ogata et al., 2014b). The debris flow (Unit 2) incised at least 22.5 m into the substrate (Unit 1; **Figure 3**). In the central sector, the basal shear surface forms ramps (up to 800 m long, >2°) and flats (up to 1,550 km long; **Figure 3B**; between the logs CML-9 and CML-10) (see Lucente and Pini, 2003; Frey Martínez et al., 2005 for flat-ramp-flat geometry). The stress applied to the substrate during the emplacement is accommodated by both stratigraphic intervals consisting of deformed packages (basal shear-zone) and interfaces consisting on a plane (basal shear-surface) (Alves and Lourenço, 2010), such as the discrete basal shear zone located in upper Unit 1. The absence of contractional features in the deposits underlying Unit 1 supports the deformation as the result of the shear stress produced by the

emplacement of the debrite rather than tectonism. The basal shear zone has variable thickness and deformation styles. It is absent in the western sector, whereas erosion and deformed intervals record a high degree of basal shear stress in the central sector (**Figure 3B**). In the central sector, the deformed package (up to 10 m thick) is characterised by decametre-scale thrusts with metre-scale offsets and drag folding (**Figure 4B**). The predominance of imbricate thrusting over folding, and lack of internal disaggregation within the package, indicate competent substrate rheology (e.g., Van Der Merwe et al., 2011). The eastward vergence of the compressional structures (**Figure 4B**) indicates an eastward emplacement direction for the debris flow (Twiss and Moores, 1992), consistent with the palaeoflow indicators in the bounding strata.

The thrusting is attributed to bulldozing by the entrenched debris flow (e.g., Jackson, 2011; Hodgson et al., 2019; Payros and Pujalte, 2019), representing the initial stage of substrate entrainment. Entrainment of megaclasts into a debris flow has been reported in other systems in the subsurface (Moscardelli et al., 2006; Alves and Cartwright, 2009; Sawyer et al., 2009; Dakin et al., 2013; Ortiz-Karpp et al., 2015; Soutter et al., 2018; Nwoko et al., 2020a) and more rarely at outcrop (Ogata et al., 2014b; Sobiesiak et al., 2016; Hodgson et al., 2019; Cumberpatch et al., 2021). The progressive increase in thickness and degree of strain along the basal shear zone of Unit 2 and the enrichment in rafted heterolithic megaclasts (**Figures 3B, 5**) suggest downdip evolution of the debris flow, which might have affected the parental debris flow rheology (e.g., Hodgson et al., 2019; Payros and Pujalte, 2019) and bulking of the flow (Gee et al., 2006; Alves and Cartwright, 2009; Butler and McCaffrey, 2010; Hodgson et al., 2019). The preferential location of heterolithic megaclast towards the top of Unit 2 might be related to internal granular convection cells created along with the debris flow, enhanced by the buoyancy of less dense rafted megaclast compared to debrite matrix (Hodgson et al., 2019) and kinetic sieving (Legros, 2002). In contrast, conglomerate megaclasts are always found at the base of the debrite due to their higher density than the surrounding debrite matrix.

Dynamic Debrite Topography and Impact on Overlying Strata

The absence of Unit 3 sandstones over the thickest part of the debrite suggests that the sediment gravity flows were strongly stratified and influenced by the debrite relief (**Figure 8**). The sandstone bodies are also disconnected at finer scales, revealing short wavelength (metre-scale) and amplitude (decimetre-scale) rugosity on the debrite surface. The existence of simultaneous short wavelength and amplitude rugosity superimposed on a large-scale wavelength relief on the upper surface of an MTD has also been reported by Armitage et al. (2009), defined as “surface-topography hierarchy,” in the Cretaceous Tres Pasos Formation at the Sierra Contreras (Chile) and by Fairweather (2014) in Carboniferous Paganzo Basin at Cerro Bola (Argentina). In this study, the deposition of sand in pre-existing lows filled the short-wavelength rugosity and triggered the loading of individual sandstone bodies onto the mud-rich

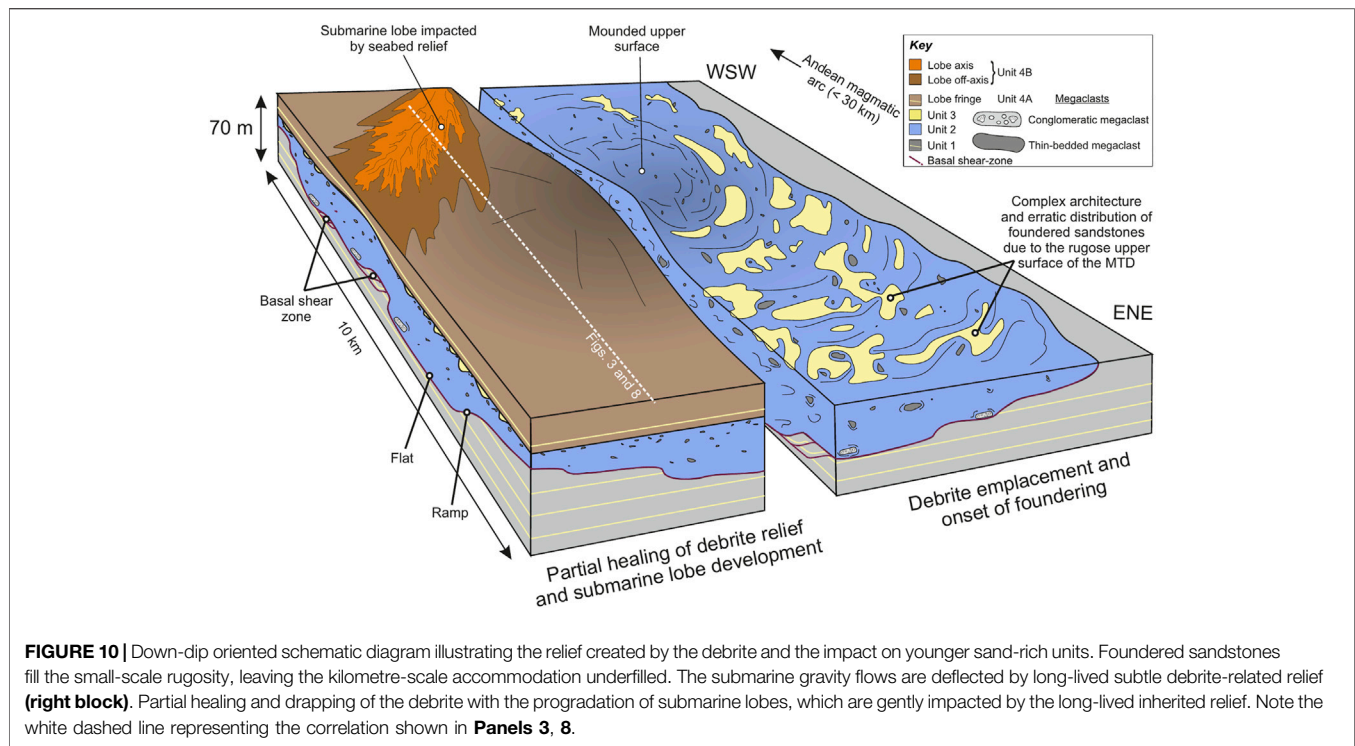
debrite (See “Small-scale architecture: Foundered sandstones” sections), leaving the large-scale relief underfilled (**Figures 3, 8**). The foundering process is evidence of substrate liquefaction and highlights the dynamic interface between the debrite and subsequent flows and their deposits. A similar scenario was proposed by Van der Merwe et al. (2009), Van der Merwe et al. (2011) in the Vischkuil Formation in the Laingsburg depocentre (Karoo Basin).

The ability of supra MTD rugosity to pond turbidity currents travelling across their upper surface is a well-known phenomenon (Kneller et al., 2016). However, the presence of Unit 3 founded sandstones up-dip and down-dip of the debrite high (**Figure 3B**), and its consistent NE paleocurrent trend, suggest connected sediment transport routes across the debrite with no evidence of flow ponding or stripping (e.g. Armitage et al., 2009; Fairweather, 2014). The highly-stratified grown-hugging parental flows of Unit 3 would have been ponded in proximal parts (western sector) if a fully enclosing topography existed given their reduced ability to surmount obstacles (Al-Ja'Aidi et al., 2004; Bakke et al., 2013), resulting in sand starvation over the debrite in distal settings (Sinclair and Tomasso, 2002; Kneller et al., 2016). The overlying Unit 4A can be traced laterally across the study area, with metre-scale thinning where the debrite is thickest (see CML-12; **Figure 3**). Apart from this, the advancing onlap geometries of the thin beds and the divergence in the overall NE-orientated paleocurrents (rose diagram Unit 4; **Figure 3**) indicate the progressive healing of the large-scale wavelength debrite relief, with some deflection of turbidity currents (**Figure 10**).

The thin sandstone beds of the upper part of Unit 4A healed the debrite high. However, the gravelly beds thin and fine from proximal to distal areas (western to eastern sectors), and the two debrites pinch out in proximal areas (western sector), suggesting subtle remnant topography (**Figure 8**). The different lateral continuity of individual beds is explained by different rheologies of individual sediment gravity flows, which affect the flow efficiency (Al Ja'Aidi et al., 2004). Cohesive debris flows are more influenced by irregular relief, while low-density turbidity currents are less affected by seafloor topography (Bakke et al., 2013; Soutter et al., 2019). This suggests that laterally continuous thick accumulations of lobe fringe deposits can develop on gentle topographies, while the submarine lobes' axial parts were restricted to lower relief areas. The interaction of thin-bedded turbidites successions with gentle topography has also been reported in other deep-water settings (i.e., “aggradational lobe fringes”; Spychala et al., 2017b). The deposition of lobe fringe successions reduced confinement, which enabled the deposition of the Unit 4B submarine lobe.

The submarine lobe is characterised by a progressive thinning and fining, developing pinch-out geometries and interfingering with Unit 4A in the area where the relief of the debrite is highest. The development of pinch-out geometries over the areas where the debrite shows a mounded relief and where the Unit 4A onlaps and thins suggests that the relief was not wholly healed with the deposition of Unit 4A and affected the parental flows of Unit 4B.

One explanation is that the exposure exhumes the Unit 4B lobe obliquely, with the medium-to thick-bedded lobe axis



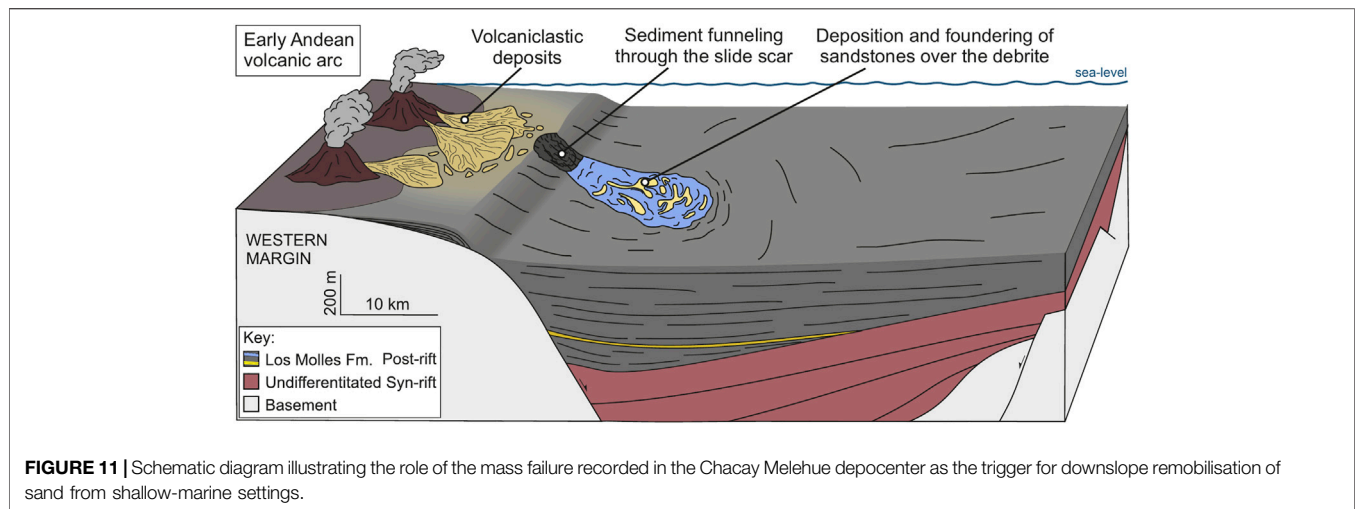
deposits in the westernmost sector (CML-1 to CML-4) transitioning into an HEB-dominated fringe, being highly impacted by gentle seafloor topography (Soutter et al., 2019; Privat et al., 2021). Alternatively, the seafloor relief could have promoted the modification of flow pathways and deflection of flows, thus changing the downdip orientation (**Figure 8**). All these scenarios suggest a confined and uncontained (see Southern et al., 2015) lobe-type depositional system. The precise dispersal pattern of the flows remains unknown due to the outcrop limitations. Nonetheless, the documented stratigraphic evolution reveals that long-lived debrite relief and progressive healing by deposition of aggradational lobe fringes enabled the progradation of sand-rich submarine lobe, albeit with changes in flow rheology the bed style and element-scale pinchout (**Figure 8**).

Another explanation is that the debrite relief in the central sector might have been rejuvenated through volume changes in the debrite due to differential compaction by loading the lobe itself in the proximal sector. However, it seems unlikely that the deposition of a 5.7 m thick lobe could promote a volume loss in an 8–47 m thick debrite, given that both units are separated by 8–22 m thick thin-bedded interval. In contrast, another two hypotheses are deemed more plausible; fluid loss and fault-controlled mechanical subsidence. Fluid loss-controlled evacuation could have promoted differential subsidence of the upper surface of the debrite and overlying units (e.g., Browne et al., 2020). Alternatively, given the early post-rift setting, mechanical subsidence by an east-facing and N-S striking fault (Mancada and Figueroa, 1995) could have generated more

accommodation in the western part of the study area (see Cristallini et al., 2006). However, this implies a very localised and rapid reactivation, and there is no other evidence for post-rift tectonism identified.

Origin and Role of the Mass-Wasting Process as a Trigger for Turbidite Systems Development

The emplacement of the >9.6 km long and erosional debrite in the Chacay Melehue depocentre reflects an abrupt change in sedimentation patterns, which were previously dominated by dilute mud-rich flows (Unit 1). The first significant sand influxes in the depocentre for ~6 Myr since the Aalenian (interval II of Gulisano and Gutiérrez Pleimling, 1995) are recorded by the sand-rich deposits (Unit 3) immediately overlying the debrite (**Figure 10**). The juxtaposition of sand-rich turbidites over debrites (metres to hundreds of meters thick) have been reported in other systems (Kleverlaan, 1987; Labaume et al., 1987; Payros et al., 1999; Fallgatter et al., 2017). These authors suggest that the debris flow underwent a period of mixing with ambient water, leading to the generation of an overriding co-genetic turbidity current. The foundering phenomenon reported here reveals a close spatiotemporal relationship between the debrite emplacement (Unit 2) and overlying sandstone deposition (Unit 3). An alternative mechanism is that the mass-failure event altered the basin margin physiography such that a sand source was captured. Mass-wasting processes responsible for the evacuation of material from shelf edge and upper slope areas alter the bathymetric configuration of basin



margins and promote the funnelling of sediment stored in shallow marine environments through slide scars (e.g., Moscardelli and Wood, 2008; Kneller et al., 2016; Steventon et al., 2020) (**Figure 11**). The role played as a trigger mechanism for sand delivery into deep-water setting by the mass-wasting event is a plausible scenario given the sand-starvation recorded in the coeval deposits of Los Molles Fm along the eastern margin of the Chacay Melehue depocentre (Veiga et al., 2013).

Given the palaeoflow and kinematic indicators, the thickness patterns of the studied units (**Figure 3B**), and previous studies on sediment supply from the volcanic arc (Vicente, 2005), we propose that the mass failure originated to the west of Chacay Melehue, where a major syn-rift fault is located close to the volcanic arc (<30 km; Manceda and Figueroa, 1995; De La Cruz and Suarez, 1997; Vicente, 2005). The role of the western volcanic arc as a source area for the early post-rift sediment supply in the Chacay Melehue depocentre is supported by the southeastwards directed paleocurrents measured in the Aalenian turbidite system at the base of the Los Molles Formation (Vicente, 2005; **Figure 2**) and the abundance of pyroclastic deposits within Los Molles Formation stratigraphy (Zöllner and Amos, 1973; Rosenfeld and Volldaeimer, 1980; Gulisano and Gutiérrez Pleimling, 1995; De La Cruz and Suarez, 1997; Llambías and Leanza, 2005). The oyster-bearing conglomerate megaclast and well-rounded volcanic epiclast within the matrix of the debrite reflect long-lived reworking in shallow-marine settings prior to the mass failure, suggesting a shallow-water origin or remobilization of older slope strata, including shallow-marine deposits. This could represent the downslope transfer of sand following the collapse of reworked volcaniclastic deposits along the magmatic arc (**Figure 9**). The evolution from the initial mass-wasting sediment supply responsible for erratically distributed foundered sandstone bodies (Unit 3) to a more mature system with the subtle distribution and diversity of lobe architectural elements (Unit 4) reflects the evolution to a more organised sediment supply

system (**Figure 10**). This was abruptly superseded by a return to sand-starved conditions dominated by dilute mud-rich flows and hemipelagic deposition until the end of the Lower Callovian (Gulisano and Gutiérrez Pleimling, 1995).

CONCLUSION

We document the anatomy and architecture of a >9.6 km long exhumed debrite and show how its twofold short- and long-wavelength relief and composition provided a likely input route for the subsequent sand-rich deep-water system and influenced flow behaviour depositional patterns. The basal surface of the debrite formed ramps and steps, indicating deep incision and entrainment of the substrate that included megaclasts. The foundering of overlying sands, their resultant geometry and spatial distribution, and the down-dip increase in mud content, indicate a dynamic and rugose upper surface to the debrite and complex flow-deposit interactions. The spatial distribution of the foundered sandstones indicates ground-hugging flows and the existence of debrite relief, which was progressively but not entirely healed by the submarine lobe. However, the architecture and facies distribution of the submarine lobe and their parental flows were still impacted by the long-lived, possibly rejuvenated, debrite-related topography.

The debrite emplacement coincided with an abrupt change in sediment supply to the Chacay Melehue depocentre from long-term mud-rich sedimentation to a transient sand-rich system. This change in depositional character is interpreted to have resulted from the funnelling of sediment stored in shallow marine environments to the west through a slide scar created by the debris flow, thus reconfiguring the sediment delivery pathway. Therefore, this study highlights that basin margin mass failures and their deposits play a key role in sediment dispersal patterns into deep-water settings, as well as the behaviour of subsequent sediment gravity flows travelling across their upper surface.

DATA AVAILABILITY STATEMENT

The original contributions presented in the study are included in the article/supplementary materials, further inquiries can be directed to the corresponding author.

AUTHOR CONTRIBUTIONS

AM-D took part in the data collection, analysis, figure drawing and wrote the manuscript. AP took part in data collection, suggested some modifications in figures, helped during the discussion of the main ideas and improved the writing. DH helped during the entire process (data collection, analysis and writing) and suggested to the author the potential of the outcrop belt that he had completed preliminary fieldwork with CJ, RD, YS and CS worked previously on it (Hodgson et al., 2019). IK helped with the discussion of the main ideas and contributed to the writing during the entire process. CJ, RD, YS and CS contributed to the data collection, discussion of ideas and improved the writing. EK field assisted AM-D during the

entire data collection campaign. ES contributed to the data collection and writing SF improved the writing and suggested modifications in the figures.

ACKNOWLEDGMENTS

This study is a collaboration between The University of Manchester (United Kingdom), The University of Leeds (United Kingdom), Leibniz University (Germany), The University of Liverpool (United Kingdom) and Centro de Investigaciones Geológicas (CIG) (Argentina). The authors would like to thank the local farmers of the Chacay Melehue region of Argentina for permission to carry out field studies on their land. The LOBE 3 consortium project of which this research forms a part is supported by sponsorship from Aker BP, BHP, BP, Equinor, HESS, Neptune, Petrobras, PetroChina, Total, Vår Energi and Woodside, for which the authors are grateful. We would like to thank reviewers Kei Ogata, Victoria Valdez and Mattia Marini for their thoughtful reviews, and Associate Editor Fabiano Gamberi for additional helpful comments that improved the manuscript.

REFERENCES

- Al Ja'Aidi, O. S., McCaffrey, W. D., and Kneller, B. C. (2004). Factors Influencing the deposit Geometry of Experimental Turbidity Currents: Implications for Sand-Body Architecture in Confined Basins. *Geol. Soc. London, Spec. Publ.* 222, 45–58. doi:10.1144/GSL.SP.2004.222.01.04
- Allen, J. R. L. (1982). *Sedimentary Structures, Their Character and Physical Basis*, 1. Amsterdam, The Netherlands: Elsevier, 663.
- Allen, J. R. L. (1971). Instantaneous Sediment Deposition Rates Deduced from Climbing-Ripple Cross-Lamination. *J. Geol. Soc.* 127, 553–561. doi:10.1144/gsl.jgs.1971.127.06.02
- Alves, T. M., and Cartwright, J. A. (2009). Volume Balance of a Submarine Landslide in the Espírito Santo Basin, Offshore Brazil: Quantifying Seafloor Erosion, Sediment Accumulation and Depletion. *Earth Planet. Sci. Lett.* 288, 572–580. doi:10.1016/j.epsl.2009.10.020
- Alves, T. M., and Lourenço, S. D. N. (2010). Geomorphologic Features Related to Gravitational Collapse: Submarine Landsliding to Lateral Spreading on a Late Miocene-Quaternary Slope (SE Crete, Eastern Mediterranean). *Geomorphology* 123, 13–33. doi:10.1016/j.geomorph.2010.04.030
- Alves, T. M. (2015). Submarine Slide Blocks and Associated Soft-Sediment Deformation in Deep-Water Basins: A Review. *Mar. Pet. Geology* 67, 262–285. doi:10.1016/j.marpetgeo.2015.05.010
- Armitage, D. A., Romans, B. W., Covault, J. A., and Graham, S. A. (2009). The Influence of Mass-Transport-Deposit Surface Topography on the Evolution of Turbidite Architecture: The Sierra Contreras, Tres Pasos Formation (Cretaceous), Southern Chile. *J. Sediment. Res.* 79, 287–301. doi:10.2110/jsr.2009.035
- Baas, J. H., Best, J. L., and Peakall, J. (2016). Comparing the Transitional Behaviour of Kaolinite and Bentonite Suspension Flows. *Earth Surf. Process. Landforms* 41, 1911–1921. doi:10.1002/esp.3959
- Baas, J. H., Best, J. L., and Peakall, J. (2011). Depositional Processes, Bedform Development and Hybrid Bed Formation in Rapidly Decelerated Cohesive (Mud-sand) Sediment Flows. *Sedimentology* 58, 1953–1987. doi:10.1111/j.1365-3091.2011.01247.x
- Baas, J. H., Best, J. L., Peakall, J., and Wang, M. (2009). A Phase Diagram for Turbulent, Transitional, and Laminar Clay Suspension Flows. *J. Sediment. Res.* 79, 162–183. doi:10.2110/jsr.2009.025
- Baker, M. L., Baas, J. H., Malarkey, J., Jacinto, R. S., Craig, M. J., Kane, I. A., et al. (2017). The Effect of clay Type on the Properties of Cohesive Sediment Gravity Flows and Their Deposits. *J. Sediment. Res.* 87, 1176–1195. doi:10.2110/jsr.2017.63
- Bakke, K., Kane, I. A., Martinsen, O. J., Petersen, S. A., Johansen, T. A., Hustoft, S., et al. (2013). Seismic Modeling in the Analysis of Deep-Water sandstone Termination Styles. *Bulletin* 97, 1395–1419. doi:10.1306/03041312069
- Blair, T. C., and McPherson, J. G. (1999). Grain-size and Textural Classification of Coarse Sedimentary Particles. *J. Sediment. Res.* 69, 6–19. doi:10.2110/jsr.69.6
- Boulestix, K., Poyatos-Moré, M., Hodgson, D. M., Flint, S. S., and Taylor, K. G. (2020). Fringe or Background: Characterizing Deep-Water Mudstones beyond the basin-floor Fan sandstone Pinchout. *J. Sediment. Res.* 90, 1678–1705. doi:10.2110/jsr.2020.048
- Brooks, H. L., Hodgson, D. M., Brunt, R. L., Peakall, J., and Flint, S. S. (2018). Exhumed Lateral Margins and Increasing Flow Confinement of a Submarine Landslide Complex. *Sedimentology* 65, 1067–1096. doi:10.1111/sed.12415
- Browne, G. H., Bull, S., Arnot, M. J., Boyes, A. F., King, P. R., and Helle, K. (2020). The Role of Mass Transport Deposits Contributing to Fluid Escape: Neogene Outcrop and Seismic Examples from north Taranaki, New Zealand. *Geo-mar Lett.* 40, 789–807. doi:10.1007/s00367-020-00641-z
- Bull, S., Cartwright, J., and Huuse, M. (2009). A Review of Kinematic Indicators from Mass-Transport Complexes Using 3D Seismic Data. *Mar. Pet. Geology* 26, 1132–1151. doi:10.1016/j.marpetgeo.2008.09.011
- Butler, R. W. H., Eggenhuisen, J. T., Haughton, P., and McCaffrey, W. D. (2016). Interpreting Syndepositional Sediment Remobilization and Deformation beneath Submarine Gravity Flows; a Kinematic Boundary Layer Approach. *J. Geol. Soc.* 173, 46–58. doi:10.1144/jgs2014-150
- Butler, R. W. H., and McCaffrey, W. D. (2010). Structural Evolution and Sediment Entrainment in Mass-Transport Complexes: Outcrop Studies from Italy. *J. Geol. Soc.* 167, 617–631. doi:10.1144/0016-76492009-041
- Cristallini, E., Bottesi, G., Gavarrino, A., Rodríguez, L., Tomezzoli, R., and Comeron, R. (2006). Synrift Geometry of the Neuquén Basin in Northeastern Neuquén Province, Argentina. *Spec. Pap. Geol. Soc. Am.* 407, 147–161. doi:10.1130/SPE407
- Cumberpatch, Z. A., Soutter, E. L., Kane, I. A., Casson, M., and Vincent, S. J. (2021). Evolution of a Mixed Siliciclastic-carbonate Deep-marine System on an Unstable Margin: The Cretaceous of the Eastern Greater Caucasus, Azerbaijan. *Basin Res.* 33, 612–647. doi:10.1111/bre.12488
- Dakin, N., Pickering, K. T., Mohrig, D., and Bayliss, N. J. (2013). Channel-like Features Created by Erosive Submarine Debris Flows: Field Evidence from the Middle Eocene Ainsa Basin, Spanish Pyrenees. *Mar. Pet. Geology* 41, 62–71. doi:10.1016/j.marpetgeo.2012.07.007
- Damborenea, S. E. (1990). Middle Jurassic Inoceramids from Argentina. *J. Paleontol.* 64, 736–759. doi:10.1017/s0022336000018965
- Davis, C., Haughton, P., McCaffrey, W., Scott, E., Hogg, N., and Kitching, D. (2009). Character and Distribution of Hybrid Sediment Gravity Flow Deposits

- from the Outer Forties Fan, Palaeocene Central North Sea, UKCS. *Mar. Pet. Geol.* 26, 1919–1939. doi:10.1016/j.marpetgeo.2009.02.015
- De La Cruz, R., and Suarez, M. (1997). El Jurásico de la cuenca de Neuquén en lonquimay, Chile: formación nacientes del biobío (38–39°S). *Rev. Geol. Chile* 24, 3–24.
- Dykstra, M. (2005). “Dynamics of Submarine Sediment Mass-Transport, from the Shelf to the Deep Sea,”. PhD Thesis Santa Barbara: University of California, Santa Barbara.
- Dykstra, M., Garyfalou, K., Kertznus, V., Kneller, B. C., Milana, J. P., Molinaro, M., et al. (2011). in *Mass-transport Deposits: Combining Outcrop Studies and Seismic Forward Modeling to Understand Lithofacies Distributions, Deformation, and Their Seismic Expression*. Editors H. Posamentier, P. Weimer, and C. Shipp (Denver: SEPM Special Publication), 95, 295–310.
- Eggenhuisen, J. T., McCaffrey, W. D., Haughton, P. D. W., and Butler, R. W. H. (2011). Shallow Erosion beneath Turbidity Currents and its Impact on the Architectural Development of Turbidite Sheet Systems. *Sedimentology* 58, 936–959. doi:10.1111/j.1365-3091.2010.01190.x
- Fairweather, L. (2014). “Mechanisms of Supra MTD Topography Generation and the Interaction of Turbidity Currents with Such Deposits,”. 242. PhD Thesis University of Aberdeen.
- Fallgatter, C., Kneller, B., Paim, P. S. G., and Milana, J. P. (2017). Transformation, Partitioning and Flow-deposit Interactions during the Run-Out of Megaflores. *Sedimentology* 64, 359–387. doi:10.1111/sed.12307
- Festa, A., Ogata, K., Pini, G. A., Dilek, Y., and Alonso, J. L. (2016). Origin and Significance of Olistostromes in the Evolution of Orogenic Belts: A Global Synthesis. *Gondwana Res.* 39, 180–203. doi:10.1016/j.gr.2016.08.002
- Flores, G. (1955). “Les résultats des études pour les recherches pétrolifères en Sicile: Discussion,” in Proceedings of the 4th World Petroleum Congress 1955 (Rome: Carlo Colombo), 121–122.
- Franzese, J. R., and Spalletti, L. A. (2001). Late Triassic-Early Jurassic continental Extension in Southwestern Gondwana: Tectonic Segmentation and Pre-break-up Rifting. *J. South Am. Earth Sci.* 14, 257–270. doi:10.1016/s0895-9811(01)00029-3
- Franzese, J., Spalletti, L., Pérez, I. G., and Macdonald, D. (2003). Tectonic and Paleoenvironmental Evolution of Mesozoic Sedimentary Basins along the Andean Foothills of Argentina (32°–54°S). *J. South Am. Earth Sci.* 16, 81–90. doi:10.1016/s0895-9811(03)00020-8
- Frey Martinez, J., Cartwright, J., and Hall, B. (2005). 3D Seismic Interpretation of Slump Complexes: Examples from the continental Margin of Israel. *Basin Res.* 17, 83–108. doi:10.1111/j.1365-2117.2005.00255.x
- Fugelli, E. M. G., and Olsen, T. R. (2007). Delineating Confined Slope Turbidite Systems Offshore mid-Norway: The Cretaceous Deep-marine Lysing Formation. *Bulletin* 91, 1577–1601. doi:10.1306/07090706137
- Gee, M. J. R., Gawthorpe, R. L., and Friedmann, S. J. (2006). Triggering and Evolution of a Giant Submarine Landslide, Offshore Angola, Revealed by 3D Seismic Stratigraphy and Geomorphology. *J. Sediment. Res.* 76, 9–19. doi:10.2110/jsr.2006.02
- Gulisano, C. A., Gutiérrez Pleimling, A. R., and Digregorio, J. H. (1984). Esquema estratigráfico de la secuencia jurásica del oeste de la provincia del Neuquén. IX Congr. *Geológico Argentino* 1, 236–259.
- Gulisano, C., and Gutiérrez Pleimling, A. R. (1995). Field Guide. The Jurassic of the Neuquén Basin. a) Neuquén Province: Asociación Geológica Argentina. *Serie E* 2, 1–111.
- Hampton, M. A., Lee, H. J., and Locat, J. (1995). Submarine Landslides. *Rev. Geophys.* 34, 33–59.
- Hansen, L. A. S., Hodgson, D. M., Pontén, A., Bell, D., and Flint, S. (2019). Quantification of basin-floor Fan Pinchouts: Examples from the Karoo Basin, South Africa. *Front. Earth Sci.* 7, 1–20. doi:10.3389/feart.2019.00012
- Hansen, L. A. S., Hodgson, D. M., Pontén, A., Thrana, C., and Obradors Latre, A. (2021). Mixed Axial and Transverse Deep-Water Systems: The Cretaceous post-rift Lysing Formation, Offshore Norway. *Basin Res.* 33, 2229–2251. doi:10.1111/bre.12555
- Haughton, P., Davis, C., McCaffrey, W., and Barker, S. (2009). Hybrid Sediment Gravity Flow Deposits - Classification, Origin and Significance. *Mar. Pet. Geology* 26, 1900–1918. doi:10.1016/j.marpetgeo.2009.02.012
- Haughton, P. D. W., Barker, S. P., and McCaffrey, W. D. (2003). ‘Linked’ Debris in Sand-Rich Turbidite Systems - Origin and Significance. *Sedimentology* 50, 459–482. doi:10.1046/j.1365-3091.2003.00560.x
- Hodgson, D. M. (2009). Distribution and Origin of Hybrid Beds in Sand-Rich Submarine Fans of the Tanqua Depocentre, Karoo Basin, South Africa. *Mar. Pet. Geol.* 26, 1940–1956. doi:10.1016/j.marpetgeo.2009.02.011
- Hodgson, D. M., Brooks, H. L., Ortiz-Karpf, A., Spychala, Y., Lee, D. R., and Jackson, C. A.-L. (2019). Entrainment and Abrasion of Megaclasts during Submarine Landsliding and Their Impact on Flow Behaviour. *Geol. Soc. Lond. Spec. Publications* 477, 223–240. doi:10.1144/sp477.26
- Howell, J. A., Schwarz, E., Spalletti, L. A., and Veiga, G. D. (2005). The Neuquén Basin: an Overview. *Geol. Soc. Lond. Spec. Publications* 252, 1–14. doi:10.1144/gsl.sp.2005.252.01.01
- Iverson, R. M. (1997). The Physics of Debris Flows. *Rev. Geophys.* 35, 245–296. doi:10.1029/97rg00426
- Jackson, C. A.-L., and Johnson, H. D. (2009). Sustained Turbidity Currents and Their Interaction with Debris-Related Topography; Labuan Island, Offshore NW Borneo, Malaysia. *Sediment. Geology* 219, 77–96. doi:10.1016/j.sedgeo.2009.04.008
- Jackson, C. A.-L. (2011). Three-dimensional Seismic Analysis of Megaclast Deformation within a Mass Transport deposit; Implications for Debris Flow Kinematics. *Geology* 39, 203–206. doi:10.1130/g31767.1
- Jobe, Z. R., Lowe, D. R., and Morris, W. R. (2012). *Climbing-ripple Successions in Turbidite Systems: Depositional Environments, Sedimentation Rates and Accumulation Times*, 59, 867–898. doi:10.1111/j.1365-3091.2011.01283.x
- Kamo, S. L., and Riccardi, A. C. (2009). A New U-Pb Zircon Age for an Ash Layer at the Bathonian-Callovian Boundary, Argentina. *Gff* 131, 177–182. doi:10.1080/11035890902867605
- Kane, I. A., and Pontén, A. S. M. (2012). Submarine Transitional Flow Deposits in the Paleogene Gulf of Mexico. *Geology* 40, 1119–1122. doi:10.1130/g33410.1
- Kane, I. A., Pontén, A. S. M., Vangdal, B., Eggenhuisen, J. T., Hodgson, D. M., and Spychala, Y. T. (2017). The Stratigraphic Record and Processes of Turbidity Current Transformation across Deep-marine Lobes. *Sedimentology* 64, 1236–1273. doi:10.1111/sed.12346
- Kleverlaan, K. (1987). Gordo Megabed: a Possible Seismitic in a Tortonian Submarine Fan, Tabernas basin, Province Almería, Southeast Spain. *Sediment. Geology* 51, 165–180. doi:10.1016/0037-0738(87)90047-9
- Kneller, B. C., and Branney, M. J. (1995). Sustained High-Density Turbidity Currents and the Deposition of Thick Massive Sands. *Sedimentology* 42, 607–616. doi:10.1111/j.1365-3091.1995.tb00395.x
- Kneller, B., Dykstra, M., Fairweather, L., and Milana, J. P. (2016). Mass-transport and Slope Accommodation: Implications for Turbidite sandstone Reservoirs. *Bulletin* 100, 213–235. doi:10.1306/09011514210
- Könitzer, S. F., Davies, S. J., Stephenson, M. H., and Leng, M. J. (2014). Depositional Controls on Mudstone Lithofacies in a Basinal Setting: Implications for the Delivery of Sedimentary Organic Matter. *J. Sediment. Res.* 84, 198–214. doi:10.2110/jsr.2014.18
- Labat, P., Mutti, E., and Seguret, M. (1987). Megaturbidites: A Depositional Model from the Eocene of the SW-Pyrenean Foreland basin, Spain. *Geo-Marine Lett.* 7, 91–101. doi:10.1007/bf02237988
- Leanza, H. A., Mazzini, A., Corfu, F., Llambías, E. J., Svensen, H., Planke, S., et al. (2013). The Chachil Limestone (Pliensbachian-Earliest Toarcian) Neuquén Basin, Argentina: U-Pb Age Calibration and its Significance on the Early Jurassic Evolution of Southwestern Gondwana. *J. South Am. Earth Sci.* 42, 171–185. doi:10.1016/j.jsames.2012.07.012
- Lee, C., Nott, J. A., Keller, F. B., and Parrish, A. R. (2004). Seismic Expression of the Cenozoic Mass Transport Complexes deepwater Tarfaya-Agadir Basin Offshore Morocco. *Proc. Annu. Offshore Technol. Conf.* 3, 1891–1908. doi:10.4043/16741-ms
- Legarreta, L. (1991). Evolution of a Callovian-Oxfordian Carbonate Margin in the Neuquén Basin of West-central Argentina: Facies, Architecture, Depositional Sequences and Global Sea-Level Changes. *Sediment. Geol.* 70 (2–4), 209–240. doi:10.1016/0037-0738(91)90142-Z
- Legarreta, L., and Gulisano, C. A. (1989). “Análisis estratigráfico secuencial de la Cuenca Neuquina (Triásico superior-Terciario inferior),” in *Cuencas Sedimentarias Argentinas*, 221–243.
- Legarreta, L., and Uliana, M. A. (1996). The Jurassic Succession in West-central Argentina: Stratal Patterns, Sequences and Paleogeographic Evolution. *Palaeogeogr. Palaeoclimatol. Palaeoecol.* 120, 303–330. doi:10.1016/0031-0182(95)00042-9

- Legros, F. (2002). Can Dispersive Pressure Cause Inverse Grading in Grain Flows? *J. Sediment. Res.* 72, 166–170. doi:10.1306/041301720166
- Lien, T. (2005). From Rifting to Drifting: Effects on the Development of Deep-Water Hydrocarbon Reservoirs in a Passive Margin Setting, Norwegian Sea. *Norwegian J. Geo.* 85 (4), 319–332.
- Llambías, E. J., Leanza, H. A., and Carbone, O. (2007). Evolución Tectono-magmática durante el pérmico al Jurásico temprano en la Cordillera del Viento (37°05'S - 37°15'S): Nuevas evidencias geológicas y geoquímicas Del Inicio de la Cuenca Neuquina. *Rev. La Asoc. Geol. Argentina* 62, 217–235.
- Llambías, E. J., and Leanza, H. A. (2005). Depósitos laháricos en la formación los molles en chacay melehue, neuquén: Evidencia de volcanismo jurásico en la cuenca neuquina. *Rev. La Asoc. Geol. Argentina* 60, 552–558.
- Llambías, E. J., Quenardelle, S., and Montenegro, T. (2003). The Choiyoi Group from central Argentina: A Subalkaline Transitional Alkaline Association in the Craton Adjacent to the Active Margin of the Gondwana Continent. *J. South. Am. Earth Sci.* 16, 243–257. doi:10.1016/S0895-9811(03)00070-1
- Lowe, D. R. (1982). Sediment Gravity Flows; II, Depositional Models with Special Reference to the Deposits of High-Density Turbidity Currents. *J. Sediment. Res.* 52, 279–297. doi:10.1306/2127f31-2b24-11d7-8648000102c1865d
- Lowe, D. R., and Guy, M. (2000). Slurry-flow Deposits in the Britannia Formation (Lower Cretaceous), North Sea: A New Perspective on the Turbidity Current and Debris Flow Problem. *Sedimentology* 47, 31–70. doi:10.1046/j.1365-3091.2000.00276.x
- Lucente, C. C., and Pini, G. A. (2003). Anatomy and Emplacement Mechanism of a Large Submarine Slide within a Miocene Foredeep in the Northern Apennines, Italy: A Field Perspective. *Am. J. Sci.* 303, 565–602. doi:10.2475/ajs.303.7.565
- Major, J. J., and Iverson, R. M. (1999). Debris-flow Deposition: Effects of Pore-Fluid Pressure and Friction Concentrated at Flow Margins. *Bull. Geol. Soc. Am.* 111, 1424–1434. doi:10.1130/0016-7606(1999)111<1424:dfdeop>2.3.co;2
- Manceda, R., and Figueroa, D. (1995). Inversion of the Mesozoic Neuquen Rift in the Malargue Fold and Thrust belt, Mendoza, Argentina. *Pet. Basins South. Am.* 62, 369–382.
- McClelland, H. L. O., Woodcock, N. H., and Gladstone, C. (2011). Eye and Sheath Folds in Turbidite Convolute Lamination: Aberystwyth Grits Group, Wales. *J. Struct. Geology* 33, 1140–1147. doi:10.1016/j.jsg.2011.05.007
- McGilvery, T. A., Cook, D. L., and Roberts, H. (2003). “The Influence of Local Gradients on Accommodation Space and Linked Depositional Elements across a Stepped Slope Profile, Offshore Brunei,” in *Shelf margin deltas and linked down slope petroleum systems: Global significance and future exploration potential: Gulf Coast Section SEPM 23rd Annual Research Conference*, 387–419. doi:10.5724/gcs.03.23.0387
- Migeon, S., Ceramicola, S., Praeg, D., Ducassou, E., Dano, A., Ketzer, J. M., et al. (2014). “Post-failure Processes on the Continental Slope of the Central Nile Deep-Sea Fan: Interactions between Fluid Seepage, Sediment Deformation and Sediment-Wave Construction,” in *Submarine Mass Movements and Their Consequences. Advances in Natural and Technological Hazards Research* (Cham: Springer), Vol 37, 117–127. doi:10.1007/978-3-319-00972-8_11
- Moscardelli, L., Wood, L., and Mann, P. (2006). Mass-transport Complexes and Associated Processes in the Offshore Area of Trinidad and Venezuela. *Bulletin* 90, 1059–1088. doi:10.1306/02210605052
- Moscardelli, L., and Wood, L. (2008). New Classification System for Mass Transport Complexes in Offshore Trinidad. *Basin Res.* 20, 73–98. doi:10.1111/j.1365-2117.2007.00340.x
- Mulder, T., and Alexander, J. (2001). The Physical Character of Subaqueous Sedimentary Density Flows and Their Deposits. *Sedimentology* 48, 269–299. doi:10.1046/j.1365-3091.2001.00360.x
- Mutti, E. (1977). Distinctive Thin-Bedded Turbidite Facies and Related Depositional Environments in the Eocene Hecho Group (South-central Pyrenees, Spain). *Sedimentology* 24, 107–131. doi:10.1111/j.1365-3091.1977.tb00122.x
- Nardin, T. R., Hein, F. J., Gorsline, D. S., and Edwards, B. D. (1979). A Review of Mass Movement Processes, Sediment and Acoustic Characteristics, and Contrasts in Slope and Base-Of-Slope Systems versus Canyon-fan-basin Floor Systems. *SEPM Spec. Publ.* 27, 61–73. doi:10.2110/pec.79.27.0061
- Nwoko, J., Kane, I., and Huuse, M. (2020a). Megaclasts within Mass-Transport Deposits: Their Origin, Characteristics and Effect on Substrates and Succeeding Flows. *Geol. Soc. Lond. Spec. Publications* 500, 515–530. doi:10.1144/sp500-2019-146
- Nwoko, J., Kane, I., and Huuse, M. (2020b). Mass Transport deposit (MTD) Relief as a Control on post-MTD Sedimentation: Insights from the Taranaki Basin, Offshore New Zealand. *Mar. Pet. Geology* 120, 104489. doi:10.1016/j.marpetgeo.2020.104489
- Ogata, K., Festa, A., Pini, G. A., and Alonso, J. L. (2019). “Submarine Landslide Deposits in Orogenic Belts: Olistostromes and Sedimentary Mélanges,” in *Submarine Landslides: Subaqueous Mass Transport Deposits from Outcrops to Seismic Profiles* (American Geophysical Union), 1–26.
- Ogata, K., Mountjoy, J. J., Pini, G. A., Festa, A., and Tinterri, R. (2014a). Shear Zone Liquefaction in Mass Transport deposit Emplacement: A Multi-Scale Integration of Seismic Reflection and Outcrop Data. *Mar. Geology* 356, 50–64. doi:10.1016/j.margeo.2014.05.001
- Ogata, K., Mutti, E., Pini, G. A., and Tinterri, R. (2012). Mass Transport-Related Stratal Disruption within Sedimentary Mélanges: Examples from the Northern Apennines (Italy) and South-central Pyrenees (Spain). *Tectonophysics* 568–569, 185–199. doi:10.1016/j.tecto.2011.08.021
- Ogata, K., Pogačnik, Ž., Pini, G. A., Tunis, G., Festa, A., Camerlenghi, A., et al. (2014b). The Carbonate Mass Transport Deposits of the Paleogene Friuli Basin (Italy/Slovenia): Internal Anatomy and Inferred Genetic Processes. *Mar. Geology* 356, 88–110. doi:10.1016/j.margeo.2014.06.014
- Ortiz-Karpf, A., Hodgson, D. M., Jackson, C. A.-L., and McCaffrey, W. D. (2017). Influence of Seabed Morphology and Substrate Composition on Mass-Transport Flow Processes and Pathways: Insights from the Magdalena Fan, Offshore Colombia. *J. Sediment. Res.* 87, 189–209. doi:10.2110/jsr.2017.10
- Ortiz-Karpf, A., Hodgson, D. M., and McCaffrey, W. D. (2015). The Role of Mass-Transport Complexes in Controlling Channel Avulsion and the Subsequent Sediment Dispersal Patterns on an Active Margin: The Magdalena Fan, Offshore Colombia. *Mar. Pet. Geology* 64, 58–75. doi:10.1016/j.marpetgeo.2015.01.005
- Owen, G. (1987). Deformation Processes in Unconsolidated Sands. *Geol. Soc. Lond. Spec. Publications* 29, 11–24. doi:10.1144/gsl.sp.1987.029.01.02
- Owen, G. (2003). Load Structures: Gravity-Driven Sediment Mobilization in the Shallow Subsurface. *Geol. Soc. Lond. Spec. Publications* 216, 21–34. doi:10.1144/gsl.sp.2003.216.01.03
- Pángaro, F., Pereira, D. M., and Micucci, E. (2009). El sinrift de la dorsal de Huinul, Cuenca Neuquina: Evolución y control sobre la estratigrafía y estructura del área. *Rev. La Asoc. Geol. Argentina* 65, 265–277.
- Payros, A., and Pujalte, V. (2019). “Eocene Mass-Transport Deposits in the Basque Basin (Western Pyrenees, Spain) Insights Into Mass-Flow Transformation and Bulldozing Processes,” in *Submarine Landslides: Subaqueous Mass Transport Deposits from Outcrops to Seismic Profiles*. Editors K. Ogata, A. Festa, and A. G. Pini (American Geophysical Union), 155–170. doi:10.1002/9781119500513.ch10
- Payros, A., Pujalte, V., and Orue-Etxebarria, X. (1999). The South Pyrenean Eocene Carbonate Megabreccias Revisited: New Interpretation Based on Evidence from the Pamplona Basin. *Sediment. Geology* 125, 165–194. doi:10.1016/s0037-0738(99)00004-4
- Pickering, K. T., and Corregidor, J. (2005). Mass-transport Complexes (MTCs) and Tectonic Control on basin-floor Submarine Fans, Middle Eocene, South Spanish Pyrenees. *J. Sediment. Res.* 75, 761–783. doi:10.2110/jsr.2005.062
- Prélat, A., Hodgson, D. M., and Flint, S. S. (2009). Evolution, Architecture and Hierarchy of Distributary Deep-Water Deposits: a High-Resolution Outcrop Investigation from the Permian Karoo Basin, South Africa. *Sedimentology* 56, 2132–2154. doi:10.1111/j.1365-3091.2009.01073
- Privat, A. M. J., Hodgson, D. M., Jackson, C. A., Schwarz, E., and Peakall, J. (2021). Evolution from Syn-rift Carbonates to Early post-rift Deep-marine Intrastope Lobes: The Role of Rift basin Physiography on Sedimentation Patterns. *Sedimentology* 68, 2563–2605. doi:10.1111/sed.12864
- Riccardi, A. C., Damborenea, S. E., Mancenido, M. O., and Leanza, H. A. (2011). *Megainvertebrados del Jurásico y su importancia geobiológica. Relat. del XVIII Congr. Neuquén: Geológico Argentino*, 441–464.
- Riccardi, A. C. (2008). The marine Jurassic of Argentina: A Biostratigraphic Framework. *Episodes* 31, 326–335. doi:10.18814/epiugs/2008/v31i3/007
- Riccardi, A., and Kamo, S. (2014). “Biostratigraphy and Geochronology of the Pliensbachian-Toarcian Boundary in Argentina,” in XIX Congr. Geológico Argentino, Córdoba, Argentina, Junio 2014, 9–11.
- Rosenfeld, U., and Volldaeimer, W. (1980). *Turbidite und andere Rhythmite im tieferen Jura des Neuquén-Beckens* Argentinien: Pascal and Francis Bibliographic Databases, 379–421.

- Sawyer, D. E., Flemings, P. B., Dugan, B., and Germaine, J. T. (2009). Retrogressive Failures Recorded in Mass Transport Deposits in the Ursa Basin, Northern Gulf of Mexico. *J. Geophys. Res. Solid Earth* 114, 1–20. doi:10.1029/2008jb006159
- Sinclair, H. D., and Tomasso, M. (2002). Depositional Evolution of Confined Turbidite Basins. *J. Sediment. Res.* 72, 451–456. doi:10.1306/111501720451
- Sobiesiak, M. S., Kneller, B., Alsop, G. I., and Milana, J. P. (2016). Internal Deformation and Kinematic Indicators within a Tripartite Mass Transport deposit, NW Argentina. *Sediment. Geology*. 344, 364–381. doi:10.1016/j.sedgeo.2016.04.006
- Southern, S. J., Patacci, M., Felletti, F., and McCaffrey, W. D. (2015). Influence of Flow Containment and Substrate Entrainment upon sandy Hybrid Event Beds Containing a Co-genetic Mud-Clast-Rich Division. *Sediment. Geology*. 321, 105–122. doi:10.1016/j.sedgeo.2015.03.006
- Soutter, E. L., Kane, I. A., Fuhrmann, A., Cumberpatch, Z. A., and Huuse, M. (2019). The Stratigraphic Evolution of Onlap in Siliciclastic Deep-Water Systems: Autogenic Modulation of Allogenic Signals. *J. Sediment. Res.* 89, 890–917. doi:10.2110/jsr.2019.49
- Soutter, E. L., Kane, I. A., and Huuse, M. (2018). Giant Submarine Landslide Triggered by Paleocene Mantle Plume Activity in the North Atlantic. *Geology* 46, 511–514. doi:10.1130/g40308.1
- Spalletti, L. A., Parent, H., Veiga, G. D., and Schwarz, E. (2012). Amonites y bioestratigrafía del Grupo Cuyo en la Sierra de Reyes (cuenca Neuquina central, Argentina) y su significado secuencial. *Andean Geol.* 39, 464–481. doi:10.5027/andgeov39n3-a06
- Spychala, Y. T., Hodgson, D. M., Prêlat, A., Kane, I. A., Flint, S. S., and Mountney, N. P. (2017a). Frontal and Lateral Submarine Lobe Fringes: Comparing Sedimentary Facies, Architecture and Flow Processes. *J. Sediment. Res.* 87, 75–96. doi:10.2110/jsr.2017.2
- Spychala, Y. T., Hodgson, D. M., Stevenson, C. J., and Flint, S. S. (2017b). Aggradational Lobe Fringes: The Influence of Subtle Intrabasinal Seabed Topography on Sediment Gravity Flow Processes and Lobe Stacking Patterns. *Sedimentology* 64, 582–608. doi:10.1111/sed.12315
- Stevenson, C. J., Jackson, C. A., Hodgson, D. M., Hubbard, S. M., and Eggenhuisen, J. T. (2015). Deep-water Sediment Bypass. *J. Sediment. Res.* 85 (9), 1058–1081. doi:10.2110/jsr.2015.63
- Stevenson, C. J., Peakall, J., Hodgson, D. M., Bell, D., and Privat, A. (2020). TB or Not TB: Banding in Turbidite Sandstones. *J. Sediment. Res.* 90, 821–842. doi:10.2110/jsr.2020.43
- Stevenson, M. J., Jackson, C. A., Johnson, H. D., and Hodgson, D. M. (2021). Evolution of a Sand-Rich Submarine Channel–Lobe System, and the Impact of Mass-Transport and Transitional-Flow Deposits on Reservoir Heterogeneity: Magnus Field, Northern North Sea. *Petroleum Geosci.* 27.
- Stevenson, M. J., Jackson, C. A.-L., Hodgson, D. M., and Johnson, H. D. (2020). Lateral Variability of Shelf-Edge and basin-floor Deposits, Santos Basin, Offshore Brazil. *J. Sediment. Res.* 90, 1198–1221. doi:10.2110/jsr.2020.14
- Stow, D. A. V., and Johansson, M. (2000). Deep-water Massive Sands: Nature, Origin and Hydrocarbon Implications. *Mar. Pet. Geology*. 17, 145–174. doi:10.1016/s0264-8172(99)00051-3
- Suárez, M., and De la Cruz, R. (1997). “Volcanismo pliniano del Lías durante los inicios de la cuenca de Neuquén, Cordillera del Viento, Neuquén, Argentina,” in *Congreso Geológico Chileno*, 266–270.
- Sumner, E. J., Amy, L. A., and Talling, P. J. (2008). Deposit Structure and Processes of Sand Deposition from Decelerating Sediment Suspensions. *J. Sediment. Res.* 78, 529–547. doi:10.2110/jsr.2008.062
- Talling, P. J., Amy, L. A., and Wynn, R. B. (2007). New Insight into the Evolution of Large-Volume Turbidity Currents: Comparison of Turbidite Shape and Previous Modelling Results. *Sedimentology* 54, 737–769. doi:10.1111/j.1365-3091.2007.00858.x
- Talling, P. J., Masson, D. G., Sumner, E. J., and Malgesini, G. (2012). Subaqueous Sediment Density Flows: Depositional Processes and deposit Types. *Sedimentology* 59, 1937–2003. doi:10.1111/j.1365-3091.2012.01353.x
- Tinterri, R. (2011). Combined Flow Sedimentary Structures and the Genetic Link between Sigmoidal-And Hummocky-Cross Stratification. *GeoActa* 10 (4), 1–43.
- Tinterri, R., Muzzi Magalhaes, P., Tagliaferri, A., and Cunha, R. S. (2016). Convolute Laminations and Load Structures in Turbidites as Indicators of Flow Reflections and Decelerations against Bounding Slopes. Examples from the Marnoso-Arenacea Formation (Northern Italy) and Annot Sandstones (South Eastern France). *Sediment. Geology*. 344, 382–407. doi:10.1016/j.sedgeo.2016.01.023
- Trabucho-Alexandre, J., Dirkx, R., Veld, H., Klaver, G., and De Boer, P. L. (2012). Toarcian Black Shales in the Dutch central Graben: Record of Energetic, Variable Depositional Conditions during an Oceanic Anoxic Event. *J. Sediment. Res.* 82, 104–120. doi:10.2110/jsr.2012.5
- Twiss, R. J., and Moores, E. M. (1992). *Structural Geology*. New York: W.H. Freeman and Company.
- Valdez, V., Milana, J. P., Sobiesiak, M. S., and Kneller, B. (2019). “The Carboniferous MTD Complex at La Peña Canyon, Paganzo Basin (San Juan, Argentina),” in *Submarine Landslides: Subaqueous Mass Transport Deposits from Outcrops to Seismic Profiles* (American Geophysical Union), p. 105–116.
- Van Der Merwe, W. C., Hodgson, D. M., and Flint, S. S. (2011). Origin and Terminal Architecture of a Submarine Slide: A Case Study from the Permian Vischkuil Formation, Karoo Basin, South Africa. *Sedimentology* 58, 2012–2038. doi:10.1111/j.1365-3091.2011.01249.x
- Van der Merwe, W. C., Hodgson, D. M., and Flint, S. S. (2009). Widespread Syn-Sedimentary Deformation on a Muddy Deep-Water basin-floor: The Vischkuil Formation (Permian), Karoo Basin, South Africa. *Basin Res.* 21, 389–406. doi:10.1111/j.1365-2117.2009.00396.x
- Veiga, G. D., Schwarz, E., and Spalletti, L. A. (2011). Análisis estratigráfico de la Formación Lotena (Calloviano superior- Oxfordiano inferior) en la Cuenca Neuquina Central, República Argentina. Integración de información de afloramientos y subsuelo. *Andean Geol.* 38, 171–197. doi:10.5027/andgeov38n1-a10
- Veiga, G. D., Schwarz, E., Spalletti, L. A., and Massafiero, J. L. (2013). Anatomy and Sequence Architecture of the Early Post-Rift in the Neuquen Basin (Argentina): A Response to Physiography and Relative Sea-Level Changes. *J. Sediment. Res.* 83, 746–765. doi:10.2110/jsr.2013.56
- Vergani, G. D., Tankard, A. J., Belotti, H. J., and Welsink, H. J. (1995/1904). *Tectonic Evolution and Paleogeography of the Neuquén Basin*. Argentina: Pet. basins South Am., 383–402.
- Vicente, J. C. (2005). Dynamic Paleogeography of the Jurassic Andean Basin: Pattern of Transgression and Localisation of Main Straits through the Magmatic Arc. *Rev. La Asoc. Geol. Argentina* 60, 221–250.
- Watt, S. F. L., Talling, P. J., Vardy, M. E., Masson, D. G., Henstock, T. J., Hühnerbach, V., et al. (2012). Widespread and Progressive Seafloor-Sediment Failure Following Volcanic Debris Avalanche Emplacement: Landslide Dynamics and Timing Offshore Montserrat, Lesser Antilles. *Mar. Geology*. 323–325, 69–94. doi:10.1016/j.margeo.2012.08.002
- Weaver, C. (1942). “A General Summary of the Mesozoic of South and Central America,” in Proceedings of the eighth American scientific congress held, Washington, May 10–18, 149–193.
- Weaver, C. (1931). *Paleontology of the Jurassic and Cretaceous of West Central Argentina*, 1. Seattle: Memoir University of Washington.
- Zöllner, W., and Amos, A. J. (1973). *Descripción geológica de la hoja 32b*. Chos Malal: Servicio Geológico Nacional, 97.

Conflict of Interest: The authors declare that the research was conducted in the absence of any commercial or financial relationships that could be construed as a potential conflict of interest.

Publisher’s Note: All claims expressed in this article are solely those of the authors and do not necessarily represent those of their affiliated organizations, or those of the publisher, the editors and the reviewers. Any product that may be evaluated in this article, or claim that may be made by its manufacturer, is not guaranteed or endorsed by the publisher.

Copyright © 2021 Martínez-Doñate, Privat, Hodgson, Jackson, Kane, Spychala, Duller, Stevenson, Keavney, Schwarz and Flint. This is an open-access article distributed under the terms of the Creative Commons Attribution License (CC BY). The use, distribution or reproduction in other forums is permitted, provided the original author(s) and the copyright owner(s) are credited and that the original publication in this journal is cited, in accordance with accepted academic practice. No use, distribution or reproduction is permitted which does not comply with these terms.



Thrust Faults Promoted Hydrocarbon Leakage at the Compressional Zone of Fine-Grained Mass-Transport Deposits

Qiliang Sun^{1,2*}, Xinong Xie¹, Shiguo Wu³ and Guorui Yin⁴

¹Hubei Key Laboratory of Marine Geological Resources, China University of Geosciences, Wuhan, China, ²Laboratory for Marine Mineral Resources, Qingdao National Laboratory for Marine Science and Technology, Qingdao, China, ³Laboratory of Marine Geophysics and Georesource, Institute of Deep-sea Science and Engineering, Chinese Academy of Sciences, Sanya, China, ⁴PetroChina Changqing Oil Field Company, Xian, China

OPEN ACCESS

Edited by:

Adam McArthur,
University of Leeds, United Kingdom

Reviewed by:

Xishuang Li,
Ministry of Natural Resources, China
Nan Wu,
Tongji University, China

*Correspondence:

Qiliang Sun
sunqiliang@cug.edu.cn

Specialty section:

This article was submitted to
Sedimentology, Stratigraphy and
Diagenesis,
a section of the journal
Frontiers in Earth Science

Received: 25 August 2021

Accepted: 15 October 2021

Published: 17 November 2021

Citation:

Sun Q, Xie X, Wu S and Yin G (2021)
Thrust Faults Promoted Hydrocarbon
Leakage at the Compressional Zone of
Fine-Grained Mass-
Transport Deposits.
Front. Earth Sci. 9:764319.
doi: 10.3389/feart.2021.764319

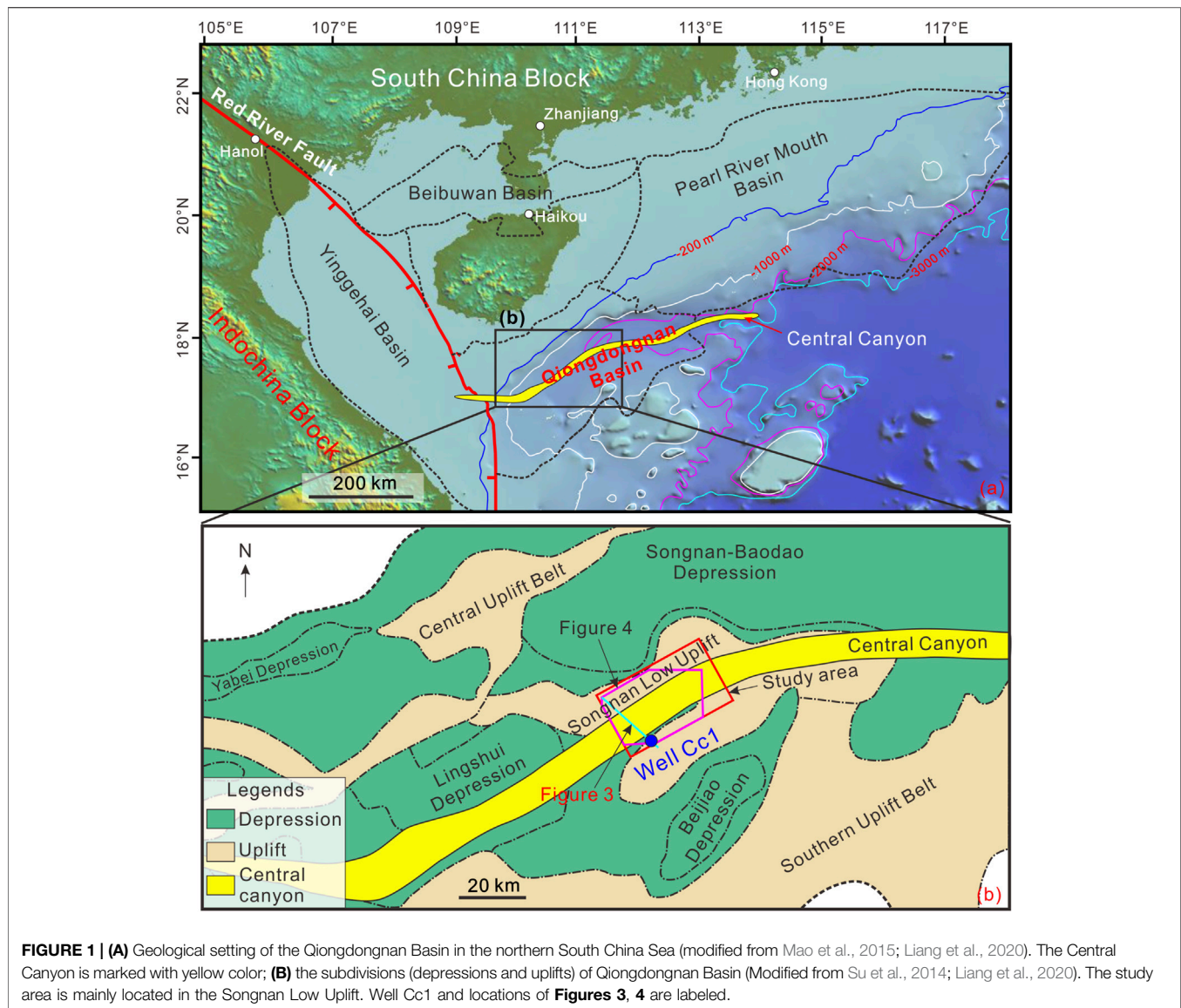
Fine-grained mass-transport deposits (MTDs), especially their compressional toe zones, are traditionally considered as effective seal in constraining the vertical fluid migration underneath. However, this study documents thrust faults at the compressional toe zone of fine-grained MTDs that could disaggregate the seal competence and promote vertical fluid flow. The investigated MTD referred to as MTD-a lies directly over a large hydrocarbon reservoir that is located within the Central Canyon of northern South China Sea, which is examined by using high-resolution 3D seismic and borehole data. Thrust faults and irregular blocks composed of coarse-grained sandstones are observed in the compressional zone of the MTD-a's toe. More importantly, seismic evidence (e.g., enhanced seismic reflections) suggests that a large amount of hydrocarbons from the underlying reservoir penetrated through the MTD-a along these thrust faults and charged into the coarse-grained sandstone blocks. This clear evidence of thrust faults compromising the MTD's seal effectiveness and thus facilitating the vertical fluid flow through the non-permeable strata demonstrate the importance of reassessing the seal capacity of MTD.

Keywords: mass-transport deposits, thrust fault, hydrocarbon leakage, block, South China Sea

INTRODUCTION

Mass-transport deposits (MTDs) widely occur at the continental margins and island flanks. They are usually composed of the headwall domain, translational domain, and toe domain (Martinsen, 1994; Lastras et al., 2002) and, accordingly, a systematic distribution of strain transferred from extensional structures in the headwall zone to compressional structures in the toe zone (Trincardi and Argnani, 1990; Canals et al., 2004; Frey Martinez et al., 2005). Thrust faults are an important component of MTDs at their compressional toe zones (Bull et al., 2009; Ogata et al., 2014; Alsop et al., 2017). They are usually caused by the translating material buttressing against a seabed obstacle (Lewis, 1971; Moscardelli et al., 2006) and typically affect the entire thickness of the MTD (Frey Martinez et al., 2005; Bull et al., 2009).

Thrust faults are mainly imaged by geophysical data (e.g., seismic reflection data) and shown as imbricated structures (Lamarche et al., 2008; Lackey et al., 2018). Because of the shear compaction and dewatering during the mass movement (e.g., decreases of porosities and permeability), MTDs,



especially those mainly composed of unlithified fine-grained sediments, are proposed as seal/barrier for the vertical fluid flow (Dugan, 2012; Alves et al., 2014; Sun and Alves, 2020). Furthermore, failed sediments are inclined to accumulate and thus thicken at the compressional toe zones (Moscardelli et al., 2006; Lamarche et al., 2008). Furthermore, the long-distance transportation of failed sediments at the toe zone is typically highly deformed and thus their fabrics are greatly damaged. These make the seal capacity of compressional toe zones of MTDs more effective. Although remnant blocks within MTDs are proposed to provide conduits for the vertical fluid flows (Alves et al., 2014; Gamboa and Alves, 2015; Cox et al., 2020), no vertical flow pathways have been identified at the compressional toe zone until now.

In this study, the investigated MTD, here referred to as MTD-a, is immediately lying on a large hydrocarbon reservoir in the Qiongdongnan Basin (QDNB) of the northern South China Sea, based on high-resolution 3D seismic and borehole data. The aims of this study are 1) to characterize the MTD-a, including the internal structures, blocks, and free gas within the MTD-a; 2) to assess the seal completeness of the compressional zone of MTD-a; and 3) to explore the vertical fluid migration system in the study area. This study demonstrates that free gas has leaked from the underlying hydrocarbon reservoir and migrated into the blocks through thrust faults. Therefore, it provides clear evidence for the thrust faults at the compressional zone of MTDs serving as fluid pathways for the first time, which suggests that the seal completeness of MTDs should be reassessed where the thrust faults develop.

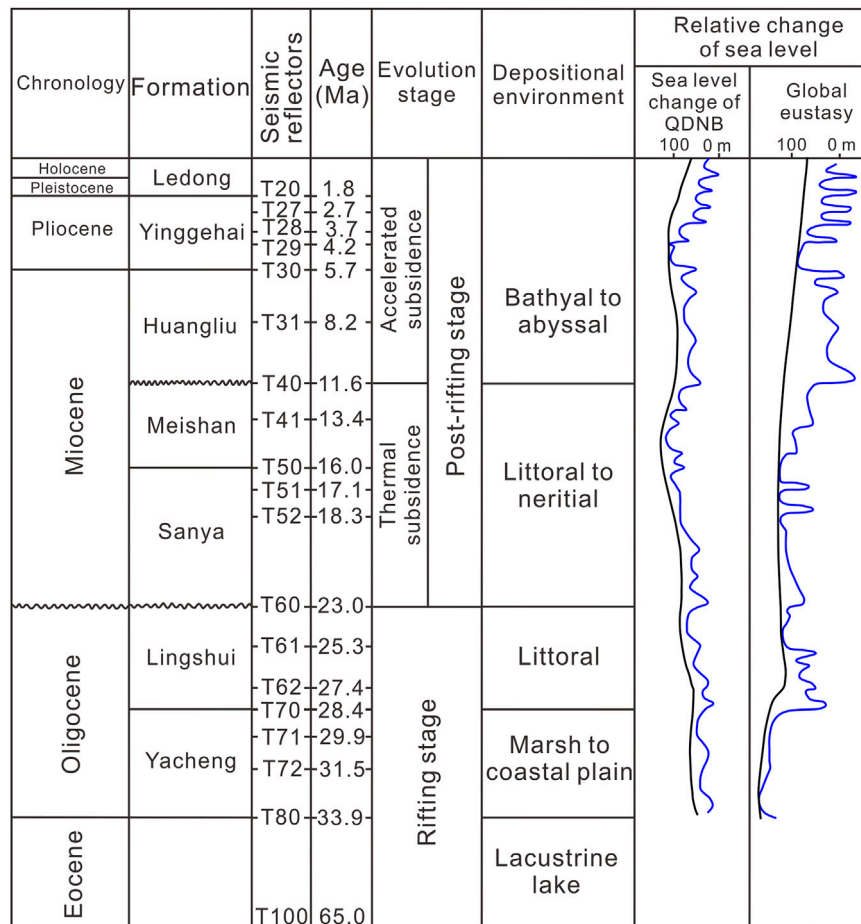


FIGURE 2 | Geological column of structural evolution stages, depositional environments, and relative sea-level changes in the Qiongdongnan Basin (modified from Su et al., 2014; Wu et al., 2018). The focused interval of this study is between T29 (4.2 Ma) and T28 (3.7 Ma).

GEOLOGICAL SETTING

The QDNB, one of the Cenozoic basins in the northern South China Sea located to the southeast of Hainan Island (**Figure 1**), covers an area of ~45,000 km² (Xie et al., 2008; Su et al., 2014). It comprises a few uplifts (massifs) and depressions (sags) (**Figure 1B**). The QDNB formed through two-stage tectonic evolutions, the Eocene-Oligocene rifting stage and the Miocene-to-Present post-rifting stage (**Figure 2**) (Gong and Li, 1997; Wu et al., 2008). During the rifting stage, deposits from the marsh-to-coastal plain Yacheng Formation and the littoral Lingshui Formation formed the main source rocks in the QDNB (Zhu et al., 2009). The post-rifting strata are composed of the littoral to neritic Sanya and Meishan formations, as well as the bathyal to abyssal Huangliu, Yinggehai, and Ledong formations (**Figure 2**) (Gong and Li, 1997; Zhu et al., 2009).

The QDNB is petroliferous, especially along the axis of the Central Canyon where numerous hydrocarbon fields have been found (Zhu et al., 2009; Wang Z. et al., 2015; Chen et al., 2015). The Central Canyon is > 425 km long and 3–16 km wide (Su

et al., 2014). Its deep incision into the strata as old as 8.2 Ma was fully filled at ~4.2 Ma (Liang et al., 2020). Moreover, the Central Canyon is mainly filled by the fine-grained mudstone and layered coarse-grained sandstone that acts as hydrocarbon reservoir (Wang Z. et al., 2015). After ~4.2 Ma, multiple MTDs are draped on the Central Canyon strata and formed the seal for the hydrocarbon reservoir (Liang et al., 2020).

MTDs widely developed in the QDNB and those in the southern QDNB (Huaguang Sag) are well studied (Sun et al., 2011; Wang et al., 2013; Wang D. et al., 2015). Those MTDs are cyclic with turbidities, such as triple packs of turbidities and MTDs, which are probably related to the sea-level changes (Sun et al., 2011). Moreover, the reactivation of major faults and associated volcanism in the late Miocene were proposed as the dominant trigger mechanisms for those MTDs (Wang et al., 2013). MTDs also frequently occurred in the central QDNB, as mentioned above (Liang et al., 2020). They may source from the northern slope area, western slope area, or Guangle Massif (Cheng et al., 2021) and mainly formed after ~4.2 Ma (Liang et al., 2020). Moreover, the slope overstepping

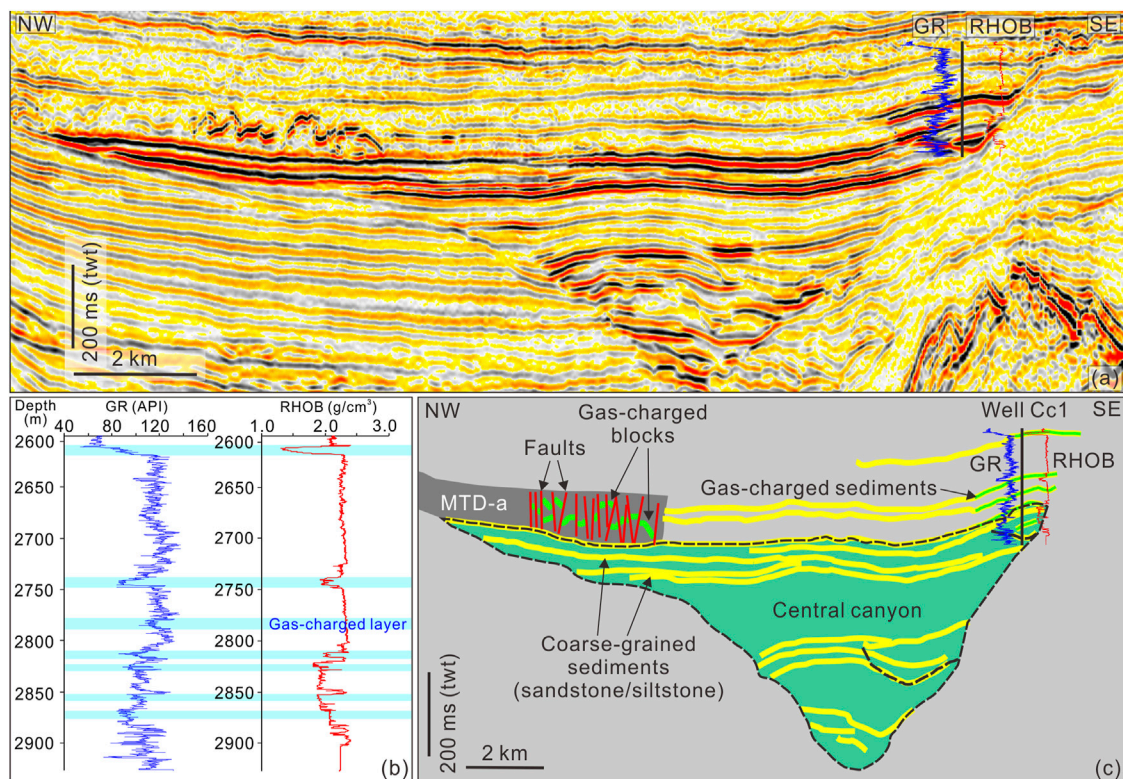


FIGURE 3 | (A) A 3D seismic profile crossing through the Well Cc1, mass transport deposit a (MTD-a), and Central Canyon. The location of Well Cc1 is marked with a black thick line, and loggings of gamma ray (GR, blue curve) and density (RHO, red curve) are also labeled. Gas-charged blocks (enhanced negative seismic reflections) within MTD-a and several gas-charged reservoirs within the Central Canyon are also clearly observed; **(B)** detailed characteristics of the GR and RHO curves. The gas-charged layers are marked with cyan squares, and they show sharp decreases of the GR and RHO; **(C)** interpretation of the seismic profile **(A)**. Green colors above the Central Canyon representing gas occurrences within the coarse-grained siltstone/sandstone.

resulting from high sediment supply likely triggered the slope instability (Qin et al., 2015; Liang et al., 2020). The occurrence of MTDs greatly changed the sediment dispersal pattern in the Central Canyon and thus influenced the hydrocarbon systems (reservoirs and seals) in the study area (Li et al., 2015; Liang et al., 2020).

DATA AND METHODS

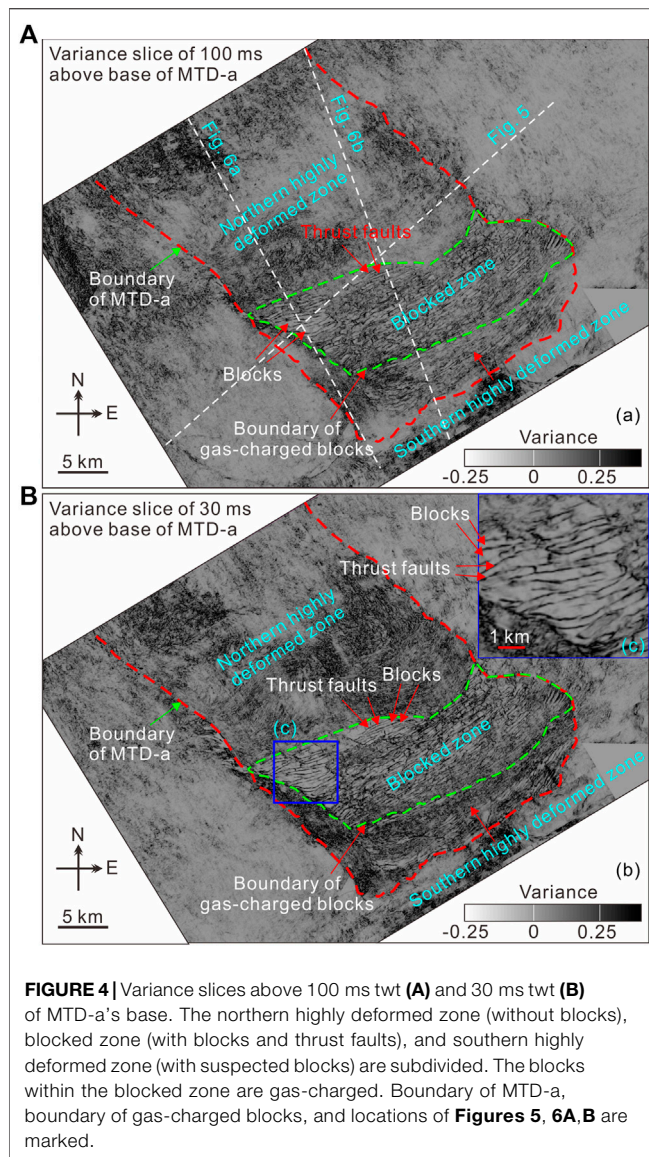
The time-migrated 3D seismic reflection data used in this study cover an area of $\sim 1,050 \text{ km}^2$ and were provided by the China National Offshore Oil Corporation (CNOOC). It was acquired in 2010 with 3,000-m-long streamers consisting of 240 channels at a spacing of 12.5 m and a sample rate of 4 ms. The bin spacing of the 3D seismic data is 25 m in the crossline and 12.5 m in the inline. The dominant frequency of the focused strata is $\sim 35 \text{ Hz}$, and thus, a vertical resolution of $\sim 20 \text{ m}$ is calculated, based on the strata velocity of 2,800 m/s from the Well Cc1 (Figure 1B). The 3D seismic reflection data are zero-phase processed and displayed with the Society of Exploration Geophysicists (SEG) normal polarity, whereby a downward increase in acoustic

impedance corresponds to a positive reflection event (red on seismic profiles) (Brown, 2004). Exploration well Cc1 is used for the lithology and strata velocity correlation. This well was located at the flank of the Central Canyon and drilled through several gas-charged sandstone layers (Figure 3). To better image the blocks, a variance attribute is used in this study (Figure 4). The variance attribute measures the variability in shape between seismic traces (Brown, 2004). It is directly derived from the processed data and thus is free of interpreter bias. The variance attribute is typically used to map structural and stratigraphic discontinuities (e.g., blocks, faults, and channels).

RESULTS

General Characteristics

The most prominent structure in the study area is the “V”-shaped Central Canyon. It quickly widens upward, and the fill sediments onlap onto its walls (Figures 3A,C, 6). The strata are mainly parallel/subparallel along the axis of the Central Canyon (Figure 5), and tapering/onlapping seismic



reflections are only occasionally observed along the axis (**Figure 5**). Many boreholes have targeted the hydrocarbon-rich Central Canyon and show that the strata mainly comprise fine-grained mudstone (Su et al., 2014; Liang et al., 2020). Coarse-grained siltstone and sandstone are also observed within the Central Canyon (**Figure 3C**), which is the main hydrocarbon reservoir (Wang Z. et al., 2015).

Multiple MTDs characterized by chaotic/blanking seismic reflections are observed above the Central Canyon, separated by continuous seismic surfaces (**Figures 3A, 5, 6**). This study is focused on the lowermost MTD, here named as MTD-a, which is directly draped on the Central Canyon (**Figure 3A**).

Many irregular blocks, characterized by short enhanced-amplitude, negative-polarity seismic reflections are identified inside the MTD-a (**Figures 3A, 5–7**). Although there is no well directly through these blocks, referencing the Well Cc1's layered

structure leads to a reasonable assumption that the blocks are mainly composed of sandstones (**Figure 3**). The blocks are surrounded by fine-grained mudstone (chaotic seismic reflections). The head zone of MTD-a has not been imaged, because of the limitation of 3D seismic coverage (**Figure 4**). It may have originated from the slope of QDNB to the north (**Figure 1**) and flowed toward the southeast part, judging from the extension of MTD-a (e.g., the direction of the lateral margins) (**Figure 4**). In the 3D seismic coverage, MTD-a could be divided into three subzones, such as a northern highly deformed zone, a blocked zone, and a southern highly deformed zone (**Figure 4**). No macroscopic blocks could be observed within the northern highly deformed zone, and it is mainly composed of chaotic seismic reflections (**Figure 6**). In the blocked zone, blocks float within the fine-grained strata (mudstone) and they are separated by high-angle thrust faults (**Figure 5**). There are suspected blocks observed on the variance slices in the highly deformed zone to the south (**Figure 4**). However, the seismic identification of these structures is not definitive (**Figures 3A, 6**).

Blocks

A total of 306 seismic-scale irregular blocks were recorded in the study area, characterized by enhanced seismic reflections as mentioned above, and are observed in the toe zone of MTD-a, especially those close to the southeastern boundary (blocked zone; green dashed zones in **Figure 4A**). However, the blocks are rarely observed at the distal termination part of MTD-a (southern highly deformed zone; **Figure 4A**). They are mainly bounded by thrust faults to their northwestern and southeastern sides and surrounded by chaotic seismic reflections (**Figures 6, 7**). In other words, they “float” within the chaotic seismic reflections. Although they are bounded by the thrust faults, the blocks are close to each other and some of them are even directly connected (**Figure 7**).

The irregular blocks are distributed in a linear fashion in plain view with orientations of E–W at the northwestern corner of the blocked zone and NE–SW at the left blocked zone (**Figure 4**). The dips of blocks are perpendicular to their strike extensions, and a few blocks are nearly horizontal elongation without any dips (**Figure 5**). The lengths of blocks range from ~0.20 to ~6.34 km with an average of ~1.48 km, while the blocks' widths are between ~0.10 and ~2.05 km, with an average of ~0.27 km. There is no apparent relationship between the lengths and widths of blocks ($R^2 = 0.03$; **Figure 8A**). The blocks cover an average area of ~0.44 km² ranging from ~0.02 to ~4.24 km². The areas of blocks are moderately related to their lengths ($R^2 = 0.54$; **Figure 8B**) and widths ($R^2 = 0.50$; **Figure 8C**). The average height of blocks is ~42.4 m (~30.3 ms twt), and thus the total volume of blocks (total area × average height) is ~5.68 km³.

Thrust Faults

A total of 350 seismic-scale thrust faults are identified in the blocked zone, which separate the blocks apart (**Figures 5, 7**).

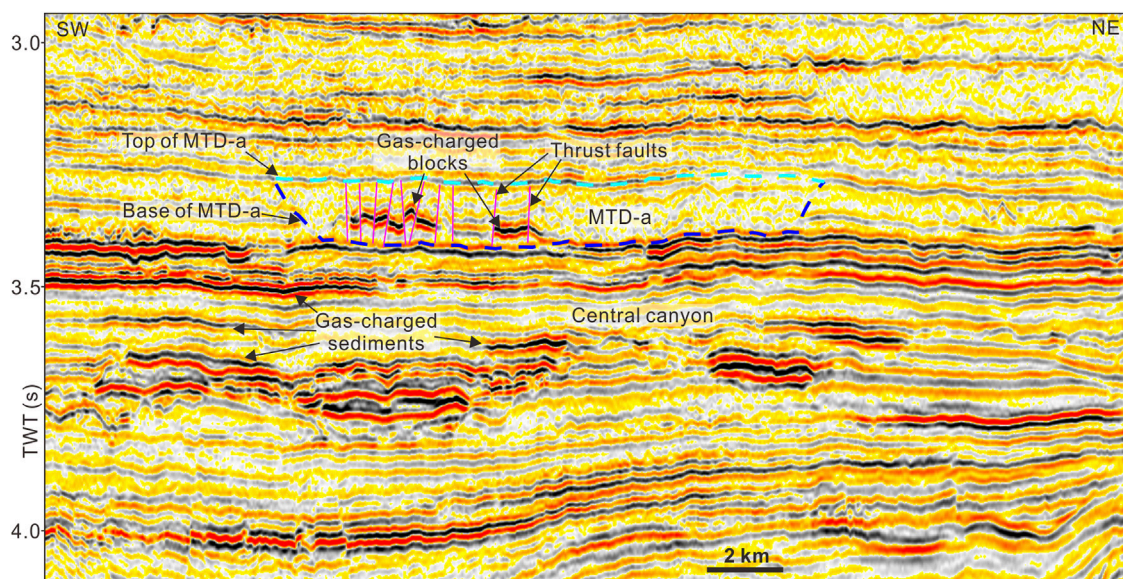


FIGURE 5 | A 3D seismic profile perpendicular to the extension of MTD-a shows its lateral boundaries. Gas-charged blocks are clearly observed within MTD-a. Central Canyon is mainly unfilled by layered sediments. Top and base of MTD-a are marked with cyan and blue dashed lines. See location in Figure 4.

Most of the thrust faults penetrate the whole MTD-a and terminate at the upper surface of the underlying Central Canyon strata (Figure 6). However, some small-scale thrust faults are mainly located in the upper part (above the blocks) of MTD-a (Figure 7B). The lengths of thrust faults range between ~0.27 and ~4.92 km with an average of ~1.4 km (Figure 8D). The strikes of thrust faults mainly extend between 40° and 70° (~84% of the total thrust faults) (Figure 8D). Less thrust faults strike 90°–147°, and they usually have short vertical extensions (<1.0 km; Figure 8D). Accordingly, the thrust faults mainly incline 130°–160° (37% of the total thrust faults) and 320°–340° (45% of the total thrust faults; Figure 8E). The dips of thrust faults range from ~25° to ~87°, and most of them (90%) are between ~30° and ~70° (Figure 8F).

Free Gas

Enhanced seismic anomalies characterized by negative reflections are observed in the Central Canyon and MTD-a's blocks (Figures 3A, 5–7), which is similar to the typical seismic characteristics of free gas (e.g., Judd and Hovland, 2007; Løseth et al., 2009; Sun et al., 2017). In fact, the exploration well Cc1 drilled through these enhanced seismic anomalies and confirmed that they are gas-charged sandstones (Figures 3A,C). Furthermore, these gas-charged sandstones characterized by sharp decreases of gamma ray (GR) and density (RHOB) are surrounded by fine-grained mudstones (Figure 3B). Accordingly, the irregular blocks within MTD-a could be interpreted as the counterparts of sandstones (Figure 3C). Moreover, the enhanced negative seismic reflections of blocks (Figures 3A, 5–7) indicate that free gas also charged into them. The average porosity of sandstone from well Cc1 is ~29.6%, and that of gas saturation

is ~71.2%; hence, the volume of free gas stored within the MTD-a' blocks can be as high as $\sim 1.2 \times 10^9 \text{ m}^3$.

DISCUSSION

Seal Disintegration and Vertical Hydrocarbon Migration

Fine-grained MTDs usually have decreased porosities and permeability, because of shear compaction and dewatering during their emplacement (Piper et al., 1997; Shipp et al., 2004; Sawyer et al., 2007; Dugan, 2012; Sun and Alves, 2020). Therefore, they usually act as effective seal to hinder the vertical migration of fluids (Alves et al., 2014; Sun and Alves, 2020). Remnant blocks that break through the MTDs could occasionally support the vertical fluid migration (Gamboa and Alves, 2015; Cox et al., 2020). However, there are no reports about vertical fluid flow in the compressional toe zone of MTDs as yet, where the compressional stress in the toe zone is proposed to strengthen the seal capacity of sediments.

Gas-charged blocks within MTD-a indicate that significant amounts of hydrocarbon have leaked from the gas field underlying the MTD-a (Figures 5–7). Because the blocks are surrounded by fine-grained sediments and are not directly connected with the underlying gas reservoir, the thrust faults are believed to act as the primary pathways for vertical fluid migration. Normally, the thrust faults in the compressional environment would be tight/closed to barrier fluids (Elmore et al., 2003; Micklethwaite, 2008). However, the thrust faults, likely with fractured medias, are mechanically weak zones (e.g., Lacroix et al., 2014; Cook et al., 2020), and they would likely reactivate under overpressure due to the underlying

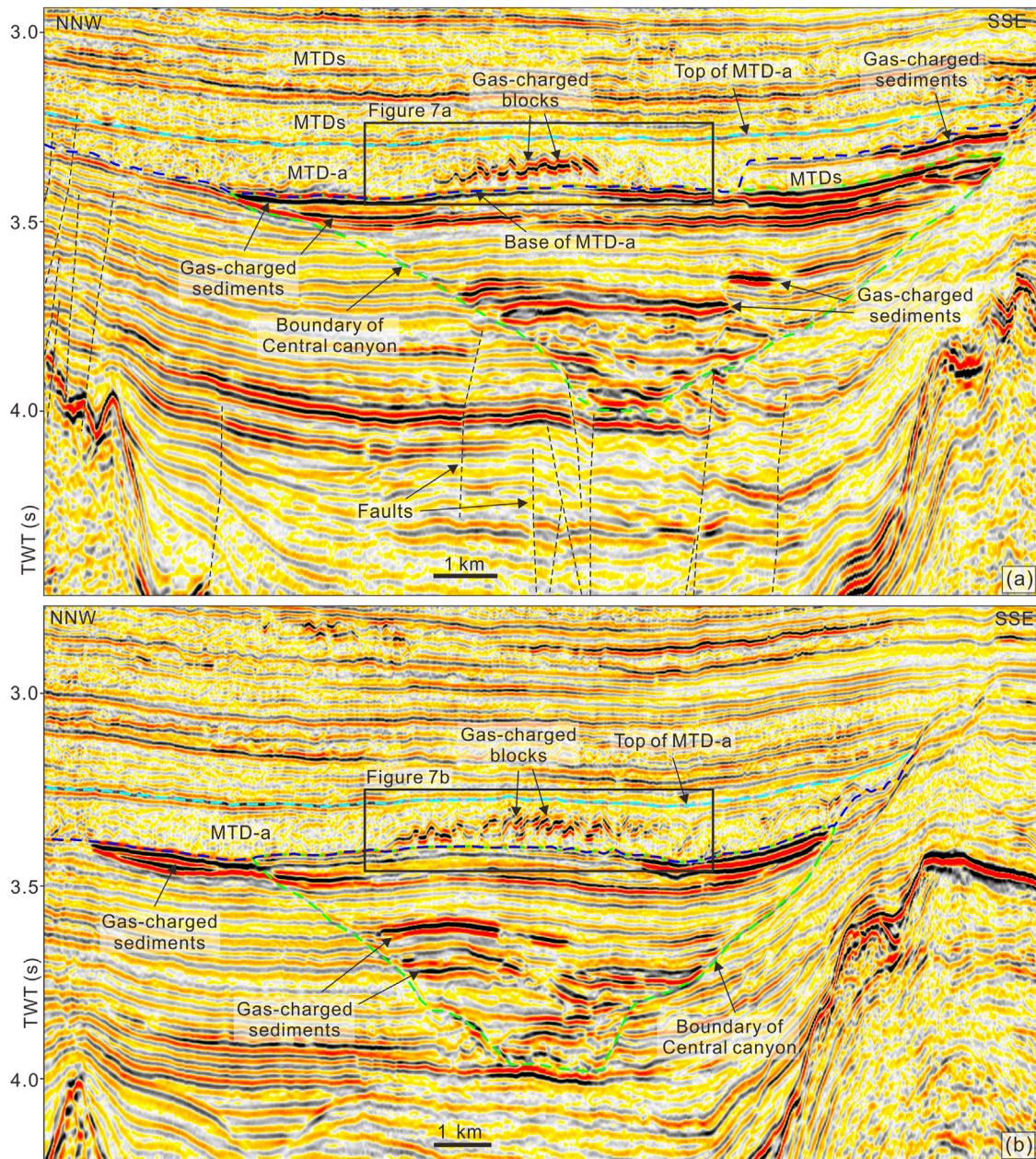


FIGURE 6 | 3D seismic profiles nearly parallel to the extension of MTD-a. MTD-a directly overlies the Central Canyon. Several gas-charged layers (enhanced negative seismic reflections), especially the uppermost layers, occurred within the Central Canyon. Gas-charged blocks within the MTD-a are surrounded by chaotic seismic reflections, interpreted as mudstone. Normal faults developed below the Central Canyon, and they provide the main pathways for the deep-seated hydrocarbon migration. Locations of **Figures 7A,B** are marked with black squares.

accumulation of hydrocarbons. Moreover, the blocked zone has weaker deformation compared to the northern and southern highly deformed zones where the failed sediments are probably fully mixed (**Figure 4**). The less mixture of sediments in the blocked zone would partly keep the fabrics of the strata, which is also in favor of reactivation of the thrust faults. This study documents the thrust faults at the compressional zone of MTDs to serve as fluid pathways for the first time. It also indicates that the fabric heterogeneity plays an important role

on the seal completeness, and certain factors (e.g., overpressure) may trigger the disintegration of seal, even for the fine-grained sediment-dominated compressional zones of MTDs.

Hydrocarbon Migration and Accumulation System

The hydrocarbon migration and accumulation system in the study area can be updated through this study together with

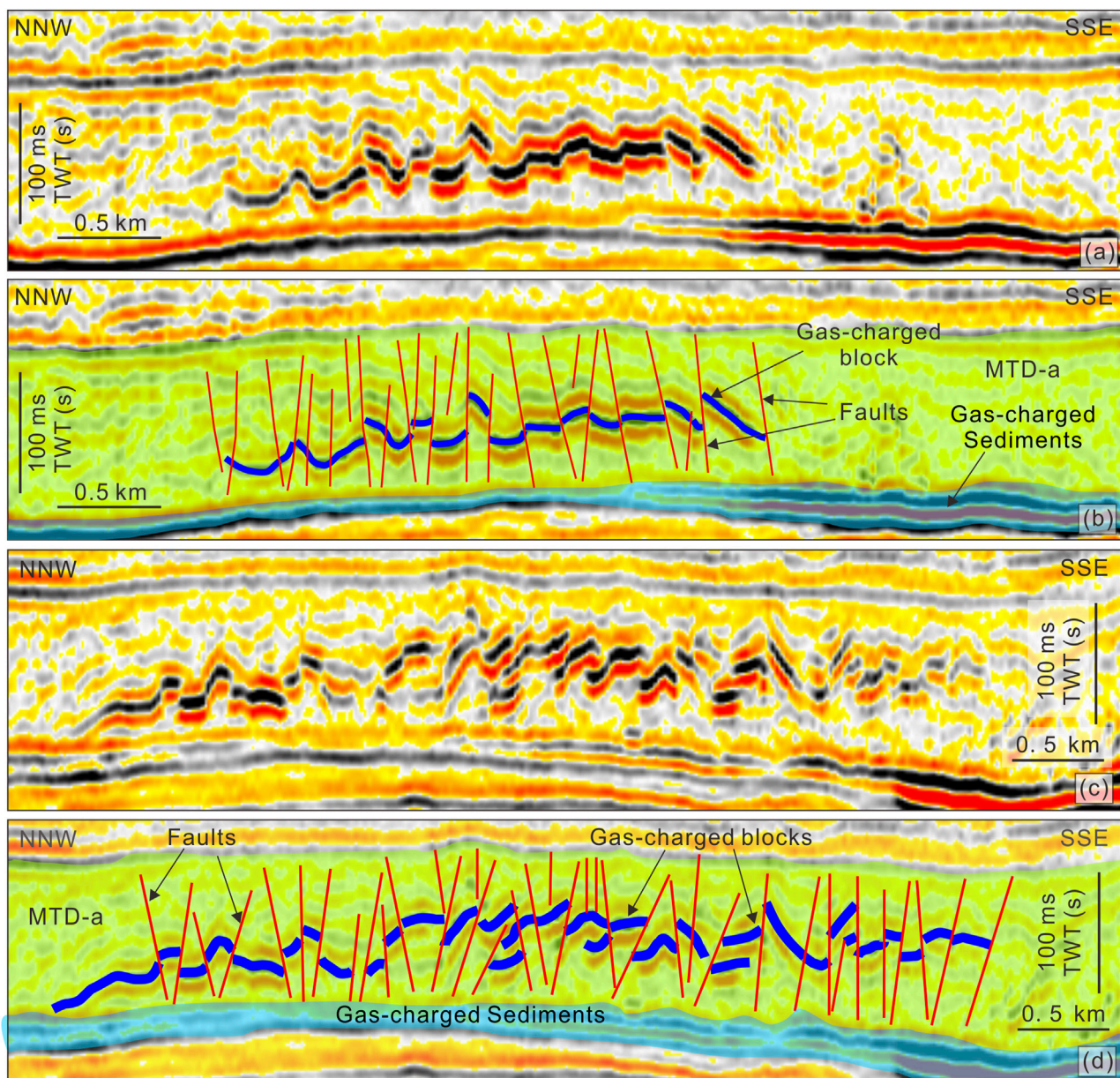
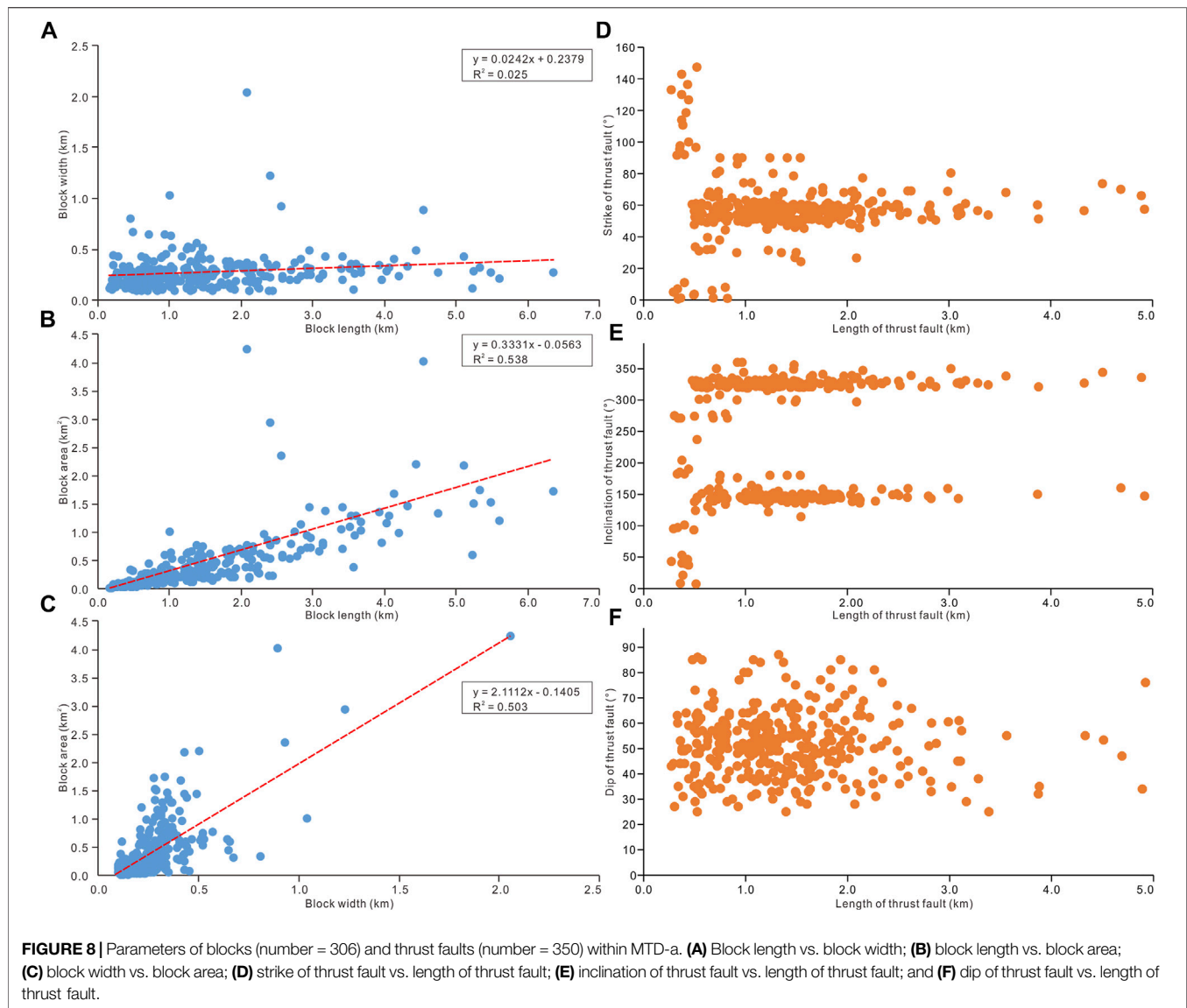


FIGURE 7 | Enlargements of seismic profiles **(A,C)** and their interpretation **(B,D)** showing the details of blocks and thrust faults within MTD-a. MTD-a directly lies on the hydrocarbon reservoir. Thrust faults link the underlying hydrocarbon reservoir and MTD-a' blocks and provide pathways for the gas leaking upward.

previous studies (Zhu et al., 2009; Li et al., 2017). The deeply buried coal-bearing strata of the lower Oligocene Yacheng Formation serve as the main source rock in the QDNB (Huang et al., 2003). The source rock entered the peak gas-generation window during the late Miocene and Pliocene (Zhu et al., 2009). Hydrocarbon (gas) from the source rock migrated upward mainly along tectonic faults (Figure 6A) and charged into the reservoir of the Central Canyon from the Pliocene to the present (Wang et al., 2014). Within the Central Canyon, the interconnected coarse-grained siltstone/sandstones provided

the lateral and vertical hydrocarbon migration pathways (Figure 9). Finally, the hydrocarbon accumulated at the topmost part of the Central Canyon where the reservoir is directly capped by the compressional zone of the fine-grained MTD-a (Figures 6, 9). The compressional zone of MTD-a is composed of a series of thrust faults and coarse-grained blocks, as mentioned above (Figure 3). Accompanying the gradual accumulation of hydrocarbon, overpressure would increase and finally exceed the yield strength of thrust faults. Therefore, the thrust faults would reactivate and allow



hydrocarbons would migrate upward along these faults and charge the blocks, as observed in this study (Figures 7, 9). This study indicates that a large amount of hydrocarbons ($\sim 1.2 \times 10^9 \text{ m}^3$) has probably leaked from the main reservoir of the gas field. Furthermore, the hydrocarbon system including the hydrocarbon migration, accumulation, and leakage in the study area is probably still dynamic, and special attention should be paid to the seal completeness where thrust faults occur within the MTDs.

CONCLUSION

This paper is focused on an MTD-a that is directly overlying a large gas field in the Central Canyon of the Qiongdongnan Basin (South China Sea), using high-resolution 3D seismic

data and borehole data. The main conclusions are drawn as follows:

- 1) Well-developed seismic-scale blocks and thrust faults are widespread in the compressional zone of MTD-a.
- 2) Thrust faults helped to penetrate MTD-a's seal and provided pathways for vertical fluid migration. This is the primary mechanism for as much as $1.2 \times 10^9 \text{ m}^3$ of hydrocarbon to escape from the reservoir, migrate upward, and eventually accumulate in the sandstone blocks.

This study provided clear evidence for the thrust faults promoting fluid flow at the compressional zone of MTDs for the first time, which has important implication on the assessment of MTDs' seal competence and underlying reservoir completeness. Moreover, reevaluation of other fine-grained

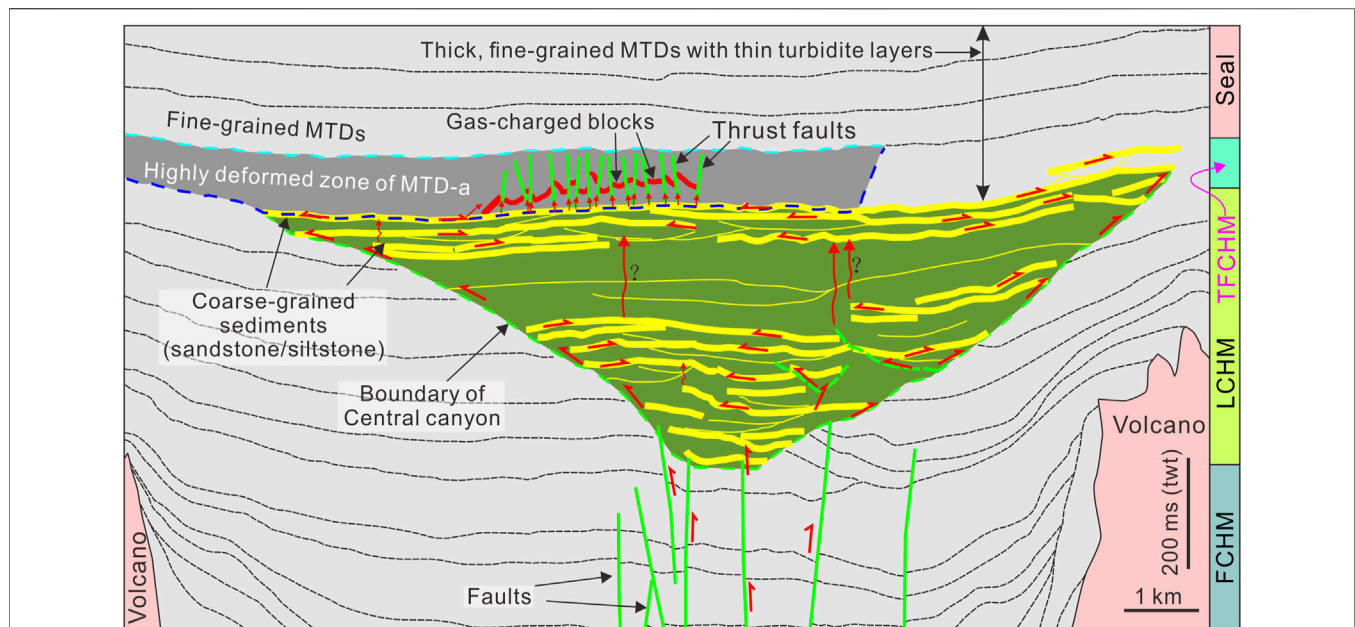


FIGURE 9 | Model for the hydrocarbon migration system in the study area. Fault-controlled hydrocarbon migration (FCHM): deep-seated normal faults provide pathways for the hydrocarbons migrating upward from the source rock; canyon-controlled hydrocarbon migration (CCHM): interconnected coarse-grained siltstone/sandstone provides pathways for the lateral/vertical hydrocarbon migration; thrust fault-controlled hydrocarbon migration (TFCHM): hydrocarbons leaked from the main reservoir in the Central Canyon and charged into blocks within MTD-a through the thrust faults.

MTDs assumed as seals is advised to reduce uncertainty in the sealing capacity of MTDs, particularly those displaying blocky and faulted textures.

DATA AVAILABILITY STATEMENT

The original contributions presented in the study are included in the article/Supplementary Material, further inquiries can be directed to the corresponding author.

AUTHOR CONTRIBUTIONS

QS is the principal author and primary seismic interpreter, and also writes and edits the paper. XX and SW contribute on the interpreting the seismic data, and writing/editing the paper. GY contributes on preparing the figures and writing the paper.

REFERENCES

- Alsop, G. I., Marco, S., Levi, T., and Weinberger, R. (2017). Fold and Thrust Systems in Mass Transport Deposits. *J. Struct. Geology*. 94, 98–115. doi:10.1016/j.jsg.2016.11.008
- Alves, T. M., Kurtsev, K., Moore, G. F., and Strasser, M. (2014). Assessing the Internal Character, Reservoir Potential, and Seal Competence of Mass-Transport Deposits Using Seismic Texture: A Geophysical and Petrophysical Approach. *Bulletin* 98, 793–824. doi:10.1306/09121313117

FUNDING

This work was supported by the National Key R&D Program of China (No. 2018YFC0310000), the National Scientific Foundation of China (No. 41676051), and the Fundamental Research Funds for the Central Universities-the China University of Geosciences (Wuhan) (No. CUG2106207).

ACKNOWLEDGMENTS

The China National Offshore Oil Company (CNOOC) is thanked for permission to release the data. The data that support the findings of this study are available from the CNOOC. Restrictions apply to the availability of these data, which were used under license for this study. Prof. Jingping Xu is thanked for his constructive comments on the original version of this paper. Guest Editor AM, Reviewer NW and an reviewer are thanked for their constructive comments that greatly improved this paper.

- Brown, A. R. (2004). Interpretation of Three-Dimensional Seismic Data: AAPG Memoir 42, in *SEG Investigations in Geophysics*. 6th Edn. Tulsa: The American Association of Petroleum Geologists and the Society of Exploration Geophysicists.
- Bull, S., Cartwright, J., and Huuse, M. (2009). A Review of Kinematic Indicators from Mass-Transport Complexes Using 3D Seismic Data. *Mar. Pet. Geology*. 26, 1132–1151. doi:10.1016/j.marpetgeo.2008.09.011
- Canals, M., Lastras, G., Urgeles, R., Casamor, J. L., Mienert, J., Cattaneo, A., et al. (2004). Slope Failure Dynamics and Impacts from Seafloor and Shallow Sub-seafloor Geophysical Data: Case Studies from the COSTA Project. *Mar. Geology*. 213, 9–72. doi:10.1016/j.margeo.2004.10.001

- Chen, H., Xie, X., Guo, J., Su, M., Zong, K., Shang, F., et al. (2015). Provenance of Central Canyon in Qiongdongnan Basin as Evidenced by Detrital Zircon U-Pb Study of Upper Miocene Sandstones. *Sci. China Earth Sci.* 58, 1337–1349. doi:10.1007/s11430-014-5038-6
- Cheng, C., Jiang, T., Kuang, Z., Ren, J., Liang, J., Lai, H., et al. (2021). Seismic Characteristics and Distributions of Quaternary Mass Transport Deposits in the Qiongdongnan Basin, Northern South China Sea. *Mar. Pet. Geology*. 129, 105118. doi:10.1016/j.marpetgeo.2021.105118
- Cook, A. E., Paganoni, M., Clennell, M. B., McNamara, D. D., Nole, M., Wang, X., et al. (2020). Physical Properties and Gashydrate at a Near-Seafloor Thrust Fault, Hikurangi Margin, New Zealand. *Geophys. Res. Lett.* 47, e2020GL088474. doi:10.1029/2020gl088474
- Cox, D. R., Huuse, M., Newton, A. M. W., Gannon, P., and Clayburn, J. (2020). Slip Sliding Away: Enigma of Large sandy Blocks within a Gas-Bearing Mass Transport deposit, Offshore Northwestern Greenland. *Bulletin* 104, 1011–1043. doi:10.1306/10031919011
- Dugan, B. (2012). Petrophysical and Consolidation Behavior of Mass Transport Deposits from the Northern Gulf of Mexico, IODP Expedition 308. *Mar. Geology*. 315–318, 98–107. doi:10.1016/j.margeo.2012.05.001
- Elmore, R. D., Blumstein, R., Engel, M., and Parnell, J. (2003). Palaeomagnetic Dating of Fluid Flow Events along the Moine Thrust Fault, Scotland. *J. Geochemical Exploration* 78–79, 45–49. doi:10.1016/s0375-6742(03)00069-4
- Frey Martinez, J., Cartwright, J., and Hall, B. (2005). 3D Seismic Interpretation of Slump Complexes: Examples from the continental Margin of Israel. *Basin Res.* 17, 83–108. doi:10.1111/j.1365-2117.2005.00255.x
- Gamboa, D., and Alves, T. M. (2015). Three-dimensional Fault Meshes and Multi-Layer Shear in Mass-Transport Blocks: Implications for Fluid Flow on continental Margins. *Tectonophysics* 647–648, 21–32. doi:10.1016/j.tecto.2015.02.007
- Gong, Z. S., and Li, S. T. (1997). *Continental Margin Basin Analysis and Hydrocarbon Accumulation of the Northern South China Sea*. Beijing: Science Press.
- Huang, B., Xiao, X., and Li, X. (2003). Geochemistry and Origins of Natural Gases in the Yinggehai and Qiongdongnan Basins, Offshore South China Sea. *Org. Geochem.* 34, 1009–1025. doi:10.1016/s0146-6380(03)00036-6
- Judd, A. G., and Hovland, M. (2007). *Seabed Fluid Flow: The Impact on Geology, Biology and the marine Environment*. Cambridge: Cambridge University Press.
- Lackey, J., Moore, G., and Strasser, M. (2018). Three-dimensional Mapping and Kinematic Characterization of Mass Transport Deposits along the Outer Kumano Basin and Nankai Accretionary Wedge, Southwest Japan. *Prog. Earth Planet. Sci.* 5, 65. doi:10.1186/s40645-018-0223-4
- Lacroix, B., Travé, A., Buatier, M., Labaume, P., Vennemann, T., and Dubois, M. (2014). Syntectonic Fluid-Flow along Thrust Faults: Example of the South-Pyrenean Fold-And-Thrust belt. *Mar. Pet. Geology*. 49, 84–98. doi:10.1016/j.marpetgeo.2013.09.005
- Lamarche, G., Joanne, C., and Collot, J. Y. (2008). Successive, Large Mass-Transport Deposits in the South Kermadec Fore-Arc basin, New Zealand: the Matakaoa Submarine Instability Complex. *Geochem. Geophys. Geosyst.* 9, Q04001. doi:10.1029/2007gc001843
- Lastras, G., Canals, M., Hughes-Clarke, J. E., Moreno, A., De Batist, M., Masson, D. G., et al. (2002). Seafloor Imagery from the BIG'95 Debris Flow, Western Mediterranean. *Geol* 30, 871–874. doi:10.1130/0091-7613(2002)030<0871:siftbd>2.0.co;2
- Lewis, K. B. (1971). Slumping on a Continental Slope Inclined at 1–4°. *Sedimentology*. 16, 97–110. doi:10.1111/j.1365-3091.1971.tb00221.x
- Li, W., Alves, T. M., Wu, S., Völker, D., Zhao, F., Mi, L., et al. (2015). Recurrent Slope Failure and Submarine Channel Incision as Key Factors Controlling Reservoir Potential in the South China Sea (Qiongdongnan Basin, South Hainan Island). *Mar. Pet. Geology*. 64, 17–30. doi:10.1016/j.marpetgeo.2015.02.043
- Li, X. S., Zhang, Y. Z., Yang, X. B., Xu, X. F., Zhang, J. X., and Man, X. (2017). New Understandings and Achievements of Natural Gas Exploration in the Yinggehai-Qiongdongnan basin, South China Sea. *China Offshore Oil and Gas* 29, 1–11. doi:10.11935/j.issn.1673-1506.2017.06.001
- Liang, C., Liu, C., Xie, X., Yu, X., He, Y., Chen, H., et al. (2020). The Role of Large-Scale Mass Wasting Processes in the Sediment Dispersal Pattern in the Deep-Water Central Canyon of the Northwestern South China Sea. *Mar. Pet. Geology*. 122, 104693. doi:10.1016/j.marpetgeo.2020.104693
- Løseth, H., Gading, M., and Wensaas, L. (2009). Hydrocarbon Leakage Interpreted on Seismic Data. *Mar. Pet. Geol.* 26, 1304–1309. doi:10.1016/j.marpetgeo.2008.09.008
- Mao, K., Xie, X., Xie, Y., Ren, J., and Chen, H. (2015). Post-rift Tectonic Reactivation and its Effect on Deep-Water Deposits in the Qiongdongnan Basin, Northwestern South China Sea. *Mar. Geophys. Res.* 36, 227–242. doi:10.1007/s11001-015-9248-x
- Martinsen, O. (1994). “Mass Movements,” in *The Geological Deformation of Sediments*. Editor A. Maltman (London: Chapman & Hall), 127–165. doi:10.1007/978-94-011-0731-0_5
- Micklethwaite, S. (2008). Optimally Oriented “Fault-valve” Thrusts: Evidence for Aftershockrelated Fluid Pressure Pulses? *Geochem. Geophys. Geosyst.* 9, Q04012. doi:10.1029/2007gc001916
- Moscaredelli, L., Wood, L., and Mann, P. (2006). Mass-transport Complexes and Associated Processes in the Offshore Area of Trinidad and Venezuela. *Bulletin* 90, 1059–1088. doi:10.1306/02210605052
- Ogata, K., Pogačnik, Ž., Pini, G. A., Tunis, G., Festa, A., Camerlenghi, A., et al. (2014). The Carbonate Mass Transport Deposits of the Paleogene Friuli Basin (Italy/Slovenia): Internal Anatomy and Inferred Genetic Processes. *Mar. Geology*. 356, 88–110. doi:10.1016/j.margeo.2014.06.014
- Piper, D. J. W., Pirmez, C., Manley, P. L., Long, D., Food, R. D., Normark, W. R., et al. (1997). “Mass-transport Deposits of the Amazon Fan,” in *The Proceedings of the Ocean Drilling Program, Scientific Results*. Editors R.D. Flood, D.J.W. Piper, A. Klaus, and L.C. Peterson (College Station, USA: Ocean Drilling Program), 109–146. doi:10.2973/odp.proc.sr.155.212.1997
- Qin, Z., Wu, S., Wang, D., Li, W., Gong, S., Mi, L., et al. (2015). Mass Transport Deposits and Processes in the north Slope of the Xisha Trough, Northern South China Sea. *Acta Oceanol. Sin.* 34, 117–125. doi:10.1007/s13131-015-0608-9
- Sawyer, D. E., Flemings, P. B., Shipp, R. C., and Winker, C. D. (2007). Seismic Geomorphology, Lithology, and Evolution of the Late Pleistocene Mars-Ursa Turbidite Region, Mississippi Canyon Area, Northern Gulf of Mexico. *Bulletin* 91, 215–234. doi:10.1306/08290605190
- Shipp, R. C., Nott, J. A., and Newlin, J. A. (2004). “Physical Characteristics and Impact of Mass Transport Complexes on deepwater Jetted Conductors and Suction Anchor Piles,” in *Offshore Technology Conference* (Houston, Texas: Extended Abstract), OTC16751. doi:10.4043/16751-ms
- Su, M., Xie, X., Xie, Y., Wang, Z., Zhang, C., Jiang, T., et al. (2014). The Segmentations and the Significances of the central canyon System in the Qiongdongnan basin, Northern South China Sea. *J. Asian Earth Sci.* 79, 552–563. doi:10.1016/j.jseas.2012.12.038
- Sun, Q.-L., Wu, S.-G., Lüdmann, T., Wang, B., and Yang, T.-T. (2011). Geophysical Evidence for Cyclic Sediment Deposition on the Southern Slope of Qiongdongnan Basin, South China Sea. *Mar. Geophys. Res.* 32, 415–428. doi:10.1007/s11001-011-9121-5
- Sun, Q., Alves, T., Xie, X., He, J., Li, W., and Ni, X. (2017). Free Gas Accumulations in Basal Shear Zones of Mass-Transport Deposits (Pearl River Mouth Basin, South China Sea): An Important Geohazard on continental Slope Basins. *Mar. Pet. Geology*. 81, 17–32. doi:10.1016/j.marpetgeo.2016.12.029
- Sun, Q. L., and Alves, T. M. (2020). Petrophysics of fine-grained Mass-Transport Deposits: A Critical Review. *J. Asian Earth Sci.* 192, 10429. doi:10.1016/j.jseas.2020.104291
- Trincardi, F., and Argnani, A. (1990). Gela Submarine Slide: a Major basin-wide Event in the Plio-Quaternary Foredeep of Sicily. *Geo-Marine Lett.* 10, 13–21. doi:10.1007/bf02431017
- Wang, D., Wu, S., Qin, Z., Spence, G., and Lü, F. (2013). Seismic Characteristics of the Huaguang Mass Transport Deposits in the Qiongdongnan Basin, South China Sea: Implications for Regional Tectonic Activity. *Mar. Geology*. 346, 165–182. doi:10.1016/j.margeo.2013.09.003
- Wang, D., Wu, S., Yao, G., and Wang, W. (2015). Architecture and Evolution of Deep-Water Cyclic Deposits in the Qiongdongnan Basin, South China Sea: Relationship with the Pleistocene Climate Events. *Mar. Geology*. 370, 43–54. doi:10.1016/j.margeo.2015.10.002
- Wang, Z., Liu, Z., Cao, S., Sun, Z., Zuo, Q., Wang, Y., et al. (2014). Vertical Migration through Faults and Hydrocarbon Accumulation Patterns in deepwater Areas of the Qiongdongnan Basin. *Acta Oceanol. Sin.* 33, 96–106. doi:10.1007/s13131-014-0579-2

- Wang, Z., Sun, Z., Zhu, J., Guo, M., and Jiang, R. (2015). Natural Gas Geological Characteristics and Great Discovery of Large Gas fields in Deep-Water Area of the Western South China Sea. *Nat. Gas Industry B* 2, 489–498. doi:10.1016/j.ngib.2016.03.001
- Wu, S. G., Yuan, S. Q., Zhang, G. C., Ma, Y. B., Mi, L. J., and Xu, N. (2008). Seismic Characteristics of a Reef Carbonate Reservoir and Implications for Hydrocarbon Exploration in Deep Water of the Qiongdongnan Basin, Northern South China Sea. *Mar. Pet. Geol.* 26, 817–823.
- Wu, W., Li, Q., Yu, J., Lin, C. S., Li, D., and Yang, T. (2018). The central canyon Depositional Patterns and Filling Process in East of Lingshui Depression, Qiongdongnan Basin Northern South China Sea. *Geol. J.* 1, 1–18. doi:10.1002/gj.3143
- Xie, X., Müller, R. D., Ren, J., Jiang, T., and Zhang, C. (2008). Stratigraphic Architecture and Evolution of the continental Slope System in Offshore Hainan, Northern South China Sea. *Mar. Geology.* 247, 129–144. doi:10.1016/j.margeo.2007.08.005
- Zhu, W., Huang, B., Mi, L., Wilkins, R. W. T., Fu, N., and Xiao, X. (2009). Geochemistry, Origin, and Deep-Water Exploration Potential of Natural Gases in the Pearl River Mouth and Qiongdongnan Basins, South China Sea. *Bulletin* 93, 741–761. doi:10.1306/02170908099

Conflict of Interest: GY was employed by the company PetroChina Changqing Oil Field Company.

The remaining authors declare that the research was conducted in the absence of any commercial or financial relationships that could be construed as a potential conflict of interest.

Publisher's Note: All claims expressed in this article are solely those of the authors and do not necessarily represent those of their affiliated organizations, or those of the publisher, the editors and the reviewers. Any product that may be evaluated in this article, or claim that may be made by its manufacturer, is not guaranteed or endorsed by the publisher.

Copyright © 2021 Sun, Xie, Wu and Yin. This is an open-access article distributed under the terms of the Creative Commons Attribution License (CC BY). The use, distribution or reproduction in other forums is permitted, provided the original author(s) and the copyright owner(s) are credited and that the original publication in this journal is cited, in accordance with accepted academic practice. No use, distribution or reproduction is permitted which does not comply with these terms.



Depositional Model for Turbidite Lobes in Complex Slope Settings Along Transform Margins: The Motta San Giovanni Formation (Miocene—Calabria, Italy)

Sébastien Rohais^{1*}, Julien Bailleul², Sandra Brocheray², Julien Schmitz¹, Paolo Paron³, Francis Kezirian⁴ and Pascal Barrier²

¹IFP Energies Nouvelles, Rueil-Malmaison, France, ²U2R 7511, Basins-Reservoirs-Resources (B2R), Geosciences Department, UniLaSalle - University of Picardie Jules Verne, Beauvais, France, ³HE Delft, Institute for Water Education, Delft, Netherlands, ⁴MARBREK-CMF, Etrochey, France

OPEN ACCESS

Edited by:

Rosanna Maniscalco,
University of Catania, Italy

Reviewed by:

Salvatore Critelli,
University of Calabria, Italy
Yvonne Therese Spychala,
Leibniz University Hannover, Germany

*Correspondence:

Sébastien Rohais
sebastien.rohais@ifpen.fr

Specialty section:

This article was submitted to
Sedimentology, Stratigraphy and
Diagenesis,
a section of the journal
Frontiers in Earth Science

Received: 30 August 2021

Accepted: 11 October 2021

Published: 26 November 2021

Citation:

Rohais S, Bailleul J, Brocheray S,
Schmitz J, Paron P, Kezirian F and
Barrier P (2021) Depositional Model for
Turbidite Lobes in Complex Slope
Settings Along Transform Margins: The
Motta San Giovanni Formation
(Miocene—Calabria, Italy).
Front. Earth Sci. 9:766946.
doi: 10.3389/feart.2021.766946

Intraslope lobes, or perched lobes, are attracting scientific interest because they represent a key archive between the shelf and the deep basin plain when looking at a complete source-to-sink depositional system across a continental margin and can form significant offshore hydrocarbon plays. In this study, we focus on a detailed characterization of intraslope lobes of the Motta San Giovanni Formation (Miocene, Calabria), which were deposited in confined conditions during the Miocene along a transform margin. We determine the typical facies associations and stratigraphic architecture of these intraslope lobes using a 3D digital outcrop model resulting from a combined Uncrewed Aerial Vehicle (UAV) and walking acquisition, together with sedimentological logging and geological mapping. We propose recognition criteria for the identification of intraslope lobes, including facies and geometries, integrated within a depositional model. A comparison with other well-known intraslope and confined lobes, as well as basin floor lobes, is finally discussed, to highlight the peculiarities of intraslope lobes deposited along transform margins. The diagnostic depositional model for these types of intraslope lobes includes four main stages of evolution: 1) Stage 1—isolated detached lobe precursor in response to a flushed hydraulic jump, 2) Stage 2—prograding and aggrading lobe elements associated with a relatively stable and submerged hydraulic jump in the Channel-Lobe Transition Zone (CLTZ), 3) Stage 3—major bypass associated with lateral accretion and local aggradation interpreted as a renewal of a normal hydraulic jump in the CLTZ, and 4) Stage 4—erosion and bypass then abandonment. The development of intraslope lobes along active transform margins is allowed by tectonically induced slope segmentation and local confinement. In such a context, flow stripping and overspill processes occurred. Resulting lobes appear to be particularly small and relatively thin sandy deposits. They could be considered end-member in a lobe classification based on the Net-to-Gross content (high) and taking into account their thickness/width ratio (intermediate between 10:1 and 100:1 lines).

Keywords: turbidites, lobe deposits, intraslope, bypass, transform margin, miocene, UAV, uncrewed aerial vehicle

INTRODUCTION

Intraslope lobes, or perched lobes (Plink-Björklund and Steel, 2002), are attracting scientific interest because they represent a key archive between the shelf and the deep basin plain when looking at a complete source-to-sink depositional system across a continental margin, and can form significant offshore hydrocarbon plays. Key subsurface studies include the Brazilian Campos basin (Albertão et al., 2011), the Niger Delta slope (Adeogba et al., 2005; Prather et al., 2012; Zhang et al., 2016; Jobe et al., 2017), the Lower Congo Basin, offshore Angola (Oluboyo et al., 2014; Picot et al., 2016; Dennielou et al., 2017), or the Gulf of Mexico (e.g. Holman and Robertson, 1994; McGee et al., 1994; Prather et al., 1998; Fiduk et al., 1999; Booth et al., 2003; 2012; Pirmez et al., 2012). Sedimentary processes and stratigraphic architecture were addressed in several examples including the Gioia Basin, southeastern Tyrrhenian Sea (Gamberi et al., 2011; Gamberi and Rovere, 2011), the Algarve Margin, offshore Portugal (Marchès et al., 2010) for modern seabed studies, and the Karoo basin, South Africa (Spychala et al., 2015), the Pab system, Pakistan (Eschard et al., 2004), and the Baiyun Sag, South China Sea (Li et al., 2012) for ancient exhumed studies.

These perched lobes are also described as confined lobes, of which an important literature is available from outcrop, with for example the world class Annot Sandstones, France (Joseph et al., 2000; Guillocheau et al., 2004; Joseph and Lomas, 2004; Mulder et al., 2010; Etienne et al., 2012), the Sorbas basin, Spain (Kleverlaan, 1989; Postma and Kleverlaan, 2018) or the Hikurangi margin, New Zealand (Burgreen and Graham, 2014; McArthur et al., 2021), and from modern system such as the Golo system, East Corsica (Gervais et al., 2004, 2006; Deptuck et al., 2008).

These lobes have common characteristics: 1) they display a smaller lateral extent and lower aspect ratio than their basin floor counterparts (Plink-Björklund and Steel, 2002; Deptuck et al., 2008; Postma and Kleverlaan, 2018), 2) they exhibit an overall mounded convex-up geometry in radial profile (e.g., Oluboyo et al., 2014), 3) they show a high proportion of relative coarse and massive sands (i.e. high Net to Gross ratio) (Komar, 1971; Ferry et al., 2005; Postma and Kleverlaan, 2018), 4) they are found in association with slumps and mass transport complexes (MTCs) (Walker, 1978; Adeogba et al., 2005; Gamberi and Rovere, 2011; Li et al., 2012), and 5) evidences for incision are frequent (Adeogba et al., 2005; Ferry et al., 2005; Flint et al., 2011; Barton, 2012; Prather et al., 2012). This final characteristic is critical as incision commonly records the bypass of sediment toward the final sink in the basin floor lobes. However, it is still unclear when sediments are exported downdip, especially the coarser material, considering the dynamic and architecture of the intraslope lobes. Guillocheau et al. (2004) proposed a stratigraphic depositional model where the topmost surface of lobe corresponds to a flattened and smooth bypass surface. Postma and Kleverlaan (2018) documented a detailed morphodynamic study to illustrate the main depositional stage of the lobe evolution in response to hydraulic jump dynamic, without addressing large erosions and related bypass processes.

Spychala et al. (2015) presented a depositional model with a final incision by a low aspect ratio channel responsible for downdip sediment export. As intraslope lobes do not represent the architectural element located in the most distal part of a turbidite system at the margin scale, understanding their depositional architecture and morphodynamics is key to characterize the record of deep-marine systems and their preserved stratigraphic successions in the abyssal plain. Amongst all tectonic margins, transform margins commonly show topographically complex slopes, and the sediment distribution as well as the geometries of turbidite architectural elements are still poorly known in this context (MacGregor et al., 2003; Pellegrini and Ribeiro, 2018).

In this study, we focus on a detailed characterization of some intraslope lobes of the Motta San Giovanni Formation (Calabria), which were deposited during the Miocene along a transform margin (Figure 1). These outcrops spectacularly expose the 3D lobes architecture thanks to rapid Pleistocene uplift, providing a unique opportunity to characterize such a complex sedimentary system along a transform margin. First, we integrate these lobes in a broader regional setting by geological mapping and paleocurrent analysis, allowing their distribution across a slope comprising perched mini-basins to be assessed. Second, we determine the typical facies associations and stratigraphic architecture of these intraslope lobes. Then, we propose recognition criteria for the identification of intraslope lobes through a depositional model. A comparison with other well-known intraslope and confined lobes, as well as basin floor lobes, is also discussed, to highlight the peculiarities of intraslope lobes deposited along transform margins.

MATERIALS AND METHODS

Fieldwork was undertaken to characterize the Miocene turbidites from the Motta San Giovanni Formation outcropping in the southeastern region of Calabria in detail (Figure 2A). Geological mapping over a survey area of $14 \times 17 \text{ km}^2$ (ca. 240 km^2) has been carried out to revise the geological maps created there by the IGAL (Institut Géologique Albert-de-Lapparent) groups and followers regularly since 1981 (e.g. Barrier, 1982; Morlo, 1985; Becue, 1988; Gallet de Saint-Aurin, 1988; Bouchet, 1990; Manoux, 1999; Schepers, 1999; Rohais, 2000; Thomaidis, 2000; Raber, 2003; Vallee, 2003; Guillois and Polard-Taine, 2016; Pichancourt and Terrier, 2016; Colas and Ripoll, 2017; Chirol et al., 2019; Marchiel and Rispal, 2019; Bourel and Degrave, 2020; Guillet de Chatelus and Prosperi, 2020) (Figure 2A).

Three areas have been studied in very high resolution for stratigraphic issues: 1) the Motta area ($1 \times 1.5 \text{ km}^2$) located in the vicinity of the Motta San Giovanni town, 2) the Saetta area located along the Saetta river ($0.8 \times 0.8 \text{ km}^2$), and 3) the Di Leo area ($0.7 \times 0.7 \text{ km}^2$) (Figure 2A).

Architecture and bed continuity in these areas were mapped by physical tracing in the field with the help of a 3-dimensional outcrop model (Virtuoso@IFPEN, Deschamps et al., 2013, 2017; Schmitz et al., 2014). The dimensions of the lobes were quantified from the 3D models using the Virtuoso interactive tool to

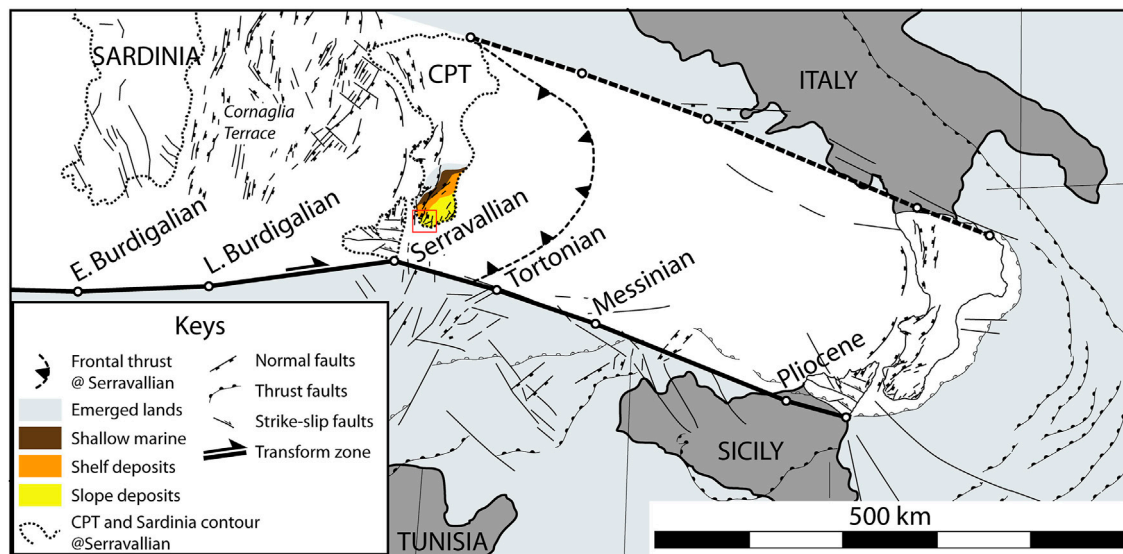


FIGURE 1 | Paleogeographic reconstruction of the Motta San Giovanni Formation during the early Serravallian. Relative position of Sardinia and CPT compared to Italy, Sicily, and Tunisia considered fixe (Gray) based on the reconstruction for the kinematic complex D2 of Vitale and Ciarcia (2013). Relative position of CPT and migration path from Vitale and Ciarcia (2013). Fault pattern is from Leprêtre et al. (2019) and Jolivet et al. (2021) and reference herein. Fault pattern in CPT is refined using Kezirian et al. (1994) (Sicily) and Brutto et al. (2018) (Calabria). Depositional environments are from the synthesis of Raber (2003) and reference herein. Red square illustrates the studied area.

preserve spatial precision and dimensionality. The images ($n = 1770$, 40 megapixels resolution) were made by land foot acquisition combined with DJI Phantom Vision 2+ drone-attached camera both with a GNSS (Global Navigation Satellite System) positioning system. The quality and resolution (<5 cm) of the 3D models provided adequate resolution for mapping purposes at the bed scale as well as for architectural and facies analysis (Figure 3).

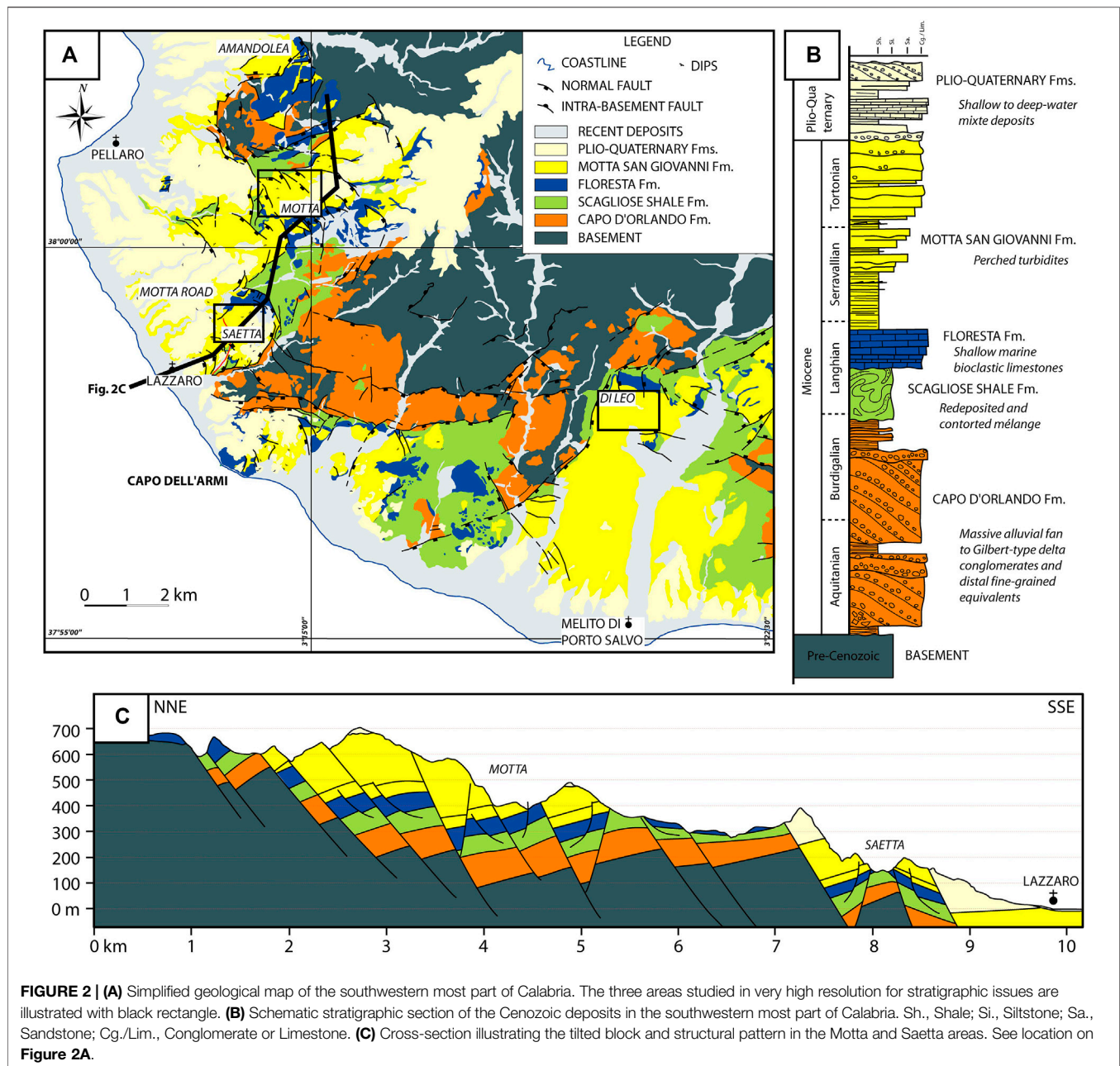
A total of 22 sedimentological sections were logged at high resolution (scale: 1:12.5, cumulative total thickness = 176 m). Turbidite facies are interpreted by using the newly proposed facies schemes of Talling et al. (2012) and Postma and Cartigny (2014) for sub- and super-critical turbidity current deposits following the recent work of Postma and Kleverlaan (2018). The Bouma sequence (Bouma, 1962) with five different facies abbreviated as Ta-Te units is used as an overall facies framework, with an expanded version for the Tb unit (Cartigny et al., 2013; Postma and Cartigny, 2014). Paleocurrents directions were acquired from ripples ($n = 679$), groove marks and channel axis ($n = 229$) all over the revised geological map.

GEOLOGICAL AND STRATIGRAPHIC SETTINGS

Calabria: A Complex Geodynamic Setting

The Calabria–Peloritani terrane (CPT) is a fault-bounded terrane comprising Calabria, i.e. the region at the southern tip of the Italy, and the Peloritani Mountains of northeastern Sicily (Figure 1). The CPT is composed of a pre-Mesozoic

crystalline basement with a thin and discontinuous Mesozoic sedimentary cover (Roda, 1965). It shows evidence of pre-Neogene tectonism and metamorphism, in marked contrast with the geology of the adjacent orogenic chains (i.e. the Apennines, including Sicily; Bonardi et al., 2001). Two main geodynamic phases characterize the construction of the CPT (Dewey et al., 1989; Faccenna et al., 2001; Critelli, 2018): 1) a Late Oligocene–Middle Miocene trench migration, accompanied by opening of the Ligurian–Provençal back-arc basin and 2) a Tortonian–Pleistocene migration, with opening of the Tyrrhenian back-arc basin. Numerous paleogeographic reconstructions of this part of the Mediterranean region have been proposed (e.g. Boullin et al., 1986; Dercourt et al., 1986; Dewey et al., 1989; Faccenna et al., 2001; Critelli et al., 2011, 2017; Vitale and Ciarcia, 2013; Critelli, 2018; Butler et al., 2020; Romagny et al., 2020; Milia et al., 2021) and controversies that go far beyond the scope of our work still exist. No matter what the paleo-reconstruction was, during Langhian to Messinian (Middle to Late Miocene), the CPT was localized to the NW of present-day Sicily (Figure 1), conforming to a transform margin setting *sensu* Type 2a of Wilson (1965). At this time, the southern portion of the CPT was facing a relatively deep basin (Algerian Basin, Sardinia Channel), where normal faults are still preserved to the south of the Cornaglia Terrace presently located to the north of Tunisia and to the west of Sicily (Figure 1). Very thick Tortonian deposits are preserved in inverted faulted blocks in the offshore of western Sicily (Milia et al., 2021). The southern margin of the CPT was recently revisited and integrated into the dynamic of the Mediterranean back-arc regions and tear faults (Jolivet et al.,



2021). It is described as a transfer zone: the Catalan-Balears-Sicily Transfer Zone (CBSTZ). It accommodates the rotation of the Corsica-Sardinia block and the related opening of the southern Tyrrhenian Sea.

Cenozoic Stratigraphy and Structures

In the study area, the Cenozoic stratigraphy is commonly subdivided into several formations (Figure 2B). The first deposits are Oligocene (Barrier et al., 1987) to Early Miocene (Aquitainian, Bonardi et al., 1980) in age while the most recent deposits are up to the Pleistocene (Barrier et al., 1987; Tripodi et al., 2013).

At base, the Capo d'Orlando Formation (uppermost Chattian–Burdigalian, Bonardi et al., 1980; Barrier et al., 1987)

is a ca. 600-m-thick siliciclastic unit composed of massive conglomerates and laterally equivalent finer-grained deposits. It is organized into a proximal-distal depositional profile ranging from alluvial fans through Gilbert-type deltas, then distal turbidites in a hemipelagic setting (Figure 2B).

The Capo d'Orlando Formation is unconformably overlain by the Scagliose shale Formation (Cortese, 1895), informally named “varicolored clays” (Figure 2B). It consists of a *mélange* composed of a pelitic, highly sheared matrix enclosing quartz-arenite and limestone–marl blocks (Cavazza et al., 1997). Strontium-isotope ages and foraminiferal biostratigraphy of the underlying and overlying units indicate that the Scagliose shale Formation was emplaced between 17 and 14 Ma (late

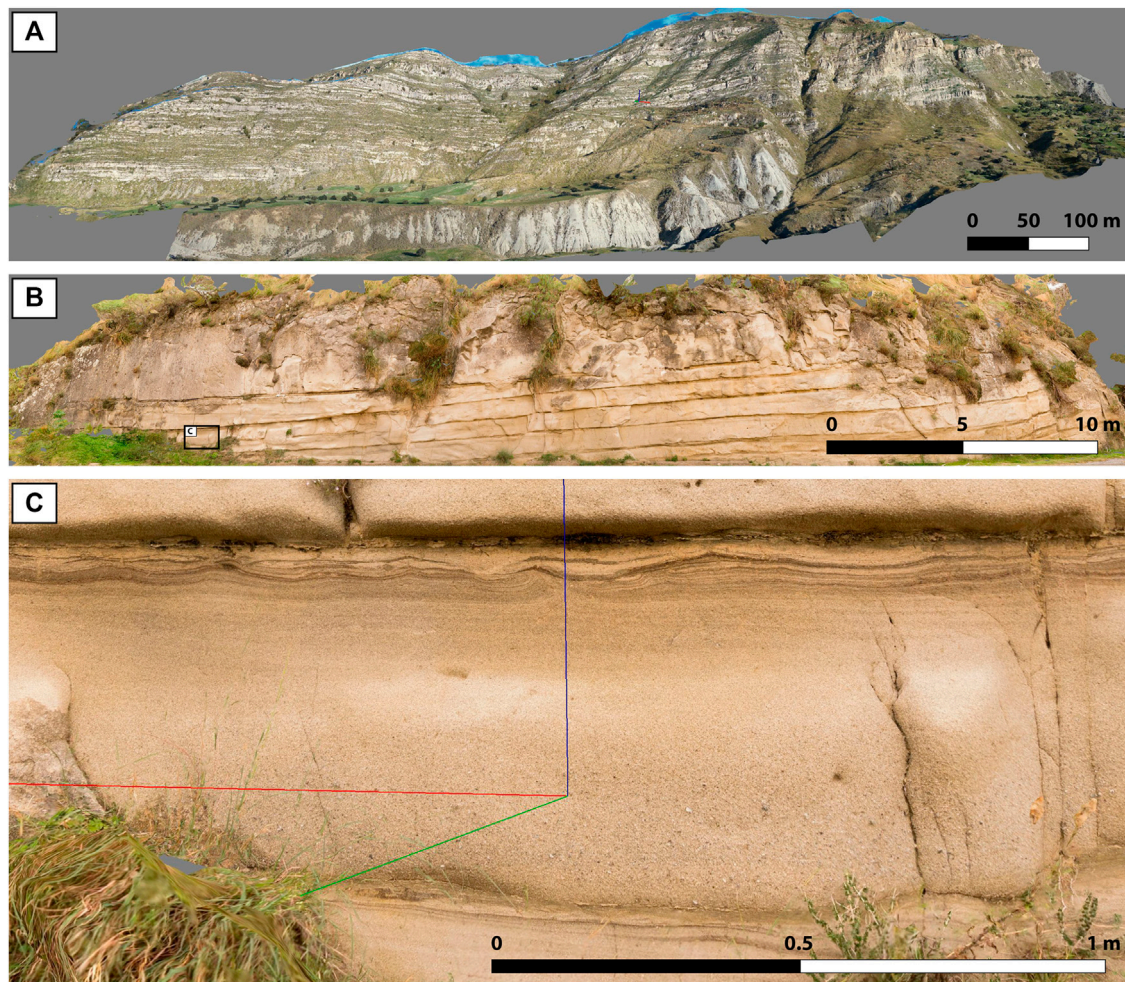


FIGURE 3 | Illustration of the resolution of the 3D drone acquisition dataset (Motta area). The embedded scale used in the present study is presented, from panoramic stratigraphic architectures of the Motta area (A), to bed sets (B) and individual beds (C). **Figure 3C** corresponds to the black rectangle on **Figure 3B**.

Burdigalian–Langhian, Bonardi et al., 1980), possibly over a shorter time span (Patterson et al., 1995; Cavazza et al., 1997). According to Cavazza et al. (1997) and Bonardi et al. (2001), the *mélange* was deposited when the southern edge of the CPT started to collide with the African plate.

The Floresta Formation (Cortese, 1895; Ogniben, 1969) is transgressive on the Scagliose shale Formation, and locally onlaps the Capo d'Orlando Formation and the pre-Cenozoic basement (Barrier et al., 1987). It consists of relatively thin (5–80 m-thick) shallow marine bioclastic mixed limestones (**Figure 2B**), evolving progressively to deeper depositional settings from the north west to the south east.

The Motta San Giovanni Formation (Barrier et al., 1987) is a thick (400–600 m-thick) transgressive unit on the Floresta Formation (**Figure 2B**). It is subdivided into a basal and an upper member, Motta 1 and Motta 2 respectively. They are interpreted to be deposited from density currents in a proximal marine environment, primarily the slope and base of slope (Cavazza et al., 1997; Cavazza and Ingersoll, 2005). The age

of the Formation is based on faunal assemblages and ranges from Tortonian, upper Serravallian to lower Messinian (Selli, 1979), to upper Langhian to Tortonian (Barrier et al., 1987).

The Plio-Quaternary deposits include several formations (Barrier et al., 1987) that have recorded major base-level changes (**Figure 2B**). They correspond to mixed deposits, from deep open marine to shallow restricted settings, and show multiple internal unconformities (Barrier et al., 1987; Cavazza et al., 1997). A Pleistocene system of perched marine and fluvial terraces discontinuously overlies older Formations (Barrier et al., 1986; 1987). These terraces are horizontal or subhorizontal and can be found at elevations reaching more than 1,000 m above present-day sea level, thus indicating a dramatic uplift of Calabria during the last 700 ka (Tortorici et al., 1995; Tripodi et al., 2018).

The geological map was revised (**Figure 2A**) highlighting major normal faults with vertical throw of >1000 m and mainly NE-SW orientation (**Figure 2C**). Three main blocks are organized as a succession of piano-like keys dipping

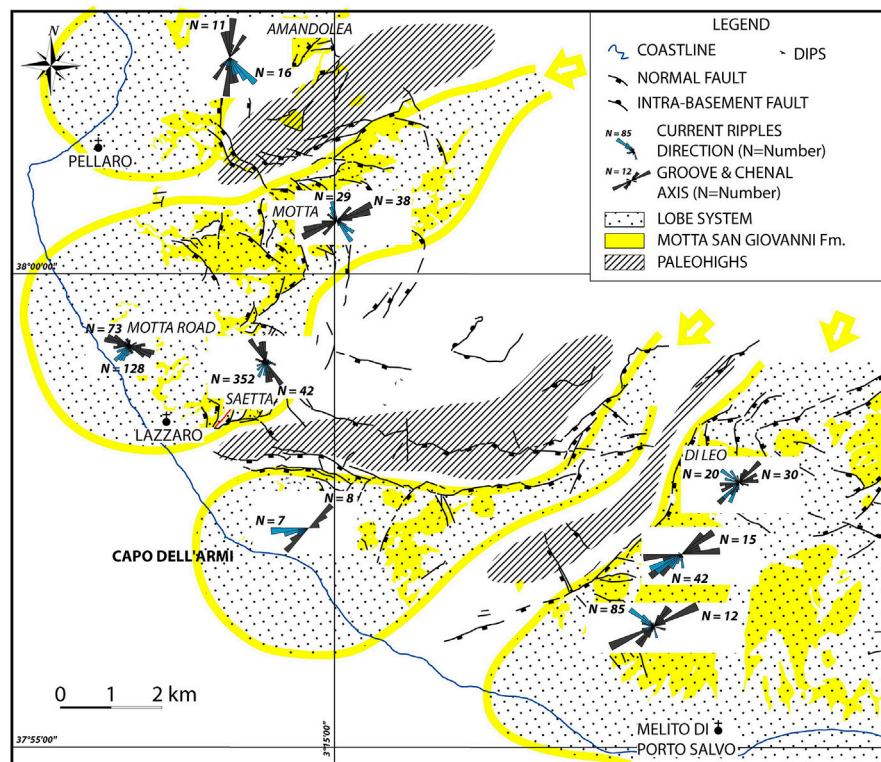


FIGURE 4 | Paleogeographic interpretation and lobe systems of the Motta San Giovanni Formation (Serravallian to Tortonian). Four systems are highlighted from NW to SE, separated by paleohighs corresponding to the crests of early Miocene tilted blocks. Yellow arrows illustrate to sediment supply entry points.

toward the SW: 1) Amandolea, 2) Motta-Saetta, and 3) Di Leo faulted blocks. Each block is affected by superimposed shallow rooted syn-sedimentary normal faults, showing spoon-shape and mainly oriented NW-SE (**Figure 2C**). Major NW-SE normal faults also crosscut the three main blocks and are mainly associated with Plio-pleistocene deformation (Barrier et al., 1987).

Miocene paleocurrents witness the sediment dispersal over the main three tilted blocks. In the Amandolea area, the main axis for the sediment transit is to the south, toward the main fault plan (**Figure 4**). In the Motta area, the main direction is aligned with the main tilted block fault, i.e. NE-SW. In the Saetta and Motta Road area, complex and multiple directions suggest sediment dispersal influenced by local normal faults. In the Di Leo area, the main axis for sediment transport is to the southwest, which is the main tilted block fault direction (**Figure 4**).

Coeval proximal depositional environments of the Motta San Giovanni Formation, including the shallow marine “Clypeaster sandstone” (Barrier et al., 1987; Cavazza et al., 1997), are preserved at north and north-east of the Messina strait (**Figure 1**), providing the opportunity to estimate the distance to the shoreline for the studied outcrops. The Amandolea area is located ca. 14–18 km, the Motta area ca. 24–28 km, the Saetta area ca. 28–32 km, and the Di Leo area ca. 32–36 km offshore the Miocene shoreline. Faunal assemblages indicate a

paleobathymetry of ca. 100–300 m in the Motta area and 300–900 m in the Di Leo area (Nicolleau et al.).

FACIES AND ARCHITECTURAL ELEMENTS

The fan lobe terminology developed by Mulder and Etienne (2010) and Gaillot et al. (2015) is followed here, as well as the facies associations and lobe subdivision proposed by Prélat et al. (2009) and Sychala et al. (2015). Facies, facies associations and architectural elements are presented in **Figures 5–7**.

Facies Association 1: Channel-Levee (C-Le) Description

This facies association is dominated by thick-bedded (2–10 m), massive to laminated, very coarse- to medium-grained sandstones, with floating gravels derived from basement rocks (gneiss, granite, micaschists). Layers with fine pebbly gravel to pebble conglomerate are commonly aligned along large-scale sigmoidal cross-stratification, as well as monogenic mud-clast breccias (**Figure 5B**). Large bioturbation (*Ophiomorpha*-like) is often preserved in the upper part of the beds (**Figure 5C**). Coarse- to very-coarse-grained cross-bedded sandstones and pebbly sandstones could be preserved just above the basal erosive surface of the facies association. The basal erosive surface

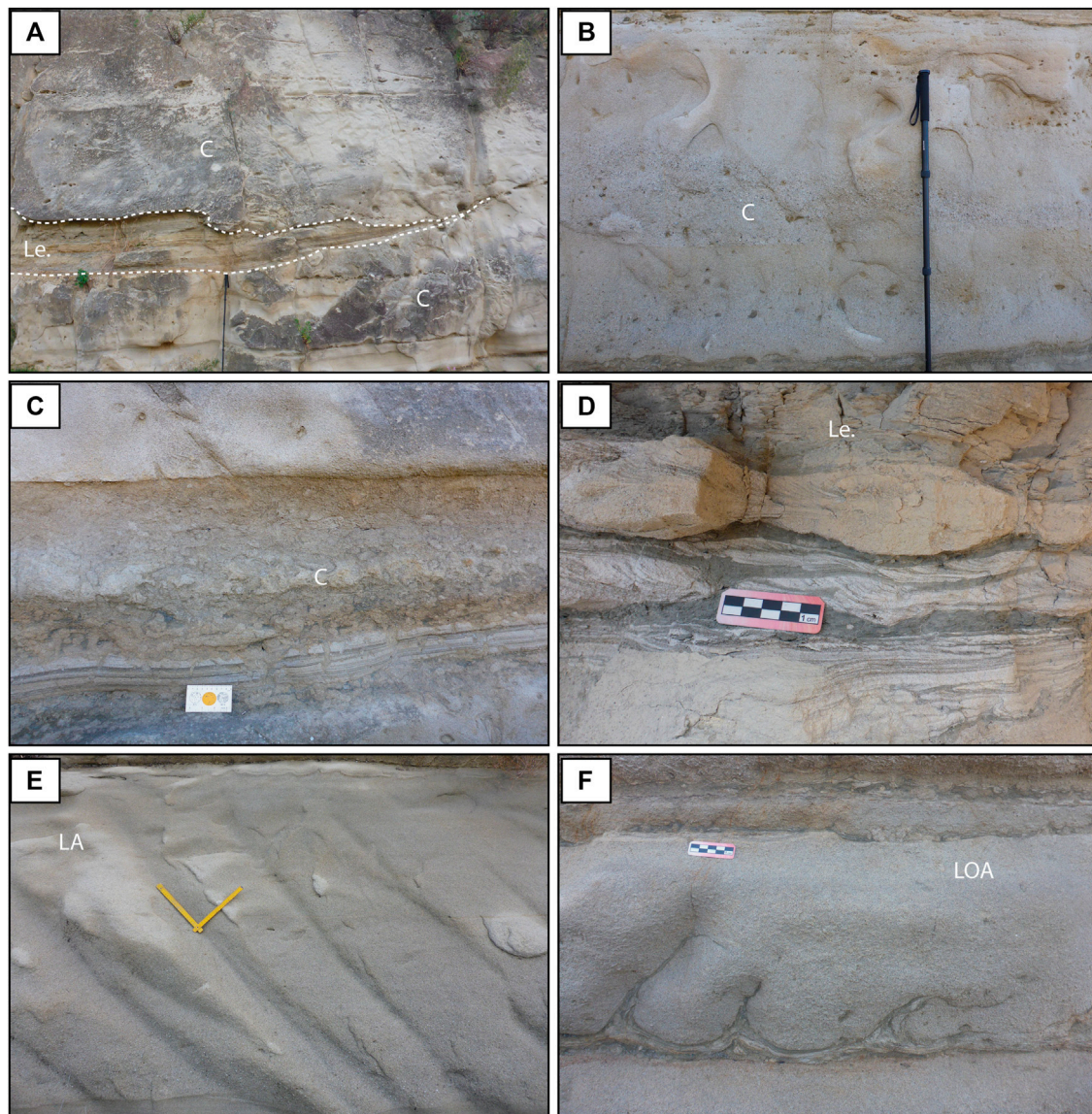


FIGURE 5 | (A) Channel and (C) Levee (Le) facies associations. 1.5 m-long Jacob staff for scale. Levee facies association is locally preserved along channel margins. **(B)** Channel, (C) facies association represented by very coarse-grained sandstones, with pebbly gravel and mud-clasts aligned along large-scale sigmoidal cross-stratification. 1.5 m-long Jacob staff for scale. **(C)** Highly bioturbated siltstones to very fine-grained sandstones commonly preserved at the top of the Channel-Levee (C-Le) facies association. **(D)** Siltstones to very fine-grained sandstones with climbing- and current-ripple structures illustrating the Levee (Le) facies association. **(E)** Lobe axis (LA) facies association represented by weak normal grading, m-thick beds of gravelly to very coarse- and medium-grained sandstones showing parallel lamination. Folding rule meter for scale, 20-cm long segments. **(F)** Lobe off-axis (LOA) facies association illustrated by normally graded coarse- to fine-grained sandstone beds with erosive base and flame structures, alternating with finer-grained deposits with current ripples.

shows multi-reactivation surfaces and lateral migration. Siltstones to very-fine-grained sandstones with climbing- and current-ripple structures are locally preserved below the basal erosive surface (**Figure 5A**). These finer-grained deposits are organized in dm to m-thick packages of 5–10 s m of lateral extent. Horizontal and vertical burrows are common in these fine-grained deposits and paleocurrents, deduced from ripples, and show an oblique flow direction away from the main channel axis. Facies association 1 has a sandstone percentage of 90% based on the reference log section (**Figure 7A**).

Interpretation

These coarse-grained deposits are mostly the product of high-density flows and are similar to the F4–F5 facies tracts described by Mutti (1992) or to the R2-3 and S1-3 divisions of Lowe (1982). Monogenic mud-clast breccias are interpreted as channel-wall collapses or internal levees reworking. Coarse-grained cross-bedded sandstones are interpreted as tractive megadunes. Such cross-bedded layers are similar to the F6 facies of Mutti (1992), Mutti and Normark (1987) and to Lowe's (1982) S1 division, interpreted as the result of waning unidirectional tractive flows

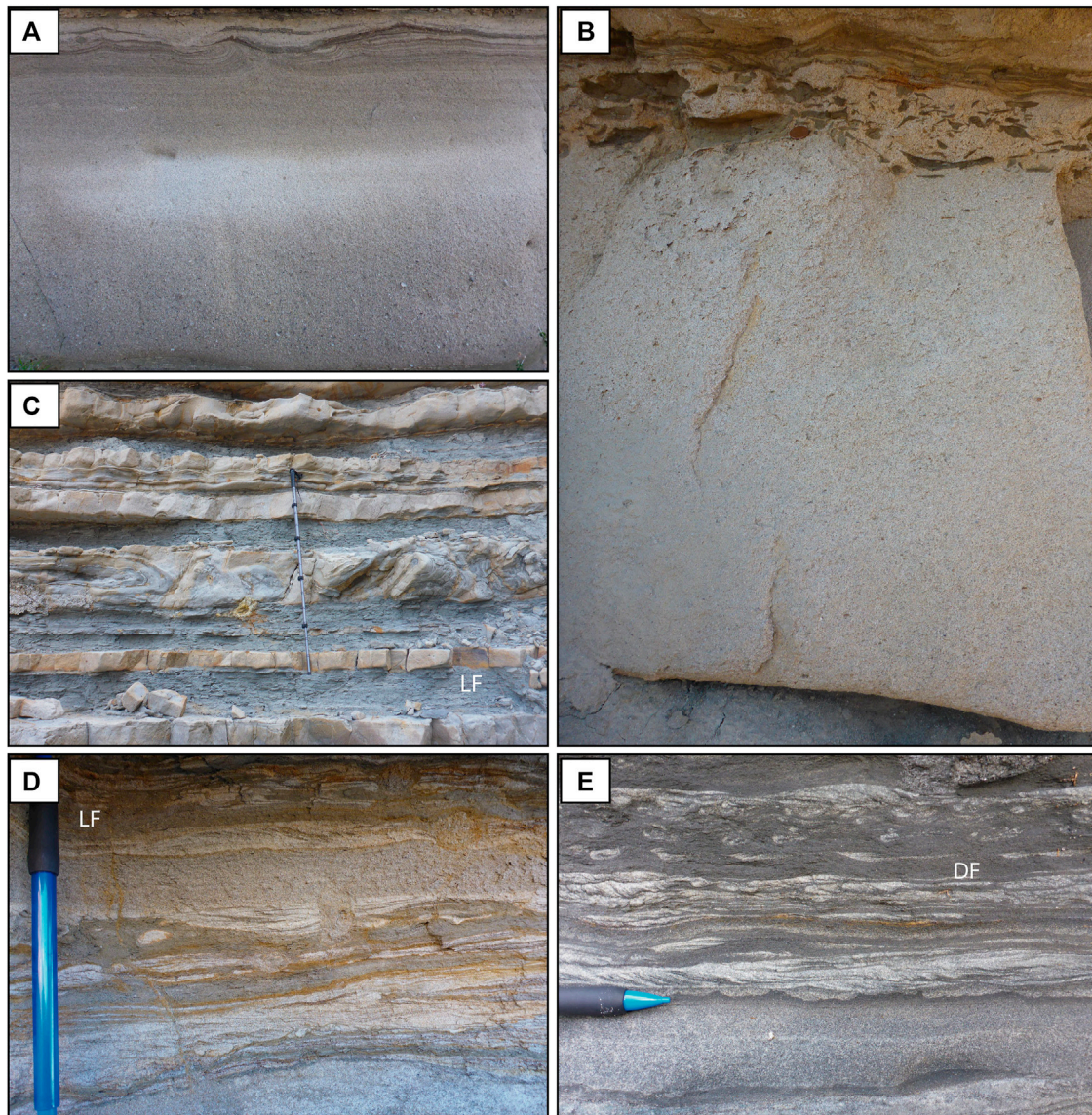


FIGURE 6 | (A) Normally graded gravelly coarse- to very fine-grained sandstone beds with erosive base (Ta-Td), very common in Lobe off-axis (LOA) facies association. Bed is 1-m thick. **(B)** Bipartite bed with a lower division of weakly normally graded coarse- to fine-grained sandstones with rare planar lamination, and an upper division comprising poorly sorted fine- to very fine-grained sandstones with dispersed cm scale mudstone clasts. Lobe fringe (LF) facies association. Bed is 70 cm-thick. **(C)** Lobe fringe (LF) facies association. Massive to normally graded fine- to medium-grained sandstones alternating with shaly-siltstones and siltstones with current ripples. Slump bed is preserved in the thicker bed, in the central part of the photo. 1.5 m-long Jacob staff for scale. **(D)** Shaly-siltstones and siltstones with current ripples of Lobe fringe (LF) facies association. Pencil for scale. **(E)** Distal fringe (DF) facies association. Silty shale intervals containing siltstones and fine- to medium-grained sandstone beds with plane bed lamination and current ripples. Pencil for scale.

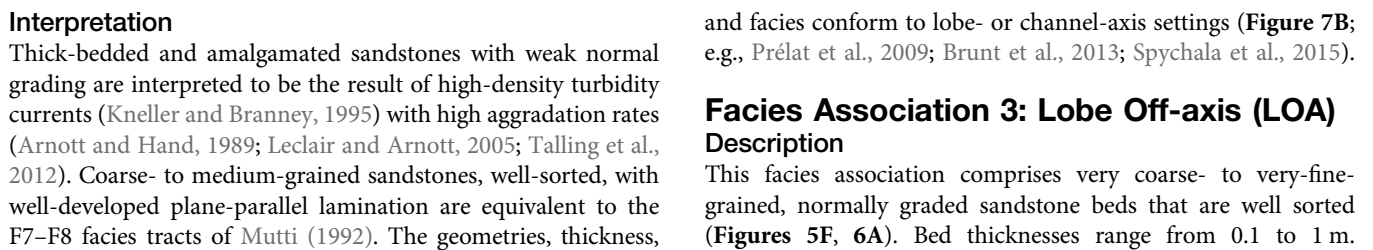
(Mutti, 1992). Fine-grained deposits are interpreted as internal levees preserved in the channel conduit (e.g. Kane and Hodgson, 2011). This facies association is representative for channel-levee turbidite deposits (Figure 7A).

Facies Association 2: Lobe Axis (LA)

Description

This facies association is dominated by weak normal grading, 0.1–2 m-thick beds of gravelly to very coarse and medium-grained sandstones showing parallel lamination (Figure 5E) with isolated cm-

sized mudstone chips aligned parallel to the internal stratification. Overall, beds are moderately to well sorted, and locally contain layers with pebbly gravel commonly preserved at the base of massive beds. Intraformational monogenic mudclasts are observed at bed bases. Bed bases are sharp, loaded, or erosive and can preserve tool marks. Bed amalgamation is common and can lead to 5–10 m-thick packages of massive sandstones. Thick-bedded sandstones show tabular to gently convex-up geometries. They are laterally extensive for up to 50–400 m. Facies association 2 has a sandstone percentage of 94% based on the reference log section (Figure 7B).



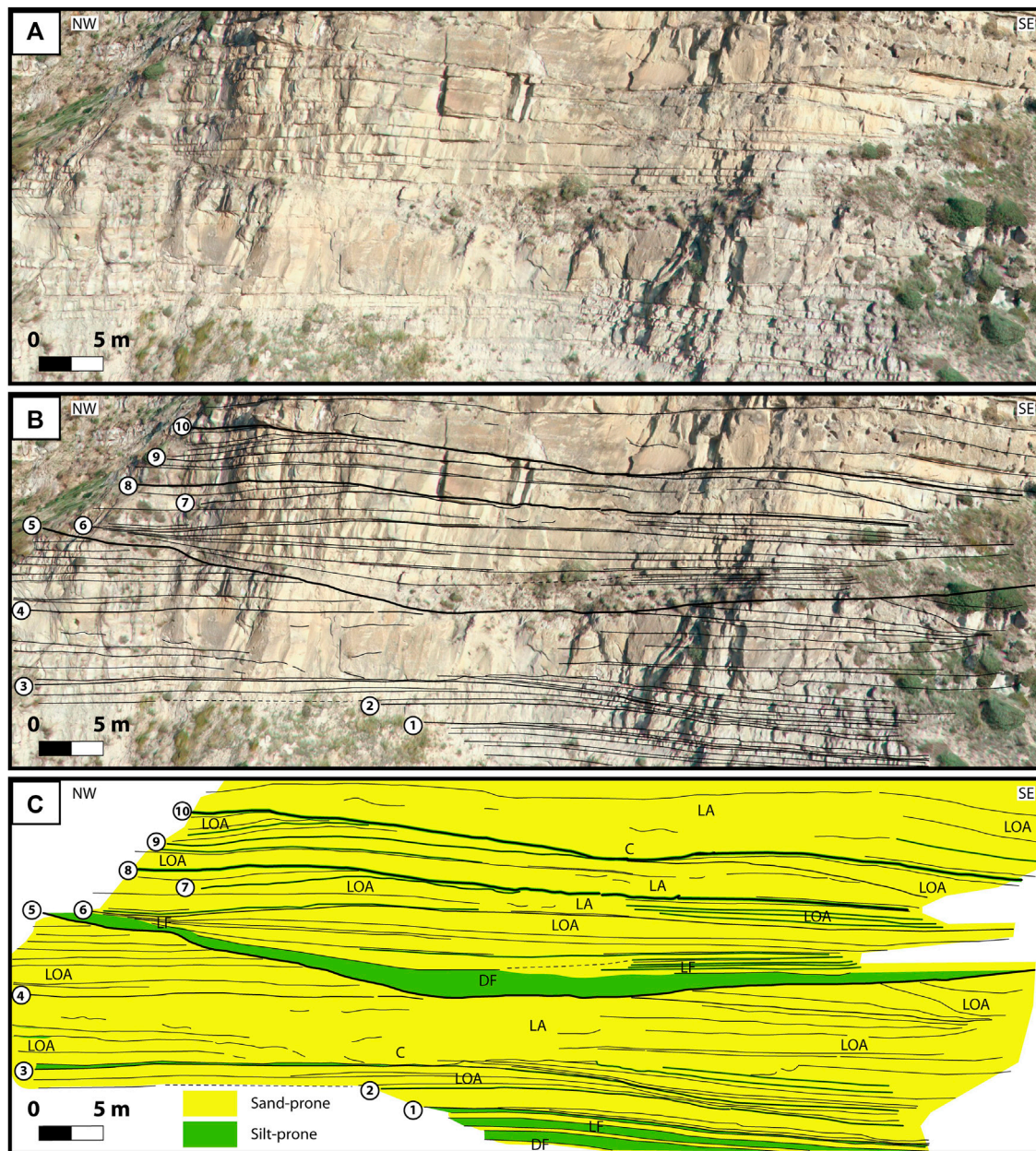


FIGURE 8 | Stratigraphic architecture of the Motta area illustrating Channel-Lobe transition zone. Panoramic view extracted from the 3D outcrop model (A) and interpretation (B,C). The main surfaces discussed in the text (1–10) are highlighted. Surfaces at the top of lobe are represented by thicker dark lines (Lines 5, 8, and 10). Lobes are composed of several lobe elements. (C) Channel, (Le) Levee, (LA) Lobe axis, (LOA) Lobe off-axis, (LF) Lobe fringe, (DF) Distal lobe fringe. See text for further explanations.

Observed sedimentary structures include planar lamination (Tb), wavy lamination, current-ripple lamination, and climbing ripple lamination (Tc), locally organized in a repetitive pattern. Bed bases are sharp or loaded with flame structures (Figure 5F). Bed tops are sharp and commonly eroded (Figure 5F). Medium- to thin-bedded sandstones show tabular to convex-up geometries and can be traced for 10's to 100's of meters down-dip and in the strike section. Facies association 3 has a sandstone percentage of 85% based on the reference log section (Figure 7C).

Interpretation

Bedforms such as planar lamination and current-ripple lamination are produced beneath dilute turbulent flows, which rework sediment along the bed (Allen, 1982; Southard, 1991; Best and Bridge, 1992). Thin beds with repeating patterns of climbing-ripples and planar lamination are interpreted to indicate highly unsteady flow behavior (Jobe et al., 2012). This facies association is interpreted to be deposited by high- to low-density turbidity currents in a lobe off-axis setting (Figure 7C; e.g. Sychala et al., 2015).

Facies Association 4: Lobe Fringe (LF)

Description

Beds are predominantly composed of fine- to medium-grained sandstones alternating with shaly-siltstones and siltstones (Figure 6C). Sandstone beds range in thickness from a few cm up to several dm and form flat to convex-up lens-shaped bodies pinching out over tens of meters. Sandstone beds show planar, current-ripple, or wavy laminations, whereas siltstone beds commonly display planar lamination with isolated starved ripples (Figure 6D). Shaly-siltstones and siltstones are commonly burrowed. Some beds show bipartite structure with a lower division of weakly normally graded fine-grained sandstones with rare planar lamination and thin mudstone-clast layers, and an upper division comprising poorly sorted very fine-grained sandstones and siltstones with dispersed mm-cm scale mudstone clasts (Figure 6B). The contact between the two divisions is commonly sharp and undulating. Slumps and contorted beds are common, ranging in thickness from a few dm up to several dm (Figure 6C). Slump beds are commonly truncated at top. Facies association 4 has a sandstone percentage of 45% based on the reference log section (Figure 7D).

Interpretation

Ripple lamination formed due to reworking by dilute turbulent flows with moderate aggradation rates, whereas climbing-ripple lamination is indicative of high aggradation rates (Allen, 1971, 1982; Southard, 1991). Bipartite beds are interpreted as hybrid event beds (Haughton et al., 2009) which primarily occurred at the bases and fringes of lobe deposits (e.g., Hodgson, 2009; Talling, 2013). Spychala et al. (2017) confirmed the lobe fringe setting for bipartite beds using a statistical approach on the Karoo example, but suggested that the occurrence at the bases was rather an artifact of lobe stacking. Ripple and planar laminated packages correspond to the Tb, Tc, and Td divisions of the Bouma sequence (1962) respectively, and shaly siltstones to Te. The abundance of Tb2, Tb1 layers in cm-thick beds indicates deposition from low-density subcritical flows (cf. Arnott and Al-Mufti, 2017; Postma and Kleverlaan, 2018). The heterolithic alternations could result from varying discharge to produce a stack of alternating low- and high-density turbidite deposits (Postma and Kleverlaan, 2018). The tabular geometry of beds in the lens-shaped convex-up bodies indicates unconfined sheet flow from an outlet point source. The intercalated and burrowed shaly siltstones suggest that outlet stability lasted for a period of time and was not related to just one flow event. Observed facies and thicknesses of this facies association conform to an interpretation of a lobe-fringe setting (Figure 7D).

Facies Association 5: Distal Fringe (DF)

Description

Thick bioturbated claystone to silty shale intervals contain rare siltstones and fine- to medium-grained sandstone beds with plane bed lamination and ripple crossbedding (Figure 6E). Rare well-sorted sandstone beds are tabular with a few cm in thickness displaying Tb2-Tb1-Tc. Some beds incorporate mudstone chips. The claystone to silty shale intervals are too strongly bioturbated and poorly outcropping to be studied in further detail. Facies

association 5 has a sandstone percentage of 15% based on the reference log section (Figure 7E).

Interpretation

Structureless beds are attributed to direct suspension fallout (Te of Bouma, 1962), whereas planar laminated beds are commonly interpreted as the product of traction processes (Stow and Piper, 1984; Mutti, 1992; Talling et al., 2012). Siltstone and thin sandstone beds (Tb2-Tb1-Tc) are interpreted as the preserved products of low-density turbidity currents. The low-density turbidity currents are characterized by bedload transport producing plane bed Tb1 term and Tc current ripples term (Postma and Cartigny, 2014). The geometries, thickness, and facies conform to a low-energy depositional environment in distal lobe-fringe settings (Figure 7E).

Facies Association 6: Hemipelagic

Background

Description

Homogenous intervals of silty shale to claystone are mainly preserved at the base of the Motta San Giovanni Formation (Motta 1 of Barrier, 1987). Layers of concretions are common and tend to be associated with distinct horizons associated to fauna, including cephalopods, scaphopods, pelecypods, gastropods, bryozoans, brachiopods, fish remains, echinoderms, and deep-water corals. Claystone intervals are laterally extensive for kilometers. Very thin-bedded (mm-scale) graded siltstone layers showing occasionally current-ripple cross stratification, are locally intercalated with claystone. Facies association 6 has a sandstone percentage of less than 2%.

Interpretation

Claystone are interpreted as hemipelagic background deposits. Where mapped over large areas, they mark episodes of sediment starvation in the deep basin and are interpreted to contain the deep-water expression of maximum flooding surfaces (e.g., Flint et al., 2011). Starved current-ripples in fine-grained deposits could be interpreted as resulting from the action of bottom currents or phases of major turbiditic inputs.

DEPOSITIONAL MODEL AND ARCHITECTURE

Motta area: Channel-lobe Transition Zone (CLTZ)

Description

The Motta area was studied in more detail in a 70 m long and 25 m high section extracted from the 3D outcrop model, which is part of a large outcrop (1.2 km long, 400 m high, Figure 8). Ten main surfaces were identified and describe the overall architecture and stacking pattern. The architecture shows a prograding trend from distal lobe fringe and hemipelagic background facies associations to lobe axis and channel facies associations.

A coarsening and thickening upward trend is observed from below surface 1 up to surface 2. The geometry of beds is

organized in lens-shaped convex-up bodies (Surface 2, 1 m-high convex-up feature) showing lateral compensation of isolated, or detached lobes. The same pattern characterizes the beds up to surface 3. This lower part of the outcrop shows a succession of prograding cycles from distal lobe-fringe to lobe off-axis facies associations. The lateral and abrupt facies change from the lobe axis to the lobe off-axis, on both the sides, is illustrated between surfaces 3 and 4. Locally, the channel facies association is observed. This unit is also organized in an overall prograding to aggrading trend. A preferential lateral migration of the lobe axis facies association is observed toward the southwest. From surfaces 4–5, the unit is characterized by an abrupt lateral migration and progradation of lobe off-axis facies association, on both sides, associated with the enlargement of an erosive and bypass surface (surface 5, 3–5 m deep). Surface 5 is draped by very fine-grained deposits from distal fringe to hemiplegic background facies associations.

The following unit from surfaces 5–6 is organized in lens-shaped convex-up bodies (3–4 m-high) showing a prograding and aggrading trend from distal lobe-fringe to lobe off-axis facies associations. Surface 5 paleo-relief is progressively filled to finally generate convex-up bodies. The lateral and abrupt facies change from the lobe axis to the distal lobe fringe is observed on both the sides in less than 40 m. From surfaces 6–7, the unit shows the same pattern as unit delimited by surfaces 3 and 4. Lateral and abrupt facies change from the lobe axis to the distal lobe fringe is also observed on both the sides, with a preferential lateral migration to the southwest. From surfaces 7–8, the unit is organized in an abrupt lateral migration associated with the progradation of the overlying erosive and bypass surface (surface 8, 1-m deep).

From surfaces 8–9, the unit shows the lateral facies change from the lobe axis to the lobe off-axis, on both the sides, forming lens-shaped convex-up bodies (2–3 m-high). Unit is organized in an aggrading trend. The following unit (surfaces 9–10) is characterized by an abrupt lateral migration and progradation of the lobe off-axis facies association, on both the sides, associated with the enlargement of an erosive and bypass surface (surface 10, 2–4 m deep). Above surface 10, a 5 to 8 m-thick massive unit is organized in an aggrading, gently prograding trend.

Interpretation

Field data show a consistent stratigraphic hierarchy, which favors an intrinsic morphodynamic process rather than a random one for lobe development. The documented facies associations reoccur in each unit and show a consistent trend at the scale of the unit (2–10 m-thick) and even higher. The identified individual units are interpreted as lobe elements (for example between surfaces 3 and 4) organized at larger scale in lobes (for example between surfaces 1 and 5). The first documented lobe, between surfaces 1 and 5, illustrated the complete cycle from distal lobe fringe and hemiplegic background facies associations to final erosive and bypass surface (surface 5). Each lobe element corresponds to a major stage of the lobe evolution, with 1) detached and isolated lobes, 2) prograding-aggrading lobe, 3) abrupt lateral migration associated with lobe overflow, spillovers, and major bypass, and 4) finally abandonment. The second lobe (surfaces 5–8) is organized in a similar pattern. The two overlying

lobes only show the two final stages with a more proximal character, suggesting that the detached and isolated lobes of the first stage are preserved down-dip.

The area is dominated by the lobe axis facies association and major bypass and erosive surfaces. These features are interpreted as representative of the channel-lobe transition zone (CLTZ) to very proximal part in the lobe (e.g. Wynn et al., 2002; Pyles et al., 2014; Hofstra et al., 2015; Hodgson et al., 2016; Brooks et al., 2018).

Saetta Area: Stacked Lobes

Description

The Saetta panorama is 90 m long for 35 m high (Figures 9, 10). Thirteen main surfaces were highlighted to describe the overall architecture and stacking pattern.

A coarsening and thickening upward trend is observed from below surface 1 up to surface 2 (Figures 7B, 10). The geometry of beds is organized in lens-shaped convex-up bodies (Surface 2) showing lateral compensation. These beds are organized in a prograding cycle from hemipelagic setting, to distal lobe-fringe then lobe fringe facies associations. From surfaces 2 to 3, the unit is organized in a rapid progradation from distal lobe-fringe to lobe fringe facies associations, and then a thick aggrading trend from lobe-axis to channel facies associations. Surface 3 is erosive, and draped with mud clast lags, as well as well-preserved reddish crust. The same pattern is observed between surfaces 3 and 4. This unit also shows the abrupt lateral facies change from the lobe axis to the lobe off-axis and lobe fringe in less than 90 m. Surface 4 is highly erosive (2-m deep) and the highest erosion is localized just on the top of the former lobe axis. The same prograding-aggrading pattern is observed between surfaces 4 and 5 and the facies belts compensate and fill the previous relief. Surface 5 is highly erosive and could entirely crosscut the previous unit down to surface 4. Surface 5 is draped by fine-grained deposits with climbing ripples diagnostics for the internal levees facies association. From surfaces 5 to 6, the paleo relief is progressively filled by m-scale prograding cycles made of lobe fringe to lobe axis facies association organized in an overall back stepping trend. Between surfaces 6 and 7, a last m-scale prograding cycle finally seals the former paleo relief by a progressive lobe compensation. All these small-scale cycles show the lateral facies change from the lobe axis to the distal lobe fringe in less than 90 m. Surface 7 is convex-up and draped with a reddish crust.

From surfaces 7 to 10, three units are organized in an overall prograding trend, and are themselves internally organized in a similar manner. These cycles illustrated the complete lateral facies change from the distal lobe fringe to the lobe axis and channel facies associations in less than 100 m.

Surface 10 is erosive (1–2 m-deep). It is associated with channel-levee facies association that rapidly laterally passes to lobe off-axis and lobe fringe facies association (<100 m).

From surfaces 11 to 13, m-scale prograding cycles are organized in an overall backstepping trend. Surface 13 is convex-up and draped with a reddish crust.

Interpretation

Intrinsic morphodynamical process rather than a random process for lobe development is one more time favored based on these

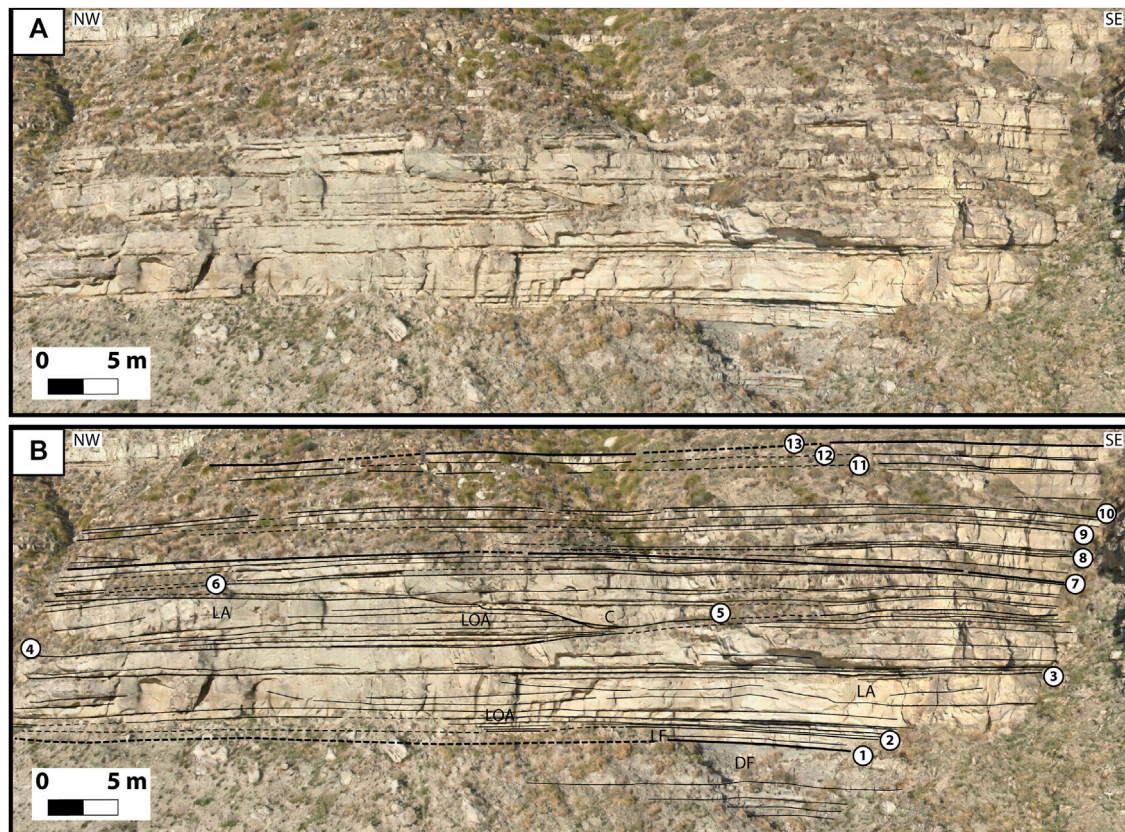


FIGURE 9 | Stratigraphic architecture of the Saetta area illustrating stacked lobes. **(A)** Panoramic view extracted from the 3D outcrop model. **(B)** The main surfaces discussed in the text (1–13) are highlighted. Surfaces at the top of lobe are represented by thicker dark lines (e.g. Lines 7 and 13). Full interpretation is presented in **Figure 10**. (C) Channel, (Le) Levee, (LA) Lobe axis, (LOA) Lobe off-axis, (LF) Lobe fringe, (DF) Distal lobe fringe.

observations. The individual identified units are interpreted as lobe elements (for example between surfaces 3 and 4) organized into lobes at a larger scale (for example between surfaces 1 and 7). Two main lobes are illustrated with the Saetta panorama. From surfaces 1 to 7, the lobe is organized with 1) a prograding trend from hemipelagic setting, to distal lobe-fringe then lobe axis facies associations (up to surface 3), then 2) an aggrading trend with lateral lobe compensation (up to surface 5), 3) a deep erosion and bypass, followed upward by 4) a backstepping trend. At the lobe element scale, the first three stages are well recorded; nevertheless, the backstepping trend is coeval with a starved and bypass surface (for example surface 3). The second lobe shows more distal facies associations, but with a similar organization characterized by 1) prograding and 2) aggrading trends (from surfaces 7 to 10), 3) deep erosion and bypass on surface 10, and 4) filling of the paleo relief and backstepping trend.

Di Leo Area: Isolated or Detached Lobe Description

The selected Di Leo panorama is 350 m-long and 6 m high (**Figures 11, 12**). Three main surfaces were highlighted to describe the overall architecture and stacking pattern of this outcrop (**Figure 11**).

Below surface 1, highly bioturbated fine-grained siltstones to medium-grained sandstones do not preserve primary sedimentary features. They share similarity with hemipelagic setting to distal lobe-fringe facies associations. Surface 1 corresponds to a sharp surface, locally erosive (>0.5 m deep) with tool marks and loading features in proximal area. Surface 1 is progressively conformable in the most distal part (**Figure 11**). The geometry of the beds is organized in lens-shaped convex-up bodies, up to surfaces 2 and 3. Surface 2 is a convex-up intermediate surface (**Figure 11**). Lobe off-axis to lobe axis facies association are dominant between surfaces 1 and 2. From surfaces 1 to 3, the unit covers the complete depositional profile from channel to lobe axis, and distal lobe fringe facies associations, in less than 350 m. Large-scale oblique backsets are observed in the lobe axis to channel facies associations (**Figure 12**). Bioturbations are well preserved on the lobe crest. Surface 3 corresponds to a sharp surface with a reddish crust, current- and undulating ripples. Hemipelagic setting to distal lobe-fringe facies associations onlap onto surface 3.

Interpretation

In the Di Leo area, beds, lobe elements, and lobe are of the same order, i.e. 1–3 m thick. The observed lobe is 350 m-long and has a maximum thickness of 3 m. The lobe is not directly connected to any channel-levee system and is fully interbedded within distal

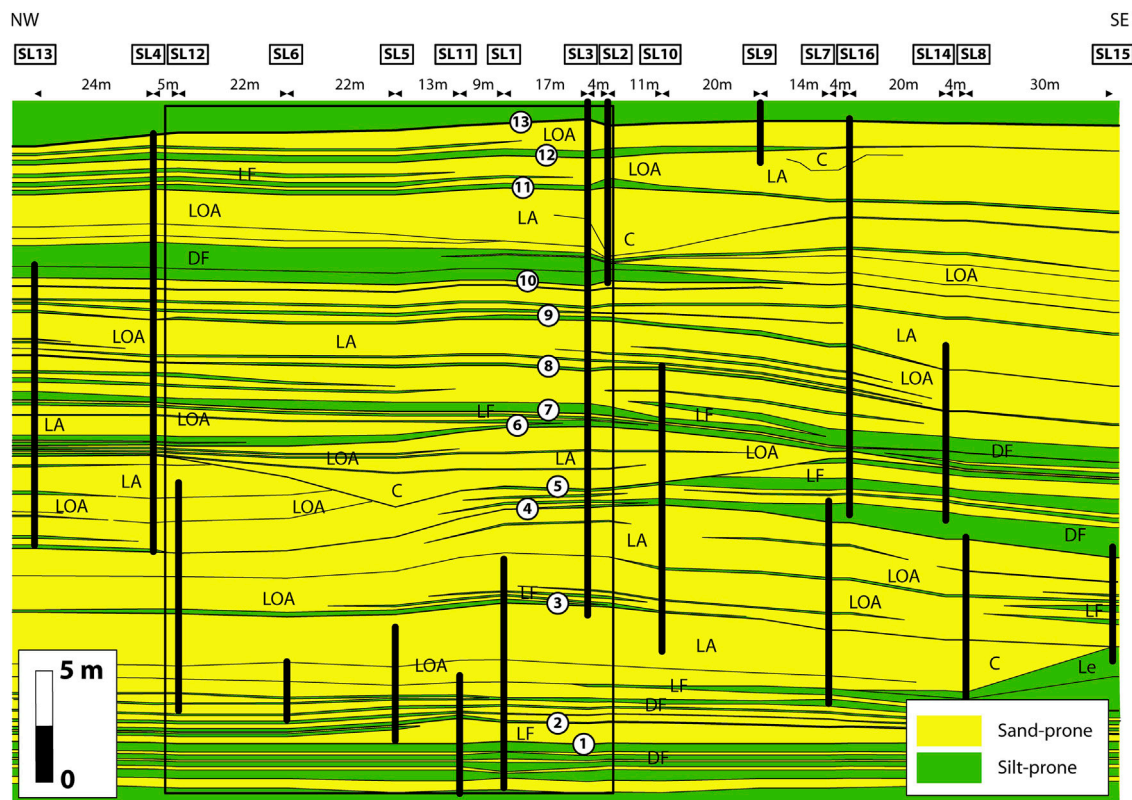


FIGURE 10 | Correlation panel of the Saetta area illustrating stacked lobes. The black rectangle corresponds to **Figure 9** with horizontal extension from sedimentological section SL12 to SL2. Thick vertical black lines correspond to the sedimentological sections. (C) Channel, (Le) Levee, (LA) Lobe axis, (LOA) Lobe off-axis, (LF) Lobe fringe, (DF) Distal lobe fringe.

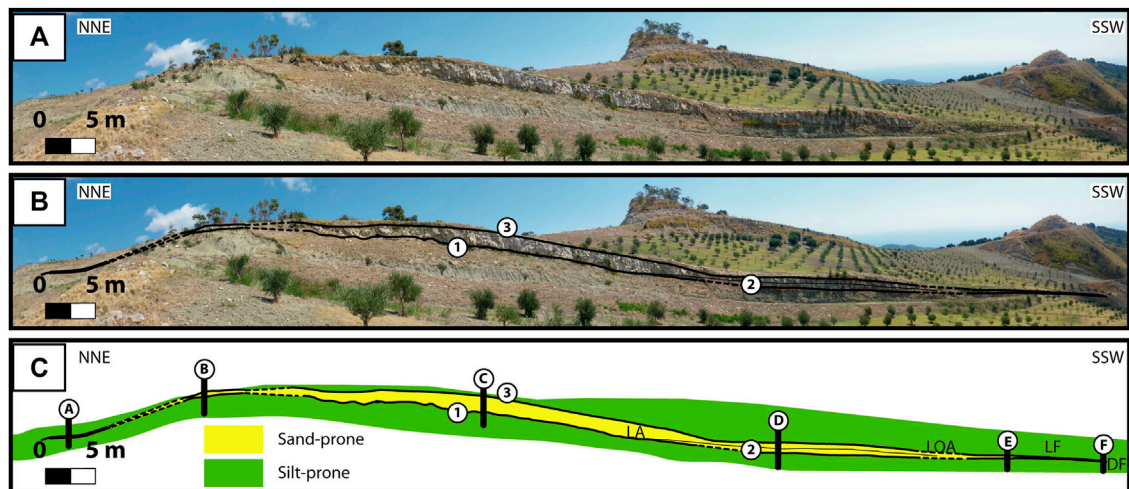
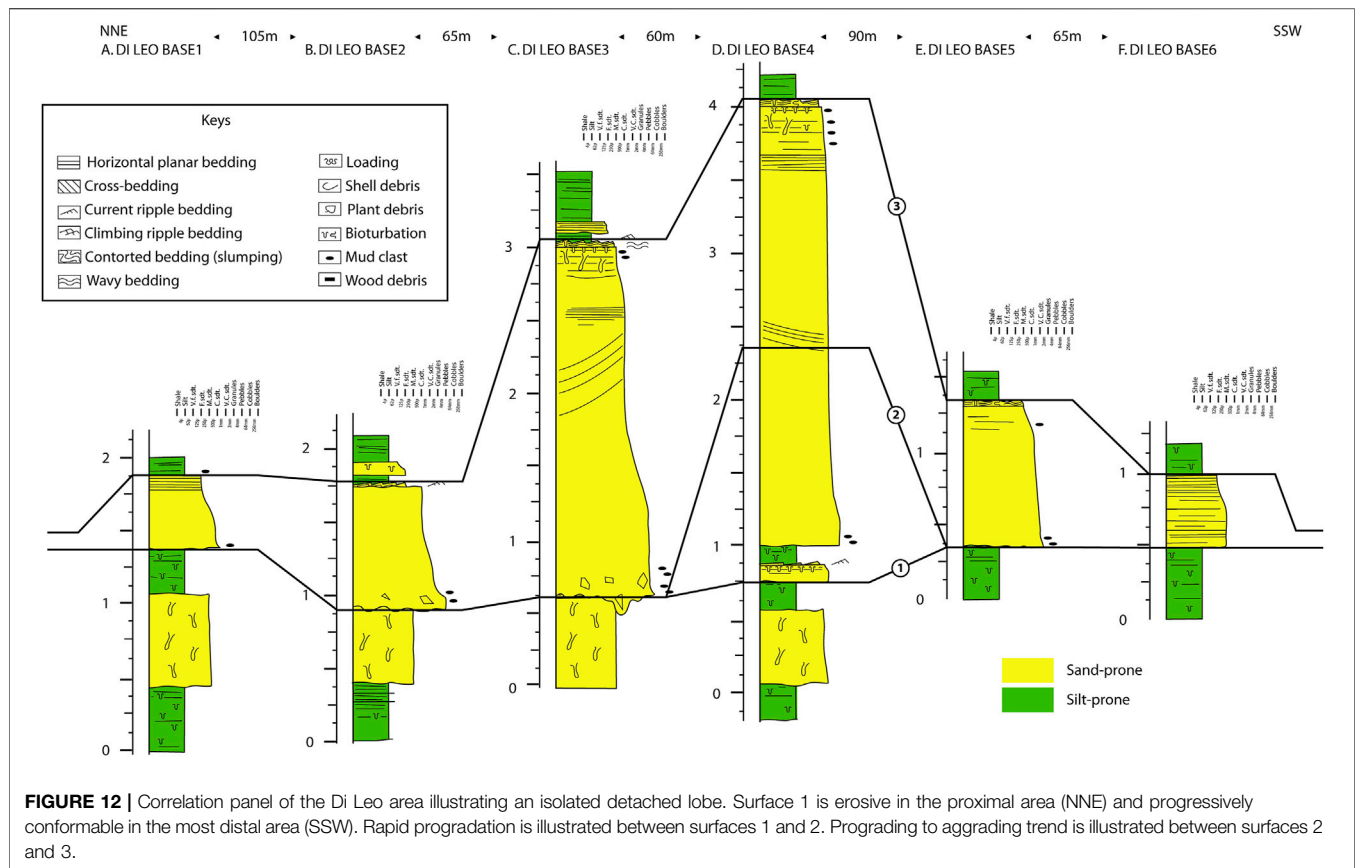


FIGURE 11 | Panoramic view of the Di Leo area illustrating the isolated detached lobe architecture. The main surface discussed in the text (1–3) is highlighted. Sedimentological sections (A–F) and interpretation are presented in **Figure 12**. Channel (C) facies association is preserved up dip of the Lobe axis (LA) facies association. (C) Channel, (LA) Lobe axis, (LOA) Lobe off-axis, (LF) Lobe fringe, (DF) Distal lobe fringe.



facies association (Figures 11, 12). We interpret the lobe evolution in three main stages with: 1) channel, lobe conduit, and lobe initiation (from surfaces 1 to 2), 2) channel extension, lobe progradation, and aggradation (from surfaces 2 to 3), and 3) lobe abandonment and bypass potentially related to avulsion (surface 3). These main stages are very similar to those of the small-radius sand-rich fan lobes of Postma and Kleverlaan (2018).

DISCUSSION

Characteristics of Perched Lobe Deposits in the Motta San Giovanni Formation Dimensions

The studied lobes are characterized by an overall convex-up morphology, locally flat or even gently concave-up in their middle axial part and with steeper slopes on their sides. The lobe dimensions were calculated using the 3D outcrop models for the three studied areas (Table 1). These lobes are architectural elements with a width of 300–3000 m, a length of 500–5000 m, and thicknesses between few to tens of meters (2–22 m thick). A stack of several lobes forms a lobe complex with a thickness of several 100's of meters (*sensu* Prélat et al., 2009; Etienne et al., 2012; Spychala et al., 2017). Lobes are composed of stacked lobe elements that are two to ten times smaller in width and thickness.

The width/max-thickness ratio is low when comparing with confined, and even more with unconfined turbidite system (Figure 13). Confined systems have generally lower width/max-thickness ratio when compared to unconfined system. The two domains are distinct with a relative superimposition. The overall trends from bed, to lobe element, lobe, and lobe complex are very similar (power law relationship) in the two domains, as well as the limit between the two domains. For example, in the Annot system, which is a text-book example for confined system, lobe width is ca. 1–5 km, for a thickness of 2–10 m (Moraes et al., 2004). Lobe width is commonly two to three times higher and thickness up to two times smaller than the studied lobes. The intraslope lobes of the Karoo basin (Spychala et al., 2015) are three to ten times larger, with the same thickness ranges, than the Motta San Giovanni lobes. In the Zaire system, which is a representative unconfined example, lobe width is ca. 10–40 km, for a thickness of 5–10 m (Jegou et al., 2008), that is ten to hundreds of times larger in width, with the same order of magnitude in thickness than the studied examples.

There is considerable variation both laterally and vertically, resulting in a complex distribution of architectural elements in the Motta San Giovanni lobes. As the lobe sizes are two to five times smaller than the tilted fault block width (Figure 4), and the paleocurrents show a clear relationship with normal fault orientation, we suggest that active tectonics influenced the intraslope lobe deposition, both in terms of topographic variation and subsequent lateral stacking. On the Log-log plots

TABLE 1 | Dimensions of Lobe Complexes, Lobes and Lobe elements in the Motta San Giovanni Formation (Miocene, Calabria) quantified from the 3D outcrop models.

Formation	Age	Type	Mode	Lobe width (m)	Lobe maximum thickness (m)
Motta San Giovanni	Miocene	Lobe Complex	Confined	4000	200
Motta San Giovanni	Miocene	Lobe Complex	Confined	5000	400
Motta San Giovanni	Miocene	Lobe Complex	Confined	4000	150
Motta San Giovanni	Miocene	Lobe Complex	Confined	6000	500
Motta San Giovanni	Miocene	Lobe	Confined	500	14
Motta San Giovanni	Miocene	Lobe	Confined	1000	17
Motta San Giovanni	Miocene	Lobe	Confined	1500	20
Motta San Giovanni	Miocene	Lobe	Confined	1000	22
Motta San Giovanni	Miocene	Lobe	Confined	300	10
Motta San Giovanni	Miocene	Lobe	Confined	290	3
Motta San Giovanni	Miocene	Lobe	Confined	600	9
Motta San Giovanni	Miocene	Lobe	Confined	800	15
Motta San Giovanni	Miocene	Lobe	Confined	600	15
Motta San Giovanni	Miocene	Lobe Element	Confined	400	4
Motta San Giovanni	Miocene	Lobe Element	Confined	200	7
Motta San Giovanni	Miocene	Lobe Element	Confined	110	4
Motta San Giovanni	Miocene	Lobe Element	Confined	105	4
Motta San Giovanni	Miocene	Lobe Element	Confined	200	5
Motta San Giovanni	Miocene	Lobe Element	Confined	500	4

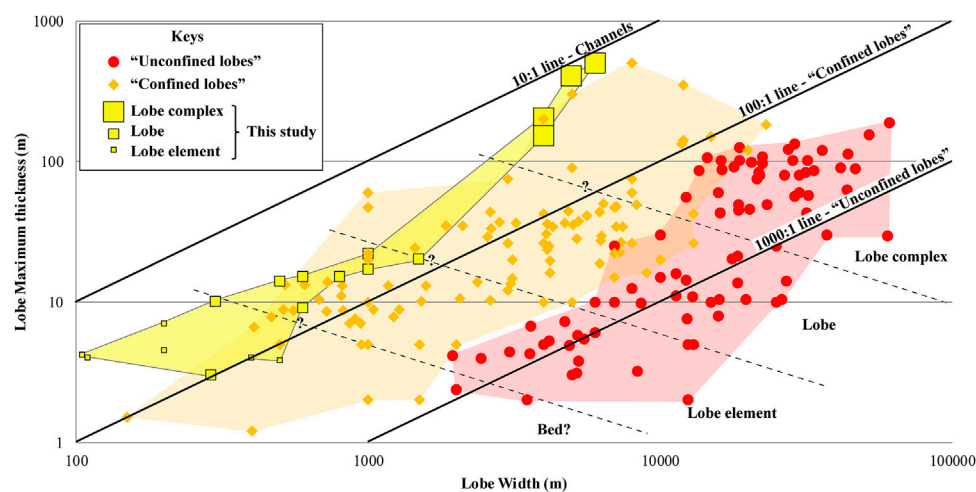


FIGURE 13 | Observed width vs. maximum thickness for studied lobes of the Motta San Giovanni Formation (green square), plotted on the log-log plot with confined systems aligned on a 100:1 line (diamond in different shades of yellowish) and unconfined systems aligned on a 1000:1 line (dot in different shades of bluish). 10:1 line illustrates the trend for channels (Pickering and Clark, 1996). Data are extracted from Pirmez et al. (2000), Bruhn et al. (2003), Moraes et al. (2004), Pr  lat et al. (2009, 2010, and reference therein), Etienne et al. (2012), Spychala et al. (2015), Marini et al. (2016), Picot et al. (2016, and reference therein), and Postma and Kleverlaan (2018), McArthur et al. (2021).

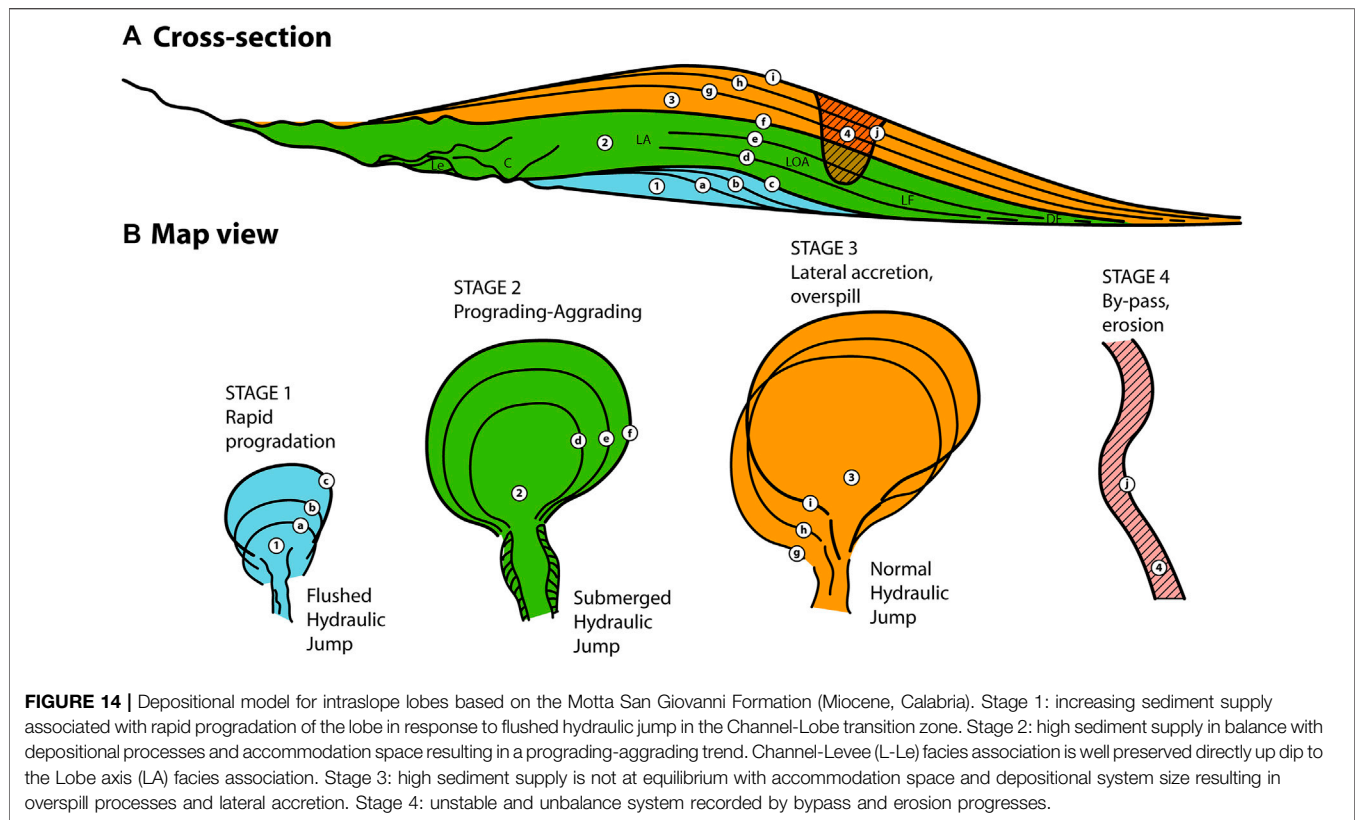
of widths vs. maximum thicknesses, our population is intermediate between 10:1 trend of channels (Pickering and Clark, 1996) and 100:1 line of confined systems (Figure 13). The transform margin perched lobes of the Motta San Giovanni Formation can be considered end-members taking into account the width/max-thickness ratio criteria.

Net-to-Gross, Facies, and Processes

In the Motta San Giovanni lobes, facies transitions occur over very short distances, typically over 10's of meters. It is consistent

with other intraslope lobe systems, such as the Karoo one (Spychala et al., 2015). It is a striking difference when comparing with basin floor lobe systems characterized by facies transitions over several kilometers (e.g., Pr  lat et al., 2009; Groeneweg et al., 2010).

The Motta San Giovanni lobes are characterized by a very high percentage of sandstone (>90–95% in lobe axis), probably because the upper fine-grained part of the flow can be stripped down-dip, overpassing the confined lows along the slope, which will increase the relative proportion of sand that



is locally accumulated. Such bypass and overspill processes are typical of intraslope sub-basins as also described from other geological contexts (Sinclair and Tomasso, 2002; Prather, 2003; McArthur et al., 2021).

Studied lobe fringes record few bipartite beds, which are diagnostic for basin floor lobe fringe deposits (Hodgson, 2009). It is in line with the observation from the intraslope lobe fringe deposits of the Karoo example (Spychala et al., 2015).

Stacking Pattern and Incisions

The studied lobes show cyclicity recorded at the lobe element scale with prograding to prograding-aggrading trends that are very common in many lobes (e.g., Guillocheau et al., 2004; Gervais et al., 2006; Deptuck et al., 2008; Prélat et al., 2009; Mulder and Etienne, 2010; Postma and Kleverlaan, 2018). An aggradational to slightly compensational style of stacking is also observed in the Motta San Giovanni lobes (Motta and Saetta areas) that are present in other intraslope and confined lobes (Guillocheau et al., 2004; Sychala et al., 2015). In contrast, basin floor lobes exhibit markedly compensational styles of stacking to form wide and spread lobe systems (Prélat et al., 2009; Groeneweg et al., 2010; Straub and Pyles, 2012).

Another diagnostic stacking pattern feature has been observed with m-deep erosion and bypass surface at the top of the lobe, and locally of lobe elements (Motta and Saetta areas). These surfaces and related paleo relief are rarely filled with channel-like facies association suggesting the system to be very instable. Intraslope

lobes are commonly incised by channels in response to transient slope accommodation (e.g., Adeogba et al., 2005; Sychala et al., 2015).

Lobe Depositional Model in Intraslope Complex Margin

Based on the Motta San Giovanni examples, we propose a depositional model including four stages of evolution for intraslope lobes deposited in perched mini-basins organized in piano-like blocks along transform margins (Figure 14).

Stage 1 corresponds to channel and lobe initiation on fine-grained deposits (substrate) with elongate fan-lobe elements (Figure 14). This stage is for example illustrated between surfaces 1 and 2 in Motta and Saetta areas (Figures 8–10). Lobe elements show coarsening and thickening upward trends indicating progradational stacking of distal lobe facies associations. There is no deposition in the CLTZ during stage 1, but rather bypass and erosion. The hydraulic jump is flushed all over the CLTZ resulting in isolated, detached lobe. Stage 1 could be considered the lobe precursor. The lobe precursor generally corresponds to a single or a few lobe beds.

Stage 2 records both progradation and aggradation of lobe elements that are coarser grained than those of the distal lobe facies association observed in stage 1 (Figure 14). This stage is for example illustrated between surfaces 3 and 4 in the Motta area (Figure 8), as well as between surfaces 2 and 3 in the Saetta area (Figures 9, 10). Channel, lobe axis to lobe fringe facies

associations are vertically stacked and progressively onlap on the former CLTZ. This aggradation of the most proximal facies association locally reduces the depositional slope gradient in the CLTZ. We propose that the hydraulic jump was progressively submerged inducing energy loss. We interpret stage 2 as recording a balance between sediment supply and accommodation space within the active lobe area.

Stage 3 is characterized by major bypass associated with lateral accretion, with locally aggradation (**Figure 14**). This stage is, for example, illustrated between surfaces 4 and 5 in the Motta area (**Figure 8**). Lobe shows overflow and spill over geometries suggesting a down-dip migration of the hydraulic jump across the propagating CLTZ on the top on the former lobe at the end of stage 2. Observed facies and geometries do not support a major progradation of the feeder channel-levee complex during this stage, but rather bypass processes in the CLTZ. The width of the lobe axis progressively increases, while other parts of the lobe start to be starved.

Stage 4 is characterized by bypass and starved deposits (reddish crusts) draping the previous paleo-relief on the top of the former lobe at the end of stage 3 (**Figure 14**). Surface 3 in the Di Leo area illustrates Stage 4 (**Figures 11, 12**). No (to very thin) channel-levees (facies association 1) are preserved in the former and initial upstream CLTZ. Deep incision across lobe or in inter lobe area suggests major final bypass and erosion, potentially in response to cascading effect on previous lobe morphology. Erosion along surface 5 in the Saetta area is a good example of Stage 4 (**Figures 9, 10**).

This dynamic shares similarities with the model proposed by Postma and Kleverlaan (2018), and their comparison to the experimental study of Hamilton et al. (2015), especially stages 1 and 2. There is nevertheless an important difference because, in their models, after the prograding-aggrading phase (Stage 2), the hydraulic jump subsequently retreated upstream over time, and avulsed to create a new channel. This point initiates the back-fill stage 3 of Postma and Kleverlaan (2018). In contrast, our stage 3 based on the Motta San Giovanni Formation cannot be considered a simple avulsion with a new cycle, as it is repetitive in many lobe-stacking patterns and records a renewal normal hydraulic jump occurrence. We interpret stage 3 as recording a progressive unbalance between available accommodation space and sediment supply. The entire lobe area would thus not be fully covered by deposition and lateral migration, thus over spilling initiated. Our stage 4 is also not comparable with the back-filling stage of Postma and Kleverlaan (2018) as it records both bypass and abrupt lobe abandonment with starved deposits. It suggests that the main period for sediment bypass through the basin floor fan is mainly recorded by a condensed bypass surface localized at the top of the lobe (Stage 4).

The proposed evolution model also shares similarities with the conceptual model of confined sandy margin of the late Quaternary Golo system established by Gervais et al. (2004, 2006). In the Golo system, the quantity and quality of sediment supply to the basin are controlled by the relative sea level changes and potential connection between canyon and sediment source. Our stage 1 could fit with the lowering sea

level and intermediate turbidity activity stage characterized by large thin sand lobes deposits. Our stage 2 could fit with the lowstand sea level phase characterized by large, thick, and stacked sand lobes deposits. It is not clear if our stage 3 fits with the previous stage or with the following rising sea level one characterized by moderate turbiditic activity with small thin sand deposits. The interglacial high stand setting could correspond to hemipelagic sedimentation preserved in between lobes. The model proposed by Gervais et al. (2004, 2006) nevertheless lacks our stage 4 (bypass and erosion).

After lobe aggradation and progradation, lobe may again be incised by the lobe channel (Bonnell et al., 2005). The progradation of lobe elements usually occurs by lobe “evitment” or “avoidance” (Turakiewicz, 2004; Jegou et al., 2008). When avulsion occurs, the channel quickly settles around the preceding lobe element and new lobe element forms downward. In this case, the channel emplacement occurs by topographic compensation (Mutti and Sonnino, 1981). In the Motta San Giovanni Formation, this topographic compensation is not always observed and the new bypass channel (Stage 3) is generally right on the top of the previous aggrading lobe axis or channel. Stage 3 cannot thus be considered a simple avulsion but rather a major milestone in the evolution of our studied intraslope lobe. An alternative interpretation would be that there was no space for the channel to avulse to a new low but was forced to stay more or less in the same position. Finally, the incisions/channels developed in the upstream CLTZ are not filled by the channel/levee facies during the back-filling stage, but by a new prograding lobe from the following cycle (new stage 1) suggesting that the hydraulic jump was very efficient in flushing sediment in the CLTZ before the next cycle.

Therefore, we speculate that this intraslope lobe system has a peculiarity, with a back-and-forth hydraulic jump dynamic. Hydraulic jump location could be described as normal jump when it occurs at the slope break (kinematic energy equals potential energy), flushed jump when occurring downstream of a slope break (kinematic > potential), or submerged jump when occurring upstream of the slope break (kinematic < potential) (Rajaratnam, 1967; Komar, 1971; Hager 1992; Cartigny et al., 2013). We propose that during Stage 1, the hydraulic jump was progressively flushed downstream the CLTZ. Then during Stage 2, it migrated upstream and stabilized in the CLTZ progressively evolving to submerged jump. The energy loss is maximal resulting in thick and massive packages of sandstones deposited all over the lobe area. Stage 3 finally recorded a renewal downstream migration with a normal jump emplacement, probably in response to the lowering of slope in the depositional lobe domain when compared to the upstream bypassed CLTZ. A new slope break marks the establishment of a normal hydraulic jump (Stage 3) following the previous submerged jump (Stage 2). Stage 4 is characterized by a rapid abandonment of the depositional system, which shares similarities with common lobe “evitment” or “avoidance.” We thus propose that intraslope lobe from the Motta San Giovanni Formation is characterized by back-and-forth migration of the hydraulic jump from flushed, to submerged and finally normal jump.

CONCLUSION

We present a detailed characterization of some outcropping intraslope lobes of the Miocene Motta San Giovanni Formation (Calabria), which were deposited and perched within sub-basins, along a transform margin. The results can be summarized in two points:

1. Based on the analysis of facies associations and stratigraphic architecture, we propose a depositional model diagnostic of intraslope lobes in a complex slope setting. Four main stages of evolution were identified with, 1) isolated detached lobe precursor during Stage 1, 2) prograding and aggrading lobe elements associated with a relatively stable submerged hydraulic jump in the CLTZ during Stage 2, 3) bypass associated with lateral accretion and local aggradation interpreted as a renewal of normal hydraulic jump emplacement, and 4) rapid abandonment during Stage 4.

2. A comparison with well-known intraslope and confined lobes, as well as basin floor lobes, is proposed, highlighting that the intraslope lobes deposited along transform margin are particularly small and relatively thin sandy deposits. Lobe elements are ca. 100–500 m wide, 200–600 m long, and 2–7 m

thick. Lobes are ca. 300–3000 m wide, 500–5000 m long, and 2–22 m thick. They could be considered end-member in a lobe classification based on their Net-to-Gross content and their thickness/width ratio, largely driven by flow stripping and overspill processes in such structurally confined basins.

DATA AVAILABILITY STATEMENT

The raw data supporting the conclusions of this article will be made available by the authors, without undue reservation.

AUTHOR CONTRIBUTIONS

SR, SB, JB, and PB contributed to conception and design of the study. SR organized the database and interpretation. JS acquired and built most of the 3D outcrop models. SR wrote the first draft of the manuscript. All authors contributed to manuscript revision, read, and approved the submitted version.

REFERENCES

- Adeogba, A. A., McHargue, T. R., and Graham, S. A. (2005). Transient Fan Architecture and Depositional Controls from Near-Surface 3-D Seismic Data, Niger Delta Continental Slope. *Bulletin* 89, 627–643. doi:10.1306/11200404025
- Albertão, G. A., Mulder, T., and Eschard, R. (2011). Impact of Salt-Related Palaeotopography on the Distribution of Turbidite Reservoirs: Evidence from Well-Seismic Analyses and Structural Restorations in the Brazilian Offshore. *Mar. Pet. Geology* 28, 1023–1046. doi:10.1016/j.marpetgeo.2010.09.009
- Allen, J. R. L. (1971). Instantaneous Sediment Deposition Rates Deduced from Climbing-Ripple Cross-Lamination. *J. Geol. Soc.* 127, 553–561. doi:10.1144/gsl.jgs.1971.127.06.02
- Allen, J. R. L. (1982). *Sedimentary Structures: Their Character and Physical Basis*. Amsterdam: Elsevier, 1, 593.
- Arnott, R. W. C., and Al-Mufti, O. (2017). Deep-Marine Pseudo Dune Cross-Stratification-Similar, but Completely Different. *J. Sediment. Res.* 87, 312–323. doi:10.2110/jsr.2017.21
- Arnott, R. W. C., and Hand, B. C. (1989). Bedforms, Primary Structures and Grain Fabric in the Presence of Suspended Sediment Rain. *J. Sediment. Pet.* 59, 1062–1069. doi:10.1306/212f90f2-2b24-11d7-8648000102c1865d
- Barrier, P. (1987). Stratigraphie des dépôts pliocènes et pleistocènes du Détroit de Messine (Italie). *Doc. Trav. Inst. Géol. Albert de Lapparent (Igal)* 11, 59–81.
- Barrier, P., Casale, V., Costa, B., Di Geronimo, L., Olivieri, O., and Rosso, A. (1986). La sezione plio-pleistocenica di Pavigliana (Reggio Calabria). *Boll. Soc. Pal. Ital.* 25 (2), 3–144.
- Barrier, P., Di Geronimo, L., and Montecat, C. (1987). Le Détroit de Messine (Italie). Evolution tectono-sédimentaire récente (pliocène et quaternaire) et environnement actuel. *Doc. Trav. Inst. Géol. Albert de Lapparent (Igal)*, 11, 3.
- Barrier, P. (1982). *Étude préliminaire des formations pliocènes et quaternaires du Sud de Reggio di Calabria (Italie); (tome I), Étude du Rione Branca (tome II)*. MS dissertation. Beauvais: M.A.G 3. Institut Géologique Albert-de-Lapparent IGAL.
- Barton, M. D. (2012). “Evolution of an Intra-slope Apron, Offshore Niger delta Slope: Impact of Step Geometry on Apron Architecture,” in *Application of the Principles of Seismic Geomorphology to Continental-Slope and Base-Of-Slope Systems: Case Studies from Seafloor and Near-Seafloor Analogues*. Editors B. E. Prather, M. E. Deptuck, D. Mohrig, B. van Hoor, and R. B. Wynn (SEPM Special Publication), 99, 181–197. doi:10.2110/pec.12.99.0181
- Becue, F. (1988). *Le Tortonien de Catanzaro (Calabre - Italie)*. Master's thesis. Beauvais: M.G. 25 Institut Géologique Albert-de-Lapparent IGAL.
- Best, J., and Bridge, J. (1992). The Morphology and Dynamics of Low Amplitude Bedwaves upon Upper Stage Plane Beds and the Preservation of Planar Laminar. *Sedimentology* 39, 737–752. doi:10.1111/j.1365-3091.1992.tb02150.x
- Bonardi, G., Cavazza, W., Perrone, V., and Rossi, S. (2001). “Calabria-Peloritani Terrane and Northern Ionian Sea,” in *Anatomy of an Orogen: The Apennines and Adjacent Mediterranean Basins: Dordrecht, The Netherlands*. Editors G. B. Vai and I. P. Martini (Kluwer Academic Publishers), 287–306. doi:10.1007/978-94-015-9829-3_17
- Bonardi, G., Giunta, G., Perrone, V., Russo, M., Zuppetta, A., and Ciampo, G. (1980). Osservazioni sull'evoluzione dell'Arco Calabro-peloritano nel Miocene inferiore: la Formazione di Stilo-Capo d'Orlando. *Bollettino Società Geologica Italiana* 99, 365–393.
- Bonnell, C., Dennielou, B., Droz, L., Mulder, T., and Berné, S. (2005). Architecture and Depositional Pattern of the Rhône Neofan and Recent Gravity Activity in the Gulf of Lions (Western Mediterranean). *Mar. Pet. Geology* 22 (6–7), 827–843. doi:10.1016/j.marpetgeo.2005.03.003
- Booth, J. R., Dean, M. C., DuVernay, A. E., and Styzen, M. J. (2003). Paleobathymetric Controls on the Stratigraphic Architecture and Reservoir Development of Confined Fans in the Auger Basin: Central Gulf of Mexico Slope. *Mar. Pet. Geology* 20, 563–586. doi:10.1016/j.marpetgeo.2003.03.008
- Bouchet, F. (1990). *Étude sédimentaire et structurale de la série oligo-miocène et plio-quaternaire de la région de Melito (Calabre - Italie)*. MS dissertation. Beauvais: M.A.G. 65 Institut Géologique Albert-de-Lapparent IGAL.
- Boullin, J. P., Durand-Delga, M., and Olivier, P. (1986). “Betic Rifian and Tyrrhenian Arc: Distinctive Features, Genesis and Development Stages,” in *The Origin of Arcs*. Editor F. Wezel (New York, NY: Elsevier), 281–304.
- Bouma, A. H. (1962). *Sedimentology of Some Flysch Deposits: A Graphic Approach to Facies Interpretation*. Amsterdam: Elsevier, 168.
- Bourel, M., and Degraeve, C. (2020). *Étude des relations entre la tectonique régionale et les formations turbiditiques du Miocène de la formation de Motta San Giovanni, Calabre, Italie*. Beauvais: M.I.R. Institut Polytechnique UniLaSalle, 875, 112.
- Brooks, H. L., Hodgson, D. M., Brunt, R. L., Peakall, J., Hofstra, M., and Flint, S. S. (2018). Deep-water Channel-Lobe Transition Zone Dynamics: Processes and Depositional Architecture, an Example from the Karoo Basin, South Africa. *GSA Bull.* 130, 1723–1746. doi:10.1130/B31714.1
- Bruhn, C. H. L., Gomes, J. A. T., Del Lucchese, C., Jr., and Johann, P. R. S. (2003). Campos Basin: Reservoir Characterization and Management – Historical Overview and Future Challenges,” in *Offshore Technology Conference*, Houston, TX, May 5–8, 2003. doi:10.4043/15220-MS
- Brunt, R. L., Hodgson, D. M., Flint, S. S., Pringle, J. K., Di Celma, C., Prélât, A., et al. (2013). Confined to Unconfined: Anatomy of a Base of Slope Succession, Karoo

- Basin, South Africa. *Mar. Pet. Geology* 41, 206–221. doi:10.1016/j.marpetgeo.2012.02.007
- Brutto, F., Muto, F., Loreto, M. F., D'Amico, S., De Paola, N., Tripodi, V., et al. (2018). “Quaternary Stress Field and Faulting in the Western Part of the Catanzaro Trough (Calabria, Southern Italy),” in *Moment Tensor Solutions*. Editor S. D'Amico (Springer Natural Hazards), 619–642. doi:10.1007/978-3-319-77359-9_28
- Burgreen, B., and Graham, S. (2014). Evolution of a Deep-Water Lobe System in the Neogene Trench-Slope Setting of the East Coast Basin, New Zealand: Lobe Stratigraphy and Architecture in a Weakly Confined basin Configuration. *Mar. Pet. Geology* 54, 1–22. doi:10.1016/j.marpetgeo.2014.02.011
- Butler, R. W. H., Pinter, P. R., Maniscalco, R., and Hartley, A. J. (2020) Deep-water Sand-Fairway Mapping as a Tool for Tectonic Restoration: Decoding Miocene central Mediterranean Palaeogeography Using the Numidian Turbidites of Southern Italy. *J. Geol. Soc.* 177, 766–783. doi:10.1144/jgs2020-008
- Cartigny, M. J. B., Eggenhuisen, J. T., Hansen, E. W. M., and Postma, G. (2013). Concentration Dependent Flow Stratification in Experimental High-Density Turbidity Currents and Their Relevance to Turbidite Facies Models. *J. Sediment. Res.* 83, 1046–1064. doi:10.2110/jsr.2013.71
- Cavazza, W., Blenkinsop, J., DeCelles, P., Patterson, R. T., and Reinhardt, E. (1997). Stratigrafia e sedimentologia della sequenza sedimentaria Oligocenico-Quaternaria del Bacino Calabro-Ionico. *Boll. Soc. Geol. It.* 116, 51–77.
- Cavazza, W., and Ingersoll, R. V. (2005). Detrital Modes of the Ionian Forearc Basin Fill (Oligocene-Quaternary) Reflect the Tectonic Evolution of the Calabria-Peloritani Terrane (Southern Italy). *J. Sediment. Res.* 75, 268–279. doi:10.2110/jsr.2005.020
- Chirol, H., and Kubiak, T. (2019). *Etude de l'architecture des corps turbiditiques miocènes de la formation de Motta San Giovanni, Secteur Ouest, Calabre, Italie*. Beauvais: M.I.R. Institut Polytechnique UniLaSalle, 839, 60.
- Colas, E., and Ripoll, A. (2017). *Etude sédimentologique et structurale de l'architecture des corps turbiditiques miocènes au niveau du village de Lazzaro*. Beauvais: M.I.R. Institut Polytechnique UniLaSalle, 839, 141.
- Cortese, E. (1895). Descrizione Geologica Della Calabria. *Memorie descrittive Carta Geologica d'Italia* 9, 310.
- Critelli, S., Muto, F., Perri, F., and Tripodi, V. (2017). Interpreting Provenance Relations from Sandstone Detrital Modes, Southern Italy Foreland Region: Stratigraphic Record of the Miocene Tectonic Evolution. *Mar. Pet. Geology* 87, 47–59. doi:10.1016/j.marpetgeo.2017.01.026
- Critelli, S., Muto, F., Tripodi, V., and Perri, F. (2011). “Relationships between Lithospheric Flexure, Thrust Tectonics and Stratigraphic Sequences in Foreland Setting: the Southern Apennines Foreland basin System, Italy,” in *New Frontiers in Tectonic Research at the Midst of Plate Convergence*. Editor U. Schattner (Rijeka, Croatia: Intech Open Access Publisher, Janeza Trdine), 9, 121–170. doi:10.5772/24120
- Critelli, S. (2018). Provenance of Mesozoic to Cenozoic Circum-Mediterranean Sandstones in Relation to Tectonic Setting. *Earth-Science Rev.* 185, 624–648. doi:10.1016/j.earscirev.2018.07.001
- Dennielou, B., Droz, L., Babonneau, N., Jacq, C., Bonnel, C., Picot, M., et al. (2017). Morphology, Structure, Composition and Build-Up Processes of the Active Channel-Mouth Lobe Complex of the Congo Deep-Sea Fan with Inputs from Remotely Operated Underwater Vehicle (ROV) Multibeam and Video Surveys. *Deep Sea Res. Part Topical Stud. Oceanography* 142, 25–49. doi:10.1016/j.dsr2.2017.03.010
- Deptuck, M. E., Piper, D. J. W., Savoye, B., and Gervais, A. (2008). Dimensions and Architecture of Late Pleistocene Submarine Lobes off the Northern Margin of East Corsica. *Sedimentology* 55, 869–898. doi:10.1111/j.1365-3091.2007.00926.x
- Dercourt, J., Zonenshain, L. P., Ricou, L.-E., Kazmin, V. G., Le Pichon, X., Knipper, A. L., et al. (1986). Geological Evolution of the Tethys belt from the Atlantic to the Pamirs since the Lias. *Tectonophysics* 123, 241–315. doi:10.1016/0040-1951(86)90199-x
- Deschamps, R., Doligez, B., Schmitz, J., Joseph, P., Rohais, S., Pellerin, M., et al. (2017). De la reconstitution numérique 3D d'affleurements au modèle de réservoir : une approche intégrée. *Géologues*, 68–71.
- Deschamps, R., Schmitz, J., Daniel, J.-M., and Joseph, P. (2013). *Method for Exploiting a Subsurface deposit Comprising at Least One Geological Outcrop by Means of Photogrammetry*.
- Dewey, J. F., Helman, M. L., Knott, S. D., Turco, E., and Hutton, D. H. W. (1989). “Kinematics of the Western Mediterranean,” in *Alpine Tectonics*. Editors M. P. Coward, D. Dietrich, and R. G. Park (Geological Society, London, Special Publications), 45, 265–283. doi:10.1144/gsl.sp.1989.045.01.15
- Eschard, R., Albouy, E., Gaumet, F., and Ayub, A. (2004). “Comparing the Depositional Architecture of basin Floor Fans and Slope Fans in the Pab Sandstone, Maastrichtian, Pakistan,” in *Confined Turbidite Systems*. Editor S. A. Lomas (Geological Society of London, Special Publications), 222, 159–185. doi:10.1144/gsl.sp.2004.222.01.09
- Etienne, S., Mulder, T., Bez, M., Desaubiaux, G., Kwasniewski, A., Parize, O., et al. (2012). Multiple Scale Characterization of Sand-Rich Distal Lobe deposit Variability: Examples from the Annot Sandstones Formation, Eocene-Oligocene, SE France. *Sediment. Geology* 273–274, 1–18. doi:10.1016/j.sedgeo.2012.05.003
- Faccenna, C., Becker, T. W., Lucente, F. P., Jolivet, L., and Rossetti, F. (2001). History of Subduction and Back-Arc Extension in the Central Mediterranean. *Geophys. J. Int.* 145, 809–820. doi:10.1046/j.0956-540x.2001.01435.x
- Ferry, J.-N., Mulder, T., Parize, O., and Raillard, S. (2005). “Concept of Equilibrium Profile in Deep-Water Turbidite System: Effects of Local Physiographic Changes on the Nature of Sedimentary Process and the Geometries of Deposits,” in *Submarine Slope Systems: Processes and Products*. Editors D. M. Hodgson and S. S. Flint (Geological Society of London, Special Publications), 244, 181–193. doi:10.1144/gsl.sp.2005.244.01.11
- Fiduk, J. C., Weimer, P., Trudgill, B. D., Rowan, M. G., Gale, P. E., Phair, R. L., et al. (1999). The Perdido Fold belt, Northwestern Deep Gulf of Mexico, Part 2: Seismic Stratigraphy and Petroleum Systems. *AAPG Bull.* 83, 578–612. doi:10.1306/00aa9c00-1730-11d7-8645000102c1865d
- Flint, S. S., Hodgson, D. M., Sprague, A. R., Brunt, R. L., van der Merwe, W. C., Figueiredo, J., et al. (2011). Depositional Architecture and Sequence Stratigraphy of the Karoo Basin Floor to Shelf Edge Succession, Laingsburg Depocentre, South Africa. *Mar. Pet. Geology* 28, 658–674. doi:10.1016/j.marpetgeo.2010.06.008
- Gaillot, G., Hoyal, D., Demko, T., and Abreu, V. (2015). *Building Blocks of the Modern Golo Submarine Fan: Insights from High-Resolution Seismic Data*. Krakow, Poland: 31st IAS Conference, 22–25.
- Gallet de Saint-Aurin, J.-M. (1988). *Approche tectono-sédimentaire du Bassin néogène et quaternaire d'Ardore-Siderno (Calabre, Italie)*. MS dissertation. Beauvais: M.A.G. 53 Institut Géologique Albert-de-Lapparent IGAL.
- Gamberi, F., and Rovere, M. (2011). Architecture of a Modern Transient Slope Fan (Villafranca Fan, Gioia Basin-Southeastern Tyrrhenian Sea). *Sediment. Geology* 236, 211–225. doi:10.1016/j.sedgeo.2011.01.007
- Gamberi, F., Rovere, M., and Marani, M. (2011). Mass-transport Complex Evolution in a Tectonically Active Margin (Gioia Basin, Southeastern Tyrrhenian Sea). *Mar. Geology* 279, 98–110. doi:10.1016/j.margeo.2010.10.015
- Gervais, A., Savoye, B., Mulder, T., and Gonthier, E. (2006). Sandy Modern Turbidite Lobes: A New Insight from High Resolution Seismic Data. *Mar. Pet. Geology* 23, 485–502. doi:10.1016/j.marpetgeo.2005.10.006
- Gervais, A., Savoye, B., Piper, D. J. W., Mulder, T., Cremer, M., and Pichevin, L. (2004). “Present Morphology and Depositional Architecture of a sandy Confined Submarine System: the Golo Turbidite System (Eastern Margin of Corsica),” in *Confined Turbidite Systems*. Editors S. A. Lomas and P. Joseph (Geological Society Special Publication), 222, 59–89. doi:10.1144/gsl.sp.2004.222.01.05
- Groeneweg, R. M., Hodgson, D. M., Prêlat, A., Luthi, S. M., and Flint, S. S. (2010). Flow-Deposit Interaction in Submarine Lobes: Insights from Outcrop Observations and Realizations of a Process-Based Numerical Model. *J. Sediment. Res.* 80, 252–267. doi:10.2110/jsr.2010.028
- Guillet de Chatelus, F., and Prosperi, A. (2020). *Impact de l'activité syn-sédimentaire sur les architectures turbiditiques miocènes de Motta San Giovanni, Calabre - Italie*. Beauvais: M.I.R. Institut Polytechnique UniLaSalle, 889, 41.
- Guillocheau, F., Quémener, J.-M., Robin, C., Joseph, P., and Broucke, O. (2004). “Genetic Units/parasequences of the Annot Turbidite System, SE France,” in *Deep Water Sedimentation in the Alpine Basin of SE France. New Perspectives on the Grès d'Annot and Related Systems*. Editors P. Joseph and S. A. Lomas (Geological Society, London, Special Publication), 221, 181–202. doi:10.1144/gsl.sp.2004.221.01.10
- Guillois, M., and Polard-Taine, P. (2016). in *Etude sédimentologique et structurale de l'architecture des corps turbiditiques miocènes au niveau du village de Motta San Giovanni* Beauvais: Institut Polytechnique Lasalle Beauvais, 131.

- Hager, W. L. (1992). *Energy Dissipators and Hydraulic Jumps*. Dordrecht: Kluwer Academic Publishers.
- Haughton, P., Davis, C., McCaffrey, W., and Barker, S. (2009). Hybrid Sediment Gravity Flow Deposits - Classification, Origin and Significance. *Mar. Pet. Geology* 26, 1900–1918. doi:10.1016/j.marpetgeo.2009.02.012
- Hodgson, D. M. (2009). Distribution and Origin of Hybrid Beds in Sand-Rich Submarine Fans of the Tanqua Depocentre, Karoo Basin, South Africa. *Mar. Pet. Geology* 26, 1940–1956. doi:10.1016/j.marpetgeo.2009.02.011
- Hodgson, D. M., Kane, I. A., Flint, S. S., Brunt, R. L., and Ortiz-Karpf, A. (2016). Time-Transgressive Confinement on the Slope and the Progradation of Basin-Floor Fans: Implications for the Sequence Stratigraphy of Deep-Water Deposits. *J. Sediment. Res.* 86, 73–86. doi:10.2110/jsr.2016.3
- Hofstra, M., Hodgson, D. M., Peakall, J., and Flint, S. S. (2015). Giant Scour-Fills in Ancient Channel-Lobe Transition Zones: Formative Processes and Depositional Architecture. *Sediment. Geology* 329, 98–114. doi:10.1016/j.sedgeo.2015.09.004
- Holman, W. E., Robertson, S. S., Lawrence, D. T., and Rossen, C. (1994). “Field Development, Depositional Model, and Production Performance of the Turbiditic ‘J’ Sands at Prospect Bullwinkle, Green Canyon 65 Field, Outer-Shelf Gulf of Mexico,” in *Submarine Fans and Turbidite Systems—Sequence Stratigraphy, Reservoir Architecture, and Production Characteristics*. Editors P. Weimer, A. H. Bouma, and B. F. Perkins (GCSSEPM Fifteenth Annual Research Conference), 139–150. doi:10.5724/gcs.94.15.0139
- Jegou, I., Savoye, B., Pirmez, C., and Droz, L. (2008). Channel-mouth Lobe Complex of the Recent Amazon Fan: The Missing Piece. *Mar. Geology* 252, 62–77. doi:10.1016/j.margeo.2008.03.004
- Jobe, Z. R., Lowe, D. R., and Morris, W. R. (2012). Climbing-ripple Successions in Turbidite Systems: Depositional Environments, Sedimentation Rates and Accumulation Times. *Sedimentology* 59, 867–898. doi:10.1111/j.1365-3091.2011.01283.x
- Jobe, Z. R., Sylvester, Z., Howes, N., Pirmez, C., Parker, A., Cantelli, A., et al. (2017). High-resolution, Millennial-Scale Patterns of Bed Compensation on a Sand-Rich Intraslope Submarine Fan, Western Niger Delta Slope. *Geol. Soc. America Bull.* 129, 23–37. doi:10.1130/b31440.1
- Jolivet, L., Menant, A., Roche, V., Le Pourhiet, L., Maillard, A., Augier, R., et al. (2021). Transfer Zones in Mediterranean Back-Arc Regions and Tear Faults. *BSGF - Earth Sci. Bull.* 192, 11. doi:10.1051/bsgf/2021006
- Joseph, P., Babonneau, N., Bourgeois, A., Cotteret, G., Eschard, R., Garin, B., et al. (2000). “The Annot Sandstone Outcrops (French Alps): Architecture Description as Input for Quantification and 3D Reservoir Modeling,” in *Deep-Water Reservoirs of the World: Gulf Coast Section SEPM Foundation 20th Annual Research Conference*. Editor P. Weimer (SEPM Special Publication), 28, 422–449. doi:10.5724/gcs.00.15.0422
- Joseph, P., and Lomas, S. A. (2004). “Deep-water Sedimentation in the Alpine Foreland Basin of SE France: New Perspectives on the Grès d’Annot and Related Systems—An Introduction,” in *Deep-Water Sedimentation in the Alpine Basin of SE France: New Perspectives on the Grès d’Annot and Related Systems*. Editors P. Joseph and S. A. Lomas Geological Society, London, Special Publications, 221, 1–16. doi:10.1144/gsl.sp.2004.221.01.01
- Kane, I. A., and Hodgson, D. M. (2011). Sedimentological Criteria to Differentiate Submarine Channel Levee Subenvironments: Exhumed Examples from the Rosario Fm. (Upper Cretaceous) of Baja California, Mexico, and the Fort Brown Fm. (Permian), Karoo Basin, S. Africa. *Mar. Pet. Geology* 28, 807–823. doi:10.1016/j.marpetgeo.2010.05.009
- Kezirian, F., Barrier, P., Bouillin, J.-P., and Janin, M.-C. (1994). L’Oligo-Miocène péloritain (Sicile) : un témoin du rift du Bassin algéro-provençal. *C. R. Acad. Sci. Paris, Série* 319, 699–704.
- Kleverlaan, K. (1989). Three Distinctive Feeder-Lobe Systems within One Time Slice of the Tortonian Tabernas Fan, SE Spain. *Sedimentology* 36, 25–45. doi:10.1111/j.1365-3091.1989.tb00818.x
- Kneller, B. C., and Branney, M. J. (1995). Sustained High-Density Turbidity Currents and the Deposition of Thick Massive Sands. *Sedimentology* 42, 607–616. doi:10.1111/j.1365-3091.1995.tb00395.x
- Komar, P. D. (1971). Hydraulic Jumps in Turbidity Currents. *Geol. Soc. America Bull.* 82, 1477–1487. doi:10.1130/0016-7606(1971)82[1477:hjtc]2.0.co;2
- Leclair, S. F., and Arnott, R. W. C. (2005). Parallel Lamination Formed by High-Density Turbidity Currents. *J. Sediment. Res.* 75, 1–5. doi:10.2110/jsr.2005.001
- Leprêtre, R., Frizon de Lamotte, D., Déverchère, J., and Graindorge, D. (2019). Géodynamique de la Méditerranée occidentale : une série de bassins d’arrière-arc dans un environnement montagneux. *Géochronique* n149, 20–34.
- Li, L., Wang, Y., Xu, Q., Zhao, J., and Li, D. (2012). Seismic Geomorphology and Main Controls of Deep-Water Gravity Flow Sedimentary Process on the Slope of the Northern South China Sea. *Sci. China Earth Sci.* 55, 747–757. doi:10.1007/s11430-012-4396-1
- Lowe, D. R. (1982). Sediment Gravity Flows: II Depositional Models with Special Reference to the Deposits of High Density Turbidity Currents. *J. Sed. Res.* 52, 279–297. doi:10.1306/212f7f31-2b24-11d7-8648000102c1865d
- MacGregor, D., Robinson, J., and Spear, G. (2003). *Play Fairways of the Gulf of Guinea Transform Margin*. London: Geological Society, Special Publications, 207, 131–150. doi:10.1144/GSL.SP.2003.207.7
- Manoux, J. (1999). *Évolution tectono-sédimentaire de la partie ouest du Bassin de Melito di Porto Salvo au Miocène et au Plio-Quaternaire. (Calabre - Italie)*. MS dissertation. Beauvais: M.A.G. 211 Institut Géologique Albert-de-Lapparent IGAL, 103.
- Marchès, E., Mulder, T., Gonthier, E., Cremer, M., Hanquiez, V., Garlan, T., et al. (2010). Perched Lobe Formation in the Gulf of Cadiz: Interactions Between Gravity Processes and Contour Currents (Algarve Margin, Southern Portugal). *Sediment. Geology* 229, 81–94. doi:10.1016/j.sedgeo.2009.03.008
- Marchiel, A., and Rispal, N. (2019). *Etude de l’architecture des corps turbiditiques Miocène de la formation de Motta San Giovanni, Secteur Est, Calabre, Italie*. Beauvais: M.I.R. Institut Polytechnique UniLaSalle, 852, 110.
- Marini, M., Patacci, M., Felletti, F., and McCaffrey, W. D. (2016). Fill to Spill Stratigraphic Evolution of a Confined Turbidite Mini-basin Succession, and its Likely Well Bore Expression: The Castagnola Fm, NW Italy. *Mar. Pet. Geology* 69, 94–111. doi:10.1016/j.marpetgeo.2015.10.014
- McArthur, A. D., Bailleul, J., Mahieux, G., Claussmann, B., Wunderlich, A., and McCaffrey, W. D. (2021). Deformation-sedimentation Feedback and the Development of Anomalous Thick Aggradational Turbidite Lobes: Outcrop and Subsurface Examples from the Hikurangi Margin, New Zealand. *J. Sediment. Res.* 91 (4), 362–389. doi:10.2110/jsr.2020.013
- McGee, D. T., Bilinski, P. W., Gary, P. S., Pfeiffer, D. S., Sheiman, J. L., Lawrence, D. T., et al. (1994). “Geologic Models and Reservoir Geometries of Auger Field, deepwater Gulf of Mexico,” in *Submarine Fans and Turbidite Systems—Sequence Stratigraphy, Reservoir Architecture, and Production Characteristics*. Editors P. Weimer, A. H. Bouma, and B. F. Perkins (GCSSEPM Fifteenth Annual Research Conference), 245–256. doi:10.5724/gcs.94.15.0245
- Milia, A., Iannace, P., and Torrente, M. M. (2021). The Meeting Place of Backarc and Foreland Rifting: The Example of the Offshore Western Sicily (Central Mediterranean). *Glob. Planet. Change* 198, 103408. doi:10.1016/j.gloplacha.2020.103408
- Moraes, M. A. S., Blaskovski, P. R., and Joseph, P. (2004). “The Grès d’Annot as an Analogue for Brazilian Cretaceous sandstone Reservoirs: Comparing Convergent to Passive-Margin Confined Turbidites,” in *Deep-Water Sedimentation in the Alpine Basin of SE France: New Perspectives on the Grès d’Annot and Related Systems*. Editors P. Joseph and S. A. Lomas (Geological Society, London, Special Publications), 221, 419–437. doi:10.1144/gsl.sp.2004.221.01.23
- Morlo, T. (1985). *Étude préliminaire des formations tortoniennes à pléistocènes du Bassin de Mesima (Italie)*. MS dissertation. Beauvais: M.A.G. 27 Institut Géologique Albert-de-Lapparent IGAL.
- Mulder, T., Callec, Y., Parize, O., Joseph, P., Schneider, J.-L., Robin, C., et al. (2010). High-resolution Analysis of Submarine Lobes Deposits: Seismic-Scale Outcrops of the Lauzanier Area (SE Alps, France). *Sediment. Geology* 229, 160–191. doi:10.1016/j.sedgeo.2009.11.005
- Mulder, T., and Etienne, S. (2010). Lobes in Deep-Sea Turbidite Systems: State of the Art. *Sediment. Geology* 229, 75–80. doi:10.1016/j.sedgeo.2010.06.011
- Mutti, E. (1992). *Turbidite Sandstones*. Milan, Italy: Agip-Instituto di Geologia. Università di Parma, 275.
- Mutti, E., and Normark, W. R. (1987). “Comparing Examples of Modern and Ancient Turbidite Systems: Problems and Concepts,” in *Marine Clastic Sedimentology: Concepts and Case Studies*. Editors J. K. Leggett and G. G. Zuffa (London: Graham and Troutman). doi:10.1007/978-94-009-3241-8_1

- Mutti, E., and Sonnino, M. (1981). *Compensation Cycles: A Diagnostic Feature of Turbidite sandstone Lobes*. Int. Ass. Sediment. Bologna, Italy: 2nd European Reg. Meet., 120–123.
- Nicolleau, P., Vadet, A., Barrier, P., Bailleul, J., Brocheray, S., Kezirian, F., et al. *About the Serravalian Cidaris with Fan-Shaped Spines from Motta San Giovanni (Calabria, Italy)*. Brest: Carnets de Géologie.
- Ogniben, L. (1969). Schema introduttivo alla geologia del confino calabro-lucano. *Memorie della Società Geologica Italiana* 8, 453–763.
- Oluboyo, A. P., Gawthorpe, R. L., Bakke, K., and Hadler-Jacobsen, F. (2014). Salt Tectonic Controls on Deep-Water Turbidite Depositional Systems: Miocene, Southwestern Lower Congo Basin, Offshore Angola. *Basin Res.* 26, 597–620. doi:10.1111/bre.12051
- Patterson, R. T., Blenkinsop, J., and Cavazza, W. (1995). Planktic Foraminiferal Biostratigraphy and $^{87}\text{Sr}/^{86}\text{Sr}$ Isotopic Stratigraphy of the Oligocene-To-Pleistocene Sedimentary Sequence in the Southeastern Calabrian Microplate, Southern Italy. *J. Paleontol.* 69, 7–20. doi:10.1017/s0022336000026871
- Pellegrini, B. d. S., and Ribeiro, H. J. P. S. (2018). Exploratory Plays of Pará-Maranhão and Barreirinhas Basins in Deep and Ultra-deep Waters, Brazilian Equatorial Margin. *Braz. J. Geol.* 48 (3), 485–502. doi:10.1590/2317-4889201820180146
- Pichancourt, T., and Terrier, J. (2016). *Etude du potentiel réservoir des corps turbiditiques Miocènes à proximité du village de Motta San Giovanni*. Beauvais: M.I.R. Institut Polytechnique UniLaSalle, 747, 83.
- Pickering, K. T., and Clark, J. D. (1996). Architectural Elements and Growth Patterns of Submarine Channels: Application to Hydrocarbon Exploration. *Am. Assoc. Pet. Geologists Bull.* 80 (2), 194–221. doi:10.1306/64ed878c-1724-11d7-8645000102c1865d
- Picot, M., Droz, L., Marset, T., Dennielou, B., and Bez, M. (2016). Controls on Turbidite Sedimentation: Insights from a Quantitative Approach of Submarine Channel and Lobe Architecture (Late Quaternary Congo Fan). *Mar. Pet. Geology* 72, 423–446. doi:10.1016/j.marpetgeo.2016.02.004
- Pirmez, C., Beaubouef, R. T., Friedmann, S. J., and Mohrig, D. C. (2000). “Equilibrium Profile and Baselevel in Submarine Channels: Examples from Late Pleistocene Systems and Implications for the Architecture of Deepwater Reservoirs,” in *Deep-Water Reservoirs of the World: 20th Annual Research Conference, Gulf Coast Section Society of Economic Paleontologists and Mineralogists*. Editor P. Weimer, 782–805. doi:10.5724/gcs.00.15.0782
- Plink-Björklund, P., and Steel, R. (2002). Sea-level Fall Below the Shelf Edge, Without Basin-floor Fans. *Geol.* 30, 115–118. doi:10.1130/0091-7613(2002)030<0115:sfbts>2.0.co;2
- Postma, G., and Cartigny, M. J. B. (2014). Supercritical and Subcritical Turbidity Currents and Their Deposits—A Synthesis. *Geology* 42, 987–990. doi:10.1130/g35957.1
- Postma, G., and Kleverlaan, K. (2018). Supercritical Flows and Their Control on the Architecture and Facies of Small-Radius Sand-Rich Fan Lobes. *Sediment. Geology* 364, 53–70. doi:10.1016/j.sedgeo.2017.11.015
- Prather, B. E., Booth, J. R., Steffens, G. S., and Craig, P. A. (1998). Classification, Lithologic Calibration, and Stratigraphic Succession of Seismic Facies of Intraslope Basins Deep Water Gulf of Mexico, U.S.A. *AAPG Bull.* 82, 701–728.
- Prather, B. E. (2003). Controls on Reservoir Distribution, Architecture and Stratigraphic Trapping in Slope Settings. *Mar. Pet. Geology* 20, 529–545. doi:10.1016/j.marpetgeo.2003.03.009
- Prather, B. E., Pirmez, C., and Winker, C. D. (2012). “Stratigraphy of Linked Intraslope Basins: Brazos-Trinity System Western Gulf of Mexico,” in *Case Studies from Seafloor and Near-Seafloor Analogues* (SEPM, Special Publication), 99, 83–109. doi:10.2110/pec.12.99.0083
- Prélat, A., Covault, J. A., Hodgson, D. M., Fildani, A., and Flint, S. S. (2010). Intrinsic Controls on the Range of Volumes, Morphologies, and Dimensions of Submarine Lobes. *Sediment. Geology* 232, 658–674. doi:10.1016/j.sedgeo.2010.09.010
- Prélat, A., Hodgson, D. M., and Flint, S. S. (2009). Evolution, Architecture and Hierarchy of Distributary Deep-Water Deposits: A High-Resolution Outcrop Investigation from the Permian Karoo Basin, South Africa. *Sedimentology* 56, 2132–2154. doi:10.1111/j.1365-3091.2009.01073.x
- Pyles, D. R., Strachan, L. J., and Jennette, D. C. (2014). Lateral Juxtapositions of Channel and Lobe Elements in Distributive Submarine Fans: Three-Dimensional Outcrop Study of the Ross Sandstone and Geometric Model. *Geosphere* 10, 1104–1122. doi:10.1130/GES01042.1
- Raber, C. (2003). *Synthèse géologique de la province de Reggio di Calabria. A 1/100 000 : carte et notice (Calabre, Italie)*. Master's thesis. Beauvais: M.I.G. 191 Institut Géologique Albert-de-Lapparent IGAL, 180.
- Rajaratnam, N. (1967). Hydraulic Jumps. *Adv. Hydroscl.* 4, 197–280. doi:10.1016/b978-1-4831-9935-1.50011-2
- Roda, C. (1965). *Il calcare portlandiano a Dasycladace di M. Mutolo*. Reggio Calabria: Geologica Romana 4, 259–290.
- Rohais, S. (2000). *Évolution tectono-sédimentaire au Miocène et au Plio-Quaternaire du bassin de Palizzi à Brancalione (Calabre, Italie)*. MS dissertation. Beauvais: M.A.G. 234 Institut Géologique Albert-de-Lapparent IGAL, 91.
- Romagny, A., Jolivet, L., Menant, A., Bessière, E., Maillard, A., Canva, A., et al. (2020). Detailed Tectonic Reconstructions of the Western Mediterranean Region for the Last 35 Ma, Insights on Driving Mechanisms. *BSGF - Earth Sci. Bull.* 191, 37. doi:10.1051/bsgf/2020040
- Russell B. Wynn, Neil H. Kenyon, R. Kenyon, N. H., Masson, D., Stow, D., and Weaver, P. (2002). Characterization and Recognition of Deep-Water Channel-Lobe Transition Zones. *Bulletin* 86, 1441–1462. doi:10.1306/61EEDCC4-173E-11D7-8645000102C1865D
- Schepers, K. (1999). *Évolution tectono-sédimentaire de la partie Est du bassin de Melito di Porto Salvo au Miocène et au Plio-Quaternaire. (Calabre - Italie du Sud)*. Beauvais: M.A.G. Institut Géologique Albert-de-Lapparent IGAL, 217, 108.
- Schmitz, J., Deschamps, R., Joseph, P., Lerat, O., Doligez, B., and Jardin, A. (2014). “From 3D Photogrammetric Outcrop Models to Reservoir Models: An Integrated Modelling Workflow,” in *Presented at the Vertical Geology Conference* (Lausanne/Switzerland, 5–7).
- Selli, R. (1979). “Geologica e sismotettonica dello stretto di Messina,” in *L'attraversamento dello stretto di Messina e la sua fattibilità*. Roma, 1978 Roma: Acad. Naz. Dei Lincei, 119–154.
- Sinclair, H. D., and Tomasso, M. (2002). Depositional Evolution of Confined Turbidite Basins. *J. Sediment. Res.* 72, 451–456. doi:10.1306/111501720451
- Southard, J. B. (1991). Experimental Determination of Bed-form Stability. *Annu. Rev. Earth Planet. Sci.* 19, 423–455. doi:10.1146/annurev.ea.19.050191.002231
- Spychala, Y. T., Hodgson, D. M., Flint, S. S., and Mountney, N. P. (2015). Constraining the Sedimentology and Stratigraphy of Submarine Intraslope Lobe Deposits Using Exhumed Examples from the Karoo Basin, South Africa. *Sediment. Geology* 322, 67–81. doi:10.1016/j.sedgeo.2015.03.013
- Spychala, Y. T., Hodgson, D. M., and Lee, D. R. (2017). Autogenic Controls on Hybrid Bed Distribution in Submarine Lobe Complexes. *Mar. Pet. Geology* 88, 1078–1093. doi:10.1016/j.marpetgeo.2017.09.005
- Stow, D. A. V., and Piper, D. J. W. (1984). “Deep-water fine-grained Sediments: Facies Models,” in *Fine-grained Sediments: Deep-Water Processes and Facies*. Editors D. A. V. Stow and D. J. W. Piper (Geological Society of London, Special Publication), 15, 611–646. doi:10.1144/gsl.sp.1984.015.01.38
- Straub, K. M., and Pyles, D. R. (2012). Quantifying the Hierarchical Organization of Compensation in Submarine Fans Using Surface Statistics. *J. Sediment. Res.* 82, 889–898. doi:10.2110/jsr.2012.73
- Talling, P. J. (2013). Hybrid Submarine Flows Comprising Turbidity Current and Cohesive Debris Flow: Deposits, Theoretical and Experimental Analyses, and Generalized Models. *Geosphere* 9, 460–488. doi:10.1130/ges00793.1
- Talling, P. J., Masson, D. G., Sumner, E. J., and Malgouyres, G. (2012). Subaqueous Sediment Density Flows: Depositional Processes and Deposit Types. *Sedimentology* 59, 1937–2003. doi:10.1111/j.1365-3091.2012.01353.x
- Thomaïdis, C. (2000). *Évolution tectono-sédimentaire du bassin de Bova au Miocène et au Plio-Quaternaire (Calabre, Italie)*. MS dissertation. Beauvais: M.A.G. 237 Institut Géologique Albert-de-Lapparent IGAL, 93.
- Tortorici, L., Monaco, C., Tansi, C., and Cocina, O. (1995). Recent and Active Tectonics in the Calabrian Arc (Southern Italy). *Tectonophysics* 243, 37–55. doi:10.1016/0040-1951(94)00190-K
- Tripodi, V., Muto, F., Brutto, F., Perri, F., and Critelli, S. (2018). Neogene-Quaternary Evolution of the Forearc and Backarc Regions Between the Serre and Aspromonte Massifs, Calabria (Southern Italy). *Mar. Pet. Geology* 95, 328–343. doi:10.1016/j.marpetgeo.2018.03.028
- Tripodi, V., Muto, F., and Critelli, S. (2013). Structural Style and Tectono-Stratigraphic Evolution of the Neogene-Quaternary Siderno Basin, Southern Calabrian Arc, Italy. *Int. Geology Rev.* 55, 468–481. doi:10.1080/00206814.2012.723859

- Turakiewicz, G. (2004). *Mécanismes forçants dans les éventails turbiditiques des marges matures: exemple de l'éventail quaternaire du Congo*. Montpellier: Unpubl. Ph.D. Thesis, Univ. Montpellier II, 367.
- Vallee, A. (2003). *Etude géologique du Monte Lepericchio : géométrie des corps sédimentaires et analyse des dépôts (Pellaro, Calabre - Italie)*. 307, Beauvais: M.A.G. Institut Géologique Albert-de-Lapparent IGAL, 57.
- Vitale, S., and Ciarcia, S. (2013). Tectono-stratigraphic and Kinematic Evolution of the Southern Apennines/Calabria-Peloritani Terrane System (Italy). *Tectonophysics* 583, 164–182. doi:10.1016/j.tecto.2012.11.004
- Walker, R. G. (1978). Deep-water Sandstone Facies and Ancient Submarine Fans: Models for Exploration of Stratigraphic Traps. *Bull. Am. Assoc. Pet. Geologists* 62, 932–966. doi:10.1306/c1ea4f77-16c9-11d7-8645000102c1865d
- Wilson, J. T. (1965). A New Class of Faults and Their Bearing on continental Drift. *Nature* 207, 343–347. doi:10.1038/207343a0
- Zhang, J.-J., Wu, S.-H., Fan, T.-E., Fan, H.-J., Jiang, L., Chen, C., et al. (2016). Research on the Architecture of Submarine-Fan Lobes in the Niger Delta Basin, Offshore West Africa. *J. Palaeogeogr.* 5, 185–204. doi:10.1016/j.jop.2016.05.005

Conflict of Interest: The authors declare that the research was conducted in the absence of any commercial or financial relationships that could be construed as a potential conflict of interest.

Publisher's Note: All claims expressed in this article are solely those of the authors and do not necessarily represent those of their affiliated organizations, or those of the publisher, the editors and the reviewers. Any product that may be evaluated in this article, or claim that may be made by its manufacturer, is not guaranteed or endorsed by the publisher.

Copyright © 2021 Rohais, Bailleul, Brocheray, Schmitz, Paron, Kezirian and Barrier. This is an open-access article distributed under the terms of the Creative Commons Attribution License (CC BY). The use, distribution or reproduction in other forums is permitted, provided the original author(s) and the copyright owner(s) are credited and that the original publication in this journal is cited, in accordance with accepted academic practice. No use, distribution or reproduction is permitted which does not comply with these terms.



Forward Modelling for Structural Stratigraphic Analysis, Offshore Sureste Basin, Mexico

Donald N. Christie^{1*}, Frank J. Peel², Gillian M. Apps² and David “Stan” Stanbrook³

¹Ocean and Earth Science, University of Southampton, Southampton, United Kingdom, ²Bureau of Economic Geology, Jackson School of Geosciences, The University of Texas at Austin, University Station, Austin, TX, United States, ³Murphy Exploration & Production Company, Houston, TX, United States

OPEN ACCESS

Edited by:

Rosanna Maniscalco,
University of Catania, Italy

Reviewed by:

Istvan Csato,
MOL, Hungary
Zoe Cumberpatch,
Equinor ASA, Norway

*Correspondence:

Donald N. Christie
Geo.D.N.C@outlook.com

Specialty section:

This article was submitted to
Sedimentology, Stratigraphy and
Diagenesis,
a section of the journal
Frontiers in Earth Science

Received: 30 August 2021

Accepted: 10 November 2021

Published: 17 December 2021

Citation:

Christie DN, Peel FJ, Apps GM and
Stanbrook DS (2021) Forward
Modelling for Structural Stratigraphic
Analysis, Offshore Sureste
Basin, Mexico.
Front. Earth Sci. 9:767329.
doi: 10.3389/feart.2021.767329

The stratal architecture of deep-water minibasins is dominantly controlled by the interplay of two factors, structure growth and sediment supply. In this paper we explore the utility of a reduced-complexity, fast computational method (*Onlapse-2D*) to simulate stratal geometry, using a process of iteration to match the model output to available subsurface control (well logs and 3D seismic data). This approach was used to model the Miocene sediments in two intersecting lines of section in a complex mini-basin in the deep-water Campeche Basin, offshore Mexico. A good first-pass match between model output and geological observations was obtained, allowing us to identify and separate the effects of two distinct phases of compressional folding and a longer-lasting episode of salt withdrawal/diapirism, and to determine the timing of these events. This modelling provides an indication of the relative contribution of background sedimentation (pelagic and hemipelagic) vs. sediment-gravity-flow deposition (e.g. turbidites) within each layer of the model. The inferred timing of the compressional events derived from the model is consistent with other geological observations within the basin. The process of iteration towards a best-fit model leaves significant but local residual mismatches at several levels in the stratigraphy; these correspond to surfaces with anomalous negative (erosional) or positive (constructive depositional) palaeotopography. We label these mismatch surfaces “informative discrepancies” because the magnitude of the mismatch allows us to estimate the geometry and magnitude of the local seafloor topography. Reduced-complexity simulation is shown to be a useful and effective approach, which, when combined with an existing seismic interpretation, provides insight into the geometry and timing of controlling processes, indicates the nature of the sediments (background vs. sediment-gravity-flow) and aids in the identification of key erosional or constructional surfaces within the stratigraphy.

Keywords: forward stratigraphic modeling, tectonostratigraphic evolution, minibasin evolution, turbidites, sediment gravity flow deposit, tectonic activity, Sureste Basin, Mexico

INTRODUCTION

The Sureste Basin, located in southern Mexico is a world class basin for hydrocarbon exploration and production with proven reserves of more than 50 Billion bbl of oil. Defined at its widest extent to cover both onshore and offshore areas (Shann, et al., 2020), it closely follows the outline of the Campeche salt basin (Figure 1) (Hudec and Norton 2019). Most wildcat exploration wells until recent years were focused onshore and in shallow-water. However, more than half of the basin is in the under-explored deep-water Campeche slope with less than 15 wildcat exploration wells in depths >500 m. Large discoveries in recent years such as Zama-1 and Polok -1 have reinvigorated offshore exploration and highlighted the long term potential of the offshore Sureste Basin.

A complex geological history and the fact that exploration has only recently begun to focus on deep-water makes the Sureste Basin an ideal area to test the stratigraphic forward modelling program *Onlapse-2D*. Within the study area there is good quality seismic, however it lacks the vertical resolution to image detailed stratigraphic relationships. The overall tectonic history of the

Sureste basin is well defined, but it is less so in the study area. Therefore, we believe that *Onlapse-2D* can be used to improve the understanding of sediment deposition and structural processes within the study area, thereby adding value to the exploration process by improving reservoir and seal predictions.

The structural history of the Sureste Basin, and indeed the whole of the Gulf of Mexico is the manifestation of complex plate tectonics resulting from the breakup of Pangea around 250–170 Ma. During the Middle Jurassic, counter-clockwise rotation of the Yucatan plate pulled the Sureste Basin away from the North American plate (Salvador 1987), (Hudec and Norton 2019), (Davison, et al., 2021).

Deposition of the Louann Salt occurred in the Bajocian (Middle Jurassic) (Pindell, et al., 2019) across stretched continental crust of the Gulf of Mexico. Oceanic spreading is believed to have begun soon after deposition of the Salt and continued until the end of the Berriasian (Early Cretaceous) (Stern and Dickinson 2010). This sea-floor spreading divided the Louann Salt into two segments with the salt provinces in the US Gulf of Mexico and Mexico's Sureste Basin (Figure 1) (Hudec and Norton 2019).

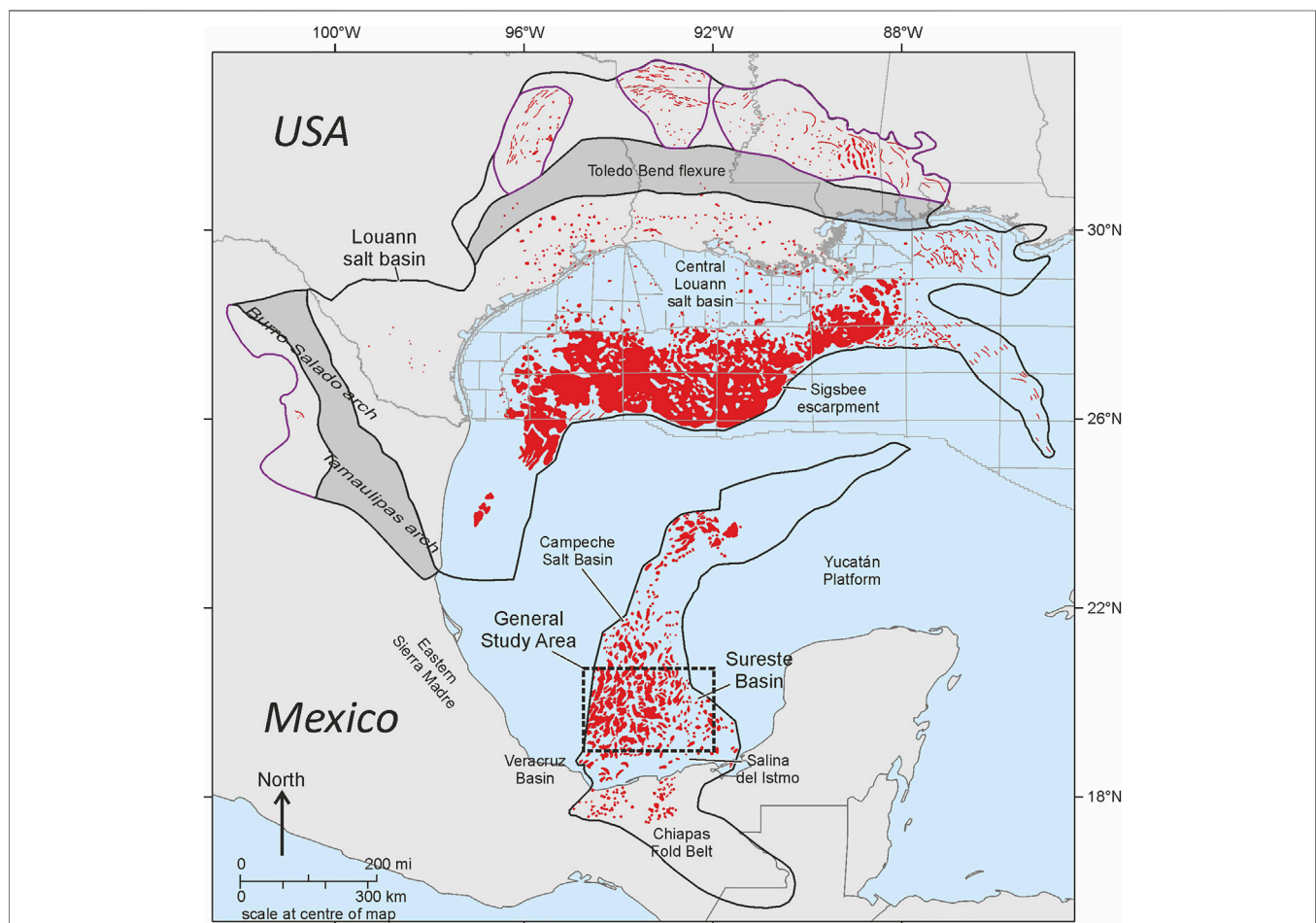


FIGURE 1 | Outline of the Sureste Basin in Southern Mexico, the study area is located in the dashed box area in offshore section of the basin, we cannot reveal the exact location due to confidentiality agreements.

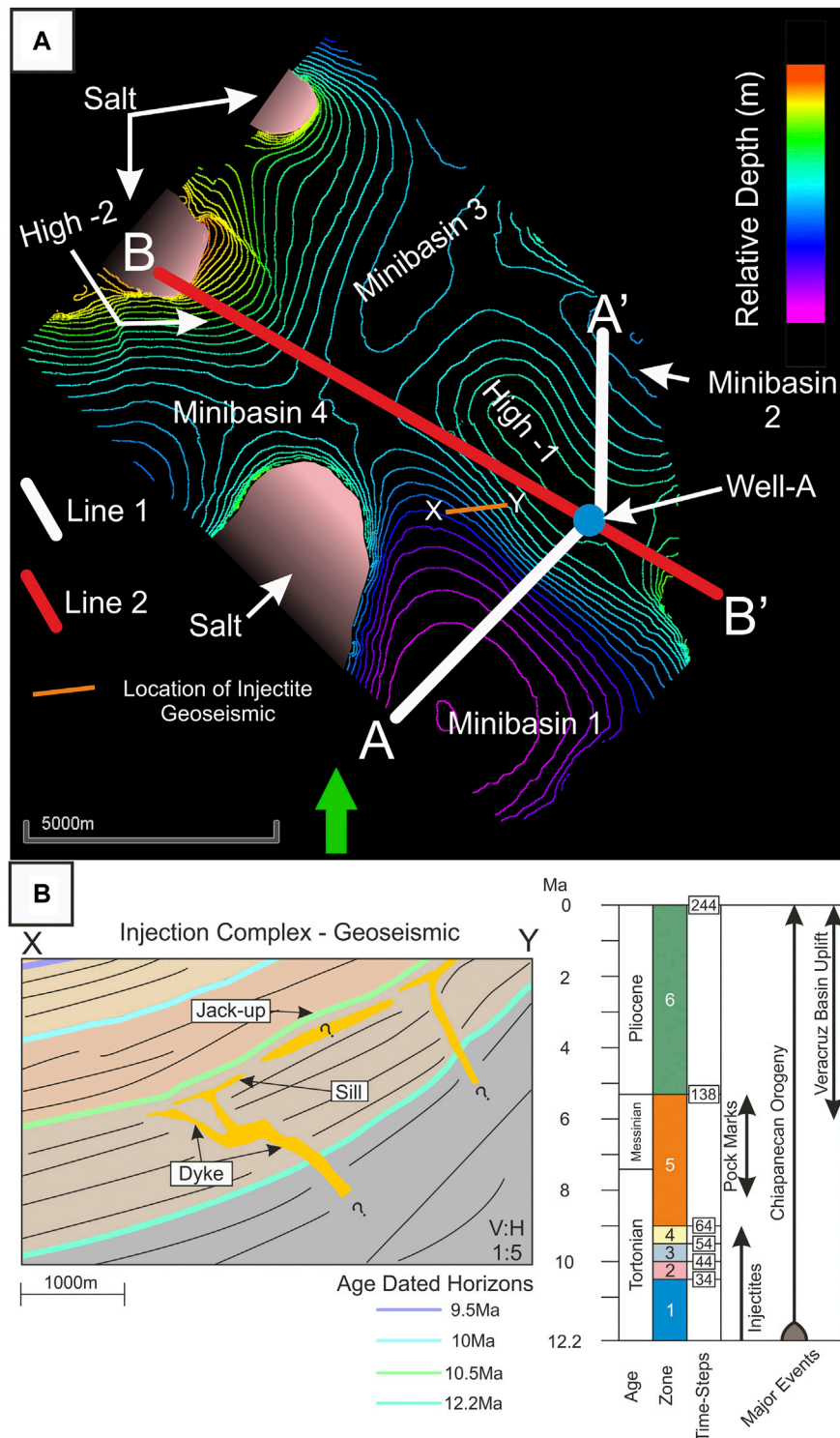


FIGURE 2 | (A) Location of Well-A superimposed over a relative depth map of the 12.2 Ma horizon interpretation, and the two modelled cross-sections Line 1 and Line 2. Frame of reference has been rotated to preserve confidentiality. **(B)** Geoseismic section X-Y, located to the southwest of High-1, showing a sand injectite dyke and sill complex within Lower Tortonian section. The interpreted timing of sand injection shown on the stratigraphic chart is based on observed sediment response to local sea floor uplift (jack-up above injectite sills). Pockmarks in the overlying Upper Tortonian to Messinian section indicate a second pulse of fluid-flow.

After cessation of rifting in the Early Cretaceous, the Gulf of Mexico began to slowly subside owing to thermal cooling and sediment loading, producing a northwest-downward tilt to the Sureste Basin (Davison 2020) (Davison, et al., 2021). For the remainder of the Cretaceous, carbonate deposition dominated the basin with shelfal systems found around the south and eastern rim of the Basin, and fine grained carbonate clastic sediments deposited in the deep-water areas of the Sureste Basin (Padilla y Sanchez, 2007; Shann, et al., 2020).

The passive margin phase of basin infill in the Sureste Basin came to an end at the start of the Late Cretaceous with the start of the Mexican Orogeny. Cover shortening, in the form of folding and thrusting, propagated north-eastwards into the Sureste Basin (Shann, et al., 2020). Pre-orogenic salt diapirs were rejuvenated by squeezing, producing allochthonous salt sheets, which are most strongly developed in the onshore and shallow water zones (Davison 2020).

The drowning of the carbonate reefs in the Lower Palaeocene marks the end of carbonate dominance in the Sureste Basin and from this point onwards deep-water siliciclastic sedimentation dominated the basin, continuing until present day. However, carbonate sedimentation continued along the eastern rim of the basin along with isolated carbonate reef build ups (Davison, et al., 2021) (Shann, et al., 2020).

Thick Lower Miocene sands are evident across the offshore Sureste Basin and correspond to onshore formations (Shann, et al., 2020). The shelf margin in the Lower Miocene is located in the present day southern onshore region of the Sureste Basin. The shelf margin migrated northwards throughout the rest of the Miocene and until its present-day position in the offshore area of the Sureste basin (Gomez Cabrera and Jackson 2009). Throughout this time the main siliciclastic sediment input into the basin came from the southern part of the Eastern Sierra Madre and Chiapas area.

The Chiapanecan Orogeny began during the Miocene (18.0 Ma) (Davison, et al., 2021) and is responsible for a short lived but crucially important phase of compressional tectonics that affected the Sureste Basin. Between 13.8–11.6 Ma, this phase triggered allochthonous salt sheet development across the basin. The tectonic event produced what is known as the Chiapas Fold-and-Thrust Belt (Mandujano-Velazquez and Keppie 2009) and is associated with onshore volcanic activity (Stanbrook, et al., 2020). This event also produced intense deformation extending across a zone up to 600 km North from the southern margin of the Sureste Basin (Davison, et al., 2021) (Shann, et al., 2020) (Davison 2020). The culmination of this tectonic event is a regional strong erosional unconformity.

This Middle Miocene event effectively subdivides the stratigraphy into three; (i) a pre-orogenic, Oligocene – Lower Miocene section, which was folded prior to emplacement of the extensive salt canopy; (ii) a syn-orogenic Middle Miocene deep-water turbidite system that is associated with the emplacement of an extensive salt canopy; (iii) a post-orogenic infill, of Late Miocene to Pliocene age, which is not affected by the Chiapaneco folding (Shann, et al., 2020).

Within the study area (Figure 2A) Sand Injectites are observed to penetrate from Middle Miocene stratigraphy through the lower

section of the Late Miocene, and cease being observed in the later stages of the Tortonian (Late Miocene). In the later stages of the Tortonian pockmarks are observed to occur above where the injectites are observed (Figure 2B). While the existence of sand injectites in other basins (e.g. North Sea, Onshore California) is well documented, and oil saturated sandstone intrusions have been recognized in some Gulf of Mexico core (Andrew Hurst, pers. comm. 2021) we are unaware of any published documentation of their presence in the southern Gulf of Mexico, including the offshore Sureste Basin.

After the development of the Mid-Miocene Chiapas Fold-and-Thrust belt due to the Chiapaneco Orogeny the tectonic development of the Sureste Basin was dominated by two events. The first was a long lived gradual downslope gravity collapse over the shelf-slope sediments into the Gulf of Mexico. This divides offshore Sureste Basin into three regions; an updip set of extensional salt withdrawal minibasins, a mid-slope translational area with widespread partly amalgamated salt canopy, and a lower-slope set of large compressional anticlinal folds (Shann, et al., 2020). The second late compressional event effects the south-eastern part of the Sureste basin, uplifting the entire Veracruz basin to the west of the Sureste Basin caused by Pliocene volcanic episodes (Padilla y Sanchez 2007).

The overall aim of this study was to utilize a forward stratigraphic modelling software, *Onlapse-2D* to better understand the tectonostratigraphic evolution of the Late Miocene section in three adjacent minibasins in a geologically complex area located in the offshore Sureste Basin. The secondary objective was to validate and develop the capability of *Onlapse-2D*. We present here the results of two modelled cross-sections, and will demonstrate how the modelling of two cross sections allowed us to better understand the spatiotemporal evolution of structural growth and how sediment input may have evolved through time. We will also demonstrate how analyzing discrepancies between the model out and subsurface data can be a vital source of information. In the process, we exhibit how *Onlapse-2D* enables the user to determine the likelihood of reservoir and seal present in a given stratigraphic interval.

METHODS

For this project, we utilized a subset of a 3D Kirchhoff Pre Stack Depth Migrated seismic. The seismic data provided good image quality allowing for the mapping of structural and stratigraphic surfaces but did not provide direct imaging of reservoir systems. Structural and seismic surface interpretations were tied to and dated by biostratigraphic data in Well-A. We were provided access to full well log data that included, Gamma Ray, Resistivity, Neutron Porosity, Density, VShale, and Image Logs interpretations.

Stratigraphic Forward Modelling

Stratigraphic Forward Modelling is the use of mathematical formulae and algorithms to create synthetic stratigraphy, with the aim of understanding and predicting dynamic sedimentary systems (Burgess 2012) (Huang, et al., 2015). Natural systems are

complex and dynamic, and consequently are difficult to model. Stratigraphic Forward Modelling can be broadly split into two end member methods, *Process Based Modelling* and *Geometric Modelling*, each with its own advantages and disadvantages (Paola 2000; Burgess 2012; Huang, et al., 2015).

Process based modelling is built on the concept of numerically modelling the physics of sediment transport through methods such as sediment diffusion (e.g. (Rivenaes 1992), (Granjeon 2014)) or the Navier-Stokes equation; for example (Griffiths, et al., 2001; Basani, et al., 2014).

Geometric models do not consider the dynamics of sediment transport. Instead they use a simple set of rules to model the overall thickness and stratal geometry of discrete stratigraphic intervals rather than the individual depositional events within the intervals; for example (Sylvester, et al., 2015).

Previous simulations of structurally active mini-basins typically use two approaches; Generic models using simple rules for sediment deposition in idealized mini-basin geometries (e.g. Sylvester et al., 2015). These are rapidly generated, and give useful insights into the general processes of mini-basin evolution, but they typically do not replicate real world examples. Models that apply more complex algorithms to simulate the flow of individual turbidity currents, stacking these to build up a synthetic stratigraphy (e.g. Burgess, et al., 2019).

In this paper we use a different approach with *Onlapse-2D*. Our fast computational model uses simple rules to match the seismic and well data in a real world example, iterating towards a best-fit solution through hundreds of simulation runs.

What is Onlapse-2D?

Onlapse-2D is a stratigraphic forward modelling program, developed in Matlab that simulates the tectonostratigraphic evolution and development of structurally controlled, deep-water minibasins. It uses four inputs; Initial Basin Structure, Background Sedimentation Rate, Structural Growth Profile and Rise, and a variable rate of rise of a Clastic Limiting Surface. The Clastic Limiting Surface is a horizontal line used to determine whether new gravity flow sediment is deposited at a given position on the cross-section. *Onlapse-2D* combines these inputs using simple rules to generate realistic looking basin architectures. *Onlapse-2D* simulates the simultaneous growth of structures and a variable rate of sediment deposition. Both rates may be derived from real data (as in this paper) to simulate structural and stratigraphic evolution of a real world basin. *Onlapse-2D* is also used to simulate idealized basins to explore how the interaction between structural growth and deposition generates different stratigraphic architecture (Christie 2021).

To achieve the stated aims in the introduction we selected an area with good quality, high resolution seismic data and well control (good age dating) in a region with 3-dimensional structural complexity. We constructed and modelled two cross sections. The first traverses Minibasin-1 passing through Well-A and into the adjacent Minibasin-2. The second cross-section, Line 2 intersects Line 1 at Well-A, traversing Minibasin-2 and Minibasin-4.

Study Area and Line Locations

This study was conducted in the offshore area of the southern Sureste Basin in Mexico (**Figure 1**). In all other maps and sections presented here cardinal points have been rotated to preserve confidentiality but we use a consistent reference direction in all figures. Two 2D intersecting cross sections were modelled, with these locations chosen to investigate different phases and different styles of deformation in different orientations. There are four minibasins within the study area which extend beyond the boundaries of the study area. The center-piece of the study area is a North-West to South-East trending long lived structural high known as High-1. Minibasin-1 is to the South-West of this high and is flanked to the North-West by the largest of the salt cored highs; at its longest and widest extent, it is 5 km by 5 km. Minibasin-2 is located off the Northern flank of High-1 and measures 4 km in length and 2 km in width. To the North of High-1 and Minibasin-2 is Minibasin-3 measuring 5 km by 6 km and is flanked to the North and West by two salt cored highs. Minibasin-4 is located off the North-West of High-1 and at its widest extent and at its maximum length is 3.5 km (**Figure 2A**). The main deep-water depositional systems of interest entered at the south of the basin in Minibasin-1 and 2, flowing axial to the long lived central high into Minibasins 3 and 4.

Boundary Conditions and Input Parameters

The boundary conditions for Lines 1 and 2 are as follows;

- Total Simulation Time: 12.2Mya (from Middle Miocene until present day)
- Time per Time-Step: 50ky
- Total number of Time-Steps: 244
- Basin Length:
 - o Line 1: 8,550 m
 - o Line 2: 10,875 m
- Horizontal Resolution: 25 m.

Line 1 and 2 modelled a total time interval of 12.2 Ma, but focused on the period 12.2– 5.3 Ma (Mid-Miocene to Late Miocene). After 5.3 Ma, the modelling was completed to a lower spatial resolution. The time interval of 12.2 Ma is split into six zones that correspond to different Time-Steps.

- Zone 1: Time-Step 1–34 (12.2–10.5 Ma)
- Zone 2: Time-Step 35–44 (10.45–10 Ma)
- Zone 3: Time-Step 45–54 (9.95–9.5 Ma)
- Zone 4: Time-Step 55–64 (9.45–9 Ma)
- Zone 5: Time-Step 65–138 (8.95–5.3 Ma)
- Zone 6: Time-Step 139–244 (5.15–0 Ma)

The four main inputs to the model and described below.

Initial Basin Structure

The initial basin structure (**Figure 3A**) represents the basin floor bathymetry at the start of the model (Time-Step 0). The starting point for constructing this is to use the isopach of the interval beneath the deepest interpreted seismic horizon that onlaps onto the strong Middle Miocene unconformity as a guide (**Figure 3E**).

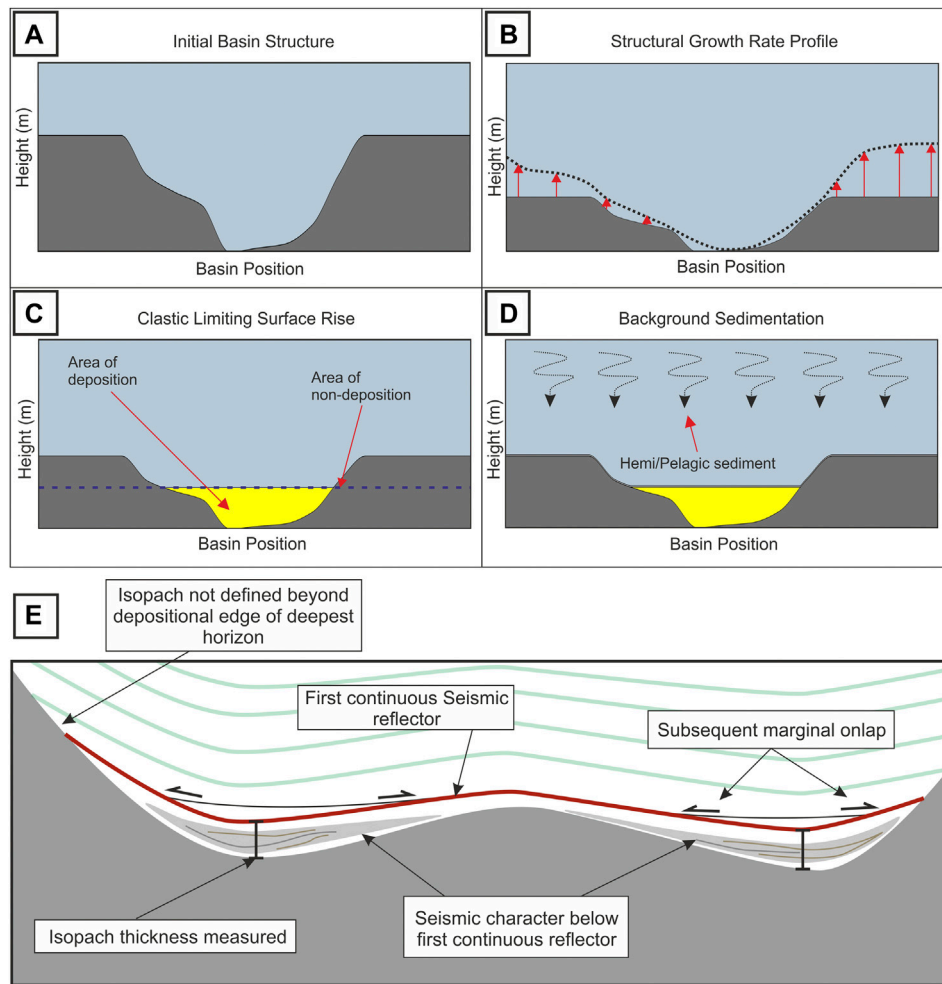


FIGURE 3 | (A) The Initial Basin Structure at Time-Step 0. **Figure 4** illustrates how we derive this from seismic data. (B) Dotted line represents the Structural Growth Profile, with red arrows indicating the rate of rise being applied to the Basin Structure (dark grey structure). The Structural Growth Rate Profile consist of multiple profiles, in this example it is a single profile. (C) Blue dotted line is the Clastic Limiting Surface, if there is available accommodation space below then gravity flow deposit packages are deposited, if not then no deposition occurs. (D) A uniform thickness of background sediment is deposited along the cross-section, through pelagic and hemi-pelagic settling. (E) The Initial Basin Structure at Time-Step 0 is derived by mapping the first continuous seismic reflector (red) and measuring the thickness of the isopach below it. Inspection of the subsequent and underlying, strata to identify patterns of onlap and geometry allow us to infer how much topography existed at Time-Step 0 and how much topography may have been created by subsequent structure growth.

Beyond the depositional edge of that deepest interpreted horizon, the isopach is not defined, and therefore the Initial Basin Structure is derived by a process of iteration.

Rate of Rise of the Structural Growth Profile

The Structural Growth Profile is a curve that defines the shape of the growing structure, this curve varies through space, but remains constant through time. The Structural Growth Rate is a user defined curve that defines the amount of growth applied to the Structural Growth Profile through time. This is spatially uniform, but varies through time. Combining the Structural Growth Profile and the Structural Growth Rate gives the *Rate of Rise of the Structural Growth Profile* (**Figure 3B**). This is the amount of rise in mm/yr converted to m/Time-Step that is applied to the basin structure through vertical shear.

The first iteration is determined through taking the *Initial Basin Structure* and measuring its height from the lowest point in the basin. We then compare each point along the cross-section to its height at the present day from the lowest point in the model, which gives us a simple way of calculating the average growth in mm/yr along the cross-section. This provides us a basic Structural Growth Profile, which is refined iteratively during the modelling process to match a predetermined set of criteria. For this study, two basic criteria were applied to the Structural Growth Profile. The first is that it must replicate the form of the final structure visually, and the second is that it must do so to a tolerance of ± 25 m. *Onlapse-2D* can model complex structural scenarios in which multiple structural processes act in the same place by combining several Structural Growth Profiles to represent different components of the structural development (salt diapirism, fold growth etc.).

Rate of Rise of the Clastic Limiting Surface

The Rate of Rise of the Clastic Limiting Surface is the amount of rise in mm/yr converted to m/Time-Step that is applied to the Clastic Limiting Surface (**Figure 3C**). The Clastic Limiting Surface is used to determine whether new gravity flow sediment is deposited at a given position on the cross-section. The Clastic Limiting Surface is a line that delineates above which, no sediment gravity flow deposits are preserved, and below which if there is accommodation, they are preserved and are given the name *Gravity Flow Deposit Packages*. This is a user-defined horizontal level that can rise or fall with time. The Clastic Limiting Surface provides a straightforward means of determining the amount of sediment being captured by a basin over time. While in nature, the amount of sediment input into a minibasin can be controlled by a variety of external geological processes (e.g. relative sea-level fall, climate, up-dip avulsion of sediment feeder channels etc.), these factors are rarely well understood and cannot be quantified. *Onlapse-2D* does not require knowledge of larger scale variables or inputs. The user makes no assumptions and instead controls only the amount of sediment captured within the minibasin at any one time, using the Clastic Limiting Surface. The Clastic Limiting Surface is not necessarily equivalent to a base-level, equilibrium surface, or even a spill point (because the user may not know that level for the basin on the chosen line of section). The Rate of Rise of the Clastic Limiting Surface is determined by local seismic and well data only (e.g. reflection seismic and well data, especially biostratigraphic data that contains information on the rate of sediment accumulation in the basin through time). It is a user-defined surface that is specific to that minibasin. It does not require knowledge of larger scale variables, nor does it require the user to know where the basin was relative to the sediment fairway, or whether the minibasin was close to the regional slope gradient, or structurally perched above the regional slope.

In this example, the initial rate of rise applied to the Clastic Limiting Surface were based on the calculated average sedimentation rates from Gomez Cabrera & Jackson (2009), which are not corrected for compaction so are likely to be an underestimate. Starting at the lowest zone, we worked progressively up through the stratigraphy, making adjustments to the Rate of Rise of the Clastic Limiting Surface so that the stratal patterns (onlap and offlap) and thickness within the zone match the subsurface data. The tolerance for thickness match is ± 25 m.

Background Sedimentation Rate

This is the amount of sediment deposited uniformly along the cross section through pelagic and hemipelagic settling (**Figure 3D**). While it is spatially constant at any one time, the rate of Background Sedimentation can change through time. We calculated this from two interpreted condensed sections within the interval of study in Well-A that had good biostratigraphic age constraint. The deeper, oldest condensed section included an average background sedimentation rate of 0.022 mm/yr, and the second condensed, younger section averaged 0.047 mm/yr.

Assumptions and Uncertainty

Several assumptions are made during the processes of producing models with *Onlapse-2D*. Within the model we assume that deposition only comes from sediment gravity flows and background sediment, and that there is no significant contributions from other processes such as carbonate build-ups. *Onlapse-2D* is unable to model erosion, and also assumes that all gravity flow deposit packages are horizontal at the time of deposition, which means that *Onlapse-2D* can't directly model positive depositional topography or depositional erosive features such as channel scours. *Onlapse-2D* also assumes that all structural movement occurs through vertical shear, and that there are no major horizontal components to structural movement. *Onlapse-2D* also inherits all the assumptions that are made when matching to subsurface data such as reflection seismic or well logs.

Compaction is not currently included within the model; therefore, estimates on the Background Sedimentation Rate and depositional rates of the Gravity Flow Deposit Packages are an underestimate. In this example this does not invalidate the model because we are able to obtain realistic simulations of the real world geometries indicating differential compaction is not a significant factor in this basin.

A Note on Gravity Flow Deposit Packages

Geoscientists commonly associate yellow coloured layers with sandy lithologies. *Onlapse-2D* does not assign a lithology to the modelled Gravity Flow Deposit Package, only stating that the rise of the Clastic Limiting Surface is generated by sediments deposited through gravity flow processes. The Gravity Flow Deposit Package represents any package of flow deposits, including low and high-density turbidites, calci-turbidites, and mass transport deposits. The interpreting geoscientist must, through their geological understanding (e.g. regional knowledge, seismic or well data, geological models) make an informed decision on what type of gravity flow deposit is represented in any given part of the active depositional package.

Workflow

The procedure for generating stratigraphy using *Onlapse-2D* is to: 1) generate an Initial Basin Structure; then for each Time-Step of the model: 2) apply the Structural Growth Profile rise for that Time-Step; 3) apply a rise to the Clastic Limiting Surface; if there is accommodation, then a gravity flow deposit package is deposited up to the Clastic Limiting Surface for each Time-Step 4) drape a uniform thickness of background sediment across the cross-section (**Figure 4**). Steps 2–4 steps are repeated until the correct number of Time-Steps is completed.

After each iteration of the simulation, we compared the generated stratigraphy to the subsurface data consider if the stratigraphy generated is consistent with the subsurface data and what, if any, differences can be found. First we measure the thickness of modelled intervals at key points along the cross-section. Key points are equally spaced points along the cross-section, for example every 1,000 m, but also include important features of interest such as the tops of anticlines, the deepest

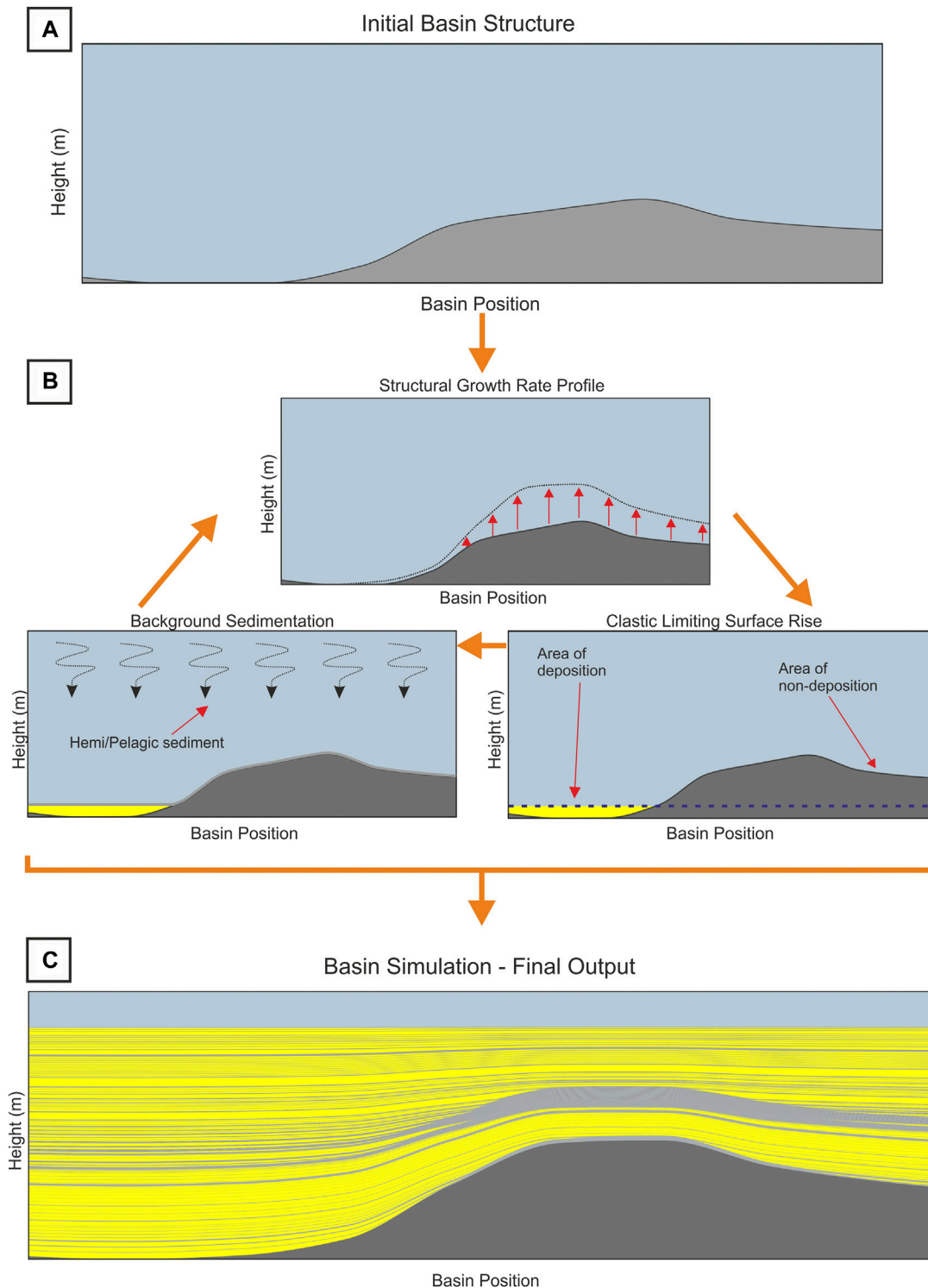


FIGURE 4 | (A): Time Step 0 shows the Initial Basin Structure with height in meters on the Y axis and Basin Position on the X axis. **(B):** Onlapse-2D applies a structural growth rate to the initial basin structure, then Onlapse-2D applies a rise to the clastic limiting surface and if there is accommodation available gravity flow deposit packages are preserved. After this, Onlapse-2D applies a uniform thickness of pelagic/hemipelagic sediment across the cross section. Section B is repeated a number of times as dictated by the number of Time-Steps. Producing a final cross section, **(C)**.

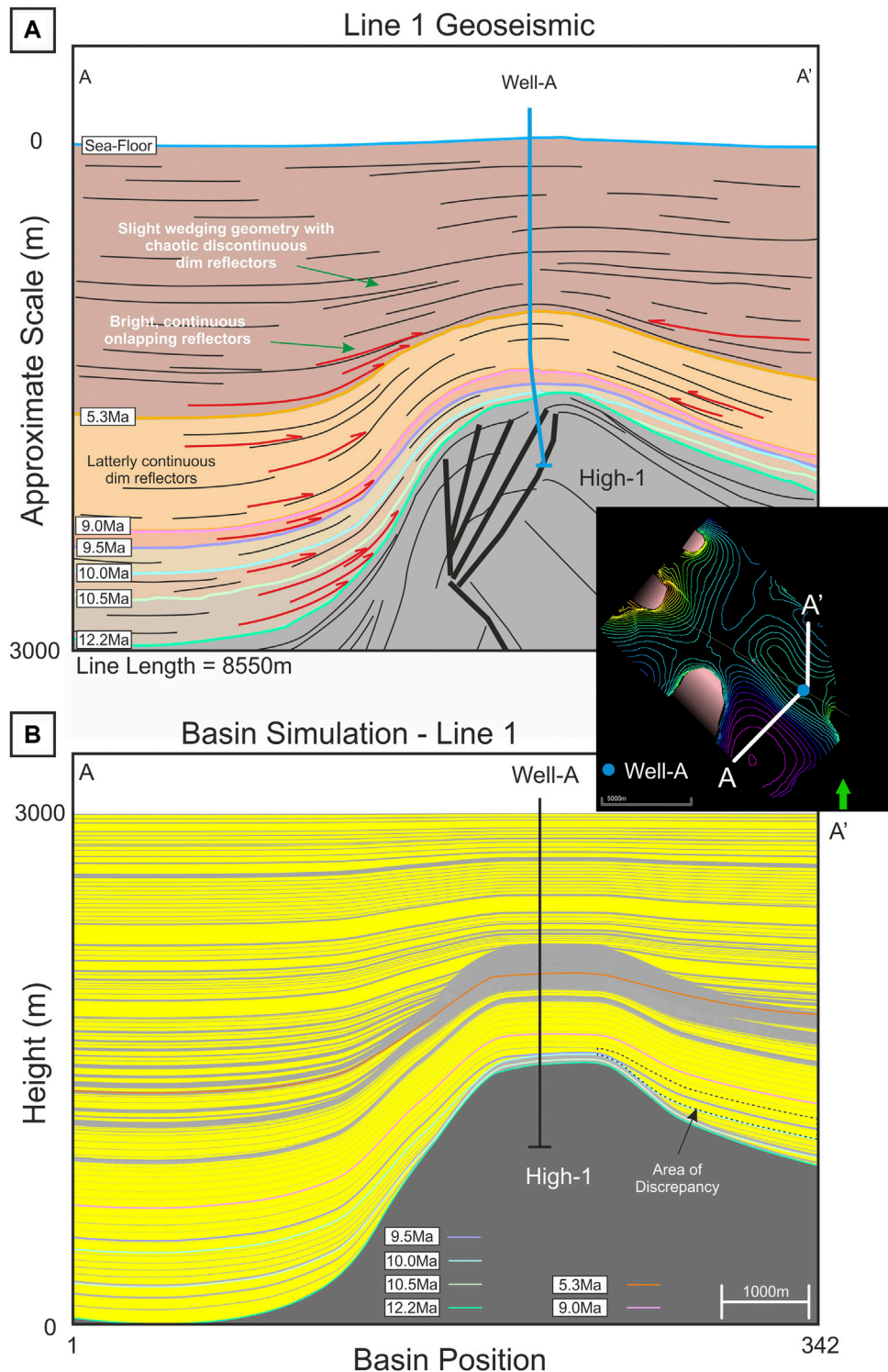


FIGURE 5 | (A) Geoseismic cross-section of Line 1 showing the position of Well-A, age-date horizons tied to Well-A, and brief annotations of the seismic character. The red arrows show some of the major onlapping reflectors and thick black lines represent faults in High-1. Modelling was completed from 12.2 Ma until present day. With 12.2–5.3 Ma being the focus and matched quantitatively to the subsurface data, while 5.3 Ma until present day was modelled to a lower, qualitative resolution only. **(B)** Onlapse-2D final simulation output of Line 1. We found there to be an overall good fit between this and the subsurface data shown in **(A)**. The model produces good fits with the overall basin structure and form, as well as the thicknesses and stratal geometries found within the interpreted horizons. An area of discrepancy is shown on the northern flank of High-1.

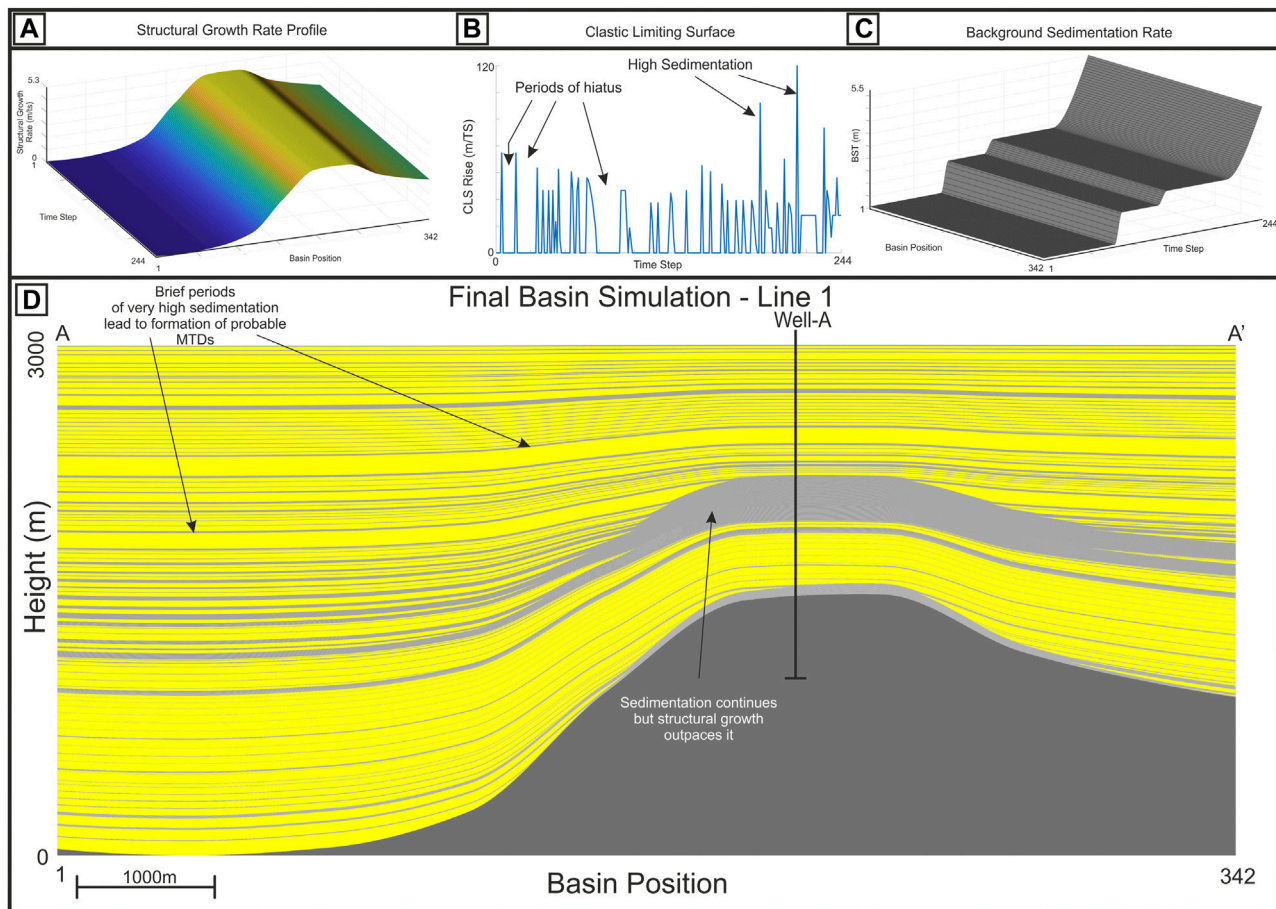


FIGURE 6 | Inputs used to model the evolution of Line 1. **(A)** 3D Representation of the Structural Growth Profile, X axis represents position in space, Y Axis represents position in Time, Z axis represents the growth that the structure grows in meters per time step. **(B)** The rate of rise of the clastic limiting surface; showing the sporadic nature and short lived time in which sediment gravity flows occur in the cross-section. **(C)** Background Sedimentation Rate; derived from data from Well-A. X Axis represents position in space along the cross section, Y axis represents position in time, and Z axis represents amount of background sediment deposited in meters. **(D)** Final simulation for Line 1, highlighting periods of very high, but short lived, sedimentation (which probably correspond to MTDs) and periods of hiatus in sedimentation.

points of synclines, or wells. This is compared to the same interval isopachs on the seismic section that is the basis for the modelled 2D profile. Second, we inspect the match between the stratal relationships generated in the model and those observed on the seismic line; for example, where there are onlaps on the seismic line, there should be onlaps on the model. Third, we consider the seismic facies of each zone, and the lithology. While Onlapse-2D does not explicitly define the lithology, the seismic facies, or mappable architectural elements within an interval, are good indicators of the type of gravity flow deposits and a proxy for the relatively speed at which the package was deposited. Intervals with active siliciclastic systems should match the zones in the *Onlapse-2D* model with high values for the Clastic Limiting Surface (more deposition per unit time). Spikes in the rate of Clastic Limiting Surface rise (i.e. zones deposited at the fastest rate) commonly correspond on seismic data to distinctive thick laterally extensive discontinuous, chaotic seismic facies

interpreted as probable mass transport complexes, however they can also represent a mega-turbidite deposit.

If a good match is not achieved, then the input variables (e.g. Clastic Limiting Surface, Structural Growth Profile, and Initial Basin Structure) are altered until the modelled stratigraphy fits within an acceptable range. For example, alteration of the input variables can include increasing or decreasing the rates of rise of the Clastic Limiting Surface or the Structural Growth Profile, adding additional Structural Growth Profiles, changing the shape of the Initial Basin Structure. For this study the iteration process continued until the generated stratigraphy matched the subsurface data. If the changes do not iterate towards a good fit to the subsurface data, there are two principal reasons. The first is that the structural simulation may not include all the structural processes within the basin (e.g. salt withdrawal) in some cases the difference may be resolved by adding additional structural growth profiles that represent some of the missing processes.

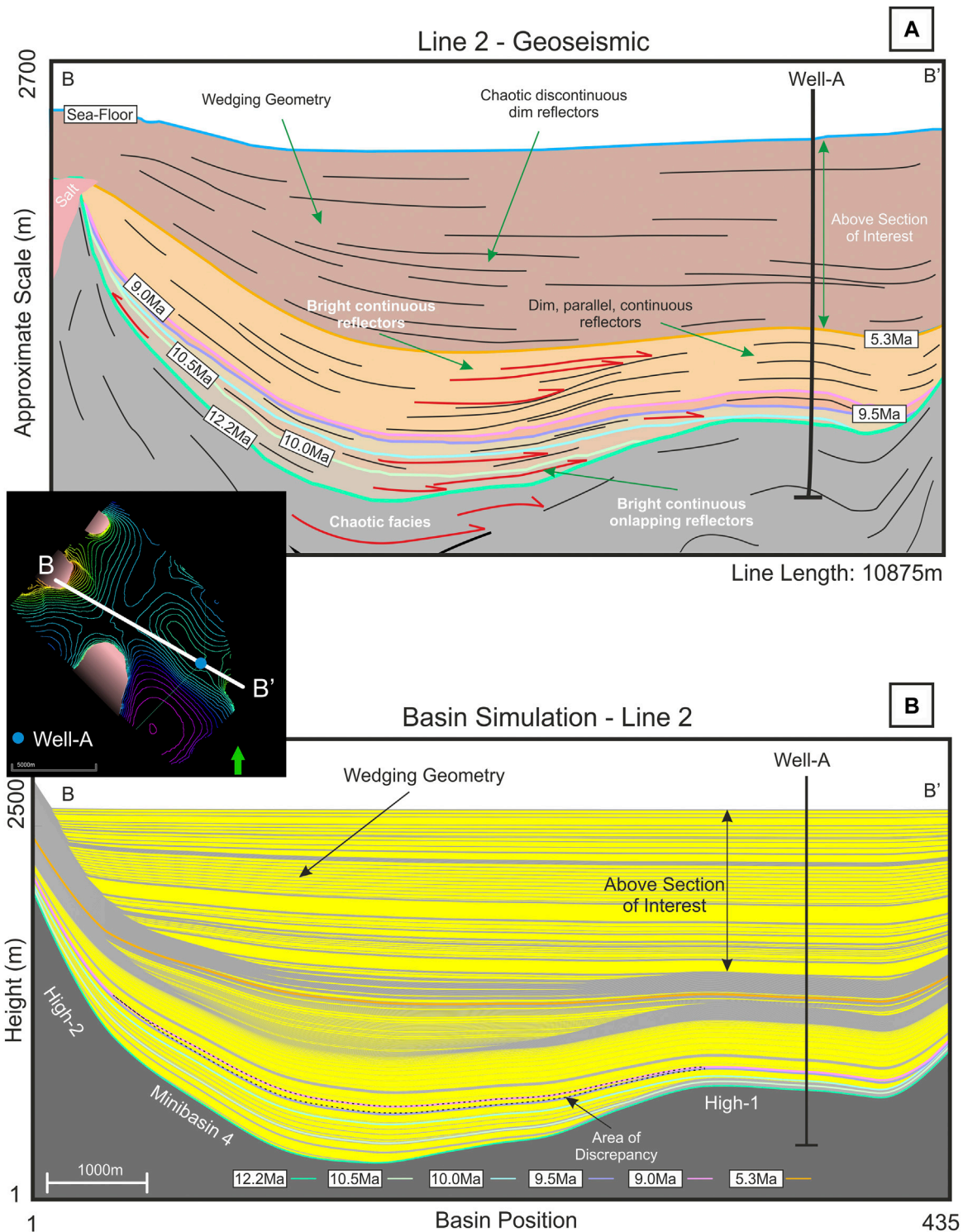
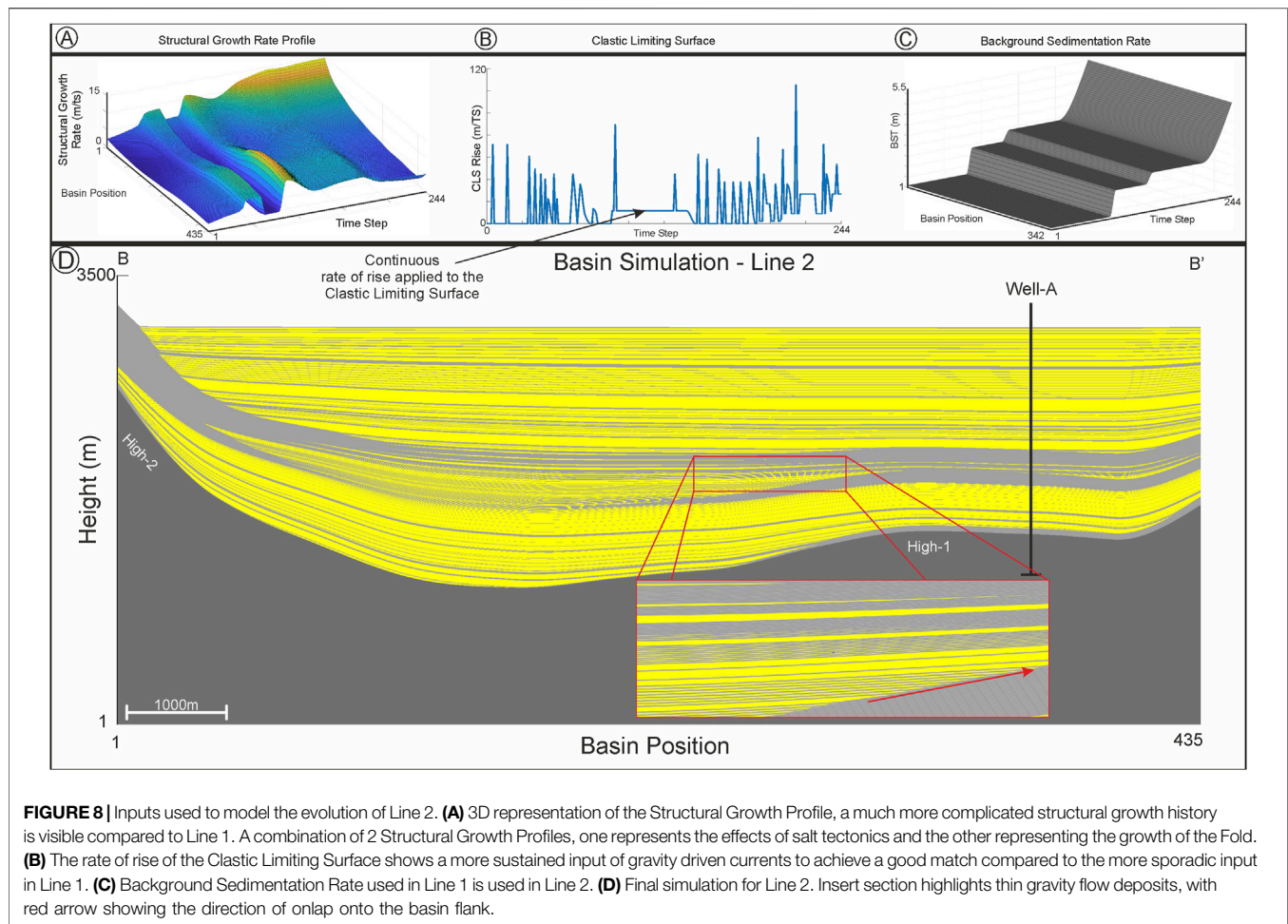


FIGURE 7 | (A) Geoseismic cross-section of Line 2. Line 2 crosses both High-1 and High-2, with High-2 containing salt. The wedging geometry seen in geoseismic cross-section is above our area of interest, but is still modelled at a lower resolution. **(B)** Onlapse-2D final simulation, overall within the section of interest there is a good match between model and the geoseismic. The model is able to match the general form of the basin as well, and major onlapping reflectors seen in 8a, occur in the modelled simulation. An area of discrepancy is highlighted within MiniBasin 4.



The second is that the discrepancy may be caused by a depositional process that cannot yet be modelled through the *Onlapse-2D* method (e.g. erosional or constructional depositional topography).

RESULTS

Line 1

We found that the modelled outputs of the final basin structure, thicknesses of modelled zones, and lateral extent of Gravity Flow Deposit packages found within them was a good fit to seismic and well data (**Figure 5**). A single, simple Structural Growth Profile that grew at a constant rate at each Time-Step was used. The Background Sedimentation Rate, derived from well based condensed section information increased in increments through time. The rate of rise of the Clastic Limiting Surface was more varied in both magnitude of rise per Time-Step and the duration of each rise (**Figure 6**). The combination in **Figure 6** is non-unique but provided us with the closest fit to the seismic and well data of multiple model runs.

Within Time-Step 45–54 (Zone 3) and Time-Step 55–64 (Zone 4) we found that on the northern flank of the High-1

there was a localized but significant mismatch between what the seismic data indicates, and what the *Onlapse-2D* model predicted to be deposited. We found there was an increasing amount of over thickening into the northern section of the basin. The implications of this discrepancy, and how we corrected for it will be discussed further in the discussion section.

Line 2

As with Line 1, we found that overall the modelled basin structure, thickness of the zones within the interval of interest, as well as the lateral extent of the Gravity Flow Deposit Packages within those zones were a good fit to both the seismic and well data (**Figure 7**). All boundary conditions were consistent with Line 1, except the Basin Length which was 10875 m. The area above the section of interest in Line 2 could not be modelled with a single, simple Structural Growth Profile (**Figure 8A**). To fit the stratigraphy above the section of interest, we required two different components of the Structural Growth Profile with different growth histories. The first component of the Structural Growth Profile was consistent with compressional folding, similar to Line 1, but with two discrete phases. The second component of the Structural Growth Profile was a longer

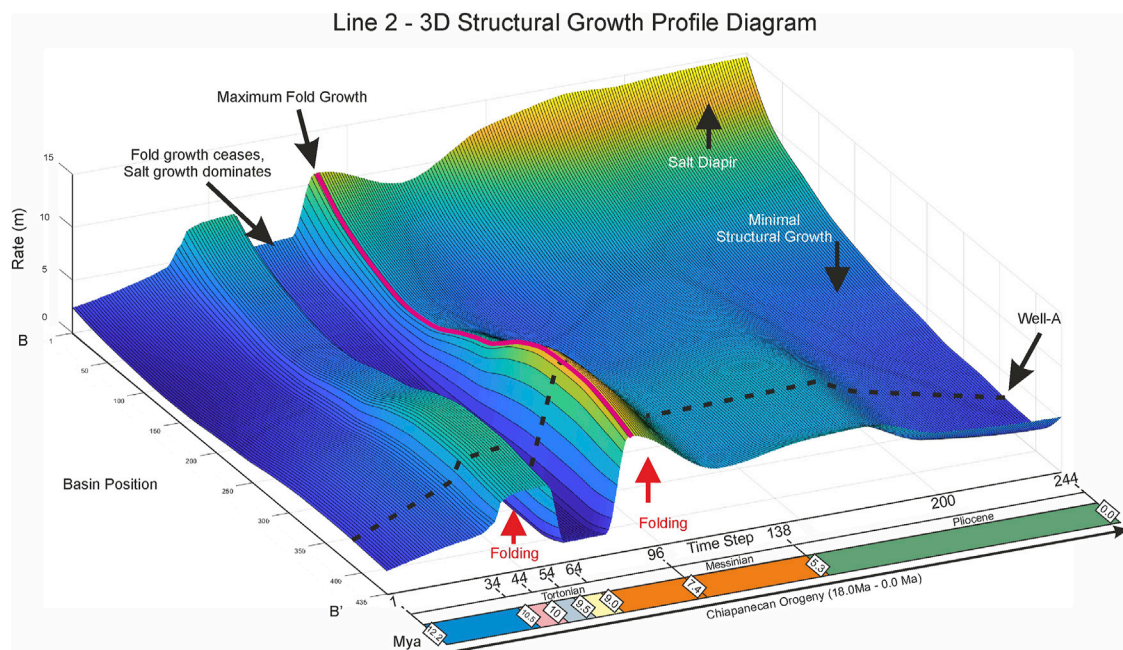


FIGURE 9 | 3D representation of the rate of rise of the Structural Growth Profile through time. X-axis represents position in time, Y-axis represents basin position along Line 2, Z-axis showing the rate of rise in meters per Time-Step. Diagram shows the combination of two Structural Growth Profiles through time. Profile 1 was consistent with compressional folding over High-1, Profile 2 is focused on salt diapirism and withdrawal at High-2. Fold growth (Profile-1) dominates in two distinct phases, phase one occurs from 12.2 Ma until ceasing at 9.0 Ma, at this point Profile 2 (salt growth) dominates until 7.8 Ma, at which point compressional folding begins again. Profile 1 continues to dominate until the middle Pliocene when fold growth tapers off. At this point, salt tectonics dominates, represented by Profile 2.

time wavelength and was required to account for the significant structural high at the NW end of Minibasin-4, and is consistent with salt withdrawal and diapirism. The timing of the interactions of the two Structural Growth Profiles is consistent with regional knowledge, and the spatial distribution is consistent with regional knowledge and structural geological principles (Padilla y Sanchez 2007) (Padilla y Sanchez 2014) (Davison 2020). We will expand on this in the discussion. As stratal patterns are generated in *Onlapse-2D* through the interaction between Structural Growth and the rise of the Clastic Limiting Surface, changes to the Structural Growth Profile meant that we needed to create a new rate of rise of the Clastic Limiting Surface. Changes to the Rate of Rise of the Clastic Limiting Surface were focused on the interval of interest (12.2–5.3 Ma), and included increasing and decreasing the rise of the Clastic Limiting Surface in M/Time-Step, changing the Time-steps in which the rise occurred, and the addition of a continuous rate of rise between 7.8–5.3 Ma. However, the Background Sedimentation Rate remains the same (Figure 8C).

Within Zone 4 (Time-Step 55–64) of Line 2 we found a localized but significant discrepancy between the final best fit simulation and the subsurface data. This mismatch could not be eliminated by simple adjustment of inputs. This discrepancy, which was focused around Well-A, is highly informative, providing additional information about the evolution of the section. If the simulation matched the thicknesses found

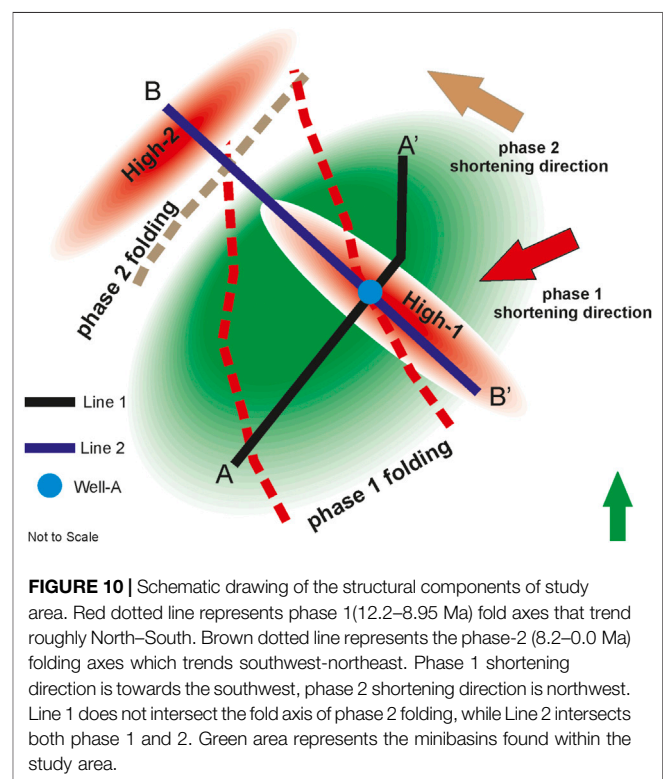


FIGURE 10 | Schematic drawing of the structural components of study area. Red dotted line represents phase 1 (12.2–8.95 Ma) fold axes that trend roughly North–South. Brown dotted line represents the phase-2 (8.2–0.0 Ma) folding axes which trends southwest–northeast. Phase 1 shortening direction is towards the southwest, phase 2 shortening direction is northwest. Line 1 does not intersect the fold axis of phase 2 folding, while Line 2 intersects both phase 1 and 2. Green area represents the minibasins found within the study area.

within Well-A, we found that there would be significant (up to 125 m) of extra siliciclastic sediment deposited within the minibasin to the north-west. The implications of this informative discrepancy, as well as how we corrected the simulation are considered in the discussion.

DISCUSSION

Structural Evolution of Line 1 and Line 2

We deliberately kept the Structural Growth Profile and its rate of rise as simple, consistent, and geologically plausible as possible in order to make comparisons between iterations easier. In the model runs of Line 1, we found keeping a single, simple Structural Growth Profile that grew at a constant rate of rise per Time-Step produced the best fit model for our subsurface data. However, we subsequently determined that the Structural Growth History for this study area is more complex than we initially supposed. As we will discuss, there are two phases of structural movement in the study area, but due to the orientation of Line 1, it did not show evidence of this. This illustrates the importance of using multiple lines of section when modelling in 2D.

For Line 2 we applied the same principle, starting with a single, simple Structural Growth Profile that grew at a constant rate of rise per time-step. The rate of rise of the Clastic Limiting Surface used for Line 1 was also used for Line 2. The rationale being that, if the modelling for Line 1 was the correct solution for Well-A, High-1 and surrounding minibasins, we would be able to produce a close fit to the seismic and well data for Line 2. We would expect minor adjustments to either the rate of rise of the Clastic Limiting Surface or the Structural Growth Profile to occur simply because of the 3D nature basin evolution. However, using a simple, single Structural Growth Profile and the rate of rise of the Clastic Limiting Surface from Line 1 did not provide a good match in Line 2 for the seismic or well data. Minor iterative changes to the rate of rise of the Clastic Limiting Surface (changing the magnitude of rise or Time-Steps of the rise), the Structural Growth Profile, or the Initial Basin Structure could not overcome the differences in the model and the subsurface data.

Instead, major changes to the Structural Growth Profile were needed to get a close match to the subsurface data. The first major change was to significantly change the Structural Growth Profile (**Figure 9**), both temporally and spatially. The first profile consisted of two phases of folding, focused on High-1 and around Well-A, phase one occurs between Time-Step 0–65 (12.2–8.95 Ma) with maximum fold growth occurring between Time-Steps 50–59 (9.7–9.45 Ma). Phase two of this folding occurs between Time-Steps 80–244 (8.2–0 Ma), with the maximum fold growth occurring at Time-Step 88 (7.8 Ma). The timing of these folding phases indicates that they are likely to be related to the Chiapanecan Orogeny (18–0 Ma) (Padilla y Sanchez 2007) (Mandujano-Velazquez and Keppie 2009) (Padilla y Sanchez 2014) (Davison, Pindell and Hull 2021). The second profile included the growth of a salt diapir at the north western end of Line 2, and that replicated the wedging geometry we

observed in Line 2, with the stratigraphy thinning north-westwards onto the salt cored high (**Figure 9**). Regional studies confirm that salt movement has continued in the Sureste Basin (Padilla y Sanchez 2007) (Gomez Cabrera and Jackson 2009) (Ruiz-Osorio, 2018) (Davison 2020). Having three distinct phases of structural growth on Line 2 allowed us to have a much closer match to both the subsurface data. The last phase of structural growth had the greatest impact on the high at the northern end of Line 2, and that high is known to be a salt diapir (**Figure 9**).

Spatial Variability

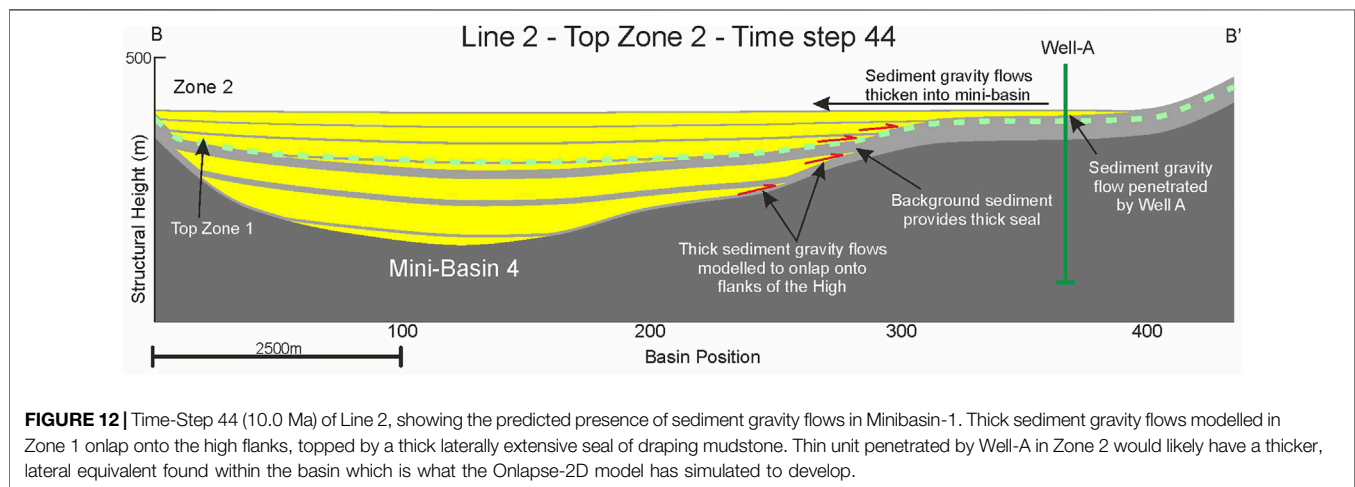
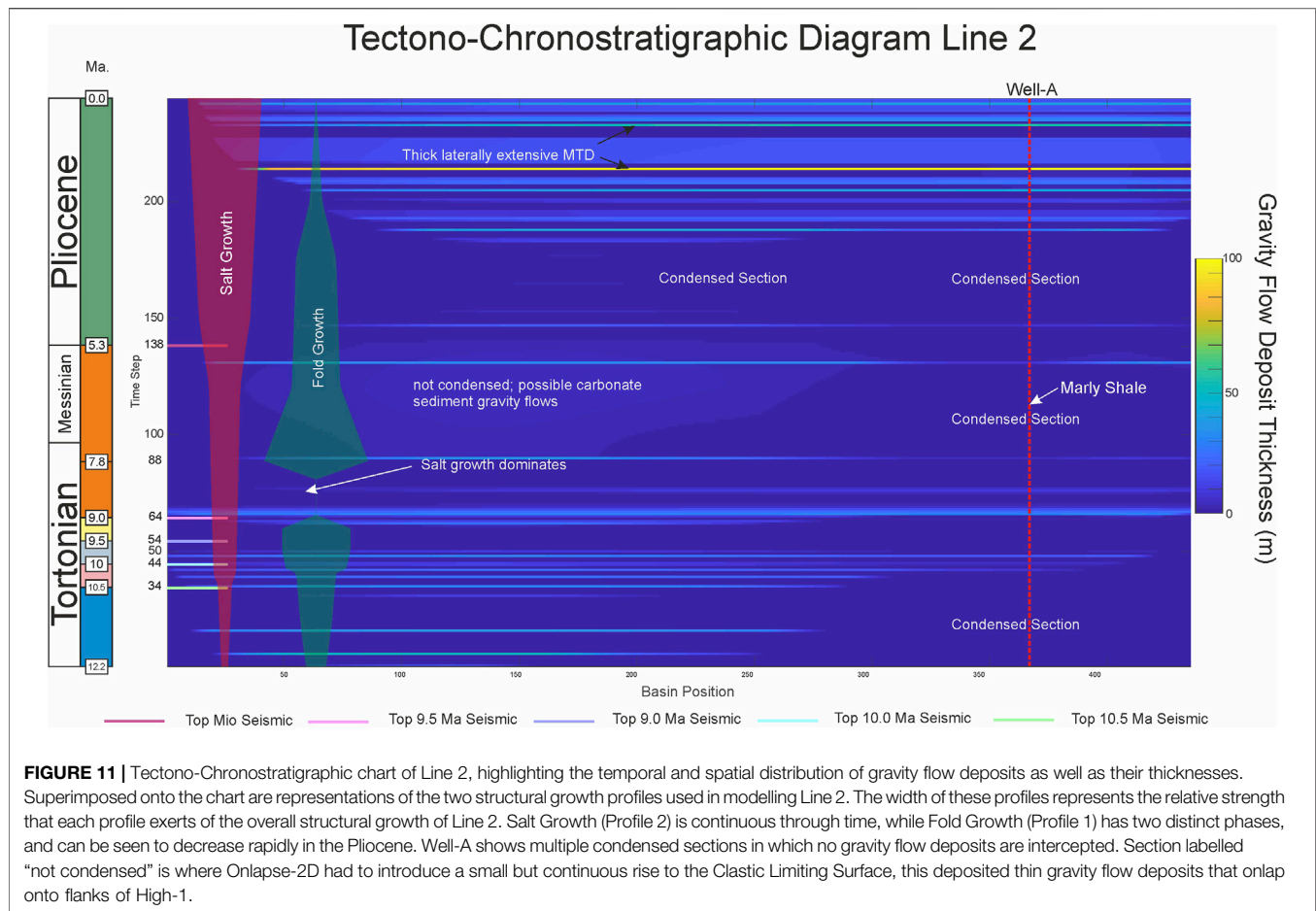
So how can we have two lines that intersect that have apparently such different structural histories? We believe this is because both salt withdrawal and compressional folding are highly three dimensional in this basin. There are three distinct phases of structural activity represented on line 2, with two distinct structural processes active within the study area: salt diapirism and withdrawal, plus two distinct phases of folding which occurred between 12.2–8.95 Ma and between 8.2–0 Ma.

Why did we not see the two phases of folding in the model for Line 1? A line of section that is parallel to the fold axis of an episode of folding (i.e. strike to the shortening direction) will not show any sign of the existence of that fold episode. That folding episode may uniformly raise or lower the line across its whole length, and we may not see differential uplift/subsidence in that direction. Conversely, a line that is at an oblique angle to a fold axis should show obvious evidence of that episode of folding.

In the study area we have 2 phases of folding whose orientations are nearly orthogonal (**Figure 10**). In the frame of reference used in this paper Phase 1 produces dominantly north-south fold axes, Phase 2 creates southwest-northeast fold axes. Line 1 is at a high angle to phase 1 and therefore shows phase 1 folding, but it does not cross any phase 2 structures. Conversely, line 2 intersects both structures of phase 1 and 2. For this reason line 1 can be modelled without requirement for phase 2 structuring as part of the model. Line 2, however, requires incorporation of both phase 1 and 2 of folding.

Likewise, we did not identify a separate signature for salt withdrawal in Line 1 because we believe the local salt is withdrawing predominantly in a north-south direction to produce the High-2 diapir at the north end of line 2. For this reason, line 2 needed to incorporate salt withdrawal and diapirism. Regionally, movement of salt found in the Sureste basin has continued until the present day, moving in a general northward direction (Gomez Cabrera and Jackson 2009) (Davison 2020).

Each component of the Structural Growth Profile reflects different structural controls on the basin, and show the amount of control that is exerted on the growth of structural accommodation through time (**Figure 9**). This is in agreement with regional studies that show the Sureste Basin is a tectonically active with compressional tectonics from the Chiapanecan Orogeny (Padilla y Sanchez 2007) (Gomez Cabrera and Jackson 2009) (Padilla y Sanchez 2014) (Davison, et al., 2021) salt tectonics playing important roles the development of the region (Gómez-Cabrera and Jackson 2009) (Ruiz-Osorio, 2018)



(Davison 2020). There are two distinct phases in the structural evolution of the cross-section where fold growth is dominant. Between these two phases, fold growth dramatically reduces from around 9.0–8.2 Ma, before increasing rapidly, peaking at around 7.8 Ma then decreasing over the course of the Pliocene (Figure 9). The timing of the first phase of folding appears to directly

correlate to a major regional event, which is the development of the Chiapas Fold-and-Thrust Belt (13.8–11.6 Ma) and the associated intense deformation in the offshore Sureste Basin (Mandujano-Velazquez and Keppie 2009) (Davison 2020). However, the results from our modelling indicates that local tectonic movement continued post 11.6 Ma, and may be also

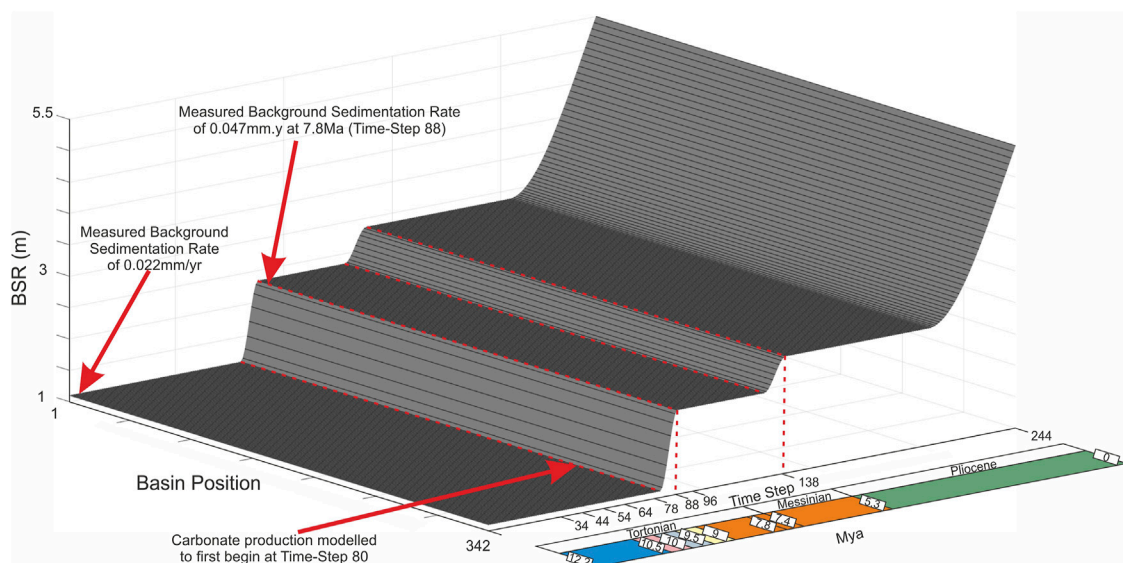


FIGURE 13 | 3D representation of Background Sedimentation Rate as it evolves through time. Derived from well data from Well-A. X axis represents position in Time, showing both Time-Step and where in the chronostratigraphic column each event is. Y axis represents position along the cross-section. Z axis represents the rate of Background Sedimentation in meters.

related to the ongoing Chiapanecan Orogeny. Salt tectonics dominates in the Pliocene, and this is what forms the wedge-shaped stratal geometry seen in the area above the Miocene section of interest in Zone 6.

Figure 11 is a tectono-chronostratigraphic chart we extracted from the *Onlapse-2D* model of Line 2, with the timing and relative importance and contribution of the two structural processes shown in red and green to the overall structural movement of Line 2. Salt tectonics exerts continual influence on the structural evolution of the cross-section throughout time, with increasing influence and becoming dominant in the Pliocene. While the fold growth of High-1, is a more variable event through time, it is dominant in the Late-Miocene before and decreases through the Pliocene.

The observation of sand injectites around the High-1 in the study area provides important independent evidence of two discrete phases of folding in the *Onlapse-2D* model output (**Figure 2**). Sand injectites are observed to penetrate from the Middle Miocene through the lower section of the Late Miocene, and are not active in the Late Tortonian. The remobilization of sands occurs when fluid overpressure forcefully injects poorly consolidated sand into the host strata (Vigorito and Hurst 2010) there are many ways in which fluid overpressure can occur; for example depositional compaction or fluid volume change. As shown by Palladino et al. (2016) contractional tectonics, such as we see here, also increases the pore-fluid pressure and can result in sand injectites. The remobilization of sand occurs throughout first phase of compression that is modelled in *Onlapse-2D* and, crucially, injectites are observed to terminate close to the time when the first phase of compression ceased in the model (Time-Step 65). No injectites are observed in the later stages of the Tortonian. Pockmarks, which are evidence of over-pressured fluid escape

(Chand, et al., 2017) are observed to occur around the time that the second phase of contraction occurs (Time-Step 80); indicating that while vertical migration of fluids continued and may be related to local compressional tectonics, the remobilization of sand ceased when the over-pressured fluids vented to the surface.

Predicting Reservoir Properties With *Onlapse-2D*

To date *Onlapse-2D* has been used to match models with existing geometries within deep-water basins. However, one of the purposes of this study is to be able to aid in the prediction of the stratigraphy prior to well placement. To this purpose we have used the interpretations of well data from Well-A provided to us, and combined this with the final simulation for Line 2 to make predictions about the stratigraphy in the Minibasin-4 (**Figure 12**).

How would the stratigraphy change in Minibasin-4 based on the modelling and what the well data shows us? Data from Zone 2 in Well-A is interpreted to be the distal lobe fringe of a deep-water turbidite system. The *Onlapse-2D* model shows packages of sediment gravity flows that thicken into the basin-axis of Minibasin-4 from Well-A in Zone 2, and thin onto and eventually onlap onto High-1. The stratal geometry here is consistent with the observations of subsurface (Mayall, et al., 2010; Doughty-Jones, et al., 2017), outcrop (Cumberpatch, et al., 2021), and numerical modelling (Sylvester, et al., 2015) of deep-water sediment gravity flows in confined tectonically active basins. These thicker sediment gravity flows could represent the sand-rich lobe axis of a confined lobe complex which progressively became unconfined through time as sediment input outpaced growth of structural accommodation. The

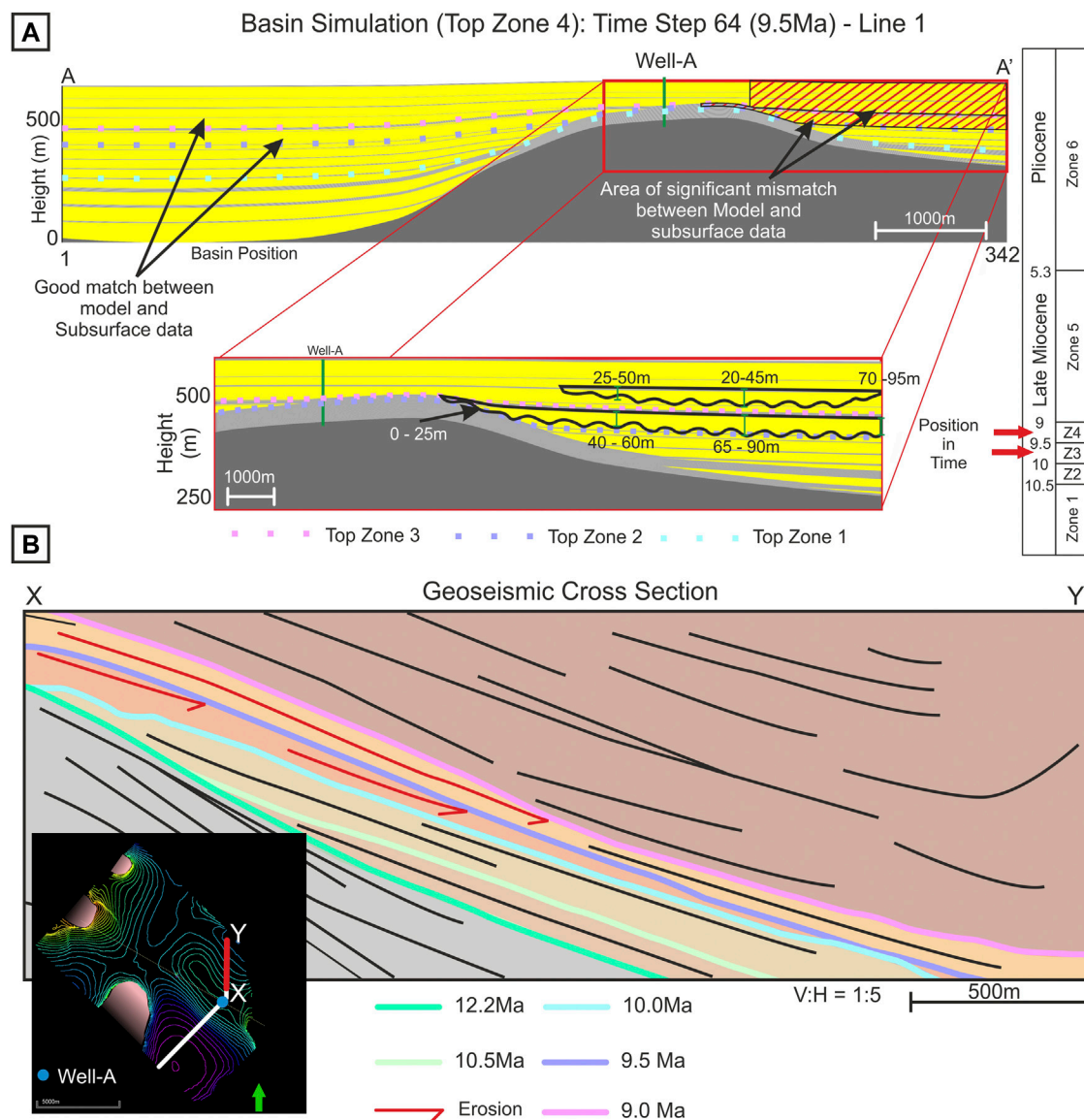


FIGURE 14 | (A) Basin simulation of Top Zone 4 of Line 1. A good match was achieved between the Onlapse-2D model and subsurface data in Zone-3 & 4 in Minibasin-1 and High-1. Red hashes show in Minibasin 2 where for Zone 3 & 4 a significant mismatch occurred. Insert shows what Onlapse-2D simulated to develop, within Zone 3, an increasing amount of over-thickening is shown, and while for Zone 4 the over-thickening is more constrained to the centre of Minibasin 2. **(B)** Geoseismic cross section focused on Minibasin-2. Map insert shows location where geoseismic is taken from. Red arrows highlight that between 10.0–9.5 Ma & 9.5–9.0 Ma, seismic reflectors are eroded into by major horizons. This provides evidence that the mismatch between simulation and subsurface data occurs because there has been erosion within Minibasin 2.

thick deposits of the lower section of Zone 2 onlap onto the flanks of, and eventually overtop the crest of High-1 (**Figure 12**).

Within Zone 1 we see thick sediment gravity flows confined within Minibasin-4 that onlap onto the flank of High-1. These sediment gravity flow packages are not penetrated by Well-A, and so we cannot definitively state what the lithology of these are. Seismically we note bright to moderate amplitude continuous reflectors which can be interpreted to be a sand-prone seismic facies. This seismic facies has a morphology and scale consistent with a lobe-complex that is experiencing a strong degree of lateral

confinement (*sensu* Pr  lat, Hodgson and Flint 2009; Groeneweg, et al. 2010). This interpretation is further supported by the context of the small-scale of the basin in that turbidity currents entering the basin are likely to experience a strong degree of relative confinement *sensu* (Stanbrook and Bentley 2021). The onlapping geometry of these sediment gravity flows represent a potential stratigraphic trap target for future consideration, and closely resembles the draping onlap (O_d) described by Bakke et al. (2013). Crucially, the modelling by Onlapse-2D predicts a thick draping of background sediment,

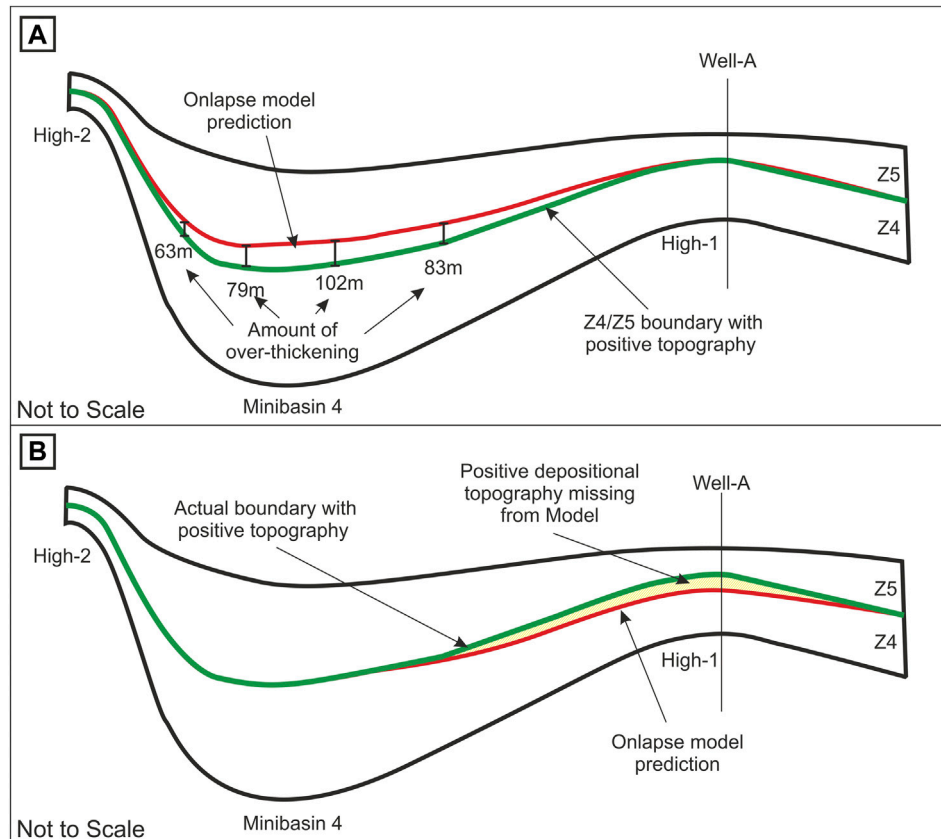


FIGURE 15 | (A) Schematic diagram of mismatch between the Onlapse-2D simulation and seismic data, with significant over-thickness within Minibasin 4 from Line 2. Red horizon represents the original simulated boundary between Zone 4 & 5 within the model. Green horizon represents boundary between Zone 4 & 5 with positive depositional topography taken from seismic data. **(B)** Schematic diagram of Onlapse-2D in final simulation of the same line, red horizon represents Onlapse-2D simulated horizon, which now matches the boundary seen in seismic in Minibasin. From the difference between red and green horizon on High-1 we can infer the amount of positive depositional topography that is present.

which could provide a thick laterally continuous seal for a potential stratigraphic trap target (Figure 12).

What is the Significance of the Different Background Sedimentation Rates?

Data from Well-A indicates the presence of two condensed zones for which we have biostratigraphic age constraints. We used these to estimate the Background Sedimentation Rate, because these are regionally interpreted as condensed zones. The oldest condensed section occurred within the Middle Miocene, and gave us a rate of 0.022 mm/yr, while the youngest condensed section occurred within the Late Miocene and gave us a rate of 0.047 mm/yr, indicating a doubling of the Background Sedimentation Rate.

Lithology data from Well-A also shows that in the Late Miocene just before this doubling occurs in the background mudstone becomes considerably more carbonate-rich compared to the section below (Figure 13). We used the first appearance of a more marl-rich lithology within Well-A to give a direct indication of when the Background Sedimentation Rate should increase as *Onlapse-2D* does not differentiate between

siliciclastic and carbonate background sediment. We interpret the cause of this increase in Background Sedimentation Rate to be an increase in carbonate productivity within the region, and this interpretation is consistent with the regional time-equivalent shelf carbonate stratigraphy. Sedimentation rates derived by Gomez Cabrera & Jackson (2009) show a marked increase in the Pliocene, which we incorporated into our Background Sedimentation Rate curve.

Possible Carbonate Sediment Gravity Flows

There are marl-rich mudrocks penetrated in Zone 5 in Well-A. When we modelled these marls as background sediment, there was a significant mismatch between the seismic and the model as the Zone 5 interval extends northwards into Minibasin-4 (Figure 2); That model run predicts a thin section in the basin centre, whereas the Zone 5 seismic interval thickens into the minibasin.

Give that the well penetrated thin sediment gravity flow deposits in Zone 5 in Well-A, in a package that onlapped onto High-1 (Figure 8) we instead modelled the interval as one of active sedimentation and added a small continuous rate of rise to

the Clastic Limiting Surface for that interval, which generated the observed thickening of this interval, confined to Minibasin-4. Doing so allowed us to account for differences in thicknesses observed between Well-A, and provide a better match to the subsurface data (**Figure 8**).

As well as the presence of marl-rich shales in this interval at Well-A, there is documentation of increases in carbonate production leading to the development of isolated carbonate build ups in shallower water sections at this time (Shann, et al., 2020). This additional line of evidence leads us to the interpretation that the modelled Gravity Flow Deposit packages which thicken northwards into Minibasin 3 in Zone 5 are likely to be calciturbidites which are derived from the shelf during this time of increased carbonate production.

Informative Discrepancies

What do we mean by an *Informative Discrepancy*? We are able to iterate towards a good solution where the model output provides a close match to the subsurface data. However, there are localized anomalies where it is not possible to iterate towards such a match using *Onlapse-2D*. We call these *Informative Discrepancies*, because they point to valuable insights. *Informative Discrepancies* identify places in the model where the basic assumptions of the *Onlapse-2D* method, do not apply; for example, no erosion or positive topography.

Our purpose with *Onlapse-2D* is to attain a close as match as possible between the model output and observed subsurface data. However, in this study, we demonstrate there is significant information and geological insight that can be obtained by quantifying the mismatch between the best fit model and the available data. Once we have identified an informative discrepancy, our objective shifts from attempting to make a perfect fit to making a best fit. Once this has been achieved, we can highlight the differences, quantify them, and then make a geological interpretation out of them; thereby enabling us to quantify the processes that lie outside the scope of the model. For example, we can estimate how much sediment at key points along the cross-section has been eroded, or predict the height of positive depositional topography. We believe this is a general learning that could be adopted in many other Stratigraphic Forward Modelling studies.

Informative Discrepancy in Line 1

Overall we found the simulation produced by *Onlapse-2D* provided a good match to the seismic and well data. However, we found a significant mismatch on the northern flank of the High-1 in Line 1 for both Zone 3 and Zone 4 (**Figure 14A**). The model was simulating a significant thickness of gravity flow deposit packages when seismic data was showing us this was not the case. There was an increasing amount of over-thickening within Zone 3 and 4 extending into Minibasin-2 off of High-1, with up to 95 m of extra sediment simulated as deposited.

To correct for this, we began by making iterative changes to the rate of rise of the Clastic Limiting Surface and the Structural Growth Profile, and we lowered the Initial Basin Structure for Time-Step 0. We were unable to lower the amount of over thickening in Zone 3 or 4 through these iterative changes,

without substantially under-thickening the model in Well-A and in Minibasin-1 (**Figure 14A**). Therefore, the discrepancy is caused by a process that we do not model in the simulation (e.g. erosion or positive depositional topography).

As there is no evidence of this over thickening within our seismic, our interpretation is that there has been substantial erosion on the northern section of the High. Close inspection of the seismic data on the northern flank shows evidence of erosive features between the mapped horizons which agrees with our assessment (**Figure 14B**). Two laterally continuous seismic reflectors from Zone 3 which are truncated by the 9.5 ma (Top Zone 3) reflector, while another major seismic reflector from within Zone 4 is truncated by the 9.0 ma (Top Zone 4) reflector. We estimate that the amount of erosion at key points in the cross-section is from 0–25 m on High-1, up to 75–95 m in the deepest section of Minibasin-2 (**Figure 14A**). We believe that this erosion is caused by the major sediment fairway that in the study area, where sediment enters Minibasin-2 from the south, flows northward running axially along High-1 into Minibasin-3. Quantifying the amount of eroded section could have implications for sediment delivery to successive minibasin downslope, and possible reservoir intervals in those minibasins.

Informative Discrepancy in Line 2

Zone 4 of Line 2 contains another major discrepancy between the modelled *Onlapse-2D* simulation and the subsurface data. Matching the model to seismic data and Well-A, produced over-thickening of the siliciclastic sediment deposited within the minibasin to the north-west, ranging from 60 to 102 m (**Figure 15A**). Quantifying the amount of eroded section could have implications for sediment delivery to successive minibasins downslope, and possible reservoir intervals in those minibasins.

Significant changes to the Structural Growth Profile, namely ceasing Fold Growth on High-1 (**Figure 9**) allowed us to lower this discrepancy between the model and the subsurface data. However, a discrepancy remained between the modelled simulation and the well and seismic data which we were unable to eliminate by means of further iterative changes in the inputs.

While there is evidence of erosion in Zone 3 and Zone 4 in the Line 1 seismic, close inspection of the seismic and well data provides no such evidence of erosion for either Zone in Line 2. This led us to the conclusion that positive topography (e.g. submarine lobes) found on High-1 was the cause of the significant mismatch between *Onlapse-2D* and the subsurface data. So we matched the thicknesses seen in Minibasin-4 instead of attempting to match the thicknesses on High-1. This provided us with a much closer fit to the subsurface data, but there was a residual discrepancy in Well-A, which allowed us to estimate how much stratigraphy was missing within the model. We can infer 5–30 m of positive depositional topography on the flanks of Minibasin-4, and at Well-A additional depositional topography of 45–70 m (**Figure 15B**). Data from Well-A for Zone 4 supports this interpretation with the sands encountered in the well representing sedimentation in a proximal to marginal lobes position with thick intervals of stacked amalgamated sands, consistent with the interpreted depositional topography.

CONCLUSION

This case study has demonstrated the value of a modelling software that integrates dynamic topographic development of real structures with active deposition in the evolving palaeotopography. Specifically, by seeking to precisely replicate the observed structural geometry and stratigraphic architecture, *Onlapse-2D* provides powerful and unexpected insights into the processes of structural and stratigraphic evolution of the study area. While this study focuses on an offshore region of the Sureste Basin, within the Gulf of Mexico we believe the workflow demonstrates the applicability of this approach in other basins with deep-water sedimentary systems such as the Northern Gulf of Mexico, offshore West Africa, or offshore Brazil.

Through the integration of both seismic and well data into the *Onlapse-2D* model we have been able to successfully simulate the tectonostratigraphic evolution of two cross sections across the study area in the Sureste Basin. We identified two distinct phases of compressional folding that were not parallel to each other and the long term effects of salt withdrawal and diapirism. We were able to integrate well data, age dated horizon interpretations, and seismic data to constrain and improve the modelled simulations produced by *Onlapse-2D* through a processes of iteration.

The best fit model for Line 2 illustrates that folding alone could not account for the stratal patterns observed in the seismic and well data and shows that structural movement resulting from salt tectonic patterns is required throughout the evolution of the cross-section. We are able to define the probable timing and rate of uplift during two distinct phases of fold growth in the Late Miocene, and this conclusion is supported by independent evidence in the timing of sand injectites. We were able to define the timing of salt withdrawal and diapirism that dominates the subsidence history in the Late Pliocene.

While we achieved a good match between the final simulation and the subsurface data for almost all intervals in both the basins modelled in the two sections, there are minor but significant intervals in which the model is unable to produce a simulation that matches the data. These model discrepancies proved to be valuable and corresponded to intervals where significant depositional topography created via erosion of previous deposits and constructional depositional topography. We term these *Informative Discrepancies*, and we are able to use their magnitude to quantify the amount of erosion or positive depositional topography (e.g. lobe palaeotopography) that the model software was not designed to replicate.

REFERENCES

- Bakke, K., Kane, I. A., Mertinsen, O. J., Petersen, S. A., Johansen, T. A., Hustoft, S., et al. (2013). Seismic Modelling in the Analysis of Deep-Water sandstone Termination Styles. *AAPG Bull.* 97 (9), 1395-1419. doi:10.1306/03041312069
- Basani, R., Janocko, M., Cartigny, M. J. B., Hansen, E. W. M., Eggenhuisen, J. T., and Eggenhuisen, J. T. (2014). "MassFLOW-3DTM as a Simulation Tool for Turbidity Currents," in *Depositional Systems to Sedimentary Successions on the Norwegian Continental Margin*. Editors A. W. Martinius, R. Ravnas, J. A. Howell, R. J. Steel, and J. P. Wonham (Chichester: International

We have also demonstrated that the *Onlapse-2D* model outputs predict the distribution of potential reservoir and seal lithologies in parts of the basin away from direct well control.

DATA AVAILABILITY STATEMENT

The raw data supporting the conclusions of this article will be made available by the authors, without undue reservation.

AUTHOR CONTRIBUTIONS

DC, FP, and D"S"S contributed to the initial design and scope of the study with D"S"S organizing access to subsurface data. Modelling and analysis of results were performed by DC, with all authors contributed to further analysis of modelling results. DC wrote the first draft of the manuscript. All authors contributed to manuscript revision, read and approved the submitted version.

FUNDING

The work contained in this paper contains work conducted during a PhD study undertaken as part of the Natural Environment Research Council (NERC) Centre for Doctoral Training (CDT) in Oil & Gas (grant number NEM00578X/1). It is sponsored by the University of Southampton whose support is gratefully acknowledged. The University of Southampton has joined the Frontiers - JISC national open access deal and once an application form is submitted with DOI information, will be paying the submission fees.

ACKNOWLEDGMENTS

We thank Murphy Oil Corporation for access to permission to use subsurface data, as well as their input and geological advice that was critical in this study. We would also like to thank the editorial team at Frontiers, as well reviews from Istvan Csato and Zoe Cumberpatch. Their insightful comments and suggestions were instrumental in improving this paper.

- Association of Sedimentologists), Special Publication 46, 587-608. doi:10.1002/9781118920435.ch20
- Burgess, P. M. (2012). A Brief Review of Developments in Stratigraphic Forward Modelling, 2000-2009. *Reg. Geology. Tectonics*, 378-404. doi:10.1016/b978-0-444-53042-4.00014-5
- Burgess, P. M., Masiero, I., Toby, S. C., and Duller, R. A. (2019). A Big Fan of Signals? Exploring Autogenic and Allogenic Process and Product in a Numerical Stratigraphic Forward Model of Submarine-Fan Development. *J. Sediment. Res.* 89, 1-12. doi:10.2110/jsr.2019.3
- Chand, S., Crémère, A., Lepland, A., Thorsnes, T., Brunstad, H., and Stoddart, D. (2017). Long-term Fluid Expulsion Revealed by Carbonate Crusts and Pockmarks Connected to Subsurface Gas Anomalies and Palaeo-Channels

- in the central North Sea. *Geo-mar Lett.* 37 (3), 215–227. doi:10.1007/s00367-016-0487-x
- Christie, D. N. (2021). Reconstructing the Ocean Floor Shape in Turbidite Basins Using Seismic Interpretations and Forward Modelling. PhD Thesis, Southampton: School of Ocean and Earth Science, University of Southampton.
- Cumberpatch, Z. A., Kane, I. A., Soutter, E. L., Hodgson, D. M., Jackson, C. A-L., Kilhams, B. A., et al. (2021). Interactinos between Deep-Water Gravity Flows and Active Salt Tectonics. *J. Sediment. Res.* 91, 34–65. doi:10.2110/jsr.2020.047
- Davison, I., Pindell, P. J., and Hull, J. (2021). *The Basins, Orogens and Evolution of the Southern Gulf of Mexico and Northern Caribbean*. London: Geological Society, 1–27. doi:10.1144/sp504-2020-218
- Davison, I. (2020). *Salt Tectonics in the Sureste Basin, SE Mexico: Some Implications for Hydrocarbon Exploration*. London: Geological Society, 147–165. doi:10.1144/SP504-2019-227
- Doughty-Jones, G., Mayall, M., and Lonergan, L. (2017). Stratigraphy, Facies, and Evolution of Deep-Water Lobe Complexes within a Solt Controlled Intralope Minibasin. *AAPG Bull.* 101 (11), 1879–1904. doi:10.1306/01111716046
- Gomez Cabrera, P. T., and Jackson, M. P. A. (2009). “Neogene Stratigraphy and Salt Tectonics of the Santa Ana Area, Offshore Salina del Istmo Basin, Southeastern Mexico,” in *Petroleum Systems in the Southern Gulf of Mexico*. Editors C. Bartolini and J. R. Román Ramos (Tulsa, Oklahoma, United States: AAPG), 237–255. doi:10.1306/13191086M9037
- Granjeon, D. (2014). “3D Forward Modelling of the Impact of Sediment Transport and Base Level Cycles on continental Margins and Incised Valleys. Vol. Special Publication 46,” in *From Depositional Systems to Sedimentary Successions on the Norwegian Continental Margin*. Editors A. W. Martinus, R. Ravnas, J. A. Howell, R. J. Steel, and J. P. Wonham (Chichester: International Association of Sedimentologists), 453–472. doi:10.1002/9781118920435.ch16
- Griffiths, C. M., Dyt, C. P., Paraschivoiu, E., and Liu, K. (2001). “Sedim in Hydrocarbon Exploration,” in *Geologic Modeling and Simulation*. Editors D. F. Merriam and J. C. Davis (Boston, MA: Springer), 71–97. doi:10.1007/978-1-4615-1359-9_5
- Groenenberg, R. M., Hodgson, D. M., Prêlat, A., Luthi, S. M., and Flint, S. S. (2010). Flow–Deposit Interaction in Submarine Lobes: Insights from Outcrop Observations and Realizations of a Process-Based Numerical Model. *J. Sediment. Res.* 80 (3), 252–267. doi:10.2110/jsr.2010.028
- Huang, X., Griffiths, C. M., and Liu, J. (2015). Recent Development in the Stratigraphic Forward Modelling and its Application in Petroleum Exploration. *Aust. J. Earth Sci.* 62, 903–919. doi:10.1080/08120099.2015.1125389
- Hudec, M. R., and Norton, I. O. (2019). Upper Jurassic Structure and Evolution of the Yucatan and Campeche Subbasins, Southern Gulf of Mexico. *AAPG Bull.* 103 (5), 1133–1151. doi:10.1306/11151817405
- Mandujano-Velazquez, J. J., and Duncan Keppie, J. (2009). Middle Miocene Chiapas Fold and Thrust belt of Mexico: a Result of Collision of the Tehuantepec Transform/Ridge with the Middle America Trench. *Geol. Soc.* 327, 55–69. doi:10.1144/SP327.4
- Mayall, M., Lonergan, L., Bowman, A., James, S., Mills, K., Primmer, T., et al. (2010). The Response of Turbidite Slope Channels to Growth-Induced Seabed Topography. *AAPG Bull.* 94 (7), 1011–1030. doi:10.1306/01051009117
- Padilla y Sanchez, R. J. (2007). Evolución geológica del sureste mexicano desde el Mesozoico al presente en el contexto regional del Golfo de México. *Boletín de la Sociedad Geológica Mexicana* 59, 19–42. doi:10.18268/BSGM2007v59n1a3
- Padilla y Sanchez, R. J. (2014). Tectonics of Eastern Mexico. *Search and Discovery Article #10622*. AAPG Available at: http://www.searchanddiscovery.com/documents/2014/10622padilla/ndx_padilla.
- Palladino, G., Grippa, A., Denis, B., Alsop, I., and Hurst, A. (2016). Emplacement of Sandstone Intrusions during Contractional Tectonics. *J. Struct. Geology.* 89, 230–249. doi:10.1016/j.jsg.2016.06.010
- Paola, C. (2000). Quantitative Models of Sedimentary basin Filling. *Sedimentology* 47 (1), 121–178. doi:10.1046/j.1365-3091.2000.00006.x
- Pindell, J., Weber, B., Elrich, W. H., Cossey, S., Bitter, M., Molina, R., et al. (2019). “Strontium Isotope Dating of Evaporites and the Breakup of the Gulf of Mexico and Proto-Caribbean Seaway (abs.),” in *AAPG Annual Convention and Exhibition* (San Antonio: AAPG).
- Prêlat, A., Hodgson, D. M., and Flint, S. S. (2009). Evolution, Architecture and Hierarchy of Distributary Deep-Water Deposits: a High-Resolution Outcrop Investigation from the Permian Karoo Basin, South Africa. *Sedimentology* 56, 2132–2154. doi:10.1111/j.1365-3091.2009.01073.x
- Rivenaes, J. C. (1992). Application of Dual Lithology, Depth Dependent Diffusion Equation in Stratigraphic Simulation. *Basin Res.* 4, 133–146. doi:10.1111/j.1365-2117.1992.tb00136.x
- Ruiz-Osorio, A. S. (2018). *Tectonostratigraphic Evolution and Salt Tectonic Processes of the Isthmus Saline Basin, South-Eastern Gulf of Mexico: Implications for Petroleum Systems and Exploration*. UK: Royal Holloway University of London.
- Salvador, A. (1987). Late-Triassic-Jurassic Paleogeography and Origin of Gulf of Mexico Basin. *AAPG Bull.* 71 (4), 419–451. doi:10.1306/94886ec5-1704-11d7-8645000102c1865d
- Shann, M. V., Vazquez-Reyes, K., Ali, H. M., and Horbury, A. D. (2020). The Sureste Super Basin of Southern Mexico. *AAPG Bull.* 104 (12), 2643–2700. doi:10.1306/09172020081
- Stanbrook, D. A., Capuzzo, N., Durcanin, M., LeCompte, B., Perez, G., and Seitchik, A. (2020). “Onshore Structural Movement Revealed Through the Presence of Volcanoclastic Deposition Offshore. Cholula-1EXP, Miocene Salinas del Istmo Basin, Mexico,” in *AAPG Annual Convention and Exhibition* (Houston, Texas: AAPG), 18.
- Stanbrook, D. S., and Bentley, M. (2021). Practical Turbidite Interpretation: The Role of Relative Confinement in Understanding Reservoir Architecture. *Mar. Pet. Geology.* 135, 105372. doi:10.1016/j.marpetgeo.2021.105372
- Stern, R. J., and Dickinson, W. R. (2010). The Gulf of Mexico Is a Jurassic Backarc basin. *Geosphere* 6 (6), 739–754. doi:10.1130/GES00585.1
- Sylvester, Z., Cantelli, A., and Pirmez, C. (2015). Stratigraphic Evolution of Intralope Minibasins: Insights from Surface-Based Mode. *AAPG Bull.* 99 (6), 1099–1129. doi:10.1306/01081514082
- Vigorito, M., and Hurst, A. (2010). Regional Sand Injectite Architecture as a Record of Pore-Pressure Evolution and Sand Redistribution in the Shallow Crust: Insights from the Panoche Giant Injection Complex, California. *J. Geol. Soc.* 167, 889–904. doi:10.1144/0016-76492010-004

Conflict of Interest: Author D“S”S is employed by Murphy Exploration and Production Company.

The remaining authors declare that the research was conducted in the absence of any commercial or financial relationships that could be construed as a potential conflict of interest.

Publisher’s Note: All claims expressed in this article are solely those of the authors and do not necessarily represent those of their affiliated organizations, or those of the publisher, the editors and the reviewers. Any product that may be evaluated in this article, or claim that may be made by its manufacturer, is not guaranteed or endorsed by the publisher.

Copyright © 2021 Christie, Peel, Apps and Stanbrook. This is an open-access article distributed under the terms of the Creative Commons Attribution License (CC BY). The use, distribution or reproduction in other forums is permitted, provided the original author(s) and the copyright owner(s) are credited and that the original publication in this journal is cited, in accordance with accepted academic practice. No use, distribution or reproduction is permitted which does not comply with these terms.



The Influence of Channel Planform and Slope Topography on Turbidity Current Overbank Processes: The Example of the Acquarone Fan (Southeastern Tyrrhenian Sea)

Elena Scacchia^{1,2*}, Roberto Tinterri¹ and Fabiano Gamberi²

¹Department of Chemistry, Life Sciences and Environmental Sustainability, Earth Sciences Unit, University of Parma, Parma, Italy,

²Istituto di Scienze Marine (ISMAR), National Research Council (CNR), Bologna, Italy

OPEN ACCESS

Edited by:

Michael Andrew Clare,
University of Southampton,
United Kingdom

Reviewed by:

Meg Baker,
Durham University, United Kingdom
Luigi Jovane,
University of São Paulo, Brazil

*Correspondence:

Elena Scacchia
elena.scacchia@unipr.it

Specialty section:

This article was submitted to
Sedimentology, Stratigraphy and
Diagenesis,
a section of the journal
Frontiers in Earth Science

Received: 28 September 2021

Accepted: 13 December 2021

Published: 10 January 2022

Citation:

Scacchia E, Tinterri R and Gamberi F
(2022) The Influence of Channel
Planform and Slope Topography on
Turbidity Current Overbank Processes:
The Example of the Acquarone Fan
(Southeastern Tyrrhenian Sea).
Front. Earth Sci. 9:785164.
doi: 10.3389/feart.2021.785164

Overbank deposits provide a potentially valuable record of flows that have passed through a submarine channel. The architecture of overbank deposits has generally assumed to relate to autogenic processes related to channel construction. In previous models, which are largely based on passive margins, the distribution and geometry of these deposits is relatively simple, and hence generally predictable. Here, we show how the interaction of different flow types with the complex morphology on a highly-tectonically modified margin can profoundly affect overbank depositional processes, and hence also the resultant deposit geometry and architecture. Our case study is the Acquarone Fan, located in the intraslope Gioia Basin in the south-eastern Tyrrhenian Sea, whose topography is mainly controlled by the presence of the Acquarone structural ridge, which results in the confinement of the left south-west side of the channel-levee system. The research is carried out through analysis of multibeam bathymetric and high-resolution Chirp sub-bottom profiler data. Seven depositional units (Units I-VII) record the recent depositional history of the fan; their thickness has been mapped and their parent flow-types have been interpreted through their seismic response. According to unit thickness maps, two main patterns of deposition are recognized in the overbank area. Their depocenters coincide with different extensive sediment wave fields developed in specific tracts of the right levee and in the frontal splay area. We show that the location of the depocenters varies in time according to the prevalent flow-type and by its interaction with the surrounding seafloor topography and channel planform. We interpret that the lateral confinement of the channel by the structural high generates episodic rebound of the overspilling flow and the inversion of the channel asymmetry. The vertical stratification of the flow strongly influences the overbank deposition where the channel planform has a non-linear shape such as bends and knick-points. In particular, the vertical stratification influences the hydraulic jump size that conditions the amount of overspill and thus the location of overbank depocenters. This study highlights that variations in the sediment distribution and composition on the overbank can be related to the way different flows interact with tectonic setting.

Keywords: overbank deposit, submarine fan, turbidity current, channel planform, slope, knick point, hydraulic jump

1 INTRODUCTION

Turbidity currents are one of the primary mechanisms for sediment transport to the deep-marine environment and their deposits represent the fundamental building blocks of submarine fans. During part of their path, turbidity currents flow within submarine channels, the principal conduits for the transport of sediment from the shelf to the basin floor (Mutti and Normark, 1991). When the thickness of the turbidity current is greater than the channel depth, the upper part of the flow can escape the channel's confinement and relatively fine-grained sediment settles beyond the channel banks and built overbank wedges (Piper and Normark, 1983).

The internal architecture and the distribution of lithologies in submarine fans and their control on the distributions of reservoir properties is fundamental information for petroleum exploration and for the advancement of the techniques for Carbon Capture Storage (CCS). As a consequence, the overbank depositional setting has recently become the focus of growing attention, since thin-bedded turbidite layers composing overbank wedges can be extremely laterally continuous (Peakall et al., 2000; Hansen et al., 2015) and contain large sand volume. As an example, a net to gross value > 50% has been reported in the Cretaceous San Fernando slope channel system of the Rosario Formation in Mexico (Hansen et al., 2015). In addition, a knowledge of the processes inherent with turbidity current behaviour is fundamental for the study of the fate of pollutants, plastics and microplastics in the marine realm (Zhong and Peng, 2021). Notwithstanding these issues with important applied outcomes, many aspects, related to turbidity current behaviour in overspilling submarine channels, remain one of the least well understood sedimentary processes.

The trends of lateral decay of levee, sand bed thickness and sand percentage transverse to the channel are thought to be predictable, and to follow power law, logarithmic or exponential decay according to the regional slope (Birman et al., 2009; Kane et al., 2010; Nakajima and Kneller, 2013). On the contrary, downslope trends in sediment distribution are less constrained. In general, levee construction involves the progressive downflow loss of fine-grained material that results in the downslope thinning of overbank wedges and increase in their sand content (Hiscott et al., 1997; Posameinter and Kolla, 2003).

However, the seafloor morphology can affect the behaviour of a turbidity current in several ways: it can halt the flow or change its velocity and alter its pathway (Kneller, 1995; Patacci et al., 2015). Those changes leave a footprint in the sedimentation pattern and in the facies and lithology distribution in submarine fans and the predictivity of those simple models can be drastically altered. The response of turbidity currents to slope topography has been investigated through several case studies specifically concentrating on their final depositional sites, corresponding to terminal lobes (Pickering and Hiscott, 1985; Haughton, 1994; Amy et al., 2004; Remacha et al., 2005; Gamberi and Marani, 2008; Tinterri and Muzzi Magalhaes, 2011; Tinterri and Piazza, 2019) and confirmed by experiments (Kneller et al., 1991; Kneller, 1995; Haughton et al., 2004;

Amy et al., 2005; Patacci et al., 2015; Howlett et al., 2019). In contrast, few studies so far have linked the development of the overbank area of leveed channels to seafloor topography (Tek et al., 2021).

Information about the variation of sediment distribution over time can be used to reconstruct changes in the flow properties. Such reconstructions can be valuable for comparison with the trends expected from the application of existing models. In addition, studies on the modern seafloor, tied to well-known morphological contexts of deposition, can be vital for unravelling the effects of seafloor topography on sedimentation. This approach is used in this study focused on the overbank wedges of the Acquarone Fan, a deep-sea fan located in the continental slope of the Gioia Basin in the southeastern Tyrrhenian Sea. The study area has a complex physiography, mainly controlled by the presence of the Acquarone structural ridge, which confines the south-west side of the channel-levee system.

The objectives of this work are: 1) integrate bathymetric and seismic data to characterize seafloor morphology and the stratigraphic architecture of the last 40 m of the sedimentary succession; 2) provide a detailed analysis of sediment thickness distribution on a submarine channel overbank area. The final purpose of our study is to investigate the effects of topographic features, resulting from tectonic processes, on overbank deposition. In particular, with the examination of overbank processes in a topographically complex slope, we aim at highlighting the divergence from the established models of overbank sedimentation in simple slope settings.

In general, our results expand our understanding of overbank flow processes and show that, particularly in active continental margin, many factors, mostly extrinsic to the turbidite system, contribute to the final fate of sediment within leveed channels.

2 GEOLOGICAL SETTING

The Acquarone Fan is located in the southern part of the Calabrian sector of the Gioia Basin, an intraslope basin in the southeastern Tyrrhenian Sea (**Figure 1A**). The Gioia Basin formed in response to the backarc extension associated with the Ionian-Calabrian subduction zone, which started in the Late Miocene (Fabbri et al., 1980; Gamberi and Marani, 2006). Since then, the Gioia Basin has been affected by major NE-SW, N-S, and E-W trending extensional faults (Fabbri et al., 1980; Casas et al., 2016). The Acquarone Fan developed in the depocenter of the Calabrian sector of the Gioia Basin, a semi-graben created by the past action of a NW-SE-trending, NE-dipping extensional fault (**Figure 1C**). Since the Middle Pleistocene, the physiography of the basin has been mainly controlled by the recent tectonic deformation, associated with high rates of vertical movement, also affecting the Sicilian and Calabrian mainland.

The submarine expression of the high rates of uplift of the basin margin is particularly evident in the Sicilian sector, where seafloor instability resulted in an extensive mass-transport complex (Gamberi and Marani, 2006; Gamberi and Rovere, 2011; Rovere et al., 2014; Gamberi et al., 2019) (**Figure 1A**).

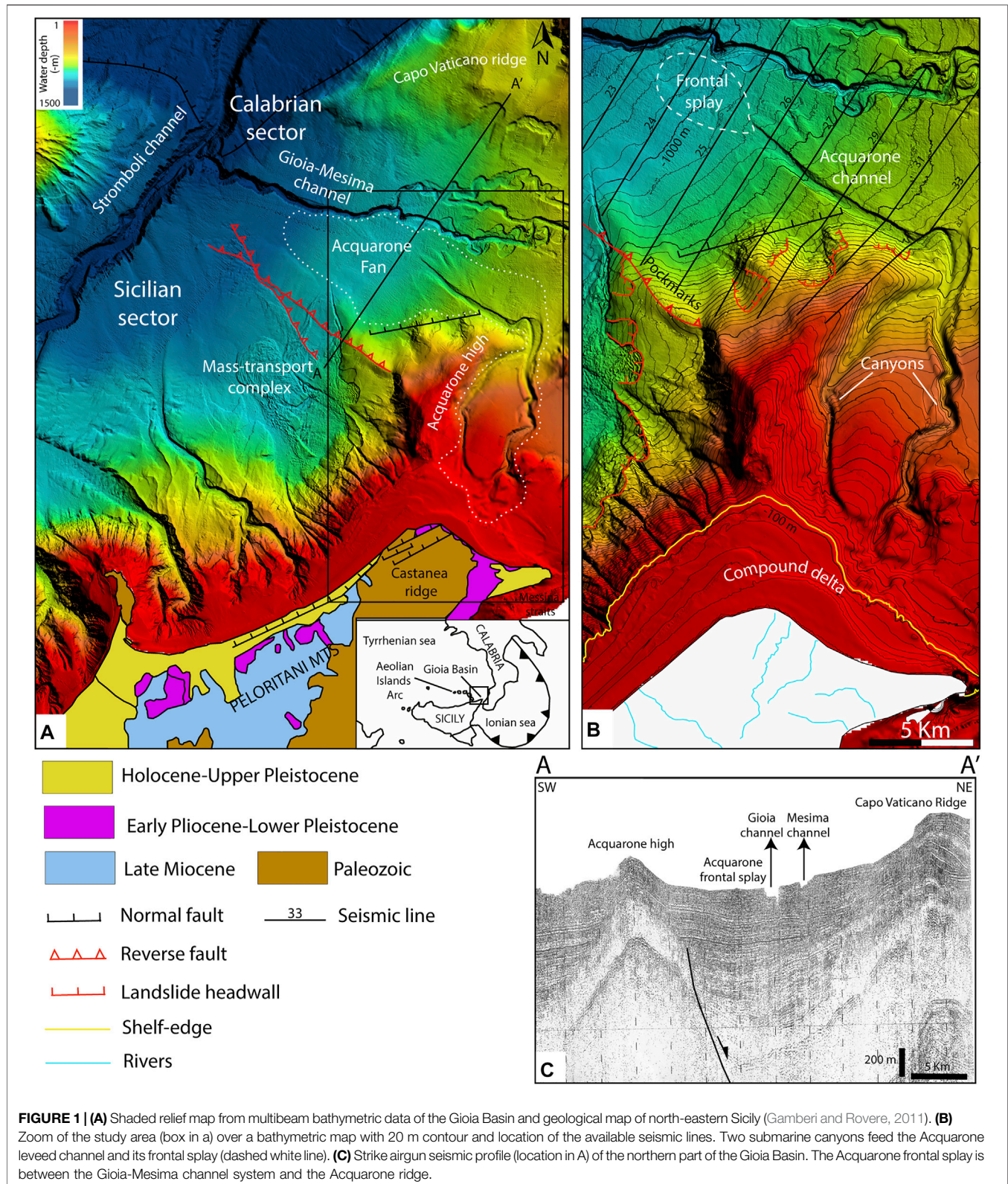


FIGURE 1 | (A) Shaded relief map from multibeam bathymetric data of the Gioia Basin and geological map of north-eastern Sicily (Gamberi and Rovere, 2011). **(B)** Zoom of the study area (box in a) over a bathymetric map with 20 m contour and location of the available seismic lines. Two submarine canyons feed the Acquarone leveed channel and its frontal splay (dashed white line). **(C)** Strike airgun seismic profile (location in A) of the northern part of the Gioia Basin. The Acquarone frontal splay is between the Gioia-Mesima channel system and the Acquarone ridge.

In the Calabrian part of the basin, tectonic unrest is shown by the presence of structural ridges that are also affected by large collapses (Gamberi and Marani, 2006; Casas et al., 2016;

Casalbore et al., 2019). The Acquarone Fan is bounded to the south by the Acquarone high, a structural ridge that represents the submarine continuation of the Castanea ridge (Figure 1A)

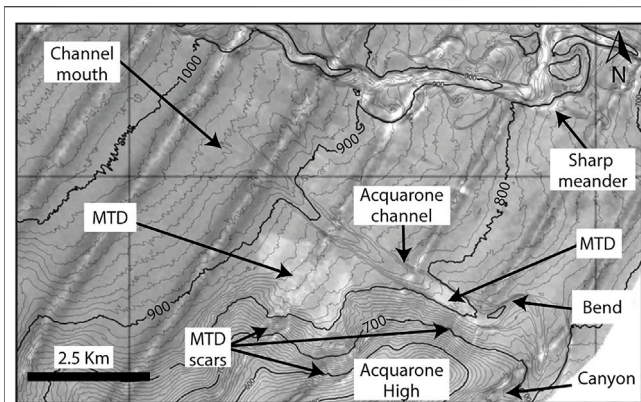


FIGURE 2 | Sea floor reflectivity image of the Acquarone Fan and of the portion of the Gioia channel to the north, draped over a bathymetric map with 10 m contours. The floor of the Acquarone channel shows mainly a low backscatter, with high backscatter only near a slide deposit (MTD) at the base of a scar on the flank of the Acquarone High. The lobate sea floor mound with high backscatter south of the Acquarone channel represents accumulation of slope-waste deposits derived from the Acquarone High. The Gioia channel floor shows patches of high backscatter, indicating recent activity. (Modified from Gamberi and Marani, 2008).

(Gamberi and Rovere, 2011), an uplifting area (1.1 mm/y) on the Peloritani Mountains (Catalano and Di Stefano, 1997; Antonioli et al., 2006). Evidence of the recent tectonic activity is given by the presence of fluid escape features (pockmarks) at the seafloor in connection with a transpressive fault (Rovere et al., 2014) (Figure 1A). An extensional fault crosses the base of the Acquarone high with a W-E direction in a sector highly affected by mass-wasting processes (Gamberi et al., 2019) (Figures 1A,B). The Acquarone fan develops southward from the Gioia-Mesima channel, a tributary to the Stromboli channel (Figure 1A). The Gioia-Mesima channel has undergone a complex evolution shown by abandoned meanders incised by a straight course due to base level deepening associated with the erosion and deepening of the Stromboli valley (Gamberi and Marani, 2008; Gamberi et al., 2019). The Acquarone Fan develops in the ENE-dipping slope and reaches a water depth of 1,000 m. The fan is fed by two submarine canyons (Figure 1B). The eastern canyon-head is at a depth of 90 m on the shelf edge and is 2.8 km off the coast; the western canyon head is at depth of 120 m and 5.3 km off the coast. On land, a small subaerial drainage basin of about 13 km² in the Paleozoic terrain of the Castanea ridge flanks the canyon head (Figure 1A). In these mountainous, tectonically active and uplifting catchments, rivers are incisional features with high gradient, torrential discharges and high sediment yield (Regione Siciliana, 2006). At present, the sediment load is ultimately deposited on the continental shelf where is interpreted to be resuspended by longshore currents and rearranged into an asymmetric compound delta (Figure 1B). The compound delta, in its apex position, is only 700 m from the shelf edge and is in front of the eastern canyon head.

3 INFLUENCE OF EXTERNAL FACTORS ON THE ACQUARONE FAN

Like the majority of submarine fans in tectonically active continental margins, the Acquarone Fan is a small turbiditic system: from the canyon head to the edge of the frontal splay it is 33 km long and is 8 km wide at the most. Its limited lateral extension is due to the topographic confinement caused by the Acquarone high to the south and the presence of the Gioia-Mesima canyon-channel system to the north.

3.1 Confinement by the Acquarone High

The Acquarone channel is bounded to the south by the Acquarone high, which stands out for about 900 m from the surrounding seafloor. The Acquarone high confines the proximal tract of the channel-levee system to its west preventing the construction of a levee in the left channel side down to a depth of 810 m (Figure 2). Moreover, the presence of the Acquarone high has “forced” the channel to develop a bend that steers the channel pathway from the N-S direction of its proximal sector to the NW-SE pathway of its distal sector (Figures 1B, 2). Further downslope, the confinement gradually decreases resulting in a partially confined area which extends until a water depth of 880 m, where the channel-levee system is no longer confined (Figure 2). The Acquarone high also controls the distribution of mass-transport deposits (MTDs), since, according to the seafloor reflectivity, recent collapses occurred on its flanks (Figure 2) (Gamberi and Marani, 2008). The recent MTDs are localized in the Acquarone channel thalweg, downslope from the meander, and on the surface of the left levee in the partially confined area (Figure 2).

3.2 The Proximity to the Gioia-Mesima Channel

The leveed Gioia-Mesima channel system limits the Acquarone Fan to the north and act as its base level (Figure 1A). Thus, the Acquarone Fan is an example of a transient fan, i.e. those fans that store part of the sediment but are connected to a deeper depositional area (Adeogba et al., 2005; Gamberi and Rovere, 2011). The distance between the Acquarone and the Gioia channels decreases downslope: the Gioia channel is 8 km far from the Acquarone channel bend and 3 km far from the Acquarone channel mouth (Figure 2). The interaction with other channels is one of the possible factors complicating thickness and sand distribution in external levees (Hansen et al., 2015). The Gioia-Mesima channel is principally characterized by erosional processes (Gamberi and Marani, 2008) as shown by an incision of about 80 m. Said incision is consistent with the erosional deepening of the Stromboli Slope Valley that lowered the base level of the Gioia-Mesima channel, which became strongly entrenched and straight (Figure 1A). Moreover, the overspilling clouds, flowing from east to west, preferentially deposit on the right-side of the Gioia-Mesima channel, and therefore the left overbank splay is exclusively alimented by the high-momentum spill-over process near a

sharp channel meander (**Figure 2**) located 7 km far from the Acquarone channel bend (Gamberi and Marani, 2008). The sediment starvation of the left overbank splay of the Gioia-Mesima channel is confirmed by its low backscatter compared to the channel floor (**Figure 2**). All these observations suggest that the proximity of the Gioia-Mesima channel does not represents a bias for the quantification of the sedimentary budget on the Acquarone overbank area.

4 DATA AND METHODS

Multibeam bathymetric data and high-resolution seismic data, imaging the Acquarone Fan in its whole length, represent our primary dataset. The major part of the study area is covered by a digital high-resolution terrain model. The latter consists of a mosaic of multibeam data acquired during two surveys carried out in 2013 and 2014 (CAT13 and MARBEEP14 respectively) on board the R/V *Urania* with the multi-beam system Kongsberg EM710 (frequency 70–100 kHz). In general, given the frequency of the multibeam instruments and the depth range of the study area, the bathymetric data have a vertical resolution less than 0.5 m. The acquired data cover depths between 300 and 1,300 m and has been merged with the EMODnet Project bathymetric data available for the shallower areas. High resolution subbottom data consists of Chirp profiles, acquired in 2013 with the Chirp Benthos III technology (frequency 2–7 kHz). Vertical resolution of the seismic profiles is in the order of 0.5 m. The Chirp sections, spaced at about 2 km, cut perpendicularly the Acquarone Fan, from the leveed channel to the fan fringe (**Figure 1B**). The penetration of the Chirp profiles depends on the type of sediment, being inversely proportional to sediment grain size and compaction.

The multibeam bathymetric data was imported and analysed using the Global Mapper® software for the production of contour and slope maps, channel and levee longitudinal profiles and cross-sections of the sediment waves. Sediment wave wavelength is calculated as the distance between two consecutive troughs, whereas wave heights as the distance from the wave crest to a straight line connecting two consecutive troughs (**Figure 3**). Following Symons et al. (2016), the cross-sectional shape of a sediment wave was defined as upslope asymmetric, when the downslope limbs are longer and shallower (**Figure 3**). Accordingly, when the downslope and upslope limbs are even, sediment waves are classified as symmetric (**Figure 3**). The principal overspilling flow direction is assumed perpendicular to the local orientation of the sediment wave crests (Normark et al., 2002). In particular, for crescentic forms the flow direction is assumed to be parallel to the principal plane of curvature of the bedform, whereas for sinuous bedforms the flow direction is assumed to be at 90° from the line connecting to two subsequent inflections in the crest of the sediment wave (**Figure 3**).

The Chirp profiles allowed us to recognize seven units (I–VII) in the last 40 m of the sedimentary succession (**Figure 3**). The boundary of the units correspond to high-amplitude reflectors, which can be followed throughout the study area. Each unit

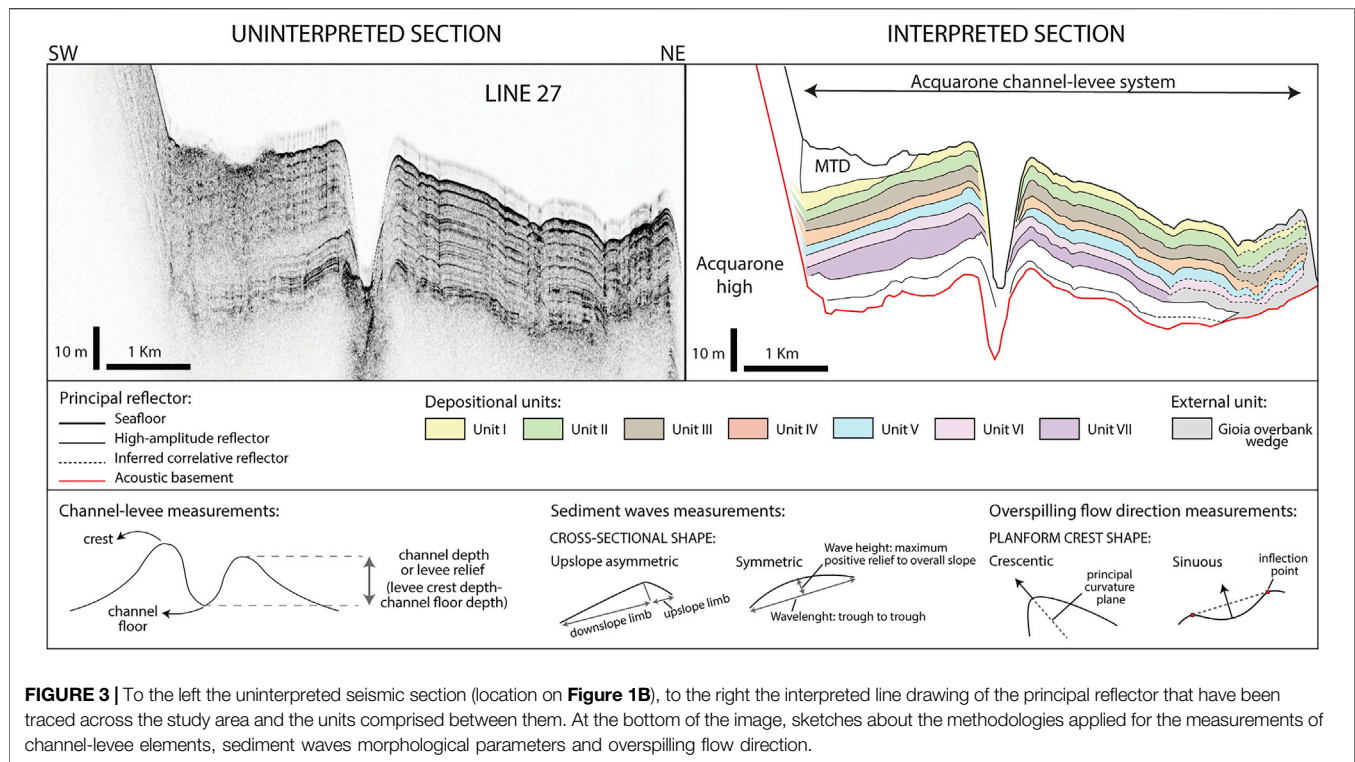
consists therefore of a coherent set of turbidites deposited, during a specific time interval, by successive flows in the different environments of the Acquarone Fan. As such, our units correspond with depositional packages deposited during discrete time interval and have a chronostratigraphic meaning. Owing to the correlatability of the units throughout the study area, spatial variations in sedimentary processes can be observed, through seismic facies and thickness analysis. In particular, the thickness distribution of the units is represented in isopach maps, which are useful to pinpoint and visualize the successive phases of construction of the Acquarone Fan. Moreover, based on the reflection character in the subbottom profiles, we defined five acoustic facies. The spatial-temporal changes in facies distribution, reconstructed from the comparison of the detailed facies maps of the seven units, are the key for interpreting sedimentary processes.

5 MORPHOLOGY OF THE ACQUARONE FAN

Based on interpretation of the multibeam bathymetric data, the morphology of the depositional environments of the fan will be presented.

5.1 Channel

The Acquarone leveed channel has formed at the slope base, at a water depth of about 750 m, at the junction of the two tributary canyons in the upper slope (channel initiation in **Figure 4A**). The two canyons are confined within a depression that cuts the slope of the Acquarone High. The Acquarone channel exits the depression confinement and makes a wide westward turn taking up a NW course, perpendicular to the slope gradient. The channel has an average gradient of about 1°, but it displays several variations in gradient as shown by its long profile in **Figure 4B**. Also the channel depth, calculated as the relief of the levee crest with respect to the channel floor for each levee (**Figure 3**) shows large variations (the red line refers to the right levee and the light blue line to the left levee in **Figure 4B**). The deepest tract of the channel is in its confined part, where, in the bend, the channel depth increases reaching its maximum of almost 60 m (**Section 1** in **Figure 4B**). The channel profile in the confined tract is affected by a recent MTD, whose topographic effect causes a drastic reduction in the channel height (**Section 2** in **Figure 4B**). At the beginning of the partially confined area, the channel depth gradually decreases to 30 m (**Section 3** in **Figure 4B**). The central tract of the channel profile has two knick-points, named KP1 and KP2, that are, respectively, 7 and 11 m high (**Figure 4B**). At KP1 the channel gradient halves abruptly, while the gradient difference in KP2 is less sharp (**Figure 4C**). Along the flat segments of the knick-points the channel depth increases (**Sections 4–5** in **Figures 4B,C**). Knick-point initiation has been linked to different processes: channel avulsion (Deptuck et al., 2007), bend cutoff (Sylvester and Covault, 2016), internally generated within channels (Heijnen et al., 2020) or tectonics (Heiniö and Davies, 2007). In the Acquarone channel there is no evidence of channel avulsion



and knick-points are located far from the bend. Also the internally generated origin has been excluded since it have been recognized in a prevalently erosional channel where turbidity currents originate knick-point far higher (about 20 m) and steeper (10° – 30°) than the knick-points in the Acquarone channel (Heijnen et al., 2020). Accordingly with the interpretation of Gamberi et al. (2019), the origin of the knick-points in the Acquarone channel can most likely be ascribed to the tectonic framework. This thesis is supported by KP1 which represent the prosecution of an extensive fault that cross the base of the Acquarone High (**Figure 4A**). Moreover, the alternation of ramp and flat segments related to the channel profile is in phase with the gradient variation in the levee crest profiles (**Figure 4C**). This configuration shows that the topographic displacement is not localized in the knick-points, but it is laterally continuous and, therefore, conceivably connected to allogenic, tectonic processes.

5.2 External Levees

The right and left levees are very different in terms of their extension, relief and distribution of sediment waves. The left levee is 6 km long, it begins at a depth of 800 m, downslope from the Acquarone ridge slope and terminates at a depth of 950 m (**Figure 4A**). On the contrary, the right levee bounds the channel for its whole length, i.e. 14 km (**Figure 4A**). In its proximal tract, the left levee is about 15 m higher than the right one (**Figure 4B**). The difference between the relief of the two levees decreases downslope and, at the end of the confined tract, at a depth of 900 m, the two levees have the same height ($H_{dx} = H_{sx}$, in **Figure 4**). Beyond this point, the left levee has a lower relief than the right one (**Figure 4B**).

Extensive sediment wave fields develop in specific tracts of the right levee (**Figure 5**). According to the classification of Symons et al. (2016), based on wavelength and amplitude, they fall into the group of small-scale sediment waves (<300 m wavelength and <8 m wave height) but, at the small scale, the sediment waves have different dimensions and cross-sectional shapes resulting in highly different morphologies. They have been subdivided into different sediment wave fields, according to their wavelength, wave height and spreading direction, occupying different areas (**Figures 5A,B**): A) *Bend area*: the outer side of the bend on the right levee; B) *Laterally confined area*: a lobe-shaped area on the right-levee; C) *Knick-points area*: a triangular shaped area with upslope apex on the levee crest laterally to KP1 and termination at the end of the channel.

The *Bend area* presents sediment waves spreading out from the outer side of the bend (**Figure 5A**). The crests are parallel to the bend suggesting that they were formed by the spreading of high-momentum spillover flows. In cross-section, they are upslope asymmetric, with amplitude and wavelength that reach a maximum of 3 and 300 m respectively; they become symmetrical, smaller and more closely spaced downslope, suggesting a rapid loss of momentum (Profile A-A', **Figure 5B**). Moreover, the seismic line 33, that cross perpendicularly part of the bedforms, highlights that the sediment waves in the *Bend area* show an initial slow up-slope migration followed by a more aggradational phase, with almost no change in trough and crest position (Profile A-A', **Figure 5B**).

Further downslope, in the *Laterally confined area*, the second sediment wave train develops on the right levee (**Figure 5A**). The trend of the sediment waves crests indicates that, initially, the overbanking flows are parallel to the course of the channel, but they rapidly become orthogonal to the channel trend and follow

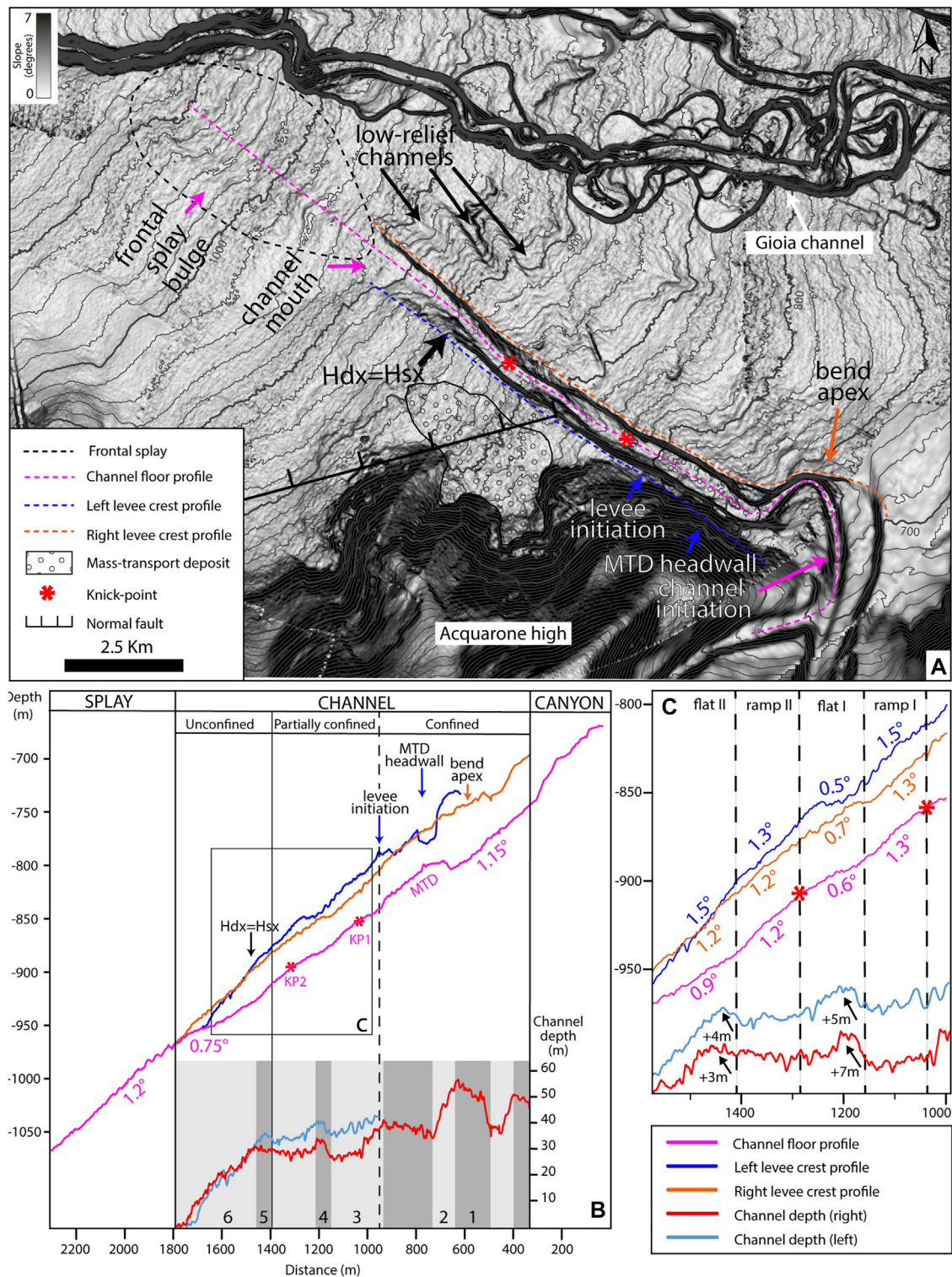


FIGURE 4 | (A) Shaded relief map in BW colours that highlights the principal morphological features of the seafloor marked by arrows. **(B)** Acquarone channel talweg (pink), right levee (orange) and left levee (blue) longitudinal depth profiles. At the bottom, the channel relief referred to the right levee (red) and to the left levee (light blue), the dark grey sections mark where the channel depth tends to increase, while in light grey where it tends to decrease. **(C)** Zoom of the channel depth and longitudinal profiles in the central sector of the channel with the related slope values.

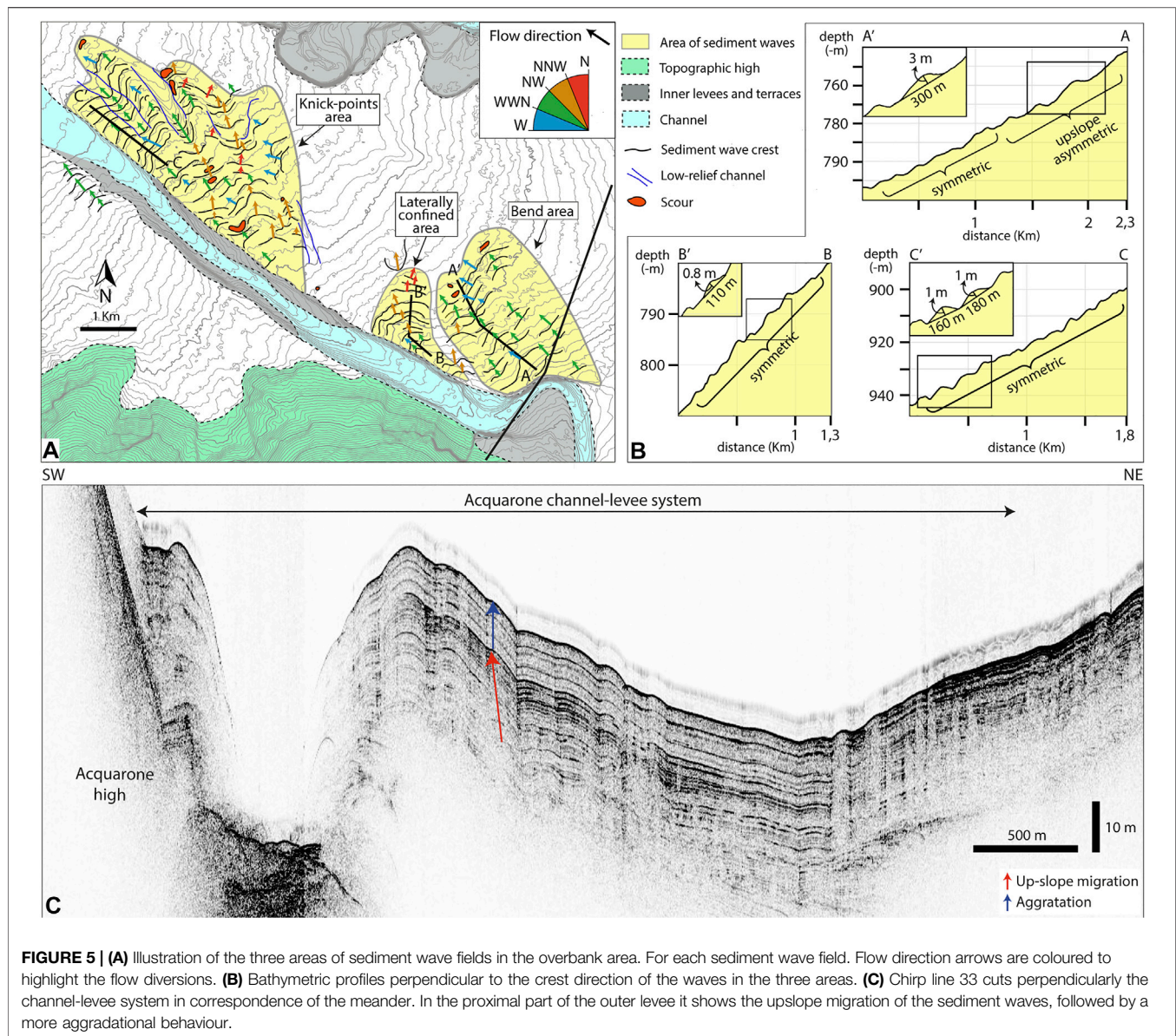


FIGURE 5 | (A) Illustration of the three areas of sediment wave fields in the overbank area. For each sediment wave field, flow direction arrows are coloured to highlight the flow diversions. **(B)** Bathymetric profiles perpendicular to the crest direction of the waves in the three areas. **(C)** Chirp line 33 cuts perpendicularly the channel-levee system in correspondence of the meander. In the proximal part of the outer levee it shows the upslope migration of the sediment waves, followed by a more aggradational behaviour.

the slope direction. They have a symmetrical profile and very low relief with an average wave height of 0.9 m and a wavelength of 140 m (Profile B-B', **Figure 5B**).

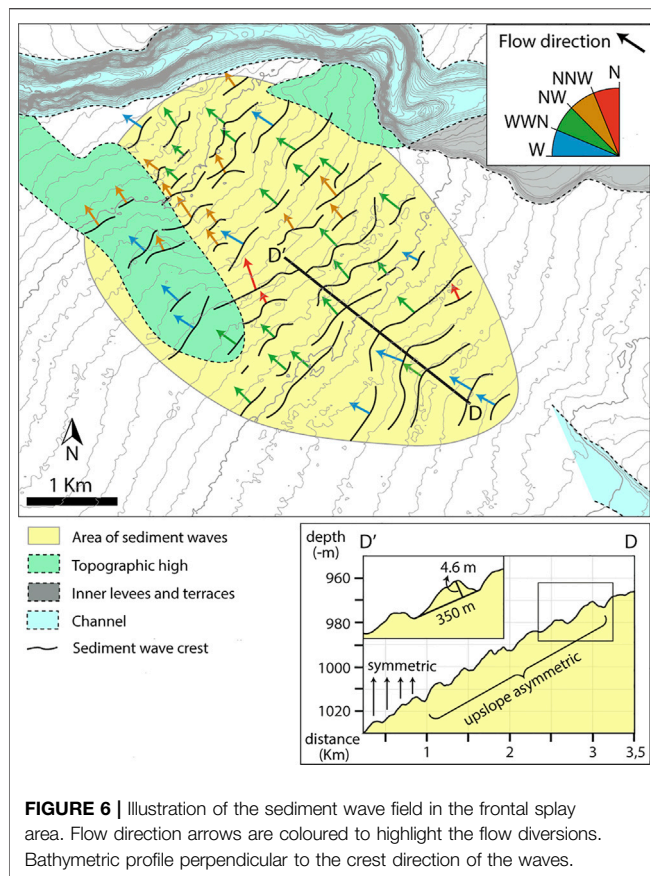
In the *Knick-points area*, the third train of sediment waves trends subparallel/oblique to the channel axis (**Figure 5A**). The waves have a symmetrical cross-section and are regularly spaced with wavelength of 150 m, while their amplitude increases downslope from 0.5 m to a maximum of 2 m (Profile C-C', **Figure 5B**). The crests have a sinuous planform; within a bedform row, the landward convex part of single bedforms are in phase and appear to form low-relief, 2–3 km-long channels, with NW-SE direction (**Figure 4A**).

5.3 Frontal splay

The Acquarone channel dies out in the lower slope forming a frontal splay that has a NW-SE-trending main elongation axis and stretches the

slope with a width of 5 km. It has an area of about 28 km² and laterally and distally passes to a fan fringe area, which occupies most of the remaining slope. The frontal splay has its apex at a depth of 950 m, at the distal end of the channel left levee, and terminates at a depth of 1,070 m where the southern flank of the Gioia-Mesima channel is (**Figure 4A**). The apex of the fan is where the slope gradient increases, from 0.75° in the distal tract of the channel, to 1.20° (**Figure 4B**). Just beyond the channel mouth, the frontal splay has a convex cross-section (**Figure 4A**). Further downslope, the fan has a central bulge flanked by two slightly depressed areas (frontal splay bulge in **Figure 4A**).

Another sediment wave field occupies the *Frontal splay area*, a lobate area that occupies the whole surface of the frontal splay (**Figure 6**). In the *Frontal splay area* the sediment waves have an upslope asymmetric cross-section shape with wavelength of about 300 m and maximum height of 4, 6 m, which decreases moving away from the channel mouth (Profile D-D', **Figure 6**).



The wave crests have a general NE-SW orientation, and they are aligned roughly parallel with the main flow pathway. The crest directions are not perfectly parallel with each other showing a deflection in their orientation, highlighted by the coloured arrows in **Figure 6**.

6 STRATIGRAPHY

The interpretation of the subbottom Chirp profiles allowed the recognition of five acoustic facies whose characteristics will be described in the following paragraph. A seismic characterization based on the distribution of the acoustic facies and their lithology interpretation is reported in the second paragraph of this chapter for each depositional environments.

6.1 Acoustic Facies

Taking into account the presence or absence of reflections, the relative amplitude of reflections, the geometry of reflectors (parallel, irregular, etc.), five different acoustic facies have been distinguished. A brief description of the acoustic facies, comprehensive of their interpretation in terms of their most likely lithology and depositional environment, is reported in **Table 1**. The first word of the acoustic facies name describe, when the reflection are present, their geometry (parallel or irregular) while, when the reflections are absent, is

labelled as transparent; the second word describe the strength of the acoustic reflection (high or low):

Transparent Low-reflectivity (TL): Intervals lacking coherent reflectors with faint reflectivity.

Parallel Low-reflectivity (PL) Parallel to subparallel, continuous to discontinuous, low-amplitude and high-frequency reflections.

Parallel High-reflectivity (PH) Parallel to subparallel, continuous to discontinuous, high-amplitude reflections and high-frequency reflections.

Irregular High-reflectivity (IH) Irregular, discontinuous, variably spaced, high-amplitude reflections.

Transparent High-reflectivity (TH) Intervals lacking coherent reflectors but highly reflective, commonly reducing the penetration of acoustic energy.

6.2 Seismic Characterization of the Slope Elements

6.2.1 Overbank Wedge and Channel Fill

At a large scale, subsurface imaging reveals the typical components of channel-levee systems, with channel floor deposits and overbank wedges. The most part of the channel axis has a transparent, highly-reflective facies, suggestive of coarse-grained channel fill deposits (**Figures 7, 8**). The only exception occurs at the channel mouth where the coarse-grained sediments of the channel-axis infill are buried under a homogeneous fine-grained deposit (TL) (**Figure 8C**).

The overbank deposits consist of a thick sedimentary wedge that tapers laterally and longitudinally. The left overbank wedge consists of relatively fine-grained sediments (TL) (**Figure 8**). At the base of the Acquarone high slope, a recent MTD can be recognized thanks to the rough seabed in the channel floor; according to its transparent, faintly reflective facies, it consists of a fine-grained MTD (**Figures 8A,B**).

In the right levee, the overbank deposits show a less homogeneous character, with varied acoustic facies. In the *Bend area* (**Figure 7A**), most of the units (I, II, III, VI and VII) are composed principally of well stratified fine-grained sediments (PL), while Units IV and V have a major coarse-grained component (PH). In the *Laterally confined area* (**Figure 7B**), there is a prevalence of well stratified fine-grained deposition (PL). At the end of the confined tract, in the *Knick-points area*, the left overbank deposits are composed by homogeneous fine-grained sediments (TL), while the right overbank by well-stratified fine-grained sediments (PL) (**Figures 8A,B**).

6.2.2 Frontal splay and Fan Fringe

The seven seismic units recognized in the overbank wedges extend downslope, in the frontal splay and fan fringe elements. The frontal splay and the fan fringe are composed of different acoustic facies that vary longitudinally and laterally. The first 8 m (Units I, II, and III) of the *Frontal splay area* consist of relatively homogeneous fine-grained sediments (TL) (**Figure 9**). This low-amplitude package drapes more reflective deposits interpreted to be composed of relatively coarse-grained sediments (TH) of Units IV and V (**Figure 9A**). Their high reflectivity strongly attenuates the acoustic signal, making

TABLE 1 | Seismic facies recognized in the Acquarone Fan.

Seismic facies	Brief description	Lithology interpretation	Depositional environment	Figure
TL	Transparent, faintly reflective	Relatively homogeneous fine-grained sediments	Left overbank, Frontal splay and Fan fringe	Figures 8, 9
PL	Parallel, low-amplitude reflections	Well stratified fine-grained sediments	Confined and partially confined right overbank—Fan fringe	Figures 7–9
PH	Parallel, high-amplitude reflections	Well stratified coarser (respect to PL)-grained sediments	Confined overbank—Inner levee	Figures 7A, 8C
IH	Irregular, discontinuous, high-amplitude reflection	Laterally discontinuous coarse-grained sediments	Frontal splay	Figure 9C
TH	Transparent, highly reflective	Relatively homogeneous coarse-grained sediments	Frontal splay, Channel fill	Figures 7–9

the recognition of the deeper units uncertain, which are thus characterized only on the basis of some minor reflections. In the fan fringe, the downslope continuation of Units IV, V, and VII present irregular high-amplitude reflectors interpreted as laterally discontinuous coarse-grained sediments, laterally the reflectors have a parallel configuration and slightly decrease in amplitude (PL) highlighting better organization and an increase in the fine content (**Figure 9C**).

7 PATTERN OF SEDIMENT DISTRIBUTION

The isopach maps of the seven units show the sediment distribution within the entire turbidite system (**Figure 10**). Each unit is characterized by a distinctive distribution of sediments, thus pointing to highly spatial variability of overspilling flow behaviour over time. In particular, the depocenters location and their seismic response are indicative of two main patterns of deposition in the Acquarone Fan. Each unit displays one of the two depositional patterns, named Case I and Case II.

Case I depositional pattern has three depocenters, in the *Bend area*, *Knick-points area* and *Frontal splay area*. This pattern is displayed by Units IV and VII and by Unit V, which, has a depocenter also in the *Laterally confined area* (**Figure 10A**). The depocenter in the *Bend area* has thicker values near the levee crest, where sediment waves are better developed and are upslope asymmetric (**Figure 5B**). The depocenter in the *Knick-points area* starts laterally to the flat sector downslope from KP1. The depocenter in the *Frontal splay area* has a convex shape, with maximum accumulation along the axis, where the sediment waves develop (**Figure 6**), and decreasing thickness laterally and downslope. In the *Frontal splay area* units IV and V are composed of homogeneous/laterally discontinuous coarse-grained sediments.

Case II depositional pattern is displayed by Units I, II, III, and VI (**Figure 10B**). The second pattern of deposition is characterized by thickness mostly constant on the overbank, with only slightly increasing values in the *Bend area*, and a slight decrease in the frontal splay. Units II and III also present a depocenter in the *Laterally confined area* with maximum values near the levee crest (**Figure 10B**). At the end of the channel, the units are homogeneously distributed on the slope with a slightly thicker accumulation in the fan fringe than in

the frontal splay. Case II units, in the *Frontal splay area*, show a homogeneous fine-grained composition.

Moreover, the thickness maps show that, concomitantly with the deposition of Units I, III, IV, and VII the Acquarone high was affected by multiple landslides, finally deposited on the left overbank. The recurrence of MTD deposits in the same position in different time intervals highlight the reactivation of the landslide headwall resulting in its retrogression (**Figure 10**).

8 INTERPRETATION

8.1 The Acquarone Channel-Levee: An Atypical Overbank Pattern in the Northern Hemisphere

Generally, in the northern hemisphere, the Coriolis force causes more sediment overspill in the right levees, which, therefore, are often higher than the left ones (Mutti and Normark, 1987; Abd El-Gawad et al., 2012; Wells and Cossu, 2013). On the contrary, in the Acquarone channel-levee system, the left levee is in general higher than the right one (**Figure 4B**). At the beginning of the partially confined area, this difference in relief is partly due to the structural setting, since the left levee grows on a more elevated terrain than the right levee, as highlighted by the relief of the acoustic basement in Line 29 (**Figure 8A**). Downslope, however, the acoustic basement reveals that the difference in relief is due to the greater aggradation of the left levee, since both the levees had initially the same height (**Figure 8B**). The left levee relief started to overcome that of the right one from the deposition of Unit VII. The isopach map shows that Unit VII presents an elongate depocenter on the left overbank running parallel to the levee crest (**Figure 10A**). It has been interpreted that part of this body is composed by an MTD coming from the retrogressive scarp located on the Acquarone high. **Figure 8B** shows that the volume of the MTD on the left overbank area, enhanced the left levee to overcome the relief of the right one, inverting the characteristic asymmetry of the channel-levee system of the northern hemisphere.

The most important parameters controlling overbank composition are vertical distribution of different grain-sizes in

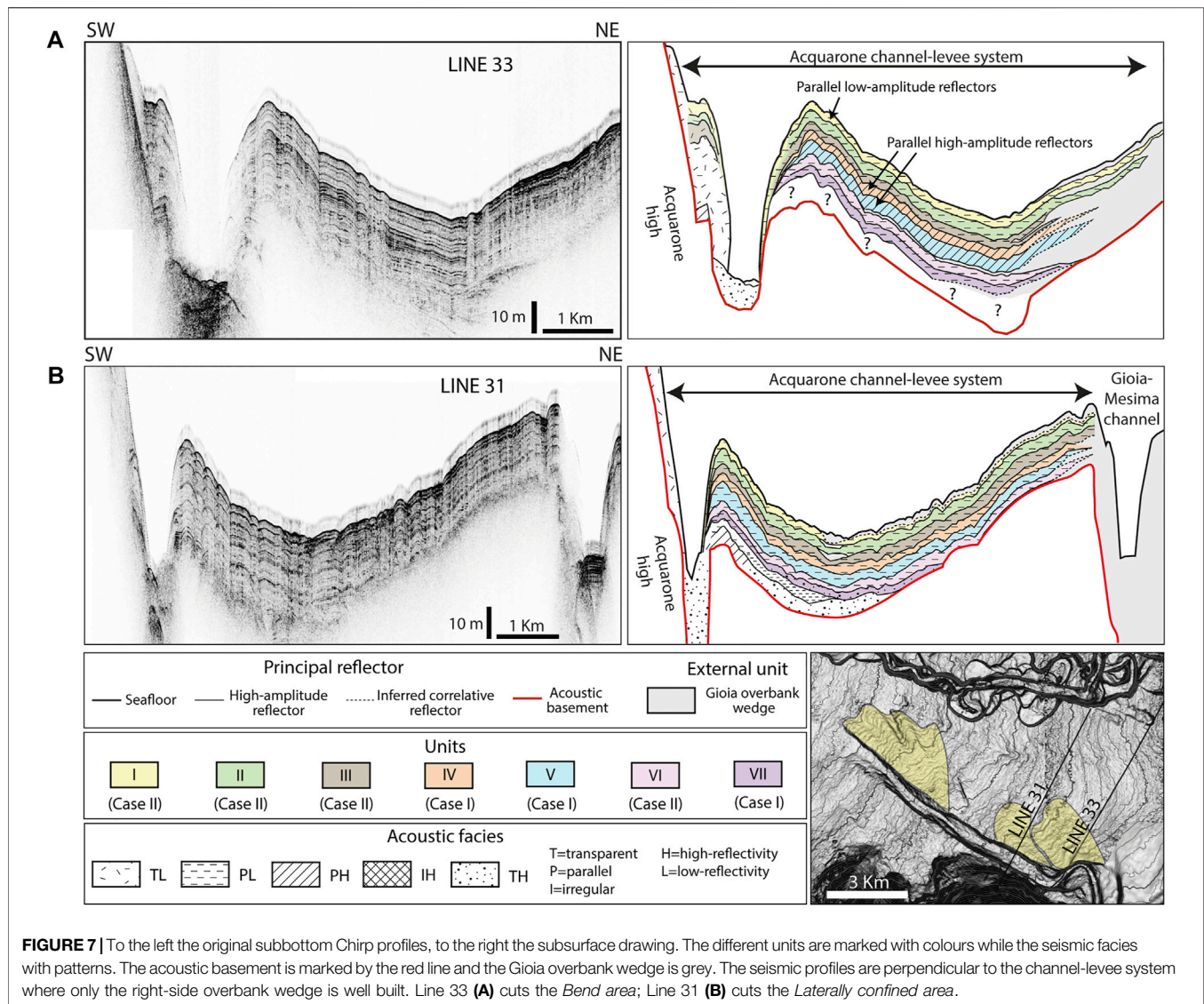


FIGURE 7 | To the left the original subbottom Chirp profiles, to the right the subsurface drawing. The different units are marked with colours while the seismic facies with patterns. The acoustic basement is marked by the red line and the Gioia overbank wedge is grey. The seismic profiles are perpendicular to the channel-levee system where only the right-side overbank wedge is well built. Line 33 **(A)** cuts the *Bend area*; Line 31 **(B)** cuts the *Laterally confined area*.

relation to the height of the levee (Straub and Mohrig, 2008; Hansen et al., 2015; Jobe et al., 2017). In fact, the relief of the levees, depending on the vertical grain-size, will control the partitioning of different grain-sizes between the in-channel flow and deposits on the levee, directly influencing the composition of the overbank wedges (Pirmez et al., 1997; Peakall et al., 2000; Pirmez and Imran, 2003).

Before the MTD deposition, the difference in relief between the right and left levee appears to have been negligible as they show the same seismic response on each side (Figures 8A,B). In this case, the same grain-sizes reached the right and left levee crest (Figure 11). However, after the deposition of the MTD, the two overbank wedges of the Acquarone fan show markedly different seismic responses. The right overbank is principally characterized by parallel low-amplitude reflector indicative of a relatively well stratified fine-grained sediment, whereas, in the left overbank wedge, the absence of any internal structure and faintly reflective seismic facies could

be indicative of homogeneous and structureless fine-grained deposition (Figures 8A,B).

Our case study shows that, the geologically-instantaneous emplacement occurrence of an MTD on the left overbank asymmetrically increased the levee relief and so the confinement of the flow towards the side interested by the failure. The stratification of the flow combined with the increase in confinement, led to the preferential overspill of coarser grain-sizes on the less elevated overbank, producing stratified deposits with sand beds (Figure 11). Instead, only fine grain-sizes, are able to reach the surface of the higher levee, creating homogenous mud-dominated deposits (Figure 11). This process led to drastic change in the resulting overbank composition that can have important consequences on facies prediction: the proximity with a structural high can originate overbank deposit with higher sand % respect to the opposite wedge where finer deposition can occur and interrupt the lateral continuity of sand beds.

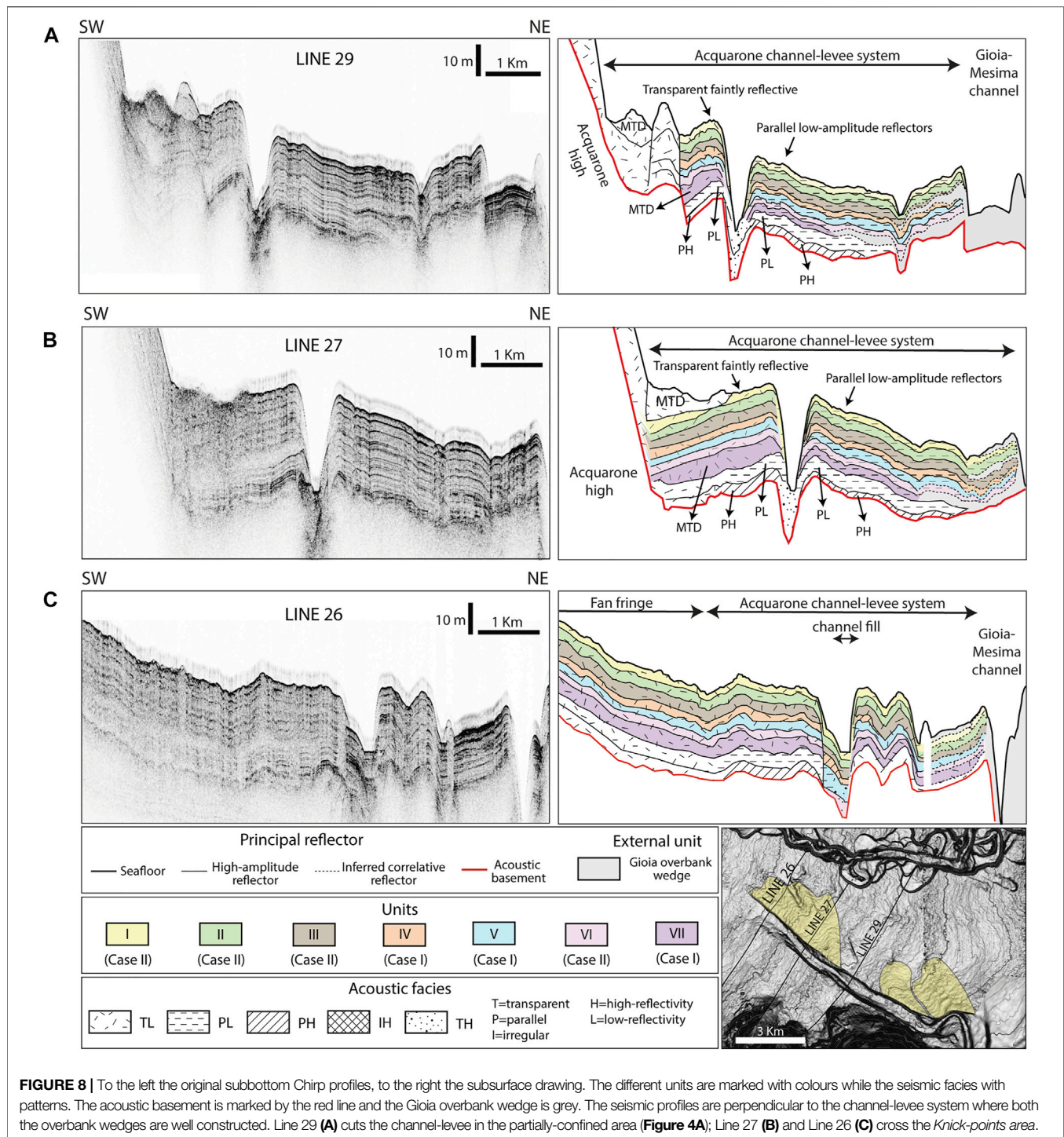
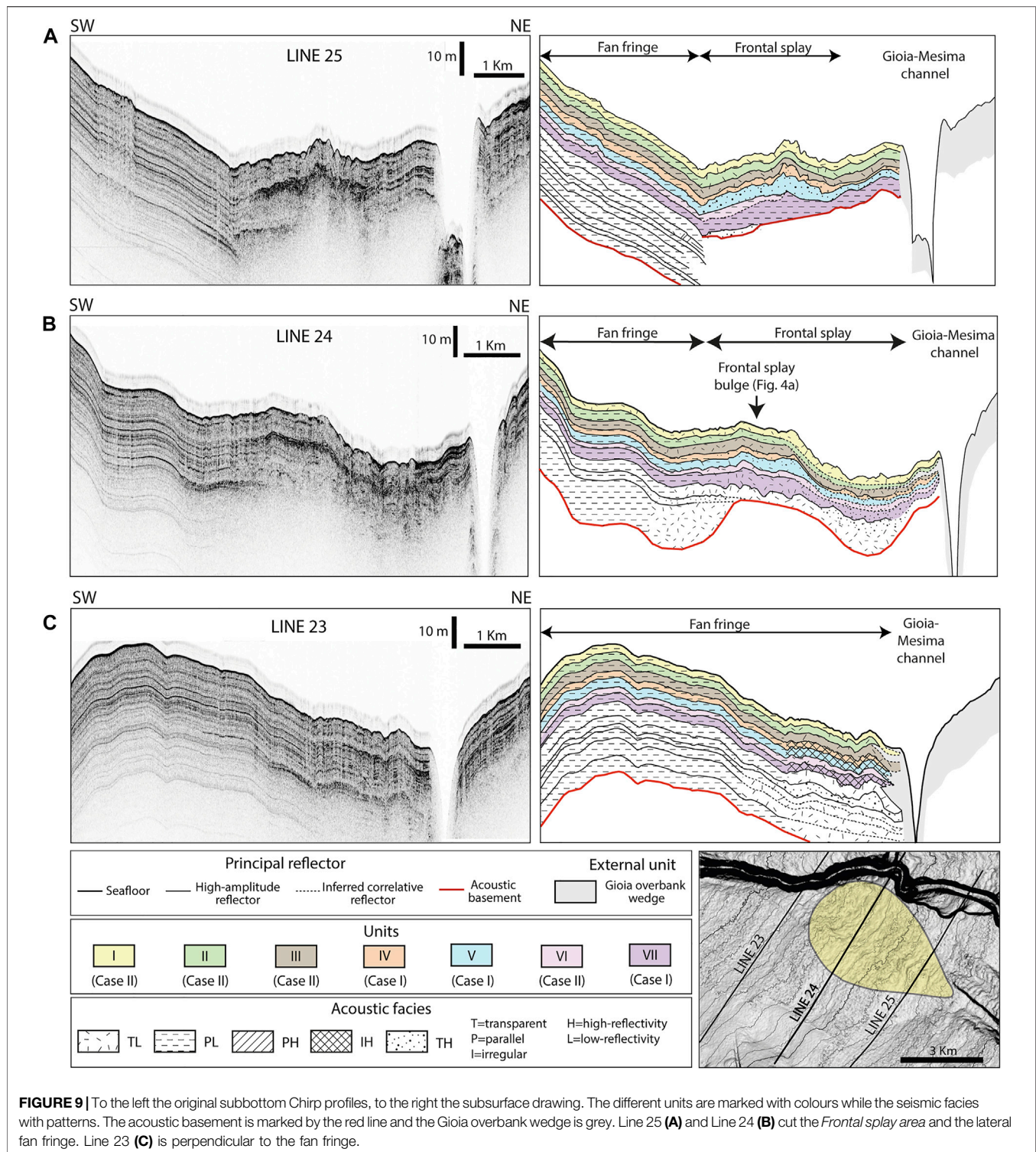


FIGURE 8 | To the left the original subbottom Chirp profiles, to the right the subsurface drawing. The different units are marked with colours while the seismic facies with patterns. The acoustic basement is marked by the red line and the Gioia overbank wedge is grey. The seismic profiles are perpendicular to the channel-levee system where both the overbank wedges are well constructed. Line 29 (A) cuts the channel-levee in the partially-confined area (Figure 4A); Line 27 (B) and Line 26 (C) cross the Knick-points area.

We conclude that the occurrence of collapses from the Acquarone high and landslide deposition on the left levee caused significant differences in the levee topography and, consequently, in the composition of the overbank wedges. Therefore, the Acquarone fan sheds light on a mechanism, i.e. slope failure, whereby channel-levee systems in topographically complex areas deviate from the characteristic asymmetry connected to the action of the Coriolis force.

8.2 Two Types of Flows

The two pattern of sediment distribution (Case I and II) and their seismic response, suggest that two types of flows, with distinct dynamics, are responsible for the different distributions of the seven depositional units in the study area. Of the many parameters that characterize turbidity currents, flow density is fundamental in controlling their depositional pattern (Lowe, 1982). We have thus explored



the possibility that flows with an initial different density and internal structure may interact differently with the seafloor topography, exploiting distinct overbank points along the channel and following different flow paths in the overbank and frontal splay areas. We follow the definition of the flow type in the classification by Lowe (1982), which distinguishes

high and low-density turbidity current depending on their dominant grain-size population.

Low density turbidity currents consist largely of clay, silt and fine-to about medium-grained sand-size particles that can be maintained in the flow by turbulence alone. Conversely, high-density turbidity currents can include particles coarser than about

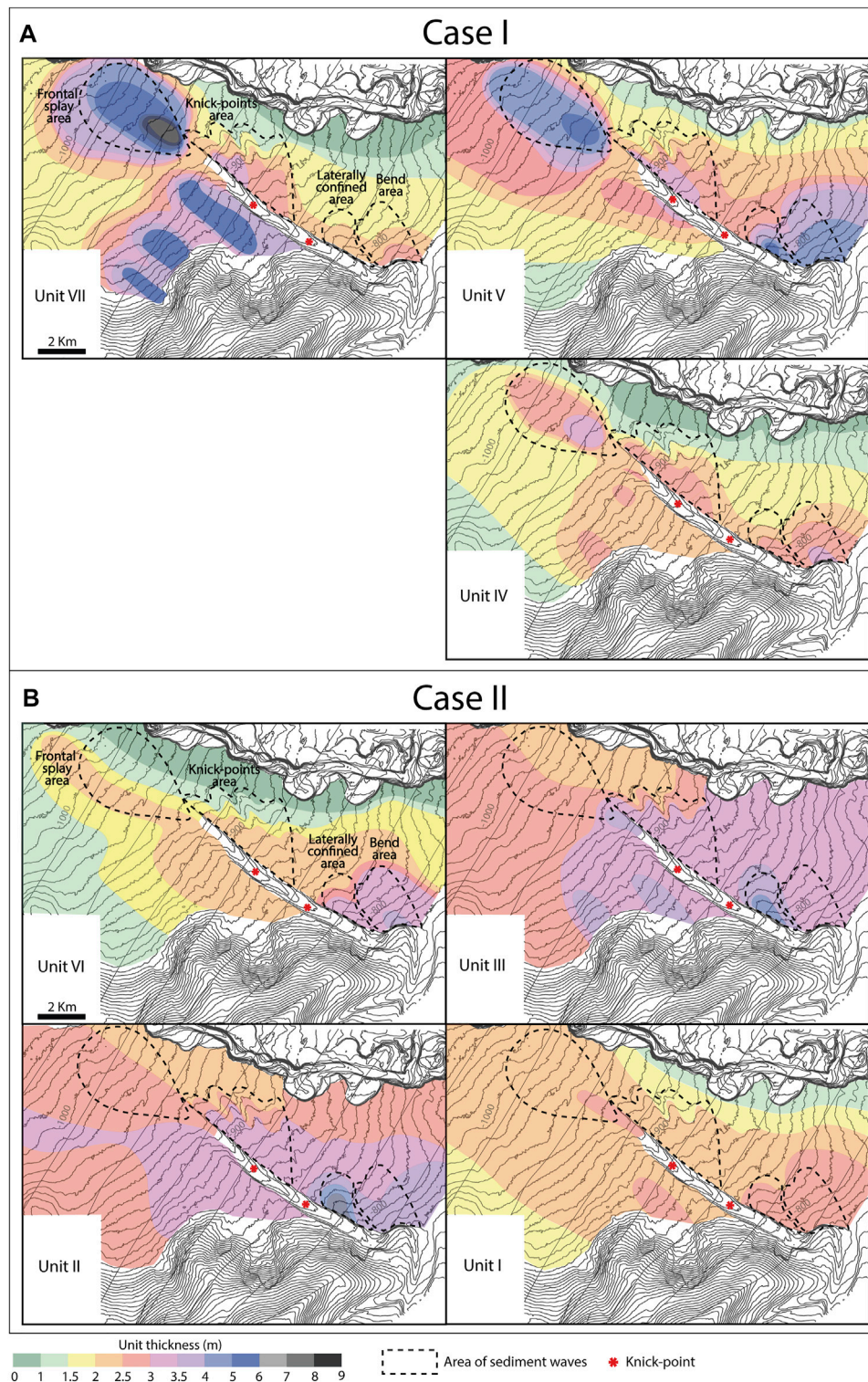
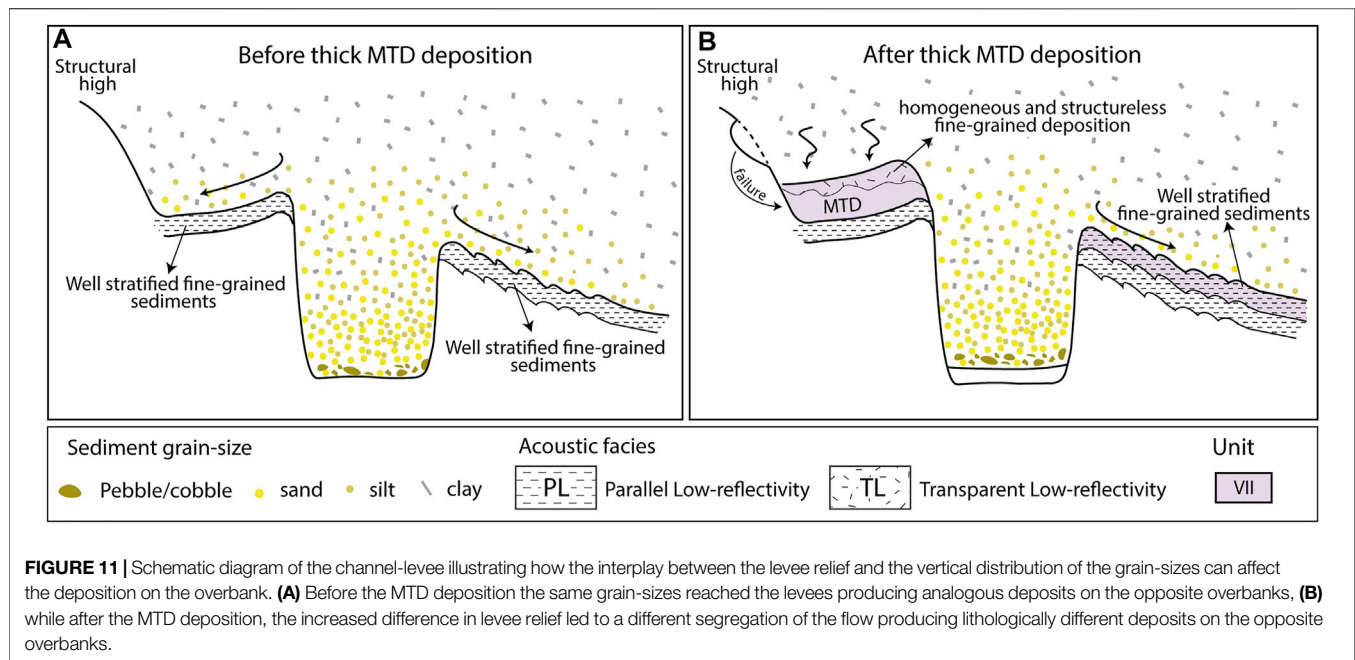


FIGURE 10 | Thickness maps of the seven (VII-I) units in the Acquarone Fan. The units have been grouped in Case I (Unit VII, V and IV) and Case II (VI, III, II, and I) since they present two different sediment distribution patterns. **(A)** Case I units have depocenters in the *Bend area*, *Knick-points area* and *Frontal splay area* (only Unit V has thick accumulation also in the *Laterally confined area*). **(B)** Case II units show more homogeneous sediment distribution on the overbank, with the exception of Units II and III that have a depocenter in the *Laterally confined area*, and slightly thin in the frontal splay.



medium-grained sand, which are supported by different mechanisms dependent on concentration effects. We have also taken into account that, in many cases, turbidite flows are bipartite, with a coarser-grained basal part behaving as high-density turbidity current and a finer-grained top behaving like a low-density one (Lowe, 1982; Mutti et al., 2003; Tinterri et al., 2003).

As summarized in **Figure 12**, in the study area, in Case I (**Figure 12A**) the bulk of sediments are deposited in the frontal splay with a transparent high-reflectivity acoustic facies indicative of prevalently coarse-grained sediment and producing a positive topography, which we interpret as resulting from high-density turbidity currents. On the contrary, in Case II (**Figure 12B**) a transparent low-reflectivity acoustic facies prevail and indicate a mud prone frontal splay, associated very likely with low-density turbidity currents even if the presence of mud-rich hybrid beds (*sensu* Haughton et al., 2009) cannot be completely ruled out.

The reason for privileging the interpretation linked to low density turbidity currents lies in the fact that, theoretically, the difference in acoustic impedance between the lithological internal divisions of hybrid beds should produce a reflection in the seismic profile whereas the frontal splay of the study area is characterized by transparent acoustic facies. Furthermore, the increase of the slope gradient downcurrent to the channel mouth (**Figure 4A**) would enhance the bypass of hybrid flows away from the frontal splay area rather than their deposition. Indeed, hybrid beds, deposited by transitional flows where the cohesive forces prevail over turbulence, tend to be more common into lateral and distal lobe fringes and basin plains and, more in general, where reduction in seafloor gradient favors flow deceleration and deposition (Haughton et al., 2009; Tinterri and Muzzi Magalhaes, 2011; Talling, 2013; Kane et al., 2016).

Our reconstruction show that the two types of flow behaviour characterize specific time intervals and alternate during the construction of the overbank wedge through the deposition from unit VII to I.

8.3 Flow Type and Sedimentation Pattern

8.3.1 Bend area

Bends are crucial morphological elements that affect sediment distribution in the channel and overbank areas. In this case study, the origin of the bend is connected to the presence of the Acquarone high that deviates the channel pathway from a N-S to a NW-SE direction. The lateral confinement imposed by the Acquarone high led to a large amount of sediment discharge outside the bend on the eastern right levee (**Figure 10**).

The backsclopes of channel levees are in general thought as sites of fine-grained turbidity currents and of predominantly mud and silt deposition (Mutti and Normark, 1987; Normark et al., 2002; Wynn and Stow, 2002; Hansen et al., 2015). In a current able to transport various grain sizes, the coarse sediment fraction is concentrated near the base of the current, while finer sediment fractions are more homogeneously distributed over the height of the current (Kneller and Buckee, 2000) (**Figure 13**). Progressive levee construction increases flow confinement and, accordingly, causes reduction in the grain-size of the sediment that can overspill the channel. As a consequence, an overall fining-upward trend generally characterizes the overbank sequence (Hansen et al., 2015).

On the outer side of the bend of the Acquarone channel, despite the high relief of the levee crest (about 60 m), Units IV and V (Case I) are characterized by a high-reflectivity interpreted as deposits with a percentage of coarse-grained sediments (**Figure 7A**). There is a drastic change of facies between Unit

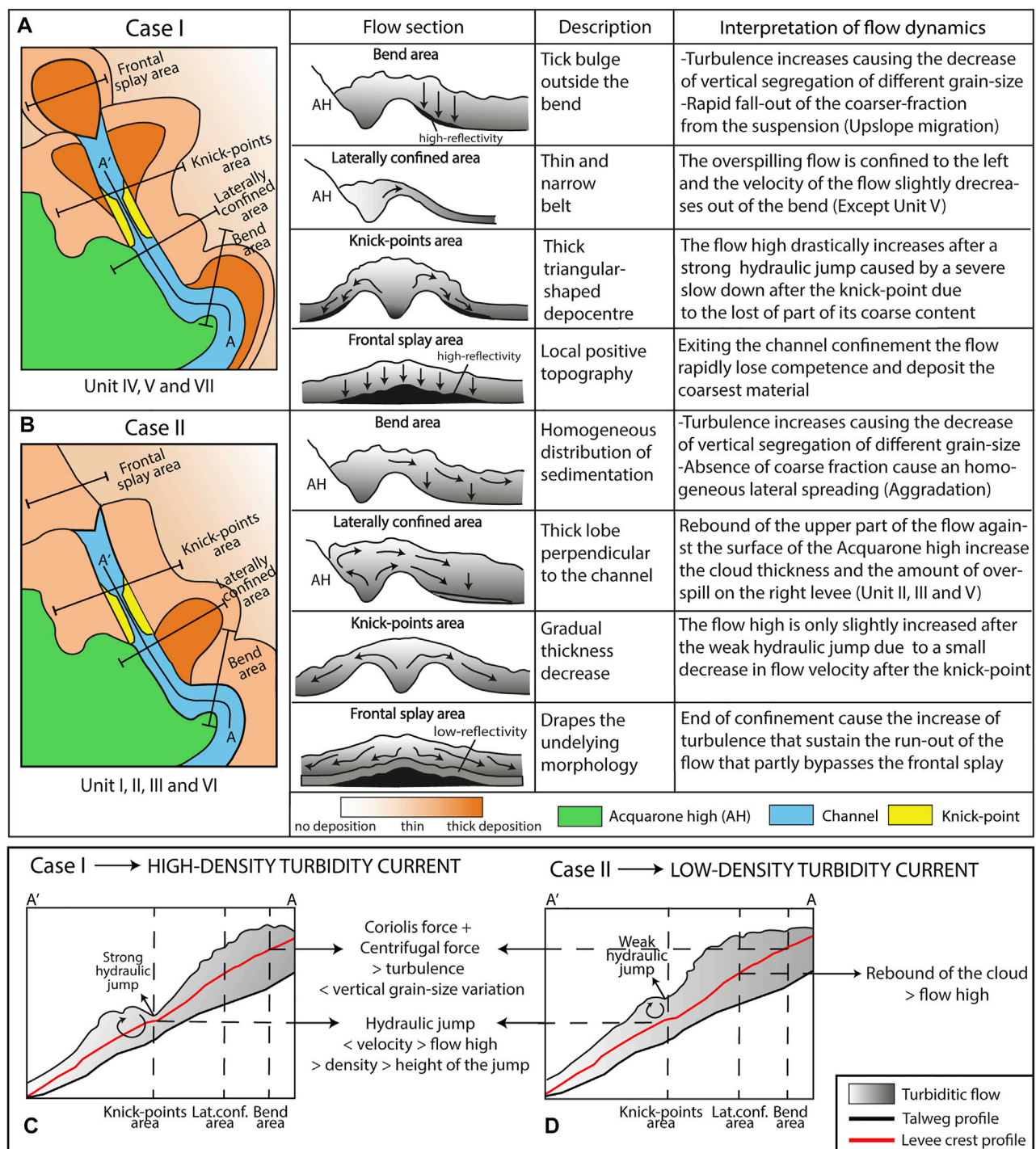


FIGURE 12 | Summary sketch of the two patterns of overbank sediment distribution, Cases I (A) and II (B) and schematic cross-sections of the flow highlighting the relevant flow dynamics. Below, the longitudinal variation in flow thickness, for Cases I (C) and II (D) and inferred variations in flow properties connected to the dynamics of the hydraulic jumps around the knick-points.

IV and the overlying units belonging to Case II consisting in 8.5 m of relatively fine-grained deposit, as inferred from the low acoustic reflectivity (Figure 7A). The passage between PH and PL facies is sharp and abrupt, indicating that a sudden change in the

properties of the flows occurred after the deposition of Unit IV. According to Baas et al. (2005), highly-turbulent flows keep the coarser particles more easily in suspension, owing to an upward directed component of turbulent velocity that overcomes the

falling velocity of most particle sizes. This effect would eventually cause a decrease in the vertical segregation of the different grain-sizes compared to flows with weaker turbulence. In the study area, the high gradient of the confined tract (1.15° , **Figure 4B**) and the centrifugal force at the bend are consistent with an increase in the flow velocity, which can develop high turbulence. So, we suggest that, in Case I, whose parent flows have a high percentage of sand fraction, the increased turbulence enhanced the coarser fraction to reach the upper part of the flows and overspill. Therefore, the overbank deposit created by high-density turbidity currents has a higher sand to mud ratio than the product of low-density turbidity currents, which does not account for a significant coarse-grained fraction to be transported over the levee crest (**Figure 13B**).

Sediment waves in the *Bend area*, in their early phase (Case I), are associated with parallel reflector with a high-reflectivity and have slow rates of up-current migration (**Figure 5C, 13A**). Anyway, later (Case II), the migration rate diminishes, the seismic response becomes less reflective and pure aggradational growth prevails (**Figure 5C, 13B**). Generally, up-current migrating sediment waves are associated with thicker and more abundant sand beds on their stoss side (Normark et al., 2002; Kostic, 2014). This general observation is consistent with a higher sand content in the overflow connected to Case I, further substantiating that they can be associated with high-density turbidity currents.

8.3.2 Laterally confined Area

Generally, in a leveed-channel system, the upper part of turbidity currents continuously over-spills onto the overbank area and the flows within the channel are progressively depleted of fine-grained material (Peakall et al., 2000; Hansen et al., 2015). As a consequence, the thickness of overbank units is expected to decrease in a downstream direction. On the contrary, in the *Laterally confined area* of the right levee, Units II, III (Case II), and V (Case I) have higher thickness than upslope (**Figure 10**). This unusual and localized increase in sedimentation can have two different explanations:

- 1) A localized reduction in the channel depth value enhances the overspill of a thicker part of the flow. Different depositional features may reduce the channel relief, such as nested mounds that develop on the outside of a specific bend (i.e. the first sharp bend) (Peakall et al., 2000) or MTD coming from the surface of the Acquarone high. However, those feature cannot be recognized, as, if present, they are now buried under the more recent MTD (**Figure 2**).
- 2) The flow experienced a reflection on the surface of the structural high.

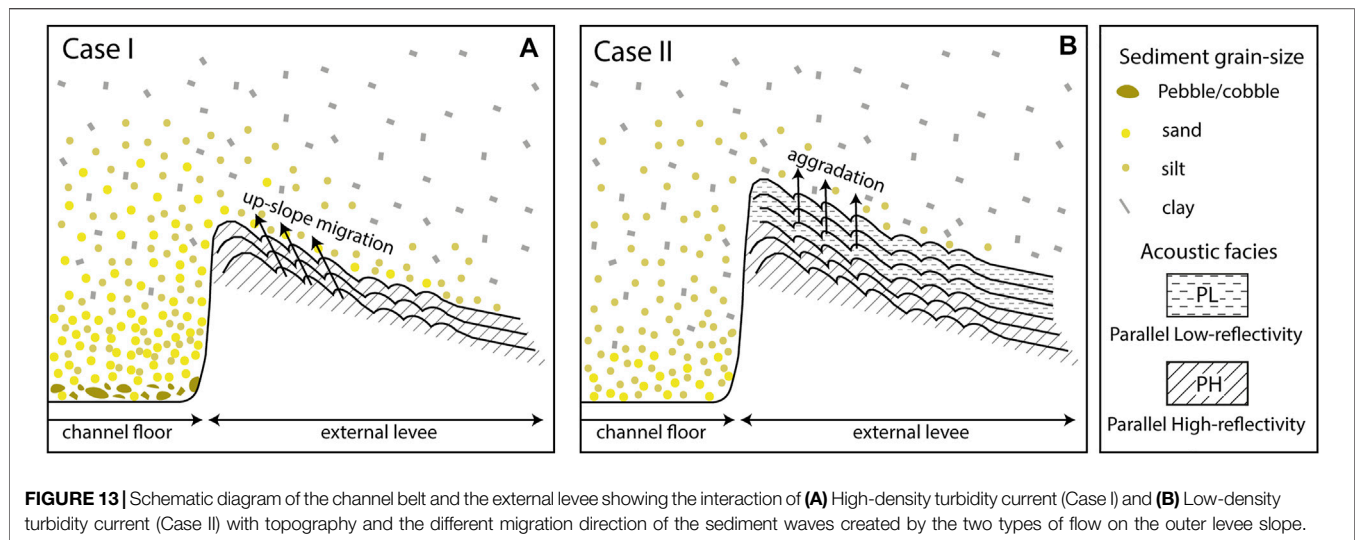
In the case of the first hypothesis, the overspill of the lower, coarser-grained part of the flows should result in a high-amplitude seismic facies, similar to what observed in the high-density flows of Case II. This is not the case, as shown by **Figure 7B**, which highlights the low-amplitude parallel reflections of the overbank wedge. Therefore, we prefer the

second hypothesis also because it is consistent with the spreading direction of the lobe-shaped depocenter in the *Laterally confined area* that is almost specular to the channel path at the bend. It can be hypothesized that the confining action of the Acquarone high could impose the thickening and the successive rebound of the upper portion of the flow outgoing from the bend (**Figures 12B,D**). In fact, a turbidity current can be reflected depending on the geometry of the bounding slope and the angle of incidence of the current (Patacci et al., 2015). This assemblage has commonly been detected in tectonically confined basins (Kneller et al., 1991; Kneller and McCaffrey, 1999; Amy et al., 2004; Tinterri et al., 2016, 2017; Tinterri and Piazza, 2019) resulting in the production of contained-reflected beds (*sensu* Pickering and Hiscott, 1985). Dalla Valle and Gamberi (2009) and Tek et al. (2021) provide other examples where changes of the overbank architecture are interpreted to be connected to flow reflection processes.

Laboratory experiments (Kneller et al., 1991; Kneller 1995; Haughton 1994; Amy et al., 2005; Patacci et al., 2015) and numerical models (Howlett et al., 2019) have shown that a reverse overflow forms as soon as a turbidity current impacts on a topographic high and a deceleration from supercritical to subcritical condition is accompanied by abrupt flow inflation. However, in order to produce a reflected overflow, the upper part of the flow should have sufficiently high momentum, so when the outbound velocity is too low at the point of incidence with the slope, turbidity-current reflection is not achieved (Patacci et al., 2015). In the case of the Acquarone channel, it is reasonable to argue that turbidity currents that spilled over the left side of the channel experienced complete reflection, being impeded in their travel by the Acquarone High (**Figure 12B**). However, the sedimentation patterns of Units I, IV, VI, and VII do not show this depocenter (**Figure 12A**). Probably the turbidity currents that generated those units had insufficient velocity due to their strongly depositional behaviour at the bend. In fact, as the current enters the bend and spills over onto the overbank, the in-channel velocity decreases significantly (Abd El-Gawad et al., 2012). Other flow properties, such as the volume of the low-density part of the flow and the height of the overspilling flow, could be involved in the occurrence of a reflected overflow, but they cannot be evaluated with the data presently available.

8.3.3 Knick-points Area

The relief of levees above the channel floor commonly diminishes in a downslope direction (Hiscott et al., 1997; Posameinter and Kolla, 2003; Hansen et al., 2015). In our case study, along the flat segments (flat I-II, **Figure 4C**) downslope from knick-points, the relief of the levees crest increase (respectively about 7 and 3 m for the right levee and 5 and 4 m for the left one) vs. the upslope levee tract (**Figure 4C**). This increase in relief could be due to a localized increase in the erosional behaviour of turbiditic flows in the channel floor or to an increase in the growth rate of levee crests. The latter hypothesis is here preferred because the flat I segment on the levee crest profiles coincides with the upslope apex of a depositional field of bedforms (**Figure 12A**).



In the *Knick-points area*, the units that fall into Case I show a marked depocenter highlighting increased capability of flows to overtop the levee crest (Figure 12A). A reduction in flow velocity is to be expected when a flow passes through a knick-point (Heijnen et al., 2020). Considering the inverse relationship between flow velocity (U) and flow height (h) marked by the Froude number

$$Fr = \frac{U}{\sqrt{\left(\frac{\rho - \rho_w}{\rho_g}\right)h}}$$

where ρ = density of the flow, ρ_w = density of water and g = acceleration of gravity, flow thickening is connected to flow deceleration.

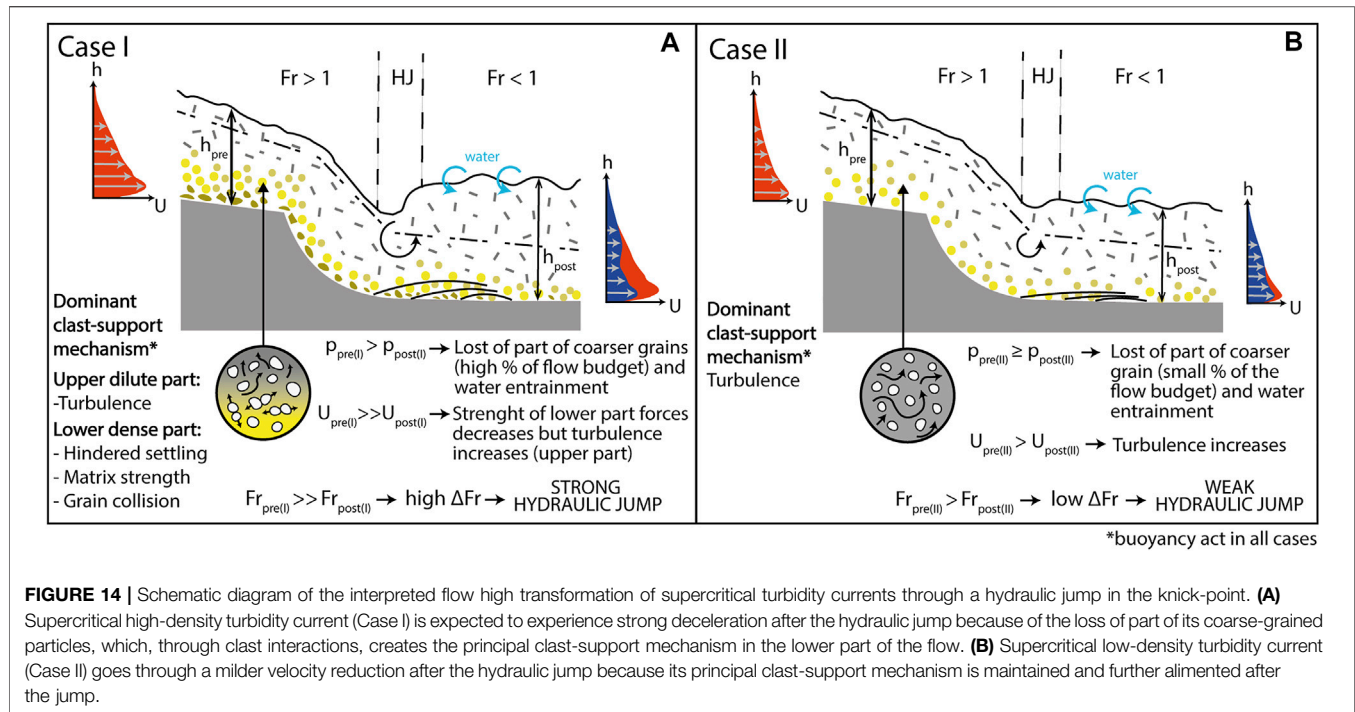
In the Acquarone channel, slopes are always one order of magnitude above the 0.1° threshold gradient for Froude supercritical flow deposits (Postma et al., 2014). This is why it is reasonable to assume that, irrespective of their nature, all the turbidity currents reached the supercritical conditions and, passing the knick-point, experienced a hydraulic jump. We suggest that in the flat I segment (Figure 4C), where the slope of the channel axis is halved, the turbidity currents rapidly slow down and go through a hydraulic jump, whose consequence is the thickening of the flow and the entrainment of water that reduce the density of the current (Figure 14) (Komar, 1971; Postma et al., 2009).

Recent experiments by Ono et al. (2021) were carried out on a mixture of sediment (including fine-sand to gravel), simulating flows equivalent to the high-density turbidity currents according to the definition of Lowe (1982). The results of Ono et al. (2021) show that after the occurrence of a large hydraulic jump, where the flow depth increased eight times respect the initial value, smaller ones, where the flow was only two times thicker than the initial value, occurs. We have interpreted that the flow behaviour of Case I in the KP1 could thus be connected to a drastic increase in flow thickness. This process can account for a

long-lasting overspill and for the formation of the depocenter associated with the *Knick-points area* (Figure 12A). Anyway, only Unit VII show a depocenter occurring after the KP2. Accordingly with the data of Ono et al. (2021), we interpreted the absence of a depocenter after KP2 for Unit V and IV to be connected to a possibly smaller hydraulic jump whose effect are potentially not related to a long-lasting overspill. The smaller size of the jump can be connected to a slow-down of the velocity of the flow following the first hydraulic jump and to the milder slope difference between the second ramp ($1, 2^\circ$) and the second flat ($0, 9^\circ$) that could have not provided sufficient deceleration to the flow.

Similarly, Case II, interpreted as associated to low-density turbidity currents, does not show any increase in sedimentation in the *Knick-points area* (Figure 12B). This occurrence is here explained as also resulting from a smaller hydraulic jump. In the crossing of a topographic step, the height of the jump has been described as the ratio of Froude number before (Fr_{pre} in Figure 14) and after the jump (Fr_{post} in Figure 14). The higher the difference between the Froude number values (ΔFr in Figure 14), before and after the jump, the higher the size of the hydraulic jump (Cartigny et al., 2014).

The lower part of bipartite turbidity currents consist of a relatively dense basal layer sustained by the combined effect of hindered settling, matrix strength and dispersive pressure controlled by sediment concentration (that may exceed 20–30% according to Lowe, 1982). In contrast, a dilute, turbulent low-density turbidity current is primarily sustained by turbulence which is largely independent from particle concentration (Lowe, 1982). The flow deceleration related to the hydraulic jump, in high-density turbidity currents, causes the en-masse deposition of the coarsest particles of the basal layer (Postma and Cartigny, 2014; Postma et al., 2014; Hage et al., 2018; Slooman and Cartigny, 2020) and the concentration of the basal dense layer is further reduced by the water entrainment effect (Figure 14A). As a consequence, we can expect that high-density



turbidity currents experience a drastic slowdown after KP1, due to the marked decrease in sediment concentration, producing a strong hydraulic jump with the consequent increase in sediment deposition on the levee (**Figure 14A**). While low-density turbidity currents, whose principal transport mechanism is the turbulence of the fine-grained sediments, are expected to experience a milder velocity reduction after KP1 producing a weak hydraulic jump (**Figure 14B**).

In summary, we suggest that the pattern of sediment distribution created by Case I in the *Knick-points* area, consisting in a localized increase in the overbank thickness, is the result of high-density turbidity currents experiencing a strong hydraulic jump (**Figure 12C**); while the sedimentation pattern of Case II does not generate a depocenter in the same area since their former flows (low-density turbidity currents) are interpreted as producing smaller and weaker hydraulic jumps (**Figure 12D**). We have interpreted the knick-points, inferred by tectonic structures transverse to the channel course whose topography is not completely healed, led to the occurrence of hydraulic jumps whose amplitude, that can be connected to the density stratification of the flow, may or not have a depositional expression on the overbank area.

8.3.4 Frontal splay Area

The thickness distribution of the seven units shows that the two different types of flow behave differently also under the rapid flow expansion regime ensuing at the end of the channel confinement. Units falling in Case I present a thick and elongate lobe with very high reflectivity (**Figure 12A**). This kind of deposition is interpreted as resulting from high-density turbidity currents that, exiting the channel confinement, rapidly lose competence, deposit the coarsest material and create a thick

frontal lobe with small-scale coarse grained sediment waves in front of the channel mouth (**Figure 6**). Moreover, the direction of the crests is indicative of another important behaviour of the lower dense portion of the turbidity current. Where the relief of the bulge in the frontal splay becomes important (**Figures 4A, 9B**), the sediment wave crests divert by about 30° eastward from their initial WNW-EES orientation (**Figure 6**). Similar results can also be observed in field studies and flume experiments related to flow deflection against lateral or oblique confining slopes (Amy et al., 2004; Tinterri et al., 2017; Piazza and Tinterri, 2020). The mud portion is completely absent, as shown by the transparent high reflectivity of the frontal splay (**Figure 9A**), indicating that the upper dilute part of the turbidity currents largely bypassed this area or were eroded by successive flows.

Units belonging to Case II do not present any thick concave upward accumulation, but, rather, deposition on the frontal splay results in a low-reflectivity package, which drapes the underlying morphology (**Figure 12B**). Sedimentation is higher towards the SW, in the fan fringe, than adjacent to the channel mouth where much of the sediment bypasses and is carried further downslope in the Gioia channel. The loss of confinement at the end of the channel is generally associated with an increase of turbulence in turbidity currents. The increase in turbulence at the mouth of submarine channels has been connected both to the occurrence of hydraulic jump (Mutti and Normark, 1987; Mutti and Normark, 1991; Mutti et al., 2003; Baas et al., 2004) and to flow relaxation mechanism (Pohl et al., 2019). In turbidity currents with a substantial mud component, as low-density turbidity currents, increase in turbulence, which, preventing sediment deposition, contributes to the flow run-out (Mutti and Normark, 1987; Mutti and Normark, 1991;

Mutti et al., 2003). Moreover, the high value of the slope (1.2°, **Figure 4B**) and the convergence created by the topography in the frontal splay caused turbidity currents to accelerate in the principal flow direction, while laterally, in the fan fringe, the gentler slope caused a little bypass and a greater amount of fine-grained deposition. In fact, low-density turbidity currents react to the end of confinement and to the morphology of the slope in the same way as the upper dilute part of high-density turbidity currents.

9 CONCLUSION

A detailed analysis of sediment thickness and facies has been performed to investigate overbank processes in a leveed channel in a slope setting located in the southeastern Tyrrhenian Sea. It reveals considerable complexity in levee facies and thickness, ultimately ensuing from the uneven seafloor topography of the study area, highlighting that, in continental slope settings, where the imprint of tectonic structures is not yet completely healed, sedimentation in overbank areas does not conform to the available, simple predictive models.

In particular, we show that structural highs can confine overbanking turbidity currents, inducing flow deflection, and forming localized depocenters in the levees. Such an interaction between overbanking flows and confining structural highs can eventually lead to reverse channel asymmetry, opposite to what would result from the effect of the Coriolis force alone.

In addition, our research also highlights that planform and gradient variations of slope channels can have a strong influence on the thickness trend in the overbank areas. In particular, we show that overbank depositional patterns change along the channel course depending on the location of bends and knickpoints. This behaviour is recognized in the majority of submarine channels and interpreted as resulting from local perturbations in channel planform and gradient depending on autogenic processes inherent with channel development. Our case study, on the contrary, shows that bends and knickpoints can have a tight connection to slope topography, thus further conjoining overbank depositional patterns and allogenic, tectonic shaping of a continental margin.

We have also shown that sediment wave fields coincide with depocenters on the overbank region, indicating that they develop from the principal sediment entry-points. According to their location, the sediment waves have different dimensions and geometries highlighting that the interaction between the

overspilling flows and slope topography, influences not only sediment distribution, but also the morphology of the sediment waves. Moreover, our study shows that the direction of migration of sediment waves is connected to the density of the turbidity current: high-density turbidity currents create upslope-migrating coarse-grained sediment waves, whereas low-density turbidity currents are associated with aggrading fine-grained sediment waves.

Finally, our study also shows that patterns of overbank deposition vary over time. We envisage that, upon interacting with gradient variations along the channel course, turbidity currents behave differently, depending on their vertical density profiles. In particular, hydraulic jumps formed by high- and low-density turbidity currents control the amount of sediment that can overspill the channel and the character and location of overbank depocenters. This finding highlights the importance of antecedent conditioning by previous flows in controlling the development of turbidite systems Migeon et al., 2000.

DATA AVAILABILITY STATEMENT

The original contributions presented in the study are included in the article/Supplementary Material, further inquiries can be directed to the corresponding author.

AUTHOR CONTRIBUTIONS

SE and GF are responsible for the conception of the study. SE performed the description and manipulation of the data, wrote the first draft of the manuscript and created the images. SE and GF are involved in the main interpretations of the paper. GF wrote the conclusion section of the manuscript. GF and TR contributed to the design of the paper and corrected the paper. All authors contributed to manuscript read and approved the submitted version.

ACKNOWLEDGMENTS

We would like to thank all the participants (ISMAR colleagues, captain and crew) of the various cruises of data acquisition. We are also grateful to Alessandra Mercorella for the processing and management of the data. Finally, we particularly thank the editor Michael Clare and two reviewers for their thorough reviews that have improved the quality of the manuscript.

REFERENCES

- Abd El-Gawad, S., Cantelli, A., Pirmez, C., Minisini, D., Sylvester, Z., and Imran, J. (2012). Three-dimensional Numerical Simulation of Turbidity Currents in a Submarine Channel on the Seafloor of the Niger Delta Slope. *J. Geophys. Res.* 117, a–n. doi:10.1029/2011JC007538
- Adeogba, A. A., McHargue, T. R., and Graham, S. A. (2005). Transient Fan Architecture and Depositional Controls from Near-Surface 3-D Seismic Data, Niger delta continental Slope. *Bulletin* 89 (5), 627–643. doi:10.1306/11200404025
- Amy, L. A., McCaffrey, W. D., and Kneller, B. C. (2004). The Influence of a Lateral basin-slope on the Depositional Patterns of Natural and Experimental Turbidity Currents. *Geol. Soc. Lond. Spec. Publications* 221, 311–330. doi:10.1144/GSL.SP.2004.221.01.17
- Antonoli, F., Ferranti, L., Lambeck, K., Kershaw, S., Verrubbi, V., and Dai Pra, G. (2006). Late Pleistocene to Holocene Record of Changing Uplift Rates in Southern Calabria and Northeastern Sicily (Southern Italy, Central Mediterranean Sea). *Tectonophysics* 422, 23–40. doi:10.1016/j.tecto.2006.05.003
- Baas, J. H., McCaffrey, W. D., Haughton, P. D. W., and Choux, C. (2005). Coupling between Suspended Sediment Distribution and Turbulence Structure in a

- Laboratory Turbidity Current. *J. Geophys. Res.* 110, C11015. doi:10.1029/2004JC002668
- Baas, J. H., van Kesteren, W., and Postma, G. (2004). Deposits of Depletive High-Density Turbidity Currents: a Flume Analogue of Bed Geometry, Structure and Texture. *Sedimentology* 51, 1053–1088. doi:10.1111/j.1365-3091.2004.00660.x
- Birman, V. K., Meiburg, E., and Kneller, B. (2009). The Shape of Submarine Levees: Exponential or Power Law? *J. Fluid Mech.* 619, 367–376. doi:10.1017/S0022112008004862
- Cartigny, M. J. B., Ventra, D., Postma, G., and Van Den Berg, J. H. (2014). Morphodynamics and Sedimentary Structures of Bedforms under Supercritical-Flow Conditions: New Insights from Flume Experiments. *Sedimentology* 61, 712–748. doi:10.1111/sed.12076
- Casalbore, D., Bosman, A., Casas, D., Chiocci, F., Martorelli, E., and Ridente, D. (2019). Morphological Variability of Submarine Mass Movements in the Tectonically-Controlled Calabro-Tyrrhenian Continental Margin (Southern Italy). *Geosciences* 9, 43. doi:10.3390/geosciences9010043
- Casas, D., Chiocci, F., Casalbore, D., Errilla, G., and de Urbina, J. O. (2016). Magnitude-frequency Distribution of Submarine Landslides in the Gioia Basin (Southern Tyrrhenian Sea). *Geo-Mar. Lett.* 36, 405–414. doi:10.1007/s00367-016-0458-2
- Catalano, S., and Di Stefano, A. (1997). Sollevamenti e tettonogenesi pleistocenica lungo il margine tirrenico dei Monti Peloritani: integrazione dei dati geomorfologici, strutturali e biostratigrafici. *Il Quaternario* 10 (2), 337–342.
- Dalla Valle, G., and Gamberi, F. (2010). Erosional Sculpting of the Caprera Confined Deep-Sea Fan as a Result of Distal basin-spilling Processes (Eastern Sardinian Margin, Tyrrhenian Sea). *Mar. Geology* 268, 55–66. doi:10.1016/j.margeo.2009.10.012
- Deptuck, M. E., Sylvester, Z., Pirmez, C., and O'Byrne, C. (2007). Migration-aggradation History and 3-D Seismic Geomorphology of Submarine Channels in the Pleistocene Benin-major Canyon, Western Niger Delta Slope. *Mar. Pet. Geology* 24, 406–433. doi:10.1016/j.marpetgeo.2007.01.005
- Fabbri, A., Ghisetti, F., and Vezzani, L. (1980). The Peloritani-Calabria Range and the Gioia basin in the Calabrian Arc (Southern Italy): Relationships between Land and marine Data. *Geologica Rom.* 19, 131–150.
- Gamberi, F., Della Valle, G., Marani, M., Mercorella, A., Distefano, S., and Di Stefano, A. (2019). Tectonic Controls on Sedimentary System along the continental Slope of the central and southeastern Tyrrhenian Sea. *Ital. J. Geosciences* 138, 317–332. doi:10.3301/IJG.2019.08
- Gamberi, F., and Marani, M. (2008). Controls on Holocene Deep-Water Sedimentation in the Northern Gioia Basin, Tyrrhenian Sea. *Sedimentology* 55, 1889–1903. doi:10.1111/j.1365-3091.2008.00971.x
- Gamberi, F., and Marani, M. (2006). Hinterland Geology and continental Margin Growth: the Case of the Gioia Basin (southeastern Tyrrhenian Sea). *Geol. Soc. Lond. Spec. Publications* 262, 349–363. doi:10.1144/GSL.SP.2006.262.01.21
- Gamberi, F., and Rovere, M. (2011). Architecture of a Modern Transient Slope Fan (Villafranca Fan, Gioia basin-southeastern Tyrrhenian Sea). *Sediment. Geology* 236, 211–225. doi:10.1016/j.sedgeo.2011.01.007
- Hage, S., Cartigny, M. J. B., Clare, M. A., Sumner, E. J., Vendettuoli, D., Hughes Clarke, J. E., et al. (2018). How to Recognize Crescentic Bedforms Formed by Supercritical Turbidity Currents in the Geologic Record: Insights from Active Submarine Channels. *Geology* 46, 563–566. doi:10.1130/G40095.1
- Hansen, L. A. S., Callow, R. H. T., Kane, I. A., Gamberi, F., Rovere, M., Cronin, B. T., et al. (2015). Genesis and Character of Thin-Bedded Turbidites Associated with Submarine Channels. *Mar. Pet. Geology* 67, 852–879. doi:10.1016/j.marpetgeo.2015.06.007
- Haughton, P., Davis, C., McCaffrey, W., and Barker, S. (2009). Hybrid Sediment Gravity Flow Deposits - Classification, Origin and Significance. *Mar. Pet. Geology* 26, 1900–1918. doi:10.1016/j.marpetgeo.2009.02.012
- Haughton, P. D. W. (1994). Deposits of Deflected and Pondered Turbidity Currents, Sorbas Basin, Southeast Spain. *J. Sediment. Res.* 64, 233–246. doi:10.1306/D4267D6B-2B26-11D7-8648000102C1865D
- Heijnen, M. S., Clare, M. A., Cartigny, M. J. B., Talling, P. J., Hage, S., Lintern, D. G., et al. (2020). Rapidly-migrating and Internally-Generated Knickpoints Can Control Submarine Channel Evolution. *Nat. Commun.* 11, 3129. doi:10.1038/s41467-020-16861-x
- Heinö, P., and Davies, R. J. (2007). Knickpoint Migration in Submarine Channels in Response to Fold Growth, Western Niger Delta. *Mar. Pet. Geology* 24, 434–449. doi:10.1016/j.marpetgeo.2006.09.002
- Hiscott, R. N., Hall, F. R., and Pirmez, C. (1997). Turbidity-current Overspill from the Amazon Channel: Texture of the silt/sand Load, Paleoflow from Anisotropy of Magnetic Susceptibility, and Implications for Flow Processes. *Proc. Ocean Drilling Program Scientific Results* 155, 53–78. doi:10.2973/odp.proc.sr.155.202.1997
- Howlett, D. M., Ge, Z., Nemecek, W., Gawthorpe, R. L., Rotevatn, A., and Jackson, C. A. L. (2019). Response of Unconfined Turbidity Current to Deep-water Fold and Thrust belt Topography: Orthogonal Incidence on Solitary and Segmented Folds. *Sedimentology* 66, 2425–2454. doi:10.1111/sed.12602
- Jobe, Z., Sylvester, Z., Bolla Pittaluga, M., Frascati, A., Pirmez, C., Minisini, D., et al. (2017). Facies Architecture of Submarine Channel Deposits on the Western Niger Delta Slope: Implications for Grain-size and Density Stratification in Turbidity Currents. *J. Geophys. Res. Earth Surf.* 122, 473–491. doi:10.1002/2016JF003903
- Kane, I. A., McCaffrey, W. D., Peakall, J., and Kneller, B. C. (2010). Submarine Channel Levee Shape and Sediment Waves from Physical Experiments. *Sediment. Geology* 223, 75–85. doi:10.1016/j.sedgeo.2009.11.001
- Kane, I. A., Pontén, A. S. M., Vangdal, B., Eggenhuisen, J. T., Hodgson, D. M., and Spychala, Y. T. (2017). The Stratigraphic Record and Processes of Turbidity Current Transformation across Deep-marine Lobes. *Sedimentology* 64, 1236–1273. doi:10.1111/sed.12346
- Kneller, B. (1995). Beyond the Turbidite Paradigm: Physical Models for Deposition of Turbidites and Their Implications for Reservoir Prediction. *Geol. Soc. Lond. Spec. Publications* 94, 31–49. doi:10.1144/GSL.SP.1995.094.01.04
- Kneller, B., and Buckee, C. (2000). The Structure and Fluid Mechanics of Turbidity Currents: a Review of Some Recent Studies and Their Geological Implications. *Sedimentology* 47, 62–94. doi:10.1046/j.1365-3091.2000.047s1062.x
- Kneller, B., Edwards, D., McCaffrey, W., and Moore, R. (1991). Oblique Reflection of Turbidity Currents. *Geol.* 19, 250–252. doi:10.1130/0091-7613(1991)019<0250:orotc>2.3.co;2
- Kneller, B., and McCaffrey, W. (1999). Depositional Effects of Flow Nonuniformity and Stratification within Turbidity Currents Approaching a Bounding Slope: Deflection, Reflection, and Facies Variation. *J. Sediment. Res.* 69, 980–991. doi:10.2110/jsr.69.980
- Komar, P. D. (1971). Hydraulic Jumps in Turbidity Currents. *Geol. Soc. America Bull.* 82, 1477–1488. doi:10.1130/0016-7606(1971)82[1477:hjtc]2.0.co;2
- Kostic, S. (2014). Upper Flow Regime Bedforms on Levees and continental Slopes: Turbidity Current Flow Dynamics in Response to fine-grained Sediment Waves. *Geosphere* 10, 1094–1103. doi:10.1130/GES01015.1
- Lowe, D. R. (1982). Sediment Gravity Flows: II Depositional Models with Special Reference to the Deposits of High-Density Turbidity Currents. *SEPM J. Sediment. Res.* 52, 279–297. doi:10.1306/212F7F31-2B24-11D7-8648000102C1865D
- Migeon, S., Savoye, B., and Faugeres, J.-C. (2000). Quaternary Development of Migrating Sediment Waves in the Var Deep-Sea Fan: Distribution, Growth Pattern, and Implication for Levee Evolution. *Sediment. Geology* 133, 265–293. doi:10.1016/S0037-0738(00)00043-9
- Mutti, E., and Normark, W. R. (1991). "An Integrated Approach to the Study of Turbidite Systems," in *Seismic Facies and Sedimentary Processes of Submarine Fans and Turbidite Systems* (New York: Springer-Verlag). doi:10.1007/978-1-4684-8276-8_4
- Mutti, E., and Normark, W. R. (1987). "Comparing Examples of Modern and Ancient Turbidite Systems: Problems and Concepts," in *Marine Clastic Sedimentology*. Editors J. K. Legget and G. G. Zuffa (Dordrecht: Springer), 1–38. doi:10.1007/978-94-009-3241-8_1
- Mutti, E., Tinterri, R., Benevelli, G., Biase, D. d., and Cavanna, G. (2003). Deltaic, Mixed and Turbidite Sedimentation of Ancient Foreland Basins. *Mar. Pet. Geology* 20, 733–755. doi:10.1016/j.marpetgeo.2003.09.001
- Nakajima, T., and Kneller, B. C. (2013). Quantitative Analysis of the Geometry of Submarine External Levées. *Sedimentology* 60, 877–910. doi:10.1111/j.1365-3091.2012.01366.x
- Normark, W. R., Piper, D. J. W., Posamentier, H., Pirmez, C., and Migeon, S. (2002). Variability in Form and Growth of Sediment Waves on Turbidite Channel Levees. *Mar. Geology* 192, 23–58. doi:10.1016/S0025-3227(02)00548-0
- Patacci, M., Haughton, P. D. W., and McCaffrey, W. D. (2015). Flow Behavior of Pondered Turbidity Currents. *J. Sediment. Res.* 85, 885–902. doi:10.2110/jsr.2015.59
- Peakall, J., McCaffrey, W. D., Kneller, B. C., Stelling, C. E., McHargue, T. R., and Schwellen, W. J. (2000). A Process Model for the Evolution of Submarine Fan

- Channels: Implications for Sedimentary Architecture *Fine-grained Turbidite Systems*. AAPG Memoir 72, 68. Tulsa, OK: SEPM Special Publication, 73–88. doi:10.1306/M72703
- Piazza, A., and Tinterri, R. (2020). Cyclic Stacking Pattern, Architecture and Facies of the Turbidite Lobes in the Macigno Sandstones Formation (Chattian-Aquitania, Northern Apennines, Italy). *Mar. Pet. Geology* 122, 104704. doi:10.1016/j.marpetgeo.2020.104704
- Pickering, K. T., and Hiscott, R. N. (1985). Contained (Reflected) Turbidity Currents from the Middle Ordovician Cloridorme Formation, Quebec, Canada: an Alternative to the Antidune Hypothesis. *Sedimentology* 32, 373–394. doi:10.1111/j.1365-3091.1985.tb00518.x
- Piper, D. J. W., and Normark, W. R. (1983). Turbidite Depositional Patterns and Flow Characteristics, Navy Submarine Fan, California Borderland. *Sedimentology* 30, 681–694. doi:10.1111/j.1365-3091.1983.tb00702.x
- Pirmez, C., Hiscott, R. N., and Kronen, J. K. (1997). Sandy Turbidite Successions at the Base of Channel-Levee Systems of the Amazon Fan Revealed by FMS Logs and Cores: Unraveling the Facies Architecture of Large Submarine Fans. *Proc. Ocean Drilling Program Scientific Results* 155, 7–33. doi:10.2973/odp.proc.sr.155.201.1997
- Pirmez, C., and Imran, J. (2003). Reconstruction of Turbidity Currents in Amazon Channel. *Mar. Pet. Geology* 20, 823–849. doi:10.1016/j.marpetgeo.2003.03.005
- Pohl, F., Eggenhuisen, J. T., Tilston, M., and Cartigny, M. J. B. (2019). New Flow Relaxation Mechanism Explains Scour fields at the End of Submarine Channels. *Nat. Commun.* 10, 4425. doi:10.1038/s41467-019-12389-x
- Posamentier, H. W., and Kolla, V. (2003). Seismic Geomorphology and Stratigraphy of Depositional Elements in Deep-Water Settings. *J. Sediment. Res.* 73, 367–388. doi:10.1306/111302730367
- Postma, G., and Cartigny, M. J. B. (2014). Supercritical and Subcritical Turbidity Currents and Their Deposits—A Synthesis. *Geology* 42, 987–990. doi:10.1130/G35957.1
- Postma, G., Cartigny, M., and Kleverlaan, K. (2009). Structureless, Coarse-Tail Graded Bouma Ta Formed by Internal Hydraulic Jump of the Turbidity Current. *Sediment. Geology* 219, 1–6. doi:10.1016/j.sedgeo.2009.05.018
- Postma, G., Kleverlaan, K., and Cartigny, M. J. B. (2014). Recognition of Cyclic Steps in sandy and Gravelly Turbidite Sequences, and Consequences for the Bouma Facies Model. *Sedimentology* 61, 2268–2290. doi:10.1111/sed.12135
- Regione Siciliana (2006). “Area Territoriale tra Capo Peloro e il bacino del Torrente Saponara (001),” in *Relazione 2006. Piano Stralcio di Bacino per l’Assetto Idrogeologico* (Palermo: Regione Siciliana).
- Remacha, E., Fernandez, L. P., and Maestro, E. (2005). The Transition between Sheet-like Lobe and Basin-Plain Turbidites in the Hecho Basin (South-Central Pyrenees, Spain). *J. Sediment. Res.* 75, 798–819. doi:10.2110/jsr.2005.064
- Rovere, M., Gamberi, F., Mercorella, A., and Leidi, E. (2014). Geomorphometry of a Submarine Mass-Transport Complex and Relationships with Active Faults in a Rapidly Uplifting Margin (Gioia Basin, NE Sicily Margin). *Mar. Geology* 356, 31–43. doi:10.1016/j.marpetgeo.2013.06.003
- Slootman, A., and Cartigny, M. J. B. (2020). Cyclic Steps: Review and Aggradation-Based Classification. *Earth-Science Rev.* 201, 102949. doi:10.1016/j.earscirev.2019.102949
- Straub, K. M., and Mohrig, D. (2008). Quantifying the Morphology and Growth of Levees in Aggrading Submarine Channels. *J. Geophys. Res.* 113, 20. doi:10.1029/2007JF000896
- Sylvester, Z., and Covault, J. A. (2016). Development of Cutoff-Related Knickpoints during Early Evolution of Submarine Channels. *Geology* 44, 835–838. doi:10.1130/G38397.1
- Symons, W. O., Sumner, E. J., Talling, P. J., Cartigny, M. J. B., and Clare, M. A. (2016). Large-scale Sediment Waves and Scours on the Modern Seafloor and Their Implications for the Prevalence of Supercritical Flows. *Mar. Geology* 371, 130–148. doi:10.1016/j.marpetgeo.2015.11.009
- Talling, P. J. (2013). Hybrid Submarine Flows Comprising Turbidity Current and Cohesive Debris Flow: Deposits, Theoretical and Experimental Analyses, and Generalized Models. *Geosphere* 9, 460–488. doi:10.1130/GES00793.1
- Tek, D. E., McArthur, A. D., Poyatos-Moré, M., Colombero, L., Allen, C., Patacci, M., et al. (2021). Controls on the Architectural Evolution of Deep-Water Channel Overbank Sediment Wave fields: Insights from the Hikurangi Channel, Offshore New Zealand. *New Zealand J. Geology Geophys.* 1–38. doi:10.1080/00288306.2021.1978509
- Tinterri, R., Drago, M., Consonni, A., Davoli, G., and Mutti, E. (2003). Modelling Subaqueous Bipartite Sediment Gravity Flows on the Basis of Outcrop Constraints: First Results. *Mar. Pet. Geology* 20, 911–933. doi:10.1016/j.marpetgeo.2003.03.003
- Tinterri, R., Laporta, M., and Ogata, K. (2017). Asymmetrical Cross-Current Turbidite Facies Tract in a Structurally-Confined Mini-basin (Priabonian-Rupelian, Ranzano Sandstone, Northern Apennines, Italy). *Sediment. Geology* 352, 63–87. doi:10.1016/j.sedgeo.2016.12.005
- Tinterri, R., and Muzzi Magalhaes, P. (2011). Synsedimentary Structural Control on Foredeep Turbidites: An Example from Miocene Marnoso-Arenacea Formation, Northern Apennines, Italy. *Mar. Pet. Geology* 28, 629–657. doi:10.1016/j.marpetgeo.2010.07.007
- Tinterri, R., Muzzi Magalhaes, P., Tagliaferri, A., and Cunha, R. S. (2016). Convolute Laminations and Load Structures in Turbidites as Indicators of Flow Reflections and Decelerations against Bounding Slopes. Examples from the Marnoso-Arenacea Formation (Northern Italy) and Annot Sandstones (South Eastern France). *Sediment. Geology* 344, 382–407. doi:10.1016/j.sedgeo.2016.01.023
- Tinterri, R., and Piazza, A. (2019). Turbidites Facies Response to the Morphological Confinement of a Foredeep (Cervarola Sandstones Formation, Miocene, Northern Apennines, Italy). *Sedimentology* 66, 636–674. doi:10.1111/sed.12501
- Wells, M., and Cossu, R. (2013). The Possible Role of Coriolis Forces in Structuring Large-Scale Sinuous Patterns of Submarine Channel-Levee Systems. *Phil. Trans. R. Soc. A* 371, 20120366. doi:10.1098/rsta.2012.0366
- Wynn, R. B., and Stow, D. A. V. (2002). Classification and Characterisation of Deep-Water Sediment Waves. *Mar. Geology* 192, 7–22. doi:10.1016/S0025-3227(02)00547-9
- Zhong, G., and Peng, X. (2021). Transport and Accumulation of Plastic Litter in Submarine Canyons—The Role of Gravity Flows. *Geology* 49, 581–586. doi:10.1130/G48536.1

Conflict of Interest: The authors declare that the research was conducted in the absence of any commercial or financial relationships that could be construed as a potential conflict of interest.

Publisher’s Note: All claims expressed in this article are solely those of the authors and do not necessarily represent those of their affiliated organizations, or those of the publisher, the editors and the reviewers. Any product that may be evaluated in this article, or claim that may be made by its manufacturer, is not guaranteed or endorsed by the publisher.

Copyright © 2022 Scacchia, Tinterri and Gamberi. This is an open-access article distributed under the terms of the Creative Commons Attribution License (CC BY). The use, distribution or reproduction in other forums is permitted, provided the original author(s) and the copyright owner(s) are credited and that the original publication in this journal is cited, in accordance with accepted academic practice. No use, distribution or reproduction is permitted which does not comply with these terms.



Submarine Channel Mouth Settings: Processes, Geomorphology, and Deposits

David M. Hodgson^{1*†}, Jeff Peakall^{1†} and Katherine L. Maier^{2†}

¹School of Earth and Environment, University of Leeds, Leeds, United Kingdom, ²National Institute of Water and Atmospheric Research (NIWA), Wellington, Aotearoa New Zealand

OPEN ACCESS

Edited by:

Fabiano Gamberi,
National Research Council (CNR), Italy

Reviewed by:

Juraj Janocko,
Technical University of Košice,
Slovakia
Luigi Jovane,
University of São Paulo, Brazil

*Correspondence:

David M. Hodgson
D.Hodgson@leeds.ac.uk

†ORCID:

Hodgson D. M.
0000-0003-3711-635X
Peakall J.
0000-0003-3382-4578
Maier K. L.
0000-0003-2908-3340

Specialty section:

This article was submitted to
Sedimentology, Stratigraphy and
Diagenesis,
a section of the journal
Frontiers in Earth Science

Received: 06 October 2021

Accepted: 13 January 2022

Published: 10 February 2022

Citation:

Hodgson DM, Peakall J and Maier KL
(2022) Submarine Channel Mouth
Settings: Processes, Geomorphology,
and Deposits.
Front. Earth Sci. 10:790320.
doi: 10.3389/feart.2022.790320

Observations from the modern seafloor that suggest turbidity currents tend to erode as they lose channel-levee confinement, rather than decelerating and depositing their sediment load, has driven investigations into sediment gravity flow behaviour at the mouth of submarine channels. Commonly, channel mouth settings coincide with areas of gradient change and play a vital role in the transfer of sediment through deep-water systems. Channel mouth settings are widely referred to as the submarine channel-lobe transition zone (CLTZ) where well-defined channel-levees are separated from well-defined lobes, and are associated with an assemblage of erosional and depositional bedforms (e.g., scours and scour fields, sediment waves, incipient channels). Motivated by recently published datasets, we reviewed modern seafloor studies, which suggest that a wide range of channel mouth configurations exist. These include traditional CLTZs, plunge pools, and distinctive long and flared tracts between channels and lobes, which we recognise with the new term channel mouth expansion zones (CMEZs). In order to understand the morphodynamic differences between types of channel mouth settings, we review insights from physical experiments that have focussed on understanding changes in process behaviour as flows exit channels. We integrate field observations and numerical modelling that offer insight into flow behaviours in channel mouth settings. From this analysis, we propose four types of channel mouth setting: 1) supercritical CMEZs on slopes; 2) plunge pools at steep slope breaks with high incoming supercritical Froude numbers; 3) CLTZs with arrays of hydraulic jumps at slope breaks with incoming supercritical Froude numbers closer to unity; and, 4) subcritical CLTZs associated with slope breaks and/or flow expansion. Identification of the stratigraphic record of channel mouth settings is complicated by the propagation, and avulsion, of channels. Nonetheless, recent studies from ancient outcrop and subsurface systems have highlighted the dynamic evolution of interpreted CLTZs, which range from composite erosion surfaces, to tens of metres thick stratigraphic records. We propose that some examples be reconsidered as exhumed CMEZs.

Keywords: submarine channel, lobe, channel-lobe transition zone, channel mouth expansion zone, supercritical flow, bedform migration

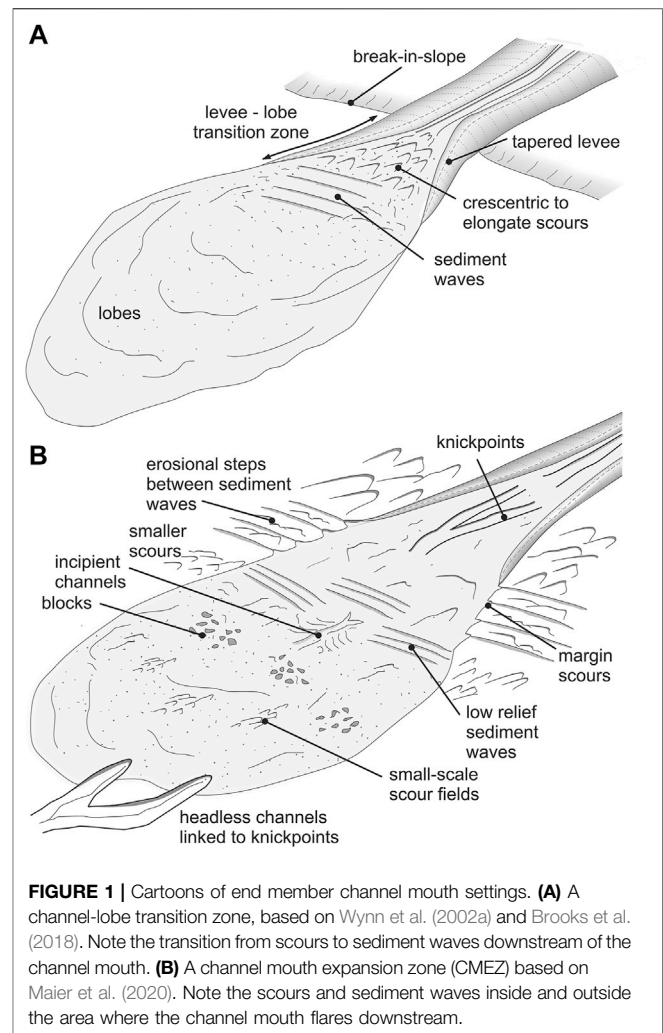
INTRODUCTION

Turbidity currents are sensitive to changes in orientation and gradient in seafloor topography, and to the nature (height and form) of lateral confinement. At submarine sites of abrupt changes in lateral confinement, such as at the mouth of submarine channels, or gradient changes, such as at the base-of-slope, flows undergo rapid changes in character (i.e., velocity, stratification, thickness) (e.g., Mutti and Normark, 1987; Mutti and Normark, 1991). These changes profoundly influence patterns of erosion and deposition, and therefore flow-topography interactions are dynamic in time and space.

Traditionally, submarine siliciclastic sedimentary systems are subdivided into 1) high gradient slope or ramp settings, dominated by erosion and sediment bypass processes, and 2) low gradient basin floor or step settings, dominated by depositional processes (e.g., Posamentier and Kolla, 2003). Commonly, the change from higher to lower gradients at the base of slope coincides with channel mouth settings. Channels in many examples appear separated from lobe deposits by transitional areas, widely referred to as channel-lobe transition zones (CLTZs; Mutti and Normark, 1987; Mutti and Normark, 1991; Wynn et al., 2002a). Mutti and Normark (1987) defined a CLTZ as “the region that, within any turbidite system, separates well-defined channels or channel-fill from well-defined lobes or lobe facies.” However, on review of the literature, including recent studies of modern seafloor systems, we propose that CLTZs are one type of a broad spectrum of configurations at channel mouth settings, and consider the likely dominant sedimentary processes and stratigraphic expression of these types.

Typically, channel mouth settings are dominated by sediment bypass (Stevenson et al., 2015; Brooks et al., 2018), and rapid flow deceleration and expansion. These processes have in turn been postulated to be associated with the occurrence of hydraulic jumps, where flows transform from supercritical to subcritical states (e.g., Komar, 1971; García and Parker, 1989; Normark and Piper, 1991; Alexander et al., 2001; Wynn et al., 2002a; Kostic and Parker, 2006; Ito, 2008; Macdonald et al., 2011a; Shaw et al., 2013; Sumner et al., 2013; Hofstra et al., 2015; Dorrell et al., 2016). Thus, it can be proposed, based on this existing literature, that there will be a relative abundance of supercritical and transcritical bedforms, including antidunes, cyclic steps, and scours, associated with channel mouth settings. Observations from modern-day channel mouth settings indicate that they are characterized by a distinctive assemblage of erosional bedforms, such as isolated or coalesced scours, and depositional bedforms, such as lags and sediment waves (e.g., Normark et al., 1979; Kenyon et al., 1995; Kenyon and Millington, 1995; Wynn et al., 2002b; Fildani and Normark, 2004; Maier et al., 2018; Droz et al., 2020; Maier et al., 2020).

There is a growing literature on CLTZs interpreted from ancient outcrops (see compilation by Navarro and Arnott, 2020), with recognition criteria proposed to support links between sedimentary processes and deposits (e.g., Bravo and Robles, 1995; Ito, 2008; Pyles et al., 2014; Hofstra et al., 2015; Pemberton et al., 2016; Postma et al., 2016; Brooks et al., 2018; Hofstra et al., 2018; Postma et al., 2021). Preserved stratigraphic



successions of interpreted CLTZs range from thick successions of aggradational beds in close association with scour-fill features (e.g., Pemberton et al., 2016; Brooks et al., 2018; Mansor and Amir Hassan, 2021; Brooks et al., 2022) to single surfaces that separate lobes from overlying channel-levee systems (e.g., Gardner et al., 2003; Hodgson et al., 2016). The wide range of expressions and dimensions (Navarro and Arnott, 2020) point to a number of parameters and configurations that control the transfer, and preservation, of channel mouth settings into the rock record.

The focus of studies on submarine channel mouth settings has shifted, evolving from largely petroleum reservoir motivations to include a renewed focus on deep-sea sediment transport processes, implications for seafloor infrastructure hazards, organic carbon flux and burial, benthic ecology, and pollutants (e.g., Kane and Clare, 2019). We aim to summarise the key observations of channel mouth settings from experimental studies, modern systems, and ancient systems to consider the feedbacks between (dynamic) seafloor topography, channel morphology, substrate, and flow rheology on changes in flow behaviour and deposits. Our objectives are to: 1) generate new

conceptual geomorphological models of channel mouth settings across a range of different geographic locations; 2) assess typical sedimentary processes associated with each of these channel mouth settings; and 3) identify examples of these channel mouth settings in the geological record, and discuss examples that may require reinterpretation.

NOMENCLATURE AND DEFINITIONS

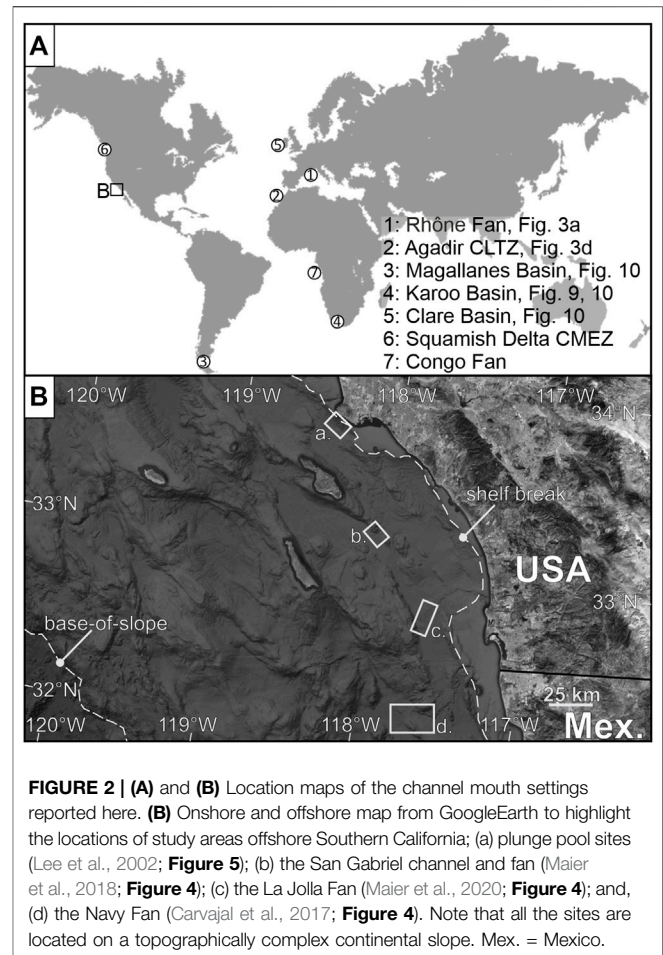
Relative to channel-levee systems and depositional lobes, the geomorphology, process sedimentology and stratigraphy of channel mouth settings are less widely documented. However, based on observations of modern systems, a more diverse suite of channel mouths settings exist that differ in scale and geomorphology from CLTZ examples.

Many parameters need to be considered when documenting submarine channel mouth settings. Physiographically, these settings commonly coincide with transitions from a slope to basin floor setting (or from a ramp to a step on a stepped slope), which can range from an abrupt gradient change (i.e., a break of slope up to several degrees) to a subtle transition over a relatively smooth seafloor profile. Similarly, submarine channel mouths can range from an abrupt termination to a broad flaring geometry, and be confined by incision or levee construction, or a combination. Furthermore, the morphodynamic configuration is likely to change in space and time through flow-deposit interactions and feedbacks.

To start, we consider a range of potential channel mouth configurations using ancient and recent studies (Figure 1): 1) broad areas of complex erosional and depositional morphologies (channel-lobe transition zones (CLTZs); e.g., Wynn et al., 2002a), and 2) channel mouth expansion zones (CMEZs), a new term we introduce to highlight distinctive examples identified in recent high-resolution seafloor surveys (e.g., Maier et al., 2020). Furthermore, we consider plunge pools (e.g., Lee et al., 2002) as part of the spectrum of channel mouth settings.

CLTZs tend to be associated with abrupt breaks in slope (Figure 1A), with a concomitant rapid change from flows confined by channels to unconfined flows. Classically, this tract is characterised by lags and scours immediately downdip of the channel with a range of forms and degree of coalescence, passing into areas dominated by sediment waves, before lobes. Reported dimensions of CLTZs range from a few kms to 10s of km in widths and lengths (e.g., Kenyon et al., 1995; Kenyon and Millington, 1995; Morris et al., 1998; Wynn et al., 2002a; Navarro and Arnott, 2020). However, this configuration can be dynamic, and can expand, contract, and migrate (Brooks et al., 2018).

In contrast, CMEZs are characterised by long and broad areas of flaring of the channel and are identified where gradient changes are subtle to absent, but are present on a slope (Maier et al., 2018; Maier et al., 2020; Fildani et al., 2021). Criteria to define where the channel component ends and the lobe component starts, such as aspect ratio or degree of incision, have not been established. Furthermore, examples have identified a complex array of scour forms, incipient channel forms, and sediment waves adjacent to

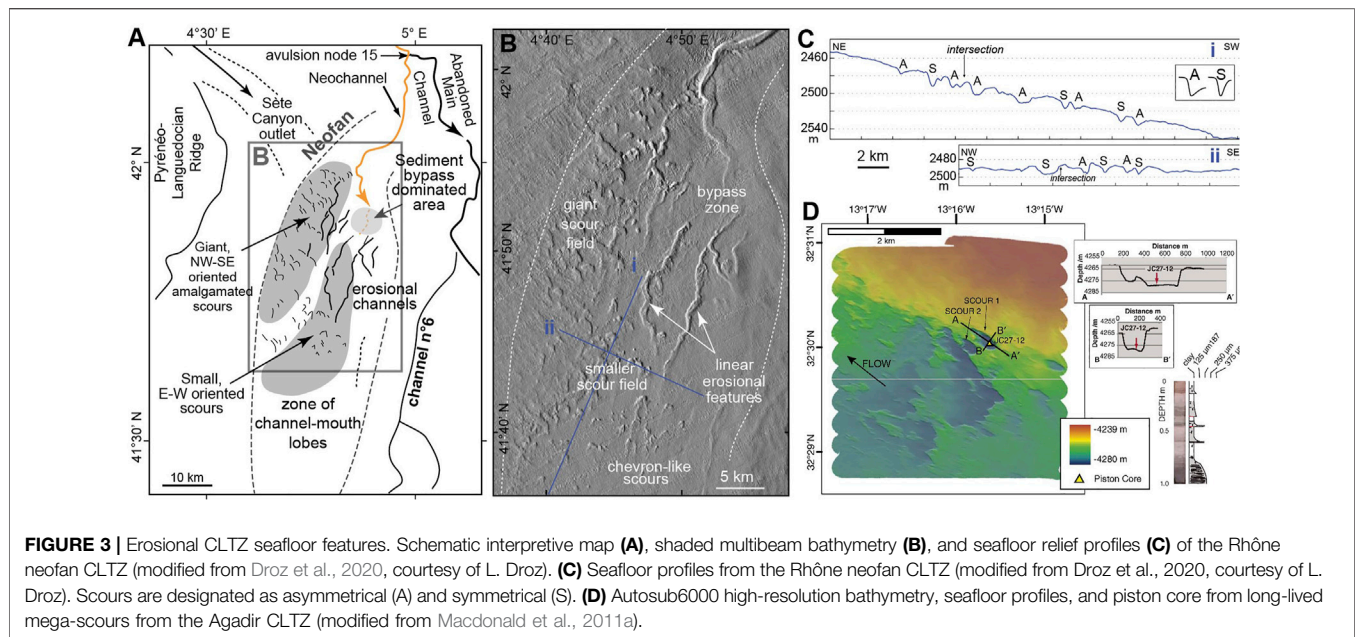


the area of channel flaring (Figure 1B; e.g., Carvajal et al., 2017; Maier et al., 2020).

We document plunge pools, CLTZs and CMEZs identified in modern systems to summarise previous work on the transition from well-defined channels to well-defined lobes. Subsequently, we consider flow process understanding derived from physical experiments, numerical simulations and real-world flow measurements, and then the stratigraphic expressions of exhumed systems interpreted to record channel mouth settings. This approach permits an alternative classification of channel mouth configurations to be proposed, which can form the basis for future investigations using modern, ancient, and experimental datasets.

COMPARISON OF MODERN SEAFLOOR SETTINGS

Seafloor studies have been key components of advancing understanding of submarine channel mouth settings for many decades, largely because they allow detailed plan-view perspectives that provide snapshots of time-transgressive morphology (e.g., Mutti and Normark, 1987; Wynn et al.,



2002a; Macdonald et al., 2011a; Macdonald et al., 2011b and references therein). Wynn et al. (2002a) summarised significant advances in morphology and processes at submarine channel mouths that were gained largely from deep-towed side-scan sonar, revealing seafloor CLTZs commonly associated with breaks in slope, scours, amalgamated erosional features, and sediment waves (Figure 1A). Subsequent advances in multibeam echosounder datasets, autonomous underwater vehicles, and remotely operated vehicles have produced seafloor datasets with increasing detail and have allowed better definition of channel and lobe environments (c.f. Mutti and Normark, 1987). Numerous studies since Mutti and Normark (1987)'s definition of a CLTZ and Wynn et al. (2002a)'s compilation have presented detailed studies of channel mouth settings on the modern seafloor. Here we discuss these advances by highlighting five examples with somewhat different character-mixed sand-mud Rhône Fan, sandy La Jolla Fan, the Squamish Delta, the mud-rich Congo Fan, and the base-of-slope plunge pools offshore North America (Figure 2).

CLTZ in the Mixed Sand-Mud Rhône Fan, Western Mediterranean Sea

The Rhône Fan, Gulf of Lions, western Mediterranean Sea (Figure 2), is a mixed sand and mud depositional system fed by the Petit-Rhône Canyon that was connected to the Rhône River during the Last Glacial Maximum (Droz et al., 2020). Imaging and interpretation of Rhône Fan CLTZs have been updated recently, following earlier recognition of erosional CLTZ features by Kenyon et al. (1995) and Wynn et al. (2002a). Multibeam bathymetry, subsurface profiles and piston cores collected across the youngest channel-fan in the Rhône system (i.e., neofan) by Bonnel et al. (2005) showed coalesced giant scours (4 km long, 1 km wide, 20 m deep) in a scour field

downslope and offset from the neofan channel mouth. Core samples from the distal neofan channel levees showed fine-grained (silt and fine sand) turbidites punctuating hemipelagic oozes (Bonnel et al., 2005).

More extensive multibeam bathymetry coverage (50 m grid) and analysis presented in Droz et al. (2020) revealed the neofan CLTZ as a region dominated by erosion and bypass of turbidity currents that separates the youngest channel and lobe. The CLTZ includes a 5-km-long smooth area out of the channel mouth, interpreted as a sediment bypass zone, and much larger adjacent and down-slope areas dominated by small scours (5–10 m deep and < 500 m wide), coalesced giant scours (10–30 m deep, 1–2 km wide, 1–5 km long), and erosional headless channels (Droz et al., 2020) (Figures 3A–C). These headless linear to sinuous erosional channels, and scours merging into megaflutes at the CLTZ, were determined to be a driver for channel inception (e.g., Gamberi and Marani, 2011; Fildani et al., 2013), development of channel confinement, and fan channel extension (Droz et al., 2020). This may contrast with the long-lived (>0.2 Myr) giant scours in the Agadir CLTZ (Figure 3D; see Macdonald et al., 2011a). Droz et al. (2020) found that, although the shape of channel-mouth lobes is controlled by the available space between channel-levee deposits and mounds created by subsurface salt diapirs, CLTZ occurrence is determined by the gradient along the channel up-slope from the channel mouth slope break, with more detachment associated with higher gradients. For example, differences in upslope gradient of only 0.13° were observed to change the amount of detachment.

CMEZ in the Sand-Rich La Jolla Fan, Offshore Southern California

The Southern California and Mexican Borderlands, offshore western North America, host many small, sand-rich canyon-

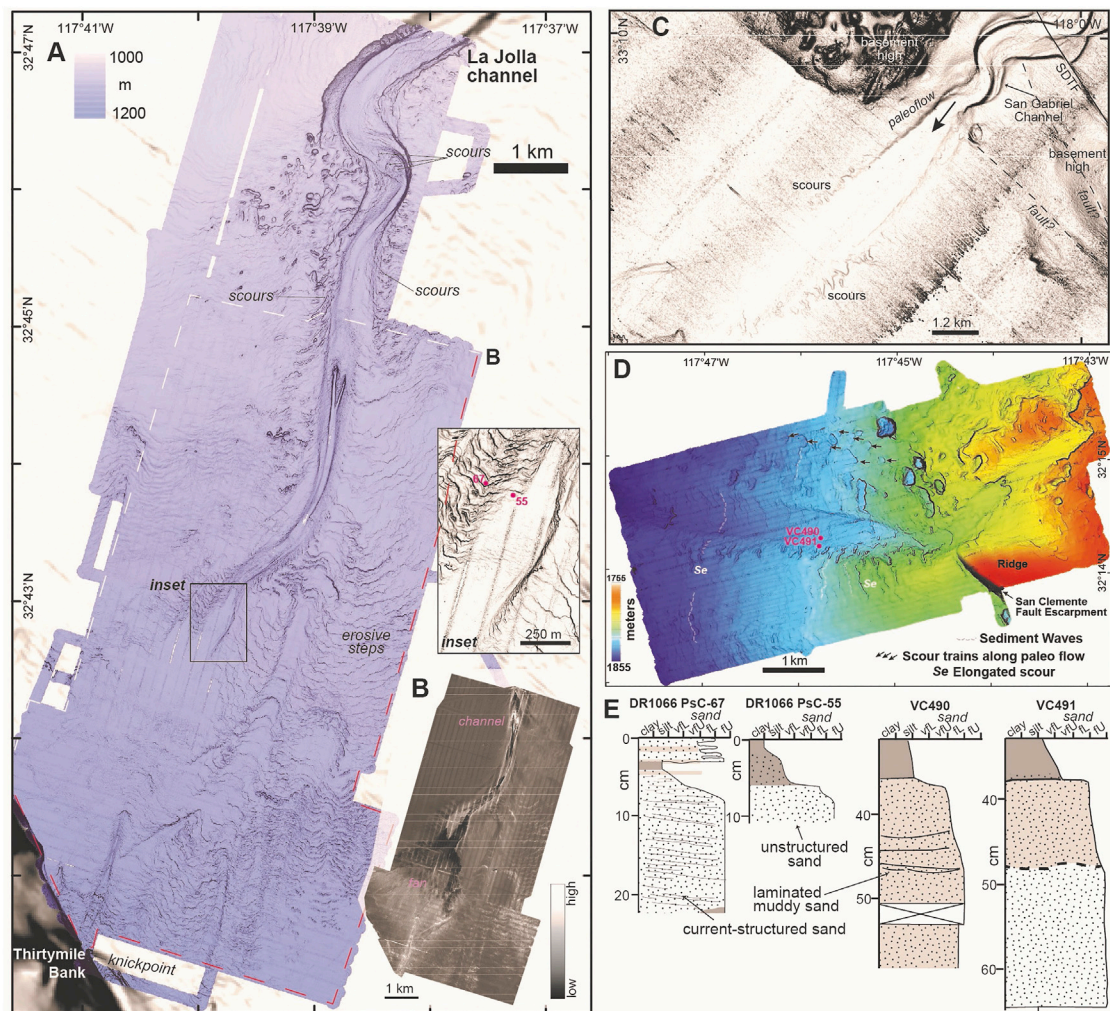


FIGURE 4 | Channel mouth expansion zone (CMEZ) examples from offshore Southern California. La Jolla Fan high-resolution (1-m grid) multibeam bathymetry **(A)** and backscatter **(B)** (modified from Maier et al., 2020). Regional bathymetry from Dartnell et al. (2015). **(C)** San Gabriel channel and fan, Catalina Basin (modified from Maier et al., 2018). **(D)** Navy Fan (modified from Carvajal et al., 2017). **(E)** Sediment cores from the Navy Fan (right; modified from Carvajal et al., 2017) and La Jolla Fan (left; from Maier et al., 2020); see inset and part **(D)**, respectively for core locations.

fan systems that route sediment across relatively steep slopes (e.g., $>0.5^\circ$; Covault et al., 2017; **Figure 2**). In many of these systems, turbidity current deposition has continued through Holocene sea-level rise via canyon incision across narrow continental shelves in this tectonically active region (e.g., Normark et al., 2009). A notable example of this is the longshore drift fed La Jolla canyon-fan (Covault et al., 2007). Here, we highlight La Jolla because 1) it has been historically important in development of canyon-fan scientific knowledge (e.g., Shepard, 1951; Normark, 1970; Piper, 1970), 2) recent examination of La Jolla channel mouth applied extensive high-resolution (1-m grid) seafloor data coverage (Maier et al., 2020) (**Figures 4A,B**), and 3) well-imaged features in La Jolla have similarities in the region (e.g., Carvajal et al., 2017; Maier et al., 2018) (**Figures 4C,D**).

High-resolution seafloor and shallow subsurface data in La Jolla Canyon (Paull et al., 2013) and fan (Maier et al., 2020) revealed the most recently active part of the La Jolla

depositional system forms a CMEZ (**Figures 4A,B**). As the channel connected to La Jolla Canyon enters the CMEZ (shift from 0.4° to 0.2°), it widens (from 150 m to 350 m), shallows (from 37 m to 3–5 m relief), and channel margins become dissected by wide (50–100 m) scours oriented perpendicular to the channel (**Figure 4A**). This widening channel morphology appears to be common in the region (Navy Fan in Carvajal et al., 2017; San Gabriel Fan in Maier et al., 2018) (**Figure 2**, **Figures 4C,D**). These share similarities with other global canyon-fan systems (e.g., Al Batha Fan in Bourget et al., 2010; Hatteras Canyon in Gardner et al., 2016; the Hudson and Wilmington Channels in Deptuck and Sylvester, 2018), and all fit with a CMEZ interpretation. In La Jolla, the wide channel-margin scours continue into laterally extensive (kms) erosive steps carved into sandy lobe deposits. These bedforms are interpreted as cyclic steps, erosional upper flow regime bedforms formed from flows not contained by the low-relief

distal channel (Fildani et al., 2021). Within the steps, scours have aligned, and are imaged at various stages of coalescing into incipient channels that are offset from, and not yet connected to, the La Jolla channel. Headless channels are also found in Monterey Fan (Normark, 1985; Klaucke et al., 2004) and San Gabriel Fan (Maier et al., 2018). Similarly, Bourget et al. (2010) interpreted the Al Batha Fan CMEZ to be dominated by scours that merged downslope into small channels. The combined La Jolla seafloor morphology, backscatter and sidescan sonar maps (Maier et al., 2020) appear similar to a braided morphology described by Ó Cofaigh et al. (2006) where the high-latitude Lofoten Channel loses confinement. Maier et al. (2020) also identified a most recent sandy lobe deposit extending as a radial fan (3×2.8 km) from the wide and shallow channel mouth across relatively flat seafloor (0.2°) with less erosional relief, but where large (up to 0.25 m height, 3–5 m width/depth) blocks are imaged. Most of the La Jolla CMEZ is dominated by erosional morphologies, with limited observation of sediment waves, which are present in the Navy Fan example to the south (Carvajal et al., 2017; Maier et al., 2020).

CMEZ in the Squamish Delta, British Columbia, Canada

The pro-delta slope of the Squamish Delta, in Howe Sound (Figure 2), is characterised by channels that widen downstream (Vendettuoli et al., 2019). The southern channel shows a marked bypass surface, prior to lobe deposition, and a reincised channel immediately updip of the bypass zone (Vendettuoli et al., 2019). The channel, bypass area, and lobe, in this system are characterised by upstream-migrating bedforms evolving during supercritical flows (Vendettuoli et al., 2019). This southern channel has been described as a CLTZ, but the flaring channel geometry, presence on a steep slope, and the lack of a significant slope break at the channel mouth, all fit with an interpretation as a CMEZ. Recent measurements of turbidity currents across kilometres from river delta to submarine lobes in the Squamish system and other fjords of British Columbia, Canada (Figure 2), provide key insights into the links between morphology, flow characteristics, frequency, and deposits (e.g., Hughes Clarke et al., 2012; Clare et al., 2016; Hughes Clarke, 2016; Hizzett et al., 2018; Vendettuoli et al., 2019; Heijnen et al., 2020). Vendettuoli et al. (2019) used repeat multibeam bathymetry to monitor >100 flows during 4 months in Squamish Delta, and less than half reached the CMEZ. As interpreted in the La Jolla Fan (Maier et al., 2020) and Rhône Fan (Droz et al., 2020), bathymetric monitoring of turbidity currents in Squamish Delta shows scours within the bedforms elongating and merging into proto-channels, progressively capturing more of flows with time (Hughes Clarke and Fedele, 2019). Vendettuoli et al. (2019) found the CMEZ to be a zone dominated by erosion in which deposits were removed by infrequent powerful flows. Erosion was largely via knickpoint retrogression, creating erosional surfaces visible as possible foresets along the CMEZ (Vendettuoli et al., 2019).

Knickpoints generated in the CMEZ propagated upstream and played a key role in channel evolution (Heijnen et al., 2020); thus, CMEZ dynamics potentially impact channel evolution and morphology along much of the system.

Linked Channel and Lobe in the Mud-Rich Congo Fan, Offshore West Africa

Large, mud-rich, river-fed submarine fans along passive margins, such as the Congo Fan (e.g., Babonneau et al., 2002; Dennielou et al., 2017), display somewhat different character at channel mouths. Wynn et al. (2002a) considered the Congo Fan to be a system without a CLTZ, and likewise, publications that are more recent have interpreted channels with attached lobes (e.g., Picot et al., 2016; Dennielou et al., 2017). Congo channel-mouth lobes have erosional bases and appear to build from connected lobe channels (~15 m relief) by bifurcation of the feeder channel (Picot et al., 2016), which Dennielou et al. (2017) interpret as facilitated by sliding at lobe sides and broad spill-over of poorly confined turbidity currents in the distal channels. Within this attached channel-lobe setting, recent bathymetric compilations across the Congo Fan, including 1-m-resolution bathymetry across parts of the active channel-lobe, reveal some features similar to the La Jolla and Rhône fans. These include wide, flat and shallow channels (up to 5 km wide, $\sim 0.14^\circ$, 8 m deep), knickpoints, sediment waves, blocks (5–10 m wide, 3 m high) with adjacent scours, and other signs of erosion or mass failure (Dennielou et al., 2017).

Plunge Pools at the Base of Slope, Offshore North America

In contrast to the examples above, the base of gullied continental slopes outside of major fan systems with large ($>4^\circ$) breaks in slope are characterised by plunge pool depressions (Lee et al., 2002). We highlight here examples offshore North America, where Lee et al. (2002) used multibeam bathymetry to document base-of-slope plunge pools on average 400 m diameter and 21 m depth, but up to 1,100 m wide and 75 m depth (Figure 2, Figure 5). These plunge pools occurred on the active tectonic margin of California and the passive margin of New Jersey. They were identified exclusively in settings with breaks in slope $>4.2^\circ$, and most commonly where breaks in slope exceed 9.8° (Lee et al., 2002). Additional coverage of continental margins with multibeam bathymetry along Cascadia (Nelson et al., 2000; Patton et al., 2013) and Gulf of Alaska (Mayer and Gardner, 2016) margins also revealed base-of-slope plunge pools (up to 2.3 km diameter and 250 m depth) at large breaks in gradient. Similarly, carbonate depositional systems of the Bahamas contain plunge pools aligned at the base of steep ($2\text{--}20^\circ$) escarpments, where they are separated by small ridges and followed down-slope by sediment wave fields (Schnyder et al., 2018).

Plunge pool depressions have been interpreted along siliciclastic submarine canyons associated with steep knickpoints within canyon thalwegs (e.g., Gamberi and Marani, 2007; Paull et al., 2011; Harris et al., 2014), and

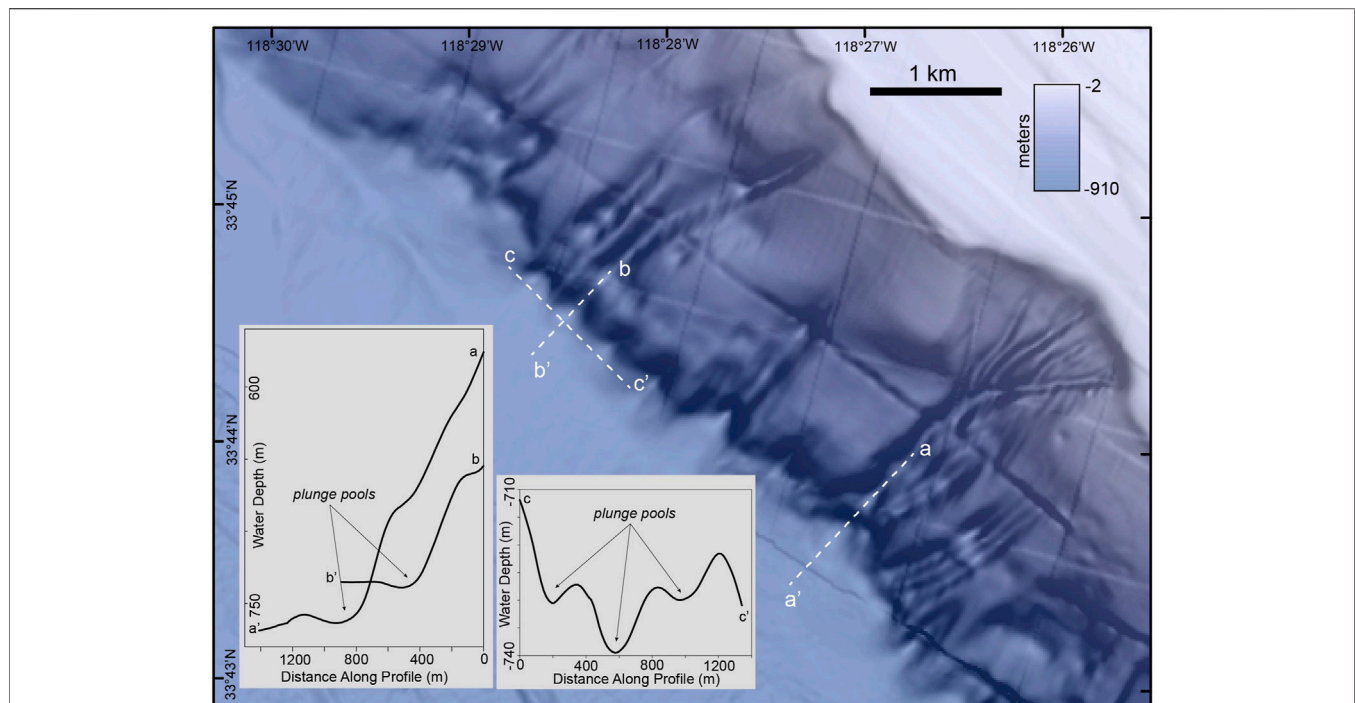


FIGURE 5 | Plunge pools at the base of slope, offshore Southern California. Map shown is colour-contoured multibeam bathymetry draped over slope-shaded bathymetry. Bathymetric grid (16 m) from Gardner and Dartnell (2002) and plunge pool interpretations after Lee et al. (2002).

plunge pools along wide carbonate canyons occur downstream from chutes (knickpoints with hundreds of metres of relief, c. f., Mulder et al., 2019; Recouvreur et al., 2021). In the central equatorial Pacific, plunge pools ~100-m-deep were recently documented where channels cross steep (5–11°) gradients and transition into sediment wave fields (Gardner et al., 2020). Plunge pools in channel and base of slope settings have been interpreted to form from down-slope sediment density flows that scour on impact at the base of slope, or they scour and deposit at a hydraulic jump caused by the break in slope, or both (Lee et al., 2002), although carbonate examples may also be influenced by erodibility of sediment and changes in underlying rock lithology (e.g., Schnyder et al., 2018; Mulder et al., 2019).

INSIGHTS FROM PHYSICAL EXPERIMENTS, NUMERICAL SIMULATIONS AND REAL-WORLD FLOW MEASUREMENTS

Process Studies of Channel Mouth Settings

Process studies on channel mouth settings have been predominantly undertaken using physical modelling (e.g., Pohl et al., 2019; Spychala et al., 2020; Lang et al., 2021). In addition, there is a broader body of experimental work on density flows crossing slope breaks (e.g., García and Parker, 1989; García, 1993; Gray et al., 2005; Gray et al., 2006; Pohl et al., 2020), which can

provide insights into channel mouth processes. No flow measurements have been reported in natural deep-sea channel mouth settings. However, the dynamics of gravity flows undergoing hydraulic jumps over scours within a subaqueous channel system has been examined (Sumner et al., 2013; Dorrell et al., 2016). Alongside these experiments and field measurements, we highlight numerical simulations and physical experiments where flows change from supercritical to subcritical in the absence of a hydraulic jump (García, 1993; Kostic and Parker, 2006; Kostic and Parker, 2007; Salinas et al., 2020), and discuss the potential implications for channel mouth settings.

Supercritical Versus Subcritical CLTZs?

It has been argued for CLTZs that these differ as a function of the Froude (*Fr*) number, with supercritical CLTZs varying from subcritical examples (Postma et al., 2016). This view is based in part on supercritical fan experiments on steep continuous slopes (Hamilton et al., 2015; Hamilton et al., 2017). Deposition at the channel mouth forms a mouth bar, leading to development of a hydraulic jump which retrogrades with associated upstream retreat of the channel-lobe transition zone (Hamilton et al., 2015; Hamilton et al., 2017). Such processes are characterised by erosive channels, and bedload-dominated systems, on steep slopes (Hamilton et al., 2017). Postma et al. (2016) contrast such supercritical systems with subcritical systems dominated by levee construction, and thus suspension-dominated load, where the channel-lobe transition is controlled by a slope break (Fernandez et al., 2014). These experiments examined

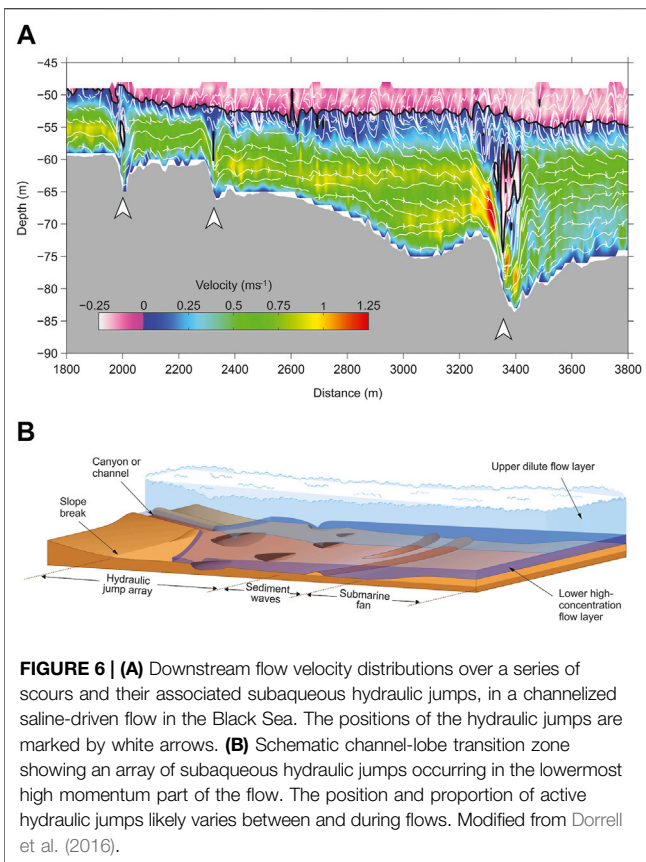


FIGURE 6 | (A) Downstream flow velocity distributions over a series of scours and their associated subaqueous hydraulic jumps, in a channelized saline-driven flow in the Black Sea. The positions of the hydraulic jumps are marked by white arrows. **(B)** Schematic channel-lobe transition zone showing an array of subaqueous hydraulic jumps occurring in the lowermost high momentum part of the flow. The position and proportion of active hydraulic jumps likely varies between and during flows. Modified from Dorrell et al. (2016).

entire submarine fans, and as such are not primarily focused on the mechanics at the channel mouth. Here we focus on the mechanics of flow and sedimentary processes within channel mouth settings, whilst considering flow criticality and breaks of slope. A number of different processes have been proposed to dominate channel mouth settings, and we consider each in turn, prior to introducing some possible additional mechanisms.

Hydraulic Jumps and Hydraulic Jump Arrays at Breaks in Slope

Experimental studies of hydraulic jumps at two-dimensional slope breaks, in net depositional fine-grained turbidity currents, show dramatic thickening and deceleration of the flow, leading to a rapid drop in bed shear stresses immediately downstream of the jump (García and Parker, 1989; García, 1993). Therefore, bedload deposition is predicted to occur rapidly downstream of the jump, but for fine-grained suspended sediment deposition may take place over distances in excess of 1,000 times the jump height (García and Parker, 1989; García, 1993). Measurements of natural subaqueous hydraulic jumps has only been undertaken in saline flows in a channel in the Black Sea, where the jumps were associated with seafloor scours (Figure 6A; Sumner et al., 2013; Dorrell et al., 2016). These flows had much lower incoming Froude numbers than the aforementioned experiments, and showed repeating hydraulic jumps, with flows becoming critical again over ~10 scour lengths. Flow

measurements showed large vertical velocities, enhanced mixing, and in contrast to the experiments, showed maintenance of near-bed shear stresses downstream of the jumps (Sumner et al., 2013; Dorrell et al., 2016). Thus, suspended sediment will be mixed and moved upwards within the flow immediately downstream of the jump, and erosion rates and flow capacity maintained, enabling bypass zones to develop. In the Black Sea, subaqueous hydraulic jumps only affected the lower part of the flow, with bypass of flow above the jump, raising the possibility that in larger flows hydraulic jumps may only affect a comparatively small fraction of the stratified flow, associated with the bulk of the momentum (Dorrell et al., 2016). These results suggest that for steep slopes with high incoming Froude numbers, just a single hydraulic jump will occur, which would fit with plunge pool formation (e.g., Lee et al., 2002; Gardner et al., 2020). In contrast, for incoming supercritical flows with Froude numbers close to unity at a slope break, then an array of hydraulic jumps will form, each associated with a scour (Figure 6B). For a given set of flow conditions, only a subset of the scours will likely have active hydraulic jumps (Figure 6B; cf. Macdonald et al., 2011a). Dorrell et al. (2016) further suggested that in the case of mud-rich channelized systems, spatial and temporal variation in the position of these stratified, subaqueous hydraulic jumps may account for the lack of an obvious supercritical to subcritical transition, and the associated absence of CLTZs, in some of these systems.

Flows Across Continuous Slopes Without Hydraulic Jumps

The influence of loss of flow confinement has been examined by comparing an instantaneous transition from a leveed channel to an unconfined setting, in the absence of a slope break, to a continuous channel over the same area (Pohl et al., 2019). These experiments showed that erosion was considerably larger in the unconfined case over a distance of ~2.5 channel widths, than at the equivalent point in the continuous channel (Pohl et al., 2019). A 'flow relaxation' mechanism is proposed where the pressure gradient expands the flow laterally, leading to the flow moving closer to the bed, lowering the height of the velocity maximum, and thus increasing basal shear stresses and enhancing erosion (Figure 7). Scours are proposed to be triggered by random irregularities on the seafloor. The experiments used the Shields scaling approach (De Leeuw et al., 2016) to balance the applied fluid shear stress and the gravity force acting on particles, thus enabling particles to remain in suspension. Sediments consisted of silt and sand up to 500 μm necessitating an 11° slope and volumetric concentrations of 17%. Froude numbers are not reported. However, consideration of the flow height and associated depth-averaged velocity, and excess density (280 kg m^{-3}) suggests that flow is subcritical, in accordance with the lack of observations of a hydraulic jump.

The flow relaxation model is in part conceptual as there are a lack of direct measurements of the vertical and lateral flow components, as the velocity measurement was undertaken using one-component probes orientated at 60° relative to the maximum bed slope. Furthermore, in order to derive

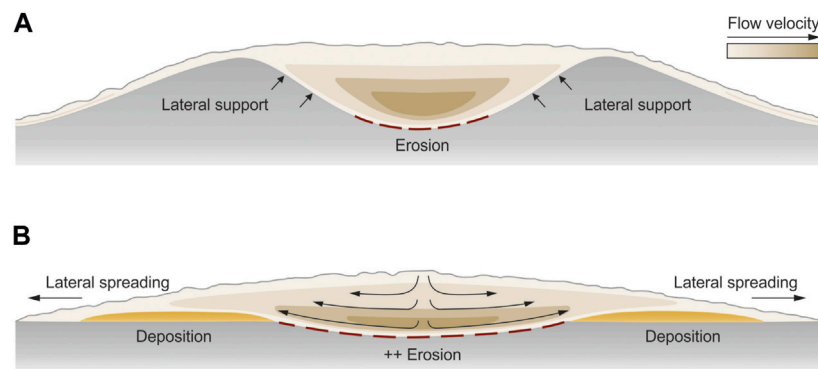


FIGURE 7 | The flow relaxation model. **(A)** Confined flow in a reference experiment at the same point on the slope as in **(B)**. **(B)** Largely unconfined flow downstream of a loss of confinement, marked by flow relaxation consisting of lateral spreading and downward movement of flow towards the base, lowering the position of the downstream velocity maximum, and therefore increasing basal shear stresses and enhancing erosion. Modified from Pohl et al. (2019).

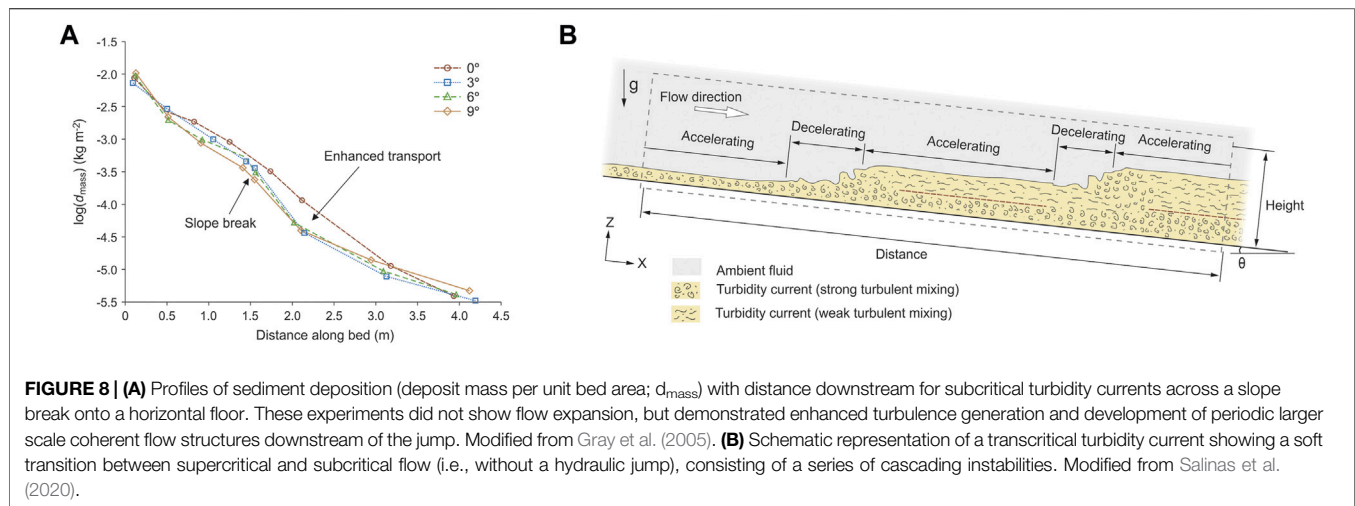
downstream velocities from such angled probes an assumption is made that net vertical velocity, and net lateral velocity, are zero, in agreement with flows of constant width and thickness on slopes (e.g., Gray et al., 2005). Consequently, if the model is correct that there is a net vertical motion of fluid towards the bed because of lateral flow, which increases in magnitude as the bed is approached (Figure 7B), then the calculated downstream velocities used to predict bed shear stresses will be inaccurate, with inaccuracies increasing towards the bed. This raises questions about the validity of the shear stress calculations given the sensitivity of these to the shapes of the velocity profiles (e.g., Yu and Tan, 2006). An alternative explanation, or a potential additional process that may contribute to the observed processes in the Pohl et al. (2019) experiments, is density stratification induced changes in velocity profiles in response to the velocity decrease. Stratification is known to increase as flows decelerate, and this leads to a lowering of the velocity maximum in turbidity currents (Wells and Dorrell, 2021). Given the very high depth-averaged concentrations (17% by volume) in these experiments, then this effect is likely to be considerable. In contrast, real-world flows are estimated to have bulk densities 1 to 2 orders of magnitude lower than these experiments (e.g., Konsoer et al., 2013; Peakall and Sumner, 2015; Simmons et al., 2020), and therefore this process will be less important. That said, stratification may lead to the lowermost parts of flows still having high sediment concentrations in certain cases (Peakall and Sumner, 2015; Wells and Dorrell, 2021), and thus this process may be important towards the base of natural turbidity currents.

Lang et al. (2021) also undertook density current experiments with a similar instantaneous transition from a channel to a slope (10°), in the absence of a slope break. The experiments, however, differ in their parameters relative to those of Pohl et al. (2019). The Lang et al. (2021) flows were supercritical throughout the measurement section, were depositional (several cm hr^{-1}), and were mixed saline-particulate suspensions (excess density 50 kg m^{-3} 1/3rd sediment, 2/3rd saline). The sediment built a channel extending beyond the fixed channel, and this widened over a distance of a metre from $\sim 20 \text{ cm}$ (the fixed channel width)

to $\sim 36 \text{ cm}$; this channel was filled with antidunes. Downstream of this widening constructional channel mouth is a lobe similarly covered in antidunes in proximal areas, and asymmetrical in-phase bedforms in distal parts, interpreted as supercritical dunes (Fedele et al., 2016; Lang et al., 2021). Lang et al. (2021) used a 3-component velocity measurement technique, and observed no lowering of the velocity maximum, even though the flow expanded laterally by $\sim 8.9^\circ$ in the initial metre, and presumably continued with a similar expansion rate.

Flows Across Slope Breaks in the Absence of Hydraulic Jumps

Recent work by Spychala et al. (2020) and Pohl et al. (2020) have used the Shields scaling approach to examine the nature and extent of flow bypass at a slope break, with and without flow expansion at the channel termination, respectively. Pohl et al. (2020) used a two-dimensional setup with no flow expansion at the slope break and varied the up-dip and down-dip slope angles whilst maintaining a constant discharge and flow concentration (17% by volume). The work shows that the slope break angle alone is a poor guide for determining the length of the bypass zone. Instead, higher up-dip slope angles extend the bypass zone basinward, whilst the angle of the lower slope controls the thickness of the down-dip deposits. A Froude number is only reported for a single case, giving a supercritical value of 2.3 (Pohl et al., 2020). However, there are a number of issues with this estimate: 1) the top of the flow does not appear to be captured (see Pohl et al., 2020, supplementary); 2) vertical velocities are assumed to be negligible even though the flow will decelerate and thicken across the slope break which by flow continuity will lead to significant vertical velocities. This leads to over-estimation of downstream velocities; 3) flow depth estimates are based on a bespoke methodology (see also Pohl et al., 2019), by taking the height to the point at which the velocity drops to half of that at the velocity maximum. This approach is equivalent to the widely used methodology for non-dimensionalising velocity profiles from runs with different flow depths (Lauder and



Rodi, 1983; Buckee et al., 2001; Gray et al., 2005). This method gives values approximately half of the true thickness (see Pohl et al., 2020, their Figure 5); 4) in turn, the depth-averaged velocity is calculated for that part of the flow below this depth, leading to a value approximately twice that of the whole flow. Adjusting for these aspects suggests that the flows were likely subcritical, in keeping with the absence of hydraulic jumps within the experiments (note that the upstream migrating “rollers” observed in a few experiments appear to be a reflected supercritical bore formed from a collapsing incoming subcritical flow; Edwards, 1993; Edwards et al., 1994).

The experiments of Spychala et al. (2020) allowed flow expansion at the channel terminus/slope break, and varied the down-dip slope angle, flow concentration (13–19% by volume) and discharge. They show that the CLTZ length increases with higher concentration and higher discharge flows, and decreases with increasing basin floor angle; this latter result is in contrast to the aforementioned 2D experiments of Pohl et al. (2020). Note that no Froude numbers are reported in Spychala et al. (2020). However, the absence of hydraulic jumps suggests that these flows are all subcritical.

Whilst the experiments of Pohl et al. (2020) and Spychala et al. (2020) examine the controlling parameters on bypass zone/CLTZ length, they do not describe the underlying flow mechanics. Gray et al. (2005), Gray et al. (2006) examined subcritical turbidity currents (1% volumetric concentration; 40–110 μm size range) across slope breaks (3°, 6°, 9°) onto a horizontal floor, in a fixed width tank. As such, there was no flow expansion. Velocity was measured in a two-component (downstream and vertical/bed-normal) grid. At, and immediately beyond, the slope break they showed that the basal part of the flow below the velocity maximum slowed rapidly, whilst the upper part was less affected. The rapidly slowing basal flow produced enhanced turbulence, whereas the upper part was characterised by the development of periodic large coherent flow structures. The currents were net depositional, but deposition was significantly reduced by about 1.75 channel widths downstream of the slope

break (Figure 8A), and linked to enhanced sediment suspension caused by increased turbulence at the slope break (Gray et al., 2005). In the lowermost parts of the flow, mean bed normal (vertical) velocities at the slope break were towards the bed (see Gray et al., 2006, their Figure 9), and became upward directed by the point where sedimentation is reduced (see Gray et al., 2006, their Figure 5B). For a flow that is not net depositional, this additional turbulence, both in terms of the total kinetic energy and the large scale coherent structures, may be expected to lead to an erosional zone downstream of the slope break, with variations in turbulence potentially triggering localised scouring within this zone.

Transition From Supercritical to Subcritical Flow Without a Hydraulic Jump

In some experiments and simulations of coarse-grained supercritical turbidity currents encountering a slope break, a hydraulic jump was not observed (García, 1989; García, 1993; Kostic and Parker, 2006; Kostic and Parker, 2007). In such cases, where settling velocity and thus sedimentation are very high the flow has been shown to be unable to undergo a hydraulic jump (Kostic and Parker, 2006; Kostic and Parker, 2007). However, this situation is unlikely to apply to CLTZs, or CMEZs, given their dominantly erosional nature. Nevertheless recent work has illustrated that there may be a mechanism by which finer-grained flows can transition from supercritical to subcritical flows in the absence of a hydraulic jump (Salinas et al., 2020). They used a direct numerical simulation of subaqueous dilute particulate density currents (concentration is not given; particles have zero settling velocity), on a constant slope (0.72°), and showed a change from supercritical to subcritical flow in the absence of a hydraulic jump. Salinas et al. (2020) referred to this as a ‘soft transition’, and it is associated with a transcritical flow characterised by a series of intermittent cascading instabilities (Figure 8B). Basal shear stress is shown to increase and decrease in a cyclical fashion reflecting these instabilities. Salinas et al. (2020) note that the associated cyclicity wavelengths (~60–140

flow depths; this will vary with slope angle) are consistent with sediment wave spacing. However, given more erosive conditions, this cyclicity might also be associated with periodic erosion. In these cases, there would then be a feedback between the flow and the aggradational/erosional bedforms, and it is unclear whether a transcritical flow state would be maintained.

Summary of Physical Experiments, Numerical Simulations and Real-World Flow Measurements

Process studies have identified a variety of mechanisms that may influence the nature of flows as they transition from channels to lobes. Many of these are dependent on the criticality of the flow, and the presence or absence of a pronounced break of slope. Supercritical flow on a relatively smooth slope produced channel mouth widening populated by a range of supercritical bedforms (i.e., a CMEZ) (Lang et al., 2021). Supercritical to subcritical transitions across a slope break may be associated with the production of a single hydraulic jump, as in plunge pools, if the incoming flow has a high Froude number (e.g., García, 1993) and the slope break angle is high (e.g., $>4^\circ$; Lee et al., 2002). Alternatively, an array of linked hydraulic jumps over broader CLTZs develop if the incoming flow has a Froude number closer to unity (Sumner et al., 2013; Dorrell et al., 2016) and likely a lower slope break angle. Single jumps across slope breaks are associated with decreased bed shear stress, and predicted enhanced sedimentation, downstream of the jump (García and Parker, 1989; García, 1993), although these are in 2D experiments that lack flow expansion. In contrast, arrays of hydraulic jumps have been shown to maintain bed shear stress downstream of the jumps (Dorrell et al., 2016).

If the up-dip flow is already subcritical, then channel mouth settings can be triggered by a slope break, a loss of confinement, or a combination of the two. Rapid deceleration of subcritical flow caused by a slope break has been shown to enhance turbulence generation at the base of the flow (Gray et al., 2005; Gray et al., 2006), albeit these were in 2D experiments. Where deceleration occurs as a result of flow expansion, in the absence of a slope break, bed shear stress is

postulated to increase, as a result of flow relaxation (Pohl et al., 2019), and/or density stratification induced lowering of the downstream velocity maximum (Wells and Dorrell, 2021) if the flow is sufficiently dense, as argued herein.

Flows may undergo a transition from supercritical to subcritical without undergoing a hydraulic jump(s) (Kostic and Parker, 2006; Kostic and Parker, 2007; Salinas et al., 2020), albeit in some cases these are associated with rapidly depositing flows that will not typically be associated with CLTZs or CMEZs. Intriguingly, Salinas et al. (2020) show that this change in Froude number state can occur via a 'soft transition' of cascading instabilities that are associated with cyclical variations in bed shear stress over wavelengths of 10–100s of flow depths. We propose that this may offer an alternative or additional process to explain the arrays of erosive scours observed in many CLTZs.

CHANNEL MOUTH SETTINGS INTERPRETED IN ANCIENT OUTCROP AND SUBSURFACE

The dominance of erosion, lack of stratigraphic completeness, and minimal preservation within modern channel mouth settings highlights the difficulty in their identification in outcrop and subsurface datasets, despite their distinct seafloor morphology and features. Furthermore, palaeogeographic context is rarely sufficient to discount some degree of attachment between submarine channels and lobes at the time of deposition, differentiating scour- and channel-fills can be difficult (Figure 9), and basinward propagation of related channels suggests that the preservation potential of channel mouth setting should be low (Hodgson et al., 2016; Pemberton et al., 2016). Therefore, outcrop examples of interpreted plunge pools and CLTZs are rare. Nonetheless, there is a growing literature on interpreted exhumed CLTZs, and their stratigraphic expression range from (composite) erosion surfaces separating underlying lobes and overlying channel-levee systems (e.g., Gardner et al., 2003) to thicker records of deposition with scour-fills and aggradational beds (e.g., Navarro and Arnott, 2020)

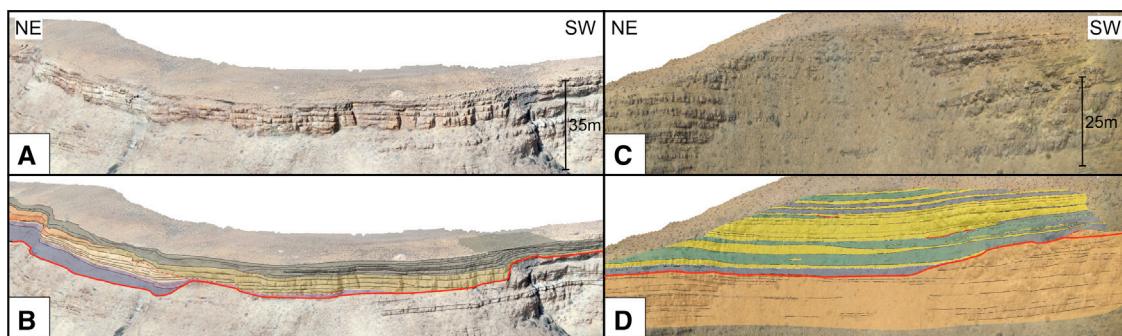


FIGURE 9 | Images from photogrammetric models built from uncrewed aerial vehicle images of giant scour-fills in interpreted channel-lobe transition zones. (A) uninterpreted and (B) interpreted images of scour-fill in Fan 3 at Kleine Reit Fonteijn, Tanqua Depocentre, Karoo Basin and (C) Uninterpreted and (D) interpreted images of a scour-fill in Unit A5 at Wilgerhout, Laingsburg Depocentre, Karoo Basin. Colours relate to sedimentary facies, which are described in detail in Hofstra et al. (2015).

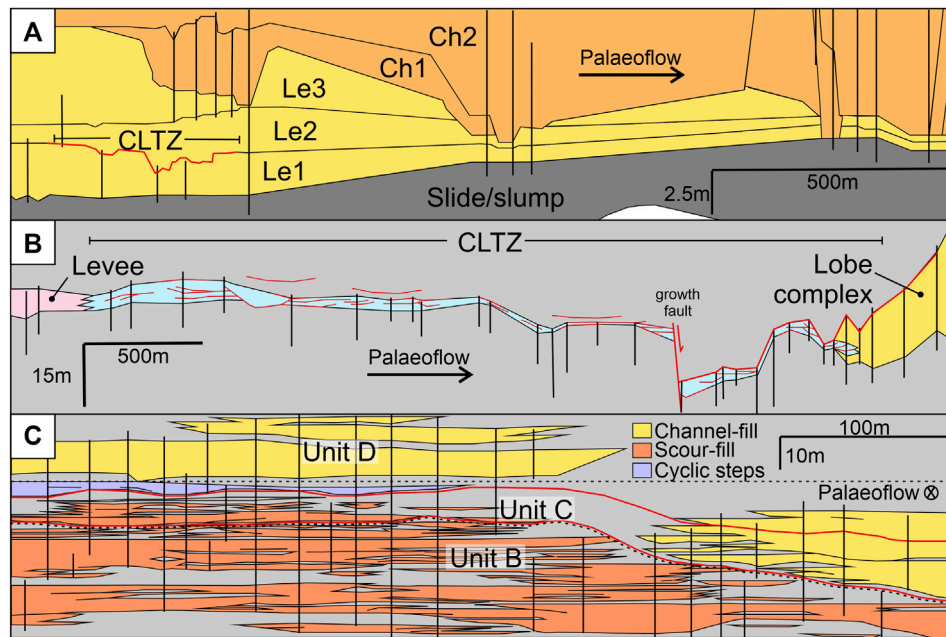


FIGURE 10 | Compilation of outcrop panels of interpreted channel mouth settings, where black vertical lines are locations of measured sections. **(A)** A CLTZ as a surface as the base of lobe element (Le) 2 at the Bridges of Ross outcrop, Loop Head Peninsula, County Clare, western Ireland (adapted from Pyles et al., 2014). **(B)** A thin CLTZ in Unit E3, Fort Brown Formation, Laingsburg depocentre, Karoo Basin, South Africa, in a base-of-slope location (adapted from Brooks et al., 2018). Red lines are scour surfaces, and the aquamarine unit is the interpreted CLTZ, which is < 10 m thick. Note the growth fault, and the abrupt thickening downdip of the sand-rich lobe complex (yellow). **(C)** A thicker succession recording the overall progradation of a lower slope succession with a large number of scour-fills, and local cyclic steps, below and adjacent to stacking channel elements from the Tres Pasos Formation, Magallanes retroarc foreland basin in southern Chile (adapted from Pemberton et al., 2016). Herein we suggest that this is a candidate CMEZ.

(Figure 10). This range of expressions suggests that the transfer and preservation of different channel mouth settings into the rock record is characterised by a range of controls and physiographic configurations.

Exhumed Plunge Pool-Fills

Lee et al. (2004) interpret deep scour-fills in the Peira Cava outlier (Eocene-Oligocene; Annot Sandstones), SE France, as plunge pool-fills. These decametre-thick sandstone bodies developed in base-of-slope settings in a foreland basin close to basin margins and immediately downstream from an inferred break-in-slope. The sandstone bodies comprise a complex basal unit of laterally pinching or inter-fingering debrites and turbidites, which is overlain abruptly by a single, thick normally graded turbidite. One sandstone body pinches out laterally in a few hundred metres and sits within a deep (>20 m) spoon-shaped erosional scour.

Henstra et al. (2016) document pervasive spoon-shaped scour-and-fill features at the base of the depositional slope in the Middle Jurassic to Lower Cretaceous Wollaston Forland half-graben, NE Greenland. They interpret the scour-fills as plunge pool-fills that formed from (and filled by) high-density supercritical turbidity currents that were forced to decelerate and undergo a hydraulic jump at the base of steep slopes.

Exhumed CLTZs as Surfaces

Several studies suggest that the expression of the CLTZ in a stratigraphic succession is a single (or composite) erosion surface

that separates underlying lobes from overlying channel fills and levees. For example, Gardner et al. (2003) use outcrops of the Permian Brushy Canyon Formation, Texas, United States, to interpret basinward then landward migration of the CLTZ by the vertical association of sandstone lobes overlain by an erosion surface and channel fills, which are capped by sandstone lobes. Hodgson et al. (2016) show several examples of frontal lobes abruptly overlain by external levee successions from the Permian Karoo Basin, which are used as evidence of basinward channel-levee propagation. The scoured surface mantled with mudclast lags separating the lobes and external levees is interpreted as the stratigraphic expression of the CLTZ. Pyles et al. (2014) used digital surveying and sedimentary logging to assess the juxtaposition of lobes and channel-fills at the Bridges of Ross outcrop in the Clare Basin, western Ireland. The upward succession at the Bridges of Ross outcrop begins with a slump (the Ross Slump), which is overlain by compensationally-stacked lobe elements that are in turn overlain by channel-fill elements (Figure 10). This succession records the stratigraphic transition from basin-floor (upper Ross Sandstone) to lower slope (Gull Island Formation). The only CLTZ they identify at outcrop is the basal surface of one of the compensationally-stacked lobe elements, which is mantled by several closely spaced megaflutes (Figure 10).

Exhumed Thin CLTZs (< 10 m Thick)

An example of a thin CLTZ is sub-unit E3 of the Fort Brown Formation, Karoo Basin, South Africa (Van der Merwe et al.,

2014). The outcrops preserve a juxtaposition of depositional and erosional elements within a < 10 m-thick unit. Intraformational sand- and mud-clast deposits are located throughout the section and interpreted as lags that record sediment bypass (Brooks et al., 2018), and supports interpretation of an erosion-dominated CLTZ (Figure 10). Metre thick, but heavily scoured sandstone beds share affinities with subcritical sediment waves identified in an interpreted CLTZ in the older Unit B stratigraphy (Hofstra et al., 2018). Sand-rich hybrid beds are noted in the proximal lobe immediately down-dip of the CLTZ where sub-unit E3 thickens abruptly (Brooks et al., 2018). The mapping of internal erosion surfaces demonstrated migration, and contraction or expansion, of the CLTZ (Brooks et al., 2018). The presence of a growth fault in this base-of-slope setting likely increased the gradient change to form this well-preserved CLTZ (Figure 10).

Exhumed Thick CLTZs (>10 m Thick)

Thicker records of interpreted CLTZs, with aggradational beds in close association with scour-fill features, have been identified where outcrop quality permits up-dip channel-complexes and down-dip lobe complexes to be mapped (e.g., Ito, 2008; Hofstra et al., 2015; Pemberton et al., 2016) or are inferred from stratigraphic relationships (e.g., Navarro and Arnott, 2020). Hofstra et al. (2015) presented recognition criteria to distinguish (giant) scour-fills from channel-fills to support interpretation of CLTZs in the Karoo Basin, South Africa. The preservation of the scour-fills (Figure 9) was attributed to their location with respect to the propagation direction of the feeder channel.

Navarro and Arnott (2020) document the stratigraphic transition from basin floor (Kaza Group) to slope (Isaac Formation) strata, which is marked by three stacked interpreted CLTZs. The lower and upper CLTZs contain more scour-fills. In contrast, the middle CLTZ has more tabular sandstone elements, which Navarro and Arnott (2020) interpret as a poorly-developed channel-lobe transition zone, resulting from inefficient, siliciclastic-rich depositional flows. The formation of multiple CLTZs with different characteristics is interpreted by Navarro and Arnott (2020) to record relative sea-level changes, and the associated changes in sediment supply and flow characteristics.

The preservation of a thicker stratigraphic record for CLTZs has been explained by high aggradation rates (e.g., Pemberton et al., 2016; Figure 10), tectonically-active settings (Ito, 2008; Mansor and Amir Hassan, 2021; Brooks et al., 2022), rapid abandonment or avulsion of feeder channels before erosion into the CLTZ (e.g., Hofstra et al., 2015; Brooks et al., 2018), or a large-scale passive margin setting allowing more net aggradation (Navarro and Arnott, 2020). Nonetheless, these studies also interpret lobes and channel-fills as part of the stratigraphic succession, which points to an aggrading and interfingering succession where the CLTZ is relatively fixed, and preserved as surfaces and thinner stratigraphic units as part of a thicker succession.

Subsurface CLTZs

There are additional challenges in the identification of channel mouth settings in the subsurface given the typical resolution of

seismic reflection data, and the scarcity of core and well intersections. Hansen et al. (2021a) used core observations to support interpretation of a 12 m thick CLTZ in the late Cretaceous Lysing Formation, offshore Norway. Observations included the presence of erosion surfaces and abundance of cross-stratified glauconite-rich sandstones interbedded with predominantly sandy bioturbated heterolithics, as well as the abundance of very fine- and medium- to coarse-grained sandstones, and the absence of fine-grained sand sizes. They interpreted the glauconite-rich cross-stratified bed types as bedforms that migrated, possibly at the base of scours, in a CLTZ setting. Based on the wells, seismic reflection data, including spectral decomposition, the CLTZ is constrained to a 5 × 3 km area, and formed on a break-in-slope above a stepped post-rift slope profile.

Wang et al. (2020) employed high-resolution 3D seismic reflection data from the Qiongdongnan Basin (South China Sea) to document downstream changes in bedforms through an interpreted CLTZ. Wang et al. (2020) document scours (1.2–5.6 m deep) at the bifurcation points of distributive channels, and steps at the confluence points, which they interpret as forming by supercritical flows and hydraulic jumps. Although in the absence of core data, the sedimentary facies of the seismically resolved bedforms remains unconstrained.

DISCUSSION

A New Classification of Submarine Channel Mouth Settings

Seafloor examples highlighted herein illustrate a range of morphologies and deposits likely resulting from different flow processes. Erosional (cyclic step) and depositional (sediment wave) bedforms dominate CMEZs from delta foreset slopes, continental slopes, and associated canyons (e.g., Covault et al., 2017; Vendettuoli et al., 2019; Fildani et al., 2021). The presence of these bedforms suggests that turbidity currents exiting or overbanking low-relief channels are supercritical, and may either undergo hydraulic jumps or still be supercritical at the point of flow expansion, creating upper flow regime bedforms. For example, in settings like the La Jolla Fan (Maier et al., 2020) and Squamish Delta (Vendettuoli et al., 2019), without a clear single break in gradient across a relatively high slope, the flows that formed the widening channel, sediment waves, and erosional step morphologies were likely supercritical, resulting in a CMEZ where flows lost confinement.

Base of slope breaks, or changes in gradient on the basin floor, appear to favour flows that are either already subcritical, or are sites for the rapid transition of flows from supercritical to subcritical conditions (Figure 11). This results in the development of broad “classic” CLTZs, such as the Rhône Fan (e.g., Droz et al., 2020), with multiple scours and sediment waves. Where the incoming slope gradient is particularly high (e.g., >4°; Lee et al., 2002), a single hydraulic jump is likely to form and develop plunge pool morphology at the base of slope (Figure 11). Conversely, large canyon-fan systems where channels extend

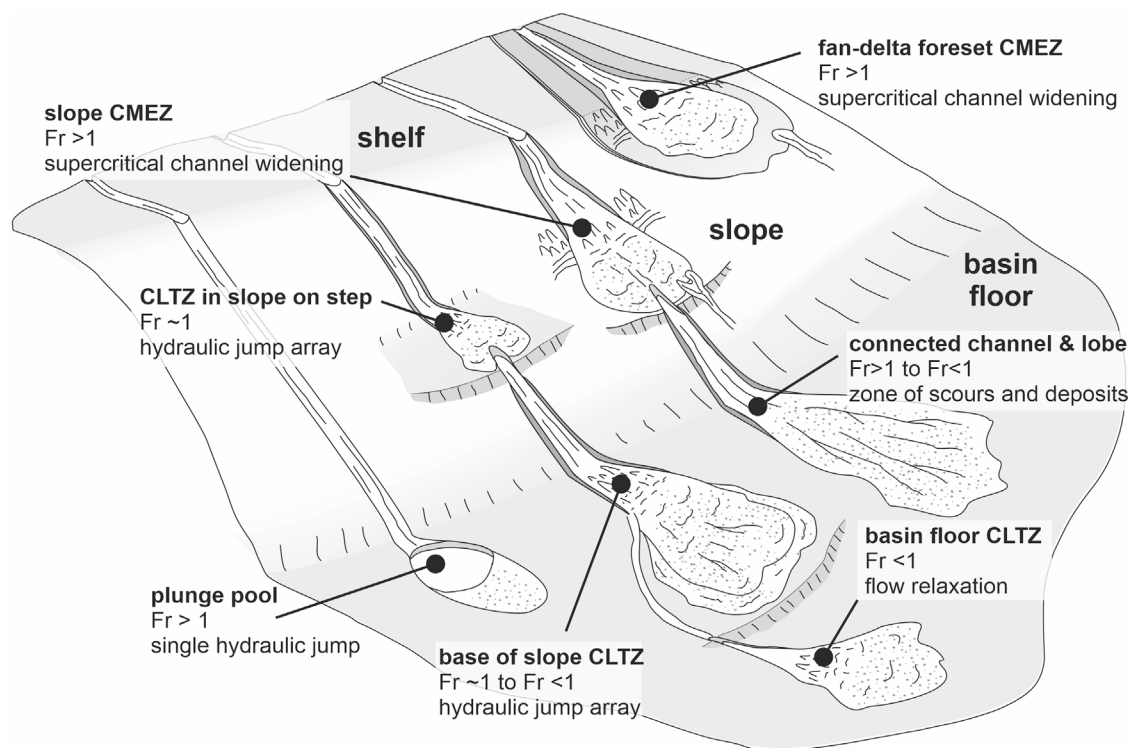


FIGURE 11 | A synthesis of different types of channel mouth settings, their likely physiographic location, and dominant flow type in terms of flow criticality. Channel mouth expansion zones (CMEZs) are present on steep slopes, including foresets of fan deltas, and are dominated by supercritical flows and bedforms. Plunge pools are located at the base of steep slopes forming a single hydraulic jump, and with flow having supercritical Froude numbers. Note that plunge pools can also form within canyons where they are related to features such as knickpoints. Channel-lobe transition zones (CLTZs) with hydraulic jump arrays form at breaks-of-slope, with supercritical flows closer to unity. Subcritical CLTZs associated with flow relaxation, typically form in relatively distal locations at points of flow expansion. Channels and lobes can also be connected, without a transition zone developing, at the base of slope with mixed erosional and depositional processes.

hundreds of kilometres onto the relatively flat basin floor, such as the Congo example (Denniellou et al., 2017), may be prone to subcritical flows, or “soft transitions”, that facilitate linked channel-lobe complexes and the absence of CLTZs (Figure 11).

The importance of supercritical aggradational bedforms in CLTZs that develop beyond the slope break is less clear. In part, this is due to the lack of high-resolution studies from these more basinward locations. Nonetheless, the amount of gradient change at a break in slope appears to be a key driver of channel mouth morphology and processes, with high gradients along channel reaches related to plunge pools (e.g., Lee et al., 2002) or development of a CLTZ (e.g., Droz et al., 2020).

The present analysis suggests a four-fold classification of channel mouth settings, expanding on the concept of supercritical and subcritical CLTZs of Postma et al. (2016). These four types are: 1) supercritical CMEZs on slopes; 2) plunge pools at steep slope breaks with high incoming supercritical Froude numbers; 3) CLTZs with arrays of hydraulic jumps at slope breaks with incoming supercritical Froude numbers closer to unity; and, 4) subcritical CLTZs associated with slope breaks and or flow expansion (Figure 11). In turn, these types of channel mouth settings will preferentially be associated with different physiographic

positions, reflecting changes in flow Froude number and slope variability (e.g., Pirmez and Imran, 2003; Dorrell et al., 2013). On continental slopes, flows are likely supercritical and CMEZs may be favoured. Hydraulic jump arrays, or plunge pools are likely favoured at the continental slope break, and enhanced turbulence and a lowered velocity maximum (flow relaxation/density stratification induced lowering) would be favoured in distal transitions out on the basin floor (Figure 11). Channels and lobes can be connected, without a transition zone developing, where erosional and depositional processes alternate (Figure 11).

Dynamic Settings and Building a Stratigraphic Record

The linked morphology and process classification provides useful ideas for further study. However, it should be noted that they can occur within a single system on the seafloor (e.g., CMEZ at the head of the San Gabriel Fan CLTZ, Maier et al., 2018). Furthermore, CLTZs and CMEZs appear to be complicated areas of flow-topography interactions that change flow-by-flow. This raises the issue of preservation potential of morphologies and deposits observed on the modern seafloor. Despite the longevity of some scours (Macdonald et al., 2011a),

the dominantly erosional CLTZs and CMEZs have low potential to accumulate over time (e.g., Vendettuoli et al., 2019) or be preserved in the rock record (e.g., Pemberton et al., 2016). However, recognising channel mouth settings is an important aspect of deciphering system dynamics because erosion (e.g., scouring, incipient channels, knickpoints) can propagate throughout the system (Hodgson et al., 2016; Heijnen et al., 2020).

Given their morphodynamic differences, can differences in flow types, and preserved bedforms, be used to distinguish CMEZs and CLTZs? Currently, there is a disconnect between recent high-resolution studies of CMEZs on the slope and/or associated with canyons (Figures 3, 4), and the most comprehensive ancient studies, which are CLTZs on, or beyond, the base-of-slope (Figure 10). The modern studies reinforce the importance of erosion and scoured surfaces, and the presence of supercritical bedforms in characterising channel mouths in CMEZs on the slope (e.g., Carvajal et al., 2017; Maier et al., 2020; Figure 11). The transfer of CLTZs into the stratigraphic record has been interpreted in several outcrop studies. Based on these examples, recognition criteria for CLTZs in the rock record include: a typically thin stratigraphic expression; amalgamated erosional features; coarse-grained lag deposits; aggradational bedforms (i.e., subcritical sediment waves); soft-sediment deformation; interfingering or juxtaposed erosional and depositional elements; and sand-rich hybrid beds in proximal lobes (e.g., Bravo and Robles, 1995; Ito, 2008; Pyles et al., 2014; Van der Merwe et al., 2014; Hofstra et al., 2015; Brooks et al., 2018; Hofstra et al., 2018; Brooks et al., 2022). However, recognition criteria for distinguishing CLTZs and CMEZs in the rock record have not been established.

Where Are the Exhumed CMEZs?

The documentation of CMEZs on the modern seafloor provide an alternative configuration for interpretation of outcrops where surfaces and successions do not conform to either channel-levee or lobe systems. Given the steeper slopes that may be required for CMEZ development, and the focus on supercritical bedforms in the rock record, many of the well-studied exhumed tectonically-active sedimentary basins that host deep-water successions are prime candidates to consider the stratigraphic transfer of CMEZs, and their recognition criteria. Furthermore, some interpreted exhumed CLTZs have identified supercritical bedforms (Pemberton et al., 2016; Postma et al., 2016; Postma et al., 2021). Therefore, given the propensity of supercritical bedforms identified in modern CMEZs, could the presence of subcritical aggradational or supercritical bedforms be a discriminating criterion between CLTZs and CMEZs, respectively?

Challenges in recognizing exhumed CMEZs include identification of the basal surface, which is likely to have a high aspect ratio, and be composite, with scour-fills inside and outside the surface. To document this requires excellent outcrops with good 3D control. The associated up-dip channels might have propagated basinward and the headless channels imaged on the modern seafloor might work updip and connect, removing much of the axial record. Furthermore, resolving a (lower) slope setting

versus basin-floor requires excellent palaeogeographic context. Nonetheless, we propose that several exhumed examples are reassessed as CMEZs based on their characteristics, including the presence of supercritical bedforms.

Postma et al. (2021) document a range of supercritical flow bedforms, including intercalated antidunes and mouth bar-related chute-and-pool-like structures, and upslope migration of hydraulic jump zones. These bedforms are preserved in a relatively short (100 s m) interpreted CLTZ that developed toward the base of a fan-delta foreset slope (the Eocene Sant Llorenç del Munt clastic wedge, near El Pont de Vilomara, NE Spain). Postma et al. (2021) sketch a flaring channel mouth setting, although outcrop limitations do not permit the planform shape to be confidently constrained. However, the foreset setting and high proportion of supercritical bedforms and erosion surfaces support an alternative interpretation of a CMEZ.

Hansen et al. (2021b) document an example of a high aspect ratio erosion surface in Unit 5 of the Permian Skoorsteenberg Formation (Tanqua Karoo, South Africa), which they interpret as a composite scour overlain by lobes. The 3–4 km wide, 1–2 km long, and up to 28 m deep basal surface, which is mantled locally with mud-clast conglomerates (lags), widens and shallows down-dip, and is above a slope, as expected in a CMEZ. However, they do not report the presence of scour-fills or supercritical bedforms outside the basal surface.

Pemberton et al. (2016) interpret scour-fills either in front of (Unit B), or lateral to (Unit C), multiple submarine channel-fills from the Tres Pasos Formation (Upper Cretaceous) of the Magallanes retroarc foreland basin in southern Chile (Figure 10). The Arroyo Picana outcrop is located ~40 km basinward of coeval shelf-edge deposits toward the lower portion of a high-relief (>900 m) slope. Interestingly, in Unit C along with scour-fills there are also cross-stratified sandstone bodies with positive-relief that record a palaeoflow at a high angle to the adjacent channel-fill. Pemberton et al. (2016) interpret these sandstones as a bedform with back-set cross-stratification formed by cyclic steps or antidunes. They interpret the stratigraphic architecture as a record of basinward progradation that preserves a channel-lobe transition zone around a break-in-slope. An alternative interpretation, which is consistent with the association of scour-fills and cyclic steps preserved in an elevated position adjacent to stacked channel-fills, is that Unit C records the lateral margin of a CMEZ on the lower slope.

The Ross Sandstone (Namurian) crops out along sea cliffs of the Loop Head Peninsula western Ireland. The interpretation and significance of extensive (>700 m wide) erosion surfaces mantled with megaflutes in the Ross Sandstone, County Clare, Ireland, has been debated (e.g., Chapin et al., 1994; Elliott, 2000a; Elliott, 2000b; Lien et al., 2003). The erosional bedforms occur on multiple stratigraphic surfaces and are associated with channel-fills and lobes (e.g., Pyles 2008; Macdonald et al., 2011b; Straub and Pyles, 2012). The Ross Sandstone preserves stacked high aspect ratio erosion surfaces with megaflutes, such as Ross Bay (Lien et al., 2003) and Kilbaha Bay (Chapin et al., 1994; Elliott, 2000a; Elliott, 2000b; Straub and Pyles, 2012). We suggest that the composite nature of these high aspect ratio erosion surfaces mantled with megaflutes are consistent with an

interpretation as CMEZs. The presence of supercritical or subcritical depositional bedforms in the underlying and overlying sandstones is hindered by the dominantly structureless nature of the sandstones in the Ross Formation, although dune-scale straight-crested bedforms are observed adjacent to megaflutes on one of the inaccessible faces (Elliott, 2000b, their Figure 6). Furthermore, the change in character across the high aspect ratio surface(s) needs detailed documentation.

Identification of exhumed CMEZs is key to investigate outstanding questions, such as the recognition of the depositional bedforms that develop within the zones of expansion, which are biased towards CLTZs, and the age relationships of erosional and depositional bedforms that develop inside and outside the zone of expansion. In the Magallanes Basin example (Pemberton et al., 2016), the scour-fills and cyclic steps lie above erosion surfaces that confine adjacent channel elements. The exact age relationships are difficult to unravel but support the interpretation that bedforms developed on the flanks of a CMEZ as the adjacent channels propagated basinward. In both the Karoo Basin and Ross Sandstone examples, the architecture of sandstones overlying the high aspect ratio erosion surface is predominantly lobes. This might be because there was no further, or limited, propagation of channel systems, and therefore the high aspect ratio composite erosion surfaces remain well preserved. However, the formation of high aspect ratio surfaces in CMEZs also lend themselves to infilling by lobes if flows become more depositional (less efficient) due to autogenic or allogenic controls (Hansen et al., 2021b). The implication is that for CMEZs preserved in the rock record we are left primarily with the (composite) erosion surface, and the associated bedforms are poorly preserved. In contrast, the candidate CMEZ documented by Postma et al. (2021) has good preservation of supercritical flow bedforms, which can be attributed to the rapid rates of progradation in a fan-delta foreset setting.

Future Opportunities for Channel Mouth and CLTZ Research

Seafloor examples will continue to be a key component of channel mouth studies, particularly as acquisition methods improve. High-resolution imaging of more submarine fans, channel mouths, CLTZs, and CMEZs, will illuminate whether features imaged in sparse high-resolution datasets (i.e., Macdonald et al., 2011a; Droz et al., 2020; Maier et al., 2020) are common across systems and settings. Increasing coverage and resolution of seafloor examples offers the opportunity to link seafloor examples with the scale of outcrop studies and provide plan-view analogues to ancient examples. Specifically, such studies are needed to evaluate the presence of CMEZs and related bedforms (e.g., laterally continuous erosional steps) in ancient outcrop examples.

Considerable opportunities also exist for future instrumentation to advance our understanding of flow processes where channels transition into lobes and provide constraints for experimental and numerical studies. Likewise, the increasing recognition of the influence of oceanographic currents on many deep-sea deposits, including turbidites (e.g., Stow and Smillie, 2020 and references therein), highlights the

opportunities for future studies of current-influenced channel mouth settings, hybrid fan-drift systems (e.g., Hikurangi Fan; Lewis, 1994), and high-latitude systems (e.g., Ó Cofaigh et al., 2006) to identify and understand modern and ancient deposits.

We have primarily focused on siliciclastic depositional systems, but lobes can also be deposited from deep-sea canyons and channels in carbonate systems. Carbonate lobes can occur at the base of slope, though often with the influence of contour currents (e.g., Mulder et al., 2012; Reijmer et al., 2015). In some cases, the lack of carbonate lobe deposition is linked to current activity (e.g., Recouvreur et al., 2021). Carbonate basin floor settings tend to be drifts instead of lobes (Reijmer et al., 2015), which may be one contributing factor to why carbonate channel mouth examples are less prevalent than siliciclastic examples. Nevertheless, there seems to be abundant opportunity in the future, with increasing seafloor mapping and resolution, to investigate channel mouth settings in carbonate systems.

Detailed outcrop research on CLTZs has primarily focused on large, relatively tectonically-quiet basins associated with mature passive margins or thermal sag basins, and influenced by glacial-interglacial cycles, such as the Karoo Basin in South Africa (e.g., Van der Merwe et al., 2014; Hofstra et al., 2015; Brooks et al., 2018). Therefore, it is important to understand if these same models can be applied to tectonically-active basins (e.g., Mansor and Amir Hassan, 2021; Brooks et al., 2022), such as forearc or retroarc foreland basins, formed in different climatic conditions in both modern environments and in the rock record. Indeed, tectonically-active basin-fills are likely to host CMEZs given the steeper slopes. In summary, identification of exhumed examples of different types of channel mouth settings will drive forward a range of recognition criteria, which at present is biased towards CLTZs.

CONCLUSION

The mouths of submarine channels are a poorly understood but crucial part of the source-to-sink sediment transport route where sediment gravity flows undergo major changes in their behaviour as confinement decreases. We integrate physical experiments, numerical modelling, and observations of modern and ancient systems, to develop insights into channel mouth settings, and their transfer into the stratigraphic record. We review the wide range of different experimental configurations that have focussed on understanding changes in process behaviour as flows exit channels. An increasing number of studies of modern systems suggest that the classic channel-lobe transition zone (CLTZ) of Wynn et al. (2002a) is one type in a range of configurations. We propose four types of channel mouth setting: 1) channel mouth expansion zones (CMEZs) that form on steep slopes and in the absence of a pronounced break in slope, and are associated with supercritical bedforms; 2) plunge pools that form at steep slope breaks in both siliciclastic and carbonate systems, with high incoming supercritical Froude numbers; 3) CLTZs with arrays of

hydraulic jumps at slope breaks with incoming supercritical Froude numbers close to unity; and, 4) subcritical CLTZs associated with slope breaks and/or flow expansion, that are the more basinward style of channel mouth setting.

Identification of the stratigraphic record of channel mouth settings is complicated by the propagation, and avulsion, of channels. Nonetheless, recent studies from ancient outcrop and subsurface systems have interpreted CLTZs, although candidate exhumed CMEZs that meet the criteria established from modern systems are postulated here, and warrant re-examination. Recent years have seen significant advances in our process understanding of these channel mouth settings. However, the total number of studies remains small, and the potential parameter space large, thus there remains much to discover.

AUTHOR CONTRIBUTIONS

DMH, JP, and KLM coordinated the work. JP led review of experimental work, KLM led review of modern systems, and DMH led review of ancient systems. All authors contributed to writing the Discussion, and design and development of the figures.

REFERENCES

- Alexander, J., Bridge, J. S., Cheel, R. J., and Leclair, S. F. (2001). Bedforms and Associated Sedimentary Structures Formed under Supercritical Water Flows over Aggrading Sand Beds. *Sedimentology* 48, 133–152. doi:10.1046/j.1365-3091.2001.00357.x
- Babonneau, N., Savoye, B., Cremer, M., and Klein, B. (2002). Morphology and Architecture of the Present canyon and Channel System of the Zaire Deep-Sea Fan. *Mar. Pet. Geology* 19, 445–467. doi:10.1016/s0264-8172(02)00009-0
- Bonnell, C., Dennielou, B., Droz, L., Mulder, T., and Berné, S. (2005). Architecture and Depositional Pattern of the Rhône Neofan and Recent Gravity Activity in the Gulf of Lions (Western Mediterranean). *Mar. Pet. Geology* 22, 827–843. doi:10.1016/j.marpetgeo.2005.03.003
- Bourget, J., Zaragosi, S., Mulder, T., Schneider, J.-L., Garlan, T., Van Toer, A., et al. (2010). Hyperpycnal-fed Turbidite Lobe Architecture and Recent Sedimentary Processes: A Case Study from the Al Batha Turbidite System, Oman Margin. *Sediment. Geology* 229, 144–159. doi:10.1016/j.sedgeo.2009.03.009
- Bravo, J. C. V., and Robles, S. (1995). “Large-scale Mesotopographic Bedforms from the Albian Black Flysch, Northern Spain: Characterization, Setting and Comparison with Recent Analogues,” in *Atlas of Deep-Water Environments: Architectural Styles in Turbidite Systems*. Editors K. T. Pickering, R. N. Hiscott, N. H. Kenyon, F. R. Lucchi, and R. D. A. Smith (London: Chapman & Hall), 216–226. doi:10.1007/978-94-011-1234-5_32
- Brooks, H. L., Hodgson, D. M., Brunt, R. L., Peakall, J., Hofstra, M., and Flint, S. S. (2018). Deep-Water Channel-Lobe Transition Zone Dynamics: Processes and Depositional Architecture, an Example from the Karoo Basin, South Africa. *Geol. Soc. Am. Bull.* 130, 1723–1746. doi:10.1130/B31714.1
- Brooks, H. L., Ito, M., Zuchuat, V., Peakall, J., and Hodgson, D. M. (2022). Channel-lobe Transition Zone Development in Tectonically-Active Settings: Implications for Hybrid Bed Development. Accepted at The Depositional Record. doi:10.1002/dep2.180
- Buckee, C., Kneller, B. C., and Peakall, J. (2001). “Turbulence Structure in Steady, Solute-Driven Gravity Currents,” in *Particulate Gravity Currents*. Editors W. D. McCaffrey, B. C. Kneller, and J. Peakall (Oxford: International Association of Sedimentologists Special Publication), 31, 173–187.
- Carvajal, C., Paull, C. K., Caress, D. W., Fildani, A., Lundsten, E., Anderson, K., et al. (2017). Unraveling the Channel-Lobe Transition Zone with High-Resolution AUV Bathymetry: Navy Fan, Offshore Baja California, Mexico. *J. Sed. Res.* 87, 1049–1059. doi:10.2110/jsr.2017.58

FUNDING

JP thanks the Natural Environment Research Council (NERC) for funding that supported the work on hydraulic jump arrays in the Black Sea (Grants NE/F020511/1, NE/F020120/1, and NE/F020279/1), and on megaflute erosion surfaces (NERC CASE Studentship NER/S/A/2006/14147 at the University of Leeds, with the National Oceanography Centre (NOC), Southampton as the CASE partner). KLM is supported by the Marine Geological Resources Programme at the National Institute of Water and Atmospheric Research (NIWA).

ACKNOWLEDGMENTS

Editor Fabiano Gamberi, and reviewers Juraj Janočko and Luigi Jovane are thanked for their constructive comments on the manuscript. We thank Gareth Keevil and Natasha Peakall for discussion and analysis, and David Lee for drafting **Figures 1, 6–8 and 11**. We thank V2Geo for hosting a publically available version of the Virtual Outcrop Model of **Figures 9C,D** at <https://v3geo.com/model/297>.

- Chapin, M. A., Davies, P., Gibson, J. L., Pettingill, H. S., Zelt, F. B., and Mutti, E. (1994). “Reservoir Architecture of Turbidite Sheet Sandstones in Laterally Extensive Outcrops, Ross Formation, Western Ireland,” in *Submarine Fans and Turbidite Systems: Sequence Stratigraphy, Reservoir Architecture and Production Characteristics*, Gulf of Mexico and International: Gulf Coast Section Society for Sedimentary Geology, GCSSEPM Foundation Annual Bob F. Perkins Research Conference Proceedings. Editors P. Weimer, A. H. Bouma, and P. F. Perkins. Tulsa, Oklahoma: SEPM Society for Sedimentary Geology, 15, 53–68. doi:10.5724/gcs.94.15.0083
- Clare, M. A., Hughes Clarke, J. E., Talling, P. J., Cartigny, M. J. B., and Pratomo, D. G. (2016). Preconditioning and Triggering of Offshore Slope Failures and Turbidity Currents Revealed by Most Detailed Monitoring yet at a Fjord-Head delta. *Earth Planet. Sci. Lett.* 450, 208–220. doi:10.1016/j.epsl.2016.06.021
- Covault, J. A., Normark, W. R., Romans, B. W., and Graham, S. A. (2007). Highstand Fans in the California Borderland: The Overlooked Deep-Water Depositional Systems. *Geology* 35, 783–786. doi:10.1130/g23800a.1
- Covault, J. A., Kostic, S., Paull, C. K., Sylvester, Z., and Fildani, A. (2017). Cyclic Steps and Related Supercritical Bedforms: Building Blocks of Deep-Water Depositional Systems, Western North America. *Mar. Geology* 393, 4–20. doi:10.1016/j.margeo.2016.12.009
- Dartnell, P., Driscoll, N. W., Brothers, D., Conrad, J. E., Kluesner, J., Kent, G., et al. (2015). Color Shaded-Relief Bathymetry, Acoustic Backscatter, and Selected Perspective Views of the Inner continental Borderland, Southern California. U.S. Geological Survey, Scientific Investigations. Map 3324, 2 sheets.
- De Leeuw, J., Eggenhuisen, J. T., and Cartigny, M. J. B. (2016). Morphodynamics of Submarine Channel Inception Revealed by New Experimental Approach. *Nat. Commun.* 7, 10886. doi:10.1038/ncomms10886
- Dennielou, B., Droz, L., Babonneau, N., Jacq, C., Bonnel, C., Picot, M., et al. (2017). Morphology, Structure, Composition and Build-Up Processes of the Active Channel-Mouth Lobe Complex of the Congo Deep-Sea Fan with Inputs from Remotely Operated Underwater Vehicle (ROV) Multibeam and Video Surveys. *Deep Sea Res. Part Topical Stud. Oceanography* 142, 25–49. doi:10.1016/j.dsr2.2017.03.010
- Deptuck, M. E., and Sylvester, Z. (2018). “Submarine Fans and Their Channels, Levees, and Lobes,” in *Submarine Geomorphology*. Editors A. Micallef, S. Krastel, and A. Savini (Cham: Springer), 273–299. doi:10.1007/978-3-319-57852-1_15
- Dorrell, R. M., Darby, S. E., Peakall, J., Sumner, E. J., Parsons, D. R., and Wynn, R. B. (2013). Superelevation and Overspill Control Secondary Flow Dynamics in Submarine Channels. *J. Geophys. Res. Oceans* 118, 3895–3915. doi:10.1002/jgrc.20277

- Dorrell, R. M., Peakall, J., Sumner, E. J., Parsons, D. R., Darby, S. E., Wynn, R. B., et al. (2016). Flow Dynamics and Mixing Processes in Hydraulic Jump Arrays: Implications for Channel-Lobe Transition Zones. *Mar. Geology*. 381, 181–193. doi:10.1016/j.margeo.2016.09.009
- Droz, L., Jégou, I., Gillet, H., Dennielou, B., Bez, M., Canals, M., et al. (2020). On the Termination of Deep-Sea Fan Channels: Examples from the Rhône Fan (Gulf of Lion, Western Mediterranean Sea). *Geomorphology* 369, 107368. doi:10.1016/j.geomorph.2020.107368
- Edwards, D. A., Leeder, M. R., Best, J. L., and Pantin, H. M. (1994). On Experimental Reflected Density Currents and the Interpretation of Certain Turbidites. *Sedimentology* 41, 437–461. doi:10.1111/j.1365-3091.1994.tb02005.x
- Edwards, D. A. (1993). *Turbidity Currents: Dynamics, Deposits and Reversals*. Berlin: Springer-Verlag, 174.
- Elliott, T. (2000a). Megaflute Erosion Surfaces and the Initiation of Turbidite Channels. *Geology* 28, 119–122. doi:10.1130/0091-7613(2000)028<0119:mesati>2.3.co;2
- Elliott, T. (2000b). “Depositional Architecture of a Sand-Rich, Channelized Turbidite System: The Upper Carboniferous Ross Sandstone Formation, Western Ireland,” in *Deep-water Reservoirs of the World. GCSSEPM Foundation 20th Annual Research Conference*, Tulsa, Oklahoma, December 3–6, 2000. Editors P. Weimer, R.M. Slatt, J. Coleman, N.C. Rosen, C.H. Nelson, A.H. Bouma, et al. 342–373. doi:10.5724/gcs.00.15.0342
- Fedele, J. J., Hoyal, D. C., Barnaal, Z., Tulenko, J., and Awalt, S. (2016). “Bedforms Created by Gravity Flows,” in *Autogenic Dynamics in Sedimentary Systems*. Editors D. Budd, E. Hajek, and S. Purkis (Tulsa: SEPM Special Publication), 106, 95–121.
- Fernandez, R. L., Cantelli, A., Pirmez, C., Sequeiros, O., and Parker, G. (2014). Growth Patterns of Subaqueous Depositional Channel Lobe Systems Developed over a Basement with a Downdip Break in Slope: Laboratory Experiments. *J. Sediment. Res.* 84, 168–182. doi:10.2110/jsr.2014.10
- Fildani, A., and Normark, W. R. (2004). Late Quaternary Evolution of Channel and Lobe Complexes of Monterey Fan. *Mar. Geology*. 206, 199–223. doi:10.1016/j.margeo.2004.03.001
- Fildani, A., Hubbard, S. M., Covault, J. A., Maier, K. L., Romans, B. W., Traer, M., et al. (2013). Erosion at Inception of Deep-Sea Channels. *Mar. Pet. Geology*. 41, 48–61. doi:10.1016/j.marpetgeo.2012.03.006
- Fildani, A., Kostic, S., Covault, J. A., Maier, K. L., Caress, D. W., and Paull, C. K. (2021). Exploring a New Breadth of Cyclic Steps on Distal Submarine Fans. *Sedimentology* 68, 1378–1399. doi:10.1111/sed.12803
- Gamberi, F., and Marani, M. (2007). Downstream Evolution of the Stromboli Slope valley (southeastern Tyrrhenian Sea). *Mar. Geology*. 243, 180–199. doi:10.1016/j.margeo.2007.05.006
- Gamberi, F., and Marani, M. (2011). Geomorphology and Sedimentary Processes of a Modern Confined Braided Submarine Channel belt (Stromboli Slope Valley, Southeastern Tyrrhenian Sea). *J. Sediment. Res.* 81, 686–701. doi:10.2110/jsr.2011.56
- García, M., and Parker, G. (1989). Experiments on Hydraulic Jumps in Turbidity Currents Near a canyon-fan Transition. *Science* 245, 393–396. doi:10.1126/science.245.4916.393
- García, M. H. (1989). *Depositing and Eroding Sediment Driven Flows: Turbidity Currents*. PhD Thesis. Minneapolis, MN: Department of Civil Engineering, University of Minnesota.
- García, M. H. (1993). Hydraulic Jumps in Sediment-Driven Bottom Currents. *J. Hydraulic Eng.* 119, 1094–1117. doi:10.1061/(asce)0733-9429(1993)119:10(1094)
- Gardner, J. V., and Dartnell, P. (2002). *Multibeam Mapping of the Los Angeles, California Margin*. Open-File Report 02-162. United States: U.S. Geological Survey.
- Gardner, M. H., Borer, J. M., Melick, J. J., Mavilla, N., Dechesne, M., and Wagerle, R. N. (2003). Stratigraphic Process-Response Model for Submarine Channels and Related Features from Studies of Permian Brushy Canyon Outcrops, West Texas. *Mar. Pet. Geology*. 20, 757–787. doi:10.1016/j.marpetgeo.2003.07.004
- Gardner, J. V., Armstrong, A. A., and Calder, B. R. (2016). Hatteras Transverse Canyon, Hatteras Outer Ridge and Environs of the U.S. Atlantic Margin: a View from Multibeam Bathymetry and Backscatter. *Mar. Geology*. 371, 18–32. doi:10.1016/j.margeo.2015.10.015
- Gardner, J. V., Peakall, J., Armstrong, A. A., and Calder, B. R. (2020). The Geomorphology of Submarine Channel Systems of the Northern Line Islands Ridge, Central Equatorial Pacific Ocean. *Front. Earth Sci.* 8, 87. doi:10.3389/feart.2020.00087
- Gray, T. E., Alexander, J., and Leeder, M. R. (2005). Quantifying Velocity and Turbulence Structure in Depositing Sustained Turbidity Currents across Breaks in Slope. *Sedimentology* 52, 467–488. doi:10.1111/j.1365-3091.2005.00705.x
- Gray, T. E., Alexander, J., and Leeder, M. R. (2006). Longitudinal Flow Evolution and Turbulence Structure of Dynamically Similar, Sustained, Saline Density and Turbidity Currents. *J. Geophys. Res.* 111, C08015. doi:10.1029/2005jc003089
- Hamilton, P. B., Strom, K. B., and Hoyal, D. C. J. D. (2015). Hydraulic and Sediment Transport Properties of Autogenic Avulsion Cycles on Submarine Fans with Supercritical Distributions. *J. Geophys. Res. Earth Surf.* 120, 1369–1389. doi:10.1002/2014jf003414
- Hamilton, P., Gaillot, G., Strom, K., Fedele, J., and Hoyal, D. (2017). Linking Hydraulic Properties in Supercritical Submarine Distributary Channels to Depositional-Lobe Geometry. *J. Sediment. Res.* 87, 935–950. doi:10.2110/jsr.2017.53
- Hansen, L. A. S., Hodgson, D. M., Pontén, A., Thrana, C., and Obradors Latre, A. (2021a). Mixed Axial and Transverse Deep-water Systems: The Cretaceous Post-Rift Lysing Formation, Offshore Norway. *Basin Res.* 33, 2229–2251. doi:10.1111/bre.12555
- Hansen, L. A. S., Healy, R. S., Gomis-Cartesio, L., Lee, D. R., Hodgson, D. M., Pontén, A., et al. (2021b). The Origin and 3D Architecture of a Km-Scale Deep-Water Scour-Fill: Example from the Skoorsteenberg Fm, Karoo Basin, South Africa. *Front. Earth Sci.* 9, 737932. doi:10.3389/feart.2021.737932
- Harris, P. T., Barrie, J. V., Conway, K. W., and Greene, H. G. (2014). Hanging Canyons of Haida Gwaii, British Columbia, Canada: Fault-Control on Submarine Canyon Geomorphology along Active Continental Margins. *Deep Sea Res. Part Topical Stud. Oceanography* 104, 83–92. doi:10.1016/j.dsr.2013.06.017
- Heijnen, M. S., Clare, M. A., Cartigny, M. J. B., Talling, P. J., Hage, S., Lintern, D. G., et al. (2020). Rapidly-Migrating and Internally-Generated Knickpoints Can Control Submarine Channel Evolution. *Nat. Commun.* 11, 3129. doi:10.1038/s41467-020-16861-x
- Henstra, G. A., Grundvåg, S.-A., Johannessen, E. P., Kristensen, T. B., Midtkandal, I., Nystuen, J. P., et al. (2016). Depositional Processes and Stratigraphic Architecture within a Coarse-Grained Rift-Margin Turbidite System: The Wollaston Forland Group, East Greenland. *Mar. Pet. Geology*. 76, 187–209. doi:10.1016/j.marpetgeo.2016.05.018
- Hizzett, J. L., Hughes Clarke, J. E., Sumner, E. J., Cartigny, M. J. B., Talling, P. J., and Clare, M. A. (2018). Which Triggers Produce the Most Erosive, Frequent, and Longest Runout Turbidity Currents on Deltas? *Geophys. Res. Lett.* 45, 855–863. doi:10.1002/2017gl075751
- Hodgson, D. M., Kane, I. A., Flint, S. S., Brunt, R. L., and Ortiz-Karpf, A. (2016). Time-Transgressive Confinement on the Slope and the Progradation of Basin-Floor Fans: Implications for the Sequence Stratigraphy of Deep-Water Deposits. *J. Sediment. Res.* 86, 73–86. doi:10.2110/jsr.2016.3
- Hofstra, M., Hodgson, D. M., Peakall, J., and Flint, S. S. (2015). Giant Scour-Fills in Ancient Channel-Lobe Transition Zones: Formative Processes and Depositional Architecture. *Sediment. Geology*. 329, 98–114. doi:10.1016/j.sedgeo.2015.09.004
- Hofstra, M., Peakall, J., Hodgson, D. M., and Stevenson, C. J. (2018). Architecture and Morphodynamics of Subcritical Sediment Waves in an Ancient Channel-Lobe Transition Zone. *Sedimentology* 65, 2339–2367. doi:10.1111/sed.12468
- Hughes Clarke, J. E., Brucker, S., Muggah, J., Hamilton, T., Cartwright, D., Church, I., et al. (2012). “Temporal Progression and Spatial Extent of Mass Wasting Events on the Squamish Prodelta Slope,” in *Landslides and Engineered Slopes: Protecting Society through Improved Understanding*. Editors E. Eberhardt, C. Froese, K. Turner, and S. Leroueil (London: Taylor and Francis Group), 1091–1096.
- Hughes Clarke, J. E. (2016). First Wide-Angle View of Channelized Turbidity Currents Links Migrating Cyclic Steps to Flow Characteristics. *Nat. Commun.* 7, 11896. doi:10.1038/ncomms11896
- Hughes Clarke, J. E., and Fedele, J. J. (2019). Lobe-channel initiation under unconfined turbidity current flow. *American Geophysical Union*, Fall Meeting 2019, abstract OS31A-08. Available at: <https://ui.adsabs.harvard.edu/abs/2019AGUFMOS31A..08H/abstract>

- Ito, M. (2008). Downfan Transformation from Turbidity Currents to Debris Flows at a Channel-To-Lobe Transitional Zone: The Lower Pleistocene Otadai Formation, Boso Peninsula, Japan. *J. Sediment. Res.* 78, 668–682. doi:10.2110/jsr.2008.076
- Kane, I. A., and Clare, M. A. (2019). Dispersion, Accumulation, and the Ultimate Fate of Microplastics in Deep-marine Environments: A Review and Future Directions. *Front. Earth Sci.* 7, 80. doi:10.3389/feart.2019.00080
- Kenyon, N. H., and Millington, J. (1995). “Contrasting Deep-Sea Depositional Systems in the Bering Sea,” in *Atlas of Deep-Water Environments: Architectural Styles in Turbidite Systems*. Editors K. T. Pickering, R. N. Hiscott, N. H. Kenyon, F. R. Lucchi, and R. D. A. Smith (London: Chapman & Hall), 196–202. doi:10.1007/978-94-011-1234-5_28
- Kenyon, N. H., Millington, J., Droz, L., and Ivanov, M. K. (1995). “Scour Holes in a Channel-Lobe Transition Zone on the Rhône Cone,” in *Atlas of Deep-Water Environments: Architectural Styles in Turbidite Systems*. Editors K. T. Pickering, R. N. Hiscott, N. H. Kenyon, F. R. Lucchi, and R. D. A. Smith (London: Chapman & Hall), 212–215. doi:10.1007/978-94-011-1234-5_31
- Klaucke, I., Masson, D. G., Kenyon, N. H., and Gardner, J. V. (2004). Sedimentary Processes of the Lower Monterey Fan Channel and Channel-Mouth Lobe. *Mar. Geology* 206, 181–198. doi:10.1016/j.margeo.2004.02.006
- Komar, P. D. (1971). Hydraulic Jumps in Turbidity Currents. *Geol. Soc. America Bull.* 82, 1477–1488. doi:10.1130/0016-7606(1971)82[1477:hjtc]2.0.co;2
- Konsoer, K., Zinger, J., and Parker, G. (2013). Bankfull Hydraulic Geometry of Submarine Channels Created by Turbidity Currents: Relations between Bankfull Channel Characteristics and Formative Flow Discharge. *J. Geophys. Res. Earth Surf.* 118, 216–228. doi:10.1029/2012jg002422
- Kostic, S., and Parker, G. (2006). The Response of Turbidity Currents to a Canyon-fan Transition: Internal Hydraulic Jumps and Depositional Signatures. *J. Hydraulic Res.* 44, 631–653. doi:10.1080/00221686.2006.9521713
- Kostic, S., and Parker, G. (2007). Conditions under Which a Supercritical Turbidity Current Traverses an Abrupt Transition to Vanishing Bed Slope without a Hydraulic Jump. *J. Fluid Mech.* 586, 119–145. doi:10.1017/s0022112007006738
- Lang, J., Fedele, J. J., and Hoyal, D. C. J. D. (2021). Three-Dimensional Submerged Wall Jets and Their Transition to Density Flows: Morphodynamics and Implications for the Depositional Record. *Sedimentology* 68, 1297–1327. doi:10.1111/sed.12860
- Lauder, B. E., and Rodi, W. (1983). The Turbulent Wall Jet Measurements and Modeling. *Annu. Rev. Fluid Mech.* 15, 429–459. doi:10.1146/annurev.fl.15.010183.002241
- Lee, S. E., Talling, P. J., Ernst, G. G. J., and Hogg, A. J. (2002). Occurrence and Origin of Submarine Plunge Pools at the Base of the US continental Slope. *Mar. Geology* 185, 363–377. doi:10.1016/S0025-3227(01)00298-5
- Lee, S. E., Amy, L. A., and Talling, P. J. (2004). “The Character and Origin of Thick Base-Of-Slope sandstone Units of the Peira Cava Outlier, SE France,” in *Deep-Water Sedimentation in the Alpine Basin of SE France: New Perspectives on the Gres d’Annot and Related Systems*. Editors P. Joseph and S. A. Lomas (Bath, UK: Geological Society, London, Special Publications), 221, 331–347. doi:10.1144/gsl.sp.2004.221.01.18
- Lewis, K. B. (1994). The 1500-Km-Long Hikurangi Channel: Trench-Axis Channel that Escapes its Trench, Crosses a Plateau, and Feeds a Fan Drift. *Geo-Marine Lett.* 14, 19–28. doi:10.1007/bf01204467
- Lien, T., Walker, R. G., and Martinsen, O. J. (2003). Turbidites in the Upper Carboniferous Ross Formation, Western Ireland: Reconstruction of a Channel and Spillover System. *Sedimentology* 50, 113–148. doi:10.1046/j.1365-3091.2003.00541.x
- Macdonald, H. A., Wynn, R. B., Huvenne, V. A. I., Peakall, J., Masson, D. G., Weaver, P. P. E., et al. (2011a). New Insights into the Morphology, Fill, and Remarkable Longevity (>0.2 m.y.) of Modern Deep-Water Erosional Scours along the Northeast Atlantic Margin. *Geosphere* 7, 845–867. doi:10.1130/GES00611.1
- Macdonald, H. A., Peakall, J., Wignall, P. B., and Best, J. (2011b). Sedimentation in Deep-Sea Lobe-Elements: Implications for the Origin of Thickening-Upward Sequences. *J. Geol. Soc.* 168, 319–332. doi:10.1144/0016-76492010-036
- Maier, K. L., Roland, E. C., Walton, M. A. L., Conrad, J. E., Brothers, D. S., Dartnell, P., et al. (2018). The Tectonically Controlled San Gabriel Channel-Lobe Transition Zone, Catalina Basin, Southern California Borderland. *J. Sed. Res.* 88, 942–959. doi:10.2110/jsr.2018.50
- Maier, K. L., Paull, C. K., Caress, D. W., Anderson, K., Nieminski, N. M., Lundsten, E., et al. (2020). Submarine-Fan Development Revealed by Integrated High-Resolution Datasets from La Jolla Fan, Offshore California, U.S.A. *J. Sed. Res.* 90, 468–479. doi:10.2110/jsr.2020.22
- Mansor, H. E., and Amir Hassan, M. H. (2021). Facies and Bed Type Characteristics of Channel-Lobe Transition Deposits from the Oligocene-Miocene Tajau Sandstone Member, Kudat Formation, Sabah, Malaysia. *Geol. J.* 56, 5642–5672. doi:10.1002/gj.4263
- Mayer, L. A., and Gardner, J. V. (2016). “Cascades and Plunge Pools on the continental Slope of the Gulf of Alaska,” in *Atlas of Submarine Glacial Landforms: Modern, Quaternary and Ancient*. Editors J. A. Dowdeswell, M. Canals, M. Jakobsson, B. J. Todd, E. K. Dowdeswell, and K. A. Hogan (Bath, UK: Geological Society of London, Memoir), 46, 389–390. doi:10.1144/M46.20
- Morris, S. A., Alexander, J., Kenyon, N. H., and Limonov, A. F. (1998). Turbidites Around an Active Fault Scarp on the Lower Valencia Fan, Northwest Mediterranean. *Geo-Marine Lett.* 18, 165–171. doi:10.1007/s003670050064
- Mulder, T., Ducassou, E., Gillet, H., Hanquiez, V., Tournadour, E., Combes, J., et al. (2012). Canyon Morphology on a Modern Carbonate Slope of the Bahamas: Evidence of Regional Tectonic Tilting. *Geology* 40, 771–774. doi:10.1130/G33327.1
- Mulder, T., Gillet, H., Hanquiez, V., Reijmer, J. J. G., Droxler, A. W., Recouvreur, A., et al. (2019). Into the Deep: A Coarse-Grained Carbonate Turbidite Valley and Canyon in Ultra-Deep Carbonate Setting. *Mar. Geology* 407, 316–333. doi:10.1016/j.margeo.2018.11.003
- Mutti, E., and Normark, W. R. (1987). “Comparing Examples of Modern and Ancient Turbidite Systems: Problems and Concepts,” in *Marine Clastic Sedimentology: Concepts and Case Studies*. Editors J. K. Leggett and G. G. Zuffa (London: Graham and Trotman), 1–38. doi:10.1007/978-94-009-3241-8_1
- Mutti, E., and Normark, W. R. (1991). “An Integrated Approach to the Study of Turbidite Systems,” in *Seismic Facies and Sedimentary Processes of Submarine Fans and Turbidite Systems*. Editors P. Weimer and M. H. Link (New York: Springer-Verlag), 75–106. doi:10.1007/978-1-4684-8276-8_4
- Navarro, L., and Arnott, R. W. C. (2020). Stratigraphic Record in the Transition from Basin Floor to Continental Slope Sedimentation in the Ancient Passive-Margin Windermere Turbidite System. *Sedimentology* 67, 1710–1749. doi:10.1111/sed.12676
- Nelson, C. H., Goldfinger, C., Johnson, J. E., and Dunhill, G. (2000). “Variation of Modern Turbidite Systems Along the Subduction Zone Margin of Cascadia Basin and Implications for Turbidite Reservoir Beds,” in *Proceedings Deep Reservoirs of the World, SEPM, Gulf Coast Section, 20th Annual Bob F. Perkins Research Conference, Houston, Texas, December 3–6, 2000*. Editors P. Weimer, R. M. Slatt, J. Coleman, N. C. Rosen, C. H. Nelson, A. H. Bouma, et al. 714–738. doi:10.5724/gcs.00.15.0714
- Normark, W. R., and Piper, D. J. W. (1991). “Initiation Processes and Flow Evolution of Turbidity Currents: Implications for the Depositional Record,” in *From Shoreline to Abyss*. Editor R. H. Osborne (Tulsa: SEPM. Spec. Publ.), 46, 207–230. doi:10.2110/pec.91.09.0207
- Normark, W. R., Piper, D. J. W., and Hess, G. R. (1979). Distributary Channels, Sand Lobes, and Mesotopography of Navy Submarine Fan, California Borderland, with Applications to Ancient Fan Sediments. *Sedimentology* 26, 749–774. doi:10.1111/j.1365-3091.1979.tb00971.x
- Normark, W. R., Piper, D. J. W., Romans, B. W., Covault, J. A., Dartnell, P., and Sliter, R. W. (2009). “Submarine canyon and Fan Systems of the California Continental Borderland,” in *Earth Science in the Urban Ocean: The Southern California Continental Borderland*. Editors H. J. Lee and W. R. Normark (Boulder: Geological Society of America Special Paper), 454, 141–168. doi:10.1130/2009.2454(2.7)
- Normark, W. R. (1970). Growth Patterns of Deep-Sea Fans. *Am. Assoc. Petrol. Geol. Bull.* 54, 2170–2195. doi:10.1306/5d25cc79-16c1-11d7-8645000102c1865d
- Normark, W. R. (1985). “Local Morphologic Controls and Effects of basin Geometry on Flow Processes in Deep marine Basins,” in *Provenance of Arenites*. Editor G. G. Zuffa (Dordrecht: NATO ASI Series. Series C: Mathematical and Physical Sciences, Reidel), 148, 47–63. doi:10.1007/978-94-017-2809-6_3
- Ó Cofaigh, C., Dowdeswell, J. A., and Kenyon, N. H. (2006). Geophysical Investigations of a High-Latitude Submarine Channel System and Associated Channel-Mouth Lobe in the Lofoten Basin, Polar North Atlantic. *Mar. Geology* 226, 41–50. doi:10.1016/j.margeo.2005.09.014
- Patton, J. R., Goldfinger, C., Morey, A. E., Romsos, C., Black, B., Djadjadhardja, Y., et al. (2013). Seismoturbidite Record as Preserved at Core Sites at the Cascadia

- and Sumatra-Andaman Subduction Zones. *Nat. Hazards Earth Syst. Sci.* 13, 833–867. doi:10.5194/nhess-13-833-2013
- Paull, C. K., Caress, D. W., Ussler, W., III, Lundsten, E., and Meiner-Johnson, M. (2011). High-Resolution Bathymetry of the Axial Channels within Monterey and Soquel Submarine Canyons, Offshore Central California. *Geosphere* 7, 1077–1101. doi:10.1130/GES00636.1
- Paull, C. K., Caress, D. W., Lundsten, E., Gwiazda, R., Anderson, K., McGann, M., et al. (2013). Anatomy of the La Jolla Submarine Canyon System; Offshore Southern California. *Mar. Geology* 335, 16–34. doi:10.1016/j.margeo.2012.10.003
- Peakall, J., and Sumner, E. J. (2015). Submarine Channel Flow Processes and Deposits: A Process-Product Perspective. *Geomorphology* 244, 95–120. doi:10.1016/j.geomorph.2015.03.005
- Pemberton, E. A. L., Hubbard, S. M., Fildani, A., Romans, B., and Stright, L. (2016). The Stratigraphic Expression of Decreasing Confinement along a Deep-Water Sediment Routing System: Outcrop Example from Southern Chile. *Geosphere* 12, 114–134. doi:10.1130/ges01233.1
- Picot, M., Droz, L., Marsset, T., Dennielou, B., and Bez, M. (2016). Controls on Turbidite Sedimentation: Insights from a Quantitative Approach of Submarine Channel and Lobe Architecture (Late Quaternary Congo Fan). *Mar. Pet. Geology* 72, 423–446. doi:10.1016/j.marpetgeo.2016.02.004
- Piper, D. J. W. (1970). Transport and Deposition of Holocene Sediment on La Jolla Deep Sea Fan, California. *Mar. Geology* 8, 211–227. doi:10.1016/0025-3227(70)90044-7
- Pirmez, C., and Imran, J. (2003). Reconstruction of Turbidity Currents in Amazon Channel. *Mar. Pet. Geology* 20, 823–849. doi:10.1016/j.marpetgeo.2003.03.005
- Pohl, F., Eggenhuisen, J. T., Tilston, M., and Cartigny, M. J. B. (2019). New Flow Relaxation Mechanism Explains Scour fields at the End of Submarine Channels. *Nat. Commun.* 10, 4425. doi:10.1038/s41467-019-12389-x
- Pohl, F., Eggenhuisen, J. T., Cartigny, M. J. B., Tilston, M. C., de Leeuw, J., and Hermidas, N. (2020). The Influence of a Slope Break on Turbidite Deposits: An Experimental Investigation. *Mar. Geology* 424, 106160. doi:10.1016/j.margeo.2020.106160
- Posamentier, H. W., and Kolla, V. (2003). Seismic Geomorphology and Stratigraphy of Depositional Elements in Deep-Water Settings. *J. Sediment. Res.* 73, 367–388. doi:10.1306/111302730367
- Postma, G., Hoyal, D. C., Abreu, V., Cartigny, M. J. B., Demko, T., Fedele, J. J., et al. (2016). “Morphodynamics of Supercritical Turbidity Currents in the Channel-Lobe Transition Zone,” in *Submarine Mass Movements and their Consequences*. Editors G. Lamarche, J. Mountjoy, S. Bull, T. Hubble, S. Krastel, E. Lane, et al. Cham: Springer. 41, 469–478. doi:10.1007/978-3-319-20979-1_47
- Postma, G., Lang, J., Hoyal, D. C., Fedele, J. J., Demko, T., Abreu, V., et al. (2021). Reconstruction of Bedform Dynamics Controlled by Supercritical Flow in the Channel-Lobe Transition Zone of a Deep-Water Delta (Sant Llorenç del Munt, North-East Spain, Eocene). *Sedimentology* 68, 1674–1697. doi:10.1111/sed.12735
- Pyles, D. R., Strachan, L. J., and Jennette, D. C. (2014). Lateral Juxtapositions of Channel and Lobe Elements in Distributive Submarine Fans: Three-Dimensional Outcrop Study of the Ross Sandstone and Geometric Model. *Geosphere* 10, 1104–1122. doi:10.1130/ges01042.1
- Pyles, D. R. (2008). Multiscale Stratigraphic Analysis of a Structurally Confined Submarine Fan: Carboniferous Ross Sandstone, Ireland. *Bulletin* 92, 557–587. doi:10.1306/01110807042
- Recouvreur, A., Fabregas, N., Mulder, T., Hanquiez, V., Fauquembergue, K., Tournadour, E., et al. (2021). Geomorphology of a Modern Carbonate Slope System and Associated Sedimentary Processes: Example of the Giant Great Abaco Canyon, Bahamas. *Sedimentology* 68, 266–293. doi:10.1111/sed.12777
- Reijmer, J. J. G., Mulder, T., and Borgomano, J. (2015). Carbonate Slopes and Gravity Deposits. *Sediment. Geology* 317, 1–8. doi:10.1016/j.sedgeo.2014.12.001
- Salinas, J., Balachandrar, S., Shringarpure, M., Fedele, J., Hoyal, D., and Cantero, M. (2020). Soft Transition between Subcritical and Supercritical Currents through Intermittent Cascading Interfacial Instabilities. *Proc. Natl. Acad. Sci. USA* 117, 18278–18284. doi:10.1073/pnas.2008959117
- Schnyder, J. S. D., Eberli, G. P., Betzler, C., Wunsch, M., Lindhorst, S., Schiebel, L., et al. (2018). Morphometric Analysis of Plunge Pools and Sediment Wave fields along Western Great Bahama Bank. *Mar. Geology* 397, 15–28. doi:10.1016/j.margeo.2017.11.020
- Shaw, J., Puig, P., and Han, G. (2013). Megaflutes in a continental Shelf Setting, Placentia Bay, Newfoundland. *Geomorphology* 189, 12–25. doi:10.1016/j.geomorph.2013.01.010
- Shepard, F. P. (1951). “Transportation of Sand into Deep Water,” in *Turbidity Currents and the Transportation of Coarse Sediment to Deep Water*. Editor J. L. Hough (Tulsa: SEPM Sp. Pub.), 2, 53–65. doi:10.2110/pec.51.02.0053
- Simmons, S. M., Azpiroz-Zabala, M., Cartigny, M. J. B., Clare, M. A., Cooper, C., Parsons, D. R., et al. (2020). Novel Acoustic Method Provides First Detailed Measurements of Sediment Concentration Structure within Submarine Turbidity Current. *J. Geophys. Res. Oceans* 125, e2019JC015904. doi:10.1029/2019jc015904
- Spychala, Y. T., Eggenhuisen, J. T., Tilston, M., and Pohl, F. (2020). The Influence of basin Setting and Turbidity Current Properties on the Dimensions of Submarine Lobe Elements. *Sedimentology* 67, 3471–3491. doi:10.1111/sed.12751
- Stevenson, C. J., Jackson, C. A.-L., Hodgson, D. M., Hubbard, S. M., and Eggenhuisen, J. T. (2015). Deep-Water Sediment Bypass. *J. Sediment. Res.* 85, 1058–1081. doi:10.2110/jsr.2015.63
- Stow, D., and Smillie, Z. (2020). Distinguishing between Deep-Water Sediment Facies: Turbidites, Contourites and Hemipelagites. *Geosciences* 10, 68. doi:10.3390/geosciences10020068
- Straub, K. M., and Pyles, D. R. (2012). Quantifying the Hierarchical Organization of Compensation in Submarine Fans Using Surface Statistics. *J. Sediment. Res.* 82, 889–898. doi:10.2110/jsr.2012.73
- Sumner, E. J., Peakall, J., Parsons, D. R., Wynn, R. B., Darby, S. E., Dorrell, R. M., et al. (2013). First Direct Measurements of Hydraulic Jumps in an Active Submarine Density Current. *Geophys. Res. Lett.* 40, 5904–5908. doi:10.1002/2013gl057862
- Van der Merwe, W. C., Hodgson, D. M., Brunt, R. L., and Flint, S. S. (2014). Depositional Architecture of Sand-Attached and Sand-Detached Channel-Lobe Transition Zones on an Exhumed Stepped Slope Mapped over a 2500 Km² Area. *Geosphere* 10, 1076–1093. doi:10.1130/ges01035.1
- Vendettuoli, D., Clare, M. A., Hughes Clarke, J. E., Vellinga, A., Hizzet, J., Hage, S., et al. (2019). Daily Bathymetric Surveys Document How Stratigraphy Is Built and its Extreme Incompleteness in Submarine Channels. *Earth Planet. Sci. Lett.* 515, 231–247. doi:10.1016/j.epsl.2019.03.033
- Wang, W., Wang, D., Sun, J., Shao, D., Lu, Y., Chen, Y., et al. (2020). Evolution of deepwater Turbidite Bedforms in the Huangguang Channel-Lobe Transition Zone Revealed by 3D Seismic Data in the Qiongdongnan Basin, South China Sea. *Geomorphology* 370, 107412. doi:10.1016/j.geomorph.2020.107412
- Wells, M. G., and Dorrell, R. M. (2021). Turbulence Processes within Turbidity Currents. *Annu. Rev. Fluid Mech.* 53, 59–83. doi:10.1146/annurev-fluid-010719-060309
- Wynn, R. B., Kenyon, N. H., Masson, D. G., Stow, D. A. V., and Weaver, P. P. E. (2002a). Characterization and Recognition of Deep-Water Channel-Lobe Transition Zones. *Am. Assoc. Petrol. Geol. Bull.* 86, 1441–1462. doi:10.1306/61eedcc4-173e-11d7-8645000102c1865d
- Wynn, R. B., Piper, D. J. W., and Gee, M. J. R. (2002b). Generation and Migration of Coarse-Grained Sediment Waves in Turbidity Current Channels and Channel-Lobe Transition Zones. *Mar. Geology* 192, 59–78. doi:10.1016/s0025-3227(02)00549-2
- Yu, G., and Tan, S.-K. (2006). Errors in the Bed Shear Stress as Estimated from Vertical Velocity Profile. *J. Irrig. Drain Eng.* 132, 490–497. doi:10.1061/(asce)0733-9437(2006)132:5(490)

Conflict of Interest: The authors declare that the research was conducted in the absence of any commercial or financial relationships that could be construed as a potential conflict of interest.

Publisher's Note: All claims expressed in this article are solely those of the authors and do not necessarily represent those of their affiliated organizations, or those of the publisher, the editors, and the reviewers. Any product that may be evaluated in this article, or claim that may be made by its manufacturer, is not guaranteed or endorsed by the publisher.

Copyright © 2022 Hodgson, Peakall and Maier. This is an open-access article distributed under the terms of the Creative Commons Attribution License (CC BY). The use, distribution or reproduction in other forums is permitted, provided the original author(s) and the copyright owner(s) are credited and that the original publication in this journal is cited, in accordance with accepted academic practice. No use, distribution or reproduction is permitted which does not comply with these terms.



Contained-Reflected Megaturbidites of the Marnoso-arenacea Formation (Contessa Key Bed) and Helminthoid Flysches (Northern Apennines, Italy) and Hecho Group (South-Western Pyrenees)

Roberto Tinterri^{1*}, Tommaso Mazza¹ and Pierre Muzzi Magalhaes²

¹Department of Chemistry, Life Sciences and Environmental Sustainability—Earth Sciences Unit, University of Parma, Parma, Italy, ²Petrobras (Petroleo Brasileiro), Rio de Janeiro, Brazil

OPEN ACCESS

Edited by:

Rosanna Maniscalco,
University of Catania, Italy

Reviewed by:

Salvatore Milli,
Sapienza University of Rome, Italy
Giacomo Dalla Valle,
National Research Council (CNR), Italy

*Correspondence:

Roberto Tinterri
roberto.tinterri@unipr.it

Specialty section:

This article was submitted to
Sedimentology, Stratigraphy and
Diagenesis,
a section of the journal
Frontiers in Earth Science

Received: 17 November 2021

Accepted: 14 January 2022

Published: 25 February 2022

Citation:

Tinterri R, Mazza T and Magalhaes PM
(2022) Contained-Reflected
Megaturbidites of the Marnoso-
arenacea Formation (Contessa Key
Bed) and Helminthoid Flysches
(Northern Apennines, Italy) and Hecho
Group (South-Western Pyrenees).
Front. Earth Sci. 10:817012.
doi: 10.3389/feart.2022.817012

Contained-reflected beds deposited by fully-ponded or partially-reflected turbidity currents are important because their correct evaluation can give important indications on the degree of basin confinement and on the type, size and orientation of the morphological obstacle. Through a detailed facies analysis of various significant megabeds in the Marnoso-arenacea Formation, including the Contessa key bed, in the helminthoid flysches in the northern Apennines (Italy) and in the Pyrenees (megaturbidite MT5), this work proposes a depositional model that is well consistent with the recent experimental data available in the literature, discussing their strengths and limits. The Contessa and flysch megabeds fit very well with the experimental conditions because they are deposited in narrow and elongated confined basins characterized by axial flows. Indeed, in the proposed model, it is possible to recognize facies deposited by: 1) a basal underflow directed towards the bounding slope (Facies A), 2) an intermediate part of the flow characterized by lateral deflections (facies B1), 3) an upper well-developed reversing flow (facies B2) and 4) an uppermost residual reversing flow recording the final collapse of the fine-grained suspended load forming a poorly-sorted slurry facies C and a very thick mudstone unit D. Facies A, B1 and B2 are usually separated by very thin fine-grained muddy drapes rich in carbonaceous matter, which can be traced throughout the basin. These drapes - very common in contained and confined beds in these settings - can be related to internal density surfaces, along which decoupling processes, separating underflows from reversing overflows, can easily occur. Conversely, as the MT5 is characterized by a source transversal to an elongated narrow basin, the large flow volume versus basin capacity hinders the generation of reversing flows and rebound layers favoring the formation of fully-ponded pulsating overflows able to deposit alternations of laminated and massive units. This facies type can be observed in the basins that are characterized by axial flows only near the basin margins where the pulsating collapse of the reversing flow can dominate. This study shows that the integration of detailed field studies are essential to validate experimental data from an applicative point of view.

Keywords: megaturbidites, contained-reflected beds, facies analyses, contessa megabed, helminthoid flysches

1 INTRODUCTION

Contained-reflected beds deposited by fully (ponded) or partly reflected turbidity currents have long been studied with experimental works, numerical modeling and facies analysis. They are very important because the correct evaluation of the flow reflection nature and direction can give important indications not only on the degree of basin confinement but also on the type, size and orientation of morphological obstacles, which, in foreland basins, are generally tectonic structures (e.g., Kneller, 1995).

In spite of the various depositional models based on field data (Pickering and Hiscott, 1985; Haughton, 1994; Remacha et al., 2005; Tinterri and Muzzi Magalhaes, 2011; Bell et al., 2018) and recent experimental and numerical models that have tried to clarify the dynamics of reflected to fully-ponded turbidity currents (Patacci et al., 2015; Howlett et al., 2019; Soutter et al., 2021), the processes and resulting facies of these types of contained-reflected flows are still poorly understood in detail and various problems remain open. First of all, a detailed depositional model aimed at recognizing the various experimental phases in ancient turbidites is not yet well defined. Secondly, other more specific open problems are the distinction between combined flow structures and mud-controlled sedimentary bedforms (e.g., Tinterri, 2011; Baker and Baas, 2020), as well as the interaction between flow reflections and the formation of mud-rich transitional flows able to deposit poorly-sorted slurry facies (e.g., Tinterri et al., 2016; Bell et al., 2018). Contained-reflected beds can be found in all depositional elements of a turbidite system but ponded beds deposited by low-density turbidity currents dominate especially the basin plains or lobe fringes where the interaction between flow decelerations and dynamics of mud rich transient turbulent flows (*sensu* Baas et al., 2011) can become important.

This work wants to present several recorded cases of bed types and facies tracts of megaturbidites deposited by high- and low-density turbidity currents related to flow reflections perpendicular and oblique to the morphology in partially or fully confined settings. These examples mainly come from turbidites in the northern Apennines (Marnoso-arenacea Formation, MAF and helminthoid flyschs, i.e., M. Cassio and Solignano Formations), and in the southern Pyrenees (megaturbidite MT5 in the Banaston turbidite system). All these deposits are suitable for discussion of open problems and try to propose depositional models that can link experimental and field data. In particular, this objective is achieved through a detailed physical stratigraphy and facies analysis of the Contessa key bed, i.e., the main key bed of the MAF (e.g., Ricci Lucchi and Valmori, 1980; Muzzi Magalhaes and Tinterri, 2010).

2 PREVIOUS WORKS: LABORATORY EXPERIMENTS AND DEPOSITIONAL MODELS

When a turbidity current encounters a topography, the flow can be laterally deflected or completely reflected, depending on the obstacle size in relation to the flow volume, the geometry of the slope and the

angle of incidence of the current (Tinterri, 2011; Patacci et al., 2015). In this case the flow can be defined as “confined” if the confining topography partially or totally traps the current, and, in case of total entrapment, the turbidity current can be also defined as “contained”. Consequently, the confined and contained turbidity currents can be also defined as ponded turbidity currents in which a flat-topped suspension cloud is established (Patacci et al., 2015).

The first laboratory experiments available in the literature focused on the processes related to lateral (Kneller et al., 1991; Haughton, 1994; Amy et al., 2004) and frontal rebounds (e.g., Pantin and Ledeer, 1987; Alexander and Morris, 1994; Edwards et al., 1994) of surge type flows discussing especially the dynamics of internal waves propagation. However, as Kneller and Branney (1995) and Kneller (1995) introduced a model that was based on various combinations of different spatial and temporal accelerations (i.e., nonuniformity and unsteadiness, respectively) and was able to produce markedly different vertical and lateral variations in the resulting turbidite bed, they highlighted, for the first time ever, the importance of submarine topography in controlling flow deflection and reflection, as well as variations in flow velocity in space (flow nonuniformity) producing anomalous intrabed vertical sequences, multiple current directions and locally enhanced deposition.

Conversely, the recent experiments by Patacci et al. (2015) focused on the behavior of sustained ponded suspension clouds showing that ponded flows are characterized by a well-determined sequence of dynamic phases. More precisely, a flow impinging a confining slope produces, firstly, a flow reversal causing a bore or soliton up current propagation that leads to an initial inflation phase of ponded suspension. Then, the progressive flow inflation forms a circulation of a ponded suspension characterized by an underflow directed towards the bounding slope and an upper return layer separated by a well-developed internal density and velocity interface where internal waves can propagate. Finally, cloud deflation on waning of input produces final settling of fines from a static cloud (**Figure 1A**).

More recently, numerical experiments by Howlett et al. (2019) have given results similar to those obtained by Patacci et al. (2015). These models discuss turbidity currents impinging against a topography perpendicular to the flow direction, and highlight that a supercritical current decelerated and thickened due to the hydraulic jump on the counter-slope, where a reverse overflow formed through current self-reflection and a reverse underflow was issued by backward squeezing of a dense near-bed sediment load (see **Figure 1B**). Very similar results can be also observed in the works by Woods et al. (1998), Lamb et al. (2004), Lamb and Parsons (2005), and Toniolo et al. (2006). The experimental results by Howlett et al., 2019 have been further investigated by Soutter et al. (2021), studying, in addition to a morphology perpendicular to the incoming flow, cases in which the topography is parallel and oblique to the flow.

Conversely, the sedimentary structures indicating flow reflections and ponding processes are relatively well established in the literature thanks especially to the depositional models by Pickering and Hiscott (1985) from the Cloridorme Formation, by Haughton (1994) from the Sorbas basin, Remacha et al. (2005) from the Hecho basin and Tinterri and Muzzi Magalhaes (2011) from the MAF (see **Figures 1D,E**).

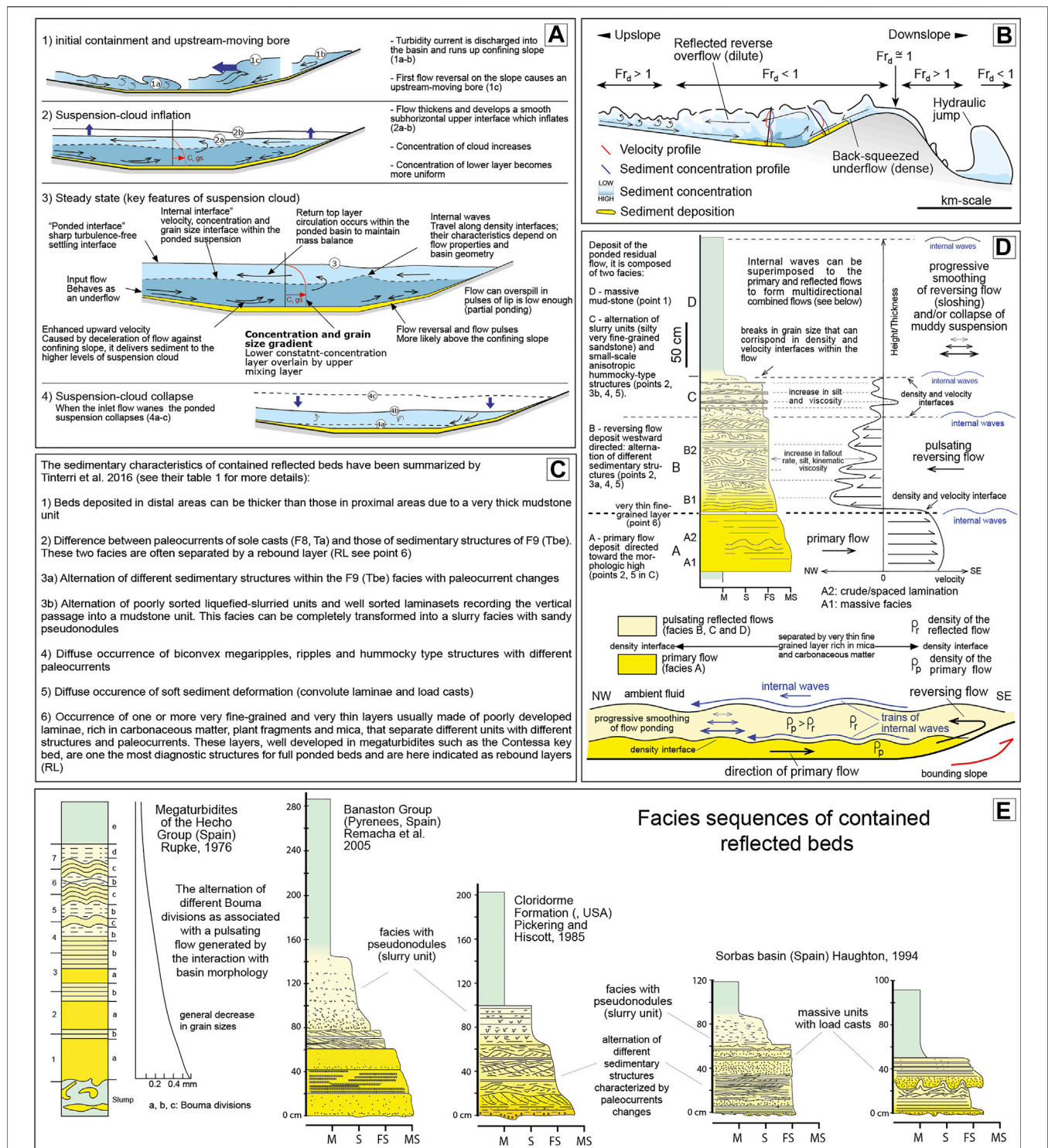


FIGURE 1 | (A) Scheme of a ponded suspension cloud from laboratory experiments by Patacci et al. (2015), **(B)** Schematic diagram summarizing the flow reflection dynamics against a morphologic obstacle (from Howlett et al., 2019), **(C)** List of the main diagnostic sedimentary structures characterizing contained-reflected beds (from Tinterri et al., 2016), **(D)** Model describing a frontal reflection, which tries to link the facies sequence of a typical contained-reflected bed in the Marnoso-arenacea Formation with the dynamics of a pulsating reflected turbidity current (from Tinterri et al., 2016); **(E)** Main facies sequences of contained-reflected beds discussed in the literature [see also (D)].

In particular, Tinterri et al., 2016 proposed a depositional model based on the studies carried out over the last 10 years in the MAF, trying to summarize the main sedimentary characteristics of the contained-reflected beds in basin plain (**Figures 1C,D**). These sedimentary structures, which are summarized in **Figure 1C**, can characterize both fully contained ponded beds and not-contained strata that undergo only lateral and frontal rebound.

Furthermore, the dynamic behavior of the turbidity currents in a confined basin changes according to flow concentration (high- and low-density) and to the degree of flow-density stratification that can favor hydraulic jumps and decoupling processes (see Postma et al., 2009; Postma and Cartigny, 2014; Tinterri et al., 2016). For these reason, facies and processes of high and low-density flows in fully-ponded basins, mainly characterized by frontal reflections, will be discussed with the aim to try to show new facies models and a possible link with the available experimental data.

3 FULLY CONTAINED AND CONFINED “PONDED” MEGATURBIDITES

These bed types can be seen as contained-reflected beds in which the degree of basin confinement versus the flow volume allows fully-ponded conditions. The turbidity currents that deposit these types of beds are able to cross the entire basin and to undergo one or more reflections. In general, these bed types can be seen as megaturbidites, i.e., very thick beds of virtually basin wide extent that usually form excellent key beds (see Mutti et al., 1984). Magnificent examples of megaturbidites are those in the south western Pyrenean foreland basin, where each megaturbidite consists of a bipartite graded bed up to 200 m thick displaying a basal megabreccia that contains large slabs of shallow water limestones and outsize rip-up marlstone clasts, which pass upward into an up to 20 m graded unit composed of a basal coarse-to fine-grained biocalcarene characterized by an alternations of horizontal and ripple lamination (Rupke, 1976; see **Figure 1E** and below) and an upper homogeneous calcareous mudstone (see Labaume et al., 1983; Labaume et al., 1987; Mutti et al., 1999; Payros et al., 1999). These megaturbidites can be interpreted as deposited by bipartite flows composed by a basal dense flow and an upper turbulent flow produced by the evolution and transformation of fast-moving, inertia-driven avalanche-blocky flows (*sensu* Ogata et al., 2012) derived from adjacent carbonate platforms triggered by major seismic shocks associated with thrust propagation. On the basis of the sedimentary structures described by Rupke (1976), it can be inferred that the upper turbulent flow must have undergone important reflections and rebound processes as occurred in other megaturbidites, such as the Gordo bed in the Sorbas basin (Kleverlaan, 1987) and Megabeds of the Cervarola Sandstones (Tinterri and Piazza, 2019; Piazza and Tinterri, 2020) and in the Cerro Bola Fm. in Argentina (Falgatter et al., 2016). Other famous examples come from the Eocene flysch of the Dalmatia in Croatia (Marjanac, 1990). Consequently, the upper graded beds characterizing these bipartite megaturbidites are the most likely to present the characteristics of ponded beds.

The Contessa key bed in the MAF, the megabeds of the Helminthoid flysches (northern Apennines, Italy) can represent very good examples of these bed types characterizing

the upper part of the megaturbidites and deposited by turbulent flows as in the case of the megabed at the top of MT5 (Hecho Group). In particular, being characterized by a massive to crudely laminated coarse-grained basal unit, the Contessa key bed and MT5 megabed can be interpreted as deposited by high-density turbidity currents, whereas the megabeds of the Cassio Fm., being characterized by fine-grained laminated basal sandstone, can be interpreted as deposited by a low-density turbidity current.

3.1 The Contessa Key Bed (Marnoso-arenacea Formation)

3.1.1 Introduction

The Contessa Key bed (CKB, Renzi, 1964; Ricci Lucchi and Piali, 1973; Ricci Lucchi and Valmori, 1980) is the most important key bed in the MAF foredeep turbidites (Langhian-Tortonian) in the northern Apennines (Italy), (**Figure 2A**). The MAF turbidites, deposited in an elongate, NW-stretched foredeep basin formed in front of the growing Northern Apennines orogenic wedge, were fed mainly by Alpine sources to the north, whereas minor sources providing hybrid and carbonate sediments included shallower water carbonate platforms along the southern and south-eastern margins of the basin (Gandolfi et al., 1983; Ricci Lucchi, 1986). The main sediment dispersal pattern was longitudinal and the northwest to southeast flowing turbidity currents had a siliciclastic composition. By contrast, carbonate and hybrid turbidites flowing in the opposite direction, i.e., towards the north-west, produced the main key beds (**Figure 2A**). Together with the fact that, among foredeep turbidites, the MAF is the best exposed and less structurally deformed one due to its relatively external position within the Apenninic orogen, these marker beds have favoured detailed physical stratigraphy studies, such as the pioneering one by Ricci Lucchi and Valmori (1980) and more recently those by Amy and Talling (2006) and Muzzi Magalhaes and Tinterri (2010) and Tinterri and Tagliaferri (2015), (see also Tagliaferri and Tinterri, 2016; Tagliaferri et al., 2018).

Thanks to the regional stratigraphic framework by Muzzi Magalhaes and Tinterri (2010), (see **Figures 2B,C**), it can be stated that the Contessa key bed is located in a stratigraphic interval characterized by tectonic quiescence allowing this megabed to be traced in the entire basin, i.e., over an area of about 125 × 25 km (Ricci Lucchi and Valmori, 1980; Muzzi Magalhaes and Tinterri, 2010).

3.1.2 Description

The high-resolution stratigraphic framework of the CKB has been carried out through the measurement and description of 23 stratigraphic logs parallel and perpendicular to the paleocurrents directed towards the northwest (**Figures 2D, 3A, 4**; see also Tinterri and Mazza, 2019).

In general, the CKB, with thickness ranging from 9 to 15 m, is a normally graded bed characterized by a well-developed bipartition highlighted by a basal sandstone unit ranging from 3.5 to 6.5 m and an upper mudstone unit with thickness ranging from 5 to 9 m (**Figure 2E**). The basal sandstone unit is characterized by high

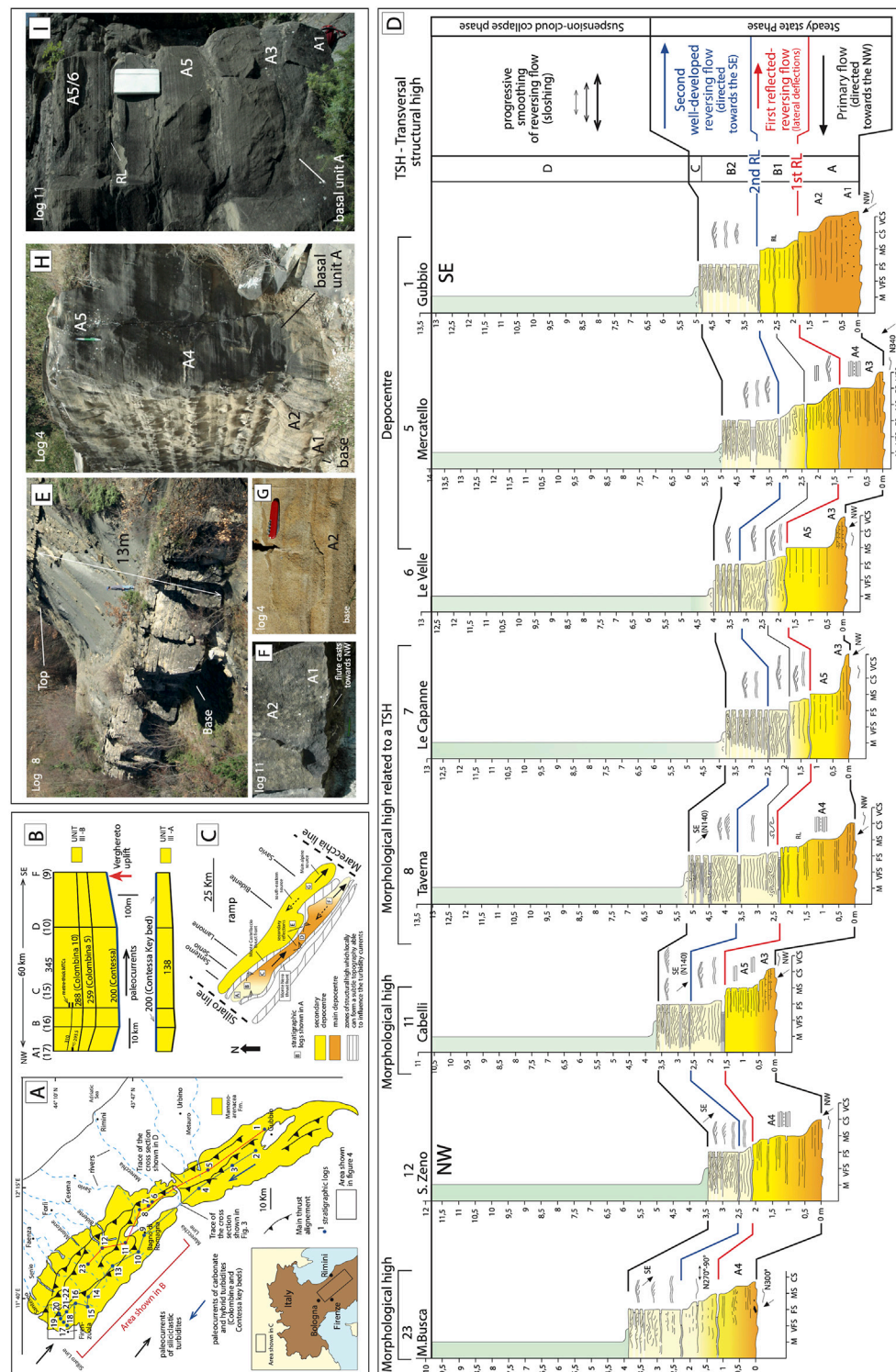


FIGURE 2 | (A) The MAF cropping out in the Northern Apennines, with the locations of the Contessa key bed stratigraphic logs, **(B)** Stratigraphic-cross section of the MAF Unit III including the Contessa key bed (from Muzzi Magalhaes and Tinterri, 2010), **(C)** Schematic paleogeography of the basin during the deposition of Unit III (from Tinterri and Muzzi Magalhaes, 2011), **(D)** Detailed stratigraphic cross section of the Contessa megabed in the outer basin (see red trace in **Figure 2A**). On the right the interpretation in terms of facies and processes is shown. The flow phases on the right are those by Patacci et al. (2015); **(E)** Contessa megabed in Log 8; **(F,G)** Details of basal coarse-grained massive facies A1 and crudely laminated facies A2 (logs 11 and 4, respectively); **(H)** Facies characterizing the basal part of the CKB deposited by the primary flow (Log 4); **(I)** Details on the basal part of the CKB below the first rebound layer (1st RL) deposited by the primary flow (Log 11). For the location of stratigraphic logs, see **(A)**.

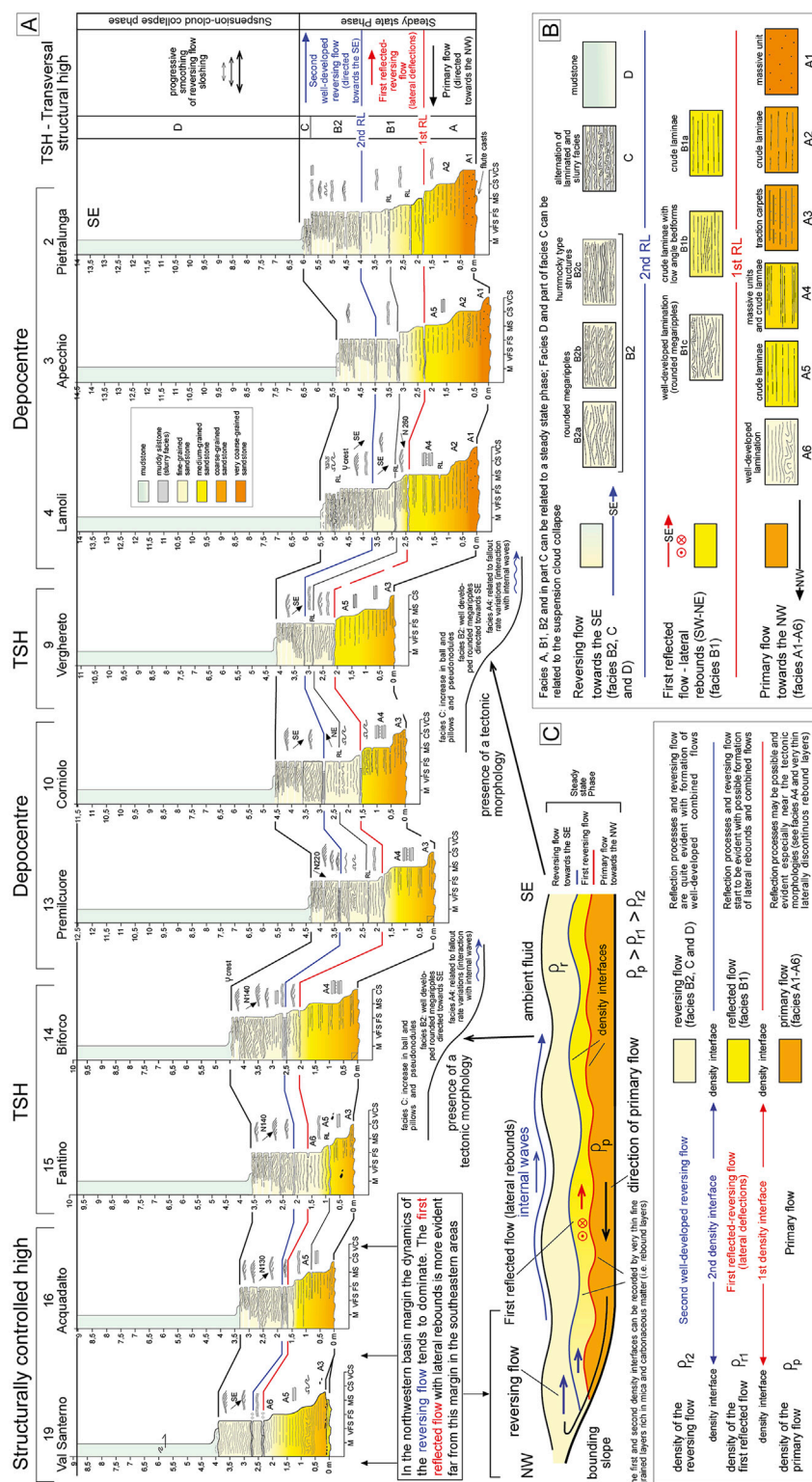
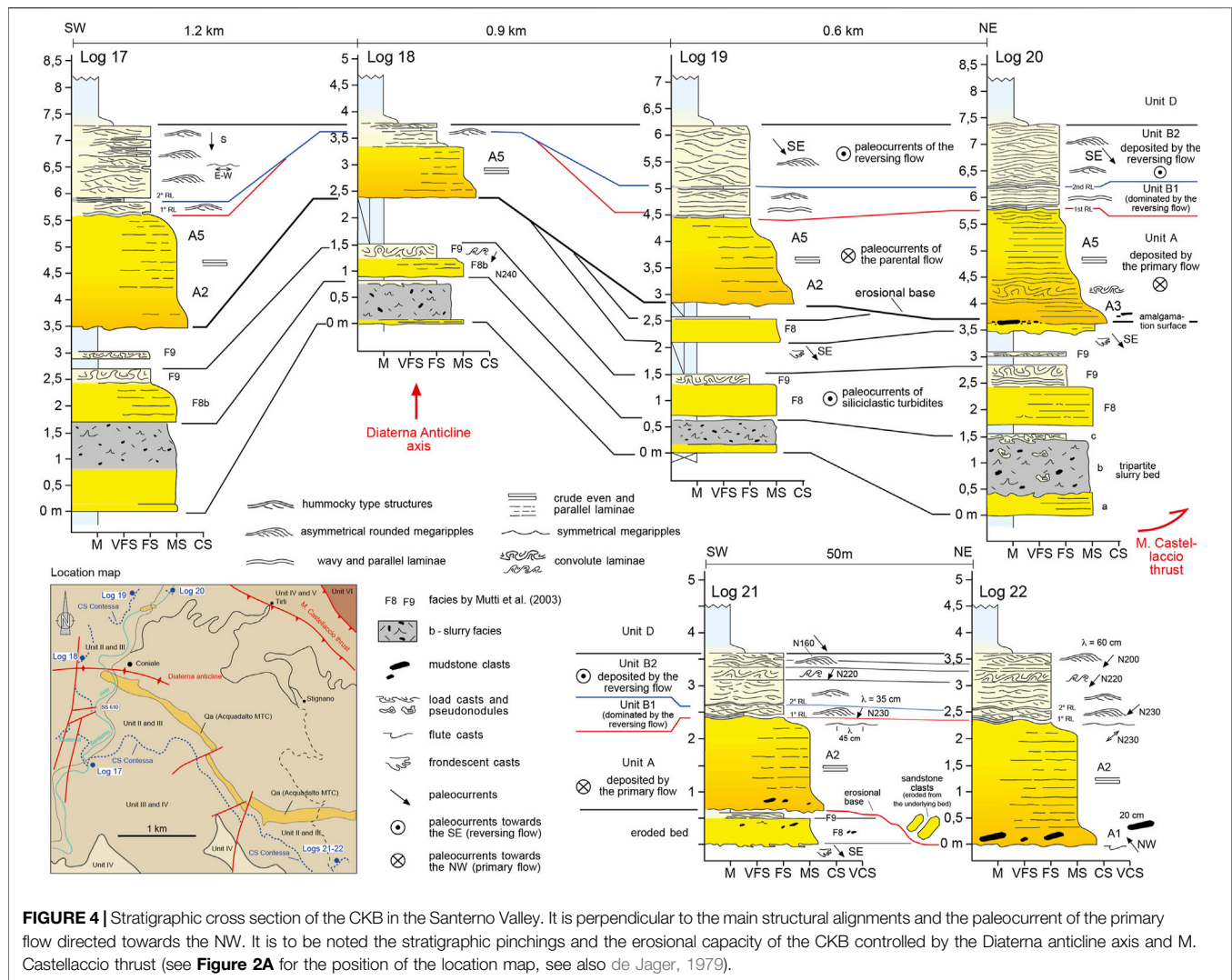


FIGURE 3 | (A) Detailed stratigraphic cross section of the Contessa megabed in the inner basin (see blue trace in **Figure 2A**). On the right, the interpretation in terms of facies and processes is also shown. The flow phases on the right are from Patucci et al. (2015); **(B)** Facies scheme of the CKB with facies deposited by the primary flow, first reflected flow characterized by lateral deflections and reversing flow; **(C)** Depositional model of the CKB.



variability in term of grain sizes, sedimentary structures and paleocurrents; however, the occurrence of two evident very thin and fine-grained layers rich in carbonaceous matter and plant fragments (i.e., the rebound layers RL by Tinterri et al., 2016) allow the sandy part of the CKB to be distinguished in three intervals, namely basal, intermediate and upper (see **Figures 2D, 3**; see also Tinterri et al., 2019b). In particular, **Supplementary Table S1** in the supplementary materials shows the list of the facies introduced in this work and their comparison to the facies scheme by Mutti et al. (2003).

The basal one is made of granular very coarse-to medium-grained sandstone characterized by well-developed flute casts indicating paleocurrents towards the northwest. On the basis of the grain sizes and sedimentary structures in this basal interval, at least six facies can be distinguished, which, from the coarsest to the finest ones, are: A1) massive granular very coarse-grained sandstone (**Figures 2F–I**). This facies can be found in the more proximal logs 1, 2, 3 and 4 (see **Figures 2D, 3A**) and can also be associated with mudstone and sandstone intraclasts, sand injections and delamination structures characterized by vertical

erosional surfaces (**Figure 4**; see also Felletti et al., 2019); A2) crude laminated very coarse to coarse-grained sandstones (**Figures 2G,H, 3**); A3) coarse-grained sandstone characterized by a well-developed traction carpets; A4) coarse to medium-grained sandstone characterized by an alternation of crudely laminated and massive units. This facies can be found especially in the intermediate logs 4, 8, 10, 13 and 14 (**Figures 2H, 3**); A5) crudely laminated medium-grained sandstones; A6) laminated fine-grained sandstone. Facies A5 and A6 are found especially in the more distal logs 16 and 19 (**Figures 3, 4**).

In general, facies A1 tends to evolve into facies A5 and A6, through intermediate facies A2, A3 and A4, both downcurrent and upward within the basal unit. The latter, mainly composed of facies A1–5, is separated from the intermediate unit by a first very thin and fine-grained layer (i.e., a rebound layer-RL). This thin layer can be traced relatively well in the entire study area (see 1st RL—red fine-grained drape in **Figures 2D, 3A, 5**) and is highlighted by the widespread occurrence of carbonaceous matter and plant fragments (**Figures 5D,E**).

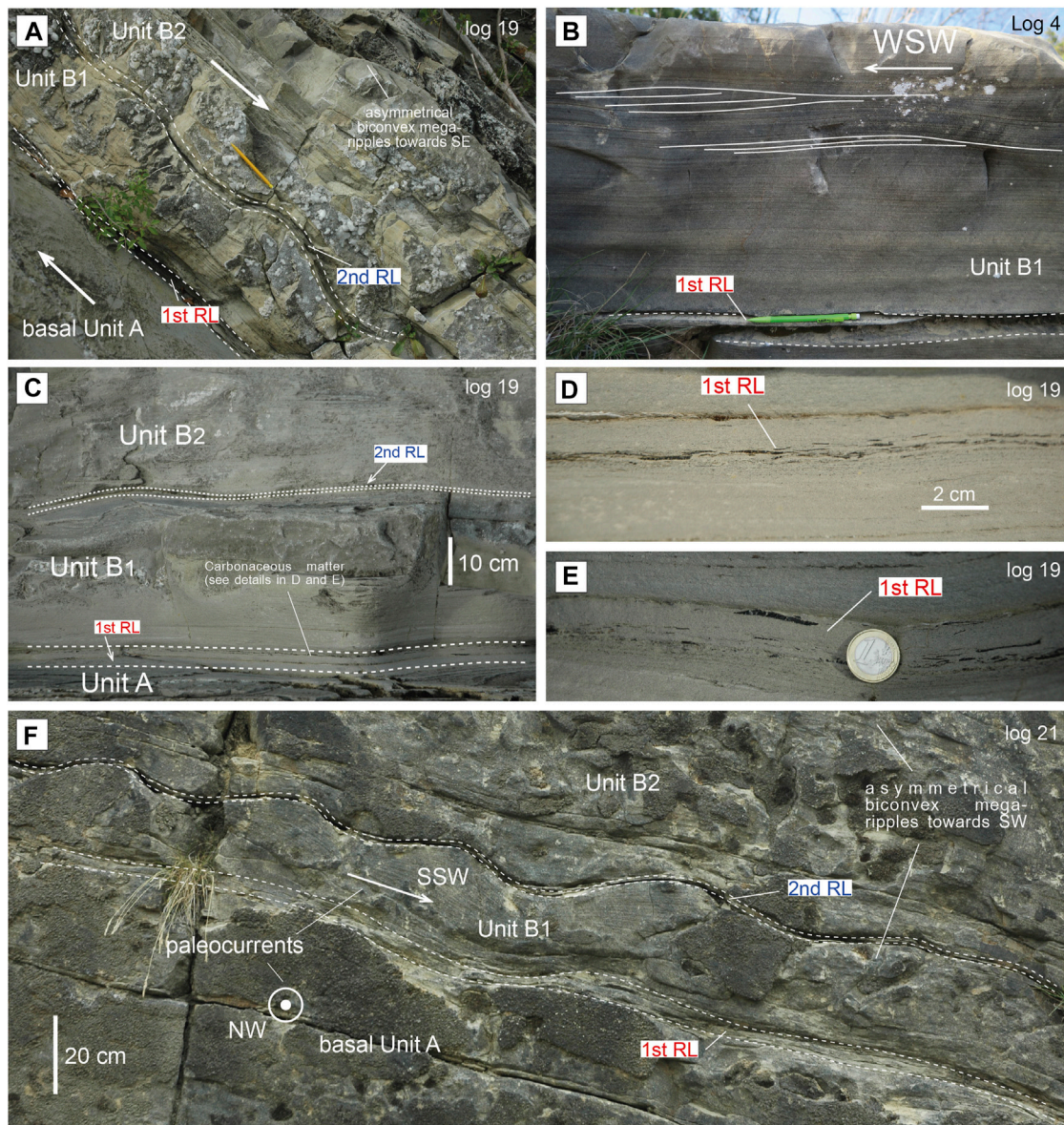


FIGURE 5 | (A) Examples of facies B1 and B2 in Log 19 (Santerno valley) separated by the 1st (red) and 2nd (blue) evident rebound layers; (B) Facies B1 in Log 4 (Lamoli) with evidence of lateral deflections; (C) Facies B1 and B2 separated by the 1st (red) and 2nd (blue) rebound layers in Log 19; (D,E) First rebound layer separating facies A and B rich in carbonaceous matter (see C for the location of the photos); (F) Facies B1 and B2 separated by the 1st (red) and 2nd (blue) rebound layers (Log 21); to be noted the slightly asymmetrical megariipples with paleocurrents towards the SW in Unit B1 (see Figure 4 for the location of the Logs).

The intermediate unit B1 is made of, at least, three facies (see Figure 3, Supplementary Table S1), namely: B1a) medium to fine-grained sandstone characterized by crude even and parallel lamination that sometimes shows subtle undulations or very low-angle laminae. This facies occurs especially in more proximal southern logs 1, 2 and 3 (see Figures 2, 3); B1b) similar to B1a, this facies is characterized by the appearance of anisotropic hummocky-like megariipples (wavelength of about 30–40 cm) showing paleocurrents roughly perpendicular to or at high angle with those indicated by the flute casts directed towards northwest (see log 4, Figures 3, 5B,C); B1c) fine-

grained sandstone characterized by a poorly-developed alternation of crude even/undulated and parallel lamination with hummocky-type megariipples showing paleocurrents directed towards the southeast, i.e., in the opposite direction vs. the north-westward paleocurrents indicated by flute casts (Figures 5A,F). In general, facies B1a tends to evolve into facies B1c, in a downcurrent direction, even if the appearance of the hummocky megariipples seems to be related to specific basin morphologies (see Figures 2D, 3).

The intermediate sandstone unit is separated from the upper sandstone unit by a second very thin and fine-grained layer,

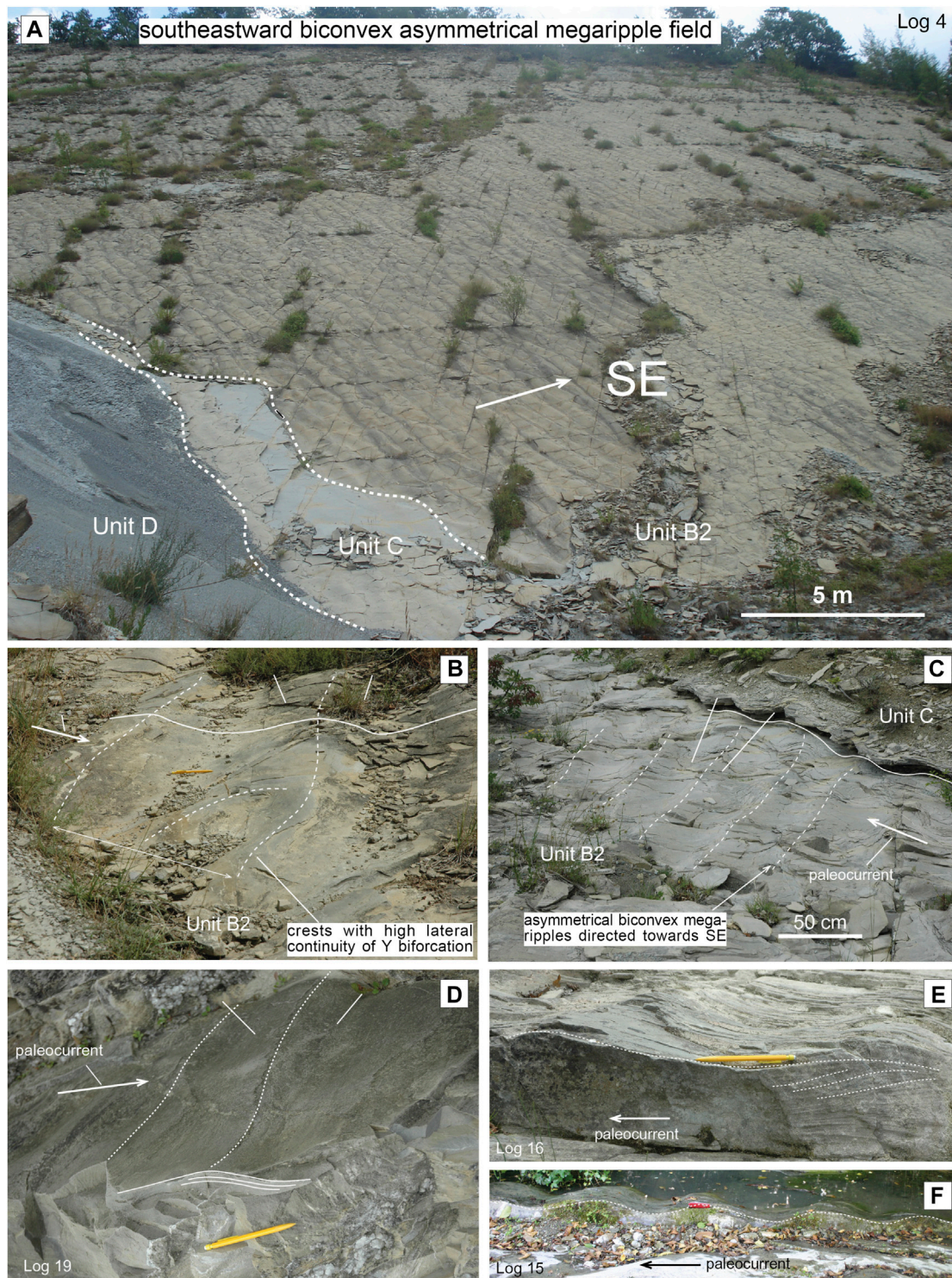


FIGURE 6 | (A) Spectacular and famous outcrop near Lamoli (Log 4) showing a field of south-eastward biconvex megaripples, where the large lateral continuity of the crests can be also observed. These megaripples characterize Unit B2 and are deposited by a well-developed reversing flow (see **Figure 3C** for the interpretation); **(B)** Biconvex megaripples characterized by a typical Y bifurcation (Log 14); **(C)** Asymmetrical biconvex megaripples with a high-lateral continuity of the crests (Taverna near Log 8); **(D–F)** Examples of biconvex (rounded) megaripples with sigmoidal-cross laminae in Logs 19, 16 and 15, respectively. See **Figures 2A,D, 3A** for the location of the logs.

which, as the first, can be traced relatively well in the entire study area (see 2nd RL—blue fine-grained drape in **Figures 2, 3, 5**). This layer is also characterized by widespread occurrence of carbonaceous matter and plant fragments.

The third upper sandstone unit is composed of two main facies indicated as B2 and C in **Figures 2D, 3, 6** and **Supplementary Table S1**. Facies B2 is made of fine to very fine-grained sandstone and is characterized by widespread occurrence of biconvex asymmetrical megaripples always indicating paleocurrents directed towards the southeast, i.e. in the opposite direction vs. the north-westward paleocurrents indicated by flute casts. These megaripples have a wavelength of about 40–50 cm and are characterized by internal sigmoidal-cross laminae (**Figure 6**). The crests have high lateral continuity (**Figures 6A–F**) showing sometimes well-developed Y bifurcations very similar to those of wave ripples (**Figure 6B**).

Facies B2 can be subdivided into three different categories (see **Figure 3, Supplementary Table S1**), namely: 1) facies B2a entirely composed of the biconvex asymmetrical megaripples described above, 2) facies B2b characterized by an alternation of undulated laminae and symmetrical biconvex megaripples and hummocky-type structures and 3) facies B2c mainly composed of wavy to even and convolute laminations. Facies B2a tend to evolve towards the south into facies B2c, i.e. in the same direction indicated by the biconvex megaripples. The megaripples of facies B2a are consistent with the reversing or back flow ripples by Parea and Ricci Lucchi, 1975 (see also Ricci Lucchi and Valmori, 1980; Ellis, 1982; Ricci Lucchi, 1995).

Facies B2 pass upward into facies C, which records the vertical transition to the upper mudstone unit D. Facies C is made of an alternation of poorly-sorted silty to muddy very fine-grained slurried sandstone and well-developed laminasets generally characterized by anisotropic hummocky-type megaripples directed towards the south-east and widespread soft-sediment deformation represented by convolute laminae and load casts. The latter are represented by ball and pillows characterizing the base of the laminasets, which can evolve in detached pseudonodules within the underlying poorly-sorted slurried facies. Facies C is not present everywhere but only in well-determined zones that generally are associated to structural highs (see logs 4, 6, 7 and 8 in **Figure 3A**).

Facies C records the vertical passage into the uppermost facies D composed of a very thick mudstone unit characterized by an apparently massive facies (**Figure 3**).

As mentioned above, the CKB is deposited in the stratigraphic Unit III by Muzzi Magalhaes and Tinterri (2010) and, although this is a unit deposited during a period of relatively tectonic quiescence, the increase and decrease in the CKB thickness tend to be consistent with the depocentres and structural highs highlighted the high-resolution stratigraphic framework carried out by Muzzi Magalhaes and Tinterri (2010). Mudstone and sandstone intraclasts in facies A and erosive delamination structures tend to be located in those logs in which a stratigraphic pinching can be observed (see **Figures 2D, 4**). Generally, these stratigraphic pinchings are located near tectonic structures as showed by the stratigraphic-cross section

of **Figure 4** where erosional features and the lowest thickness in the CKB are located above the Diaterna anticline axis.

3.1.3 Interpretation

Based on the facies descriptions the CKB can be interpreted as a typical contained and reflected bed in which the degree of basin confinement allows fully-ponded conditions (see Parea and Ricci Lucchi, 1975; Ellis, 1982; Ricci Lucchi, 1995; Tinterri and Muzzi Magalhaes, 2009, Tinterri and Muzzi Magalhaes, 2011). Indeed, facies A, B, C and D are consistent with the facies categories introduced by Tinterri et al. (2016) for contained-reflected beds (see also Tinterri et al., 2012; Tinterri et al., 2019b). However, thanks to the detailed facies analysis of the CKB, a detailed depositional model can be advanced in which the two very fine-grained layers that can be interpreted as rebound drapes (RL; see Tinterri et al., 2016; Tinterri et al., 2019a), play a key role.

The basal sandstone unit of the CKB can be divided into three units (A, B and C) thanks to two main fine-grained very thin levels rich in carbonaceous matter (1st and 2nd rebound drapes, see **Figure 3** and **Supplementary Table S1**). The first one (red line) separates the basal facies A deposited by a high-density primary flow (directed towards the NW) from the intermediate unit composed of facies B1 in which sedimentary structures indicating lateral reflections and reversing flow start to be common. Conversely, the second RL (blue line) separates the intermediate unit from the upper sandstone unit dominated by biconvex asymmetrical megaripples and hummocky-type structures (facies B2 and C) indicating paleocurrents directed towards the SE and produced by a well-developed reversing flow directed towards the same direction, i.e., SE. These very thin rebound drapes must record a deposition from a relatively quiescent period after reflected or reversing flows had bypassed.

As well known in the literature, the CKB, characterized by a hybrid composition (Gandolfi et al., 1983), was deposited by a turbidity current coming from the south. The source area, able to supply terrigenous and intrabasinal sediment, is thought to be located in a southeastern area of the Apenninic margin (Gandolfi et al., 1983). Consequently, facies A1 to A6 were deposited by the basal part of a bipartite flow represented by a high-density primary flow evolving towards the northwest. This flow can be highly erosive as testified by well-developed bulbous flute casts and delamination structures able to erode the underlying beds (see also Felletti et al., 2019). In this case, in the basal facies A1, mudstone and sandstone clasts can be common (see Log. 15 in **Figure 3A** and **Figure 4**). Delaminations structures, however, seem to be associated with tectonically-controlled basin morphologies that can enhance flow impacts and erosive processes (see **Figure 4**). Log 15 is associated with the Val Lamone tectonic structure separating an uplifted northwestern area from a depocentral southeastern zone (see Muzzi Magalhaes and Tinterri, 2010) whereas the stratigraphic cross section in **Figure 4**, perpendicular to the paleocurrents and to the Diaterna anticline axis and M. Castellaccio thrust shows that these structures can enhance the erosive capacity of the flows and bed amalgamations (see Log 19).

In particular, massive facies A1 is interpreted as deposited by high rates of fallout able to suppress the turbulence at the boundary layer, whereas facies A3, dominated by traction carpets, can be seen as a traction-dominated facies recording the bypass of a sandy high-density turbidity current able to transport northwards the medium-grained sand that would then form the depositional crudely laminated facies A4 and A5 (see **Supplementary Table S1**). The crude or spaced lamination indicates progressive aggradation under a high rate of fallout forming a near-bed suspension in which well-developed tractive structures are prevented by the absence of a sharp rheological interface between the lowest parts of the flow and the just-formed deposit (Kneller and Branney, 1995). In particular, the alternation of crude laminations and massive units characterizing facies A4 may be interpreted as related to decreases and increases in fallout rates generated by increases and decreases, respectively, in flow velocity and turbulence energy. These types of variations can be induced by constructive and destructive interferences between internal wave trains, produced by lateral reflections against the basin margins, and the unidirectional turbidity current directed towards the north (Tinterri, 2011; Patel et al., 2021). Indeed, facies A4 is well developed to the south of the following tectonic structures: Verghereto (Log 4), Lamone (Logs 13, 14, 15) and Diaterna anticline (Logs 21, 22) (see **Figures 3A, 4**).

The basal unit A is separated from the upper unit B1 by the first RL, which can be deposited by the tail rich in carbonaceous matter and mica of the upper turbulent flow bypassing the deposits of unit A. This bypass can be induced by lateral flow reflections rather than a well-developed reversing flow, since no well-developed reversing megariipples directed towards the southwest are present. These lateral rebounds and decelerations of the bipartite flow can favor decoupling processes with the detachment and partial bypass of the upper turbulent flow (see **Section 6.1** for more details). Indeed, in the second sandstone unit B1, facies B1a tends to decrease in thickness towards the northeast, passing into facies B1c through facies B1b in which megariipples directed towards northeast and southwest, i.e., roughly perpendicular to the primary flow, are common. The reversing megariipples directed towards the south start to be present especially in distal zones, i.e., in Logs 14, 17, 21 (**Figures 3A, 4**) and this can be associated with the beginning of a complete reflection of the upper turbulent flow favoured by the presence of important transversal tectonic structures, such as those of the Sillaro and Val Lamone lines (see Tinterri et al., 2019a, **Figure 3A**). According to the stratigraphic framework by Muzzi Magalhaes and Tinterri (2010), in the northwestern area, the stratigraphic unit III including the CKB is deposited in a tectonically uplifted zone as testified by the stratigraphic pinching of this unit towards the northwest and the occurrence of large-volume mass-transport deposits (see **Figures 2A–C**). In particular, the area of the Lamone valley (Logs 14, 15, **Figure 3A**) separates a northwestern uplifted area from a southeastern depocenter located in the Bidente valley (see Log 10); it is here supposed that this zone may be associated to a transversal tectonic structure related to the Sillaro line that could produce a barrier able to induce complete reflection of a turbidity current coming from the south,

as also supposed by Ellis (1982). Consequently, in distal areas near the northern basin margin, facies B1 passes into a thin B1c facies testifying that the flow is dominated by processes related to the reversing flow (see **Figure 3**).

The evidence of a clear reversing overflow directed towards the southeast is present in the upper sandstone units B2 and C where well-developed biconvex megariipples and anisotropic hummocky-type structures can be found (see **Figure 6**). In general, climbing-biconvex megariipples with sigmoidal-cross laminae (facies B2a) pass downcurrent (i.e., towards the southeast) into symmetrical small-scale hummocky-type structures and wavy to even laminae (facies B2c) suggesting a south-eastward evolution of the reversing flow.

These megariipples have been interpreted as traction-plus-fallout structures related to a unidirectional backflow (Parea and Ricci Lucchi, 1975; Ricci Lucchi and Valmori, 1980; Ellis, 1982), or as antidunes by Ricci Lucchi (1985) and more recently as supercritical dunes propagating in the same direction of the backflow (see Fedele et al., 2016). These megariipples, however, are very similar to the biconvex megariipples reproduced in laboratory under combined flows dominated by unidirectional components (see Yokokawa, 1995; Dumas et al., 2005; Tinterri, 2011). This evidence suggests that they can be deposited by asymmetrical combined flows in which also the fallout rate must play an important role (e.g. Tinterri, 2011).

These structures can be evidence of an interaction between a unidirectional turbidity current and an oscillatory component associated with different trains of internal waves produced by reflection processes. These internal waves propagating along the internal density surfaces can be characterized by very complex interferences resulting from the overlapping of different wave trains able to produce high-velocity multidirectional combined flows, which are at the base of hummocky-type structures. The downcurrent passage from biconvex megariipples into isotropic hummocky structures and low-angle wavy to even laminae can be related to progressive deceleration of the reversing flow that favor the progressive increase in the fallout rate and traction-plus-fallout processes. This, together with a multidirectional oscillatory component, hinder the development of flow separations on the lee side and relative vortices, preventing the formation of regular bedforms (ripples and dunes) and favoring plane beds or quasi-planar laminations which, draping low-angle erosive surfaces, can produce hummocky-type structures (Tinterri, 2011). The long straight crests of the megariipples characterized by large lateral continuity and by Y bifurcations, typical of wave ripples (**Figure 6D**), suggest that the oscillatory component had to be important, reinforcing the interpretation of current-dominated combined flow structures (see Harms, 1969; Tinterri, 2011).

The interpretation of a reversing flow explains very well the second rebound drape separating the upper facies B2 by the underlying intermediate facies B1. Indeed, it is interpreted to be deposited by a diluted tail of the upper turbulent flow bypassed towards the northwest. Undergoing a reflection produced by a northern basin margin, this flow can form a reversing flow directed towards the southeast, able to deposit the megariipples of facies B2 (see **Section 6.1**).

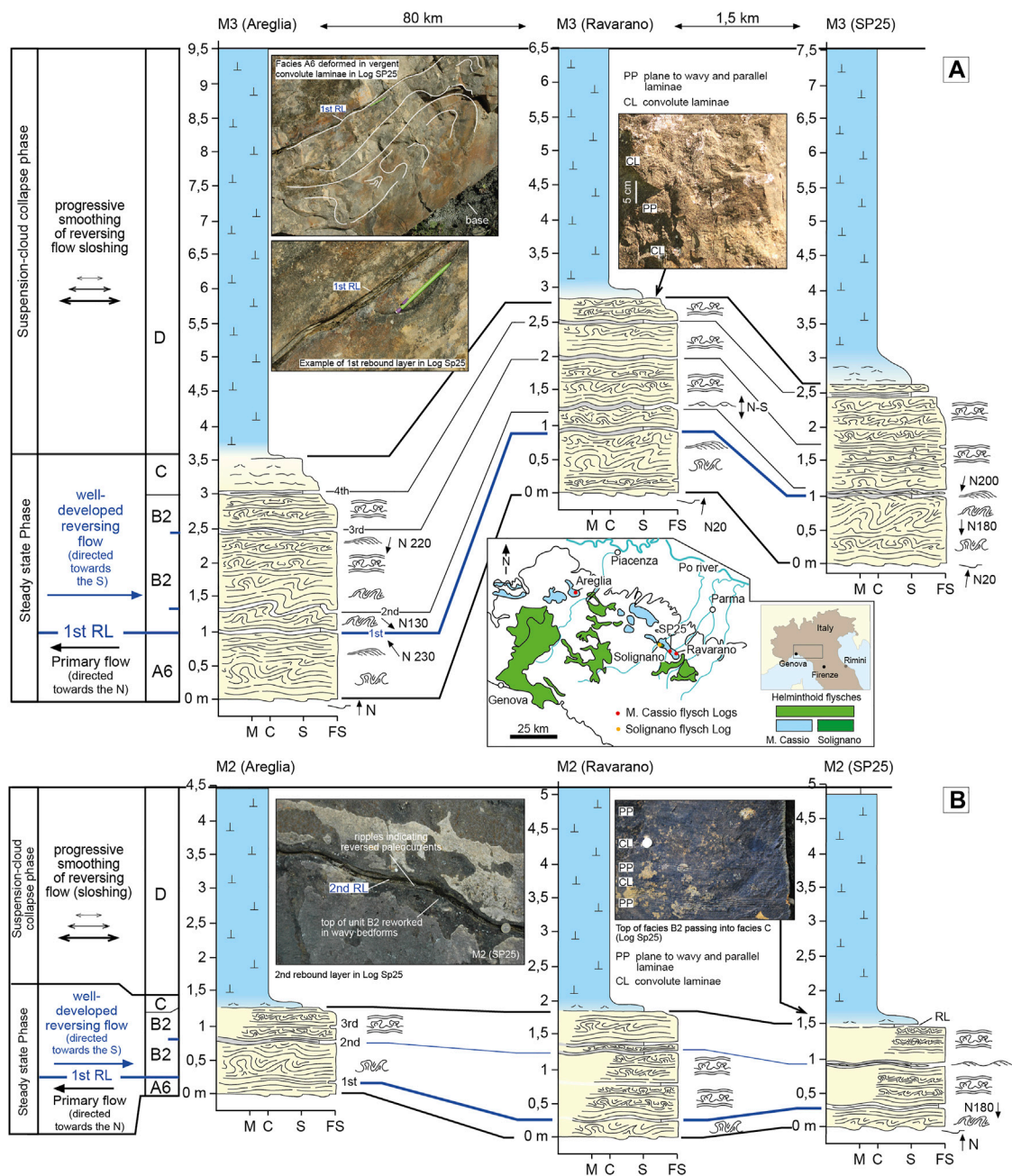


FIGURE 7 | (A) Stratigraphic cross section of megabed M3. Details of the 1st RL, of vergent convolute laminae in facies A6 and the alternations of plane-parallel and convolute laminae at the top of Unit B2 are also shown. A location map of the stratigraphic logs is also shown; **(B)** Stratigraphic cross section of megabed M2, details of the 2nd RL and alternations of plane-parallel and convolute laminae at the top of facies B2 are also shown (see **Supplementary Figure S1** in the supplementary materials for more details).

Facies B2 passes upward into facies C characterized by an alternation of poorly-sorted slurried units and well-sorted laminasets. This facies is very common in contained-reflected beds, and can be interpreted as deriving from an interaction of collapse of final suspension cloud (see Patacci et al., 2015), cyclic-wave loading of reflected flows (testified by the combined flow structures and the changes in paleocurrents, Tinterri et al., 2016)

and the dynamics of the silty and muddy grain sizes (see Baas et al., 2011; Baker and Baas, 2020). This facies records the passage to the upper very thick mudstone unit D in its turn recording the deposition of the residual muddy turbulent flow.

In conclusion, the CKB depositional model may be consistent with the steady state phase 3 and suspension-cloud collapse phase 4 of the experimental model proposed by Patacci et al. (2015) (see

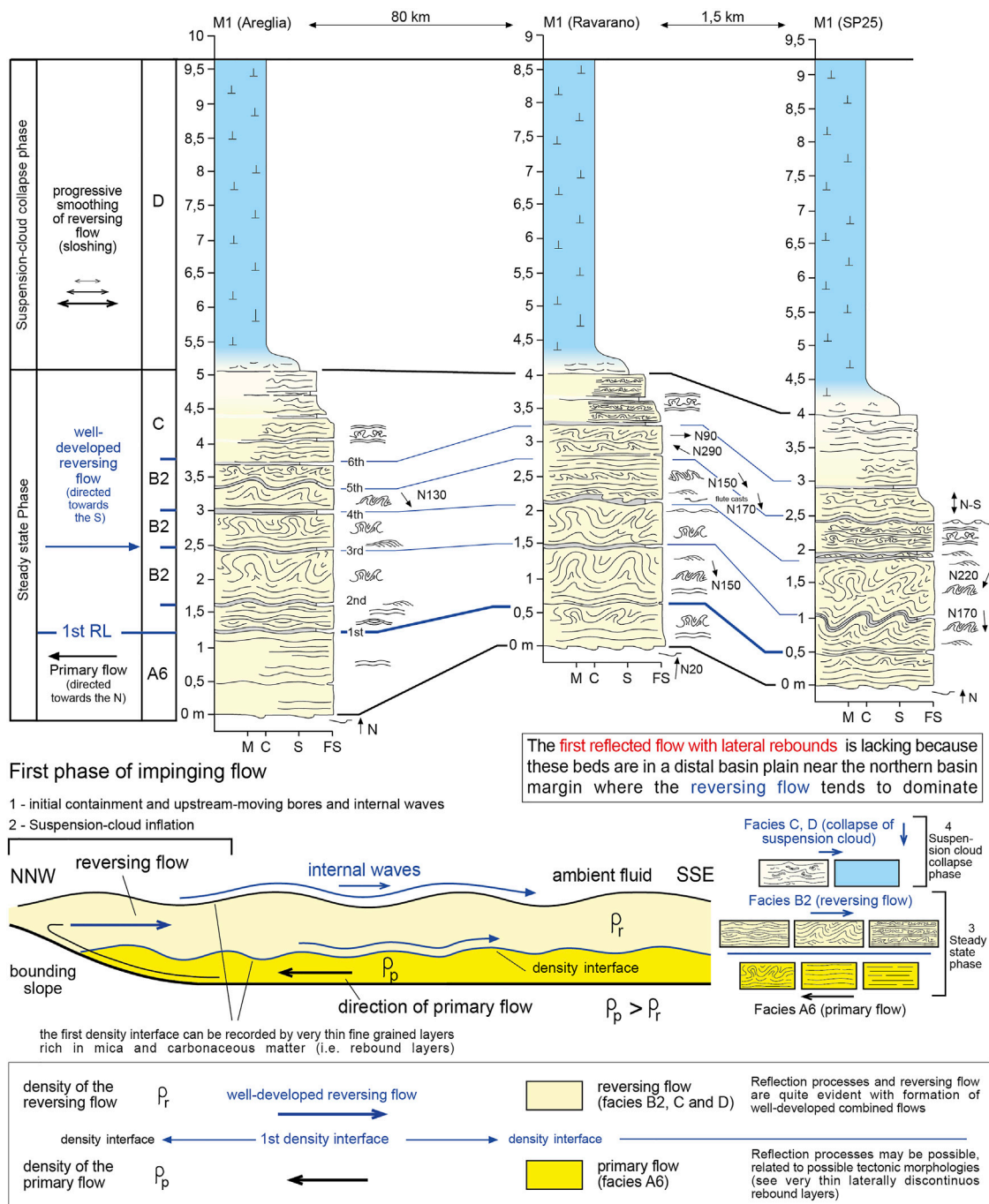


FIGURE 8 | Stratigraphic cross section of megabed M1. Below, facies scheme and depositional model of the M. Cassio Flysch megabeds are also shown (compare to CKB depositional model in **Figure 3C**).

Figure 1A), where two main rebound drapes (1st and 2nd RLs) recording two density interfaces, allow to subdivide the turbidity current, able to deposit the CKB, into three parts (see **Figure 3** and **Supplementary Table S1**): I) a first basal high-density primary flow deriving from to the south and that decelerates towards the north (Facies A), II) a second more diluted turbulent upper part that, although still related to a flow coming from to the

south, starts to record lateral rebound processes, and, in more distal zones (i.e., the north western areas), the first evidence of reversing flow (Facies B1c) and III) a third uppermost more diluted turbulent flow that records a well-developed reversing flow that, after the reflection against a northern morphological barrier, evolves towards the south east (Facies B2 and partially C; **Figure 3**). The final deposition

of the mud (Facies D) can be related to the deflation of a steady cloud characterizing the entire basin even if an interaction with sloshing internal waves cannot be completely ruled out as testified by the thickness variations consistent with the basin morphology controlled by the main tectonic structures. This interaction can also enhance decelerations and suspension-cloud collapses that can contribute to the formation of slurry facies C (Figure 3).

3.2 The M. Cassio Flysch Megabeds: Fully-Contained (Ponded) Beds

3.2.1 Introduction

The Monte Cassio Flysch (MCF) is composed of deep water turbidites that belong to the External Ligurian Units in the Northern Apennines (Italy) and mark, together with the other Upper Cretaceous helminthoid flyschs, the beginning of the Tethys Ocean closure and, consequently, of the alpine orogenesis (Vescovi et al., 1999; Marroni et al., 2001). The MCF thickness, more than 1800 m, consists of basin plain siliciclastic, carbonate and mixed turbidites of the Late Campanian age (Rio e Villa, 1987), deposited in a narrow and elongate basin below the CCD (Scholle, 1971; Sagri e Marri, 1980; Baruffini and Papani, 2017; Marroni et al., 2017). The MCF stratigraphic succession consists of beds whose composition indicates mixing of sediments derived from intrabasinal and terrigenous sources; some of these beds are megabeds characterized by a graded laminated hybrid sandstone passing upward into a very thick marlstone. The biogenic particles that characterize these megabeds range from fine-grained sand (fragments of echinoderms and bryozoans, benthic and planktonic foraminifera, fine pelecypods, sponge spicules, calcareous algae) to mud (coccoliths and fine spicules) (see Zuffa et al., 2004).

3.2.2 Descriptions

The MCF stratigraphic succession is characterized by more than twenty megabeds that represent regional key beds; however, a detailed facies analysis of three of these megabeds (i.e., beds M1, M2 and M3 in Supplementary Figure S1) highlights facies sequences very similar to that of CKB. Megabeds M1, M2 and M3 are consistent with beds 1,040, 1,080 and 1,100 by Baruffini and Papani (2017) and, thanks to the high-resolution stratigraphic framework performed by Mazza and Tinterri (in preparation), these beds can be traced for about 100 km (Figure 7A, see also Baruffini and Papani, 2017). These correlations show that these beds are characterized by a basal fine-grained sandstone with well-developed laminations that pass upward into a very thick marlstone.

In all studied beds, the basal sandstone units are characterized by a well-developed alternation of different types of sedimentary structures, such as wavy to even and parallel laminae, hummocky-type structures, convolute laminations with different degrees of vergence and ripples (Figure 7). Vergent convolute laminae, anisotropic hummocky structures and ripples show different paleocurrents from those of flute casts indicating flows towards the north.

In particular, as for the CKB, the presence of various fine-grained drapes (i.e., rebound layers) allows the basal sandstone units to be divided into different facies that show these paleocurrent changes.

The first fine-grained drape (1st blue line in Figures 7, 8) divides a basal laminaset generally composed of even to wavy and parallel laminae with flute casts indicating paleocurrents towards the north-northeast (facies A6) from upper laminasets dominated by ripples and vergent convolute laminae showing paleocurrents in the opposite direction (i.e. towards the south-southwest, see facies B2 in Figures 7A, 8 and Supplementary Table S1). In particular, in its upper part, facies A can already show vergent convolute laminae and ripples indicating paleocurrent towards the south (Figures 7, 8).

Facies B2 is made of various laminasets separated by fine-grained drapes that are characterized by various very peculiar structures, such as large-scale hummocky geometries, very thin laminates made of ripples, deformations associated with vergent convolutes. In some cases, flute casts at the base of B2 laminasets indicating paleocurrents in the opposite direction vs. the flute casts of facies A6, are found (see the 2nd drapes in the bed M1 at the Log Ravarano, Figure 8 and Supplementary Figure S1E).

The vertical passage to the marlstone unit D is recorded by facies C made of silty very fine-grained sandstone and is characterized by widespread soft-sediment deformations consisting of convolute laminae, ball-and-pillows and pseudonodules. In some cases, however, in facies C, well-developed alternations of even to wavy and parallel laminae, low-angle bedforms and small-scale convolute laminae can be recognized (see bed M1 in the Ravarano Log, Figure 8). This evidence suggests that a continuum between these two facies types can exist.

Finally, Facies D is composed of a very thick marlstone, which generally has thickness similar or higher than that of the basal sandstone unit. This unit apparently shows a massive facies, although very thick faint laminations can be observed.

3.2.3 Interpretations

Facies descriptions allow the MCF megabeds to be interpreted as typical confined and contained beds, in which the degree of basin confinement allows fully-ponded conditions. Facies A, B, C and D, as for CKB, are perfectly consistent with the facies categories introduced by Tinterri et al. (2016), and the fine-grained and very-thin drapes can be interpreted as rebound layers recording a deposition during a relatively quiescent period occurring after the bypass of reflected or reversing flows (see Section 6.1, Tinterri et al., 2016). They highlight the three facies, A, B and C, of the basal sandstone unit (see Figures 7, 8 and Supplementary Table S1).

In particular, the first rebound drape (1st blue line in Figures 7, 8) separates the basal facies A, which can be interpreted as deposited by a low-density primary turbidity current directed towards the N from an upper unit deposited by a reversing flow represented by a low-density turbidity current flowing in the opposite direction. This is testified by ripples, vergent convolute laminae and anisotropic hummocky-type structures indicating paleocurrents towards the S. The basal facies A in comparison to those of the CKB is dominated by A6, since it represents a more

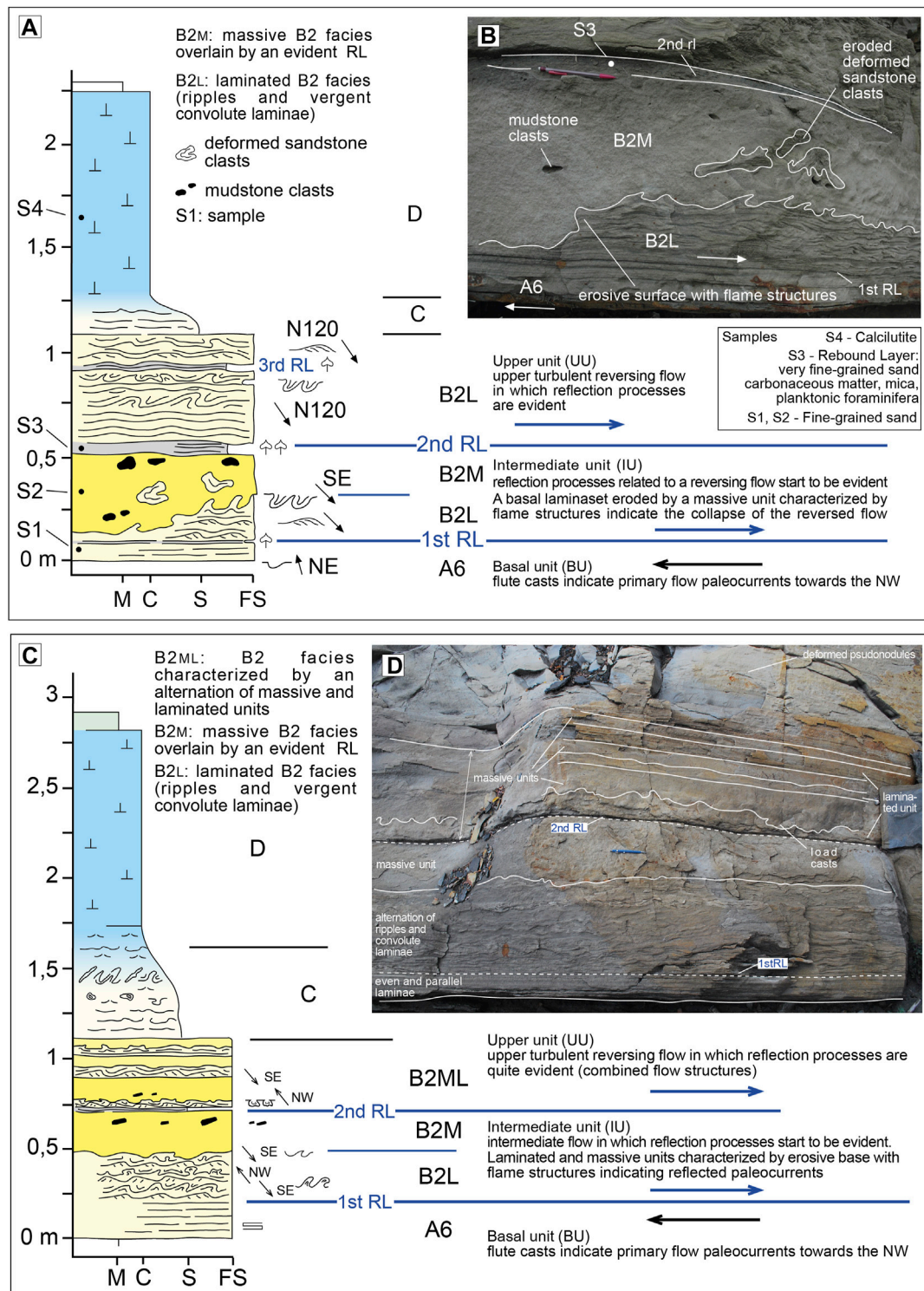


FIGURE 9 | (A) Description and interpretation of a megabed in the Solignano Flysch characterized by massive units with an erosional base and flame structures. The location of the samples used for the grain-size analysis is also shown; **(B)** Detail of massive facies B2M characterized by folded mudstone and sandstone clasts, erosional base and flame structures (see Log in A); **(C)** Description and interpretation of another megabed in the Solignano Flysch characterized by massive units with an erosional base and load structures. These bed types have been interpreted as indicating proximity to the bounding slope; **(D)** Megabed shown in C in which the main facies are also indicated (see **Supplementary Figures S2, S3** in the supplementary materials for more details). See **Figure 7A** for the beds location.

distal facies than the A5 facies in CKB (**Figures 4, 8**; see **Supplementary Table S1**). From this point of view, the megabeds of the MCF may be seen as a downcurrent evolution of beds showing a facies sequence similar to that of the CKB.

However, unlike the CKB, the MCF megabeds do not seem to be characterized by the intermediate facies B1 with lateral deflections. Conversely, the basal facies A6 is directly overlain by facies B2 indicating a well-developed reversing flow. This evidence may be explained by the fact that these beds represent a downcurrent evolution of megabeds similar to the CKB suffering more from the effects of frontal reflections with development of a reversing flow.

The laminasets of facies B2 are generally separated by various rebound layers that are generally less developed than those associated with the reversing flow (**Figures 7A, 8** and **Supplementary Figure S1**). A possible explanation is that the reversing flow can undergo various minor lateral reflections sufficient to produce a delay in the lateral bores allowing the formation of fine-grained rebound layers. In this case reversing flows can propagate in a unsteady pulsating way, i.e., through low-frequency reversing surges where the tail of every surge has the time to deposit an RL through a mechanism similar to that described by Kane et al. (2009), (see **Section 6.1** for more details; see also Patel et al., 2021). Indeed, a pulsating reversing flow can be considered the rule in ponded confined basins, where the interaction with lateral rebounds due to basin margins or uneven (bumpy) intrabasinal morphologies can produce complex flow velocity variations at different frequency and scales (see Tinterri, 2011; see also; Patacci et al., 2015; Howlett et al., 2019). At large-scale, low-frequency pulsating reversing surges can play an important role in the deposition of the rebound layers, whereas, at small-scale, multidirectional combined flows can be related to an interaction between pulsating reversing flows and different trains of internal waves due to multiple lateral rebounds (Tinterri, 2011).

From this point of view, the formation of alternations of different structures, such as convolute and plane to wavy parallel laminae, can be related to these flow velocity variations (see **Figure 7A**), while symmetrical ripples with a dominant trochoidal geometry and low-angle hummocky-type structures having different degree of anisotropy show that an oscillatory component must be present within the flow, supporting the interpretation of multidirectional-combined flows (**Figures 7A, 8**). However, in the formation of low amplitude hummocky-type structures, the dynamics of mud and silt at the boundary layer in transient turbulent flows should also be taken into account (see Baas et al., 2011; Baker and Baas, 2020).

The same very common convolute laminae can be related to an interplay between fine-grained sediment (silt and mud) and cyclic-wave loading associated with multidirectional combined flows (see Tinterri et al., 2016). This process must have been particularly efficient during the deposition of Unit C that can be characterized by an alternation of convolute laminae and low-amplitude bedforms that can pass laterally into slurry facies with pseudonodules (**Figure 8**). This transition can be related to the increase in cyclic-wave loading and mud percentage in

decelerating combined flows able to form transient flows characterized by progressive attenuation of the near bed turbulence. Indeed, facies C record the vertical passage into the very thick mudstone unit D, whose thickness is due to the ponded condition. This last phase probably records a depositional phase similar to the cloud deflation phase by Patacci et al. (2015), which produces the final settling of fines from an essentially static cloud. Nevertheless, the presence of faint bandings within the upper mudstone unit does not rule out the occurrence of waning sloshing bores. Indeed, the concentration of cohesive mud in a flow can considerably affect processes of sediment deposition and resulting types of deposit (Amy and Talling, 2006; Talling et al., 2012). Investigating bedload transport and deposition of clay floccules, Schieber and Southard (2009) clearly showed that this process can occur at flow velocities that transport and deposit sand, pointing out that the formation of floccule ripples develop into low-angle foresets and mud beds appearing laminated after post-depositional compaction. Talling et al. (2012) showed that laminated mud (TE-1) and graded mud (TE-2) very likely result from floc settling at lower mud concentrations, while Ungraded (TE-3) mud intervals very likely form through *en-masse* consolidation of relatively dense cohesive mud suspensions due to gelling (see also McCave and Jones, 1988). From this point of view, it is plausible to think that a continuum from facies C to an uppermost massive ungraded mud of facies D can exist, related to the interaction between a progressive decrease in sloshing surges and dynamics of cohesive mud in the residual turbulent flow.

In conclusion, MCF megabeds fit very well with the model by Patacci et al. (2015) with a northeastward primary flow overlaid directly by a south-westward reversing flow separated by a density interface that can produce the RLs (see **Figure 8**).

4 SOLIGNANO FLYSCH AND MARNOSO-ARENACEA FORMATION CONFINED AND PARTIALLY CONTAINED BEDS

4.1 Introduction

The Solignano flysch (late Campanian-Maastrichtian in age) is part of the helminthoid flysch of the northern Apennines, such as the MCF (see location map in **Figure 7A**). Like the latter, the Solignano flysch is characterized by three main types of beds, namely: 1) micritic-marly beds, 2) arenitic-siliciclastic beds and 3) mixed beds exhibiting a basal arenitic-siliciclastic unit grading upward into a micritic-marly interval (Fontana et al., 1994). Some of the mixed beds can be megaturbidites showing characteristics similar to that of the MCF megabeds except for the fact that the Solignano beds are more siliciclastic and coarser than those of the MCF and are often characterized by erosive massive sandstone units rich in mudstone clasts.

The Solignano megabeds are always characterized by flute casts indicating a primary flow directed towards the northwest and ripples, vergent convolute laminae and flame structures, located just above the base, indicating paleocurrents exactly in

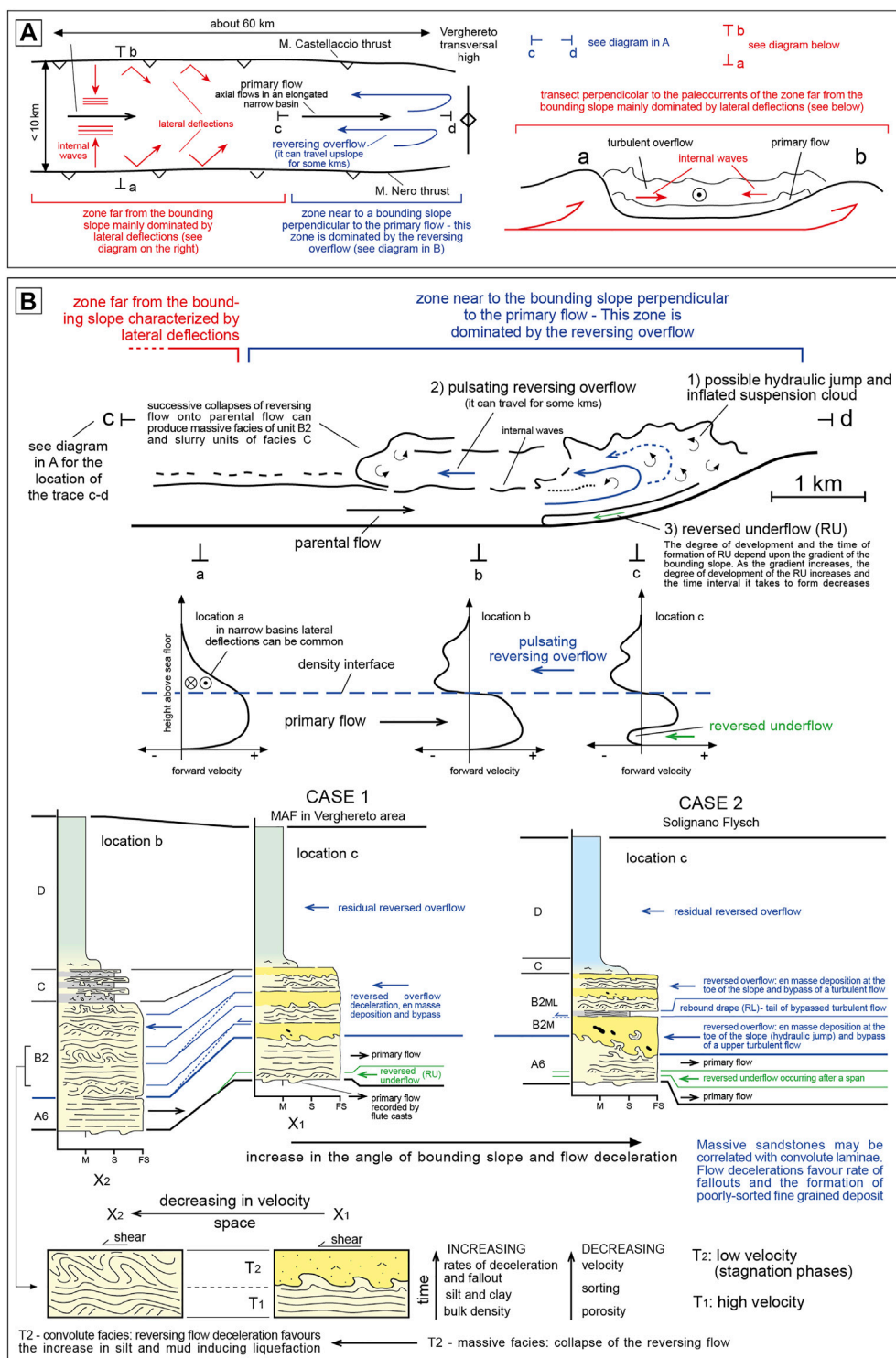


FIGURE 10 | (A) Schematic paleogeography of the MAF inner basin in which the main reflection processes related to the lateral and frontal basin margins are illustrated. Trace a-b indicates a cross-section perpendicular to the paleocurrents and to the main structural alignments represented by the M. Nero and M. Castellaccio thrusts (i.e., the lateral margins of the basin). Conversely, trace c-d indicates a cross-section parallel to the main structural alignments but perpendicular to the Verghereto high in a distal basin plain (see **Figures 2B,C**; modified from Tinterri and Muzzi Magalhaes, 2011). **(B)** Depositional model describing a flow perpendicular to the bounding slope (inspired by Howlett et al., 2019; see also Patacci et al., 2015). The model tries to link the facies variations in a direction towards the bounding slope with the different flow phases occurring during the reflection process. Below, a scheme illustrating facies and processes at the basis of the relationship between massive facies with load casts (near the bounding slope) and convolute laminae (in more distant zone).

the opposite direction, i.e., towards the southeast. This evidence allows an interesting comparison with the contained and reflected beds of the MAF near the Verghereto transversal tectonic feature, described by Tinterri et al. (2016) (see their **Figures 5, 6**).

4.2 Description

The most part of the Solignano beds and megabeds are composed of a basal laminaset made of plane-parallel laminae (Facies A6) passing upward (sometimes through a first fine-grained drape, RL) into an alternation of ripples and vergent convolute laminae generally indicating paleocurrents directed towards the southeast (i.e., in the opposite direction vs. those indicated by the flute casts), (see Facies B2 in **Figure 9**). This laminated facies is often overlain by a massive fine-grained sandstone (Ta Bouma division) where mudstone and laminated sandstone intraclasts, eroded from the underlying unit, can be common. The base of the massive unit is erosive and is usually characterized by load and flame structures indicating paleocurrents towards the southeast and for this reason this facies is indicated as B2M (see **Figures 9A,B, Supplementary Figure S2A and Supplementary Table S1**). The grain-size analysis in thin section shows that these basal facies have the same grain-sizes, i.e., fine-grained sandstones (**Figure 9A**).

In general, above the first basal massive facies, there is a fine-grained drape rich in carbonaceous matter, mica and foraminifera (2nd RL in **Supplementary Figure S2D**), which divides the basal units from upper laminasets dominated by an alternation of ripples and vergent convolute laminae showing paleocurrents in the opposite direction (i.e., towards the south-southwest, see facies B2 in **Figure 9 and Supplementary Figures S2B,C**). Sometimes, laminasets of this type are alternated with massive units with ball and pillows whose thickness tends to decrease upward; this facies has been indicated as B2ML (see **Figures 9C,D, Supplementary Figures S2E, S3 and Supplementary Table S1**). These types of B2 facies passes upward into a very thick marlstone unit (facies D) through facies C made of silty very fine-grained sandstone dominated by soft-sediment deformations in which pseudonodules and contorted very thin laminasets characterized by ball-and-pillows, can still be recognized (**Supplementary Figure S2F**).

The Solignano bed types show strong analogies with the contained-reflected beds of the MAF near the Verghereto structural high, which is oriented perpendicularly to the general paleocurrents directed towards the SE (Unit IV by Muzzi Magalhaes and Tinterri, 2010, **Figure 10B**). These beds, 4 km away from the structural high, are composed of fine-grained sandstones characterized by even and parallel laminae passing upward into an alternation of vergent convolutes and ripples indicating reversing palaeocurrents directed towards the W and WNW (i.e., in the opposite direction vs. those indicated by sole casts directed towards the Verghereto high, see **Figures 1C, 10B**). However, many contained-reflected beds in this zone are characterized by reversing ripples even in the most basal part of the beds, whereas the vertical passage into thick mudstone unit D is recorded, again, by a type-C unit characterized by an alternation of slurried units made of very fine sandy siltstone and thin laminasets composed of small-scale anisotropic

hummocky-type structures characterized by ball and pillows and pseudonodules. These bed types pass downcurrent (i.e., towards the structural high) into beds composed of plane or slightly undulated laminae passing upward into an alternation of vergent convolute laminae, reversing ripples and massive units characterized by load structures, very similar to those described in the Solignano Flysch (see **Figure 10B**). In these zones, near the structural high, the vertical passage into the mudstone unit D tends to occur without the development of any unit C (**Figure 10B**). Essentially, the general model of **Figure 10B** emphasizes the facies tract of the beds characterizing the MAF in the Verghereto area and Solignano Flysch.

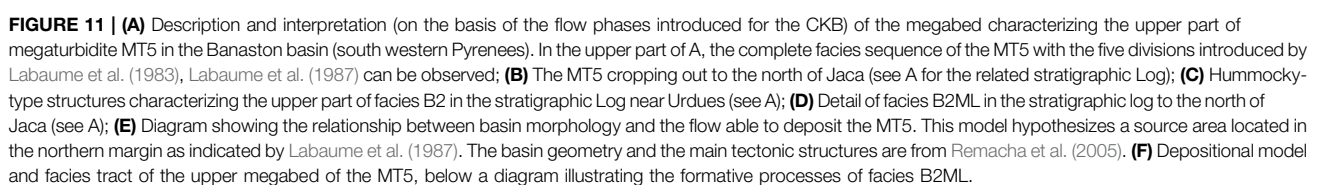
4.3 Interpretation

Facies B, C and D of the Solignano Flysch and the MAF beds in the Verghereto area are consistent with the facies categories introduced by Tinterri et al. (2016). In particular, these beds show many analogies with bed types cropping out in the Sorbas basin (southern Spain) and described by Haughton (1994), Haughton (2001).

In the MAF, for example, the beds towards the Verghereto structural high are all dominated by sedimentary structures indicating a very important role of the reversing flow and are generally characterized by a progressive increase, towards the bounding slope, in thin massive units with basal load casts (see **Figure 10**). This evidence can be interpreted as linked to an increase in deceleration and fallout rates and, more probably, to the collapse of the reversing-reflected flow that must occur in a pulsating way as testified by the alternation of laminated and massive units characterized by load casts near the bounding slope (see Postma et al., 2009; Tinterri et al., 2016).

More precisely, following the experimental phases described by Patacci et al. (2015) and Howlett et al. (2019), the basal facies, consisting of even or slightly undulated parallel basal laminae with flute casts indicating paleocurrents towards the NE, can be interpreted as recording the basal underflow directed against the bounding slope (Facies A6). However, the occasional occurrence of reversing ripples exactly at the base of the beds may suggest basal reversing flows consistent with the basal flow reversal by Patacci et al. (2015) or with the back squeezed underflow by Howlett et al. (2019) (see **Figures 1A,B**). Indeed, in this case, the structural high is relatively near (few kms) and flows impinge perpendicularly the bounding slope as in the aforementioned laboratory experiments.

Conversely, the facies characterized by the alternation of reversing ripples and vergent convolute laminae (Facies B2) can record the reversed overflow. As mentioned above, this alternation tends to evolve, moving towards the bounding slope, into a facies constituted by an alternation of even and parallel laminae and massive units with load casts (Facies B2M and B2ML, see **Figure 10B**). This lateral facies change can be related to a pulsating reversed overflow characterized by stagnation phases due to the repeated collapse, against the bounding slope, of the reflected overflow (Patacci et al., 2015; see also; Howlett et al., 2019). These stagnation phases must have produced a high rate of fallout near the obstacle generating massive units with load casts and relatively lower fallout rate far



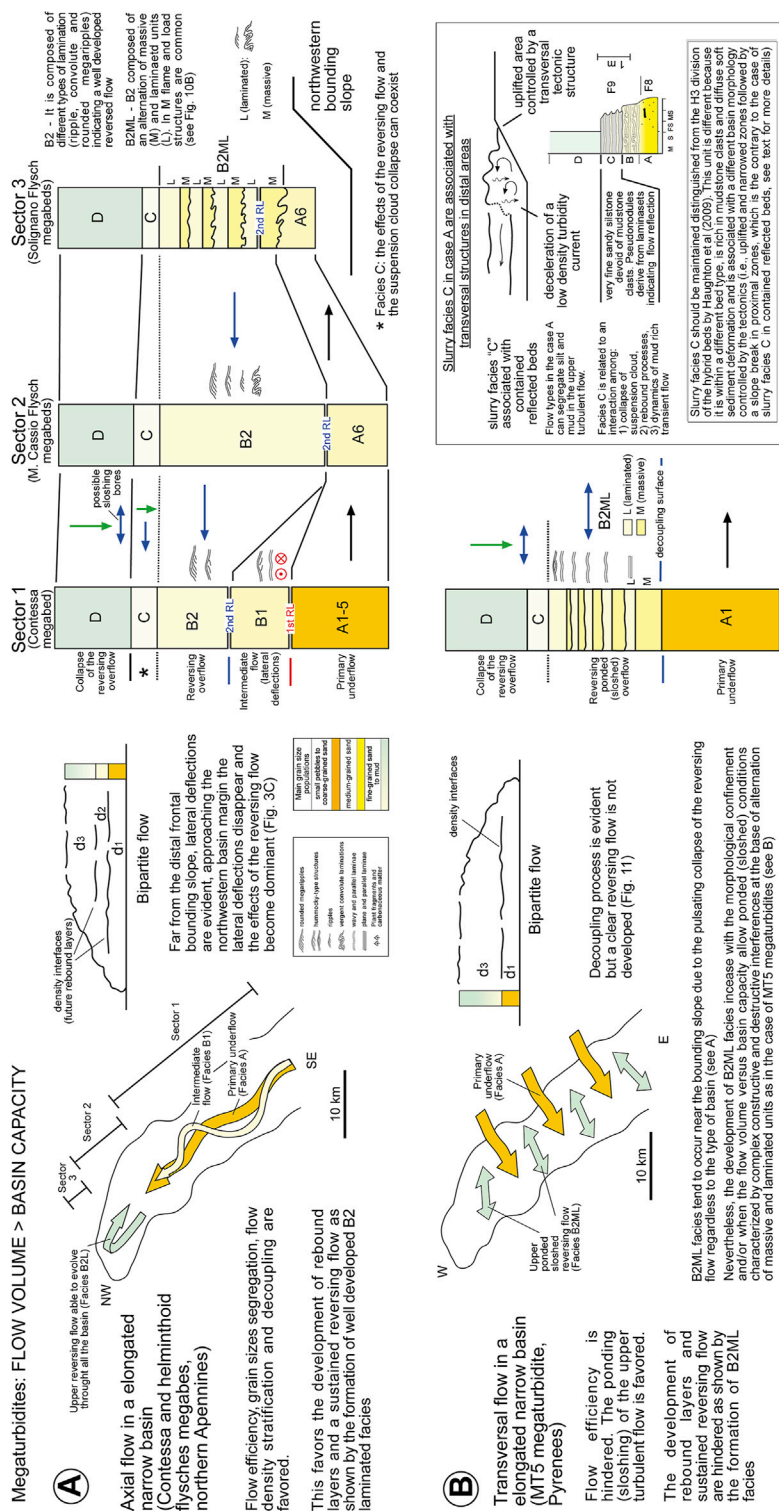


FIGURE 12 | Depositional models that summarize the different study cases in this work. In **(A)**, the cases of the Contessa Key bed and helminthoid flysches, which are deposited by axial flows in elongated and narrow basins. In **(B)**, conversely, the case of megaturbidite MT5 in the south western Pyrenees deposited by a flow transversal to an elongated and narrow basin.

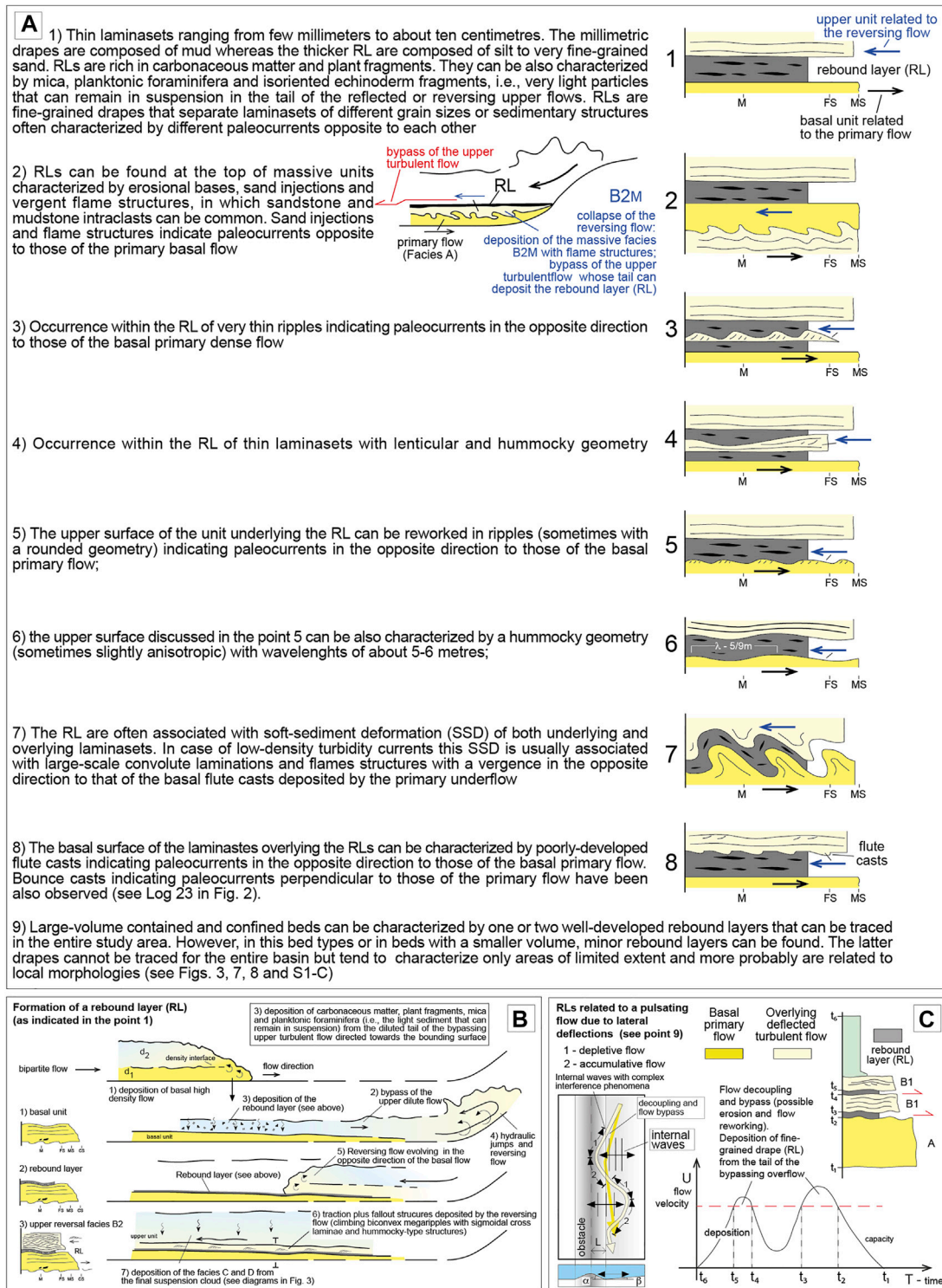


FIGURE 13 | (A) Main sedimentary characteristics of the different types of rebound layers (RLs). In the point 2 a scheme illustrating the formation of a RL associated with the collapse of a reversing flow induced by a bounding slope can be also observed; **(B,C)** Two different depositional models showing how RLs can form, are shown (see points 1 and 9). Diagram in C is inspired from Kane et al. (2009) and Tinterri et al. (2016).

from the bounding slope generating convolute laminae. In other words, in zones far from the bounding slope the fallout rates associated to the stagnation phases may be sufficient to produce

deposits rich in silt and mud that can favor liquefaction processes and consequently convolute laminae (see also Tinterri et al., 2016; Gladstone et al., 2018). From this point

of view, a possible relationship is proposed between massive units and convoluted laminasets as indicated in **Figure 10B**.

In these situations, however, constructive and destructive interferences between different trains of reflected bores or internal waves may further contribute to the pulsating nature of the reversed overflow and to the convolute formation through cyclic-pressure variations (Tinterri et al., 2016).

This facies B2, in turn, can pass upward into a facies C characterized by a fine-grained sandy siltstone that can be interpreted as a slurry facies (*sensu* Lowe and Guy, 2000). This facies is generally characterized by an alternation of thin slurry units and laminasets consisting of large-scale hummocky-type structures and low-angle megaripples that can indicate paleocurrents opposed to those of flute casts. It tends to taper and disappear towards the structural high, presumably above the bounding slope (**Figure 10B**). This facies is interpreted as the collapse of the fine-grained sediment (very fine-grained sand, silt and mud) characterizing the residual reversed flow at the toe of the obstacle where the slope change and the deceleration degree are the highest. In this process, however, a key role must have been played not only by the dynamics of the fine-grained sediment (e.g., Schreiber et al., 2007; Baas et al., 2011) but also by reflection processes as testified by the occurrence of laminated units characterized by reversed sedimentary structures. Consequently, the origin of this facies cannot be merely a simple collapse of the reversing flow as indicated by Patacci et al. (2015) but rather, as the alternated facies suggest, in the same way of facies B2, a pulsating collapse of the mud-rich residual reversing flow with the deposition of slurry facies, during the deceleration phases in which the cohesive strength of mud prevails, and laminated units during acceleration phases in which traction-plus-fallout processes must prevail. In the latter case, combined flows (see Tinterri et al., 2016) and the dynamics of the fine-grained sediment (mud and silt) (see Baker and Baas, 2020) may both contribute to produce the hummocky-type structures and large-scale low-angle megaripples. The erosion of mud on the bounding slope by the reflected flows as indicated by Bell et al. (2018) may surely contribute to the formation of slurry facies, even if, in the case of MAF, this facies is not characterized by the presence of mudstone clasts but only by load structures, such as pseudonodules, deriving from laminated units. Facies C, therefore, is interpreted as mainly associated with the pulsating collapse of the mud rich residual reversing flow at the toe of the structural high where the slope change produces the highest rates of deceleration (see Sumner et al., 2009; Baas et al., 2011). Following the experimental phases described by Patacci et al. (2015) facies C and the thick mudstone facies D can record the final phase of suspension-flow collapse modified, however, by the aforementioned processes.

The Solignano Flysch beds (**Figure 9**) are very similar to those described in the Verghereto area and thus are interpreted as recording similar sedimentary processes and similar basin morphologies, i.e., primary flows directed

towards a northwestern obstacle and reflected flows in the opposite direction, i.e., towards the southeast. This evidence, together with the occurrence of well-developed rebound layers above thick massive units characterized by folded mudstone and sandstone clasts and erosional bases with flame structures indicating reversed paleocurrents, are evidence of a more drastic deceleration and collapse of the reversing flow (**Figures 9, 10B**). This is probably due to the obstacle being in closer proximity or a more pronounced slope change than those of the MAF beds in the Verghereto area. In this case, it is plausible to think that decoupling processes, with a drastic collapse of the basal part of the reversing flow and bypass of its uppermost turbulent portion, can occur in a very efficient way with the consequent formation of a tail able to deposit a fine-grained drape rich in plant fragments, carbonaceous matter, mica and planktonic foraminifera, i.e., particles able to remain more efficiently in suspension (**Figure 9A**). Above this first rebound layer, in the same way as for the MAF beds, facies B2ML is characterized by an alternation of vergent convolute laminae, reversing ripples and massive units with load casts, which can be interpreted as associated with a pulsating reversing flow suffering repeated gravitational collapses and re-accelerations. In the same way, the slurry Facies C, with soft-sediment deformation, and Facies D can record the final phase of suspension-flow collapse where, however, the faint laminations of facies D suggest traction-plus-fallout processes in mud sediment as indicated by Schieber and Southard (2009).

Essentially, contained-reflected beds characterized by thin massive units with load structures can be present not only in small-scale confined basin, as indicated by Patacci et al. (2015), but also in relatively large basins as in the case of the MAF beds deposited in a foredeep and M. Cassio and Solignano helminthoid flyschs deposited in an ocean basin. Consequently, their presence should be ascribed to the proximity of a bounding slope rather than to the dimension and the degree of basin confinement, even if the data coming from the MAF and MT5 megaturbidite in the Pyrenees show that these massive units within the strata become more and more evident as the degree of tectonic confinement versus flow volume increases (see below). In the same way, the rebound layers (RL) near the bounding slope seem to be more developed in large-volume beds in which the decoupling processes are enhanced by flow stratification and by the degree of flow deceleration related to the proximity of the obstacle and the size of the slope change.

5 MT5 MEGATURBIDITE (SOUTH WESTERN PYRENEES)

The considerations just made seem to be confirmed by the facies analysis of the calcarenite at the top of the MT5 megaturbidite in the Banaston turbidite system (south-western Pyrenees) (**Figure 11**). This megabed, deposited at the top of very thick calcareous megabreccia, is related to the upper high-density

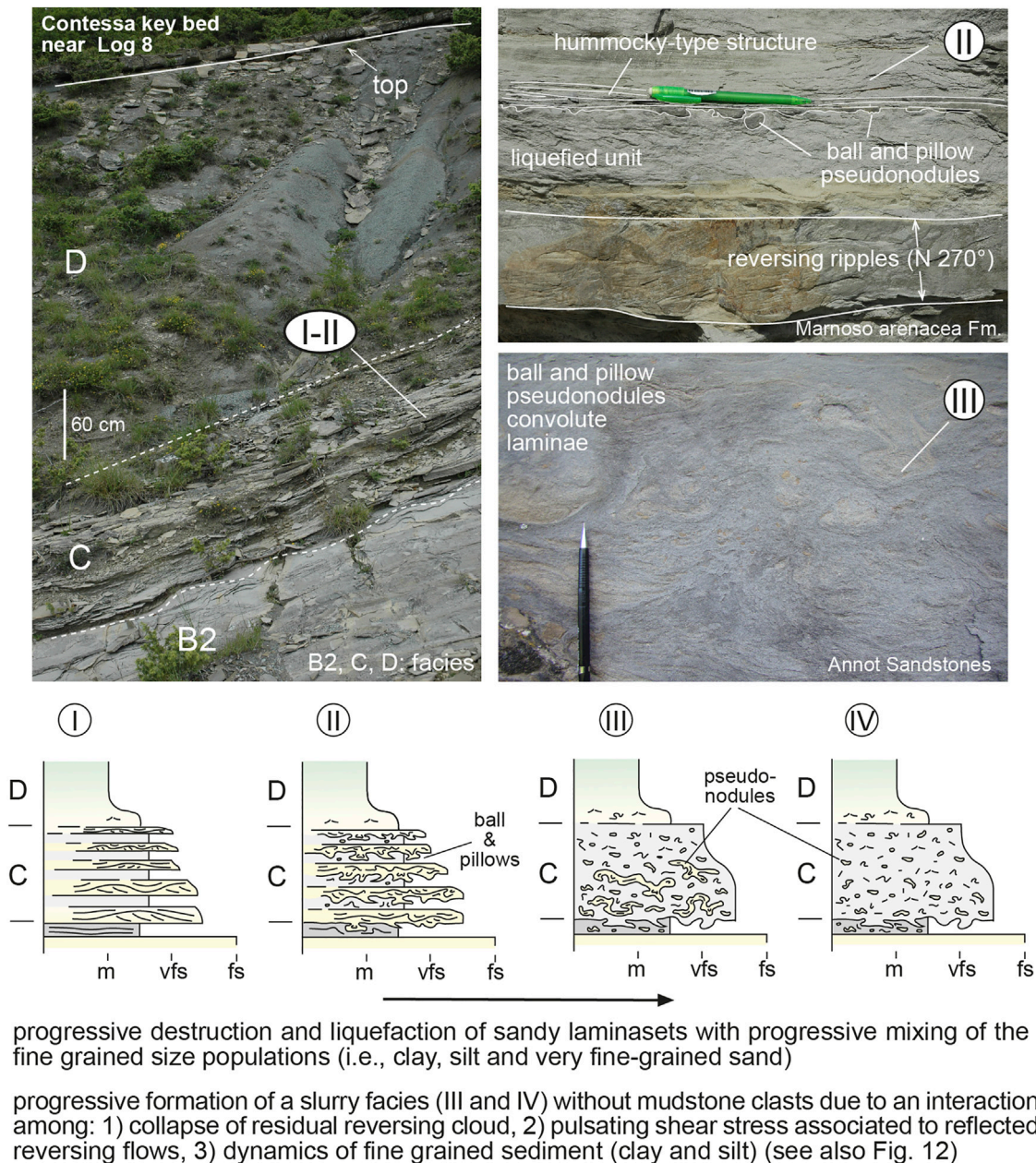


FIGURE 14 | Diagrams illustrating the different types of slurry facies C in relation to the progressive increase (from I to IV) in soft sediment deformation with the consequent destruction of the sandy laminasets.

turbidity current characterizing the bipartite flow able to deposit the MT5 (Labaume et al., 1987; Mutti et al., 1999; Ogata et al., 2012; see also **Figure 11**). Consequently, this megabed shows strong analogies with the megabeds discussed so far and especially with those in **section 4** (see **Figure 9**); indeed, it consists of a basal coarse-grained massive facies A1 passing upward into a facies B2ML made of an alternation of fine-grained laminated (L) and massive (M) units where the former are mainly characterized by hummocky-type structures and low-angle wavy laminae (**Figures 11A,C,D**).

The rebound layers are not well developed and are often absent (**Figure 11A**).

The main difference from the Contessa and helminthoid flysch megabeds is that the MT5 is deposited by a flow transversal to the elongated and narrow basin of the Banaston turbidite system (**Figures 11E,F**). Therefore, these conditions can create a fully ponded suspension cloud (*sensu* Patacci et al., 2015) where the upper reversing flow, which can be reflected from both the southern and northern margin, can combine itself with various types of bores coming from

different zones due to the basin geometry (**Figure 11E**). Consequently, the formation of complex constructive and destructive interference processes must result in a strongly unsteady multidirectional pulsating ponded overflow. Said overflow prevents the formation of a relatively steady reversing flow and, consequently, of well-developed reversing megaripples and rebound layers, such as in the case of the Contessa and MCF megabeds, and favours the formation of the alternation of laminated and massive units (Facies B2ML) and the hummocky-type structures (**Figure 11F**). Facies B2ML is related to a pulsating flow where the massive units can be associated with destructive interferences, which cause velocity to decrease and the fallout rate to increase, while the laminated units can be related to constructive interferences with consequent increase in velocity and decrease in the fallout rate (**Figure 11F**). The same hummocky structures, low-angle wavy and plane and parallel laminae are favoured by the unsteady multidirectional nature of the overflow as indicated by Tinterri (2011).

6 DISCUSSION: DEPOSITIONAL MODEL FOR FULLY-PONDED CONFINED BEDS

The depositional model and facies tracts proposed for the megaturbidites of the MAF (Contessa bed) and helminthoid flysches (**Figures 3, 8**) are essentially consistent with depositional phases 3 and 4 of the recent laboratory experiments by Patacci et al. (2015) (see also Howlett et al., 2019, **Figure 1**). In these geological settings, axial turbidity currents evolving towards NW in narrow NW-SE stretched basins, can maintain the flow efficiency and have the time for producing a well-developed reversing flow (see **Figure 12A**). The field data, indeed, indicate that these megaturbidites are characterized by four parts recording the basal primary flow (facies A), an intermediate flow characterized especially by lateral deflections and a reversing flow (facies B1), a well-developed reversed flow (facies B2) and an upper residual flow recording the final collapse of the suspended load (facies C and D) (**Figures 3, 8, 12A**). More precisely, facies A is consistent with the underflow (*sensu* Patacci et al., 2015) directed towards the bounding slope where the downcurrent facies change from facies A1 to facies A6 describes the evolution from a high-density to a low-density turbidity current (**Figure 3**). Conversely, facies B is well consistent with the development of an upper reversing flow, even if the field data deriving especially from the CKB highlight that, between basal facies A and facies B2 characterized by megaripples indicating a south-eastward reversed flow, there is an intermediate facies B1 in which the sedimentary structures indicate a flow characterized by SW-NE oriented lateral deflections. It is interesting to note that facies A, B1 and B2 are well separated by two evident rebound layers (1st and 2nd RL in **Figure 12A**) that can be consistent with the internal density surfaces by Patacci et al. (2015). Finally, facies C and D can be related with the final phase of collapse of the residual suspended load cloud modified by a complex interaction between combined flows associated with rebound processes and the

dynamics of a mud rich suspension which must control the formation of the slurry facies and low-angle hummocky-type structures and megaripples.

However, the evidence that facies B1 is not present in the MCF megaturbidites more probably depends upon their proximity to the northern basin margin where the effects of the reversed flows can be much higher than those of lateral deflections that, conversely, should be more evident away from the northern basin margin as it occurs for the CKB and MAF beds (see **Figure 10A** and sector 2 of **Figure 12A**; see also Tinterri et al., 2016).

This evidence is also confirmed by the data of the MAF beds in the Verghereto area and of the Solignano flysch beds (**Figure 10**). Indeed, these strata are located very near to a morphologic obstacle and can give important information about the reflection phases near the bounding slope (i.e., phase 1 by Patacci et al., 2015; see also Howlett et al., 2019). These beds are all dominated by sedimentary structures indicating a well-developed upper reversing flow (**Figure 10**), also testified by progressive increase, towards the bounding slope, in thin massive units with load casts alternated with laminated units characterized by ripples, convolute laminae and hummocky-type structures indicating reversing paleocurrents (facies B2ML in **Figure 12A**). This facies can be related to the pulsating collapse of the reversing overflow consistent with repeated stagnation phases as described in the laboratory experiments (Patacci et al., 2015; Howlett et al., 2019). These stagnation phases can be also at the basis of the formation of slurry facies characterizing facies C (**Figure 12A**).

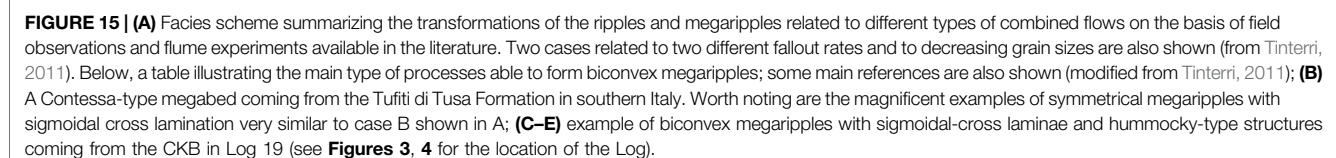
Facies B2ML featuring this type of alternation is also common in the upper megabed characterizing the MT5 in the southern Pyrenees (**Figure 12B**). This megabed is deposited by a flow transversal to an elongated narrow basin, and its large volume versus basin capacity tends to hinder the generation of a sustained reversing flow and rebound layers favoring the formation of a fully-ponded sloshing pulsating overflow able to deposit alternations of laminated and massive units that must be related to constructive and destructive interference processes (**Figure 12B**).

The comparison between field and experimental data allows more detailed discussions of some key topics characterizing contained-reflected beds, such as the significance of rebound layers (RL), the slurry deposits of facies C and the low-angle sedimentary structures featuring facies C and B.

6.1 Sedimentary Characteristics and Formation of the Rebound Layers

Although discussed briefly by Pickering and Hiscott (1985) and Edwards et al. (1994), rebound layers (RLs) are one of the most common and diagnostic structure of fully-ponded contained and confined beds (see Tinterri and Muzzi Magalhaes, 2011; Tinterri et al., 2016). The comparison between MAF megaturbidites and helminthoid flysches shows the main sedimentary characteristics of these rebound layers that are summarized in **Figure 13**.

On the basis of these sedimentary characteristics, RLs are interpreted as recording the deposition of a residual very fine-grained suspended load during a relatively quiescent period after



the deposition of the basal sandstone by the primary flow (**Figure 13B**). Indeed, during this period, the tail of the upper bypassed flow can deposit a thin drape of mud or very fine-grained sand characterized by particles able to remain easily in suspension, as indicated in point 1. The reversed flow generally is not able to erode the fine-grained drape of the RL; in fact, flute casts indicating reversed paleocurrents at the base of the laminaset just above the RL have been observed in only one case (see point 8, **Figure 13A**). However, the sedimentary characteristics listed in points 2, 3, 6 and 7 (**Figure 13**) show that RLs could also be associated with the tail of the reversed flow; ripples at the top of the basal sandstone unit clearly show that the flow had already been reflected before the RL deposition. Likewise, RLs just above massive units with flame structures indicating reversed paleocurrent can be evidence of an efficient decoupling process with the collapse of a basal part of the reversing flow and the bypass of an upper more diluted turbulent flow whose tail can deposit the RL drape (**Figure 13A**, point 2). In general, this case is more likely to occur in zones near the obstacle and, indeed, the collapse of a part of the reversed flow can be related to a slope change with the possibility to form an internal hydraulic jump, ball and pillows and flame structures due to the high rate of fallout (see Postma et al., 2009; Tinterri et al., 2016). Folded RLs due to soft-sediment deformation, which is usually represented by large-scale vergent convolute lamination (point 7, **Figure 13A**), can be related to a similar process or a pulsating shear stress associated with a combined reversed flow (see Tinterri et al., 2016). The same thin laminasets within the RL, characterized by reversing ripples (see point 3), are evidence that, at least in part, the fine-grained drape is deposited by the reversing flow even if these ripples can be also deposited by local reflection processes associated to local morphologies. Indeed, their geometry is usually characterized by strong lenticularity, such as the laminasets composed of hummocky-type structures (point 4), that, besides indicating a combined reversed flow, can be evidence of compensation phenomena of the hummocky geometry of the basal sandstone upper surface (see point 6 in **Figure 13A**). This geometry can be related to reworking processes associated with the bypass of upper low-density primary flow as well as reversing flow that, also given the presence of biconvex ripples, could have combined flow characteristics.

The possibility that RLs can be associated with local flow reflections is also substantiated by the presence of minor RLs traceable only over short distances. In this case, RLs may be related to unsteady pulsating flows reflecting local seafloor reliefs and recombination of deflected reversed flows with a mechanism similar to that described by Kane et al. (2009) as shown in **Figure 13C** (see also Patel et al., 2021).

However, it appears evident that well-developed RLs that can be traced throughout the basin are those associated with megaturbidites deposited by large-volume turbidity currents capable of crossing the basin several times (point 9 in **Figure 13A**). In particular, the comparison between CKB and MT5 megabeds (**Figure 12**) suggests that the development of RLs is associated with highly-stratified axial flows in elongated and narrow basins, as in the CKB where the maintenance of flow efficiency allows the formation of a well-developed reversing flow. In this case, RLs can be consistent with the internal density surfaces

along which decoupling processes can occur and internal waves at different frequencies can propagate (see Tinterri, 2011; Patacci et al., 2015). This process can be at the basis of the combined flow structures as well as the hummocky surface, which features the top of the basal sandy unit A6 deposited by the primary flow.

6.2 Formation and Significance of Slurry Facies in Contained and Confined Beds

The formation of slurry facies within contained-reflected beds in distal basin plains is another important topic that deserves to be discussed. These facies indicated in this work as facies C, record the passage between the fine-grained sandstone facies B and the uppermost mudstone facies D. In general, the slurry unit is composed of a very fine-grained sandy siltstone and is characterized by a continuum of facies whose end members are: 1) a completely homogeneous facies rich in soft-sediment deformations, such as contorted pseudonodules and convoluted laminae and 2) an alternation of thin slurry units and laminasets characterized by hummocky-type structures and low-angle megaripples indicating paleocurrents opposite to those of the flute casts and, in some cases, opposite one to the other (**Figure 14**). The latter facies passes to the completely homogenized facies through a progressive increase in the soft-sediment deformation represented by load structures (ball and pillows and detached pseudonodules) as shown in **Figure 14**. It is considered important to stress that mudstone intraclasts were never found in any facies C of the cases studied.

This facies is a typical characteristic of contained-reflected beds and was discussed for the first time by Pickering and Hiscott (1985) and later by Haughton (1994), Remacha et al. (2005), Muzzi Magalhaes and Tinterri (2010). More recently, this facies formation process was discussed also by Patacci et al. (2015) and Bell et al. (2018). The former gives more emphasis to the processes of cyclic-wave loading linked to various types of internal waves or bores resulting in the slurry facies, whereas the latter tends to give more emphasis to the collapse phases of fine residual flows. In particular, Bell et al. (2018) see the formation of this type of slurry as due to the collapse of a deflected turbidity current enriched of mud through erosion processes occurring on the bounding slope. In this study, however, the slurry facies is always devoid of mudstone clasts and, in many cases, also of arenaceous pseudonodules, showing a poorly-sorted liquefied homogeneous very fine-grained sandy siltstone.

From this point of view, it is more likely that this facies is the result of a combination of several factors rather than just one, such as: 1) the collapse, enhanced by the basin morphology, of the fine residual part of a contained-reflected current where the presence of bores still slowly move back and forth across the basin cannot be completely ruled out, 2) the dynamics of combined flows characterized by pulsations of different frequencies. Lower frequency pulsations linked to the alternation of the flow stagnation and re-acceleration phases can contribute to the formation of the alternation of slurry and laminated units, whereas high-frequency internal waves can contribute to the formation of combined flow structures

and to the liquefaction processes linked to cyclic shear stresses, 3) the dynamics of mud rich turbulent flows that, through the formation of transitional flows (*sensu* Baas et al., 2009, Baas et al., 2011), can favor the formation of slurry units and low-angle mixed sand-mud bedforms (see below).

Facies C tends to be associated with intrabasinal morphologies that favour flow decelerations and an increase in sediment fallout, as in the case of CKB where this facies is better developed near important transversal tectonically-controlled highs (see **Figures 2, 3**). Likewise, in contained and confined turbidites having relatively small volumes (in comparison with megaturbidites), facies C tends to develop in distal basin plains against important morphological barriers, such as in the case of MAF beds at the toe of the Verghereto structural high (**Figure 10B**). This is evidence that the role of the collapse of fine-grained residual suspension is certainly fundamental, as well as reflection processes as testified by the occurrence of sedimentary structures indicating paleocurrents different one from the other and from those of the flute casts.

The progressive passage from a facies characterized by an alternation of different units to a well-developed homogeneous slurry facies must depend upon an increase in the fallout rate, related to the rate of deceleration and to an increase in silt and mud content towards the basal part of the flow, which favor the formation of transitional flow (see **Figure 14**).

Lastly, it is considered important to point out that this slurry facies C should be kept distinguished from the intermediate slurry unit of the classic tripartite hybrid beds as described by Haughton et al., 2009 (i.e., H3 division; see also Talling et al., 2004; Muzzi Magalhaes and Tinterri, 2010). The former, consisting of very fine-grained sandy siltstone rich in load structures without mudstone clasts, is associated with deceleration and reflection of low-density turbidity currents in basin plains against distal morphological obstacles. On the contrary, the latter consists of muddy sandstone rich in mudstone clasts and soft-sediment deformation produced by decelerations, induced by a gradient decrease, of mud-rich turbidity currents, whose mud enrichment must occur upcurrent, generally induced by a tectonic confinement that favor erosive processes (Tinterri et al., 2020; see **Figure 12**).

6.3 Asymmetrical Biconvex Megaripples and Hummocky-Type Structures

Contained-reflected beds usually show various typical bedforms that characterize especially facies B and C (**Figures 3, 6, 15**). These sedimentary structures are: 1) biconvex asymmetrical to symmetrical megaripples with sigmoidal-cross laminae, 2) isotropic to anisotropic small-scale hummocky-type structures, and 3) low-angle undulated laminae. Megaripples and hummocky-type structures are generally characterized by wavelengths of about 40–60 cm and are often associated with reversing flows since they indicate paleocurrents opposite to those of flute casts. Magnificent examples of symmetrical 2D megaripples separated by evident RLs can also be observed in another Contessa-type megabed in the Tufiti di Tusa Formation in the southern Apennines (see **Figure 15B**; see also Cerone et al., 2017). This evidence led to interpret these structures as related to

combined flows deriving from the interference processes between reflected turbidity currents and different trains of internal waves or bores (Tinterri, 2011; Tinterri et al., 2016; see also Kneller et al., 1991; Edwards et al., 1994; Haughton, 1994). Indeed, experimental data show that an oscillatory component in combined flows, dominated by a unidirectional component, favours the formation of biconvex ripples and megaripples with sigmoidal-cross laminae (Yokokawa et al., 1995; Dumas et al., 2005). This is related to how the sand is redistributed by the vortices relating to forward and backward strokes of the oscillatory components (**Figure 15A**). In general, in a combined flow dominated by a unidirectional component, the sandy load lifted in suspension by the vortex formed in front of the lee side, associated with the stronger stroke, is not redistributed completely on the stoss side as in the purely oscillatory flows, but a large part of said load is deposited on the lee side near the brinkpoint, forming a bulge structure materialized by a convex lamina. The latter, joining with the lower part of the concave-upward foresets, produces a sigmoidal lamina. In these cases, however, an increase in the fallout rate or a decrease in grain sizes or a combination of both processes may favor ripple roundness and the vertical passage into small-scale hummocky-type structures (see Tinterri, 2011) (**Figure 15A**). In these cases, however, a contribution given by a supercritical unidirectional component producing asymmetrical rounded megaripples cannot be completely ruled out (see Fedele et al., 2016) (see table in **Figure 15A**).

It is also possible that the dynamics of mud and silt forming transient turbulent flows and mixed sand-mud bedforms can have played an important role (see Baker and Baas, 2020; Baas et al., 2021). This is particularly valid for the sedimentary structures characterizing facies C, which are made of muddy very fine-grained sandy siltstone.

Recent laboratory experiments, indeed, have shown that current ripples can transform into large-scale ripples and then into low-amplitude bedwaves, under decelerating sand-mud flows where the increase in viscosity due to mud-rich suspension can produce transitional flows with attenuated turbulence (Baker and Baas, 2020; Baas et al., 2021). The same vertical passage from megaripples into convolute laminae (see **Figure 10B**) can be associated with an increase in mud content as indicated by Tinterri et al. (2016) and Gladstone et al. (2018), which could be related to an increase in flow deceleration and fallout rate associated with stagnation or destructive interference phases of the reversed/deflected flow (**Figure 10B**). The same lateral facies variation in facies B, where alternations of megaripples and convolute laminae pass, towards the bounding slope, into alternations of even/undulated low-amplitude laminations and massive units with load structures, can be related to an increase in fallout and deceleration rate allowing a relationship between convolute laminae and massive units to be assumed, as indicated in **Figure 10B**.

7 CONCLUSION

This work discusses facies and processes of contained and confined beds of the MAF and helminthoid flysches in the northern

Apennines. In particular, thanks to the comparison of the Contessa megabed and some particularly significant megabeds of the MCF, on the hand, with the MT5 megaturbidite in the Pyrenees, a depositional model for fully-ponded beds, which is well consistent with the experimental data available in the literature (see **section 2**), can be proposed (see **Figure 12**). These megaturbidites, which are deposited by turbidity currents having larger volumes than those of the respective basins, are characterized by four main facies (A, B, C and D in **Figure 12**), whose characteristics change depending on whether the flows are characterized by an axial source (parallel to the basin axis), as in the case of the CKB and helminthoid flyschs, or by a source transversal to the basin (perpendicular to the basin axis), as in the case of the MT5.

In the former case the lateral confinement favours the conservation of flow efficiency and the development of a steady phase 3 by Patacci et al. (2015) (**Figure 12A**). In this case, indeed, Facies A, consisting of six facies (A1 to A6), records the evolution of the basal primary underflow, while Facies B, made of two subfacies B1 and B2, records an intermediate flow with lateral deflections and a well-developed reversed overflow, respectively. Conversely, Facies C and D, consisting of a slurry facies C and a very thick mudstone unit D, record the final collapse of the suspended load characterizing a residual reversing flow (**Figures 3, 8, 12**). In the case of **Figure 12A**, facies A, B1 and B2, are usually separated by evident very thin fine-grained muddy drapes (rebound layer, RL) that can be related to the internal density surfaces highlighted also by flume experiments, along which decoupling processes separating the underflow from the reversing overflow can occur more easily (**Figure 13**). Facies C, however, tends to be more developed near the morphological highs, where the rates of deceleration, the dynamics of muddy transient flows and interference of reflected internal waves can play a key role in the formation of sandy siltstone slurry facies, when turbulent flows impinge perpendicularly a distal basin margin.

Conversely in the case of MT5 (**Figure 12B**), flows transversal to the basin axis tend to favor the formation of fully-ponded pulsating (sloshing) overflows hindering the generation of sustained reversing flows and, consequently, of evident rebound layers, favoring instead the deposition of alternations of laminated and massive units (B2ML facies) deriving from complex interference processes associated with pulsating overflows (**Figure 11**). A similar facies, however, can be also observed in the basins characterized by axial flows only near the basin margin where the pulsating collapse of the reversing flow dominates (see **Figures 10B, 12A**).

REFERENCES

- Alexander, J., and Morris, S. (1994). Observations on Experimental, Nonchannelized, High-Concentration Turbidity Currents and Variations in Deposits Around Obstacles. *Jour. Sed. Res.* 64, 899–909. doi:10.1306/d4267f00-2b26-11d7-8648000102c1865d
- Allen, P. A., and Underhill, J. R. (1989). Swaley Cross-Stratification Produced by Unidirectional Flows, Bendcliffe Grit (Upper Jurassic), Dorset, UK. *J. Geol. Soc.* 146, 241–252. doi:10.1144/gsjgs.146.2.0241
- Amy, L. A., McCaffrey, W. D., and Kneller, B. C. (2004). “The Influence of a Lateral basin-slope on the Depositional Patterns of Natural and Experimental Turbidity

This study shows that field studies integrating high-resolution physical stratigraphy, facies analysis and regional-structural geology are essential for a correct interpretation of any type of structure, at any scale, and, consequently, for tangible validation of experimental data from an applicative point of view.

DATA AVAILABILITY STATEMENT

The original contributions presented in the study are included in the article/**Supplementary Material**, further inquiries can be directed to the corresponding author.

AUTHOR CONTRIBUTIONS

RT contributed to the Conceptualization, Methodology, Investigation, Writing—original draft and Project administration; TM and PM contributed to the Investigation; All the Authors contributed to manuscript revision, read, and approved the submitted version.

ACKNOWLEDGMENTS

We would like to thank Alessio Tagliaferri, Alberto Piazza, Rogerio Soares Cunha, Vanni Pizzati, Elena Scaccia and Simone Lombardi for the discussions in the field and their help in the final editing phase. Luca Baruffini is thanked for the discussions on the helminthoid Flyschs. Emiliano Mutti and Eduard Remacha are thanked for their teachings and discussions on the Hecho Group. We also wish to thank Dave Hodgson (Chief Editor), Rosanna Maniscalco (Guest Editor) and the reviewers Salvatore Milli and Giacomo Dalla Valle for their helpful and constructive comments which helped to improve the manuscript. This research was partially funded by ENI SpA and Petróleo Brasileiro S.A. (Petrobras). In particular, we thank Giancarlo Davoli (Eni) and Mario Carminatti (Petrobras).

SUPPLEMENTARY MATERIAL

The Supplementary Material for this article can be found online at: <https://www.frontiersin.org/articles/10.3389/feart.2022.817012/full#supplementary-material>

- Currents,” in *Deep-water Sedimentation in the Alpine Foreland Basin of the SE France: New Perspectives on the Grès d'Annot and Related Systems*. Editors P. Joseph, and S. A. Lomas (Bath, United Kingdom: Geological Society of London, Special Publications), 221, 311–330. doi:10.1144/gsl.sp.2004.221.01.17
- Amy, L. A., and Talling, P. J. (2006). Anatomy of Turbidites and Linked Debrisites Based on Long Distance (120 X 30 Km) Bed Correlation, Marnoso Arenacea Formation, Northern Apennines, Italy. *Sedimentology* 53, 161–212. doi:10.1111/j.1365-3091.2005.00756.x
- Arnott, R. W., and Southard, J. B. (1990). Exploratory Flow-Duct Experiments on Combined-Flow Bed Configurations, and Some Implications for Interpreting Storm-Event Stratification. *Jour. Sed. Petr.* 60, 211–219. doi:10.1306/212f9156-2b24-11d7-8648000102c1865d

- Baas, J. H., Best, J. L., and Peakall, J. (2011). Depositional Processes, Bedform Development and Hybrid Bed Formation in Rapidly Decelerated Cohesive (Mud-sand) Sediment Flows. *Sedimentology* 58, 1953–1987. doi:10.1111/j.1365-3091.2011.01247.x
- Baas, J. H., Best, J. L., Peakall, J., and Wang, M. (2009). A Phase Diagram for Turbulent, Transitional, and Laminar clay Suspension Flows. *J. Sediment. Res.* 79, 162–183. doi:10.2110/jsr.2009.025
- Baas, J. H., Best, J., and Peakall, J. (2021). Rapid Gravity Flow Transformation Revealed in a Single Climbing Ripple. *Geology* 49, 493–497. doi:10.1130/g48181.1
- Baker, M. L., and Baas, J. H. (2020). Mixed Sand-Mud Bedforms Produced by Transient Turbulent Flows in the Fringe of Submarine Fans: Indicators of Flow Transformation. *Sedimentology* 67, 2645–2671. doi:10.1111/sed.12714
- Baruffini, L., and Papani, L. (2017). An Introduction to the Physical Stratigraphy and Facies of the Upper Cretaceous Helminthoid Flysch, Western Alps and NW Apennine. *33rd Int. Meet. Sedimentology – Toulouse*, 10–12.
- Bell, D., Stevenson, C. J., Kane, I. A., Hodgson, D. M., and Poyatos-Moré, M. (2018). Topographic Controls on the Development of Contemporaneous but Contrasting basin-floor Depositional Architectures. *Jour. Sed. Res.* 88, 1166–1189. doi:10.2110/jsr.2018.58
- Cartigny, M. J. B., Ventra, D., Postma, G., and Van den Berg, J. H. (2014). Morphodynamics and Sedimentary Structures of Bedforms under Supercritical-Flow Conditions: New Insights from Flume Experiments. *Sedimentology* 61, 712–748. doi:10.1111/sed.12076
- Cerone, D., Gallicchio, S., Moretti, M., and Tinterri, R. (2017). Vertical facies evolution of the Tufiti di Tusa Formation cropping out in the Lucanian Apennines (Southern Italy). *Jour. Med. Earth Sci.* 9, 109–112.
- Chough, S. K., and Sohn, Y. K. (1990). Depositional Mechanics and Sequences of Base Surges, Songaksan Tuff Ring, Cheju Island, Korea. *Sedimentology* 37, 1115–1135. doi:10.1111/j.1365-3091.1990.tb01849.x
- de Jager, J. (1979). The Relation between Tectonics and Sedimentation Along the “Sillaro line” (northern Apennines, Italy). *Geol. Ultraiectina*, 19, 97.
- Dumas, S., Arnott, R. W. C., and Southard, J. B. (2005). Experiments on Oscillatory-Flow and Combined-Flow Bed Forms: Implications for Interpreting Parts of the Shallow-Marine Sedimentary Record. *J. Sediment. Res.* 75, 501–513. doi:10.2110/jsr.2005.039
- Edwards, D. A., Leeder, M. R., Best, J. L., and Pantin, H. M. (1994). On Experimental Reflected Density Currents and the Interpretation of Certain Turbidites. *Sedimentology* 41, 437–461. doi:10.1111/j.1365-3091.1994.tb02005.x
- Ellis, D. (1982). *Palaeohydraulics and Computer Simulation of Turbidites in the Marnoso-Arenacea, Northern Apennines, Italy*. PhD Thesis. Scotland: University of St. Andrews.
- Fallgatter, C., Kneller, B. C., Paim, P., and Milana, J. P. (2016). Hybrid Megabeds Deposition and the Influence of Related Topography in Ponding Subsequent Co-genetic Flow: Cerro Bola Area, Paganzo Basin, Argentina. *Sedimentology* 64, 357–387.
- Fedele, J. J., Hoyal, D. C. J. D., Barnaal, Z., Tulenko, J., and Awalt, S. (2016). “Bedforms Created by Gravity Flows,” in *Autogenic Dynamics and Self-Organization in Sedimentary Systems* (Broken Arrow, OK, United States: SEPM Special Publication), 106, 95–121.
- Felletti, F., Marini, M., Bellin, N., and Talling, P. (2019). Geometry and Internal Facies Partitioning of the Contessa Megaturbidite from Long Distance (130–30 Km) Correlation (Miocene Marnoso Arenacea Fm; Northern Apennines, Italy). *34th Int. Meet. Sedimentology – Rome*, 10–13.
- Fontana, D., Spadafora, E., and Stefani, C. (1994). The Upper Cretaceous Helminthoid Flysch of the Northern Apennines: Provenance and Sedimentation. *Mem. Soc. Geol. It.* 48, 237–250.
- Gandolfi, G., Paganelli, L., and Zuffa, G. G. (1983). Petrology and Dispersal Pattern (Miocene, Northern Apennines). *Jour. Sed. Petrol.* 53, 493–507.
- Ghienne, J. F., Girard, F., Moreu, J., and Rubino, J. L. (2010). Late Ordovician Climbing-Dune Cross-Stratification: a Signature of Outburst Floods in Proglacial Outwash Environments? *Sedimentology* 57, 1175–1198.
- Gladstone, C., McClelland, H. L. O., Woodcock, N. H., Pritchard, D., and Hunt, J. E. (2018). The Formation of Convolute Lamination in Mud-rich Turbidites. *Sedimentology* 65, 1800–1825. doi:10.1111/sed.12447
- Hand, B. M., and Bartberger, C. E. (1988). Leeseide Sediment Fallout Patterns and the Stability of Angular Bedforms. *Jour. Sed. Petr.* 58, 33–43.
- Harms, J. C. (1969). Hydraulic Significance of Some Sand Ripples. *Geol. Soc. America Bull.* 80, 363–396. doi:10.1130/0016-7606(1969)80[363:hsossr]2.0.co;2
- Haughton, P. (2001). Contained Turbidites Used to Track Sea Bed Deformation and basin Migration, Sorbas Basin, South-East Spain. *Basin Res.* 13, 117–139. doi:10.1046/j.1365-2117.2001.00143.x
- Haughton, P. D. W. (1994). Deposits of Deflected and Ponded Turbidity Currents, Sorbas Basin, Southeast Spain. *J. Sediment. Res.* 64, 233–246. doi:10.1306/d4267d6b-2b26-11d7-8648000102c1865d
- Howlett, D. M., Ge, Z., Nemec, W., Gawthorpe, R. L., Rotevatn, A., and Jackson, C. A. L. (2019). Response of Unconfined Turbidity Current to Deep-water Fold and Thrust belt Topography: Orthogonal Incidence on Solitary and Segmented Folds. *Sedimentology* 66, 2425–2454. doi:10.1111/sed.12602
- Haughton, P. D. W., Davis, C., McCaffrey, W. D., and Barker, S. (2009). Hybrid sediment gravity flow deposits – classification, origin and significance. *Mar. Petrol. Geology* 26, 1900–1918.
- Kane, I. A., McCaffrey, W. D., and Martinsen, O. J. (2009). Allogenic vs. Autogenic Controls on Megaflute Formation. *J. Sediment. Res.* 79, 643–651. doi:10.2110/jsr.2009.072
- Kleverlaan, K. (1987). Gordo Megabed: a Possible Seismitic in a Tortonian Submarine Fan, Tabernas basin, Province Almería, Southeast Spain. *Sediment. Geology* 51, 165–180. doi:10.1016/0037-0738(87)90047-9
- Kneller, B. (1995). “Beyond the Turbidite Paradigm: Physical Models for Deposition of Turbidites and Their Implications for Reservoir Prediction,” in *Characterization of Deep Marine Clastic Systems*, 4. Editors A. J. Hartlet, and D. J. Prosser (Bath, UK: Geological Society, London, Special Publications), 94, 31–49. doi:10.1144/gsl.sp.1995.094.01.04
- Kneller, B. C., and Branney, M. J. (1995). Sustained High-Density Turbidity Currents and the Deposition of Thick Massive Sands. *Sedimentology* 42, 607–616. doi:10.1111/j.1365-3091.1995.tb00395.x
- Kneller, B., Edwards, D., McCaffrey, W., and Moore, R. (1991). Oblique Reflection of Turbidity Currents. *Geol.* 19, 250–252. doi:10.1130/0091-7613(1991)019<0250:orotc>2.3.co;2
- Koller, D., Manica, R., Borges, A. L., and Fedele, J. (2019). Experimental Bedforms by saline Density Currents. *Braz. J. Geology* 49, 20180118. doi:10.1590/2317-4889201920180118
- Lababe, P., Mutti, E., and Seguret, M. (1987). Megaturbidites: A Depositional Model from the Eocene of the SW-Pyrenean Foreland Basin, Spain. *Geo-Marine Lett.* 7, 91–101. doi:10.1007/bf02237988
- Lababe, P., Mutti, E., Seguret, M., and Rosell, J. (1983). Megaturbidites carbonates du bassin turbiditique de l'Eocene inferieur et moyen sud-pyreneen. *Bull. de la Societe Geologique de France S7-XXV*, 927–941. doi:10.2113/gssgfbull.s7-xxv.6.927
- Lamb, M. P., Hickson, T., Marr, J. G., Sheets, B., Paola, C., and Parker, G. (2004). Surging versus Continuous Turbidity Currents: Flow Dynamics and Deposits in an Experimental Intrallope Minibasin. *J. Sediment. Res.* 74, 148–155. doi:10.1306/062103740148
- Lamb, M. P., and Parsons, J. D. (2005). High-density Suspensions Formed under Waves. *J. Sediment. Res.* 75, 386–397. doi:10.2110/jsr.2005.030
- Lowe, D. R., and Guy, M. (2000). Slurry-flow Deposits in the Britannia Formation (Lower Cretaceous), North Sea: a New Perspective on the Turbidity Current and Debris Flow Problem. *Sedimentology* 47, 31–70. doi:10.1046/j.1365-3091.2000.00276.x
- Marjanac, T. (1990). Reflected Sediment Gravity Flows and Their Deposits in Flysch of Middle Dalmatia, Yugoslavia. *Sedimentology* 37, 921–929. doi:10.1111/j.1365-3091.1990.tb01834.x
- Marroni, M., Meneghini, F., and Pandolfi, L. (2017). A Revised Subduction Inception Model to Explain the Late Cretaceous, Double-Vergent Orogen in the Precollisional Western Tethys: Evidence from the Northern Apennines. *Tectonics* 36, 2227–2249. doi:10.1002/2017tc004627
- Marroni, M., Molli, G., Ottria, G., and Pandolfi, L. (2001). Tectono-sedimentary Evolution of the External Liguride Units (Northern Apennines, Italy): Insights in the Pre-collisional History of a Fossil Ocean-Continent Transition Zone. *Geodinamica Acta* 14, 307–320. doi:10.1080/09853111.2001.11432449
- Masuda, F., and Yokokawa, M. (1992). Combined Flow Ripples Produced by Flume Experiments. *Sci. Rep. Col. Gen. Educ. Osaka Univ.* 41, 1–13.

- McCave, I. N., and Jones, K. P. N. (1988). Deposition of Ungraded Mud from High-Density Non-turbulent Turbidity Currents. *Nature* 333, 250–252. doi:10.1038/333250a0
- Mutti, E., Lucchi, F. R., Seguret, M., and Zanzucchi, G. (1984). Seismoturbidites: a New Group of Resedimented Deposits. *Mar. Geology* 55, 103–116. doi:10.1016/0025-3227(84)90135-x
- Mutti, E., Tinterri, R., Benevelli, G., Biase, D. d., and Cavanna, G. (2003). Deltaic, Mixed and Turbidite Sedimentation of Ancient Foreland Basins. *Mar. Pet. Geology* 20, 733–755. doi:10.1016/j.marpetgeo.2003.09.001
- Mutti, E., Tinterri, R., Remacha, E., Mavilla, N., Angella, S., and Fava, L. (1999). *An Introduction to the Analysis of Ancient Turbidite Basins from an Outcrop Perspective*, 39. Tulsa, OK: AAPG Continuing Education Course Notes Series, 93.
- Muzzi Magalhaes, P., and Tinterri, R. (2010). Stratigraphy and Depositional Setting of Slurry and Contained (Reflected) Beds in the Marnoso-Arenacea Formation (Langhian-Serravallian) Northern Apennines, Italy. *Sedimentology* 57, 1685–1720. doi:10.1111/j.1365-3091.2010.01160.x
- Myrow, P. M., and Southard, J. B. (1991). Combined-flow Model for Vertical Stratification Sequences in Shallow marine Storm Deposited Beds. *Jour. Sed. Petr.* 61, 202–211. doi:10.1306/d42676d1-2b26-11d7-8648000102c1865d
- Nøttvedt, A., and Kreisa, R. D. (1987). Model for the Combined-Flow Origin of Hummocky Cross-Stratification. *Geology* 15, 357–361.
- Ogata, K., Mutti, E., Pini, G. A., and Tinterri, R. (2012). Mass Transport-Related Stratal Disruption within Sedimentary Mélanges: Examples from the Northern Apennines (Italy) and South-central Pyrenees (Spain). *Tectonophysics* 568–569, 185–199. doi:10.1016/j.tecto.2011.08.021
- Pantin, H. M., and Leeder, M. R. (1987). Reverse Flow in Turbidity Currents: the Role of Internal Solitons. *Sedimentology* 34, 1143–1155. doi:10.1111/j.1365-3091.1987.tb00597.x
- Parea, G. C., and Ricci Lucchi, F. (1975). Turbidite Key-Beds as Indicators of Ancient Deep-Sea plains. *Proc. IX Int. Cong. Sed., Nice, Theme 1*, 235–245.
- Patacci, M., Houghton, P. D. W., and McCaffrey, W. D. (2015). Flow Behavior of Pondered Turbidity Currents. *J. Sediment. Res.* 85, 885–902. doi:10.2110/jsr.2015.59
- Patel, U. S., Gardiner, A., and Stow, D. A. V. (2021). Bed-scale Vertical and Lateral Distribution of Massive sandstone in a Topographically Confined basin (Peira Cava, SE France): Implications for Flow Processes. *Sediment. Geology* 424, 106001. doi:10.1016/j.sedgeo.2021.106001
- Payros, A., Pujalte, V., and Orue-Etxebarria, X. (1999). The South Pyrenean Eocene Carbonate Megabreccias Revisited: New Interpretation Based on Evidence from the Pamplona Basin. *Sediment. Geology* 125, 165–194. doi:10.1016/s0037-0738(99)00004-4
- Piazza, A., and Tinterri, R. (2020). “Mass-Transport Deposits in the Foredeep Basin of the Cervarola Sandstones Formation (Miocene, Northern Apennines, Italy),” in *Submarine Landslides: Subaqueous Mass-Transport Deposits from Outcrops to Seismic Profiles*. Editors K. Ogata, A. Festa, and G. A. Pini Geophysical Monograph 247, First Edition. American Geophysical Union (Hoboken NJ: John Wiley & Sons, Inc.), 27–44.
- Pickering, K. T., and Hiscott, R. N. (1985). Contained (Reflected) Turbidity Currents from the Middle Ordovician Cloridorme Formation, Quebec, Canada: an Alternative to the Antidune Hypothesis. *Sedimentology* 32, 373–394. doi:10.1111/j.1365-3091.1985.tb00518.x
- Postma, G., and Cartigny, M. J. B. (2014). Supercritical and Subcritical Turbidity Currents and Their Deposits—A Synthesis. *Geology* 42, 987–990. doi:10.1130/g35957.1
- Postma, G., Cartigny, M., and Kleverlaan, K. (2009). Structureless, Coarse-Tail Graded Bouma Ta Formed by Internal Hydraulic Jump of the Turbidity Current? *Sediment. Geology* 219, 1–6. doi:10.1016/j.sedgeo.2009.05.018
- Remacha, E., Fernandez, L. P., and Maestro, E. (2005). The Transition between Sheet-like Lobe and basin plain Turbidites in the Hecho basin (Southcentral Pyrenees, Spain). *Jour. Sed. Res.* 75, 789–819. doi:10.2110/jsr.2005.064
- Renzi, G. (1964). Un probabile Livello guida nella Formazione Marnoso-arenacea romagnola nei dintorni di Marradi e Palazzuolo. *Quaderni Studi Romagnoli* 1, 15–20.
- Ricci Lucchi, F. (1995). Contessa and Associated Megaturbidites: Long Distance (120 × 25 Km) Correlation of Individual Beds in a Miocene Foredeep. *Atlas of Deep Water Environments*, 300–302. doi:10.1007/978-94-011-1234-5_45
- Ricci Lucchi, F., and Piali, G. (1973). Apporti secondari nella Marnoso arenacea: 1. Torbiditi di conoide e di pianura sottomarina ad est-nord-est di Perugia. *Bollettino della Società Geologica Italiana* 92, 669–712.
- Ricci Lucchi, F. (1985). *Small-scale Antidune Forms on Top of a Megaturbidite sandstone, Northern Apennines*. Lleida, Abs: IAS 5th Regional Meeting, 387–390.
- Ricci Lucchi, F. (1986). “The Oligocene to Recent Foreland Basins of the Northern Apennines,” in *Foreland Basins, IAS Spec. Publ.* Editors P. A. Allen, and P. Homewood (Oxford: Blackwell Scientific), Vol. 8, 105–139.
- Ricci Lucchi, F., and Valmori, E. (1980). Basin-wide Turbidites in a Miocene, Over-supplied Deep-Sea plain: a Geometrical Analysis. *Sedimentology* 27, 241–270. doi:10.1111/j.1365-3091.1980.tb01177.x
- Rio, D., and Villa, G. (1987). On the age of the “Salti del Diavolo” conglomerates and of the Monte Cassio Flysch “Basal Complex” (Northern Apennines, Parma province). *Giornale di Geologia* 49 (1), 63–79.
- Rupke, N. A. (1976). Sedimentology of Very Thick Calcarenite-Marlstone Beds in a Flysch Succession, Southwestern Pyrenees. *Sedimentology* 23, 43–65. doi:10.1111/j.1365-3091.1976.tb00038.x
- Sagri, M., and Marri, C. (1980). Paleobatimetria e ambienti di deposizione delle unità torbiditiche cretaceo-superiori dell’Appennino settentrionale. *Società Geologica Italiana Memorie* 21, 231–240.
- Saunderson, H., and Lockett, F. P. J. (1983). “Flume Experiments on Bedforms and Structures at the Dune-Plane Bed Transition,” in *Modern and Ancient Fluvial Systems, IAS Spec.* Editors J. D. Collinson, and J. Lewin (Blackwell: Publ.), 6, 49–58.
- Schieber, J., and Southard, J. B. (2009). Bedload Transport of Mud by Floccule Ripples—Direct Observation of Ripple Migration Processes and Their Implications. *Geology* 37, 483–486. doi:10.1130/g25319a.1
- Schieber, J., Southard, J., and Thaisen, K. (2007). Accretion of Mudstone Beds from Migrating Floccule Ripples. *Science* 318, 1760–1763. doi:10.1126/science.1147001
- Scholle, P. A. (1971). Sedimentology of fine-grained Deep-Water Carbonate Turbidites, Monte Antola Flysch (Upper Cretaceous), Northern Apennines, Italy. *Geol. Soc. America Bull.* 82, 629–658. doi:10.1130/0016-7606(1971)82[629:sodfct]2.0.co;2
- Soutter, E. L., Bell, D., Cumberpatch, Z. A., Ferguson, R. A., Sychala, Y. T., Kane, I. A., et al. (2021). The Influence of Confining Topography Orientation on Experimental Turbidity Currents and Geological Implications. *Front. Earth Sci.* 8, 540633. doi:10.3389/feart.2020.540633
- Stevenson, C. J., Talling, P. J., Masson, D. G., Sumner, E. J., Frenz, M., and Wynn, R. B. (2014). The Spatial and Temporal Distribution of Grain-Size Breaks in Turbidites. *Sedimentology* 61, 1120–1156. doi:10.1111/sed.12091
- Sumner, E. J., Talling, P. J., and Amy, L. A. (2009). Deposits of Flows Transitional between Turbidity Current and Debris Flow. *Geology* 37, 991–994. doi:10.1130/g30059a.1
- Tagliaferri, A., and Tinterri, R. (2016). The Tectonically-Confined Firenzuola Turbidite System (Marnoso-Arenacea Formation, Northern Apennines, Italy). *It. Jour. Geoscience* 135, 425–443. doi:10.3301/ijg.2015.27
- Tagliaferri, A., Tinterri, R., Pontiggia, M., Da Pra, A., Davoli, G., and Bonamini, E. (2018). Basin-scale, High-Resolution Three-Dimensional Facies Modeling of Tectonically Confined Turbidites: An Example from the Firenzuola System (Marnoso-Arenacea Formation, Northern Apennines, Italy). *AAPG Bulletin* 102, 1601–1626. doi:10.1306/12081716521
- Talling, P. J., Amy, L. A., Wynn, R. B., Peakall, J., and Robinson, M. (2004). Beds Comprising Debrite Sandwiched within Co-genetic Turbidite: Origin and Widespread Occurrence in Distal Depositional Environments. *Sedimentology* 51, 163–194. doi:10.1111/j.1365-3091.2004.00617.x
- Talling, P. J., Masson, D. G., Sumner, E. J., and Malgesini, G. (2012). Subaqueous Sediment Density Flows: Depositional Processes and deposit Types. *Sedimentology* 59, 1937–2003. doi:10.1111/j.1365-3091.2012.01353.x
- Tinterri, R., Civa, A., Laporta, M., and Piazza, A. (2020). “Turbidites and Turbidity Currents,” in *Regional Geology and Tectonics: Principles of Geologic Analysis*. Editors N. Scarselli, A. Jürgen, D. Chiarella, D. G. Roberts, and A. W. Bally. 2nd ed. (Elsevier), 1, 441–479.
- Tinterri, R. (2011). Combined Flow Sedimentary Structures and the Genetic Link between Sigmoidal and Hummocky-Cross Stratification. *GeoActa* 10, 43–85.
- Tinterri, R., and Mazza, T. (2019). Contained-reflected Beds: Examples from Foredeep Turbidites and Helminthoid Flysches of the Northern Apennines (Italy). *34th Int. Meet. Sedimentology – Rome* 10–13, 1879.

- Tinterri, R., Muzzi Magalhaes, P., Piazza, A., and Tagliaferri, A. (2019a). Comparing Two Foredeeps: Cervarola Sandstones and Marnoso-Arenacea Formations (Miocene, Northern Apennines, Italy). *34th Int. Meet. Sedimentology – Rome* 10–13, 1601.
- Tinterri, R., and Muzzi Magalhaes, P. (2011). Synsedimentary Structural Control on Foredeep Turbidites: an Example from Miocene Marnoso-Arenacea Formation, Northern Apennines, Italy. *Mar. Pet. Geology*. 28, 629–657. doi:10.1016/j.marpetgeo.2010.07.007
- Tinterri, R., Muzzi Magalhaes, P., Tagliaferri, A., and Cunha, R. S. (2016). Convolute Laminations and Load Structures in Turbidites as Indicators of Flow Reflections and Decelerations against Bounding Slopes. Examples from the Marnoso-Arenacea Formation (Northern Italy) and Annot Sandstones (South Eastern France). *Sediment. Geology*. 344, 382–407. doi:10.1016/j.sedgeo.2016.01.023
- Tinterri, R., Muzzi Magalhaes, P., Tagliaferri, A., and Piazza, A. (2019b). *Foredeep Turbidites of the Marnoso-Arenacea Formation*. In Field Trips Guide book, 34th IAS Meeting, Rome 10–13 september 2019. (Italy; northern Apennines), 323–339.
- Tinterri, R., and Muzzi Magalhaes, P. (2009). “The Miocene Turbidite Deposits of the Marnoso-Arenacea Formation (Northern Apennines, Italy),” in *Field Trips Guidebook*. 249–277, *27th IAS Meeting of Sedimentology, Alghero 20–23 September 2009, Post Congress Field Trip*. Editors V. Pascucci and S. Andreucci, 12, 24–28.
- Tinterri, R., and Piazza, A. (2019). Turbidites Facies Response to the Morphological Confinement of a Foredeep (Cervarola Sandstones Formation, Miocene, Northern Apennines, Italy). *Sedimentology* 66, 636–674. doi:10.1111/sed.12501
- Tinterri, R., and Tagliaferri, A. (2015). The Syntectonic Evolution of Foredeep Turbidites Related to basin Segmentation: Facies Response to the Increase in Tectonic Confinement (Marnoso-Arenacea Formation, Miocene, Northern Apennines, Italy). *Mar. Pet. Geology*. 67, 81–110. doi:10.1016/j.marpetgeo.2015.04.006
- Tinterri, R., Muzzi Magalhaes, P., and Tagliaferri, A. (2012). Foredeep turbidites of the Miocene Marnoso-arenacea Formation (Northern Apennines). *AAPG International Conference & Exhibition-Milan, Geological Field Trips* 4, 1–132. doi:10.3301/GFT.2012.03
- Toniolo, H., Lamb, M., and Parker, G. (2006). Depositional Turbidity Currents in Diapiric Minibasins on the continental Slope: Formulation and Theory. *Jour. Sed. Res.* 76, 783–797. doi:10.2110/jsr.2006.071
- Vescovi, P., Fornaciari, E., Rio, D., and Valloni, R. (1999). The Basal Complex Stratigraphy of the Helminthoid Monte Cassio Flysch: a Key to the Eoalpine Tectonics of the Northern Apennines. *Rivista Italiana di Paleontologia e Stratigrafia* 105, 101–128. doi:10.13130/2039-4942/5367
- Woods, A. D., Bursik, M. I., and Kurbatov, A. V. (1998). The Interaction of Ash Flows with Ridges. *Bull. Volcanology*. 60, 38–51.
- Yokokawa, M. (1995). Combined Flow Ripples: Genetic Experiments and Application for Geologic Records. Kyushu University, Faculty of Science. *Mem. Ser. D, Earth Planet. Sci.* 29, 1–38.
- Yokokawa, M., Masuda, F., and Endo, N. (1995). Sand Particle Movement on Migrating Combined-Flow Ripples. *Jour. Sed. Res.* A65, 40–44.
- Zuffa, G. G., Fontana, D., Morlotti, E., Premoli, S. I., Sighinolfi, G. P., Stefani, C., et al. (2004). *Anatomy of Carbonate Turbidite Mega-Beds (M. Cassio Formation, Upper Cretaceous, Northern Apennines, LXI. Italy: Mem. Descr. Carta Geol. It.*, 129–144.

Conflict of Interest: Author PM was employed by the company Petrobras.

The remaining authors declare that the research was conducted in the absence of any commercial or financial relationships that could be construed as a potential conflict of interest.

Publisher’s Note: All claims expressed in this article are solely those of the authors and do not necessarily represent those of their affiliated organizations, or those of the publisher, the editors and the reviewers. Any product that may be evaluated in this article, or claim that may be made by its manufacturer, is not guaranteed or endorsed by the publisher.

Copyright © 2022 Tinterri, Mazza and Magalhaes. This is an open-access article distributed under the terms of the Creative Commons Attribution License (CC BY). The use, distribution or reproduction in other forums is permitted, provided the original author(s) and the copyright owner(s) are credited and that the original publication in this journal is cited, in accordance with accepted academic practice. No use, distribution or reproduction is permitted which does not comply with these terms.



Possible Tsunami-Induced Sediment Transport From Coral Reef to Deep Sea Through Submarine Canyons on the Southern Ryukyu Forearc, Japan

Ken Ikehara^{1*}, Toshiya Kanamatsu² and Kazuko Usami^{3,4}

¹Research Institute of Geology and Geoinformation, Geological Survey of Japan, National Institute of Advanced Industrial Science and Technology (AIST), Tsukuba, Japan, ²Research Institute of Marine Geodynamics, Japan Agency for Marine-Earth Science and Technology (JAMSTEC), Yokosuka, Japan, ³Japan NUS Co., Ltd., Tokyo, Japan, ⁴Japan Oil, Gas and Metals National Corporation (JOGMEC), Chiba, Japan

OPEN ACCESS

Edited by:

Fabiano Gamberi,
National Research Council (CNR), Italy

Reviewed by:

Susanne Pohler,
University of Graz, Austria
Ángel Puga-Bernabéu,
University of Granada, Spain

*Correspondence:

Ken Ikehara
k-ikehara@aist.go.jp

Specialty section:

This article was submitted to
Sedimentology, Stratigraphy and
Diagenesis,
a section of the journal
Frontiers in Earth Science

Received: 05 August 2021

Accepted: 20 April 2022

Published: 11 May 2022

Citation:

Ikehara K, Kanamatsu T and Usami K
(2022) Possible Tsunami-Induced
Sediment Transport From Coral Reef
to Deep Sea Through Submarine
Canyons on the Southern Ryukyu
Forearc, Japan.
Front. Earth Sci. 10:753583.
doi: 10.3389/feart.2022.753583

Submarine canyons are efficient sediment transport pathways from shallow marine areas to deep sea. Along active margins, large tsunamis are a trigger for sediment transport to deep sea. However, sediment transport through submarine canyons by such extreme wave events in the carbonate depositional environments has not been fully understood. Large tsunamis have repeatedly struck the coral reef islands of the southern Ryukyu Islands and have transported large boulders composed of coral from the reef to shore. In this study, we examined sediment cores collected near the mouths of submarine canyons and basin floor on the southern Ryukyu arc's forearc. The presence of coarse calciturbidites containing coral, molluscan fragments, and coral reef benthic foraminifera was limited on the submarine fan formed at the mouth of the reef-connected and shelf-incised submarine canyon. In cores collected near the mouth of shelf-incised submarine canyons with no reef connection and slope-confined canyons, no coarse calciturbidite is observed. Few calciturbidites were found in more downslope cores, implying that most calcareous grains derived from shallow marine areas were deposited on this fan. Depositional intervals of turbidites were calculated to be several hundred–a few thousand years, which agree with the recurrence intervals of large tsunamis estimated from onshore tsunami deposits, based on radiocarbon dates in hemipelagic mud intervals. No temporal change in the depositional intervals of calciturbidites in the cores from the submarine fan since the last glacial maximum. Therefore, the tsunamis may be an important mechanism for surface sediment reworking in coral reefs, and shelf-incised and reef-connected submarine canyons can play an important role in the efficient transport of shallow marine calcareous grains to the deep sea.

Keywords: turbidite, coral reef, tsunami, submarine canyon, submarine fan, Ryukyu islands

INTRODUCTION

Submarine canyons have been recognized as preferential sediment transport pathways from continental margins to deep sea (e.g., Gardner, 1989; Xu et al., 2002, 2010; Palanques et al., 2005; Liu et al., 2016). Erosion and deposition by sediment gravity flows are the main overarching processes in submarine canyons (e.g., Pickering and Hiscott, 2016). However, modern submarine canyons in carbonate settings have been poorly understood because most submarine canyon studies

focused on the siliciclastic depositional environments (Harris and Whiteway, 2011). Sediment production in carbonate settings is highest when the carbonate platform is flooded during high sea-level; sediment is commonly produced in excess of the available accommodation on the platform, and excess sediment is exported to the deep-sea (Mullins, 1983; Eberli, 1991). This differs from the siliciclastic system, in which the maximum export to the deep-sea commonly occurs during the low sea-level stands. Further, Eberli (1991) showed that sediment export from carbonate platform rims, either along a volcanic island or along a continental shelf differs from that from pure carbonate platforms. Several studies on submarine canyons and their role in sediment transport in pure carbonate and mixed carbonate-siliciclastic depositional settings along passive margins such as Bahamas, Great Barrier Reef and Mozambique Channel have been conducted (Grammer and Ginsberg, 1992; Jorry et al., 2010, 2020; Mulder et al., 2012a, b, 2017; Webster et al., 2012; Puga-Bernabéu et al., 2014; Wunsch et al., 2017; Tournadour et al., 2017; Counts et al., 2018, 2021). However studies on carbonate sediment export to the deep-sea, from small reefs surrounding a small island along an active margin are still limited. More acquisition of knowledge is therefore necessary to better understand the role of submarine canyons in source-to-sink in carbonate environments.

Tsunamis have been repeatedly generated by interplate mega-earthquakes along active plate margins. Large earthquakes and tsunamis have enough potential to disturb sea floor, remobilize surface sediments and form submarine earthquake- and tsunami-induced event deposits (e.g., Ikehara and Usami, 2018). Recent studies have suggested that tsunami-induced sediment resuspension and tsunami backwash can transport shallow marine sediments to the deep sea (Feldens et al., 2009; Ikehara et al., 2021a). Tsunami-induced turbidity currents by the 2011 Tohoku-oki earthquake were observed by instrumental records at two sites off Sanriku upper slope (Arai et al., 2013) and tsunami-induced turbidites were recognized on the outer shelf-upper slope (Ikehara et al., 2014, 2021b; Usami et al., 2017) along the Japan Trench. In the tropical-subtropical coastal zones, large tsunamis transported meter-sized coral boulders and calcareous coral reef sediments onshore (e.g., Goto et al., 2010; Fujiwara et al., 2020). Therefore, tsunamis can significantly disturb the seafloor and remobilize coral reef sediments. Notwithstanding a few studies in ancient environments (e.g., Puga-Bernabéu et al., 2007), our knowledge on tsunami-induced sediment transport from the shelf to deep sea, especially in carbonate settings, is insufficient because of the limited number of post-tsunami offshore surveys. Composition of carbonate sediments in the southern Ryukyu arc show zonal distribution with water depths (e.g., Tsuji, 1993), providing a unique opportunity to trace the sediment transport from a shallow marine reef (source) to deep sea (sink).

The southern Ryukyu arc is located in a subtropical region, and small islands in the arc are surrounded by coral reefs (Hori, 1977; Hori and Kayanne, 2000). Large tsunamis have repeatedly struck these islands with 500–1,000 years intervals (Kawana and Nakata, 1994; Ando et al., 2018; Fujita et al., 2020) from studies of onshore sandy tsunami deposits and tsunami boulders, although Araoka et al. (2013) inferred 150–400 years intervals during the

last 2,400 years. The latest tsunami was the Meiwa tsunami in 1771, which had run-up heights of 30 m and approximately 12,000 deaths (Goto et al., 2010). Kitamura et al. (2018) estimated that the sizes of the two tsunamis that occurred before the 1771 event were comparable to the 1771 tsunami. However, because of the limited distribution of onshore tsunami deposits, long-term evaluation on tsunami recurrence are not available. There are several submarine canyons along the forearc slope of the southern Ryukyu. The heads of some canyons are near the coral reef around the southern Ryukyu islands. Ujiie et al. (1997) indicated a frequent occurrence of turbidites, which include coral reef species of benthic foraminifera in a core collected from a submarine fan in a pioneer study on sedimentation on the forearc slope. This suggests that this slope is a potential area for the detailed analysis of the source-to-sink sediment transport related to the tectonic events, such as large tsunamis and earthquakes, and for examination of response of sediment export from coral reef to the deep-sea to sea-level variations in this carbonate setting.

In this study, we examine sediment cores collected from the forearc slope to the basin area, off the southern Ryukyu arc, determine the spatiotemporal distribution pattern of calciturbidites in these cores, and discuss the source-to-sink movement of the carbonate sediment and the role of the submarine canyons in the transport of coral reef sediments to deep sea.

SOUTHERN RYUKYU ARC

The Ryukyu subduction zone extends >1,200 km from Kyushu to Taiwan (Figure 1). At the southern Ryukyu Trench, the Philippine Sea plate subducts northwestward beneath the Eurasian plate at a rate of >10 cm/yr (Taylor and Goodliffe, 2004; Argus et al., 2011). However, only two great interplate earthquakes ($M_w > 8$) have occurred along the Ryukyu Trench in the last 300 years; the 1771 Yaeyama earthquake at the southern Ryukyu and the 1911 earthquake off Kikai Island at the central Ryukyu (Usami, 2003; Ando et al., 2009), implying that overall plate coupling is weak (Peterson and Seno, 1984). Recent geodetic, geophysical, and seismological observations, such as the occurrence of slow slip events, low- and very-low-frequency earthquakes, and small repeating earthquakes, which support the weak coupling, suggest fluids are present at the plate boundary (Heki and Kataoka, 2008; Igarashi, 2010; Ando et al., 2012; Nishimura, 2014; Nakamura and Sunagawa, 2015; Arai et al., 2016). The Meiwa tsunami in 1771 was generated by either a tsunami earthquake, which assumed a slip on the plate boundary along a trench (Nakamura, 2009) or a submarine landslide induced by an intraplate earthquake (Imamura et al., 2001, 2008; Miyazawa et al., 2012). Another possible source is splay faults branching from the plate boundary (Hsu et al., 2013; Arai et al., 2016). Recently, Okamura et al. (2018) proposed an accretionary prism collapse as a new hypothesis for giant tsunami generation. However, an exact mechanism to produce such a large tsunami in 1771 remains controversial.

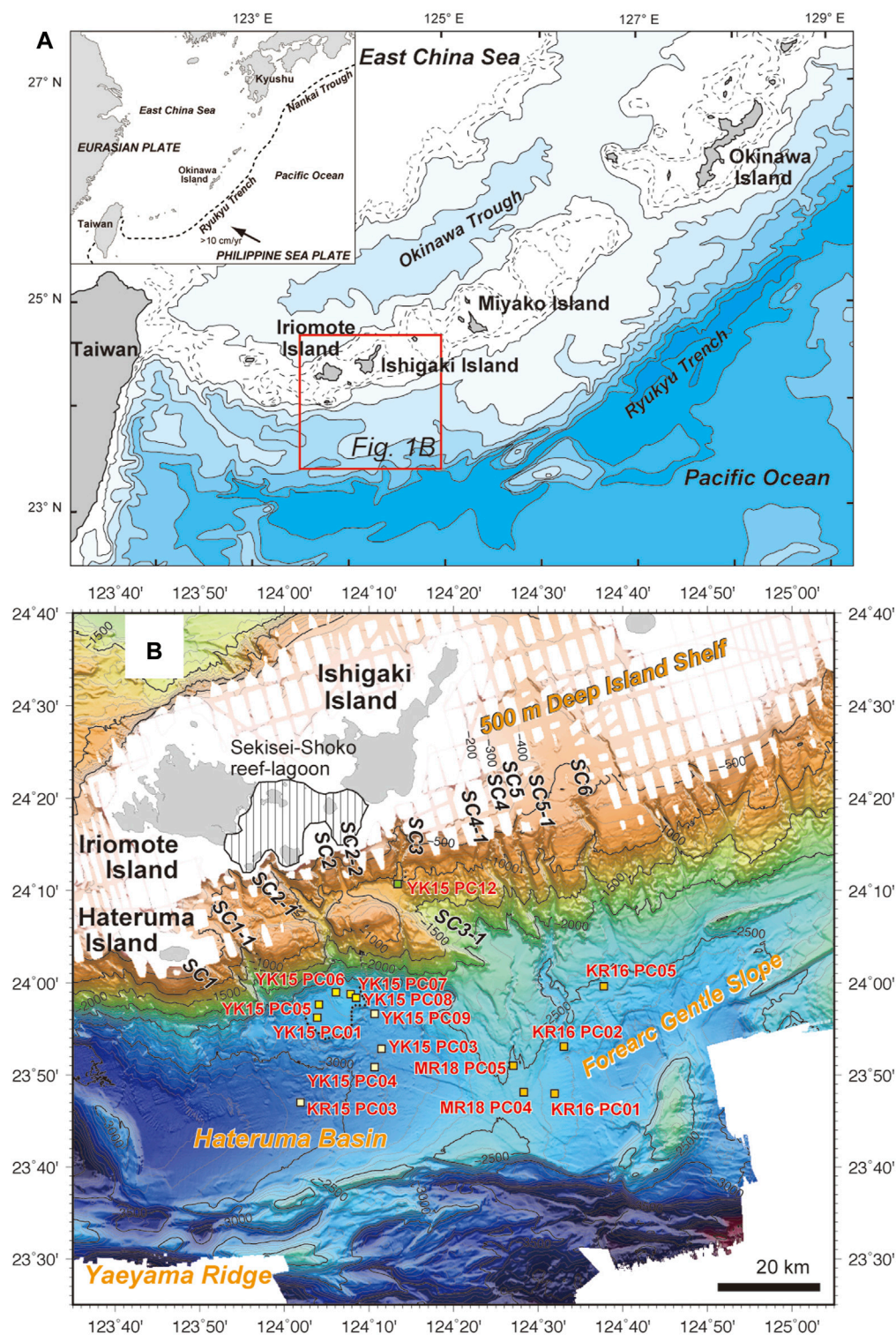


FIGURE 1 | Location (A) and bathymetry (B) of the study area with piston coring locations. SC means submarine canyon listed in **Supplementary Table S4**.

The southern Ryukyu Islands have a subtropical climate, and fringing coral reefs have developed around the islands. The development of modern coral reefs in the southern Ryukyu

Islands began around 10–11 ka (Hori and Kayanne, 2000). The Sekisei-Shoko reef-lagoon between Ishigaki and Iriomote islands (**Figure 1**) is the largest reef in Japan. The Ryukyu arc

extends NE-SW and changes direction southeast of Ishigaki Island to ESE-WNW direction (**Figure 1**). Trench-parallel right-lateral tectonic movements due to the oblique subduction along the Ryukyu Trench has developed a complex geomorphic structure in this forearc area (Lallemand et al., 1999). The southern Ryukyu forearc has a narrow shelf, a wide forearc basin, a deep and flat trench floor, separated by steep slopes (**Figure 1**). A wide terrace with a water depth of 200–500 m, which is called a “500 m deep island shelf” (Ujiié, 1980), is found between Iriomote and Miyako islands. A steep slope exists between the wide terrace and forearc basins and gentle slope. The water depth of the base of the steep slope is shallower to the east (~2,200 m), than to the west (~2,500–2,800 m) of ~124°25'E. Many submarine canyons and gullies occur in the slope. At least six major submarine canyons (SC1 to SC6 from west to east) incise the slope between 123°50'E and 124°40'E. In some canyons, a major canyon diverges into a few branches, which are called as SC*-1 to SC*-2 from west to east (**Figure 1** and **Supplementary Table S4**). Several forearc basins occur between Taiwan and Ishigaki Island with ESE-WNW direction. The Hateruma Basin, with its water depth of 3,400–3,500 m, is the easternmost forearc basin located to the south of Iriomote Island. The northern margin of the Hateruma Basin is a steep slope with small gullies and submarine canyons (**Figure 1B**). The direction of the forearc slope changes at ~124°25'E from ESE-WNW to E-W in the west to NE-SW in the east according to the bending of the Ryukyu arc. No forearc basin exists eastward of the arc-bending point, but a wide forearc gentle slope, which tilts southward, occurs. The Yaeyama Ridge is a topographic high that extends the E-W direction along the offshore margin of the forearc basins.

MATERIALS AND METHODS

We obtained 15 sediment cores from the forearc of the southern Ryukyu Islands during YK15-01 (YK15) cruise of R/V Yokosuka, KR15-18 (KR15) and KR16-E06 (KR16) cruises of R/V Kairei and MR18-01C (MR18) cruise of R/V Mirai of JAMSTEC (**Figure 1** and **Supplementary Table S1**) using a piston corer; 5 cores (cores YK15 PC01, PC05, PC06, PC07, and PC08) from a submarine fan near the mouth of SC2 (Kuroshima submarine canyon), 4 cores (cores YK15 PC03, PC04, PC09, and KR15 PC03) from the forearc (Hateruma) basin floor [note; core KR15 PC03 near the mouth of SC1 (Hateruma submarine canyon)], 1 core (core YK15 PC12) at the mouth of SC3 (Shiraho submarine canyon), 2 cores (cores MR18 PC04 and PC05) at the mouth of SC4, 2 cores (cores KR16 PC01 and PC02) at the mouth of SC5 (Nishi-Ishigaki submarine canyon) and 1 core (core KR16 PC05) at the mouth of SC6 (Higashi-Ishigaki submarine canyon). Cores ranging in length from ~1.8 to 5.0 m were recovered (**Supplementary Table S1**). The cores were cut vertically and one-half of the cut surface was visually logged. Sediment colors were determined using Revised Standard Soil Color Charts (Oyama and Takehara, 1967). To observe detailed sedimentary structures, two-dimensional (2D) soft-X radiographs were taken from 1 cm-thick slab samples. The other half of the cores was sampled continuously using a standard paleomagnetic cube

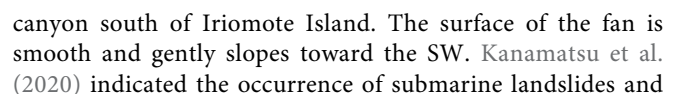
(7 cm³). The magnetic susceptibility of samples was measured using a KLY-4 magnetic susceptibility meter (Agico Co.). Accelerator mass spectrometry radiocarbon age-determinations using single species (*Globigerinoides sacculifer*) or mixed planktonic foraminifera in hemipelagic mud (bioturbated silt) intervals were conducted for cores YK15 PC01 (10 horizons), PC05 (14 horizons), PC07 (12 horizons), PC08 (15 horizons), PC09 (4 horizons), KR15 PC03 (10 horizons) and KR16 PC02 (8 horizons) (**Figure 2** and **Supplementary Table S2**). Radiocarbon dating was conducted at Beta Analytics Co. Ltd. Obtained radiocarbon ages are calibrated to calendar ages using Calib8.20 calibration program with Marine 20 calibration curve (Heaton et al., 2020) and local marine reservoir value of 35 ± 25 years, which was obtained for coral on Ishigaki Island (Hideshima et al., 2001). Benthic foraminiferal assemblage analysis was also conducted at the selected intervals both from calcareous sand layers and hemipelagic mud of cores YK15 PC01 (11 calcareous sands and 4 hemipelagic muds) and PC08 (10 calcareous sands and 6 hemipelagic muds) (**Supplementary Table S3**) at Palynosurvey Co. Ltd. Samples were washed gently through a 63- μ m sieve. The residues were observed under stereoscopic microscopy to perform planktonic foraminiferal tests as well as count and identify approximately 200 individuals of benthic foraminifera.

Bathymetric surveys were conducted during cruises YK15-01 of R/V Yokosuka, KR15-18 and KR16-E01 of R/V Kairei and MR18-01C of R/V Mirai. Bathymetric data were collected using multibeam echosounder SeaBeam 2012 and Kongsberg EM 122 at 12 kHz frequency. Seafloor bathymetry obtained during the cruises was reported by Kanamatsu et al. (2020). We also used the existing bathymetric data collected during the GH17 and GH18 cruises by the Geological Survey of Japan (GSJ), AIST.

RESULTS

Seafloor Morphology of the Slope and Submarine Canyons

The slope between Ishigaki Island (~124°40'E) and Iriomote Island (~123°50'E) is steep and its average gradient ranges from 5° to 14°. On this slope, at least six major submarine canyons can be found (**Figure 1** and **Supplementary Table S4**). A small N-S trending topographic high occurs offshore of Ishigaki Island at ~124°25'E, where the southern Ryukyu arc bends, and the morphology of the slope is different between the east and west of the topographic high. To the east of the topographic high, the upper slope (500–2,200 m in water depth) has an average gradient of 5°–7° with some canyons. Gentle slope (2,200–2,700 m in water depth and 2°–3° in average gradient) with a few canyons exist at the foot of the steep slope, and a wide and gentle slope with its water depth of 2,500–2,800 m exists offshore. To the west of the topographic high, a steep slope and a wide forearc basin (Hateruma Basin) are prominent features. The steep slope has its base at 2,500–2,800 m in water depth and an average gradient of ~12°–14°. No gentle slope exists at the northern slope of the eastern part of Hateruma Basin, but a gentle slope exists



scattered blocks of a few km in length in the eastern margin of the fan.

Many submarine canyons and gullies incise the steep slopes. Submarine canyons have low sinuosity and incise the slope ~200–600 m (**Supplementary Table S4**). Submarine canyons in the east are slope-confined canyons (Puga-Bernabéu et al., 2011), which do not breach the shelf-break. Canyon heads locate at ~500–550 m in water depths near the edge of “500 m deep island shelf” (Ujiié, 1980). Canyon heads become shallower toward the west and canyon incises the shelf break (~140 m) south of Ishigaki Island (SC3 canyon). Canyon heads locate at ~50–60 m in the south of Sekisei-Shoko reef-lagoon (SC2-1 (Aragusukushima submarine canyon) and SC2 canyons). Canyons in the west (SC2-1 and SC2 canyons) are partly blocked by reefs and classified as shelf-incised and partly reef-blocked canyons (sensu Puga-Bernabéu et al., 2011). The westernmost two canyons (SC1 and SC1-1 canyons) are slope-confined canyons, whose heads locate at ~200–300 m. Reflecting the steeper upper slope of the western side and the occurrence of the gentle lower slope at the foot-of-steep-slope of the eastern area, the submarine canyons are longer in the eastern area than in the western area. However, SC3 canyon is short and open to a small basin at the middle of forearc slope. Extension of the submarine canyon (SC3-1 canyon) incises the lower part of the slope. The longest submarine canyon (SC4) occurs at the eastern slope of the topographic high and has ~50 km in length. The submarine canyons at the steep slope are narrow with 0.8–2 km in widths but relatively wider and flatter floor in the western canyons (SC2-1, SC2, SC2-2, and SC3). SC5 canyon has incised the lower slope larger than those of SC4 and SC6 canyons.

Sediment Core Lithology, Sedimentary Structures and Sediment Compositions

All collected cores are mainly composed of yellowish-gray–grayish olive slightly calcareous and bioturbated silt intercalated with yellowish-orange calcareous very fine to coarse sand layers (**Figure 2**). Bioturbated silt of the uppermost part of all cores is yellowish gray, but those of the other parts are grayish olive. The thickness of the calcareous sand layers ranges from a few cm to >300 cm. Most sand layer exhibits parallel- or cross-lamination with a sharp basal contact and a fining-upward grading. Sandy grains are mainly composed of calcareous bioclasts such as fragments of molluscan shells, corals, bryozoa, and benthic and planktonic foraminifera. Preservation of benthic foraminifera is moderate, being slightly better in bioturbated silts and fine calcareous sand layers than in coarse calcareous sand layers (**Supplementary Table S3**). Benthic foraminiferal assemblages of sandy layers of cores YK15 PC01 and PC08 contain shallow-water species (S) of Inoue (1980a, b), which mainly live in shallow water <200 m water depth, such as *Quinqueloculina* spp., *Textularia* spp., *Miliolinella* spp., and *Glabratella* spp., and coral reef species (C) of Fujita (2013), such as *Acervulina* spp., *Calcarina* spp., *Amphisorus* sp., *Operculina* spp., and *Dendritina striata*, and are different from those of bioturbated silt, which contains the middle and deep-water species (M-D) of Inoue (1980a, b), such as *Globocassidulina*

subglobosa, *Globocassidulina* spp., *Bolivina decussata*, *Cassidulina carinata*, and *Gyroidina* spp. (**Figure 3** and **Supplementary Table S3**). Coral reef species occur in a higher percentage in calcareous sand layers of medium–coarse sand size than in calcareous sand layers of fine sand size. The calcareous sand have a composition in agreement with a shallow marine and coral reef origin (**Figure 3** and **Supplementary Table S3**). The sedimentary structures show that the calcareous sand layers are calciturbidites (division Tb–Tc of Bouma, 1962) of shallow marine origin. The upper boundary of each sand layer is sharp and no or little turbidite mud without bioturbation occurs above the calcareous sand layer. On the contrary, the bioturbated nature and benthic foraminiferal assemblages of the similar water depths to the coring sites in slightly calcareous silt show that the bioturbated silt is hemipelagic mud deposited at the coring place.

The frequent occurrence of calcareous sand layers (calciturbidites) is characteristic of cores from the submarine fan (cores YK15 PC01, PC05, PC07 and PC08). The frequency and thickness of sand layers in the upper part of cores YK15 PC01 and PC05 is higher than those in the lower part, whereas those in the upper part of core YK15 PC08 is lower than those in the lower part (**Figure 2**). Instead, frequency is low in the Hateruma Basin floor cores in cores YK15 PC03, 04, PC09, and KR15 PC03, and in the forearc gentle slope cores (cores KR16 PC01, PC02, PC05, MR18 PC04, and PC05) (**Figure 2**). Sands are coarser and layers are thicker in the submarine fan cores than in the forearc basin and gentle slope cores. Thick calcareous sand with a fining-upward grain-size trend from coarse sand at the base to very fine sand at the top occurs in core YK15 PC06 from SC2 canyon mouth on the submarine fan (**Figure 2**). A similar thick calcareous sand layer with a fining-upward grain size trend occurs in core YK15 PC12 from SC3 canyon mouth of the upper slope (**Figure 2**).

Magnetic Susceptibility

Values of the measured volumetric magnetic susceptibility range from $\times 0.3 \text{ E-04}$ to $1.3 \times \text{E-03}$ (**Figure 2**). Calcareous sand layers have magnetic susceptibility of $< 2 \times \text{E-04}$ and show negative peaks, indicating lower content of magnetic minerals than bioturbated silt (magnetic susceptibility of $> 4 \times \text{E-04}$) despite their coarser grain size (**Figure 2**). Therefore, it is easy to distinguish calcareous sand layers from the background (hemipelagic) bioturbated silt.

Radiocarbon Dates

In seven cores, 73 radiocarbon dates were obtained: cores YK15 PC01 (10 horizons), PC05 (14 horizons), PC07 (12 horizons), PC08 (15 horizons), PC09 (4 horizons), KR15 PC03 (10 horizons) and KR16 PC02 (8 horizons) (**Figure 2** and **Supplementary Table S2**). Although some overturns in age are probably due to a mixture of reworked, older foraminifera from the calcareous sand layers by benthic organisms, the obtained radiocarbon dates generally become older with increasing sub-bottom depths. Assuming no erosion at the base of the sand layer and constant sedimentation within hemipelagic mud (bioturbated silt), the averaged sedimentation rates of hemipelagic mud are calculated as

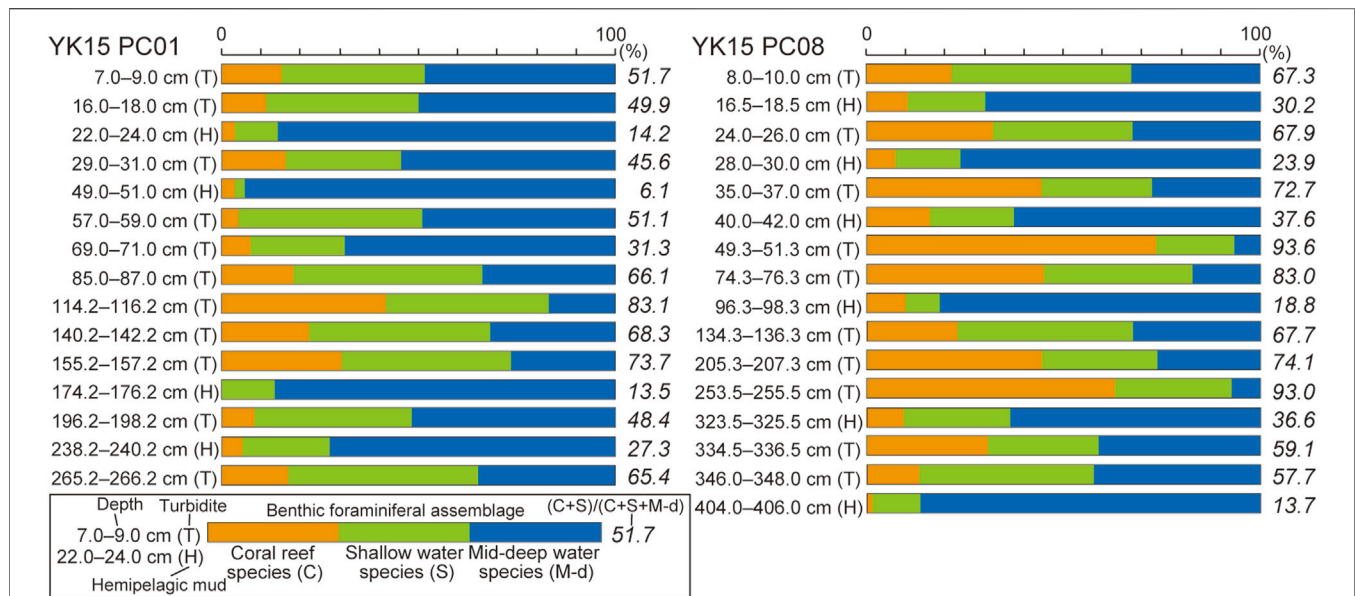
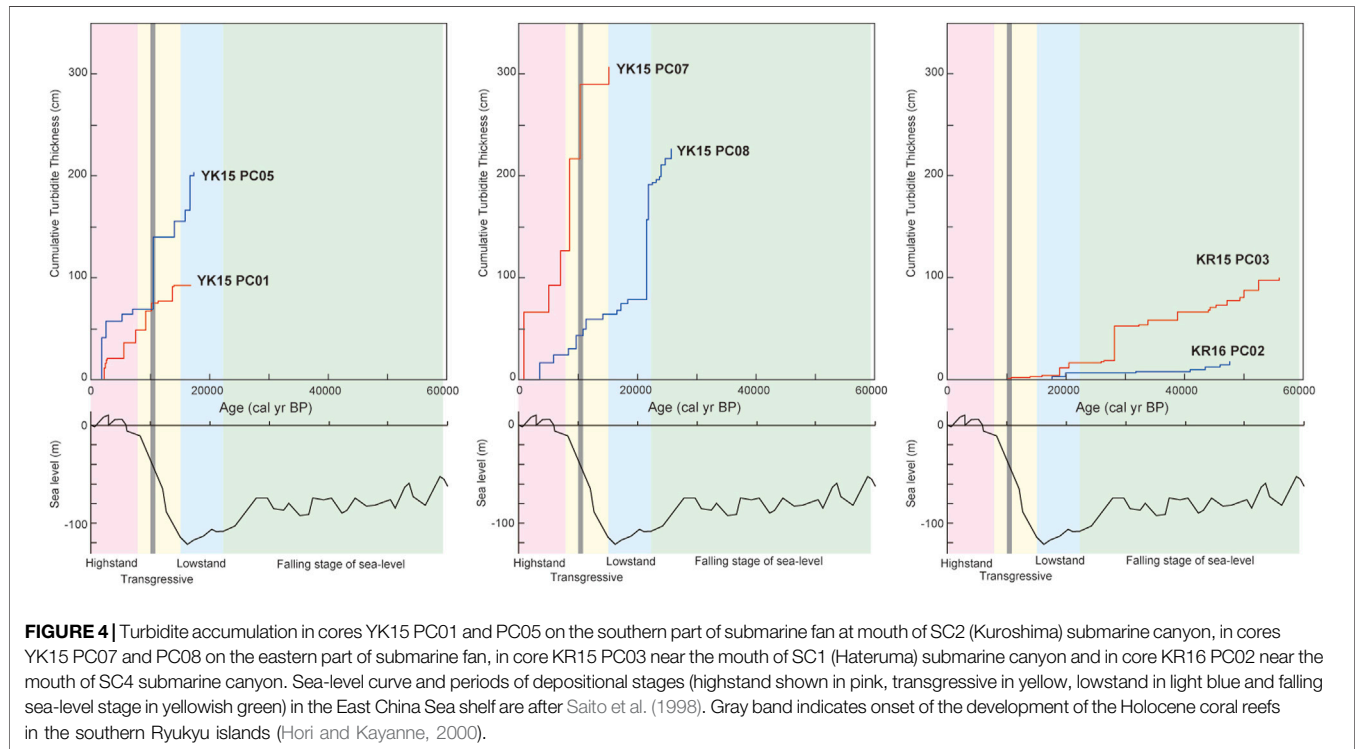


FIGURE 3 | Ratios of coral reef–shallow water–mid-deep water benthic foraminiferal species in calciturbidite (T) and hemipelagic muds (H) of cores YK15 PC01 and PC08.



~10 cm/ky (6.8 cm/ky for core YK15 PC07 to 11.8 cm/ky for core YK15 PC01) throughout the study area. Recurrence intervals of calcareous sand layers are calculated as 46–2,857 years (average: 1,042 years) for core YK15 PC01, 126–3,572 years (1,556 years) for core YK15 PC05,

1,608–4,760 years (2,850 years) for core YK15 PC07, 73–3,180 years (1,169 years) for core YK15 PC08, 86–5,517 years (2,103 years) for core KR15 PC03 and 1745–11,851 years (4,987 years) for core KR16 PC02, respectively (**Figure 4** and **Supplementary Table S5**).

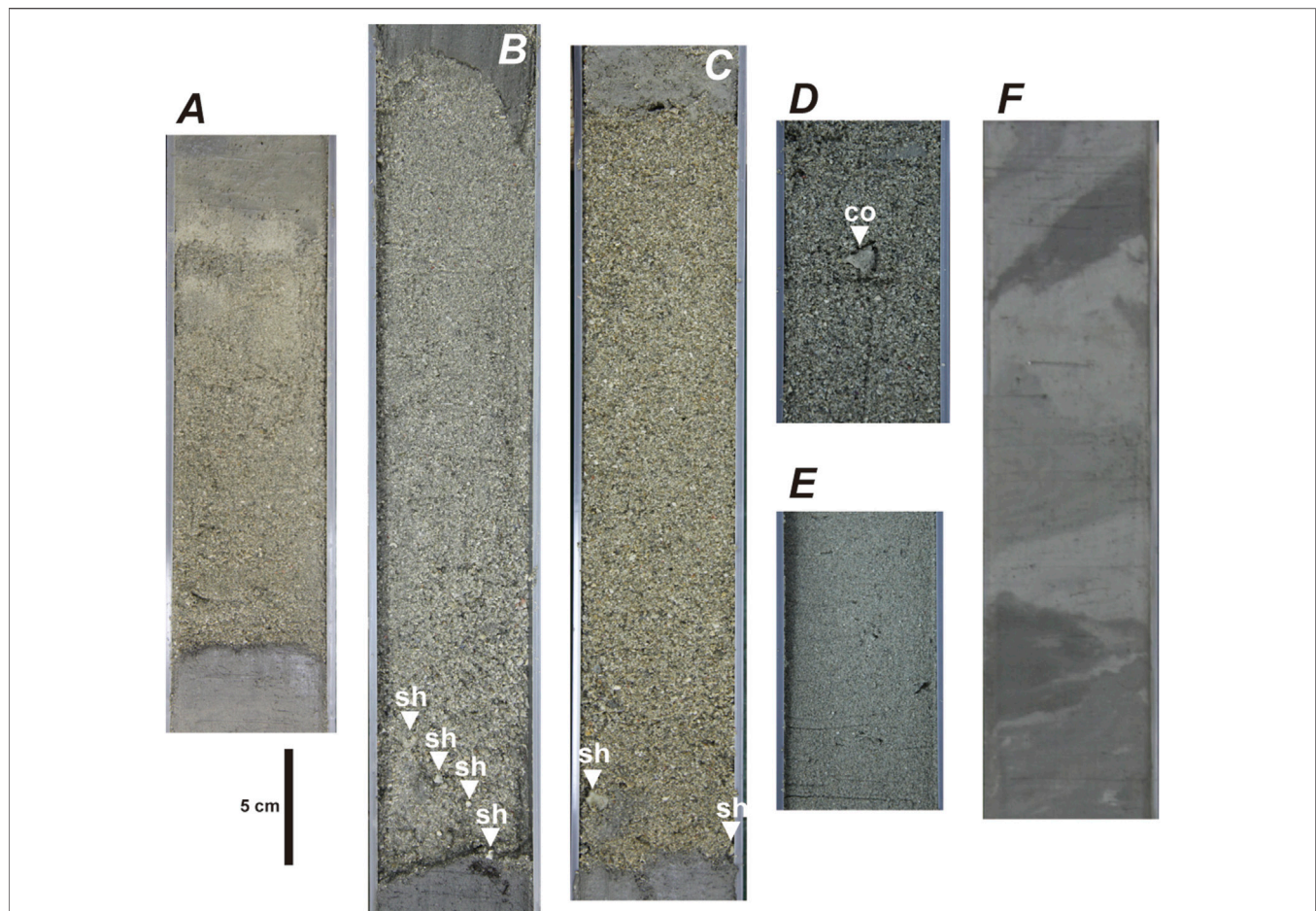


FIGURE 5 | Typical examples of calciturbidite (A–E) and chaotic mass-transported deposit facies (F) in the obtained cores. (A) fining-upward calcareous medium-very fine sand with a sharp base (core YK15 PC01 at 100.2–126.2 cm), (B) fining-upward calcareous coarse-fine sand with a sharp base (core YK15 PC08 at 267.5–305.5 cm), (C) fining-upward calcareous medium-coarse sand with shell fragments (core YK15 PC07 at 117.5–154.5 cm), (D) calcareous medium-coarse sand with a coral fragment (core YK15 PC06 at 286.5–299.5 cm), (E) calcareous very fine sand (core YK15 PC12 at 132.2–145.2 cm), (F) varicolored chaotic silt (core YK15 PC09 at 287.3–312.3 cm). sh: shell fragment, co: coral fragment.

DISCUSSION

Connectivity of Submarine Canyon Heads With Coral Reefs and Sediment Core Lithology

Sediment core lithology around submarine canyon mouths of the southern Ryukyu forearc varies depending on the connectivity of submarine canyon heads with coral reefs. In pure carbonate and mixed carbonate-siliciclastic settings, sediment exports from shallow carbonate platforms and reefs to the deep-sea is controlled by the carbonate and clastic sediment productivity, type of canyon, and connectivity of shelf channel with the submarine canyon (Mullins, 1983; Eberli, 1991; Jorjy et al., 2010, 2020; Puga-Bernabéu et al., 2011, 2014; Counts et al., 2018, 2021). First, we will examine the relationship between sediment core lithology and the type and connectivity of submarine canyons. In the eastern part of the study area, where the submarine canyons are slope-confined and the

canyon heads lie at ~500–550-m water depths far from modern coral reef distribution (Figure 1), only several thin (a few cm order) and fine-grained (very fine sand–coarse silt-sized) calciturbidites occur in the cores (Figure 2). These sand layers are mainly composed of fine-carbonate grains such as planktonic foraminifera, and lack large bioclasts such as coral, bryozoa, and molluscan (bivalve) fragments. On the contrary, sediment cores from a submarine fan at mouth of SC2 canyon, which is shelf-incised and partly reef-blocked, in the western part of the study area contain several thick (several cm–m scale) and coarse-grained (fine sand–coarse sand-sized) calciturbidites (Figures 2, 5A,5B). In the Great Barrier Reef, the shelf-connection type of submarine canyons influences the type of sedimentary gravity flow deposits (Puga-Bernabéu et al., 2011, 2014). Although SC2-1 and SC2 canyons belong to shelf-incised and partly reef-blocked canyon, sedimentary dynamics are more complicated owing to the multiple sediment sources, no shelf channels connected to the land in the Sekisei-Shoko lagoon, and low clastic sediment supply from nearby small islands may contribute to form carbonate

deposits at the mouth of these canyons. The frequency and thickness of calciturbidites in core KR15 PC03 collected near SC1 canyon mouth is larger than in cores collected from the eastern forearc gentle slope (cores KR16 PC01, PC02, PC05, MR18 PC04, and PC05) but smaller than in cores from the submarine fan (cores YK15 PC01, PC05, PC07, and PC08) (**Figure 2**). SC1 canyon head is located near the Hateruma Island coral reef based on a bathymetric map “Hateruma Sima” (Japan Coast Guard, 1988). This suggests that distance between canyon head and sediment source (coral reef) plays some roles on sediment transport to deep-sea through submarine canyon.

Next, we will examine the relationship between composition of calciturbidites and the connectivity of submarine canyon heads with coral reefs. In the western part of the study area, molluscan (bivalve and gastropoda) and bryozoa fragments and benthic foraminifera are common (**Figures 3, 5**) whereas coral fragments rarely occur in coarse-medium sand-sized calciturbidites (**Figure 5**) in the cores collected from the submarine fan at SC2 canyon mouth. Molluscan fragments and benthic foraminifera are also found in fine-medium sand-sized calciturbidites (**Figure 5**). Benthic foraminiferal assemblages in calciturbidites consist mainly of coral reef (C) and shallow-water (S) species with a low percentage of middle-deep-water (M-D) species ($>60\%$ in $(C + S)/(C + S + M-D)$ ratio). A larger number of coral reef species is observed in the coarse-medium sand-sized calciturbidites than in the very fine-fine sand-sized calciturbidites (**Figure 3**). Ujiie et al. (1997) also reported the occurrence of coral reef benthic foraminifera in calciturbidites in the Holocene sequence of a core collected from the same fan. These benthic foraminiferal assemblages indicate that these calciturbidites are shallow water-origin, and the coral reef is the most likely source of coarse calciturbidites. Instead, very fine-fine calcareous sands originate from shallow-water areas including the coral reefs. In the eastern part of the study area, no intercalation of coarse calciturbidites and a few fine calciturbidites occur in cores MR18 PC04 and PC05, KR16 PC01, PC02, and PC05 at the mouths of submarine canyons (SC4, SC5, and SC6) without connection to the coral reef. Although no precise report on the distribution and characteristics of surface sediments near the heads of submarine canyons exist, Tsuji (1993) showed a wide distribution of planktonic foraminiferal sand and mud at the water depths of 200–900 m around Miyako Island. Planktonic foraminiferal tests in surface sediments are the most likely origin of fine calciturbidite sands. Even in the western part, the sediment lithology of cores YK15 PC06 and PC12 at SC2 and SC3 submarine canyon mouths, respectively, suggest that the distance from the submarine canyon head and coral reef edge is a factor for the transport of coarse-grained coral reef materials to deep sea through the submarine canyon. The closer location of submarine canyon head to the coral reef for core YK15 PC06 [0.6 km at SC2-1, ~1 km at SC2-2, and 1.4 km at SC2 based on the bathymetric map “Southern Part of Isigaki Sima” (Japan Coast Guard, 1992)] than for core YK15 PC12 [2.6 km at SC3] may be related to coarser grain-size nature (**Figure 2**) with many coral and molluscan bioclasts of core YK15 PC06 (**Figure 5D**) than core YK15 PC12 (**Figure 5E**). Therefore, the connectivity of

submarine canyon heads with coral reefs is a possible factor for thick deposition of calcareous bioclasts at the deep-sea floor and efficient sediment transport from shallow- to deep sea through submarine canyons in the carbonate depositional system.

Reflecting such differences in frequency and thickness of calciturbidites transported through submarine canyons between the eastern and western parts of the study area, topography near the submarine canyon mouth is also different. No fan and lobe topography is observed near the two eastern submarine canyon (SC5 and SC6) mouths where a few thin and fine-grained calciturbidites are obtained (**Figure 1**). Only a distinct fan-shaped relief is found at the mouth of SC2 canyon where many thick and coarse-grained calciturbidites are obtained (**Figure 2**). Smooth surface of this fan shows an active deposition of sediments on the fan. Larger widths in the western submarine canyons (SC2-1, SC2, SC2-2, and SC3) than those in the eastern canyons (SC4-1, SC4, SC5, SC5-1, and SC6) may relate to larger coarse sediment transport through canyons and to larger lateral erosion of canyon walls in the western canyons than in the eastern canyons.

Temporal Change in the Frequency of Calciturbidites

Carbonate production on carbonate platform tops and sediment exports from platforms to surrounding deep seas by plumes and gravity flows have been influenced by late Quaternary large scale oscillations of sea level (e.g., Mullins 1983; Droxler and Schlager, 1985; Eberli, 1991; Jorjy et al., 2010, 2020; Webster et al., 2012; Counts et al., 2021). In many studies, a general correlation has been found between an increase in calciturbidite frequency and periods of sea-level highstand (Droxler and Schlager, 1985; Jorjy et al., 2010, 2020; Webster et al., 2012; Wunsch et al., 2017; Counts et al., 2018, 2021). However, the exact occurrence patterns of calciturbidites are variables, reflecting the bank-top water depths (the timing of the flooding of bank-top), type of submarine canyon, and shelf-edge morphology (Jorjy et al., 2010; Puga-Bernabéu et al., 2014). Interestingly, the frequency of deposition, thickness, and grain size of calciturbidites in the four cores from the submarine fan (cores YK15 PC01, PC05, PC07 and PC08; **Figures 2, 4**) do not show a relationship with glacial-interglacial variability. For example, during the sea-level highstand, the frequency of calciturbidites is highest in cores YK15 PC01 and PC05 but lowest in core YK15 PC08 and is almost even in core YK15 PC07. This suggests that another control on coral reef sediment exports other than carbonate production exist in this carbonate system. Moreover, the frequency of calciturbidites is high before the last glacial maximum (LGM) and low in the Holocene in cores from the eastern part (core KR16 PC02) and Hateruma Basin (core KR15 PC03) (**Figures 2, 4** and **Supplementary Table S5**). No and only three thin (<1 cm thick) Holocene calciturbidite occurs in cores KR16 PC02 and KR15 PC03, respectively. In core KR15 PC03 two and three calciturbidites are formed in early transgressive stage and in the lowest sea-level stand (LGM) with their recurrence intervals of ~1,300–3,300 years. The frequency of calciturbidites (~550–5,500 years intervals) in core KR15 PC03 is slightly high in

the falling sea-level stage before the LGM. A high occurrence of calciturbidites is also found in the lower part of Hateruma Basin cores (cores YK15 PC03 and PC04), although there is no radiocarbon date in the two cores. A similar decrease of calciturbidite frequency in the LGM was reported from the Gulf of Papua, western Caribbean Sea, Bahamas (Jorry et al., 2010), and Mozambique Channel (Jorry et al., 2020). Lack of the Holocene turbidite in the eastern part and Hateruma Basin cores may reflect core top disturbance in the recovery of the piston cores and low sedimentation rates. Sea-level oscillation is a likely control on down-slope sediment transport along the forearc slope in the southern Ryukyu, except at the submarine fan. However, it is necessary to obtain many radiocarbon ages to examine the relationship between calciturbidite frequency and sea-level state in these basin floor cores.

The development of modern coral reefs in water depths shallower than 50–55 m in the middle–southern Ryukyu Islands began around 10–11 ka (Hori and Kayanne, 2000). Five to ten calciturbidites are found on the submarine fan after the development of modern coral reefs (**Figure 4** and **Supplementary Table S5**). Coral reefs could form during the lowest-sea-level glacial period in southern Ryukyu (Sasaki et al., 2006). Although there is no report on the glacial coral reefs around the study area, the occurrence of coral reef materials in calciturbidites of the LGM to last deglaciation sequence in core YK15 PC08 show that mound-like (Webster et al., 2004; Sasaki et al., 2006) or small shelf-edge reef (Webster et al., 2018) had been formed near the submarine canyon head throughout the LGM to the last deglaciation.

Deposition of Coral Reef–Shallow-Water Origin Carbonate Sand on a Submarine Fan

The calciturbidites become thinner and finer-grained from proximal to distal locations on the submarine fan (**Figure 2**). The submarine fan has a radial in shape and has a sand-dominated character (Shanmugam and Moiola, 1988; Pickering and Hiscott, 2016). The thickest (>3 m) and coarsest (coarse–fine sand) turbidite occurs at SC2 canyon mouth in core YK15 PC06 (**Figure 2**). Sand thickness and grain size decrease quickly toward distally to a few tens cm in thickness and very fine–fine sand in cores YK15 PC01 and PC08, through several tens cm and medium–fine sand in cores YK15 PC05 and PC07. This shows that coarse-grained sand transported from the coral reef through the submarine canyon has been deposited near the canyon mouth according to rapidly decreasing flow velocity. A narrow topographic high at the submarine canyon mouth (**Figure 1**) may reflect such rapid deposition of coarse-grained materials on the upper fan.

Although a similar spatial change in sand thickness and grain size is found both toward east and south, temporal depositional patterns of calciturbidites on the eastern and southern parts of the fan are different. In the lower part of cores YK15 PC07 and PC08 on the eastern part of the fan, calciturbidites are thicker and coarser than those in the upper part of the cores (**Figure 2**). Contrarily, on the southern part of the fan (cores YK15 PC01 and PC05), calciturbidites are more frequent, coarser, and thicker in the upper part than in the lower part (**Figure 2**). Ujiie et al. (1997)

reported the occurrence of 10 calciturbidites during the last ~15 ky in a core collected near core YK15 PC01, and relatively low frequency before ~10 ka. This trend is similar to our record in core YK15 PC01. This shows that the turbidite depocenter shifted on the submarine fan, at ~11 cal ky BP (**Figures 2, 4**).

Almost no coarse calciturbidite occurs in cores collected from the forearc basin floor (cores YK15 PC03, PC04, and PC09) apart from core KR16 PC03, which was collected near SC1 canyon mouth. This means that most coarse calcareous materials transported from coral reefs through the submarine canyon have been deposited on the submarine fan. Therefore, canyon-connected submarine fan plays an important role in the deposition (sink) of coarse-grained materials from the coral reef. The rapid and thick accumulation of sediments on the fan at the foot of the slope can cause instability of the seafloor. Kanamatsu et al. (2020) reported the presence of a submarine landslide at the margin of the submarine fan. They also discussed the age of the submarine landslide as ~7 ky BP in conventional radiocarbon date from thin-sandy layer (turbidite) in core YK15 PC03 based on the radiocarbon ages at the correlative horizon of the sand layer in core YK15 PC13. Interestingly, these thin calciturbidites with very fine–fine sand are traceable among the sediment cores collected from the Hateruma Basin floor near the horizon of sediment color change from yellowish to grayish (**Figure 2**). Although newly obtained radiocarbon dates in this study show that the sediment color change occurred at ~7–9 cal ky BP (**Figure 2**), this turbidite deposition might be a basin-wide event in the Hateruma Basin. Another evidence on submarine landslide near the margin of the fan is the occurrence of a varicolored chaotic mud layer (mass-transported deposit; MTD), which occurred just below the sediment color change in core YK15 PC09 (**Figures 2, 5F**). Newly obtained radiocarbon dates in this core suggest that the MTD deposited before ~5 cal ky BP and after ~11 cal ky BP (**Figure 2** and **Supplementary Table S2**). Secondary gravitational sediment transport from the fan to the peripheral basin floor may contribute to sediment dispersal of calcareous sediments in the deep-sea environments.

Repeated Transport of Coral Reef Calcareous Grains to a Submarine Fan

Transport of calcareous sand from the coral reef to deep sea through SC2-1 and SC2 submarine canyons has repeatedly occurred (**Figures 2, 4**). Large earthquakes and tsunamis are possible mechanisms for the transport of shallow marine sediments to the deep-sea (e.g., Feldens et al., 2009, 2012; Ikehara and Usami, 2018; Ikehara et al., 2021b). Especially in coral reefs, large tsunamis have enough potential to transport coral reef materials to both onshore (Goto et al., 2010; Kitamura et al., 2018; Fujita et al., 2020) and offshore (Feldens et al., 2009, 2012; Paris et al., 2010; Sukuna-Schwartz et al., 2015). Recurrence intervals of calciturbidite depositions in cores YK15 PC01, PC05, PC07, and PC08 are calculated as several hundred–a few thousand years (average: 1,388 years) (**Figure 4** and **Supplementary Table S5**). The intervals are likely concordant with those (500–1,000 years) of large tsunamis as reconstructed

from coral boulders and onshore tsunami deposits in the southern Ryukyu Islands (Kawana and Nakata, 1994; Ando et al., 2018; Kitamura et al., 2018; Fujita et al., 2020), and slightly larger than those (150–400 years) from coral boulders on Ishigaki Island (Araoka et al., 2013). Remobilization of coral reef sediments and collapse of reef slopes by strong earthquake ground shaking might be another mechanism for the transport of coral reef sediments to the deep-sea. Although there is no evidence on strong shaking, such as soft-sediment deformations in our cores, the possibility of the association between that large earthquakes and down-slope sediment transport in the study area cannot be denied. Intervals of ~50–300 years may be too small as recurrence intervals of large tsunamis. The erosion of surficial hemipelagic mud during calciturbidite deposition is a likely mechanism to shorten the intervals. Another explanation is sediment transport by large typhoons. Typhoon-induced hyperpycnal flows and megarips may transport shallow marine materials to deep-sea (Liu et al., 2016; Porcile et al., 2020). Although no large hinterland and large river is expected in the small islands of the southern Ryukyu arc, extreme waves by large typhoon may remobilize coral reef calcareous sediments to deep-sea through reef-connected submarine canyons. However, the coincidence in the recurrence intervals suggests that a large tsunami is likely to trigger the mechanism of sediment transport from the coral reef to the deep sea through a reef-connected submarine canyon in southern Ryukyu. However, longer intervals in our turbidite records than those of onshore records from tsunami deposits and tsunami boulders show that not all large tsunami events have been recorded as turbidites in a core. The shift of turbidite depocenter may influence such an incomplete record in a core, because no turbidite might deposit when the depocenter moved far from the coring site. Moreover, no direct evidence on the 1771 Meiwa tsunami-induced calciturbidite is found in our cores. This may be due to core top disturbance during the piston corer recovery and thin surface sediment cover after the 1771 Meiwa tsunami because of the low background sedimentation rate of hemipelagic mud. Some studies suggested that submarine landslides play an essential role in generating large tsunamis in this region (Imamura et al., 2001, 2008; Miyazawa et al., 2012; Okamura et al., 2018). Based on the detailed bathymetry of the forearc slope, Kanamatsu et al. (2020) stated that there is no large submarine landslide along the forearc slope, except for a submarine landslide at the submarine fan's margin. Based on our core data, there is a possibility that the submarine landslide was related to the deposition of a thin turbidite distributed basinwide, as discussed above. However, no other direct evidence to connect submarine landslides and turbidite depositions exists at present. In addition, we do not have any sediment data from lower slope and trench floor to determine the submarine landslides at the lower slope, as suggested by Okamura et al. (2018). We need further study to clarify the relationship between submarine landslides and turbidite depositions.

CONCLUSION

Bathymetry and sediment core data along the southern Ryukyu forearc indicate that coral reef-connected submarine canyons play an important role in the delivery of coarse calcareous sand from shallow water to the deep sea. The connection between the submarine canyon head with the coral reef (source) is a crucial factor for the efficiency of coarse sediment transport. The volume and frequency of coarse sediment transport through the submarine canyon decrease with the increase in the distance between the coral reef and the canyon head. Coarse calcareous sediment transported through the coral reef-connected submarine canyon were deposited as calciturbidites near the submarine canyon's mouth, forming a submarine fan (sink) at the toe of the slope. Depocenters of calciturbidites on the fan has been shifted at ~11 cal ky BP. The calciturbidites' recurrence intervals (several hundred–a few thousand years) show that a large tsunami is the most likely trigger mechanism for sediment transport of coarse calcareous sands from the coral reef to the deep sea through submarine canyons. The lack of temporal changes in the recurrence intervals of the calciturbidites in the cores from the submarine fan since the LGM implies that tectonic-driven trigger mechanisms, such as large tsunamis, are a more important factor than climatic-controlled sediment production and supply from the coral reef, in this carbonate source-to-sink system in the southern Ryukyu forearc. This also suggests that, where the tsunami-induced turbidity currents could occur repeatedly, the tsunamis may contribute to maintain submarine canyons.

DATA AVAILABILITY STATEMENT

The original contributions presented in the study are included in the article/**Supplementary Material**, further inquiries can be directed to the corresponding author.

AUTHOR CONTRIBUTIONS

KI and TK projected the study and the survey cruises. KI and KU conducted sedimentological analysis. TK performed paleomagnetic and rock magnetic measurements. KI drafted the manuscript. All authors contributed to the data acquisitions and have read and approved the final manuscript.

FUNDING

This work was funded as part of the “Research Project for Compound Disaster Mitigation on the Great Earthquakes and Tsunamis around the Nankai Trough Region” by the Ministry of Education, Culture, Sports, Science and Technology of Japan.

ACKNOWLEDGMENTS

We thank the captains, crews, marine technicians and onboard scientists of the R/Vs Yokosuka (YK15-01), Kaiei (KR15-18 and KR16-E01), and Mirai (MR18-01) for their efforts and supports in data collection. We also thank Dr. A. Misawa of the GSJ, AIST for providing us bathymetric data obtained by the survey cruises conducted by the GSJ, AIST, for **Figure 1**, and Dr. K. Arai of the GSJ, AIST for discussion on the glacial coral reefs in the southern Ryukyu Islands and carbonate depositional

systems. We thank Dr. Á. Puga-Bernabéu and an anonymous reviewer for their constructive comments, and Enago for the English language review.

SUPPLEMENTARY MATERIAL

The Supplementary Material for this article can be found online at: <https://www.frontiersin.org/articles/10.3389/feart.2022.753583/full#supplementary-material>

REFERENCES

- Ando, M., Kitamura, A., Tu, Y., Ohashi, Y., Imai, T., Nakamura, M., et al. (2018). Source of High Tsunamis along the Southernmost Ryukyu Trench Inferred from Tsunami Stratigraphy. *Tectonophysics* 722, 265–276. doi:10.1016/j.tecto.2017.11.007
- Ando, M., Nakamura, M., Matsumoto, T., Furukawa, M., Tadokoro, K., and Furumoto, M. (2009). Is the Ryukyu Subduction Zone in Japan Coupled or Decoupled? -The Necessity of Seafloor Crustal Deformation Observation. *Earth Planet Sp.* 61, 1031–1039. doi:10.1186/BF03352954
- Ando, M., Tu, Y., Kumagai, H., Yamanaka, Y., and Lin, C.-H. (2012). Very Low Frequency Earthquakes along the Ryukyu Subduction Zone. *Geophys. Res. Lett.* 39, L04303. doi:10.1029/2011GL050559
- Arai, K., Naruse, H., Miura, R., Kawamura, K., Hino, R., Ito, Y., et al. (2013). Tsunami-generated Turbidity Current of the 2011 Tohoku-Oki Earthquake. *Geology* 41, 1195–1198. doi:10.1130/G34777.1
- Arai, R., Takahashi, T., Kodaira, S., Kaiho, Y., Nakanishi, A., Fujie, G., et al. (2016). Structure of the Tsunamiogenic Plate Boundary and Low-Frequency Earthquakes in the Southern Ryukyu Trench. *Nat. Commun.* 7, 12255. doi:10.1038/ncomms12255
- Araoka, D., Yokoyama, Y., Suzuki, A., Goto, K., Miyagi, K., Miyazawa, K., et al. (2013). Tsunami Recurrence Revealed by Porites Coral Boulders in the Southern Ryukyu Islands, Japan. *Geology* 41, 919–922. doi:10.1130/G34415.1
- Argus, D. F., Gordon, R. G., and DeMets, C. (2011). Geologically Current Motion of 56 Plates Relative to the No-Net-Rotation Reference Frame. *Geochim. Geophys. Geosyst.* 12, Q1101. doi:10.1029/2011GC003751
- Bouma, A. H. (1962). *Sedimentology of Some Flysch Deposits*. Amsterdam: Elsevier, 168p.
- Counts, J. W., Jorry, S. J., Vazquez Riveiros, N., Jouet, G., Giraudeau, J., Cheron, S., et al. (2019). A Late Quaternary record of highstand shedding from an isolated carbonate platform (Juan de Nova, southern Indian Ocean). *Depositional Rec.* 5, 540–557. doi:10.1002/dep2.57
- Counts, J. W., Jorry, S. J., Vazquez-Riveiros, N., Amy, L. A., Dennielou, E., and Jouet, G. (2021). Sedimentology and Distribution of Late Quaternary Calciturbidites and Calcidibrites in the Mozambique Channel (Southwest Indian Ocean). *Facies* 67, 17. doi:10.1007/s10347-021-00624-1
- Droxler, A. W., and Schlager, W. (1985). Glacial versus Interglacial Sedimentation Rates and Turbidite Frequency in the Bahamas. *Geology* 13, 799–802. doi:10.1130/0091-7613(1985)13<799:gvisra>2.0.co;2
- Eberli, G. P. (1991). "Calcareous Turbidites and Their Relationship to Sea-Level Fluctuations and Tectonism," in *Cycles and Events in Stratigraphy*. Editors G. Einsele, W. Ricken, and A. Seilacher (Springer-Verlag), 340–359.
- Feldens, P., Schwarzer, K., Sakuna, D., Szczuciński, W., and Sompongchaiyakul, P. (2012). Sediment Distribution on the Inner Continental Shelf off Khao Lak (Thailand) after the 2004 Indian Ocean Tsunami. *Earth Planet Sp.* 64, 875–887. doi:10.5047/eps.2011.09.001
- Feldens, P., Schwarzer, K., Szczuciński, W., Stattegger, K., Sakuna, D., and Sompongchaiyakul, P. (2009). Impact of 2004 Tsunami on Seafloor Morphology and Offshore Sediments, Pakarang Cape, Thailand. *Pol. J. Environ. Stud.* 18, 63–68.
- Fujita, K. (2013). Ecology of Large Benthic Foraminifers; a Review. *Nihon Sangoshō Gakkaishi* 15, 57–77. doi:10.3755/jcrs.15.57
- Fujita, R., Goto, K., Iryu, Y., and Abe, T. (2020). Millennial Paleotsunami History at Minna Island, Southern Ryukyu Islands, Japan. *Prog. Earth Planet Sci.* 7, 53. doi:10.1186/s40645-020-00365-9
- Fujiwara, O., Goto, K., Ando, R., and Garrett, E. (2020). Paleotsunami Research along the Nankai Trough and Ryukyu Trench Subduction Zones - Current Achievements and Future Challenges. *Earth-Science Rev.* 210, 103333. doi:10.1016/j.earscirev.2020.103333
- Gardner, W. D. (1989). Baltimore Canyon as a Modern Conduit of Sediment to the Deep Sea. *Deep Sea Res. Part A. Oceanogr. Res. Pap.* 36, 323–358. doi:10.1016/0198-0149(89)90041-1
- Goto, K., Kawana, T., and Imamura, F. (2010). Historical and Geological Evidence of Boulders Deposited by Tsunamis, Southern Ryukyu Islands, Japan. *Earth-Science Rev.* 102, 77–99. doi:10.1016/j.earscirev.2010.06.005
- Grammer, G. M., and Ginsburg, R. N. (1992). Highstand versus Lowstand Deposition on Carbonate Platform Margins: Insight from Quaternary Foreslopes in the Bahamas. *Mar. Geol.* 103, 125–136. doi:10.1016/0025-3227(92)90012-7
- Harris, P. T., and Whiteway, T. (2011). Global Distribution of Large Submarine Canyons: Geomorphic Differences between Active and Passive Continental Margins. *Mar. Geol.* 285, 69–86. doi:10.1016/j.margeo.2011.05.008
- Heaton, T. J., Köhler, P., Butzin, M., Bard, E., Reimer, R. W., Austin, W. E. N., et al. (2020). Marine20-The Marine Radiocarbon Age Calibration Curve (0–55,000 Cal BP). *Radiocarbon* 62, 779–820. doi:10.1017/RDC.2020.68
- Heki, K., and Kataoka, T. (2008). On the Biannually Repeating Slow-Slip Events at the Ryukyu Trench, Southwestern Japan. *J. Geophys. Res.* 113, B11402. doi:10.1029/2008JB005739
- Hideshima, S., Matsumoto, E., Abe, O., and Kitagawa, H. (2001). Northwest Pacific Marine Reservoir Correction Estimated from Annually Banded Coral from Ishigaki Island, Southern Japan. *Radiocarbon* 43, 473–476. doi:10.1017/s003822200038352
- Hori, K., and Kayanne, H. (2000). Submarine Morphology of the Island Shelf off the Middle and South Ryukyu Islands, Southwest Japan. *Geogr. Rev. Jpn. Ser. A, Chirigaku Hyoron* 73, 161–181. (in Japanese with Eng. Abstract). doi:10.4157/grj1984a.73.3_161
- Hori, N. (1977). A Morphometrical Study on the Geographical Distribution of Coral Reefs. *Geogr. Rep. Tokyo Metropol. Univ.* 12, 1–75.
- Hsu, S.-K., Yeh, Y.-C., Sibuet, J.-C., Doo, W.-B., and Tsai, C.-H. (2013). A Mega-Splay Fault System and Tsunami Hazard in the Southern Ryukyu Subduction Zone. *Earth Planet. Sci. Lett.* 362, 99–107. doi:10.1016/j.epsl.2012.11.053
- Igarashi, T. (2010). Spatial Changes of Inter-plate Coupling Inferred from Sequences of Small Repeating Earthquakes in Japan. *Geophys. Res. Lett.* 37, L20304. doi:10.1029/2010GL044609
- Ikehara, K., Irino, T., and Saito, Y. (2021a). The 2011 Tohoku-Oki Tsunami-Induced Sediment Remobilization on the Sendai Shelf, Japan, from a Comparison of Pre- and Post-tsunami Surface Sediments. *Sci. Rep.* 11, 7864. doi:10.1038/s41598-021-87152-8
- Ikehara, K., Irino, T., Usami, K., Jenkins, R., Omura, A., and Ashi, J. (2014). Possible Submarine Tsunami Deposits on the Outer Shelf of Sendai Bay, Japan Resulting from the 2011 Earthquake and Tsunami off the Pacific Coast of Tohoku. *Mar. Geol.* 358, 120–127. doi:10.1016/j.margeo.2014.11.0004
- Ikehara, K., Usami, K., Irino, T., Omura, A., Jenkins, R. G., and Ashi, J. (2021b). Characteristics and Distribution of the Event Deposits Induced by the 2011 Tohoku-Oki Earthquake and Tsunami Offshore of Sanriku and Sendai, Japan. *Sediment. Geol.* 411, 105791. doi:10.1016/j.sedgeo.2020.105791

- Ikehara, K., and Usami, K. (2018). Submarine Earthquake- and Tsunami-Induced Event Deposits. *Synth. Engl. Ed.* 11, 13–23. doi:10.5571/syntheng.11.1_13
- Imamura, F., Goto, K., and Ohkubo, S. (2008). A Numerical Model for the Transport of a Boulder by Tsunami. *J. Geophys. Res.* 113. doi:10.1029/2007JC004170
- Imamura, F., Yoshida, Y., and Moore, A. (2001). Numerical Study of the 1771 Meiwa Tsunami at Ishigaki Island, Okinawa and the Movement of the Tsunami Stones. *Proc. Coast. Eng. Jpn. Soc. Civ. Eng.* 48, 346–350. (in Japanese with English abstract). doi:10.2208/proce1989.48.346
- Inoue, Y. (1980a). Distribution of Recent Benthic Foraminifera in the Adjacent Seas of Japan (Part 1). *Spec. Rep. Tech. Lab. Jpn. Pet.Explor. Co.* 41-1, 1–114.
- Inoue, Y. (1980b). Distribution of Recent Benthic Foraminifera in the Adjacent Seas of Japan (Part 2). *Spec. Rep. Tech. Lab. Jpn. Pet.Explor. Co.* 41-2, 1–307.
- Japan Coast Guard (1988). *Bathymetric Chart “Hateruma Sima”*, Tokyo.
- Japan Coast Guard (1992). *Bathymetric Chart “Southern Part of Isigaki Sima”*, Tokyo.
- Jorry, S. J., Droxler, A. W., and Francis, J. M. (2010). Deepwater Carbonate Deposition in Response to Re-flooding of Carbonate Bank and Atoll-Tops at Glacial Terminations. *Quat. Sci. Rev.* 29, 2010–2026. doi:10.1016/j.quascirev.2010.04.016
- Jorry, S. J., Jouet, G., Edinger, E. N., Toucanne, S., Counts, J. W., Miramontes, E., et al. (2020). From Platform Top to Adjacent Deep Sea: New Source-To-Sink Insights into Carbonate Sediment Production and Transfer in the SW Indian Ocean (Glorieuses Archipelago). *Mar. Geol.* 423, 106144. doi:10.1016/j.margeo.2020.106144
- Kanamatsu, T., Ikehara, K., and Misawa, A. (2020). “Seafloor Morphology and Sediment Magnetic Fabric in a Putative 1771 Meiwa Tsunami Source Region in the Southern Ryukyu Islands, SW Japan.”. Editors Bath; Japan Coast Guard, 1988 and 1992 b Tokyo, Y. Dilek, Y. Ogawa, and Y. Okubo. Bath; Japan Coast Guard, 1988 and 1992 b Tokyo. *Geol. Soc. London Spec. Publ.*, 501, 289–299. doi:10.1144/SP501-2019-94
- Kawana, T., and Nakata, T. (1994). Timing of Late Holocene Tsunamis Originated Around the Southern Ryukyu Islands, Japan, Deduced from Coralline Tsunami Deposits. *J. Geogr. (Chigaku Zasshi)* 103, 352–376. (in Japanese with English abstract). doi:10.5026/jgeography.103.4_352
- Kitamura, A., Ito, M., Ikuta, R., and Ikeda, M. (2018). Using Molluscan Assemblages from Paleotsunami Deposits to Evaluate the Influence of Topography on the Magnitude of Late Holocene Mega-Tsunamis on Ishigaki Island, Japan. *Prog. Earth Planet Sci.* 5, 41. doi:10.1186/s40645-018-0200-y
- Lallemant, S., Liu, C.-S., Dominguez, S., Schnürle, P., and Malavieille, J. (1999). Trench-parallel Stretching and Folding of Forearc Basins and Lateral Migration of the Accretionary Wedge in the Southern Ryukyus: A Case of Strain Partition Caused by Oblique Convergence. *Tectonics* 18, 231–247. doi:10.1029/1998TC900011
- Liu, J. T., Hsu, R. T., Hung, J.-J., Chang, Y.-P., Wang, Y.-H., Rendle-Bühning, R. H., et al. (2016). From the Highest to the Deepest: The Gaoping River-Gaoping Submarine Canyon Dispersal System. *Earth-Science Rev.* 153, 274–300. doi:10.1016/j.earscirev.2015.10.012
- Miyazawa, K., Goto, K., and Imamura, F. (2012). “Re-evaluation of the 1771 Meiwa Tsunami Source Model, Southern Ryukyu Islands, Japan,” in *Submarine Mass Movements and Their Consequences*. (Springer), 497–506. Dordrecht: doi:10.1007/978-94-007-2162-3_44
- Mulder, T., Ducassou, E., Eberli, G. P., Hanquiez, V., Gonthier, E., Kindler, P., et al. (2012a). New Insights into the Morphology and Sedimentary Processes along the Western Slope of Great Bahama Bank. *Geology* 40, 603–606. doi:10.1130/g32972.1
- Mulder, T., Ducassou, E., Gillet, H., Hanquiez, V., Tournadour, E., Combes, J., et al. (2012b). Canyon Morphology on a Modern Carbonate Slope of the Bahamas: Evidence of Regional Tectonic Tilting. *Geology* 40, 771–774. doi:10.1130/g33327.1
- Mulder, T., Jomes, M., Hanquiez, V., Gillet, H., Reijmer, J. J. G., Tournadour, E., et al. (2017). Carbonate Slope Morphology Revealing Sediment Transfer from Bank-To-Slope (Little Bahama Bank, Bahamas). *Mar. Petroleum Geol.* 83, 26–34. doi:10.1016/j.marpetgeo.2017.03.002
- Mullins, H. T. (1983). Comments and Reply on ‘Eustatic Control of Turbidites and Winnowed Turbidites’. *Geol* 11, 57–58. doi:10.1130/0091-7613(1983)11<57:caroc>2.0.co;2
- Nakamura, M. (2009). Fault Model of the 1771 Yaeyama Earthquake along the Ryukyu Trench Estimated from the Devastating Tsunami. *Geophys. Res. Lett.* 36, L19307. doi:10.1029/2009GL039730
- Nakamura, M., and Sunagawa, N. (2015). Activation of Very Low Frequency Earthquakes by Slow Slip Events in the Ryukyu Trench. *Geophys. Res. Lett.* 42, 1076–1082. doi:10.1002/2014GL062929
- Nishimura, T. (2014). Short-term Slow Slip Events along the Ryukyu Trench, Southwestern Japan, Observed by Continuous GNSS. *Prog. Earth Planet. Sci.* 1, 22. doi:10.1186/s40645-014-0022-5
- Okamura, Y., Nishizawa, A., Fujii, Y., and Yanagisawa, H. (2018). Accretionary Prism Collapse: a New Hypothesis on the Source of the 1771 Giant Tsunami in the Ryukyu Arc, SW Japan. *Sci. Rep.* 8, 13620. doi:10.1038/s41598-018-31956-8
- Oyama, M., and Takehara, H. (1967). *Revised Standard Soil Color Charts*. Tokyo: Japan Color Enterprise.
- Palanques, A., El Khatab, M., Puig, P., Masqué, P., Sánchez-Cabeza, J. A., and Isla, E. (2005). Downward Particle Fluxes in the Guadiaro Submarine Canyon Depositional System (North-western Alboran Sea), a River Flood Dominated System. *Mar. Geol.* 220, 23–40. doi:10.1016/j.margeo.2005.07.004
- Paris, R., Fournier, J., Poizot, E., Etienne, S., Morin, J., Lavigne, F., et al. (2010). Boulder and Fine Sediment Transport and Deposition by the 2004 Tsunami in Lhok Nga (Western Banda Aceh, Sumatra, Indonesia): A Coupled Offshore-Onshore Model. *Mar. Geol.* 268, 43–54. doi:10.1016/j.margeo.2009.10.011
- Peterson, E. T., and Seno, T. (1984). Factors Affecting Seismic Moment Release Rates in Subduction Zones. *J. Geophys. Res.* 89, 10233–10248. doi:10.1029/JB089iB12p10233
- Pickering, K. T., and Hiscott, R. N. (2016). *Deep Marine Systems, Processes, Deposits, Environments, Tectonics and Sedimentation*. Oxford: AGU and Wiley, 657p.
- Porcile, G., Bolla Pittaluga, M., Frascati, A., and Sequeiros, O. E. (2020). Typhoon-induced Megarips as Triggers of Turbidity Currents Offshore Tropical River Deltas. *Commun. Earth Environ.* 1, 2. doi:10.1038/s43247-020-0002-1
- Puga-Bernabéu, Á., Webster, J. M., Beaman, R. J., Reimer, P. J., and Renema, W. (2014). Filling the Gap: A 60 Ky Record of Mixed Carbonate-Siliciclastic Turbidite Deposition from the Great Barrier Reef. *Mar. Pet. Geol.* 50, 40–50. doi:10.1016/j.marpetgeo.2013.11.009
- Puga-Bernabéu, Á., Webster, J. M., Beaman, R. J., and Guilbaud, V. (2011). Morphology and Controls on the Evolution of a Mixed Carbonate-Siliciclastic Submarine Canyon System, Great Barrier Reef Margin, North-Eastern Australia. *Mar. Geol.* 289, 100–116. doi:10.1016/j.margeo.2011.09.013
- Puga-Bernabéu, Á., Martín, J. M., and Braga, J. C. (2007). Tsunami-related Deposits in Temperate Carbonate Ramps, Sorbas Basin, Southern Spain. *Sed. Geol.* 199, 107–127. doi:10.1016/j.sedgeo.2007.01.20
- Saito, Y., Katayama, H., Ikehara, K., Kato, Y., Matsumoto, E., Oguri, K., et al. (1998). Transgressive and Highstand Systems Tracts and Post-glacial Transgression, the East China Sea. *Sediment. Geol.* 122, 217–232. doi:10.1016/s0037-0738(98)00107-9
- Sakuna-Schwartz, D., Feldens, P., Schwarzer, K., Khokiatwong, S., and Stattegger, K. (2015). Internal Structure of Event Layers Preserved on the Andaman Sea Continental Shelf, Thailand: Tsunami vs. Storm and Flash-Flood Deposits. *Nat. Hazards Earth Syst. Sci.* 15, 1181–1199. doi:10.5194/nhess-15-1181-2015
- Sasaki, K., Omura, A., Miwa, T., Tsuji, Y., Matsuda, H., Nakamori, T., et al. (2006). ²³⁰Th/²³⁴U and ¹⁴C Dating of a Lowstand Coral Reef beneath the Insular Shelf off Irabu Island, Ryukyu, Southwestern Japan. *Isl. Arc* 15, 455–467. doi:10.1111/j.1440-1738.2006.00541.x
- Shanmugam, G., and Moiola, R. J. (1988). Submarine Fans: Characteristics, Models, Classification, and Reservoir Potential. *Earth-Science Rev.* 24, 383–428. doi:10.1016/0012-8252(88)90064-5
- Taylor, B., and Goodliffe, A. M. (2004). The West Philippine Basin and the Initiation of Subduction, Revisited. *Geophys. Res. Lett.* 31, L12602. doi:10.1029/2004GL020136
- Tournadour, E., Mulder, T., Borgomano, J., Gillet, H., Chabaud, L., Ducassou, E., et al. (2017). Submarine Canyon Morphologies and Evolution in Modern Carbonate Settings: The Northern Slope of Little Bahama Bank, Bahamas. *Mar. Geol.* 391, 76–97. doi:10.1016/j.margeo.2017.07.014
- Tsuji, Y. (1993). Tide Influenced High Energy Environments and Rhodolith-Associated Carbonate Deposition on the Outer Shelf and Slope off the Miyako

- Islands, Southern Ryukyu Island Arc, Japan. *Mar. Geol.* 113, 255–271. doi:10.1016/0025-3227(93)90021-m
- Ujiie, H., Nakamura, T., Miyamoto, Y., Park, J.-O., Hyun, S., and Oyakawa, T. (1997). Holocene Turbidite Cores from the Southern Ryukyu Trench Slope: Suggestions of Periodic Earthquakes. *Jour. Geol. Soc. Jpn.* 103, 590–603. doi:10.5575/geosoc.103.590
- Ujiie, H. (1980). Significance of “500 M Deep Island Shelf” Surrounding the Southern Ryukyu Island Arc for its Quaternary Geological History. *Quat. Res. (Daiyonki-Kenkyu)* 18, 209–219.
- Usami, K., Ikehara, K., Jenkins, R. G., and Ashi, J. (2017). Benthic Foraminiferal Evidence of Deep-Sea Sediment Transport by the 2011 Tohoku-Oki Earthquake and Tsunami. *Mar. Geol.* 384, 214–224. doi:10.1016/j.margeo.2016.04.001
- Usami, T. (2003). *New Comprehensive Summary of Historical Destructive Earthquakes in Japan*. Tokyo: Univ. Tokyo Press, 605p.
- Webster, J. M., Beaman, R. J., Puga-Bernabéu, Á., Ludman, D., Renema, W., Wust, R. A. J., et al. (2012). Late Pleistocene History of Turbidite Sedimentation in a Submarine Canyon off the Northern Great Barrier Reef, Australia. *Palaeogeogr. Palaeoclimatol. Palaeoecol.* 331–332, 75–89. doi:10.1016/j.palaeo.2012.02.034
- Webster, J. M., Braga, J. C., Humblet, M., Potts, D. C., Iryu, Y., Yokoyama, Y., et al. (2018). Response of the Great Barrier Reef to Sea-Level and Environmental Changes over the Past 30,000 Years. *Nat. Geosci.* 11, 426–432. doi:10.1038/s41561-018-0127-3
- Webster, J. M., Clague, D. A., Riker-Coleman, K., Gallup, C., Braga, J. C., Potts, D., et al. (2004). Drowning of the –150 M Reef off Hawaii: A Casualty of Global Meltwater Pulse 1A? *Geology* 32, 249–252. doi:10.1130/G20170.1
- Wunsch, M., Betzler, C., Lindhorst, S., Lüdmann, T., and Eberli, G. P. (2017). Sedimentary Dynamics along Carbonate Slopes (Bahamas Archipelago). *Sedimentology* 64, 631–657. doi:10.1111/sed.12317
- Xu, J. P., Noble, M., Eittreim, S. L., Rosenfeld, L. K., Schwing, F. B., and Pilskaln, C. H. (2002). Distribution and Transport of Suspended Particulate Matter in Monterey Canyon, California. *Mar. Geol.* 181, 215–234. doi:10.1016/s0025-3227(01)00268-7
- Xu, J. P., Swarzenski, P. W., Noble, M., and Li, A.-C. (2010). Event-driven Sediment Flux in Hueneme and Mugu Submarine Canyons, Southern California. *Mar. Geol.* 269, 74–88. doi:10.1016/j.margeo.2009.12.007

Conflict of Interest: KU is employed by Japan NUS Co. Ltd.

The remaining authors declare that the research was conducted in the absence of any commercial or financial relationships that could be construed as a potential conflict of interest.

Publisher’s Note: All claims expressed in this article are solely those of the authors and do not necessarily represent those of their affiliated organizations, or those of the publisher, the editors and the reviewers. Any product that may be evaluated in this article, or claim that may be made by its manufacturer, is not guaranteed or endorsed by the publisher.

Copyright © 2022 Ikehara, Kanamatsu and Usami. This is an open-access article distributed under the terms of the Creative Commons Attribution License (CC BY). The use, distribution or reproduction in other forums is permitted, provided the original author(s) and the copyright owner(s) are credited and that the original publication in this journal is cited, in accordance with accepted academic practice. No use, distribution or reproduction is permitted which does not comply with these terms.



Tectonic Influence on the Geomorphology of Submarine Canyons: Implications for Deep-Water Sedimentary Systems

Laura H. Bührig^{*†}, Luca Colombero[‡], Marco Patacci[‡], Nigel P. Mountney[‡] and William D. McCaffrey[‡]

School of Earth and Environment, Institute of Applied Geoscience, University of Leeds, Leeds, United Kingdom

OPEN ACCESS

Edited by:

Rosanna Maniscalco,
University of Catania, Italy

Reviewed by:

Daniele Casalbore,
Sapienza University of Rome, Italy
Andrea Fildani,
Deep Time Institute, United States

*Correspondence:

Laura H. Bührig
lhbuehrig@gmail.com

[†]This author has first authorship

[‡]These authors have contributed
equally to this work and share senior
authorship

Specialty section:

This article was submitted to
Quaternary Science, Geomorphology
and Paleoenvironment,
a section of the journal
Frontiers in Earth Science

Received: 15 December 2021

Accepted: 21 April 2022

Published: 02 June 2022

Citation:

Bührig LH, Colombero L, Patacci M,
Mountney NP and McCaffrey WD
(2022) Tectonic Influence on the
Geomorphology of Submarine
Canyons: Implications for Deep-Water
Sedimentary Systems.
Front. Earth Sci. 10:836823.
doi: 10.3389/feart.2022.836823

A database-informed metastudy of 294 globally distributed submarine canyons has been conducted with the aim of elucidating the role of tectonic setting on submarine-canyon geomorphology. To achieve this, data from seafloor and subsurface studies derived from 136 peer-reviewed publications and from open-source worldwide bathymetry datasets have been statistically analyzed. In particular, relationships between margin type (active vs. passive) or plate-boundary type (convergent vs. transform vs. complex) have been assessed for key morphometric parameters of submarine canyons, including: streamwise length, maximum and average width and depth, canyon sinuosity, average canyon thalweg gradient, and maximum canyon sidewall steepness. In addition, possible scaling relationships between canyon morphometric parameters and characteristics of the associated terrestrial catchment, continental shelf and slope, and of the broader physiographic setting for canyons along both active and passive margins have been evaluated. The following principal findings arise: 1) overall canyon geomorphology is not markedly different across tectonic settings; 2) slope failure might be more important in passive-margin canyons compared to active ones, possibly due to seismic strengthening in the latter; 3) some aspects of canyon geomorphology scale with attributes of the source-to-sink system and environmental setting, but the strength and sign in scaling might differ between active and passive margins, suggesting that the extent to which canyon geomorphology can be predicted depends on the tectonic setting. Insights from our analysis augment and improve conceptual, experimental and numerical models of slope systems at the scale of individual canyons and source-to-sink systems, and increase our understanding of the complex role played by tectonic setting in shaping deep-water systems.

Keywords: global, quantitative analysis, geometry, scaling relationships, source-to-sink, active margin, passive margin

1 INTRODUCTION

As major conduits for the exchange of sediment, organic matter, nutrients, pollutants and water masses across continental margins (e.g., Fildani, 2017; Santora et al., 2018; Maier et al., 2019; Zhong and Peng, 2021), submarine canyons are important components of deep-water environments and of broader source-to-sink (S2S) systems.

Canyon fills and deep-water fans collectively provide a depositional record of the sediment funneled through a connected canyon, and hold valuable information on the long-term evolution of continental margins (e.g., Normark and Carlson, 2003; Hessler and Fildani, 2019). They are more likely preserved when small in size, accommodated on continental crust, and associated with an active-margin setting (e.g., Normark et al., 1993; Normark and Carlson, 2003); this creates bias in the sedimentary record of deep-water systems. As a consequence, insights from ancient systems only provide a selective view on controls on deep-water systems and have limited applicability to modern environments. Moreover, current knowledge of the role of submarine-canyon geomorphology in shaping the configuration of deep-water systems largely relies on insights from a small number of modelling studies based on datasets from passive-margin settings (e.g., Wan et al., 2021) and a small number of comparative global studies with focus on specific aspects of canyon geomorphology (e.g., Normark and Carlson, 2003; Covault et al., 2011a). Furthermore, despite the importance of canyons for the delivery of sediment to deep-water basins, relationships between the geometry of submarine canyons and linked controls have not yet been fully considered in source-to-sink models; previous analyses were limited to the assessment of scaling relationships between canyon morphometric parameters with attributes of terrestrial catchments and continental shelves and slopes, which demonstrate that canyon geomorphology is partially controlled by the configuration of S2S systems (e.g., Sømme et al., 2009; Casalbore et al., 2011; Nyberg et al., 2018; Bührig et al., in review).

The quantitative investigation of modern canyons can increase our understanding of the importance of tectonic controls on their geomorphology, and in turn of the potential role of canyon geomorphology on sediment dispersal to deep-marine sinks. Insights in such relationships may also be useful for the reconstruction and prediction of geometries of deep-water systems and superordinate S2S systems, where these are only partially preserved in outcrop or are partially resolved in surveys of the seafloor and subsurface.

Submarine-canyon geomorphology is governed by multiple environmental factors including their hydrodynamic regime, oceanographic environment, regional climate, and tectonic setting (e.g., Harris and Whiteway, 2011; Huang et al., 2014; Puig et al., 2014; Bührig et al., in review), which control mechanisms of sediment routing from terrestrial source areas to marine sinks. In active-margin settings, relatively steep gradients and short transport distances across terrestrial catchments and the adjoining continental shelf promote rapid delivery of solids from the terrestrial hinterland to the deep-marine environment (e.g., Bouma and Scott, 2003; Sømme et al., 2009; Gamberi et al., 2015; Nyberg et al., 2018; Pierdomenico

et al., 2019). In systems with wide shelves along passive margins, sediment routing to slopes and basin floors is facilitated *via* shelf channels, shelf-edge deltas and submarine canyons that have cut across the shelf to connect to a river (e.g., Sylvester et al., 2012; Rona et al., 2015).

Some global studies indicate that the overall geomorphology of canyons might not differ fundamentally between tectonically active and passive margins (e.g., Harris and Whiteway, 2011; Bührig et al., in review). Yet tectonic activity molds the basin topography *via* its control on the distribution and type of faulting and mass-failures, which have been shown to leave characteristic signatures in the morphology of submarine canyons of active continental margins (e.g., Greene et al., 1991; Chiang and Yu, 2006; Micallef et al., 2014; Corradino et al., 2021; Soutter et al., 2021). Moreover, active margins encompass both convergent and strike-slip tectonic domains, and are characterized by variability in sedimentary basin-morphology and sediment generation, transport and dispersal mechanisms (e.g., Ingersoll, 2012; Ju et al., 2020). Although tectonically active margins host over 50% of submarine canyons globally (Harris and Whiteway, 2011), studies of the genesis and evolution of submarine canyons associated with active margins are relatively underrepresented in the scientific literature (Micallef et al., 2014).

The aim of this study is to increase understanding of the influence of tectonic setting on the geomorphology of submarine canyons. To achieve this, the geomorphology of 294 modern canyons has been investigated in their S2S context, considering parameters describing their physiographic and tectonic setting. Specific research objectives are as follows: 1) to quantitatively characterize the variability in selected canyon geomorphologic parameters across active (both convergent and strike-slip) and passive continental-margin types; 2) to evaluate scaling relationships in canyon morphometry and of individual canyon morphometric parameters with attributes describing their environmental setting, discriminating between active and passive margins; 3) to assess the characteristics of canyon-associated terrestrial catchments, shelves and slopes in active-versus passive-margin settings, and their scaling relationships.

2 DATASET AND METHODS

2.1 Dataset

The dataset used in this study has been extracted from a database of submarine canyons collated by Bührig et al. (in review), who have investigated controlling factors on canyon geomorphology in a global metastudy. For the present study, the database has been extended by defining and characterizing new attributes and by integration with additional data to facilitate the analyses. The data presented in this article are made available in the Supplementary Material.

Data on the geomorphology of the canyons have been extracted from high-resolution seabed and subsurface studies from 136 peer-reviewed publications and from open-source worldwide bathymetry (NOAA National Centers for Environmental Information, 2021; Google Earth). The dataset is organized as 97 individual case studies, with each case

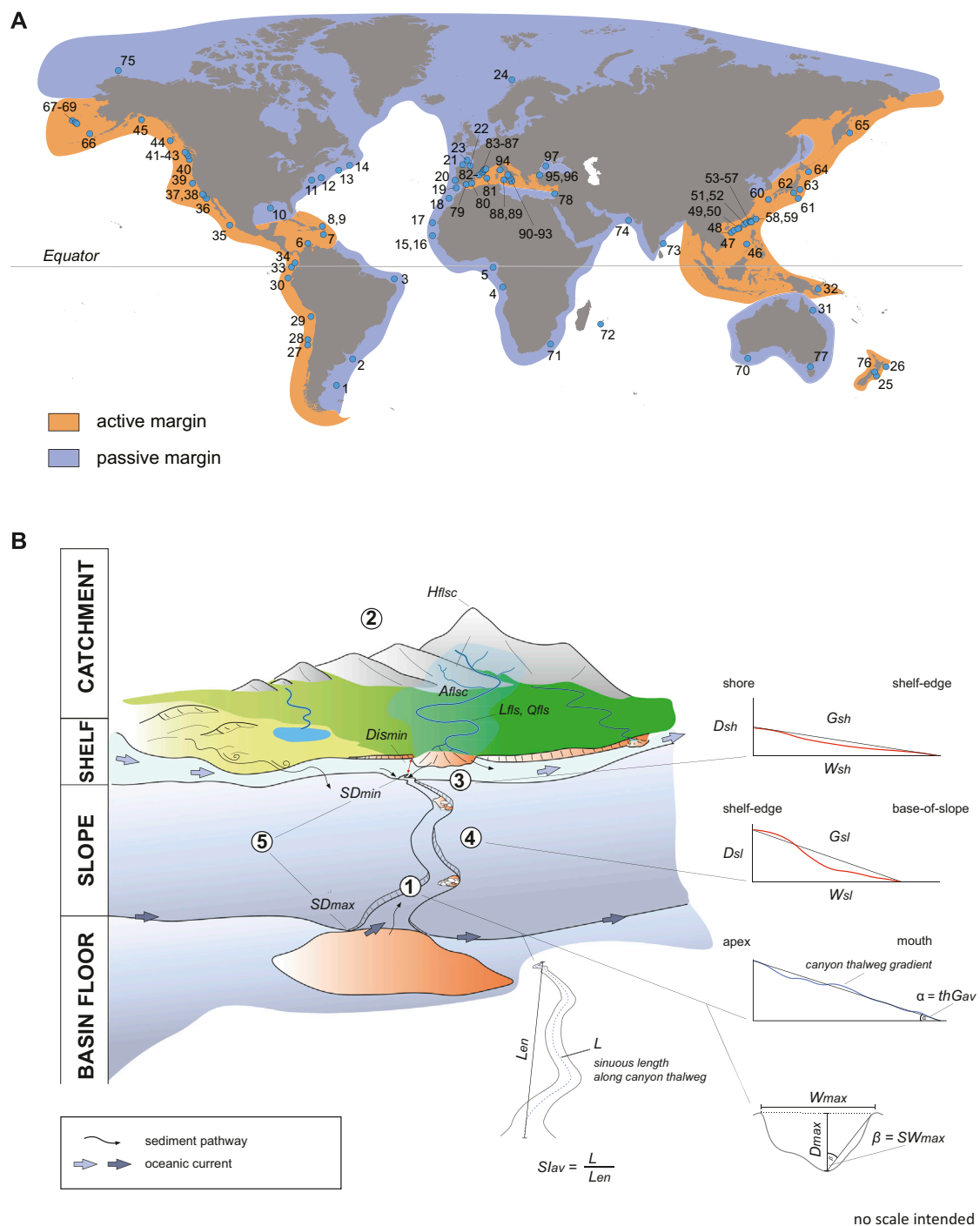


FIGURE 1 | (A) Overview map of the distribution of the 97 case studies and their associated margin-type setting. Continental-margin classification after Harris et al. (2014b) (World map from freevectormaps.com). **(B)** Key parameters investigated in the study: 1) Submarine canyon: L , canyon length along thalweg; L_{en} , canyon length along endpoints; W_{max} , maximum canyon width; D_{max} , maximum canyon depth; $Slav$, average canyon sinuosity index; thG_{av} , average canyon thalweg gradient; SW_{max} , maximum canyon sidewall steepness. 2) Terrestrial catchment: L_{fls} , fluvial system length; Q_{fls} , average annual fluvial discharge; A_{flsc} , catchment size; H_{flsc} , maximum catchment elevation. 3) Shelf configuration: W_{sh} , shelf width; D_{sh} , shelf-break depth; G_{sh} , average shelf gradient. 4) Slope configuration: W_{sl} , slope width; D_{sl} , slope-break depth; G_{sl} , average slope gradient. 5) Canyon-physiographic setting: SD_{min} , seafloor depth at canyon apex; SD_{max} , seafloor depth at canyon mouth; Dis_{min} , minimum distance of canyon to shoreline.

TABLE 1 | Summary of the 97 case studies considered in this study.

ID	Case study	No. of canyons	Oceanic region	Reference(s)
1	Patagonia canyons, SE Argentina	8	South Atlantic Ocean	Lastras et al. (2011a)
2	Mar del Plata Canyon, E Argentina	1	South Atlantic Ocean	Krastel et al. (2011), Warratz et al. (2019)
3	Potiguar Basin canyons, NE Brazil	14	South Atlantic Ocean	de Almeida et al. (2015)
4	Congo Canyon, W Democratic Republic of Congo	1	South Atlantic Ocean	Babonneau et al. (2002), Ferry et al. (2004)
5	Avon & Mahin canyons, SW Nigeria	2	South Atlantic Ocean	Jimoh et al. (2018)
6	Aguja Canyon, N Colombia	1	North Atlantic Ocean (Caribbean Sea)	Restrepo-Correa and Ojeda (2010)
7	Guayanilla canyon system, S Puerto Rico	4	North Atlantic Ocean (Caribbean Sea)	Trumbull and Garrison (1973)
8	Arecibo & Quebradillas canyons, NW Puerto Rico	2	North Atlantic Ocean	Gardner et al. (1980)
9	Mona Canyon, NW Puerto Rico	1	North Atlantic Ocean	Mondziel et al. (2010)
10	Mississippi Canyon, S United States	1	North Atlantic Ocean (Gulf of Mexico)	Coleman et al. (1982)
11	Hudson Canyon, NE United States	1	North Atlantic Ocean	Rona et al. (2015)
12	Lydonia & Oceanographer canyons, NE United States	2	North Atlantic Ocean	Valentine et al. (1980)
13	Logan Canyon, SE Canada	1	North Atlantic Ocean	Li et al. (2019)
14	SW Grand Banks Slope canyons, SE Canada	3	North Atlantic Ocean	Armitage et al. (2010)
15	Dakar Canyon, W Senegal	1	North Atlantic Ocean	Pierau et al. (2010), Pierau et al. (2011)
16	Cayar Canyon, W Senegal	1	North Atlantic Ocean	Dietz et al. (1968)
17	Timiris Canyon, NW Mauritania	1	North Atlantic Ocean	Krastel et al. (2004), Antobreh and Krastel (2006)
18	Agadir Canyon	1	North Atlantic Ocean	Ercilla et al. (1998), Wynn et al. (2002)
19	Faro & Portimao canyons, SW Portugal	2	North Atlantic Ocean (Gulf of Cadiz)	Mulder et al. (2006)
20	Nazaré, Cascais & Setubal-Lisbon canyons, W Portugal	4	North Atlantic Ocean	Arzola et al. (2008), Lastras et al. (2009), Allin et al. (2016)
21	Aviles Canyon system & Navia canyon, N Spain	5	North Atlantic Ocean (Bay of Biscay)	Gómez-Ballesteros et al. (2014)
22	Capbreton Canyon, SW France	1	North Atlantic Ocean (Bay of Biscay)	Mazières et al. (2014)
23	Audierne & Blackmud canyons, SW France	2	North Atlantic Ocean (Bay of Biscay)	Mulder et al. (2012)
24	Lofoten-Vesterålen canyons (incl. Andøya Canyon), NW Norway	15	North Atlantic Ocean	Rise et al. (2013)
25	Kaikoura Canyon, E New Zealand	1	South Pacific Ocean	Lewis and Barnes (1999)
26	Lachlan Canyon, NE New Zealand	1	South Pacific Ocean	Walsh et al. (2007)
27	Biobio Canyon system, SW Chile	2	South Pacific Ocean	Bernhardt et al. (2015)
28	San Antonio Canyon, NW Chile	1	South Pacific Ocean	Hagen et al. (1996), Laursen and Normark (2002)
29	E Arequipa Basin canyons, NW Chile	3	South Pacific Ocean	Hagen et al. (1994)
30	Guayaquil & Santa Elena canyons, NW Ecuador	2	South Pacific Ocean	Michaud et al. (2015)
31	N Great Barrier Reef canyons, NE Australia	15	South Pacific Ocean (Coral Sea)	Puga-Bernabéu et al. (2011)
32	Solomon Sea canyons, E & SE Papua New Guinea	8	South Pacific Ocean (Solomon Sea)	Davies et al. (1987), Galewsky and Silver (1997)
33	Esmeraldas Canyon, NW Ecuador	1	North Pacific Ocean	Michaud et al. (2015)
34	Mira & Patia canyons, SW Colombia	2	North Pacific Ocean	Ratzov et al. (2012)
35	Ipala Canyon, W Mexico	1	North Pacific Ocean (South China Sea)	Urrías Espinosa et al. (2016)
36	La Jolla, Scripps, Sur, Carmel, Noyo & Eel canyons, SW United States	6	North Pacific Ocean	Le Dantec et al. (2010), Paull et al. (2013)
37	Redondo, Santa Monica & Dume canyons, SW United States	3	North Pacific Ocean	Gardner et al. (2003), Tubau et al. (2015)
38	Mugu & Hueneme canyons, SW United States	2	North Pacific Ocean	Piper et al. (1999)
39	Monterey, Soquel, Año Nuevo & Cabrillo canyons, SW United States	4	North Pacific Ocean	Greene et al. (2002), Xu and Noble (2009)
40	Astoria Canyon, NW United States	1	North Pacific Ocean	Hickey (1997), Bosley et al. (2004)
41	Quinault Canyon, NW United States	1	North Pacific Ocean	Baker and Hickey (1986), Carson et al. (1986)
42	Juan de Fuca Canyon, NW United States	1	North Pacific Ocean (heads in the Juan de Fuca Strait)	Alford and MacCready (2014)
43	Barkley Canyon, SW Canada	1	North Pacific Ocean	Allen et al. (2001)
44	Haida Gwaii canyons, SW Canada	6	North Pacific Ocean	Harris et al. (2014a)
45	Tarr Canyon, NW United States	1	North Pacific Ocean (Gulf of Alaska)	Carlson et al. (1990)
46	North Palawan Canyon, S China	1	North Pacific Ocean (South China Sea)	Yin et al. (2018)
47	Modern Central Canyon, S China	1	North Pacific Ocean (South China Sea)	Su et al. (2015)
48	3 canyons & 4 gullies, S China	3 (4)	North Pacific Ocean (South China Sea)	Chen et al. (2017)
49	Pearl River Mouth Basin canyons, S China	17	North Pacific Ocean (South China Sea)	Han et al. (2010), Su et al. (2020)
50	Zhujiang/Pearl River Canyon, S China	1	North Pacific Ocean (South China Sea)	Han et al. (2010), Ding et al. (2013)
51	Dongsha Canyon, S China	1	North Pacific Ocean (South China Sea)	Yin et al. (2015)
52	Taiwan Canyon, SW Taiwan	1	North Pacific Ocean (South China Sea)	Xu et al. (2014)
53	Hongtsai Canyon, SW Taiwan	1	North Pacific Ocean (South China Sea)	Yu and Chiang (1995)
54	Fangliao Canyon, SW Taiwan	1	North Pacific Ocean (South China Sea)	Yu and Lu (1995), Chiang et al. (2012)
55	Kaoping Canyon, SW Taiwan	1	North Pacific Ocean (South China Sea)	Chiang and Yu (2006), Liu et al. (2016)
56	Kaohsiung Canyon, SW Taiwan	1	North Pacific Ocean (South China Sea)	Yu et al. (1992)

(Continued on following page)

TABLE 1 | (Continued) Summary of the 97 case studies considered in this study.

ID	Case study	No. of canyons	Oceanic region	Reference(s)
57	Penghu Canyon, SW Taiwan	1	North Pacific Ocean (South China Sea)	Yu and Chang (2002), Hsiung and Yu (2011), Su et al. (2015)
58	Taitung Canyon, SE Taiwan	1	North Pacific Ocean (Philippine Sea)	Schnürle et al. (1998)
59	Hualien Canyon, SE Taiwan	1	North Pacific Ocean (Philippine Sea)	Hsiung et al. (2017)
60	Goto Canyon, SW Japan	1	North Pacific Ocean (East China Sea)	Oiwane et al. (2011)
61	Aoga Shima Canyon, SE Japan	1	North Pacific Ocean (Philippine Sea)	Klaus and Taylor (1991)
62	Tenryu Canyon, SE Japan	1	North Pacific Ocean	Soh and Tokuyama (2002)
63	Boso Canyon, SE Japan	1	North Pacific Ocean	Soh et al. (1990)
64	Kushiro Canyon, NE Japan	1	North Pacific Ocean	Noda et al. (2008), Noda and Tuzino (2010), Tuzino and Noda (2010)
65	Submarine canyons of Kamchatka, NE Russia	7	North Pacific Ocean	Gribidenko and Svarichevskaya (1984)
66	Bering Canyon, Bering Sea	1	North Pacific Ocean (Bering Sea)	Carlson and Karl (1988), Harris and Whiteway (2011)
67	Zhemchug, Pervenets & Navarin canyons, Bering Sea	3	North Pacific Ocean (Bering Sea)	Carlson and Karl (1988)
68	Middle canyon system, Bering Sea	2	North Pacific Ocean (Bering Sea)	Carlson and Karl (1984), Carlson and Karl (1988)
69	St. Matthew canyon system, Bering Sea	2	North Pacific Ocean (Bering Sea)	Carlson and Karl (1984), Carlson and Karl (1988)
70	Albany canyons, SW Australia	11	Indian Ocean	Exon et al. (2005)
71	Tugela Canyon, E South Africa	1	Indian Ocean	Wiles et al. (2013)
72	Saint-Etienne & Pierrefonds canyons, SW La Reunion	2	Indian Ocean	Babonneau et al. (2013)
73	Palar Basin canyons, E India	20	Indian Ocean	Susanth et al. (2021)
74	Indus Canyon, SE Pakistan	1	Indian Ocean (Arabian Sea)	Von Rad and Tahir (1997), Salmanidou et al. (2019)
75	Barrow Canyon, NW United States	1	Arctic Ocean	Eittreim et al. (1982), Pisareva et al. (2019)
76	Cook Strait canyons, E New Zealand	9	Cook Strait	Mountjoy et al. (2009), Mountjoy et al. (2014), Micallef et al. (2014)
77	Bass canyon system, SE Australia	10	Bass Strait	Mitchell et al. (2007)
78	Akhviz & Sour canyons, NW Israel	2	Mediterranean Sea	Mart (1989), Almagor (1993)
79	Almeria, Western, Eastern & Guadiaro canyons, S Spain	4	Mediterranean Sea	Alonso and Ercilla (2003), Palanques et al. (2005)
80	Alías-Almanzora canyon system, SE Spain	4	Mediterranean Sea	Puig et al. (2017)
81	Menorca Canyon, SW Menorca, Balearic Islands	1	Mediterranean Sea	Acosta et al. (2002)
82	Orpesa Canyon, NE Spain	1	Mediterranean Sea	Amblas et al. (2012)
83	Foix Canyon system, NE Spain	3	Mediterranean Sea	Puig et al. (2000), Tubau et al. (2013)
84	Blanes Canyon, SE France	1	Mediterranean Sea	Lastras et al. (2011b)
85	Palamós/La Fonera Canyon, NE Spain	1	Mediterranean Sea	Martin et al. (2006), Palanques et al. (2006), Lastras et al. (2011b)
86	Cap de Creus Canyon, NE Spain	1	Mediterranean Sea	Baztan et al. (2005), Lastras et al. (2007), Lastras et al. (2011b)
87	Bourcart Canyon, SE France	1	Mediterranean Sea	Mauffrey et al. (2015)
88	Gulf of Palermo canyons, NW Sicily, Italy	7	Mediterranean Sea	Lo Iacono et al. (2011), Lo Iacono et al. (2014)
89	Gulf of Castellammare canyons, NW Sicily, Italy	2	Mediterranean Sea	Lo Iacono et al. (2014)
90	Messina Canyon, NE Sicily, Italy	1	Mediterranean Sea	Ridente et al. (2014)
91	Petrace, Gioia & Mesima canyons, SW Italy	3	Mediterranean Sea	Pierdomenico et al. (2016), Casalbone et al. (2018)
92	Luna & Infreschi canyons, SW Italy	2	Mediterranean Sea	Budillon et al. (2011)
93	Dohrn Canyon, SW Italy	1	Mediterranean Sea	Milia (2000)
94	Golo system canyons, NE Corsica, France	4 (2)	Mediterranean Sea	Gervais et al. (2004), Gervais et al. (2006)
95	North İmralı Canyon, NW Turkey	1	Sea of Marmara	Vardar (2019)
96	Sarköy & İzmit canyons, NW Turkey	2	Sea of Marmara	Çağatay et al. (2015)
97	Danube/Viteaz Canyon, SE Romania	1	Black Sea	Popescu et al. (2004)

The numbers of canyons reported in brackets indicate channel forms that were termed as "submarine gullies" by the authors of the original data sources.

corresponding to one or several submarine canyons from a geographic location or region, detailed as a self-contained study by the original authors (**Figure 1A**; **Table 1**).

2.2 Methods

Data on individual canyon morphometric parameters, the physiographic setting of the canyon and characteristics of its associated S2S system have been coded in the Deep-Marine

Architecture Knowledge Store (DMAKS; Cullis et al., 2019), a relational database storing data on characteristics of deep-water sedimentary systems and their environmental settings (see Cullis et al., 2019).

2.2.1 Canyon Definition

In this study, a submarine canyon is defined as a throughgoing erosional channel form incised into the continental slope; this

TABLE 2 | Overview of the parameters investigated in the study and their definitions.

Study parameter	Definition
Canyon morphometrics	
L (km)**	Streamwise length of the canyon between canyon apex and canyon mouth as measured along the canyon thalweg
W_{max} (km)**	Maximum width of the canyon orthogonal to the canyon length
W_{av} (km)*	Average canyon width over the length of the entire canyon
D_{max} (m)*	Maximum depth of the canyon, i.e., depth of the canyon thalweg relative to the elevation of the canyon margins
D_{av} (m)*	Average canyon thalweg depth over the length of the entire canyon
SI_{av} (-)**	Average canyon sinuosity index, i.e., ratio between the sinuous canyon length measured along its thalweg and the straight distance between canyon apex and canyon mouth
thG_{av} (°)**	Average canyon thalweg gradient, evaluated between canyon apex and canyon mouth
SVW_{max} (°)*	Maximum canyon-sidewall steepness, representing the maximum value of gradient between canyon rim and canyon bottom evaluated along the entire length of the canyon
Physiographic setting	
Dis_{min} (km)**	Minimum distance between the canyon and the shoreline
SD_{min} (m)**	Seafloor depth at the top of the canyon
SD_{max} (m)**	Seafloor depth at the mouth of the canyon
Canyon terrestrial catchment	
L_{fls} (km)**	Length of the river with a present-day or previous connection with the canyon, from headwater to river mouth; for canyons connected with several rivers the cumulative length has been considered
Q_{fls} (km ³ /yr)*	Mean annual discharge of the fluvial system; for canyons connected with several rivers the cumulative mean annual discharge has been considered
A_{flsc} (km ²)*	Size of the catchment associated with the fluvial system; for canyons connected with several rivers the cumulative catchment area size has been considered
H_{flsc} (m)**	Maximum elevation of the catchment associated with the fluvial system; for canyons connected with several rivers, the elevation of the highest peak in the combined catchments has been considered
Continental shelf	
W_{sh} (km)**	Width of the shelf at the canyon location
G_{sh} (°)**	Average shelf gradient at the canyon location
D_{sh} (m)**	Shelf-break depth at the canyon where the shelf edge is intact and not eroded into by the latter; for shelf edges displaying some degree of variability in their bathymetry the maximum depth of the shelf break has been chosen
Continental slope	
W_{sl} (km)**	Width of the slope at the canyon location
G_{sl} (°)**	Average slope gradient between the shelf break and the slope break
D_{sl} (m)**	Slope-break depth at the canyon
Other parameters	
Continental-margin type	For canyons located along continental margins, including canyons associated with islands: 1) active margin, including transform margins; 2) passive margin [classification after Figure 2 of Harris et al. (2014b)]
Active-margin plate boundary type	Based on the type of plate boundary, active margins are distinguished into 1) convergent, 2) transform, and 3) complex margins. The latter category includes settings which involve more than one plate boundary, and margins which display an additional direction of motion, e.g., convergent margins with a transform component

definition does not therefore consider ancillary criteria that are sometimes used by some authors, such as their origin or minimum size (cf. Harris and Whiteway, 2011). The general definition used herein encompasses smaller channelforms, which are sometimes referred to as “submarine gullies” (e.g., Gervais et al., 2006), “submarine gulley” (e.g., Normark et al., 2009) or “potential submarine canyons” (e.g., de Almeida et al., 2015), and which might represent forms at the early stage of development of a canyon (e.g., Nelson et al., 2011; Sanchez et al., 2012; Amblas et al., 2017 and references therein). The terms “canyon” and “gully” (or “gulley”) are not clearly distinguished in terms of size in the wider literature, and both terms are used when referring to smaller channelforms.

2.2.2 Study Parameters

2.2.2.1 Canyon Morphometrics

Canyon geomorphology has been assessed based on the following morphometric parameters: streamwise canyon length, maximum and average canyon width and depth, canyon sinuosity, average

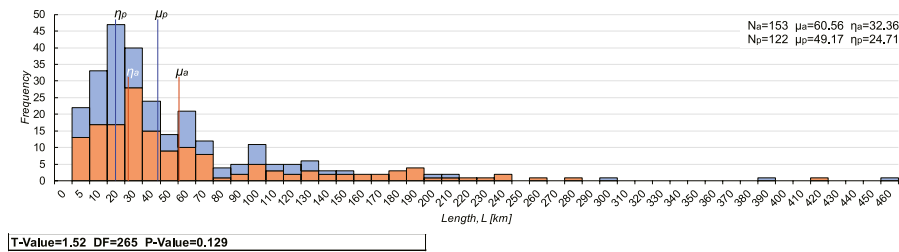
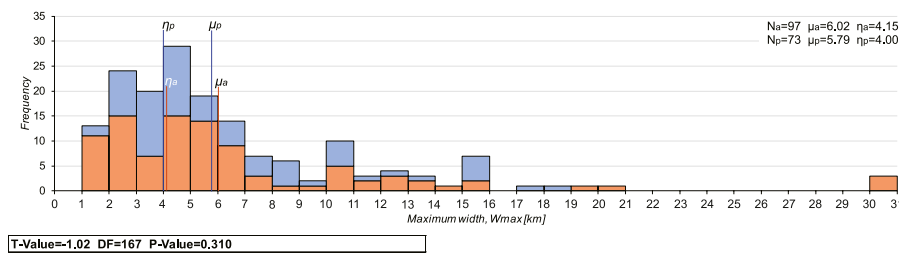
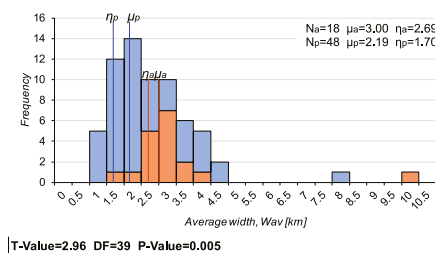
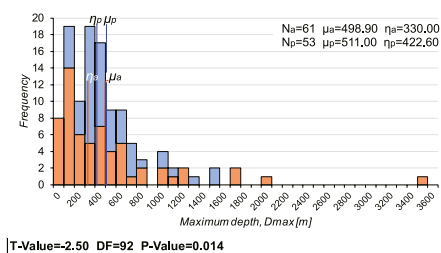
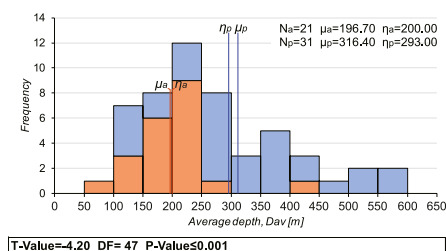
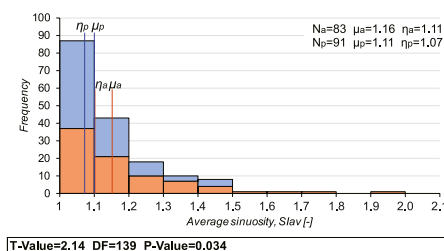
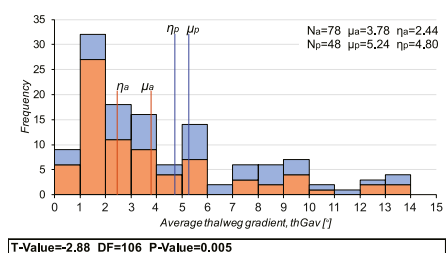
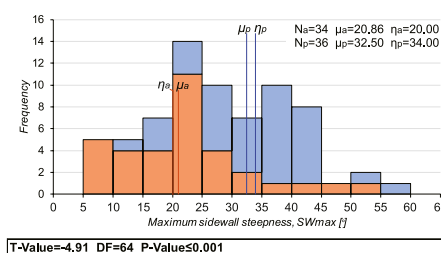
canyon thalweg gradient, and maximum canyon sidewall steepness. Values reported in textual form in the literature sources have only been considered where underpinned by observations on bathymetric surveys with full coverage of the canyon.

2.2.2.2 Physiographic Setting

The physiographic setting of the studied canyons has been characterized by means of attributes describing the bathymetry of the canyon apex and mouth, and the minimum distance of the canyon to the shoreline.

2.2.2.3 Source-to-Sink System Attributes

For canyons with a present or past sediment connection with a fluvial system, the length and average annual water discharge of the river have been recorded, as well as the size and maximum elevation of its catchment. In cases where canyons are linked with several rivers, the sum of the length of the individual rivers, the sum of their mean annual fluvial discharges and catchment areas, and the maximum

A Canyon length**B Maximum canyon width****C Average canyon width****D Maximum canyon depth****E Average canyon depth****F Average canyon sinuosity****G Average canyon thalweg gradient****H Maximum canyon sidewall steepness**

● active margin ● passive margin

FIGURE 2 | (A–H) Stacked histograms of morphometric values in studied canyons in active (a) vs. passive (p) margins. N , number of readings; μ = mean value; η = median value; DF, degrees of freedom.

elevation of the highest peak in the combined catchments have been recorded; this enables comparison with canyons fed by single fluvial systems. The geometric configuration of the continental margin at the

canyon location has been characterized in terms of average gradient of shelf and slope, and depth of shelf break and base of slope below present-day mean sea level.

2.2.2.4 Tectonic Setting

Canyon-hosting continental margins have been classified as active or passive following the classification by Harris et al. (2014b) (see **Figure 1A**). Active margins have been further differentiated based on the plate-boundary type with which they are associated, as convergent, transform and complex margins. The term “complex” is used here to refer to settings that involve more than one type of plate boundary and sense of motion (e.g., convergent margins with a transform component).

Definitions of the studied parameters are provided in **Table 2** and illustrated in **Figure 1B**.

2.3 Statistical Analyses

Different types of statistical analyses have been conducted to evaluate scaling relationships within submarine canyons, and between canyon geomorphology and attributes of its environment as a function of the tectonic setting.

- 1) *Descriptive statistics*: Frequency distributions of the studied canyon morphometric parameters have been summarized in terms of minimum, maximum, mean and median values, to reveal differences across margin types and active-margin plate boundary types.
- 2) *Hypothesis testing*: Hypothesis testing has been used to evaluate the statistical significance of differences in mean values of canyon morphometric parameters across classes of canyons for different tectonic settings and attributes of the source-to-sink system along active and passive margins. The Welch's two sample t-test (only referred to as “t-test” hereafter) has been used for comparisons between active and passive margins; Welch's ANOVA (only “ANOVA” hereafter) has been used for comparisons between convergent, transform and complex plate-boundary settings of active margins. The chosen tests allow testing of datasets with non-equal variances. For skewed frequency distributions, a logarithmic variable transformation has been conducted prior to the analyses. In these instances, where differences in mean values are reported in the text, they refer to the transformed variables and not the variables themselves. To enable a pairwise comparison of mean values between the three different active-margin settings, ANOVA has been complemented with Games-Howell post-hoc tests. Test statistics (t-test: *T*-value; ANOVA: *F*-value; Games-Howell: *T*-value), *p*-values and degrees of freedom (DF) are presented for all tests below each individual figure. To limit the number of false positives, the confidence interval has been set at 99%, with results where *p*-values are ≤ 0.01 treated as statistically significant.
- 3) *Correlation analysis*: Correlation analyses have been undertaken to assess pairwise scaling relationships between study parameters. Correlation coefficients quantify the sign and strength of correlation: the Pearson's correlation coefficient (*r*) describes linear relationships, whereas Spearman's rank correlation coefficient (*r_s*) describes monotonic relationships. The statistical significance of a correlation between two variables is indicated by *p*-values. A confidence interval of 99% is employed to indicate significant correlations.

2.4 Limitations of the Study

Data analyses and interpretations are subject to some limitations, including the following:

- 1) Metastudies might inherit unidentified data errors from the original literature data sources. This has been minimized by exclusively considering data from peer-reviewed publications and government agency sources.
- 2) Although care has been taken to avoid potential bias in the geographic distribution of case studies (see Matos et al., 2018), some geographic bias may exist for canyons from transform margins specifically, which are only considered for two regions (offshore California, Sea of Marmara), both located at temperate latitudes.
- 3) Some statistical analyses are based on datasets of limited size. This is the case for data on morphometric parameters of canyons from transform and complex settings, but also for pairs of variables whose correlation is evaluated. Correlation analyses are typically only considered and discussed where the number of observations (*N*) is equal to or larger than 15, making it explicit when $N < 15$.
- 4) Some relationships might represent covariance related to factors that were not assessed in this study, but which may influence canyon geomorphology, such as lithology (e.g., Smith et al., 2017) and rate and direction of relative sea-level changes (e.g., Covault et al., 2011b), among others.

3 RESULTS

3.1 Scaling Between Canyon Morphometric Parameters and the Tectonic Setting

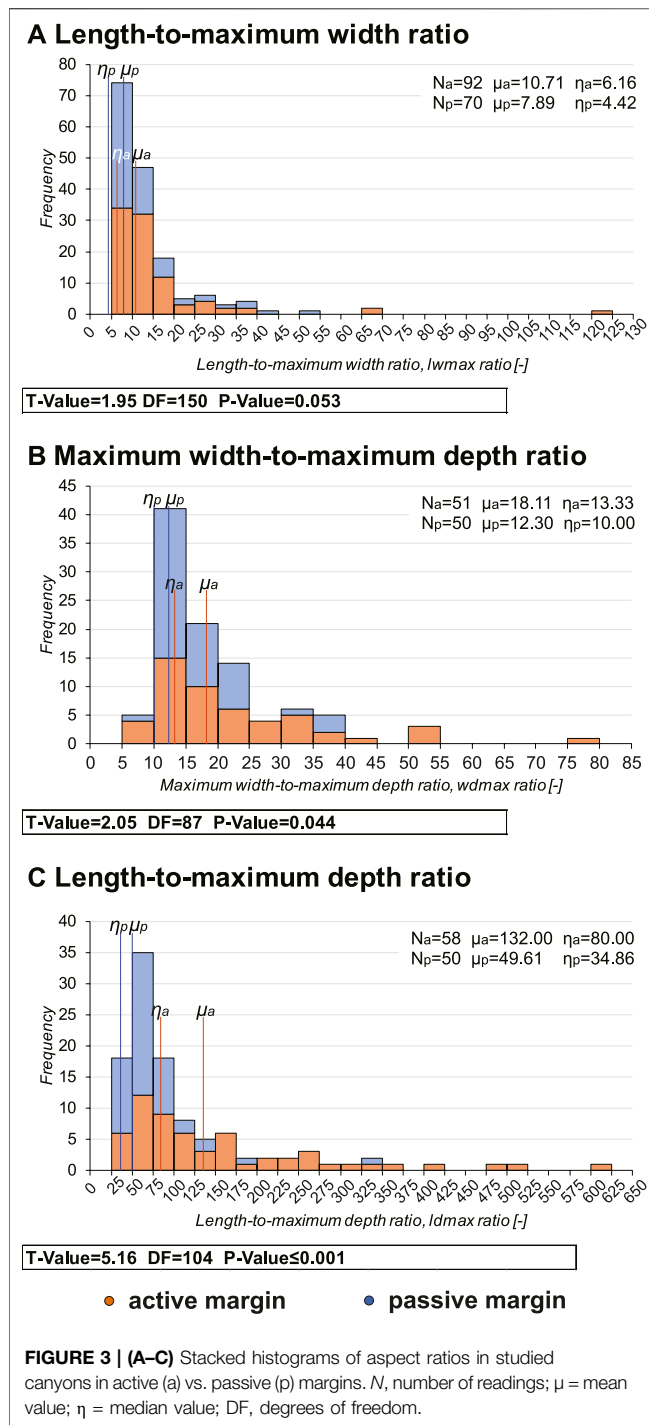
3.1.1 Continental-Margin Type

3.1.1.1 Canyon Dimensions and Aspect Ratios

Comparisons of the maximum and average dimensions of submarine canyons along tectonically active and passive margins demonstrate how canyon geometry varies between the two canyon groups.

Canyons in active margins are, on average, longer than those along passive margins—by a factor 1.23—but the difference in mean is not statistically significant. The longest canyon in the study is associated with a passive margin, but lengths of more than 400 km occur in both groups (**Figure 2A**). The deepest and widest canyons are seen on active margins. However, these values of depth and width represent individual outliers; ranges in maximum widths and depths are similar for the vast majority of studied canyons in both margin types, and their mean values are very similar (**Figures 2B,D**).

Canyons in the two margin types exhibit average widths within the same range. On average, mean canyon width is 1.37 times greater in studied active-margin examples, which show a narrower range in values than their counterparts from passive margins (**Figure 2C**). However, average-width data relating to canyons from an active-margin setting are associated with two case studies only, both from the South China Sea, whereas average width data for canyons in passive-margin settings are derived from examples from only three



geographic regions; therefore, these findings need to be corroborated by additional data in future research. In contrast, the mean average canyon depth is significantly greater for passive margins, by a factor 1.6. The maximum average depth of passive-margin canyons (594 m) is notably higher than that of active-margin ones (400 m) (Figure 2E).

Despite a greater range in aspect ratios of maximum canyon dimensions for examples from active margins, the mean values of

streamwise length-to-maximum width (lw_{max}) (Figure 3A) and maximum width-to-maximum depth (wd_{max}) (Figure 3B) ratios are similar for the two margin types. In contrast, a statistically significant difference in the mean value of length-to-maximum depth (ld_{max}) ratio (Figure 3C) is seen; this parameter is on average 2.66 times larger for active-margin canyons.

3.1.1.2 Average Canyon Sinuosity, Average Canyon Thalweg Gradient and Maximum Canyon Sidewall Steepness

The studied active-margin canyons show a greater range in average canyon sinuosity than passive-margin ones, but mean average canyon sinuosity is equally low in both margin types, ~1.1 (Figure 2F).

The range in average canyon thalweg gradient is very similar for the two margin types; thalwegs are, on average, steeper in the studied passive-margin examples to a statistically significant level (Figure 2G).

Canyons situated in passive settings have steeper canyon sidewalls compared to those in tectonically active settings. On average, the maximum sidewall gradient varies significantly between the two canyon groups, and is larger by a factor 1.56 for passive-margin examples (Figure 2H).

3.1.2 Active Margin Plate-Boundary Type

3.1.2.1 Canyon Dimensions and Aspect Ratios

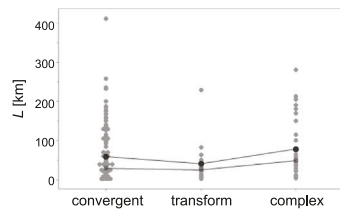
Canyons in convergent settings display the highest maximum values of length, maximum width and depth. Yet, on average, maximum canyon dimensions are greater in canyons located at complex plate boundaries (Figures 4A–C). The maximum width (Figure 4B) and depth (Figure 4C) of canyons from this type of setting are on average significantly higher than that of canyons in convergent settings, by a factor of 1.77 and 1.29, respectively.

The length (Figure 4A) and maximum width (Figure 4B) of canyons along transform plate boundaries are, on average, lower than those of canyons in the other two settings. The mean canyon length does not vary significantly across the three active-margin settings (Figure 4A). Instead, the mean maximum canyon width differs at a statistically significant level between transform and complex settings (Figure 4B), but this variable could only be constrained for twelve transform-setting canyons. Although data on maximum canyon depth for canyons along transform plate boundaries could only be derived for four examples, the data demonstrate that the depth range of canyons in such settings is similar to that of canyons in convergent settings, and larger than that of canyons from complex settings (Figure 4C).

Mean aspect ratios are similar across all three active-margin settings, but relatively few data are available for canyons in transform- and complex-margin settings. Aspect ratios based on maximum canyon dimensions for canyons in convergent settings are highly variable and display the greatest range in values (Figures 4G–I).

3.1.2.2 Average Canyon Sinuosity, the Average Canyon Thalweg Gradient and Maximum Canyon Sidewall Steepness

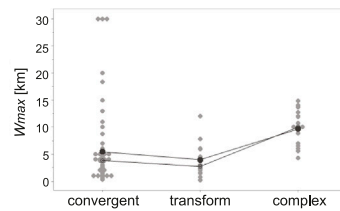
Frequency distributions of average canyon sinuosity for convergent, transform and complex plate boundaries exhibit similar mean and median values. Based on results of Welch's

A Canyon length

	N	min	mean	StDev	median	max
conv.	108	2,00	59,00	68,47	29,09	411,00
trans.	17	2,50	40,90	52,80	25,10	229,70
comp.	28	3,90	78,50	78,20	48,90	279,70

Welch's ANOVA
F-Value=1.01 DF Num=2 DF Den=36,7576 P-Value=0,373

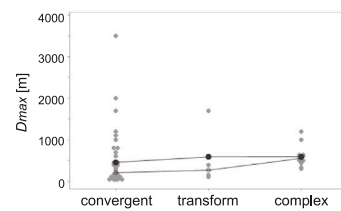
	Dmean	SE	T-Value	adjusted P-Value
conv. vs trans.	-0,100	0,119	-0,84	0,682
conv. vs comp.	0,118	0,119	1,00	0,584
comp. vs trans.	0,218	0,152	1,43	0,335

B Maximum canyon width

	N	min	mean	StDev	median	max
conv.	67	0,25	5,42	6,60	3,83	30,00
trans.	12	0,15	3,98	3,46	2,73	12,00
comp.	18	4,30	9,62	3,21	10,00	14,80

Welch's ANOVA
F-Value=25,72 DF Num=2 DF Den=27,0868 P-Value<0,001

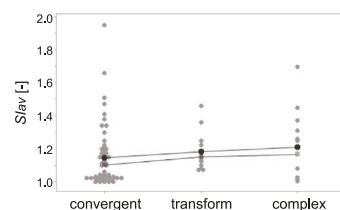
	Dmean	SE	T-Value	adjusted P-Value
conv. vs trans.	-0,124	0,158	-0,78	0,718
conv. vs comp.	0,4356	0,0647	6,73	<0,001
comp. vs trans.	0,560	0,154	3,64	0,008

C Maximum canyon depth

	N	min	mean	StDev	median	max
conv.	43	35,00	459,60	647,90	210,00	3500,00
trans.	4	110,00	588,00	752,00	270,00	1700,00
comp.	15	310,00	594,30	240,50	555,00	1200,00

Welch's ANOVA
F-Value=8,50 DF Num=2 DF Den=7,84612 P-Value=0,011

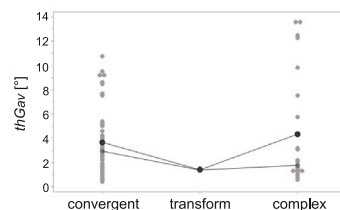
	Dmean	SE	T-Value	adjusted P-Value
conv. vs trans.	0,133	0,278	0,48	0,886
conv. vs comp.	0,3686	0,0865	4,26	<0,001
comp. vs trans.	0,236	0,271	0,87	0,690

D Average canyon sinuosity

	N	min	mean	StDev	median	max
conv.	58	1,00	1,14	0,18	1,10	1,95
trans.	13	1,07	1,18	0,12	1,15	1,46
comp.	12	1,00	1,21	0,22	1,17	1,70

Welch's ANOVA
F-Value=0,94 DF Num=2 DF Den=22,2231 P-Value=0,405

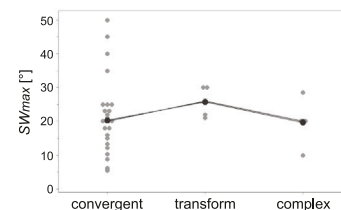
	Dmean	SE	T-Value	adjusted P-Value
conv. vs trans.	0,0163	0,0139	1,18	0,477
conv. vs comp.	0,0222	0,0231	0,96	0,613
comp. vs trans.	0,0059	0,0245	0,24	0,969

E Average canyon thalweg gradient

	N	min	mean	StDev	median	max
conv.	52	0,40	3,67	2,63	2,93	10,77
trans.	3	1,30	1,39	0,10	1,38	1,50
comp.	23	0,60	4,34	4,65	1,77	13,60

Welch's ANOVA
F-Value=21,66 DF Num=2 DF Den=37,9576 P-Value<0,001

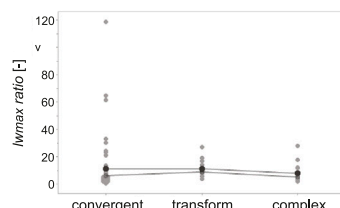
	Dmean	SE	T-Value	adjusted P-Value
conv. vs trans.	-0,3078	0,0498	-6,18	<0,001
conv. vs comp.	-0,039	0,103	-0,38	0,924
comp. vs trans.	0,2686	0,0943	2,85	0,024

F Maximum canyon sidewall steepness

	N	min	mean	StDev	median	max
conv.	26	5,40	20,30	11,75	20,00	50,00
trans.	4	21,00	25,75	4,92	26,00	30,00
comp.	4	10,00	19,63	7,56	20,00	28,50

Welch's ANOVA
F-Value=1,47 DF Num=2 DF Den=7,23013 P-Value=0,291

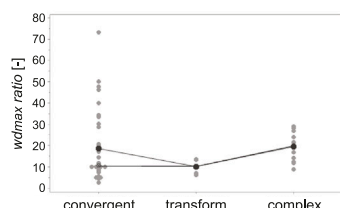
	Dmean	SE	T-Value	adjusted P-Value
conv. vs trans.	5,45	3,37	1,62	0,285
conv. vs comp.	-0,68	4,43	-0,15	0,987
comp. vs trans.	-6,12	4,51	-1,36	0,426

G Length-to-maximum width ratio

	N	min	mean	StDev	median	max
conv.	64	0,46	11,31	18,06	6,20	118,88
trans.	12	3,88	11,32	6,92	8,94	27,11
comp.	16	1,91	7,85	7,04	5,13	27,97

Welch's ANOVA
F-Value=2,33 DF Num=2 DF Den=28,0361 P-Value=0,116

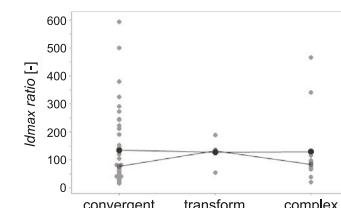
	Dmean	SE	T-Value	adjusted P-Value
conv. vs trans.	0,1683	0,0904	1,86	0,172
conv. vs comp.	-0,0525	0,0991	-0,53	0,857
comp. vs trans.	-0,221	0,112	-1,97	0,140

H Maximum width-to-maximum depth ratio

	N	min	mean	StDev	median	max
conv.	34	2,45	18,54	16,71	10,33	73,33
trans.	4	6,15	10,05	3,99	10,20	13,64
comp.	13	8,75	19,48	6,49	19,83	28,86

Welch's ANOVA
F-Value=4,53 DF Num=2 DF Den=9,57062 P-Value=0,041

	Dmean	SE	T-Value	adjusted P-Value
conv. vs trans.	-0,145	0,110	-1,32	0,434
conv. vs comp.	0,1451	0,0763	1,90	0,150
comp. vs trans.	0,290	0,101	2,87	0,083

I Length-to-maximum depth ratio

	N	min	mean	StDev	median	max
conv.	42	14,30	133,80	134,4	75,70	593,30
trans.	4	52,60	126,00	56,10	131,20	188,90
comp.	12	18,90	127,70	133,80	82,40	466,10

Welch's ANOVA
F-Value=0,47 DF Num=2 DF Den=9,60212 P-Value=0,641

	Dmean	SE	T-Value	adjusted P-Value
conv. vs trans.	0,136	0,137	1,00	0,609
conv. vs comp.	0,026	0,126	0,21	0,977
comp. vs trans.	-0,110	0,160	-0,69	0,776

FIGURE 4 | (A–I) Dot plots of morphometric values and aspect ratios for the studied canyons from active margins, classified on plate-boundary type. *N*, number of readings; min, minimum value; mean, mean value; SD, standard deviation; median, median value; max, maximum value. Results of Welch's ANOVA test: DF Num, degrees of freedom numerator; DF Den, degrees of freedom denominator. Games-Howell *post hoc* test: *D*_{mean}, difference of means; SE, standard error.

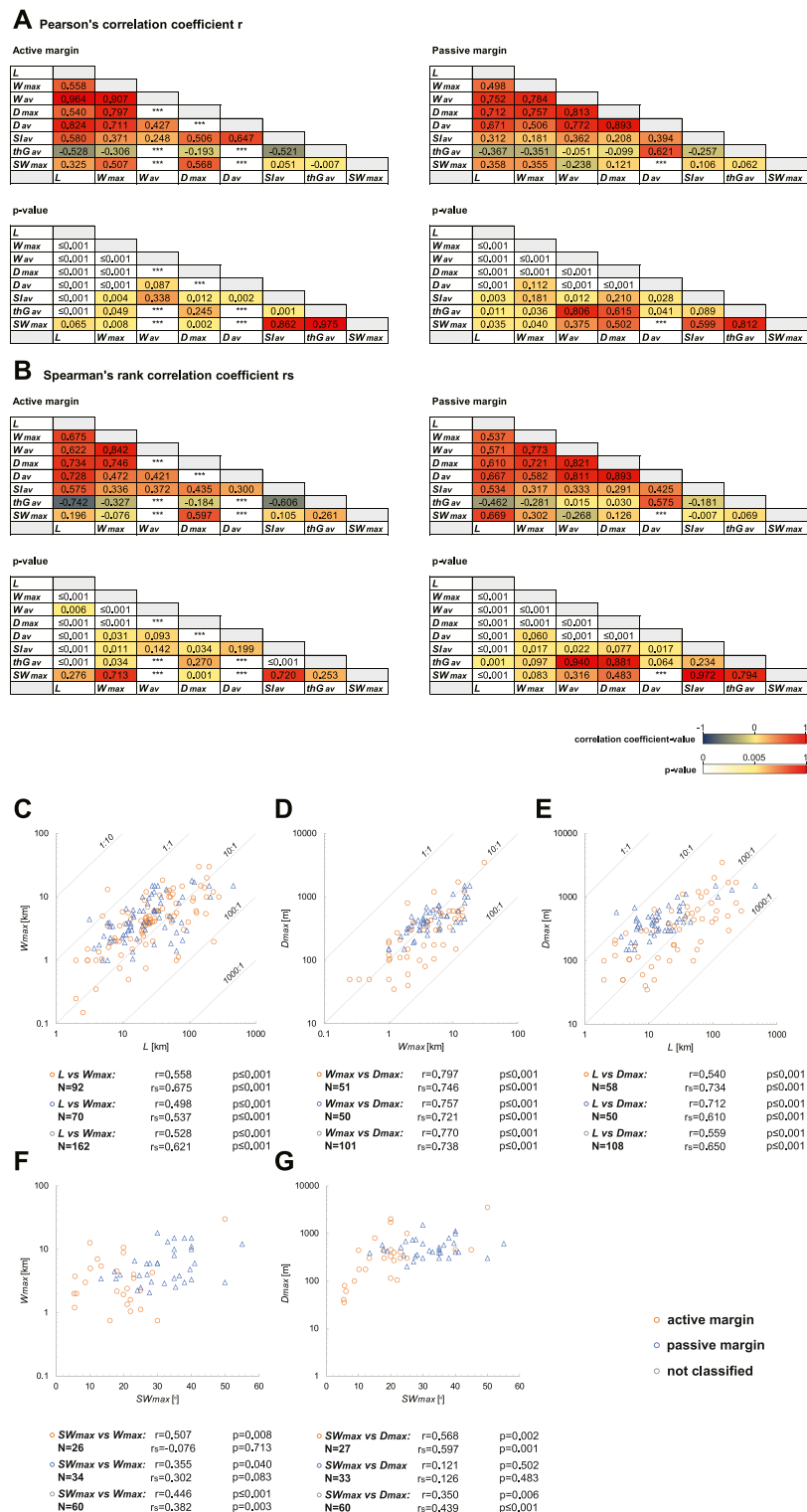


FIGURE 5 | (A–G) Results of the correlation analyses of canyon morphometric parameters with attributes of the physiographic setting at the canyon in active vs. passive margins. **(A,B)** Overview of results presented as heat maps. **(C–G)** Scatter plots of results. L , canyon length; W_{max} , maximum canyon width; W_{av} , average canyon width; D_{max} , maximum canyon depth; D_{av} , average canyon depth; Sl_{av} , average canyon sinuosity index; thG_{av} , average canyon thalweg gradient; SW_{max} , maximum canyon sidewall steepness; N , number of readings; r , Pearson's correlation coefficient; r_s , Spearman's rank correlation coefficient.

ANOVA and Games-Howell post-hoc tests, no significant differences are seen for average values across the different active-plate boundary types (Figure 4D).

Submarine canyons in complex settings exhibit a greater range in values of the average canyon thalweg gradient than those in convergent margins, but on average, the overall thalweg gradient is only 1.18 times steeper, and not significantly different (Figure 4E).

Canyons in convergent settings display a great range in maximum sidewall steepness, which is on average 20.3° . There exists insufficient data on margin steepness in canyons located in transform and complex settings to conduct meaningful analyses on these, but the data available demonstrate that canyons in these settings can reach gradients of 30.0° and 28.5° , respectively; these values are higher than those recorded in the majority of convergent-margin canyons (Figure 4F).

3.2 Scaling in Submarine Canyons in Active Versus Passive Margins

Results of the correlation analyses of canyon morphometric parameters with each other are presented as heat maps (Figures 5A,B). Additionally, correlations between maximum canyon dimensions and their aspect ratios (Figures 5C–E) and between maximum canyon sidewall steepness and maximum width (Figure 5F) and depth (Figure 5G) are also displayed as scatter plots.

3.2.1 Canyon Dimensions

Moderate and statistically significant scaling between maximum canyon dimensions is seen for submarine canyons along both active and passive margins (Figures 5A–E).

3.2.2 Maximum Canyon Sidewall Steepness vs. Maximum Canyon Width and Depth

A moderate linear correlation is seen between maximum sidewall steepness and maximum width in active-margin canyons, whereas the same parameters are weakly correlated in passive-margin canyons (Figure 5F).

Correlations of maximum sidewall steepness with maximum depth (Figure 5G) are weak and not significant for passive-margin examples. In contrast, maximum sidewall steepness displays moderate correlations with maximum depth in canyons along active margins, which are statistically significant.

3.3 Scaling Between Canyon Morphometric Parameters and Characteristics of Their Physiographic Setting in Active Versus Passive Margins

Results of the correlation analyses of canyon morphometric apex (Section 3.3.1) and mouth, and with the distance of the canyon to the nearest shoreline (Section 3.3.2) are presented as heat maps (Figures 6A,B). In addition, discussed scaling relationships are presented as scatter plots (Figures 7A–H).

3.3.1 Seafloor Depth at the Canyon Apex

In canyons from active and passive margins, the seafloor depth at the canyon apex correlates weakly with canyon length, maximum canyon width and average canyon thalweg gradient (Figures 6A,B). For average canyon width and seafloor depth at the canyon apex, moderate to modest negative correlations are seen in both active and passive margins, which are only significant for the latter (Figure 7A). A negative and significant moderate correlation between seafloor depth and maximum canyon depth is seen for passive-margin canyons; the corresponding relationship is instead weak for canyons along active margins (Figure 7B). Average canyon depth displays negative and modest correlations with the seafloor depth at the canyon apex along passive margins, but these are not significant for the chosen alpha value (Figure 7C).

Moderate inverse relationships between seafloor depth and both average canyon sinuosity (Figure 7D) and maximum canyon sidewall steepness (Figure 7E) exist in active margins, which are statistically significant. For canyons in passive margins, the correlations with apex depth are weak for both morphometric parameters (Figures 7D,E).

For the investigated aspect ratios, significant and moderate positive scaling exists with wd_{\max} ratios of canyons in active settings (Figure 7F). The remaining correlations in both margin types are all weak (Figures 6A,B).

3.3.2 Minimum Canyon-Shoreline Distance

Correlations between the shortest distance of the canyon to the shoreline with canyon morphometric parameters are weak for all maximum and average canyon dimensions for canyons from both margin types. Relationships with average canyon width in active-margin canyons were not assessed due to insufficient data for the statistical analyses (Figures 6A,B).

Average canyon sinuosity demonstrates modest negative scaling with the minimum distance of the canyon to the shoreline in active margins, whereas weak positive scaling is seen for passive margins; correlations are statistically significant for both margins (Figures 6A,B).

Inverse scaling between the minimum canyon-shoreline distance and the average canyon thalweg gradient is seen in canyons from both margin types. The correlation is weak for examples from active margins, whereas modest, linear negative correlation is seen for passive-margin settings (Figures 6A,B).

With decreasing distance of the canyon to the coastline, the maximum sidewall steepness in active-margin canyons tends to increase, but the strength of this correlation is moderate to modest. Correlation between the two parameters is very weak in examples from passive margins (Figure 7G).

Correlations of aspect ratios with minimum distance to the shoreline are weak for maximum canyon dimensions across both margin types (Figures 6A,B), with the exception of significant moderate and modest scaling displayed for wd_{\max} ratios in active-margin canyons (Figure 7H).

A Pearson's correlation coefficient r **Active margin**

<i>L</i>	-0.043	0.670	0.006
<i>W_{max}</i>	0.184	0.429	-0.195
<i>W_{av}</i>	-0.373	0.909	***
<i>D_{max}</i>	-0.292	0.774	-0.106
<i>D_{av}</i>	0.073	0.834	0.158
<i>Sl_{av}</i>	-0.223	0.636	-0.440
<i>thG_{av}</i>	0.197	-0.315	-0.124
<i>SW_{max}</i>	-0.622	0.387	-0.667
<i>lw_{max}</i>	-0.210	0.434	-0.188
<i>wd_{max}</i>	0.628	-0.230	0.552
<i>ld_{max}</i>	0.068	0.229	0.103
<i>SD_{min}</i>			
<i>SD_{max}</i>			
<i>Dis_{min}</i>			

Passive margin

<i>L</i>	-0.081	0.570	0.194
<i>W_{max}</i>	0.105	0.376	-0.023
<i>W_{av}</i>	-0.423	0.062	0.323
<i>D_{max}</i>	-0.218	0.615	0.107
<i>D_{av}</i>	-0.457	0.568	0.328
<i>Sl_{av}</i>	-0.090	0.450	0.331
<i>thG_{av}</i>	-0.304	-0.477	-0.459
<i>SW_{max}</i>	-0.017	0.339	0.081
<i>lw_{max}</i>	-0.102	0.629	0.244
<i>wd_{max}</i>	0.185	0.114	0.087
<i>ld_{max}</i>	-0.040	0.559	-0.114
<i>SD_{min}</i>			
<i>SD_{max}</i>			
<i>Dis_{min}</i>			

p-value

<i>L</i>	0.647	≤0.001	0.942
<i>W_{max}</i>	0.116	≤0.001	0.062
<i>W_{av}</i>	0.140	≤0.001	***
<i>D_{max}</i>	0.052	≤0.001	0.426
<i>D_{av}</i>	0.752	≤0.001	0.495
<i>Sl_{av}</i>	0.081	≤0.001	≤0.001
<i>thG_{av}</i>	0.135	0.010	0.319
<i>SW_{max}</i>	≤0.001	0.042	≤0.001
<i>lw_{max}</i>	0.076	≤0.001	0.080
<i>wd_{max}</i>	≤0.001	0.171	≤0.001
<i>ld_{max}</i>	0.659	0.135	0.454
<i>SD_{min}</i>			
<i>SD_{max}</i>			
<i>Dis_{min}</i>			

p-value

<i>L</i>	0.459	≤0.001	0.037
<i>W_{max}</i>	0.471	0.018	0.848
<i>W_{av}</i>	0.003	0.710	0.025
<i>D_{max}</i>	0.183	≤0.001	0.447
<i>D_{av}</i>	0.011	0.004	0.072
<i>Sl_{av}</i>	0.439	≤0.001	0.002
<i>thG_{av}</i>	0.042	0.003	0.002
<i>SW_{max}</i>	0.932	0.098	0.641
<i>lw_{max}</i>	0.496	≤0.001	0.048
<i>wd_{max}</i>	0.272	0.557	0.548
<i>ld_{max}</i>	0.812	0.002	0.430
<i>SD_{min}</i>			
<i>SD_{max}</i>			
<i>Dis_{min}</i>			

B Spearman's rank correlation coefficient r_s **Active margin**

<i>L</i>	-0.097	0.768	0.103
<i>W_{max}</i>	0.028	0.537	0.045
<i>W_{av}</i>	-0.432	0.115	***
<i>D_{max}</i>	-0.242	0.816	-0.088
<i>D_{av}</i>	0.079	0.632	0.286
<i>Sl_{av}</i>	-0.500	0.350	-0.464
<i>thG_{av}</i>	-0.087	-0.192	-0.148
<i>SW_{max}</i>	-0.610	0.208	-0.429
<i>lw_{max}</i>	-0.235	0.361	-0.115
<i>wd_{max}</i>	0.520	-0.084	0.424
<i>ld_{max}</i>	-0.023	0.200	0.132
<i>SD_{min}</i>			
<i>SD_{max}</i>			
<i>Dis_{min}</i>			

Passive margin

<i>L</i>	-0.198	0.590	0.169
<i>W_{max}</i>	-0.256	0.358	-0.216
<i>W_{av}</i>	-0.553	0.123	0.381
<i>D_{max}</i>	-0.614	0.398	-0.161
<i>D_{av}</i>	-0.412	0.609	0.250
<i>Sl_{av}</i>	-0.104	0.402	0.112
<i>thG_{av}</i>	-0.323	-0.501	-0.262
<i>SW_{max}</i>	0.091	0.549	-0.156
<i>lw_{max}</i>	-0.129	0.383	0.147
<i>wd_{max}</i>	0.115	-0.014	-0.001
<i>ld_{max}</i>	0.019	0.098	-0.208
<i>SD_{min}</i>			
<i>SD_{max}</i>			
<i>Dis_{min}</i>			

p-value

<i>L</i>	0.304	≤0.001	0.234
<i>W_{max}</i>	0.812	≤0.001	0.671
<i>W_{av}</i>	0.083	0.650	***
<i>D_{max}</i>	0.109	≤0.001	0.511
<i>D_{av}</i>	0.734	0.002	0.208
<i>Sl_{av}</i>	≤0.001	0.005	≤0.001
<i>thG_{av}</i>	0.513	0.122	0.231
<i>SW_{max}</i>	≤0.001	0.289	0.014
<i>lw_{max}</i>	0.047	0.003	0.284
<i>wd_{max}</i>	0.001	0.620	0.002
<i>ld_{max}</i>	0.880	0.192	0.337
<i>SD_{min}</i>			
<i>SD_{max}</i>			
<i>Dis_{min}</i>			

p-value

<i>L</i>	0.067	≤0.001	0.070
<i>W_{max}</i>	0.076	0.025	0.075
<i>W_{av}</i>	≤0.001	0.457	0.008
<i>D_{max}</i>	≤0.001	0.029	0.249
<i>D_{av}</i>	0.024	0.002	0.176
<i>Sl_{av}</i>	0.372	0.001	0.300
<i>thG_{av}</i>	0.031	0.002	0.086
<i>SW_{max}</i>	0.653	0.004	0.365
<i>lw_{max}</i>	0.386	0.018	0.239
<i>wd_{max}</i>	0.498	0.944	0.997
<i>ld_{max}</i>	0.909	0.612	0.146
<i>SD_{min}</i>			
<i>SD_{max}</i>			
<i>Dis_{min}</i>			

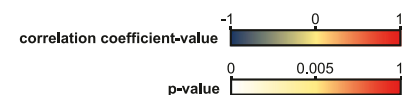


FIGURE 6 | (A,B) Results of the correlation analyses of canyon morphometric parameters and aspect ratios with parameters of the physiographic setting at the canyon in active vs. passive margins presented as heat maps. *L*, canyon length; *W_{max}*, maximum canyon width; *W_{av}*, average canyon width; *D_{max}*, maximum canyon depth; *D_{av}*, average canyon depth; *Sl_{av}*, average canyon sinuosity index; *thG_{av}*, average canyon thalweg gradient; *SW_{max}*, maximum canyon sidewall steepness; *lw_{max}*, length-to-maximum width ratio; *wd_{max}*, maximum width-to-maximum depth ratio; *ld_{max}*, length-to-maximum depth ratio; *SD_{min}*, seafloor depth at canyon apex; *SD_{max}*, seafloor depth at canyon mouth; *Dis_{min}*, minimum distance between canyon and shoreline; *** = correlations not reported due to small dataset size.

3.4 Scaling Between Canyon Morphometry and Characteristics of the Source-to-Sink System

Scaling relationships between canyon morphometric parameters and attributes of the terrestrial catchment (Figures 8A–L), shelf (Figures 8M–Q, 9A) and slope (Figures 8R, 9B) have been assessed.

3.4.1 Terrestrial Catchment (Fluvial System Length, Average Annual Fluvial Water Discharge, Catchment Size, Maximum Catchment Elevation)

For the studied canyons with a present and/or past sediment connection with one or several fluvial systems, scaling of canyon length and average canyon sinuosity with attributes of the terrestrial catchment in active and passive margins can be quantified. Statistical analyses on maximum canyon width are limited to active-margin settings in view of data coverage.

3.4.1.1 Fluvial System Length

Correlations of river length with canyon length are weak and not significant for canyons in passive margins. Along active margins, positive and moderate scaling of canyon length with fluvial

system length is demonstrated, which is statistically significant (Figure 8A). In contrast, maximum width correlates weakly with river length in canyons along active margins, but relatively strongly for canyons located in passive-margin settings. However, findings for the latter group are based on thirteen observations only (Figure 8E). For average canyon sinuosity, the correlations are weak and not significant for any margin type (Figure 8I).

3.4.1.2 Average Annual Fluvial Water Discharge

The average annual water discharge of the fluvial system displays positive, moderate monotonic correlations with canyon length in canyons of both margin types, as well as overall in the entire dataset; these relationships are statistically significant (Figure 8B). Correlations of average annual fluvial discharge and maximum width are weak in active-margin canyons (Figure 8F). Positive and monotonic correlations of average canyon sinuosity with this catchment attribute exist for active and passive margins, but these are respectively moderate and weak, and neither is statistically significant (Figure 8J).

3.4.1.3 Catchment Size

Scaling of canyon length with catchment size is weak for canyons from passive margins (Figure 8C). Moderate, positive monotonic

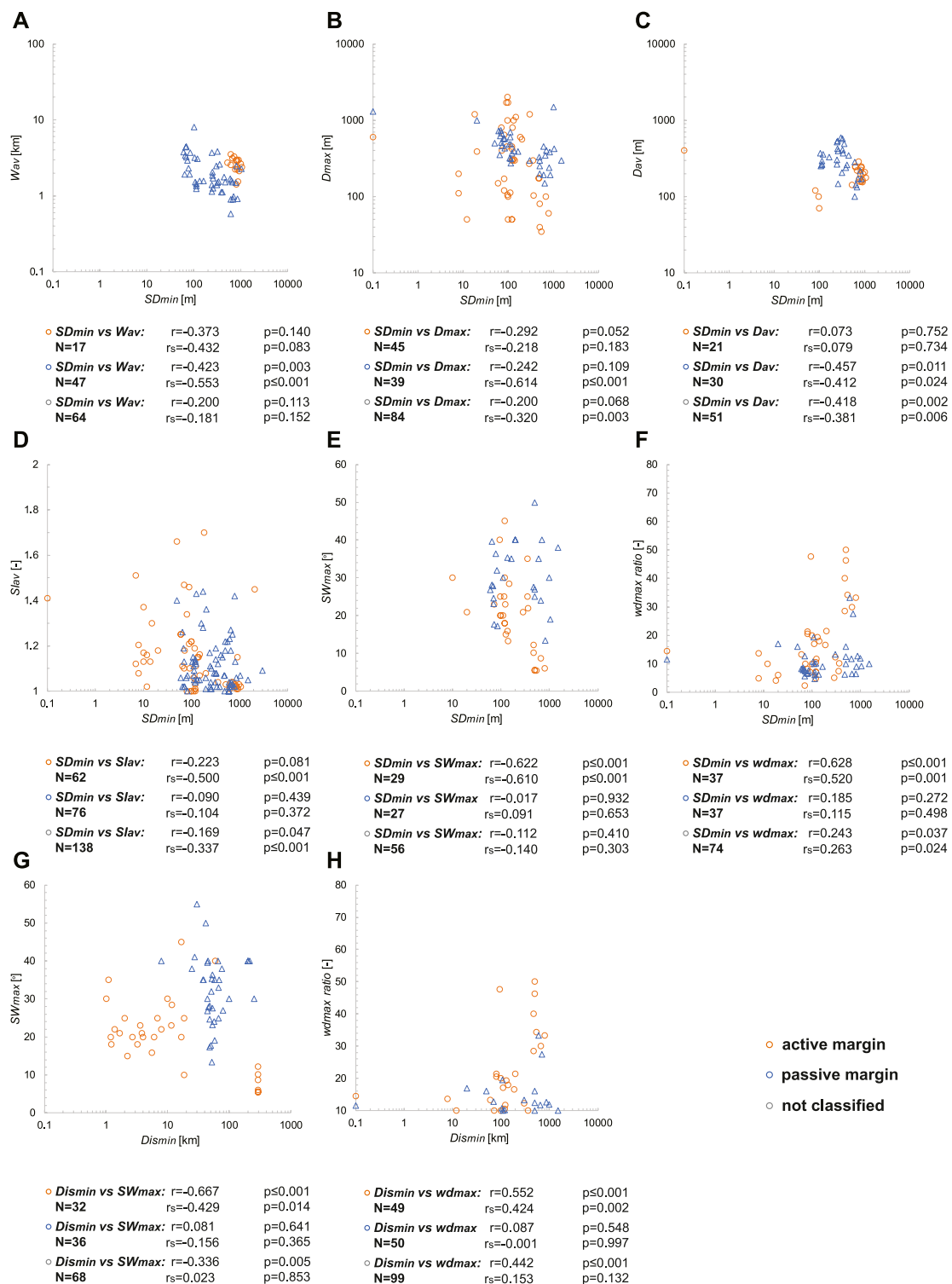


FIGURE 7 | (A–H) Scatterplots of attributes of the canyon-physiographic setting with canyon morphometric parameters for submarine canyons of the study in active vs. passive margins. W_{av} , average canyon width; D_{max} , maximum canyon depth; D_{av} , average canyon depth; Sl_{av} , average canyon sinuosity index; SW_{max} , maximum canyon sidewall steepness; wd_{max} ratio, maximum width-to-maximum depth ratio; SD_{min} , minimum water depth at the canyon apex; Dis_{min} , minimum canyon distance to the shoreline; N , number of readings; r , Pearson's correlation coefficient; r_s , Spearman's rank correlation coefficient.

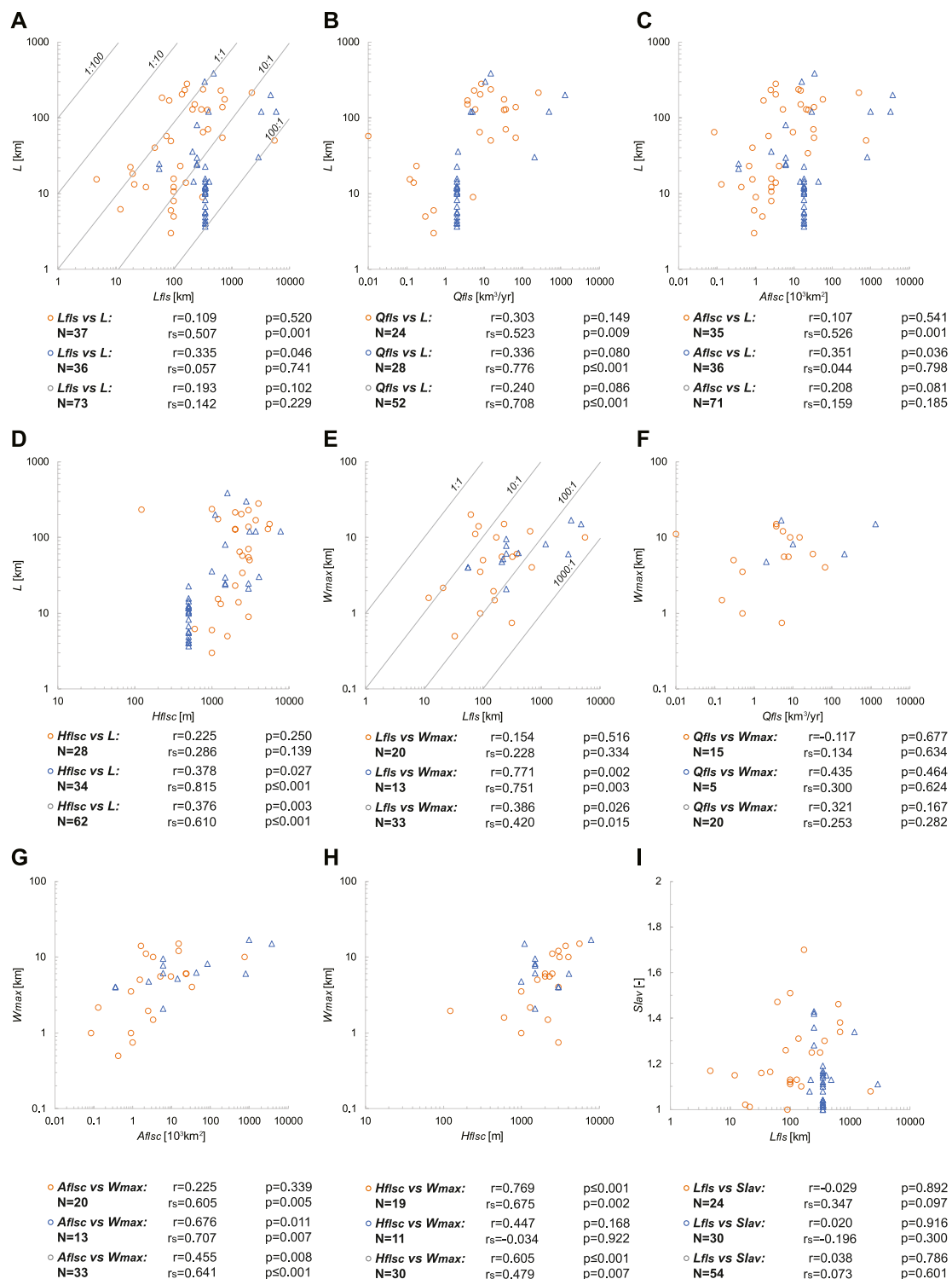


FIGURE 8 | (A–I) Scatterplots of attributes of the terrestrial catchment, shelf and slope with canyon morphometric parameters for submarine canyons of the study in active vs. passive margins. L , canyon length; W_{max} , maximum canyon width; S_{lav} , average canyon sinuosity index; SW_{max} , maximum canyon sidewall steepness; L_{fls} , fluvial system length; Q_{fls} , average annual fluvial discharge; A_{flsc} , catchment size; H_{flsc} , Maximum catchment elevation; D_{sh} , shelf-break depth; W_{sh} , slope width. N , number of readings; r , Pearson's correlation coefficient; r_s , Spearman's rank correlation coefficient.

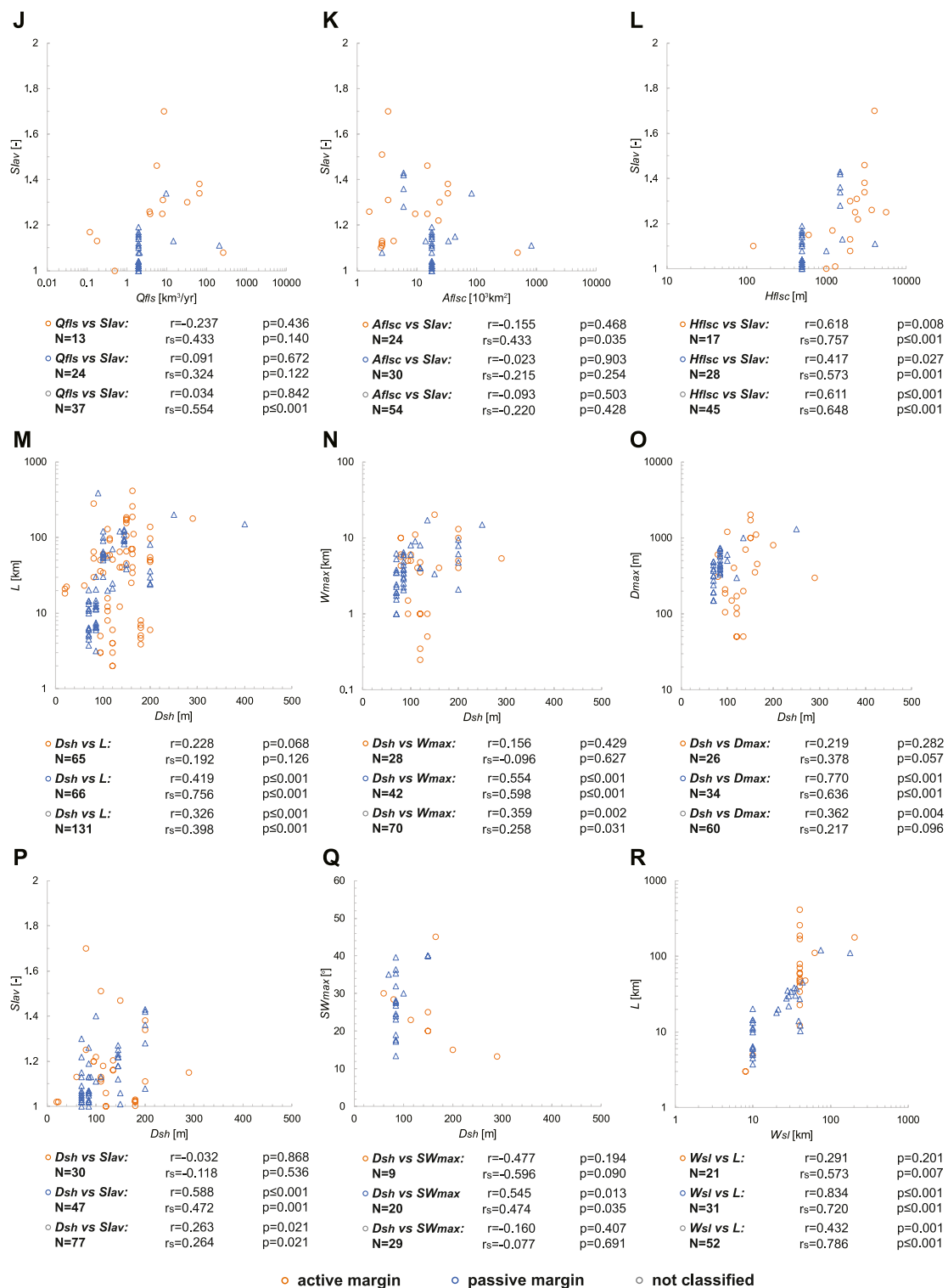


FIGURE 8 | (Continued)

correlations exist for the length (Figure 8C) and maximum width (Figure 8G) in canyons associated with active margins. No correlation is seen between average canyon sinuosity and

catchment area for passive-margin canyons; a modest, positive monotonic correlation is seen for active-margin settings, but this is not significant (Figure 8K).

A Shelf

Pearson's correlation coefficient r

Active margin

L	0.227	0.228	-0.414
W _{max}	0.066	0.156	-0.422
D _{max}	0.227	0.219	-0.407
Slav	-0.368	-0.032	0.029
thG _{av}	-0.179	0.210	0.180
SW _{max}	0.373	-0.477	-0.418
lw _{max}	-0.188	0.207	0.059
wd _{max}	-0.033	-0.066	-0.095
ld _{max}	-0.101	0.404	-0.092
W _{sh}		D _{sh}	G _{sh}

Passive margin

L	0.245	0.419	0.083
W _{max}	0.133	0.554	0.283
D _{max}	0.198	0.770	-0.193
Slav	0.260	0.588	0.645
thG _{av}	-0.490	-0.343	-0.178
SW _{max}	0.533	0.545	-0.466
lw _{max}	0.267	0.515	0.490
wd _{max}	0.413	0.285	-0.481
ld _{max}	0.059	0.838	-0.674
W _{sh}		D _{sh}	G _{sh}

Spearman's rank correlation coefficient rs

Active margin

L	0.365	0.192	-0.537
W _{max}	0.339	-0.096	0.283
D _{max}	0.525	0.378	-0.525
Slav	-0.344	-0.118	0.089
thG _{av}	-0.339	0.238	0.298
SW _{max}	0.288	-0.596	-0.370
lw _{max}	0.013	0.165	-0.086
wd _{max}	0.093	-0.100	-0.196
ld _{max}	0.270	0.236	-0.171
W _{sh}		D _{sh}	G _{sh}

Passive margin

L	0.356	0.756	-0.168
W _{max}	-0.052	0.598	0.192
D _{max}	0.202	0.636	0.205
Slav	0.049	0.472	0.036
thG _{av}	-0.302	-0.311	0.200
SW _{max}	0.322	0.474	-0.333
lw _{max}	0.325	0.377	-0.139
wd _{max}	0.105	0.234	-0.304
ld _{max}	-0.080	0.041	-0.281
W _{sh}		D _{sh}	G _{sh}

p-value

L	0.014	0.068	0.001
W _{max}	0.572	0.429	0.025
D _{max}	0.149	0.282	0.035
Slav	0.001	0.868	0.880
thG _{av}	0.153	0.171	0.242
SW _{max}	0.087	0.194	0.263
lw _{max}	0.115	0.299	0.769
wd _{max}	0.857	0.796	0.689
ld _{max}	0.535	0.045	0.655
W _{sh}		D _{sh}	G _{sh}

p-value

L	0.016	≤0.001	0.521
W _{max}	0.353	≤0.001	0.073
D _{max}	0.240	≤0.001	0.281
Slav	0.022	≤0.001	≤0.001
thG _{av}	0.001	0.028	0.265
SW _{max}	0.013	0.013	0.039
lw _{max}	0.066	0.001	0.002
wd _{max}	0.014	0.107	0.005
ld _{max}	0.735	≤0.001	≤0.001
W _{sh}		D _{sh}	G _{sh}

p-value

L	≤0.001	0.126	≤0.001
W _{max}	0.003	0.627	0.073
D _{max}	≤0.001	0.057	0.005
Slav	0.002	0.536	0.640
thG _{av}	0.006	0.119	0.050
SW _{max}	0.193	0.090	0.327
lw _{max}	0.913	0.409	0.671
wd _{max}	0.606	0.692	0.408
ld _{max}	0.092	0.256	0.403
W _{sh}		D _{sh}	G _{sh}

p-value

L	≤0.001	≤0.001	0.192
W _{max}	0.715	≤0.001	0.228
D _{max}	0.231	≤0.001	0.252
Slav	0.670	0.001	0.810
thG _{av}	0.044	0.047	0.209
SW _{max}	0.154	0.035	0.152
lw _{max}	0.024	0.016	0.405
wd _{max}	0.550	0.190	0.091
ld _{max}	0.647	0.819	0.119
W _{sh}		D _{sh}	G _{sh}

B Slope

Pearson's correlation coefficient r

Active margin

L	0.291	0.305	0.221
W _{max}	0.018	0.342	0.289
D _{max}	-0.034	0.655	0.566
Slav	***	0.244	0.201
thG _{av}	-0.262	-0.066	-0.018
SW _{max}	***	0.222	0.424
lw _{max}	0.970	0.438	-0.085
wd _{max}	-0.038	-0.203	-0.647
ld _{max}	0.960	0.282	-0.530
W _{sl}		D _{sl}	G _{sl}

Passive margin

L	0.834	-0.034	-0.327
W _{max}	0.639	-0.428	-0.707
D _{max}	0.730	0.150	-0.740
Slav	-0.383	0.328	-0.308
thG _{av}	-0.341	0.279	0.638
SW _{max}	-0.271	-0.344	0.149
lw _{max}	0.333	0.490	0.089
wd _{max}	0.170	-0.183	-0.381
ld _{max}	0.512	0.259	-0.690
W _{sl}		D _{sl}	G _{sl}

Spearman's rank correlation coefficient rs

Active margin

L	0.573	0.381	0.309
W _{max}	0.236	0.244	0.319
D _{max}	0.285	0.535	0.652
Slav	***	0.170	0.423
thG _{av}	-0.171	0.161	0.044
SW _{max}	***	0.118	0.725
lw _{max}	0.736	0.402	-0.091
wd _{max}	0.204	-0.082	-0.675
ld _{max}	0.801	0.214	-0.644
W _{sl}		D _{sl}	G _{sl}

Passive margin

L	0.720	0.152	-0.578
W _{max}	0.671	-0.372	-0.700
D _{max}	0.446	0.111	-0.553
Slav	-0.420	0.344	-0.325
thG _{av}	-0.397	0.295	0.742
SW _{max}	-0.402	-0.598	0.020
lw _{max}	0.153	0.486	0.017
wd _{max}	0.564	-0.129	-0.569
ld _{max}	0.736	0.533	-0.707
W _{sl}		D _{sl}	G _{sl}

p-value

L	0.201	0.005	0.166
W _{max}	0.956	0.016	0.152
D _{max}	0.911	≤0.001	0.004
Slav	***	0.157	0.511
thG _{av}	0.278	0.623	0.930
SW _{max}	***	0.360	0.170
lw _{max}	≤0.001	0.003	0.686
wd _{max}	0.912	0.256	0.002
ld _{max}	≤0.001	0.091	0.009
W _{sl}		D _{sl}	G _{sl}

p-value

L	≤0.001	0.788	0.030
W _{max}	≤0.001	0.005	≤0.001
D _{max}	≤0.001	0.517	≤0.001
Slav	0.087	0.036	0.081
thG _{av}	0.278	0.209	0.001
SW _{max}	0.293	0.149	0.567
lw _{max}	0.072	0.002	0.626
wd _{max}	0.368	0.441	0.038
ld _{max}	0.003	0.284	≤0.001
W _{sl}		D _{sl}	G _{sl}

p-value

L	0.007	≤0.001	0.049
W _{max}	0.460	0.091	0.112
D _{max}	0.346	≤0.001	0.001
Slav	***	0.329	0.150
thG _{av}	0.484	0.227	0.831
SW _{max}	***	0.629	0.008
lw _{max}	0.010	0.006	0.666
wd _{max}	0.548	0.650	0.001
ld _{max}	0.002	0.203	0.001
W _{sl}		D _{sl}	G _{sl}

p-value

L	≤0.001	0.228	≤0.001
W _{max}	≤0.001	0.017	≤0.001
D _{max}	0.012	0.632	0.001
Slav	0.058	0.028	0.065
thG _{av}	0.202	0.183	≤0.001
SW _{max}	0.109	0.007	0.938
lw _{max}	0.419	0.002	0.928
wd _{max}	0.001	0.588	0.001
ld _{max}	≤0.001	0.019	≤0.001
W _{sl}		D _{sl}	G _{sl}

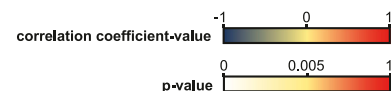


FIGURE 9 | (A,B) Results of the correlation analyses of canyon morphometric parameters with attributes of the **(A)** shelf and **(B)** slope at the canyon in active vs. passive margins presented as heat maps. L, canyon length; W_{max}, maximum canyon width; D_{max}, maximum canyon depth; Slav, average canyon sinuosity index; thG_{av}, average canyon thalweg gradient; SW_{max}, maximum canyon sidewall steepness; lw_{max}, length-to-maximum width ratio; wd_{max}, maximum width-to-maximum depth ratio; ld_{max}, length-to-maximum depth ratio; W_{sh}, shelf width; D_{sh}, shelf-break depth; G_{sh}, average shelf gradient; W_{sl}, slope width; D_{sl}, slope-break depth; G_{sl}, average slope gradient; *** = correlations not reported due to small dataset size.

3.4.1.4 Maximum Catchment Elevation

The length of submarine canyons scales positively with the maximum catchment elevation of associated fluvial systems on passive margins. A corresponding relationship is absent for active

margins (Figure 8D), whereas maximum canyon width shares positive and moderate correlations with maximum catchment elevation in active-margin canyons (Figure 8H). Moderate, significant correlations are seen between average canyon

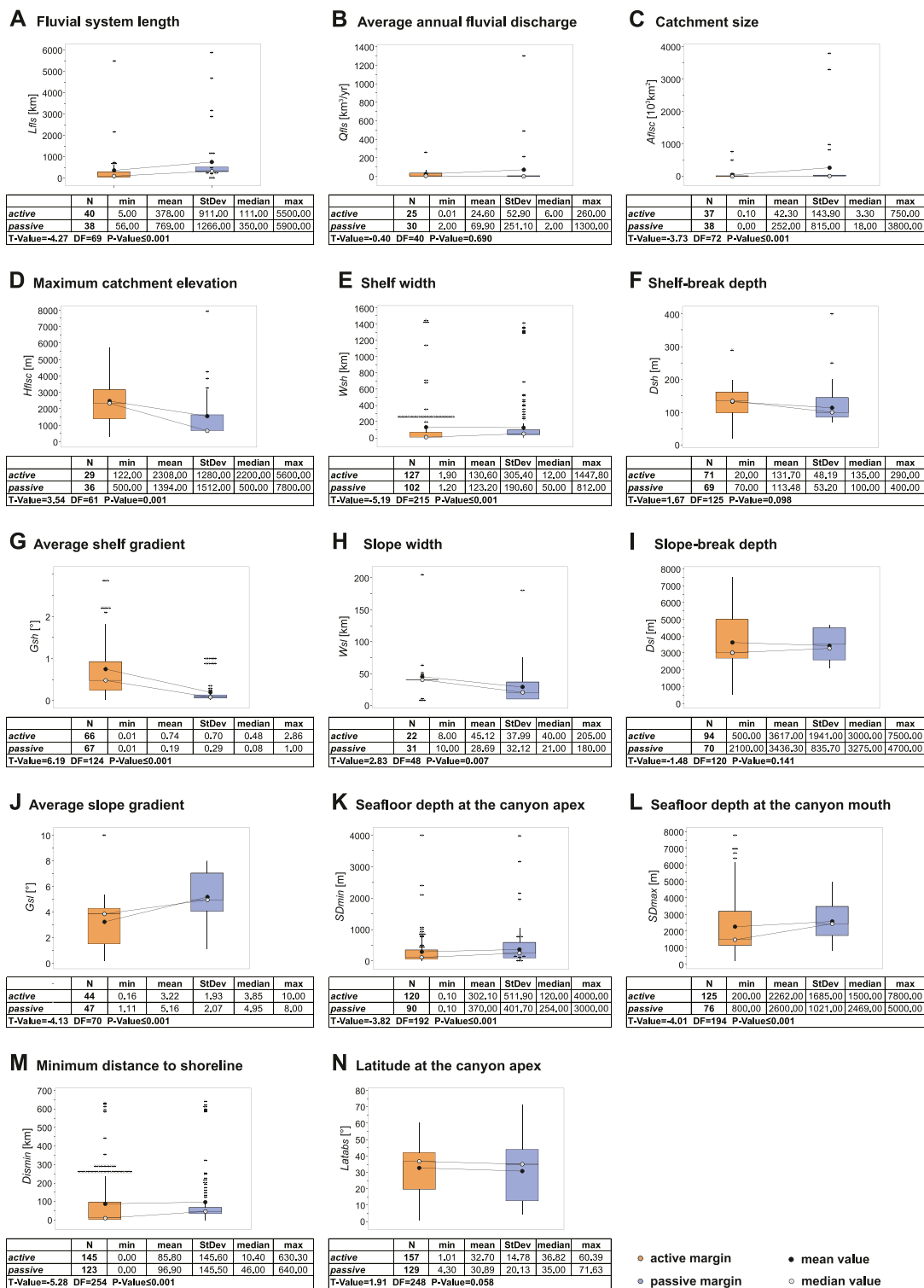


FIGURE 10 | (A–N) Boxplots of frequency distributions of attributes of source-to-sink systems and of the canyon-physiographic setting linked to submarine canyons of active and passive margins. *N*, number of readings; min, minimum value; mean, mean value; SD, standard deviation; median, median value; max, maximum value; DF, degrees of freedom.

A Active margin

Pearson's correlation coefficient r

Q_{fls}	0.339								
A_{flsc}	0.966	0.505							
H_{flsc}	0.146	0.010	0.081						
W_{sh}	0.935	0.983	0.979	0.028					
D_{sh}	0.460	0.752	0.479	0.143	0.277				
G_{sh}	-0.342	-0.463	-0.470	-0.267	-0.397	-0.198			
W_{sl}	***	***	***	***	-0.147	0.913	-0.345		
D_{sl}	0.125	0.200	0.232	-0.078	-0.104	0.077	-0.001	0.788	
G_{sl}	0.082	0.015	0.314	0.161	0.397	-0.167	-0.532	-0.660	-0.542
L_{fls}	Q_{fls}	A_{flsc}	H_{flsc}	W_{sh}	D_{sh}	G_{sh}	W_{sl}	D_{sl}	

p-value

Q_{fls}	0.097								
A_{flsc}	≤0.001	0.010							
H_{flsc}	0.457	0.962	0.681						
W_{sh}	≤0.001	≤0.001	≤0.001	0.895					
D_{sh}	0.021	0.002	0.021	0.612	0.027				
G_{sh}	0.111	0.151	0.032	0.378	0.001	0.117			
W_{sl}	***	***	***	***	≤0.001	0.226			
D_{sl}	0.579	0.474	0.340	0.759	0.399	0.593	0.895	≤0.001	
G_{sl}	0.861	0.880	0.411	0.781	0.037	0.405	0.006	0.001	0.004
L_{fls}	Q_{fls}	A_{flsc}	H_{flsc}	W_{sh}	D_{sh}	G_{sh}	W_{sl}	D_{sl}	

Spearman's rank correlation coefficient r_s

Q_{fls}	0.851								
A_{flsc}	0.924	0.835							
H_{flsc}	0.404	0.303	0.404						
W_{sh}	0.687	0.680	0.678	0.322					
D_{sh}	0.444	0.659	0.288	0.170	0.707				
G_{sh}	-0.316	-0.783	-0.772	-0.382	-0.809	-0.301			
W_{sl}	***	***	***	***	0.154	0.955	-0.249		
D_{sl}	0.039	0.283	0.246	-0.036	0.058	0.187	-0.155	0.571	
G_{sl}	-0.147	0.158	0.026	0.353	0.600	0.017	-0.700	-0.206	-0.084
L_{fls}	Q_{fls}	A_{flsc}	H_{flsc}	W_{sh}	D_{sh}	G_{sh}	W_{sl}	D_{sl}	

p-value

Q_{fls}	≤0.001								
A_{flsc}	≤0.001	≤0.001							
H_{flsc}	0.033	0.141	0.033						
W_{sh}	≤0.001	0.001	≤0.001	0.116					
D_{sh}	0.026	0.010	0.182	0.545	≤0.001				
G_{sh}	0.141	0.004	≤0.001	0.197	≤0.001	0.016			
W_{sl}	***	***	***	***	0.585	≤0.001	0.390		
D_{sl}	0.864	0.306	0.309	0.888	0.636	0.194	0.299	0.007	
G_{sl}	0.753	0.800	0.948	0.493	0.001	0.934	≤0.001	0.357	0.676
L_{fls}	Q_{fls}	A_{flsc}	H_{flsc}	W_{sh}	D_{sh}	G_{sh}	W_{sl}	D_{sl}	

B Passive margin

Pearson's correlation coefficient r

Q_{fls}	0.785								
A_{flsc}	0.939	0.917							
H_{flsc}	0.525	0.137	0.334						
W_{sh}	0.547	0.252	0.396	0.469					
D_{sh}	0.244	0.740	0.424	-0.516	0.352				
G_{sh}	-0.431	-0.323	-0.403	-0.524	-0.319	0.506	***		
W_{sl}	***	***	***	***	***	***	***	***	
D_{sl}	-0.479	-0.449	-0.526	-0.559	-0.352	0.477	0.901	0.881	
G_{sl}	-0.365	***	-0.378	***	-0.780	***	0.272	-0.864	0.261
L_{fls}	Q_{fls}	A_{flsc}	H_{flsc}	W_{sh}	D_{sh}	G_{sh}	W_{sl}	D_{sl}	

p-value

Q_{fls}	≤0.001								
A_{flsc}	≤0.001	≤0.001							
H_{flsc}	0.001	0.472	0.047						
W_{sh}	≤0.001	0.187	0.015	0.004					
D_{sh}	0.400	0.093	0.131	0.086	0.004				
G_{sh}	0.141	0.479	0.172	0.098	0.009	≤0.001			
W_{sl}	***	***	***	***	***	***	***	***	
D_{sl}	0.115	0.372	0.079	0.059	0.018	0.005	≤0.001	≤0.001	
G_{sl}	0.002	***	0.001	***	≤0.001	***	0.161	≤0.001	0.149
L_{fls}	Q_{fls}	A_{flsc}	H_{flsc}	W_{sh}	D_{sh}	G_{sh}	W_{sl}	D_{sl}	

Spearman's rank correlation coefficient r_s

Q_{fls}	0.654								
A_{flsc}	0.997	0.654							
H_{flsc}	0.103	0.954	0.099						
W_{sh}	0.638	0.591	0.666	0.084					
D_{sh}	-0.002	0.058	-0.183	-0.772	0.182				
G_{sh}	-0.366	-0.587	-0.432	-0.428	-0.327	-0.109			
W_{sl}	***	***	***	***	***	***	***	***	
D_{sl}	-0.372	-0.647	-0.372	-0.817	-0.421	0.587	0.406	0.522	
G_{sl}	-0.896	***	-0.896	***	-0.509	***	0.512	-0.924	0.181
L_{fls}	Q_{fls}	A_{flsc}	H_{flsc}	W_{sh}	D_{sh}	G_{sh}	W_{sl}	D_{sl}	

p-value

Q_{fls}	≤0.001								
A_{flsc}	≤0.001	≤0.001							
H_{flsc}	0.552	≤0.001	0.566						
W_{sh}	≤0.001	0.001	≤0.001	0.630					
D_{sh}	0.994	0.913	0.532	0.003	0.146				
G_{sh}	0.218	0.166	0.141	0.189	≤0.001	0.396			
W_{sl}	***	***	***	***	***	***	***	***	
D_{sl}	0.234	0.165	0.234	0.001	0.004	≤0.001	0.023	0.032	
G_{sl}	0.016	***	0.016	***	0.004	***	0.005	≤0.001	0.322
L_{fls}	Q_{fls}	A_{flsc}	H_{flsc}	W_{sh}	D_{sh}	G_{sh}	W_{sl}	D_{sl}	

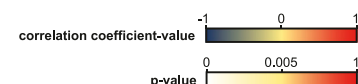


FIGURE 11 | (A,B) Results of the correlation analyses of attributes of the source-to-sink system in active vs. passive margins presented as heat maps. L_{fls} , fluvial system length; Q_{fls} , average annual fluvial discharge; A_{flsc} , catchment size; H_{flsc} , maximum catchment elevation; W_{sh} , shelf width; D_{sh} , shelf-break depth; G_{sh} , average shelf gradient; W_{sl} , slope width; D_{sl} , slope-break depth; G_{sl} , average slope gradient; *** = correlations not reported due to small dataset size.

sinuosity and maximum catchment elevation for both margin types (Figure 8L).

3.4.2 Shelf-Break Depth

Correlations of shelf-break depth at the canyon location with attributes of canyon geomorphology are weak and not significant for canyons in active-margin settings; in the studied canyons from passive margins, instead, maximum canyon dimensions (Figures 8M–O), average canyon sinuosity (Figure 8P) and maximum canyon sidewall steepness (Figure 8Q) correlate moderately or strongly with the shelf-break depth (Figure 9A).

3.4.3 Slope Width

Canyon length increases with slope width in active and passive margins; the strength of the relationship is moderate in the former and strong in the latter (Figure 8R). Maximum canyon width and depth do not correlate with the slope width in active margins, but both variables show moderate correlation with the width of

passive-margin slopes. However, more data are needed to support the findings for active-margin canyons (Figure 9B).

3.5 Characterization of Canyon Source-to-Sink System and Physiographic Setting by Tectonic Setting

Analyses have been undertaken of 1) attributes of the S2S system and of the physiographic setting, and of how these vary with the margin type (Section 3.5.1), and of 2) scaling between attributes of the S2S systems in active and passive margins (Section 3.5.2). This has been done for the following reasons: 1) to assess commonalities and differences in characteristics of the two margin types, which can be used to refine existing S2S system models; and 2) to aid recognition of covariance between variables that may be related to the studied canyon morphometric parameters, rendered necessary by data gaps that prevent the application of multivariate techniques.

3.5.1 Attributes of the Canyon Geological Contexts and Their Variations Across Margin Types

Two-sample t-tests undertaken on frequency distributions of the attributes describing canyon terrestrial catchments, continental shelves and slopes (**Figures 10A–N**) demonstrate that significant differences in mean values of the studied variables are seen for all investigated attributes except for average annual fluvial discharge (**Figure 10B**), shelf-break depth (**Figure 10F**), slope-break depth (**Figure 10I**) and latitude at the canyon apex (**Figure 10N**).

On average, the length (**Figure 10A**), average annual water discharge (**Figure 10B**) and catchment size (**Figure 10C**) of fluvial systems supplying sediment to the studied canyons are each greater in terrestrial catchments along passive margins. Although the greatest maximum catchment elevation recorded in the study occurs in a passive-margin drainage basin, terrestrial catchments associated with active margins tend to be higher than along passive margins (**Figure 10D**).

The widest continental shelves in the study are associated with the submarine canyons of the Bering Sea, but the mean shelf widths of the studied active and passive margins are very similar, albeit slightly greater along the former (**Figure 10E**). Shelf-breaks tend to be deeper along active margins, but the results do not indicate a significant difference between the two margin types (**Figure 10F**). The average shelf gradient is on average higher in active-margin systems (**Figure 10G**).

Canyons of the study along active margins are hosted on wider (**Figure 10H**) and deeper (**Figure 10I**) slopes, whereas the average slope gradient tends to be higher in S2S systems associated with the studied passive margins (**Figure 10J**).

With regard to aspects of the physiographic setting, mean values of seafloor depth at the canyon apex and mouth, of the minimum distance of the canyon to the shoreline, and of the latitude of the canyon apex are similar across the two margin types. Active-margin canyons show a greater bathymetric range, and several of the studied canyons in passive margins are located at higher latitudes (**Figures 10K–N**).

3.5.2 Scaling Between Attributes of the Source-to-Sink Systems of Active and Passive Margins

Correlations between attributes of the terrestrial catchment, shelf and slope in canyon-associated S2S systems grouped into active- and passive-margin settings share similarities, yet exhibit differences regarding their sign, strength and statistical significance. For some attributes, the amount of data prevents meaningful analyses to be undertaken (**Figures 11A,B**).

Statistically significant scaling relationships are seen across both margin types, but these vary in strength. Strong and positive significant correlations of catchment area with fluvial-system length and average annual fluvial discharge are seen for both margin types. Also, shelf width correlates positively with catchment area and fluvial system length in both margin types, but the relationship with the latter is stronger in active-margin settings. Strong inverse scaling across both margin types exists between shelf width and the average shelf gradient and between slope width and the average slope gradient in passive margins (**Figures 11A,B**).

For other pairs of attributes, significant relationships may be seen for a particular margin type only. For example, the maximum elevation of passive-margin catchments shows significant and positive scaling with fluvial system length and average annual fluvial discharge, which is moderate for the former and strong for the latter. For active margins, correlations are weak and modest and not statistically significant. Shelf-break depth and the average shelf gradient display linear, moderate and significant positive correlation with each other in passive margins, but along active margins the same trend is weak, negative and not statistically significant (**Figures 11A,B**).

4 DISCUSSION

4.1 Tectonic Influence on Controlling Factors on Submarine-Canyon Geomorphology

Findings from this study suggest that certain aspects of the morphometry of submarine canyons, and some scaling relationships of canyon morphometric parameters mutually and with attributes of their geological setting, are more strongly expressed in a specific margin type (see **Figures 2–9**), indicating a possible tectonic control. Although commonalities seen in scaling across both margin types indicate that a scaling relationship might not be generally sensitive to factors related to tectonic activity, the possibility exists that tectonic influences might be overridden by other controlling factors or that different controls in passive and active margins have led to similar geomorphologic expressions in canyons.

In the following sections, the main findings of the study are discussed in the context of a potential tectonic influence on controlling factors on submarine-canyon geomorphology, including intra-canyon sedimentary processes, sediment connection to fluvial and littoral sources, sediment supply to shelf margins and structural controls.

4.1.1 Intra-Canyon Sedimentary Processes

The contrast in relative importance of intra-canyon processes along active and passive margins may contribute to certain differences seen in scaling relationships between canyons of the two margin types. For example, intra-canyon-wall failure might be less important as a geomorphic agent in canyons from active margins compared to passive-margin ones (Bührig et al., in review). This is because slope failures are thought to occur less commonly along active margins compared to passive margins, due to strengthening of the seafloor from recurrent seismic activity (e.g., Strozyk et al., 2010; Nelson et al., 2011; Sawyer and DeVore, 2015; Molenaar et al., 2019); on active margins, large-scale slope failures tend to be linked to high-magnitude earthquakes (e.g., Strozyk et al., 2010; Molenaar et al., 2019). By contrast, active-margin settings with steep terrestrial catchments and narrow and steep shelf configurations promote maintenance of sediment connection of submarine canyons with fluvial outlets and littoral cells even during periods of sea-level highstand, as at

present (e.g., Gamberi et al., 2015; Bernhardt and Schwanghart, 2021). Hence, moderate correlations of maximum sidewall steepness with maximum canyon width (**Figure 5F**) and depth (**Figure 5G**) in canyons along active margins might reflect the tendency of sediment gravity flows to predominate over intra-canyon slope failure in shaping canyon geomorphology in these settings, *via* their ability to concurrently control canyon width, depth and bank steepness by thalweg erosion (e.g., McHargue et al., 2011; Peakall and Sumner, 2015) and canyon margin aggradation from flow overspilling (e.g., Armitage et al., 2010; Soulet et al., 2016). In contrast, the weaker correlations seen for passive-margin canyons (**Figures 5F,G**) may be linked to the combined effect of a subordinate influence of sediment gravity flows from the disconnection of canyons to fluvial and intrashelf sources during periods of sea-level highstand (e.g., Harris and Whiteway, 2011), paired with the variable impact of canyon-wall failure on canyon-wall slopes, canyon width and canyon depth. As a result, relationships between these morphometrics linked to intracanyon erosion by flows might be overprinted. When deposited near their source, mass failures and their depositional products will lead to lower canyon depths and greater canyon-floor widths over the affected areas, whereas the maximum width between the canyon banks will only increase where the wall collapse extends to the uppermost canyon margin. Intra-canyon slope failures may also have an indirect effect on canyon geomorphology away from the site of failure, particularly when the mass failure transitions into a sediment gravity flow (e.g., Stow, 1986; Hsu et al., 2008), or when the deposit is remobilized at a later point in time and is transported down canyon (e.g., Khrapounoff et al., 2012); as a consequence, mass-failure impact on canyon width, depth and sidewall gradients might vary.

Thus, the co-occurrence of wall failure and sediment gravity flows, which is recognized to act as an autogenic control on the variability in width-to-depth ratios of submarine channels (see **Figure 11** and text in Shumaker et al., 2018), may also be effective in controlling maximum width-to-maximum depth ($w_{d_{max}}$) ratios of submarine canyons (Bührig et al., in review). The smaller mean value and range of $w_{d_{max}}$ ratio seen for passive-margin canyons compared to active-margin ones (**Figures 3B, 5D**) suggest that width-to-depth aspect ratios in canyons hosted on passive margins tend to be constrained in their magnitude by the way in which wall-collapse may limit canyon-margin aggradation. By contrast, the subordinate role of intra-canyon failure combined with the effect of structural controls on canyon depths and widths (see **Section 4.1.4**) can explain the greater range in $w_{d_{max}}$ ratios seen in active-margin canyons (**Figures 3B, 5D**).

4.1.2 Sediment Connection to Fluvial and Littoral Sources

4.1.2.1 Sediment Discharge From Rivers

Some geomorphic features of submarine canyons are seen to scale, to some degree, with fluvial system length, average annual water discharge, catchment size and maximum catchment elevation. These observations are interpreted to reflect the importance of sediment discharge from rivers as controls on

how canyon geomorphology is shaped by erosional and depositional processes (cf. Casalbore et al., 2011; Bührig et al., in review).

For submarine canyons in active margins, potential causal links between fluvial sediment supply and their length and maximum width are suggested by: 1) moderate scaling of the former with fluvial system length (**Figure 8A**), average annual water discharge (**Figure 8B**) and catchment size (**Figure 8C**), and 2) moderate scaling of the latter with the area (**Figure 8G**) and maximum elevation (**Figure 8H**) of the associated terrestrial catchment. These relationships probably reflect how erosive intracanyon flows related to fluvial discharge promote lengthening at the canyon head (e.g., Piper and Normark, 2009) and mouth (e.g., Hodgson et al., 2016), as well as canyon widening (e.g., Casalbore et al., 2011).

By contrast, weak correlations of passive-margin canyon length with fluvial system length (**Figure 8A**) and catchment size (**Figure 8C**) indicate a lack of control of sediment discharge from rivers on canyon length. This might in part reflect how retrogressive slope failure tends to be a more prominent process along passive margins compared to active ones, and how sediment connection of canyons with fluvial sources in passive-margin settings tend to diminish through time at times of marine transgression (see **Section 4.1.1**). For example, incised valleys along passive margins are thought to be more prone to infill during transgressive and highstand intervals due to their commonly shallower depths compared to those along active margins, promoting the disconnection of canyon heads from fluvial sediment sources in passive-margin settings (Harris and Whiteway, 2011). Also, flooding events are less likely to trigger hyperpycnal flows at the mouth of rivers along passive margins, due to the increased sand-grade sediment segregation in their larger coastal and alluvial floodplains (e.g., Milliman and Syvitski, 1992; Sømme et al., 2009). In addition, larger terrestrial catchments are less affected by extreme weather events, in proportion to their size, compared to smaller ones (e.g., Sømme et al., 2009; Reid and Frostick, 2011).

Despite this, comparably strong scaling of canyon length with average annual fluvial discharge for passive-margin canyons (**Figure 8B**) might reflect that long-lived sediment-laden turbulent flows (*sensu* Zavala, 2020) linked to discharge from rivers are efficient in traversing wide shelves and entire canyons even during periods of sea-level highstand, and are effective in increasing canyon lengths by erosion at the canyon head and at its mouth. Such hyperpycnal flows are thought to be common at the mouths of medium to large rivers associated with low-gradient terrestrial catchments, and to be able to cover distances of up to several hundred kilometers (Zavala, 2020).

4.1.2.2 Seafloor Depth at the Canyon Apex

Inverse relationships of average canyon width (**Figure 7A**) and maximum (**Figure 7B**) and average canyon depth (**Figure 7C**) with seafloor depth at the canyon apex seen for canyons from passive margins might reflect how canyons with apices located at greater water depths are more likely to be disconnected from terrestrial and intrashelf sources, at present and during past sea-level lowstands. Unless such canyons are coupled with a

contouritic system (e.g., Warratz et al., 2019), intra-canyon erosion would be limited to mass-wasting events on the slope proximal to and within the canyon, and to wave erosion.

Active-margin canyons tend to have steeper sidewalls if their canyon apex is closer to the shoreline (**Figure 7G**) and/or at shallower seafloor depth (**Figure 7E**), whereas in passive margins the maximum canyon sidewall steepness does not correlate with either physiographic parameter (**Figures 7E,G**). This finding supports our hypothesis that erosive flows originating from within the shelf and terrestrial catchment may be more important in carving steep canyon walls in active settings compared to passive ones (**Section 4.1.1**). We also find that average canyon sinuosity and w_{\max} ratios of canyons in active settings show moderate scaling with canyon bathymetry at the apex, inverse for the former (**Figure 7D**) and positive for the latter (**Figure 7F**), which can also be ascribed to the influence of such erosive flows.

4.1.3 Sediment Supply to Shelf Margins

The moderate scaling of shelf-break depth with canyon length (**Figure 8M**), maximum width (**Figure 8N**) and depth (**Figure 8O**), and average canyon sinuosity (**Figure 8P**) for passive-margin canyons might reflect to some degree how higher rates of sediment supply from terrestrial source areas promote subsidence along continental margins and act to push the slope break into deeper waters (cf. Sweet and Blum, 2016; Wang et al., 2019). In contrast, relationships between the shelf-break depth and maximum canyon dimensions and overall canyon sinuosity are weak for active-margin canyons (**Figures 8M–P**), even though terrestrial catchments in active margins can be characterized by high rates of sediment supply (see also **Section 4.1.2** and **Section 4.1.4**), which can be associated with narrow shelves promoting sediment routing to canyons (e.g., Blum and Hattier-Womack, 2009). Our observation may reflect, in part, the relative importance of structural controls on geomorphologic evolution in active settings (see **Section 4.1.4**), including the structural control of shelf-break migration (e.g., Han et al., 2016).

4.1.4 Structural Controls

Faulting and diapirism and their effects related to both gravitational failure and tectonic activity (e.g., Rowan et al., 2004; Hudec and Jackson, 2007; Yang et al., 2020) constitute structural controls that might affect canyon geomorphology in different ways through their influence on sediment-transport and canyon pathways (e.g., Chiang et al., 2012; Doo et al., 2015; Urías Espinosa et al., 2016); they can also do so by reshaping canyon walls (e.g., Yu and Chang, 2002; Bernhardt et al., 2015).

The greater impact of faulting and diapirism linked to tectonic activity on margin configuration, seafloor topography and sedimentary processes in active-margin settings compared to passive-margin ones (e.g., Yang et al., 2020) may explain some of the differences in scaling and canyon-morphometric characteristics seen between canyons across different tectonic settings.

The value of slope width for predicting canyon length (Sømme et al., 2009; Bührig et al., in review) is lower in active margins than

in passive ones (**Figure 8R**), which is possibly related to a greater and more prolonged impact of tectonic convergence on slope physiography in active margins compared to passive margins (e.g., Pratson et al., 2007; Yang et al., 2020), and its variable influence on canyon length. Canyon pathways can be deflected by positive topography created by faults and diapirs (e.g., Li et al., 2021), or develop along intraslope depressions as transform faults (e.g., Greene et al., 1991), or axes of intraslope basins (e.g., Bourget et al., 2010), thereby increasing canyon length relative to the width of the slope. On the other hand, emerging seafloor topography can lead to canyon abandonment by redirecting sediment pathways (e.g., Chiang et al., 2012), whereas the presence of intraslope basins (e.g., Harris et al., 2014a) and highs (e.g., Hsiung et al., 2014) can inhibit further extension of the canyon across the slope.

Given the general importance of structural controls on canyon length and average canyon sinuosity in active margins, it is unsurprising that our results indicate that both canyon morphometric parameters are not generally different between the different categories of active margins (convergent, transform and complex settings; **Figures 4A,D**).

In contrast, the fact that the maximum width of canyons from complex settings is on average larger compared to that of canyons from convergent and transform ones (**Figure 4B**) suggests that such settings may be inherently more favorable to the development of wide canyons. In tectonically complex settings with strike-slip tectonics, such as the Cook Strait sector, New Zealand, and offshore Taiwan in the East China Sea, a local widening of canyons might be promoted by the concurrence of transform faulting coupled with recurrent sediment gravity flows, where canyons intersect with strike-slip faults (e.g., Schnürle et al., 1998; Micallef et al., 2014).

In case of the SW Taiwan margin canyons, instead, the development of very wide canyons might be explained by the high frequency of hyperpycnal flows at river mouths (e.g., Milliman and Kao, 2005; Liu et al., 2013). The formation of hyperpycnal flows in the region is favored by enhanced erosion rates in terrestrial catchments from earthquake-related landslides (e.g., Dadson et al., 2005), extended periods of precipitation during the monsoonal wet season (e.g., Zhang et al., 2022) and associated with typhoons (e.g., Dadson et al., 2005; Milliman and Kao, 2005; Zhang et al., 2018), as well as from decreased levels of salinity of the ambient oceanic water due to high freshwater discharge along the margin (e.g., Dadson et al., 2005).

Despite the fact that both mean canyon length (**Figure 2A**) and mean maximum canyon depth (**Figure 2D**) are not significantly different in active and passive margins, length-to-maximum depth (ld_{\max}) ratios are on average significantly higher in active margins (**Figure 3C**). The findings might reflect how enhanced seafloor relief linked to tectonics tends to increase canyon length, while simultaneously inhibiting canyon deepening. A downcanyon decrease in the erosive power of canyon-traversing flows may be caused by the capture of coarser sediment fractions by intraslope depressions (e.g., Soutter et al., 2021) and by flow deceleration upstream of slope topography leading to deposition of coarser sediment (e.g., Soutter et al., 2020). Although our data on the average

depth of canyons from active and passive margins show that active-margin canyons tend to be significantly shallower (**Figure 2E**), further investigation is needed to corroborate our findings in view of the limited geographic coverage of the dataset.

4.2 Canyon Geomorphology and Associated Characters of Deep-Water Systems

Despite the importance of sediment connection of submarine canyons to sediment sources in terrestrial catchments, shelves and slopes, and the lithological characteristics of source areas for the evolution of deep-water systems (e.g., Normark and Carlson, 2003; Smith et al., 2017; Hessler and Fildani, 2019; Bernhardt and Schwanghart, 2021), the character of a deep-water system is ultimately controlled by the efficiency of sediment transport through canyons to deep-marine sinks (Hessler and Fildani, 2019).

Stratigraphic forward modelling experiments by Wan et al. (2021) for delta-canyon-fan systems in a passive-margin setting suggest that sediment routing to basin floor sinks is promoted for shallow and low-sinuosity canyons.

Results by Wan et al. (2021) suggest that intracanyon basinward transport of coarser grain-size fractions is more efficient in shallower canyons. Canyons along active margins tend to be shallower than passive-margin canyons (**Figure 2E**), but they also tend to exhibit increased intra-canyon relief, which can inhibit the down-canyon erosive strength of flows *via* mass extraction (see **Section 4.1.4**). This suggests that the relationship identified by Wan et al. (2021) might not be applicable for canyons in active-margin settings. Similarly, the impact of canyon depth on grain-size segregation within canyons might be subdued in canyons associated with passive-margin settings where slope relief is increased by gravitational loading.

The rate of thalweg lateral migration, which determines the canyon sinuosity, controls the caliber of sediment transported down-canyon; in more sinuous canyons, a relatively larger proportion of coarse sediment is deposited along the inner bends and the proximal part of the canyon, whereas in canyons with lower sinuosity the coarser sediment can be more effectively transported down-slope (Wan et al., 2021). Given that the average sinuosity of canyons is neither generally different between active and passive margins (**Figure 2F** this study; Harris and Whiteway, 2011; Bührig et al., in review), nor seemingly different across the considered active-margin settings (**Figure 4D**), the control of canyon sinuosity on sediment transport dynamics and grain-size segregation is probably not fundamentally different between active- and passive-margin settings and across active margins with different types of plate boundaries.

However, the influence of canyon geomorphology on sediment connection across deep-water environments might be absent or less prominent for active margins where canyons experience “flushing” initiated by large-magnitude earthquakes (e.g., Goldfinger et al., 2012; Atwater et al., 2014), due to the remobilization of large volumes of sediment, including coarser grain size fractions, and related substrate erosion within the canyon (e.g., Mountjoy et al., 2018).

These aspects highlight the need for modelling studies and conceptual models of S2S and deep-water systems to better consider the wide range of boundary conditions associated with characteristics of continental margins.

4.3 Implications of the Findings and Future Work

Our comparisons of frequency distributions of canyon morphometric parameters for different tectonic settings (**Figures 2A–H, 4A–I**) corroborate results of earlier quantitative global studies, showing that canyon morphometrics are variably sensitive to factors related to the tectonic-margin type (e.g., Harris and Whiteway, 2011; Bührig et al., in review). These insights suggest that overall canyon geomorphology cannot be predicted from the tectonic setting alone. Our findings that canyons along active margins display a greater variability in aspect ratios of maximum canyon dimensions (**Figures 3A–C**) indicate that the size of canyon fills in the stratigraphic record might be less reliably estimated from outcrop and subsurface data in active-margin settings compared to passive margins. Moreover, aspects of canyon morphometry in canyons associated with convergent settings are not fundamentally different compared to those in complex settings (**Figures 4A–I**), suggesting that canyon geomorphology is not primarily controlled by the complexity of the tectonic regime in active-margin settings. Despite this, complex tectonics may be preferentially associated with canyons with larger maximum widths and depths (**Figures 4B,C**, see also **Section 4.1.4**).

Our analysis also shows that scaling relationships of canyon morphometric parameters with attributes of the physiographic setting (**Figures 6A,B, 7A–H**) and source-to-sink (S2S) system (**Figures 8A–R, 9A,B**) might vary between active and passive margins. The same applies for scaling relationships between the different canyon morphometric parameters (**Figures 5A–G**), and for scaling between attributes of S2S systems (**Figures 11A,B**). These findings are important because they demonstrate that the relationships between continental-margin types and the configuration of deep-water systems is more complex than hitherto recognized in conceptual, experimental and numerical models.

The variable and complex influence of the tectonic setting on sediment routing along S2S systems, on canyon geomorphology, and on the degree of confinement of deep-water fans in settings such as intraslope basins (e.g., Budillon et al., 2011; Hsiung et al., 2014), lower slopes with complex seafloor topography (e.g., Hsiung et al., 2018), and trenches (e.g., Thornburg et al., 1990; McArthur and Tek, 2021) raises the question whether scaling relationships between submarine canyons and deep-water fans can be predicted. This needs to be investigated in future work.

5 CONCLUSION

A global metastudy of geomorphic characteristics of submarine canyons as a function of the tectonic setting has been conducted. The key findings of the study are that:

- 1) Overall canyon geomorphology is not generally different between active and passive margins and across different plate-boundary types in tectonically active settings.
- 2) The role of slope failure as a mechanism governing the morphology of canyons may be subordinate for canyons associated with active margins, compared to passive-margin examples, possibly due to seismic strengthening of seafloors in the former. This indicates that width-to-depth ratios might be inherently limited in their magnitude in canyons in passive-margin settings due to the interplay of intracanyon sediment flows and canyon-wall failure, with the latter counteracting canyon-margin accretion while promoting canyon widening and aggradation of canyon floors.
- 3) Scaling relationships of individual canyon morphometric parameters and aspect ratios of maximum canyon dimensions with attributes of the S2S system and the physiographic setting have been demonstrated for 1) active margins, 2) passive margins, and 3) across both margin types. The scaling relationships vary broadly in magnitude of correlation, but are seldom strong; this reflects how canyon geomorphology is shaped by the complex interplay of different controls, which are only in part influenced by the tectonic setting.
- 4) Our findings suggest that canyon geomorphology can be to some degree predicted in S2S systems in active and passive margins, but that the predictive value of attributes of the environmental setting might vary across different tectonic settings.
- 5) Insights from this study suggest possible genetic links between aspects of canyon geomorphology and characteristics of the physiographic environment related to the tectonic setting. This finding can be applied to improve and help constrain conceptual, experimental and numerical models of submarine canyons and canyon-associated sedimentary systems at source-to-sink scale by 1) demonstrating how the relative importance of controlling factors on canyon morphometry might vary across different tectonic settings; 2) providing a quantitative characterization of canyon morphometric attributes and associated parameters of the physiographic and environmental setting that can be applied to constrain models in a realistic manner; and 3) illustrating how insights from our analyses can augment existing semi-quantitative models of source-to-sink systems for different tectonic settings, which have not yet expressly considered submarine-canyon morphometry (e.g., Sømme et al., 2009; Nyberg et al., 2018).

REFERENCES

- Acosta, J., Canals, M., López-MartínezMuñoz, A., Herranz, P., Urgeles, R., et al. (2002). The Balearic Promontory Geomorphology (Western Mediterranean): Morphostructure and Active Processes. *Geomorphology* 49, 177–204.
- Alford, M. H., and MacCready, P. (2014). Flow and Mixing in Juan de Fuca Canyon, Washington. *Geophys. Res. Lett.* 41, 1608–1615. doi:10.1002/2013GL058967
- Allen, S. E., Vindeirinho, C., Thomson, R. E., Foreman, M. G., and Mackas, D. L. (2001). Physical and Biological Processes Over a Submarine Canyon During an Upwelling Event. *Can. J. Fish. Aquat. Sci.* 58, 671–684. doi:10.1139/cjfas-58-4-67110.1139/f01-008

DATA AVAILABILITY STATEMENT

The raw data supporting the conclusion of this article will be made available by the authors, without undue reservation.

AUTHOR CONTRIBUTIONS

LB conceptualized and led the investigation, conducted the analyses, drafted the figures and wrote the original draft. LC, MP, NM, and WM supervised the project. LC, MP, NM, and WM provided specialist technical input for the interpretation of geomorphological and geological datasets and the application of statistical analytical techniques; they additionally contributed to the scientific writing of the manuscript and to manuscript revisions.

FUNDING

This research was funded by the sponsors of the Turbidites Research Group (AkerBP, CNOOC, ConocoPhillips, Harbour, Murphy, Occidental, OMV) and of the Fluvial, Eolian & Shallow-Marine Research Group [AkerBP, Areva (now Orano), BHP, Cairn India (Vedanta), Chevron, CNOOC International, ConocoPhillips, Equinor, Murphy Oil, Occidental, Petrotechnical Data Systems, Saudi Aramco, Shell, Tullow Oil, Woodside, YPF], School of Earth and Environment, University of Leeds. Financial support to this research was also provided by NERC (NE/P01691X/1).

ACKNOWLEDGMENTS

We thank the sponsors of the Turbidites Research Group and of the Fluvial, Eolian & Shallow-Marine Research Group for financial support. We thank DC and AF for their constructive comments, which helped improve the paper.

SUPPLEMENTARY MATERIAL

The Supplementary Material for this article can be found online at: <https://www.frontiersin.org/articles/10.3389/feart.2022.836823/full#supplementary-material>

- Allin, J. R., Hunt, J. E., Talling, P. J., Clare, M. A., Pope, E., and Masson, D. G. (2016). Different Frequencies and Triggers of Canyon Filling and Flushing Events in Nazaré Canyon, Offshore Portugal. *Mar. Geol.* 371, 89–105. doi:10.1016/j.margeo.2015.11.005
- Almagor, G. (1993). Continental Slope Processes off Northern Israel and Southernmost Lebanon and Their Relation to Onshore Tectonics. *Mar. Geol.* 112, 151–169. doi:10.1016/0025-3227(93)90166-s
- Alonso, B., and Ercilla, G. (2003). Small Turbidite Systems in a Complex Tectonic Setting (SW Mediterranean Sea): Morphology and Growth Patterns. *Mar. Pet. Geol.* 19, 1225–1240. doi:10.1016/S0264-8172(03)00036-9
- Amblas, D., Ceramicola, S., Gerber, T. P., Canals, M., Chiocci, F. L., Dowdeswell, J. A., et al. (2017). “Submarine Canyons and Gullies,” in *Submarine*

- Geomorphology*. Editors A. Micallef, S. Krastel, and A. Savini (Berlin, Germany: Springer), 251–272. doi:10.1007/978-3-319-57852-1_14
- Amblas, D., Gerber, T. P., De Mol, B., Urgeles, R., Garcia-Castellanos, D., Canals, M., et al. (2012). Survival of a Submarine Canyon during Long-Term Outbuilding of a Continental Margin. *Geology* 40 (6), 543–546. doi:10.1130/G33178.1
- Antobreh, A. A., and Krastel, S. (2006). Morphology, Seismic Characteristics and Development of Cap Timiris Canyon, Offshore Mauritania: a Newly Discovered Canyon Preserved-Off a Major Arid Climatic Region. *Mar. Petroleum Geol.* 23, 37–59. doi:10.1016/j.marpetgeo.2005.06.003
- Armitage, D. A., Piper, D. J. W., McGee, D. T., and Morris, W. R. (2010). Turbidite Deposition on the Glacially Influenced, Canyon-Dominated Southwest Grand Banks Slope, Canada. *Sedimentology* 57, 1387–1408. doi:10.1111/j.1365-3091.2010.01149.x
- Arzola, R. G., Wynn, R. B., Lastras, G., Masson, D. G., and Weaver, P. P. E. (2008). Sedimentary Features and Processes in the Nazaré and Setúbal Submarine Canyons, West Iberian Margin. *Mar. Geol.* 250, 64–88. doi:10.1016/j.margeo.2007.12.006
- Atwater, B. F., Carson, B., Griggs, G. B., Johnson, H. P., and Salmi, M. S. (2014). Rethinking Turbidite Paleoseismology Along the Cascadia Subduction Zone. *Geology* 42, 827–830. doi:10.1130/G35902.1
- Babonneau, N., Delacourt, C., Cancouët, R., Sisavath, E., Bachélery, P., Mazuel, A., et al. (2013). Direct Sediment Transfer From Land to Deep-Sea: Insights into Shallow Multibeam Bathymetry at La Réunion Island. *Mar. Geol.* 346, 47–57. doi:10.1016/j.margeo.2013.08.006
- Babonneau, N., Savoye, B., Cremer, M., and Klein, B. (2002). Morphology and Architecture of the Present Canyon and Channel System of the Zaire Deep-Sea Fan. *Mar. Petroleum Geol.* 19, 445–467. doi:10.1016/s0264-8172(02)00009-0
- Baker, E. T., and Hickey, B. M. (1986). Contemporary Sedimentation Processes in and Around an Active West Coast Submarine Canyon. *Mar. Geol.* 71, 15–34. doi:10.1016/0025-3227(86)90031-9
- Baztan, J., Berné, S., Olivet, J.-L., Rabineau, M., Aslanian, D., Gaudin, M., et al. (2005). Axial Incision: The Key to Understand Submarine Canyon Evolution (In the Western Gulf of Lion). *Mar. Pet. Geol.* 22 (6–7), 805–826. doi:10.1016/j.marpetgeo.2005.03.011
- Bernhardt, A., Melnick, D., Jara-Muñoz, J., Argandoña, B., González, J., and Strecker, M. R. (2015). Controls on Submarine Canyon Activity during Sea-Level Highstands. The Biobío Canyon System Offshore Chile. *Geosphere* 11 (4), 1226–1255. doi:10.1130/GES01063.1
- Bernhardt, A., and Schwanghart, W. (2021). Where and Why Do Submarine Canyons Remain Connected to the Shore during Sea-Level Rise? Insights from Global Topographic Analysis and Bayesian Regression. *Geophys. Res. Lett.* 48, e2020GL092234. doi:10.1029/2020GL092234
- Blum, M. D., and Hattier-Womack, J. (2009). “Climate Change, Sea-Level Change, and Fluvial Sediment Supply to Deepwater Depositional Systems,” in *External Controls on Deep Water Depositional Systems: Climate, Sea-Level, and Sediment Flux*. Editors B. Kneller, O. J. Martinsen, and B. McCaffrey (Tulsa, OK: SEPM), 15–40. doi:10.2110/sepm.092.015
- Bosley, K. L., Lavelle, J. W., Brodeur, R. D., Wakefield, W. W., Emmet, R. L., Baker, E. T., et al. (2004). Biological and Physical Processes in and Around Astoria Submarine Canyon, Oregon, USA. *J. Mar. Syst.* 50, 21–37. doi:10.1016/j.jmarsys.2003.06.006
- Bouma, A. H., and Scott, E. D. (2003). “Source-to-sink: the Importance of the Updip Coastal Area in Defining Deep-Water Sand Characteristics,” in *Shelf Margin Deltas and Linked Down Slope Petroleum Systems – Global Significance and Future Exploration Potential*. Editors H. H. Roberts, N. C. Rosen, R. H. Fillon, and J. B. Anderson (Houston, TX: GCSSEPM), 597–617. doi:10.5724/gcs.03.23.0597
- Bourget, J., Zaragosi, S., Ellouz-Zimmermann, N., Mouchot, N., Garlan, T., Schneider, J.-L., et al. (2010). Turbidite System Architecture and Sedimentary Processes along Topographically Complex Slopes: the Makran Convergent Margin. *Sedimentology* 58 (2), 376–406. doi:10.1111/j.1365-3091.2010.01168.x
- Budillon, F., Conforti, A., Tonielli, R., De Falco, G., Di Martino, G., Innangi, S., et al. (2011). The Bulgheria Canyon-Fan: A Small-Scale Proximal System in the Eastern Tyrrhenian Sea (Italy). *Mar. Geophys. Res.* 32, 83–97. doi:10.1007/s11001-011-9138-9
- Bührig, L. H., Colomera, L., Patacci, M., Mountney, N. P., and McCaffrey, W. D. (in review). A Global Analysis of Controls on Submarine-Canyon Geomorphology. *arXiv*. doi:10.31223/X5RK9H
- Çağatay, M. N., Uçarkus, G., Eriş, K. K., Henry, P., Gasperini, L., and Polonia, A. (2015). “Submarine Canyons of the Sea of Marmara,” in *Submarine Canyon Dynamics in the Mediterranean and Tributary Seas – an Integrated Geological, Oceanographic and Biological Perspective*. Editor F. Briand (Monaco:CIESM), 123–135.
- Carlson, P. R., Bruns, T. R., and Fisher, M. A. (1990). “Development of Slope Valleys in the Glacimarine Environment of a Complex Subduction Zone, Northern Gulf of Alaska,” in *Glacimarine Environments; Processes and Sediments*. Editors J. A. Dowdeswell and J. D. Scourse (London: GEOLOGICAL SOCIETY), 139–153. doi:10.1144/gsl.sp.1990.053.01.08
- Carlson, P. R., and Karl, H. A. (1988). Development of Large Submarine Canyons in the Bering Sea, Indicated by Morphologic, Seismic, and Sedimentologic Characteristics. *Geol. Soc. Am. Bull.* 100, 1594–1615. doi:10.1130/0016-7606(1988)100<1594:dolsci>2.3.co;2
- Carlson, P. R., and Karl, H. A. (1984). Discovery of Two New Large Submarine Canyons in the Bering Sea. *Mar. Geol.* 56, 159–179. doi:10.1016/0025-3227(84)90011-2
- Carson, B., Baker, E. T., Hickey, B. M., Nittrouer, C. A., DeMaster, D. J., Thorbjarnarson, K. W., et al. (1986). Modern Sediment Dispersal and Accumulation in Quinault Submarine Canyon – A Summary. *Mar. Geol.* 71, 1–13. doi:10.1016/0025-3227(86)90030-7
- Casalbore, D., Chiocci, F. L., Scarascia Mugnozza, G., Tommasi, P., and Sposato, A. (2011). Flash-flood Hyperpycnal Flows Generating Shallow-Water Landslides at Fiumara Mouths in Western Messina Strait (Italy). *Mar. Geophys. Res.* 32, 257–271. doi:10.1007/s11001-011-9128-y
- Casalbore, D., Falcini, F., Martorelli, E., Morelli, E., Bosman, A., Calarco, M., et al. (2018). Characterization of Overbanking Features on the Lower Reach of the Gioia-Mesima Canyon-Channel System (Southern Tyrrhenian Sea) through Integration of Morpho-Stratigraphic Data and Physical Modelling. *Prog. Oceanogr.* 169, 66–78. doi:10.1016/j.pcean.2018.02.020
- Chen, H., Zhan, W., Li, L., and Wen, M.-M. (2017). Occurrence of Submarine Canyons, Sediment Waves and Mass Movements along the Northern Continental Slope of the South China Sea. *J. Earth Syst. Sci.* 126, 73. doi:10.1007/s12040-017-0844-9
- Chiang, C.-S., and Yu, H.-S. (2006). Morphotectonics and Incision of the Kaoping Submarine Canyon, SW Taiwan Orogenic Wedge. *Geomorphology* 80, 199–213. doi:10.1016/j.geomorph.2006.02.008
- Chiang, C.-S., Yu, H.-S., Noda, A., TuZino, T., and Su, C.-C. (2012). Avulsion of the Fangliao Submarine Canyon off Southwestern Taiwan as Revealed by Morphological Analysis and Numerical Simulation. *Geomorphology* 177–178, 26–37. doi:10.1016/j.geomorph.2012.07.011
- Coleman, J. M., Prior, D. B., and Lindsay, J. F. (1982). Formation of the Mississippi Canyon. *GCAGS Trans.* 32, 519.
- Corradino, M., Pepe, F., Burrato, P., Kanari, M., Parrino, N., Bertotti, G., et al. (2021). An Integrated Multiscale Method for the Characterization of Active Faults in Offshore Areas. The Case of Sant’Eufemia Gulf (Offshore Calabria, Italy). *Front. Earth Sci.* 9, 670557. doi:10.3389/feart.2021.670557
- Covault, J. A., Fildani, A., Romans, B. W., and McHargue, T. (2011a). The Natural Range of Submarine Canyon-And-Channel Longitudinal Profiles. *Geosphere* 7 (2), 313–332. doi:10.1130/GES00610.1
- Covault, J. A., Romans, B. W., Graham, S. A., Fildani, A., and Hilley, G. E. (2011b). Terrestrial Source to Deep-Sea Sink Sediment Budgets at High and Low Sea Levels: Insights from Tectonically Active Southern California. *Geology* 39 (7), 619–622. doi:10.1130/G31801.1
- Cullis, S., Patacci, M., Colomera, L., Bührig, L., and McCaffrey, W. D. (2019). A Database Solution for the Quantitative Characterisation and Comparison of Deep-Marine Siliciclastic Depositional Systems. *Mar. Pet. Geol.* 102, 321–339. doi:10.1016/j.marpetgeo.2018.12.023
- Dadson, S., Hovius, N., Pegg, S., Dade, W. B., Horng, M. J., and Chen, H. (2005). Hyperpycnal River Flows from an Active Mountain Belt. *J. Geophys. Res.* 110, F04016. doi:10.1029/2004JF000244
- Davies, H. L., Keene, J. B., Hashimoto, K., Joshima, M., Stuart, J. E., and Tiffin, D. L. (1987). Bathymetry and Canyons of the Western Solomon Sea. *Geo-Mar. Lett.* 6, 181–191.

- de Almeida, N. M., Vital, H., and Gomes, M. P. (2015). Morphology of Submarine Canyons along the Continental Margin of the Potiguar Basin, NE Brazil. *Mar. Pet. Geol.* 68, 307–324. doi:10.1016/j.marpetgeo.2015.08.035
- Dietz, R. S., Knebel, H. J., and Somers, L. H. (1968). Cayar Submarine Canyon. *Geol. Soc. Am. Bull.* 79, 1821–1828. doi:10.1130/0016-7606(1968)79[1821:nadcsj]2.0.co;2
- Ding, W., Li, J., Li, J., Fang, Y., and Tang, Y. (2013). Morphotectonics and Evolutionary Controls on the Pearl River Canyon System, South China Sea. *Mar. Geophys. Res.* 34, 221–238. doi:10.1007/s11001-013-9173-9
- Doo, W.-B., Hsu, S.-K., Lo, C.-L., Chen, S.-C., Tsai, C.-H., Lin, J.-Y., et al. (2015). Gravity Anomalies of the Active Mud Diapirs off Southwest Taiwan. *Geophys. J. Int.* 203, 2089–2098. doi:10.1093/gji/ggv430
- Eittrheim, S., Grantz, A., and Greenberg, J. (1982). Active Geologic Processes in Barrow Canyon, Northeast Chukchi Sea. *Mar. Geol.* 50, 61–76. doi:10.1016/0025-3227(82)90061-5
- Ercilla, G., Alonso, B., Perez-Belzuz, F., Estrada, F., Baraza, J., Farran, M., et al. (1998). Origin, Sedimentary Processes and Depositional Evolution of the Agadir Turbidite System, Central Eastern Atlantic. *J. Geol. Soc. Lond.* 155 (6), 929–939. doi:10.1144/gsjgs.155.6.0929
- Exon, N. F., Hill, P. J., Mitchell, C., and Post, A. (2005). Nature and Origin of the Submarine Albany Canyons off Southwest Australia. *Aust. J. Earth Sci.* 52 (1), 101–115. doi:10.1080/08120090500100036
- Ferry, J.-N., Babonneau, N., Mulder, T., Parize, O., and Raillard, S. (2004). Morphogenesis of Congo Submarine Canyon and Valley: Implications about the Theories of the Canyons Formation. *Geodin. Acta.* 17, 241–251. doi:10.3166/ga.17.241-251
- Fildani, A. (2017). Submarine Canyons: A Brief Review Looking Forward. *Geology* 45 (4), 383–384. doi:10.1130/focus042017.1
- Galewsky, J., and Silver, E. A. (1997). Tectonic Controls on Facies Transitions in an Oblique Collision: The Western Solomon Sea, Papua New Guinea. *Am. Geol. Soc. Bull.* 109 (10), 1266–1278. doi:10.1130/0016-7606(1997)109<1266:tcft>2.3.co;2
- Gamberi, F., Rovere, M., Marani, M. P., and Dykstra, M. (2015). Modern Submarine Canyon Feeder-System and Deep-Sea Fan Growth in a Tectonically Active Margin (Northern Sicily). *Geosphere* 11 (2), 307–319. doi:10.1130/GES01030.1
- Gardner, J. V., Dartnell, P., Mayer, L. A., and Hughes Clarke, J. E. (2003). Geomorphology, Acoustic Backscatter, and Processes in Santa Monica Bay from Multibeam Mapping. *Mar. Environ. Res.* 56, 15–46. doi:10.1016/S0141-1136(02)00323-9
- Gardner, W. D., Glover, L. K., and Hollister, C. D. (1980). Canyons off Northwest Puerto Rico: Studies of Their Origin and Maintenance with the Nuclear Research Submarine NR-1. *Mar. Geol.* 37, 41–70. doi:10.1016/0025-3227(80)90011-0
- Gervais, A., Mulder, T., Savoye, B., and Gonthier, E. (2006). Sediment Distribution and Evolution of Sedimentary Processes in a Small Sandy Turbidite System (Golo System, Mediterranean Sea): Implications for Various Geometries Based on Core Framework. *Geo-Mar. Lett.* 26, 373–395. doi:10.1007/s00367-006-0045-z
- Gervais, A., Savoye, B., Piper, D. J. W., Mulder, T., Cremer, M., and Pichevin, L. (2004). “Present Morphology and Depositional Architecture of a Sandy Confined Submarine System: the Golo Turbidite System (Eastern Margin of Corsica),” in *Confined Turbidite Systems*. Editors S. A. Lomas and P. Joseph (London: Geological Society), 59–89. doi:10.1144/gsl.sp.2004.222.01.05
- Gnibidenko, H. S., and Svarichevskaya, L. V. (1984). The Submarine Canyons of Kamchatka. *Mar. Geol.* 54, 277–307. doi:10.1016/0025-3227(84)90043-4
- Goldfinger, C., Nelson, C. H., Morey, A. E., Johnson, J. R., Patton, J., Karabanov, E., et al. (2012). Turbidite Event History – Methods and Implications for Holocene Paleoseismicity of the Cascadia Subduction Zone. *USGS Prof. Pap.* 1661-F, 170. doi:10.3133/PP1661F
- Gómez-Ballesteros, M., Druet, M., Muñoz, A., Arrese, B., Rivera, J., Sánchez, F., et al. (2014). Geomorphology of the Avilés Canyon System, Cantabrian Sea (Bay of Biscay). *Deep Sea Res. Part II Top. Stud. Oceanogr.* 106, 99–117. doi:10.1016/j.dsr2.2013.09.031
- Greene, H. G., Clarke, S. H., Jr., and Kennedy, M. P. (1991). “Tectonic Evolution of Submarine Canyons along the California Continental Margin,” in *From Shoreline to Abyss: Contributions in Marine Geology in Honor of Francis Parker Shepard*. Editor R. H. Osborne (Tulsa, OK: SEPM), 231–248. doi:10.2110/pec.91.09.0231
- Greene, H. G., Maher, N. M., and Paull, C. K. (2002). Physiography of the Monterey Bay National Marine Sanctuary and Implications about Continental Margin Development. *Mar. Geol.* 181, 55–82. doi:10.1016/S0025-3227(01)00261-4
- Hagen, R. A., Bergersen, D. D., Moberly, R., and Coulbourn, W. T. (1994). Morphology of a Large Meandering Submarine Canyon System on the Peru-Chile Forearc. *Mar. Geol.* 119, 7–38. doi:10.1016/0025-3227(94)90138-4
- Hagen, R. A., Vergara, H., and Naar, D. F. (1996). Morphology of San Antonio Submarine Canyon on the Central Chile Forearc. *Mar. Geol.* 129, 197–205. doi:10.1016/0025-3227(96)83345-7
- Han, J., Xu, G., Li, Y., and Zhuo, H. (2016). Evolutionary History and Controlling Factors of the Shelf Breaks in the Pearl River Mouth Basin, Northern South China Sea. *Mar. Pet. Geol.* 77, 179–189. doi:10.1016/j.marpetgeo.2016.06.009
- Han, X., Li, J., Chu, F., Li, J., and Yang, F. (2010). “Geomorphology and Tectonic Interpretation of Zhujiang Submarine Canyon, in the Northern South China Sea,” in *OCEANS’10 IEEE SYDNEY*, Sydney, NSW, Australia, May 24–27, 2010. doi:10.1109/OCEANSSYD.2010.5603638
- Harris, P. T., Barrie, J. V., Conway, K. W., and Greene, H. G. (2014a). Hanging Canyons of Haida Gwaii, British Columbia, Canada: Fault-Control on Submarine Canyon Geomorphology along Active Continental Margins. *Deep Sea Res. Part II Top. Stud. Oceanogr.* 104, 83–92. doi:10.1016/j.dsr2.2013.06.017
- Harris, P. T., Macmillan-Lawler, M., Rupp, J., and Baker, E. K. (2014b). Geomorphology of the Oceans. *Mar. Geol.* 352, 4–24. doi:10.1016/j.margeo.2014.01.011
- Harris, P., and Whiteway, T. (2011). Global Distribution of Large Submarine Canyons: Geomorphic Differences between Active and Passive Continental Margins. *Mar. Geol.* 285, 69–86. doi:10.1016/j.margeo.2011.05.008
- Hessler, A. M., and Fildani, A. (2019). Deep-sea Fans: Tapping into Earth’s Changing Landscapes. *J. Sediment. Res.* 89 (11), 1171–1179. doi:10.2110/jsr.2019.64
- Hickey, B. M. (1997). The Response of a Steep-Sided, Narrow Canyon to Time-Variable Wind Forcing. *J. Phys. Oceanogr.* 27 (5), 697–726. doi:10.1175/1520-0485(1997)027<0697:troass>2.0.co;2
- Hodgson, D. M., Kane, I. A., Flint, S. S., Brunt, R. L., and Ortiz-Karpf, A. (2016). Time-transgressive Confinement on the Slope and the Progradation of Basin-Floor Fans: Implications for the Sequence Stratigraphy of Deep-Water Deposits. *J. Sediment. Res.* 86, 73–86. doi:10.2110/jsr.2016.3
- Hsiung, K.-H., Kanamatsu, T., Ikehara, K., Shiraishi, K., Horng, C.-S., and Usami, K. (2017). Morpho-sedimentary Features and Sediment Dispersal Systems of the Southwest End of the Ryukyu Trench: a Source-To-Sink Approach. *Geo-Mar. Lett.* 37, 561–577. doi:10.1007/s00367-017-0509-3
- Hsiung, K.-H., Yu, H.-S., and Chiang, C.-S. (2014). Seismic Characteristics, Morphology and Formation of the Ponged Fangliao Fan off Southwestern Taiwan, Northern South China Sea. *Geo-Mar. Lett.* 34, 59–74. doi:10.1007/s00367-013-0351-1
- Hsiung, K.-H., Yu, H.-S., and Chiang, C.-S. (2018). The Modern Kaoping Transient Fan Offshore SW Taiwan: Morphotectonics and Development. *Geomorphology* 300, 151–163. doi:10.1016/j.geomorph.2017.10.013
- Hsiung, K.-H., and Yu, H.-S. (2011). Morpho-Sedimentary Evidence for a Canyon-Channel-Trench Interconnection Along the Taiwan-Luzon Plate Margin, South China Sea. *Geo-Mar. Lett.* 31, 215–226. doi:10.1007/s00367-010-0226-7
- Hsu, S.-K., Kuo, J., Lo, C.-L., Tsai, C.-H., Doo, W.-B., Ku, C.-Y., et al. (2008). Turbidity Currents, Submarine Landslides and the 2006 Pingtung Earthquake off SW Taiwan. *Terr. Atmos. Ocean. Sci.* 19 (6), 767–772. doi:10.3319/tao.2008.19.6.767(pt)
- Huang, z., Nichol, S. L., Harris, P. T., and Caley, M. J. (2014). Classification of Submarine Canyons of the Australian Continental Margin. *Mar. Geol.* 357, 362–383. doi:10.1016/j.margeo.2014.07.007
- Hudec, M. R., and Jackson, M. P. A. (2007). Terra Infirma: Understanding Salt Tectonics. *Earth-Sci. Rev.* 82, 1–28. doi:10.1016/j.earscirev.2007.01.001
- Ingersoll, R. V. (2012). “Chapter 1: Tectonics of Sedimentary Basins, with Revised Nomenclature,” in *Tectonics of Sedimentary Basins: Recent Advances*. Editors C. Busby and A. Azor (Oxford, UK: Blackwell Publishing), 3–43.
- Jimoh, R. O., Tang, Y., Li, J., Awosika, L. F., Li, H., Akininbade, E. A., et al. (2018). The Architecture of the Lower Parts of Submarine Canyons on the Western

- Nigerian Continental Margin. *Acta Oceanol. Sin.* 37 (7), 28–40. doi:10.1007/s13131-018-1242-0
- Ju, Y., Wang, G., Li, S., Sun, Y., Suo, Y., Somerville, I., et al. (2020). Geodynamic Mechanism and Classification of Basins in the Earth System. *Gondwana Res.* 2020. In press. doi:10.1016/j.gr.2020.08.017
- Khrifounoff, A., Crassous, P., Bue, N. L., Dennielou, B., and Jacinto, R. S. (2012). Different Types of Sediment Gravity Flows Detected in the Var Submarine Canyon (Northwestern Mediterranean Sea). *Progr. Oceanogr.* 106, 138–153. doi:10.1016/j.pocan.2012.09.001
- Klaus, A., and Taylor, B. (1991). Submarine Canyon Development in the Izu-Bonin Forearc: a SeaMARC II and Seismic Survey of Aoga Shima Canyon. *Mar. Geophys. Res.* 13, 131–152.
- Krastel, S., Hanebuth, T. J. J., Antobreh, A. A., Henrich, R., Holz, C., Kölling, M., et al. (2001). Cap Timiris Canyon: a Newly Discovered Channel System Offshore of Mauritania. *Eos Trans. Am. Geophys. Union.* 85 (42), 417–432. doi:10.1029/2004eo420001
- Krastel, S., Wefer, G., Hanebuth, T. J. J., Antobreh, A. A., Freudenthal, T., Preu, B., et al. (2011). M78/3 shipboard scientific party Sediment dynamics and geohazards off Uruguay and the de la Plata River region (northern Argentina and Uruguay). *Geo-Mar. Lett.* 31, 271–283. doi:10.1007/s00367-011-0232-4
- Lastras, G., Acosta, J., Muñoz, A., and Canals, M. (2011a). Submarine Canyon Formation and Evolution in the Argentine Continental Margin Between 44°30'S and 48°S. *Geomorphology* 128, 116–136. doi:10.1016/j.geomorph.2010.12.027
- Lastras, G., Arzola, R. G., Masson, D. G., Wynn, R. B., Huvenne, V. A. I., Hühnerbach, V., et al. (2009). Geomorphology and Sedimentary Features in the Central Portuguese Submarine Canyons, Western Iberian Margin. *Geomorphology* 103, 310–329. doi:10.1016/j.geomorph.2008.06.013
- Lastras, G., Canals, M., Amblas, D., Lavoie, C., Church, I., De mol, B., et al. (2011b). Understanding Sediment Dynamics of Two Large Submarine Valleys from Seafloor Data: Blanes and La Fonera Canyons, Northwestern Mediterranean Sea. *Mar. Geol.* 280, 20–39. doi:10.1016/j.margeo.2010.11.005
- Lastras, G., Canals, M., Urgeles, R., Amblas, D., Ivanov, M., Droz, L., et al. (2007). A Walk Down the Cap de Creus Canyon, Northwestern Mediterranean Sea: Recent processes inferred from morphology and sediment bedforms. *Mar. Geol.* 246, 176–192. doi:10.1016/j.margeo.2007.09.002
- Laursen, J., and Normark, W. R. (2002). Late Quaternary Evolution of the San Antonio Submarine Canyon in the Central Chile Forearc (~33°S). *Mar. Geol.* 188, 365–390. doi:10.1016/s0025-3227(02)00421-8
- Le Dantec, N., Hogarth, L. J., Driscoll, N. W., Babcock, J. M., Barnhardt, W. A., and Schwab, W. C. (2010). Tectonic Controls on Nearshore Sediment Accumulation and Submarine Canyon Morphology Offshore La Jolla, Southern California. *Mar. Geol.* 268, 115–128. doi:10.1016/j.margeo.2009.10.026
- Lewis, K. B., and Barnes, P. M. (1999). Kaikoura Canyon, New Zealand: Active Conduit from Near-Shore Sediment Zones to Trench-Axis Channel. *Mar. Geol.* 162, 39–69. doi:10.1016/s0025-3227(99)00075-4
- Li, M. Z., Prescott, R. H., and Robertson, A. G. (2019). Observation of Internal Tides and Sediment Transport Processes at the Head of Logan Canyon on Central Scotian Slope, Eastern Canada. *J. Mar. Syst.* 193, 103–125. doi:10.1016/j.jmarsys.2019.02.007
- Li, W., Li, S., Alves, T. M., Rebesco, M., and Feng, Y. (2021). The Role of Sediment Gravity Flows on the Morphological Development of a Large Submarine Canyon (Taiwan Canyon), North-East South China Sea. *Sedimentology* 68, 1091–1108. doi:10.1111/sed.12818
- Liu, J. T., Hsu, R. T., Hung, J.-J., Chang, Y.-P., Wang, Y.-H., Rendle-Bührling, R. H., et al. (2016). From the Highest to the Deepest: The Gaoping River-Gaoping Submarine Canyon Dispersal System Earth-. *Sci. Rev.* 153, 274–300. doi:10.1016/j.earscrev.2015.10.012
- Liu, J. T., Kao, S.-J., Huh, C.-A., and Hung, C.-C. (2013). Gravity Flows Associated with Flood Events and Carbon Burial: Taiwan as Instructional Source Area. *Annu. Rev. Mar. Sci.* 5, 47–68. doi:10.1146/annurev-marine-121211-172307
- Lo Iacono, C., Sulli, A., Agate, M., Lo Presti, V., Pepe, F., and Catalano, R. (2011). Submarine Canyon Morphologies in the Gulf of Palermo (Southern Tyrrhenian Sea) and Possible Implications for Geo-Hazard. *Mar. Geophys. Res.* 32, 127–138. doi:10.1007/s11001-011-9118-0
- Lo Iacono, C., Sulli, A., and Agate, M. (2014). Submarine Canyons of North-Western Sicily (Southern Tyrrhenian Sea): Variability in Morphology, Sedimentary Processes and Evolution on a Tectonically Active Margin. *Deep Sea Res. Part II Top. Stud. Oceanogr.* 104, 93–105. doi:10.1016/j.dsr2.2013.06.018
- Maier, K. L., Rosenberger, K. J., Paull, C. K., Gwiazda, R., Gales, J., Lorenson, T., et al. (2019). Sediment and Organic Carbon Transport and Deposition Driven by Internal Tides along Monterey Canyon, Offshore California. *Deep Sea Res. Part I Oceanogr. Res. Pap.* 153, 103108. doi:10.1016/j.dsr.2019.103108
- Mart, Y. (1989). Sediment Distribution in Akhziv Canyon off Northern Israel. *Geo-Mar. Lett.* 9, 77–83. doi:10.1007/bf02430427
- Martín, J., Palanques, A., and Puig, P. (2006). Composition and Variability of Downward Particulate Matter Fluxes in the Palamós Submarine Canyon (NW Mediterranean). *J. Mar. Syst.* 60, 75–97. doi:10.1016/j.jmarsys.2005.09.010
- Matos, F. L., Ross, S. W., Huvenne, V. A. I., Davies, J. S., and Cunha, M. R. (2018). Canyons Pride and Prejudice: Exploring the Submarine Canyons Research Landscape, a History of Geographic and Thematic Bias. *Prog. Oceanogr.* 169, 6–19. doi:10.1016/j.pocan.2018.04.010
- Mauffrey, M. A., Berné, S., Jouet, G., Giresse, P., and Gaudin, M. (2015). Sea-level Control on the Connection between Shelf-Edge Deltas and the Bourcart Canyon Head (Western Mediterranean) during the Last Glacial/interglacial Cycle. *Mar. Geol.* 370, 1–19. doi:10.1016/j.margeo.2015.09.010
- Mazières, A., Gillet, H., Castelle, B., Mulder, T., Guyot, C., Garlan, T., et al. (2014). High-Resolution Morphobathymetric Analysis and Evolution of Capbreton Submarine Canyon Head (Southeast Bay of Biscay—French Atlantic Coast) over the Last Decade Using Descriptive and Numerical Modelling. *Mar. Geol.* 351, 1–12. doi:10.1016/j.margeo.2014.03.001
- McArthur, A. D., and Tek, D. E. (2021). Controls on the Origin and Evolution of Deep-Ocean Trench-Axial Channels. *Geology* 49 (8), 883–888. doi:10.1130/G48612.1
- McHargue, T., Pyrcz, M. J., Sullivan, M. D., Clark, J. D., Fildani, A., Romans, B. W., et al. (2011). Architecture of Turbidite Channel Systems on the Continental Slope: Patterns and Predictions. *Mar. Pet. Geol.* 28, 728–743. doi:10.1016/j.marpetgeo.2010.07.008
- Micallef, A., Mountjoy, J. J., Barnes, P. M., Canals, M., and Lastras, G. (2014). Geomorphic Response of Submarine Canyons to Tectonic Activity: Insights from the Cook Strait Canyon System, New Zealand. *Geosphere* 10 (5), 905–929. doi:10.1130/GES01040.1
- Michaud, F., Proust, J. N., Collot, J. Y., Lebrun, J. F., Witt, C., Ratzov, G., et al. (2015). Quaternary Sedimentation and Active Faulting along the Ecuadorian Shelf: Preliminary Results of the ATACAMES Cruise. *Mar. Geophys. Res.* 36, 81–98. doi:10.1007/s11001-014-9231-y
- Milia, A. (2000). The Dohrn Canyon: A Response to the Eustatic Fall and Tectonic Uplift of the Outer Shelf along the Eastern Tyrrhenian Sea Margin. *Italy. geo-mar. Lett.* 20, 101–108. doi:10.1007/s003670000044
- Milliman, J. D., and Kao, S.-J. (2005). Hyperpycnal Discharge of Fluvial Sediment to the Ocean: Impact of Super-typhoon Herb (1996) on Taiwanese Rivers. *J. Geol.* 113, 503–516. doi:10.1086/431906
- Milliman, J. D., and Syvitski, P. M. (1992). Geomorphic/Tectonic Control of Sediment Discharge to the Ocean: The Importance of Small Mountainous Rivers. *J. Geol.* 100, 525–544. doi:10.1086/629606
- Mitchell, J. K., Holdgate, G. R., Wallace, M. W., and Gallagher, S. J. (2007). Marine Geology of the Quaternary Bass Canyon System, Southeast Australia: a Cool-Water Carbonate System. *Mar. Geol.* 237, 71–96. doi:10.1016/j.margeo.2006.10.037
- Molenaar, A., Moernaut, J., Wiemer, G., Dubois, N., and Strasser, M. (2019). Earthquake Impact on Active Margins: Tracing Surficial Remobilization and Seismic Strengthening in a Slope Sedimentary Sequence. *Geophys. Res. Lett.* 46, 6015–6023. doi:10.1029/2019GL082350
- Mondziel, S., Grindlay, N., Mann, P., Escalona, A., and Abrams, L. (2010). Morphology, Structure, and Tectonic Evolution of the Mona Canyon (Northern Mona Passage) from Multibeam Bathymetry, Side-Scan Sonar, and Seismic Reflection Profiles. *Tectonics* 29, TC2003. doi:10.1029/2008TC002441
- Mountjoy, J. J., Barnes, P. M., and Pettinga, J. R. (2009). Morphostructure and Evolution of Submarine Canyons across an Active Margin: Cook Strait Sector of the Hikurangi Margin, New Zealand. *Mar. Geol.* 260, 45–68. doi:10.1016/j.margeo.2009.01.006
- Mountjoy, J. J., Howarth, J. D., Orpin, A. R., Barnes, P. M., Bowden, D. A., Rowden, A. A., et al. (2018). Earthquakes Drive Large-Scale Submarine Canyon

- Development and Sediment Supply to Deep-Ocean Basins. *Sci. Adv.* 4 (3), eaar3748. doi:10.1126/sciadv.aar3748
- Mountjoy, J. J., Micallef, A., Stevens, C. L., and Stirling, M. W. (2014). Holocene Sedimentary Activity in a Non-terrestrially Coupled Submarine Canyon: Cook Strait Canyon System, New Zealand. *Deep Sea Res. Part II Top. Stud. Oceanogr.* 104, 120–133. doi:10.1016/j.dsr2.2013.09.001
- Mulder, T., Ducassou, E., Gillet, H., Hanquiez, V., Tournadour, E., Combes, J., et al. (2012). Canyon Morphology on a Modern Carbonate Slope of the Bahamas: Evidence of Regional Tectonic Tilting. *Geology* 40 (9), 771–774. doi:10.1130/G33327.1
- Mulder, T., Lecroart, P., Hanquiez, V., Marches, E., Gonthier, E., Guedes, J.-C., et al. (2006). The Western Part of the Gulf of Cadiz: Contour Currents and Turbidity Currents Interactions. *Geo-Mar. Lett.* 26 (1), 31–41. doi:10.1007/s00367-005-0013-z
- Nelson, C. H., Escutia, C., Damuth, J. E., and Twichell, D. C., Jr. (2011). “Interplay of Mass-Transport and Turbidite-System Deposits in Different Active Tectonic and Passive Continental Margin Settings: External and Local Controlling Factors,” in *Mass-Transport Deposits in Deepwater Settings*. Editors R. C. Shipp, P. Weimer, and H. W. Posamentier (Tulsa, OK: SEPM), 39–66. doi:10.2110/sepm.096.039
- NOAA National Centers for Environmental Information (2021). Available at <https://www.ncei.noaa.gov/maps/bathymetry/> [Accessed October 28, 2021]
- Noda, A., TuZino, T., Furukawa, R., Joshima, M., and Uchida, J. (2008). Physiographical and Sedimentological Characteristics of Submarine Canyons Developed upon an Active Forearc Slope: the Kushiro Submarine Canyon, Northern Japan. *Geol. Soc. Am. Bull.* 120 (5/6), 750–767. doi:10.1130/B26155.1
- Noda, A., and TuZino, T. (2010). Shelf-Slope Sedimentation during the Late Quaternary on the Southwestern Kuril Forearc Margin, Northern Japan. *Sediment. Geol.* 232, 35–51. doi:10.1016/j.sedgeo.2010.09.008
- Normark, W. R., and Carlson, P. R. (2003). “Giant Submarine Canyons: Is Size Any Clue to Their Importance in the Rock Record?,” in *Extreme depositional Environ. Mega end members Geol. time* Editors M. A. Chan and A. W. Archer (Boulder, CO: GSA), 175–190. doi:10.1130/0-8137-2370-1.175
- Normark, W. R., Piper, D. J. W., Romans, B. W., Covault, J. A., Dartnell, P., and Sliter, R. W. (2009). “Submarine Canyon and Fan Systems of the California Continental Borderland,” in *Earth Science in the Urban Ocean: The Southern California Continental Borderland*. Editors H. J. Lee and W. R. Normark (Boulder, CO: GSA), 141–168. doi:10.1130/2009.2454(2.7)
- Normark, W. R., Posamentier, H., and Mutti, E. (1993). Turbidite Systems: State of the Art and Future Directions. *Rev. Geophys.* 31 (2), 91–116. doi:10.1029/93rg02832
- Nyberg, B., Helland-Hansen, W., Gawthorpe, R. L., Sandbakken, P., Eide, C. H., Somme, T., et al. (2018). Revisiting Morphological Relationships of Modern Source-To-Sink Segments as a First-Order Approach to Scale Ancient Sedimentary Systems. *Sediment. Geol.* 373, 111–133. doi:10.1016/j.sedgeo.2018.06.007
- Oiwane, H., Tonai, S., Kiyokawa, S., Nakamura, Y., Suganuma, Y., and Tokuyama, H. (2011). Geomorphological Development of the Goto Submarine Canyon, Northeastern East China Sea. *Mar. Geol.* 288, 49–60. doi:10.1016/j.margeo.2011.06.013
- Palanques, A., El Khatab, M., Puig, P., Masqué, P., Sánchez-Cabeza, J. A., and Isla, E. (2005). Downward Particle Fluxes in the Guadiaro Submarine Canyon Depositional System (North-western Alboran Sea), a River Flood Dominated System. *Mar. Geol.* 220, 23–40. doi:10.1016/j.margeo.2005.07.004
- Palanques, A., Martín, J., Puig, P., Guillén, J., Company, J. B., and Sardá, F. (2006). Evidence of Sediment Gravity Flows Induced by Trawling in the Palamós (Fonera) Submarine Canyon (Northwestern Mediterranean). *Deep Sea Res. Part I Oceanogr. Res. Pap.* 53, 201–214. doi:10.1016/j.dsr.2005.10.003
- Paull, C. K., Caress, D. W., Lundsten, E., Gwiazda, R., Anderson, K., McGann, M., et al. (2013). Anatomy of the La Jolla Submarine Canyon System; Offshore Southern California. *Mar. Geol.* 335, 16–34. doi:10.1016/j.margeo.2012.10.003
- Peakall, J., and Sumner, E. J. (2015). Submarine Channel Flow Processes and Deposits: a Process-Product Perspective. *Geomorphology* 244, 95–120. doi:10.1016/j.geomorph.2015.03.005
- Pierau, R., Hanebuth, T. J. J., Krastel, S., and Henrich, R. (2010). Late Quaternary Climatic Events and Sea-Level Changes Recorded by Turbidite Activity, Dakar Canyon, NW Africa. *Quat. Res.* 73, 385–392. doi:10.1016/j.yqres.2009.07.010
- Pierau, R., Henrich, R., Preiß-Daimler, I., Krastel, S., and Geersen, J. (2011). Sediment Transport and Turbidite Architecture in the Submarine Dakar Canyon off Senegal, NW-Africa. *J. Afr. Earth Sci.* 60, 196–208. doi:10.1016/j.jafrearsci.2011.02.010
- Pierdomenico, M., Casalbore, D., and Chiocci, F. L. (2019). Massive Benthic Litter Funnelled to Deep Sea by Flash-Flood Generated Hyperpycnal Flows. *Sci. Rep.* 9, 5530. doi:10.1038/s41598-019-41816-8
- Pierdomenico, M., Martorelli, E., Dominguez-Carrio, C., Gili, J. M., and Chiocci, F. L. (2016). Seafloor Characterization and Benthic Megafaunal Distribution of an Active Submarine Canyon and Surrounding Sectors: The Case of Gioia Canyon (Southern Tyrrhenian Sea). *J. Mar. Syst.* 157, 101–117. doi:10.1016/j.jmarsys.2016.01.005
- Piper, D. J. W., Hiscott, R. N., and Normark, W. R. (1999). Outcrop-scale Acoustic Facies Analysis and Latest Quaternary Development of Hueneme and Dume Submarine Fans, Offshore California. *Sedimentology* 46, 47–78. doi:10.1046/j.1365-3091.1999.00203.x
- Piper, D. J. W., and Normark, W. R. (2009). Processes that Initiate Turbidity Currents and Their Influence on Turbidites: a Marine Geology Perspective. *J. Sediment. Res.* 79, 347–362. doi:10.2110/jsr.2009.046
- Pisareva, M. N., Pickart, R. S., Lin, P., Frattantoni, P. S., and Weingartner, T. J. (2019). On the Nature of Wind-Forced Upwelling in Barrow Canyon. *Deep Sea Res. Part II Top. Stud. Oceanogr.* 162, 63–78. doi:10.1016/j.dsr2.2019.02.002
- Popescu, I., Lericolais, G., Panin, N., Normand, A., Dinu, C., and Le Drezen, E. (2004). The Danube Submarine Canyon (Black Sea): Morphology and Sedimentary Processes. *Mar. Geol.* 206, 249–265. doi:10.1016/j.margeo.2004.03.003
- Pratson, L. F., Nittrouer, C. A., Wiberg, P. L., Steckler, M. S., Swenson, J. B., Cacchione, D. A., et al. (2007). “Seascape Evolution on Clastic Continental Shelves and Slopes,” in *Continental Margin Sedimentation: From Sediment Transport to Sequence Stratigraphy*. Editors C. A. Nittrouer, J. A. Austin, M. E. Field, J. H. Kravitz, J. P. M. Syvitski, and P. L. Wiberg (Oxford, UK: Blackwell Publishing), 339–380.
- Puga-Bernabéu, A., Webster, J. M., Beaman, R. J., and Guilbaud, V. (2011). Morphology and Controls on the Evolution of a Mixed Carbonate-Siliciclastic Submarine Canyon System, Great Barrier Reef Margin, North-Eastern Australia. *Mar. Geol.* 289, 100–116. doi:10.1016/j.margeo.2011.09.013
- Puig, P., Durán, R., Muñoz, A., Elvira, E., and Guillén, J. (2017). Submarine Canyon-Head Morphologies and Inferred Sediment Transport Processes in the Alías-Almanzora Canyon System (SW Mediterranean): on the Role of the Sediment Supply. *Mar. Geol.* 393, 21–34. doi:10.1016/j.margeo.2017.02.009
- Puig, P., Palanques, A., Guillén, J., and García-Ladona, E. (2000). Deep Slope Currents and Suspended Particle Fluxes in and Around the Foix Submarine Canyon (NW Mediterranean). 47. *Deep Sea Res. Part I Oceanogr. Res. Pap.* 47, 343343–366366. doi:10.1016/s0967-0637(99)00062-x
- Puig, P., Palanques, A., and Martín, J. (2014). Contemporary Sediment-Transport Processes in Submarine Canyons. *Annu. Rev. Mar. Sci.* 6, 53–77. doi:10.1146/annurev-marine-010213-135037
- Ratzov, G., Sosson, M., Collot, J.-Y., and Migeon, S. (2012). Late Quaternary Geomorphologic Evolution of Submarine Canyons as a Marker of Active Deformation on Convergent Margins: The Example of the South Colombian Margin. *Mar. Geol.* 315–318, 77–97. doi:10.1016/j.margeo.2012.05.005
- Reid, I., and Frostick, L. E. (2011). “Chapter 13: Channel Form, Flows and Sediments of Endogenous Ephemeral Rivers in Deserts,” in *Arid Zone Geomorphology: Process, Form and Change in Drylands*. Editor D. S. G. Thomas (Oxford, UK: John Wiley & Sons), 301–332. doi:10.1002/9780470710777.ch13
- Restrepo-Correa, I. C., and Ojeda, G. Y. (2010). Geologic Controls on the Morphology of La Aguja Submarine Canyon. *J. South. Am. Earth. Sci.* 29, 861–870. doi:10.1016/j.jsames.2010.07.001
- Ridente, D., Martorelli, E., Bosman, A., and Chiocci, F. L. (2014). High-resolution Morpho-Bathymetric Imaging of the Messina Strait (Southern Italy). New Insights on the 1908 Earthquake and Tsunami. *Geomorphology* 208, 149–159. doi:10.1016/j.geomorph.2013.11.021
- Rise, L., Boe, R., Riis, F., Bellec, V. K., Laberg, J. S., Eidvin, T., et al. (2013). The Lofoten-Vesterålen Continental Margin, North Norway: Canyons and Mass-

- Movement Activity. *Mar. Pet. Geol.* 45, 134–149. doi:10.1016/j.marpetgeo.2013.04.021
- Rona, P., Guida, V., Scranton, M., Gong, D., Macelloni, L., Pierdomenico, M., et al. (2015). Hudson Submarine Canyon Head Offshore New York and New Jersey: A Physical and Geochemical Investigation. *Deep Sea Res. Part II Top. Stud. Oceanogr.* 121, 213–232. doi:10.1016/j.dsr2.2015.07.019
- Rowan, M. G., Peel, F. J., and Vendeville, B. C. (2004). “Gravity-driven Fold Belts on Passive Margins,” in *Thrust Tectonics and Hydrocarbon Systems*. Editor K. R. McClay (Tulsa, OK: AAPG), 157–182.
- Salmanidou, D. M., Heidarzadeh, M., and Guillas, S. (2019). Probabilistic Landslide-Generated Tsunamis in the Indus Canyon, NW Indian Ocean, Using Statistical Emulation. *Pure Appl. Geophys.* 176, 3099–3114. doi:10.1007/s00024-019-02187-3
- Sanchez, C. A., Fulthorpe, C. S., and Steel, R. J. (2012). Miocene Shelf-Edge Deltas and Their Impact on Deepwater Slope Progradation and Morphology, Northwest Shelf of Australia. *Basin Res.* 24, 683–698. doi:10.1111/j.1365-2117.2012.00545.x
- Santora, J. A., Zeno, R., Dorman, J. G., and Sydeman, W. J. (2018). Submarine Canyons Represent an Essential Habitat Network for Krill Hotspots in a Large Marine Ecosystem. *Sci. Rep.* 8, 7579. doi:10.1038/s41598-018-25742-9
- Sawyer, D. E., and DeVore, J. R. (2015). Elevated Shear Strength of Sediments on Active Margins: Evidence for Seismic Strengthening. *Geophys. Res. Lett.* 42, 10216–10221. doi:10.1002/2015GL066603
- Schnürle, P., Liu, C.-S., Lallemand, S. E., and Reed, D. (1998). Structural Controls of the Taitung Canyon in the Huatung Basin East of Taiwan. *TAO* 9 (3), 453–472.
- Shumaker, L. E., Jobe, Z. R., Johnstone, S. A., Pettinga, L. A., Cai, D. X., and Moody, J. D. (2018). Controls on Submarine Channel-Modifying Processes Identified through Morphometric Scaling Relationships. *Geosphere* 14 (5), 2171–2187. doi:10.1130/GES01674.1
- Shyu, J. B. H., Sieh, K., and Chen, Y.-G. (2005). Tandem Suturing and Disarticulation of the Taiwan Orogen Revealed by its Neotectonics Elements. *Earth Planet. Sci. Lett.* 233, 167–177. doi:10.1016/j.epsl.2005.01.018
- Smith, M. E., Finnegan, N. J., Mueller, E. R., and Best, R. J. (2017). Durable Terrestrial Bedrock Predicts Submarine Canyon Formation. *Geophys. Res. Lett.* 44, 10332–10340. doi:10.1002/2017GL075139
- Soh, W., Tokuyama, H., Fujioka, K., Kato, S., and Taira, A. (1990). Morphology and Development of a Deep-Sea Meandering Canyon (Boso Canyon) on an Active Plate Margin, Sagami Trough, Japan. *Mar. Geol.* 91, 227–241. doi:10.1016/0025-3227(90)90038-1
- Soh, W., and Tokuyama, H. (2002). Rejuvenation of Submarine Canyon Associated with Ridge Subduction, Tenryu Canyon, off Tokai, Central Japan. *Mar. Geol.* 187, 203–220. doi:10.1016/s0025-3227(02)00267-0
- Sømme, T. O., Helland-Hansen, W., Martinsen, O. J., and Thurmond, J. B. (2009). Relationships between Morphological and Sedimentological Parameters in Source-to-Sink Systems: A Basis for Predicting Semi-quantitative Characteristics in Subsurface Systems. *Basin Res.* 21, 361–387. doi:10.1111/j.1365-2117.2009.00397.x
- Soulet, W., Migeon, S., Gorini, C., Rubino, J.-L., Raison, F., and Bourges, P. (2016). Erosional versus Aggradational Canyons along a Tectonically-Active Margin: the Northeastern Ligurian Margin (Western Mediterranean Sea). *Mar. Geol.* 382, 17–36. doi:10.1016/j.margeo.2016.09.015
- Soutter, E. L., Bell, D., Cumberpatch, Z. A., Ferguson, R. A., Sychala, Y. T., Kane, I. A., et al. (2020). The Influence of Confining Topography Orientation on Experimental Turbidity Currents and Geological Implications. *Earth Sci.* 8, 540633.
- Soutter, E. L., Kane, I. A., Hodgson, D. M., and Flint, S. (2021). The Concavity of Submarine Canyon Longitudinal Profiles. *J. Geophys. Res. Earth. Surf.* 126, e2021JF006185. doi:10.1029/2021JF006185
- Stow, D. (1986). “Deep Clastic Seas,” in *Sedimentary Environments and Facies*. Editor H. G. Reading (Boston, MA: Blackwell), 399–443.
- Strozyk, F., Strasser, M., Förster, A., Kopf, A., and Huhn, K. (2010). Slope Failure Repetition in Active Margin Environments: Constraints from Submarine Landslides in the Hellenic Fore Arc, Eastern Mediterranean. *J. Geophys. Res. Earth.* 115, B08103. doi:10.1029/2009JB006841
- Su, M., Hsiung, K.-H., Zhang, C., Xie, X., Yu, H.-S., and Wang, Z. (2015). The Linkage between Longitudinal Sediment Routing Systems and Basin Types in the Northern South China Sea in Perspective of Source-To-Sink. *J. Asian Earth Sci.* 111, 1–13. doi:10.1016/j.jseas.2015.05.011
- Su, M., Lin, Z., Wang, C., Kuang, Z., Liang, J., Chen, H., et al. (2020). Geomorphologic and Infilling Characteristics of the Slope-Confining Submarine Canyons in the Pearl River Mouth Basin, Northern South China Sea. *Mar. Geol.* 424, 106166. doi:10.1016/j.margeo.2020.106166
- Susanth, S., Kurian, P. J., Bijesh, C. M., Twinkle, D., Tyagi, A., and Rajan, S. (2021). Controls on the Evolution of Submarine Canyons in Steep Continental Slopes: Geomorphological Insights from Palar Basin, Southeastern Margin of India. *Geo-Mar. Lett.* 41, 14. doi:10.1007/s00367-021-00685-9
- Sweet, M. L., and Blum, M. D. (2016). Connections between Fluvial to Shallow Marine Environments and Submarine Canyons: Implications for Sediment Transfer to Deep Water. *J. Sediment. Res.* 86, 1147–1162. doi:10.2110/jsr.2016.64
- Sylvester, Z., Deptuck, M., Prather, B. E., Pirmez, C., and O’Byrne, C. (2012). “Seismic Stratigraphy of a Shelf-Edge Delta and Linked Submarine Channels in the Northeastern Gulf of Mexico,” in *Application of the Principles of Seismic Geomorphology to Continental Slope and Base-Of-Slope Systems: Case Studies from Seafloor and Near-Seafloor Analogues*. Editors B. E. Prather, M. E. Deptuck, D. Mohrig, B. Van Hooen, and R. B. Wynn (Tulsa, OK: SEPMP), 31–59. doi:10.2110/pec.12.99.0031
- Thornburg, T. M., Kulm, L. D., and Hussong, D. M. (1990). Submarine-fan Development in the Southern Chile Trench: A Dynamic Interplay of Tectonics and Sedimentation. *Am. Geol. Soc. Bull.* 102, 1658–1680. doi:10.1130/0016-7606(1990)102<1658:sfdits>2.3.co;2
- Trumbull, J. V. A., and Garrison, L. E. (1973). Geology of a System of Submarine Canyons South of Puerto Rico. *J. Res. U.S. Geol. Surv.* 1 (3), 293–299.
- Tubau, X., Lastras, G., Canals, M., Micallef, A., and Amblas, D. (2013). Significance of the Fine Drainage Pattern for Submarine Canyon Evolution: the Foix Canyon System, Northwestern Mediterranean Sea. *Geomorphology* 184, 20–37. doi:10.1016/j.geomorph.2012.11.007
- Tubau, X., Paull, C. K., Lastras, G., Caress, D. W., Canals, M., Lundsten, E., et al. (2015). Submarine Canyons of Santa Monica Bay, Southern California: Variability in Morphology and Sedimentary Processes. *Mar. Geol.* 365, 61–79. doi:10.1016/j.margeo.2015.04.004
- TuZino, T., and Noda, A. (2010). Architecture and Evolution of the Kuroshio Submarine Canyon in the Kurile Trench Forearc Slope, North-western Pacific. *Sedimentology* 57, 611–641. doi:10.1111/j.1365-3091.2009.01107.x
- Urias Espinosa, J., Bandy, W. L., Mortera Gutiérrez, C. A., Núñez Cornú, F. J., and Mitchell, N. C. (2016). Multibeam Bathymetric Survey of the Ipa Submarine Canyon, Jalisco, Mexico (20°N): The Southern Boundary of the Banderas Forearc Block? *Tectonophysics* 671, 249–263. doi:10.1016/j.tecto.2015.12.029
- Valentine, P. C., Uzzmann, J. R., and Cooper, R. A. (1980). Geology and Biology of Oceanographer Submarine Canyon. *Mar. Geol.* 38, 283–312. doi:10.1016/0025-3227(80)90004-3
- Vardar, D. (2019). Morphological Definition of the North İmralı Canyon in the Sea of Marmara. *Arab. J. Geosci.* 12, 76. doi:10.1007/s12517-019-4257-8
- von Rad, U., and Tahir, M. (1997). Late Quaternary Sedimentation on the Outer Indus Shelf and Slope (Pakistan): Evidence from High-Resolution Seismic Data and Coring. *Mar. Geol.* 138, 193–236. doi:10.1016/s0025-3227(96)00090-4
- Walsh, J. P., Alexander, C. R., Gerber, T., Orpin, A. R., and Sumners, B. W. (2007/2007). Demise of a Submarine Canyon? Evidence for Highstand Infilling on the Waipaoa River Continental Margin, New Zealand. *Geophys. Res. Lett.* 34, L20606. doi:10.1029/2007GL031142
- Wan, L., Bianchi, V., Hurter, S., Salles, T., Zhang, Z., and Yuan, X. (2021). Morphological Controls on Delta-Canyon-Fan Systems: Insights from Stratigraphic Forward Models. *Sedimentol. Early View* 2021. doi:10.1111/sed.12930
- Wang, R., Colomera, L., and Mountney, N. P. (2019). Geological Controls on the Geometry of Incised-Valley Fills: Insights from a Global Dataset of Late-Quaternary Examples. *Sedimentology* 66 (6), 2134–2168. doi:10.1111/sed.12596
- Warratz, G., Schwenk, T., Voigt, I., Bozzano, G., Henrich, R., Violante, R., et al. (2019). Interaction of a deep-sea current with a blind submarine canyon (Mar del Plata Canyon, Argentina). *Mar. Geol.* 417, 106002. doi:10.1016/j.margeo.2019.106002
- Wiles, E., Green, A., Watkeys, M., Jokat, W., and Kroker, R. (2013). The Evolution of the Tugela Canyon and Submarine Fan: A Complex Interaction between Margin Erosion and Bottom Current Sweeping, Southwest Indian Ocean, South Africa. *Mar. Pet. Geol.* 44, 60–70. doi:10.1016/j.marpetgeo.2013.03.012
- Wynn, R. B., Weaver, P. P. E., Masson, D. G., and Stow, D. A. V. (2002). Turbidite Depositional Architecture across Three Interconnected Deep-Water Basins on

- the North-West African Margin. *Sedimentology* 49, 669–695. doi:10.1046/j.1365-3091.2002.00471.x
- Xu, J. P., and Noble, M. A. (2009). Currents in Monterey Submarine Canyon. *J. Geophys. Res.* 114, C03004. doi:10.1029/2008JC004992
- Xu, S., Wang, Y., Peng, X., Zou, H., Qiu, Y., Gong, C., et al. (2014). Origin of Taiwan Canyon and its Effects on Deepwater Sediment. *Sci. China Earth Sci.* 57 (11), 2769–2780. doi:10.1007/s11430-014-4942-0
- Yang, X., Peel, F. J., McNeill, L. C., and Sanderson, D. J. (2020). Comparison of Fold-Thrust Belts Driven by Plate Convergence and Gravitational Failure. *Earth-Sci. Rev.* 203, 103136. doi:10.1016/j.earscirev.2020.103136
- Yin, S., Li, J., Ding, W., Gao, J., Ding, W., and Wang, Y. (2018). Migration of the Lower North Palawan Submarine Canyon: Characteristics and Controls. *Int. Geol. Rev.* 6287–8, 988–1005. doi:10.1080/00206814.2018.1522519
- Yin, S., Wang, L., Guo, Y., and Zhong, G. (2015). Morphology, Sedimentary Characteristics, and Origin of the Dongsha Submarine Canyon in the Northeastern Continental Slope of the South China Sea. *Sci. China Earth Sci.* 58, 971–985. doi:10.1007/s11430-014-5044-8
- Yu, H.-S., and Chang, J.-F. (2002). The Penghu Submarine Canyon off Southwestern Taiwan: Morphology and Origin. *Terr. Atmos. Ocean. Sci.* 13 (4), 547–562. doi:10.3319/tao.2002.13.4.547(o)
- Yu, H.-S., and Chiang, C.-S. (1995). Morphology and Origin of the Hongtsai Submarine Canyon West of the Hengchun Peninsula, Taiwan. *J. Geol. Soc. China* 38 (1), 81–93.
- Yu, H.-S., Liu, C. S., and Lee, J.-T. (1992). The Kaohsiung Submarine Canyon: a Modern Aborted Canyon and its Morphology and Echo Character. *Acta Ocean. Taiwan* 28, 19–30.
- Yu, H.-S., and Lu, J. C. (1995). Development of the Shale Diapir-Controlled Fangliao Canyon on the Continental Slope off Southwestern Taiwan. *J. Asian Earth Sci.* 11 (4), 265–276. doi:10.1016/0743-9547(95)00004-c
- Zavala, C. (2020). Hyperpycnal (Over Density) Flows and Deposits. *J. Palaeogeogr.* 9, 17. doi:10.1186/s42501-020-00065-x
- Zhang, F., Hu, Y., Fan, X., Yu, W., Liu, X., and Jin, Z. (2022). Controls on Seasonal Erosion Behavior and Potential Increase in Sediment Evacuation in the Warming Tibetan Plateau. *Catena* 209, 105797. doi:10.1016/j.catena.2021.105797
- Zhang, Y., Liu, Z., Zhao, Y., Colin, C., Zhang, X., Wang, M., et al. (2018). Long-term *In Situ* Observations on Typhoon-Triggered Turbidity Currents in the Deep Sea. *Geology* 46 (8), 675–678. doi:10.1130/G45178.1
- Zhong, G., and Peng, X. (2021). Transport and Accumulation of Plastic Litter in Submarine Canyons – The Role of Gravity Flows. *Geology* 49, 581–586. doi:10.1130/G48536.1

Conflict of Interest: The authors declare that the research was conducted in the absence of any commercial or financial relationships that could be construed as a potential conflict of interest.

Publisher's Note: All claims expressed in this article are solely those of the authors and do not necessarily represent those of their affiliated organizations, or those of the publisher, the editors and the reviewers. Any product that may be evaluated in this article, or claim that may be made by its manufacturer, is not guaranteed or endorsed by the publisher.

Copyright © 2022 Bührig, Colomera, Patacci, Mountney and McCaffrey. This is an open-access article distributed under the terms of the Creative Commons Attribution License (CC BY). The use, distribution or reproduction in other forums is permitted, provided the original author(s) and the copyright owner(s) are credited and that the original publication in this journal is cited, in accordance with accepted academic practice. No use, distribution or reproduction is permitted which does not comply with these terms.



Coexistence of Adjacent Siliciclastic, Carbonate, and Mixed Sedimentary Systems: An Example From Seafloor Morphology in the Northern Lesser Antilles Forearc

Pierre Morena^{1,2*}, Gueorgui Ratzov², Antonio Cattaneo¹, Frauke Klingelhoefer¹, Christian Beck³, Chloé Seibert⁴, Boris Marcaillou² and Nathalie Feuillet⁴

¹Geo-Ocean, Univ Brest, CNRS, Brest, France, ²Université Côte d'Azur, CNRS, IRD, Observatoire de la Côte d'Azur, Géoazur, Valbonne, France, ³CNRS ISTERre, Université Savoie-Mont-Blanc, Le Bourget du Lac, France, ⁴Institut de Physique du Globe de Paris, CNRS, Université de Paris-Cité, Paris, France

OPEN ACCESS

Edited by:

Adam McArthur,
University of Leeds, United Kingdom

Reviewed by:

Barbara Claussmann,
Schlumberger, United Kingdom
Lesli Wood,
Colorado School of Mines,
United States

*Correspondence:

Pierre Morena
pierre.f.morena@gmail.com

Specialty section:

This article was submitted to
Sedimentology, Stratigraphy and
Diagenesis,
a section of the journal
Frontiers in Earth Science

Received: 12 December 2021

Accepted: 07 June 2022

Published: 13 July 2022

Citation:

Morena P, Ratzov G, Cattaneo A,
Klingelhoefer F, Beck C, Seibert C,
Marcaillou B and Feuillet N (2022)
Coexistence of Adjacent Siliciclastic,
Carbonate, and Mixed Sedimentary
Systems: An Example From Seafloor
Morphology in the Northern Lesser
Antilles Forearc.
Front. Earth Sci. 10:834029.
doi: 10.3389/feart.2022.834029

Three main types of factors commonly control the nature of the clasts, the arrangement of the distinctive lithologies, and the general architecture of turbidite systems: sedimentation rate and carbonate production; climates and glacio-eustatism; and morphology and tectonics. The coexistence of adjacent systems of distinctive nature is, however, scarcely documented, and the relative influence of each factor needs better constrain. In the Northern Lesser Antilles Segment (NLAS), carbonate and siliciclastic sediment sources coexist within a 150 km lateral distance, with carbonate platforms lying onto a volcanic substratum, and by a succession of spurs and triangular valleys that are bounded by active normal faulting. To better understand the factors controlling sedimentary processes from the carbonate platform sources to the deep-sea sinks, we used backscatter, bathymetry, multichannel seismic, and sub-bottom profiles. Sedimentary systems are dominated by siliciclastic input (by retrogressive erosion of confined canyons affecting the volcanic slope), carbonate input (by carbonate sediment transported by oceanic- and wind-driven submarine currents beyond the leeward edges of carbonates platforms), or both. In the mixed systems, the retrogressive erosion of the canyon head determines the nature of the source (volcanic on the slope, carbonate when the canyons reach the shelf edge). Glacio-eustatism has a key role in carbonate availability on the platform, as attested by the presence of drowned platforms. The main contribution of this study is the identification of the major role that tectonic activity plays in the short-distance coexistence of the distinctive sedimentary systems since fault-bounded V-shaped valleys in map view offer alternating leeward and windward edges favoring carbonate or mixed systems. Additionally, the steep slope gradient induced by normal faults and regional subsidence seems to be the main factor controlling sediment dispersal. It causes multiple line sources and the dispersion of gravity-driven currents under the effect of hydraulic jumps, thus preventing the formation of a channelized system. Our study provides a modern analog of adjacent systems dominated by distinctive lithologies in a tectonically active area. The results appear particularly appropriate to decipher the nature of ancient

source-to-sink systems dominated by complex tectonics, paleo-bathymetry, and sediment routings.

Keywords: sediment pathways, mixed turbidite system, subduction zone, submarine canyon, plunge-pool, active tectonics

1 INTRODUCTION

The identification of the main depositional elements in sedimentary systems, especially for the lowest part of the systems where gravity flows and turbidity currents dominate, was proposed first in siliciclastic systems, in particular concerning the architecture of turbidite systems that include sediment sources on land and on the shelf, canyons on the continental slope, channel-levee systems, and distal fan systems in the abyssal plain (Mutti and Normark, 1991; Shanmugam, 2016). Gravity flows typically funneled into point sources constitute a morphological control leading to such architecture (Yose and Heller, 1989 and references therein). Differences in sedimentary systems, such as morphology and timing of clastic production, do exist. Indeed, carbonate gravity flows are commonly triggered from a line of sources at the shelf edge or along the slope (Mullins et al., 1984; Droxler and Schlager, 1985; Reijmer et al., 1988; Haak and Schlager, 1989; Mulder et al., 2012b), diluting the amount of sediment, thus deep water carbonates systems are considered to lack well-developed channel-levee and lobe deposits (Yose and Heller, 1989). The timing of sediment transfer may also differ, with carbonate systems being more productive during sea-level high stands (Reijmer et al., 1988), while pure siliciclastic systems are more active during relative sea-level low stands (Posamentier et al., 1991; Vail et al., 1991; Hübscher et al., 1997). Likewise, in the mixed systems, the dominance of the carbonate sources during sea-level highstands/warm periods and dominance of the siliciclastic sources during sea-level low stands/cool periods are generally observed (Schlager et al., 1994; Jorjy et al., 2008). The “dominant” system usually restrains the other system (e.g., carbonate reefs prevent the siliciclastic input, Puga-Bernabéu et al., 2011; 2014; Moscardelli et al., 2019).

Over the two last decades, a series of studies conducted in ancient (Dorsey and Kidwell, 1999; Braga et al., 2001; Payros and Pujalte, 2008; Sola et al., 2017; Chiarella et al., 2017; 2019) and modern depositional systems (Mulder et al., 2012a; 2012b; Principaud et al., 2015; Tournadour et al., 2015, 2017; Counts et al., 2018; Jorjy et al., 2020) reveal multiple examples with similar morphologies and architectural elements between siliciclastic, carbonate, and mixed turbidite systems. To predict the nature of the clasts, the arrangement of the distinctive types of deposits, and the general architecture of the turbidite systems, the authors emphasize the influence of three main types of factors. These include first, the sedimentation rate and carbonate production (Dorsey and Kidwell, 1999; Jorjy et al., 2008; Counts et al., 2018; Jorjy et al., 2020); second, climate, and eustatism (Spence and Tucker, 1997; McArthur et al., 2013; Puga-Bernabéu et al., 2014; Cumberpatch et al., 2021); third, the morphology and tectonic displacements of the source areas (Bailleul et al., 2007; Reijmer et al., 2012; Ćosović et al., 2018; Claussmann et al., 2021a; Claussmann et al., 2021b). The

coexistence of adjacent systems of distinctive nature is however scarcely documented, and the relative influence of each factor needs to be better constrained.

In this study, we propose a detailed morphological analysis of a marine dataset from the Northern Antilles area, and in particular from the Northern Lesser Antilles Segment (NLAS). This area extends from the inactive volcanic arc to the subduction front between Antigua and Anguilla banks (**Figure 1**). The NLAS is composed of carbonate shelves resting on a volcanic basement where structural features control the overall morphology of the margin (Feuillet et al., 2002; Laurencin et al., 2017; Boucard et al., 2021), and the connectivity of carbonate reefs to the deeper part of turbiditic sedimentary systems. The coexistence of adjacent siliciclastic, carbonate or mixed sedimentary systems make the NLAS an ideal case to identify the mechanisms and controls of sediment distribution from the carbonate shelf sources to deep-sea sinks in the forearc. We anticipate the application of this case in both modern and ancient systems dominated by tectonics and presenting complex morphologies, sediment pathways, and sediment accumulation. We present new backscatter and bathymetric data, multichannel seismic profiles (MCS profiles), and sub-bottom profile data (**Figure 2**) to: 1) identify the sediment sources and pathways of gravity-driven currents and sediment transfer, from the carbonate shelf down to the slope in the forearc zone of the NLAS, 2) identify the signature of dominant processes that influence sediment remobilization and transfer, and 3) infer their variability over time.

2 GEOLOGICAL SETTING

2.1 Geodynamics of the Lesser Antilles

The Lesser Antilles Volcanic Arc results from the subduction of the upper Cretaceous (~100 Ma) oceanic lithosphere (Stein et al., 1982; Stéphan et al., 1990), part of the North and South American plates, beneath the Caribbean plate (**Figure 1A**). The present-day convergence rate is ~20 mm/year along a ~N254° direction (De Mets et al., 2010).

The primary arc of the Lesser Antilles was formed during the Eocene to the early or the middle Miocene (Bouysse and Guennoc, 1983; Legendre et al., 2018). It comprises volcanic islands from Dog Island to Guadeloupe and from St. Lucia to Grenade (**Figure 1**). Tectonic uplift was responsible for the emergence of some carbonate platforms such as Marie-Galante, Barbuda, and Anguilla (Budd et al., 1995; Feuillet et al., 2004; Cornée et al., 2012; Weil-Accardo et al., 2022). The uplift results either from backarc spreading in the Kalinago Basin (**Figures 1B,C**) during the earliest-middle Miocene (Boucard et al., 2021) or from long-term processes along the subduction megathrust during the Pliocene (Feuillet et al., 2004; Leclerc and Feuillet, 2019).

The subduction of Tiburón ridge (**Figure 1**) during the middle to the late Miocene (Pichot et al., 2012) and Barracuda ridge

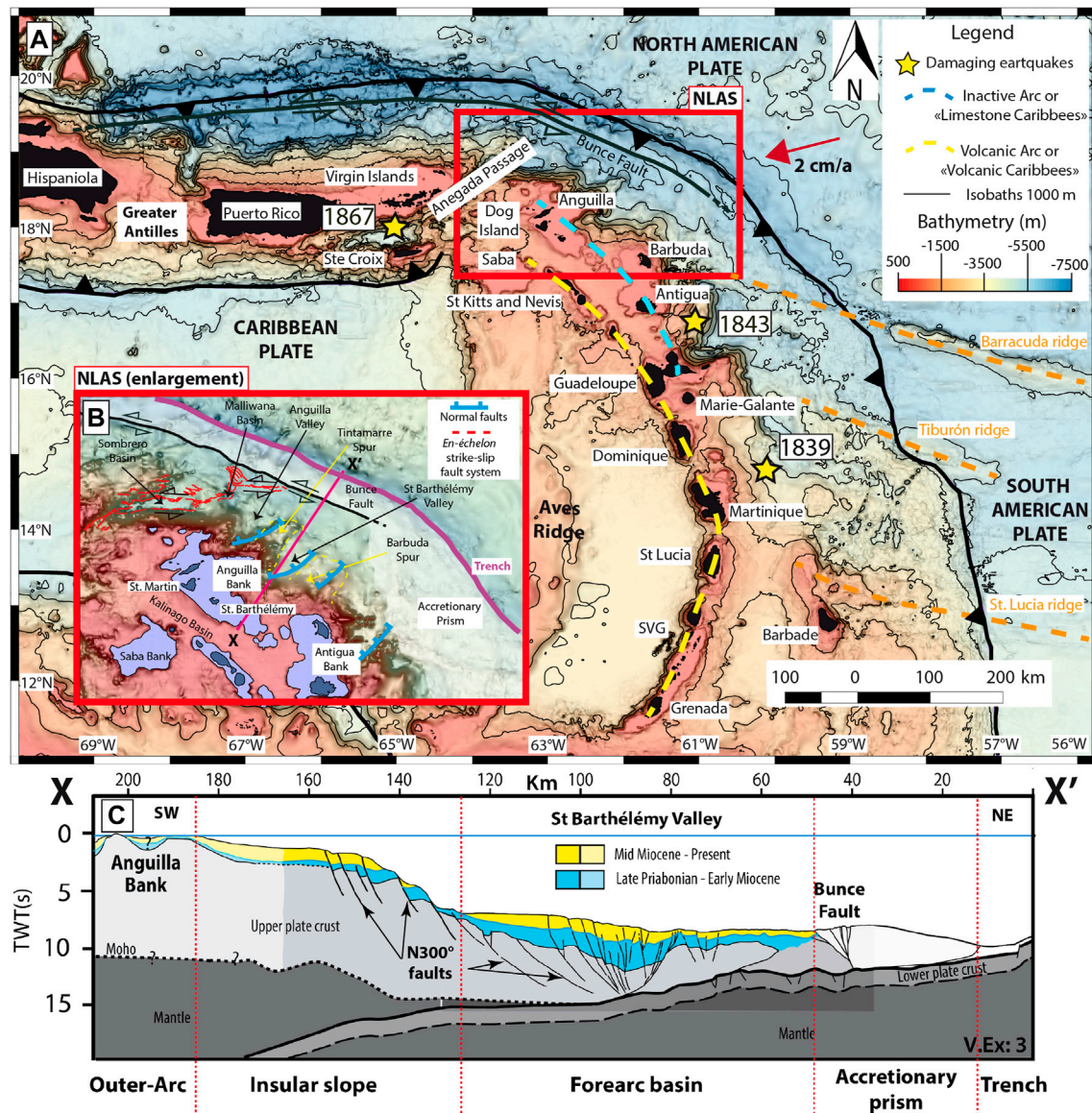


FIGURE 1 | (A) General map of the Lesser Antilles subduction zone. The red box indicates the study area (the NLAS) and refers to **Figure 1B** and **Figure 2**. The orange dashed lines represent the ridges. **(B)** Enlargement of the Northern Lesser Antilles Segment. **(C)** XX' cross-section (modified from Boucard et al., 2021).

(Figure 1) during the Pleistocene (Pichot et al., 2012) may have caused a slight transverse shift of the volcanic front (Bouysse and Westercamp, 1990) and resulted in a morphological segmentation of the forearc. The subduction of these ridges may have in addition promoted a change in the dip of the subducting slab (Bouysse and Westercamp, 1990). Consequently, the volcanism migrated southwestward and formed, during the late Miocene (Bouysse and Westercamp, 1990), the islands of the inner, secondary and active arc called “Volcanic Caribbees”, which include islands from Saba to Grenada (Figure 1). The northward increasing obliquity of the subduction (from 16° east of Guadeloupe to 75° northeast of the Virgin Islands) is partially accommodated by sinistral strike-slip deformation along the “Volcanic Caribbees” (Feuillet et al., 2002;

Feuillet et al., 2004; Feuillet et al., 2010; Feuillet et al., 2011), in the Aneгада Passage (Laurencin et al., 2017), and by strike-slip faults in the accretionary prism (Laurencin et al., 2019, or; Benâtre et al., 2020).

2.2 The Northern Lesser Antilles Segment (NLAS)

The NLAS is limited to the northwest by the Aneгада Passage (Jany et al., 1990), which separates the Lesser Antilles to the east from the Greater Antilles to the west (Christman, 1953). The Aneгада Passage extends eastward to the accretionary prism through a continuous set of *en-échelon* strike-slip faults (Figure 1B) and pull-apart basins (Sombrero, Malliwana,

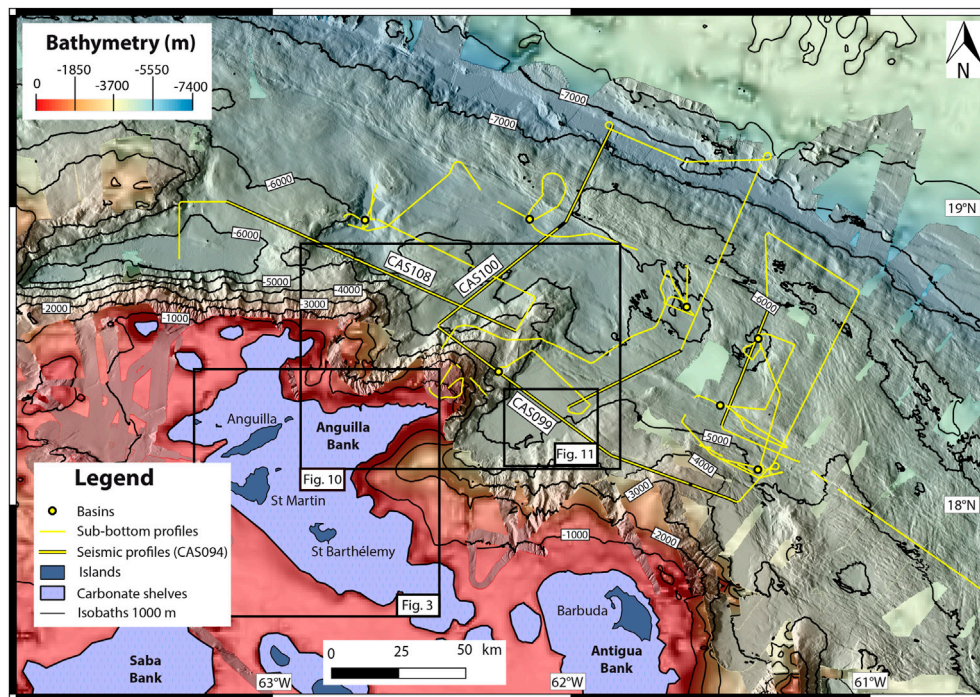


FIGURE 2 | Data from ANTITHESIS (2013–2016) and CASEIS (2016) cruises in the NLAS. Black lines represent the seismic profiles: CAS108 (**Figures 7A, 10**), CAS099 (**Figure 7B**), and CAS100 (**Figure 10**). Black boxes locate **Figures 3, 10, 12**.

Figure 1B) called the Aneгада Passage Eastern Segment (Laurencin et al., 2017). At its eastern limit, the passage connects to the sinistral strike-slip Buncce Fault (**Figure 1B**) that extends from Puerto Rico (ten Brink et al., 2004) to offshore Barbuda (Laurencin et al., 2019). To the west, the 800-m-deep Kalinago Basin (**Figures 1B,D**; Legendre et al., 2018), which opened as an intra-arc basin during the late Eocene-early Oligocene (Cornee et al., 2021), separates the NLAS from the inner and active arc (**Figure 1A**; Bouysse et al., 1985; Jany et al., 1990).

In the NLAS, the Eocene to Miocene volcanic basement is overlain by shallow Miocene to Holocene carbonate platforms such as the Antigua Bank or the Anguilla Bank (**Figures 1B, 2, 3**). These banks include a few islands (Antigua and Barbuda on the Antigua Bank and Anguilla, St. Barthélemy and St. Martin for the Anguilla Bank; **Figure 1**) that were probably connected during the Pliocene and the Pleistocene when the sea-level was lower (Christman, 1953; Cornee et al., 2021). The volcanic basement outcrops in the islands of the Anguilla Bank, where it was tilted by NE-SW faults (Cornee et al., 2021). It consists of late Paleocene to Eocene volcanoclastic turbidites (Andréieff et al., 1988a; Andréieff et al., 1988b), late Eocene-early Oligocene intruded granodiorites (Nagle et al., 1976), and Oligocene to early Miocene volcanic pipes and intrusions (Nagle et al., 1976). On the Antigua Bank, volcanic rocks are only observed in Antigua Island and consist of a middle Eocene to Oligocene basal volcanic complex (Briden et al., 1979) and Oligocene volcanoclastic deposits (Masclé and Westercamp, 1983).

The seafloor morphology presents a steep insular slope (Bouysse and Guennoc, 1983; **Figures 1B,C**) and a succession of arc-perpendicular spurs (Barbuda, Tintamarre, **Figure 1B**) and V-shaped valleys in map view (Anguilla, St-Barthélemy;) bounded by NE-SW (N40°–90°) normal faults in the forearc (Feuillet et al., 2002; Boucard et al., 2021). The N40°–90° normal faults and the strike-slip faults of the Aneгада Passage Eastern Segment either accommodated since the late Paleogene (Pindell and Kennan, 2009) the Bahamas Bank collision, and the subsequent margin convex bending (Pindell and Baret, 1990; Mann et al., 2005; Boucard et al., 2021) or plate-scale slip-partitioning (Feuillet et al., 2002; Feuillet et al., 2004; Feuillet et al., 2010; Feuillet et al., 2011). The V-shaped valleys opened during a trench-parallel extension phase that triggered crustal normal faulting before the earliest middle Miocene when an emersion phase occurred (Boucard et al., 2021). Additionally, the margin is cut by a series of ~N300° trending normal faults (**Figure 1B**) generated during a trench-perpendicular extension, and associated with post-Miocene drastic subsidence (estimated about 340 m/Myr since 16 Ma, Boucard et al., 2021), a Pliocene to Present basal erosion of the upper plate and a major basement thinning (Boucard et al., 2021). The NLAS is similar to the “Rough area” defined by Seibert et al. (2020) north of the Désirade normal fault comprising wide carbonate platforms, straight canyons incising a steep insular slope, and deep basins.

The accretionary prism (**Figures 1B,C**) is 20–30 km wide on average (Laurencin et al., 2019; Boucard et al., 2021), which is relatively narrow compared to its width in the south (~240 km,

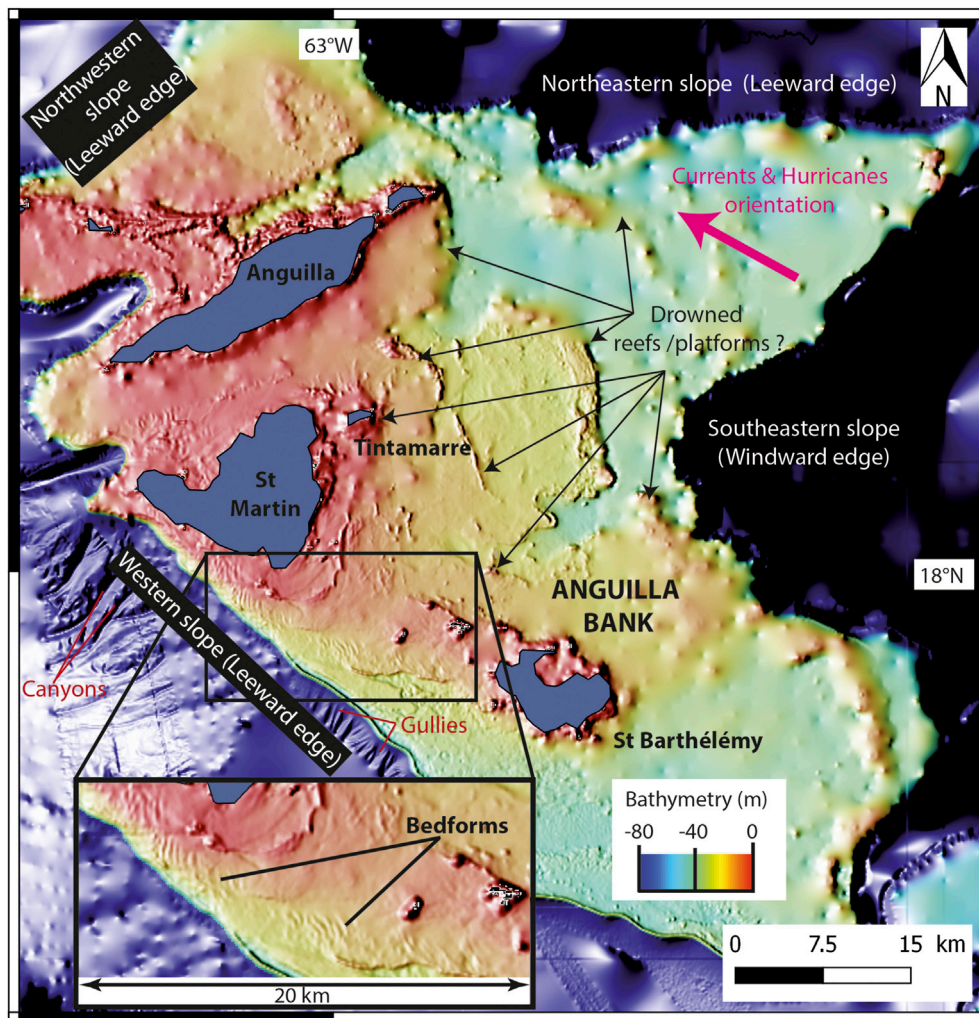


FIGURE 3 | Illustration of the Anguilla Bank with shallow-water bathymetry from the SHOM (2018). A sediment wave field on the shelf presents bedforms with an orientation N-S south of St Martin Island and NW-SE towards the St Barthélémy Island.

Seibert et al., 2020). The fold and thrust structure of the prism draws N120°-trending bathymetric linear features with positive elevation, which are parallel to the deformation front (Laurencin et al., 2019; Boucard et al., 2021). Northwestward, the accretionary prism is well delimited by the Bunce Fault (Laurencin et al., 2019); southeastward, this fault ends (black dots, **Figure 1B**) in an anastomosing system (Laurencin et al., 2019). With an average depth of 7,000 km, the trench (**Figures 1B,C**) has a flat bottom and a “U-form” morphology in front of the Barbuda-Anguilla segment (Laurencin, 2017). The trench presents variations in its depth and in its form eastwards and northwards (Laurencin, 2017).

2.3 Sedimentation and Climate

Pelagic carbonates, shallow-water carbonates redeposited by density cascading or gravity currents, and volcanoclastic silts and clays (including ashfall from the now inactive arc) represent the main sources of the deep-water sedimentation in

the Lesser Antilles (Reid et al., 1996). Eolian dust from Africa represents another minor source (Reid et al., 1996). Distant sediment supply from the Orinoco delta is trapped by the accretionary prism and the ridges (Tiburón and Barracuda) and then confined in the trench (Deville et al., 2015). In the NLAS, sediment accumulation rates are relatively constant between glacial and interglacial periods, but vary significantly between the forearc and the arc platform, from 1 to 3 cm/kyr and more than 9 cm/kyr, respectively (Reid et al., 1996).

The Lesser Antilles are located in the tropical climate zone. They are exposed to large storms and tropical hurricanes, mostly between June and November (Saunders et al., 2017). In the NLAS, the mean orientation of the hurricane's tracks is similar to the subsurface submarine currents (**Figure 3**) oriented ESE-WNW to SE-NW (Richardson, 2005). According to Malaizé et al. (2011), periods of severe drought and hurricanes have alternated with periods of more uniform climate over the last 3,700 years. These variations are likely linked to the migration of the Inter-Tropical

Convergence Zone (ITCZ) combined with changes in the trajectory of cyclones (Bertran et al., 2004).

3 DATA AND METHODS

3.1 Data

This study is based on the analysis of geophysical data (backscatter and bathymetry) acquired during the ANTITHESIS 1 and ANTITHESIS 3 cruises (Marcaillou and Klingelhoefer, 2013; Marcaillou and Klingelhoefer, 2016) and of geophysical data (backscatter, bathymetry, MCS profiles, and sub-bottom profiles) from the CASEIS cruise (Feuillet, 2016) (Figure 2).

Backscatter and bathymetry data include Reson 7,150 multibeam echo sounder (MBS; 12 or 24 kHz) and 7111 MBS (100 kHz) acquired on board the *R/V POURQUOI PAS?* These data were complemented with Kongsberg-EM122 multibeam sounder bathymetry and backscatter data from the *R/V L'ATALANTE*. The horizontal resolution is $0.5 \times 0.5^\circ$ for the 24 kHz echo sounder (corresponding to ~25 m at about 3,000 m water depth and ~44 m at about 5,000 m water depth) and $1 \times 1^\circ$ for the 12 kHz echo sounder (corresponding to ~50 m at about 3,000 m water depth and ~85 m at about 5,000 m water depth).

Backscatter mosaic and bathymetric grids were produced using the IFREMER CARAIBES, GLOBE, and SONARSCOPE software. The grid size of the backscatter mosaics is 50 m for the 24 kHz mode in the study area. Grid size of bathymetry is about 20 m for high-frequency/shallow-water data and 50–100 m for low-frequency/deep-sea data. The bathymetric data of the Anguilla Bank (Figure 3) were acquired during the HOMONIM project (SHOM, 2018).

Forty-two multichannel seismic reflection profiles (48-traces) were acquired at 10 knots speed using a solid streamer with a shot interval of 50 m. Two GI guns were used as sources and covered frequencies between 50 and 150 Hz. The uninterpreted versions of the seismic reflection profiles are available in the supplementary material (Supplementary Figures S1, S2). Sub-bottom profiles were acquired with a hull-mounted source of 1.8–5.1 kHz and were processed using the SUBOP software (IFREMER).

3.2 Methods

Backscatter data are fundamental in reconstructing the sedimentary sources and pathways (Counts et al., 2018) and are shown in Figures 4A,B. Due to the strong heterogeneity of reflectivity, backscatter data were separated into different backscatter echo-facies characterized by their reflectivity level. As a result, the seafloor backscatter map (Figure 4A) was divided into five main echo-facies: [a] very high heterogeneous reflective (red), [b] high heterogeneous reflective (orange), [c] middle heterogeneous reflective (yellow), [d] low heterogeneous reflective (blue), and [e] very low heterogeneous reflective (dark blue), (Figure 4B). Highly reflective zones (light tones in Figure 4A, yellow areas in Figure 4B) are generally interpreted as active sediment transfer areas (Counts et al., 2018) such as canyons, gullies, or valleys where deposits are coarser, or alternately the areas where the seafloor is rougher, such as

along scarps (Iacono et al., 2008). Low reflective zones (dark tones in Figure 4A, purple in Figure 4B) are generally interpreted as morphologically smooth, less active sedimentation areas (Counts et al., 2018), or areas of fine-grained sediment accumulation (Iacono et al., 2008).

A morpho-bathymetric map (Figure 5) was made from the available data although some areas were incomplete due to the lack of survey coverage (e.g., the outer arc or the insular slope). Detailed descriptions and interpretations were made from this map, from enlargements and seismic profiles (Figures 6–11). These descriptions are supported by morphometric quantification computed using QGIS software: areas of carbonate platforms and basins, width and length of structures, and the water depth range of all the features (Table 1). On maps of each insular slope (Figures 6, 8, 9), three canyons are highlighted to present their diversity in terms of length, form, and thalweg depth.

Along with the seismic profiles (Figures 2, 7), we identified two main seismic facies [α] a facies with few reflectors and with no structure within or below, that we interpreted as the acoustic basement, and [β] a facies with continuous and parallel reflectors corresponding to stratified sedimentary deposits (interpretations based on principles developed by Payton, 1977). The nature of the acoustic basement is mostly volcanic as it is characterized by 4.7–6 km/s P-wave velocities (Laurencin et al., 2018) compatible with those of an uppermost volcanoclastic layer (Christeson et al., 2008; Kopp et al., 2011) and retrieved inland (Bouysse et al., 1985). Within facies [β], seismic units separated by unconformities are identified. We labeled them U1 to U5 (Figure 10) and Ua to Ud (Figure 7B) in the Anguilla and St-Barthélemy valleys, respectively. We used distinctive nomenclature for the units in both valleys since no temporal constraints allow correlating the units across valleys. The seismic facies [β] seems to be similar to the U4 sedimentary unit of Boucard et al. (2021), who interpret this unit as fan-shaped deposits filling the basins and the valleys. In the seismic facies [β], reflectors are often crosscut and offset by numerous faults (Figure 7B).

4 RESULTS: PHYSIOGRAPHY AND MAIN MORPHOLOGIC FEATURES OF THE NORTHERN LESSER ANTILLES SEGMENT (NLAS)

The seafloor of the NLAS (Figure 5) presents five morpho-structural areas: 1) the outer arc (from 0 to 1,000 mbsl), 2) the steep insular slopes (from 200 mbsl to 5,000 mbsl), 3) the forearc basin (from 5,000 mbsl to 7,000 mbsl), 4) the accretionary prism (from 5,600 mbsl to 5,900 mbsl) and 5) the trench (~7,000 mbsl). We focus the description of the area from the outer arc to the forearc basin, where the sedimentary sources, the turbiditic systems, and the distal sinks appear.

4.1 The Outer Arc and Carbonate Platforms

The outer arc consists of wide, relatively flat carbonate platforms lying on the old inactive volcanic arc at water depths shallower than ~100 m (Figure 5). The Anguilla Bank is the largest

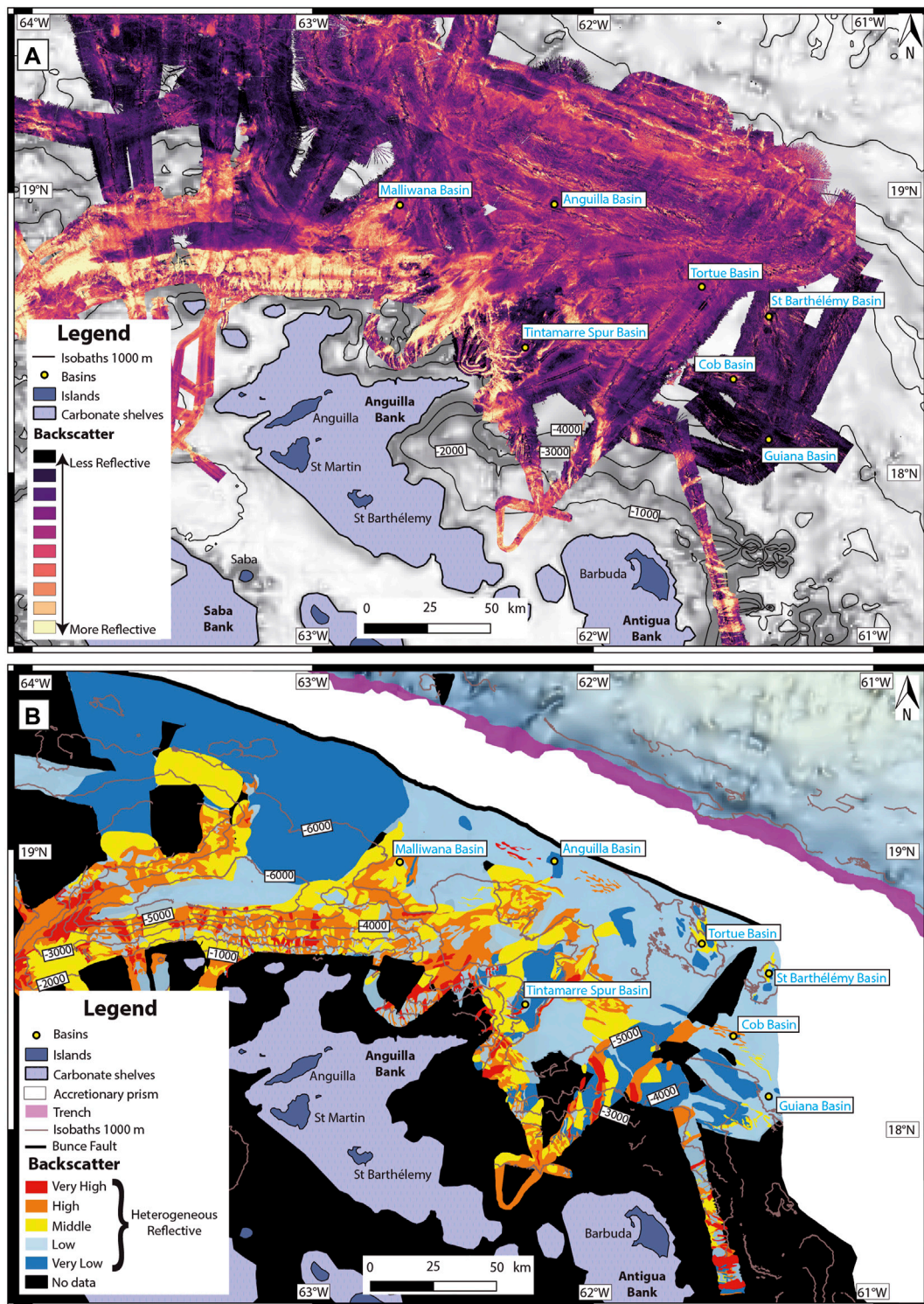


FIGURE 4 | Backscatter map: **(A)** Data (color scale plasma). **(B)** Interpretation. Five echo-facies: (a) Very High Heterogeneous Reflective (in red), (b) High Heterogeneous Reflective (in orange), (c) Middle Heterogeneous Reflective (in yellow), (d) Low Heterogeneous Reflective (in blue), (e) Very Low Heterogeneous Reflective (in dark blue). Please note that generally, highly reflective echo-facies (a,b) are present especially in the canyon floor and areas cut by gullies, the medium reflective facies highlight some valleys, and less reflective facies (d,e) are present in spurs and deep basins.

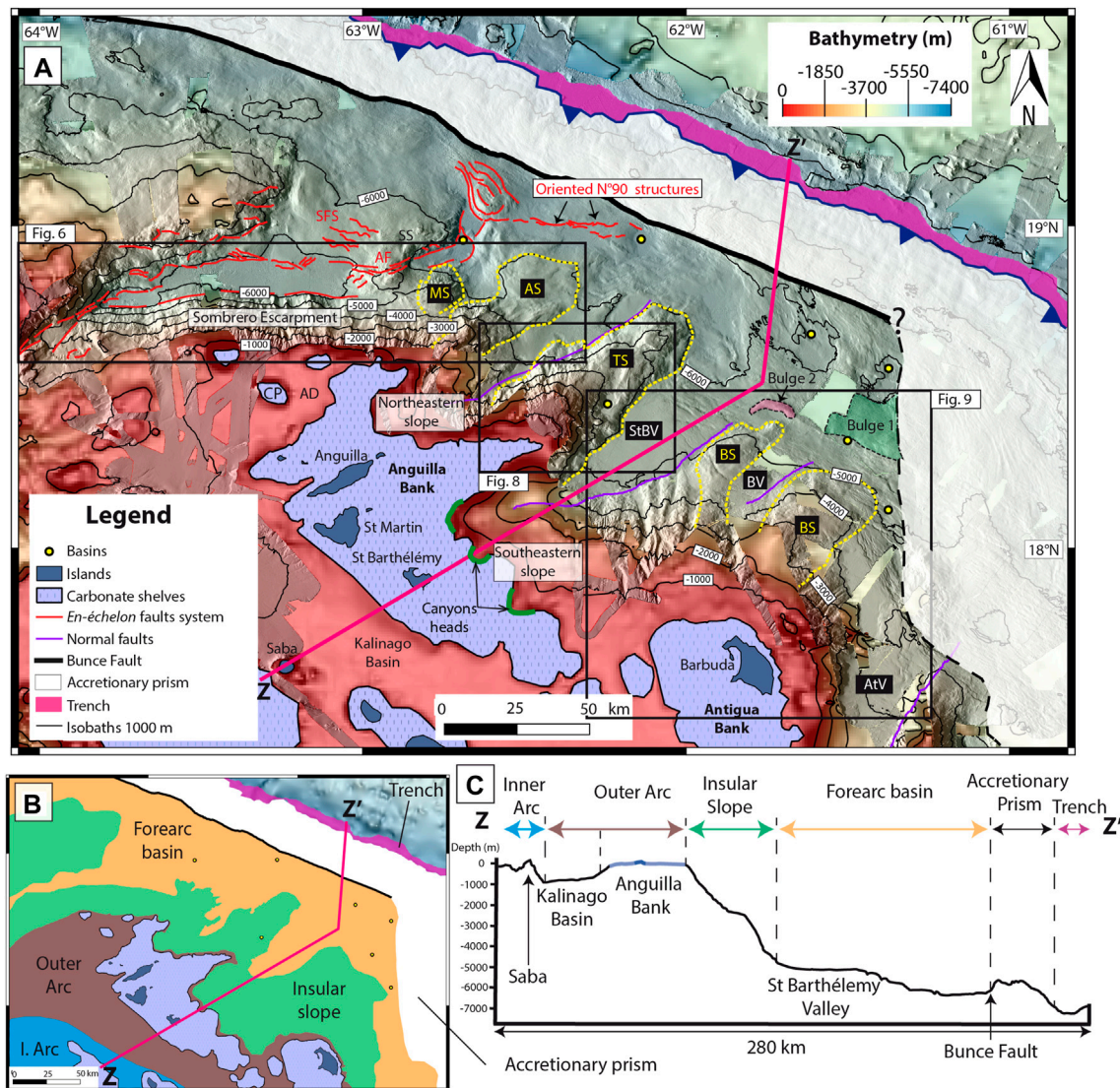


FIGURE 5 | (A) Morpho-bathymetric map of the NLAS. The cross-section AB is represented in pink in the main map and in the reduced map, it refers to **Figure 5B**. Red faults demarcate the Anegada Passage Eastern Segment, yellow dots indicate four main spurs. AB: Anguilla Basin, AD: Anguilla Depression, AF: Anguilla Faults, AS: Anguilla Spur, AV: Antigua Valley, BS: Barbuda Spur, BV: Barbuda Valley, CP: Crocus Platform, MS: Malliwana Spur, SFS: Sombrero Faults System, SS: Sombrero Saddle, StBV: St Barthélemy Valley, TS: Tintamarre Spur. **(B)** Reduced map of the main domains. **(C)** ZZ' cross-section. The colors of the main domains double arrows are the same as in the insert map in **Figure 5B**.

carbonate platform (area of about 4,660 km², **Table 1**). The data reveals that the carbonate platform is not protected by shelf-edge barriers along most of its rim. Indeed, bathymetric highs are only visible east of Saint-Barthélemy and scarcely visible on the northeastern edge of the bank (**Figure 3**). However, the lack of multibeam coverage prevents precise mapping. Additionally, at ~40 mbsl, flat areas alternate with elongated highs rimmed at their seaward boundaries. We interpreted these successions of features as drowned platforms and reefs, as attested by previous studies (Christman, 1953; Cornee et al., 2021). Smaller carbonate platforms (30–53 km², **Table 1**) are also located north of the Anguilla bank in a 200-to-700-m-deep depression (Anguilla

Depression, **Figure 5; Table 1**): Crocus (**Figure 5; Table 1**), Malliwana and Sombrero platforms (**Figure 6; Table 1**).

On the southern edge of the Anguilla Bank, south of Saint-Martin, ~2 m-high, ~400 m-long bedforms lie on the seafloor, trending N/S to NNW/SSE. The bedforms are observable to the western shelf edge and seem to be connected to NE-SW canyons incising the western slope of the Anguilla Bank. Given their shape and orientation perpendicular to the direction of the main submarine current (Richardson, 2005) (**Figure 3**), we interpreted these features as submarine dunes caused by the main currents (see Gonzalez and Eberli, 1997). The second-largest carbonate platform (area of about 3,800 km², **Table 1**)

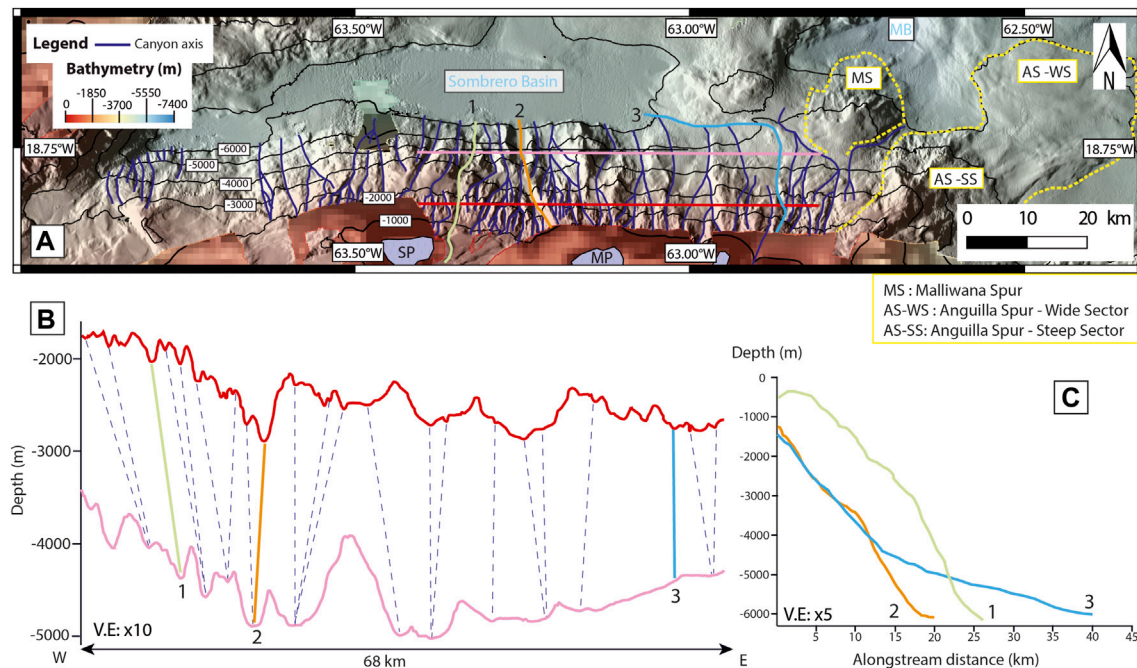


FIGURE 6 | (A) Enlargement of the Sombrero Escarpment. MB: Malliwana Basin, MP: Malliwana Platform, SP: Sombrero Platform. **(B)** W-E cross-section of the Sombrero Escarpment. The red cross-section is between 1,700 and 2,900 m and the light pink cross-section is between 3,500 and 5,100 m. Blue dots follow canyons axis between the two cross-sections. Three canyons axis (1, 2, and 3) are represented and referred to **Figure 6C**. **(C)** Bathymetric profiles of three canyons axis (1, 2, and 3).

is the Antigua Bank (**Figure 5**). However, we lack multibeam data to describe its detailed morphology.

4.2 The Insular Slopes

4.2.1 Sombrero Escarpment

The Sombrero Escarpment (**Figures 5A, 6**) is oriented E-W with an average slope gradient of 14.7° and extends from 900 mbsl down to 6,000 mbsl. This escarpment is incised by numerous canyons (15–20 km long, up to 38 km for the longest, **Figure 6**), mostly linear and dipping northwards (**Figure 6A**) toward the Sombrero Basin. The shortest canyons present a 30 m-deep thalweg while the longest is up to 600 m-deep. For instance, canyons 1, 2, and 3 are representative of the erosional patterns on the Sombrero escarpment: Canyon 1 is a single and sinuous canyon presenting a continuous slope angle ($\sim 14.7^\circ$, **Figure 6C**). Canyon 2 is linear and merges with two northward-oriented tributary canyons between 2000 mbsl and 4,100 mbsl (**Figure 6C**). Canyon 3 is more sinuous and the longest, (38 km), merging with three S-N linear canyons between 5,000 mbsl and 6,000 mbsl. In their upper part, most canyons are slope-confined and show no connection with feeding channels from the Anguilla Depression (**Figure 5**). The canyons are highlighted by an alternation of highly reflective echo-facies [a] and [b], contrasting with less reflective facies [c] and [d] (**Figure 4B, Table 1**) in between. Given the high seafloor reflectivity within the canyons, we interpreted them as major sediment transfer paths as observed in similar contexts (Counts

et al., 2018). The amount of sediment transfer is however probably limited given the disconnection with the upper slope.

4.2.2 Northeastern Slope of the Anguilla Bank

The northeastern slope of the Anguilla Bank, which extends from 100 mbsl down to 5,000 mbsl, is oriented NE-SW and shows a mean gradient value of 7.7° (**Figure 5, Table 1**). As observed along the Sombrero Escarpment, the northeastern slope of the Anguilla bank is incised by several canyons highlighted by reflective echo-facies [a] and [b] (**Figure 4B, Table 1**). Its northern tip, the Anguilla Spur (**Figures 5A, 6A**), includes two sectors: a steep one (11.8°) from 2000 mbsl down to 5,000 mbsl, and an extended, wide sector ($\sim 550 \text{ km}^2$, 2.3°) from 5,000 mbsl to 6,000 mbsl.

In the Anguilla spur, seismic profiles reveal almost directly in the subsurface the acoustic basement (facies [a] in **Figure 7A**), with a limited number of discontinuous reflectors near the surface. Locally, a chaotic unit lies on top (enlargement in **Figure 7A**). We interpreted it as Mass Transport Deposit (MTD) (Weimer and Shipp, 2004), which attests to the occurrence of local destabilizations within the spur.

4.2.3 Tintamarre Spur

The Tintamarre Spur (**Figures 5A, 8**) is a SW-NE trending structure located along with the eastward extension of the Anguilla Bank. The spur is slightly asymmetric, revealing a steeper mean gradient on its northwestern flank (12°) compared to the southeastern one (9.7°), most likely related to

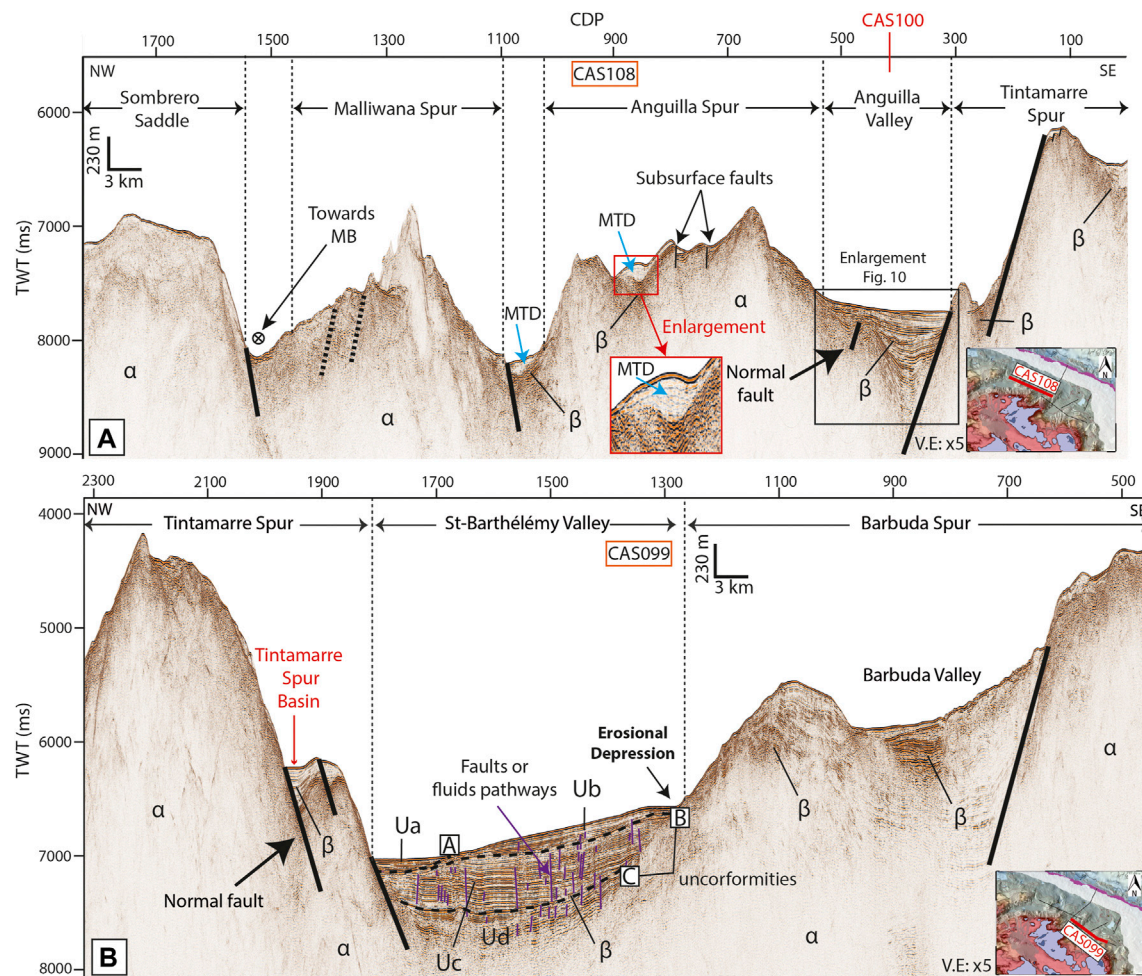


FIGURE 7 | Seismic profiles: **(A)** CAS108, uncertain faults are in dashed black. A, B, and C are unconformities, Ua to Ud are different seismic units. The black box locates an enlargement reporting to **Figure 10**; **(B)** CAS099. Acoustic facies in the seismic profiles [α] chaotic unit (acoustic basement) and [β] unit with evidence of numerous and stratified reflectors (basins, valleys). Red lines in the insert maps indicate the position of the seismic profiles. The vertical exaggeration (V.E) is x5 for the two seismic profiles.

the presence of normal faults on the western flank (Feuillet et al., 2002; and **Figure 7A**). The top of the spur reveals remarkable morphologies: two particularly planar and gently dipping surfaces (respectively $\sim 2^\circ$ and 4.5°) (**Figure 8**, **Table 1**), with an area of 37 and $\sim 85 \text{ km}^2$, occur at $\sim 700 \text{ mbsl}$ and at $\sim 1,600 \text{ mbsl}$. These features stand out from all other morphologies visible on the insular slopes, and we interpreted them as tilted strata. Given their location on the upper slope, at the edge of Anguilla Bank, these could be interpreted as subsided platforms (such structures have already been identified close to carbonate banks, Eberli and Ginsburg, 1987); we have named them paleo-platform PP1 and paleo-platform PP2 (**Figure 8A**).

On the northern part of the Tintamarre Spur, from 1,000 mbsl to 4,000 mbsl, numerous 10 to 18 km-long, northward-oriented canyons and/or gullies pour out into the Anguilla Valley (**Figure 8A**). These canyons/gullies are highlighted by the reflective echo-facies [α] and [β] while the rest of the spur is less reflective (echo-facies [c] to [e], **Figure 4B**, **Table 1**). Most

canyons are slope-confined, with a spoon-shaped canyon head located at the edge of paleo-platform PP2 (**Figure 8A**). Similar headscarps also incise the edge of the upper paleo-platform PP1, with some gullies at its foot, streaming down to PP2. For instance, Canyons 4 and 5 incise both paleoplatforms *via* gullies in-between, while Canyon 6 is limited to PP2 (**Figure 8B**).

In the northeastern part of the Tintamarre Spur, from 4,000 to 6,000 mbsl, no canyon is identified. On the southeastern flank of the spur, only a few gullies and sinuous canyons occur (for instance Canyon 6 (Line 6, **Figure 8B**). Its slope gradient is locally steep between 1700 and 3,800 mbsl (14.5°), and decreases from 4,100 mbsl to 4,600 mbsl (11.9°). The canyon pours out in a relatively small slope basin located at 4,680 mbsl, (15 km^2 , **Table 1**) called Tintamarre Spur Basin (**Figures 7B**, **8**). Its reflectivity is very low (echo-facies [e], **Figure 4B**, **Table 1**). It is highlighted by the seismic facies [β] on seismic profiles (**Figure 7B**). This basin is confined by the height of its flanks.

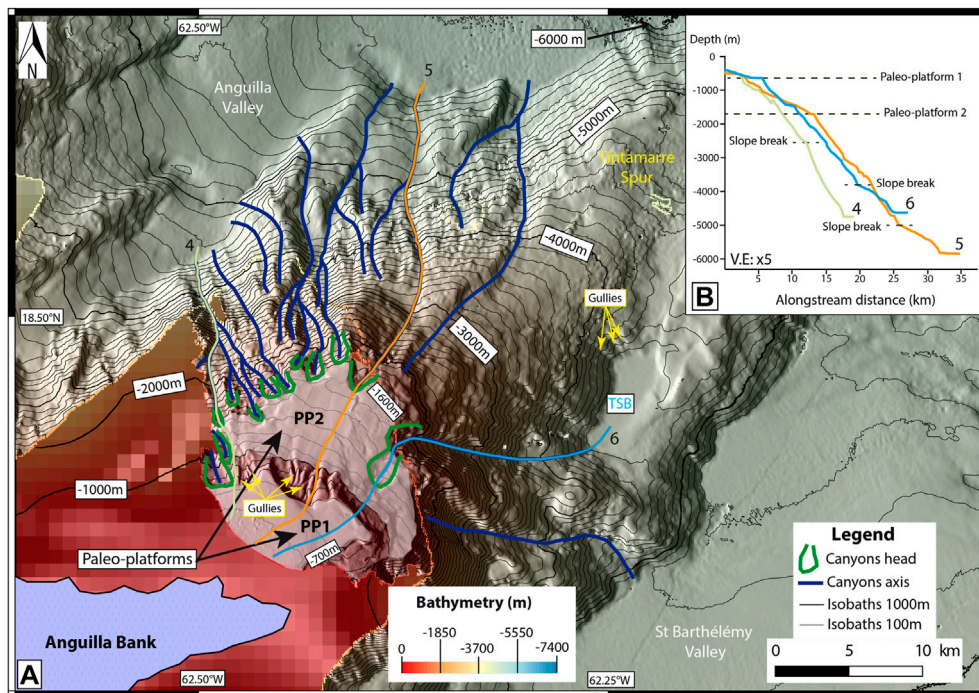


FIGURE 8 | (A) Enlargement of the Tintamarre Spur. PP1: Paleo-platform 1; PP2: Paleo-platform 2; TSB: Tintamarre Spur Basin. Three canyons axis (4, 5, and 6) are represented and referred to **Figure 8B**. Please note that canyons are more numerous in the northern part of the Tintamarre Spur than in the southern part. **(B)** Bathymetric profiles of three canyons axis (4, 5, and 6).

The southeastern slope of the Anguilla Bank (oriented NW-SE, **Figures 3, 5**) is not imaged by multibeam data, but based on GEBCO Satellite bathymetry the shape of the 1000-m isobaths and some spoon-shaped (Canyons heads, **Figure 5A**) in the Anguilla Bank, which we interpreted as canyon heads, suggest the existence of SW-NE oriented canyons reaching the St-Barthélemy Valley.

4.2.4 Barbuda Spur and Valley

The northern slope of the Antigua Bank is composed of a major SW-NE trending spur called Barbuda Spur, cut by the 1000 m-deep Barbuda Valley (**Figures 5A, 9**). The Barbuda Spur shows generally a low to very low reflective seafloor (echo-facies [d] and [e], **Figure 4B, Table 1**). With an average slope gradient of 5.7° from 120 mbsl to 5,000 mbsl, the SW-NE northern slope of Antigua Bank is also incised by northward oriented canyons, over 30 km long, 3 km wide, and ~500 m deep. The canyons, highlighted by echo-facies [a] and [b] (**Figure 4B, Table 1**), seem either slope-confined or connected at their head by gullies themselves connected upwards to the Antigua Bank (**Figure 9A**). These gullies are located downstream from passes across the reefs of Barbuda (yellow dashed arrows, towards gullies, **Figure 9E**). Four main canyons are visible between 4,000 mbsl and 5,000 mbsl (light pink cross-section, **Figures 9A,B**) and present a “U-shape”. They result from the merger of other canyons between 1,500 mbsl and 3,500 mbsl. The 50-km-long canyon shown in line 7 (yellow line, **Figures 9B,D**) presents 400-m-high walls while the three other canyons have smaller walls, between 50 and 300 m (**Figure 9B**).

The Barbuda Valley has a depth of about 4,600 mbsl and is connected to the Antigua Bank through the main canyon (Canyon 8, **Figure 9A**) collecting sediment from several secondary canyons (**Figure 9D**). Between 2000 mbsl and 4,000 mbsl, where the secondary canyons spatially merge with the main one, the slope is steep ($\sim 7.4^\circ$) then flattens ($\sim 2.2^\circ$) below 4,000 mbsl (**Figure 9D**). The Barbuda Valley (**Figures 5A, 9**) is highlighted by highly reflective echo-facies [a] and [b] (**Figure 4B, Table 1**) and is partially filled with stratified deposits illustrated by the seismic facies [β] on seismic profiles (**Figure 7B**). Additionally, the valley is bounded by a normal fault on its eastern flank (**Figure 7B**).

With an average slope gradient of 6.4° , the NNW-SSE oriented Antigua northeastern slope is incised by numerous and very reflective (echo-facies [a], **Figure 4B, Table 1**) SW-NE oriented linear canyons which are also linked to gullies at the top of the slope (**Figure 9**). With a length of at least 20 km, these narrow (<1 km width) canyons present 80-m-high walls between 2000 mbsl and 3,000 mbsl (orange cross-section, **Figure 9C**) and 10-to-100-m-high walls between 3,000 mbsl and 4,000 mbsl (brown cross-section, **Figure 9C**). They pour out onto a 4,000 mbsl deep terrace (**Figure 9**). Canyon 9 is linear and its thalweg presents an average slope of 10.1° between 1,000 mbsl and 4,000 mbsl.

To summarize, compared to the eastern flank, the north-western flank of the spur is dominated by a greater number of canyons, which moreover appear more incised and more reflective, probably supporting a more active sediment transfer as observed in other studies (Iacono et al., 2008; Counts et al.,

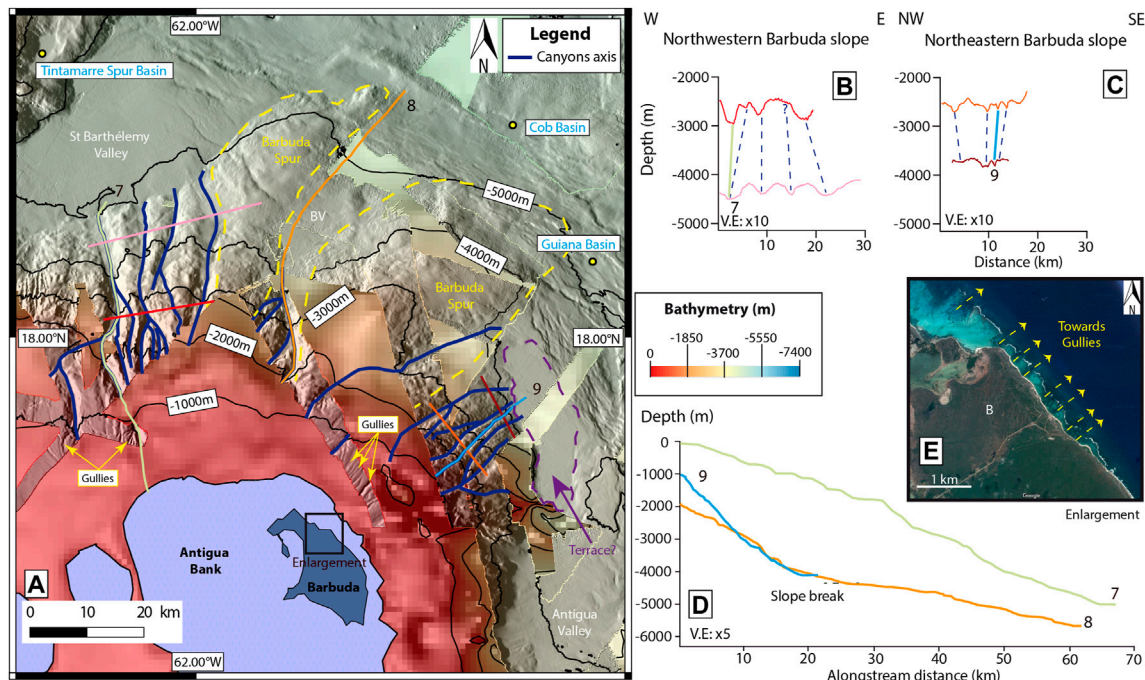


FIGURE 9 | (A) Enlargement of the northern slope of the Antigua Bank. BB: Barbuda Basin, BV: Barbuda Valley. Three canyons axis (7, 8, and 9) are represented and referred in **Figures 9B–D**. (B) W-E cross-sections of the northwestern slope of the Antigua Bank. The red cross-section is between 2,500 and 3,000 mbsl, the light pink cross-section is between 4,300 and 4,600 mbsl. (C) W-E cross-sections of the northeastern slope of the Antigua Bank. The orange cross-section is between 2,400 and 2,900 mbsl and the brown cross-section is between 3,700 and 3,900 mbsl. Blue dots follow canyons axis between the two cross-sections. (D) Bathymetric profiles of three canyons axis (7, 8, and 9). (E) Enlargement of Barbuda Island's passes. The Enlargement comes from Google Maps.

2018). The origins of these differences will be assessed in the discussion.

4.3 The Forearc

4.3.1 The Sombrero Basin

The Sombrero Basin, located at the toe of the Sombrero Escarpment, is 8 km wide and 86 km long, lying at ~6,200 mbsl (**Figure 6; Table 1**). This structure is bounded by transtensive faults (Laurencin et al., 2017). The seafloor is flat, and poorly reflective, highlighted by echo-facies [d] (**Figure 4B**). However, in front of the numerous canyons, the seafloor is slightly more reflective but still represented by the same echo-facies. We interpreted the infill as being either fine-grained (as observed by Iacono et al., 2008), and/or the sediment transfers being inactive, apart from in front of the canyons where accumulation is limited.

4.3.2 Deep Submarine Valleys

Two valleys are identified between the spurs: the Anguilla Valley (**Figures 5A, 10**), delimited by the Tintamarre and Anguilla Spurs, and the St-Barthélemy Valley (**Figures 5A, 10**), delimited to the SE by the Barbuda Spur. These two valleys, filled with stratified deposits illustrated by the seismic facies [β] (**Figures 7A,B**), are bounded by normal faults (Feuillet et al., 2002). Their seafloor however presents a contrasting backscatter signature (**Figure 10A**).

The Anguilla Valley, from 5,100 mbsl to 5,350 mbsl, (**Figures 5A, 10**), is narrow (~10 km). In its distal part (**Figure 10B**), the seafloor is poorly reflective along the Tintamarre spur, while the axis of the

valley and its distal vicinity is highly reflective (**Figure 10B**). This highly reflective seafloor correlates with truncated reflectors (**Figure 10C**). We interpreted these features as the presence of an active sediment transfer and erosional turbidity currents (active currents **Figure 10C**), as attested by the backscatter signature of turbidites in other studies (Iacono et al., 2008). Five units separated by four unconformities are visible in this valley (**Figures 10C,D**). U1 to U3 present continuous reflectors; U4 is more chaotic and onlaps in its southwestern part while U5 appears very chaotic, with few strong and parallel reflectors. U1 and U4 share a similarity: an erosive depression is visible in U1 at the foot of the slope, and a similar buried feature is identified in U4 (**Figure 10D**).

Conversely, the St-Barthélemy Valley (**Figures 5A, 7–10**) is a broader submarine valley (~28 km wide, 4,900–5,200 mbsl) presenting a low reflective seafloor (**Figure 10A**, echo-facies [d], **Figure 4B; Table 1**) compared to the Antigua valley. At the foot of the southeastern slopes off the Anguilla Bank, the seafloor is locally more reflective (echo-facies [a] to [c], **Figure 4B, Table 1**) describing a lobate shape (Lobate Structures, **Figure 10**). The infill of the valley is well stratified and shows at least 4 units (Ua to Ud) separated by three unconformities (A to C in **Figure 7B**). The most recent infill shows well-stratified reflections (**Figure 7B**), lying unconformably on top of truncated reflectors. We interpreted the sediment transfer within the valley as being less active and/or comprising finer-grained deposits than within the Anguilla valley (as observed in other studies (Iacono et al., 2008; Counts et al., 2018).

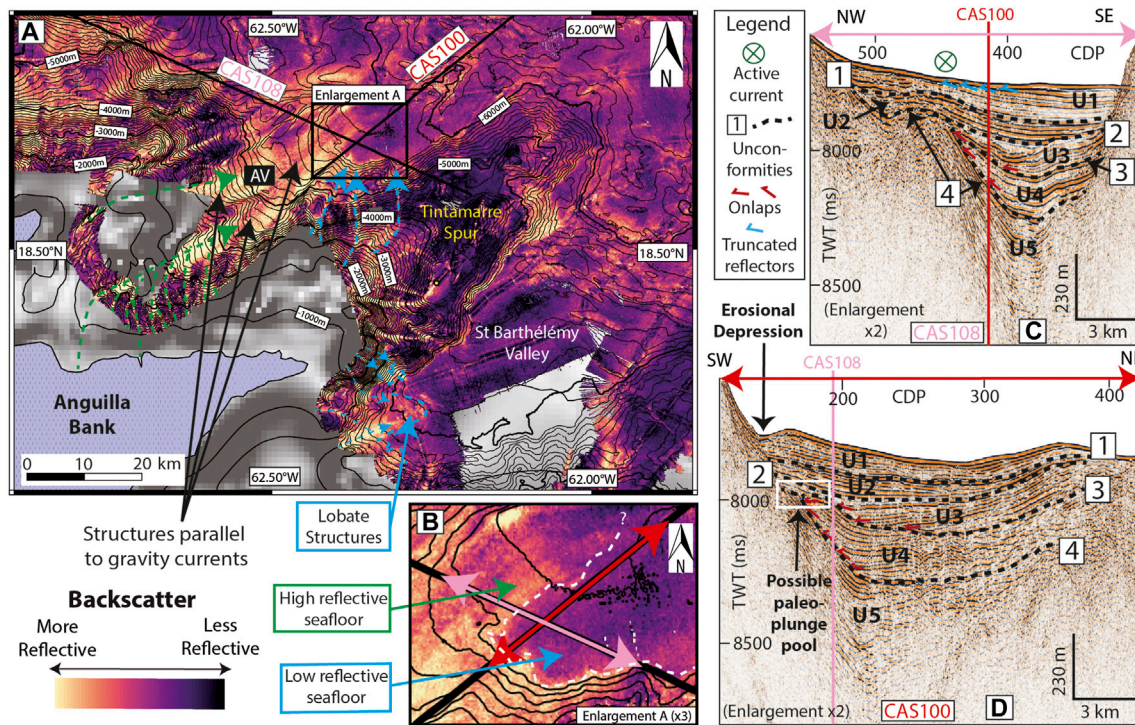


FIGURE 10 | Enlargement of the two main valleys. **(A)** Interpreted backscatter map. Blue dashed arrows represent sediment transfer from the northeastern Anguilla Bank. Blue dots delimit lobate structures in the St-Barthélémy Valley. Green dashed arrows represent sediment transfer from the paleo-platforms of the Tintamarre Spur. AV: Anguilla Valley. Please note that the backscatter pattern is totally different between the two valleys. **(B)** Enlargement of Figure 10A. The light pink double arrow locates the enlargement C coming from the seismic line CAS108 (Figure 7A). The red double arrow locates the enlargement D coming from the seismic line CAS100. The white dots separate the active transfer area (indicated by a green arrow) and the transfer and deposition area (indicated by a blue arrow). **(C)** Enlargement of the seismic line CAS108 (Figure 7A). The red line indicates where the seismic line CAS100 cut the seismic line CAS108. The vertical exaggeration is x5 for the seismic profile. **(D)** Enlargement of the seismic line CAS100. U1 to U5 refers to the number of units. The light pink line indicates where the seismic line CAS108 cut the seismic line CAS100. The vertical exaggeration is x5 for the seismic profile.

The presence of unconformities in both valleys suggests successive periods of sediment transfer (as attested by other studies, e.g. Laban et al., 1984) but also at least one subsidence phase, attested by the divergent geometry of the reflectors of U3, U4, and U5 in the Anguilla Valley. Drastic subsidence in the area has already been identified on MCS profiles (Boucard et al., 2021), suggesting the importance of tectonics in the Northern Lesser Antilles Segment.

4.3.3 Plunge Pools

In the St-Barthélémy Valley, erosional depressions (Figures 7B, 11) occur along the 5,000 m isobaths and are located at the foot of the northern slope of the Antigua Bank (Figure 11A). They are 540–1,200 m long and 16–20 m deep, where the slope break ranges from 4° to 7° (Figures 11B–E). In detail, sub-bottom profiles reveal a small, highly reflective depression located at the foot of the slope, with a mounded shape located immediately basinward from the depression (Figure 11B). The mound shows stratified acoustic facies with low amplitude continuous reflectors. A similar structure, visible in the Anguilla Valley (Figure 10), is 1,450 m long and 22 m deep, at a break in slope of ~7° and corresponds to the erosive depression associated with U1 (Figure 10D). Due to their stratified composition with low amplitude continuous reflectors, corresponding to alternating

fine- and coarse-grained material (e.g., Hassoun et al., 2009), we inferred that these features have a sedimentary origin. We interpreted these features as plunge pools, characterized by an erosional scour at the foot of a steep slope, and a depositional slope-break deposit downstream (Komar, 1971; Mulder and Alexander, 2001; Lee et al., 2002; Bourget et al., 2011; Migeon et al., 2012). Given their similarities, we interpreted the erosional and depositional features described at the slope break in Units U1 and U4 (Figure 10D) as active and buried plunge pools, respectively.

4.4 Deep Basins and Seismic Stratigraphy of Basin Fill

The study of deep sub-basins helps to determine the occurrence—or not—of sediment transfer and deposition in the area. Several forearc sub-basins have been identified, from 5,000 mbsl to 7,000 mbsl (Figure 5). They are dominated by low reflective seafloor or echofacies [d] to [e] (Figure 4B, Table 1), implying mostly fine-grained sediment accumulation (Counts et al., 2018). Seven basins or sinks of varying geological contexts in this area are illustrated by sub-bottom profiles and are in different geological contexts. Groups of black reflectors alternating with transparent and thick units are visible on the sub-bottom profiles (Figure 12). The proximal sub-

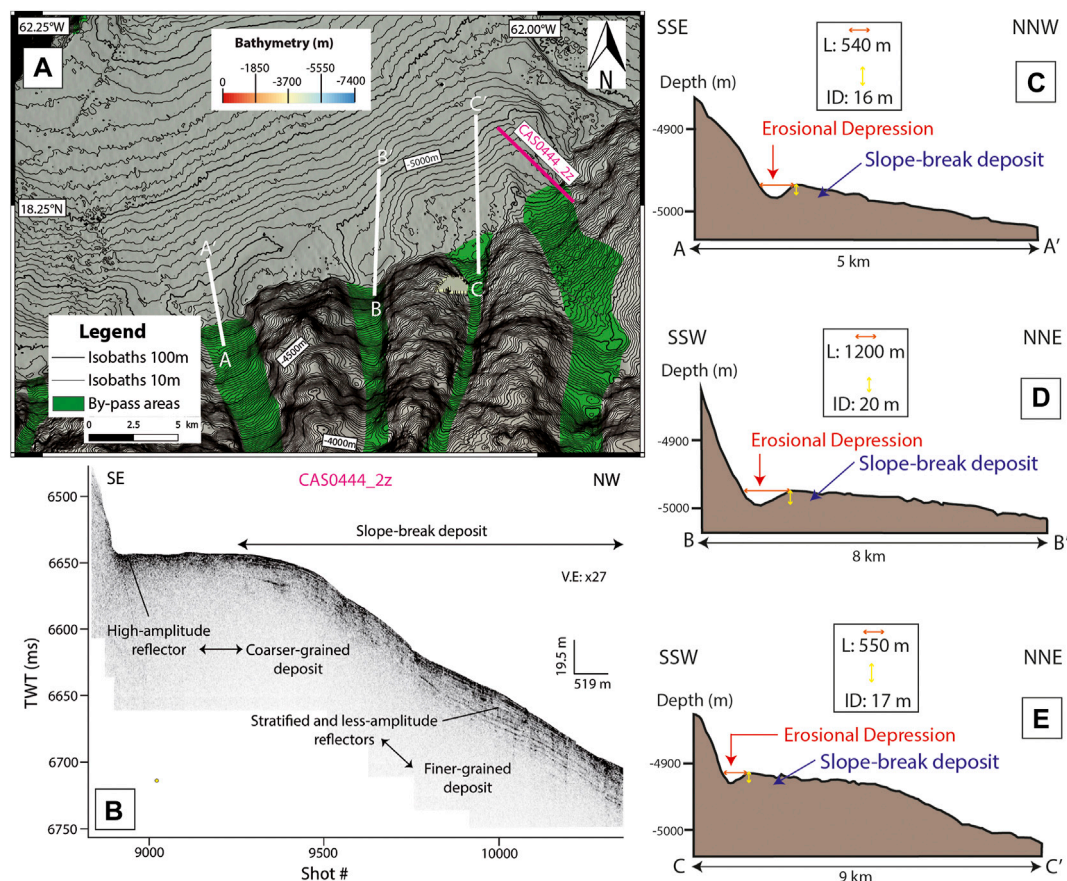


FIGURE 11 | (A) Identification of unusual sediment structures in the St-Barthélémy Valley. These structures are illustrated in a sub-bottom profile and in three cross-sections. **(B)** Enlargements on sub-bottom profile CAS0444_2z. The enlargement was realized using QC SBP5.0_64bits (Ifremer, Brest). **(C)** Cross-section AA' **(D)** Cross-section BB' **(E)** Cross-section CC'. L = Length, ID = Incision Depth for the Erosional Depression.

basins (Guiana Basin, Cob Basin, and Tintamarre Spur Basin) contain at least one thick transparent unit, while the distal sub-basins contain at least two thick transparent units (Figure 12):

- the Guiana Basin (Figures 4, 9, 12A, 13) and the Cob Basin (Figures 4, 9, 12B, 13) are small sinks (~3 km², Table 1) located close to the insular slope at 5,150 and 5,800 mbsl, respectively (Table 1).
- the St-Barthélémy Basin (~10 km², Table 1) and the Tortue Basin (~17 km², Table 1) are basins at great depth (~6,100 mbsl, Table 1), located close to the accretionary prism and far from the slopes of the Antigua Bank (Figures 4, 12C,D, 13).
- the Tintamarre Spur Basin (Figure 12E) is a small slope-confined basin (~15 km², Table 1) located on the Tintamarre Spur (Figures 4, 7B, 8, 13) at 4,600 mbsl (Table 1).
- the Anguilla Basin (Figure 12F) is larger (~45 km², Table 1) and deeper (~6,700 mbsl, Table 1) than the previous basins and is located close to the accretionary prism and far from the slopes of the Anguilla Bank (Figures 4, 13).
- the Malliwana Basin (Figures 12G,H) is a wide (~155 km², Table 1) and deep (~6,900 mbsl, Table 1) pull-apart basin located close to the northeastern slope of the Anguilla Bank (Figures 4, 6, 13) in an *en-échelon* fault system (Laurencin et al., 2018). In this basin, another acoustic transparent unit is visible in the subsurface of the basin but does not fill the entire basin (Figure 12H). This unit seems to be correlated with a spoon-shaped structure visible on the backscatter (Figure 12G). Thus, at around 5,000 mbsl, in the Malliwana Spur, some semi-circular structures are observable (Figure 12G). We interpreted these structures as evacuation areas (see Moscardelli and Wood, 2016) while the spoon-shaped structure could be interpreted as an MTD, suggesting local destabilizations on the Malliwana Spur. It also implies different triggering mechanisms for the MTD and the others megabeds filling the entire surface of the basin.

Acoustically transparent and thick units identified in sub-bottom profiles are similar to units identified elsewhere and called the term “unifite” (Stanley, 1981), then megaturbidites (San Pedro et al., 2017), or homogenites (Kastens and Cita, 1981; Beck, 2009; Beck,

TABLE 1 | Main characteristics of the structures of the Northern Lesser Antilles Segment.

Physiographic domain	Detail zone	Structures	Ab.	Water depth range (m)	~Area (km ²)	Length (km)	Width (km)	Backscatter echo-facies	Related figures
Outer Arc		Kalinago Basin	KB	200–800	—	200	20	d	1b, 5, 13
		Anguilla Bank	AngB	0–100	4,660	110	40	ND	1b, 2, 3, 5, 8, 13
		Antigua Bank	AntB	0–200	3,800	90	45	ND	1b, 2, 5a, 9, 13
		Crocus Platform	CP	35–180	53	11	7	ND	5a, 13
		Maliwana Platform	MP	35–150	30	8.5	5.2	ND	6, 13
		Sombrero Platform	SP	2–20	33	9	5.3	ND	6, 13
Insular Slope	Northern slope	Sombrero Escarpment	—	200–6,000	—	90	—	a to b (canyons) c to d (interfluvies)	5a, 6
		Maliwana Spur	MS	4,000–6,000	150	~15	10 to 15	b to d	6, 7a, 13
	Anguilla Bank slopes	Northeastern slope	—	100–5,000	—	~50	—	a to b	3, 5a
		Anguilla Spur	AS	2000–6,000	900	~40	15 to 26	b to d	6, 7a, 13
	Antigua Bank slopes	Tintamarre Spur	TS	1,000–6,000	2000	~60	35–22	a to c (upper spur) c to e (lower spur)	1b, 7a, 7b, 8, 10, 13
		Tintamarre Spur Basin	TSB	4,600	15	7	2.5	d	7b, 8, 9, 12, 13
		Southeastern slope	—	100 to 5,000	—	~70	—	ND	3, 5a, 5b
		Barbuda Spur (NW)	BS	120 to 5,000	670	37	10 to 16	d to e	1b, 7b, 9, 13
		Barbuda Spur (SE)		120 to 5,000	1,070	40	28		7b, 9, 13
		Barbuda Valley	BV	4,600	—	~30	5	a to c	7b, 9, 13
		Northwestern slope	—	120 to 5,000	—	36	—	a to b (canyons)	9
		Northeastern slope	—	120 to 5,000	—	21	—	c to d (interfluvies)	9
Forearc	Northwestern forearc	Anguilla Valley	AngV	2000 to 6,000	—	~50	10	a to c (shallower valley) c to e (deeper valley)	1b, 7a, 8, 10, 13
		Sombrero Basin	SB	6,000 to 6,400	905	86	8	d	6, 13
		Maliwana Basin	MB	6,800 to 7,000	145	18.5	8.5	c to d	6, 12, 13
	Southeastern forearc	Anguilla Basin	AB	6,700	45	10	8.5	d	5a, 12, 13
		StBarthélemy Valley	StBV	4,900 to 5,200	—	~65	28	c to d	1b, 5b, 7b, 8, 9, 10, 11, 13
		Guiana Basin	GB	5,150	3	3.5	1	d	4, 9, 12, 13
		Cob Basin	CB	5,800	3	2.5	1	d	4, 9, 12, 13
		St Barthélemy Basin	StB	6,100	10	4	2	d	4, 12, 13
		Tortue Basin	TB	6,110	17	7	2	c	4, 12, 13
		Antigua Valley	AntV	4,000	—	~85	17	ND	9

The two values of width of the spurs correspond respectively to the width of the upper spur and the width of the lower spur, and backscatter echo-facies refers to **Figure 4**.

2012; Polonia et al., 2017; San Pedro et al., 2017; McHugh et al., 2020). Without sedimentological analysis to decipher their nature, we called these units “megabeds” (**Figure 12**).

5 DISCUSSION

The study area presents evidence of sediment transfer, identifiable despite the absence of deep-sea channels in the forearc basin

thanks to highly reflective seafloor in the Anguilla Valley (**Figure 10A**), reflective lobate patches in the St-Barthélemy Valley (**Figure 10A**), plunge pools (**Figures 7B, 10D, 11**), MTDs (**Figures 7A, 12D,H**), and megabeds in the deep basins (**Figure 12**). This evidence implies the occurrence of gravity processes (slope failures, density currents, etc.). To infer controls on the sediment transfer and tentatively the nature of deposits, we discuss the present-day links between morphology and sediment transfer, deduce the nature of deposits and the type

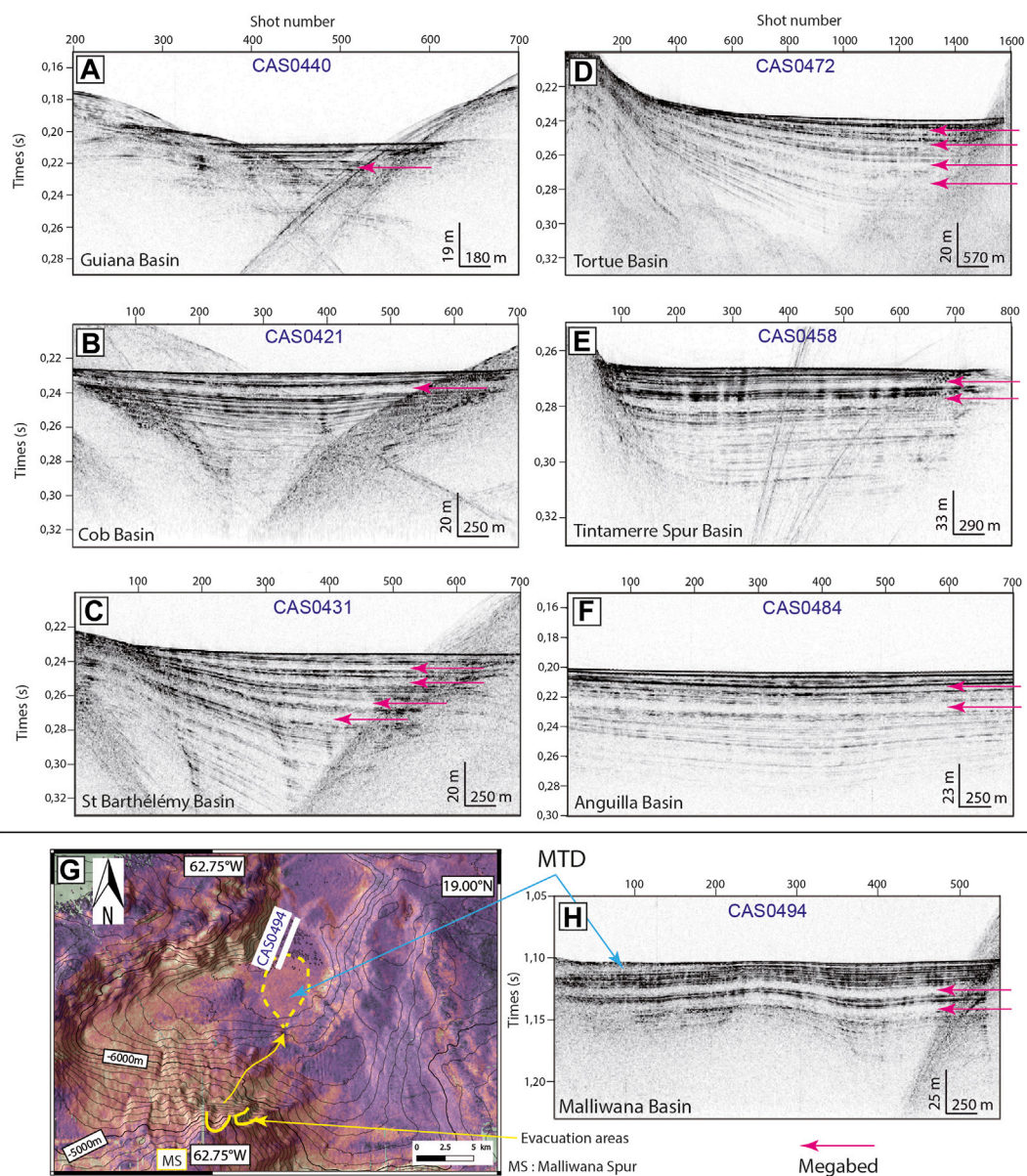


FIGURE 12 | Identification of thick acoustically transparent units in the sub-bottom profiles of the basins. Numerous thick “acoustic megabeds” can be identified but only the most visible are highlighted by the arrows. (A) Guiana Basin. (B) Cob Basin. (C) St Barthélemy Basin. (D) Backscatter map of the Malliwan Basin. Yellow dotted line highlights a MTD. (E) Tortue Basin. (F) Tintamarre Spur Basin. (G) Anguilla Basin. (H) Malliwan Basin. The basins are located in **Figures 4, 13**. MTD: Mass-Transport Deposit.

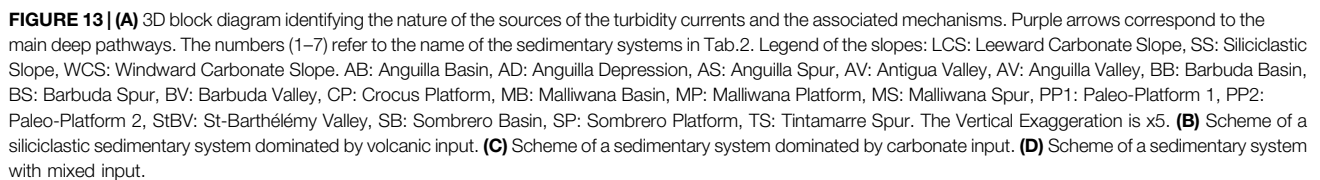
of mixing, and discuss the longer-term (Kyr to Myr) external controls on these systems.

5.1 Morphological Factors Influencing the Sediment Transfer

5.1.1 Connection Between Canyons and Reef Passes

The northeastern slope of Antigua Bank (**Figure 9**) is the only area illustrating a direct spatial relation between reef passes, gullies, and canyons (Sedimentary system 1, **Figure 13A**,

Table 2). The northeastern edge of Barbuda Island shows a narrow fringing reef disrupted by a series of passes visible in satellite photographs (**Figure 9E**). Relatively large gullies are identified on the upper slope in front of the passes (**Figure 9A**), likely acting as pathways for sediment flux. Such features are very similar to those observed off the Bahamas Banks (Mulder et al., 2017; Fauquembergue et al., 2018). They most likely result from sediment resuspension in the lagoon during cold fronts and hurricanes, leading to sediment export by density cascading and ebb currents (Wilson and Robert, 1995; Mulder



The orientation of the carbonate platforms and shelf edges with respect to major winds and oceanic currents plays an important role in sediment transfer down to deep basins (Gonzalez and Eberli, 1997; Rankey et al., 2006; Counts et al., 2018). In the study area, the Anguilla Valley is located in the continuity of canyons incising the northeastern slope of the Anguilla Bank (**Figure 10**), which represents a leeward (i.e. downwind) edge of the bank (**Figure 3**). The Anguilla Valley seafloor is highly reflective (**Figure 10**), likely indicative of coarse sediment and/or efficient sediment transport. Upstream, numerous bedforms,

July 2022 | Volume 10 | Article 834029

TABLE 2 | Identification of sedimentary systems (or turbiditic systems) and their nature (siliciclastic/carbonate/mixed) based on morphological and reflectance evidences.

Name of the sedimentary system (nb)	Elements	From (mbsl) to (mbsl)	Total length (km)	Av. slope (°)	Comments/evidences	Interpretation
NE Antigua Bank (1)	Lagoon, passes, gullies canyons	100–5,000	95 (until CB)	6.4	The only continuous system reef to deep sea	Carbonate (mainly)
NW Antigua Bank (2)	Canyons	100–6,000	105 (until StBB and TB)	5.7	Plunge-pools in St Barthélemy Valley	Carbonate (mainly)
SE Anguilla Bank (3)	Rare canyons	100–6,000	140 (until TB)	—	—	Mixed
Tintamarre Spur (4)	Gullies	700–4,600	20 (until TSB)	—	Local system	Mixed
NE Anguilla Bank (5)	Canyons	100–7,000	110 (until AB)	7.7	Anguilla Valley	Carbonate (mainly)
N Anguilla Bank (6)	Canyons	100–7,000	100 (until MB)	—	—	Carbonate (mainly)
Sombrero Escarpment (7)	Canyons	900–6,000	20 (until SB)	14.7	—	Siliciclastic

The number of each sedimentary system refers to **Figure 13**; AB, Anguilla Basin; CB, Cob Basin; MB, Malliwana Basin; SB, Sombrero Basin; StBB, St-Barthélemy Basin; TB, Tortue Basin; TSB, Tintamarre Spur Basin.

A similar configuration, with a shelf edge favorably oriented for overspill and canyons located downslope, exists off the northwest Antigua Bank (Sedimentary system 2; **Figure 13A**, **Table 2**). However, the Barbuda and Saint-Barthélemy valleys located downwards present a less reflective seafloor, likely transferring less or finer-grained sediment (Counts et al., 2018) compared to the Anguilla Valley. This fining is probably due to the greater distance (~50 km, **Figure 9**) of the canyon heads from the shelf break, but also to the gentler slope gradient, which could favor deposition rather than transport.

The southeastern slope of the Anguilla Bank presents an opposite configuration, being located off a windward edge (i.e., facing the wind; **Figures 3, 13A**). In this sediment system, canyon heads have been identified on the platform edge (**Figure 5A**) and numerous highly reflective lobate patches are found in the downstream reaches of the St-Barthélemy Valley (**Figure 10**). Due to their high to medium reflectivity (**Figure 10A**), these features are interpreted as coarse-grained deposits, located close to the slope break. Given their lobate structure and based on other case studies, they could be interpreted as MTDs (Moscardelli and Wood, 2016) or submarine fans (Shanmugam, 2016).

5.1.3 Retrogressive Erosion on the Slopes

Retrogressive erosion is a common process on submarine slopes in siliciclastic (Pratson et al., 1994; Pratson and Coakley, 1996), carbonate (Tournadour et al., 2017), or mixed sedimentary systems (Puga-Bernabéu et al., 2011). This process mainly affects the slopes disconnected from any input from the carbonate banks, for example on the Sombrero Escarpment or the Tintamarre Spur (**Figures 6, 8**).

The Sombrero Escarpment (**Figure 6**) is incised by numerous submarine canyons that are not directly connected to the Anguilla Bank. It is separated from the Anguilla Bank by the ~60-km-wide Anguilla Depression located below the storm-wave base (300 mbsl), where waves generate no water motion (Peters and Loss, 2012 and references therein), preventing the entrainment of sediment particles down the canyons of the Sombrero Escarpment. The Sombrero Escarpment canyons are mostly slope-confined and

disconnected from any feeding channel. Additionally, a ~100 m-high bathymetric elevation at the edge of the Anguilla Depression (**Figure 5C**) most likely acts as a dam, preventing sediment overspill onto the slope. The canyons incise the seafloor composed of volcanic basement or mostly volcanoclastic deposits as attested by dredged rocks collected along the escarpment (Bouysse et al., 1985) supporting that the deposits transferred within this siliciclastic system derived from volcanic sources. The low reflectivity downstream of the canyons (**Figure 4**) suggests that the deposits are probably fine-grained, but also that the sediment transfer is limited.

On the Tintamarre Spur (Sedimentary system 4, **Figure 13A**, **Table 2**), two paleo-platforms are situated at 700 mbsl and 1,600 mbsl (**Figure 8**). Between the shallowest paleo-platform and the shelf edge, no gullies, no bedforms, and no areas of high reflectivity are identified, suggesting that there is no sediment transfer from the Anguilla Bank at the moment. Both paleo-platforms show a gently dipping surface (2.4–6.6°), with a sharp slope break (16.6–18.6°) affected by spoon-shaped head scarps with gullies and canyons downwards. Due to the absence of connection with the Anguilla Bank, these canyons were probably formed by retrogressive erosion.

5.1.4 Role of Slope Gradient on the Distribution of Canyons and Plunge Pools

Many canyons (and gullies) are clearly identified on the steep insular slopes of the NLAA (**Figures 6, 8–11**), but they are generally scarcely incised and slope-confined. This diffuse distribution leads to the presence of multiple but relatively small point sources along the insular slopes. The canyons feed the foot of the slope, resulting in a scattering of sediment fluxes, which, combined with the very low accumulation rates (from 1 to 3 cm/kyr, Reid et al., 1996), supports a sediment supply insufficient to build a channelized fan turbidite system (Yose and Heller, 1989; Nelson et al., 1999). Such scattered distribution is observed along and at the base of the entire steep and rough slope (slope gradient up to 25°, Seibert et al., 2020) down to Guadeloupe, while southwards from Guadeloupe, the smoother

physiography shows well-identified single point sources, and associated distinct and long canyons and channels at their base (Seibert et al., 2020).

Additionally, the presence of a plunge pool associated with a slope-break deposit at the base of the slope in the Saint-Barthélemy (**Figure 11**) and Anguilla valleys (**Figure 10**) supports the occurrence of hydraulic jumps. Indeed, a slope-break deposit can be formed due to a significant change in slope gradient (Mulder and Alexander, 2001; Bourget et al., 2011; Migeon et al., 2012) close to a canyon mouth (Komar, 1971). The slope break that we observe ranges from 4° to 7°, and is consistent with other observations compatible with the formation of hydraulic jumps (Lee et al., 2002). One effect of hydraulic jumps is to disrupt the gravity flow, and thus maintain sediment in suspension and favor transport at the slope break (Gray et al., 2005). This process may contribute to lateral sediment dispersal towards distal sites and thus prevents a point source of sediment and channelization at the foot of the slope.

5.2 Types of Sediment Mixing

The sources of a turbidite system are a key control in their properties (Stow and Mayall, 2000). We identified two main types of sources: carbonate, due to the presence of the carbonate platforms, and siliciclastic, due to the erosion of the volcanic basement. In the study area, turbidite systems dominated by carbonate sediment overspill, are observed on the leeward edges of the shelves (Leeward Carbonate Slope—LCS; **Figures 3, 13A,C**). From the shelf break to the deep basins, these systems extend from 65 to 130 km and are dominated by carbonate sediment overspill or direct sediment transfer from the shallow carbonate reefs through reef passes and gullies, such as on the northeastern slope of the Antigua Bank (**Figures 9A,E**). The Sombrero Escarpment is the only siliciclastic turbidite system, as it is mostly fed by the retrogressive erosion of the volcanic basement and volcanoclastic deposits (Sedimentary system 7, **Figures 13A,B, Table 2**). This sedimentary system is short (~20/30 km; **Table 2**) compared to the other systems in the study area. Finally, mixed systems (i.e., with carbonate and siliciclastic sources) are also identified in the study area. If two sediment sources settle in the same place, mixed systems can be defined at the “bed scale” (the mixing occurs within each bed), at the “lithofacies scale” (the mixing represents an alternation of beds for each lithology), or at “stratigraphic scale” (Chiarella et al., 2017).

In the study area, the two distinct sources are vertically arranged, since the carbonate source sits on top of the volcanic source, rather than “frontally arranged”, with two distinct lateral lithologies (e.g., Cumberpatch et al., 2021). The mixed systems of this study are observable on the windward edges of the shelves (Sedimentary system 3, **Figure 13A, Table 2**). Indeed, these systems are fed by retrogressive erosion (**Figure 13D**) from both the platforms and shelf-edge (carbonate fraction) and the volcanic basement (volcanic fraction). This process is in accordance with other mixed systems as described offshore Australia (Puga-Bernabéu et al., 2011), where submarine canyons grow by retrogressive erosion after their initiation by a localized slope failure and/or sediment

gravity flows. Depending on their stage of formation (juvenile stage with canyon on the lower slope, transitional stage on the middle slope, mature stage on the upper slope, Puga-Bernabéu et al., 2011), the nature of the dominant source varies, with dominance of the siliciclastic source (located on the slope) during young stages and a dominance of the carbonate source in the mature stages, when the canyon reaches the platform edge (canyons heads, **Figure 5A**). We, therefore, expect the mixing to occur mostly at a “bed-scale” (Chiarella et al., 2017), with both carbonate and siliciclastic sources mixed within each deposit. The proportion of each lithology should depend on the stage of formation of the canyon. We however anticipate a dominant carbonate fraction: low reflectivity in the Sombrero basin supports a limited siliciclastic delivery compared to in the carbonate valleys. We also expect some limited amount of mixing at the lithofacies scale, because of the presence of, either juvenile systems with canyons affecting solely the volcanic basement, or, slope failures.

5.3 Long-Term (Kyr to Myr) Controls on Sediment Transfer

5.3.1 Glacio-Eustatism

Some features of the NLAS support the importance of eustatism on carbonate sediment productivity and transfer: A) drowned reefs or platforms on the Anguilla Bank indicate past periods of exposure and/or drowning of the platform (Schlager, 1989, 1998; Leclerc et al., 2014; Leclerc and Feuillet, 2019; Carey et al., 2020), and B) unconformities between seismic units in the Anguilla Valley (**Figures 10C,D**) and the St-Barthélemy Valley (**Figure 7B**) highlight periods with variation in sediment transport.

In tropical carbonate turbidite systems, eustatic fluctuations have generally a high impact on sedimentation (Dunbar and Dickens, 2003; Tcherepanov et al., 2008). During sea-level highstands, carbonate productivity is usually enhanced (Reijmer et al., 1988; Schlager et al., 1994; Chabaud et al., 2016), providing high amounts of bioclasts and carbonate muds available for sediment transport. Conversely, during sea-level lowstands, production and off-bank transport are generally reduced while cementation, lithification, and induration of shallow-water carbonates are increased (Schlager et al., 1994; Chabaud et al., 2016), and thus prevent remobilization by currents and waves. Moreover, dissolution rather than erosion of carbonates prevails onshore (Chabaud et al., 2016), furthermore reducing sediment input during lowstands. Limited deposition of gravity flows may however also occur during lowstands, mainly at proximal locations of turbidite systems as documented for the Glorieuses islands (Jorry et al., 2020) and supported by higher seafloor reflectivity, suggesting some reworking on the upper slope.

Carbonate systems of the NLAS are therefore most likely active during sea-level highstands and less active during sea-level lowstands, such as in other mixed systems (Schlager et al., 1994; Jorry et al., 2008; McArthur et al., 2013). In contrast, the top of the siliciclastic system is too deep (~900 mbsl) to be influenced by glacio-eustatic sea-level fluctuations as usually observed in

siliciclastic systems, which are more active during sea-level lowstands (Posamentier et al., 1991; Vail et al., 1991; Hübscher et al., 1997).

5.3.2 Tectonics

Tectonics can play an important role in sediment transfer and destabilization, particularly along active margins, where vertical motions can deflect or dam transfer axis, modify the availability of sediment supply or drive the failure of over-steepened slopes (Laursen and Normark, 2002; Mountjoy et al., 2009; Michaud et al., 2011; Ratzov et al., 2012; Collot et al., 2019; Seibert et al., 2020; Claussmann et al., 2021a). Subsidence outlined by the presence of two tilted carbonate paleo-platforms at 700 mbsl and 1,600 mbsl (Figure 8) is consistent with the drastic subsidence of the forearc identified by Boucard et al., 2021. The present-day relatively deep position of these features, which were formed at a very shallow depth, attests to the important role of subsidence, probably accentuated along the Tintamarre Spur. For instance, at Les Saintes (offshore Guadeloupe), the subsidence of the Quaternary coral reef (Leclerc et al., 2014) is estimated at a rate of -0.3 to -0.45 mm/yr since the late Pleistocene (Leclerc and Feuillet, 2019), while in the north, this estimation reaches 340 m/Myr (0.34 mm/yr) in the deepest outer forearc since middle Miocene (Boucard et al., 2021). Possible causes of subsidence are debated, but include: A) a thermal origin caused by the cooling of the lithosphere related to a decline in volcanic activity and westward migration of the volcanic arc since the Miocene (Bouysse and Westercamp, 1990; Legendre et al., 2018); B) regional subsidence of the arc due to long-term plate motion along the subduction megathrust over several seismic cycles (Leclerc and Feuillet, 2019); or C) basal erosion of the upper plate by over pressured fluids related to a fully-hydrated subduction zone (Paulatto et al., 2017; Marcaillou et al., 2021).

Independently of the causes of tectonics in the area, two general effects are directly induced. The first is the opening of V-shaped valleys in map view (*sensu* Boucard et al., 2021), which created a complex morphology departing from a classical circular or elongated shape of the banks and shelf-edges; this promotes multiple edges that are either windward or leeward oriented, thus favoring, or not, carbonate transport off-bank. The second is the over-steepening of valley walls (or spurs, or flanks) bounded by normal faults. This last effect directly influences slope stability, the amount of retrogressive erosion, sediment production, and the formation of plunge pools due to hydraulic jumps. Indeed, the stability of plunge pools over time; demonstrated by the presence of a buried and tilted plunge pool along with unconformity U4, would have involved a slope-break angle of a few degrees to allow for a hydraulic jump (Komar, 1971). This break is probably maintained by fault activity, preventing sediment accumulation and progressive flattening at the foot of the slope (Bourget et al., 2011). The two combined effects of tectonics thus account for the long-term lack of point sources, scattered sediment delivery, and the mixing of the system.

5.3.3 Seismicity

The main particularity of the NLAS is the proximity of a subduction zone, implying possible seismically-triggered gravity-driven currents (see for example Goldfinger et al., 2003; Ratzov et al., 2015). In at least seven separate forearc sub-basins, thick transparent units (megabeds) are visible in sub-bottom profiles (Figure 12) and could correspond to homogenites or megaturbidites. Similar deposits are explained in the literature as resulting from surficial sediment remobilization (McHugh et al., 2016; McHugh et al., 2020), or from a seiche effect induced by seismic waves in a confined basin or in a lake (Chapron et al., 1999; Beck et al., 2007). Alternative explanations include the waning flow of a turbidity current triggered by an earthquake (Polonia et al., 2017) or the resuspension of shallow sediment due to a tsunami (San Pedro et al., 2017). The identification of MTDs (Figures 7A, 12D,H), which can be triggered by earthquakes (Moscardelli and Wood, 2016 and reference therein), confirms that seismicity is an important parameter considering sediment transfer in the study area. Ongoing detailed chronostratigraphy and dating of these deposits (Morena, 2020) should define the timing and spatial correlation across the margin, to infer a regional trigger, most likely caused by an earthquake as documented by Goldfinger et al. (2003).

6 CONCLUSION

The study of modern depositional sedimentary systems, especially concerning multi-sources (siliciclastic, carbonate, or mixed) sedimentary systems has significantly progressed over the last decade (e.g., Chiarella et al., 2017), even if the coexistence of adjacent systems of distinctive nature is scarcely documented. In the Northern Lesser Antilles Segment, carbonate and siliciclastic sources coexist within 150 km on two wide and shallow carbonate shelves (carbonate sources) and a steep insular and mainly volcanic slope (siliciclastic source). Morphological factors, such as the slope gradient or the orientation of the shelf edge with respect to wind and current, are determining factors for the nature of the source:

- Siliciclastic sedimentary systems are disconnected by a morphological dam from the main carbonate platforms or sources and are likely fed by retrogressive erosion of the steep volcanic slopes
- Carbonate sedimentary systems are sourced from the leeward edges of the carbonate platforms by carbonate overspill through numerous small, narrow canyons originating at the shelf edge
- Mixed sedimentary systems are identified on the windward edges of carbonate platforms incised by slope-confined canyons through retrogressive- and downward-cutting erosion

Tectonic activity plays a major role in the coexistence of adjacent distinctive sedimentary systems, since the normal

faults created a complex morphology dominated by V-shaped valleys in map view, which offer an alternation of leeward, and windward edges favoring carbonate- or mixed-systems. Additionally, the steep slope gradient induced by normal faults and tilting seems to be the main factor controlling sediment dispersal, for example by causing multiple line sources, and the dispersion of gravity-driven currents under the effect of hydraulic jump in areas of marked slope break. Evidence of paleo-platforms in the Tintamarre Spur and unconformities in the valleys also support the importance of tectonics in the area for all the sedimentary systems, while drowned platforms might imply the strong influence of glacio-eustatism on the carbonate system. Ongoing marine paleoseismic studies could allow us to verify the role of seismicity as a triggering-factor for slope destabilizations leading to the occurrence of gravity-driven currents and their deposit in the forearc basin.

Our study provides a modern analog of adjacent systems dominated by distinctive lithologies in a tectonically active area. The results appear particularly appropriate to decipher the nature of ancient source-to-sink systems dominated by complex tectonics, paleo-bathymetry, and sediment routings.

DATA AVAILABILITY STATEMENT

The original contributions presented in the study are included in the article and **Supplementary Material**; further inquiries can be directed to the corresponding author or to SISMER. The DOIs of the oceanographic cruises are: <https://doi.org/10.17600/16001800> for ANTITHESIS 1 cruise, doi: 10.17600/13010070 for ANTITHESIS 3 cruise and doi: 10.17600/16001700 for CASEIS cruise.

AUTHOR CONTRIBUTIONS

PM was involved in all the stages of the production of the study, including data analysis, figures realization and writing of the paper. GR was involved in the data acquisition and was involved in all the stages of the production of the study. AC was involved in all the stages of the production of the manuscript. FK was involved in the production of the manuscript and was co-Principal Investigator of the ANTITHESIS cruises. CB was involved in the data acquisition and was involved in the final

reading of the manuscript. CS was involved in the data acquisition and processing, and was involved in the final reading of the manuscript. BM was the Principal Investigator of the ANTITHESIS cruises and was involved in the data acquisition and in the final reading of the manuscript. NF was the Principal Investigator of the CASEIS cruise, was involved in the data acquisition and in the final reading of the manuscript.

ACKNOWLEDGMENTS

The authors thank the Captain, crew, and scientific team of CASEIS cruise (DOI:10.17600/16001800) and ANTITHESIS cruises (DOI: 10.17600/13010070). This study was accomplished within the framework of the French ANR CARQUAKES project, contract number ANR-17-CE3-0006, the LABEX UnivEearthS project WP2.1, the PREST interreg Caraïbe project, the BQR IPGP, the CNRS-INSU, the BQR Observatoire Côte d'Azur, and the Université Côte d'Azur (CSI 2016-DR-066). The PhD of Pierre Morena was funded by IFREMER and Région Bretagne. The authors thank Alison Chalm (Ifremer, Brest) for her efficiency in the English correction of the manuscript. The authors also thank Sébastien Migeon (Geoazur, Valbonne) for scientific discussions. The authors thank Jenny Trévisan (Geoazur, Valbonne) for DEM processing; Frédérique Leclerc (Geoazur, Valbonne), Muriel Laurencin (UBO, Brest), Jean-Marie Saurel (IPGP, Paris), Gaëlle Bénâtre (IPGP, Paris), and Eric Jacques (IPG, Paris) for MCS data processing; and Hervé Bisquay and Laurence Morvan (Genavir, Brest) for multibeam data processing. The authors finally thank Barbara Claussmann (Schlumberger, United Kingdom), Lesli Wood (Colorado School of Mines, United States) and Adam McArthur (University of Leeds, United Kingdom) for their constructive review, as well as Ángel Puga-Bernabéu (University of Granada, Spain) for his comments on an early version of the manuscript.

SUPPLEMENTARY MATERIAL

The Supplementary Material for this article can be found online at: <https://www.frontiersin.org/articles/10.3389/feart.2022.834029/full#supplementary-material>

REFERENCES

- Andréieff, P., Baubron, J. C., and Westercamp, D. (1988a). Histoire géologique de la Martinique (Petites Antilles): biostratigraphie (foraminifères), radiochronologie (potassium-argon), évolution volcano-structurale. *Géologie Fr.* 2-3, 39–70.
- Andréieff, P., Westercamp, D., Garrabé, F., and Bonneton, J. R. (1988b). Stratigraphie de l'île de Saint-Martin. *Géologie Fr.* 2-3, 71–88.
- Bailleul, J., Robin, C., Chanier, F., Guillocheau, F., Field, B., and Ferriere, J. (2007). Turbidite Systems in the Inner Forearc Domain of the Hikurangi Convergent Margin (New Zealand): New Constraints on the Development of Trench-Slope Basins. *J. Sediment. Res.* 77 (4), 263–283. doi:10.2110/jsr.2007.028
- Beck, C. (2009). "Late Quaternary Lacustrine Paleo-Seismic Archives in North-Western Alps: Examples of Earthquake-Origin Assessment of Sedimentary Disturbances". *Earth-Science Rev.* 96, 327–344. doi:10.1016/j.earscirev.2009.07.005
- Beck, C., Mercier de Lepinay, B., Schneider, J.-L., Cremer, M., Çağatay, N., Wendenbaum, E., et al. (2007). Late Quaternary Co-seismic Sedimentation in the Sea of Marmara's Deep Basins. *Sediment. Geol.* 199 (1-2), 65–89. doi:10.1016/j.sedgeo.2005.12.031
- Beck, C., Reyss, J.-L., Leclerc, F., Moreno, E., Feuillet, N., Barrier, L., et al. (2012). Identification of Deep Subaqueous Co-seismic Scarps through Specific Coeval Sedimentation in Lesser Antilles: Implication for Seismic Hazard. *Nat. Hazards Earth Syst. Sci. Eur. Geosciences Union* 12, 1–13. doi:10.5194/nhess-12-1755-2012

- Benâtre, G., Feuillet, N., Carton, H., Jacques, E., and Pichot, T. (2020). *Main Active Structures in the Barbados Accretionary Wedge of the Lesser Antilles Subduction: Implications for Slip Partitioning*. Vienna: EGU Fall Meeting.
- Bertran, P., Bonnissent, D., Imbert, D., Lozouet, P., Serrand, N., and Stouvenot, C. (2004). Paléoclimat des Petites Antilles depuis 4000 ans BP : l'enregistrement de la lagune de Grand-Case à Saint-Martin. *Comptes Rendus Geosci.* 336 (16), 1501–1510. doi:10.1016/j.crte.2004.09.009
- Boucard, M., Marcaillou, B., Lebrun, J. F., Laurencin, M., Klingelhoefer, F., Laigle, M., et al. (2021). Paleogene V-Shaped Basins and Neogene Subsidence of the Northern Lesser Antilles Forearc. *Tectonics* 40, e2020TC006524. doi:10.1029/2020TC006524
- Bourget, J., Zaragosi, S., Ellouz-zimmermann, N., Mouchot, N., Garlan, T., Schneider, J.-L., et al. (2011). Turbidite System Architecture and Sedimentary Processes along Topographically Complex Slopes: the Makran Convergent Margin. *Sedimentology* 58 (2), 376–406. doi:10.1111/j.1365-3091.2010.01168.x
- Bouysse, P., Andréieff, P., Richard, M., Baubron, J. C., Mascle, A., Maury, R. C., et al. (1985). “Aves Swell and Northern Lesser Antilles Ridge: Rock-Dredging Results from ARCANTE 3 Cruise,” in *Géodynamique des Caraïbes, Symposium* (Paris: Editions Technip), 65–76.
- Bouysse, P., and Guennoc, P. (1983). Données sur la structure de l'arc insulaire des petites antilles, entre Ste-Lucie et Anguilla. *Mar. Geol.* 53 (1-2), 131–166. doi:10.1016/0025-3227(83)90038-5
- Bouysse, P., and Westercamp, D. (1990). Subduction of Atlantic Aseismic Ridges and Late Cenozoic Evolution of the Lesser Antilles Island Arc. *Tectonophysics* 175 (4), 349–380. doi:10.1016/0040-1951(90)90180-g
- Braga, J. C., Martin, J. M., and Wood, J. L. (2001). Submarine Lobes and Feeder Channels of Redeposited, Temperate Carbonate and Mixed Siliciclastic-Carbonate Platform Deposits (Vera Basin, Almería, Southern Spain). *Sedimentology* 48, 99–116. doi:10.1046/j.1365-3091.2001.00353.x
- Briden, J. C., Rex, D. C., Faller, A. M., and Tomblin, J. F. (1979). K-ar Geochronology and Palaeomagnetism of Volcanic Rocks in the Lesser Antilles Island Arc. *Philosophical Trans. R. Soc. B Biol. Sci.* 291, 485–528. doi:10.1098/rsta.1979.0040
- Brink, U. t., Danforth, W., Polloni, C., Andrews, B., Llanes, P., Smith, S., et al. (2004). New Seafloor Map of the Puerto Rico Trench Helps Assess Earthquake and Tsunami Hazards. *Eos Trans. AGU* 85 (Issue 37), 349–354. doi:10.1029/2004EO370001
- Budd, A. F., Johnson, K. G., and Edwards, J. C. (1995). Caribbean Reef Coral Diversity during the Early to Middle Miocene: An Example from the Anguilla Formation. *Coral Reefs* 14, 109–117. doi:10.1007/bf00303432
- Carey, S., Sparks, R. S. J., Tucker, M. E., Li, T., Robinson, L., Watt, S. F. L., et al. (2020). The Polygenetic Kahouanne Seamounts in the Northern Lesser Antilles Island Arc: Evidence for Large-Scale Volcanic Island Subsidence. *Mar. Geol.* 419, 106046. doi:10.1016/j.margeo.2019.106046
- Chabaud, L., Ducassou, E., Tournadour, E., Mulder, T., Reijmer, J. J. G., Conesa, G., et al. (2016). Sedimentary Processes Determining the Modern Carbonate Periplatform Drift of Little Bahama Bank. *Mar. Geol.* 378, 213–229. doi:10.1016/j.margeo.2015.11.006
- Chapron, E., Beck, C., Pourchet, M., and Deconinck, J.-F. (1999). 1822 Earthquake-Triggered Homogenite in Lake Le Bourget (NW Alps). *Terra nova*. 11 (2-3), 86–92. doi:10.1046/j.1365-3121.1999.00230.x
- Chiarella, D., Longhitano, S. G., and Tropeano, M. (2019). Different Stacking Patterns along an Active Fold-And-Thrust Belt-Acerenza Bay, Southern Apennines (Italy). *Geology* 47 (2), 139–142. doi:10.1130/g45628.1
- Chiarella, D., Longhitano, S. G., and Tropeano, M. (2017). Types of Mixing and Heterogeneities in Siliciclastic-Carbonate Sediments. *Mar. Petroleum Geol.* 88, 617–627. doi:10.1016/j.marpetgeo.2017.09.010
- Christeson, G. L., Mann, P., Escalona, A., and Aitken, T. J. (2008). Crustal Structure of the Caribbean-Northeastern South America Arc-Continent Collision Zone. *J. Geophys. Res.* 113, 1–19. doi:10.1029/2007jb005373
- Christman, R. A. (1953). Geology of St. Bartholomew, St. Martin and Anguilla, Lesser Antilles. *Geol. Soc. Am. Bull.* 64 (1), 65–96. doi:10.1130/0016-7606(1953)64[85:gosbsm]2.0.co;2
- Claussmann, B., Bailleul, J., Chanier, F., Caron, V., Mearthur, A. D., Mahieux, G., et al. (2021b). Contrasting Mixed Siliciclastic-Carbonate Shelf-Derived Gravity-Driven Systems in Compressed Intra-slope Basins (Southern Hikurangi Margin, New Zealand). *Mar. Petroleum Geol.* 134, 105252. doi:10.1016/j.marpetgeo.2021.105252
- Claussmann, B., Bailleul, J., Chanier, F., Mahieux, G., Caron, V., Mearthur, A. D., et al. (2021a). Shelf-derived Mass-Transport Deposits: Origin and Significance in the Stratigraphic Development of Trench-Slope Basins. *N. Z. J. Geol. Geophys.* 65 (1), 17–52. doi:10.1080/00288306.2021.1918729
- Collot, J. Y., Ratzov, G., Silva, P., Proust, J. N., Migeon, S., Hernandez, M. J., et al. (2019). The Esmeraldas Canyon: A Helpful Marker of the Pliocene-Pleistocene Tectonic Deformation of the North Ecuador-Southwest Colombia Convergent Margin. *Tectonics* 38, 3140–3166. doi:10.1029/2019TC005501
- Cornée, J.-J., Léticée, J.-L., Münch, P., Quillévéré, F., Lebrun, J.-F., Moissette, P., et al. (2012). Sedimentology, Palaeoenvironments and Biostratigraphy of the Pliocene-Pleistocene Carbonate Platform of Grande-Terre (Guadeloupe, Lesser Antilles Forearc). *Sedimentology* 59, 1426–1451. doi:10.1111/j.1365-3091.2011.01311.x
- Corne, J. J., Münch, P., Philippon, M., Boudagher-Fadel, M., Quillévéré, F., Melinte-Dobrinescu, M., et al. (2021). Lost Islands in the Northern Lesser Antilles: Possible Milestones in the Cenozoic Dispersal of Terrestrial Organisms between South-America and the Greater Antilles. *Earth-Science Rev.* 2021, 103617. doi:10.1016/j.earscirev.2021.103617
- Ćosović, V., Mrinjek, E., Nemec, W., Španiček, J., and Terzić, K. (2018). Development of Transient Carbonate Ramps in an Evolving Foreland Basin. *Basin Res.* 30 (4), 746–765.
- Counts, J. W., Jorry, S. J., Leroux, E., Miramontes, E., and Jouet, G. (2018). Sedimentation Adjacent to Atolls and Volcano-Cored Carbonate Platforms in the Mozambique Channel (SW Indian Ocean). *Mar. Geol.* 404, 41–59. doi:10.1016/j.margeo.2018.07.003
- Cumberpatch, Z. A., Soutter, E. L., Kane, I. A., Casson, M., and Vincent, S. J. (2021). Evolution of a Mixed Siliciclastic-carbonate Deep-marine System on an Unstable Margin: The Cretaceous of the Eastern Greater Caucasus, Azerbaijan. *Basin Res.* 33 (1), 612–647. doi:10.1111/bre.12488
- DeMets, C., Gordon, R. G., and Argus, D. F. (2010). Geologically Current Plate Motions. *Geophys. J. Int.* 181, 1–80. doi:10.1111/j.1365-246X.2009.04491.x
- Deville, E., Mascle, A., Callec, Y., Huyghe, P., Lallemand, S., Lerat, O., et al. (2015). Tectonics and Sedimentation Interactions in the East Caribbean Subduction Zone: An Overview from the Orinoco Delta and the Barbados Accretionary Prism. *Mar. Petroleum Geol.* 64, 76–103. doi:10.1016/j.marpetgeo.2014.12.015
- Dorsey, R. J., and Kidwell, S. M. (1999). Mixed Carbonate-Siliciclastic Sedimentation on a Tectonically Active Margin: Example from the Pliocene of Baja California Sur, Mexico. *Geol.* 27 (10), 935–938. doi:10.1130/0091-7613(1999)027<0935:mcssoa>2.3.co;2
- Droxler, A. W., and Schlager, W. (1985). Glacial versus Interglacial Sedimentation Rates and Turbidity Frequency in the Bahamas. *Geol.* 13 (11), 799–802. doi:10.1130/0091-7613(1985)13<799:gvisra>2.0.co;2
- Dunbar, G. B., and Dickens, G. R. (2003). Late Quaternary Shedding of Shallow-Marine Carbonate along a Tropical Mixed Siliciclastic-Carbonate Shelf: Great Barrier Reef, Australia. *Sedimentology* 50 (6), 1061–1077. doi:10.1046/j.1365-3091.2003.00593.x
- Eberli, G. P., and Ginsburg, R. N. (1987). Segmentation and Coalescence of Cenozoic Carbonate Platforms, Northwestern Great Bahama Bank. *Geol.* 15 (1), 75–79. doi:10.1130/0091-7613(1987)15<75:sacocc>2.0.co;2
- Fauquembergue, K., Ducassou, E., Mulder, T., Hanquiez, V., Perello, M.-C., Poli, E., et al. (2018). Genesis and Growth of a Carbonate Holocene Wedge on the Northern Little Bahama Bank. *Mar. Petroleum Geol.* 96, 602–614. doi:10.1016/j.marpetgeo.2018.05.013
- Feuillet, N., Beauducel, F., and Tapponnier, P. (2011). Tectonic Context of Moderate to Large Historical Earthquakes in the Lesser Antilles and Mechanical Coupling with Volcanoes. *J. Geophys. Res.* 116, B10. doi:10.1029/2011JB008443
- Feuillet, N. (2016). CASEIS Cruise, RV Pourquoi Pas ? <https://campagnes.flotteoceanographique.fr/campagnes/16001800/>. doi:10.17600/16001800
- Feuillet, N., Leclerc, F., Tapponnier, P., Beauducel, F., Boudon, G., Le Friant, A., et al. (2010). Active Faulting Induced by Slip Partitioning in Montserrat and Link with Volcanic Activity: New Insights from the 2009 GWADASEIS Marine Cruise Data. *Geophys. Res. Lett.* 37, 19. doi:10.1029/2010gl042556
- Feuillet, N., Manighetti, I., Tapponnier, P., and Jacques, E. (2002). Arc Parallel Extension and Localization of Volcanic Complexes in Guadeloupe, Lesser Antilles. *J. Geophys. Res.* 107 (B12), 3–1. doi:10.1029/2001JB000308
- Feuillet, N., Tapponnier, P., Manighetti, I., Villemant, B., and King, G. C. P. (2004). Differential Uplift and Tilt of Pleistocene Reef Platforms and Quaternary Slip

- Rate on the Morne-Piton Normal Fault (Guadeloupe, French West Indies). *J. Geophys. Res. Solid Earth* 109, B2. doi:10.1029/2003jb002496
- Goldfinger, C., Nelson, H. C., and Johnson, J. E. (2003). Shipboard Scientific Party Deep-Water Turbidites as Holocene Earthquake Proxies: the Cascadia Subduction Zone and Northern San Andreas Fault Systems. *Ann. Geophys.* 46 (5), 1169–1194.
- Gonzalez, R., and Eberli, G. P. (1997). Sediment Transport and Bedforms in a Carbonate Tidal Inlet; Lee Stocking Island, Exumas, Bahamas. *Sedimentology* 44 (6), 1015–1030. doi:10.1046/j.1365-3091.1997.d01-59.x
- Gray, T. E., Alexander, J., and Leeder, M. R. (2005). Quantifying Velocity and Turbulence Structure in Depositing Sustained Turbidity Currents across Breaks in Slope. *Sedimentology* 52 (3), 467–488. doi:10.1111/j.1365-3091.2005.00705.x
- Haak, A. B., and Schlager, W. (1989). Compositional Variations in Calciturbidites Due to Sea-Level Fluctuations, Late Quaternary, Bahamas. *Geol. Rundsch* 78 (2), 477–486. doi:10.1007/bf01776186
- Hans Nelson, C., Karabanov, E. B., Colman, S. M., and Escutia, C. (1999). Tectonic and Sediment Supply Control of Deep Rift Lake Turbidite Systems: Lake Baikal, Russia. *Geol. Zool.* 27 (2), 163–166. doi:10.1130/0091-7613(1999)027<0163:tassco>2.3.co;2
- Hassoun, V., Migeon, S., Cattaneo, A., Larroque, C., and Mercier de Lepinay, B. (2009). “Imbricated Scars on the Ligurian Continental Slope: Evidence for Multiple Failure Events in the 1887 Earthquake Epicentral Area,” in International Conference on Seafloor Mapping for Geohazard Assessment, Ischia, Italy, May 11–13, 2009 (World Academy of Science, Engineering and Technology), 7, 11–13.
- Hübscher, C., Spieß, V., Breizke, M., and Weber, M. E. (1997). The Youngest Channel-Levee System of the Bengal Fan: Results from Digital Sediment Echosounder Data. *Mar. Geol.* 141, 125–145.
- Iacono, C. L., Gràcia, E., Diez, S., Bozzano, G., Moreno, X., Dañoibeitia, J., et al. (2008). Seafloor Characterization and Backscatter Variability of the Almería Margin (Alboran Sea, SW Mediterranean) Based on High-Resolution Acoustic Data. *Mar. Geol.* 250 (1–2), 1–18. doi:10.1016/j.margeo.2007.11.004
- Jany, I., Scanlon, K. M., and Mauffret, A. (1990). Geological Interpretation of Combined Seabeam, Gloria and Seismic Data from Anegada Passage (Virgin Islands, North Caribbean). *Mar. Geophys. Res.* 12 (3), 173–196. doi:10.1007/bf02266712
- Jorry, S. J., Camoin, G. F., Jouet, G., Roy, P. L., Vella, C., Courgeon, S., et al. (2016). Modern Sediments and Pleistocene Reefs from Isolated Carbonate Platforms (Iles Eparses, SW Indian Ocean): a Preliminary Study. *Acta Oecol.* 72, 129–143. doi:10.1016/j.actao.2015.10.014
- Jorry, S. J., Droxler, A. W., Mallarino, G., Dickens, G. R., Bentley, S. J., Beaufort, L., et al. (2008). Bundled Turbidite Deposition in the Central Pandora Trough (Gulf of Papua) since Last Glacial Maximum: Linking Sediment Nature and Accumulation to Sea Level Fluctuations at Millennial Timescale. *J. Geophys. Res.* 113. doi:10.1029/2006JF000649
- Jorry, S. J., Jouet, G., Edinger, E. N., Toucanne, S., Counts, J. W., Courgeon, S., et al. (2020). From Platform Top to Adjacent Deep Sea: New Source-to-Sink Insights into Carbonate Sediment Production and Transfer in the SW Indian Ocean (Glorieuses archipelago). *Marine Geology* 423, 106144. doi:10.1016/j.margeo.2020.106144
- Kastens, K. A., and Cita, M. B. (1981). Tsunami-induced Sediment Transport in the Abyssal Mediterranean Sea. *Geol. Soc. Am. Bull.* 92 (11), 845–857. doi:10.1130/0016-7606(1981)92<845:tstlita>2.0.co;2
- Komar, P. D. (1971). Hydraulic Jumps in Turbidity Currents. *Geol. Soc. Am. Bull.* 82 (6), 1477–1488. doi:10.1130/0016-7606(1971)82[1477:hjtc]2.0.co;2
- Kopp, H., Weinzierl, W., Becel, A., Charvis, P., Evain, M., Flueh, E. R., et al. (2011). Deep Structure of the Central Lesser Antilles Island Arc: Relevance for the Formation of Continental Crust. *Earth Planet. Sci. Lett.* 304, 121–134. doi:10.1016/j.epsl.2011.01.024
- Laban, C., Cameron, T. D. J., and Schüttenhelm, R. T. E. (1984). Geologie van het Kwartair in de zuidelijke bocht van de Noordzee. *Meded. Werkgr. Tert. Kwartaire Geol.* 21 (3), 139–153.
- Laurencin, M. (2017). *Etude de la géométrie, de la nature et des déformations de la zone de subduction des Petites Antilles du Nord*. Brest: University of Bretagne Loire, 294. PhD Thesis.
- Laurencin, M., Graindorge, D., Klingelhoefer, F., Marcaillou, B., and Evain, M. (2018). Influence of Increasing Convergence Obliquity and Shallow Slab Geometry onto Tectonic Deformation and Seismogenic Behavior along the Northern Lesser Antilles Zone. *Earth Planet. Sci. Lett.* 492, 59–72. doi:10.1016/j.epsl.2018.03.048
- Laurencin, M., Marcaillou, B., Graindorge, D., Klingelhoefer, F., Lallemand, S., Laigle, M., et al. (2017). The Polyphased Tectonic Evolution of the Anegada Passage in the Northern Lesser Antilles Subduction Zone. *Tectonics* 36 (5), 945–961. doi:10.1002/2017TC004511
- Laurencin, M., Marcaillou, B., Graindorge, D., Lebrun, J. F., Klingelhoefer, F., Boucard, M., et al. (2019). The Bunce Fault and Strain Partitioning in the Northern Lesser Antilles. *Geophys. Res. Lett.* 46, 9573–9582. doi:10.1029/2019GL083490
- Laursen, J., and Normark, W. R. (2002). Late Quaternary Evolution of the San Antonio Submarine Canyon in the Central Chile Forearc (33°S). *Mar. Geol.* 188 (3–4), 365–390. PII:S0025-3227(02)00421-8. doi:10.1016/s0025-3227(02)00421-8
- Leclerc, F., Feuillet, N., Cabioch, G., Depluys, C., Lebrun, J. F., Bazin, S., et al. (2014). The Holocene Drowned Reef of Les Saintes Plateau as Witness of a Long-Term Tectonic Subsidence along the Lesser Antilles Volcanic Arc in Guadeloupe. *Mar. Geol.* 355, 115–135. doi:10.1016/j.margeo.2014.05.017
- Leclerc, F., and Feuillet, N. (2019). Quaternary Coral Reef Complexes as Powerful Markers of Long-Term Subsidence Related to Deep Processes at Subduction Zones: Insights from Les Saintes (Guadeloupe, French West Indies). *Geosphere* 15 (4), 983–1007. doi:10.1130/GES02069.1
- Lee, S. E., Talling, P. J., Ernst, G. G. J., and Hogg, A. J. (2002). Occurrence and Origin of Submarine Plunge Pools at the Base of the US Continental Slope. *Mar. Geol.* 185 (3–4), 363–377. PII:S0025-3227(01)00298-5. doi:10.1016/s0025-3227(01)00298-5
- Legendre, L., Philippon, M., Münch, P., Leticée, J. L., Noury, M., Maincent, G., et al. (2018). Trench Bending Initiation: Upper Plate Strain Pattern and Volcanism. Insights from the Lesser Antilles Arc, St. Barthélemy Island, French West Indies. *Tectonics* 37 (9), 2777–2797. doi:10.1029/2017TC004921
- Malaizé, B., Bertran, P., Carbonel, P., Bonnissent, D., Charlier, K., Galop, D., et al. (2011). Hurricanes and Climate in the Caribbean during the Past 3700 Years BP. *Holocene* 21 (6), 911–924. doi:10.1177/0959683611400198
- Mann, P., Prentice, C. S., Hippolyte, J.-C., Grindlay, N. R., Abrams, L. J., and Lao ‘-Da’ vila, D. (2005). “Reconnaissance Study of Late Quaternary Faulting along Cerro Goden Fault Zone, Western Puerto Rico,” in *Active Tectonics and Seismic Hazards of Puerto Rico, the Virgin Islands and Off-Shore Areas*. Editor P. Mann (America: Geological Society of America), 115–138. doi:10.1130/0-8137-2385-x.115
- Marcaillou, B., and Klingelhoefer, F. (2013). *ANTITHESIS-1-Leg1 Cruise*. RV L’Atalante. doi:10.17600/13010070
- Marcaillou, B., and Klingelhoefer, F. (2016). *ANTITHESIS-3 Cruise*. RV Pourquoi Pas? doi:10.17600/16001700
- Marcaillou, B., Klingelhoefer, F., Laurencin, M., Lebrun, J.-F., Laigle, M., Lallemand, S., et al. (2021). Pervasive Detachment Faults within the Slow Spreading Oceanic Crust at the Poorly Coupled Antilles Subduction Zone. *Commun. Earth Environ.* 2. doi:10.1038/s43247-021-00269-6
- Masclé, A., and Westercamp, D. (1983). Géologie d’Antigua, Petites Antilles. *Bull. Société géologique Fr.* S7-XXV, 855–866. doi:10.2113/gssgfbull.s7-xxv.6.855
- McArthur, A. D., Hartley, A. J., and Jolley, D. W. (2013). Stratigraphic Development of an Upper Jurassic Deep Marine Syn-Rift Succession, Inner Moray Firth Basin, Scotland. *Basin Res.* 25 (3), 285–309. doi:10.1111/j.1365-2117.2012.00557.x
- McHugh, C. M., Kanamatsu, T., Seeber, L., Bopp, R., Cormier, M.-H., and Usami, K. (2016). Remobilization of Surficial Slope Sediment Triggered by the A.D. 2011 Mw9 Tohoku-Oki Earthquake and Tsunami along the Japan Trench. *Geology* 44, 391–394. doi:10.1130/G37650.1
- McHugh, C. M., Seeber, L., Rasbury, T., Strasser, M., Kioka, A., Kanamatsu, T., et al. (2020). Isotopic and Sedimentary Signature of Megathrust Ruptures along the Japan Subduction Margin. *Mar. Geol.* 428, 106283. doi:10.1016/j.margeo.2020.106283
- Michaud, F., Calmus, T., Ratzov, G., Royer, J. Y., Sossou, M., Bigot-Cormier, F., et al. (2011). Active Deformation along the Southern End of the Tosco-Abrejos Fault System: New Insights from Multibeam Swath Bathymetry. *Pure Appl. Geophys.* 168 (8), 1363–1372. doi:10.1007/s00024-010-0193-y
- Migeon, S., Mulder, T., Savoye, B., and Sage, F. (2012). Hydrodynamic Processes, Velocity Structure and Stratification in Natural Turbidity Currents: Results

- Inferred from Field Data in the Var Turbidite System. *Sediment. Geol.* 245–246, 48–62. doi:10.1016/j.sedgeo.2011.12.007
- Morena, P. (2020). *Paléosismologie et potentiel sismogène de la zone de subduction des Petites Antilles à partir de l'enregistrement sédimentaire*. Brest: University of Bretagne Occidentale, 340. PhD Thesis.
- Moscardelli, L., Ochoa, J., Hunt, I., and Zahm, L. (2019). Mixed Siliciclastic-Carbonate Systems and Their Impact for the Development of Deep-Water Turbidites in Continental Margins: A Case Study from the Late Jurassic to Early Cretaceous Shelburne Subbasin in Offshore Nova Scotia. *Bulletin* 103 (10), 2487–2520. doi:10.1306/02151917318
- Moscardelli, L., and Wood, L. (2016). Morphometry of Mass-Transport Deposits as a Predictive Tool. *Bulletin* 128 (1–2), 47–80.
- Mountjoy, J. J., Barnes, P. M., and Pettinga, J. R. (2009). Morphostructure and Evolution of Submarine Canyons across an Active Margin: Cook Strait Sector of the Hikurangi Margin, New Zealand. *Mar. Geol.* 260 (1–4), 45–68. doi:10.1016/j.margeo.2009.01.006
- Mulder, T., and Alexander, J. (2001). Abrupt Change in Slope Causes Variation in the Deposit Thickness of Concentrated Particles-Driven Density Currents. *Mar. Geol.* 175 (1–4), 221–235. PII: S0025-3227(01)00114-1. doi:10.1016/S0025-3227(01)00114-1
- Mulder, T., Ducassou, E., Eberli, G. P., Hanquiez, V., Gonthier, E., Kindler, P., et al. (2012a). New Insights into the Morphology and Sedimentary Processes along the Western Slope of Great Bahama Bank. *Geology* 40 (7), 603–606. doi:10.1130/G32972.1
- Mulder, T., Ducassou, E., Gillet, H., Hanquiez, V., Tournadour, E., Combes, J., et al. (2012b). Canyon Morphology on a Modern Carbonate Slope of the Bahamas: Evidence of Regional Tectonic Tilting. *Geology* 40 (9), 771–774. doi:10.1130/G33327.1
- Mulder, T., Joumes, M., Hanquiez, V., Gillet, H., Reijmer, J. J. G., Tournadour, E., et al. (2017). Carbonate Slope Morphology Revealing Sediment Transfer from Bank-To-Slope (Little Bahama Bank, Bahamas). *Mar. Petroleum Geol.* 83, 26–34. doi:10.1016/j.marpetgeo.2017.03.002
- Mullins, H. T., Heath, K. C., Buren, H. M., and Newton, C. R. (1984). Anatomy of a Modern Open-Ocean Carbonate Slope: Northern Little Bahama Bank. *Sedimentology* 31, 141–168. doi:10.1111/j.1365-3091.1984.tb01956.x
- Mutti, E., and Normark, W. R. (1991). “An Integrated Approach to the Study of Turbidite Systems,” in *Seismic Facies and Sedimentary Processes of Submarine Fans and Turbidite Systems* (New York, NY: Springer), 75–106. doi:10.1007/978-1-4684-8276-8_4
- Nagle, F., Stipp, J. J., and Fisher, D. E. (1976). K–Ar Geochronology of the Limestone Caribbees and Martinique, Lesser Antilles, West Indies. *Earth Planet. Sci. Lett.* 29, 401–412. doi:10.1016/0012-821x(76)90145-x
- Pamela Reid, R., Carey, S. N., and Ross, D. R. (1996). Late Quaternary Sedimentation in the Lesser Antilles Island Arc. *Geol. Soc. Am. Bull.* 108 (1), 78–100. doi:10.1130/0016-7606(1996)108<0078:LQSTL>2.3.CO;2
- Paulatto, M., Laigle, M., Galve, A., Charvis, P., Sapin, M., Bayrakci, G., et al. (2017). Dehydration of Subducting Slow-Spread Oceanic Lithosphere in the Lesser Antilles. *Nat. Commun.* 8 (1), 1–11. doi:10.1038/ncomms15980
- Payros, A., and Pujalte, V. (2008). Calciclastic Submarine Fans: An Integrated Overview. *Earth Sci. Rev.* 86, 203–246. doi:10.1016/j.earscirev.2007.09.001
- Payton, C. E. (1977). Seismic Stratigraphy - Applications to Hydrocarbon Exploration. *Am. Assoc. Petroleum Geol.* 26, 1. doi:10.1306/M26490
- Peters, S. E., and Loss, D. P. (2012). Storm and Fair-Weather Wave Base: A Relevant Distinction? *Geology* 40 (6), 511–514. doi:10.1130/g32791.1
- Pichot, T., Patriat, M., Westbrook, G. K., Nalpas, T., Gutscher, M. A., Roest, W. R., et al. (2012). The Cenozoic Tectonostratigraphic Evolution of the Barracuda Ridge and Tiburon Rise, at the Western End of the North America-South America Plate Boundary Zone. *Mar. Geol.* 303–306, 154–171. doi:10.1016/j.margeo.2012.02.001
- Pindell, J. L., and Barret, S. F. (1990). “The Caribbean Region, The Geology of North America,”. *Geological Evolution of the Caribbean Region*, 339–374
- Pindell, J. L., and Kennan, L. (2009). Tectonic Evolution of the Gulf of Mexico, Caribbean and Northern South America in the Mantle Reference Frame: an Update. *Geol. Soc. Lond. Spec. Publ.* 328 (1), 1–55. doi:10.1144/sp328.1
- Polonia, A., Nelson, C. H., Romano, S., Vaiani, S. C., Colizza, E., Gasparotto, G., et al. (2017). A Depositional Model for Seismo-Turbidites in Confined Basins Based on Ionian Sea Deposits. *Mar. Geol.* 384, 177–198. doi:10.1016/j.margeo.2016.05.010
- Posamentier, H. W., Erskine, R. D., and Mitchum, R. M., Jr. (1991). “Models for Submarine-Fan Deposition within a Sequence-Stratigraphic Framework,” in *Seismic Facies and Sedimentary Processes of Submarine Fans and Turbidite Systems*. Editors P. Weimer and M. H. Link (New York: Springer), 127–136. doi:10.1007/978-1-4684-8276-8_6
- Pratson, L. F., and Coakley, B. J. (1996). A Model for the Headward Erosion of Submarine Canyons Induced by Downslope-Eroding Sediment Flows. *Geol. Soc. Am. Bull.* 108 (2), 225–234. doi:10.1130/0016-7606(1996)108<0225:amfthe>2.3.co;2
- Pratson, L. F., Ryan, W. B. F., Mountain, G. S., and Twichell, D. C. (1994). Submarine Canyon Initiation by Downslope-Eroding Sediment Flows: Evidence in Late Cenozoic Strata on the New Jersey Continental Slope. *Geol. Soc. Am. Bull.* 106 (3), 395–412. doi:10.1130/0016-7606(1994)106<0395:scibde>2.3.co;2
- Principaud, M., Mulder, T., Gillet, H., and Borgomano, J. (2015). Large-scale Carbonate Submarine Mass-Wasting along the Northwestern Slope of the Great Bahama Bank (Bahamas): Morphology, Architecture, and Mechanisms. *Sediment. Geol.* 317, 27–42. doi:10.1016/j.sedgeo.2014.10.008
- Puga-Bernabéu, Á., Webster, J. M., Beaman, R. J., and Guilbaud, V. (2011). Morphology and Controls on the Evolution of a Mixed Carbonate-Siliciclastic Submarine Canyon System, Great Barrier Reef Margin, North-Eastern Australia. *Mar. Geol.* 289 (1–4), 100–116. doi:10.1016/j.margeo.2011.09.013
- Puga-Bernabéu, Á., Webster, J. M., Beaman, R. J., Reimer, P. J., and Renema, W. (2014). Filling the Gap: A 60 Ky Record of Mixed Carbonate-Siliciclastic Turbidite Deposition from the Great Barrier Reef. *Mar. Petroleum Geol.* 50, 40–50. doi:10.1016/j.marpetgeo.2013.11.009
- Rankey, E. C., Riegl, B., and Steffen, K. (2006). Form, Function and Feedbacks in a Tidally Dominated Ooid Shoal, Bahamas. *Sedimentology* 53 (6), 1191–1210. doi:10.1111/j.1365-3091.2006.00807.x
- Ratzov, G., Cattaneo, A., Babonneau, N., Déverchère, J., Yelles, K., Bracene, R., et al. (2015). Holocene Turbidites Record Earthquake Supercycles at a Slow-Rate Plate Boundary. *Geology* 43 (4), 331–334. doi:10.1130/g36170.1
- Ratzov, G., Sosson, M., Collot, J.-Y., and Migeon, S. (2012). Late Quaternary Geomorphologic Evolution of Submarine Canyons as a Marker of Active Deformation on Convergent Margins: the Example of the South Colombian Margin. *Mar. Geol.* 315–318, 77–97. doi:10.1016/j.margeo.2012.05.005
- Reijmer, J. J. G., Palmieri, P., and Groen, R. (2012). Compositional Variations in Calciturbidites and Calcidebrites in Response to Sea-Level Fluctuations (Exuma Sound, Bahamas). *Facies* 58 (4), 493–507. doi:10.1007/s10347-011-0291-z
- Reijmer, J. J., Schlager, W., and Droxler, A. W. (1988). 15. Site 632: Pliocene-Pleistocene Sedimentation Cycles in a Bahamian Basin. *Proc. ocean Drill. program Bahamas Cover. Leg* 101, 626–636.
- Richardson, P. L. (2005). Caribbean Current and Eddies as Observed by Surface Drifters. *Deep Sea Res. Part II Top. Stud. Oceanogr.* 52 (3–4), 429–463. doi:10.1016/j.dsr2.2004.11.001
- San Pedro, L., Babonneau, N., Gutscher, M.-A., and Cattaneo, A. (2017). Origin and Chronology of the Augias Deposit in the Ionian Sea (Central Mediterranean Sea), Based on New Regional Sedimentological Data. *Mar. Geol.* 384, 199–213. doi:10.1016/j.margeo.2016.05.005
- Saunders, M. A., Klotzbach, P. J., and Lea, A. S. R. (2017). Replicating Annual North Atlantic Hurricane Activity 1878–2012 from Environmental Variables. *J. Geophys. Res. Atmos.* 122, 6284–6297. doi:10.1002/2017JD026492
- Schlager, W. (1989). “Drowning Unconformities on Carbonate Platforms,” in *Controls on Carbonate Platform and Basin Development*. Editors P. D. Crevello, J. L. Wilson, J. F. Sarg, and J. F. Read (SEPM Special Publication), Vol. 44, 15–25. doi:10.2110/pec.89.44.0015
- Schlager, W. (1998). “Exposure, Drowning and Sequence Boundaries on Carbonate Platforms,” in *Reefs and Carbonate Platforms in the Pacific and Indian Oceans*. Editors G. F. Camoin and P. J. Davies (London: International Association of Sedimentologists/Blackwell), 3–21.
- Schlager, W., Reijmer, J. J. G., and Droxler, A. (1994). Highstand Shedding of Carbonate Platforms. *Sepm Jsr* 64B (3b), 270–281. doi:10.1306/D4267FAA-2B26-11D7-8648000102C1865D
- Seibert, C., Feuillet, N., Ratzov, G., Beck, C., and Cattaneo, A. (2020). Seafloor Morphology and Sediment Transfer in the Mixed Carbonate-Siliciclastic Environment of the Lesser Antilles Forearc along Barbuda to St. Lucia. *Mar. Geol.* 428, 106242. doi:10.1016/j.margeo.2020.106242

- Shanmugam, G. (2016). Submarine Fans: A Critical Retrospective (1950–2015). *J. Palaeogeogr.* 5 (2), 110–184. doi:10.1016/j.jop.2015.08.011
- SHOM (2018). MNT bathymétrique de façade de Saint-Martin et Saint-Barthélemy (Projet Homonim). Available at: <https://geo.data.gouv.fr/fr/datasets/8302fdbac53efdc82fc83d06b24589623b8ec648>. doi:10.17183/MNT_ANTN100m_HOMONIM_WGS84
- Sola, F., Puga-Bernabéu, A., and Aguirre, J. (2017). Heterozoan Carbonate Deposition on a Steep Basement Escarpment (Late Miocene, Almería, South-East Spain). *Sedimentology* 64, 1107–1131. doi:10.1111/sed.12343
- Spence, G. H., and Tucker, M. E. (1997). Genesis of Limestone Megabreccias and Their Significance in Carbonate Sequence Stratigraphic Models: a Review. *Sediment. Geol.* 112 (3–4), 163–193. doi:10.1016/s0037-0738(97)00036-5
- Stanley, D. J. (1981). Unifites: Structureless Muds of Gravity-Flow Origin in Mediterranean Basins. *Geo-Marine Lett.* 1, 77–83.
- Stein, S., Engeln, J. F., Wiens, D. A., Fujita, K., and Speed, R. C. (1982). Subduction Seismicity and Tectonics in the Lesser Antilles Arc. *J. Geophys. Res.* 87 (B10), 8642–8664. doi:10.1029/JB087iB10p08642
- Stéphan, J. F., Mercier-de-Lepinay, B., Calais, E., Tardy, M., Beck, C., Carfantan, J. C., et al. (1990). Paleogeodynamic Maps of the Caribbean: 14 Steps from Lias to Present. *Bull. Soc. Geol. Fr.* 6 (8), 6–919.
- Stow, D. A. V., and Mayall, M. (2000). Deep-water Sedimentary Systems: New Models for the 21st Century. *Mar. Petroleum Geol.* 17 (2), 125–135. doi:10.1016/s0264-8172(99)00064-1
- Tcherepanov, E. N., Droxler, A. W., Lapointe, P., and Mohn, K. (2008). Carbonate Seismic Stratigraphy of the Gulf of Papua Mixed Depositional System: Neogene Stratigraphic Signature and Eustatic Control. *Basin Res.* 20 (2), 185–209. doi:10.1111/j.1365-2117.2008.00364.x
- Tournadour, E., Mulder, T., Borgomano, J., Gillet, H., Chabaud, L., Ducassou, E., et al. (2017). Submarine Canyon Morphologies and Evolution in Modern Carbonate Settings: The Northern Slope of Little Bahama Bank, Bahamas. *Mar. Geol.* 391, 76–97. doi:10.1016/j.margeo.2017.07.014
- Tournadour, E., Mulder, T., Borgomano, J., Hanquiez, V., Ducassou, E., and Gillet, H. (2015). Origin and Architecture of a Mass Transport Complex on the Northwest Slope of Little Bahama Bank (Bahamas): Relations between Off-Bank Transport, Bottom Current Sedimentation and Submarine Landslides. *Sediment. Geol.* 317, 9–26. doi:10.1016/j.sedgeo.2014.10.003
- Vail, P. R., Audemard, F., Bowman, S. A., Eisner, P. N., and Perez-Cruz, G. (1991). “The Stratigraphic Signatures of Tectonics, Eustasy and Sedimentation—An Overview,” in *Cyclic Stratigraphy*. Editors G. Einsele, W. Ricken, and A. Seilacher (New York: Springer), 617–659.
- Weil-Accardo, J., Feuillet, N., Philibosian, B., Guihou, A., Jacques, E., Cabioch, G., et al. (2022). Interaction between Climate and Tectonics in the Northern Lesser Antilles Inferred from the Last Interglacial Shoreline on Barbuda Island. *Geochim. Geophys. Geosystems* 23, e2021GC010045. doi:10.1029/2021GC010045
- Weimer, P., and Shipp, C. (2004). “Mass Transport Complex: Musing on Past Uses and Suggestions for Future Directions,” in Paper presented at the Offshore Technology Conference, Houston, TX, May 2004 (OnePetro). doi:10.4043/16752-ms
- Wilson, P. A., and Robert, H. H. (1995). Density Cascading: Off-Shelf Sediment Transport, Evidence and Implications, Bahama Banks. *Sepm Jsr* 65A, 45–56. doi:10.1306/D426801D-2B26-11D7-8648000102C1865D
- Yose, L. A., and Heller, P. L. (1989). Sea-level Control of Mixed-Carbonate-Siliciclastic, Gravity-Flow Deposition: Lower Part of the Keeler Canyon Formation (Pennsylvanian), Southeastern California. *Geol. Soc. Am. Bull.* 101 (3), 427–439. doi:10.1130/0016-7606(1989)101<0427:slcomc>2.3.co;2

Conflict of Interest: The authors declare that the research was conducted in the absence of any commercial or financial relationships that could be construed as a potential conflict of interest.

Publisher’s Note: All claims expressed in this article are solely those of the authors and do not necessarily represent those of their affiliated organizations, or those of the publisher, the editors, and the reviewers. Any product that may be evaluated in this article, or claim that may be made by its manufacturer, is not guaranteed or endorsed by the publisher.

Copyright © 2022 Morena, Ratzov, Cattaneo, Klingelhofer, Beck, Seibert, Marcaillou and Feuillet. This is an open-access article distributed under the terms of the Creative Commons Attribution License (CC BY). The use, distribution or reproduction in other forums is permitted, provided the original author(s) and the copyright owner(s) are credited and that the original publication in this journal is cited, in accordance with accepted academic practice. No use, distribution or reproduction is permitted which does not comply with these terms.

Advantages of publishing in Frontiers



OPEN ACCESS

Articles are free to read
for greatest visibility
and readership



FAST PUBLICATION

Around 90 days
from submission
to decision



HIGH QUALITY PEER-REVIEW

Rigorous, collaborative,
and constructive
peer-review



TRANSPARENT PEER-REVIEW

Editors and reviewers
acknowledged by name
on published articles

Frontiers

Avenue du Tribunal-Fédéral 34
1005 Lausanne | Switzerland

Visit us: www.frontiersin.org

Contact us: frontiersin.org/about/contact



REPRODUCIBILITY OF RESEARCH

Support open data
and methods to enhance
research reproducibility



DIGITAL PUBLISHING

Articles designed
for optimal readership
across devices



FOLLOW US

@frontiersin



IMPACT METRICS

Advanced article metrics
track visibility across
digital media



EXTENSIVE PROMOTION

Marketing
and promotion
of impactful research



LOOP RESEARCH NETWORK

Our network
increases your
article's readership